

# CONTENT

<b>PREFACE</b>	<b>3</b>
<b>ACKNOWLEDGEMENTS</b>	<b>4</b>
<b>Plenary Lectures</b>	<b>9</b>
I. URSU, Rezonanța magnetică, metodă de investigare a sistemelor moleculare.....	11
M. PECULEA, Discuție asupra unor soluții tehnologice pentru schimbul izotopic apă-hidrogen.....	16
KENJI TAKESHITA, MASAMI SHIMIZU, Analysis of Heavy Water Production Plant Using Bithermal and Monothermal H <sub>2</sub> /H <sub>2</sub> O-Isotopic Exchange Processes.....	24
GRAZYNA ZAKRZEWSKA-TRZNADEL, ANDRZEJ G. CHEMIELEWSKI, NADA MILJEVIĆ, ALEXANDER VAN HOOK, Separation of Hydrogen and Oxygen Isotopes by Membrane Method.....	39
ETIENNE ROTH, Solving Problems by Isotope Abundance Measurements.....	47
RAMESH R. SADHANKAR, ALISTAIR I. MILLER, New Heavy Water Production and Processing Technologies.....	55
ISTVÁN FÓRIZS, Isotopes as Natural Tracers in the Water Cycle: Examples from the Carpathian Basin.....	69
BRANDSCH J., BRANDSCH R., MERCEA P., PIRINGER O., Analysis and Modelling of Molecular Mass Transfer from Plastic Metherials into Environmental Systems.....	78
DETLEF BRINKMANN, Microscopic Dynamics in Cuprate Superconductors: NMR and NQR Studies.....	88
M.R. CAIRA, E.J.C DE VRIES, M. BOGDAN, D. BOGDAN, S.I. FARCAS, Inclusion of Alkylparabens in Cyclodextrins.....	95
<b>Oral communications</b>	<b>103</b>
<b>Isotopic separation, labelled compounds and applications</b>	
DUMITRU OHÂI, Use of Slightly Enriched Uranium (SEU) in PHWR.....	105
KAUCSÁR M., V. COSMA, D. AXENTE, A. BÁLDEA, V. BUNEA, Fuzzy Logic Control of <sup>15</sup> N Separation Plant ...	112
ANDRZEJ G. CHEMIELEWSKI, RYSZARD WIERZCHNICKI, MALGORZATA DERDA, AGNIESZKA MIKOLAJCZUK, GRAZYNA ZAKRZEWSKA-TRZNADEL, Application of Stable Isotopes in Environmental Studies and in Food Authentication.....	119
ILIE HODOR, The Theory of the Thermal-Diffusion Column: a Critical Review.....	125
JOVAN ZOTO, Results of the Application of Stable Isotopes of Light Elements in Geology and Hydrology.....	131
<b>Advanced molecular systems</b>	
R. TURCU, I. PETER, A. BOT, M.N. GRECU, O. PANA, I. CHICINAS, R. GRECU, Supramolecular Electroactive Structures Based on Conducting Polymer.....	136
D. LUPU, A.R. BIRIȘ, I. MIȘAN, G. MIHĂILESCU, L. OLENIC, S. PRUNEANU, A. JIANU, C. BUNESCU, A. WEIDENKAFF, C. DIECKER, Synthesis of Carbon Nanostructures by Induction Heating Assisted CCVD Method.....	142
SIMION ASTILEAN, Metallic Nanostructures for Controlling Light-Molecules Interactions.....	147
DANA DOROHAI, Cycloimmonium Ylid UV VIS Spectroscopy.....	153
N. ALDEA, ANDREEA GLUTHOI, B. BARZ, P. MARGINEAN, MIHAELA LAZAR, XIE YANING, HU TIANDOU, LIU TAO, ZONGHUA WU, ZIYU WU, The Complete Local and Global Structure of the Nickel Catalysts Characterized by Synchrotron Radiation.....	162
M. BOGDAN, DIANA BOGDAN, M.R. CAIRA, S.I. FĂRCAȘ, Bimodal Molecular Encapsulation of Mefenamic Acid by β-CD in Solution and Solid State.....	167
<b>Mass spectrometry, chromatography, atomic and molecular spectroscopy</b>	
ADRIAN BOT, RODICA TURCU, IZABELLA PETER, VIOREL COSMA, VASILE SURDUCAN, New Concepts and Sensing Materials for Thermal Conductivity Detectors in Gas Chromatography.....	173
DAMASCHIN IOANOVICIU, Potpourri of Ion Optics.....	179
T. ILIESCU, M. BOLBOACA, S. AȘTILEAN, D. MANIU, W. KIEFER, Surface-Enhanced Raman Spectroscopy and Theoretical Investigations of Diclofenac Sodium.....	188
CLAUDIU FILIP, Solid-State NMR Techniques for Structural Investigations of Proteins.....	197
C. COSMA, V. BENEĂ, TLD Using in Ceramics Dating.....	202
E. CULEA, I. BRATU, LIDIA POP, Magnetic and IR Spectroscopic Behaviour of some Glasses Containing Gadolinium and Neodymium Ions.....	207
<b>Biophysics and environmental physics</b>	
DAN GRECU, ANCA VISINESCU, IOAN TURCU, Ratchet Motion and Quantum Motors in Biological Systems.....	213
Z. MOLDOVAN, D.J.M. BAYONA, Characterisation of Organic Pollutants Detected in Somes River by GC/MS.....	218

D. BĂRBOS, M. MLADIN, A. DATCU, Multi-Element Determination by Neutron-Induced Prompt Gamma-Ray Analysis.....	222
MONICA CULEA, ONUC COZAR, DUMITRU RISTOIU, Biomedical Applications of Gas Chromatography-Mass Spectrometry .....	227
V.V. MORARIU, Stationary and Nonstationary Characteristics of the Atomic Vibrations in Proteins.....	234
I. TURCU, CHRISTIAN V.L.POP, SILVIA NEAMTU, Intensity Fluctuating Pattern of Light Scattered on Microparticles .....	240
E. SURDUCAN, V. SURDUCAN, C. NEAMTU, S.V. FILIP, G. NAGY, C. VILICHE, M. POSTOLACHE, Overview on Microwaves Power Applications in Molecular Physics.....	246

## **Posters** **253**

### ***Isotopic separation, labelled compounds and applications***

FLOAREA POP, CORNELIA CROITORU, MIHAI CULCER, MARIANA ILIESCU, GHEORGHE TITESCU, IOAN STEFANEASCU, MARIUS PECULEA, Analysis of Measurement Errors Influence on Experimental Determination of Mass and Heat Transfer Coefficients.....	255
GH. IONITA, IRINA POPESCU, TEODORA RETEGAN, IOAN STEFANESCU, New Improved Hydrophobic-Pt-Catalyst for Hydrogen Isotopes Separation .....	259
GHEORGHE IONITA, ASASHI KITAMOTO, DUMITRU MIRICA, CROITORU CORNELIA, IOAN STEFANESCU, RETEGAN TEODORA, New Improved Counter-Current Multi-Stage Centrifugal Extractor for Solvent Extraction Proces .....	263
MIHAELA PAVEL, DAMIAN AXENTE, The Recovery of Gold from Chloride Solutions Using the Selective Ion Exchange Resin Ionac SR3.....	266
I. COROIU, H. R. COROIU, Evaluation of the Isotopic Thermal Diffusion Factor from Morse - Morse - Spline - Van der Waals Intermolecular Potential .....	270
MIHAELA LIGIA UNGURESAN, LORENTZ JÄNTSCHI, Interactive Students Training and Evaluation Software for Radioisotopes.....	274
LORENTZ JÄNTSCHI, DELIA GLIGOR, MIHAELA LIGIA UNGURESAN, Acid-Base Titration Numerical Simulator .....	278
MIHAELA LIGIA UNGURESAN, LORENTZ JÄNTSCHI, Simulation of Kinetics Chemical Reactions.....	285
STEFANESCU IOAN, TITESCU GHEORGHE, TAMAIAAN RADU, Deuterium - Depleted Water. Effects on Living Organisms.....	289
OVIDIU BALTEANU, CARMEN MARIA RETEVOI, IULIANA STEFAN, Safety System in a Heavy Water Detritiation Plant.....	291
CARMEN MARIA RETEVOI, IULIANA STEFAN, ANISIA BORNEA, OVIDIU BALTEANU, Data Acquisition System for Optimization and Control the Processes from Isotopic Exchange Column .....	295
IULIANA STEFAN, CARMEN RETEVOI, LIVIU STEFAN, OVIDIU BALTEANU, Data Acquisition and Control System for a Heavy Water Detritiation Plant .....	299
LUCIA FEURDEAN, VICTOR FEURDEAN, MIHAI GLIGAN, Origin and Flow Dynamic of Groundwater in Movile Cave Area, Romania, Based on Environmental Isotopes .....	303

### ***Advanced molecular systems***

FERIDE SEVERCAN, DANA DOROHAI, Phospholipid Model-Membranes Studied by FTIR Spectroscopy.....	309
IOAN ZAHARIE, DANIELA ZAHARIE, On the Determination of the Crystallization Energy in Non-Isothermal Processes by Using Evolutionary Algorithms.....	317
AL. DARABONT, K. KERTÉSZ, C. NEAMTU, ZS. SÁRKÓZI, L. TAPASZTÓ, L.P. BIRÓ, Z.E. HORVÁTH, A.A. KOÓS, Z. OSVÁTH, Z. VÉRTESY, Production of Carbon Nanotubes by the catalysed Vapour Phase Pyrolysing Process.....	321
DAN CHICEA, JOHN DASH, On Surface Morphology and Composition Changes of Uranium Samples After Hydrogen Absorption.....	325
T.D. SILIPAS, V. TOSA, DANA GARGANCIUC, GH. BATRINESCU, GABRIELA ROMAN, B. ALBU, Gas Permeation Trough Polyamides and Polyimides Polymers Membranes .....	329
STELA PRUNEANU, LILIANA OLENIC, G. MIHAILESCU, D. LUPU, A.R. BIRIS, L. RADU-TUDORAN, Synthesis of Metallic and Semiconducting Nanostructures .....	332
D. RISTOIU, C. COSMA, T. RISTOIU, D. CENAN, Study of Internal Heat Transfer in Stainless Steel-Water two-Phase Thermosyphons .....	335
V. SURDUCAN, E. SURDUCAN, C. NEAMTU, Modular - Microwave Power System, Based on Microcontroller Unit.....	338
CLAUDIA VILICHE, E. SURDUCAN, V. SURDUCAN, Wine Probes Processing in Microwave Power Field for Analyses .....	342
E. SURDUCAN, V. SURDUCAN, Microwave Dielectric Resonator (DRO) Transducer for Molecular Dynamics Studies ..	345
IZABELLA PETER, RODICA TURCU, ADRIAN BOT, IONEL CHICINAS, RODICA GRECU, LIANA MURESAN, IONEL CATALIN POPESCU, Polypyrrole - Zeolites Composites for Electroanalytical Application.....	349

MIHAI CHIRTOC, ILEANA CHIRTOC, EMANOIL SURDUCAN, VASILE SURDUCAN, CAMELIA NEAMTU, CRISTIAN V.L. POP, DANE BICANIC, M. WUBBENHORTS, Complementary Methods for Monitoring Thermal Phenomena Associated with the Polymerisation Process of Epoxific Resins .....	353
M. BOLBOACA, L. BAI, I. CHICINAS, D. MANIU, T. ILIESCU, S. ASTILEAN, Optical and Structural Investigations of Ordered Metallic Nanostructures for Sers Experiments.....	357
C. MORARI, S. ASTILEAN, Theoretical Investigations of the Surface Polaritons Density of States on Silver Surfaces .....	360
C.I. MORARI, C. IONESCU, Investigations of the Penicilin - $\beta$ -Cyclode4xtrine Complex by Semiempirical Methods .....	363
ANA-MARIA KAZONI PRICOP, ELISABETH-JEANNE POPOVICI, DORU ROIBAN, TRAIAN URSALES, RODICA GRECU, EMIL INDREA, Alumina Based Composite Material for Catalytic Purposes .....	366
TRAIAN-NICOLAE URSALES, ELISABETH-JEANNE POPOVICI, IOAN SILAGHI-DUMITRESCU, NICOLAE POPOVICI, ADINA URSALES, Synthesis and Characterisation of Some New Calix[n] Arene Derivatives.....	370
SIMONA COBZAC, OLAH NELI, CARMEN BATIU, S. GOCAN, E. SURDUCAN, Microwave Assisted Solvent Extraction of some Bioactive Compounds from <i>Vaccinium Myrtillus</i> L. Leaves .....	374
MARGARETA BAKO, SIMINA DREVE, I. BRATU, E. INDREA, Uptake of Uranyl Ions by Chitosan and Cellulose Derivatives .....	378
SIMINA DREVE, E. INDREA, MARGARETA BAKO, GH. MIHAILESCU, LILIANA OLENIC, STELA PRUNEANU, V. ZNAMIROVSKY, L. BARBU TUDORAN, Template-Based Preparation of Nanostructures Polyvinylformaldehyde Thin-Film.....	381
I. COROIU, E. CULEA, AL. DARABONT, I. BRATU, GH. BORODI, Study of Some Ceramic Systems Based on Silicium Oxide .....	385
<b>Mass spectrometry, chromatography, atomic and molecular spectroscopy</b>	
D. IOANOVICIU, C. CUNA, A. PAMULA, I. ALBERT, T. NEDA, Ion Optical Solutions Involved in Forensic Mass Spectrometry .....	389
A. PAMULA, I. DOBOCAMN, N. GLIGAN, ADRIANA BENTA, Multifunctional Ion Detector for a Thermal Ionization Mass Spectrometer .....	395
STELA CUNA, GABRIELA MURESAN, ONUC COZAR, NICOLAE LUPSA, VALENTIN MIREL, Photosynthetic Fractionation of Carbon Isotopes.....	397
IOSIF CHEREJI, WOLFANGO PLATINO, STELA CUNA, NICOLAE LUPSA, GABRIELA MURESAN, VALENTIN MIREL, PETRE BERDEA, CALIN BACIU, Tritium Enrichment of Environmental Waters by Electrolysis.....	400
Z. MOLDOVAN, CORINA IONESCU, FLORINA TUSA, N. PALIBRODA, A. PAMULA, The Structural Characterisation of Fossil Resins Based on Mass Spectra Obtained in GC/MS Mode on Pyrolysed Sample .....	404
Z. MOLDOVAN, PH. BETTEN, N. PALIBRODA, ILEANA CHRTOC, Determination of Chemical Structure of Polymers by PY-GC/MS .....	408
S. NICOARA, N. PALIBRODA, Z. MOLDOVAN, M. CULEA, O. COZAR, I. FENESAN, Kinetic Energy Release in Some Thiophosphorylic p-Carboxybenzene Sulfoamides.....	411
SIMION GOCAN, SIMONA COBZAC, EDA PRODAN, VLADIMIR CIOVARNACHE, Supercritical Fluid Extraction of <i>Acorus Calamus</i> L. Analysis by Gas Chromatography - Mass Spectrometry.....	416
Z. MOLDOVAN, VIRGINIA COMAN, MIUTA FILIP, Mass Spectrometry Characterization of Some n-Octadecyl Chemically Modified Adsorbents Used as Stationary Phases in TLC .....	420
NICOLAE LUPSA, VALENTIN MIREL, STEFAN POPESCU, Vacuum System Protection and Automation Unit (VSPAU) Destined to Modernize the Izotopic Analysis Mass Spectrometer .....	424
VIRGINIA COMAN, VERONICA AVRAM, LOREDANA SORAN, RODICA GRECU, Z. MOLDOVAN, HAJNALKA FARKAS, HPLC Determination of Some Antibiotics .....	427
CORINA ANCA SIMION, M.O. Calculations of Vibrational Spectra of Some Ureides and Thioureides; Theoretical Contributions to C=S Group Localization on I.R. Spectra.....	430
GEORGETA CAZACU, CARMEN-MIHAELA POPESCU, V.I. POPA, GH. SINGUREL, CORNELIA VASILE, FT-IR Spectroscopy for Lignins Characterization .....	434
MARIA-CRISTINA POPESCU, CORNELIA VASILE, DANIELA FILIP, DOINA MACOCINSCHI, GH. SINGUREL, Spectroscopical Study of Some Systems Containing Liquid Crystalline Components .....	438
FELICIA POP-GOZMAN, I. BRATU, O. COZAR, M. BOJITA, Spectroscopic Investigation of Cu(I) Molecular Complexes of Atenolol and Metoprolol Tartate.....	442
DIANA BOGDAN, C. MORARI, M. BOGDAN, NMR Study of Homo- and Heteroassociation of Aromatic Molecules in Aqueous Solution. Numerical Simulations .....	445
DANIELA DOLHA, About the Extraordinary Refractive Index in VIS - In ADP Single - Crystals.....	450
A. BENDE, V. TOSA, <i>Ab Initio</i> Density Functional Theory Study of CF <sub>3</sub> HCl and its Isotopic Species .....	453
T. JURCA, S. CAVALU, S. CANTA PINZARU, V. SIMON, Vibrational and EPR Analysis of New Complexes of Pyrazinamide with Cu(II).....	457
NICOLAE LEOPOLD, ONUC COZAR, CONSTANTIN COSMA, BERNHARD LENDL, A New Analytical Method for Trace Detection at Femtogram Level Employing Surface-Enhanced Raman Spectroscopy .....	460
RODICA GRECU, VIRGINIA COMAN, MIUTA FILIP, Characterization by FTIR Spectroscopy of Different Alumina Samples Used in TLS .....	463

DORU ROIBAN, ELISABETH-JEANNE POPOVICI, ANA-MARIA KASZONI PRICOP, LAURA SILAGHI-DUMITRESCU, RODICA GRECU, Evaluation of Apple Quality by Reflectance Spectrometry .....	466
MARIA LADAR, ELISABETH-JEANNE POPOVICI, LIGIA PASCU, RODICA GRECU, IONEL CATALIN POPESCU, EMIL INDREA, Spectroscopic Characterisation of Cadmium Sulphide Thin Layers Deposited on ITO Coated Glass.....	469
RODICA GRECU, ELISABETH-JEANNE POPOVICI, MARIA LADAR, LAURA SILAGHI-DUMITRESCU, E. INDREA, Investigation of Optical Properties of Chemical Bath Deposited Zinc Sulphide Thin Films .....	472
L. BAIA, R. STEFAN, W. KIEFER, S. SIMON, Structural Investigations of Iron Doped Bi <sub>2</sub> O <sub>3</sub> -GeO <sub>2</sub> Glasses by Means of Micro-Raman and Infrared Spectroscopies .....	476
LAURA MURESAN, ELISABETH-JEANNE POPOVICI, AMALIA HRISTEA, EMIL INDREA, MARILENA VASILESCU, Spectral Investigation on Terbium Activated Yttrium Oxysulphide Phosphors.....	479
CEZARA VOICA, LIANA GAGEA, E. INDREA, SIMINA DREVE, I. BRATU, Microstructural Investigations of New Vitreous Material for Ceramic Industry .....	482
D. ENIU, S. SIMON, Silica-Lime-Phosphate Vitroceramics with Iron .....	486
MIHAELA TOMA, I. BRATU, A. HERNANZ, GH. BORODI, O. COZAR, GH. BORA, The Inclusion Complex of Nimodipine with $\beta$ -Cyclodextrin. FT IR Spectroscopy and X-Ray Diffraction Studies .....	490
V. SIMION, LAURA BARZA, S.G. CHIUZBAIAN, M. NEUMANN, XPS Investigation of Bismuth Gallate Glasses Containing Iron.....	494
<b><i>Biophysics and environmental physics</i></b>	
V.V. MORARIU, The Information Content of DNA and the Origin of Life .....	498
C. I. MORARI, C.M. MUNTEAN, Theoretical Simulation of the Raman Spectra of DNA Bases.....	501
S. CINTA PINZARU, N. PEICA, I. PAVEL, W. KIEFER, Food Additives Study: Vibrational Approach.....	504
NICOLAE-MARIUS BARLEA, ADINA MAN, The Importance of the Skin Galvanic Response on Certain Points.....	507
CRISTIAN V.L. POP, IOAN TURCU, CALIN VAMOS, Simulation of Fluctuating Interference Pattern for Light Scattered on Erythrocytes in Suspension .....	511
ADRIANA ISVORAN, Simulation of the Molecular Dynamics of a Polypeptide in Vacuum .....	515
G. DAMIAN, Atr FT-IR Investigations of Secondary Structure of Lyophilized Proteins in Water and Deuterated Water .....	518
MIHAELA RACUCIU, DORINA CREANGA, Low Intensity Gamma Radiation Effects in Young Plantlet Assimilatory Pigments .....	522
P. BERDEA, STELA CUNA, M. CAZACU, M. TUDOSE, Deuterium Depletion in Blood, Blood Plasma and Neoplasm Tissue from Patients. Diagnosis and Treatments Implications .....	526
C. BINDEA, GABRIELA BINDEA, ST. POPESCU, T. SIMPLACEANU, The Effect of High Magnetic Field on Li <sup>+</sup> Transport Through Human Erythrocyte Membranes .....	530
GABRIELA BINDEA, C. BINDEA, ST. POPESCU, T. SIMPLACEANU, The Effect of Low Magnetic Field on Li <sup>+</sup> Influx in Human Erythrocytes .....	533
S. CAVALU, S. CANTA-OANZARU, W. KIEFER, Advantages and Shortcomings in FT-Raman and Surface Enhanced Raman Scattering of Two Different Enzymes.....	536
ALINA RAPA, SERVILIA OANCEA, DANA DOROHAI, Hemoglobin Solutions in Ultrasonic Field .....	540
SILVIA NEAMTU, V.V. MORARIU, E. BOLDIZSAR, Metabolic Activity of Bacteria in Zero Magnetic Field. The Influence of Geomagnetic Fluctuations .....	544
ALEXANDRA FLORE, CONSTANTIN COSMA, Radon Epidemiologic Studies. Uncertainties in Assessing Health Risks from Natural Radiation .....	548
VALER TOSA, Modeling the Propagation of Femtosecond Laser Pulses in Gaseous Media.....	551
C. COSMA, CORINA RUDEI, IRINA CIOTOTARU, KINGA HENING, Radon Content in Schools from Cluj and Onești Cities .....	554
Z. MOLDOVAN, FLORINA TUSA, The Separation of Polycyclic Aromatic Hydrocarbons (Pahs) by High Resolution Gas Chromatography .....	557
IOAN I. SUCIU, CONSTANTIN C. COSMA, Determination by ICP Spectrometry of Heavy Metals Concentration in Some Concerned Areal of Romania.....	562
C. CUNA, P. ARDELEAN, STELA CUNA, The Analysis of Atmospheric Methane Concentration in the Areal of Cluj....	565
G. DAMIAN, V. MICLAUS, I. MOLDOVAN, M. PUJA, Vibrational Studies of Adsorbed Carvone on Some Surfaces....	568
ANISOARA PREDA, FELICIA VASUT, NICOLAE BIDICA, COSMIN DRAGOIU, Influence of Radioactive Isotopes Upon Environment .....	571
NICOLAE MARIUS BARLEA, SINZIANA IULIA BIRLEA, Semiconductor Gas Sensor for Detecting Air Pollution ...	574
V. A. SZABO, C. IONESCU, V. SIMION, Structural Changes in Dental Alloys Investigated by Microscopy.....	578
GEORGETA TARALUNGA, Solid State Cells for Cardiac Pacemakers.....	582
D.E. CREANGA, Electrical Field Action on Lipid Bilayer - Mathematical Model.....	586
D. E. CREANGA, Mathematical Approach on the Free Ca <sup>2+</sup> Kinetics in the Muscle Cell.....	590

## PREFACE

*The 3<sup>rd</sup> Conference “Isotopic and Molecular Processes” held in Cluj-Napoca, Romania, on September 25-27, 2003, was organized by the National Research and Development Institute of Isotopic and Molecular Technologies together with the Physics Faculty of the “Babeș-Bolyai” University under the aegis of the Ministry of Education, Research and Youth. There were more than 160 participants, including 12 foreign invited lecturers from 9 countries.*

*The scientific program of the conference included papers on original research and covered the full range of isotopic and molecular processes and their application in physics, chemistry, chemical physics and biophysics.*

*The plenary lecturers presented by invited speakers were held in the morning, followed by four parallel oral communications sessions. The papers scheduled as posters were presented in the afternoon in two sessions arranged in the Physics Faculty “Babeș-Bolyai” University. All the received materials are published in this volume, which constitutes the proceeding of the 3<sup>rd</sup> Conference on Isotopic and Molecular Processes.*

*At the opening held in the “Petru Maior” Hall of the Physics Faculty, the president (rector) of the “Babeș-Bolyai” University, Prof. Dr. Andrei Marga welcomed the participants. The conference was then opened by the Director of the National Research and Development Institute of Isotopic and Molecular Technologies, Dr. Mircea Bogdan, than Acad. Ioan Ursu, Acad. Marius Peculea and Prof. Dr. Simion Simon, the Dean of the Physics Faculty addressed the conference.*

*During the conference, a reception was held in the Glass Hall of the Institute and a Conference Dinner in the University hotel restaurant.*

*The financial support given by the Ministry of Education, Research and Youth was greatly appreciated. The help received from the president of the Cluj County Council, Ing. Șerban Grațian is gratefully acknowledged. On behalf of the Organizing Committee we wish to express to many persons who helped in the successful organization of the 3<sup>rd</sup> “Isotopic and Molecular Processes” conference our most cordial thanks for their enthusiasm and friendly cooperation. Finally, we wish to thank the chairmen, plenary lecturers and all the participants who made the Conference a stimulating and successful event.*

**M. Bogdan and V. Cosma**

*Chairman – Organizing Committee*

**A. Pamula**

*Secretary*

## **ACKNOWLEDGEMENTS**

The Conference could be organized due to the substantial support of the  
**MINISTRY OF EDUCATION, RESEARCH AND YOUTH,**  
and the **COUNTY COUNCIL** of Cluj-Napoca.

The organizers are also indebted to the following sponsors:

- “Banca Comercială Română” – Sucursala Cluj
- “Romceh Import-Export S.R.L.” Focșani
- “REDOX SRL” București
- “COCA-COLA S.A.” Cluj-Napoca
- “Regia Autonomă de Termoficare” Cluj-Napoca
- “PRODVINALCO” Cluj-Napoca
- “Mineral Quantum S.A.” Sâncrăieni, Harghita
- “URSUS S.A.” Cluj-Napoca
- “International Paper S.R.L.” Cluj-Napoca
- “COMCEREAL S.A.” Cluj-Napoca
- “ECRED Comimpex S.R.L.” Cluj-Napoca
- “Stațiunea de Cercetări Pomicole” Cluj-Napoca
- “FARMEC S.A.” Cluj-Napoca
- “Vâlcele S.A.”
- “S.C. ONCOS S.R.L.” Cluj-Napoca
- “NAPOCHIM S.A.” Cluj-Napoca

## REZONANȚA MAGNETICĂ, METODĂ DE INVESTIGARE A SISTEMELOR MOLECULARE

### I. URSU

Colective de rezonanță magnetică (RMN, RES) din INCDTIM Cluj-Napoca au desfășurat și continuă să desfășoare sub conducerea Prof. Ioan Ursu cercetări în două domenii de vîrf, și anume:

- Studiul sistemelor moleculare utilizate în energetica nucleară ( $\text{UF}_6$  și  $\text{U}(\text{OCH}_3)_6$ )
- Conductorii moleculari unidimensionali

Studiile privind sistemele moleculare utilizate în energetica nucleară au vizat aspecte distincte ale aceleiași clase de substanțe, și anume:

- A. Utilizarea Rezonanței Magnetice Nucleare ca posibilă metodă de determinare indirectă a prezenței izotopului  $^{235}\text{U}$  în  $\text{UF}_6$  aflată în fază lichidă
- B. Studiul potențialelor intermoleculare în gaze poliatomiche  $\{\text{XF}_6; \text{X} = \text{S}, \text{Mo}, \text{W}, \text{U}\}$  prin relaxometrie RMN
- C. Dinamica moleculară în  $\text{U}(\text{OCH}_3)_6$  în fază solidă investigată prin RMN

Întrucît topica acestei Conferințe o constituie procesele izotopice și moleculare, în cele ce urmează vom prezenta doar principalele rezultate obținute cu privire la "**efectul de îmbogățire**" în izotopul  $^{235}\text{U}$  a  $\text{UF}_6$ , fază lichidă, prin  $^{19}\text{F}$  RMN.

#### $\text{UF}_6$ – FAZA LICHIDĂ

Efectul de îmbogățire în  $^{235}\text{U}$  pus în evidență de către noi constă într-o dependență liniară a vitezelor de relaxare ( $R_1$  și  $R_2$ ) ale  $^{19}\text{F}$  în funcție de gradul de îmbogățire,  $I$ , în izotopul  $^{235}\text{U}$ , conform **Fig. 1** și **Fig. 2**.

După cum rezultă din analiza acestor figuri, viteza de relaxare  $R_2$  prezintă un puternic "efect de îmbogățire", valoarea sa variind cu aproximativ un ordin de mărime pentru  $0,4\% \leq I \leq 93\%$ .

Efectul de îmbogățire este mult mai mic în cazul vitezei de relaxare longitudinală,  $R_1$ .

Evoluțiile în timp ale celor două magnetizări sînt monoexponențiale și demonstrează faptul că în  $\text{UF}_6$  lichidă este prezentă o interacțiune scalară indirectă la nivel intermolecular responsabilă pentru schimbul "informației magnetice" între moleculele  $^{235}\text{UF}_6$  și  $^{238}\text{UF}_6$ .

Analiza principalelor mecanisme de relaxare a condus la concluzia că responsabile pentru evoluția magnetizării  $^{19}\text{F}$  sînt:

- interacțiunea spin - rotație ( $(R_i)_{\text{SR}}$ )
- cuplajul scalar indirect ( $(R_i)_{\text{S}}$ )

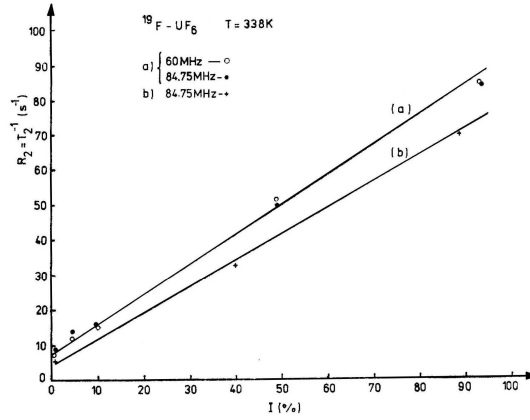


**Fig. 1.**  $^{19}\text{F}$  transverse nuclear magnetic relaxation ( $R_2$ ) versus  $^{235}\text{U}$  enrichment in liquid  $\text{UF}_6$  at  $T = 338\text{ K}$ ; (a) the BNF-samples measured at  $\nu_0 = 60\text{ MHz}$  and  $84.75\text{ MHz}$ ; (b) the samples prepared by us and measured at  $\nu_0 = 84.75\text{ MHz}$ .

Responsabilă pentru "efectul de îmbogățire" observat este interacțiunea scalară indirectă  $^{19}\text{F} - ^{235}\text{U}$ .

Această interacțiune este modulată termic de relaxarea quadropolară rapidă a  $^{235}\text{U}$ . Izotopul  $^{235}\text{U}$  avînd o valoare relativ ridicată a momentului electric de quadropol, micile distorsiuni în simetria octaedrală a moleculei  $\text{UF}_6$  reprezintă un mecanism eficient de relaxare.

Pe baza acestui model, vitezele de relaxare totale ( $R_{1,2}$ ) pentru  $^{19}\text{F}$  sînt descrise de relațiile:

$$R_1 = R_1^{(SR)} + R_1^{(S)} \cdot I$$

$$R_2 = R_2^{(SR)} + R_2^{(S)} \cdot I$$

unde:

$(R_{1,2})_{SR}$  sînt vitezele de relaxare în cazul  $I = 0$   
 $(R_{1,2})_S$  descriu relaxarea produsă de cuplajul scalar  $^{19}\text{F} - ^{235}\text{U}$   
 $I$  este gradul de îmbogățire în izotopul  $^{235}\text{U}$

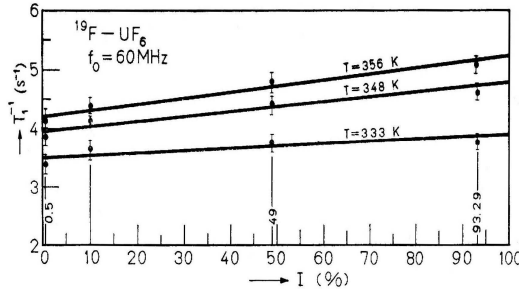


**Fig. 2.** Longitudinal relaxation rate  $T_1^{-1}$  of  $^{19}\text{F}$  in  $\text{UF}_6$  vs. the enrichment at three different temperatures.



Vitezele de relaxare corespunzătoare mecanismului scalar au forma:

$$R_{1,S} = \frac{21}{2} J_{F-U}^2 \cdot \left[ \frac{T_{1,U}}{1 + (\omega_0^F - \omega_0^U)^2 \cdot T_{1,U}^2} \right]$$

$$R_{2,S} = \frac{21}{2} J_{F-U}^2 \cdot \left[ T_{1,U} + \frac{T_{1,U}}{1 + (\omega_0^F - \omega_0^U)^2 \cdot T_{1,U}^2} \right]$$

unde:

$T_{1,U}$  este timpul de relaxare longitudinal de  $^{235}\text{U}$   
 $J_{F-U}$  este constanta de cuplaj scalar indirect  
 $\omega_0^F, \omega_0^U$  sînt frecvențele unghiulare de rezonanță ale  $^{19}\text{F}$  și  $^{235}\text{U}$

Deoarece  $\omega_0^F \gg \omega_0^U$ , iar  $(\omega_0^F - \omega_0^U) \cdot T_{1,U} > 1$ , rezultă că:

$$R_{1,S} \cong 0$$

$$R_{2,S} = \frac{21}{4} \cdot J_{F-U}^2 \cdot T_{1,U}$$

Aceste ecuații explică selectivitatea efectului de îmbogățire observat, precum și dependența lui liniară de gradul de îmbogățire, I.

Deoarece spectrele de înaltă rezoluție pe  $^{19}\text{F}$  înregistrate la  $T = 345 \text{ K}$  pentru două probe avînd  $I = 0,5 \%$  și  $88,9 \%$  nu prezintă structură de multiplet, singura diferență fiind lărgimea de linie diferită:

$$\Delta\nu_{1/2}(I = 0,5\%) = 7 \text{ Hz}$$

$$\Delta\nu_{1/2}(I = 88,9\%) = 36 \text{ Hz}$$

rezultă că în  $\text{UF}_6$  lichidă mecanismul de relaxare quadrupolară a izotopului  $^{235}\text{U}$  este foarte eficient.

Pentru evaluarea acestui mecanism și pentru a obține parametrii  $J_{F-U}$  și  $T_{1,U}$  s-a măsurat contribuția relaxării scalare la  $R_{1p}^{\text{exp}}$ .

$$R_{1p}^{\text{exp}} = R_1^{\text{dd}} + R_1^{\text{SR}} + I \cdot R_{1p}^{\text{SC}}$$

cu

$$R_{1p}^{\text{SC}} = \frac{I_{F-U}^2 \cdot S(S+1)}{3} \cdot \frac{T_{1,U}}{1 + \omega_1^2 \cdot T_{1,U}^2}$$

Contribuția interacțiunii scalare s-a obținut prin măsurători de  $T_{1p}$  în funcție de  $\omega_1$  pentru două probe de  $\text{UF}_6$  lichide cu  $I_a = 93 \%$  și  $I_b = 0,4 \%$  conform relației:

$$R_{1,p}^{\text{SC}} = \frac{(R_1^{\text{exp}})_a - (R_1^{\text{exp}})_b}{I_a - I_b}$$

După cum era de așteptat, pentru proba de UF<sub>6</sub> cu <sup>235</sup>U în abundență naturală, T<sub>1ρ</sub> este practic independent de ω<sub>1</sub> și are valoarea T<sub>1ρ</sub> = 225 ms la T = 343 K.

Pentru aceeași probă și la aceeași temperatură

$$T_1 = 236,7 \text{ ms}$$

$$T_2 = 2221,4 \text{ ms}$$

Ținând cont de faptul că eroarea de măsură în determinarea timpilor de relaxare este de ±5%, putem concluziona că în UF<sub>6</sub> lichidă cu <sup>235</sup>U în abundență naturală:

$$T_1 \approx T_2 \approx T_{1,\rho}$$

Valorile experimentale ale contribuției cuplajului scalar la T<sub>1ρ</sub> funcție de ω<sub>1</sub><sup>2</sup> sînt prezentate în Fig. 3.

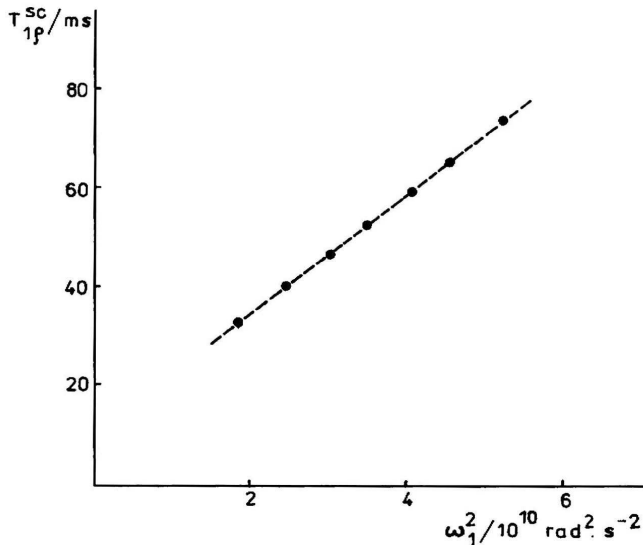


Fig. 3. The  $\omega_1^2$  dependence of  $T_{1\rho}^{SC}$  for <sup>19</sup>F in UF<sub>6</sub> at T = 343 K.

Din panta graficului și intersecția la ω<sub>1</sub> = 0, rezultă:

$$J_{F-U} = 213 \text{ Hz}$$

$$T_{1,U} = 11,8 \mu\text{s}$$

Lărgimea de linie Δv<sub>1/2</sub> calculată cu acești parametri, în cazul unei interacțiuni scalare pure, conduce la valoarea:

$$\Delta v_{1/2}^{\text{calc}} = 33 \text{ Hz}$$

în perfectă concordanță cu valoarea

$$\Delta v_{1/2}^{\text{exp}} = 36 \text{ Hz}$$

Acest rezultat demonstrează cu prisosință faptul că "efectul de îmbogățire" observat experimental se datorează unei interacțiuni scalare <sup>19</sup>F – <sup>235</sup>U modulate de către o relaxare quadropolară rapidă a izotopului <sup>235</sup>U.

În plus, s-au analizat diverse modele fizice bazate pe crearea unui gradient instantaneu de câmp electric care să justifice apariția unui mecanism de relaxare quadropolar în cazul moleculelor cu simetrie octaedrală.

Modelele investigate au fost:

- i) distorsiunea vibrațională
- ii) gradienti de câmp electric induși de momentul de hexadecapol
- iii) deformarea prin ciocnire

Valorile calculate pentru timpul de relaxare longitudinal  $T_{1,U}$  pe baza acestor modele la  $T = 343$  K sînt:

Model	$T_{1,U}$
distorsiune vibrațională	11,46 s
gradient indus	0,10 s
deformare prin ciocnire	8,92 $\mu$ s

Valoarea obținută în cazul mecanismului de generare a unui gradient de câmp electric în urma "deformării prin ciocnire" are același ordin de mărime cu cea determinată experimental,  $T_{1,U}^{\text{exp}} = 11,8 \mu$ s .

Putem deci concluziona că, în cazul  $^{235}\text{UF}_6$  lichide, doar acest mecanism este capabil să explice relaxarea quadropolară rapidă a izotopului  $^{235}\text{U}$ .

## DISCUȚIE ASUPRA UNOR SOLUȚII TEHNOLOGICE PENTRU SCHIMBUL IZOTOPIC APĂ-HIDROGEN

MARIUS PECULEA\*

**REZUMAT.** Se prezintă evoluția în timp a spațiului de schimb pentru transferul izotopic succesiv apă-vapori de apă-hidrogen, utilizând catalizatori de hidrogenare inițial hidrofilii, apoi hidrofobi, analizând, în fiecare caz în parte, profilul izotopic în direcția de curgere a fluidelor. Din analiză a rezultat practic forma ideală pentru spațiul de schimb și modelele de calcul pentru descrierea procesului, cu utilitate în studiile de cercetare (modelul cu trei fluide) și în proiectarea coloanelor de separare (modelul cu două fluide)

Lucrarea se bazează pe studiul de caz prezentat la Călimănești [1], studiu care evidențiază, în principal, contribuția cercetării românești a schimbului izotopic apă-hidrogen, cu vădită intenție de a elabora o tehnologie competitivă cu recente realizări din domeniul separării deuteriului și tritiului.

Prima tehnologie bazată pe schimbul izotopic apă-hidrogen a fost realizată industrial la Trail, Canada, și a funcționat între anii 1944-1956 [2].

Caracteristic pentru schimbul izotopic apă-hidrogen este transferul succesiv de izotop, respectiv de la apă la vaporii de apă, o distilare în prezența unui gaz inert, urmate de o reacție catalitică în fază gazoasă între vaporii de apă și hidrogen. Catalizatorul utilizat este unul de hidrogenare și, în funcție de proprietatea lui de a fi hidrofil sau hidrofob, determină geometria spațiului în care are loc transferul integral de izotop. Practic, proprietățile catalizatorului au determinat evoluția spațiului de schimb și, prin urmare, atenția cercetătorilor de la IFA-Cluj, urmată de a celor de la Uzina G-Râmnicu Vâlcea s-a polarizat asupra elaborării de catalizatori performanți.

Evoluția și comportarea izotopică a geometriei spațiului de schimb pot fi urmărite în Figurile 1 și 2.

Utilizarea catalizatorului hidrofil a impus ca temperatura de cataliză  $T_C$  să fie mai mare decât temperatura de distilare,  $T_D$ , asigurându-se astfel o supraîncălzire a vaporilor pentru a evita otrăvirea catalizatorului cu vaporii de apă. Soluția Trail (Figura 1/①) reprezenta un schimb izotopic succesiv, discret, cu circulația separată a fluidelor [2] și cu un model de calcul grafico-analitic adaptat geometriei spațiului de schimb [3].

Transformarea schimbului succesiv discret într-un schimb succesiv continuu, păstrînd circulația separată a fluidelor și catalizatorul de tip hidrofil, a fost realizată la IFA-Cluj [4] (Figura 1/②). Modelul de calcul a fost elaborat de Palibroda [5] și își păstrează și astăzi actualitatea.

Valorificarea cercetărilor s-a materializat prin construcția și experimentarea cu succes a unei instalații pilot biterm-binară [6], care a fost o premieră mondială. Instalația pilot poate fi văzută în Figura 3.

Soluția spațiului de schimb [4] a fost extinsă, cu rezultate notabile, și la schimbul amoniac-hidrogen [7].

---

\* *Romanian Academy, Bucharest*

Cu toate rezultatele încurajatoare, soluția IFA-Cluj (Figura 1/②) nu a fost industrializată. Două au fost cauzele principale:

- Sarcina redusă a coloanei de separare (debite specifice mici), ceea ce conducea la volume mari ale instalației
- Utilizarea unui catalizator hidrofil care impunea termostatări diferite ( $T_C > T_D$ ) la cataliză și distilare, complicând astfel tehnologia și, implicit, realizarea instalației.

Descoperirea catalizatorului de hidrogenare hidrofob [8] a revoluționat geometria spațiului de schimb, eliminând dezavantajele semnalate: spațiul de schimb putea fi realizat prin utilizarea umpluturilor de coloană care permiteau vehicularea de debite specifice mari și, datorită hidrofobicității catalizatorului, coloana putea fi operată izoterm ( $T_C = T_D$ ).

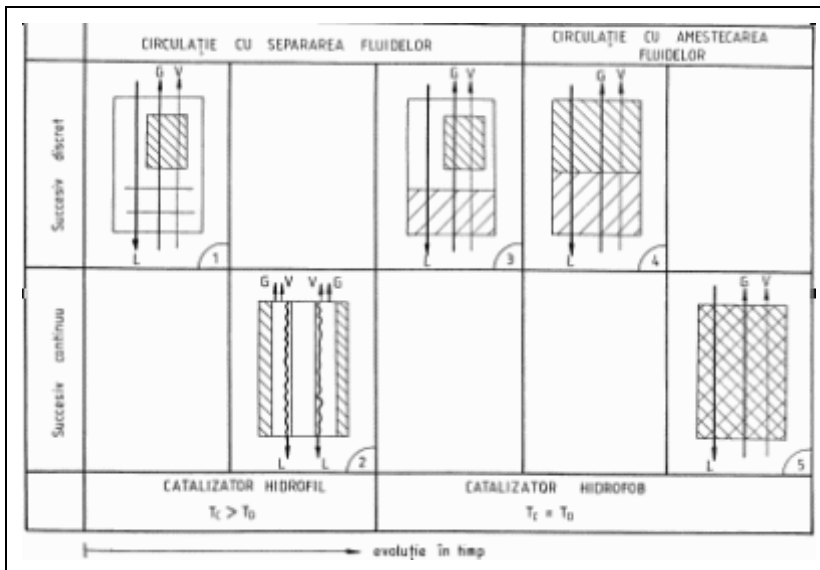


**Fig. 1.** Evoluția în timp a geometriei spațiului de schimb izotopic

Primul pas a fost realizarea la Uzina G a unui spațiu de schimb care a avut ca model Trail (Figura 1/①), însă cu două îmbunătățiri [9], conform schemei reprezentate în Figura 1/③: distilarea se realiza pe o umplutură [10] și, datorită catalizatorului hidrofob [11], procesul a devenit izoterm ( $T_C = T_D$ ). În Figura 4 este reprezentat spațiul de schimb realizat după schema din Figura 1/③.

Evoluția înspre simplificare și creștere corespunzătoare a eficienței spațiului de schimb a făcut ca circulația cu separarea fluidelor să fie înlocuită cu o circulație în care fluidele se amestecă, rezultatul fiind o umplutură mixtă [12], conform schemei reprezentate în Figura 1/④, în care straturile de umplutură pentru distilare se succed cu straturile de umplutură catalitică.

Este interesant și util de urmărit și de analizat modul în care se realizează transferul succesiv de izotop pentru cele patru tipuri de spații de schimb și evoluția profilului izotopic de-a lungul elementului de coloană. Schemele și diagramele din Figura 2 ilustrează acest lucru.

DISCUȚIE ASUPRA UNOR SOLUȚII TEHNOLOGICE PENTRU SCHIMBUL IZOTOPIC

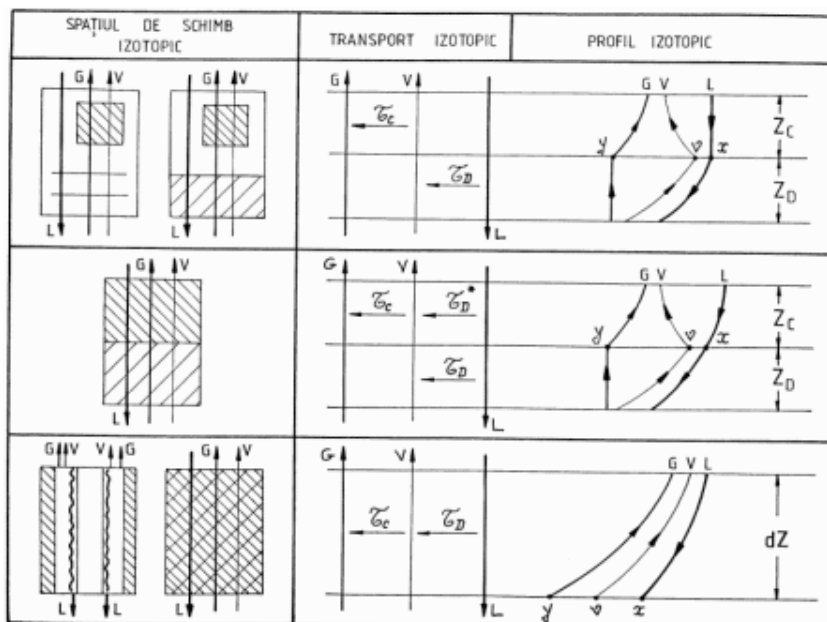


Fig. 2. Transportul succesiv de izotop și profilul izotopic în lungul spațiului de schimb

Tipurile ① și ③ prezintă un schimb succesiv discret, cu circulație separată a fluidelor. Transferul izotopic se realizează distinct pentru porțiunea de distilare și pentru porțiunea de cataliză, ceea ce permite un calcul succesiv și independent pentru cele două procese. Se constată o discontinuitate în evoluția profilelor izotopice ale celor trei faze apă-vapori de apă-hidrogen, datorită caracteristicii de curgere a fluidelor, respectiv în contracurent pentru distilare și echicurent pentru reacția catalitică, ceea ce produce o creștere de entropie în sistem, fapt nedorit.

Tipul ④ prezintă o comportare asemănătoare cu ① și ③, cu excepția faptului că și pe umplutura catalitică are loc un proces de distilare. Evoluția profilelor izotopice de-a lungul elementului de coloană este îmbunătățită prin procesul de distilare suplimentară de pe umplutura catalitică. Modelul matematic este mai complicat decât la ① și ③ și, în funcție de autori, sînt oferite soluții diferite [13].

Tipul ②, datorită schimbului succesiv continuu, prezintă o evoluție continuă a profilelor izotopice și are un model de calcul, [5], care descrie, fără echivoc, procesul de transfer izotopic pentru geometria dată.

Analiza evoluției spațiului de schimb [1] de la tipul ① la tipul ④ ne conduce la o soluție tehnologică reprezentată în Figura 1/⑤, în care separarea izotopică are loc pe o umplutură catalitică hidrofobizată, cu proprietăți de udabilitate asemănătoare cu umpluturile de distilare care întrunește următoarele calități:

- Circulația fluidelor este amestecată
- Operarea este izotermă ( $T_C = T_D$ )
- Schimbul izotopic este succesiv și continuu
- Evoluția profilului concentrațiilor izotopice este continuă

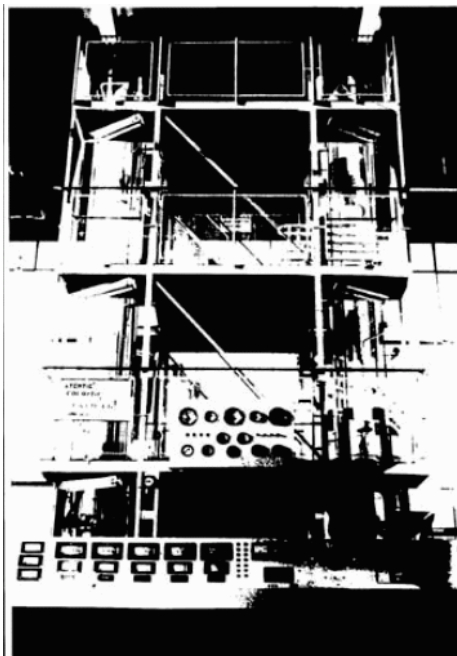


Fig. 3. Instalația pilot biterm-bibară pentru separarea deuteriului

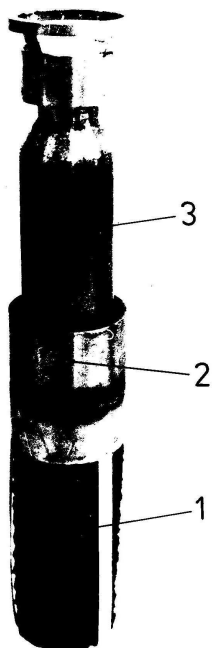


Fig. 4. Umplutura de coloană cu catalizator hidrofob, cu schimb succesiv și circulație separată a fluidelor: 1 - umplură pentru distilare; 2 - separator de faze; 3 - umplură catalitică

DISCUȚIE ASUPRA UNOR SOLUȚII TEHNOLOGICE PENTRU SCHIMBUL IZOTOPIC

- Modelul matematic [5] este ușor adaptabil noii geometrii
- Umplutura este compactă, simplă geometric și ușor de montat, practic soluția tehnologică așteptată

Modelul matematic pentru descrierea procesului de separare pe o umplutură catalitică de tipul © (Figura 1/©) poate avea două variante:

- modelul cu trei fluide [5], în care transferul de izotopi este caracterizat de către două constante de transport (de distilare, respectiv de cataliză), model care se pretează în special studiilor de laborator și analizei comparate între cele două procese succesive
- modelul cu două fluide [1], unde transferul de izotopi este caracterizat de către o constantă de transport globală, model care se pretează la proiectarea coloanei de separare pe baza eficienței umpluturii, definită de înălțimea unității de transfer.

Principiul celor două modele matematice este prezentat în Figura 5.

Studiul de caz [1] a verificat cele două modele matematice în raport cu datele obținute pe standul experimental [4], determinînd, prin calcul, valorile concentrațiilor izotopice de la partea superioară a coloanei ( $y_1, v_1, x_1$ ) față de datele de intrare de la partea inferioară, ținînd cont de parametrii de operare și de valoarea constantelor de transport determinate experimental. Rezultatele calculului comparativ cu concentrațiile măsurate sînt prezentate în Tabelul 1.

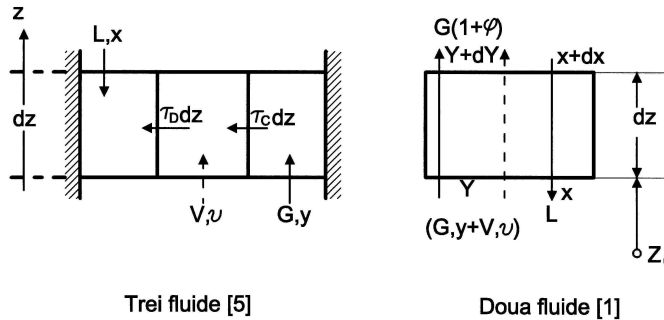


Fig. 5. Descrierea modelelor matematice pentru schimbul izotopic succesiv apă-vapori de apă-hidrogen, cu trei fluide și cu două fluide

Tabelul 1

Validarea modelelor matematice care descriu procesul de separare succesiv al schimbului izotopic apă-hidrogen

$P/T_D/L$	1,5 / 92,5 / 3,02			2,75 / 106,5 / 2,62			4,0 / 117,5 / 2,59		
Variante	$y_1$	$v_1$	$x_1$	$y_1$	$v_1$	$x_1$	$y_1$	$v_1$	$x_1$
Măsurat	1440	7500	13300	2970	13500	23100	3520	13200	21900
Relații articol	1626	7248	12884	3447	13770	22900	3701	13251	21834
a	60	138	142	62	140	144	64	142	145
$b(\alpha_c)$	2850	7011	13353	5614	13249	23902	5603	12719	22753
Relații explicite	1626	7296	12937	3343	13565	22847	3600	12735	21620
$b(\alpha_c)$	1569	7563	13948	3183	13655	20678	3757	13525	22012
$G(1+\varphi)$	1378	6642	12505	2816	12081	21798	3560	12816	21642

Valorile  $y, v, x$  se multiplică cu  $10^{-6}$



Tabelul 1 necesită câteva explicații. Regimurile experimentale [4] care au fost alese pentru comparație au fost acelea care au prezentat erori ale bilanțului izotopic sub 1 %; de asemenea, ele au fost alese pentru cele trei nivele de presiune: 1.5; 2.75 și 4 bari.  $T_D$  corespunde temperaturii de distilare a lichidului, iar  $L$  este debitul de lichid ( $\text{mol} \cdot \text{sec}^{-1} \cdot 10^{-2}$ ). Variantele comparate cu valorile experimentale au fost:

- “relații articol” au fost calculate după [5], unde, spre exemplu, concentrația izotopică a gazului are expresia:

$$y = A + B \cdot e^{-f_1 \cdot \lambda \cdot z} + C \cdot e^{-f_2 \cdot \lambda \cdot z} \quad (1)$$

- varianta “a” consideră distilarea ca avînd un echilibru instantaneu [5]

$$x = \alpha_D \cdot V \quad (2)$$

și astfel sistemul [5] se simplifică

- varianta “b( $\alpha_C$ )” consideră reacția catalitică ca avînd un echilibru instantaneu [5]

$$V = \alpha_C \cdot y \quad (3)$$

simplificînd sistemul [5]

- “relații explicite” reprezintă explicitarea relației (1) în funcție de datele de intrare [1]

$$y = y_0 + B \cdot (e^{-f_1 \cdot \lambda \cdot z} - 1) + C \cdot (e^{-f_2 \cdot \lambda \cdot z} - 1) \quad (4)$$

- varianta “b( $\alpha_C^*$ )” reprezintă varianta “b( $\alpha_C$ )” modificată, unde factorul de separare  $\alpha_C$  este corectat cu randamentul reacției catalitice  $\eta$ :

$$\alpha_C^* = \frac{\alpha_C}{\eta} = \frac{V}{y} \quad (5)$$

- varianta “G(1+ $\varphi$ )” reprezintă modelul cu două fluide [1].

Relația (5) este de importanță majoră pentru modelul cu două fluide, atît pentru determinarea factorului de echilibru între faza gazoasă (G+V) și faza lichidă (L)

$$\alpha_0 = \alpha_D \cdot \alpha_C^* \cdot \frac{1 + \varphi}{1 + \alpha_C^* \cdot \varphi} \quad (6)$$

unde  $\varphi = \frac{V}{G}$ , cît și pentru descrierea echilibrului izotopic între cele două faze, determinînd legătura dintre  $y$ ,  $v$  și  $Y$ , după cum rezultă din Figura 5.

$$y = \frac{1 + \varphi}{1 + \alpha_C^* \cdot \varphi} Y = \frac{\alpha_0}{\alpha_D \cdot \alpha_C^*} Y = \frac{V}{\alpha_C^*} \quad (7)$$

Echivalentul relației (4) pentru două fluide este:

$$Y = Y_0 + \frac{\Delta_0}{\alpha_0 - \rho} \cdot \left[ 1 - e^{-\lambda \cdot (\alpha_0 - \rho) \cdot z} \right] \quad (8)$$

cu  $\Delta_0 = x_0 + \alpha_0 Y_0$ .

Valoarea randamentului reacției catalitice,  $\eta$ , se determină experimental și, pentru cazul discutat aici, el a fost determinat pe baza datelor măsurate pe standul experimental [4].

Diferențele minore dintre valorile măsurate și cele calculate din Tabelui 1 se datoresc, în cea mai mare parte, efectului de capăt de la partea inferioară a coloanei standului experimental [1]. Diferențe majore prezintă variantele “a” și “b( $\alpha_C$ )”, care nu pot fi luate în considerare pentru descrierea corectă a procesului de separare.

DISCUȚIE ASUPRA UNOR SOLUȚII TEHNOLOGICE PENTRU SCHIMBUL IZOTOPIC

Se poate afirma că cele două modele care descriu procesul de separare al schimbului izotopic succesiv apă-hidrogen, și anume cel cu trei fluide [5] și cel cu două fluide [1], sînt echivalente și pot fi aplicate în funcție de problema urmărită și de preferințele utilizatorului.

O testare corectă a umpluturii catalitice presupune, în primul rînd, o compatibilitate perfectă între modelul matematic și instalația experimentală. Mă refer aici la instalația experimentală [4] și nu numai, și amintesc o maximă a lui Publilius Syrus, un mare actor contemporan cu Iulius Cezar: “Clipele din urmă judecă totdeauna pe cele dinainte”.

De amintit este efectul de capăt, care a avut drept urmare unele abateri de la modelul matematic considerat în testarea umpluturii și instalația experimentală. În dezvoltarea modelului matematic [5] se consideră raportul potențialelor de schimb izotopic ca fiind constant în lungul coloanei, respectiv:

$$\frac{\Delta_C}{\Delta_D} = \frac{\alpha_C y - v}{\alpha_D v - x} = const. \quad (9)$$

lucru care, prin studiul de caz [1], s-a dovedit a nu fi respectat. Acesta este motivul pentru care se propune schema unui stand experimental pentru testarea performanțelor umpluturilor de schimb izotopic, conform Figurii 6.

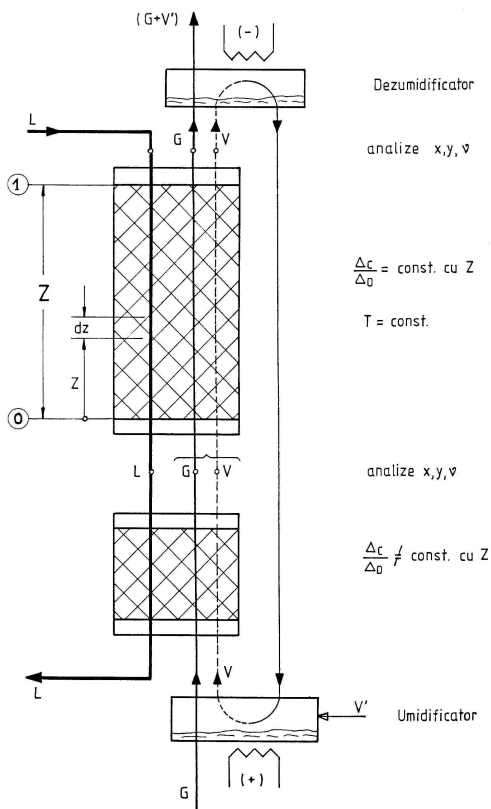


Fig. 6. Schema standului experimental pentru determinarea comportării izotopice a umpluturilor de coloană

În partea inferioară a coloanei este prevăzută o zonă în lungul căreia fluidele L / V / G se echilibrează izotopic, astfel încât de-a lungul coloanei de testare să fie îndeplinită condiția (9) prevăzută în modelul matematic. Se recomandă ca alegerea debitelor L / V / G să reprezinte un raport echimolar, presiunea de operare să fie în medie cu 10 % mai mare decât cea atmosferică și concentrația izotopică a reactanților să corespundă domeniului de sensibilitate maximă a aparatelor de analiză izotopică (a se evita extremele).

Evoluția spațiului de schimb în procesul de separare izotopică apă-hidrogen confirmă importanța care trebuie acordată soluțiilor tehnologice pentru același fenomen fizic. Este meritorie perseverența cercetării care nu a abandonat ideea de a face din procesul de separare apă-hidrogen o tehnologie competitivă atât pentru producerea apei grele, cât și pentru extragerea și îmbogățirea tritiului. Viitorul rămîne mereu deschis ideilor de valoare și nu trebuie uitat ce a spus Leonardo da Vinci “*nu ceea ce știi, ci ceea ce faci rămîne*”.

## BIBLIOGRAFIE

1. M. Peculea, *Critica schimbului izotopic apă-hidrogen, studiu de caz, Progress of Cryogenics and Isotopes Separation*, **9-10**, 3 (2002)
2. M. Peculea, *Apa grea-procese industriale de separare*, Ed. Scrisul Românesc, Craiova, 1984
3. H. R. C. Pratt, *Countercurrent Separation Processes*, Ed. Elsevier, Amsterdam-London-New York, 1967
4. I. Hodor, N. Morar, M. Peculea, L. Sâmpăleanu, “*Determinarea constantelor de transport ale schimbului izotopic complex hidrogen-vapori de apă-apă în condițiile unui stand experimental*”, Studii și Cercetări de Fizică, **21** (10)1105 (1969)
5. N. Palibroda, *Approach to the Theory of Separating Columns with Successive Exchange between three Fluids*, Zeitschrift für Naturforschung, **21a** (6), 745 (1966)
6. M. Peculea, M. Boian, *Instalație biterm-bibară pentru separarea deuteriului prin schimb izotopic între trei fluide*, Revista de Chimie, **20** (7), 429 (1969)
7. I. Hodor, M. Peculea, R. Străulea, *Continuous isotopic exchange column for hydrogen-water or hydrogen-ammonia*, Isotopenpraxis, **1** (9), 6 (1973)
8. W. H. Stevens, Canadian Patent, Nr. 907292, August 15, 1972
9. M. Peculea, *Trends in the technology of the H<sub>2</sub>O-H<sub>2</sub> isotopic exchange*, Rev. Roum. Phys., **4** (33), 4 (1988)
10. Brevete de invenție, România, **Nr. 69866** (1979) și **Nr. 115529** (1984)
11. Brevet de invenție, România, **Nr. 107842** (1991)
12. D. Ștefănescu, M. Peculea, I. Ursu, *Mixed packing for the successive isotopic exchange between water-water vapours and hydrogen*, Rev. Roum. Phys., **7-8** (36), 377 (1991)
13. C. Croitoru, M. Peculea, I. Ursu, *Model matematic pentru schimbul izotopic (H<sub>2</sub>O)<sub>L</sub>-(H<sub>2</sub>O)<sub>V</sub>-H<sub>2</sub>*, Studii și Cercetări de Fizică, **4** (37), 328 (1985)

# ANALYSIS OF HEAVY WATER PRODUCTION PLANT USING BITHERMAL AND MONOTHERMAL H<sub>2</sub>/H<sub>2</sub>O-ISOTOPIC EXCHANGE PROCESSES

KENJI TAKESHITA<sup>1</sup> and MASAMI SHIMIZU<sup>2</sup>

<sup>1</sup>*Chemical Resources Laboratory, Tokyo Institute of Technology,  
4259 Nagatsuta, Midori-ku, Yokohama 226-8503, Japan*

<sup>2</sup>*Isotope Science Laboratory, 1198 Isshiki, Kanagawa 240-0111, Japan*

**ABSTRACT.** Concerning the heavy water production plant composed of the 3 stages of multi-section separated-bed type bithermal H<sub>2</sub>/H<sub>2</sub>O-isotopic exchange columns and the same type monothermal H<sub>2</sub>/H<sub>2</sub>O-isotopic exchange ExEl-finisher was carried out numerically the analysis of the heavy water production rate influenced by the isotopic exchange efficiency in the hydrophobic Pt-catalyst bed ( $\eta_c$ ) and that in the scrubbing bed ( $\eta_b$ ) and by the water stream cut from the first stage to the second one ( $\theta_1$ ) and from the second stage to the third one ( $\theta_2$ ) and from the third stage to the ExEl-finisher ( $\theta_3$ ). The optimum operation conditions of heavy water production plant were evaluated from these calculation results and the D-concentration profile in the ExEl-finisher was calculated under these operation conditions. It was confirmed that the proposed plant with bithermal and monothermal exchange processes can be designed reasonably

## I. Introduction

At present the heavy water production plants are based mainly on the H<sub>2</sub>S/H<sub>2</sub>O-isotopic exchange process in USA, Canada, Romania, India, Argentina and China (1). From the environmental point of view, the heavy water production process was researched and developed by way of using H<sub>2</sub>/H<sub>2</sub>O-isotopic exchange process instead of using the H<sub>2</sub>S/H<sub>2</sub>O-process (2). The multi-section type H<sub>2</sub>/H<sub>2</sub>O-isotopic exchange column using the hydrophobic Pt-catalyst without the superheating section was developed by the Japan Nuclear Cycle Development Institute (JNC) and the Institute of Physical and Chemical Research (IPCR) (2).

In this paper, the authors show the basic design theory of the 3-stage bithermal H<sub>2</sub>/H<sub>2</sub>O-isotopic exchange column cascade with the monothermal ExEl-finisher and the heavy water extraction yields influenced by the isotopic exchange efficiencies in the hydrophobic Pt-catalyst bed and that in the scrubbing bed ( $\eta_c$  and  $\eta_b$ ) and those by the water stream cuts between stages ( $\theta_1$ ,  $\theta_2$  and  $\theta_3$ ) were evaluated numerically. The optimum operation conditions were determined from these calculation results. Finally, the D-concentration profile in the ExEl-finisher is calculated under the optimum operation conditions and the dimensions of proposed process were evaluated.

## II. Description of Heavy Water Production Process

The flow scheme of the proposed 3-stages bithermal H<sub>2</sub>/H<sub>2</sub>O-isotopic exchange column process combined with the monothermal ExEl-finisher was shown in **Fig. 1**. Natural water is fed to the top of the cold exchange column of the first stage and the depleted water is drawn from the bottom of the hot exchange column of the same stage. Hydrogen gas

ANALYSIS OF HEAVY WATER PRODUCTION PLANT

containing water vapor is circulated through these exchange columns and then deuterium is extracted from natural water flown counter-currently. In the second stage, the hydrogen gas and water vapor drawn from the hot exchange column of the first stage are fed to the bottom of the hot exchange column of the second stage. The hydrogen gas with water vapor flows up through the hot and cold exchange columns and then is returned to the first stage. Water flows counter-currently to the hydrogen gas as a deuterium transfer medium and is circulated between the cold and hot exchange columns. In the third stage, hydrogen gas with water vapor is drawn from the hot exchange column of the second stage and fed to the bottom of the hot exchange column of the third stage. The hydrogen gas flows up through the hot and cold exchange columns and is returned to the second stage. Water is circulated between the cold and hot exchange columns and plays a role for recovering deuterium from the hydrogen stream. The enriched water is drawn from the bottom of the cold exchange column and fed to the monothermal ExEl-finisher. At the same time, the auxiliary natural water is fed to both the top of the hot exchange column of the third stage and the top of monothermal H<sub>2</sub>/H<sub>2</sub>O-isotopic exchange column. The feed rate of natural water to the third stage is the same as the flow rate of enriched water drawn from the third stage.

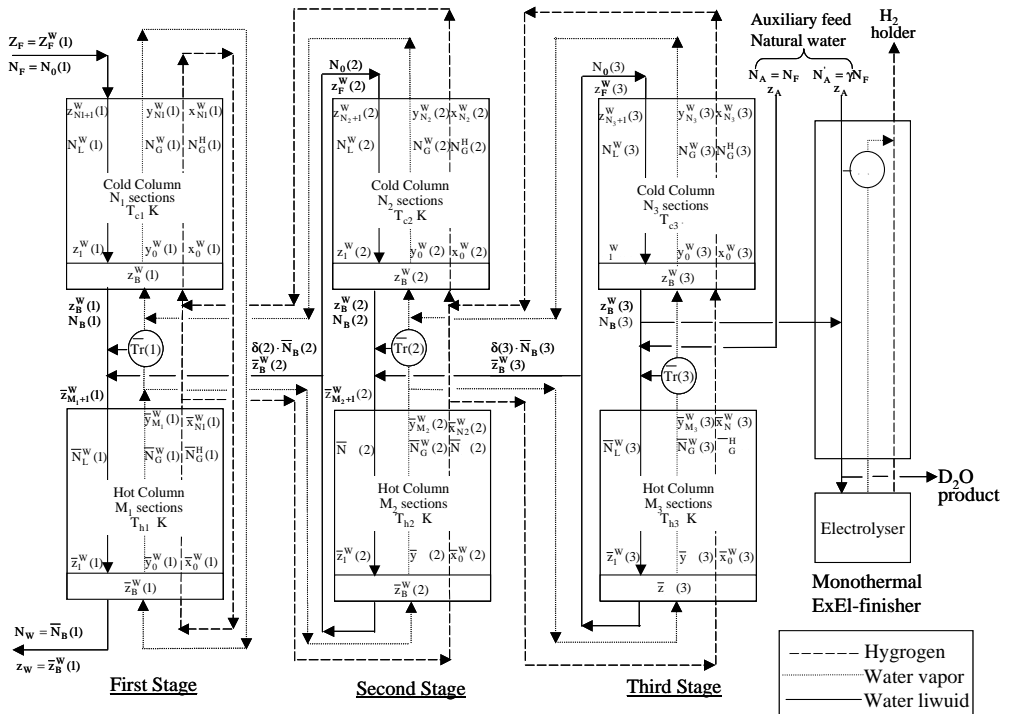
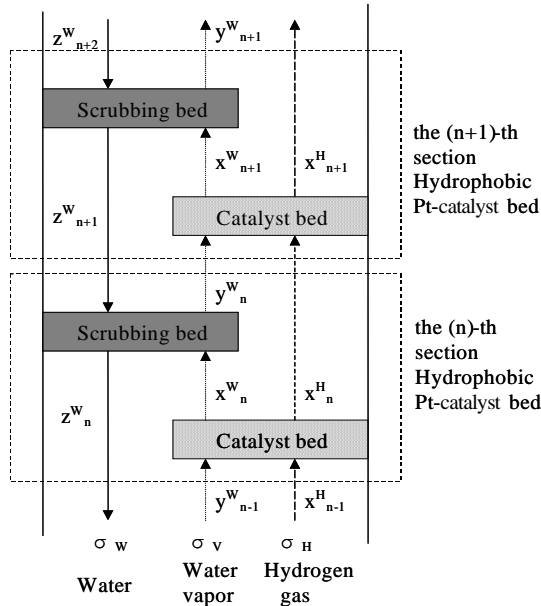


Figure 1 Flow scheme of proposed H<sub>2</sub>/H<sub>2</sub>O - isotopic exchange process

In each exchange column, there are alternatively hydrophobic Pt catalyst bed for catalytic reaction section and packed bed or perforated plates for scrubbing section, as shown in **Fig. 2**, and heat exchanger with a function of humidification at the bottom as shown in the previous paper (4). There is also a vapor/liquid separator with a function of heat exchange between the cold and hot exchange columns. The schematic description of the monothermal ExEl-finisher is shown in **Fig. 3**.

The exchange column is composed of the monothermal separated-bed column and a water electrolyser as a phase converter from liquid water to hydrogen gas. The product water of the third stage bithermal exchange column cascade is fed to the center of the separated-bed column of the ExEl-finisher. The auxiliary natural water is fed to the top of the separated-bed column. The D-enriched product is extracted from the electrolyser. The D-depleted hydrogen is drawn from the top of column and stored into the hydrogen gas holder.



**Figure 2** Schematic inner structure of separated-bed column

### III. Numerical Analysis of Heavy Water Production Plant

#### 3.1 3-stage Bithermal H<sub>2</sub>/H<sub>2</sub>O-isotopic Exchange Column Cascade

The design equations for the 3-stage cascade composed of the multisection-type bithermal exchange columns was described by the finite difference equation shown in the previous paper (3,4). Assuming that the D-mole fraction is less than 0.20, the separation factors for catalytic exchange ( $\alpha_g$ ) and phase transition of water ( $\alpha_l$ ) can be described approximately as the ratio of D-mole fraction of water vapor to that of hydrogen gas and that of liquid water to that of water vapor, respectively.

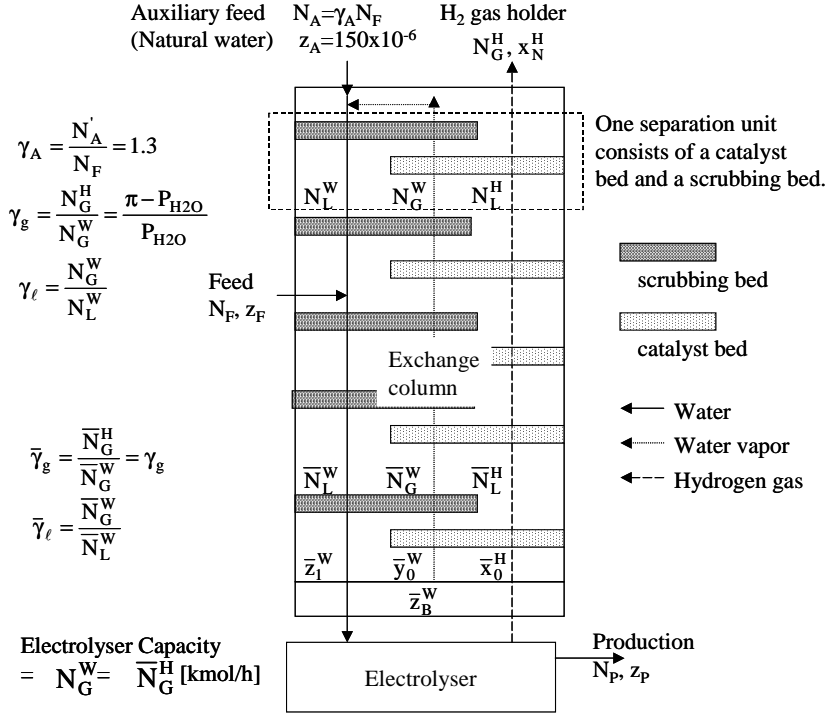


**Figure 3** Schematic diagram of monothermal Ex El -finisher with auxiliary feed.

Then, the catalytic exchange efficiency  $\eta_c$  and the scrubbing efficiency  $\eta_b$  are defined as follows:

$$\eta_c = \frac{x_{n-1}^H - x_n^H}{x_{n-1}^H - (x_n^H)_e}, \quad \eta_b = \frac{x_{n-1}^W - y_n^W}{x_n^W - (y_n^W)_e} \quad (1)$$

From the previous papers by Shimizu (4), the following expressions are written:

$$\begin{aligned} x_n^H &= A x_{n-1}^H + B y_{n-1}^W \\ x_n^W &= C x_{n-1}^H + D y_{n-1}^W \\ y_n^W &= E z_n^W + F x_n^W \\ z_{n+1}^W &= G z_n^H + h x_n^W \end{aligned} \quad (2)$$

where

$$A = \left(1 - \frac{\alpha_g \eta_c}{\alpha_g + \gamma_g}\right), \quad B = \frac{\eta_c}{\alpha_g + \gamma_g}, \quad C = \frac{\alpha_g \gamma_g \eta_c}{\alpha_g + \gamma_g}, \quad D = \left(1 - \frac{\gamma_g \eta_c}{\alpha_g + \gamma_g}\right)$$

$$E = \frac{\eta_b}{\alpha_1 - \gamma_1 \eta_b}, \quad F = (1 - \eta_b) - \frac{\gamma_1 \eta_b^2}{\alpha_1 - \gamma_1 \eta_b}, \quad G = \frac{\alpha_1}{\alpha_1 - \gamma_1 \eta_b}, \quad H = \frac{-\alpha_1 \gamma_1 \eta_b}{\alpha_1 - \gamma_1 \eta_b}$$

$$\gamma_g = \frac{N_G^H}{N_G^W} = \frac{\pi - P_{H_2O}}{P_{H_2O}}, \quad \gamma_1 = \frac{N_G^W}{N_L^W}$$

From Eq.(2), the following finite difference equation concerning xH can be derived:

$$x_{n+3}^H + p x_{n+2}^H + q x_{n+1}^H + r x_n^H = 0 \quad (3)$$

where, the coefficients of p, q and r denote as  $p = -(A + DF + G)$ ,  $q = (ADF - BDF + AG + DFG + DEH)$  and  $r = (BC - AD)(FG - EH)$ . The section becomes as follows:

$$x_n^H = K_1 g_1^n + K_2 g_2^n + K_3 g_3^n \quad (n \geq 0) \quad (4)$$

where  $K_1$ ,  $K_2$  and  $K_3$  are constants and  $g_1$ ,  $g_2$ , and  $g_3$  are real roots of the following characteristic equation:  $g^3 + pg_2 + qg + r = 0$  ( $g \neq 0$ ).

For the first stage of the 3-stages bithermal H<sub>2</sub>/H<sub>2</sub>O-exchange cascade the following expressions can be derived concerning the deuterium concentration: for the cold column,

$$x_n^H(1) = \sum_{i=1}^3 K_i(1) g_i^n(1) \quad (5)$$

$$x_n^W(1) = \sum_{i=1}^3 K_i(1) [C(1) + \frac{D(1)}{B(1)} (g_i(1) - A(1))] g_i^{n-1}(1) \quad (n \geq 1) \quad (6)$$

$$y_n^W(1) = \sum_{i=1}^3 K_i(1) \left( \frac{g_i(1) - A(1)}{B(1)} \right) g_i^n(1) \quad (7)$$

$$z_n^W(1) = \sum_{i=1}^3 K_i(1) \frac{1}{B(1)E(1)} [(g_i(1) - A(1))g_i(1) - F(1)(B(1)C(1) + D(1)(g_i(1) - A(1)))] g_i^{n-1}(1) \quad (8)$$

For the hot column, the similar deviation can be made concerning the hot column. In this case, a bar must be attached to each symbol and Eqs.(9) to (12) corresponding to Eqs(5) to (8) can be expressed as an example of the following equation (9).

$$\bar{x}_n^H(1) = \sum_{i=1}^3 \bar{K}_i(1) \bar{g}_i^n(1) \quad (9)$$

$$\bar{x}_n^W(1) = \sum_{i=1}^3 \bar{K}_i(1) [C(1) + \frac{D(1)}{B(1)} (\bar{g}_i(1) - A(1))] \bar{g}_i^{n-1}(1) \quad (n \geq 1) \quad (10)$$

$$\bar{y}_n^W(1) = \sum_{i=1}^3 \bar{K}_i(1) \left( \frac{\bar{g}_i(1) - A(1)}{B(1)} \right) \bar{g}_i^n(1) \quad (11)$$

$$\bar{z}_n^W(1) = \sum_{i=1}^3 \bar{K}_i(1) \frac{1}{B(1)E(1)} [(\bar{g}_i(1) - A(1))\bar{g}_i(1) - F(1)(B(1)C(1) + D(1)(\bar{g}_i(1) - A(1)))] \bar{g}_i^{n-1}(1) \quad (12)$$

For the second stage of bithermal H<sub>2</sub>/H<sub>2</sub>O-exchange process the similar treatments can be made. In this case, (1) of each symbol in Eqs (5) to (12) must be replaced by (2). For example,



$$x_n^H(2) = \sum_{i=1}^3 K_i(2)g_i^n(2) \quad (13)$$

For the third stage of bithermal H<sub>2</sub>/H<sub>2</sub>O-exchange process the similar treatments can be made, too. In this case, (2) of each symbol in Eq.(13) must be replaced by (3), For example,

$$x_n^H(3) = \sum_{i=1}^3 K_i(3)g_i^n(3) \quad (14)$$

The constants

$$\begin{aligned} &K_1(1), \quad K_2(1), \quad K_3(1), \quad \bar{K}_1(1), \quad \bar{K}_2(1), \quad \bar{K}_3(1); \\ &K_1(2), \quad K_2(2), \quad K_3(2), \quad \bar{K}_1(2), \quad \bar{K}_2(2), \quad \bar{K}_3(2); \\ &K_1(3), \quad K_2(3), \quad K_3(3), \quad \bar{K}_1(3), \quad \bar{K}_2(3), \quad \bar{K}_3(3); \end{aligned}$$

can be obtained from the 18 boundary conditions.

By substituting Eqs.(5) to (14) and the flow relations to the 18 boundary conditions, a matrix equation composed of 18 simultaneous simple equations was obtained. The matrix equation was solved under the operating conditions, the concentrations and flow rates for each part of the cascade were determined.

### Monothermal ExEl-finisher (refer to Figures 2 and 3)

From the mass balance for the monothermal ExEl-finisher, the following equations are derived.

$$\beta = \frac{z_p / (1 - z_p)}{z_f / (1 - z_f)} \quad (15)$$

$$\gamma_A = N_A / N_F \quad (16)$$

$$N_F + \gamma_A N_F = N_P + N_R \quad (17)$$

$$N_F z_F + \gamma_A N_F z_A = N_P z_P + N_R x_R \quad (18)$$

$$N_G^H = \bar{N}_G^H = N_R = N_F \left\{ 1 + \gamma_A - \frac{\eta_{ex}}{\beta} [(\beta - 1)z_F + 1] \right\} \quad (19)$$

where

$$\eta_{ex} = z_p N_p / z_f N_f$$

$$\gamma_g = \bar{\gamma}_g = (\pi - P_{H_2O}) / P_{H_2O} \quad (20)$$

$$N_G^W = \bar{N}_G^W = N_R / \gamma_g \quad (21)$$

$$N_L^W = \gamma_A N_F + (N_R / \gamma_g), \quad \bar{N}_L^W = (1 + \gamma_A) N_F + (N_R / \gamma_g) \quad (22)$$

$$\gamma_\ell = (N_G^W / N_L^W) = (N_R / \gamma_g) / (\gamma_A N_F + N_R / \gamma_g) \quad (23)$$

$$\bar{\gamma}_\ell = (\bar{N}_G^W / \bar{N}_L^W) = (N_R / \gamma_g) / [(1 + \gamma_A) N_F + N_R / \gamma_g] \quad (24)$$

From the definition of electrolytic separation factor ( $\alpha_{El}$ ) and the concentration factor ( $\beta$ ), the following equation is derived,

$$\bar{x}_0^H = \frac{\beta z_F}{\alpha_{EI}(1-z_F) + \beta z_F} \quad (25)$$

where  $\alpha_{EI} = \alpha_{EI}^{H/D} = 3.4$  at 303 K as shown in Appendix (1)  
 The mass balance around the electrolytic cell is given as

$$\bar{z}_B^W (\bar{N}_L^W - \bar{N}_G^W) = z_P N_P + \bar{x}_0^H \bar{N}_G^H \quad (26)$$

By substituting Eqs(19), (22) and  $z_P N_P = \eta_{ex} z_F N_F$  to Eq.(26), we get

$$\bar{z}_B^W = \frac{\eta_{ex} + \frac{\beta\{(1+\gamma_A) - (\eta_{ex}/\beta)[(\beta-1)z_F + 1]\}}{\alpha_{EI}(1-z_F) + \beta z_F}}{(1+\gamma_A)} \cdot z_F \quad (27)$$

Equilibrium relation at the bottom of exchange column is given as

$$\bar{y}_D^W = \frac{\bar{z}_B^W}{\alpha_\ell - (\alpha_\ell - 1)\bar{z}_B^W} \quad (28)$$

Mass balance at the bottom of exchange column:

$$\bar{z}_1^W = \bar{y}_\ell \bar{y}_0^W + (1 - \bar{y}_\ell) \bar{z}_B^W \quad (29)$$

In the case of D-concentration more than 10%, the following procedure of calculation must be adopted in the catalyst bed and in the scrubbing bed.

(In the catalyst bed)

$$\left. \begin{aligned} \eta_c &= \frac{x_{n-1}^H - x_n^H}{x_{n-1}^H - (x_n^H)_e} \\ \alpha_g &= \frac{(x_n^W)_e / [1 - (x_n^W)_e]}{(x_n^H)_e / [1 - (x_n^H)_e]} \\ (x_n^W - y_{n-1}^W) &= \gamma_g (x_{n-1}^H - x_n^H) \\ [(x_n^W)_e - y_{n-1}^W] &= \gamma_g [x_{n-1}^H - (x_n^H)_e] \end{aligned} \right\} \quad (30)$$

(In the scrubbing bed) ( $\alpha_l > \gamma_l$ )

$$\left. \begin{aligned} \eta_b &= \frac{x_n^W - y_n^W}{x_n^W - (y_n^W)_e} \\ \alpha_\ell &= \frac{(z_{n+1}^W)_e / [1 - (z_{n+1}^W)_e]}{(y_n^W)_e / [1 - (y_n^W)_e]} \\ (z_n^W - z_{n+1}^W) &= \gamma_\ell (x_n^W - y_n^W) \end{aligned} \right\} \quad (31)$$

(In the enriching section)

The values of  $\bar{x}_n^H$ ,  $\bar{x}_n^W$ ,  $\bar{y}_n^W$  and  $\bar{z}_n^W$  can be calculated successively from the bottom to the feed point of the column by using Eqs.(30) and (31) with the variables attached with bar.

(Around the feed point)

$$x_0^H = \bar{x}_M^H \quad (32)$$

$$y_0^W = \bar{y}_M^W \quad (33)$$

$$z_1^W = \bar{z}_{M+1}^W (\bar{N}_L^W / N_L^W) - z_F (N_F / N_L^W) \quad (34)$$

where  $(\bar{z}_{M+1}^W - z_F) \approx 0$

(In the stripping section)

The values of  $x_n^H$ ,  $x_n^W$ ,  $y_n^W$  and  $z_{n+1}^W$  can be calculated successively from the feed point to the top of the column by using Eqs.(30) and (31). The successive calculation must be finished, when  $x_n^H - x_R \leq 0$ . Then, n can be written as N, where xR is given as less than  $150 \times 10^{-6}$ .

#### IV. Results of Numerical Calculation and Discussion

In this section, the heavy water extraction yields (Y) influenced by the isotopic exchange efficiencies in the hydrophobic Pt-catalyst bed and that in the scrubbing bed ( $\eta_c$  and  $\eta_b$ ) and those by the water stream cuts between stages ( $\theta_1$ ,  $\theta_2$  and  $\theta_3$ ) are evaluated numerically. From these calculation results, the optimum operation conditions can be determined.

##### (1) Effects of $\eta_c$ and $\eta_b$ on the D-extraction yield Y

The calculation results were shown in **Fig. 4**. The Y-value was increased rapidly in the efficiency range more than 70%. Both the  $\eta_c$  and  $\eta_b$  values were reported as 0.9 in the previous paper (7). Therefore, the D-extraction yield of 15% is achieved.

##### (2) Effects of $\theta_1$ , $\theta_2$ and $\theta_3$ on the D-extraction yield Y and the concentration of the product zWP.

The calculation results were shown in **Fig. 5**. According to the increase of  $\theta_1$ ,  $\theta_2$  and  $\theta_3$ , the D-extraction yield Y increases and the D- concentration of the product zWP decreases. The higher  $\theta_1$  and  $\theta_2$  should be selected for increasing the efficiency of 3-stages cascade, however, the D-concentration of product decreases with increasing these cuts. It is reasonable to select 0.3 as  $\theta_1$  and  $\theta_2$ . Then,  $\theta_3$  should be given as 0.0025, because the higher D-concentration of product is obtained without decreasing the D-extraction yield largely.

##### (3) Effect of Tc and Th on the D-extraction yield Y

The calculation results were shown in **Fig. 6**. The optimum temperature of cold columns is given as about 363K. Then, the higher temperature of hot columns should be obtained for increasing the D-extraction yield.

##### Influences of Number of Sections in Columns on D-extraction yield Y

The calculation results were shown in **Fig.7**. The number of sections in the first stage of the cascade influences strongly on the D-extraction yield, compared with these of the second stage and the third stage. A large number of sections in the first stage are required for increasing the D-extraction yield. However, the required amount of catalyst

should be depressed from the viewpoint of economy. A number of sections in the first stage were given as 50 sections for the hot column and 150 sections for the cold column. The optimum numbers of sections in the second and third stages were shown in **Table 1**.

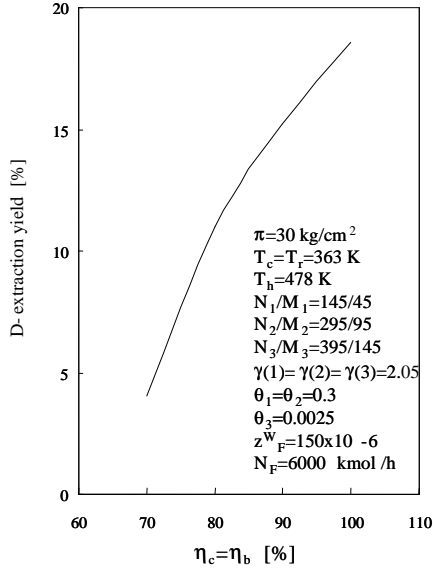


**Figure 4** The effects of  $\eta_c$  and  $\eta_b$  on  $Y$

**Table 1** Dimensions of proposed plant

	No. of sections	Size of column		No. of columns
		Diameter [m]	Height [m]	
<b>Bithermal H<sub>2</sub>/H<sub>2</sub>O exchange column cascade</b>				
<b>First stage</b>				
Cold column	150	2.1	30	2
Hot column	50	3.7	20	1
<b>Second stage</b>				
Cold column	300	1.2	30	4
Hot column	100	2.0	20	2
<b>Third stage</b>				
Cold column	450	0.7	30	6
Hot column	150	1.2	20	3
Vcat [m <sup>3</sup> ]	193			
<b>Monothermal ExEl-finisher</b>				
Column	67	0.21	26.8	1
Electrolyser Cw [W]	3.33x10 <sup>5</sup>			
V cat [m <sup>3</sup> ]	0.42			

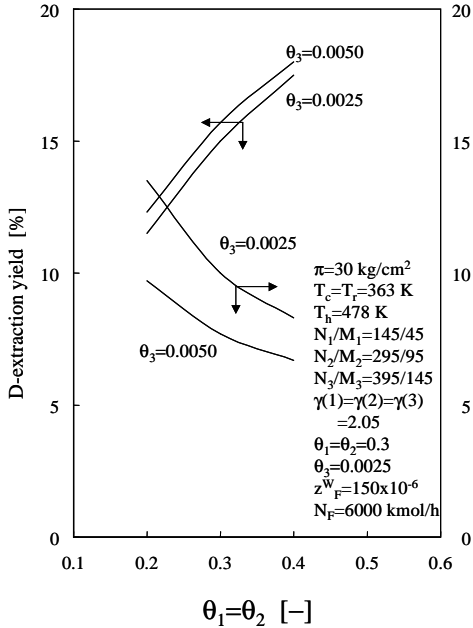


Figure 5 Effects of  $\theta_1$ ,  $\theta_2$  and  $\theta_3$  on  $Y$

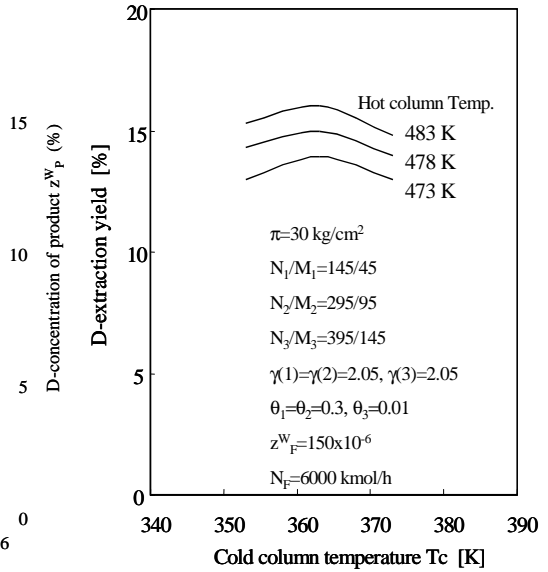


Figure 6 Effects of  $T_c$  and  $T_h$  on  $Y$

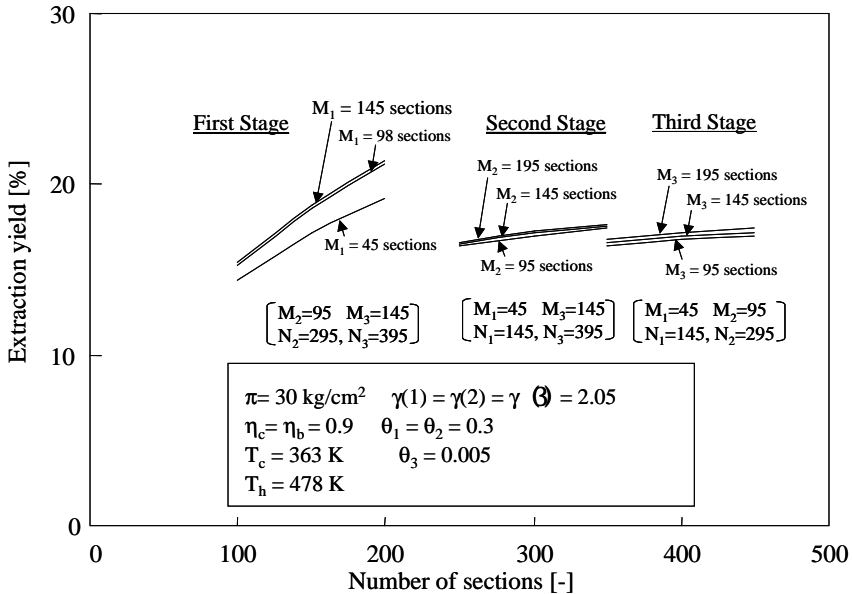


Fig.7 Influence of number of sections in column on extraction yield

**Evaluation of dimensions of 3-stages bithermal H<sub>2</sub>/H<sub>2</sub>O-exchange column cascade**

From Figs.4 to 7, the conditions required for the calculation of mass balance of 3-stage bithermal H<sub>2</sub>/H<sub>2</sub>O-exchange column cascade were assumed as follows,

$$NF=6000 \text{ kmol/h, } zF=150 \times 10^{-6}, \gamma(1)=\gamma(2)=\gamma(3)=2.05,$$

$$\pi(1) = \pi(2) = \pi(3) = \bar{\pi}(1) = \bar{\pi}(2) = \bar{\pi}(3) = 30 \text{ kg/cm}^2,$$

$$T_c=363\text{K, } T_h=478 \text{ K, } u_G(1) = u_G(2) = u_G(3) = \bar{u}_G(1) = \bar{u}_G(2) = \bar{u}_G(3) = 1 \text{ m/s opc},$$

$$\theta_1 = \theta_2 = 0.3, \theta_3 = 0.0025 \text{ and}$$

$$H_s(1) = H_s(2) = H_s(3) = \bar{H}_s(1) = \bar{H}_s(2) = \bar{H}_s(3) = 0.4 \text{ m/section}$$

By using the equations shown in Appendix (1) and (2), the dimensions of the H<sub>2</sub>/H<sub>2</sub>O-bithermal column cascade can be evaluated. The calculation results were summarized in Table 1. The D-concentration at the outlet of cascade reaches to 10% and the D-extraction yield is maintained at 15% by operating the column cascade under the conditions given above.

The D-concentration profile in the monothermal ExEl-finisher is shown in **Fig. 8**.

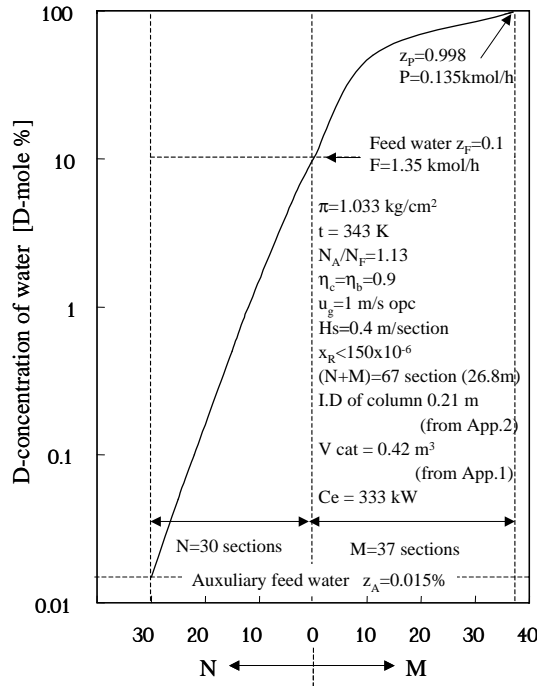


**Figure 8** Profile of D-concentration in ExEl-finisher

The concentration of deuterium in water at the bottom of column reaches to 99.8%. By introducing the proposed plant, the D<sub>2</sub>O in commercial grade can be produced at the rate of 0.135 kmol/h.

## V. Conclusion

Dimensions of heavy water production plant using the bithermal and monothermal H<sub>2</sub>/H<sub>2</sub>O-isotopic exchange process were evaluated numerically. The effects of the design and operation factors (hc, hb; Th, Tc; q1, q2, q3; N1, N2, N3 and M1, M2, M3 ) on the D-extraction yield Y were estimated quantitatively and the optimum operation conditions and column size were determined. Finally the concentration profile of deuterium in the monothermal ExEl-finisher was calculated by using the calculation results of bithermal column cascade. The concentration of deuterium in water at the bottom of column was evaluated as 99.8%. These calculation results suggest that D<sub>2</sub>O in commercial grade can be produced reasonably by introducing the proposed heavy water plant.

### Appendix (1)

From the previous papers, the equilibrium separation factors required for the calculation,  $\alpha_g^{(5)}$ ,  $\alpha_l^{(5)}$  and  $\alpha_{El}^{H/D(7,8)}$ , were given as follows,

$$\ln \alpha_g = -0.2218 + \frac{413.3}{(t+273)} + \frac{8497}{(t+273)^2} \quad (A-1)$$

$$\ln \alpha_l = 0.0588 - \frac{80.05}{(t+273)} + \frac{25440}{(t+273)^2} \quad (A-2)$$

$$\ln \alpha_{El}^{H/D} = \frac{\ln \alpha_{El}^{H/T}}{1.40} \quad (A-3)$$

$$(\alpha_{El}^{H/T} = 6.5 \text{ at } 303 \text{ K})$$

Total volume of catalyst bed, V<sub>cat</sub>, and the electrolytic power required for the decomposition of water in the electrolyser were gives as follows,

$$V_{cat} = (1/4)\pi(\text{dia})^2(\text{Hc})(\text{Number of Sections}) \quad (A-4)$$

where 'dia' denotes the inner diameter of column . The height of catalyst bed for a section, Hc, was assumed as 0.1m. The electrolytic power of electrolyser in the monothermal H<sub>2</sub>/H<sub>2</sub>O-isotopic exchange column is evaluated as

$$\text{Electrolytic power } C_w \text{ [ kW ]} = (N_F + N_A) \times 22.4 \times 5 \quad (A-5)$$

### Appendix (2)

The diameters of cold and hot columns, the height of these columns and the fluxes of hydrogen gas in these columns were calculated by the following equations, respectively.

$$\text{Dia}(i) = \left( \frac{N_G^H(i) + N_G^W(i)}{0.7854 \cdot \sigma_G(i)} \right)^{0.5}, \quad \bar{\text{Dia}}(i) = \left( \frac{\bar{N}_G^H(i) + \bar{N}_G^W(i)}{0.7854 \cdot \bar{\sigma}_G(i)} \right)^{0.5} \quad (A-6)$$

$$H(i) = N_i \cdot H_s(i), \quad \bar{H}(i) = \bar{N}_i \cdot \bar{H}_s(i) \quad (A-7)$$

$$\sigma_G(i) = u_G(i) \left( \frac{3600}{22.4} \right) \pi(i) \left( \frac{273}{T_{ci}} \right), \quad \bar{\sigma}_G(i) = \bar{u}_G(i) \left( \frac{3600}{22.4} \right) \bar{\pi}(i) \left( \frac{273}{\bar{T}_{hi}} \right) \quad (A-8)$$

where i denotes the stage number of column (i=1,2,3).

### Appendix (3)

The  $\gamma_A$  value in the monothermal ExEl-finisher was given as 1.13 in Fig.8. This value was derived according to the following procedure.

(1) The mass balance in the ExEl-finisher are given as

$$N_F(1+\gamma_A) = N_G^H + N_P \quad (\text{A-9})$$

$$N_F z_F + \gamma_A N_F z_A - N_P z_P = N_G^H x_N^H \quad (\text{A-10})$$

where  $x_N^H < x_R$  ( $x_R=150 \times 10^{-6}$ ). From these equations,

$$N_G^N \leq N_F \frac{(z_P - z_F) + (z_P - z_A) \cdot \gamma_A}{(z_P - x_R)} \quad (\text{A-11})$$

Since the mole fractions,  $z_P$ ,  $z_F$  and  $z_A$ , are given as 0.998, 0.1,  $150 \times 10^{-6}$ , respectively,

$$N_G^H = N_F(0.90 + \gamma_A) \quad (\text{A-12})$$

On the other hand, since  $\gamma_g = (N_G^H / N_G^W) = (\pi - P_{H_2O}) / P_{H_2O} = 2.25$  from the initial conditions,

$$\begin{aligned} N_L^W &= N_F \gamma_A + N_G^H / \gamma_g \\ &= N_F \gamma_A + N_F(0.90 + \gamma_A) / 2.25 \\ &= N_F(1.44\gamma_A + 0.40) \end{aligned} \quad (\text{A-13})$$

From Eqs. (A-12) and (A-13)

$$\frac{N_G^H}{N_L^W} = \frac{(0.90 + \gamma_A)}{(1.44\gamma_A + 0.40)} \quad (\text{A-14})$$

In the case of  $(N_G^H / N_L^W) = 1$ , the  $\gamma_A$  value is determined as 1.13 from Eq.(A-14).

### Nomenclature

Dia(i) : Diameter of cold column of the i-th stage (i=1,2,3)	[m]
$\bar{\text{Dia}}(i)$ : Diameter of hot column of the i-th stage (i=1,2,3)	[m]
<b>Mi</b> : Number of (catalytic+scrubbing) sections in hot column of the i-th stage (i=1,2,3)	[-]
<b>Ni</b> : Number of (catalytic+scrubbing) sections in hot column of the i-th stage (i=1,2,3)	[-]
$N_L^W(i)$ : Water flow rate in cold column of the i-th stage (i=1,2,3)	[kmol/h]
$\bar{N}_L^W(i)$ : Water flow rate in hot column of the i-th stage (i=1,2,3)	[kmol/h]
$N_G^W(i)$ : Vapor flow rate in cold column of the i-th stage (i=1,2,3)	[kmol/h]
$\bar{N}_G^W(i)$ : Vapor flow rate in hot column of the i-th stage (i=1,2,3)	[kmol/h]
$N_G^H(i)$ : Hydrogen flow rate in cold column of the i-th stage (i=1,2,3)	[kmol/h]
$\bar{N}_G^H(i)$ : Hydrogen flow rate in hot column of the i-th stage (i=1,2,3)	[kmol/h]
$N_F$ : Feed rate of water	[kmol/h]
$N_0(i)$ : Feed rate of water to cold column of the i-th stage (i=1,2,3)	[kmol/h]



ANALYSIS OF HEAVY WATER PRODUCTION PLANT

$\bar{N}_0(i)$ : Feed rate of water to hot column of the i-th stage (i=1,2,3)	[kmol/h]
$N_B(i)$ : Flow rate of water leaving cold column of the i-th stage (i=1,2,3)	[kmol/h]
$\bar{N}_B(i)$ : Flow rate of water leaving hot column of the i-th stage (i=1,2,3)	[kmol/h]
$N_W$ : Flow rate of depleted water from the bottom of the first hot column	[kmol/h]
$N_P$ : Production rate	[kmol/h]
$N_A$ : Auxiliary water feed rate	[kmol/h]
$P_{H_2O}(i)$ : Vapor pressure in cold column of the i-th stage (i=1,2,3)	[kg/cm <sup>2</sup> ]
$\bar{P}_{H_2O}(i)$ : Vapor pressure in hot column of the i-th stage (i=1,2,3)	[kg/cm <sup>2</sup> ]
$x_n^H(i)$ : D - concentration of hydrogen gas leaving the n-th section in cold column of the i-th stage	[-]
$\bar{x}_n^H(i)$ : D-concentration of hydrogen gas leaving the n-th section in hot column of the i-th stage	[-]
$x_n^W(i)$ : D-concentration of water vapor leaving the n-th section in cold column of the i-th stage	[-]
$\bar{x}_n^W(i)$ : D-concentration of water vapor leaving the n-th section in hot column of the i-th stage	[-]
$y_n^W(i)$ : D-concentration of water leaving the n-th section in cold column of the i-th stage (i=1,2,3)	[-]
$\bar{y}_n^W(i)$ : D-concentration of water leaving the n-th section in hot column of the i-th stage (i=1,2,3)	[-]
$z_F^W(i)$ : D-concentration of feed water to cold column of the i-th stage (i=1,2,3)	[-]
$\bar{z}_F^W(i)$ : D-concentration of feed water to hot column of the i-th stage (i=1,2,3)	[-]
$z_F$ : D-concentration of feed	[-]
$z_P$ : D-concentration of product	[-]
$z_A$ : D-concentration of auxiliary feed water	[-]
$Y$ : D-extraction yield [ = 100 · $\theta_3 \cdot z_B^W(3) / (N_F z_F + N_A z_A)$ ]	[%]

<Greeks>

$\alpha_g(i)$ : Separation factor for catalytic exchange reaction in cold column of the i-th stage (i=1,2,3)	[-]
$\bar{\alpha}_g(i)$ : Separation factor for catalytic exchange reaction in hot column of the i-th stage (i=1,2,3)	[-]
$\alpha_\ell(i)$ : Separation factor for scrubbing reaction in cold column of the i-th stage (i=1,2,3)	[-]
$\bar{\alpha}_\ell(i)$ : Separation factor for scrubbing reaction in hot column of the i-th stage (i=1,2,3)	[-]
$\gamma(i)$ : Flow rate ratio defined as $N_G^H(i) / N_0(i)$ at the i-th stage (i=1,2,3)	[-]

$\gamma_g(i)$ : Flow rate ratio of hydrogen to vapor in cold column of the i-th stage (i=1,2,3)	[-]
$\bar{\gamma}_g(i)$ : Flow rate ratio of hydrogen to vapor in hot column of the i-th stage (i=1,2,3)	[-]
$\gamma_\ell(i)$ : Flow rate ratio of vapor to water in cold column of the i-th stage (i=1,2,3)	[-]
$\bar{\gamma}_\ell(i)$ : Flow rate ratio of vapor to water in hot column of the i-th stage (i=1,2,3)	[-]
$\eta_c(i)$ : Catalytic efficiency in cold column of the i-th stage (i=1,2,3)	[-]
$\bar{\eta}_c(i)$ : Catalytic efficiency in hot column of the i-th stage (i=1,2,3)	[-]
$\eta_b(i)$ : Scrubbing efficiency in cold column of the i-th stage (i=1,2,3)	[-]
$\bar{\eta}_b(i)$ : Scrubbing efficiency in hot column of the i-th stage (i=1,2,3)	[-]
$\eta_{ex} := z_P N_P / z_F N_F$	[-]
$\theta_1, \theta_2$ : Cut of gas stream of the first stage and second stage	[-]
$\theta_3$ : Cut of gas stream from the third stage to ExEl-finisher	[-]

## REFERENCES

- (1) Brochure given in Drobeta Turun Severin, Romania in 2001
- (2) Shimizu, M., Kiyota, S. and Ninomiya, R.: Hydrogen Isotope Enrichment by Hydrophobic Pt-catalyst in Japan and Western Countries, Proc. of the Intern. Symposium on Isotope Separation and Chrm. Exch. Uranium Enrichment, Tokyo ,Japan, Oct.29-Nov.1, 1990, p.56-73
- (3) Ahn, D.H., Paek, S.W., Lee, H.S., Chung, H. and Shimizu, M.: Analysis of heavy water separation cascade using bithermal H<sub>2</sub>/H<sub>2</sub>O Exchange Process, Proc. of Korean Nucl. Soc. Autumn Meeting, Toejon, Korea, Oct., 1996, p.571-576.
- (4) Shimizu, M., Doi, T., Kitamoto, A. and Takashima, Y.: Numerical analysis on heavy water separation characteristics for a pair of dual temperature multistage-type H<sub>2</sub>/H<sub>2</sub>O-exchange columns, J.Nucl.Sci. and Techmol., 17(6), 446-460 (1980)
- (5) Rolston, J.H., den Hartog, J. and Butler, J.P.: The deuterium isotope separation factor between hydrogen and liquid water, AECL-5025, 1975
- (6) Jones, W.M.: Vapor pressures of tritium oxide and deuterium oxides, Interpretation of the isotope effect, USAEC Report LADC-5905
- (7) Shimizu, M., Takeshita, K.: Comparison between water distillation process and hydrogen isotope exchange process for depletion and enrichment of tritium in light water, Studia Universitatis Babes-Bolyai, Physica, Special Issue, 2001, Romania
- (8) Bigeleisen, J.: Correlation of tritium and deuterium isotope effects, Tritium in the Physical and Biological Sciences, p.161, IAEA, Vienna (STI/PUB/39) (1962)

## SEPARATION OF HYDROGEN AND OXYGEN ISOTOPES BY MEMBRANE METHOD

**GRAZYNA ZAKRZEWSKA-TRZNADEL<sup>1</sup>, ANDRZEJ G. CHMIELEWSKI<sup>1</sup>  
NADA MILJEVIĆ<sup>2</sup>, ALEXANDER VAN HOOK<sup>3</sup>**

<sup>1</sup>*Institute of Nuclear Chemistry and Technology, Dorodna 16, 03-195 Warsaw  
Poland*

<sup>2</sup>*Vinca Institute of Nuclear Sciences, P.O. Box 522, 11001 Belgrade, Yugoslavia*

<sup>3</sup>*Department of Chemistry, University of Tennessee, Knoxville, TN 37996-1600*

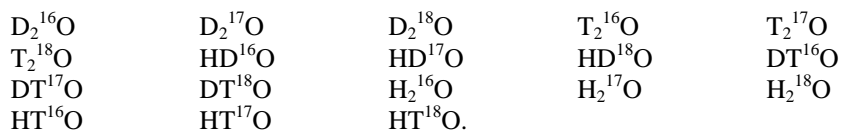
**ABSTRACT.** In this work the unit H/D and <sup>16</sup>O/<sup>18</sup>O separation factors in permeation of natural water with phase transition (membrane distillation) were determined. Isotope effect of permeation was compared with vapour pressure isotope effect (VPIE). The experimental separation factors of H/D and <sup>16</sup>O/<sup>18</sup>O in permeation through hydrophobic PTFE membrane were higher than those for distillation of water.

The cascade system for deuterium and oxygen-18 enrichment was proposed. On the basis of experimental results and separation cascade theory the parameters of such a unit (number of stages, total flow, separative power, energy consumption, etc.) were calculated and compared with parameters of counter-current distillation cascade. It was demonstrated that permeation is competitive to the other methods commonly used for production of heavy isotopes of hydrogen and oxygen.

The process was examined for separation of trace concentrations of HTO from light water. The method is considered as a possible way for separation of HTO created within the light water coolant in nuclear power plants or other nuclear centres.

### 1. Introduction

Hydrogen isotopes: H, D, T, together with the stable isotopes of oxygen can form 18 isotopomers of water:



All isotopomers are present in natural water but due to natural composition of isotopes only molecules of H<sub>2</sub><sup>16</sup>O, H<sub>2</sub><sup>18</sup>O, HD<sup>16</sup>O and H<sub>2</sub><sup>17</sup>O can be determined with sufficient level of accuracy. Determination of tritium concentration in natural water is usually preceded by previous enrichment of water samples by electrolysis.

Water enriched with its stable isotopes plays an important role in research and technology. Heavy water (HDO, D<sub>2</sub>O) is used in nuclear technology and research and its role may become more important should nuclear fusion reactors ever be used for energy production.

Water enriched in <sup>18</sup>O is used in research and medicine in trace experiments, as is water enriched in <sup>17</sup>O. In contrast to <sup>16</sup>O and <sup>18</sup>O, <sup>17</sup>O has a nuclear magnetic moment which permits easy NMR detection and makes it particularly valuable. There appears to be

significant market demand for increasing production of heavy oxygen. Large amounts of  $^{18}\text{O}$  is used by positron emission tomography and an increasing need in PET scanning is observed last time and continuous increase of  $^{18}\text{O}$  is expected in future.

The simplest method for isotope enrichment in natural water is distillation, but due to the very low values of the separation factors coupled with low concentrations in raw material, the method requires a large number of theoretical plates and inordinately long column equilibration times.

The production of heavy water by the enrichment of natural water in heavy isotopes has been known for many years. Several methods have been used among other distillation, electrolysis, isotope exchange and low-temperature distillation of hydrogen [1-6]. Chemical exchange or low-temperature hydrogen distillation technologies are economically useful, even though these technologies are extremely complicated, employ dangerous and toxic materials, and are hostile to the environment. For oxygen enrichment, however, chemical exchange rates are too slow, and in recent years, distillation of water appears to be the only method used for production.

The separation of tritium is connected with the problem of nuclear reactors operation. Tritiated water (HTO) is created in nuclear power plants, in the coolant of nuclear reactors. It is also formed during spent fuel reprocessing by neutron absorption. Low concentrations of HTO are predicted in the coolant of fusion reactors. Since tritium is a radioactive isotope, emitting mild beta radiation it is necessary to remove it from the cooling water and minimize the environmental release.

The methods of elimination of tritium include electrolysis, catalytic exchange and water distillation, but all these methods operate well with high HTO concentration. There is a need of testing the new, more economic methods, characterized by high separation factors.

The method of separation of water isotopomers proposed in the paper is a thermal evaporation through a polymer membrane (membrane distillation), described by a number of authors [7-11]. The principle of the method is an application of hydrophobic barrier between two separate phases. The hydrophobic properties of the porous membrane avoid the penetration of the liquid phase into the pores. The process is considered to be a good method for concentration of different kinds of solute, water purification and desalination. Vacuum membrane distillation is used for removal of organic admixtures from water.

## 2. Experimental

### 2.1. Apparatus

The apparatus shown in Fig. 1 consists of permeation cell 1 divided into two compartments (liquid and vapour) by the membrane, kept at fixed temperature by thermostat 2, radiator 3, sample collecting system 4, manometer 5, vacuum pump 6, compensation vessel 7, needle valve 8, drying columns 9.

The experiments were conducted with flat-sheet hydrophobic *PTFE* membrane: polish-made *Tarflen* and commercial *Millipore FGLP* filters. The isotopic analyses of water samples (deuterium, heavy oxygen) were performed by mass spectrometry (*SIRA 12 V6 Isogas mass spectrometer*, Vinca Institute of Nuclear Sciences) with relation to Vienna-SMOW standard ( $\pm 0.05$  ppm of accuracy). Tritium content in the samples was measured by use of Liquid Scintillator Spectrometer *TRI CARB (Packard)* with accuracy of  $\pm 2.5$  Bq/dm<sup>3</sup>.

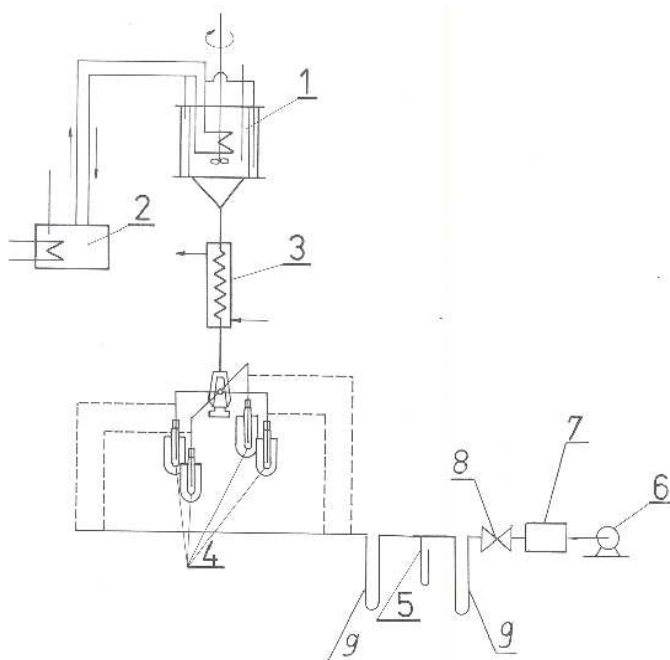


**Fig. 1.** Experimental apparatus. 1- permeation cell, 2 – thermostat, 3 – radiator, 4 – sample collecting system, 5 – manometer, 6 – vacuum pump, 7 – compensation vessel, 8 - needle valve, 9 - drying columns.

On the basis of experimental results the separation factors in permeation were determined using a formula:

$$\alpha = \frac{(x'/x)_P}{(x'/x)_R} \quad (1)$$

where:

$x'$  – concentration of light isotope and  $x$  – concentration of heavy isotope in permeate ( $P$ ) and retentate ( $R$ ).

Since the concentration of heavy isotopes in the sample is small, the formula (1) can be reduced to simple concentrations ratio:

$$\alpha = \frac{x_R}{x_P} \quad (2)$$

The  $x_R$  and  $x_P$  are the mean values from successive spectrometric measurements of the same sample with their standard deviations. The error of evaluation of separation factor was determined as:

$$\sigma_\alpha = \pm \frac{x_R}{x_P} \sqrt{\left(\frac{\sigma_R}{x_R}\right)^2 + \left(\frac{\sigma_P}{x_P}\right)^2} \quad (3)$$

where  $\sigma_R$  and  $\sigma_P$  are standard deviations of  $x_R$  and  $x_P$ .

### 2.2. Deuterium enrichment in natural water

H/D separation factors for different Tarflen membranes are shown in Figure 2. The relative volatility factors of H<sub>2</sub>O/HDO vs. temperature were added in the same graph for comparison. Since membrane distillation is the thermal evaporation through the hydrophobic polymer barrier, the process is similar to the distillation. That is the reason why it is convenient to discuss the process with a reference to distillation and vapour pressure isotope effect (VPIE), which is expressed by a logarithmic relative volatility of two components. All separation factors for membrane permeation are higher than separation factors for distillation (relative volatility factors). They decrease with temperature as does vapour pressure isotope effect. The dependence of separation factors on pressure in vapour compartment was observed. The highest separation factors for small pressures in vapour chamber were obtained, when driving force (pressure difference) was big. Experimental data show the  $\alpha$  value increases while pressure on permeate side decreases up to c.a. 40 Torr, and then the further variation of separation factor is not observed. The behaviour of separation factor can be discussed on the basis of capillary model of permeation. When the driving force ( $\Delta P$ ) in the process is small the permeate flux is also small. Since the membrane pores are the system of capillaries of different diameter, under small pressure difference narrow capillaries are closed for the flow and only big pores take part in the mass transport. Such a transport may not cause the differentiation of the components and finally the separation factor in the process is small. When the pressure difference increases the narrow capillaries are getting opened and when all of them take part in the transport the further increase of separation factor is not observed.

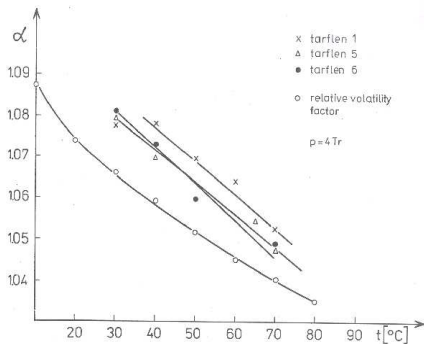


Fig. 2. H/D separation factors in membrane distillation.

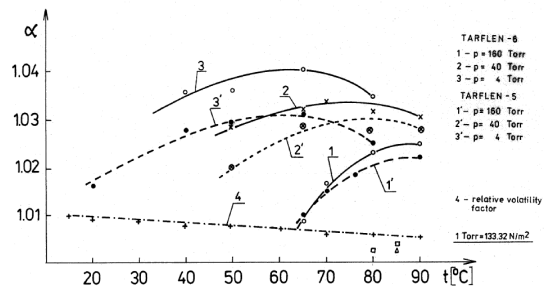


Fig. 3. <sup>16</sup>O/<sup>18</sup>O separation factors in membrane distillation

### 2.3. Heavy oxygen enrichment

<sup>18</sup>O/<sup>16</sup>O separation factors for different downstream pressures versus the temperature are shown in the Figure 3. As in previous experiments the factors are related to the relative volatility factors for H<sub>2</sub><sup>16</sup>O/H<sub>2</sub><sup>18</sup>O mixture. All separation factors for permeation are higher than those for distillation. However  $\alpha(t)$  curves for <sup>18</sup>O/<sup>16</sup>O separation run in different way than H/D curves. <sup>18</sup>O/<sup>16</sup>O separation factors increase with temperature up to the certain extreme point and then further temperature increase causes the decrease of separation factor. The pressure dependence of <sup>18</sup>O/<sup>16</sup>O separation factor shows the same tendency as H/D separation factor.

#### 2.4. Isotope effect in permeation process coupled with phase transition

Since permeation coupled with phase transition shows some similarity with distillation it is convenient to compare both processes introducing parameter  $R$ , which is the ratio of the separation effects in two discussed processes: the effect observed in membrane permeation and vapour pressure isotope effect.

$$R = \frac{\ln(\alpha_M)}{\ln(\alpha_{l/v})} = \frac{\ln\left(\frac{(x'/x)_P}{(x'/x)_R}\right)}{\ln\left(\frac{P^{o'}}{P^o}\right)} \quad (4)$$

where:

$\alpha_M$  – separation factor in membrane process,

$\alpha_{l/v}$  – separation factor in distillation,

$x'$  – concentration of light isotope in permeate ( $P$ ) or retentate ( $R$ ),

$x$  – concentration of heavy isotope in permeate ( $P$ ) or retentate ( $R$ ),

$P^{o'}$  – vapour pressure of light isotope,

$P^o$  – vapour pressure of heavy isotope.

There is a proved relation for hydrogen and oxygen isotopes:

$$\ln(\alpha_M) > \ln(\alpha_{l/v}) = \ln(P^{o'}/P^o) = \ln((x'/x)_P/(x'/x)_R) \quad (5)$$

For both hydrogen and oxygen isotopes  $R > 1$ , but there is a significant difference between  $R_{HD}$  and  $R_{16/18}$ . While  $R_{HD}$  is rather modest (~1.2-1.6), the  $R_{16/18}$  seems large (~6-7).

To explain large separation factors and their nature it was necessary to know the transport character through the membrane.

Therefore a study of the membrane structure was done:

- by Electron Scanning Microscopy (200-90000 times magnification) - the images of PTFE membranes showed fibrous structure with not precisely defined pore diameter,
- by gas-liquid porometry to determine the pore size distribution, average pore size, porosity, etc.

The description of phenomena occurring in permeation of water isotopomers through the porous PTFE membranes was performed using mass transport equations: molecular diffusion equation, Knudsen diffusion and Poiseuille flow models and combined Present and Pollard model.

Since the mass transport in membrane distillation occurs in a sequence of three steps (evaporation, transport of vapour through the membrane, condensation) the selectivity of the process will be determined by difference in partial pressures of separated substances and their transport rate through the pores of the hydrophobic barrier. We assumed that the total enrichment by permeation coupled with phase transition is a result of two effects:  $VPIE$  and the effect connected with water vapour transport through the membrane:

$$\alpha_{MD} = \alpha_{l/v} \cdot \alpha_M \quad (6)$$

where  $\alpha_M$  represents all the effects coupled with the transport of water through the membrane. The factor  $\alpha_M$  can be estimated from models of mass transport through the membrane.

### 2.5. Production of heavy water an heavy oxygen water in permeation cascade

The cascade system for deuterium and oxygen-18 enrichment was proposed. Double counter-current cascade, re-utilising part of the heat of condensation seemed to be the best solution for such a process. Two cascades work at different pressures and temperatures; product from cascade I forms the feed for cascade II, condensed waste liquid from cascade I is used to supply process heat to cascade II. The only use of external thermal energy is to heat feed for cascade I.

On the basis of experimental results and separation cascade theory the parameters of such a unit (number of stages, total flow, separative power, energy consumption, etc.) were calculated and compared with parameters of counter-current distillation cascade. The results are presented in Tables 1 and 2. For both isotopes enrichment the permeation looks more advantageous than distillation. The process is characterised by less number of stages, less total flow and energy consumption than simple distillation.

**Table 1.**

**Comparison of parameters of double permeation cascade with parameters of counter-current distillation cascade - deuterium enrichment.**

	Permeation	Distillation
The mass of the feed per 1 kg of the product [ $10^3$ kg]	9 - 19	200 - 250
Material efficiency [%]	33 - 70	2,5-3,0
Number of stages	360 - 600	1100-1200
Total flow per 1 kg of the product [ $10^6$ kg]	8 - 27	77
Separative power per $10^3$ kg of the feed [kg]	475-1200	25-35
Energy consumption per 1 kg of the product [GJ]	3-10	70 -100

**Table 2.**

**Comparison of parameters of double permeation cascade with parameters of counter-current distillation cascade - heavy oxygen enrichment.**

	Permeation	Distillation
The mass of the feed per 1 kg of the product [ $10^3$ kg]	5-100	12-20
Material efficiency [%]	0,5-1,5	2,5-4
Number of stages	700-2000	6100-6200
Total flow per 1 kg of the product [ $10^6$ kg]	3-30	250
Separative power per $10^3$ kg of the feed [kg]	5-110	25-40
Energy consumption per 1 kg of the product [GJ]	1-12	4-8

### 2.6. Removal of tritiated water

MD was proposed for the separation of small concentration of tritiated water from the light water. The process was arranged in the same way as previous tests with heavy water. The batch-type apparatus (Fig. 1) was used in experiments. The experiments were run in the temperature range  $20-80\pm 0,5$  °C, and downstream pressure  $2-260\pm 2$  Torr. The feed solution was a distilled water enriched in tritiated water to the concentration  $148$  Bq/dm<sup>3</sup>.

The experimental data for PTFE-Millipore membrane shown the separation factors  $\alpha_{\text{H}_2\text{O}/\text{HTO}}$  were in most cases higher than vapour pressure ratio ( $\alpha_{\text{H}_2\text{O}} = P^{\circ}/P^{\circ}$ ). Table 3 shows the parameters  $R$  defined by equation (4) and calculated for the experimental conditions. Since the  $R$  values are mostly higher than 1, permeation seems more efficient than gas-liquid equilibrium process.



**Table 3.**
**Tritium enrichment in membrane process (PTFE Millipore membrane)**

P [mmHg]	T [degC]	P/P <sup>0</sup>	R
0	28	0,0000	1,2399
0	30	0,0000	2,2376
0	33,5	0,0000	1,7015
0	50	0,0000	0,8469
0	50	0,0000	1,1541
0	75	0,0000	1,6290
2	17	0,1394	0,9323
2	21	0,1089	1,1508
2	50	0,0216	1,0171
3	20	0,1737	1,1832
4	40	0,0729	0,9421
6	50	0,0648	0,7520
7	17,5	0,4729	0,8940
7	18	0,4584	1,0039

P [mmHg]	T [degC]	P/P <sup>0</sup>	R
7	25	0,2995	1,4582
7	66	0,0352	1,7583
8	56	0,0642	2,3012
8	74	0,0284	0,4665
8	75	0,0273	1,1660
9	65	0,0474	1,3476
9	76	0,0294	2,4721
11	40	0,2005	1,0406
11	64	0,0606	1,3777
34	40	0,6198	1,8314
53	75	0,1807	1,5897
54	80	0,1502	0,8103
84	82	0,2159	1,4581

### 3. Conclusions

The experiments show the membrane process is characterised by higher H/D/H/T and  $^{16}\text{O}/^{18}\text{O}$  separation factors than distillation of water. Since distillation is the only method for heavy oxygen production the process has particular importance for  $^{18}\text{O}$  separation. In some cases it can be applied for production of heavy water and for removal of trace HTO concentrations from reactor waters. Preliminary engineering calculations based on the cascade theory showed many advantages of membrane permeation. Employing the system of two counter-current cascades combined in series results in savings in stage number, reflux ratio, and energy demand. The technical and economic evaluation of permeation as compared to other enrichment methods showed the competitiveness of the membrane process.

The method can be applied for a separation of isotopes of hydrogen and oxygen in natural water. It can be employed for a removal of small concentrations of tritiated water from the light water coolant in nuclear power plants and fusion reactors. The method can be used separately or in combination with other separation processes.

### REFERENCES

1. Rae H. K., *Separation of Hydrogen Isotopes*, ACS Symposium Series, Washington (1978).
2. Chemla M., Perie J., *La separation les isotopes*, Presses Universitaires de France, (1974).
3. Murphy G. M., Urey H. C., Kirschenbaum I., *Production of Heavy Water*, Mc Graw-Hill Book Co., Inc., New York, (1955).

## SEPARATION OF HYDROGEN AND OXYGEN ISOTOPES BY MEMBRANE METHOD

4. Hammerli M., Stevens W. H., Butler J. P., *Separation of Hydrogen Isotopes*, p. 110, American Chemical Society, Washington, 1978.
5. Rolston J. H., Stevens W. H., Den Hartog J., Butler J. P., Can. Pat. Appl. No 199, 402, (1971).
6. Nitschke E., Ilguer H., Walter S., *Separation of Hydrogen Isotopes*, p 77, American Chemical Society, Washington, (1978).
7. Gostoli C., Sarti G. C., *Separation of Liquid Mixtures by Membrane Distillation*, J. Membrane Sci., 41, 211, (1989).
8. Schofield R. W. Fane A. G. Fell C. J. D., *Heat and Mass Transfer in Membrane distillation* J. Membrane Sci., 33, 299, (1987).
9. Schofield R. W. Fane A. G. Fell C. J. D., Macoun R., *Factors Affecting Flux in Membrane Distillation*, Desalination 77, 279, (1990).
10. Hogan P. A., Sudjito, Fane A. G., Morrison G. L., *Desalination by Solar Heated Membrane Distillation*, Desalination, 81, 81, (1991).
11. G. Zakrzewska-Trznadel, M. Harasimowicz, A. G. Chmielewski, *Concentration of radioactive components in liquid low-level radioactive waste by membrane distillation*, J. Membrane Science, 163 (1999) 257-264.
12. Hwang Sun-Tak, Kammermaeyer K., *Membranes in Separations*, Techniques of Chemistry, Vol. VII, John Wiley and Sons, Inc., New York-London-Sydney-Toronto (1975).

## SOLVING PROBLEMS BY ISOTOPE ABUNDANCE MEASUREMENTS

ETIENNE ROTH

*103 rue BRANCAS, F- 92310, Sèvres France  
e-mail: etienneroeth@compuserve.com*

**ABSTRACT.** A variety of problems studied at Saclay with the use of deuterium, and isotopes of sulphur and rare earth, are explained in their historical context. They illustrate how techniques developed to solve applied problems were used to foster cognitive research; and conversely how analytical systems, set up for pure research purposes, provided data enabling to build plants that detritiate tons of heavy water. The role of instrumentation in authorising the discovery of disulphur monoxide, or to facilitate medical applications is underscored. In conclusion an expansion of applications of isotope abundance measurements is foreseen, and publication policies improving the possibility of comparisons of results from different laboratories are suggested.

### Introduction

The discovery of stable isotopes, made in 1910 by J.J.Thompson, was not followed by applications before the 1930ies after the discovery of deuterium by H.C. Urey, and heavy water preparation. The latter was used first as tracer in human physiology. But it took less than six years for artificial radioactivity, discovered in 1934 by Irène and Frédéric Joliot-Curie, to be used in research.

Experimentation with isotopes was dependent, either on the possibility to procure spikes having a stable isotope composition different from that of the system to investigate, or of production of radioactive tracers by irradiation in accelerators, or later in nuclear reactors.

The gradual discovery of natural isotope fractionations, in nearly fifty elements having two or more isotopes, opened specific fields of applications to stable isotope measurements in addition to providing sources of natural spikes. This field is still expanding because all ranges of natural isotope composition have not yet been tied to mechanisms helpful in problem solving. For practical purposes isotopes with half lives of the order of, or longer than, the estimated age of the universe, i.e. 15 Ga, are considered as stable. One may add two uranium isotopes to them because their half lives, though smaller, are long enough.

A largely unexplored field opened when non mass dependent isotope effects were observed in phenomena in the upper atmosphere. More recently similar occurrences have been found in sulphur minerals. Considering that all elements of even atomic number, from oxygen up, possess a minimum of three stable isotopes, one may anticipate that studies of non mass dependent isotope effects will develop and may reveal new mechanisms of natural isotope fractionation.

We restrict this account of problems solved by the use of isotope abundance measurements to problems studied at Saclay. We describe first early work, at Saclay, which started with problems relative to deuterium concentration and sulphur isotope determinations.

*We do not report isotope abundance measurements in dating nor in isotope dilution analysis, though it enabled for instance to date the Oklo phenomenon, or with deuterium, to measure a solubility as small as that of water in carbon tetrachloride.*

## Deuterium abundance

### *Earlier deuterium natural abundance measurements*

#### *Variations in deuterium content of natural waters*

They have been found, even before World War two, by methods relying on density measurements, as delicate as the falling drop technique. Though mass spectrometry was *the* method of isotope analysis, in the fifties very few laboratories could make reliable measurements of deuterium by mass spectrometry. Either mass spectrometers could not work in the very low mass range, or, if they could, the distance between mass two ( $H_2$ ) and mass three (HD) was so large that mass discrimination prevented ratios of peak heights to be representative of abundance ratios

In Saclay there was an apparatus dedicated to mass three to mass two determinations, that was built in H.G. Thode's laboratory, from a prototype inherited from A. O. Nier. It consisted of a small tube equipped with two ion collectors, enclosed in an all glass envelop in which a small permanent magnet provided the deflecting field.

Hydrogen gas, not water could be admitted into the ion source. When samples are under water form, in early days deuterium was analysed by equilibrating water with hydrogen at a well controlled temperature and using a platinum oxide as catalyst in the water phase. The equilibrium constant was assumed from the literature. The preferred technique however soon became reducing water to hydrogen, initially over zinc, and later over uranium metal turnings, following a course advocated by J. Bigeleisen.

When other molecules were investigated their hydrogen had to be converted to water. Several pitfalls had to be averted. To study deuterium in  $H_2S$  exchange,  $H_2S$  had to be burnt. An exchange with water before combustion would modify drastically the measured deuterium content, because this exchange is very fast and its equilibrium ratio, under working conditions, was always bigger than two. When analysing methane, errors due to incomplete catalytic conversion had to be avoided.

#### *Work on D concentration in rivers*

It started around 1955 with the purpose of choosing the best source of water for heavy water production. A location close to the natural gas wells of Lacq was considered because gas from Lacq contains about fifteen percent hydrogen sulphide. Advantage of this particularity was first taken to build a pilot plant to study <sup>1</sup>production of heavy water by the hydrogen sulphide water isotope exchange, saving the labour of preparing hydrogen sulphide in large quantities, and perhaps later a production plant might follow.

Lacq is located close to the Pyrénées. Investigations soon revealed that streams flowing down from hills had a deuterium content in small but characteristic excess over that of the main river originating from the mountains. An explanation was soon put forward: rains falling on the hills would deplete clouds from deuterium before they would deposit snow on the mountains where the river had its source.

In addition to survey of waters, however, we had, for the pilot plant operation, to be able to analyse deuterium in hydrogen sulphide. In the natural gas, collected at the exit of the pipes, its deuterium content was 86 atoms per million. As very small quantities of water are carried to the surface in the gas, the deuterium content of hydrogen sulphide

---

1. Coplen Ty et al. *Isotopic Abundance Variations of Selected Elements* Pure & Appl. Chem. Vol.74 N° 10 pp.1987 – 2012 (2002)

corresponds to isotope equilibrium with water at the bottom of the well. Estimating temperature at the bottom of the well to be around 140°C assigns a deuterium content of this water at 152 atoms per million, a content close to that of local surface water. Reciprocally temperature at the bottom of the well can be estimated by the same reasoning when one considers that water in rocks forming the gas reservoir was in large quantity with respect to hydrogen sulphide, so that exchange did not modify its isotope composition supposed to be 150 ppm of deuterium<sup>2</sup>.

It is worthwhile mentioning that to study isotope exchange reactions, absolute isotope abundance must be measured. Relative deuterium contents of stream and rivers could have been established using relative values, expressed by deltas, but temperature determinations call for absolute figures.

The same can be said of the requirements for any thermometer, e.g. that of the well known <sup>18</sup>O one developed by Epstein and Urey.

### ***Deuterium measurements at higher concentrations***

#### *Heavy water analysis*

Mass spectrometric analysis of water concentrated in deuterium is inevitably affected by contamination by background, whichever procedure is used. It introduces uncertainties that check endeavours to use mass spectroscopy.

Fortunately in the near infrared region of the water spectrum, there is an interval where absorption is due to HDO<sup>3</sup>. Water is analysed in the liquid form, and contamination from absorption cells that can be dried is not observed. This enables to measure D concentrations of heavy water safely and fast up to around 99.9 percent. Infrared analysis of heavy water was performed first with this technique when concentration was checked on every drum during filling the tank of the first nuclear reactor at Saclay, late in 1952.

#### *Medical application*

This easy analytical procedure was attractive to workers outside Saclay.. In particular medical doctors interested in different body water pools. The most sophisticated application was to measure extravascular lung water<sup>4</sup>. When injecting a few cc. of D<sub>2</sub>O in a vein, they mix with lung water by diffusion within the lungs. The transit time to an artery of an induced deuterium signal in blood depends on the water volume with which this spike mixes. This volume is calculated by comparison with the transit time of the non diffusible indocyanide green. A special infrared machine was designed that enabled to work "on line" on a patient's bedside. A by product of the technique is to give a value of the blood flow to the heart.

### ***Sulphur isotope abundance measurements***

#### *Work on sulphur samples from volcanic origin*

This work was carried out in parallel with the early deuterium work. A problem was whether they were anomalies in sulphurs collected from volcano eruptions. The ground to start this research, in 1949, was to check an hypothesis put forward by a volcanologist, Dr. Noetzelin.

---

2.Roth E. *Composition isotopique du soufre et de l'hydrogène des gaz de Lacq*, Comitato Nazionale per l'Energia Nucleare, Summer Course on Nuclear Geology Varenna 1960, pp.187-190.

3.Lecomte J., Ceccaldi M., Roth E., *Dosage isotopique de l'eau par mesure d'absorption dans l'infrarouge*, J. Chem. Phys. Fr. vol. 50 pp. 168 – 169 (1953)

4.Roth E., Basset G., Sutton J., Apfelbaum M., Marsac J. *Use of Water Labeled with Deuterium for Medical Applications* Stable Isotopes – pp. 337 – 344 Elsevier (1982)

In March 1939, two months only after the discovery of fission, he had made the supposition that energy liberated by fission might be the driving force of volcanic eruptions<sup>5</sup>. During the intervening years he wrote several papers developing this hypothesis, and made calculations resting on what became known, little by little, of the theory of chain reactions. He thus decided to look for isotopes that might have captured neutrons, and wanted to investigate sulphur isotopes because sulphur samples could be obtained from many volcanic sites and would lend themselves easily to generate SO<sub>2</sub> for mass spectrometric analysis. This, of course was not a choice resting on optimum nuclear reaction considerations! However Saclay could measure sulphur isotope ratios because there was at Saclay a mass spectrometer of the same type as the one with which H.G. Thode had measured natural variations of sulphur isotope abundance as soon as 1947

Half a dozen volcanic samples were analysed for <sup>34</sup>S/<sup>32</sup>S ratios<sup>6</sup>. Little or no variation between samples from volcanoes of different parts of the world was found, and no difference either with native sulphur from non volcanic origin. A comprehensive review of isotope abundances of sulphur is found in Coplen's report (ref.1). One may compare these findings with the evidence given in ref.2 that <sup>34</sup>S abundance in Lacq sulphur was significantly different, though by a small amount, from what it was in neighbouring sulphuretted water sources.

*S<sub>2</sub>O, an interesting side result of this research.*

Peaks in the background spectrum of the mass spectrometer were found around mass 80. A first interpretation was to assign them to a small amount of SO<sub>3</sub>. But peaks at mass 82 were much too big to be due to <sup>34</sup>SO<sub>3</sub><sup>+</sup>, but they could originate from <sup>34</sup>S in S<sub>2</sub>O<sup>+</sup> ions. One was to find whether such ions were due to reactions within the mass spectrometer, or belonged to bona fide molecules of a sulphur oxide. The only oxide described in the literature that could generate those ions would have been the dubious (SO)<sup>n</sup>. A series of experiments showed that an S<sub>2</sub>O molecule could be prepared. Its stability region and thermodynamic properties were established<sup>7</sup>. We gave it the name "*Sulphur hemioxide*". It is surprising that this molecule was not discovered sooner because it is formed when burning sulphur under a low oxygen pressure, or alternatively under action of an electric discharge. When condensed in a dry ice cold trap, it gives a red precipitate instead of the white one of sulphur dioxide. Ignoring preceding publications, the same molecule has been described under the name of *disulphur monoxide* from its raman spectrum in 1975<sup>8</sup>. It may be pointed out that working with instruments that are equipped with programs that limit exploration of masses to the "most interesting" ones would have prevented making this discovery.

***Later deuterium work at natural concentration, at Saclay,***

Such work has mainly been done on samples fractionated during transition from condensed to vapour phase, or the reverse, and been compared to, or associated with, <sup>18</sup>O and tritium measurements

---

5.Noetzelin J *Volcanisme et Chimie Nucléaire* Comptes Rendus Acad. Sci. Paris (1939)

6.Lazard B., Nief G., Roth E. *Variations de l'abondance du <sup>34</sup>S* J. Chim. Phys. Fr. vol. 49, pp. 60 – 63 (1952).

7.Hagemann R., *Etude thermodynamique de l'hémioxyde de soufre par spectrométrie de masse* Thesis Paris (1964), and Botter R., Hagemann R., Nief G., et Roth E. *Same title* In Advances in Mass Spectrometry vol. 3 The Institute of Petroleum editions (1966)

8.Tang Sheng-Yuh and Brown Chris W., *Raman Spectrum of Matrix Isolated S<sub>2</sub>O; Evidence for the Formation, of S<sub>2</sub> and SO<sub>2</sub> from S<sub>2</sub>O* Inorg. Chem. **14** N° 11 pp.2856-7 (1975)

*Exploration of ice caps*

When it became known that Saclay could routinely analyse deuterium in water at its natural concentrations, it started requests for measurements from several parts. Under impulse from a Swiss teacher, Dr. Renaud, the french explorer Paul Emile Victor proposed to bring samples from ice caps to make isotope determinations. This would be parallel to work done in Chicago by Sam Epstein, to estimate annual precipitation, relying on seasonal variations of  $^{18}\text{O}$  in ice. The aim was essentially of geographical interest. In Europe W. Dansgaard studied Greenland. and equipped his laboratory for  $^{18}\text{O}$  abundance measurements.

Saclay could not look routinely at  $^{18}\text{O}$ , and it was decided to analyse deuterium.

Seasonal variations showed up nicely in ice cores; fear that diffusion would rapidly erase seasonal variations of D contents were alleviated. It was nevertheless necessary to prove that determinations of deuterium and of  $^{18}\text{O}$ , reputedly less diffusible in ice, gave the same results. For this purpose, we analysed deuterium in samples from an iceberg, in collaboration with Dansgaard, who did the  $^{18}\text{O}$  determinations. The linear relationship found between D and  $^{18}\text{O}$  values. proved the two techniques to be equivalent<sup>9</sup>.

*Climatology*

In a more general formulation Harmon Craig established his well known linear relation between deltas of D and  $^{18}\text{O}$ . This became a tool in climatology, as both the intercepts at the origin and deviations from the straight line may be interpreted. At Saclay analysed ice cores came from drillings by Expéditions Polaires Françaises, but also from those of the Russians and Americans<sup>10</sup>. Cores several thousand meter long have now been drilled, reaching the bottom rock in one place, and an unexpected lake in the other. One is reluctant to sample the lake by fear of pollution by a drill. Ice reached at the bottom has an estimated age of more than 400.000 years. Data accumulated that initially appeared to be of purely scientific interest have acquired a very big role in efforts to predict greenhouse phenomenon effects. Analysis of gases trapped in the ice are made simultaneously with isotope analysis that provide a temperature estimation. Results at Saclay show that there is undoubtedly a parallelism between increase in temperature and greenhouse gas concentration. It may be argued that this does not solve an egg and hen kind of dilemma, it should nevertheless incite to minimise greenhouse gas emissions. An unexpected recent result is also that very fast temperature changes occurred in the past: temperature drops of ten degrees celsius, that were thought to take centuries were observed to have happened in decades<sup>11</sup>.

*Hail formation*

Understanding the growth of hailstones was considered necessary to efficiently fight damage caused by hailstorms, but it was a puzzle that no tool helped to solve when our assistance was requested. Work started on the hypothesis that, should hailstones grow layer by layer, the isotopic composition of these layers might vary if their temperatures of formation differed. This assumption was confirmed, first on small hailstones, later on specimens the size of

---

9. Dansgaard W., Nief G., Roth E., *Isotopic distribution in a Greenland Iceberg* Nature G. B. **185**, 232, p. 4708 (1959)

10. Merlivat L, Lorius C., Majzoub M., Nief G., et Roth E., *Etudes Isootopiques en profondeur d'un glacier en Antarctique* dans *Isotopes in Hydrology*, Proc. Of the *Symposium on isotopes in hydrology* IAEA IUGC Vienna , Proceedings series (1967)

11. Jouzel J. *personal communications*

grapefruits, obtained from american colleagues. The next step was to interpret temperatures in terms of altitudes within hail clouds. Isotopic equilibrium between the superficial ice sheet of the stone and water vapour in the cloud had been assumed. It was to be confirmed, because kinetic effects would invalidate our estimations. Simultaneous analysis of  $^{18}\text{O}$  and D demonstrates equilibrium when fractionations are in the ratio predictable from the vapour to ice condensation coefficients. As hailstone's homogeneous isotopic layers are very thin, correlation had to be established on exactly the same samples. To do this a special ion source was built, enabling part of the samples to be introduced as water vapour into the mass spectrometer for  $^{18}\text{O}$  analysis, while another fraction was conventionally reduced to hydrogen for D analysis. This facility enabled to establish that equilibrium was reached<sup>12</sup>.

A picture of hailstone formation resulted from a three dimensional isotopic mapping. The nuclei are formed at the bottom of clouds, growth takes place in the violent ascending air current that characterises hail storms. Having reached the top of the cloud hailstones fall. Unexpectedly it was found that they may be caught a second, or even a third time in the ascending draft, which explains some of their biggest dimensions. The model was refined<sup>13</sup> But a publication claiming that tritium had been detected in the nucleus of hailstones gave rise to further experiments. As tritium formed naturally, or as debris from nuclear explosions, originates on upper atmosphere, it was claimed that, contrary to our results, nuclei were formed on top of clouds. We endeavoured to measure also tritium, and disproved this claim, which probably relied on contaminated samples<sup>14</sup>.

#### *Balancing input and output flows of water in a lake*

Lake Tahoe, in the US, has no visible outflow. Is the stream water coming in evacuated entirely by evaporation, or is there a hidden outlet? To answer this question we applied the model of a constant volume pool with a steady inlet flow, losing water by evaporation only. It would have at equilibrium a deuterium concentration one alpha above that of the incoming flow, in order that the pool would be not only at constant water volume, but also at constant deuterium content. Within the applicability of the model to the real situation pure loss by evaporation was established<sup>15</sup>.

#### *Deuterium content of gas from lunar samples*

The motivation to establish deuterium concentrations of lunar hydrogen was to investigate the possibility of presence of water on the moon. It appeared however that lunar gases were entirely due to protons from the solar wind, i.e. at a D content that could be less than  $10^{-16}\%$ <sup>16</sup>. A major difficulty in this research was to avoid contamination of samples by ordinary water before

- 
12. Majoube M., Roth E. *Etude des variations des teneurs en oxygène 18 et en deutérium dans des grêlons* Note CEA 1540 juillet 1972
  13. Merlivat L., Nief G., Roth E. *Etude de la formation de la grêle par une méthode isotopique* C. R. Acad. Sci. Paris **258**, pp. 6500 – 6502 ( 29 juin 1964)
  14. Jouzel J., Merlivat L., Roth E., *Isotopic Study of Hail* J. of Geophys. Res. Vol. 80 N°36 pp. 5015 – 5030 (1975)
  15. Bonner F. T., Roth E., Schaeffer O. A., and Thompson S. O., *Chlorine 36 and deuterium study of Great Basin lake waters* Geochim. et Cosmochim. Acta, **25**, pp. 261 – 266 (1961)
  16. Merlivat L., Lelu M., Nief G., Roth E., *Deuterium, hydrogen and water content of lunar material* Proc. of the 5<sup>th</sup> lunar science conf.(supplement 5, Geochim. And Cosmochim. Acta Vol. 2 pp.1885 – 1996 (1974)



analysis, and by background residual peaks in the mass spectrometer. Spallation deuterium, found in the course of this work, later became a subject of investigation in meteorites<sup>17</sup>.

#### ***Detritiation of heavy water a byproduct of tritium work***

A special concentration technique was developed to analyse tritium at very low levels at Saclay to minimize the risk of contamination by the ambient atmospheres they were two heavy water research reactors operating at Saclay and a biology department using tritium as tracer. The method consisted in transferring the tritium to be analysed from water to “dead” hydrogen from natural gas by catalytic exchange. Tritium was then concentrated by thermal diffusion. No exposure to air nor addition of electrolyte, was involved as in other techniques.

When asked to develop a method of detritiating heavy water of the high flux reactor built at Grenoble, it was found that processes used to prepare heavy water would necessitate gigantic plants. The solution was obtained by adapting the analytical scheme by replacing in the design hydrogen by deuterium and thermal diffusion by liquid deuterium distillation, a well known process. No further experimentation was needed to build a detritiation unit in Grenoble<sup>18</sup> that has been in operation since 1971 with only one replacement of the catalyst. This unit can produce circa 100g of tritium per year. A plant using the french patent<sup>19</sup>, on the process, is operating at Darlington in Canada to detritiate heavy water from the CANDU reactors. It has a separating capability of several kilograms of tritium per year.

#### ***Measuring burnups of nuclear fuels and the OKLO phenomenon***

Detritiation techniques developed for pure research gave the answer to a technical problem of reactors. Conversely, when it was found, in 1972, that uranium samples from OKLO in Gabon were depleted in <sup>235</sup>U it was the similarity with problems met in the study of spent fuels, that were examined routinely in laboratories at Saclay, led to study rare earths and their isotope composition, that eventually was the key to understand the phenomenon<sup>20</sup>. Depletion in <sup>235</sup>U was a consequence of nuclear chain reactions originating spontaneously 1.8 Ga B.C. within the OKLO uranium deposit. Isotope abundance measurements across and around the deposit were a powerful tool to understand how chain reactions were formed, sustained, propagated and came to an end. To answer to the query whether OKLO was the unique uranium deposit to undergo nuclear chain reactions, ruthenium isotopes were investigated on the following grounds. An OKLO type phenomenon can only have happened after the earth's atmosphere became oxidising enough to allow the formation of uranium deposits, but before concentration of <sup>235</sup>U had decayed to too small values. Ruthenium from fission is very abundant and isotopically quite different from “normal” ruthenium. As samples from rocks formed before the atmosphere became oxidising and samples from recent ones have the same isotope composition, the latter can not be contaminated by fission ruthenium. It sets a very low probability to chances of finding sites similar to OKLO, in regions outside “cratons”<sup>21</sup>.

- 
17. Merlivat L., Lelu M., Nief G., Roth E., *Spallation deuterium in rock 70215* Proc. 7<sup>th</sup> lunar science conference Houston ( 15 - 16 March 1976, pp. 649 – 658 Pergamon Press (1976).
  18. Leger D., Dirian G., Roth E., *Détitiation de l'eau lourde des réacteurs nucléaires* Enrgie Nucléaire Vol N°2 p. 135 (mars – avril 1970)
  19. Roth E.A, *French process for tritium removal from Canadian heavy water* Nuclear Technology Fusion (March 1984)
  20. Roth E., *The discovery and study of the nuclear reactor in OKLO* J. Radioanalyt. Chem., **37**, 1, pp. 65 - 78
  21. Roth E., Lucas M. Lecomte T., Devillers C, Hagemann R, *Essai de contribution par la géochimie à l'évaluation de l'importance et de la fréquence des phénomènes de type « OKLO »* dans : Le Phénomène d'OKLO, Compte rendu d'un colloque sur le phénomène d'OKLO, AIEA, Vienne SM – 204/25, pp. 489 - 498 (1975).

It is *piquant* to observe the following a) Conditions of occurrence of OKLO anomalies had been described as soon as 1956 by Pr. Kuroda, but were forgotten or ignored when they were discovered b), Kuroda, in his 1956 work was inspired by Noetzelin's hypothesis of a role of nuclear reactions in volcanism<sup>22</sup>.

### Conclusion

Describing the amount of work done at Saclay on deuterium should not obscure the fact that worldwide a much larger amount of work is done using carbon and nitrogen isotopes than deuterium. Yet the variety of subjects in this paper should convince of the versatility of isotope abundance measurements as tools in problem solving. And their field of application is still growing for two reasons. Firstly non mass dependent fractionations are only starting to be explored. Secondly progress in instrumentation has, in the past paved the way to applications such as the use of infrared analysis introducing the medical use of breath tests using labelled carbon, or NMR fostering the exploration of intramolecular isotope effects. Today significant isotope analysis can be made on spots of only a few microns diameter on solids. Already inhomogeneities have been found when dating minerals on this scale. Further work is bound to increase

This variety of subjects and number of applications make it desirable that published data from all laboratories be comparable. It probably is not the case for results expressed in delta units, for two reasons. Several reference samples have become "virtual", PDB for instance. Secondary references, provided inter alia by AIEA and renamed V- samples, are used, with a small scale correction. But, as deltas are not additive when they are large or published with two significant decimal figures, the correction to be introduced is not only of one additive term translation but involves a multiplicative term that may be overlooked when wrongly believed to be small.

In the future, changes of reference samples will make the comparison of older and more recent publications akin to that of comparing old "physical" and "chemical"<sup>23</sup> atomic weights. To remedy this situation a first step should be that absolute isotope abundance ratios of all reference samples be determined, and that, as much as possible, laboratories, use references certified in absolute ratios and publish results in absolute values. This problem is discussed now within IUPAC that has already published the report mentioned earlier (ref.1) reporting results in both scales.

Finally the variety of subjects studied make conferences like those at Cluj-Napoca, where so many different works are presented, very useful by giving an opportunity to attendants to familiarise themselves with progresses that may bring helpful ideas for their work though outside their own line.

---

22. Kuroda P. *Personal communication*

## NEW HEAVY WATER PRODUCTION AND PROCESSING TECHNOLOGIES

RAMESH R. SADHANKAR and ALISTAIR I. MILLER

*AECL, Chalk River Laboratories, Chalk River, Ontario, Canada, K0J 1J0*

**ABSTRACT.** The use of heavy water ( $D_2O$ ) as a neutron moderator is one of the distinctive features of CANDU<sup>\*</sup> reactors. Using heavy water as a moderator results in CANDU reactors' well-known fuel cycle flexibility, including the ability to burn natural, un-enriched uranium. Ensuring the availability of economic processes for the supply and management of heavy water is a major goal of AECL's CANDU development program.

AECL has developed several approaches to ensure affordable supplies of  $D_2O$ . The Combined Industrial Reforming and Catalytic Exchange (CIRCE) process offers an effectively unlimited production capability since it is based on extraction of  $D_2O$  from steam-methane reformers (SMR), the standard method of producing hydrogen on a large scale. CIRCE uses exchange of deuterium between water and hydrogen, an exchange that depends on an effective catalyst. AECL's wetproofed catalysts, developed over three decades, is the key to CIRCE and other processes that depend on this reaction.

CIRCE is a combination of three process steps. In the first, before being evaporated, water entering the SMR is enriched in deuterium by contact with the hydrogen produced in the SMR. As a result, deuterium concentrations in the SMR are 15- to 25-fold higher than natural and about 50% of the deuterium content of the hydrogen is recovered. In the second step, deuterium is further enriched (in one or two stages) using a bithermal water-hydrogen process. Final enrichment is completed in a Combined Electrolysis and Catalytic Exchange (CECE) stage, where electrolysis is used to produce deuterium gas for countercurrent exchange with a small water flow.

From mid-2000 to late-2002, AECL operated a Prototype CIRCE Plant (the "PCP") at the site of a small SMR owned by Air Liquide Canada (ALC). All three CIRCE process steps performed as expected. The catalyst maintained its activity very well in this industrial setting. Integration of the SMR and CIRCE processes was fully satisfactory and routine operation of the plant easily performed by ALC's SMR operator.

Upgrading and detritiation of heavy water can also employ processes based on the wetproofed platinum catalyst. CECE is an alternative process to water distillation (DW) for heavy-water upgrading and CECE is also provides a highly effective way to detritiate  $D_2O$ . AECL has operated a prototype CECE plant to demonstrate both upgrading and detritiation. Feedwater concentrations ranging from 1-99 mol%  $D_2O$  were upgraded to >99.9 mol%  $D_2O$  and heavy water was detritiated up to factors exceeding 50 000.

This paper describes the CIRCE and CECE prototypes and reviews the requirements for large-scale CIRCE deployment.

### 1. Introduction

Of the entire periodic table, more atoms of the isotopes of hydrogen have been separated than of any other element and to extremes of separation unmatched by any other element. Achieved concentrations of tritium range from natural levels in fossil material of

---

\* CANDU®: Canada Deuterium Uranium

essentially zero—and far below the  $\sim 10^{-17}$  mole fraction levels currently in the biosphere—to well over 99% produced in kilogram quantities from Ontario Power Generation's Darlington Tritium Removal Facility. AECL has water with deuterium concentrations ranging from 0.2 ppm to 99.994 mol %. There are both commercial and technical reasons for these vast ranges.

With deuterium, the main interest is in water with high deuterium concentrations though there are rare applications for deuterium below 1 ppm for nuclear physics experiments. Commercially, reactors moderated with heavy water generally operate with 99.8 to slightly over 99.9 mol %  $D_2O$  and small amounts of very high purity  $D_2O$  command a price premium for use in magnetic resonance imaging. With tritium, more often because of the ease with which this radio-isotope can be detected than for sound environmental reasons, removal of tritium from ground waters is periodically considered. The main interest in manipulating concentrations of tritium in heavy water is for its reclamation when a reactor is decommissioned. By reducing its tritium content, used heavy water can be recycled to new reactors.

Technically, none of these manipulations of hydrogen isotopes are really difficult and the main factors that drive process costs are either the need to process large feed streams or the radiotoxic nature of tritium. Large feed streams are highly significant in producing heavy water, because hydrogen is predominantly protium (mass=1) and the natural occurrence of deuterium is only about 0.015 mol %.

Innumerable physical and chemical processes have been proposed as the basis for hydrogen-isotope separations but only two classes have been used for separation of large quantities: chemical exchange and distillation. Both of these approaches exploit the capacity for gravity-driven counterflow of a liquid and a gas. This feature is useful since hundreds of contacts between the two streams are needed to meet the requirements for separation. Because of its simplicity, distillation has been deployed for a few limited, niche applications. Water distillation is often used to “upgrade”—that is remove light water contamination—heavy water. The same process has been used as a finishing process for heavy water already upgraded to at least 10 mol % by the Girdler-Sulphide (G-S) process. Hydrogen distillation is the process of choice for separating tritium from deuterium for tritium concentrations exceeding a few hundred parts per million. The attractions of hydrogen distillation are the high integrity of a process that needs no moving parts within the pressure boundary and the relatively low radiotoxicity of elemental tritium compared to that of tritiated water.

Chemical exchange processes require two chemical species, one gaseous and one liquid and both containing hydrogen atoms that can be readily exchanged. Both should be otherwise stable at process conditions. To lead to competitive processes, by broad cost comparisons for chemical compounds, both species should be relatively inexpensive. There also needs to be a reasonably large difference in the preference of one species over the other for hydrogen isotopes (the separation factor). Only four pairs of chemical species have been developed to any significant extent: water-hydrogen sulphide (the G-S process), ammonia-hydrogen, aminomethane-hydrogen and water-hydrogen. None of the four is ideal. Only the G-S process does not need a catalyst for hydrogen exchange but it has many detractors: toxicity, corrosiveness, poor separation factor, and a limited range of accessible pressure and temperature conditions. Ammonia-hydrogen and aminomethane-hydrogen both require moderate levels of refrigeration ( $\sim -30^\circ C$ ) and depend on potassium salts to catalyse hydrogen exchange. Even with these catalysts, the kinetics are so poor that mechanical agitation is needed to achieve acceptable rates of exchange. With development of AECL's wetproofed catalyst, processes based on exchange between water and hydrogen

have arguably displaced all of the other existing processes (except for hydrogen distillation for high tritium concentrations for the already-mentioned radiotoxicity of tritiated water).

Chemical exchange can be applied in two distinct ways: monothermal and bithermal processes. Both processes involve repeated contacts between a gas and a liquid flowing countercurrently. For the four chemical systems that have been developed, the liquid species always has a higher affinity for the heavier isotopes than the gaseous species and the relative affinities are greater at lower temperatures. The description below is for deuterium-protium separation but the same principles apply to tritium-deuterium or tritium-protium separations.

In monothermal processes, the downflowing liquid gains deuterium from the upflowing gas, which is in turn stripped of deuterium. The process is simple and its control is easy since fluctuations of the flows have a relatively weak effect. If a deuterium concentration substantially below that of the feed is required, a second liquid feed of suitably low concentration becomes essential. If necessary, this can be synthesized from some of the effluent gas. Also to their advantage, because the equilibrium ratio between the two species is usually quite large, monothermal processes consequently require a relatively small number of contacts. The large disadvantage of a monothermal process is that almost all of the liquid must be chemically converted into the gas—a requirement that precludes all monothermal applications of the water-hydrogen sulphide system and many monothermal applications of the other three chemical pairs.

Bithermal processes avoid chemical conversion. Instead, they utilize the variation of separation factors with temperature. So, with the G-S process, the ratio of concentrations at equilibrium between water and H<sub>2</sub>S is 2.3 at 32°C and 1.8 at 130°C<sup>i</sup>. As with a monothermal process, deuterium transfers from the gas to the liquid in the cold tower. The liquid leaving this tower goes next to a hot tower, where the separation factor is weaker. With careful control of the ratio of liquid to gas flows, the liquid can now find itself in contact with gas with less than its equilibrium concentration of deuterium. In this situation, deuterium transfers from the liquid to the gas in the hot tower. Because the variations in separation factor between the two temperatures are fairly small, the concentrations in the gas and liquid are always very close to equilibrium. So bithermal processes require a relatively large number of contacts between the two species and hence exchange columns that are much longer than for monothermal processes.

## 2. Processes Based on Water-Hydrogen Exchange

Once the problem of an effective catalyst has been overcome, processes based on water-hydrogen exchange have many advantages: they operate in convenient temperature ranges (either near ambient or between ambient and about 175°C); water and hydrogen are available in very large quantities; these two species are easily interconverted; neither is toxic or markedly corrosive; though flammable, hydrogen is routinely handled in large quantities in the chemical and petrochemical industries; the separation factors are large and have a good variation with temperature (for deuterium:protium separation, from 3.8 at 25°C to 2.1 at 175°C); and there are no practical constraints on the pressure or temperature of a process.

AECL defines three distinct processes based on water-hydrogen exchange. The first process is Combined Electrolysis and Catalytic Exchange (CECE), where electrolysis converts water to hydrogen to provide hydrogen feed to the exchange column enriched in the heavier isotope. Fig. 1 gives two CECE configurations.

<sup>i</sup> G-S operating temperatures are limited by the formation of hydrates below about 30°C and the liquefaction of H<sub>2</sub>S at pressures exceeding 2.2 MPa – inaccessibility of higher pressure constrains the hot tower temperature to avoid excessive humidity.

Demonstration of the CECE process for upgrading and detritiation is discussed later in this paper.

Ideally, one would apply the CECE process to the primary production of D<sub>2</sub>O but the scale on which electrolysis is usually deployed today is far too small to provide useful rates of D<sub>2</sub>O production and the stand-alone value of the small amount of D<sub>2</sub>O produced could not possibly defray the cost of electrolysis of the far larger feed stream<sup>ii</sup>. However, hydrogen is already produced on a large enough scale for effectively unlimited production of D<sub>2</sub>O but its production is overwhelmingly by steam-methane reforming (SMR). So the second process, Combined Industrial Reforming and Catalytic Exchange (CIRCE), produces heavy water as a byproduct of SMR-hydrogen production. Practical CIRCE plants also incorporate the third process, Bithermal Hydrogen-Water (BHW), though this could also be a stand-alone process.

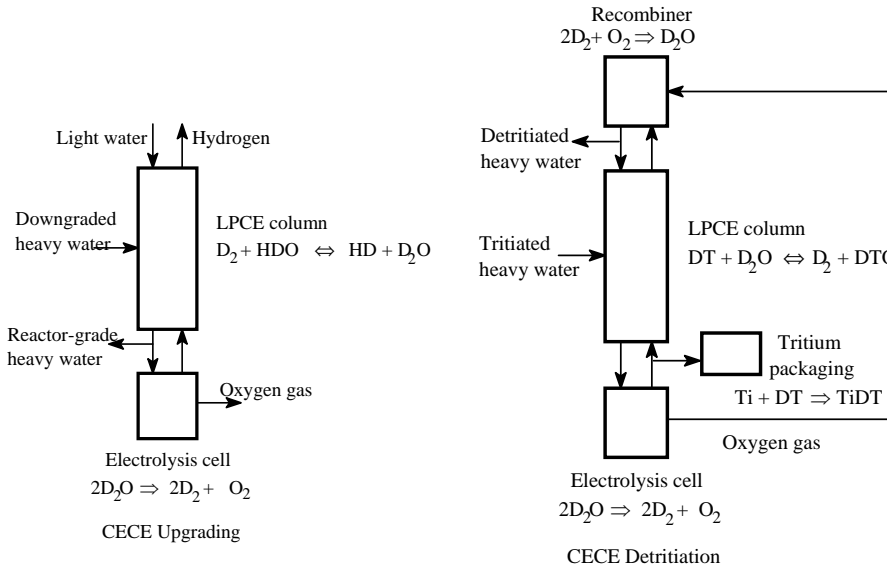


**Fig. 1.** Schematic of the CECE Process for Heavy Water Upgrading and Heavy Water Detritiation (CECE-UD)

### 3. The CIRCE Process

Conceptually, CIRCE is fairly similar to the CECE process except that electrolytic conversion of water to hydrogen is replaced by the SMR. Practically, however, there are large and important differences. The layouts of an SMR with and without a Prototype CIRCE Plant (PCP) are shown schematically in Figure 2.

<sup>ii</sup> This could change as the world begins a widely-expected move toward a “hydrogen economy”, with hydrogen displacing conventional hydrocarbon fuels.

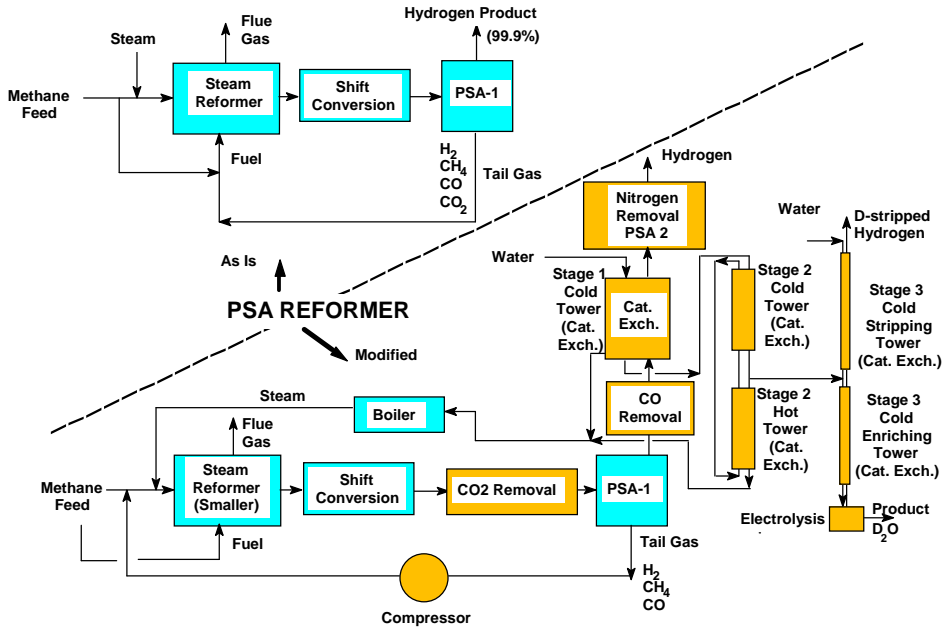


Fig. 2. Schematic of a typical SMR before (top left) and after (bottom right) adaptation to the CIRCE process.

There are two broad types of SMR, both of which are suitable for adaptation to CIRCE. The one shown in Figure 2 is of the Pressure Swing Absorption (PSA) type. (The other type is usually associated with ammonia production and is expected to be somewhat simpler to adapt.)

All SMRs have a primary, high-temperature converter, which reacts steam and methane to produce hydrogen and a mixture of carbon dioxide and carbon monoxide as well as some unconverted water vapour and methane. One or more shift converters then contribute additional hydrogen by “shifting” CO to CO<sub>2</sub> through further reaction with steam. So the predominant products of an SMR are hydrogen and carbon dioxide. Depending on the SMR, varying amounts of carbon monoxide and unconverted methane also leave the SMR. The hydrogen must be further purified, in the case illustrated, with a PSA unit. The PSA contains a series of beds of molecular sieve through which the hydrogen passes unabsorbed. All other gases are absorbed on the molecular sieve, with varying degrees of binding. The flow is cycled between beds, which are regenerated by a complex sequence of pressure reductions and flushings with streams of intermediate purity. From the perspective of the CIRCE process, the PSA is both helpful and unhelpful. Helpfully, it produces a very pure hydrogen stream that needs only modest further purification before it passes over the exchange catalyst; unhelpfully, it diverts considerable amounts of hydrogen and hydrogen-containing compounds to its low-pressure blow-down.

Looking in detail at the adapted flowsheet in Figure 2, the water feed to the SMR first undergoes enrichment with deuterium, which is stripped from the SMR’s hydrogen product. At the high temperatures of the reformer and the shift converters, hydrogen isotopes are freely exchanged so methane, steam and hydrogen all become enriched in deuterium within the SMR. In the unadapted SMR, blow-down from the PSA is used as fuel to heat the reformer. With

CIRCE, most of the deuterium would escape by this route if one were to allow the PSA blow-down to be used in this way. So, in the CIRCE-adapted SMR, the blow-down is recompressed and recycled as process feed. To allow recycle, the CO<sub>2</sub> co-product of the SMR process must be removed. This is done by adding a conventional CO<sub>2</sub> absorption process, a standard component in other types of SMR. Nitrogen, present in small amounts in the natural gas feed, would also build up. It can either be removed from the feed by cryogenic pre-purification or (because it is only weakly absorbed in the PSA) allowed to leave the PSA with the main hydrogen flow. The latter is the approach illustrated in Figure 2 and used in AECL's PCP. For the SMR with which the PCP is integrated, the specification for the hydrogen product requires it to be both N<sub>2</sub>-free and dry. Nitrogen removal and drying are easily accomplished by a second PSA unit, PSA-2.

There are several other components of the PCP that illustrate significant differences between the CECE and CIRCE processes. With CECE, the hydrogen stream from the electrolysis cells is exceedingly pure and can be passed straight to an isotope exchange column. With CIRCE, even the hydrogen purified by a PSA contains a small, fluctuating amount of CO (~1 ppm CO). CO is a cumulative, though reversible, poison of the exchange catalyst. So, for CIRCE, these traces of CO are converted to methane by an AECL-proprietary catalytic process before the hydrogen enters the catalytic exchange column. A second difference arises from the smaller water-to-hydrogen flow ratio in the exchange column (1:2 compared to the 1:1 ratio of the CECE process) since half the hydrogen originates in the methane feed to the SMR. With less water to remove deuterium from the hydrogen, the deuterium concentrations are generally closer to equilibrium and more catalyst is required. A third difference is that CIRCE operates at the pressure of the reformer (typically 2 to 4 MPa, compared to near ambient pressure for most electrolysis). Higher pressure reduces catalyst activity somewhat, again leading to a requirement for more catalyst. However, catalyst activity increases rapidly with rising temperature so using a rather higher exchange temperature can significantly offset the requirement for more catalyst, though this causes a modest reduction in deuterium recovery. Overall, CIRCE requires a substantially greater volume of exchange catalyst than CECE. Hence maximizing catalyst activity and reducing catalyst cost are important objectives of AECL's program of catalyst development.

The final difference between the CECE and CIRCE processes is in their different potentials for losses. Electrolysis cells are very leak-tight and loss of material from them is not a significant issue. SMRs, on the other hand, are somewhat more prone to leakage, though the amounts remain very small. The main loss issue concerns design of the SMR to allow the export of surplus steam without also exporting deuterium. Steam exports must either be produced from separate steam coils using water not enriched in deuterium or the condensate must be recycled.

All of these key factors to adapt an SMR for heavy water production by CIRCE have been successfully addressed with AECL's PCP, at an Air Liquide Canada site in Hamilton, Ontario.

#### **4. AECL's CIRCE Prototype**

##### ***The SMR and its Adaptation for Heavy Water Production***

Air Liquide Canada's Hamilton SMR is an excellent facility at which to prototype the new technology since, by industrial standards, it is a very small SMR, designed to produce 2600 normal m<sup>3</sup>/h of hydrogen. (While SMRs come in a wide range of sizes, the typical scale



of an SMR of the sort associated with ammonia production or heavy-oil upgrading is about 120 000 normal m<sup>3</sup>/h of hydrogen.) Further, since the SMR and AECL's PCP were designed and built at the same time, their integration was simplified. The SMR supplies a mix of continuous and intermittent demand and so its production fluctuates somewhat.

As Figure 2 shows, heavy water enrichment occurs in three stages. Strictly speaking, Stage 1 is the CIRCE process and only this stage is deeply integrated with the SMR. The two further stages of enrichment use other processes.

#### *Stage 1: The CIRCE Process*

In the PCP, the CIRCE process enriches hydrogen-containing chemical species to around 2000 ppm of deuterium in the SMR. This is a blend of water enriched to around 4000 ppm from the catalytic exchange column and of methane at about 100 ppm. A small part of the water leaving the catalytic exchange column is further enriched to about 6000 ppm by bringing it very close to equilibrium with the hydrogen stream leaving the SMR. This small stream is fed to Stage 2.

Operating conditions are 80°C and 1 MPa (the pressure of the SMR). Physically, Stage 1 comprises four exchange columns arranged in series.

The AECL wetproofed catalyst used in this stage is "structured", made up of plates of stainless steel screens. The plates alternate between a hydrophobic, corrugated plate coated with noble-metal catalyst (to allow the transfer of isotopes between hydrogen and water vapour) and a flat plate coated for increased hydrophilicity (to promote exchange of isotopes between water vapour and liquid water). Stage 1 columns are 430 mm in diameter.

#### *Stage 2: A Bithermal Hydrogen-Water Process*

Stage 2 also utilizes a novel process, BHW, the third process made possible by the AECL exchange catalyst. Bithermal processes have been used to produce D<sub>2</sub>O using other chemical exchange pairs: widely by the G-S process using water-H<sub>2</sub>S and by ammonia-hydrogen at Talcher, India. However, this is the first deployment of water-hydrogen in a bithermal process.

In contrast with the bithermal G-S process, as already noted, BHW offers far superior separation factors: the cold tower of the PCP's Stage 2 operates at 60°C (separation factor = 3.15) and the hot tower at 150°C (2.25). For the cold tower, 60°C is the appropriate temperature for minimum catalyst volume (higher activity offsetting a lower separation factor as the temperature is raised). The choice of 150°C for the hot-tower temperature was conservatively low. It was based on AECL's testing of the catalyst at that time. Experience with exchange catalyst subsequent to design of the PCP has shown that a hot tower temperature of as high as 175°C could be used. (The limit on hot tower temperature is set by rising humidity and the energy input needed for its evaporation.) Unlike Stage 1, the operating pressure is not fixed by the SMR and was set at 2.2 MPa to maintain reasonably low humidity for the 150°C temperature.

Stage 2 has its own recirculating gas flow of hydrogen. Stage 2 receives the small stream of water at 6000 ppm from Stage 1 and enriches it by a further factor of about twelve, to 7.5 mol % deuterium.

The catalyst in Stage 2 is of the same type as Stage 1 and the eight exchange columns are all 154-mm diameter.

### *Stage 3: A Monothermal CECE Stage*

Finally in the PCP, a very small stream of water is drawn from between the cold and the hot towers of Stage 2 and sent for further enrichment to Stage 3, which uses CECE technology. Unlike most designs of heavy water plants where stages are connected by both a forward and return flow, Stage 3 interfaces with Stage 2 only through this single stream from Stage 2. The Stage 3 exchange columns operate at 60°C where the separation factor is amply large enough to accommodate a stripping water flow of less than half the total flow that is converted to hydrogen in a 7.2-kA electrolysis cell.

This CECE unit is not novel; indeed, it is almost identical to the AECL's CECE-UD prototype, used to demonstrate CECE upgrading and detritiation and which is discussed in detail below. The catalyst in Stage 3 is of the random type, a mixture of catalyst-coated hydrophobic and hydrophilic rings.

### ***Important Aspects of Demonstration of the New Technology***

The PCP was declared to be in operation in 2000 July and completed the planned test program in 2002 October. (The slight dilation in time arises from a few occasions when the SMR was off-line.)

As with any new process, the PCP has to provide satisfactory demonstration of many aspects of the technology. About 20 elements were identified explicitly for verification. One can divide these elements into four broad categories of demonstration:

- successful integration with the SMR
- performance of the catalysts
- operability of the process
- validation of the process model

### *Integration*

Integration with the SMR has been fully demonstrated. No adverse effects have been observed arising from the presence of the PCP and its SMR modifications and the PCP CIRCE.

### *Catalyst Performance*

Demonstration of catalyst performance in this industrial setting has been generally satisfactory. Where there has been no external cause, the exchange catalyst has shown very little loss of activity over the two-year period of the demonstration. When a small proportion of catalyst was accidentally exposed to significant concentrations of carbon monoxide (due to inadvertent bypassing of the final CO removal step, a methanation bed), the expected loss of activity was observed. With both of the expected sources of catalyst poisoning—from carbon monoxide and traces of organics entering with the feed water—we have succeeded in demonstrating that catalyst activity can be restored *in-situ* using a flow of nitrogen plus a small amount of oxygen at about 100°C. Oil in-leakage, from a failed compressor seal, caused local catalyst degradation and this could not be regenerated. This provided a good test of field replacement of the catalyst. The catalyst has shown no adverse effect from sustained operation at the high temperature of the Stage 2 hot tower. However, parts of the water distributors in the hot tower unexpectedly lost a hydrophobic coating and this led to some temporary loss of catalyst performance. They were replaced with a redesigned type.

Since the methanation catalyst used to protect the Stage 1 exchange catalyst from traces of CO in the main hydrogen stream has performed flawlessly, a test of its effectiveness at lower temperature was carried out and established that lower-temperature operation was effective.

### *Operability*

Despite the four separate exchange columns, Stage 1 showed no discernable effects attributable to fluctuations in the rate of hydrogen production. Measurement of catalyst activity in the exchange catalyst was broadly consistent with the design assumptions. This demonstrated (1) that the catalyst has intrinsically stable performance in an industrial hydrogen stream, (2) that water purification is effective in excluding water-soluble catalyst poisons, and (3) that the methanation catalyst is completely effective in removing CO from the hydrogen stream.

Obviously, when the SMR's production fluctuated, there was a lag in the response of the water flow, which both fed the SMR and stripped deuterium from the hydrogen. However, as expected from the intrinsic insensitivity to flow ratio of any monothermal process, the resulting ripples in the liquid-to-gas ratio showed no discernable effect on the plant's performance.

Total interruptions of the hydrogen flow and/or bypassing of the Stage 1 exchange column occasionally caused substantial losses of extracted deuterium. However, the PCP was always expected to be sensitive to this type of disruption because its small SMR had a disproportionately large water inventory. Data collected on this effect and on leakage rates from the SMR provided necessary scaling information for larger plants.

Because it is bithermal, analysis of catalyst performance in Stage 2 was very sensitive to the precise ratio of liquid-to-gas flows. This made measurement of the performance of catalyst at the two temperatures somewhat less precise but the overall performance of catalyst in Stage 2 matched the design. This is an important observation since its calculated performance would have been adversely affected if the liquid-to-gas ratio had fluctuated appreciably. Since there were physically four cold and four hot columns, we must have achieved appropriately good control of the liquid flow through the entire stage. (This is quite an important demonstration since previous bithermal processes have been designed with only one or two columns.) However, an on-line densitometer—a prototype instrument developed for this purpose—revealed considerable short-term fluctuation in the deuterium concentrations in the middle of the cold and hot columns. This implies some fluctuation in local flow ratios though the overall analysis of the Stage's performance indicating little detrimental effect.

As a monothermal process with a large separation factor, the CECE stage is particularly suited to developing very large factors of enrichment and depletion. The PCP Stage 3 has demonstrated a comparable capability by producing D<sub>2</sub>O at over 99.994 mol % purity. Similarly, as described below, the CECE-UD prototype achieved detritiation factors exceeding 50 000.

### *Model Validation*

The PCP was designed using process simulation. Data from its operation—including large sets of deuterium analyses of both liquid and gas samples—provided extensive comparisons both of the basic design and of the effects of temperature, flows and pressure on catalyst performance. Except when perturbed by significant variations in flows, agreement between the plant and the model was generally good and consistent with design assumptions.

The model had one striking success in predicting a significant improvement in Stage 2 performance if water and gas flows in the Stage were cut by 22%. When the flows were cut, the Plant responded as predicted.

A dynamic model of the process has also undergone limited testing and confirms broad trends observed with redistribution of deuterium in Stage 2.

This validation of the plant models has firmly established AECL's ability to provide accurate process designs for future, commercial CIRCE plants. With the design tools validated, designs of full-scale plants can be produced with a high level of confidence that their performance will be as predicted. With confidence in the design modelling, the exchange columns can be designed without unusually large margins of catalyst volume.

### ***Project Execution***

The PCP project was designed and constructed within schedule and budget. The demonstrated stability of the process and good availability of the PCP plant indicate that performance and operating costs of CIRCE plants will be highly predictable. Both the fidelity of the cost basis and the consistent operating experience directly establish the superior economics of the CIRCE plant process for future heavy water production.

The PCP's operation unequivocally demonstrated the soundness of the CIRCE technology and of the wetproofed catalyst on which it is based. All of the key aspects required for the future deployment of full-scale CIRCE plants have been fully demonstrated, including the design model validity, process integration with an industrial SMR plant, plant operating reliability and process stability.

While the superior economics of the CIRCE process for D<sub>2</sub>O production have now been established, it is not yet clear when the first full-scale plant will be committed. AECL has substantial quantities of heavy water in its stockpile—especially in the context of the much smaller D<sub>2</sub>O inventory of the Advanced CANDU Reactor™, AECL's next-generation CANDU. Reactor sales will, of course, determine when the stockpile needs to be augmented but suitable opportunities will be sought for deploying CIRCE technology, possibly as a convenient local source of make-up heavy water for existing or planned heavy water reactors. CIRCE is well suited to this supply role with the natural capacity of individual plants ranging up to 50 to 70 Mg per year production.

Overall, the significant achievement of the PCP program is that the knowledge gained from it provides AECL with confidence that CIRCE technology is now fully market-ready for commercial deployment either when needed to add to heavy water stockpiles or earlier if a suitable opportunity arises.

## **6. CECE Upgrading and Detritiation**

### ***Background***

The CECE process for water detritiation has been the subject of pilot-scale demonstrations in many countries<sup>1-8</sup> and has been investigated on a laboratory scale in several others.<sup>9-11</sup> The CECE process is a viable detritiation technology that can achieve high detritiation factors (DFs) as a front-end to a cryogenic distillation column (CD) or as a stand-alone plant. Two characteristics that make the CECE process an attractive detritiation option are the relatively uncomplicated and inexpensive Liquid-Phase Catalytic Exchange (LPCE) technology used to separate isotopes and the capability to be configured as a conventional distillation system, that is, simultaneously producing a product stream depleted of tritium and another product stream enriched in tritium.

In typical large-scale water detritiation facilities, the front-end water detritiation system is combined with a cryogenic distillation (CD) system to minimize the amount of deuterium removed from the process. For example, in a detritiation process coupled to an

operating CANDU® nuclear reactor, a front end process such as vapour-phase catalytic exchange (VPCE) or LPCE is used to transfer tritium from water to deuterium gas, which is then fed to the CD system. For detritiation attached to a CANDU, a detritiation process designed to remove 97-98% tritium is sufficient, and the DF for the CD is typically limited to 50 or less.

A significant advantage of the CECE process is that very high detritiation factors, which would exceed the demonstrated performance limits of cryogenic distillation, are readily achievable. This can be done without incurring excessive cost due to the combination of high separation factor for deuterium-tritium separation and the relatively low cost of catalyst.<sup>12</sup> Hence the CECE process offers considerable advantage for the reclamation of existing reserves of used heavy water through upgrading and detritiating, as it can readily provide more complete detritiation than alternative front-end processes.<sup>13</sup> For recycled heavy water to be reused in place of new water, 99 - 99.9%, or even greater, tritium removal is desirable (depending on the tritium content of the feed). For this purpose, the front-end CECE can be designed to provide a very high overall DF simply by adding catalyst, while the detritiation factor of the cryogenic distillation can be limited to about 99%. Also, since the CECE can enrich tritium in the feed gas to the CD, the CD can be sized to process a smaller feed flow rate. (Detritiation by cryogenic distillation is then within a range that is well proven and does not add excessive cost.)

### *Upgrading*

In 1998 June, AECL began operation in upgrading mode of a CECE Upgrading and Detritiation (CECE-UD) Demonstration Facility at Chalk River Laboratories using its wetproofed catalyst. The design feed rate ranged up to 25 Mg/a for 95 mol% D<sub>2</sub>O feed water. Table 1 gives other key design parameters.

**Table 1.**

**Key Design Parameters for the CECE Demonstration Facility**

<b>Item</b>	<b>Specification</b>
Electrolysis Cell	7.2 kA, 2.7 L/h D <sub>2</sub> O
Electrolysis Cell - maximum concentration	600 Ci/kg
Catalyst	75 L, AECL random catalyst
Catalyst Column diameter, operating temperature, operating pressure	0.05 m, ~50°C, 100-120 kPa
Upgrading Capacity	25 Mg/annum (maximum, varies with feed isotopic)
Detritiation Capacity	5 Mg/annum
Maximum Tritium-in-Deuterium concentration	100 ppm DT in D <sub>2</sub>
Storage Method for Recovered Tritium	Titanium metal

This Demonstration Facility was designed, built, and operated under the CAN/CSA N286 Quality Assurance Program series<sup>4</sup>, and a safety analysis report prepared to support the application to the Canadian nuclear regulator for operating approval. The facility was also designed with a computer-based control and data acquisition system to minimize operator interaction and enhance system performance and safety. A simple schematic of the CECE process for heavy-water upgrading appears in Figure 1. For the upgrading application, downgraded heavy-water is fed to an intermediate point in the LPCE catalyst column and a product stream of reactor-grade heavy water is removed at the bottom of the column. A small flow of natural water is fed to the top of the column to strip deuterium from the hydrogen gas

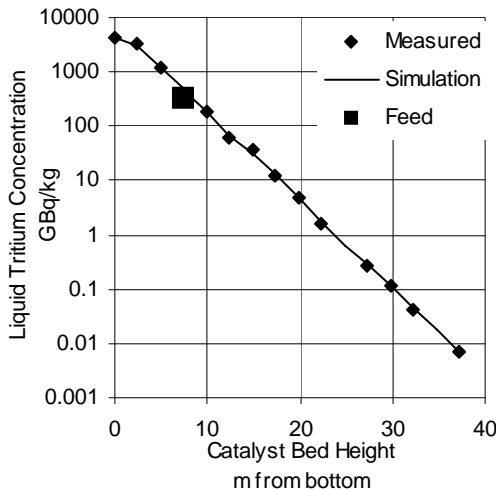


Fig. 3. LPCE Profile – DF = 46 000

tritium, which is purified and somewhat further enriched in tritium by diffusion through a palladium membrane before being packaged on titanium metal. The overhead product is tritium-depleted deuterium gas and this and oxygen from the electrolysis cell are converted to heavy water by a trickle-bed recombiner, using another version of AECL's wetproofed catalyst. Passing the oxygen stream through the gas-phase recombiner and mass-transfer column is even more important than with upgrading since this avoids contamination of the product with tritium in the oxygen either from water vapour or deuterium impurity. The scrubbing water stream enters the main detritiation column. The Demonstration Facility has been described in detail in a paper at the 2000 Pacific Basin Nuclear Conference<sup>13</sup>.

#### *Detritiation Factors*

Because it was designed to validate the CECE process for on-stream reactor detritiation, the Demonstration Facility was designed for a DF of 100. However, it proved possible to demonstrate the much higher levels of detritiation that would be required for detritiation of used heavy water down to levels acceptable for new reactor fills. Detritiation factors up to 56 000 were achieved. Figure 3 shows the experimental and fitted profiles for one test set where the DF was 46 000.

Excellent agreement was obtained between the measured tritium concentrations and the profile produced by computer simulation of the process.

Simulated verification of the process demonstrates that there is no discernable, adverse effect from the inevitable small fluctuations in liquid flow through the exchange columns and that there is no significant contamination with tritium carried in the oxygen stream.

#### *Status of CECE Technology*

The operation of the CECE-UD in both upgrading and detritiating modes establishes CECE technology for both applications. CECE upgraders appear to be lower cost than the traditional water distillation (D-W) units and the very deep levels of detritiation achievable with the CECE process allows tritiated heavy water from decommissioned reactors to be refurbished for use in new reactors.

above the main feed point as it flows up the column. Tritium follows the deuterium in this process and is removed with the reactor-grade heavy water product.

The oxygen from the electrolysis cell passes through a gas-phase recombiner and scrubber column to remove deuterated and tritiated hydrogen and water from the oxygen stream, from the electrolysis cell, before discharge.

#### *Detritiation*

The configuration of the Demonstration Facility for detritiation is somewhat different than for upgrading. The product from the vicinity of the electrolysis cell is now deuterium gas enriched in

## 7. Acknowledgement

Implementation of the PCP was a major undertaking. So many people contributed to its success in significant ways as to preclude individual recognition. Instead, we appreciatively acknowledge the contributions of many people currently or previously working for AECL, Air Liquide Canada, SNC-Lavalin, the Laframboise Group, and Howe-Baker Engineers. Their collective efforts have transformed the CIRCE concept into a proven process.

The CECE Demonstration Facility was almost as large an undertaking and we particularly wish to acknowledge our use of our colleagues' reports presented at the 2000 PBNC meeting<sup>13</sup> and at the 6<sup>th</sup> International Conference on Tritium Science and Technology in 2001<sup>14</sup>.

## REFERENCES

1. J.M. Miller, S.L. Celovsky, A.E. Everatt, W.R.C. Graham, and J.R.R. Tremblay, "Design and Operational Experience with a Pilot-Scale CECE Detritiation Process", Proceedings of the Sixth Topical Conference Tritium, Japan (2001).
2. D.A. Spagnolo, A.E. Everatt, P.W.K. Seto, and K.T. Chuang, "Enrichment and Volume Reduction of Tritiated Water Using Combined Electrolysis Catalytic Exchange", *Fusion Technology*, **14**, (1988), p 501.
3. C.J. Sienkiewicz and J.E. Lentz, "Recovery of Tritium from Water", *Fusion Technology*, **14**, (1988) p 444.
4. I.M. Shimizu, S. Kiyota and R. Ninomiya, "Hydrogen Isotope Enrichment by Hydrophobic Pt-Catalyst in Japan and Western Countries", *Bull. Res. Lab. Nucl. React.*, Special Issue No. 1, Tokyo Inst. Technol., (1992).
5. S. Isomura, K. Suzuki, and M. Shibuya, "Separation and Recovery of Tritium by Hydrogen-Water Isotopic Exchange Reaction", *Fusion Technology*, **14**, (1988), p 518.
6. K. Takeshita, Y. Wei, M. Kumagai, Y. Takashima and M Shimizu, "Application of H<sub>2</sub>/HTO Isotopic Exchange Method to Recovery of Tritium from Waste Water Generated in Spent Nuclear Fuel Reprocessing Plant", *Fusion Technology*, **28**, (1995), p 1572.
7. L. Greens, A. Bruggeman, L. Meynendockx, C. Parmentier, H. Belien, E. Ooms, D. Smets, J. Stevens, and J. Van Vlerken, "Separation of Tritium from Aqueous Effluents, Final Report", *EUR 1151 EN*, (1988).
8. U. Berndt, E. Kirste, V. Prech, F. Ruckert, A. Sameh, S.A. Ali, and H.J. Ache, "Final Report on the Tritium Enrichment Facility", *Report KfK 4780*, (1991).
9. G. Ionita and I. Stefanescu, "The Separation of Deuterium and Tritium on Pt/SDB/PS and Pt/C/PTFE Hydrophobe Catalysts", *Fusion Technology*, **28**, (1995), p 641.
10. B.M. Andreev, Y.A. Sakharovsky, M.B. Rozenkevich, E.P. Magomedbekov, Y.S. Park, V.V. Uborskiy, V.D. Trenin, I.A. Alekseev, O.A. Fedorchenko, S.P. Karpov, and K.A. Konoplev, "Installations for Separation of Hydrogen Isotopes by the Method of Chemical Isotopic Exchange in the Water-Hydrogen System", *Fusion Technology*, **28**, (1995), p 515.
11. V.D. Trenin, I.A. Alekseev, S.P. Karpov, S.D. Bondarenko, T.V. Vasyanina, K.A. Konoplev, O.A. Fedorchenko, V.V. Uborski, and T. Voronina, "Full-Scale Experimental Facility for the Development Technologies for the Reprocessing of Tritium Contaminated Light and Heavy Water Wastes by CECE Process and Cryogenic Distillation", *Fusion Technology*, **28**, (1995), p 767.

12. D.A. Spagnolo and A.I. Miller, "The CECE Alternative for Upgrading/Detritiating in Heavy Water Nuclear Reactors and for Tritium Recovery in Fusion Reactors, *Fusion Technology*, **28**, (1995), p 748.
13. C.J. Allan, A.R. Bennett, C.A. Fahey, C.H. Knight, A.I. Miller and J.M. Miller, "New Heavy Water Processing Technologies", Proceedings of the 12<sup>th</sup> Pacific Basin Nuclear Conference, 2000 October 29 –November 2, Seoul, Korea (2000).
14. W.R.C. Graham, A.E. Everatt, , J.R.R. Tremblay, J.M. Miller, and D.A. Spagnolo, "Demonstration of Very High Detritiation Factors with a Pilot-Scale CECE Facility", Presented at the 6th International Conference on Tritium Science and Technology, Tsukuba, Ibaraki, Japan, 2001 November 11-16. To be published in *Fusion Science and Technology*.



## ISOTOPES AS NATURAL TRACERS IN THE WATER CYCLE: EXAMPLES FROM THE CARPATHIAN BASIN

ISTVÁN FÓRIZS

*Laboratory for Geochemical Research,  
Hungarian Academy of Sciences  
H-1112 Budapest, Budaörsi út 45.,  
Hungary, forizs@geochem.hu*

**ABSTRACT.** Environmental isotopes are very good tracers for studying the subsurface water flow systems, and to determine the origin of water or pollutants. The stable isotope composition of precipitation linearly correlates with the air temperature, so the water infiltrated during the Ice Age (>10 000 years ago) into the subsurface aquifers is characterized by an isotope composition different from that infiltrated during the Holocene (>10 000 years) providing a tool to study groundwater mixing processes and vulnerability of water resources. The stable oxygen isotope composition of the Danube River shows seasonal variability giving a possibility to determine the Danube water transit time from the river to the production wells installed along the riverbank. The stable isotope composition of groundwater together with age determination can be used for paleoclimate reconstruction.

### INTRODUCTION

Environmental isotopes are the best tracers in the natural water cycle, and at the same time they are environment friendly, because introduction of artificial tracers into the flow system is not necessary. These isotopes can be grouped by different point of views, e.g. 1) stable or radioactive; 2) incorporated in the water molecule or not incorporated in the water molecule. Those incorporated in the water molecule gives information about the water itself (origin of water, water-rock interaction, mixing, evaporation, etc.), while the others give information about the solutes (including origin and fate of pollutants) or physical conditions during the infiltration of water.

The major stable environmental isotopes:  $^1\text{H}$ ,  $^2\text{H}$  (D),  $^3\text{He}$ ,  $^4\text{He}$ ,  $^6\text{Li}$ ,  $^7\text{Li}$ ,  $^{10}\text{B}$ ,  $^{11}\text{B}$ ,  $^{12}\text{C}$ ,  $^{13}\text{C}$ ,  $^{14}\text{N}$ ,  $^{15}\text{N}$ ,  $^{16}\text{O}$ , ( $^{17}\text{O}$ ),  $^{18}\text{O}$ ,  $^{20}\text{Ne}$ ,  $^{22}\text{Ne}$ ,  $^{32}\text{S}$ ,  $^{34}\text{S}$ ,  $^{35}\text{Cl}$ ,  $^{37}\text{Cl}$ ,  $^{79}\text{Br}$ ,  $^{81}\text{Br}$ ,  $^{86}\text{Sr}$ ,  $^{87}\text{Sr}$ .

The major radioactive environmental isotopes:  $^3\text{H}$  (T),  $^{14}\text{C}$ ,  $^{37}\text{Cl}$ ,  $^{39}\text{Ar}$ ,  $^{85}\text{Kr}$ ,  $^{129}\text{I}$ ,  $^{222}\text{Rn}$ ,  $^{226}\text{Ra}$ ,  $^{230}\text{Th}$ ,  $^{234}\text{U}$ ,  $^{238}\text{U}$ .

Among the above isotopes the most commonly used ones in hydrogeology are  $^2\text{H}/^1\text{H}$ ,  $^{18}\text{O}/^{16}\text{O}$ ,  $^{13}\text{C}/^{12}\text{C}$ ,  $^{15}\text{N}/^{14}\text{N}$ ,  $^{34}\text{S}/^{32}\text{S}$  (stable isotopes); T,  $^{14}\text{C}$  (radioactive isotopes).

### TERMINOLOGY

*Stable isotope* composition is always expressed in a special way as  $\delta$  (delta) value, what is a dimensionless number in parts per thousand:

$$\delta = \frac{R_{\text{sample}} - R_{\text{standard}}}{R_{\text{standard}}} * 1000 \text{ [‰]},$$

where R denotes the ratio of the heavy to light isotope (e.g.  $^2\text{H}/^1\text{H}$  or  $^{18}\text{O}/^{16}\text{O}$ ) in the sample and international standard, respectively. For the major material types international standards with known isotope compositions are used, e.g. for water the international standard is the Vienna

Standard Mean Ocean Water (VSMOW) distributed by the International Atomic Energy Agency. For instance oxygen composition of a water sample is reported as  $\delta^{18}\text{O}$  value in [‰]<sub>VSMOW</sub>, and in the case of other elements it is done in similar way ( $\delta\text{D}$ ,  $\delta^{13}\text{C}$ ,  $\delta^{15}\text{N}$ , etc).

The stable isotope composition is usually measured by gas-source mass spectrometers, less frequently by solid-source mass spectrometers.

Concentrations of *radioactive isotopes* are reported in different way regarding different isotopes. For examples: 1) tritium is reported in tritium unit, TU, where 1 TU = 1 tritium among  $10^{18}$  hydrogen atoms; 2)  $^{14}\text{C}$  is reported in percent modern carbon, pmC, where “modern carbon” is defined as 100%  $^{14}\text{C}$  activity of a wood grown in fossil- $\text{CO}_2$ -free environment (just before the  $\text{CO}_2$  emission from firing coal and crude oil increased by magnitudes, for more details and other isotopes see [1]).

The content of radioisotopes are usually measured by scintillation methods, but recently the accelerator mass spectrometry is getting to be more widely used as before.

### THE WATER CYCLE

The majority of the water is accumulated in the oceans. Clouds are formed from the vapour coming mainly from the oceans and in less amount coming from the terrestrial areas by evaporation and transpiration. Liquid (rain) and solid (snow) precipitation fall to the surface partly gets back to the oceans through rivers, and partly infiltrates into the ground (a very small part evaporates). The infiltrated groundwater moves from the recharge (infiltration) area through the flow path to the discharge area, where it gets back to the surface. These flow paths vary greatly, in some of them water spends only few days while in others tens of thousands of years. During the whole way of the water both the water molecules and the solutes have characteristic isotope composition determined by the physical and chemical processes and the rock-water interaction. If we know these characteristics then measuring the isotope composition of a water sample and/or its solutes, we can tell a lot about them.

#### *Isotopic characteristics of the precipitation in the Carpathian Basin*

There is an indirect linear relationship between the stable isotope composition of the precipitation ( $\delta\text{D}$ ,  $\delta^{18}\text{O}$ ) and the mean annual or monthly temperature of the air (T) on global scale and local scale as well (see e.g. [1] pp. 64-65, or [2]). The decreasing temperature comes together with decreasing  $\delta^{18}\text{O}$  and  $\delta\text{D}$  values, with other words as the temperature of the air decreases the precipitation becomes more depleted in heavier isotopes of hydrogen and oxygen.

In the Carpathian Basin the first study on the T- $\delta^{18}\text{O}$  and T- $\delta\text{D}$  relationships was made by Deák [3] who measured the stable isotope composition of precipitation collected at Abádszalók (Great Hungarian Plain) between 1977 and 1988. He found that  $\delta^{18}\text{O}_{\text{monthly}} = 0.37 \cdot T_{\text{monthly}} - 12.8\text{‰}$ , where T is temperature in °C (Fig. 1). Palcsu et al. [4] have got similar correlation for precipitation collected in Debrecen (Hungary) in the years 2001 and 2002:  $\delta^{18}\text{O}_{\text{monthly}} = 0.28 \cdot T_{\text{monthly}} - 11.6\text{‰}$ . These relationships are not far away from the global relationship:  $\delta^{18}\text{O}_{\text{monthly}} = 0.338 \cdot T_{\text{monthly}} - 11.99\text{‰}$  ([1], p. 64).

According to this relationship the stable isotope composition of precipitation at a location varies seasonally. The precipitation in wintertime is isotopically very light, while summertime it is rather heavy. Deák measured  $\delta^{18}\text{O}$  values between -2‰ and -22‰ [3]. Considering the mean annual stable isotope composition of precipitation, if the climate changes it changes as well mostly according to the above relationship. As a result of this

rule, there is a great difference between the stable isotope composition of today's precipitation and that of the Ice Age, when the temperature was considerable lower (for details see chapter "Groundwater").

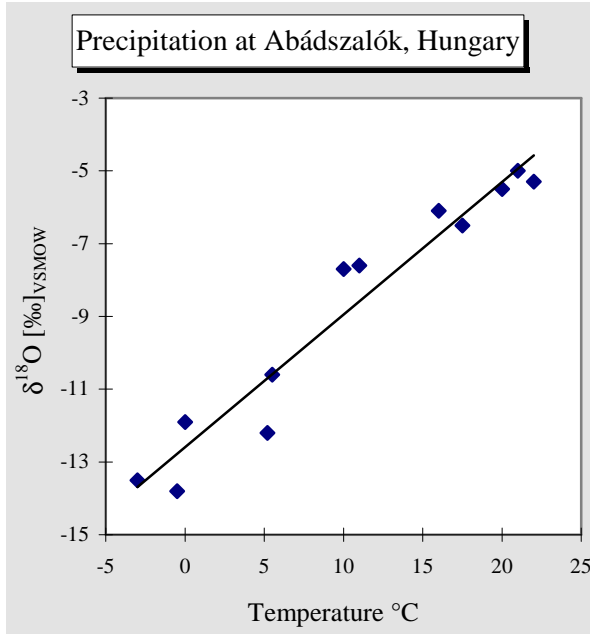


**Fig. 1.** The linear relationship between the mean monthly air temperature and the  $\delta^{18}\text{O}$  value of the precipitation collected at Abádszalók Meteorological Station (Hungary) between 1977 and 1988, [3].

not make big error if we use the same  $\delta^{18}\text{O}$  value for the fallen and for the infiltrated precipitation in the Carpathian Basin for paleoclimate reconstruction.

### *Groundwater*

Subsurface water resources are very important from the point of view of drinking water supply. The Carpathian Basin has a unique morphology; high mountains in an almost perfect circular form surround the basin. Water infiltrated in the mountains moves through the rock fissures and in the sedimentary layers to the lower parts, to the lowlands. These flow systems are discharged by the rivers, or on the Great Hungarian Plain there are places, where the old water gets to the surface forming shallow lakes or gets close to the surface. In both cases the majority of the water evaporates and the result is salt accumulation on the surface or in the soil. The transit time or the flow through time of the regional flow systems in the Carpathian Basin is usually few tens of thousands of years (20-40 ka). The intermediate and local scale flow systems have shorter, sometimes much shorter flow through time.

The latest glaciation (Ice Age) ended cca. 10 000 years ago, when the temperature changed a lot, raised more or less to the present level. According to this climate change there is a

The stable isotope composition of the infiltrating precipitation is rather close to the mean annual isotope composition of the precipitation. In the Carpathian Basin the bigger portion of the precipitation falls in spring and autumn and infiltration occurs mostly in these seasons. Summer-time, when the precipitation is isotopically heavy, the infiltration is not characteristic (it occurs rarely), therefore the average stable isotope composition of the infiltrated water is expected to be characterized by a little bit more negative  $\delta^{18}\text{O}$  value than that of the precipitation. And indeed, Deák has got average  $\delta^{18}\text{O}$  value of  $-9.1\text{‰}$  for precipitation of 12 years (1977-1988) and  $-9.3 \pm 0.4\text{‰}$  for shallow groundwater in Hungary [3]. It is worth mentioning that the difference between the two values is within the uncertainty of the measured numbers. So we do

great difference between the  $\delta^{18}\text{O}$  values of the groundwater infiltrated in the Ice Age and the groundwater infiltrated during the latest 10 000 years (Holocene). In Hungary the  $\delta^{18}\text{O}$  value of the Holocene infiltrated groundwater varies between -9‰ and -10‰ depending on the geographical area, while that of the Ice Age infiltrated groundwater varies between -11‰ and -14‰ depending on the time of infiltration and also on the geographical area.

Usual problem is the overexploitation of groundwater, when the amount of abstracted (exploited) water is higher than what the aquifer can provide, and as a result, the potentially or actually polluted near surface water flows down to the aquifer and mixes to the deeper water. In the Carpathian Basin in many cases this deep groundwater was infiltrated in the Ice Age, while the near surface water is a young Holocene water, so the stable isotope compositions of the two types of water differ, and monitoring the  $\delta^{18}\text{O}$  value of the exploited water allows us to catch the arrival of the down-flowing water far before the arrival of any pollution front.

A good example for this phenomenon is the Újkígyós Regional Water Works situated on the Great Hungarian Plain. The production wells had been installed into the Maros/Mureş alluvial fan close to the villages Újkígyós and Szabadkígyós [5]. In the original conditions the area is a regional discharge area of the flow system in the Maros/Mureş alluvial fan. The piezometric head of the deeper groundwater was higher than those of the shallow ones, so the deeper groundwater, which is an old, Ice Age infiltrated groundwater, could get to nearby the surface, where it mixed with the infiltrating modern precipitation. The start of the exploitation changed the conditions a lot in the depth range of 0-80 meters (see Figure 2). The piezometric head (water pressure) in the exploited aquifers decreased so much

that the shallow groundwater (in some places polluted by nitrate) could seep down and mix to the ascending old groundwater.

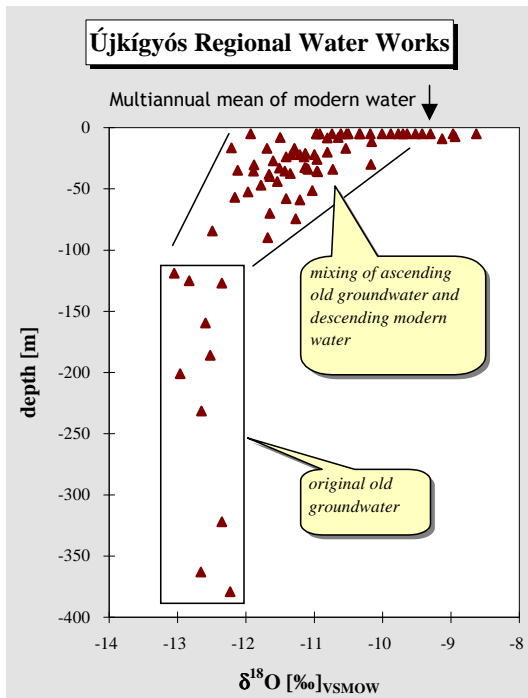


**Fig. 2.** The  $\delta^{18}\text{O}$  value of the groundwater vs. depth in the area of the Újkígyós Regional Water Works in 1992.

Below 100 m down to 400 m the  $\delta^{18}\text{O}$  values of the groundwater varies between -12‰ and -13‰. This is the original old groundwater (20-30 ka according to radiocarbon age determinations). This water mixes with the descending shallow groundwater resulting in  $\delta^{18}\text{O}$  values between -10‰ and -12.2‰ in the depth of 20-80 meters. The multiannual mean  $\delta^{18}\text{O}$  value of the infiltrating precipitation is -9.3‰.

*Rivers and riparian resources*

Riparian water resources along the river banks also have great importance, because many people are supplied with drinking water from this kind of water resources including, for example, the inhabitants of Budapest (almost two million people), capital of Hungary.

The catchment area of the Danube River upstream from the Great Hungarian Plain is mostly the high elevation Alps, so the Danube water is isotopically lighter (mean  $\delta^{18}\text{O}$  value is  $-11\text{‰}$ ) than the local meteoric water ( $-9.3\text{‰}$ ) providing a tool for tracing the flow of river water into the riparian aquifers and its mixing to the background water, latter one is infiltrated from precipitation.

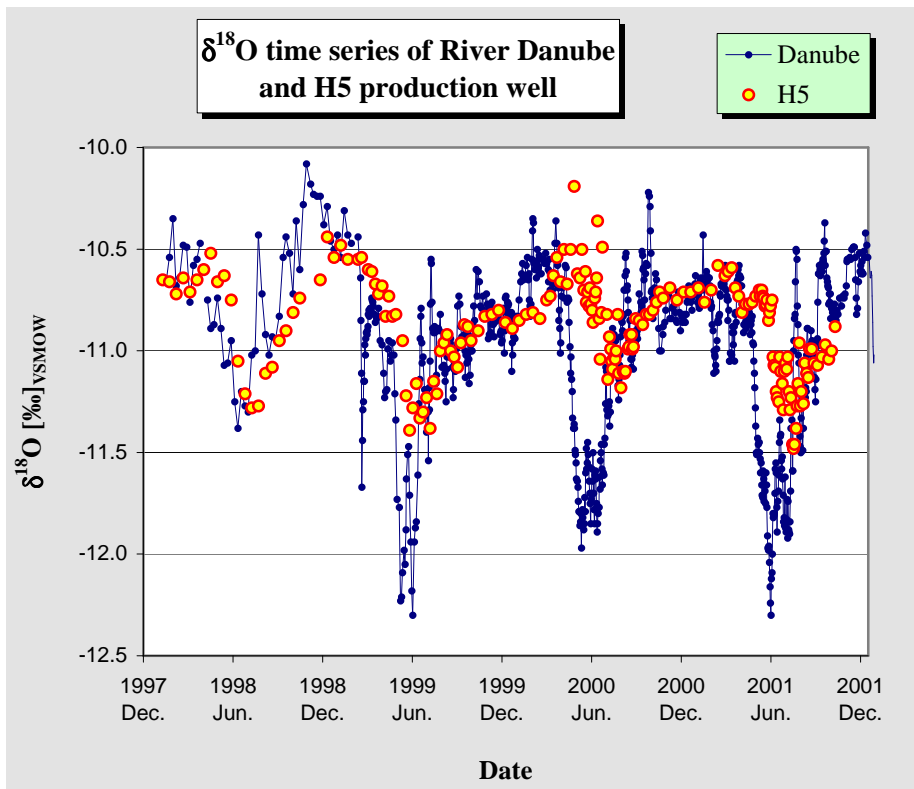


**Fig. 3.** The  $\delta^{18}\text{O}$  time series of the Danube River at Budapest and of the Halásztelek-5 (H5) production well on the Csepel Island (south of Budapest) in the years of 1998-2001.

The stable isotope composition of the Danube River has special feature. It has a seasonal variation, which is almost the opposite to that of the precipitation. The most negative  $\delta^{18}\text{O}$  values occur usually in May-July (see Fig. 3), because the precipitation in the high elevation Alps fallen in wintertime (in the form of snow) melts and gets to the Danube in this part of the year. In wintertime on the high elevation parts of the catchment area the air temperature is continuously below the freezing point, so the precipitation is snow, which does not get to the river in this time, so the Danube river at Budapest has a water originat-

ing only from the shallowest groundwater of the lower part of the catchment area. This groundwater is recharged from the whole year precipitation, therefore the  $\delta^{18}\text{O}$  value of the Danube River in wintertime is more positive than in summertime.

This seasonality in the stable isotope composition of the Danube River provides a good tool to calculate some hydrodynamic parameters of the riparian flow system. Production wells close to the riverbank exploit mostly river water (close to 100%). If we measure the time series of the stable isotope composition of the exploited water and compare it to that of the river water, then we can calculate the transit time of the river water to the production well. Figure 3 shows a good example, where the time series of the  $\delta^{18}\text{O}$  value of the H5 production well has a delay comparing to that of the Danube. This delay is shows the transit time. Beside this delay, the amplitude of the  $\delta^{18}\text{O}$  curve of the H5 smaller, which is related to the dispersion phenomenon. Applying appropriate mathematical formulations describing the dispersion, we can calculate the transit time with an uncertainty of  $\pm 1\text{-}2$  days [6].

The average  $\delta^{18}\text{O}$  value of the Danube for the period of 1998-2002 at Budapest is  $-10.9\text{‰}$ , which differs from  $\delta^{18}\text{O}$  value the infiltrated precipitation in Hungary. On the Csepel Island (a river island south of Budapest) the shallowest groundwater is exploited for providing drinking water. This water is a mixture of river water and background water, latter is an infiltrated precipitation. In this area the  $\delta^{18}\text{O}$  value of the infiltrated precipitation is between  $-9\text{‰}$  and  $-9.5\text{‰}$ , which differs considerable from the mean  $\delta^{18}\text{O}$  value of the Danube water. Using a two component mixing model based on the  $\delta^{18}\text{O}$  value of the shallowest groundwater of the Csepel Island we can calculate the mixing ratio of 'river water'/'background water' [7]. These data are very important for the validation of the three dimensional hydraulic model of the area under construction at the Budapest Technical University.

#### **PALEOCLIMATE APPLICATIONS**

When we know the relationship between the temperature and the stable isotope composition of the infiltrating water, then we can use it for paleotemperature reconstruction. Measuring the stable isotope composition of groundwater of a regional flow system (any flow system with a long enough flow through time), we can calculate the air temperature of the infiltration area for the time of infiltration. If we measure the age of water by radiocarbon (or other) method, then we can reconstruct the air temperature variation of the infiltration area in the past. Since temperature is one of the main parameters of the climate, in this way we can infer climate change happened in the past.

Figure 4 shows the stable oxygen isotope composition vs. calculated radiocarbon age of some groundwaters of deep aquifers on the Csepel Island (river island south of Budapest). It is interesting to notice that samples with the most negative  $\delta^{18}\text{O}$  values are not the oldest ones. Both younger and older samples have less negative  $\delta^{18}\text{O}$  values. Although the radiocarbon age determination has big uncertainty (uncertainty originating only from the analytical error is indicated on the figure 4, uncertainty of the correction method is not indicated, but it is bigger), the variation of  $\delta^{18}\text{O}$  values by time showed on Fig. 4 clearly demonstrates that the temperature changed in that period of time from less cool to cooler and back to less cool. We must know that the mean temperature was not the same during the Ice Age. There were cooler and less cool periods. The last cooler period was the Würm III between about 29 000 and 18 000 years BP (before present). The three points, which lie in the Würm III period have more negative  $\delta^{18}\text{O}$  values than those, which lie outside of this period. One point on the left side and one on the right side are outside the Würm III. From

the  $\delta^{18}\text{O}$ -T relation [3] we calculated the mean annual air temperature of the infiltration area (Fig. 4). If the  $\delta^{18}\text{O}$ -T relation determined in the 20<sup>th</sup> century was valid in the Ice Age as well, then we can conclude, that the mean annual temperature in a part of the Würm III was lower than zero °C.

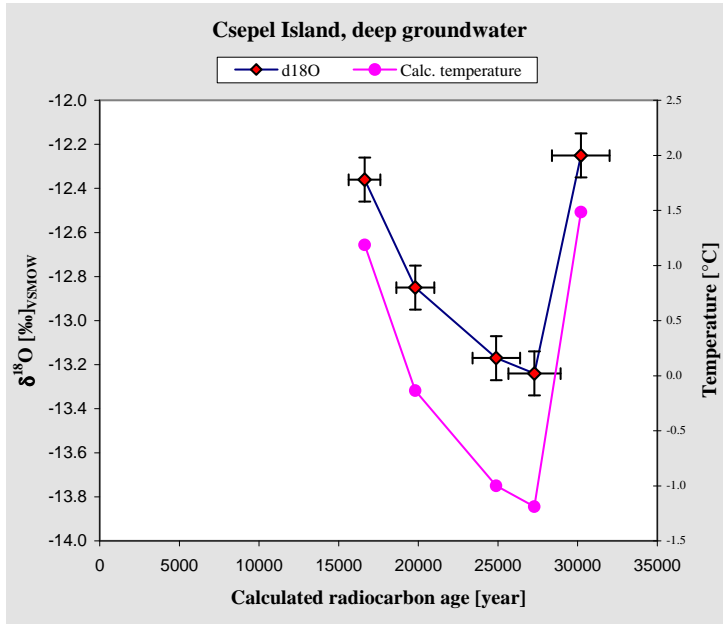


**Fig. 4.** The stable oxygen isotope composition and calculated air temperature vs. calculated,  $^{13}\text{C}$  corrected radiocarbon age of some old deeper groundwater on the Csepel Island (south of Budapest).

The stable isotope composition of river water reflects the climate of its catchment area. Although the river water flows away, it does not remain in time, shells of molluscs living in the river are in somehow isotopic equilibrium with the water, so the isotopic composition of the remaining carbonate shells in the river sediments can be a good proxy for the climate of the catchment area.

Since the catchment area of the Tisza River is lower than that of the Danube, the annual mean  $\delta^{18}\text{O}$  value of the Tisza is less negative than that of the Danube. Molluscs grow their carbonate shells from about April to October. If we consider the difference between the  $\delta^{18}\text{O}$  values of the two rivers in this period, it is 1.5‰ [8]. This difference is well reflected by the stable oxygen isotope composition of carbonate shells of Unionidae living in these rivers (Fig. 5). The difference between the mean  $\delta^{18}\text{O}$  values of shells of the Danube and Tisza Rivers is also 1.5‰. This nowadays difference between the two rivers is good basis for studying whether the climate on the catchment areas changed in the same way or not. We can study this problem by measuring the  $\delta^{18}\text{O}$  values of the shells in the Holocene and Ice Age sediments of the two rivers.

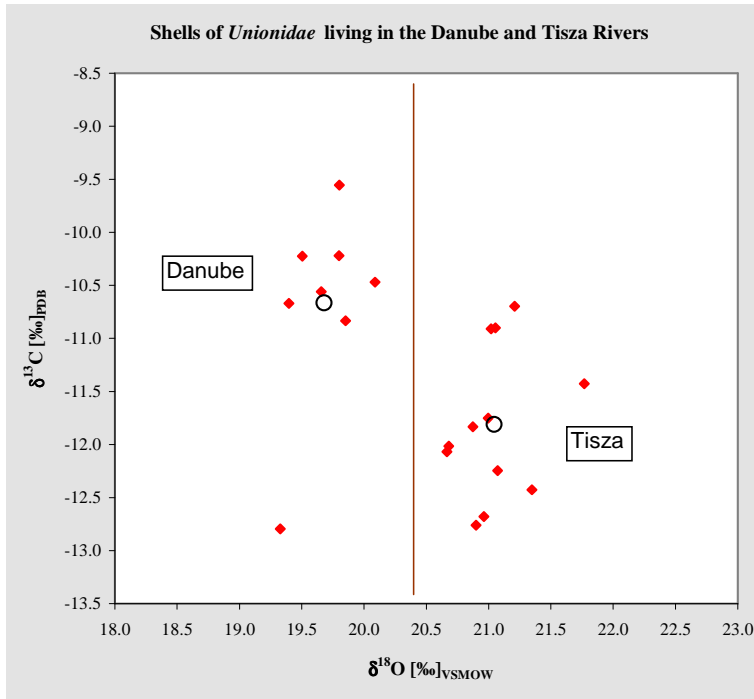


**Fig. 5.** The stable carbon isotope composition vs. stable oxygen isotope composition of carbonate shells of *Unionidae* molluscs living in the Danube and Tisza rivers. Samples were collected in the year 2001. The big open circles indicate the average values for the Danube and Tisza groups.

#### ACKNOWLEDGEMENTS

The author thanks the great help of Tamás Berecz (Ph.D. student at the Eötvös University) regarding the isotope hydrogeochemical research made on the Csepel Island. The isotope hydrological research of the Danube and Tisza rivers has been funded by the Hungarian Scientific Research Fund (project Nr. T 035032).

#### REFERENCES

- [1] Clark, I., Fritz, P. 1997. Environmental Isotopes in Hydrogeology. Lewis Publishers, Boca Raton – New York
- [2] Siegenthaler, U., Matter, H.A. 1983. Dependence of  $\delta^{18}\text{O}$  and  $\delta\text{D}$  in precipitation on climate. In: Palaeoclimates and palaeowaters: A collection of environmental isotope studies. IAEA, Vienna, p. 37-51
- [3] Deák, J. 1995. Groundwater recharge studies on the Great Hungarian Plain by environmental isotope data. VITUKI (Water Resources Research Centre, Institute of Hydrology) Report, Budapest (in Hungarian)



- [4] Palcsu, L., Svingor, É., Szántó, Zs., Molnár, M., Futó, I., Major, Z., Rinyu, L. 2003. Isotopic composition of precipitation in Hungary in 2001 and 2002. *Hydrological Processes*, special issue "International Symposium on Isotope Hydrology and Integrated Water Resources Management, Vienna, 19-23 May 2003" (manuscript submitted).
- [5] Deák, J., Fórizs, I., Deseő, É., Hertelendi, E. 1993. Origin of Groundwater and Dissolved Ammonium in SE Hungary: Evaluation by Environmental Isotopes. In: *Tracers in Hydrology*, IAHS Publ. no. 215, p. 117-124.
- [6] Małozzewski, P., Moser, H., Stichler, W., Bertleff, B., Hedin, K. 1990. Modelling of groundwater pollution by river bank filtration using oxygen-18 data. In: *Groundwater Monitoring Management*. IAHS Publ. no. 173: Wallingford; p. 153-161.
- [7] Fórizs, I., Deák, J. 1998. Origin of bank filtered groundwater resources covering the drinking water demand of Budapest, Hungary. In: *Application of isotope techniques to investigate groundwater pollution*, IAEA-TECDOC-1046, Vienna, pp.133-165.
- [8] Fórizs, I., Juhász, P. (2002) Differences in the climates of catchment areas as reflected by isotopic characteristics of the Danube and Tisza Rivers, Hungary. *Abstracts, VI Isotope Workshop*. Tallinn, 29 June – 4 July, p. 32-33.

## **ANALYSIS AND MODELLING OF MOLECULAR MASS TRANSFER FROM PLASTIC MATERIALS INTO ENVIRONMENTAL SYSTEMS**

**BRANDSCH J., BRANDSCH R., MERCEA P., PIRINGER O.**

*FABES Forschungs-GmbH, Schragenhofstraße  
35, D-80992 München*

**ABSTRACT.** Plastic materials contain a variety of compounds which can diffuse into their environment. In order to guarantee the protection of health many interdisciplinary research activities are necessary. Typical examples of such activities are presented which cover high performance instrumental trace analysis in combination with theoretical models for estimation of mass transfer processes occurring in many practical applications.

### **1. Introduction**

The early ages of man are classified according to the most important materials used for making tools and other articles. After the *Stone Age*, the *Bronze Age* and the *Iron Age* a continual enlargement of the material variety occurred. The biggest enlargement came during the last century with the plastic materials. The enormous impact of these materials on all facets of life justify to speak now of a *Plastic Age*. The world-wide plastic consumption increased from 86 million tons in 1990 to 155 mill. tons in 2001 with a prognosis of 258 mill. tons in 2010.

As a result of today's multitude of plastic applications there is a corresponding enormous variety of plastic materials. The polymer matrix as well as the incorporated additives can be made to differ in such a variety of ways with respect to their chemical composition and structure, that one finds or can develop a tailor made product for every application.

The widespread use of plastics has not been achieved without large-scale investment in research and development. But currently a change in the focus of these activities can be observed. That means, the plastic producer is mainly interested in optimised low cost production and consequently in minimization of research and development (R&D) for new processes and applications. The appearing gaps demand new activity fields for independent R&D services (Figure 1). This paper presents a few results of such an activity focused on a specific demand for many application fields of plastic materials: the quality assurance from the viewpoint of the environment protection and the protection of human health.

The variety of tailor made products needs many processing aids and additives from all chemical classes: inorganic and metal-organic compounds used as catalysts, emulsifiers and other aids as well and organic compounds as additives in a large molecular mass range for stabilization of plastic materials during processing and application. Antioxidants and other stabilizers are by definition reactive substances and consequently many of their reaction products can be found in the polymer matrix.

All these compounds can in principle diffuse (migrate) from the plastic material into the neighbouring systems. Of special interest, due to their connection with human health are plastic materials used for packaging of foodstuffs and pharmaceutical products, household and agriculture products. With the aim of health protection in mind the organization of a research service is based on the following three fundamental supports (Figure 2): 1) plastic producing and converting industry, 2) health organisations and 3) research funds.

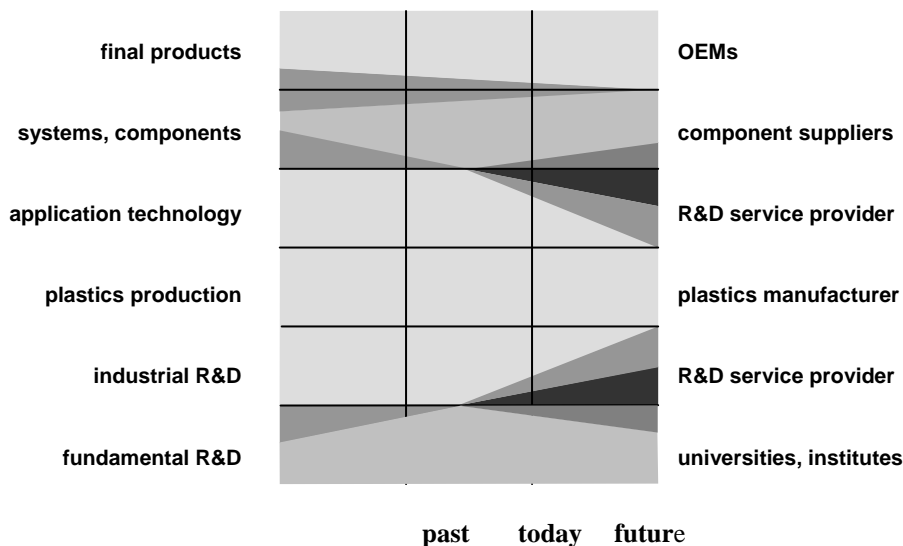


Fig. 1. Future demand of research and development services

The starting impulse comes from the health law which force industry to react by supporting research services to develop adequate methods for quality control. During these activities a permanent interaction and feedback between the three supports occurs with high impacts in the future structure and contents of them. Of particular actual interest for the organization of the research services are the harmonization of health law within the European Community (EU) and the globalization processes within the industry.

## 2. Experimental methods

### 2.1 Migration measurements

A primary step in the risk assessment of a chemical compound used in a plastic material is the knowledge of its migration rate from the polymer matrix into an adjacent medium, e.g. a liquid which simulates a food or a pharmaceutical product. Adequate devices (cells) made of glass or metal are used for migration measurements. A sheet or plastic film is brought in contact, one-sided or by full immersion with the liquid phase during a certain time at a certain temperature. In order to avoid interactions with the liquid, the plastic film or sheet can be covered with a solid powder with a high absorption capacity, e.g. Tenax. In this manner in addition to the diffusion rate of the migrant within the plastic sample the evaporation rate of the migrant from the plastic surface can be measured as well.

### 2.2 Identification and quantitative analysis of the migrants.

A considerable challenge is the qualitative and quantitative analysis of the migrants in both phases, the plastic sample and the liquid phase after the contact time as well. An immense power of instrumental methods for all kinds of chemical compounds exists actually. But one must never forget the necessity of optimisation all activity steps in a laboratory of research services with an interdisciplinary character ranging from pure chemical and technological

demands, through instrumental trace analysis and development of evaluation methods until their connection with the different laws for health protection. Consequently, a limited number of state of the art methods can be provided to answer the most important questions. Among these are high resolution gas-chromatography (GC) in combination with mass spectrometry (MS), high performance liquid-chromatography (HPLC) with ultra-violet (UV) or MS-detectors and direct MS and MS/MS for non-volatiles using electrospray ionisation sources (ESI). A few examples are shown in the following which illustrate the power of these instrumental methods used for specific analysis of migrated compounds in the range of ppb ( $\mu\text{g}/\text{kg}$ ) to ppm ( $\text{mg}/\text{kg}$ ).

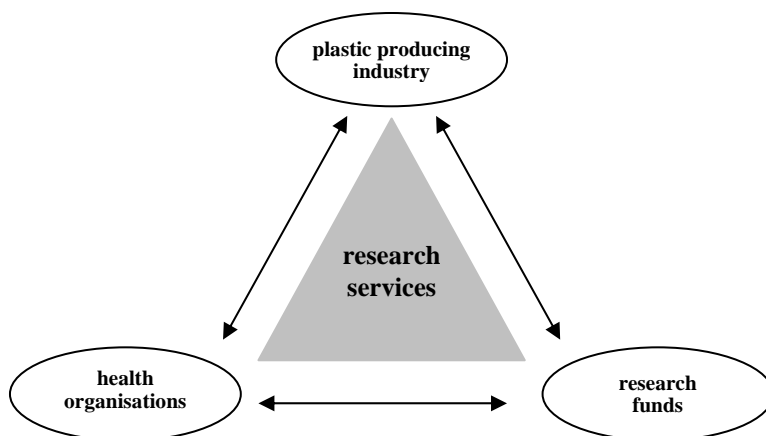
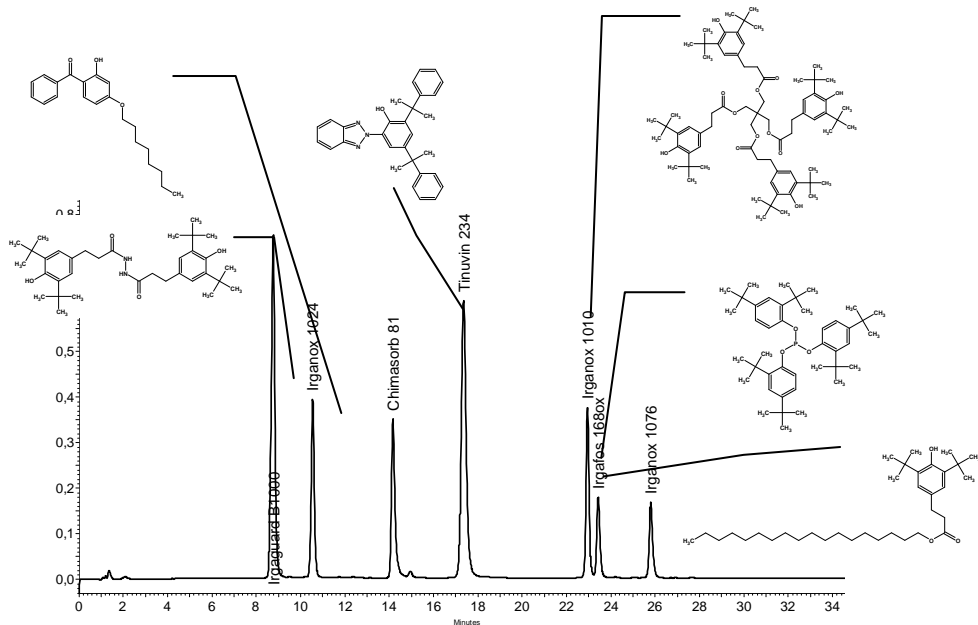


Fig. 2. The fundamental supports of the quality assurance activity.

For processing and long-term heat stabilization of many polymers hindered phenols are used preferentially as antioxidants. The efficiency of the phenolic antioxidants is very effectively improved in combinations with compounds of trivalent phosphor and derivatives from other chemical classes. The method of choice for the analysis of these classes of plastic additives is HPLC with UV detectors. In Figure 3 a typical HPLC-chromatogram of a mixture of antioxidants is shown.

Another class of efficient compounds for long-term heat stabilization contains the hindered amine light stabilizers (HALS) (Fig. 4). A very selective and sensitive method of analysis is the ESI-MS/MS method. The sample solution is introduced into the sprayer nozzle. With a nitrogen stream the liquid is sprayed into the ESI-source. The ions are separated in the ion-trap. Although the upper mass limit of the *Finnigan LCQ-MS/MS* used is  $m/z = 2000$ , the detection of molecules with relative molecular masses,  $M_r > 2000$  Dalton is also possible if multiple charged ions are produced.

This method allows the identification of all important decomposition products of HALS and impurities with  $M_r < 1000$  Dalton as well, by using the direct flow injection mode of operation without prior chromatographic separation. From a toxicological point of view only molecules with  $M_r < 1000$  are of primary interest for human exposure assessments and safety evaluations.



**Fig. 3.** HPLC-chromatogram of phenolic and phosphite antioxidants.

Organo-tin compounds represent an important class of metal-organic stabilizers in Poly(vinyl-chloride) (PVC). Mixtures of alkyl-tin-isoctylthioglycolates and their reaction and decomposition products appearing in very low concentrations in the migration solutions are a challenge for the analyst. Main components were monobutyl-tin-tris(alkylthioglycolate) and dibutyl-tin-bis(alkylthioglycolate) with R = C12 or C14:

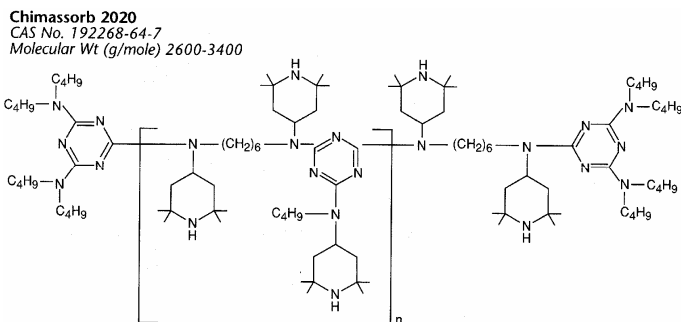
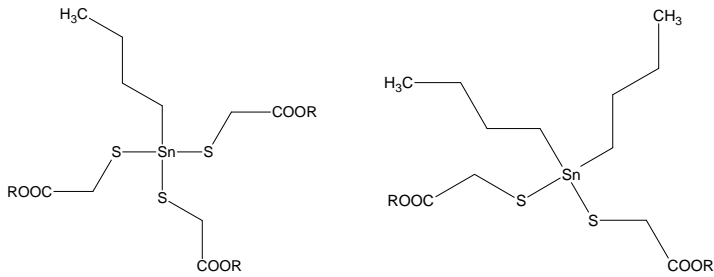
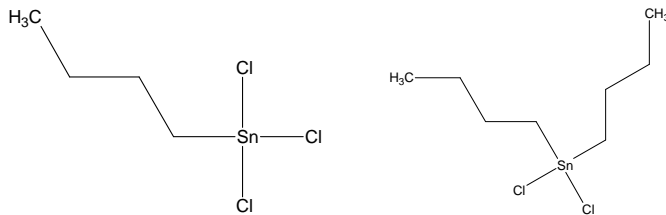


**Fig. 4.** A typical HALS-compound for which the ESI-MS is a very sensitive analysis method.

## ANALYSIS AND MODELLING OF MOLECULAR MASS TRANSFER



During processing the organo-tin stabilizers are chemically transformed and the migrating species changes from the alkyl-tin-(alkylthioglycolates) to alkyl-tin-chlorides:



In Figure 5 the ESI-MS spectrum of a typical organotin compound is presented showing the isotope pattern of Sn.

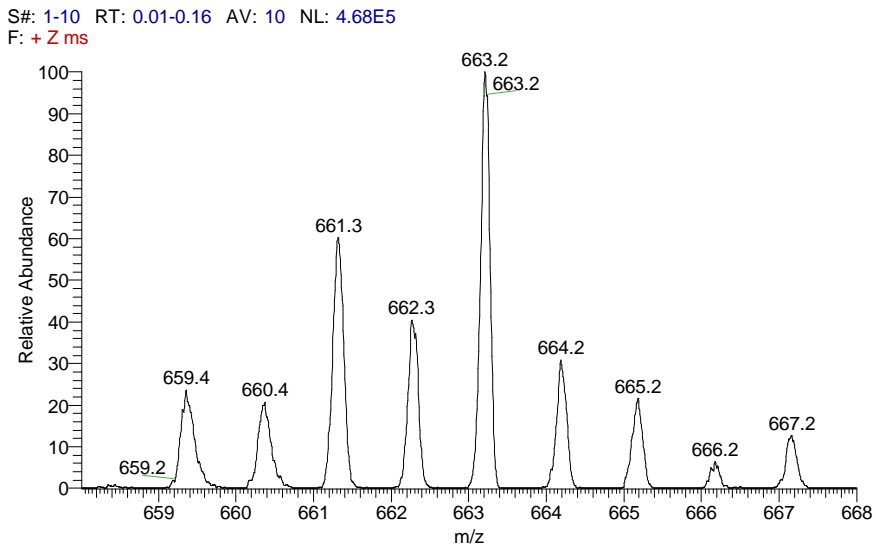


**Fig. 5.** The zoomed MS-spectrum of an organo-tin migrant with the Sn isotopes.

Decomposition products of the organo-tin stabilizers in PVC are toxicologically important specimens which must be considered in environmental systems, for example in closed rooms containing PVC-floors as shown later.

Last but not least, an ESI-MS analysis of a polymeric additive mixture is given in Figure 6, which shows the distribution of the masses and relative concentrations of the mixture components.

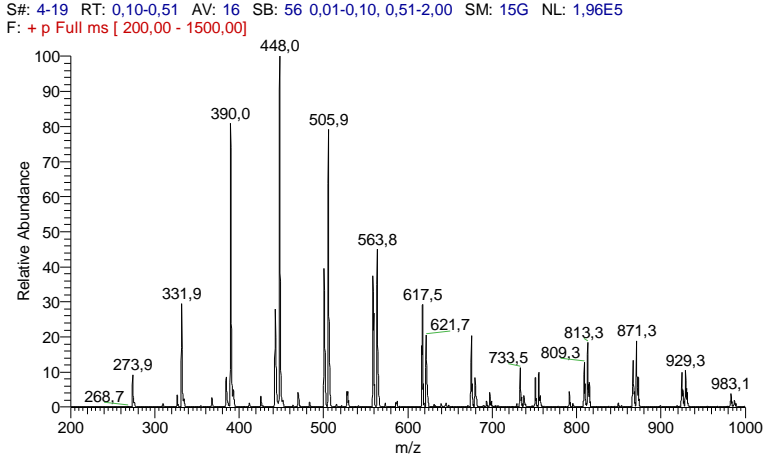


Fig. 6. ESI-MS spectrum obtained with a polymeric additive migrated from Polyethylene into ethanol.

Polymeric additives are of increasing importance for future developments due to their lower migration rates in comparison with low molecular additives and other technological advantages.

### 3. Migration modelling

The few examples shown above emphasize the complexity of the required experimental measurements and consequently the high costs of quality assurance in these applications. But the mass transport of compounds solved in plastics is a predictable physical process if a set of assumptions is fulfilled. The molecular transport generally obeys Fick's diffusion laws and this opens the possibility of modelling the migration of the solutes from plastic into the environment. Let us consider a plastic sheet (P) in contact with a liquid (L) as an adequate system for modelling these processes. Fick's 2<sup>nd</sup> diffusion equation:

$$\frac{\partial c}{\partial t} = D_P \frac{\partial^2 c}{\partial x^2} \quad (1)$$

provides an analytical solution for many practical applications [1]:

$$\frac{m_{L,t}}{A} = c_{P,0} \rho_P d_P \left( \frac{\alpha}{1+\alpha} \right) \left[ 1 - \sum_{n=1}^{\infty} \frac{2\alpha(1+\alpha)}{1+\alpha+\alpha^2 q_n^2} \exp\left(-D_P t \frac{q_n^2}{d_P^2}\right) \right] \quad (2)$$

with  $\alpha = \frac{1}{K_{P,L}} \frac{V_L}{V_P} = \frac{c_{L,\infty}}{c_{P,\infty}} \frac{\rho_L}{\rho_P} \frac{V_L}{V_P}$ ,  $K_{P,L} = \frac{c_{P,\infty}}{c_{L,\infty}} \frac{\rho_P}{\rho_L}$  and  $\tan q_n = -\alpha q_n$

where:  $m_{L,t}$  = mass of migrant in L after time t, A = area of P in contact with L,  $c_{P,0}$  = initial concentration of migrant in P,  $\rho_P$  = density of P,  $\rho_L$  = density of L,  $D_P$  = diffusion coefficient of

migrant in P,  $t$  = migration time,  $d_p$  = thickness of P,  $V_p$  = volume of P,  $V_L$  = volume of L,  $c_{p,\infty}$  = equilibrium concentration of migrant in P (w/w),  $c_{L,\infty}$  = equilibrium concentration of migrant in L (w/w),  $K_{p/L}$  = the partition coefficient of the migrant between P and L, and  $q_n$  = the non-zero, positive roots of the transcendental equation.

### 3.1 A polymer specific mass transport constant

One key parameter in the above equation is the diffusion coefficient  $D_p$ . There are enormous differences between the  $D_p$ -values within the actually known plastic materials. Despite of a large scientific literature about diffusion coefficients [2], a prediction of  $D_p$ -values is seldom possible due to the many unknown parameter values requested by these models. Indeed the  $D_p$ -value depends on many parameters but for practical applications only equations for  $D_p$ -estimation with a very limited set of parameters which can easily be provided are useful. To pursue the goal of obtaining a simple formula for the estimation of  $D_p$ , an equation for a reference amorphous polyolefin material was developed [3], [4], [5]:

$$D_p = 10^4 \exp \left[ A_p - 0.1351M_r^{2/3} + 0.003M_r - \frac{10454R}{RT} \right] \quad (\text{cm}^2/\text{s}) \quad (3)$$

with: 
$$A_p = A'_p - \frac{\tau}{T} \quad (4)$$

where  $M_r$ ,  $T$  and  $R = 8.3145 \text{ (J mol}^{-1}\text{K}^{-1}\text{)}$  represent, respectively, the relative molecular mass of migrant in Dalton, the temperature in K and the gas constant. The parameter  $A_p$  has the role of a “conductance” of the polymer matrix towards the diffusion of the migrant. Higher  $A_p$ -values in such polymers as Low Density Polyethylene (LDPE) with  $A_p \cong 10$  lead to increased  $D_p$  while in stiffer polymers, e.g. in High Density Polyethylene (HDPE)  $A_p \cong 7$  accounts for smaller diffusion coefficients for the same migrant at the same temperature. Whereas the mean diffusion activation energy for most additives in LDPE is well approximated with the reference activation energy  $E_A = 10454R = 86.7 \text{ kJ/mol}$  from equation (3), an additional account results for HDPE which is given with equation (4) and  $\tau > 0$  ( $A_p = 12 - 1577/T$ ). One important aim of our research activity is the determination of  $A_p$ -values for the actually used plastic materials [6].  $A_p$ -values are only little affected by the migrant structure and consequently equation (3) can be used with a characteristic  $A_p$ -value for a certain polymer in the whole range of  $M_r$ -values  $< 2000$ , which is of interest from the toxicological viewpoint.

## 4. Applications

### 4.1 Measurement and modelling of material properties

By fitting the migration curve calculated with the above equation (2) to the experimentally obtained migration points as shown in Figure 7, the  $D_p$ - and  $K_{p/L}$ -values for a given system at temperature  $T$  can be obtained and in addition the  $A_p$ -value of a not previously studied polymer matrix can be determined with equation (3). As an example, Figure 7a shows the migration behavior of di-octyl-phthalate (DOP) from a plasticized PVC-sample into iso-octane and the experimental data points are well described by the calculated curve.

A much lower migration value is observed, however, when Tenax is used as absorbant (Figure 7b). In this case the evaporation rate of DOP at the PVC surface competes with the diffusion rate of DOP in the polymer matrix and must be taken into account with the differential equation:



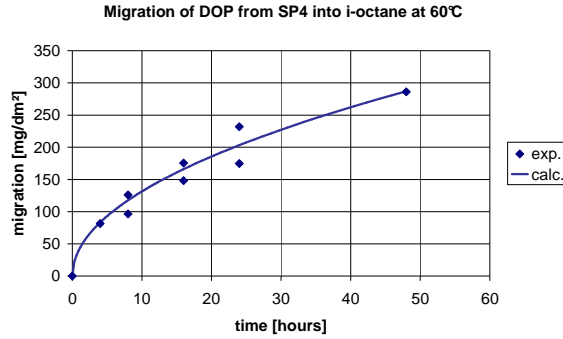


Fig. 7. a) Migration kinetic of DOP from PVC into iso-octane.

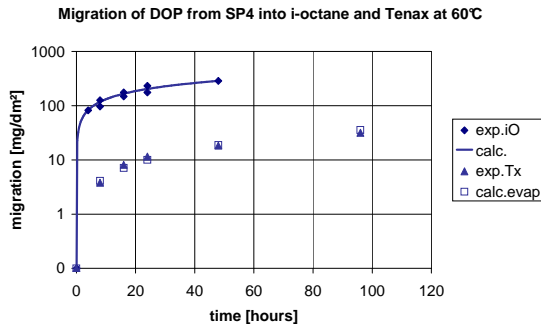


Fig. 7. b) Migration kinetic of DOP from PVC into Tenax in comparison with iso-octane.

$$-D_p \frac{\partial c_p}{\partial x} = k(c_{A,G} - c_{A,P})$$

(5)

and its analytical solution [1]:

$$\frac{m_{L,t}}{A} = c_{p,0} \rho_p d_p \left( \frac{\alpha}{1+\alpha} \right) \left[ 1 - \sum_{n=1}^{\infty} \frac{2L^2}{\beta_n^2 (\beta_n^2 + L^2 + L)} \exp\left(-D_p t \frac{\beta_n^2}{d_p^2}\right) \right] \quad (6)$$

with  $L = d_p k / D_p$  and  $\beta \tan \beta = L$ ,

where  $c_{A,G}$  and  $c_{A,P}$  are the concentrations of the migrant in the gas and polymer at the polymer surface, respectively,  $k$  is a transport coefficient and  $\beta_n$  are the positive roots of the above transcendental equation.

The different behaviour of the migration kinetic of the same migrant from the same polymer into two different environmental systems provides the way for modelling practical situations.

Due to the complexity of a specific situation concerning modelling of the mass transfer from a certain plastic material into a certain environment surrounding it, an user-friendly software for modelling such phenomena can be of great help. A corresponding software for modelling the migration from monolayers of plastic materials has been developed by FABES and is available as MIGRATEST Lite 2001. The use of migration modelling as an

additional tool for quality assurance in the large application field of plastics in contact with foodstuffs has been recently legalized in the EU Directive 2002/72/EC, Article 8 [7]. Future articles in this field cover the migration modelling from multilayer structures [9].

#### 4.2 *The emission of organo-tin compounds from PVC-floors into closed atmospheres.*

In order to exemplify the above described activities with an additional practical problem, the following study is summarized [8]. The basic aim of a project initiated by the German Plastic Industry was the estimation of consumer exposure with organo-tin species from PVC floorings based on the knowledge of the basic mass transfer phenomena. Of special toxicological concern is for example tributyl-tin-chloride for which a legal maximal concentration of  $0.5 \text{ mg/m}^3$  in the atmosphere of a PVC converting working area is allowed. It has been considered that the organo-tin species from the PVC flooring can be removed from the PVC/air interface by evaporation in the surrounding atmosphere in a room or by cleaning with aqueous media. Consequently two simulating media have been chosen, e.g. a solid absorbent (Tenax<sup>®</sup>) which takes up organo-tin species evaporating from the PVC flooring and water as contact medium during the cleaning process. The migration studies have been performed at  $40^\circ\text{C}$  to simulate worst case conditions. The organotin stabiliser was a technical mixture of monobutyl-tin-tris(alkylthioglycolate) and dibutyl-tin-bis(alkylthioglycolate), as shown above in section 2.2, with small impurities of mono- and dioctyl-tin-bis(alkylthioglycolate). The level of use of the organo-tin stabiliser in the PVC flooring was approx. 0,5%.

The alkyl-tin chlorides have been quantified in the PVC flooring by dissolution of the PVC matrix for example in tetra-hydro-furane (THF), precipitation of the polymer, derivatization and GC analysis. The migration experiments have been performed by full immersion in the migration cell at  $40^\circ\text{C}$  with water and by one-sided contact with Tenax. The following conclusions resulted from these measurements:

The migration of the organotin species into water decreases dramatically with increasing number of butyl groups in the order monobutyl-SnCl<sub>3</sub> > dibutyl-SnCl<sub>2</sub> > tributyl-SnCl > tetrabutyl-Sn. This observation is directly related to the water solubility (polarity) of the different organo-tin species, which increases with the number of Cl-atoms.

In opposition to the migration experiments into water, the migration of the organotin species onto Tenax increases dramatically with the increasing number of organic groups in this series. These observations are attributed to the decrease in evaporation rate of the different organo-tin species from the PVC surface with increasing number of Cl-atoms in the molecule. The character of the molecules changes from covalent to ionic with increasing number of Cl-atoms in the molecule.

The whole evaluation of these experiments were done by using the above considerations about the experimental and modelling steps. As a conclusion, the maximal concentration of tri-butyl-Sn-Cl in the room atmosphere under worst case conditions was < 1 % of the allowed toxicological limit.

## REFERENCES

- [1] Crank J., *The Mathematics of Diffusion*, 2<sup>nd</sup> ed., 1975, Clarendon Press, Oxford.
- [2] Mercea, P., *Models of diffusion in polymers*, Chapter 5, in Piringer, O.-G., Baner, A. L. (ed.), *Plastic Packaging Materials for Food.*, 2000, Wiley-VCH, Weinheim, New York.
- [3] Piringer O., *Evaluation of Plastics for Food Packaging*, Food Additives and Contaminants, *11*, 221-230, 1994.

- [4] Piringer, O.-G., Baner, A. L. (ed.), *Plastic Packaging Materials for Food.*, 2000, Wiley-VCH, Weinheim, New York.
- [5] Brandsch J., Mercea P., Piringer O.-G., *Modelling of Additive Diffusion Coefficients in Polyolefins.*, Chapter 4 in Risch, S. J., (ed), *Food Packaging – Testing Methods and Applications.*, 2000, ACS Symposium Series 753, American Chemical Society, Washington, DC.
- [6] Baunemann R., Brandsch J., Brandsch R., Mercea P., Piringer O., *Migrationsmodelle zur Bewertung von Kunststoffprodukten*, *Kunststoffe*, 93 (7), 22-25., 2003.
- [7] Hinrichs K., Piringer O., (Eds.), *Evaluation of Migration Models*, Final Report of the EU-project contract SMT-CT98-7513. Brussels 2001.
- [8] Baunemann R., Brandsch J., Piringer O., *Migration zinnorganischer Verbindungen aus PVC-Böden*. Studie im Auftrag von VKE, 2000.
- [9] Brandsch J., Mercea P., Piringer O., Rüter M., Tosa V., *Migration modelling as a tool for quality assurance of food packaging*, *Food Additives and Contaminants*, 19, Supplement, 29-41, 2002.

# MICROSCOPIC DYNAMICS IN CUPRATE SUPERCONDUCTORS: NMR AND NQR STUDIES

DETLEF BRINKMANN

*Physik-Institut, University of Zürich,  
CH-8057 Zürich, Switzerland*

**ABSTRACT.** The paper reviews some examples how the NMR/NQR spectroscopic technique can be applied to explore problems on the microscopic level in cuprate high-temperature superconductors. We are dealing with the following questions: Is there long-range magnetic order in these compounds? How do we detect the presence of antiferromagnetic fluctuations? Is the single-spin fluid model valid? What is the spatial symmetry of the pairing state? How do we confirm an inter-layer coupling in the cuprates? Are out-of-plane nuclei like Ba affected by the antiferromagnetic fields?

## 1. Introduction

The cuprate compounds  $\text{YBa}_2\text{Cu}_3\text{O}_7$ ,  $\text{YBa}_2\text{Cu}_4\text{O}_8$ , and  $\text{Y}_2\text{Ba}_4\text{Cu}_7\text{O}_{15}$  belong to those high-temperature superconductors which have most extensively been studied by Nuclear Magnetic Resonance (NMR) and Nuclear Quadrupole Resonance (NQR). These spectroscopic methods are apt to reveal details about the dynamics of solids at the atomic scale, hence, a wealth of information from these compounds has been collected during the last decade. A selection of some general review papers on this subject are References [1] to [6]. Our presentation will give a personal review of such studies mainly dealing with the compound  $\text{YBa}_2\text{Cu}_4\text{O}_8$ , known for its homogeneity and thermal stability, with many examples from the Zürich laboratory. The studies were performed in both the normal and the superconducting state thereby using various NMR isotopes (*e.g.*  $^{17}\text{O}$ ,  $^{63,65}\text{Cu}$ ,  $^{135}\text{Ba}$ ).

Our presentation will be organized like this. We will discuss, one after the other, several important characteristics of cuprate superconductors, each of them will be followed by a description of the appropriate NMR/NQR experiments or models that support or "prove" this feature. This way we will gain an overview of typical properties of cuprate superconductors.

## 2. Antiferromagnetic fluctuations

Cuprate superconductors form an unique class of superconductors quite different from conventional superconductors and metals because they can be derived from antiferromagnetic (AF) parent compounds whose magnetic order arises from  $\text{Cu}^{2+}$  spins in the  $\text{CuO}_2$  planes. For instance,  $\text{YBa}_2\text{Cu}_3\text{O}_7$  is obtained by doping  $\text{YBa}_2\text{Cu}_3\text{O}_6$  with oxygen. This process creates electron holes in the  $\text{CuO}_2$  planes and eventually destroys the AF long-range order. However, AF short-range order is still present in the superconductors and even in the superconducting phase.

How can we prove by NMR/NQR that there is no long-range magnetic order? We must perform an NQR experiment with the nuclei of plane Cu atoms. If this is done in zero external magnetic field, both Cu isotopes,  $^{63}\text{Cu}$  and  $^{65}\text{Cu}$ , yield a single NQR signal due to their nuclear spin  $3/2$ , with a frequency given by

$$\nu_Q = \frac{eQV_{zz}}{2h} \left( 1 + \frac{1}{3} \eta^2 \right)^{1/2} .$$

Here,  $eQ$  is the quadrupole moment of the respective isotope,  $V_{zz}$  and  $\eta$  are largest principle component and asymmetry parameter, respectively, of the electric field gradient tensor present at the Cu nucleus site. Since  $V_{zz}$  and  $\eta$  are the same for both isotopes, the ratio of the NQR frequencies,  $\nu_Q$ , must be exactly equal to the ratio of the quadrupole moments - if there are no internal magnetic fields! And this has been confirmed by experiment, that means: long-range magnetic order is absent in these compounds, at least on the time scale of NQR.

### 3. Relaxation by antiferromagnetic fluctuations

The next question is: "How do we know the presence of the AF fluctuations?" The short answer is: "Because the Cu spin-lattice relaxation time is so short!" Indeed, it is a central problem of NMR/NQR studies in cuprates how to explain properly the behavior of the Cu relaxation. I have discussed some of these issues at the 2nd PIM Conference in 2001 [7].

The electron spin fluctuations give a dominating contribution to the total plane Cu relaxation rate. This contribution is related to the imaginary part of the wavevector,  $\vec{q}$ , dependent dynamical spin susceptibility,  $\chi(q, \omega_0)$ , and it is given by the Moriya formula:

$$\left(\frac{1}{T_1 T}\right)_\alpha = \frac{\gamma_n^2 k_B}{2\mu_B^2} \sum_{\vec{q}, \alpha' \neq \alpha} F_\alpha(\vec{q}) \frac{\chi''_{\alpha\alpha'}(\vec{q}, \omega_0)}{\omega_0} \quad \text{where } F_\alpha(\vec{q}) = \left| \sum_j A_{j,\alpha\alpha'} \exp(i\vec{q} \cdot \vec{r}_j) \right|^2.$$

$F_\alpha(\vec{q})$  is the form factor,  $\omega_0$  is the nuclear resonance frequency,  $\alpha$  denotes the direction of quantization, *i.e.*, the direction of either the maximum component of the field gradient in NQR or of the steady magnetic field in NMR, and  $\alpha'$  is the direction perpendicular to  $\alpha$ .  $A_j$  is the on-site ( $\vec{r}_j = 0$ ) and transferred ( $\vec{r}_j \neq 0$ ) hyperfine coupling tensor for the nuclei under consideration. Therefore,  $1/T_1 T$  provides information about the  $\vec{q}$  averaged imaginary part of  $\chi(\vec{q}, 0)$ .

One of the first attempts to explain the temperature dependence of  $1/T_1$ , is the phenomenological MMP model by Millis, Monien, and Pines [6]. The essential assumption of this model is that the complex electron susceptibility,  $\chi(q, \omega_0)$ , consists of two contributions: the real and imaginary part describe the quasi-particle (normal Fermi-liquid-like) contribution and the AF correlation, respectively. Together with its variants, the model has, among others, quantitatively described the normal state relaxation of Cu, O, and Y in  $\text{YBa}_2\text{Cu}_3\text{O}_7$  and  $\text{La}_{1.85}\text{Sr}_{0.15}\text{CuO}_4$ .

During further studies, however, it turned out that a microscopic model is required to properly calculate the dynamic spin susceptibility. The  $t$ - $J$  model [9] is a good starting point, at least for compounds with moderate doping. Here,  $t$  denotes the hopping energy of the holes and  $J$  represents the strong repulsion between holes residing on the same square. When calculating the susceptibility, an essential point is how one is treating the AF correlation length which depends on temperature and doping. We decided to calculate  $\chi''(\vec{q}, \omega_0)$  for an AF structure within a constraint-free theory based on the presentation of the  $t$ - $J$  model in terms of Hubbard operators [10]. Both electron and AF spin correlation were taken into account. The model is able to reproduce the main features of the temperature and doping dependence of the correlation length in both the pure Heisenberg AF  $\text{La}_2\text{CuO}_4$  and in the doped compound,  $\text{La}_{2-x}\text{Sr}_x\text{CuO}_4$ . We then determined  $1/T_1$  for  $^{63}\text{Cu}$ ,  $^{17}\text{O}$ , and  $^{89}\text{Y}$  in  $\text{YBa}_2\text{Cu}_3\text{O}_7$ ; the results (see Fig. 1) are in good agreement with experimental data [11]. The spin gap effect is a separate topic which we have already discussed at the previous PIM conference [7] and which we will not repeat here.

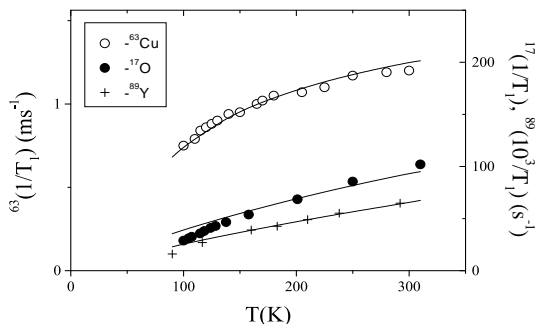


**Fig. 1.** Temperature dependence of the copper, oxygen, and yttrium relaxation rates in  $\text{YBa}_2\text{Cu}_3\text{O}_7$  (solid lines) compared with experimental data. From [11].

#### 4. The single-spin fluid model

When discussing NMR/NQR in the cuprates, one quite often assumes, within the framework of the  $t$ - $J$  model we mentioned above, that the pseudoparticles are Zhang-Rice singlets [5]: the holes due to doping are allowed to delocalize (with the hopping integral  $t$ ) and the hole spin forms a singlet state with the electronic Cu spin. Adopting this picture, one needs one degree of freedom to describe the physics at the atomic scale of cuprate superconductors; this is the single-spin fluid (SSF) model. What is the comment of NMR/NQR on this concept? The copper and oxygen Knight shift data favor this view, however, oxygen and yttrium relaxation anisotropy data do not fit into this picture.

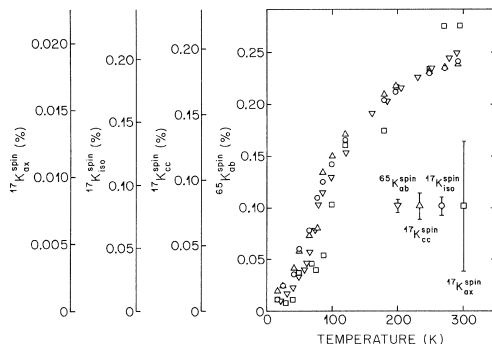


**Fig. 2.** Normalized Knight shift components of plane Cu and O in  $\text{YBa}_2\text{Cu}_4\text{O}_8$ . From [12].

In NMR experiments, the magnetic coupling between the nuclear spin and its electronic environment can be viewed as a coupling of the nuclear spin with a time dependent local magnetic hyperfine field generated by the electron spin and the electron orbital motion. The static part of this field gives rise to a magnetic NMR line shift which can be decomposed in a spin and an orbital part. The spin part is usually called the Knight shift which is a tensor. In high-temperature superconductors, the orbital shift is predominantly temperature independent, whereas the temperature dependent Knight shift is expected to vanish in the superconducting state due to singlet spin pairing.

The Knight shift of planar Cu and O in cuprate superconductors has been measured in several laboratories including our own studies of  $\text{YBa}_2\text{Cu}_4\text{O}_8$  [12]. The major result (see Fig. 2) is the following: The various shift components exhibit the same temperature dependence over a large temperature range extending from 8.5 K to about 300 K with a decline which starts already well above  $T_c$ . Thus, these data support the SSF model. We also found [12] that all Knight shift components of the chain Cu are proportional to the respective component of O, hence the chains also form a single-spin fluid, however, the susceptibilities of both systems are different. As already mentioned before, the plane oxygen and yttrium relaxation anisotropy data do not fit into the SSF model. Using the abbreviation  $W_{\square}/T_1$ , the anisotropy of the plane oxygen relaxation rate is defined as  $^{17}(W_{\parallel}/W_c)$  [with the magnetic field either in the plane or parallel to the  $c$  axis]. It displays a pronounced temperature dependence (*e.g.* [13]) while the SSF model predicts an almost temperature independent rate. Zha *et al.* [14] tried to explain the behavior of  $^{17}(W_{\parallel}/W_{c,\perp})$  in the framework of the MPP model by including additional next-nearest neighbor and incommensurate AF fluctuations. This model is able to describe the temperature dependence of  $^{17}(W_{\parallel}/W_{c,\perp})$  quite well. However, when calculating the ratio  $^{17}W_c/^{89}W_c$  for  $\text{YBa}_2\text{Cu}_4\text{O}_8$  by following the MPP model and including the new form factor proposed by Zha as well as the incommensurability, our result failed to reproduce the data.

As an alternative, we proposed [13,15] the presence of an additional relaxation mechanism which can provide a coherent description of the temperature dependence of both  $^{17}(W_{\parallel}/W_{c,\perp})$  and  $^{17}W_c/^{89}W_c$ . As shown in [13], there are enhanced charge fluctuations in the chain and the plane at temperatures which lie below the temperature associated with the opening of the spin gap [7]. These fluctuations provide an additional relaxation mechanism which is of quadrupolar origin. This would easily explain the temperature dependence of  $^{17}W_c/^{89}W_c$  since only  $^{17}W_c$  of oxygen is enhanced while yttrium, because of its spin 1/2, cannot couple to the charge fluctuations. Using a double irradiation method, we found that, below around 200 K, the relaxation rate of plane oxygen is not only driven by magnetic, but also significantly by quadrupolar fluctuations, *i.e.* low-frequency charge fluctuations. This implies that, with the opening of the pseudo spin gap, a charge degree of freedom is present in the electronic low-energy excitation spectrum. So, the SSF model is only partially correct: two degrees of freedom are involved in the system, one of them is the single-spin degree whereas the other one is the *charge* degree of freedom with predominantly oxygen character.

### 5. The spatial symmetry of the pairing wave function

We will now address the question whether measurements of spin-lattice relaxation and Knight shift provide evidence for a certain spatial symmetry of the pairing state. With the angular momentum denoted by  $l$ , one usually discusses the two cases:  $l = 0$  ( $s$  wave) and  $l = 2$  ( $d$  wave). Many experiments are compatible with  $d$  wave symmetry. There are several ways to check this symmetry with the aid of NMR/NQR although they are less straightforward than other techniques.

It is usually assumed that the susceptibility of the superconducting state,  $\chi_s$ , is related to the normal state susceptibility,  $\chi_n$ , which is taken as temperature independent, via the equation  $\chi_{s(T)} = Y_l(T) \chi_n$ . For  $l = 0$ ,  $Y_0(T)$  is called the Yosida function, it describes the conventional BCS weak coupling spin singlet  $s$  wave pairing mechanism. Because the calculation of  $Y_l(T)$  for  $l \neq 0$  is

more involved, no results seem to be available for  $\text{YBa}_2\text{Cu}_4\text{O}_8$ ; therefore, a decision in favor for  $d$  wave pairing, based on Knight shift data, could not be made. Another possibility to check the symmetry of the pairing state is offered by spin-lattice relaxation, for instance by measuring the spatial anisotropy of the plane Cu relaxation. The analysis is, however, quite involved [12]. A better clue to the pairing state symmetry is provided by the individual behavior of the relaxation rates in the superconducting state. We note that both the planar Cu and O rates show no coherence peak just below  $T_c$ , nor does the rate diminish exponentially with decreasing temperature as observed in conventional  $s$  wave superconductors. Instead, the temperature dependence of  $1/T_1$  is rather power-law like, that is  $1/T_1$  is proportional to  $T^n$  with  $n$  between 2.5 and 3. This points to the existence of nodes in the superconducting gap as one expects, for instance, for  $d$  wave pairing superconductivity.

### 6. Inter-layer coupling

There is a fascinating question: What is the coupling between sequential conducting planes formed in cuprate superconductors? In  $\text{YBa}_2\text{Cu}_3\text{O}_7$  and  $\text{YBa}_2\text{Cu}_4\text{O}_8$ , the  $\text{CuO}_2$  planes form double planes separated by Y ions. The structure of  $\text{Y}_2\text{Ba}_4\text{Cu}_7\text{O}_{15}$  consists of a sequence of alternating  $\text{YBa}_2\text{Cu}_3\text{O}_7$  and  $\text{YBa}_2\text{Cu}_4\text{O}_8$  blocks. Due to this alternation, the individual planes of a  $\text{CuO}_2$  double plane in  $\text{Y}_2\text{Ba}_4\text{Cu}_7\text{O}_{15}$  are *inequivalent* and hence can separately be monitored by NMR/NQR methods allowing one to investigate the coupling between these planes [16]. We therefore measured various NMR/NQR parameters of Cu in these inequivalent planes, namely the Knight shift, the spin-lattice relaxation, and the so-called “indirect part to the Gaussian contribution” to the spin-spin relaxation rate. This rate is a measure for the coupling among nuclear spins and the indirect part arises from an enhanced Cu nuclear-nuclear spin coupling induced through an *indirect* coupling via electron spins.

The ratio of these parameters (for instance of  $T_1$  values of the two planes) turned out to be constant above 100 K. The analysis revealed that both the static and the dynamic electron susceptibilities of the two single planes of each double-plane are governed by the *same* temperature dependence which means common spin dynamics in both planes, and hence these planes must be strongly coupled. To confirm independently and directly the existence of the inter-plane coupling in the compound  $\text{Y}_2\text{Ba}_4\text{Cu}_7\text{O}_{15}$ , we have performed an NQR spin-echo double resonance (SEDOR) experiment [17]. Observing a SEDOR effect proves that the two nuclei involved in SEDOR are coupled by a spin-spin interaction [18]. By choosing partners from inequivalent planes we confirmed the inter-plane coupling.

### 7. Effects on out-of-plane nuclei

So far we have been concerned with those properties of the cuprates which can be checked by NMR/NQR studies with *plane* nuclei. At the end of our presentation we will address the question: “Do the AF spin fluctuations in the  $\text{CuO}_2$  affect the spin-lattice relaxation of the out-of-plane Ba nuclei?” Our answer has been: The nuclei, with isotopes  $^{135}\text{Ba}$  and  $^{137}\text{Ba}$ , relax by the interaction of their quadrupole moments,  $eQ$ , with fluctuating electric field gradients due to phonons [19]. This mechanism is different from the quadrupole interaction we mentioned in Sect. 4. It turned out that the Ba relaxation is caused by a two-phonon Raman process, i.e. the absorption of one phonon and the emission of another. Such a process leads, assuming a Debye type phonon spectrum, to the following relaxation rate:

$$\frac{1}{T_1} = A Q^2 \int_0^{kT_D/\hbar} \frac{\exp(\hbar\omega/kT)}{[\exp(\hbar\omega/kT) - 1]^2} \left( \frac{\hbar\omega}{kT_D} \right)^6 d\omega$$



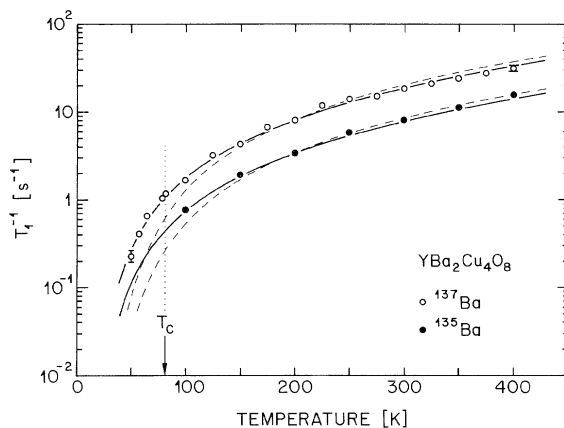


**Fig. 3.** Temperature dependence of the  $^{135}\text{Ba}$  and  $^{137}\text{Ba}$  spin-lattice relaxation rates in  $\text{YBa}_2\text{Cu}_4\text{O}_8$ . Solid and dashed lines are fits to the theoretical expression with Debye temperatures of 185 K and 350 K, respectively. From [19].

Here,  $T_D$  is the Debye temperature and the factor  $A$  is assumed to be temperature independent. This expression has been fitted to the relaxation data of both isotopes with  $T_D$  as the only adjustable parameter, beside the scaling factor  $A$ . According to Fig. 3, the fit is very good for both isotopes and yields the same Debye temperature,  $T_D = 185(20)$  K. In the high- and low-temperature limit, the relaxation rates vary as  $T^2$  and  $T^7$ , respectively, which is a well-known behavior of relaxation in ionic crystals. It is worthwhile to note that the Ba relaxation rates pass smoothly “through  $T_c$ ” which implies that those phonons causing Ba relaxation do not change appreciably at the phase transition.

Our result for the Debye temperature agrees quite well with  $T_D$  values of 155-185 K deduced from an analysis of the thermal conductivity. This is expected since heat is mostly carried by acoustical phonons and the Debye model, which was used to derive the relaxation formula, works best for acoustical phonons.

## REFERENCES

- [1] C.H. Pennington, C.P. Slichter, in: *Physical Properties of High Temperature Superconductors*, edited by D.M. Ginsburg (World Scientific, Singapore, 1990) Vol. 2, p. 269.
- [2] H. Alloul, in: *Temperature Superconductivity*, edited by D.P. Tunstall, W. Barford (Adam Hilger, Bristol, 1991) p. 207.
- [3] D. Brinkmann and M. Mali, in *NMR - Basic Principles and Progress*, edited by P. Diehl, E. Fluck, H. Günther, R. Kosfeld, J. Seelig (Springer, Berlin-Heidelberg, 1994) Vol. 31, p. 171.
- [4] C. Berthier, M.H. Julien, M. Horvaticš, Y. Berthier, *J. Physique I* 6, 2205 (1996).
- [5] A. Rigamonti, F. Borsa, P. Carretta, *Report Prog. Phys.* 61, 1367 (1998).

- [6] D. Brinkmann, *High-temperature Superconductors, Cuprate: Magnetic Properties by NMR/NQR*, Encyclopedia of Materials: Science and Technology, (2nd Update, Elsevier Science, 2002).
- [7] D. Brinkmann, Proc. of 2nd Conference on *Isotopic and Molecular Processes* (Studia Universitatis Babes-Bolyai Physica, 2001) Vol. I, p. 81. The paper contains an incorrect combination of figures and figure captions. The correct combination is: the first, second, and third figure belong to the second, third, and first figure caption, respectively.
- [8] A.J. Millis, H. Monien, D. Pines, Phys. Rev. B 42, 167 (1990).
- [9] F.C. Zhang and T.M. Rice, Phys. Rev. B 37, 3759 (1988).
- [10] A.Yu. Zavidonov and D. Brinkmann, Phys. Rev. B 58, 12486 (1998).
- [11] A.Yu. Zavidonov and D. Brinkmann, Phys. Rev. B 63, 132506-1 (2001).
- [12] M. Bankay, M. Mali, J. Roos, D. Brinkmann, Phys. Rev. B 50, 6416 (1994).
- [13] A. Suter, M. Mali, J. Roos, D. Brinkmann, Phys. Rev. B 56, 5542 (1997).
- [14] Y. Zha, V. Barzykin, D. Pines, Phys. Rev. B 54, 7561 (1996).
- [15] A. Suter, M. Mali, J. Roos, D. Brinkmann, Phys. Rev. Lett. 84, 4938 (2000).
- [16] D. Brinkmann, Z. Naturforschung 51a, 786 (1996).
- [17] R. Stern, M. Mali, J. Roos, D. Brinkmann, Phys. Rev. B 52, R15734 (1995).
- [18] C.P. Slichter, in *Nuclear Magnetic Double Resonance*, edited by B. Maraviglia (North-Holland, 1993), p. 69.
- [19] A. Lombari, M. Mali, J. Roos, D. Brinkmann, A. Yakubowskii, Physica C 235-240, 1651 (1994).

## INCLUSION OF ALKYLPARABENS IN CYCLODEXTRINS

**M.R. CAIRA<sup>1</sup>, E.J.C. DE VRIES<sup>1</sup>, M. BOGDAN<sup>2</sup>, D. BOGDAN<sup>2</sup>, S.I. FARCAS<sup>2</sup>**

<sup>1</sup> Department of Chemistry, University of Cape Town, Rondebosch 7701, South Africa

<sup>2</sup> National Institute for R&D of Isotopic and Molecular Technologies, P.O. Box 700, Cluj-Napoca, Romania

**ABSTRACT.** The alkyl esters of 4-hydroxybenzoic acid, with formula  $\text{HO-C}_6\text{H}_4\text{-COOR}$  and  $\text{R} = \text{Me}$ , Et, *n*-Pr, *n*-Bu, are well known as antibacterial preservatives. Owing to their poor aqueous solubilities, their inclusion in cyclodextrins has been investigated by numerous workers as a means of enhancing their dissolution properties. This paper reports salient results of a systematic study of the inclusion of the alkylparabens in native and methylated cyclodextrins, with emphasis on the thermal and structural properties of the solid inclusion complexes. Techniques used to study the interaction between the various hosts and guests included X-ray diffraction, thermal analysis, FTIR spectroscopy and high-resolution NMR spectroscopy.

### 1. Introduction

Inclusion of drugs in cyclodextrins (CDs) is an attractive, widely used strategy for improving their performance [1]. Increased drug solubility, as well as physical and chemical stability are some of the advantages offered by this approach. The special features of cyclodextrins (cyclic oligosaccharides composed of  $\alpha$ -1,4-linked glucopyranose units) which enable them to encapsulate and solubilise hydrophobic guest molecules are their toroidal shape, hydrophobic interior cavity and hydrophilic exterior (Figure 1).

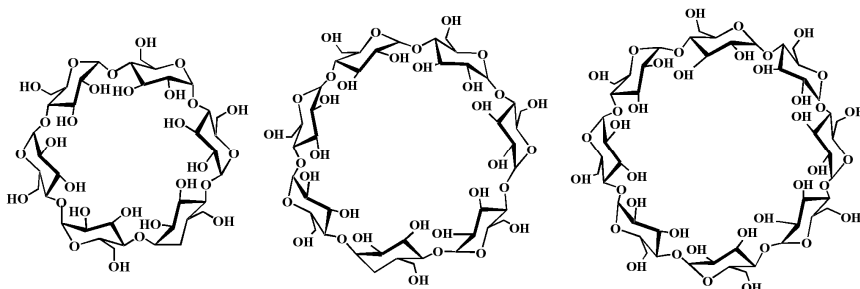


**Fig. 1.** Structures of the native cyclodextrins: from left to right  $\alpha$ -,  $\beta$ -, and  $\gamma$ -cyclodextrin.

The guest molecules relevant to the present study are the alkylparabens, alkyl esters of 4-hydroxybenzoic acid (Figure 2), commonly employed as antibacterial preservatives in cosmetics, food products and pharmaceutical formulations [2]. These compounds, which are used singly or in combination, have broad spectrum antimicrobial activity in the pH range 4-8 and are most effective against yeasts and moulds. For the series shown in Figure 2, the aqueous solubilities at 25°C are very low, ranging from 0.016-0.001M as the chain length of the alkyl moiety increases [3]. Consequently, methods for improving their solubility have been sought and one strategy for achieving this is cyclodextrin inclusion. Recent reports documenting

increased aqueous solubility of alkylparabens effected by cyclodextrins include those on the use of heptakis(2,6-di-O-methyl-3-O-acetyl)- $\beta$ -cyclodextrin [4] and 2-hydroxypropyl- $\beta$ -cyclodextrins with different degrees of substitution [5].

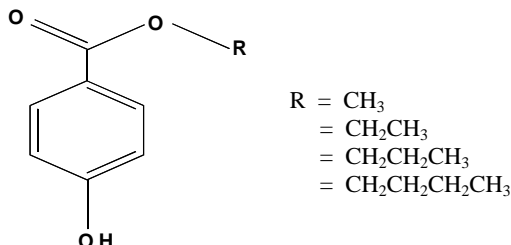


**Fig. 2.** Structures of the guest molecules, methyl-, ethyl-, *n*-propyl- and *n*-butylparaben.

Our interest in the area of cyclodextrin-drug complexation prompted us to investigate the physical stabilities and structures of solid inclusion compounds formed between alkylparabens and a range of cyclodextrins [6]. Apart from the pharmaceutical interest, the availability of this homologous series of guests allowed investigation of the mode of guest inclusion as a function of alkyl-chain length. Here we report some pertinent results gleaned primarily from thermal analysis and X-ray diffraction. Additional information on the interaction between the four alkylparabens shown in Figure 2 and  $\beta$ -cyclodextrin in solution was obtained by NMR experiments. Owing to the large mass of available data we have accumulated on this topic and limited space, only selected aspects of the work are alluded to here. Full accounts which describe the detailed structures and thermal decompositions of the complexes with native and derivatised cyclodextrins are in preparation and will be published *in extenso* elsewhere as indicated under individual sections of this paper.

## 2. General Experimental Procedures

Proton NMR experiments were performed at 298K in  $\text{D}_2\text{O}$  solution and at 300 MHz on a Varian-Gemini 300 spectrometer to study the interaction between  $\beta$ -cyclodextrin and each of the four guests. The continuous variation method was used to determine complex stoichiometry in solution. This involved plotting measured changes in chemical shifts for both host and guest protons,  $\Delta\delta_{\text{obs}}[\text{X}]$ , against the mole fraction ratio *r*. Computation of the association constants followed. The procedures used were described in detail recently [7].

Solid inclusion complexes with  $\beta$ - and  $\gamma$ -cyclodextrins as hosts were generally prepared by kneading and co-precipitation methods, using the individual pure alkylparabens as guests in 1:1 molar ratio with the host. With the methylated cyclodextrins DIMEB [heptakis(2,6-di-O-methyl)- $\beta$ -cyclodextrin] and TRIMEB [heptakis(2,3,6-tri-O-methyl)- $\beta$ -cyclodextrin], the technique of incubating a solution of the drug and cyclodextrin at 50-60°C was employed, leading to crystallization of inclusion complexes.

Putative complexes were examined by hot stage microscopy, thermogravimetric analysis (TGA) and differential scanning calorimetry (DSC). Recorded powder X-ray diffraction (PXRD) patterns were compared with reference patterns [8] to establish complex formation and possible space groups. Single crystal X-ray diffraction was applied to complexes that yielded crystals of adequate quality. Intensity data were collected on a Nonius Kappa CCD diffractometer with the crystals generally cooled in a stream of nitrogen to improve diffraction quality. Structures were solved by a variety of methods including Patterson search and isomorphous replacement techniques. For structure refinement, full-matrix least-squares methods were employed.

### 3. Interaction between the parabens and $\beta$ -cyclodextrin

In solution, inclusion complex formation between the parabens and  $\beta$ -cyclodextrin was inferred from the NMR experiments which showed upfield shifts of the host H3, H5 and H6 protons, the first two of which are located inside the cavity and the last at the narrow primary rim of the macrocycle. No significant shifts were observed for the host H1, H2 and H4 protons. Distinct peaks were not observed for a bound and a free form. This observation implied that complexation is a dynamic process, the included drug undergoing fast exchange (relative to the NMR time scale) between the free and bound states and only the shifts of the spectral lines were observed. Therefore the exchange rate between the free and bound states must exceed the reciprocal of the largest observed shift difference (in Hz) for any proton of the guest molecule [9]. The stoichiometries of the complexes were determined using the continuous variation method by following the changes in the chemical shifts of the host protons which showed the greatest variations *viz.* H3, H5 and H6. The Job plot of the  $\beta$ -CD proton shifts is more accurate than that of the paraben proton shifts, as the  $\beta$ -CD signals are strengthened by the seven chemically equivalent protons (one from each glucose monomer). The Job plots for the  $\beta$ -CD H3, H5 and H6 protons are unremarkable, having an almost symmetric appearance, indicating that only one type of complex had formed [9]. For each  $\beta$ -CD-paraben complex, the Job plot showed a maximum at  $r = 0.5$ , indicating the existence of a complex with 1:1 stoichiometry within the range of concentrations investigated. The association constants for the 1:1 complexes were evaluated by a non-linear least-squares regression analysis of the observed chemical shift changes of the drug and  $\beta$ -CD NMR lines, as a function of  $\beta$ -CD concentration. For consistency,  $K$  was evaluated from the observed differences in chemical shifts for the H3, H5, and H6 protons of  $\beta$ -CD in each case. The overall association constants ( $K$ ) obtained were 1631, 938, 460 and 2022  $M^{-1}$  for complex formation with methyl-, ethyl-, propyl- and butylparaben respectively. The  $\Delta\delta(H5)$  (range 0.24-0.28 ppm) was generally found to exceed  $\Delta\delta(H3)$  (range 0.13-0.26 ppm) and it was concluded that the guests penetrate the cavity fairly deeply and that the host primary side is also involved in inclusion. The general decrease in  $K$  with increasing guest alkyl chain length (up to propyl-) is consistent with this part of the guest finding itself outside the cavity in the hydrophilic water environment. However the butylparaben complex is inconsistent with this trend and the calculated association constant suggests that this guest has the tightest fit within the CD cavity.

Regarding complex structure in solution, some conclusions were drawn from the complexation-induced shifts. The signals of the included paraben were shifted by complexation to a variable extent and a similar trend for each of the guest proton resonances was observed, suggesting a comparable mode of insertion of each paraben guest in the  $\beta$ -CD cavity. An increase in the concentration of the CD for each  $\beta$ -CD-paraben mixture caused down-field shifts of the alkyl chain and ester moiety signals and up-field shifts of the aromatic ring protons. The latter was interpreted as a consequence of the inclusion of the phenyl ring in the host while the former suggested that the alkyl protons lay outside the host cavity. The guest position is consistent with the up-field shifts of the  $\beta$ -CD cavity protons, as the  $\beta$ -CD protons experience anisotropic shielding attributed to the inclusion of the guest aromatic ring. Regarding guest orientations, further consideration of the available data suggested that the guest hydroxyl groups are located at the host primary rim for the higher homologues propyl- and butylparaben, while the reverse orientation for methylparaben was inferred. Near equality of the chemical shifts for the aromatic protons of ethylparaben prevented definite conclusions regarding its orientation in the host cavity.

Complex formation in the solid state *via* both kneading and co-precipitation methods was confirmed by a variety of methods [10], PXRD proving to be the most definitive. DSC traces of 1:1 physical mixtures of each paraben with  $\beta$ -CD showed the corresponding fusion endotherm of the guest. The latter disappeared in the traces for kneaded and co-precipitated products, where only peaks for complex dehydration and final decomposition (around 300°C) were evident. UV spectrophotometry indicated 1:1 host-guest stoichiometry in each case and TGA enabled water contents to be assessed, leading to a range of 7.0-7.3 water molecules per complex unit. FTIR spectra were also useful, showing significant shifts of the guest C=O absorption band to higher frequencies in the complexes relative to the pure guests. Comparison of experimental PXRD traces with reference patterns [8, 10] immediately furnished proof of inclusion complex formation as well as indicating probable crystal packing arrangements. All four inclusion complexes yielded a PXRD pattern consistent with channel-packing of dimeric  $\beta$ -CD inclusion complexes.

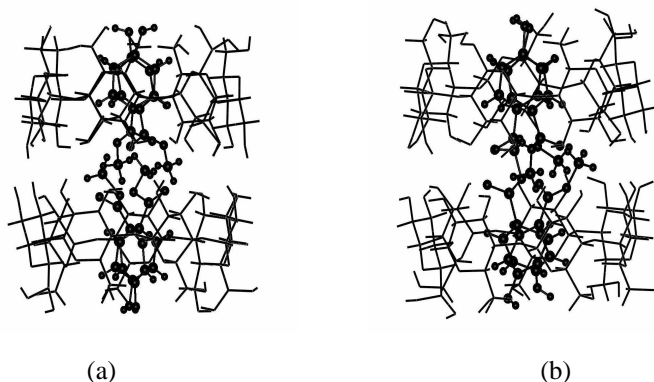
Single crystals of each of the four crystalline inclusion complexes were grown and attempts were made to determine their detailed structures by X-ray diffraction. Table 1 lists the unit cell parameters for the complexes crystallized at ambient temperature (20°C). All four crystallize in the monoclinic space group C2 with  $Z = 4$ , implying a unit cell content of two dimeric  $\beta$ -CD inclusion complexes. Crystals of the complexes with ethylparaben and butylparaben diffracted weakly and only a set of imprecise unit cell data could be recorded.

Table 1.

Crystal data for  $\beta$ -CD complexes with the four guest alkylparabens

Complex formula	$\beta$ CD-M-7.2H <sub>2</sub> O	$\beta$ CD-E-7.0H <sub>2</sub> O	$\beta$ CD-P-7.0H <sub>2</sub> O	$\beta$ CD-B-7.3H <sub>2</sub> O
<i>a</i> /Å	18.8632(4)	18.88(1)	19.137(2)	19.05(1)
<i>b</i> /Å	24.4542(45)	24.44(1)	24.523(1)	24.48(1)
<i>c</i> /Å	15.5942(5)	15.73(1)	15.793(1)	15.73(1)
$\beta$ /°	110.668(1)	109.8(1)	109.52(2)	110.9(1)

The near equality of unit cell data for the complexes is consistent with the inference of isostructurality from PXRD analysis. Detailed single crystal X-ray analysis was only possible for  $\beta$ CD-M-7.2H<sub>2</sub>O and  $\beta$ CD-P-7.0H<sub>2</sub>O. However, in the latter case, severe disorder of the guest prevented its modelling despite the well-ordered nature of the host molecule. This phenomenon has been observed previously with channel-packed inclusion complexes crystallizing in the space group C2. The only reliable structure available is therefore that of  $\beta$ CD-M-7.2H<sub>2</sub>O [11], whose dimeric 1:1 host-guest unit is shown in Figure 3(a). The guest M was found to be disordered over two sites with equal statistical occupancy within the host cavity. In this structure, the two halves of the dimeric complex are related by a horizontal two-fold rotation axis and the guest hydroxyl groups are located at the host primary rim. Here they engage in hydrogen bonding with water molecules and hydroxyl groups of neighbouring counterparts. This orientation is the reverse of that established in solution, where at low solute concentration the secondary side of the host may be exposed to the aqueous environment, allowing hydration of the guest hydroxyl group. The dimeric complex units pack in the 'channel-mode', characterized by linear channels produced when close-packed layers of dimers stack in exact alignment.



**Fig. 3.** Structures of the dimeric  $\beta$ -CD complex units in (a)  $\beta$ CD-M·7.2H<sub>2</sub>O (monoclinic) and (b)  $\beta$ CD-M·14.0H<sub>2</sub>O (triclinic). All disordered components of the guest molecules are shown.

Earlier, we had alluded to the possibility that cyclodextrin inclusion complexes should in principle display polymorphism [8]. This was realized by our recent discovery that when the complex  $\beta$ CD-M is crystallized at reduced temperature (7°C), a modification crystallizing in the triclinic space group P1 results. The structure of the complex unit in this crystal (Figure 3(b)) is also a dimer containing disordered guests in the same orientation as found in the monoclinic form. As indicated in a recent communication [11], the isolation of two crystalline forms of a cyclodextrin inclusion complex by systematic variation of crystallization conditions is a novel finding of general significance. The monoclinic and triclinic crystals were furthermore shown to have significantly different temperatures of dehydration and complex decomposition. A full account of the interaction between the parabens and  $\beta$ -cyclodextrin in solution and in the solid state is in preparation [12].

#### 4. Interaction between the parabens and $\gamma$ -cyclodextrin

Attempted complexation between the parabens and  $\gamma$ -cyclodextrin by the kneading method led to crystalline powders whose PXRD patterns matched those of physical mixtures of the components. However, inclusion complexes with H:G stoichiometry 1:2 were obtained by the co-precipitation method [6]. These complexes displayed similar thermal behaviour to the inclusion complexes with  $\beta$ -CD in that the DSC traces were devoid of the guest melting endotherms. Definitive identification of these species was obtained by noting that their common PXRD traces were practically superimposable on the reference pattern for the unique tetragonal family of  $\gamma$ -CD inclusion complexes with  $a \sim 23.8$ ,  $c \sim 23.2\text{\AA}$  crystallizing in space group P4<sub>2</sub>2 [8].

#### 5. Interaction between the parabens and dimethylated $\beta$ -CD (DIMEB)

Inclusion complexes of H:G stoichiometry 1:1 were obtained in crystalline form and were characterized by HSM, TGA, DSC, PXRD and single crystal X-ray diffraction methods. Here we focus on preliminary results of the X-ray study. Table 2 lists crystal data for these complexes which crystallize in the orthorhombic space group P2<sub>1</sub>2<sub>1</sub>2<sub>1</sub> with four molecules per unit cell in each case. The complexes clearly fall into two distinct isostructural series.

Table 2.

Crystal data for DIMEB (DMB) complexes with the four guest alkylparabens

Complex formula	DMB·M·3.7H <sub>2</sub> O	DMB·E·4.0H <sub>2</sub> O	DMB·P·3.9H <sub>2</sub> O	DMB·B·3.7H <sub>2</sub> O
a/Å	10.6014(1)	10.6560(1)	15.1399(2)	15.3735(2)
b/Å	15.4760(2)	15.3073(2)	18.8943(3)	18.8114(2)
c/Å	48.2438(6)	49.0417(6)	28.4009(5)	28.3989(4)

The presence of two crystal packing modes implied by the above data is consistent with the detailed modes of guest inclusion (shown schematically in Figure 4) determined from single crystals. In the first isostructural pair of complexes (guests M, E), the guest hydroxyl group is located at the host secondary rim while the aromatic portion occupies the central part of the host cavity. The guest orientation is reversed in the case of P and B, the greater portion of their respective phenolic groups extending from the host primary sides.

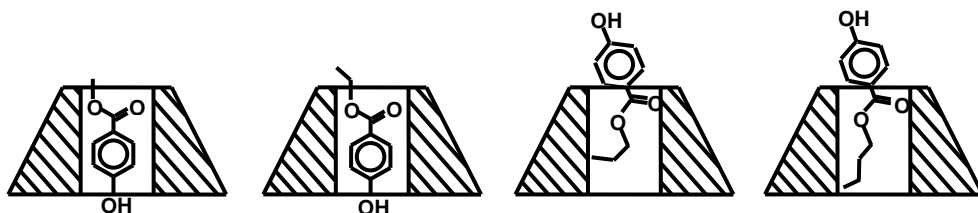


Fig. 4. Schematic diagram showing the modes of guest inclusion in the host DIMEB.

In contrast to the  $\beta$ -CD complexes of the parabens which are dimeric, the DIMEB complexes are monomeric and thus both ends of the DIMEB host molecule can provide a favourable aqueous environment to the guest hydroxyl group, enabling the two guest orientations to occur. However, the specific orientations adopted may only be explained after a detailed study of the host-guest interactions in the four complexes has been undertaken. Such a study is underway and a full account is in preparation [13].

## 6. Interaction between the parabens and permethylated $\beta$ -CD (TRIMEB)

Crystalline inclusion complexes between TRIMEB (TMB) and the parabens were isolated and characterized using the same methods as for the DIMEB complexes. Table 3 lists crystal data for the TMB complexes, all of which crystallize in space group  $P2_12_12_1$  with four molecules per unit cell. In this series the complex with methylparaben has unique unit cell data while complexes with E, P and B are isostructural, corresponding to a 'screw-channel' crystal packing mode [8].

Table 3.

Crystal data for TRIMEB (TMB) complexes with the four guest alkylparabens

Complex formula	TMB·M·2.6H <sub>2</sub> O	TMB·E·5.0H <sub>2</sub> O	TMB·P·5.2H <sub>2</sub> O	TMB·B·5.6H <sub>2</sub> O
a/Å	10.718(1)	14.886(2)	14.863(1)	14.866(2)
b/Å	26.353(1)	22.024(3)	21.862(2)	21.967(2)
c/Å	30.018(2)	27.602(1)	27.627(3)	27.635(4)



Comparison of the host geometries in the four structures showed that TMB in the complex with methylparaben has a distinctly different conformation from the common one found in the other three complexes. As shown schematically in Figure 5, the complex with ethylparaben is unique in having the guest phenolic group situated at the primary side of the host molecule. In the other three complexes, the alkyl chains are located at, or protrude through, the host primary rim. Again these preferred modes of guest inclusion require detailed investigation and full details will be published elsewhere [13].

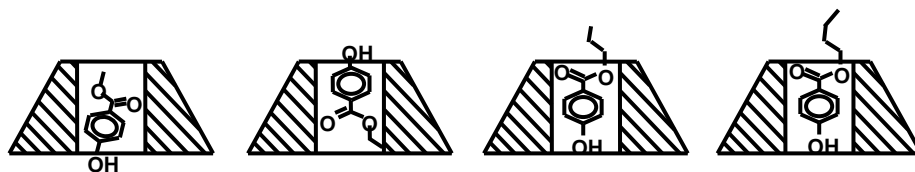


Fig. 5. Schematic diagram showing the modes of guest inclusion in the host TRIMEB.

### 7. Concluding remarks

The most significant result that emerged from a study of the inclusion of the parabens in  $\beta$ -CD was the finding that in the solid state two distinct crystals of the complex with methylparaben can form, depending on the temperature conditions during crystallization. This is the first well-documented example of this phenomenon for cyclodextrin inclusion complexes [11]. The fact that these complexes have different physical properties indicates that crystallization temperature should be considered more critically in future as an experimental variable as it may enable a richer variety of cyclodextrin inclusion complexes to be generated. A systematic study of the effect of temperature on the crystallization of analogous complexes is in progress [14].

The solution NMR data for inclusion of the parabens in  $\beta$ -CD confirmed 1:1 host-guest stoichiometry and yielded stability constants. This study, based on the continuous variation method, represents a significant advance on previous work on the same four complexes [15] where NMR data for only a single concentration of each paraben were considered.

Inclusion complex formation in the solid state between the parabens and  $\gamma$ -CD was confirmed and the complexes behaved uniformly under thermal analysis. No single crystal structure determinations were attempted as the guests are known to be generally disordered in such high symmetry crystals [8].

Successful structural elucidation of the inclusion complexes of the parabens with both partially and fully methylated  $\beta$ -CDs showed that the guest alkyl chain length is a defining factor in determining both the guest orientation within these macrocycles as well as crystal packing modes. Specific findings have yet to be rationalised on the basis of host-guest compatibility, hydrophobicity and polarity, which are some of the determinants involved.

**Acknowledgements:** MRC and E J C de V thank the University of Cape Town and the NRF (Pretoria) for research support.

## REFERENCES

1. K.-H. Frömring and J. Szejtli, "Cyclodextrins in Pharmacy", Kluwer Academic Press, Dordrecht, 1998.
2. A. Wade and P. J. Weller (Eds): Handbook of Pharmaceutical Excipients, 2<sup>nd</sup> Ed., American Pharmaceutical Association, Washington DC, 1994, 340-344.
3. F. Giordano, R. Bettini, C. Donini, A. Gazzaniga, M. R. Caira, G. G. Z. Zhang and D. J. W. Grant, *Physical properties of Parabens and their mixtures: solubility in water, thermal behavior, and crystal structures*, J. Pharm. Sci., 88, 1999, 1210-1216.
4. S. Mieda, F. Hirayama, K. Uekama., *Preparation and pharmaceutical evaluation of heptakis(2,6-di-O-methyl-3-O-acetyl)- $\beta$ -cyclodextrin*, Proceedings of the International Symposium on Cyclodextrins, 9<sup>th</sup>, Santiago de Compostela, Spain, 1998. 309-312.
5. H. Matsuda, K. Ito, Y. Sato, D. Yoshizawa, M. Tanaka, A. Taki, H. Sumiyoshi, T. Utsuki, F. Hirayama and K. Uekama, *Inclusion complexation of p-hydroxybenzoic acid Esters with 2-hydroxypropyl-)- $\beta$ -cyclodextrins. On changes in solubility and Antimicrobial activity*. Chem. Pharm. Bull., 41, 1993, 1448-1452.
6. E. J. C. de Vries, *Inclusion of Alkylparabens in Cyclodextrins*, PhD thesis, University of Cape Town, April 2003 (291 pp).
7. M. Bogdan, M. R. Caira and S. I. Farcas, *Inclusion of the niflumic acid anion in  $\beta$ -cyclodextrin: a solution NMR and X-ray structural investigation*. Supramol Chem., 14, 2002, 427-435.
8. M. R. Caira, *On the isostructurality of cyclodextrin inclusion complexes and its practical utility*, Rev. Roum. Chim., 46, 2001, 371-386.
9. F. Djedaini, S. Z. Lin, B. Perly, D. Wouessidjewe, *High-field nuclear magnetic resonance techniques for the investigation of a beta-cyclodextrin:indomethacin inclusion complex*, J. Pharm. Sci., 79, 1990, 643-646.
10. M. R. Caira, E. J. C. de Vries and L. R. Nassimbeni, *Cyclodextrin inclusion of p-hydroxybenzoic acid esters*, J. Therm. Anal. Cal., 73, 2003, 647-651.
11. M. R. Caira, E. J. C. de Vries and L. R. Nassimbeni, *Crystallization of two forms of a cyclodextrin inclusion complex containing a common organic guest*, J. Chem. Soc., Chem. Commun., 2003, 2058-2059.
12. M. R. Caira, E. J. C. de Vries, M. Bogdan, D. Bogdan and S. I. Farcas, in preparation.
13. M. R. Caira and E. J. C. de Vries, in preparation.
14. M. R. Caira and N. Stellenboom, in preparation.
15. L. W. Chan, T. R. Kurup and A. Muthaiah, *Interaction of p-hydroxybenzoic acid esters with beta-cyclodextrin*, Int. J. Pharm., 195, 2000, 71-79.

**ISOTOPIC SEPARATION, LABELLED COMPOUNDS AND APPLICATIONS**

**USE OF SLIGHTLY ENRICHED URANIUM (SEU) IN PHWR**

**DUMITRU OHĂI**

*Institute for Nuclear Research-Pitești,  
P.O. Box 78, ROMANIA*

**ABSTRACT.** The flexibility of CANDU reactor permits use of different fissile materials: natural Uranium (NU), Slightly Enriched Uranium (SEU), Recovered Uranium (RU) from LWR spent fuel reprocessing, Thorium or Plutonium (Mixed Oxide – MOX) and even, PWR spent fuel (Direct Use of spent fuel in CANDU - DUPIC). That is possible using as carrier in pressure tube an advanced fuel bundle. AECL Canada developed a new fuel bundle concept named CANFLEX (Canadian Flexible). In the demonstration irradiation to Point Lepreau Reactor, using CANFLEX fuel bundle with natural Uranium, the burn up was about 10,000 MWd/tU comparatively with 7000 MWd/tU for standard fuel bundle with natural Uranium. Slightly Enriched Uranium is Uranium having the enrichment 0.9 – 1.2%U<sup>235</sup>. There are estimations that the Uranium enrichment increasing up to 1.2% U<sup>235</sup> can to obtain burn up about 21,000 MWd/tU. In Romania, also, Institute for Nuclear Research Pitești develops a new fuel bundle concept (named SEU 43), compatible with CANDU 6 Reactor. The intention is to use slightly enriched Uranium for burn up increasing and to reduce spent fuel amounts.

**INTRODUCTION**

The IAEA-sponsored International Symposium on “Nuclear Fuel Cycle and Reactor Strategies: Adjusting to New Realities” identified the factors influencing the choice of fuel-cycle strategy, and development requirements and directions [1]. The fuel-cycle path chosen by a particular country or utility will depend on many local and global factors, a few of which are short-and long-term availability, cost, security, and diversity of energy resources; the state of industrial development; availability and cost of fuel-cycle technologies both domestically and off-shore (such as enrichment, and reprocessing); back-end considerations, including total inventories of used fuel and high-level waste requiring permanent disposal, environmental impact, availability, cost, and public acceptance of permanent disposal facilities; government policy on energy and industrial development; and non-proliferation considerations.

Given the historical difficulty in predicting the availability and cost of energy resources and fuel-cycle technologies, and the large uncertainties and variability in many of the factors, a superior nuclear energy strategy should be based on fuel-cycle flexibility. An inherent feature of the CANDU design is its very high degree of fuel-cycle flexibility. This enables a country, or utility, to optimize its fuel-cycle strategy based on its own unique circumstances. CANDU reactor development follows an evolutionary path, allowing custom tailoring of the fuel cycle to fit local requirements.

**NATURAL URANIUM FUEL IN CANDU REACTORS**

In considering the CANDU fuel-cycle, it is important to understand the benefits derived from the use of natural uranium fuel to appreciate why it remains such an attractive option for CANDU owners.

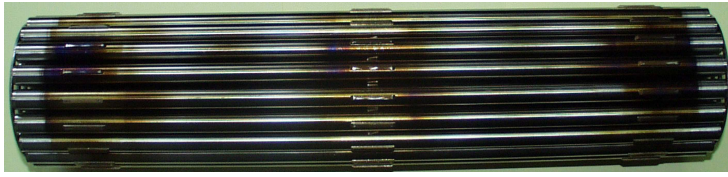


Fig. 1. Standard CANDU fuel bundle

The standard CANDU fuel bundle (Figure 1) is relatively small (0.5 m in length, 10 cm in diameter), and easily handled (about 24 kg). It consists of only 7 distinct components (pellets, sheath, CANLUB coating inside the sheath, spacer pads, bearing pads, end-plugs and end-plates). Hence it is an easily manufactured product that client countries have found straightforward to localize. The use of natural uranium fuel itself simplifies manufacture, handling, as well as sourcing and diversity of fuel supply.

The uranium requirements (mined uranium required per unit of electricity generated) are about 30% lower than for a PWR. The use of natural uranium generates no depleted-uranium tails waste from the enrichment plant – in total, a more environmentally friendly front-end of the fuel cycle.

After 350 reactor-years of operation, the failure rate of natural uranium CANDU fuel is very low – less than 0.1% bundle failure rate. A consequence of these factors is that fuelling costs in CANDU reactors are a factor of 2 lower than for PWRs.

Nor is the lower CANDU fuel burnup a disadvantage in the back-end of the fuel cycle [2]. An extensive assessment of the Canadian concept for geological disposal confirms its technical soundness [3]. The concept is based on deep geological disposal in an underground vault located in plutonic rock. Primarily the heat load of the used fuel determines the density of fuel emplacement in such a facility. Its lower heat load offsets the higher quantity of used natural uranium CANDU fuel, compared to higher burnup PWR fuel. The simplicity and small size and weight of the CANDU bundle also reduce the cost of the emplacement system. The overall disposal cost per unit of electricity produced is very similar for used natural uranium CANDU fuel and used PWR fuel. This is borne out in the OECD/NEA assessment of disposal costs [4].

Also, the size of the repository is small, considering the electricity produced.

Given all of these benefits then, it is likely that any new fuel or fuel cycle will need to offer compelling advantages before it is introduced. The rest of this paper will identify some of these compelling benefits.

### **THE CANFLEX FUEL BUNDLE**

Despite the outstanding performance of existing fuel designs, the first “compelling” product that is likely to be introduced is the new CANFLEX fuel bundle (Figure 2), fuelled initially with natural uranium. The CANFLEX fuel bundle has been under development by AECL since 1986, and jointly with the Korea Atomic Energy Research Institute (KAERI) since 1991 [5,6]. It is now ready for commercial implementation. In 1998 September, a demonstration irradiation of 24 bundles was initiated in the Point Lepreau power reactor in New Brunswick, Canada. In 2000 August, this demonstration irradiation was successfully completed, with the last 4 CANFLEX fuel bundles being discharged from the reactor. Selective bundles are now under going post-irradiation examination (PIE) at the Chalk River Laboratories, to

confirm acceptable fuel performance. A full-scale water critical heat flux (CHF) test has also been completed, culminating an extensive series of qualification tests that establishes the thermal hydraulic performance of the bundle. The improvement in critical channel power (corresponding to the first occurrence of dry out of the fuel sheath) over the 37-element bundle is around 8%, depending on the age of the pressure tube.

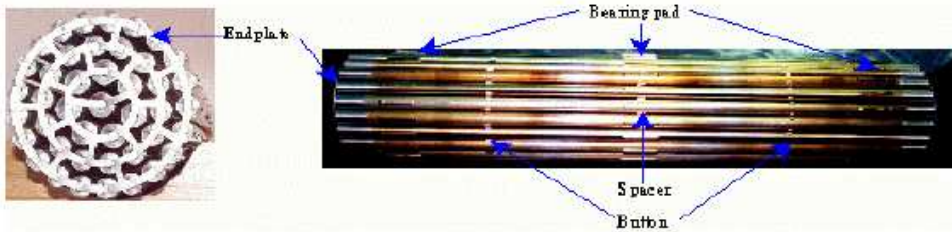


Fig. 2. CANFLEX fuel bundle

CANFLEX is a 43-element bundle, with 2 element sizes. The increased number of element size-grading reduces peak linear element ratings by 20% compared with those of the 37-element bundle. This improvement applies to natural uranium, as well as to a variety of enriched fuels and burnups. Patented CHF-enhancing appendages improve the thermal hydraulic performance.

What will make the initial introduction of CANFLEX a “compelling” product is its application in plant-life extension, for recovering the loss of thermal hydraulic margins that can occur because of various aging phenomena, thereby enabling the reactor to remain at full power.

### ROMANIAN SEU 43 FUEL BUNDLE CONCEPT

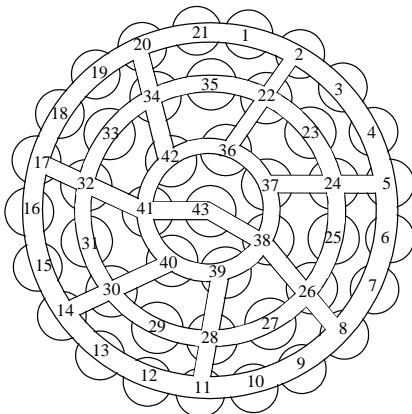


Fig. 3. SEU 43 (cross section)

This fuel bundle type is destined to a high burn up and it is compatible with CANDU 6 Reactor systems. To this purpose, the basic overall dimensions of SEU-43 (Figure 3) fuel bundle were designed to be the same as those of the 37-element bundle [7]. The type of assembly is welded bundles of 43 elements in circular array with brazed appendages. The major feature of SEU-43 bundle is an increase in the number of fuel elements from 37 in the standard CANDU-6 bundle to 43 elements. The SEU-43 bundle consists of 2 fuel element sizes: the 11.50 mm diameter elements (35) in the outer and intermediate ring, and the 13.50mm diameter elements (8) in the inner and center rings. The small-diameter elements in the outer

ring allow the peak element ratings in the bundle to be reduced comparatively with the standard 37-element bundle. The larger-diameter elements in the inner rings of the bundle compensate for the fuel volume lost due to the smaller-diameter outer ring elements.

### SEU IN CANDU REACTORS

In many countries, including Canada and Korea, we would anticipate that after the introduction of CANFLEX bundles containing natural uranium fuel, the next step in the evolution of CANDU fuel cycles would be the introduction of SEU fuel, using the CANFLEX bundle as the carrier. The 20% lower linear element ratings in CANFLEX reduces the peak operating temperatures and hence, fission-gas release, facilitating the achievement of higher burnups. Moreover, the increased thermal hydraulic margins obtained with CANFLEX fuel provide a significant performance enhancement in addition of the other benefits of enrichment.

The inherent differences in the neutronics, and the low fabrication cost of CANDU fuel, mean that the optimal enrichment that minimizes the fuel cycle cost in CANDU reactors is much lower than in a PWR: between 0.9% and 1.2%  $^{235}\text{U}$ , with most of the benefits already achieved between 0.9% and 1.0%. This lower enrichment (and burn up) avoids the life-limiting phenomena that must be addressed in high-burn up LWR fuel. Enrichments around 0.9% are below the threshold at which critically considerations result in restrictions and complications in fuel fabrication and fuel handling. Moreover, with this level of enrichment, fuel management is extremely simple: a regular 2- or 4-bundle shift, bi-directional (adjacent channels are fuelled in the opposite direction) fuelling scheme results in excellent axial power distributions, with or without the presence of the adjuster rods (which are required with natural uranium fuel to flatten the axial power distribution, and lower peak bundle powers)[8]. It is also anticipated that at these enrichments, the transition from a natural uranium-fuelled core to an SEU-fuelled core can be achieved in a straightforward fashion, by simply replacing natural uranium fuel with SEU during the normal course of refueling. Operational considerations are easily met with enrichment at this level, with no changes to the reactor.

Enrichments between 0.9% and 1.2% would reduce fuel-cycle costs by 20 to 30%. This cost savings is partly due to an improvement in uranium utilization: natural uranium requirements (per units of electricity generated) are reduced by about 25% compared to natural uranium fuel in CANDU reactors. Moreover, with enrichments in this range, spent fuel disposal costs are reduced relative to natural uranium by much as 30% [9].

In reactors that have surplus heat removal capability, or in which this can be provided in a cost-effective manner during a planned outage, SEU can be used to uprate the reactor power without increasing the limits on maximum bundle or channel power, by flattening the channel power distribution across the core. This power uprating is done by increasing the power in the outer channels (by reducing their burn up through increasing their refueling rate). Fuel burn up is hence traded-off against higher core power. Power uprating can provide a large economic benefit to operating plants.

In new reactor, SEU provides greater flexibility in design. Using power flattening to obtain more power from a given-sized core has an advantage in capital costs over simply adding more channels to the reactor. In the SEU-fuelled CANDU 9 reactor, using enrichment of around 0.9% to flatten the channel power distribution in the core results in 1100 MW(e) from a 480-channel, Darlington-size core, nominally rated at 935 MW(e). SEU could also be used to increase the pressure-tube thickness to extend pressure tube lifetime, or to upgrade the primary-heat-transport system conditions, thereby achieving

higher thermodynamic efficiency. Decreasing the moderator and reflector volumes could reduce the moderator inventory. SEU also offers greater flexibility in fuel-bundle design, providing, for example, a means of tailoring reactivity coefficients. The use of SEU in the CANFLEX fuel bundle is a key enabling technology in achieving a significant reduction in the capital costs of next-generation CANDU reactors [10].

Finally, the use of RU from reprocessed spent LWR fuel offers access to a potentially very economical supply of enrichment at the optimal enrichment level [11-13]. Previous studies with COGEMA confirmed the suitability of this material as feedstock for CANDU fuel pellets. An earlier preliminary assessment identified the potential advantages of this material in CANDU reactors, especially compared to re-enrichment in a PWR. A detailed assessment of the use of RU in CANDU reactors is currently underway as part of a collaborative program between AECL, BNFL, and KAERI. If this assessment confirms the business case for RU, then the next step will be a demonstration irradiation in a power reactor with CANFLEX fuel. In this context, RU is considered to be available on the open market, and is not linked to a utility's decision to reprocess.

### **CANDU/PWR SYNERGISM**

An attractive opportunity is DUPIC (Direct use of PWR spent fuel in CANDU) fuel cycle. There are two important advantages: reprocessing process is removed and both fissile materials <sup>235</sup>U and Pu are burned.

One example of direct use would be to simply cut the PWR fuel elements to CANDU fuel element length (~50cm), straighten, them, then weld new end-caps to the ends. (Optionally, the elements could be double-clad). The smaller size of PWR fuel would enable the use of a 48- or 61-element fuel bundle, which would significantly reduce the linear element ratings compared with those of a 37-element bundle and enhance fuel performance, and would help to accommodate the variation in fissile content between elements.

Another option in the OREOX process—a thermal-mechanical process that reduces the used PWR pellets to a powder, after the cladding has been removed. The powder would be pressed and sintered as “new” CANDU pellets, and loaded into standard sheaths that would be assembled into standard bundles. The technical feasibility of this second option is the focus of a collaborative program involving AECL, KAERI, and the U.S. Department of State [14]. The IAEA also participates in the safeguards aspects of this program. As part of this program, AECL and KAERI staff fabricated three DUPIC fuel elements from used PWR fuel, in AECL's hot-cell facility at its Whiteshell Laboratories [15], and inserted these elements into the NRU research reactor at the Chalk River Laboratories. The elements have now reached a burn up of 10MWd/kg HE (heavy elements) a little greater than natural uranium burn up. This is half of the target burn up, and one element has now been removed for PIE.

This DUPIC recycling options offer advantages over conventional reprocessing. They all use only dry processes: no wet chemistry is involved, and indeed, there are virtually no liquids. They are simpler than conventional reprocessing, and the expectation is that they will be cheaper. While very preliminary economic analysis suggests that this is the case, much more technical work will be required to define the processes before more credible costs can be confirmed.

A perhaps unexpected benefit of the DUPIC fuel cycle is a reduction in the cost of geological disposal (per unit electricity produced in the system of CANDU reactors and PWRs). The heat load of the used DUPIC fuel (after it has been irradiated in CANDU reactors), is not much different from the decay heat from the original used PWR fuel. That

means that approximately 50% more energy can be derived from the PWR fuel by burning it as DUPIC fuel in CANDU reactors, with no additional penalty in heat load. Because the decay heat determines the density of used fuel packing in a geological repository, this extra energy's obtained with virtually no increase in disposal cost. As a result, the disposal cost for DUPIC fuel (in \$/kWh) is significantly lower than for either used PWR or CANDU fuel [9].

### REMARKS

Whereas natural uranium fuel provides many advantages, the use of slightly enriched uranium (SEU) in CANDU reactors offers lower fuel-cycle costs and other benefits, such as up rating capability through flattening the channel power distribution across the reactor core. Recycled uranium (RU) from reprocessing used ("spent") PWR fuel is a subset of SEU that has significant economic promise. AECL views the use of SEU/RU in the CANFLEX bundle as the first logical step from natural uranium.

High neutron economy enables the use of low-fissile-content fuel in CANDU reactors, which opens up a spectrum of unique fuel-cycle opportunities that exploit the synergism between CANDU reactors and light water reactors (LWRs). At one end of this spectrum is the use of materials from conventional reprocessing of used LWR fuel: CANDU reactors can utilize the RU directly without re-enrichment. At the other end of the spectrum is the DUPIC cycle (Direct Use of Spent PWR Fuel In CANDU), employing only thermal-mechanical processes to convert used PWR fuel into CANDU fuel, with no purposeful separation of isotopes from the fuel, and processing a high degree of proliferation resistance. Between these two extremes are other advanced recycling options that offer particular advantages in exploiting the CANDU reactor's high neutron economy to reuse spent LWR fuel without the need to separate, then enrich the contained fissile material.

### REFERENCES

1. IAEA International Symposium, "Nuclear Fuel Cycle and Reactor Strategies: Adjusting to New Realities", Vienna, Austria, 1997 June 3-6, IAEA-SM-346.
2. Allan, C.J., Baumgartner, P., "Back-End of the Nuclear Fuel Cycle: A Comparison of The Direct Disposal and Reprocessing Options". Proc. Global '97, Yokohama, Japan, 1997 Oct.5-10.
3. Nuclear Fuel Waste Management and Disposal Concept Environmental Assessment Panel. 1998. *Nuclear Fuel Waste Management and Disposal Concept*. Canadian Environmental Assessment Agency, 13<sup>th</sup> Floor, Fontaine Bldg., 200 Sacre-Coeur Blvd., Hull, Quebec, K1A 0H3.
4. OECD/NEA, "The Cost of High-Level Waste Disposal in Geological Repositories. An Analysis of Factors Affecting Cost Estimates", Paris (1993).
5. Suk,H.C. Sim, K-S., Kim, B.G.,Choi, C.B.,Chung, C.H.Lane, A.D., Sears, D.F.,Lau,J.H.K.,Oldaker,I., Boczar,P.G., "CANFLEX as a CANDU Advanced Fuel Bundle", Proc. 5<sup>th</sup> Intl. Topical Mtg. On Nuclear Thermal Hydraulics, Operations and Safety, 1997 April 14-18, Beijing, China.
6. Inch,W.W.R., Thompson, P.,Suk,H.C. "CANFLEX: From Development Concept to a Proven Fuel" Proc. Korea Atomic Industry Forum/Korea Nuclear Society (KAIF/KNS) Annual Conf., Seoul, Korea, 1998 April 15-16.



## USE OF SLIGHTLY ENRICHED URANIUM (SEU) IN PHWR

7. G.Olteanu, "SEU 43 Fuel Bundle Design, ed.1, act.1", ICN Internal Report No 5984/2001
8. Donnelly, J.V., D'Antonio, M., "Fuel-Management Simulations for 0.9% SEU in CANDU 6", Proc. IAEA Technical Committee Meeting on Fuel Cycle Options for Light Water Reactors and Heavy Water Reactors, Victoria, Canada, 1998 April 28-May 1; IAEA-TECDOC-1122.
9. Baumgartner, P., Ates, Y., Boczar, P.G., Ellis, R., Johnson, L., "Disposal Costs for Advanced CANDU Fuel Cycles", Proc. 11<sup>th</sup> Pacific Basin Nuclear Conference (PBNC), Banff, Canada, 1998 May 3-7.
10. Duffey, R.B., Hancox, W.T., Torgerson, D.F., "The Future Of CANDU", presented at this conference.
11. Boczar, P.G., Sullivan, J.D., Hamilton, H., Townes, B.M., Lee, Y.O., Jeong, C.J., Suk, H.C., Mugnier, C., "Recovered Uranium in CANDU: A Strategic Opportunity", Proc. International Nuclear Congress and Exhibition, Toronto, Canada, 1993 October 3-6.
12. Wash, M.R., Inch, W.W.R., Page, R.J., Marsh, G., "Recycled Uranium – An Advanced Fuel for CANDU Reactors", Proc. IAEA Technical Committee Meeting on Fuel Cycle Options for Light Water Reactors and Heavy Water Reactors, Victoria, Canada, 1998 April 28-May 1; IAEA-TECDOC-1122.
13. Suk, H.C. Sim, K-S., Kim, B.G., "CANFLEX-RU Fuel Development Program as One Option of Advanced Fuel Cycles in Korea", Proc. IAEA Technical Committee Meeting on Fuel Cycle Options for Light Water Reactors and Heavy Water Reactors, Victoria, Canada, 1998 April 28-May 1; IAEA-TECDOC-1122.
14. Sullivan, J.D., Boczar, P.G., Cox, D.S., Baumgartner, P., Fehrenbach, P., Yang, M.S., Lee, J.S., "Benefits of the DUPIC Fuel Cycle Strategy", Proc. GLOBAL '99 International Conference on Future Nuclear Systems, Nuclear Technology-Bridging the Millennia, 1999 Aug. 29 – Sept.3, Jackson, Wyoming, USA.
15. Sullivan, J.D., Ryz, M.A., Lee, J.W., "Fabrication of CANDU DUPIC Fuel", Proc. IAEA Technical Committee Meeting on Fuel Cycle Options for Light Water Reactors and Heavy Water Reactors, Victoria, Canada, 1998 April 28-May 1; IAEA-TECDOC-1122.

## FUZZY LOGIC CONTROL OF $^{15}\text{N}$ SEPARATION PLANT

**KAUCSÁR M., V. COSMA, D. AXENTE, A. BÂLDEA, V. BUNEA**

*National Institute for Research and Development of Isotopic  
and Molecular Technologies*

*P. O. BOX 700, 3400 Cluj - Napoca 5, ROMANIA*

### **1. Introduction**

The first paper on fuzzy logic was written by Professor Lotfi Zadeh of the University of California at Berkeley, he is considered to be the founding father of the entire field of fuzzy logic [10]. Zadeh recognized that the true or false nature of the Boolean logic did not account for the many shades of gray found in the real world. To account for the infinite gradations between true and false declaration, Zadeh expanded the idea of a classical set to a fuzzy set. Fuzzy logic – in contrast to the bivalent Boolean logic – is a multi-valued logic. The fuzzy basis function expansion is very powerful because its basis function can be derived from either numerical data or linguistic knowledge, both of which can be cast into the forms of if-then rules.

The process of  $^{15}\text{N}$  separation by chemical exchange in Nitrox system is automatically maintained in optimal operation conditions using a fuzzy logic control system. By automatic control results a maximum production of  $^{15}\text{N}$  with a minimum of raw materials and energy consumption. Comparing with conventional control systems this system responds more intelligently to the imprecise and often contradictory conditions of the outside conditions. By explicitly dealing with noisy information, shades-of-gray control signals, and imprecise input this system mimics, in closer fashion, the way we humans use the mathematical model to maintain the optimal isotopic exchange ratio. Such similarity between machine behaviour and human behaviour will reduce the need for complex external controls, make the system more “reasonable”.

### **2. The configuration and the structure of the fuzzy controller**

In developing the fuzzy logic control system the above basic configurations of the fuzzy controllers are considered: direct control, feedforward control and parameter adaptive control.

The *direct control* is the most obvious fuzzy controller configuration. In a feedback control system the fuzzy controller is placed in the forward path and replaces the conventional P, PI or PID controller. (Fig. 1). The process output is compared with the reference input, and if there is a deviation, the controller takes action according to the control strategy.

In *feedforward control* (Fig. 2) the fuzzy controller compensates an external disturbance. The figure shows only the controller and the fuzzy compensator, the process and the feedback loop are omitted. This scheme, disregarding the disturbance input, can be viewed as a collaboration of linear and nonlinear control actions. The controller may be a linear controller, while the fuzzy controller is a supplementary nonlinear controller.

Fuzzy rules are also used to correct tuning parameters in *parameter adaptive control* configuration (Fig. 3). If the nonlinear separation plant changes the operating point, it make possible to change the parameters of the controller according to each operating point. This is called *gain scheduling* because originally was used to change process gain.

## FUZZY LOGIC CONTROL OF $^{15}\text{N}$ SEPARATION PLANT

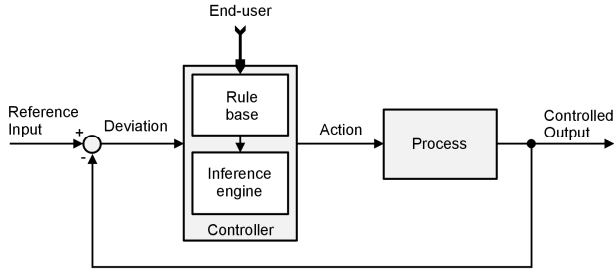


**Fig. 1.** Direct control configuration

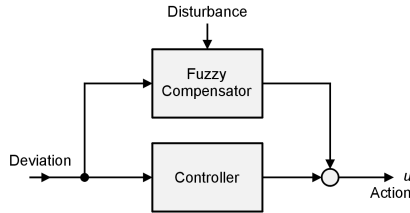


**Fig. 2.** Feedforward configuration

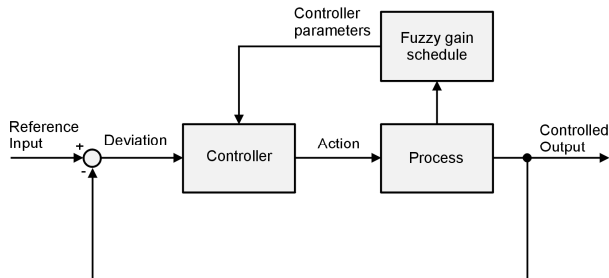


**Fig. 3.** Adaptive control configuration

The basic components of a fuzzy controller are shown in Figure 4. In this simplified general block diagram, the controller is placed between the pre-processing and post-processing block and it contains four functional blocks: fuzzifier, rules, inference engine, and defuzzifier. The fuzzifier maps crisp input numbers into fuzzy sets. The fuzzy set is needed in order to activate rules, which are in terms of linguistic variables. The inference engine maps fuzzy sets into fuzzy sets. It handles the way in which rules are combined. In our applications, crisp numbers must be obtained at the output of the fuzzy controller. The defuzzifier serves this purpose, maps output fuzzy sets into crisp numbers.

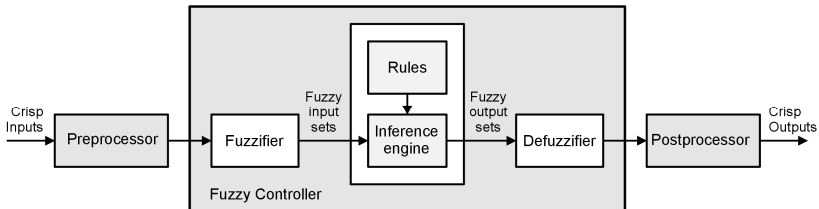


**Fig. 4.** General bloc diagram of the fuzzy controller

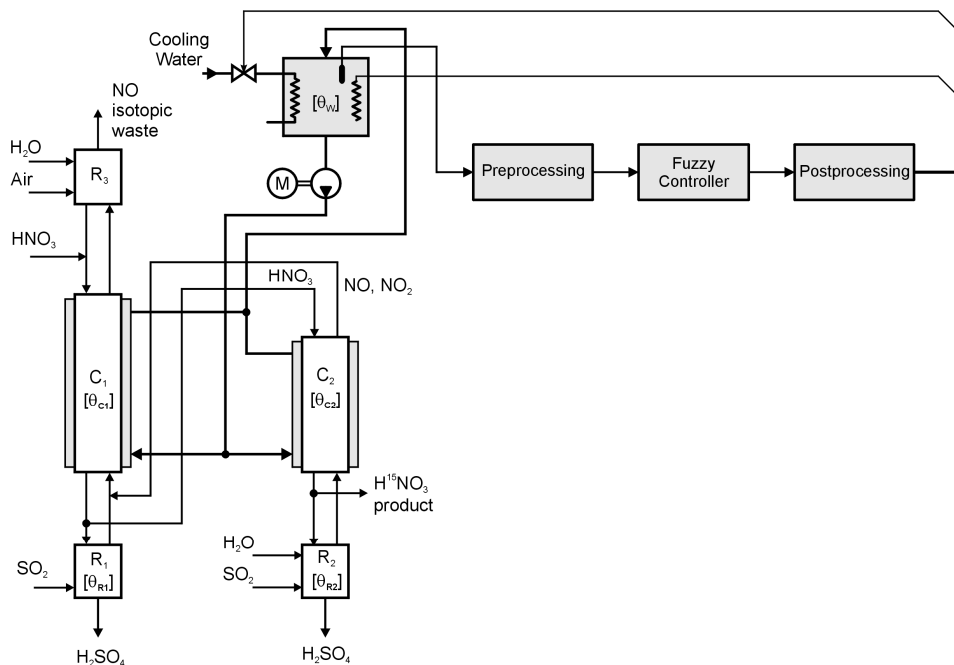


Fig. 5. Simplified block diagram of the auxiliary water temperature fuzzy logic controller

In controlling the  $^{15}\text{N}$  separation plant the temperature of the separation columns is one important parameter. Thus, the temperature  $\theta_{C1}$  and  $\theta_{C2}$  of the separation columns must be maintained at a constant level, therefore the columns are surrounded by auxiliary water with controlled temperature. Using a fuzzy controller in direct control configuration (Fig. 5) the temperature of this water is maintained at  $26\text{ }^\circ\text{C}$ . In refluxors R1 and R2 the exothermal chemical reactions take place in about a 10-20 cm zone. These zones must be maintained at a given optimal height, and are localized measuring the temperature gradient over the height of the refluxors. Therefore each refluxor is provided by a temperature sensor array (Fig. 6). The position of the reaction zone is controlled in function of two main parameters: the flow of the nitric acid ( $L_{C1}$  and  $L_{C2}$ ) and the flow of the sulfur dioxide ( $G_1$  and  $G_2$ ).  $L_{C1}$  and  $L_{C2}$  flow are maintained at an optimal level using constant flow rate feeding pumps. The fuzzy controller with two precision flow regulators controls  $G_1$  and  $G_2$  flow so the position of the reaction zones falls in the predefined zone for optimal isotopic exchange [2], [3].

### 2.1. Preprocessing

The preprocessor performs signal-conditioning steps applied to the crisp inputs:

- quantization in connection with sampling and rounding to integers
- normalization and scaling onto the standard input range
- filtering in order to remove the superimposed noise.

The crisp inputs are the measurements from sensors and transducers of the separation plant. The preprocessor passes the data on to the controller.

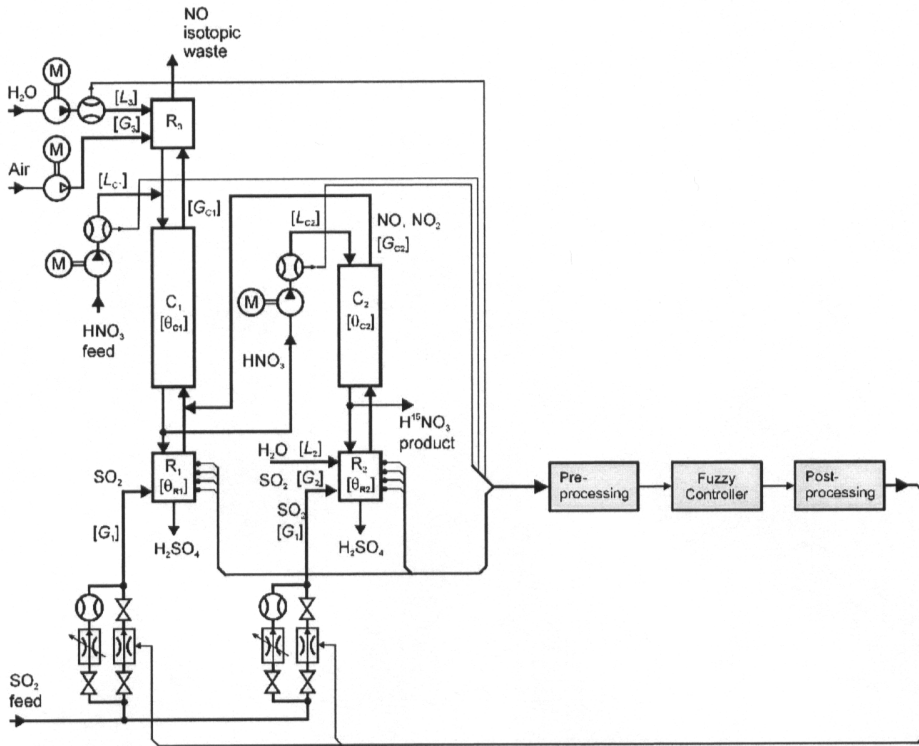


Fig. 6. Simplified block diagram of the reaction zone position fuzzy logic controller

## 2.2. Fuzzification

The first block inside the controller is the fuzzifier, which converts the crisp inputs into fuzzy sets so that it can be operated by the system. Each value of input data is converted to degrees of membership by a lookup in one or several membership functions.

A fuzzy set  $F$  in  $U$  may be represented as a set of ordered pairs of a generic element  $x$  and its grade of membership function:  $F = \{(x, \mu_F(x)) \mid x \in U\}$ . When  $U$  is continuous (e.g., the real numbers),  $F$  is commonly written as  $F = \int_U \mu_F(x)/x$ . When  $U$  is discrete  $F$  is commonly written as  $F = \sum_U \mu_F(x)/x$ . Referring to the given application the fuzzifiers uses triangular, trapezoidal, s-curve, z-curve,  $\pi$ -curve and bell-shaped membership functions (Fig. 7 and 8).

## 2.3. Rule Evaluation – Inference engine

Rule evaluation, also referred to as fuzzy inference, applies the rules to the fuzzy inputs that were generated in the fuzzification process. The inference engine uses linguistic rules to determine what control action should occur in response to a given set of input values. The rules may use several variables both in the antecedent and the consequent. The fuzzy rule base consists in a collection of IF-THEN rules, which generally are expressed as:

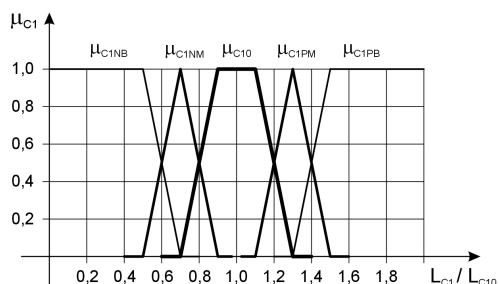


**Fig. 7.** Membership functions for  $L_{C1}$  and  $L_{C2}$  flow of nitric acid

$\mu_{C1O}$  – optimal flow

deviations from optimal:

$\mu_{CPM}$  – positive medium;

$\mu_{CPB}$  – positive big;

$\mu_{CNM}$  – negative medium;

$\mu_{CNB}$  – negative big

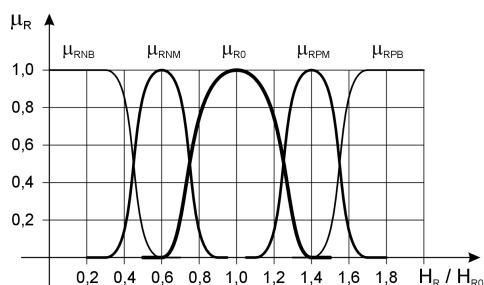


**Fig. 8.** Membership functions for the position of reaction zone:

$\mu_{R0}$  – optimal height

deviations from optimal:

$\mu_{RPM}$  – positive medium;

$\mu_{RPB}$  – positive big;

$\mu_{RNM}$  – negative medium;

$\mu_{RNB}$  – negative big

$$R^{(l)} : \text{IF } u_1 \text{ is } F_1^l \text{ AND } u_2 \text{ is } F_2^l \text{ AND } \dots u_p \text{ is } F_p^l \text{ THEN } v \text{ is } G^l$$

where  $l=1,2, \dots, M$ ,  $F_2^l$  and  $G^l$  are fuzzy sets in  $U_i \subset R$  and  $V \subset R$  ( $R$  denotes

the set of real numbers), the linguistic variables  $\mathbf{u} = \text{col}(u_1, \dots, u_p) \in U_1 \times \dots \times U_p$ , and  $v \in V$ .

The fuzzy rules in our application are presented in multidimensional table format. The input variables are laid out along the axes, and the output variable is inside the table. In case the table has an empty cell, it is an indication of a missing rule, and this format is useful for checking completeness.

In order to maintain the temperature of the auxiliary water the output of the fuzzy controller acts two actuators – heater and cooler. If temperature is lower than the reference value only the heater is actioned. If temperature is higher than the reference value the cooler is actioned only. If the temperature is inside the tolerance interval no action is taken. The optimal isotopic exchange is assured by a sophisticated control of the position of reaction zones. If the flow of the nitric acid ( $L_{C1}$ ,  $L_{C2}$ ) is inside the tolerance interval corresponding to the optimal isotopic exchange then the flow of the dioxide sulfur ( $G_1$ ,  $G_2$ ) is controlled taking into consideration only the position of the reaction zone. If the flow of the nitric acid ( $L_{C1}$ ,  $L_{C2}$ ) is out of the tolerance interval then the flow of the dioxide sulfur ( $G_1$ ,  $G_2$ ) is controlled in function of the flow of the nitric acid ( $L_{C1}$ ,  $L_{C2}$ ) and the position of the reaction zone.

#### 2.4. Defuzzification

The fuzzy set which results after the inference engine must be converted into a crisp signal that can be sent to the process control. This operation is called defuzzification. There are several defuzzification methods. The most used methods are: center of gravity, 116

center of gravity method for singletons, bisector of area, mean of maxim, leftmost maximum and rightmost maximum. In this separation plant control the defuzzification is based on the center of gravity. The crisp output value  $u$  is the abscissa under the center of gravity of the fuzzy set:

$$u = \frac{\sum_i \mu(x_i) x_i}{\sum_i \mu(x_i)}$$

Here  $x_i$  is a running point in a discrete universe, and  $\mu(x_i)$  is its membership value in the membership function. The expression can be interpreted as the weighted average of the elements in the support set.

### 3. Conclusions

The integration of fuzzy logic into the separation plant control offers a series of major implications of higher machine intelligence and includes such benefits as:

- a higher degree of user friendliness
- higher degrees of autonomy
- better performance
- lower power consumption
- self-diagnostic capabilities
- a higher degree of adaptability
- a potential for outperforming a skilled human operator

### REFERENCES

1. Adcock, T. A. – “*What is Fuzzy Logic? An Overview of the Latest Control Methodology*”, Digital Signal Processing – Semiconductor Group, Texas Instruments Incorporated, 1993.
2. Axente, D. – “*Metodica separării pe coloane a izotopului  $^{15}\text{N}$* ”, Studii cercetări chimie, tom.19, nr.4, 1971, pp. 395-415.
3. Benedict, M., Pigford, T.H., Levy, H.W. – “*Nuclear Chemical Engineering*”, McGraw-Hill Book Co., Boston, 1998.
4. Fullér R. – “*Neural Fuzzy Systems*”, Åbo Akademis tryckeri, Åbo, ESF Series A: 443, 1995, 249 pages.
5. Jantzen, J. – “*Design of Fuzzy Controllers*”, Technical University of Denmark, Department of Automation, Denmark, Tech. report no 98-E 864, September 30, 1999.
6. Kosko, B. – “*Fuzzy systems as universal approximators*”, Proc. IEEE 1992 Int. Conference Fuzzy Systems, San Diego, 1992, pp. 1153-1162.
7. Kosko, B. – “*Neural networks and fuzzy systems*”, Prentice-Hall, New Jersey, 1992.
8. Mamdani, E.H. – “*Applications of fuzzy logic to approximate reasoning using linguistic synthesis*”, IEEE Transactions on Computers, Vol. 26, No. 12, 1977, pp.1182-1191.

9. Mendel, J.M. – “*Fuzzy Logic Systems for Engineering: A Tutorial*”, Proceedings of the IEEE, Vol.83, No.3, March 1995, pp. 345-377
10. Zadeh, L.A. – “*Fuzzy sets*”, Information and Control, Vol. 8, 1965, pp. 383-353.
11. Zadeh, L.A. – “*Knowledge representation in fuzzy logic*”, IEEE Transactions on Knowledge and Data Engineering, Vol. 1, 1989, pp. 89-100.
12. Zadeh, L.A. – “*Outline of a new approach to the analysis of complex systems an decision processes*”, IEEE Transactions on Systems, Man and Cybernetics, Vol. SMC-3, No. 1, 1973, pp. 28-44.
13. Zadeh, L.A. – “*the concept of a linguistic variable and its application to approximate reasoning*”, Information Sciences, 1975, Vol. 8, pp. 199-249, and Vol. 9, pp. 43-80.



## APPLICATION OF STABLE ISOTOPES IN ENVIRONMENTAL STUDIES AND IN FOOD AUTHENTICATION

ANDRZEJ G. CHMIELEWSKI, RYSZARD WIERZCHNICKI, MAŁGORZATA DERDA, AGNIESZKA MIKOŁAJCZUK, GRAZYNA ZAKRZEWSKA-TRZNADEL

*Institute of Nuclear Chemistry and Technology  
Dorodna 16, 03-195 Warsaw (Poland)*

**ABSTRACT.** Environmental isotopes of light elements are used as modern, specific and reliable technique for studies of global element cycles, hydrology, and recently more and more for pollution monitoring. After the identification and quantification of pollution, it is of interest to characterize the sources and determine whether the pollution is locally derived or has been transported over long distances. Surface sources of pollution can be designated as natural, industrial, agricultural or domestic.

Atmospheric sulphur compounds e.g.  $\text{SO}_2$  and  $\text{SO}_4^{2-}$  originate from coal combustion, volcano eruption or are produced by sea microorganisms. Measurements of  $^{34}\text{S}/^{32}\text{S}$  in the samples are a useful way to distinguish of the sources. Isotopic ratio  $^{34}\text{S}/^{32}\text{S}$  can be considered as a natural marker for the pollution origin study.

Among other hydrological and chemical methods, tritium analysis and methods based on measurement of isotopic ratio of  $^2\text{H}/^1\text{H}$ ,  $^{34}\text{S}/^{32}\text{S}$  and  $^{18}\text{O}/^{16}\text{O}$  in  $\text{SO}_4^{2-}$  ions are used for monitoring and prognosis of the ground water quality in the vicinity of Bełchatów lignite mine. INCT carries on periodical monitoring of ground water in that industrial region.

Natural products such as wine, spirits, fruit juices, flavours, oils, and honey are prime targets for fraudulent adulteration because of their high prices. The stable isotope techniques based on measuring the natural abundance of isotope ratios  $^2\text{H}/^1\text{H}$ ,  $^{13}\text{C}/^{12}\text{C}$ , and  $^{18}\text{O}/^{16}\text{O}$  in organic molecules have become the most efficient method to authenticate foodstuffs.

The relative abundance of stable isotopes in food from different areas in Poland was measured by the isotopic ratio mass spectrometer Delta Plus, Finnigan MAT, equipped with auxiliary accessories, as the difference relative to a standard (Vienna - Standard Mean Ocean Water).

### 1. Introduction

The chemistry of isotopes experienced a true revival during the 90s. Firstly, in response to the discovery of new experimentally confirmed phenomena new theoretical concepts were proposed, enabling a more efficient approach to the separation set-up design. Secondly, substances of altered isotopic composition found new practical applications thus becoming desirable products. Stable isotopes found new fields of application, such as medicine, environment protection as well as the areas of science and industry relating directly to the improvement of quality of human life. This work is intended to present some examples of stable isotopes application in environmental research and food authentication.

### 2. Stable isotopes in environmental studies

#### 2.1. Water resources management

In addition to classical geologic/hydrologic methods, isotopic abundance of  $^2\text{H}$ ,  $^3\text{H}$ ,  $^{13}\text{C}$ ,  $^{14}\text{C}$ ,  $^{15}\text{N}$ ,  $^{18}\text{C}$ ,  $^{34}\text{S}$  is widely applied for investigation of the history and pathway of water in different parts of hydrological cycle. Isotopic content has been employed to determine

- the origin and age of different water bodies
- the location and proportion of water recharge
- the degree of mixing
- velocity of groundwater flow

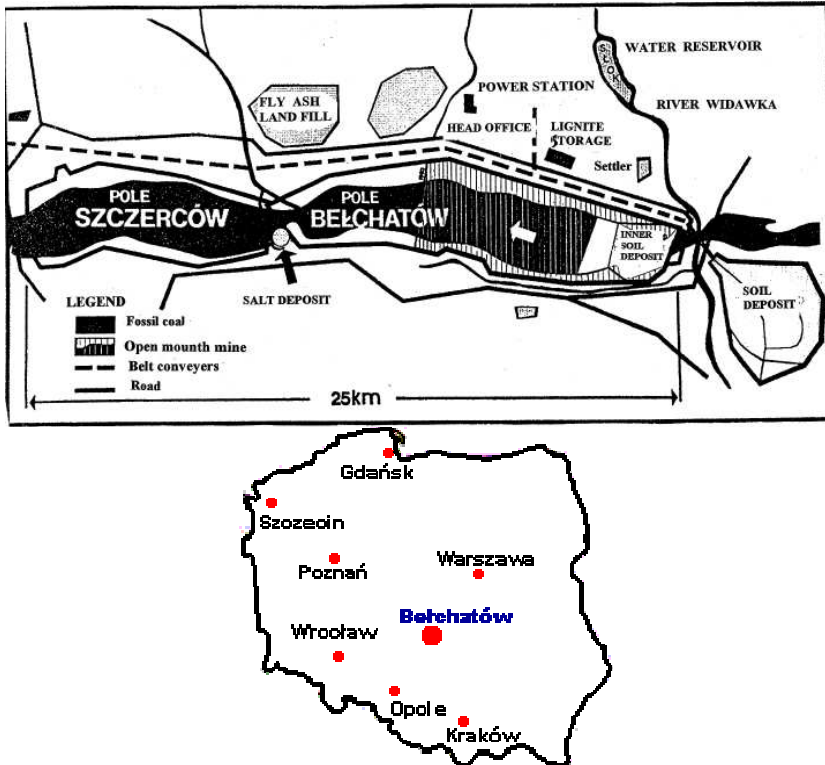


Fig. 1. BĘŁCHATÓW the Polish biggest lignite mine.

Among other hydrological and chemical methods, tritium analysis and methods based on measurement of isotopic ratio of  $2\text{H}/^1\text{H}$ ,  $^{34}\text{S}/^{32}\text{S}$  and  $^{18}\text{O}/^{16}\text{O}$  in  $\text{SO}_4^{2-}$  ions are used for monitoring and prognosis of the ground water quality in the vicinity of Belchatow lignite mine [1]. This is the biggest Polish open mouth mine, and with a new proposed expansion (the Szczercow field) will be in operation for the next 50 years. The general scheme of the region is presented in Fig. 1. The large salt deposit lies between the fields. Ground waters are pumped to allow exploitation of the mine.

The main physico-chemical features as well as micro and macro components and environmental isotope concentrations were measured in the surface and ground waters in the hypothetical strip interaction region. It has been found that the outfall of mine pumped waters to the Widawka river do not spoil water quality, which preserves the first class of purity in the course between Ruszczyń and up to the Warta river. The forecast of the salinity increase for ground waters pumped by the protection barrier of salt deposit Debina have been worked out for water table altitude = 50.0 m below the sea level (state in December 2000). The range of the wet ash deposit interaction on water quality pumped by the Belchatow mine drainage system have been determined and evaluated.

### 2.2. Determination sulphur isotope ratio ( $^{34}\text{S}/^{32}\text{S}$ ) in coal combustion process.

Atmospheric sulphur compounds e.g.  $\text{SO}_2$  and  $\text{SO}_4^{2-}$  originate from coal combustion, volcano eruption or are produced by sea microorganisms. Measurements of  $^{34}\text{S}/^{32}\text{S}$  in the samples are a useful way to distinguish the sources [2] of pollution. Intensive researches concerning analyses of sulphur isotope ratio in coal and different combustion streams (gases, desulphurisation product) are going on [3].

The aim of the work is determination of sulphur isotope composition in products of coal combustion process and application of sulphur isotopes ratio ( $\delta^{34}\text{S}$ ) as an environmental tracer. There are two main tasks of this work. The first is characteristic of sulphur isotopes composition in Polish coals from Upper Silesia and Lublin. Preliminary results shows, that sulphur in coal has a different isotopic composition (Tables 1 and 2) and occurs in many different forms (pyrite sulphur, sulphate and organic sulphur). Three samples from Sosnica Mine were taken from different depths (Table 2). There is a big differentiation not only between the concentration of the sulphur, but also between the composition of this element in source materials.

The chemical compounds separation and determination of isotope composition may provide an information concerning the era and mechanism of sulphur incorporation in organic-rich sediments. The stable isotope composition of sulphur compounds of industrial origin present in atmosphere, biosphere, hydrosphere, groundwater, soil, etc., may differ from natural analogues. The analysis of stable isotope of sulphur is the only method to distinguish anthropogenic and natural source of sulphur.

**Table.1.**

Sulphur isotopes ratio for sulphur present in Polish coals

Coal mine	S[%]	$\delta^{34}\text{S}$ [‰]		
		Pyrite sulphur	Organic sulphur	Sulphate sulphur
Bogdanka	1.23	1.29	-2.50	-1.95
Kazimierz Juliusz	0.79	6.37	6.18	7.27
Chwalowice	0.81	1.97	3.85	1.19
Jankowice	0.64	0.33	15.88	-
Slask	0.74	10.50	4.40	13.71
Sosnica	2.06	-6.62	4.66	-1.88
Belchatow*	0.30	-	9.37	-

\*lignite

**Table 2.** $\delta^{34}\text{S}$  of coals from the Sosnica Mine

Total S[%]	Sulphur content S[%]			$\delta^{34}\text{S}$ [‰]		
	Pyrite	Sulphate	Organics	Pyrite	Sulphate	Organics
0.51	0.36	0.08	0.07	4.05	4.08	4.29
0.75	0.37	0.03	0.35	7.32	10.88	9.71
2.06	1.28	0.10	0.68	-6.62	-1.88	4.66

The technique may be used for:

- monitoring of water;
- investigation of gypsum dissolution;
- investigation of ashes leaching;
- investigation of deposition of sulphur from gases after desulphurisation process;

### 3. Stable isotopes in food authentication

Natural products such as wine, spirits, fruit juices, flavours, oils, and honey are prime targets for fraudulent adulteration because of their high prices. Traditional analytical methods like HPLC, GS and GC-MS make possible the identification and quantification of all the major molecules present, but more sophisticated analytical methods are required to detect whether natural ingredients have been mixed with similar materials from cheaper (synthetic) sources. Stable isotope composition is an important tool for food authenticity and control of the origin. It allows detecting the origin from a geographic point of view or from the point of view of the production processes. The measurement of various isotopic

ratios (hydrogen, oxygen, carbon and nitrogen) in different fractions of a product often enables the characterisation of the origin of starting materials. The isotopic fractionation of those elements in the environment undergoes complex patterns allowing to establish the correlation between the food (fruits, vegetables etc.) and raw materials (water and CO<sub>2</sub>). The aim of the study is to find the relationship between isotope composition of different sorts of food and its geographical origin and to compare the data from different regions of Poland. The samples are received directly from a producer. Stable isotopic composition (<sup>18</sup>O/<sup>16</sup>O, <sup>13</sup>C/<sup>12</sup>C, <sup>15</sup>N/<sup>14</sup>N and D/H) was measured for food (apples, tomatoes, potatoes, champignons and red beet) from different region of Poland. The collected data gives a possibility to find the relationship between time and place of origin and isotope ratio.

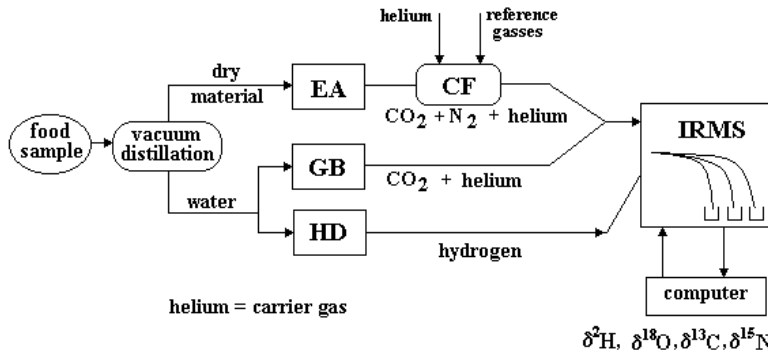


**Fig. 2.** Block diagram of the sample preparation and measuring arrangement. EA - Elemental Analyzer, GB - GasBench II, HD - H/Device, CF -ConFloIII, IRMS - Isotope Ratio Mass Spectrometer

The composition of water present in the food was tested. Hydrogen was measured by H/Device and oxygen isotope ratio by Gasbench II (both instruments connected with mass spectrometer). For the comparison the water samples from the region of plant growing was collected and measured. In this study for measurements of carbon and nitrogen composition in food, we use our new instrument Elemental Analyser coupled with mass spectrometer (Fig.2). Fig.3 shows the places where samples were collected. The results of measurements of stable isotope composition <sup>18</sup>O/<sup>16</sup>O, <sup>13</sup>C/<sup>12</sup>C, <sup>15</sup>N/<sup>14</sup>N, D/H and geographical origin of tested food: apples, potatoes, tomatoes, red beet and champignons are presented at the Figures 4 and 5.

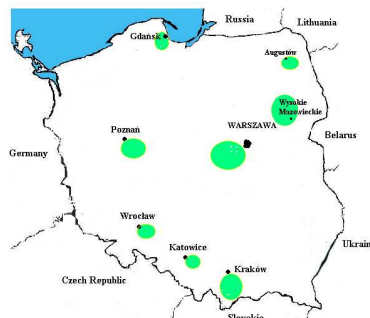


**Fig. 3.** Regions of sample collection

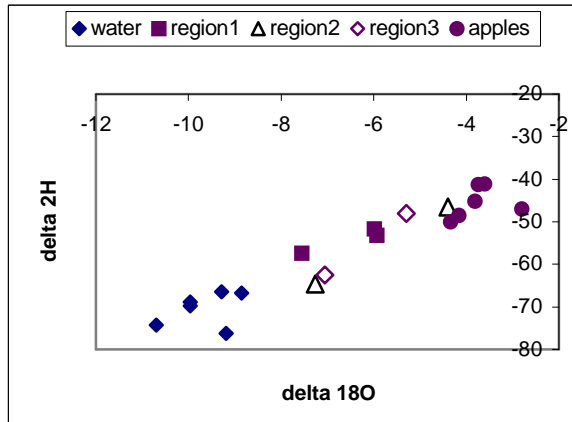


Fig. 4. Relation between  $\delta\text{D}$  and  $\delta^{18}\text{O}$  in water and food samples

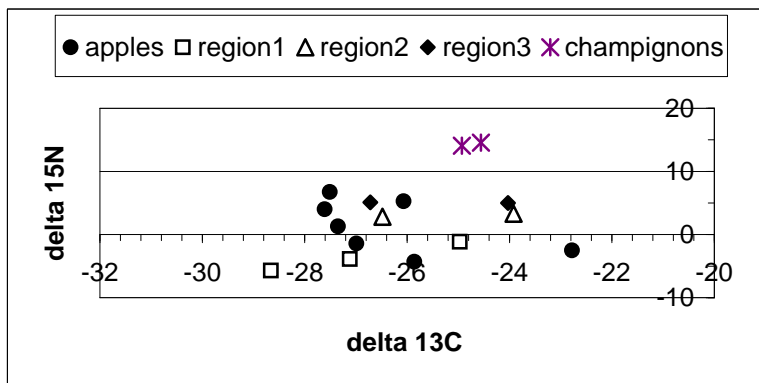


Fig. 5. Relation between  $\delta^{15}\text{n}$  and  $\delta^{13}\text{C}$  in water and food samples

#### 4. Conclusions

The isotope ratio analysis seems an efficient tool for environmental monitoring. It can be used to predict the ground water quality in industrially devastated regions and as a tracer to track the products of the combustion of particular coal.

The new field of application of this technique is food quality control and food authenticity confirmation. The detection of frauds by analysis of the isotopic composition of the food is a well-established technique for a range of substances, but it still requires a huge effort to spread its applications. Isotopic methods become a reliable tool for checking the compliance of goods with and international regulations and several isotopic methods have already been included as a official standards for food quality and authenticity control.

## REFERENCES

1. Sołtyk W., Owczarczyk A., Walendziak J., Methods of monitoring and prognosis of ground water quality changes in the region of power-mine complex „Belchatów” 2001, INCT Report 2/2001, Warsaw, 34 pp.
2. Andrews J.E., Brimblecombe P., Jicklus T.D., Liss P.S., An Introduction to Environmental Chemistry, WNT, Warszawa, 1999 (Polish Edition).
3. Chmielewski A. G., et al., (2002), Sulfur isotope composition of Polish coals, *Nukleonika*, 47, 569-570.

## THE THEORY OF THE THERMAL-DIFFUSION COLUMN: A CRITICAL REVIEW

**ILIE HODOR**

*National Institute for R&D of Isotopic and Molecular Technologies  
P.O.Box 700, 400293 Cluj-Napoca, Romania*

**ABSTRACT.** It is critically reviewed the theoretical literature of the thermal-diffusion column: the original and improved Furry-Jones-Onsager theories, the forgotten effect, the involvement of the chemical exchange reactions, and the application of separation-of-variables to the linearized problems. A series of weaknesses are pointed out and tentative plans for more rigorous theoretical approach are mentioned.

### Introduction

Thermal-diffusion (TD) consists in the fact that a temperature gradient in a mixture of fluids gives rise to a flow of one component relative to the mixture as a whole. The phenomenon has a small separation effect, which is very small for isotopic mixtures.

In 1938 Clusius and Dickel<sup>[1]</sup> found their *thermal-diffusion column*, which can multiply considerably the TD elementary separation effect with a countercurrent convection in the column. The mixture is placed between two vertical walls, one hot, and one cold. There are two typical geometries: (a) the plane case, when the two walls are plan-parallel, and (b) the cylindrical case, when the two walls are coaxial cylinders. The horizontal temperature gradient gives rise to a density gradient, which, at its turn, gives rise to the convective countercurrent flow. The geometrical conditions are chosen so that the flow is lamellar.

In 1938, Furry, Jones, and Onsager (FJO)<sup>[2-4]</sup> published their famous theory of the TD column, which has played a central role in numerous studies that have followed.

A few years ago I discovered an error in the FJO theory and decided to re-examine the main theoretical TD literature. The purpose of this communication is to show the present state of this undertaking.

### FJO theory

The FJO theory is derived for a binary mixture and assumes the validity of the following equations for the mass flux  $J_1^*$  due to molecules of species 1 and for the molecular average velocity of all species  $\mathbf{v}$  respectively,

$$J_1^* = \rho[\mathbf{v}c_1 + D(-\nabla c_1 + \alpha c_1 c_2 \nabla \ln T)] \quad (1)$$

$$r^{-1}(\partial/\partial r)r\eta(\partial\mathbf{v}/\partial r) = (dp/dz) + \rho g \quad (2)$$

where  $\rho$  - mass density,  $c_i$  - mole fraction of species  $i$ ,  $D$  - coefficient of ordinary diffusion,  $T$  - absolute temperature,  $\alpha$  - thermal diffusion constant,  $p$  - pressure,  $\eta$  - viscosity,  $g$  - acceleration of gravity, and  $(r, z)$  - cylindrical coordinates. Eq. (2)

involves the assumption that  $\mathbf{v}$  is parallel to  $z$ -axis. The main result of the column theory is the transport equation

$$\tau_1^* = \sigma^* c_1 + H^* c_1(1 - c_1) - (K_c^* + K_d^*)(dc_1/dz), \quad (3)$$

where  $\tau_1^*$  stands for mass transport of the species 1 through the column,  $\sigma^*$  stands for total mass transport through the column, and  $H^*$ ,  $K_c^*$ ,  $K_d^*$  are some definite integrals.

### ***An error in the FJO theory***

In 1984 I published an overall axiomatic theory of the separation column<sup>[5]</sup> and, as an application, derived an independent theory of the TD column. My result and that of FJO were similar and I thought, at that time, that they coincide.

Kitamoto *et al.*<sup>[6]</sup> studied hydrogen isotope separation using thermal-diffusion column for hydrogen gas. When the mixture is binary, say H-D, three molecular species D<sub>2</sub>-DH-H<sub>2</sub> are present and the exchange reaction H<sub>2</sub>+D<sub>2</sub>=2HD takes place at the hot wall. For such a system Kitamoto *et al.*<sup>[6]</sup> developed a theory with 12 column constants instead of the three constants ( $H^*$ ,  $K_c^*$ ,  $K_d^*$ ) in Eq. (3).

From the theory in Ref. 5 it follows that if only two isotopes are present and if the isotopic effects are small, then an equation of the type (3) can be derived, with only three constants, indifferent of how many molecular types and what kind of exchange reactions are involved. Thus, I derived an equation of the type (3)<sup>[8]</sup> for the Kitamoto *et al.*'s problem. To verify my result I considered the limit case when deuterium concentration is very small, in which case, my coefficients ( $H$ ,  $K_c$ ,  $K_d$ ) must coincide with those of FJO. After repeated verification I concluded that the two results did not coincide. Then I analyzed the original FJO papers and made an astonishing discovery: the discrepancy was due to an error in the FJO theory. Namely, in the FJO theory, it is constantly assumed that: *the mass of a component in a binary mixture is given by the product between the mass of the whole mixture and the molar concentration of that component*. This is strictly correct only if  $m_2/m_1 = 1$ , where  $m_1$  and  $m_2$  (with  $m_2 > m_1$ ) are the molecular masses of the two components. The same error is included in Eq. (1), the corresponding correct equation of the flux being

$$\mathbf{J}_1 = m_1 n [c_1 \mathbf{v} - D(\nabla c_1 - \alpha c_1 c_2 \nabla \ln T)] \quad (4)$$

where  $n$  is the total molar density.

I corrected<sup>[9]</sup> the FJO theory using the original FJO method of derivation though the more rigorous method from Ref. 5 could be applied. The result was similar to Eq. 3,

$$\tau_1 = m_1 \hat{\tau} c_1 + H c_1(1 - c_1) - (K_c + K_d)(dc_1/dz) \quad (5)$$

where  $\hat{\tau}$  is the total molar transport through column. For distinction, the quantities affected of the FJO error are marked with asterisk; that is, the equations for ( $H$ ,  $K_d$ ,  $K_c$ ) differ from those corresponding to ( $H^*$ ,  $K_c^*$ ,  $K_d^*$ ). The correlation between corrected and original theory is given in Ref. 8.

The derivation procedure of the FJO theory is not rigorous; it uses a series of intuitive simplifying assumptions. This circumstance has generated discussions in literature and attempts have been made to improve the theory. However, the FJO error was not noticed in an interval of about sixty years; there are two explanations for that:



1. As shown in Ref. 8, the effect produced by FJO error is really large only if the following two conditions are simultaneously fulfilled:

- i. The TD-column is operated with extraction (not at total reflux);
- ii. The ratio  $m_2/m_1$  is sufficiently large (for a  $^3\text{He}$ - $^4\text{He}$  mixture, when  $m_2/m_1 = 1.25$ , the error effect can be up to 33%; if  $m_2/m_1 = 10$  the error effect can be huge).

2. Usually, a paper is not analyzed in order to find elementary errors in it, the more so when the authors are eminent (Onsager won Nobel Pries in 1968). (It is to note that I discovered the error by verifying a new theory for which I took FJO theory for granted.)

It seems that the two conditions (i and ii) have not been fulfilled in the experimental research. For simplicity, the TD column was generally studied at total reflux (closed column) and not many studies were made with a ratio  $m_2/m_1$  sufficiently greater than unity.

One could assert that the curious FJO-assumption is not an error but merely a simplifying assumption. That cannot be true as this assumption is not necessary in the derivation of the theory and, on the other hand, FJO had in view to apply their theory to helium isotope separation<sup>[4]</sup> where the ratio  $m_2/m_1$  is substantially greater than unity.

#### Other comments on TD column theory

The comments that follow are based on a series of previous theoretical studies<sup>[5,7-11]</sup>.

1. Besides of the original<sup>[2,4]</sup> and corrected<sup>[9]</sup> FJO theory, a *variant derived by Rutherford*<sup>[12]</sup> should be mentioned.

Rutherford<sup>[12]</sup> affirmed that “the FJO theory was originally developed for mixtures of heavy isotopes” even if Jones and Furry applied their theory also to helium isotope separation (Ref. 4, pg. 210). He considered that “the theory can be extended to include mixtures of light isotopes” merely by using mass fraction  $w_i$  instead of mole fractions  $c_i$  and mass average velocity  $\mathbf{v}_m$  instead of molar average velocity  $\mathbf{v}$ . Doing this change, Rutherford re-derived the theory using the flux equation

$$\mathbf{J}_1 = \rho w_1 \mathbf{v}_m - \rho D (\nabla w_1 - \alpha w_1 w_2 \nabla \ln T). \quad (6)$$

One can demonstrate by algebraic manipulation that this flux is identical with that given by Eq. (4). That is, Rutherford used a correct flux so that he derived a correct theory, but he did not mention this essential quality as compared with the FJO theory.

Both theories, Rutherford’s<sup>[12]</sup> and mine<sup>[9]</sup>, are similar corrected FJO theories, but strictly speaking they do not coincide: in the first<sup>[12]</sup> it is supposed that  $\mathbf{v}_m$ , in the second<sup>[9]</sup> that  $\mathbf{v}$  is parallel with z-axis; or it was shown<sup>[9]</sup> that the two conditions generally cannot be fulfilled simultaneously. However, both theories assume that  $\alpha$  is small, which mathematically means  $\alpha \rightarrow 0$ , and for this limit  $(\mathbf{v}_m - \mathbf{v}) \rightarrow 0$ . It follows that the two theories coincide to the limit, or that the difference between them is a term of the second order (proportional to  $\alpha^2$ ).

Rutherford tested his theory by separation experiments at total reflux with mixtures of  $^3\text{He}$  and  $^4\text{He}$ . In spite of the fact that the experimental errors were quite large, he considered that his theory is suitable for mixtures of light isotopes. We know now that, at total reflux, all three theories FJO, (<sup>[9]</sup>), and (<sup>[12]</sup>) are equally suitable, the difference between them being only a term of the second order which should be covered by experimental errors.

2. *Forgotten effect.* In the original<sup>[2-4]</sup> and corrected<sup>[9,12]</sup> FJO-theory, it is assumed that the horizontal gradient of density is caused only of temperature gradient. De Groot et al.<sup>[13]</sup> drew the attention upon a “forgotten effect” which consists in the influence of the concentration gradient upon the density gradient. Numerous attempts<sup>[14-19]</sup> have been made to derive the phenomenological theory of the TD-column with forgotten effect included but to date there has no rigorous derivation.

Prigogine et al.<sup>[20]</sup> published batch experiments on TD-column of some binary organic solutions in which they obtained bizarre separation results: the difference in concentration between top and bottom started in one direction, slowed, and then went in the opposite direction, giving separations opposite from the original direction. This behavior, which has been called *concentration reversal*, was attributed by them to the influence of concentration on density, that is to forgotten effect. Concentration reversal was also observed experimentally by Jones and Milberger<sup>[21]</sup>.

Using carefully constructed and operated columns, Korchinsky and Emery<sup>[22]</sup> were unable to obtain concentration reversal under conditions similar to those in which it has been reported in the literature<sup>[20,21]</sup>. They also solved numerically the basic equations that describe the TD-column, including the forgotten effect. They concluded that: “When density of the liquid in the column varies with concentration, the forgotten effect is important in transient batch operation of columns, increasingly so as the wall spacing decreases, but it has no influence at the steady state.” This last part of the conclusion that the forgotten effect “has no influence at the steady state” cannot be true. Indeed, let us suppose a binary mixture with the property  $\partial\rho/\partial T = 0$ . In this case the countercurrent convection is caused only of the concentration gradient. With other words, the multiplication of the elementary separation effect on the TD-column is produced only of the forgotten effect. It means that the numerical method used by Korchinsky and Emery, which is not presented in detail in Ref. 22, has weaknesses.

Horne and Bearman<sup>[23]</sup>, observing that their results does not agree with the new literature data<sup>[22,24]</sup>, reanalyzed their theory and added a corrective term to their forgotten effect. However, this correction was not sufficient to obtain an agreement with Korchinsky and Emery’s result<sup>[22]</sup>.

The conclusion is that in spite of the fact that many authors have studied the forgotten effect; there is not a satisfactory theoretical treatment of this subject.

3. The thermal diffusion term in Eq. (4) contains the product  $c_1c_2 = c_1(1 - c_1)$ , which is not linear. When  $c_1$  does not vary much along column, this term can be linearized and the whole mathematical problem became linear in  $c_1$ . The linearized problem can be solved by *separation-of-variables* method. Tsay and Yen<sup>[25]</sup> used this method but they did not arrived to understand and overcome the encountered special difficulties. However, there are studies on similar systems<sup>[7,10,11,26,27]</sup> so that linearized TD problems could be correctly solved.

4. Spindel and Taylor<sup>[28]</sup> studied the concentration of  $^{15}\text{N}$  by chemical exchange  $^{14}\text{NO}_2 + ^{15}\text{NO}_2 = ^{15}\text{NO}_2 + ^{14}\text{NO}$  in a TD column. No theory was derived so far for such complex processes on a TD column.

The chemical exchange in the TD column represents a domain that is insufficiently explored and it is possible to find in it processes of remarkable practical interest. For this reason it would be worth to develop adequate theoretical means.

### Tentative plans for future theoretical studies

Much theoretical work on TD column have been done so far, nevertheless, as shown above, many important problems are not satisfactorily solved. My tentative plans are to complete the TD-column theory by finalization and publication of the following series of theoretical works:

- a. The rigorous theory of the TD column (without forgotten effect; done<sup>[8]</sup>);
- b. The rigorous theory of the TD column with forgotten effect included;
- c. Theory of the TD column with chemical exchange at the wall (done<sup>[8]</sup>);
- d. Theory of the TD column with chemical exchange in inner fluid mixture;
- e. Theory of the TD column with misaligned cylindrical walls (problem studied numerically by Sørensen *et al.*<sup>[29]</sup>);
- f. Second order terms in the theory of the TD-column (the theories a—e refer to the first order terms obtained in the supposition that  $\alpha$  is small);
- g. Solving linearized problems of the TD-column by separation-of-variables method.

These problems can be solved using the methods developed in Refs. 5 and 11.

### REFERENCES

- [1] K. Clusius and G. Dickel: *Naturforschung*, **26**, 546 (1938)
- [2] W. H. Furry, R. C. Jones, and L. Onsager: *Phys. Rev.* **55**, 1083 (1939)
- [3] W. H. Furry and R. C. Jones: *Phys. Rev.*, **69**, 459 (1946)
- [4] R. C. Jones and W. H. Furry: *Rev. Mod. Phys.*, **18**, 151 (1946)
- [5] I. Hodor: *Isotopenpraxis*, **20(9)**, 330 (1984)
- [6] A. Kitamoto, M. Otha, K. Hasegawa: In *Proceedings of the International Symposium on Isotope Separation and Chemical Exchange Uranium Enrichment*, Tokyo, Oct 29 – Nov 1, 1990; Fujii, Y., Ishida, T., Takeuchi, K., Eds.; Bull. Res. Lab. for Nucl. Reactors, Tokyo Institute of Technology, Tokyo 1992, pp. 460-471.
- [7] I. Hodor: *ibid.*, pp. 482-485
- [8] I. Hodor: Unpublished works
- [9] I. Hodor: *Sep. Sci. Technol.*, **38(5)**, 1229 (2003)
- [10] I. Hodor: Thesis (Univ. Babeş-Bolyai, Romania, 1971)
- [11] I. Hodor: *Studia Universitatis Babeş-Bolyai, Physica*, **28**, 15 (1983)
- [12] W. M. Rutherford: *J. Chem. Phys.*, **53**, 4319 (1970)
- [13] S. R. De Groot, W. Hoogenstraaten, and C. J. Gorter: *Physica*, **9**, 923 (1942)
- [14] S. R. De Groot, C. J. Gorter, and W. Hoogenstraaten: *Physica*, **10**, 81 (1943)
- [15] S. R. DeGroot: "L'Effet Soret," N. V. Noord Hollandsche Uitgeveres Maatschappij, Amsterdam (1945)
- [16] E. Von Halle: E. Ph.D. thesis, Univ. Tennessee, Knoxville (1959)
- [17] J. D. Baleschwieler: *A.I.Ch.E. J.*, **7**, 34 (1961)

THE THEORY OF THE THERMAL-DIFFUSION COLUMN: A CRITICAL REVIEW

- [18] F. H. Horne and R. J. Bearman: *J. Chem. Phys.*, **37**, 2842, 2857 (1962)
- [19] F. H. Horne and R. J. Bearman: *J. Chem. Phys.*, **46**, 4128 (1967)
- [20] I. Prigogine, L. de Brouckère, and R. Amand.: *Physica* **16** 577, 851 (1950)
- [21] A. L. Jones and E. C. Milberger: *Ind. Eng. Chem.*, **45**, 2689 (1953)
- [22] W. J. Korchinsky and A. H. Emery Jr.: *A.I.Ch.E. J.* **13** 224 (1967)
- [23] F. H. Horne and R. J. Bearman: *J. Chem. Phys.*, **49**, 2457 (1968)
- [24] J. C. R. Turner, B. D. Butler, and M. J. Story: *Trans. Faraday. Soc.* **63**, 1906 (1967)
- [25] S-W Tsai and H-M Yen: *Sep. Sci. Technol.*, **21(10)**, 1142 (1986)
- [26] R. P. Stein: *Chem. Eng. Prog. Symposium Ser.*, **61(59)**, 64, 76 (1965; *AIChE J.*, **12**, 1217 (1966); *Chem. Eng. Prog. Symposium Ser.*, **64(82)**, 219 (1968)
- [27] R. Beals: *J. Math. Phys.*, **22**, 954 (1981)
- [28] W. Spindel and T. I. Taylor: *J. Chem. Phys.*, **23**, 1318 (1955)
- [29] J. P. Sørensen, M. S. Willis, and W. E. Stewart: *Effects of Column Asymmetry on Thermal Diffusion Separation*, Univ. of Wisconsin, Jan. (1974)

## RESULTS OF THE APPLICATION OF STABLE ISOTOPES OF LIGHT ELEMENTS IN GEOLOGY AND HYDROLOGY

JOVAN ZOTO

*Institute of Nuclear Physics, Tirana, Albania*

**ABSTRACT.** Stable isotopes of light elements there are using for study of many problems of different fields; the extended of their application and improvement of the analytical methods there are the objections of scientists. Geology, agriculture, hydrogeology, hydrology, precipitation, geology of petroleum there are the fields of application of stable isotopes in our country. Follow there are some results of application in geology and hydrology.

A - Determination of absolute geological age it is very important for geological studies. There are known some methods of determination, but, for some specific analytical problems we have used the potassium - argon method; the formula of the determination of the geological age there is:

$$t = 1 / \lambda \times \ln (\lambda / \lambda_k \times {}^{40}\text{Ar} / {}^{40}\text{K} + 1)$$

$$\text{where: } \lambda = \lambda_k + \lambda_\beta ;$$

The  ${}^{40}\text{K}$  content of the monomineral geological sample is calculated by the content of K of the sample which is determined by the flame photometer, but the  ${}^{40}\text{Ar}$  content is determined by the mass spectrometer ZH-1301. The results of our determination there are between  $23.6 \times 10^6$  million years and  $446.2 \times 10^6$  years, and, generally, there are in good correlation with the geological evaluations and in good agreement with the determinations of other laboratories.

B - The stable isotopes of hydrogen and oxygen there are used in the study of many problems of the hydrology in our country, but, more interesting there is the study of underground connection between Prespa and Ohrid lakes. Prespa and Ohrid lakes there are in the east part of Albania and the bordery between Albania - Greece - Fyr. of Makedonia. The altitude of Prespa and Ohrid lakes there are respectively 850 m. and 690 m. asl. and between lakes there are Mali i Thate and Galitica mountains. At the lake side of Ohrid there are two big springs, Tushemishti in Albania territory and Sveti Naum in Fyr. of Makedonia territory. Referring the our data of  $\delta^{18}\text{O}$  and  $\delta^2\text{H}$ , the underground connection exist between Prespa lake and big springs at the lake side of Ohrid.

### Introduction

The development of the science and economy it is attendanted with the using of the new methods of the studies. The method of mass spectrometry analysis is very important in the frame of physico - chemical methods; the high sensitivity, the high accuracy, quick analyse and small quantity of samples for analyses there are some advantages of mass spectrometry method.

A - The determination of absolute geological age, as is known, it is an important problem of the geology. The radioactivity disintegration is a process that occurred with the constant speed, so, it is used as unit of time. The base of radioactivity dating there is the law of radioactivity disintegration  $N = N_0 \times e^{-\lambda t}$ , where  $\lambda$  is the constant of the process [2]. There are some radioactivity methods of geological dating, but, for some reasons of the analytical techniques we have used the potassium - argon method, which is based on the radioactivity transformation of the  ${}^{40}\text{K}$  to the  ${}^{40}\text{Ar}$  by the "k" capture reaction. The melt of the mineral samples and the cleaning of the argon gas from the other gases there are made

in the quartz - glass vacuum system and the calculation of the argon gas is made by the volumetric method. The isotope ratio of Argon is made by the mass spectrometer ZhH-1301, while the K content of the samples there is made by the flamephotometer. The our experimental data of the geological ages there are in good agreement with the geological considerations.

**B** - The isotopic compositions of elements with low atomic numbers are variable because their isotopes are fractionated in the course of certain chemical and physical processes occurring in the nature. The most important elements in which natural variations of the isotopic composition have been observed include hydrogen, carbon, nitrogen, oxygen and sulfur. Isotope ratios, defined by the expression:  $R = \text{abundance of rare isotope} / \text{abundance of abundant isotope}$ , generally, there are not reported as absolute numbers [6]. Therefore, an isotope abundance is expressed as a deviation of the isotope ratio of a sample "s" relative to that of a reference or standard "r", as below:

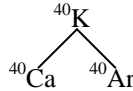
$$\delta_{s/r} = R_s - R_r / R_r ; \quad [8]$$

The  $\delta$  has a dimensionless value and their values are expressed in per mille (‰) because its are very small; the  $\delta$  values are expressed with respect to SMOW.

For the determination of  $\delta^2\text{H}$  and  $\delta^{18}\text{O}$  of the water samples of the Prespa - Ohrid lakes system have used the SIRA 10 mass spectrometer, the ISOPREP 18 system for the equilibration method of water with  $\text{CO}_2$  and the line preparation of the  $\text{H}_2$  by the reduction of water with Zinc. The experimental data of  $\delta$  concerning the underground connection between Prespa and Ohrid lakes there are interesting.

**Material and method**

**A** - The isotope  $^{40}\text{K}$  there is radioactive and its radioactive transformations are:  $\beta$  disintegration (about 88.4 %) and k - capture (about 11.6 %). The constant of disintegrations there are known and respectively there are  $\lambda_\beta = 4.7 \times 10^{-10} \text{ years}^{-1}$  and  $\lambda_k = 5.8 \times 10^{-11} \text{ years}^{-1}$ . The scheme of disintegration of  $^{40}\text{K}$  there is:



The mean content of the Potassium to the earth's crust is evaluated at the 2.6 % and it is mixture of three isotopes  $^{39}\text{K}$ ,  $^{40}\text{K}$  and  $^{41}\text{K}$  and with relatively content, respectively 93.08 %, 0.0119 %, 6.91 %; while, the mean content of the Argon at the air is about 0.9 - 1 % and there is mixture of stable isotopes  $^{36}\text{Ar}$ ,  $^{38}\text{Ar}$ ,  $^{40}\text{Ar}$  and with relatively content respectively 0.337 %, 0.063 % and 99.6% [3]. Experimentally there is observed the increase of the Argon at the air as a result of formation of radiogenic  $^{40}\text{Ar}$  and its coming out in the air.

The fundamental relations of the absolute age determination by the potassium argon method there are:

$$\frac{d^{40}\text{K}}{dt} = -\lambda \times ^{40}\text{K} \quad \text{and} \quad \frac{d^{40}\text{Ar}}{dt} = \lambda_k \times ^{40}\text{K}$$

but, the formula of the age determination there is:

$$t = \frac{1}{\lambda} \times \ln \left( \frac{\lambda}{\lambda_k} \times \frac{^{40}\text{Ar}}{^{40}\text{K}} + 1 \right) \quad [2]$$

The determination of the  $^{40}\text{K}$  of the monomineral geological sample is made by the relation of  $^{40}\text{K}$  and total Potassium of the sample ( $^{40}\text{K} / ^{39}\text{K} + ^{40}\text{K} + ^{41}\text{K} = 0.0122$  % weight), while for the determination of the total Potassium it is used the flamephotometer method after the treatment of the geological sample with  $\text{HNO}_3$ ,  $\text{H}_2\text{SO}_4$ ,  $\text{HF}$  etc. The Potassium content of the geological samples of our determinations there is between 2.4 % to 8 % [5].

The treatment of the monomineral geological samples for the extraction of the Argon and its cleaning from other gases of the samples is made at the quartz - glass vacuum system. The geological samples there are melted at the temperature between  $1100^\circ\text{C}$  and  $1300^\circ\text{C}$  and the argon it is cleaning from the gases as  $\text{CO}$ ,  $\text{CO}_2$ ,  $\text{H}_2$ ,  $\text{H}_2\text{O}$ ,  $\text{N}_2$ ,  $\text{O}_2$ ,  $\text{Kr}$  etc. by the different absorbents incorporated at the vacuum system such as  $\text{CuO}$ ,  $\text{Ti}$ , active Carbon etc.; the temperature of the absorbents there are different (high temperature for the  $\text{CuO}$ ,  $\text{Ti}$  and very low temperature for the Carbon). The quantity of the cleaning Argon it is measured by the Mak Leod manometer incorporated at the vacuum system.

The cleaning Argon of the geological samples it is analysed for the isotopic ratio using mass spectrometer ZhH-1301 and by the following formula it is calculated the radigenic  $^{40}\text{Ar}$  of the samples.

$$^{40}\text{Ar}_{\text{rad}} = \left[ 1 - \left( \frac{^{40}\text{Ar}}{^{36}\text{Ar}} \right)_{\text{air}} \times \left( \frac{^{36}\text{Ar}}{^{40}\text{Ar}} \right)_{\text{samp}} \right] \times Q \quad [2]$$

where  $Q$  is the total quantity of the argon of the sample ( $Q = ^{40}\text{Ar} + \text{Ar}_{\text{nonrad}}$ ). At the Table No.1 there are results of the geological age for some samples:

**Table 1**

**Results of the geological age for some samples**

Sample	Age
Kersantit	$269.2 \times 106 \pm 12$ %;
Sericit	$446.2 \times 106 \pm 16.5$ %;
Ortofir	$373.1 \times 106 \pm 13.6$ %; [5]
Glaukonit	$23.7 \times 106 \pm 15$ %;

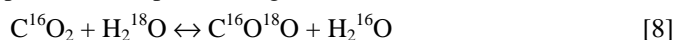
Our results of the geological age by the potthassium - argon method, generally, there are in good agreement with the geological considerations. We have compared our result of the age determination with the result of foreign laboratory for the same sample; the used method of the age determination is the same (potthassium - argon method ) but, the used method of the treatment of the geological sample and cleaning of the argon there is different. The taken results for the sample Biotit 0190 there are:  $t = (179 \pm 26) \times 10^6$  years of our laboratory and  $t_1 = (188 \pm 6) \times 10^6$  years of the foreign laboratory [4].

**B** - The isotopic compositions of elements having low atomic numbers are variable because their isotopes are fractionated in the course of certain chemical and physical processes occurring in nature. Isotope fractionation there is a consequence of the fact that certain thermodynamic properties of molecules depend on the masses of the atoms of which they are composed. The major changes in the isotopic composition of natural waters occur in the atmospheric part of the water cycle and in surface waters which are exposed to the atmosphere [6]. The different isotopes of the Hydrogen and Oxygen and their isotopic compositions in the water molecules we have used for the study of underground communication between Prespa and Ohrid lakes.

The Prespa and Ohrid lakes there are in the east part of Albania and in the border between Greece and Fyr. of Makedonia. The altitude of Ohrid lake there is 695 m. asl., while the altitude of Prespa lakes (Big Prespa and Small Prespa) there is about 850 m. asl. The three lakes constitute a common hydraulic system. A natural surface communication exists between two Prespa lakes and water flows from Small to Big Prespa lake. Between Prespa and Ohrid lakes there are situated Mali i Thate mountain in Albania territory and Galichitsa mountain in the Fyr. of Makedonia territory. The mountains there are composed of carbonate karstic rocks. At the western part of Mali i Thate and Galichitsa mountains there are some big springs (Tushemishti and Saint Naum, the average discharge, respectively, is about  $2.5 \text{ m}^3 / \text{s}^{-1}$  and  $5.58 \text{ m}^3 / \text{s}^{-1}$ ) and some small springs at the lakeside of Ohrid lake [9].

The sampling net of the water of the lakes, springs and rivers there was created; every two months was the frequency of the sampling process for a period of two years. The determination of  $\delta^2\text{H}$  and  $\delta^{18}\text{O}$  of the water samples it is realised using mass spectrometer SIRA 10, which in principle is derived from the Nier's mass spectrometer [1]. The mass spectrometer, essentially, consists of a tube in which high vacuum is maintained, with an ion source placed at one end and ion collectors at the other end. The middle part of the tube is curved and immersed in a magnetic field normal to the curvature plane. The vacuum in the mass spectrometer SIRA 10, is in order  $(1 - 2) \text{ E-}09$  torr; it is realised by two rotary pumps and two diffusion pumps and it is measured by two Pirani gauges and by means of ionization gauge.

The determination of  $\delta^{18}\text{O}$  in the water samples it is made using  $\text{CO}_2$  gas in the isotopic equilibrium with the water samples; the ISOPREP 18 system of the isotopic equilibration of the water and gas  $\text{CO}_2$  is used and it is based to the Roether method. The 5 ml. of water is introduced in a glass container, which is then coupled to a stopcock and connected to the line by means of ground joints; the air is pumping through a capillary tube and the pressure drops to a few tens of torrs for a short time; the water loss is too small. After eliminating the air, the carbon dioxide is introduced in the samples containers which are in the thermostatic bath at the temperature  $25^\circ\text{C}$ . The isotopic equilibrium it is reaches after 5 hours shaking the samples; the isotopic exchange reaction is:



The ISOPREP 18 is connected online with mass spectrometer.

For the determination of the  $\delta^2\text{H}$  of the water samples it is used the hydrogen gas getting by the reduction of water samples with granulated Zinc at the high temperature and vacuum conditions. The reaction which occur is:



The preparation of the  $\text{H}_2$  gas samples is made in the separated line from the mass spectrometer. The  $\delta^2\text{H}$  and  $\delta^{18}\text{O}$  are normalized with respect to SMOW.

Referring the experimental data of  $\delta^2\text{H}$  and  $\delta^{18}\text{O}$  for the sampling points at the region of Prespa - Ohrid lakes, the respective correlation function of the precipitation there is:

$$\delta^2\text{H} = 8 \times \delta^{18}\text{O} + 13.8 \quad [9]$$

For the sampling points at the Prespa lakes and big springs Tushemishti and Saint Naum the slope of the correlation there is 5.2 that is attributed to waters with a significant rate of evaporation relative to input. The isotopic composition of the above springs is constituted by mixing in different proportions of precipitations and Prespa lake waters.



**REFERENCES**

1. Mass Spectrometry, Edited by C. A. McDowell, 1963;
2. I. E. Starik: Jadernaja geohronologija, 1961;
3. O. Schaefer, I. Zahringer: Potassium Argon dating, 1966;
4. Biotite Albanese, Pisa - Italy, 1985, personal communication;
5. J. Zoto, E. Millona: Disa rezultate te moshes absolute gjeologjike te marra me metoda te ndryshme, Punime te Institutit te Fizikes Berthamore, Nr. 5, 1987;
6. Stable Isotope Hydrology, IAEA, Technical Reports No. 210, 1981;
7. G. Faure: Oxygen and Hydrogen in the hydrosphere and the atmosphere (Principles of Isotope Geology), 1977;
8. J. R. Gat: Variability of the isotopic composition of precipitation, IAEA, 1987;
9. R. Eftimi, J. Zoto: Isotope study of the connection of Ohrid and Prespa lakes, PPNEA, 1997.

## **SUPRAMOLECULAR ELECTROACTIVE STRUCTURES BASED ON CONDUCTING POLYMER**

**R. TURCU<sup>1</sup>, I. PETER<sup>1</sup>, A. BOT<sup>1</sup>, M.N. GRECU<sup>2</sup>, O. PANA<sup>1</sup>, I. CHICINAS<sup>3</sup>, R. GRECU<sup>4</sup>**

<sup>1</sup> *National Institute R&D for Isotopic and Molecular Technologies, P.O.Box 700, 3400, Cluj-Napoca 5, Romania*

<sup>2</sup> *National Institute R&D for Materials Physics, P.O.Box MG-7 Bucuresti-Magurele, Romania*

<sup>3</sup> *Materials Science and Technology Department, Technical University of Cluj-Napoca, 3400, Romania*

<sup>4</sup> *Institute of Chemistry "Raluca Ripan", Cluj-Napoca, 3400, Romania*

**ABSTRACT.** In this paper we focus on several types of composites obtained by combining conducting polypyrrole (PPY) with inorganic or organic nonconducting components like: zeolite, Fe<sub>2</sub>O<sub>3</sub>, polystyrenesulfonate (PSS), polyvinylalcohol (PVA). The composites were obtained by two different synthesis methods: a) electrochemical polymerization of pyrrole in the presence of the inorganic (zeolite) or organic (PSS, PVA) component; b) chemical oxidative polymerization of pyrrole followed by the formation of Fe<sub>2</sub>O<sub>3</sub> nanoparticles into the host PPY matrix. The properties of the as-synthesized composites were investigated by d.c. conductivity measurements, FTIR spectroscopy, magnetization and electron spin resonance (ESR). Our results show that the electrical, optical and magnetic properties of the PPY composites are correlated with their supramolecular structure. The nonconducting component from the composite influences the chains conformations of the electroactive polypyrrole during the polymerization process. Modifications of the composite properties can be induced by the change of the components nature and their concentrations.

### **INTRODUCTION**

The synthesis of supramolecular electroactive structures based on conducting polymer represents a new strategy to obtain the specific requirements of physical properties for different applications like chemical sensors, biosensors, metals ion uptake from solutions, electromagnetic interference shielding, and microwave absorbing. These new composites materials contain a conducting polymer, as electroactive component and an inorganic or organic nonconducting component.

In this paper we report the physical properties of polypyrrole (PPY) composites like: PPY-zeolite (PPY-Z), PPY-Fe<sub>2</sub>O<sub>3</sub>, PPY-polystyrenesulfonate (PPY-PSS), PPY-polyvinylalcohol (PPY-PVA). Modifications of the electrical, optical, structural and magnetic properties of the investigated composites can be induced by changing the nature of the nonconducting component and by the synthesis parameters.

### **EXPERIMENTAL**

#### ***Composites synthesis***

Free standing films of composites PPY-zeolite, PPY-PSS, PPY-PVA were synthesized electrochemically by anodic oxidation of pyrrole in an aqueous solution containing the nonconducting component (zeolite NaX or NaPSS or PVA) and an electrolyte as doping agent. For the composites PPY-PSS, the component PSS represents the dopant. PPY-PVA and PPY-

zeolite composites were obtained by using p-toluensulfonate [TSO<sup>-</sup>] or hexacyanoferrate [Fe(CN)<sub>6</sub>]<sup>3-</sup> as doping ions. The electropolymerization was carried out at room temperature in potentiostatic conditions at +0.8V vs. SCE by using an AUTOLAB experimental set-up. The composites were obtained by using the following molar ratios: i) pyrrole/zeolite  $1,3 \times 10^3 - 1,3 \times 10^2$ ; pyrrole/PSS = 28; pyrrole/PVA = 28. In the synthesis of PPY-Fe<sub>2</sub>O<sub>3</sub> composite, the host PPY matrix was prepared by chemical oxidative polymerization of pyrrole by using ammonium persulfat (APS) as oxidant and dodecylsulfonic acid sodium salt (DSNa) as doping agent. PPY doped with DS ions results as a black powder which was filtered, washed with deionized water and methanol several times and dried. PPY(DS) was poured into a 1 M NaOH aqueous solution under stirring. During this reaction of polymer reduction the sodium cations are inserted into PPY matrix. After 2 h the resulting reaction mixture was washed with deionized water and methanol, and dried. Then, the reduced PPY was reoxidized into 1 M FeCl<sub>3</sub> aqueous solution under stirring 2 h, to allow the exchange of sodium cations by iron cations into the polymer. The resulting reaction mixture was washed with deionized water and methanol and dried, too. The treatment of PPY containing Fe<sup>2+</sup> with 1 M NH<sub>4</sub>OH aqueous solution at 70° C, 30 min under stirring results in the formation of Fe<sub>2</sub>O<sub>3</sub> particles into the PPY matrix.

### Measurements

The electrical conductivity of the composites was determined by the standard four-contacts methods by using silver painted electrodes. Temperature dependence of the conductivity was measured in the range -60 ÷ +70°C under vacuum by using a home-made cell with thermoelectric modules for temperature control.

FTIR transmission spectra of PPY composites in the range 400-4000 cm<sup>-1</sup> were recorded by using a JASCO FTIR 610 spectrophotometer.

The electron spin resonance (ESR) spectra of PPY composites were determined by a JEOL JES-ME-3X spectrometer.

The magnetic properties of the composite PPY-Fe<sub>2</sub>O<sub>3</sub> were investigated by using a SQUID device.

## RESULTS AND DISCUSSIONS

### Electrical conductivity

The values of the electrical conductivity,  $\sigma$  at room temperature for the electrochemically synthesised PPY composites are given in the Table 1.

**Table 1**  
**Room temperature conductivities of electrochemically synthesised PPY composites**

Sample	Doping ion	C <sub>ions</sub> [M]	Polymerization time [s]	Film thickness [ $\mu$ m]	$\sigma$ [S/cm]
PPY-Z1	TSO <sup>-</sup>	0.1	3600	70	28
PPY-Z4	TSO <sup>-</sup>	0.1	1800	26	71
PPY-Z7	[Fe(CN) <sub>6</sub> ] <sup>3-</sup>	0.1	1800	40	2
PPY-Z9	TSO <sup>-</sup>	0.5	1800	90	13
PPY-PSS	PSS	0.005	1800	20	0.5
PPY-PVA	TSO <sup>-</sup>	0.005	1800	36	13

The Figure 1 shows the temperature dependences of the electrical conductivity for PPY-zeolite composites (samples PPY-Z4 and PPY-Z7 from Table 1). The behavior of  $\sigma$  vs. T for sample PPY-PVA from Table 1 is similar to that of PPY-Z4 from Figure 1. A common characteristic of the investigated PPY composites is the conductivity decrease after the first heating under vacuum (curves 1-2 from Figure 1). During the subsequent cooling-heating processes the conductivity

exhibits different trends. For all TSO<sup>-</sup> doped composites the conductivity values on the cooling branch (curves 2-3) and on the second heating branch (curves 3-4) overlap, see Figure 1. For [Fe(CN)<sub>6</sub>]<sup>3-</sup> doped composite PPY-Z7 shown in the Figure 1, a hysteresis loop with  $\sigma$  values on the cooling branch (curve 2-3) lower than those on the second heating branch (curve 3-4) was observed. An explanation of  $\sigma$  vs. T variation for the investigated samples is based on the water desorption process and different interactions of the composite components with oxygen and hydroxyl groups coming from water dissociation [1].

The electrical conductivity of PPY-PSS exhibits a good reversibility during subsequent heating-cooling processes, Figure 2. This fact is due to the good stability of PSS component as compared to PVA or zeolite which can incorporate more water.

The conductivity of PPY composites is strongly influenced by the doping ions since there is an electrostatic interactions of these ions with the positive charges from the PPY chains.

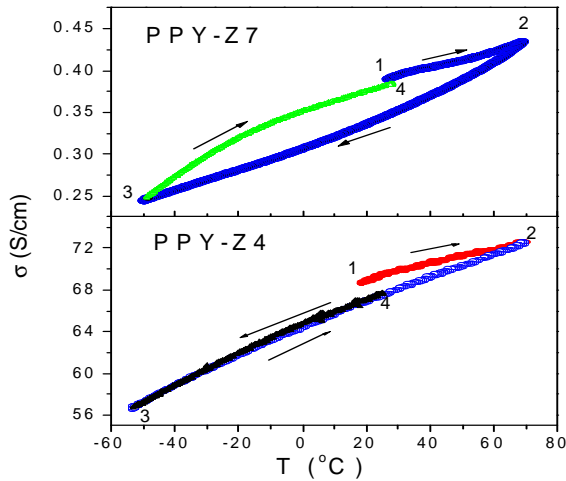


**Fig. 1.**  $\sigma$  vs.T behavior during heating-cooling processes for PPY-zeolite composites (PPY-Z4 and PPY-Z7 from Table 1)

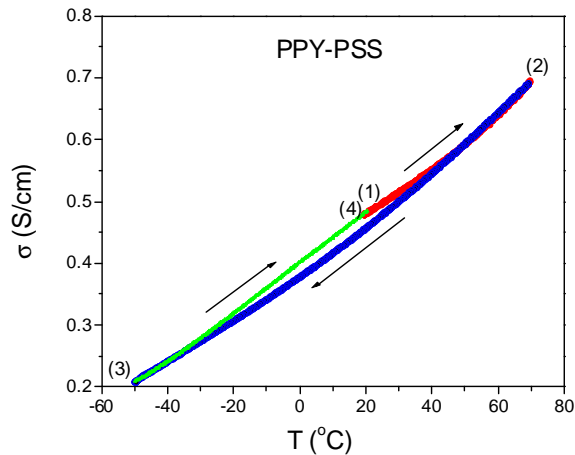


**Fig. 2.**  $\sigma$  vs.T behavior during heating-cooling processes for PPY-PSS.

The nature of the doping ions could result in different behavior of the conductivity at successive exposures from vacuum ( $p=10^{-2}$  torr) to ambient air. From the Figure 3 one can see that for  $[\text{Fe}(\text{CN})_6]^{-3}$  doped composite the conductivity decrease under vacuum and increase upon exposure to air, in contrast to  $\text{TSO}^-$  doped one.

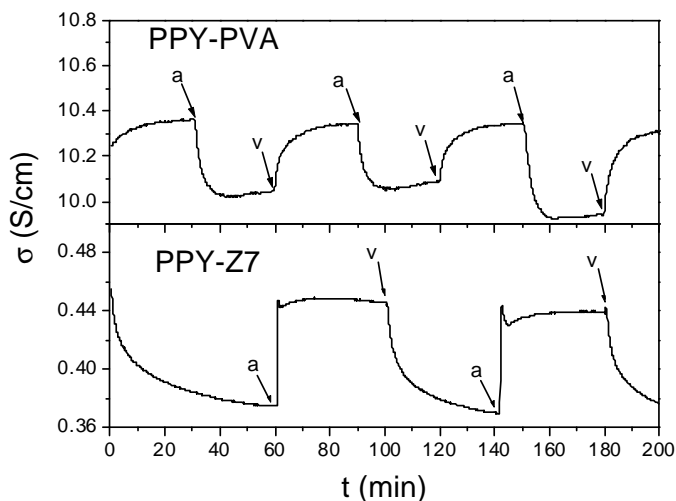


**Fig. 3.** Conductivity behavior at successive exposures from vacuum (v) to ambient air (a) for the composites PPY-PVA and PPY-Z7.

#### **FTIR spectra**

The positions of the characteristic absorption bands for PPY are influenced by the oxidation state of the polymer and the conjugation chains length [2]. In the Figure 4 are represented the absorption spectra for the composite PPY-Z7 from Table 1.

The spectrum of the composite PPY-PSS, Figure 5 contains the characteristic absorption bands of PPY ( $1559, 1477, 1323, 1047, 966, 915 \text{ cm}^{-1}$ ) and those of PSS. The absorption bands for PPY into the composites PPY-zeolite, PPY-PSS are shifted to higher frequencies as compared to those of pure PPY. This fact indicates a lower oxidation state or shorter conjugated chains for PPY formed into the supramolecular structure of these composites.

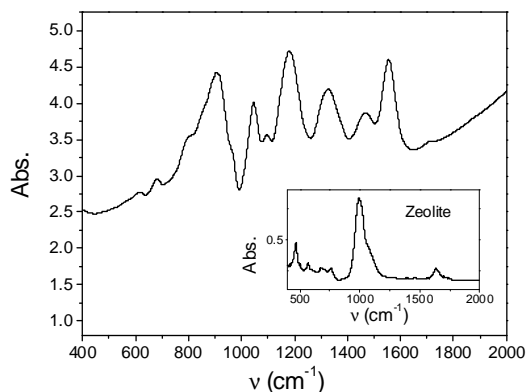


**Fig. 4.** FTIR spectrum for the composite PPY-Z7 and for zeolite (the inset).

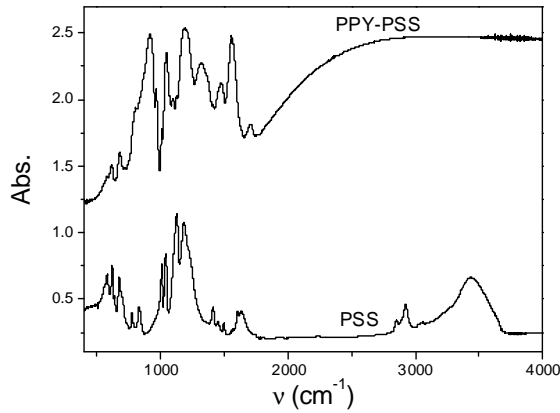


**Figure 5.** FTIR spectra for PPY-PSS and PSS

***Magnetic properties of the composite PPY-Fe<sub>2</sub>O<sub>3</sub>***

The magnetization, *M* of PPY-Fe<sub>2</sub>O<sub>3</sub> composite measured versus increasing and decreasing magnetic field shows no hysteresis loop, Figure 6. This fact is typical for fine magnetic particles, with nanodimensions and is consistent with a super-paramagnetic behavior [3].

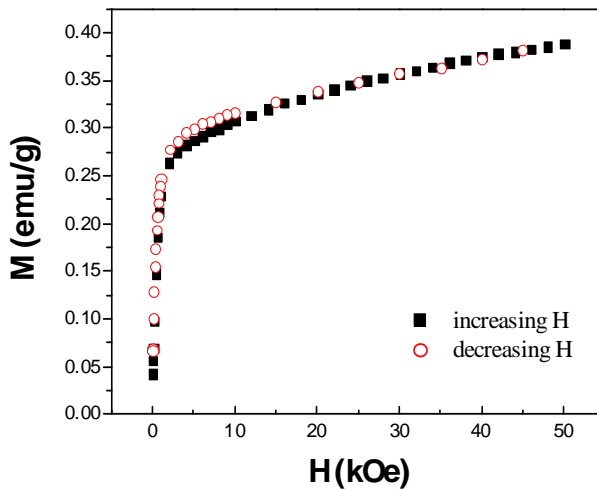


**Fig. 6.** Magnetization vs. applied magnetic field at T=300K for PPY-Fe<sub>2</sub>O<sub>3</sub>

The ESR spectrum presented in the Figure 7 shows two resonance lines: a narrow one attributed to the paramagnetic PPY matrix and a broad one due to the super paramagnetic Fe<sub>2</sub>O<sub>3</sub> nanoparticles. The integrated ESR signals have both Lorentzian line

shapes with “g” factors,  $g=2.02$  for PPY and  $g=2.16$  for  $\text{Fe}_2\text{O}_3$  respectively. The line widths at half height,  $\Delta H_{1/2}$  are 13 G for PPY matrix and  $\Delta H_{1/2} = 1486$  G for  $\text{Fe}_2\text{O}_3$  system.

The reported results are the first step in the investigation of a new type of nanostructured magnetic materials with improved processability and low cost, obtained by the combination of a conducting polymer and magnetic particles.

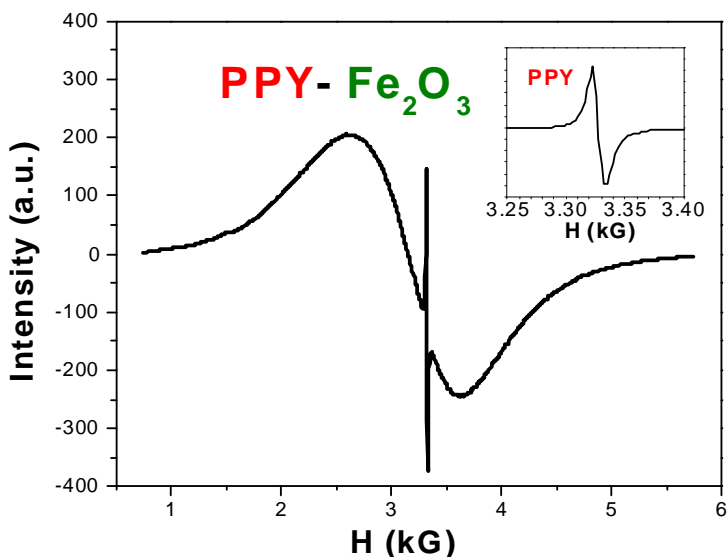


Fig. 7. The ESR spectrum for PPY-  $\text{Fe}_2\text{O}_3$  composite. In the inset : ESR spectrum for PPY

## CONCLUSIONS

The association of conducting PPY with organic (PVA, PSS) or inorganic nonconducting materials (zeolite,  $\text{Fe}_2\text{O}_3$ ) in order to prepare composites which combine the properties of both components is one very promising way to obtain the specific requirements of physical properties for different applications.

Our results show that the electrical, optical and magnetic properties of PPY composites are controllable by the nature of the nonconducting component and by doping with different ions.

## REFERENCES

1. H. Okuzaki, T. Kondo, T. Kunugi, *Characteristics of water in polypyrrole films*, Polymer 40 (1999) 995
2. R.Turcu, W.Graupner, C.Filip, A.Bot, M.Brie, R.Grecu, *Studies of the Intermolecular Interactions in Polypyrrole and Conjugated Composites based on Polypyrrole*, Adv.Mater. Opt. Electron. 9 (1999), 157
3. M. Kryszewski, J. K. Jeszka, *Nanostructured conducting polymer composites-superparamagnetic particles in conducting polymers*, Synthetic Metals, 94 (1998) 99

## SYNTHESIS OF CARBON NANOSTRUCTURES BY INDUCTION HEATING ASSISTED CCVD METHOD

**D. LUPU<sup>1</sup>, A.R. BIRIŞ<sup>1</sup>, I. MIŞAN<sup>1</sup>, G. MIHĂILESCU<sup>1</sup>, L. OLENIC<sup>1</sup>, S. PRUNEANU<sup>1</sup>,  
A. JIANU<sup>2</sup>, C. BUNESCU<sup>3</sup>, A. WEIDENKAFF<sup>4</sup>, C. DIECKER<sup>4</sup>**

<sup>1</sup> National Institute for Research and Development of Isotopic and Molecular Technologies, P.O. Box 700, R-3400 Cluj-Napoca, Romania

<sup>2</sup> National Institute of Materials Physics, P.O. Box MG-7, RO-76900

<sup>3</sup> Hochschule Wismar, PO Box 1210, D-23952, Wismar, Germany

<sup>4</sup> Institute of Solid State Chemistry, Universität Augsburg, Universitäts str. 1, D-86159 Augsburg, Germany

**ABSTRACT.** Experiments on the catalytic chemical vapour deposition for the synthesis of carbon nanostructures are reported, both with the outer furnace technique and with induction heating. The results are analysed comparatively and the advantage of the induction heating is revealed.

### 1. Introduction

The carbon-based materials and nano-scale sciences are envisaged as major fields of the 21<sup>st</sup> Century technology. The extensive work on carbon nanotubes (CNT), started just after their discovery [1], resulted in an exponential increase of the patent filings and publications [2]. Their applicability has been investigated in various technological areas such as aerospace, aeronautic, nanoelectronics, energy, medicine or chemical industry in which they can be used as gas adsorbents, templates, actuators, composite reinforcements, catalyst supports, probes, chemical sensors, nano-reactors. The ability of the CNTs to immobilise biologically active substances [3-5] opens new ways for bio-nanotechnologies.

The main challenge in working with carbon nanotubes is their synthesis [6] and new techniques are examined in many laboratories to develop methods able to lead to carbon nanotubes with controlled characteristics and suitable for large-scale production. It is usually accepted that the catalytic decomposition of hydrocarbons (CCVD) on solid (catalyst) surfaces seems a viable method for large-scale production with low energy consumption.

The use of the induction heating to reach high temperatures during the laser synthesis of single-wall carbon nanotubes [7] pointed out to the ability of this particular heating mode to control the temperature of the reaction even at high temperatures, without significant heat transfer to the quartz tube confining the reaction region. This made us to explore the possibilities of coupling the induction heating (IH) with the CCVD method for the synthesis of carbon nanotubes. By this CCVD-IH route, various types of carbon nanostructures were indeed obtained [8], the attempts showing that it can be used even for the vertical, floating catalyst method.

In this paper, the results obtained with outer furnace technique and induction heating, keeping the same all the other reaction conditions (hydrocarbon and carrier gas flow, reaction temperature and time) are comparatively reported, trying to find out some possible advantages of the CCVD-IH coupling.

### 2. The experimental set-up of CCVD with induction heating

The catalytic chemical vapor decomposition of hydrocarbons for the synthesis of carbon nanofibers, single-wall nanotubes (SWNT), multi-wall nanotubes (MWNT) is usually performed at temperatures over 500 °C, in a quartz tube containing the catalyst which may be displayed in a



convenient way to be kept at the reaction temperature. In our experiments, both heating with an electric outer furnace (referred to as CCVD) and induction heating (CCVD-IH) have been used. In the later, the outer furnace has been replaced by the coils of an high frequency inductor working at 1.3 MHz as described in Fig. 1. The catalyst is placed on the susceptor within the quartz tube – an electric conductor of suitable shape which can be inductively heated.

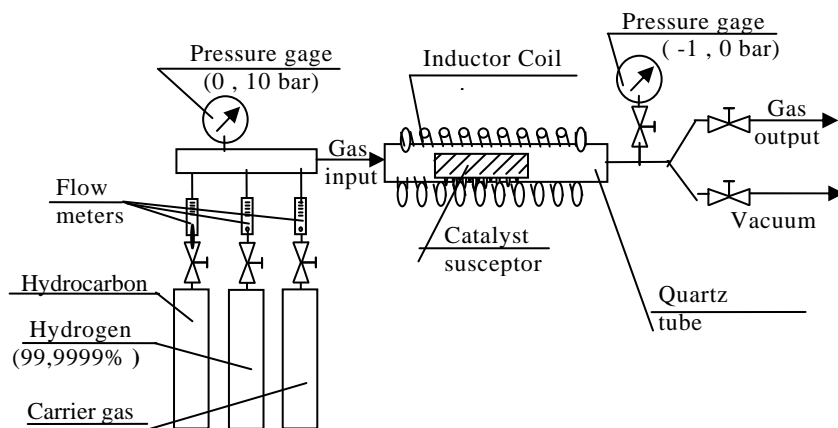


**Fig.1.** Scheme of the experimental set-up for CCVD syntheses of carbon nanostructures using induction heating

Some peculiarities of the two heating modes need a brief review. The heating of the catalyst (either as a powder in a ceramic boat or deposited on a substrate) with an outer furnace is achieved through heat transfer by radiation and convection from the hot tube walls. Conversely, in the induction heating case, the thermal gradient is in the opposite direction: the heat transfer flows from the inductively heated susceptor to the catalyst displayed on its surface. The inductive heating (IH) occurs due to the confinement of the induced currents and magnetic flux to a thin layer of an electric conductor subjected to the high-frequency field- the *skin effect*. The thickness of this layer decreases with the increasing frequency, at high frequencies the electromagnetic energy being confined essentially to the surface [9] with the skin depth depending on the frequency, relative permeability and electric conductivity – the parameters on which the selection of a suitable susceptor should depend on. Due to the permeability, for example, the skin depth of magnetic steel increase from 0.014 mm below the Curie point to 0.55 mm above 780 °C. The power absorbed by the IH heated body depends on the same parameters and on the magnetic field. Because the catalyst involves metallic clusters it may be directly influenced by the high-frequency field with direct consequences on the processes related to the CCVD occurring on its surface. These effects, which are not present in the conventional heating mode, may ultimately result in influences on the morphology and growth of the carbon nanostructures synthesized by CCVD-IH. The experiments showed that the materials used for the susceptor can be titanium, graphite, molybdenum or even iron.

With the modified CCVD-IH method, the activation of the catalyst can be performed also at the desired temperature as for the CCVD with outer furnace technique, by the control of the high-frequency generator at the required conditions.

### 3. Comparative results obtained by CCVD and CCVD-IH

#### 3.1 Hollow core nanofibers

With a Ti rod used as a susceptor, its surface was previously prepared to obtain a thin layer of  $\text{TiO}_2$  as the titanium oxide proved to be good as support of metal catalyst [10] for the synthesis of carbon nanostructures. The surface of the rod was oxidized electrochemically in a 3% aqueous solution at constant voltage (20 V, DC) for 10 min. After that, nitrate solutions were evaporated to obtain Fe:Co (1:1 mole ratio)/ $\text{TiO}_2$  and the deposit was heated in air at 400 °C for 1 h. Both for the CCVD and CCVD-IH synthesis, the catalyst was previously activated “in situ” at 350 °C for 1 h, after which the temperature of the rod was increased at 600 °C and an ethylene:hydrogen mixture (4:1 volume ratio) at 0.35 bar was admitted in the quartz tube. After 1 h, the sample was cooled to the room temperature.

The carbonaceous products, collected by scraping from the Ti rod were maintained in HCl 37% for 24 h, washed with distilled water and dried at 150 °C for 1h.

The results reported comparatively in Fig. 2 for synthesis in exactly the same conditions show some interesting differences. Hollow core nanofibers of 20-50 nm o.d. (5-20 nm i.d.) many of them with catalyst particles encapsulated at their tips are obtained by CCVD. On the other hand, CCVD-IH results in significantly thinner nanofibers of 8-15 nm o.d. (3-5 nm i.d.), without catalyst particles at the tip. This suggests a higher growth rate in the IH case as the thin fibers grow faster than the thick ones [11]. Further studies seem very interesting to elucidate if this might be a direct effect of the induction currents.

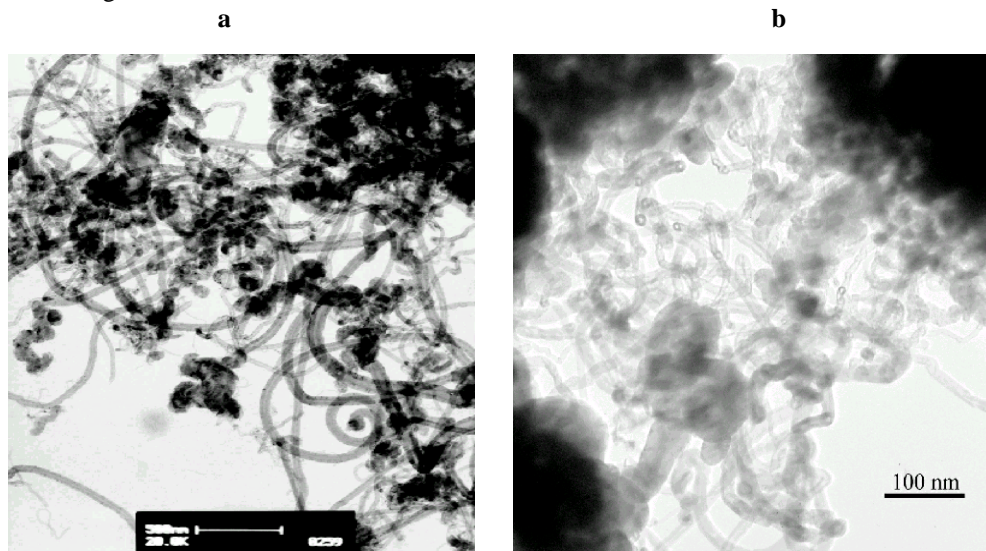


**Fig. 2.** TEM images of the carbon nanostructures obtained in the same reaction conditions from ethylene:hydrogen (4:1) at 0.35 bar and 600 °C on Fe:Co(1:1)/ $\text{TiO}_2$ , using: a) outer furnace and b) induction heating

#### 3.2 Single wall nanotubes

Experiments on the synthesis of SWNT have been also performed, using the Fe:Mo:Al<sub>2</sub>O<sub>3</sub> (1:0.2:16 weight ratios) reported in literature [12] to be good for SWNT synthesis even without activation. The catalyst was prepared as described [12] and 20-30 mg were introduced in a graphite cylinder of 14 mm o.d. (1 mm wall thickness) as susceptor. The synthesis

was conducted at 800 °C with 12 ml/min methane flow and 80 ml/min purified argon as carrier gas for 1 h after which the sample was allowed to cool at the room temperature. Fig.39a,b) show images very similar to the bundles of SWNT reported in [7]. They are more abundant in the case of CCVD-IH (Fig. 3b) as compared to the outer furnace technique (Fig. 3a). Raman studies will be performed to obtain more detailed informations about the SWNTs diameters and some possible differences between the two methods.

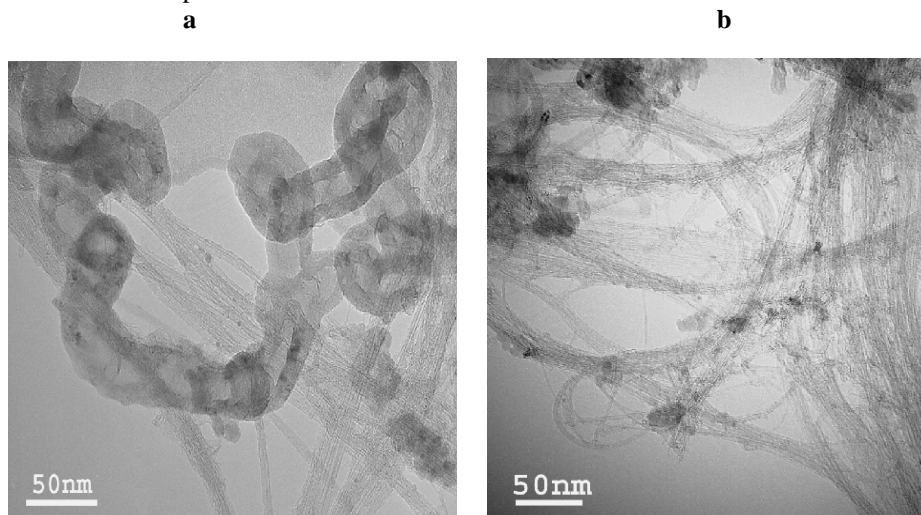


**Fig. 3.** TEM images for as-prepared carbon nanotubes from methane/argon at 800 °C on Fe:Mo:Al<sub>2</sub>O<sub>3</sub> catalyst by: a) CCVD and b)CCVD-IH techniques

The average yield was 19-20% both for CCVD and for CCVD-IH but the consumed energy was 2.5 kWh for CCVD and only 0.6 kWh for IH.

### 3.3 Multi-wall nanotubes

With CCVD-IH, thin hollow core nanofibers of 15-20 nm outer diameter, 5-6 nm inner hollow core, (possibly MWNT), were obtained from ethylene (16% vol) in hydrogen flow (100 ml/min) at 600 °C with Ni/Al<sub>2</sub>O<sub>3</sub> on molybdenum susceptor. The catalyst was prepared by evaporating Ni and Al nitrates on a rolled Mo foil. The TEM image shown in Fig. 4 does not allow a firm conclusion about the identification as MWNT and the work needs to be continued by HRTEM studies.

Recently it was reported [13] that high quality multi-wall carbon nanotubes are obtained from acetylene on Co<sub>3</sub>O<sub>4</sub>/MgO catalyst with nitrogen as carrier gas. Preliminary results, within a cooperation with Prof. L. Duclaux and Dr. Y. Soneda, show that in the same reaction conditions, better MWNT are obtained with the CCVD-IH method [14], as revealed by HRTEM. The work is now in progress to establish the suitable synthesis conditions and to characterize the morphology and structure of the products. It is worth to note that the energy consumed in this case, even using a short electric outer furnace is 420 Wh for CCVD but only 175 Wh for CCVD-IH.

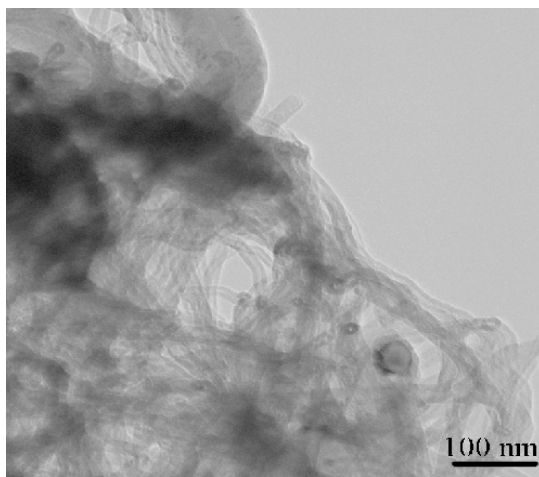


**Fig. 4.** TEM image of carbon nanostructures obtained by CCVD-IH from ethylene: hydrogen (16 % vol) at 600 °C on Ni/Al<sub>2</sub>O<sub>3</sub>

### Conclusions

The induction heating can be used to synthesize all the main type of carbon nanostructures (nanofibers, SWNT, MWNT) by the CCVD method. This CCVD-IH method show some advantages as compared to the outer furnace technique: 2-3 times lower energy consumption, lowering of the overall time for a batch due to the fast heating and cooling rates, versatility in the temperature control with much higher temperatures available for synthesis and thermal annealing, reduced extent of the heating zone. The influence of IH on the morphology, structure and growth rate of the carbon nanostructures deserves further studies.

### REFERENCES

- [1]. S. Iijima, *Nature* 354(1991)56
- [2]. R. H. Baughman, A. A. Zakhidov, W. A. de Heer, *Science* 297(2002)787
- [3]. G. A. Kovalenko, E. V. Kuznetsova, Yu. I. Mogilnykh, I. S. Andreeva, D. G. Kuvshinov, N. A. Rudina, *Carbon* 39(2001)1033
- [4]. X. Yu, D. Chattopadhyay, I. Galeska, F. Papadimitrakopoulos, J. F. Rusling, *Electrochemistry Communications* 5(2003)408
- [5]. W. Huang, S. Taylor, K. Fu, D. Zhang, T.W. Hanks, A.M. Rao, Y-P. Sun, *Nano Letters* 2(2002)311
- [6]. M. Dresselhaus in *Materials Today* 2002, 5: 11: 48
- [7]. T. Gennett, A. C. Dillon, J. L. Alleman, K. M. Jones, P. A. Parilla, M. J. Heben, *Mat. Res. Soc. Symp. Proc.* vol. 633 (2001): A2.3.1-6
- [8]. D. Lupu, A. R. Biris, A. Jianu, C. Bunescu, E. Burkel, E. Indrea, G. Mihailescu, S. Pruneanu, L. Olenic, I. Misan, *Carbon* (2003) accepted for publication
- [9]. C. P. Poole Jr., *Electron spin resonance*, New York, John Wiley Ed. 1967, pp72-73
- [10]. S. Takenaka, H. Ogihara, I. Yamanaka, K. Otsuka, *Applied Catalysis A* 217(2001)101
- [11]. K.P. de Jong, J.W. Geus, *Catalysis Review-Sci. and Eng.* 42(2000)481
- [12]. A.R. Harutyunyan, B.K. Pradhan, U.J. Kim, G. Chen, P.C. Eklund, *Nano Letters* 2(2002)525
- [13]. Y. Soneda, L. Duclaux, F. Beguin, *Carbon* 40(2002)965
- [14]. Y. Soneda, private communication

## METALLIC NANOSTRUCTURES FOR CONTROLLING LIGHT – MOLECULES INTERACTIONS

SIMION ASTILEAN

*Molecular Spectroscopy Department,  
Faculty of Physics, Babes-Bolyai University,  
3400 Cluj-Napoca, Romania*

**ABSTRACT.** We investigate the optical properties of ordered silver nanostructures with the goal of optimizing and controlling the specific spectroscopic signatures of molecules, i.e. the fluorescence decay and surface-enhanced Raman scattering.

### Introduction

The density of states of electromagnetic excitations  $D(\omega)$  at optical frequencies, both photons and surface plasmons, is a basic concept underlying the theory of light-matter interaction. For instance the probability of spontaneous emission of an emitter is given by Fermi's [1] golden rule as:

$$\Gamma_{ij} \sim |M_{ij}|^2 D(\omega_{ij}) \quad (1)$$

where  $\Gamma_{ij}$  is the rate for the transition between the excited state  $i$  and lower energy state  $j$ ,  $M_{ij}$  is a matrix element that connects the excited and lower energy levels and is determined by the wavefunctions associated with those levels and  $D(\omega_{ij})$  is the density of the optical field at the transition frequency. A similar relation works for the probability of spontaneous Raman scattering of light [2]. According to relation (1), the fluorescence emission rate or the Raman scattering probability of molecules are not an intrinsic property of the molecule but a possible exchange between molecule and all available light states. This idea was first pointed out at radio frequencies by Purcell [3] in 1946.

To control the density of optical modes  $D(\omega)$  in order to manipulate the optical properties of fundamental light emitters (atoms, molecules, quantum dots) has been the great motivating force of intensive investigations during the last decade in the field of photonic crystals (PCs). Photonic crystals are dielectric or metallic materials which possess a periodic modulation of their refractive index on the scale of the wavelength of light. Contrary to homogeneous materials, PCs exhibit a discrete density of states  $D(\omega)$ , that is, a range of frequencies ( $\omega$ ) and wavevectors ( $\mathbf{k}$ ) wherein the propagation of light can be allowed or blocked [4].

In this paper we employ an inexpensive nanofabrication method, i.e. the nanosphere lithography [5], to produce two-dimensional PCs consisting of arrays of silver nanoparticles or ordered nanoscopic holes in metallic films. We investigate their photonic structure and hereafter their potential to control light – molecules interaction. Specifically, we demonstrate that the spectroscopic signature, i.e. the fluorescence decay or surface-enhanced Raman scattering of molecules are strongly dependent on the “photonic environment”.

Metallic PCs with specific “plasmonic” band structures  $D(\omega)$  are consistent with the manipulate of both *the spontaneous emission rate* and *the Raman scattering efficiency*. The control of spectroscopic signal on the nanoscale is useful in ultrasensitive analysis and chemo- or biosensing applications.

### Experimental

a) *Nanostructures preparation*. The samples were prepared according to the nanosphere lithography procedure [5]. A suspension of polystyrene nanospheres was dropcoated onto the substrate where they self-assembled into hexagonally close-packed 2D colloidal crystal that served as a deposition mask. Polystyrene nanospheres were supplied by Interfacial Dynamics Corporation and by Duke Scientific Ltd as monodispersed suspensions in deionised water. Once the 2D colloidal crystal deposition mask was formed, the substrate were mounted into the vacuum chamber of a vapour deposition system. Silver or gold films of controlled thickness (usually between 20-120 nm) were thermally evaporated onto the substrate under a pressure of  $5 \times 10^{-6}$  Torr. The film thickness was monitored using a calibrated quartz crystal oscillator. The silver was evaporated from a molybdenum boat, having been thoroughly out-gassed under high vacuum. A voltage of  $\sim 90$ V was required to melt and then vaporise the metal, and once the metal had been deposited, the sample was left under vacuum for half an hour in order to allow the film to cool and stabilize, so that there was the minimum of oxidation and sulphidisation on the metal surface. The evaporated silver or gold coats the regions of the substrate not covered with polymer spheres. A solvent (dichloromethane or chloroform) wash is then used to remove the polystyrene nanospheres from the substrate. The solvent wash removes the nanospheres but does not affect the silver or gold that has been deposited onto the substrate, resulting in a glass substrate metallized with repeatable spaced metallic nano-triangles. The period of nanostructures is determined by the initial period of hexagonally close-packed nanosphere arrays and the size of metallic features can be easily tuned by the diameter of spheres. The versatility of nanosphere lithography was extended by using reactive ion etching (RIE) of polystyrene nanospheres. The sample consisting of crystalline assemblies of polystyrene nanospheres was placed in a RIE chamber and exposed to oxygen ( $O_2$ ) plasma. The nanospheres are reduced in size by RIE after which silver film was thermally evaporated. The thinned spheres were removed by sonication in dichloromethane leaving the silver film patterned with periodic array of nanoholes.

The spectroscopic experiments were performed on two representative dyes: rhodamine 700 (R700) and rhodamine 6G. All materials involved in sample and substrate preparation were purchased from commercial sources as analytical pure reagents. For recording the fluorescence and SERS spectra rhodamine  $10^{-6}$  M methanol solution was used.

b) *Experimental measurements*. Scanning electron microscopy investigations were performed with a Hitachi electronic microscope.

Fluorescence emission decays were measured with a time correlated single photon counting (TCSPC) system. A pulsed laser diode emitting at 635 nm served as the excitation source. It provides a pulse of  $< 200$  ps (FWHM) duration at a repetition rate of 1 MHz. The output optics of the laser diode allows collimating or focusing the beam to a spot size of approx. 200  $\mu$ m in diameter. Measurements were performed with an average power of less than 1mW at the sample. In order to acquire time-resolved data, the signal was recorded with a time-correlated single photon counting module and fluorescence decay signals were collected in typical fluorescence lifetime histograms with a timing resolution 6.1 ps/channel. The experimental determination of fluorescence lifetime was performed by using a non-linear fitting procedure to fit sampling photon arrival times to a single exponential decay function.

The SERS measurements were performed on a Dilor Labram system for excitation with 514 nm laser line and Renishaw's inVia Raman microscopes for excitation with 785 diode laser line.

## Results and discussion

### *a) Structural and optical characterization of fabricated metallic nanostructures.*

Figure 1a and 1b show the scanning electron microscope (SEM) pictures of fabricated periodic metallic nanostructures. The first picture represents an array of triangular silver particles left on the substrate after polystyrene spheres removing. One can see the regular arrangement of metal particles as well as their shape reflecting the voids between polystyrene spheres (about of 65 nm height and 120 nm length). The second picture shows highly regular hole-arrays in the deposited film. The diameter of holes (250 nm) can be easily tuned by the etching time, as Haginoya *et al.* had reported partially [6].

We measured the dispersion of the surface plasmon modes by recording optical transmission through the samples as a function of light frequency and in-plane wave vector. The experimental set-up used to obtain dispersion data consists of a white light source focused through two apertures to reduce beam divergence and grating spectrometer to select light with frequency ranging from  $1.15 \mu\text{m}^{-1}$  to  $2.3 \mu\text{m}^{-1}$  (where  $\omega(\mu\text{m}^{-1}) = \omega(\text{rad/s})/2\pi c$ ). The in-plane wave vector,  $\mathbf{k}_{\parallel}$  was varied by adjusting the angle of incidence to take a value dependent on the frequency  $\omega$  of the incident radiation according to the equation  $k_{\parallel} = k_0 \sin \theta$ , where  $k_0 = \omega/c$  for which  $n$  is the refractive index of the dielectric

Experimental plasmonic bands for the two nanostructures are presented in Fig 2b and Fig. 2b, respectively. As mentioned, the signature optical property of noble metal nanoparticles is the localized surface plasmon resonances (LSPR). The first experimental plasmonic band illustrates SPR modes localized on nanoparticles whereas the second one that of SPR modes localized inside of hole-arrays [7]. The primary consequence of SPR excitation is the enhancement of the local electromagnetic field, that is why such metallic nanostructures play the role of active substrates for surface-enhanced Raman spectroscopy (SERS) and controlling molecular fluorescence.

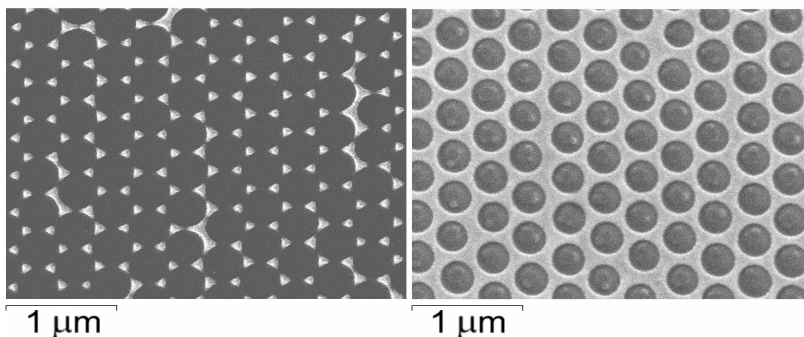


**Fig. 1.** SEM images: a) periodic array of silver nanoparticle  
b) periodic array of nanoholes in silver film.

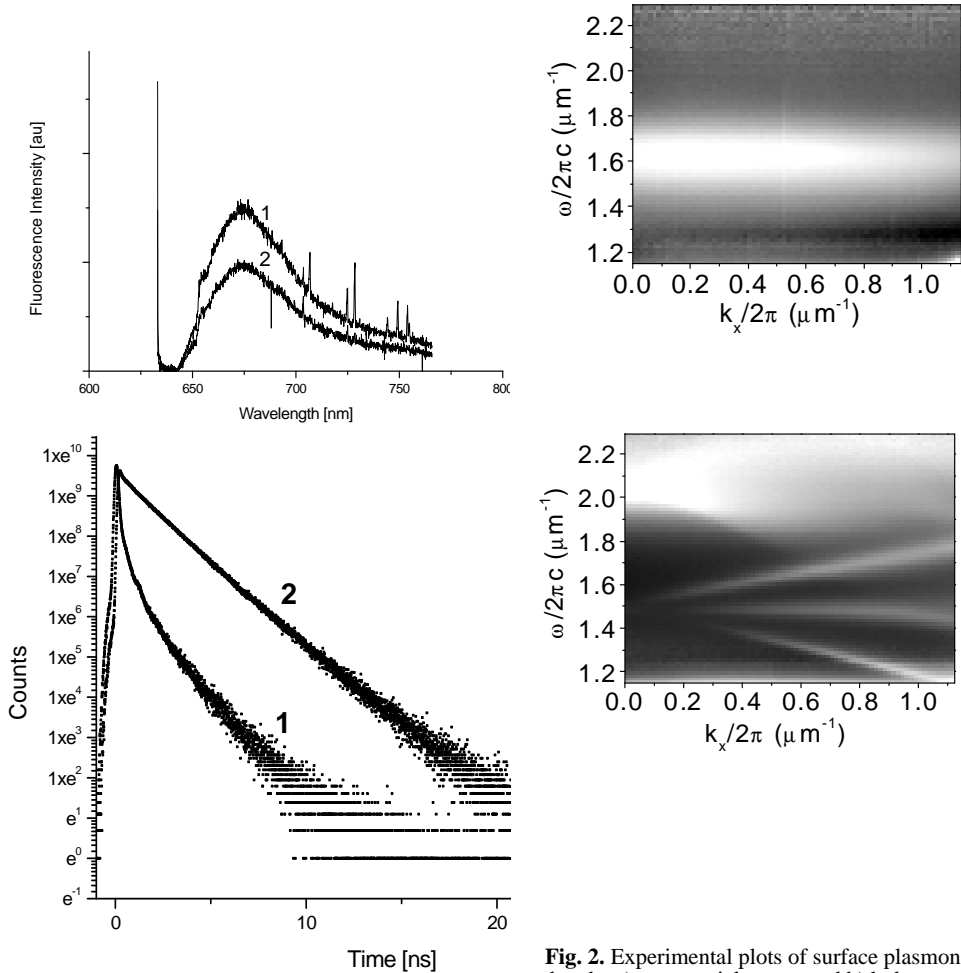


**Fig. 3.** Steady-state fluorescence spectra and time-resolved fluorescence profiles of rhodamine 700 molecules located on flat silica substrate (1) with regular arrays of silver nanoparticles and (2) without metal.

**Fig. 2.** Experimental plots of surface plasmons bands: a) nanoparticle array and b) hole-array (white color means high extinction coefficient)

b) *Controlling the fluorescence emission.* Figure 3 shows representative examples of fluorescence data, steady-state fluorescence spectra (Fig. 3a) and time-resolved profiles (Fig. 3b) of rhodamine 700 (R700). We measured the fluorescence of dye positioned directly on the silica substrate in two distinct cases. In the first case (data marked with (1)) the molecules were located on silica substrate in the presence of nearby regular arrays of silver nanoparticles whereas in the second case (data (2)) without any metal particles. Both types of measurements show important effects induced by the presence of metallic nanostructures. As we have studied the emission in a virtually identical chemical environment on silica substrate, the relative differences in data result exclusively from different  $D(\omega)$ . The alteration in the fluorescence lifetime is important and prove clearly the ability of such metallic nanostructure to manipulate



the fluorescence signal of dye molecules. The theoretical model to study the emission rate of dye induced by a nearby flat silver mirror is described in literature [8]. The lifetime and quantum efficiency of R700 was previously determined and found to be 2.8 ns and 0.65, respectively.

c) *Controlling the surface-enhanced Raman scattering (SERS)*. We investigate the SERS efficiency of the structure presented in Fig 1b using rhodamine 6G molecules as model compound. The SERS spectrum of Rh6G recorded with the 785 nm line, presented together with the SERRS recorded with the 514 nm laser line and FT-Raman spectra in Fig. 4, demonstrates the great capability of this substrate to provide SERS enhancements, when various laser lines are employed for excitation. The surface plasmons dispersion band (Fig 2b) provides only electromagnetic enhancement when using for excitation the laser line of 785 nm. Rh6G exhibits an electronic absorption maximum at 526 nm and therefore both resonance and surface enhancements are expected to contribute to the observed SERS spectra recorded with the 514 nm laser line. The differences between the SERRS and SERS spectra can be explained by considering the resonant contribution to the overall SERS enhancement. The electromagnetic field responsible for SERS is likely localized inside the holes, where giant local fields corresponding to Raman enhancement factors of the order of  $10^{11}$  are conceivable. This implies that the majority of the SERS signal measured from our sample is due to the excitation of very small percentage of adsorbate situated inside the holes, the individual enhancements being greater than the surface-averaged values [9].

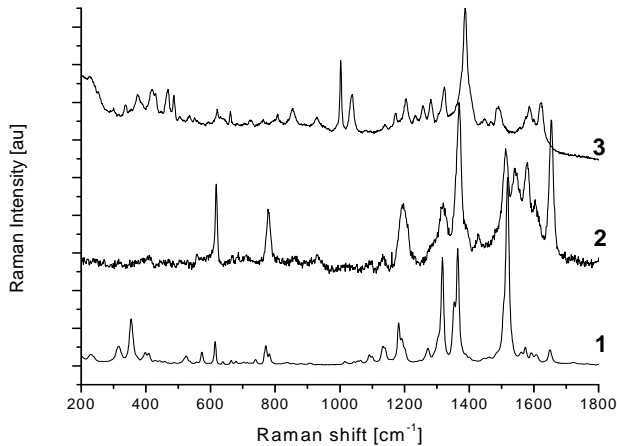


**Fig. 4.** (1) Ordinary FT-Raman spectrum of Rh6G polycrystalline sample (excitation line: 1064 nm); (2) SERRS spectrum (excitation line: 514 nm) of adsorbed Rh6G molecules; (3) SERS spectrum (excitation line: 785 nm) of adsorbed Rh6G.

### Conclusions

We have investigated the optical properties of ordered silver nanostructures with the goal of controlling the specific spectroscopic signatures of molecules, i.e. the fluorescence decay and surface-enhanced Raman scattering. The fluorescence emission depends strongly of the coupling between molecules and regular arrays of metallic nanoparticles via their plasmonic environment and the enhancement of SERS signal can be correlated with the plasmonic band structure  $D(\omega)$ .

## REFERENCES

1. E. Fermi, *Rev. Mod. Phys.*, 4, 87, (1932).
2. S. V. Gaponenko, *Effects of photon density of states on Raman scattering in mesoscopic structures*, *Phys Rev B*, 65, 140303(R), (2002).
3. E. M Purcell, *Phys. Rev.*, 69, 681, (1946).
4. K. Sakoda, *Optical properties of photonic crystals*, Springer, Berlin, (2001).
5. Y. Xia, B. Gates, Y. Yin, and Y. Lu, *Monodispersed colloidal spheres: old materials with new applications*, *Adv. Materials*, 12 (10), 693, (2000).
6. C. Haginoya, M. Ishibashi, K. Koike, *Nanostructure array fabrication with a size-controlable natural lithography*, *Appl. Phys. Lett.* 71 (20), 2934 (1997).
7. W. A. Murray, S. Astilean, P. Andrew , W. L. Barnes, The European Conf. on Lasers and Electro-Optics and the European Quant. Electronics Conf, Munich, Germany 23-27 June 2003.
8. S. Astilean and W. L. Barnes, *Quantum efficiency and the photonic control of molecular fluorescence in the solid state*, *Applied Physics B*, 75, 1, (2002).
9. S. Astilean, M. Bolboaca, T. Iliescu, D. Maniu, *Ordered metallic nanostructures for surface-enhanced Raman spectroscopy*, *Romanian Journal of Physics* (to be published), (2003).

## CYCLOIMMONIUM YLID UV VIS SPECTROSCOPY.

DANA DOROHOI

“Al.I.Cuza” University, Faculty of Physics, 11A Bd. Carol I,  
Iași, Romania, E-mail <ddorohoi@uaic.ro>

**ABSTRACT.** Cycloimmonium ylids are exciting subjects from spectral point of view. Their intramolecular charge transfer electronic band is very sensitive to the solvent nature, offering information on the intermolecular interactions in solutions. From spectral shifts measured in visible absorption and fluorescence spectra of cycloimmonium ylids the dipole moments and the structure of their first solvation sphere in ternary solutions were estimated.

### 1. Structure, stability and applicability of cycloimmonium ylids.

The term ylid was introduced in 1944 by G. Wittig and Felletschin [1] and reports the ending of the name given to a nitrogen organic derivative; trimethylammoniummethyloid. In cycloimmonium ylids [2,3] nitrogen belonging to the azo-heterocycle is covalently bonded to a mono- or di-substituted carbanion (Fig.1). The R –groups bonded up with the ylid carbon atom are strong electron-withdrawing groups such as  $-\text{COC}_6\text{H}_5$ ,  $-\text{COOR}$ ,  $-\text{CN}$ ,  $-\text{CONHC}_6\text{H}_5$ .



**Fig. 1.** Carbanion mono-substituted (a) and di-substituted (b) cycloimmonium ylids.

The ylid aromatic nitrogen is near  $sp^2$  hybridized in all circumstances, while for the ylid carbanion  $sp^2$  and  $sp^3$  are two limits of hybridization.

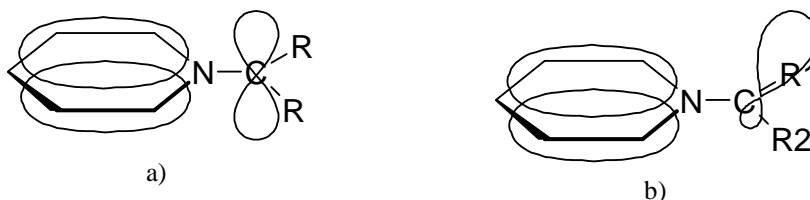


**Fig. 2.** Two limits of the carbanion hybridization in cycloimmonium ylids:  
a)  $sp^2$  hybridization, b)  $sp^3$  hybridization.

The isolation of the ylids as unitary compounds depends on their molecular stability. The nature both of the heterocycle and of the group covalently bonded to the carbanion is an essential factor determining the stability of these dipolar structures [2-6].

Usually carbanion disubstituted cycloimmonium ylids are more stable than the carbanion monosubstituted ones. The most stable carbanion disubstituted ylids are those with strong electron- acceptor substituents. The cycloimmonium ylid stability increases by passing through azinium to the diazinium [3].

The stable cycloimmonium ylids have interesting applications such as analytical reagents [7,8], semi-conducting materials [9-12], or substances with antimicrobial and antifungal action. They are used in various heterocycle synthesis of new classes of aza-heterocycle compounds [3,7,8] and as acid-basic indicators by their specific color.

Cycloimmonium ylids are nucleophilic reagents by their carbanion [3]. The carbanion monosubstituted cycloimmonium ylids have a larger nucleophilic character than the carbanion disubstituted ones. They act as 1,3 dipole in the [3+2] or [3+3] or as 1,5 dipoles in [5+2] cycloaddition reactions [13-17]. Cycloaddition and dimerization reactions are made "in situ", so knowledge about intermolecular interactions in cycloimmonium solutions, as well as about their structural parameters are very usefully in organic chemistry.

Recently the biological activity of some pyridazinium ylids [18-20] was revealed. The tests on Cock Bacillus evidenced anticonsumption properties of pyridazinium ylids, the diameter of the inhibition zone being about 90%. They are also moderate active compounds against Escherichia Coli and Staphylococcus Aureus.

## 2. Electronic absorption and fluorescence spectra of cycloimmonium ylids.

All cycloimmonium ylids have ultraviolet (UV) and visible (VIS) electronic absorption bands [21-30]. UV bands are attributed to  $\pi \rightarrow \pi^*$  transition. An increase of the conjugation in the case of carbanion disubstituted planar cycloimmonium ylids determined by electron withdrawing groups attached to the carbanion shifts hypsochromically the maximum of the UV absorption bands.

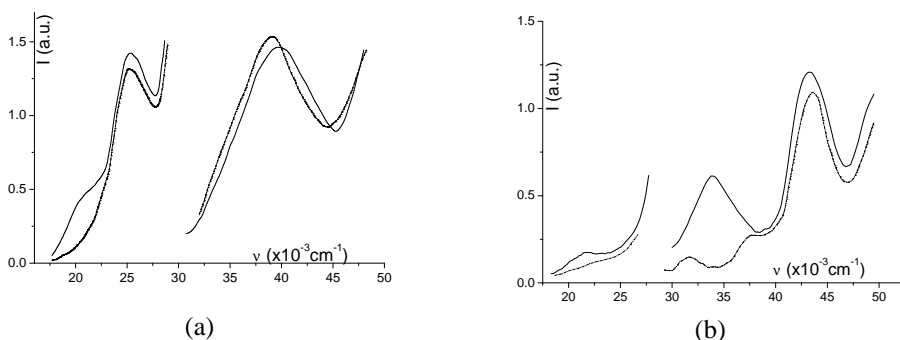


**Fig. 3.** UV VIS spectra of (a) p-phenyl pyridazinium-p-nitro-phenacylid and (b) isoquinolinium-carbomethoxy-thioanilido methylid in ethanol and ethanol +propionic acid (dot-dash line)

The visible electronic absorption band of cycloimmonium ylids has been attributed to an intramolecular charge transfer from the carbanion to the heterocycle, of the  $n - \pi^*$  type [21-32]. This band has a low intensity as compared with UV bands, shifts hypsochromically when passing from nonpolar to polar solvents as well as from non-protic to protic ones and disappears in acid solutions in which the non-participant electrons of the carbanion are blocked by the free protons. Kosower and Ramsey [31] suggested mechanism illustrated in Fig. 4 for the visible absorption band appearance.

The greater the delocalization, the higher wavenumber in the ICT visible absorption band maximum.

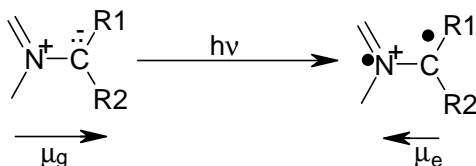


**Fig. 4.** Intramolecular charge transfer for visible absorption band of cycloimmonium ylids.

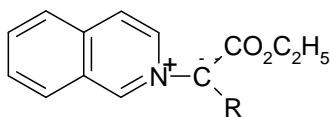
The wavenumber in the maximum of ICT visible absorption band depends on the degree of the negative charge delocalization on the carbanion substituents.

In a given non-polar solvent, the visible ICT band of cycloimmonium ylids with common both heterocycle and one from the carbanion substituents, has been used to evaluate the electron withdrawing character of the second group attached to the carbanion.

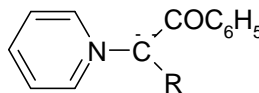
A series of isoquinolinium-R carboethoxy methylids with R=H, -Br, -Cl, has been synthesized. Atomic electronegativities  $\chi$  (eV) of these atoms were correlated with the energies in the maximum of ICT visible band  $E_{\max}$  (kcal/mol.) registered in benzene for the corresponding ylids. A linear dependence of the type (1) has been graphically established.

$$\chi(\text{eV}) = 0.07E_{\max} - 1.3 \quad (1)$$

The values of the atomic group electronegativity were determined with equation (1), supposing that no essential changes occur in the ylid structure by the change of R= atom by one atomic group. I. Zugrăvescu et al. [24,28,33] listed a series with increasing electronegativity atomic groups from Table 2. These values are in agreement with those estimated by the other methods [36,37].



(A)



(B)

**Fig. 5.** Isoquinolinium- and pyridinium- ylids used for electronegativity determination.

**Table1**

**Group electronegativities  $\chi$  (eV) determined in a series of isoquinolinium-R carboethoxymethylids (A) with -R variable, in benzene.**

Nr	-R	$\nu$ (cm <sup>-1</sup> )	$\chi$ (eV)	Nr.	-R	$\nu$ (cm <sup>-1</sup> )	$\chi$ (eV)
1	H	18020	2.2	8	CSSH	20850	2.87
2	Br	20570	2.8	9	CO <sub>2</sub> C <sub>2</sub> H <sub>5</sub>	21200	2.93
3	Cl	21550	3.0	10	COCH <sub>3</sub>	21840	3.07
4	CSNHC <sub>6</sub> H <sub>5</sub>	19310	2.52	11	COC <sub>3</sub> H <sub>7</sub>	21890	3.08
5	SO <sub>4</sub> C <sub>6</sub> H <sub>4</sub> CH <sub>3</sub>	20190	2.74	12	COC <sub>2</sub> H <sub>5</sub>	22110	3.10
6	CONHC <sub>6</sub> H <sub>5</sub>	20610	2.82	13	CN	22220	3.14
7	SO <sub>2</sub> C <sub>6</sub> H <sub>5</sub>	20800	2.86	14	COC <sub>6</sub> H <sub>4</sub> NO <sub>2</sub> -p	22260	3.20

Hine [38] showed that the bonds CF or CO in the same molecule tend to strong one another. This effect of thermodynamic stabilization was named symbiosis by Jorgenson [39]. Symbiosis permits us to explain the disagreements between the group electronegativities of the substituents R=-CO<sub>2</sub>C<sub>2</sub>H<sub>5</sub> and R=-COC<sub>6</sub>H<sub>5</sub> determined in systems with symmetric and asymmetric carbanions. In system (A) of isoquinolinium-carboethoxyRmethylid R=-CO<sub>2</sub>C<sub>2</sub>H<sub>5</sub> is attached to a symmetric carbanion, while R=COC<sub>6</sub>H<sub>5</sub> is affected by symbiosis

in system (B) pyridinium-benzoyl-R-methylid (Fig. 5). The resonant effect in the case of symmetric substituted cycloimmonium ylids has been described in [28,33]. It underlines the resonant intramolecular interaction role in the electronic levels stabilization.

**Table 2**  
Wavenumber of ICT visible absorption band for pyridinium-R benzoyl methylid in benzene solutions.

Nr.	Substitute R	$\nu$ (cm <sup>-1</sup> )	$\chi$ (eV)	Let us consider some pyridazinium-ylids from Fig.6 having substituents from Table 4. The wavenumbers of the ICT visible absorption band measured in benzene and ethanol and the spectral shifts by passing from benzene to ethanol, $\Delta\nu$ (cm <sup>-1</sup> ), listed in Table 4, are determined by the cycloimmonium-ylid structure.
1	CONHC <sub>6</sub> H <sub>5</sub>	22390	2.82	
2	CO <sub>2</sub> C <sub>2</sub> H <sub>5</sub>	23230	2.93	
3	COCH <sub>3</sub>	23540	3.07	
4	COC <sub>6</sub> H <sub>5</sub>	23300	3.10	
5	CN	24100	3.14	

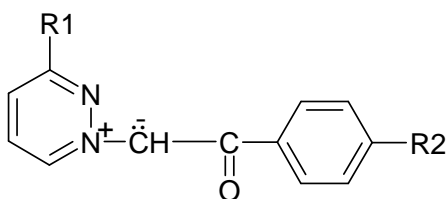


**Fig. 6.** Structure of 3-R<sub>1</sub>-Pyridazinium-p-R<sub>2</sub>-phenacylids and pyrimidinium - p-R<sub>2</sub>-phenacylids

**Table 3**  
Wavenumbers in the maximum of ICT visible absorption band of some 3-R<sub>1</sub>-Pyridazinium-p-R<sub>2</sub>-phenacylids (Fig.6) and spectral shift  $\Delta\nu$  by passing from benzene to ethanol solutions.

Ylid	1	2	3	4	5
-R <sub>1</sub>	H	C <sub>6</sub> H <sub>5</sub>	C <sub>6</sub> H <sub>4</sub> CH(C H <sub>3</sub> ) <sub>2</sub>	C <sub>6</sub> H <sub>4</sub> Br <sub>p</sub>	C <sub>6</sub> H <sub>4</sub> Cl <sub>p</sub>
-R <sub>2</sub>	NO <sub>2</sub>	NO <sub>2</sub>	NO <sub>2</sub>	NO <sub>2</sub>	NO <sub>2</sub>
Benzene	21480	20990	20810	20520	20600
Ethanol	22280	20890	21660	22080	21410
$\Delta\nu$ (cm <sup>-1</sup> )	800	900	850	1560	810
Ylid	6	7	8	9	10
-R <sub>1</sub>	C <sub>6</sub> H <sub>4</sub> Cl <sub>p</sub>	C <sub>6</sub> H <sub>4</sub> Cl <sub>p</sub>	C <sub>6</sub> H <sub>4</sub> Cl <sub>p</sub>	C <sub>6</sub> H <sub>4</sub> Br <sub>p</sub>	H
-R <sub>2</sub>	H	Br	OCH <sub>3</sub>	H	OCH <sub>3</sub>
Benzene	20020	20500	19630	19950	21100
Ethanol	20420	20920	20900	20500	21400
$\Delta\nu$ (cm <sup>-1</sup> )	420	270	270	550	300

Based on Table 3 the following remarks can be mentioned:

For the series of pyridazinium ylids 1-5 with common carbanion (-R<sub>2</sub>=NO<sub>2</sub>) and variable heterocycle, the wavenumbers of the ICT visible absorption band decrease in order: R<sub>1</sub>=-H > -C<sub>6</sub>H<sub>5</sub> > -C<sub>6</sub>H<sub>4</sub>-p-CH(CH<sub>3</sub>)<sub>2</sub> > -C<sub>6</sub>H<sub>4</sub>-p-Cl > -C<sub>6</sub>H<sub>4</sub>-p-Br, indicating an increase of the positive charge delocalization on the heterocycle.

Within series of pyridazinium ylids 5-8 having a common heterocycle, R<sub>1</sub>=-C<sub>6</sub>H<sub>4</sub>-p-Cl, and variable carbanion, the wavenumbers in the maximum of ICT absorption band depend on the unscreening ability of the carbanion substitutes [24,28,40,41].

Let be a class of cycloimmonium ylids with the same carbanion and different heterocycles [29-35]. The wavenumbers of the ICT visible band of some cycloimmonium ylids with common carbanion recorded in benzene and in ethanol are listed in Table 4.

**Table 4**

The ICT band wavenumbers for cycloimmonium-dibenzoylmethylids with common carbanion ( $R_1=R_2=-COC_6H_5$ ) and different heterocycles and spectral shift  $\Delta\nu$  by passing from benzene to ethanol solutions.

Nr.	Heterocycle	$\nu$ (cm <sup>-1</sup> )		$\Delta \nu$ (cm <sup>-1</sup> )
		benzene	ethanol	
1	pyridine	22550	24970	2420
2	Iso quinoline	22770	24540	1770
3	Pyridazine	20090	21400	1310
3	p-Phenyl pyridazine	20000	21280	1280
4	p-Cumyl pyridazine	19610	20880	1270
5	3 diphenyl- pyridazine	20800	19230	1970
6	Benzo[f]quinoline	22000	23600	1600
7	phthalazine	20100	23150	3050

From Table 4 it results a great sensitivity of ICT absorption band of cycloimmonium-dibenzoylmethylids to the heterocycle as well as to the solvent nature.

### 3. Solvent influence upon the electronic visible bands of cycloimmonium ylids.

In solutions, intermolecular interactions stabilize energy levels of the spectrally active molecules, determining changes in the wavenumber values in the maxima of the electronic absorption and emission bands.

As it results from Table 4, ICT visible absorption band of cycloimmonium ylids is strongly dependent on the nature of the solvent in which spectrally active molecules are solved. In this way, cycloimmonium ylids can be used as "probes" able to measure, by the spectral shifts, the intensity of intermolecular interactions in solutions. The visible ICT band modifications by passing from the gaseous state (g) to liquid solution (l) are directly proportional with the difference between the solvation energies of the electronic states participating to the transition. Let us consider two states of an electronic transition –fundamental state (0) and excited state (e)-, whose solvation energies are  $\Delta E_0$  and  $\Delta E_e$  (Fig. 7). From Fig.7 it results that if  $\Delta E_0 > \Delta E_e$ , electronic bands shift to blue (hypsichromically) and contrarily, if  $\Delta E_0 < \Delta E_e$ , electronic bands shift to red (bathochromically).

From such spectral shifts measured in different solvents one can obtain information on intermolecular interactions in cycloimmonium ylid solutions.

Due to their diversity, it is very difficult to separate the contributions of each interaction type from the total spectral shift of the electronic band. In order to establish what are the intermolecular interactions in a solution containing spectrally active molecules, the wavenumbers of the electronic bands are usually subjected to multiple linear regression (MLR) or multilinear regression of main components (MLRMC) by means of versions MULTIREG and HKA programs [43]. In this way estimations of the type;

$$\nu = \nu_0 + C_1 P_1 + C_2 P_2 + C_3 P_3 + \dots + C_N P_N \quad (3)$$

can be obtained [37, 39, 43, 71].

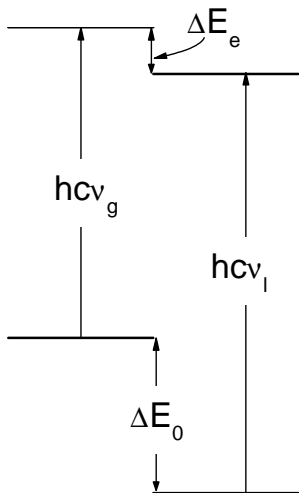


**Fig.7.** Solvation energies and the spectral shift by passing from gaseous state (g) to solution(s).

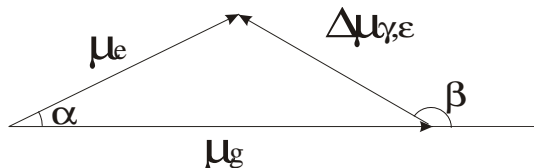


**Fig. 8.** Diagram of dipole moments in ICT process.

The change of wavenumber in the maximum of the electronic transition by passing from the gaseous state (g) to solution state (l), can be written:

$$hc(\nu_l - \nu_g) = hc\Delta\nu_{e0} = \Delta E_e - \Delta E_0 \quad (2)$$

From (4) it results that the spectral shifts by passing from gaseous to solution state are the greatest for the highest difference between solvation energies  $\Delta E_0$  and  $\Delta E_e$ .

The parameters  $P_i$  ( $i=1,N$ ) chosen as regressors in (3) could be functions from theories describing solvent influence on electronic absorption spectra. The coefficients  $C_i$  ( $i=1,N$ ) of regression indicate the contribution of each solvent parameters in the wavenumber modification.

The dependence between the spectral shift and the solvent microscopic parameters (3) evaluated from the solvent influence on the ICT visible absorption band is of the form:

$$\Delta\nu = C_1 \frac{\epsilon - 1}{\epsilon + 2} + C_2 \frac{n^2 - 1}{n^2 + 2} + C_3 \delta(\text{ppm}) \quad (4)$$

In relation (4)  $\Delta\nu$  represents the spectral shift measured when the spectrally active molecule passes from the gaseous state in solution with a given solvent and  $\epsilon$  and  $n$  are electric permittivity and refractive index of the solvents. Chemical shift  $\delta(\text{ppm})$  of the OH proton has been measured in the protic solutions.

In non-polar solvents cycloimmonium ylids participate at inductive-dispersive interactions and in polar solvents additionally at orientation-induction interactions.

The third term in (4) describes specific interactions of the type proton donor-acceptor, between the negative carbanion (or its substituents) and the -OH or -NH groups of the solvent.

As it results from Bakhshiev theory [44], parameters  $C_j$ ,  $j=1,N$  are dependent on the microscopic parameters of the spectrally active molecule, such as electric dipole moments or electric polarizabilities, in the electronic state participating to the intramolecular charge transfer. Coefficient  $C_1$  from (4) in Bakhshiev's theory is expressed by (5).

$$C_{1,or}^a = \frac{2}{hcr_0^3} \frac{2n^2 + 1}{n^2 + 2} [\mu_e(s)\mu_0(s) \cos \varphi - \mu_0^2(s)] \quad (5)$$

$$C_{1,or}^f = \frac{2}{hcr_0^3} \frac{2n^2 + 1}{n^2 + 2} [\mu_e^2(s) - \mu_e(s)\mu_0(s) \cos \varphi]$$

a and f refer to absorption and fluorescence spectra.



From the solvent influence on the absorption and fluorescence spectra one can estimate the electric dipole moment in the excited state of the molecules, as well as the angle between the molecular dipole moments in the two electronic states participating to the transition. In the case when the molecular microscopic parameters in the ground state of cycloimmonium ylid are known, the use of Bakhshiev's theory permits to evaluate the dipole moments in the excited states of the spectrally active molecules. A series of the microscopic parameters evaluated from the solvent influence on the ICT visible band based on Bakhshiev's theory are listed in the Table 5 for some new pyridazinium-ylids: p-phenyl-pyridazinium-p-nitro-phenacylid ( $P_1$ ), p-cumyl-pyridazinium-p-nitro-phenacylid ( $P_2$ ), p-phenyl-pyridazinium-benzoyl-p-nitro-benzoylmethylid ( $P_3$ ), p-cumyl-pyridazinium-benzoyl-p-nitro-benzoyl methylid ( $P_4$ ).

**Table 5.**

Microscopic parameters of some cycloimmonium ylids estimated from the solvent influence.

Ylid	$\mu_g (D)$	$r(A)$	$C_1^a$ (erg)	$C_1^f$ (erg)	$\mu_e (D)$	$\alpha$ (grd)	$\Delta\mu_{g,e} (D)$	$\beta$ (grd)
$P_1$	7.3	8	1840.6	-420.8	5.0	60	7.4	130
$P_2$	8.9	9	1755.9	-291.3	6.1	57	8.3	123
$P_3$	7.1	8	1581.0	-98.8	4.6	54	5.8	140
$P_4$	8.4	9	2024.2	-395.4	5.	71	8.6	142

The model of ternary solutions [46-48] permits us to estimate the composition of the first solvation sphere of cycloimmonium ylids when they are solved in binary solvent. For example, in the case of pyridinium-anilido benzoyl methylid solved in pairs of solvents benzene + ethanol and benzene + dimethylformamide, the molar ratios of protic solvent in solution ( $x_1$ ) and the statistic average weights ( $p_1$ ) have the values from Table 6.

**Table 6**

Molar ratios of protic solvent in solution ( $x_1$ ) and statistic average weights ( $p_1$ ) for pyridinium anilido-benzoylmethylids.

Benzene + Ethanol				Benzene + DMF			
Nr.	$x_1(\%)$	$\nu (cm^{-1})$	$p_1(\%)$	Nr.	$x_1(\%)$	$\nu (cm^{-1})$	$p_1(\%)$
1	0	21960	0	1	0	21960	0
2	7.4	22800	39	2	4.7	22320	24
3	14.5	23080	52	3	9.4	22480	34
4	27.6	23340	64	4	19.1	22720	50
5	50.4	23640	78	5	38.7	23000	68
6	82.0	23720	72	6	73.9	22920	63
7	100	24100	100	7	100	23480	100

Data from Table 5 show that ternary solutions of cycloimmonium ylids are not homogeneous systems. The polar, or protic solvent tends to occupy the places near the zwitterionic compound. So, the first solvation sphere of cycloimmonium ylid molecule is enriched with the molecules of the more active solvent from point of view of intermolecular interactions.

### Conclusions

ICT visible band of cycloimmoniu-methylids can be used in solvent influence studies due to its sensibility both to the ylid molecular structure and to the solvent nature.

Using the specificity of the cycloimmonium ylid spectra and their changes induced by the solvent nature, some structural features, such as dipole moments in the excited states of these compounds can be easily obtained. These estimations could not be made by the other experimental means.

### REFERENCES

1. G. Wittig and G. Felletschin, *Ann.* 555, 133, (1994).
2. A. W. Johnson, *N-Ylid Chemistry*, Academic Press, NY, (1966).
3. I. Zugrăvescu and M. Petrovanu, *N-Ylid Chemistry*, Mc Graw-Hill, NY, London, (1976).
4. Y. Kazarzi and G. Surpăţeanu, *Heterocycles*, 51, 4, 863, (1999).
5. P. Woisel, G. G. Surpăţeanu and G. Surpăţeanu, *Targets in Heterocycles Systems*, 5, 461, (2001).
6. W. E. Doering and K. Hoffmann, *J. Amer. Chem. Soc.*, 77, 521, (1955).
7. A. Pawda, *1,3-Dipolar Cycloaddition Chemistry*, Wiley Interscience, NY, (1984).
8. M. Petrovanu and I. Zugrăvescu, *Cycloaddition Reactions*, Academic Press, Bucuresti, (1987).
9. G. Surpăţeanu, V. Ştefan, E. Rucinschi and I. Zugrăvescu, *An. Ştiin. Univ. Iaşi, s. Chimie*, 20, 71, (1974).
10. L. Leontie, M. Roman, I. Caplanuş, G.I. Rusu, *Progr. Org. Coat.*, 44, 287, (2002).
11. L. Leontie, M. Roman, F. Brînză, C. Podaru, G.I. Rusu, *Synthetic Metals*, 138, 57, (2003).
12. L. Leontie, I. Olariu, G.I. Rusu, *Mater. Chem. Phys.*, 80, 506, (2003).
13. A. Couture, A. Lablache-Combiere, P. Grandclaude, *Heterocycles*, 31, 2111, (1990).
14. M. Petrovanu, C. Luchian, G. Surpăţeanu and V. Bărboiu, *Tetrahedron*, 37, 2805, 1981; 37, 2813, (1981).
15. R. Hoffmann, D. B. Boyd and S. Z. Goldberg, *J. Amer. Chem. Soc.*, 92, 3929, (1970).
16. D.B. Boyd and R. Hoffmann, *J. Amer. Chem. Soc.*, 94, 2382, (1972).
17. I. Zugrăvescu, E. Rucinschi, G. Surpăţeanu, *An. Ştiin. Univ. Iaşi, s. Chimie*, 14 41, (1970).
18. M. Ungureanu, I. Mangalagiu, G. Grosu, M. Petrovanu, *Ann. Pharm. Fr.*, 55(2), 69, (1997).
19. I. Olariu, M. Caproşu, G. Grosu, M. Ungureanu, M. Petrovanu, *Roum. Biotech. Lett.*, 4(5), 365, (1999).
20. I. Mangalagiu, G. Mangalagiu, M. Roman, M. Caproşu, M. Petrovanu, *Ann. Pharm. Fr.*, 58, 86, (2000).
21. D. Dorohoi, G. Surpăţeanu and C. Mihul, *An. Şt. Univ. Al.I.Cuza, Iaşi, T. XX*, nr.1, 59, (1974).
22. D. Dorohoi, L. Sitaru, G. Surpăţeanu and C. Mihul, *An. Şt. Univ. Al.I.Cuza, Iaşi, T. XX*, nr.2, 147, (1974).
23. C. Mihul and D. Dorohoi, *An. Şt. Univ. Al.I.Cuza, Iaşi, T. XXI*, 57, (1975).
24. G. Surpăţeanu, D. Dorohoi and I. Zugrăvescu, *An. Şt. Univ. Al.I.Cuza, Iaşi, T. XXI*, 89, (1975).
25. D. Dorohoi, E. Lupu, Mai Van Tri, *An. Şt. Univ. Al.I.Cuza, Iaşi, T. XXII*, 35, (1976).

26. M. Petrovanu, D. Dorohoi, Mai Van Tri, An. Șt. Univ. Al.I.Cuza, Iași, T. XXII, 41, (1976).
27. D. Dorohoi, M. Rotariuc and Mai Van Tri, An. Șt. Univ. Al.I.Cuza, Iași, T. XXII, 46, (1976).
28. G. Surpățeanu and D. Dorohoi, An. Șt. Univ. Al.I.Cuza, Iași, T. XXIII, 99, (1976).
29. D. Dorohoi, Contributions to the study of intermolecular interactions by spectral means, PHD-Thesis, Al.I.Cuza University, Iași, (1977).
30. D. Dorohoi, V. Tatu, An. Șt. Univ. Al.I.Cuza, Iași, T. XXV, 55, (1979).
31. R.M. Kosower and B.G. Ramsey, J. Amer. Chem. Soc., 81, 856, (1959).
32. C.A. Henrick, E. Ritchie and W.C. Taylor, Austr. J. Chem., 20, 2457, (1967); 20, 2467, (1967).
33. D. Dorohoi, D. Partenie, Do Nhat Van, I. Zugrăvescu, An. Șt. Univ. Al.I.Cuza, Iași, T. XXVI, 52, (1980).
34. D. Dorohoi, D. Creangă, G. Surpățeanu, An. Șt. Univ. Al.I.Cuza, Iași, T. XXVII, 59, (1980).
35. D. Dorohoi, D. Partenie, Do Nhat Van, An. Șt. Univ. Al.I.Cuza, Iași, T. XXIX, 27, (1983).
36. J.E. Huheey, J. Phys. Chem., 70, 2086, (1966).
37. J. M. Dereppe, R. Tonilaux, R. Schanch, J. Meerssche and M. Van, Ind. Chem. Belg., 38, 247, (1973).
38. J. Hine, J. Am. Chem. Soc., 85, 3230, (1963).
39. C. K. Jorgenson, Inorg. Chem. 3, 1201, (1964).
40. D. Dorohoi, V. Holban, J. Mol. Struct., 293, 1-3, 133, (1993).
41. D. Dorohoi, H. Partenie, J. Mol. Struct., 293, 1-3, 129, (1993).
42. V. Pop, D. Dorohoi and V. Holban, Spectrochim. Acta, part A 50(4), 2281, (1994).
43. G. Henrion, A. Henrion and R. Henrion, Biespiele zur Datenanalyse mit BASIC Programmen VEB D.V.W. Berlin, (1988).
44. N. G. Bakhshiev, Spectroscopia Mejmoleculiar'h Vzaimodeistviah, Izd. Nauka, (1972).
45. D. Dorohoi, G. Surpățeanu and L. Gheorghies, Balkan Physics Letters, 6(3), 198, (1998).
46. Iy.G. Mazurenko, Opt. i Spektros. T. XXXIII, 1060, 1972.
47. V. Pop, D. Dorohoi and M. Delibaș, An. Șt. Univ. Al.I.Cuza, Iași, T. XXXII, s.Ib, 79, (1986).
48. D. Dorohoi, V. Pop, An. Șt. Univ. Al.I.Cuza, Iași, T. XXXII, s. Ib Fizică, 79-82, (1987).

## THE COMPLETE LOCAL AND GLOBAL STRUCTURE OF THE NICKEL CATALYSTS CHARACTERIZED BY SYNCHROTRON RADIATION

**N. ALDEA<sup>1</sup>, ANDREEA GLUHOI<sup>1</sup>, B. BARZ<sup>1</sup>, P. MARGINEAN<sup>1</sup>, MIHAELA LAZAR, XIE YANING<sup>2</sup>, HU TIANDOU<sup>2</sup>, LIU TAO<sup>2</sup>, ZONGHUA WU<sup>2</sup> and ZIYU WU<sup>2</sup>**

<sup>1</sup> *National Institute for Research and Development of Isotopic and Molecular Technologies, R-3400 Cluj-Napoca, P.O. 5, Box 700, Romania*

<sup>2</sup> *Beijing Synchrotron Radiation Facilities of Beijing Electron Positron Collider National Laboratory, Beijing, People's Republic of China*

**ABSTRACT.** The supported Ni catalysts were analyzed by Extended X-ray Absorption Fine Structure (EXAFS) and X-Ray Diffraction (XRD) in order to determine their local and global structure. The present study evidenced by EXAFS method a strong deformation of the local structure of the metal due to its interaction with oxide support. The average particle size, the mean square of the microstrain the probability of the faults and the particle distribution function of the supported Ni catalysts were determined by XRD method. The method is based on Fourier analysis of the experimental X-ray line profiles (XRLP) (111), (200) and (220). The global structure is obtained with a fitting method based on the generalized Fermi function (GFF) facilities for approximation. The local and global microstructures of the catalysts are modified by the strong interaction between the metal clusters and oxidic supports. As a result the chemisorption and catalytic processes which occur at the Ni-support interface are also changed.

### Introduction

The theoretical background of EXAFS and XRD analysis was presented in previous papers [1,2]. The main mathematical properties of the GFF used for approximation and deconvolution of the experimental XRLP were described in Ref. [1,3]. A completed description of the methods for preparation of the supported nickel catalysts, experimental details using synchrotron radiation and data processing were presented in Ref. [1,3-5]. The present paper offers the complete local and global structure characterization by analyzing the first to fourth coordination shells and (111), (200) and (220) XRLP using X-ray absorption spectroscopy method and X-ray diffraction, respectively. We have investigated the following systems: 60 at. % Ni/ZnO, 89.6 at. % Ni/UO<sub>2</sub>, 88.4 at. % Ni/ThO<sub>2</sub>, 60 at. % Ni/MgO, 80 at. % Ni/SiO<sub>2</sub>, 70 at. % Ni/ZrO<sub>2</sub> and 85 at. % Ni/Al<sub>2</sub>O<sub>3</sub>. The transmission EXAFS and XRD measurements were carried out in 4W1B and 4W1C beamlines in Beijing Synchrotron Radiation Facilities (BSRF) operating at 30-50 mA and 2.2 GeV at room temperature [6].

### Results and discussion

#### EXAFS results

Fig. 1-(a) shows the absorption coefficients for investigated catalysts. The extraction of the EXAFS signal is based on  $E_0$  determination, followed by background removal before pre-edge and after edge baseline fitting with different possible modeling functions. The local structure of these samples corresponding to each coordination shell have been determined by Fourier transform technique of the EXAFS function defined in the range 20-150 nm<sup>-1</sup>. The local structure of the standard Ni black powder for each coordination shell is described by the following parameters:  $N_1=12$ ,  $R_1=0.249$ ,  $N_2=6$ ,  $R_2=0.352$ ,  $N_3=24$ ,  $R_3=0.431$ ,  $N_4=12$  atoms and  $R_4=0.497$  nm, respectively.

The diminution of the Fourier transform magnitude is a result of the reduced average coordination number. Each peak from  $|\Psi(r)|$  is shifted from the true distance due to the phase shift function which is included in the EXAFS signal. By assuming that each radial distribution

function  $|\Psi(r)|$  can be a Gaussian distribution and based on Lavenberg-Marquard [1] fit, the total radial distribution function  $|\Psi(r)|$  is split into four contributions. Thus, the broadening and center of each coordination shell is represented in Fig. 1-(b). By taking the inverse Fourier transform of the Gaussian distribution given in Fig. 1-(b), we obtained the experimental EXAFS function attached to each coordination shell. Then, the theoretical amplitude envelope and the phase shift functions were extracted from a black nickel powder as a standard sample.

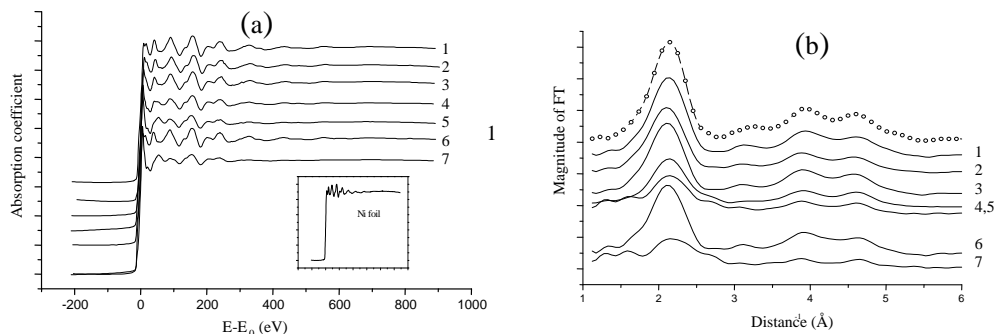


**Fig. 1.** (a) The normalized absorption coefficients versus photoelectron energies: binding energy  $E_0 = 8332$  eV, lower box - Ni foil as standard sample; (b) the Fourier Transforms of the EXAFS spectra ( $\circ$ ) black Ni powder; (1)- 60 at % Ni/ZnO, (2) - 89.6 at % Ni/UO<sub>2</sub>, (3) - 88.4 at % Ni/ThO<sub>2</sub>, (4) - 60 at % Ni/MgO, (5) - 80 at % Ni/SiO<sub>2</sub>, (6) - 70 at % Ni/ZrO<sub>2</sub>, (7) - 85 at % Ni/Al<sub>2</sub>O<sub>3</sub>

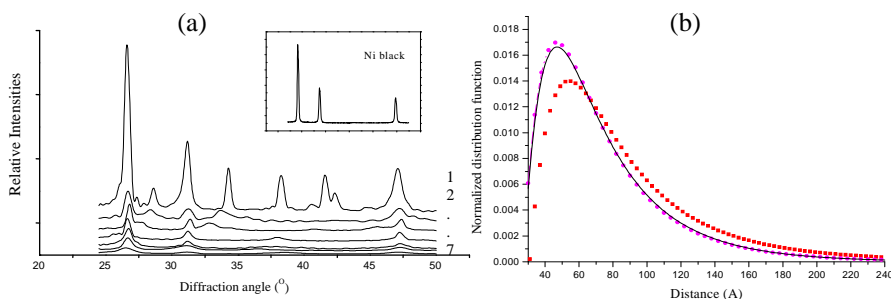


**Fig. 2.** (a) The XRLP (111), (200) and (220):, (1) - 60 at % Ni/ZnO, (2) - 89.6 at % Ni/UO<sub>2</sub>, (3) - 88.4 at % Ni/ThO<sub>2</sub>, (4) - 60 at % Ni/MgO, (5) - 80 at % Ni/SiO<sub>2</sub>, (6) - 70 at % Ni/ZrO<sub>2</sub>, (7) - 85 at % Ni/Al<sub>2</sub>O<sub>3</sub>; (b), the crystallite distribution function: ■ (111), ● (200) and (—) (220) X-ray line profiles for 60 at. % Ni/ZnO.

**Table 1.**

**The local structural parameters of the investigated samples**

Sample	Shell	R $\pm\Delta$ R Shell radius(nm)	N $\pm\Delta$ N Atomic numbers
60 at % Ni/ZnO	1	0.25 $\pm$ 0.01	1.0 $\pm$ 0.1
89.6 at % Ni/UO <sub>2</sub>		0.25 $\pm$ 0.01	9.01 $\pm$ 0.1
88.4 at % Ni/ThO <sub>2</sub>		0.25 $\pm$ 0.01	10.15 $\pm$ 0.12
60 at % Ni/MgO		0.25 $\pm$ 0.005	7.17 $\pm$ 0.1
80 at % Ni/SiO <sub>2</sub>		0.25 $\pm$ 0.006	9.32 $\pm$ 0.11
70 at % Ni/ZrO <sub>2</sub>		0.25 $\pm$ 0.003	9.16 $\pm$ 0.2
85 at % Ni/Al <sub>2</sub> O <sub>3</sub>		0.256 $\pm$ 0.001	6.08 $\pm$ 0.12

Sample	Shell	R±ΔR Shell radius(nm)	N±ΔN Atomic numbers	
60 at % Ni/ZnO	2	0.35±0.01	5.53±0.1	
89.6 at% Ni/UO <sub>2</sub>		0.351±0.03	4.32±0.05	
88.4 at % Ni/ThO <sub>2</sub>		0.349±0.02	4.46±0.02	
60 at % Ni/MgO		0.352±0.01	3.73±0.04	
80 at % Ni/SiO <sub>2</sub>				
70 at % Ni/ZrO <sub>2</sub>		0.35±0.02	4.46±0.02	
85 at % Ni/Al <sub>2</sub> O <sub>3</sub>				
60 at % Ni/ZnO	3	0.433±0.008	25.05±0.03	
89.6 at% Ni/UO <sub>2</sub>		0.433±0.05	17.58±0.022	
88.4 at % Ni/ThO <sub>2</sub>				
60 at % Ni/MgO		0.432±0.007	12.92±0.03	
80 at % Ni/SiO <sub>2</sub>				
70 at % Ni/ZrO <sub>2</sub>		0.433±0.01	18.64±0.04	
85 at % Ni/Al <sub>2</sub> O <sub>3</sub>				
60 at % Ni/ZnO	4	0.499±0.001	9.1±0.1	
89.6 at% Ni/UO <sub>2</sub>		0.498±0.001	10.10±0.05	
88.4 at % Ni/ThO <sub>2</sub>		0.5±0.003	10.34±0.02	
60 at % Ni/MgO		0.5±0.001	7.09±0.01	
80 at % Ni/SiO <sub>2</sub>				
70 at % Ni/ZrO <sub>2</sub>		0.502±0.003	10.10±0.05	
85 at % Ni/Al <sub>2</sub> O <sub>3</sub>				

Table 1 contains the best values of the local structural parameters for all investigated coordination shells. In according with our previous data reported in [1-3], we found that the average interatomic distances of the first to the fourth coordination shells are closely related with standard sample. The atom number of the first shell decreases with 15% (88.4 at. % Ni/ThO<sub>2</sub>) up to 49% (85 at. % Ni/Al<sub>2</sub>O<sub>3</sub>) relative to the standard sample. By analyzing the atom number of the second coordination shell, we also obtained a diminution between 8% (60 at. % Ni/ZnO) and 38% (60 at. % Ni/MgO). The structural model of the third coordination shell gives an increase of the atom number with 4% for 60 at. % Ni/ZnO and a decrease between 22% (70 at. % Ni/ZrO<sub>2</sub>) and 46% (60 at. % Ni/MgO). The last coordination shell shows a decrease between 14% (88.4 at. % Ni/ThO<sub>2</sub>) and 41% (60 at. % Ni/MgO). Therefore, we consider that this diminution of the atom number is due to a strong interaction between the Ni atoms and the support surface. The metal-support interface can have influence upon the electronic properties of the metal clusters, and as a consequence their reactivity for adsorption of the molecules are modified. Also, the nature of the interaction of the metal clusters with the support was expected to influence both the electronic properties and morphology of the clusters and thus their catalytic properties.

### ***XRD results***

The XRLP (111), (200) and (220) were processed in manner of the Ref. [1-2]. Their relative intensities with respect to the diffraction angle for standard sample as well as for investigated samples are shown in Fig. 2-(a). Nobody has ever used the GFF for the XRLP approximation and its Fourier Transform before. In former section we have shown that the coordination shell radius of investigated sample have similar values as Ni standard sample. An additional proof is given by the position and the shape of each Ni K edge around to 8333 eV; it means that all the samples contain only metallic nickel. These important results are strongly correlated with the positions of (111), (200) and (220) XRLP from the experimental spectra

presented in Fig. 2-(a). Therefore, these results explain the metallic features of the investigated clusters despite the strong deformation of the crystalline structure. Fig. 2-(b) shows the particle size distribution for 60 at. % Ni/ZnO sample. The main results regarding the investigated supported nickel catalyst microstructure are summarised in Table 2. As a measure of the discrepancy between the XRLP approximated by the GFF and pseudo-Voigt or Pearson V we defined a residual index [1-2]. By analysing the values of the residual index for each of the distributions, we demonstrated the validity and reliable of the GFF approximation. The values of the crystallite size can be correlated with the mean value of the grain diameter [7], if we take into consideration the physical meaning of the crystallite size and the grain one. It is possible that a grain of nickel cluster be built up from more nickel crystallites. In this case, the adsorption probability of the hydrogen on the interface of the crystallites, inside the metal cluster, is much reduced.

**Table 2**

**The global structural parameters of the investigated samples**

Name of sample	$\delta_i(\rho_h, \rho_g)$ [nm] <sup>-1</sup>	$D_{eff}^{(hkl)}$ [nm]	$\langle \epsilon^2 \rangle_{hkl} 10^{-4}$	SFP <sup>(hkl)</sup> [%]
(111), $\delta_g=0.0029 \text{ nm}^{-1}$				
60 at % Ni/ZnO	0.075	9.5	0.14	0.2
89.6at%Ni/VO <sub>2</sub>	0.963	7.3	0.22	0.07
88.4 at % Ni/ThO <sub>2</sub>	0.728	10.4	0.12	0.4
60 at % Ni/MgO	0.07	10.2	0.13	0.3
80 at % Ni/SiO <sub>2</sub>	0.134	5.9	0.36	1.4
70 at % Ni/ZrO <sub>2</sub>	0.141	5.1	0.41	1.3
85 at % Ni/Al <sub>2</sub> O <sub>3</sub>	0.228	3.2	1.04	0.04
(200), $\delta_g=0.0031 \text{ nm}^{-1}$				
60 at % Ni/ZnO	0.093	7.9	0.14	0.2
89.6at%Ni/VO <sub>2</sub>	0.104	6.9	1.8	0.1
88.4 at % Ni/ThO <sub>2</sub>	0.083	8.8	0.12	0.3
60 at % Ni/MgO	0.104	6.7	0.19	0.1
80 at % Ni/SiO <sub>2</sub>	0.164	4.7	0.37	0.6
70 at % Ni/ZrO <sub>2</sub>	0.241	2.9	1.01	0.8
85 at % Ni/Al <sub>2</sub> O <sub>3</sub>	0.214	3.4	0.73	0.7
(220), $\delta_g=0.0028 \text{ nm}^{-1}$				
60 at % Ni/ZnO	0.112	6.8	0.1	0.2
89.6at%Ni/VO <sub>2</sub>	0.104	6.9	0.34	1.5
88.4 at % Ni/ThO <sub>2</sub>	0.083	8.8	0.4	0.19
60 at % Ni/MgO	0.096	6.7	0.06	0.13
80 at % Ni/SiO <sub>2</sub>	0.163	4.7	0.20	0.42
70 at % Ni/ZrO <sub>2</sub>	0.179	2.9	0.24	0.89
85 at % Ni/Al <sub>2</sub> O <sub>3</sub>	0.228	3.4	0.4	1.5

$\delta_g(\rho_g)$  - integral width for standard black Ni powder,  $\delta_i(\rho_h, \rho_g)$  - integral width for true samples,

$D_{eff}^{(hkl)}$  - effective particle size,  $\langle \epsilon^2 \rangle_{hkl}$  - mean square of the microstrain, SFP<sup>(hkl)</sup> - stacking fault probability (Ref. [1] contains the meaningful of each parameters).

## Conclusions

The information presented in this paper describes the whole local and global structure of supported nickel catalysts determined by EXAFS and XRD analysis. The additional results give a complete image of the strong deformation of the crystalline structure. The conclusions that can be drawn from these studies are:

(i) The local structure of the investigated systems shows a strong morphological deformation of the nickel clusters caused by the metal-support interaction. These morphological modifications can be accompanied by modification of the electronic structure that has a large effect on the reactant adsorption. A result of these modifications induced by the supports is the enhancement of the catalytic activity for H/D exchange reaction between hydrogen and water vapor.

(ii) The numerical results obtained from (111), (200) and (220) XRLP show that by using the GFF distribution we can also obtain reliable microstructural parameters.

## REFERENCES

- [1]. N. Aldea, Andreea Gluhoi, P. Marginean, C. Cosma and Xie Yaning, *Extended X-ray Absorption Fine Structure and X-ray Diffraction studies on supported Ni catalysts*, Spectrochim. Acta Part B 55, 997 (2000).
- [2]. N. Aldea, Andreea Gluhoi, P. Marginean, C. Cosma, Xie Yaning, Hu Tiandou, Whongua Wu and Baozhong Dong, *Investigation of supported nickel catalysts by X-ray absorption spectrometry and X-ray diffraction using synchrotron radiation*, Spectrochim. Acta Part B 57, 1453 (2002).
- [3]. B. Barz, N. Aldea, Andreea Gluhoi, P. Marginean, Xie Yaning, Hu Tiandou, Liu Tao and ZonhuaWu and Ziyu Wu *The analysis of the interaction metal-support in Ni-catalysts by extended x-ray absorption fine structure and x-ray diffraction using synchrotron radiation*, Colloquium Spectroscopicum Internationale CSI XXXIII, 7-12 Sept. 2003, Granada, Spain.
- [4]. A. Gluhoi, B. Barz, P. Marginean, N. Aldea, *X-ray diffraction analysis on supported nickel catalysts*, National Conference of Physics, Targu-Mures, Romania 2002.
- [5]. B.Barz, Andreea Gluhoi, P. Marginean, N. Aldea, Xie Yaning and Baozhong Dong, *X-Ray diffraction analysis on supported nickel catalysts and their physical-chemical properties*, CERES Programme, Annual Scientific Session, Dec. 2-3 2002, Bucharest.
- [6]. B.S.R.F. Activity Report 2001, Beijing Electron Positron Collider Laboratory.
- [7]. P. Marginean and A. Olariu, *Metal /oxide support effects in H<sub>2</sub>-H<sub>2</sub>O deuterium exchange reaction catalyzed by nickel*, J. Catal. 95 (1985) 1-12.



## BIMODAL MOLECULAR ENCAPSULATION OF MEFENAMIC ACID BY $\beta$ -CD IN SOLUTION AND SOLID STATE

**M. BOGDAN<sup>1</sup>, DIANA BOGDAN<sup>1</sup>, M.R. CAIRA<sup>2</sup>, S.I. FĂRCAȘ<sup>1</sup>**

<sup>1</sup> National Institute for Research and Development of Isotopic and Molecular Technologies, P.O. Box 700, Donath Str. # 71-103, 400293 Cluj-Napoca 5, Romania Tel. +4-0264-584037, Fax: +4-0264-420042

<sup>2</sup> University of Cape Town, Department of Chemistry, Rondebosch 7701, South Africa; Tel. 021 6503071, Fax. 021 6897499; E-mail: xraymino@science.uct.ac.za

**ABSTRACT.** Inclusion complexes of mefenamic acid anion (MF<sup>-</sup>), a non-steroidal anti-inflammatory drug, with  $\beta$ -cyclodextrin ( $\beta$ -CD) were prepared and characterized both in solution and in solid state using <sup>1</sup>H NMR and X-ray diffraction studies. Inclusion of the mefenamic acid anion in the host molecule is shown by changes in the chemical shifts of some of the guest and host protons, in comparison with the chemical shifts of the same protons in the free compounds. The continuous variation method was used to establish the stoichiometry. The obtained results indicate that simultaneous inclusion of both rings occur, giving rise to two isomeric 1:1 complexes. The association constants for the two 1:1 complexes were calculated by a non-linear least-squares regression analysis of the changes in observed chemical shifts of the drug and  $\beta$ -CD lines as a function of  $\beta$ -CD concentration. The obtained results were compared with those obtained by X-ray powder diffraction in combination with molecular mechanics calculations. The geometry of the two 1:1 complexes according to the obtained X-ray data is given.

### Introduction

Mefenamic acid is a non-steroidal drug with strong analgesic anti-inflammatory and anti-pyretic properties, widely applied in therapeutics. The therapeutic single oral dose of mefenamic acid is 0.25 g; it is absorbed from the alimentary canal and after 2 hours the maximal concentration in the blood is reached. Unfortunately, it may produce a number of side effects such as nausea, vomiting, bleeding from the alimentary canal, rash, etc. The side effects can be reduced by increasing the drug solubility, which enhances its biological availability and permits decrease of the required dose. Moreover, this drug is not stable and products of its decomposition can enhance undesirable effects. In the modern technology of drug formulation, cyclodextrins are used as stability and solubilising agents [1].

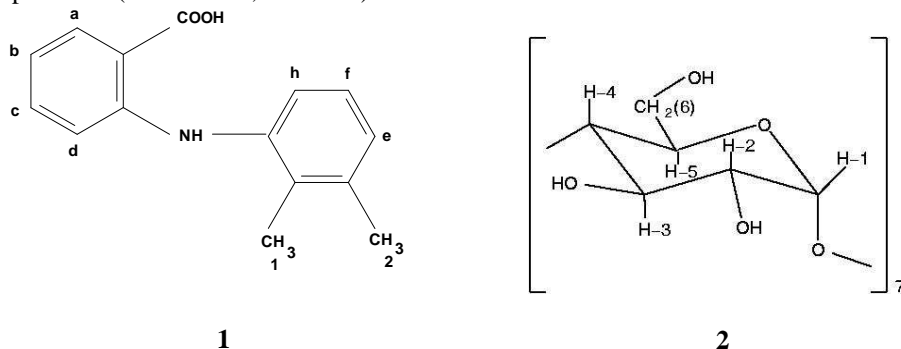
Cyclodextrins (CDs) have homogeneous toroidal structures of different molecular size: most typical are cyclohexaamylose ( $\alpha$ -CD), cycloheptaamylose ( $\beta$ -CD) and cyclooctaamylose ( $\gamma$ -CD). All glucose units are slightly tilted so they form a hollow truncated cone. The primary hydroxyl groups are located at the wider rim and the secondary hydroxyl groups are found at the narrower rim. The toroidal structure has a hydrophilic surface, making them water soluble, whereas the cavity is composed of the glycoside oxygens and methine hydrogens, giving it a hydrophobic character. As a consequence, the CDs are capable of forming inclusion complexes with compounds having a size compatible with dimensions of their size [2].

In a thoroughly study of an inclusion complex, three main points need to be clarified: stoichiometry, association constant and geometry of the complexes. Such a complete characterization of the inclusion complexes should contribute to a better understanding of the therapeutic properties.

In this work, we investigated the complexation of mefenamic acid anion **1** (MF<sup>-</sup>) and  $\beta$ -CD, **2**, in water by NMR and showed that two 1:1 complexes coexist. The structure of these complexes in solid state was estimated from the X-ray diffraction data in combination with molecular mechanics calculations.

## Materials and Methods

$\beta$ -cyclodextrin ( $\beta$ -CD) containing an average of 8 water molecule/ molecule was purchased from Sigma Chemie GmbH (Germany). The  $\beta$ -CD was used without further purification and the water content was considered in the calculation of solute concentrations. The  $D_2O$  (deuterium content 99,7 %) was purchased from Institute for Cryogenics and Isotope Separations (Rm. Vâlcea, Romania).



The NMR experiments were performed at 300 MHz with a Varian-Gemini spectrometer. The  $^1H$  NMR spectra were recorded in  $D_2O$  solution at  $293 \pm 0.5$  K and all chemical shifts were measured relative to external TMS. Typical conditions were as follows: 16 K data points, sweep width 4500 Hz, giving a digital resolution of 0.28 Hz/point. The  $90^\circ$  pulse width was  $13 \mu s$  and the spectra were collected by co-addition of 32 or 64 scans. In some cases, an appropriate Gaussian function was applied before Fourier transformation to enhance the spectral resolution.

In order to study the complexation process between mefenamic acid (MF) and  $\beta$ -CD in solution, two stock solutions in  $D_2O$ , both having  $10 \text{ mM}$  were prepared. Due to extremely low solubility of mefenamic acid in water [3], it was converted to its sodium salt by titration with NaOD to a final pH = 12. Based on these two equimolar solutions, a series of nine samples ( $i = 1 \div 9$ ) containing both the  $MF^-$  and the  $\beta$ -CD molecules were prepared. This was accomplished by mixing the two solution to constant volume ( $2 \text{ ml}$ ) at varying proportions, so that a complete range ( $0 < r < 1$ ) of the ratio  $r = [X]/([H] + [G])$  was sampled.  $X = G$  or  $H$  and  $[H]$  and  $[G]$  are the total concentrations of the host ( $\beta$ -CD) and guest ( $MF^-$ ), respectively. Thus, the total concentration  $[H] + [G] = [M] = 10 \text{ mM}$  was kept constant for each solution. The same set of samples was used both for the determination of the stoichiometry and association constant,  $K_a$ .

For X-ray diffraction study, the powder sample was prepared as follows. Equal amounts ( $25 \text{ ml}$ ) of  $\beta$ -CD and  $MF^-Na$  solutions were mixed, shaken for  $8 \text{ h}$  and then stored for 7 days at 313 K. The precipitate of the inclusion complex was washed twice with small portions of distilled water and was dried first in air and then in a dryer at 325 K. A capillary of diameter  $0.7 \text{ mm}$  was filled with powder and measured at the high-resolution powder station of BM16 at the European Synchrotron Radiation Facility (Grenoble) with  $\lambda = 0.80081 \text{ \AA}$ . Continuous scans were made from  $0.0^\circ$  to  $48.0^\circ$  in  $2\theta$  with  $0.5^\circ 2\theta \text{ min}$  and a sampling time of  $50 \text{ ms}$ .

## Results and Discussion

### Determination of the stoichiometry

Several techniques like IR, CD and UV-VIS spectroscopy can establish if guest molecules form an inclusion complex with  $\beta$ -CD, but they cannot provide information about the structural configuration of the complex. In contrast, NMR is a technique which provides the

most evidence for the inclusion of a guest into the hydrophobic CD cavity in solution. Inclusion of  $\text{MF}^-$  in  $\beta$ -CD is shown by the change in the chemical shift of some of the guest and host protons in comparison with the chemical shifts of the same protons in the free components. Partial  $^1\text{H}$  NMR spectra of pure components and  $\text{MF}^-$ : $\beta$ -CD mixture in a 3:2 molar ratio are shown in **Figures 1 and 2**.

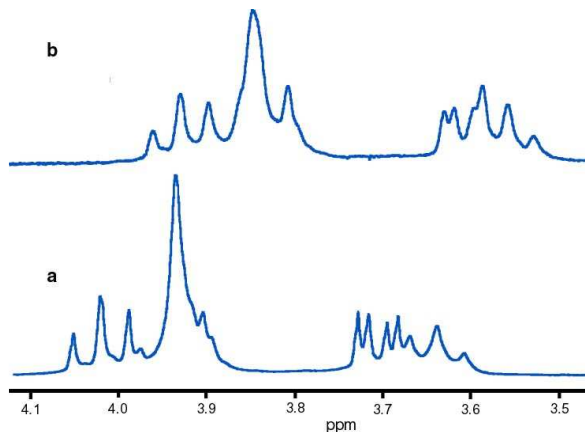


**Fig. 1.** Partial 300 MHz spectra of (a) 10 mM  $\beta$ -CD and (b) 4 mM  $\beta$ -CD and 6 mM mefenamic acid anion.

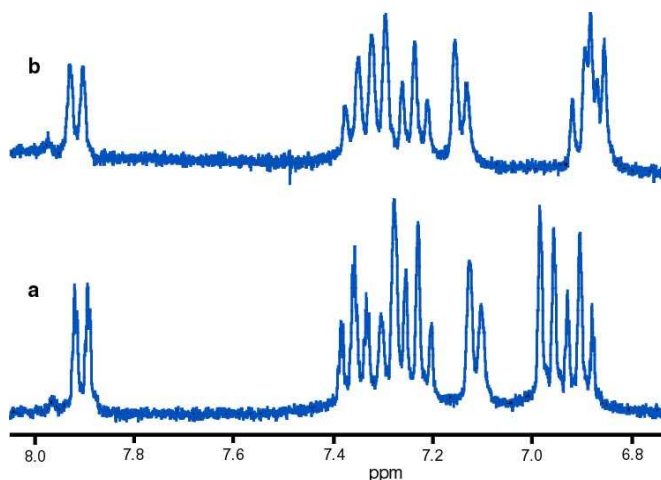


**Fig. 2.** Partial 300 MHz spectra of (a) 10 mM mefenamic acid anion and (b) 6 mM mefenamic acid anion and 4 mM  $\beta$ -CD. Only the spectral region for aromatic protons (Ha, Hc, Hh, Hf, He, Hd, Hb) of mefenamic acid anion is displayed.

The absence of new peaks that could be assigned to the complex suggested that complexation is a dynamic process, the included  $\text{MF}^-$  being in a fast exchange between the free and bound states.

Determination of the stoichiometry of the  $\text{MF}^-$ : $\beta$ -CD complex by continuous variation method was based on  $^1\text{H}$  NMR spectra obtained for  $\text{MF}^-$  and  $\beta$ -CD mixtures in which the initial concentrations of the two species were maintained constant and the ratio  $r$  varied between 0 and 1. The continuous variation plots (Job plots) of  $|\Delta\delta|$  [ $\beta$ -CD] against  $r_1 = m/(m+n)$ , where  $m$  and

n are, respectively, the proportions of  $\beta$ -CD and MF-Na in the  $(\text{MF-Na})_n : (\beta\text{-CD})_m$  complex are presented in **Figure 3**. The induced shift,  $\Delta\delta$ , is defined as the difference in chemical shifts in the absence and in the presence of the other reactant for a given ratio  $r$ .

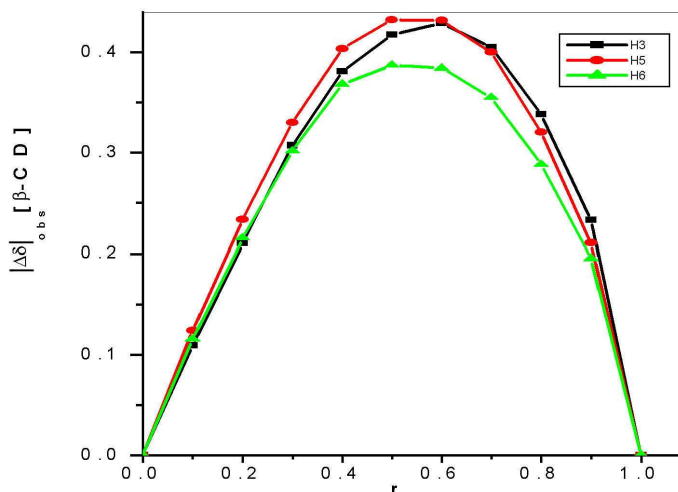


**Fig. 3.** Job plots for protons H3, H5, and H6 of  $\beta$ -CD in the presence of different concentrations of mefenamic acid anion

Thus, for H3, H5 and H6 protons of  $\beta$ -CD, significant upfield shifts, attributable to the inclusion of an aromatic part, were observed. The Jobs plots show a maximum at  $r_1 = 0.5$  and quite symmetrical shapes indicating that the complex has 1:1 stoichiometry. The MF-Na protons can be split into two groups, one shifted upfield (Ha, He, Hh and H2) and the other (Hd) downfield. Because the protons belonging to both the aromatic rings of MF-Na show chemical shift differences upon inclusion, suggests that multiple equilibria may exist in solution. Although the shapes of the Job plots for MF-Na protons are not smoothly and highly symmetrical, the maximum does not deviate significantly from  $r_2 = 0.5$ , indicating, in our opinion, the existence of two isomeric 1:1 complexes. Similar behavior was reported for other non-steroidal anti-inflammatory agents such as diclofenac [4], piroxicam [5], naproxen [6] and an anticholinergic drug, oxyphenonium bromide [7].

#### ***Evaluation of the binding constants***

In order to determine the extent of the intermolecular binding between the two aromatic rings of MF-Na and  $\beta$ -CD, the association constants have been evaluated.

The association constant,  $K_a$ , for a 1:1 complex can be determined according to the following equation [8]:

$$\Delta\delta^{(i,j)} = \frac{\Delta\delta_c^{(j)}}{2[X]} \left\{ [M] + \frac{1}{K_a} - \left[ \left( [M] + \frac{1}{K_a} \right)^2 - 4[H]^{(i)}[G]^{(i)} \right]^{1/2} \right\} \quad (1)$$

where  $i$  counts the sample number and  $j$  the investigated protons.

If the studied proton belongs to the guest or host molecule, then  $X = G$  or  $H$ , respectively.  $\Delta\delta_c^{(i)}$  represents the chemical shift difference (for a given proton) between the free component and a pure inclusion complex.

We developed a computer programme based on an iteration procedure following specific algorithms in order to fit the experimental values  $\Delta\delta_c^{(i,j)}$  to the appropriate equation. Each iteration sets up a quadratic programme to determine the direction of search and the loss function:

$$E = \sum_i \sum_j \left( \Delta\delta^{(i,j)} - \Delta\delta_{calc}^{(i,j)} \right)^2 \quad (2)$$

until search converges. The fitting procedure reaches an end when the difference between two consecutive E values is smaller than  $10^{-6}$ . The treatment of the whole set of protons studied yields one single  $K_a$  value for the whole process and a set of calculated  $\delta_c^{(i,j)}$  values.

In our particular case, we applied eq. (1) for a set of protons consisting in H3, H5 and H6 of  $\beta$ -CD and Ha and Hd of MF-Na and then for H3, H5 and H6 of  $\beta$ -CD and He, Hh and H2 of MF-Na. This means that we considered first the case when the xylyl moiety is inserted in the  $\beta$ -CD cavity and then the inclusion of benzoic acid moiety. The association constants obtained, using the above described procedure are:

$K_{1:1'} = 172.32 \text{ M}^{-1}$ $E = 3.11 \cdot 10^{-3}$ $r = 0.993$	Based on the observed chemical shift changes of H3, H5, H6, Ha and Hd
$K_{1:1} = 435.54 \text{ M}^{-1}$ $E = 2.14 \cdot 10^{-3}$ $r = 0.995$	Based on the observed chemical shift changes of H3, H5, H6, He, Hh and H2

$$K_a = K_{1:1} + K_{1:1'} = 607.86 \text{ M}^{-1}$$

It is worth mentioning that there is a striking similarity between the  $K_a$  value obtained by us and the values reported by Ikeda *et al.* [9] using CD ( $K_a = 620 \text{ M}^{-1}$ ), UV-VIS spectroscopy ( $K_a = 630 \text{ M}^{-1}$ ) and solubility measurements ( $K_a = 570 \text{ M}^{-1}$ ).

#### **Structure determination in solid state**

The crystal structure of the inclusion complex of  $\beta$ -CD with MF-Na has been determined from a combination of high-resolution synchrotron powder diffraction data and molecular mechanics calculations [10]. A grid search indicates two possible solutions, which are corroborated by molecular mechanics calculations, while Rietveld refinement (RR) results suggest the crystal structure that is more likely to be formed in the solid state. Thus, MF-Na is partially included in  $\beta$ -CD with either the xylyl or the benzoic acid moiety being inside its cavity.

After energy minimization, the two models presented in **Figure 5** (to be referred as **I** and **II**) were found to be almost isoenergetic and MF-Na had become only partially encapsulated in the CD macrocycle. Either the xylyl (**I**) or the benzoic acid (**II**) moiety was inside the cavity and the N atom that linked the two phenyl rings was found at the secondary face of the macrocycle in both cases. After RR was performed, a significantly better fit was obtained for (**I**), suggesting that in the solid state, the solution that has the xylyl moiety partially included in the CD cavity is more likely to be formed than solution (**II**). In our calculations, water molecules were not considered because of the lack of stoichiometric information.

After convergence, the calculated solvent-accessible areas for (**I**) allow for the presence of one water molecule inside CD cavity and of five more in the space between the CD molecules while for (**II**) there is only space for about nine water molecules outside the CD cavity. We can conclude that in solid state both models (**I** and **II**) MF-Na and  $\beta$ -CD form a monomeric complex (occupancy factor 0.9) in a herringbone-packing scheme in which CD faces are blocked by adjacent CD molecules.

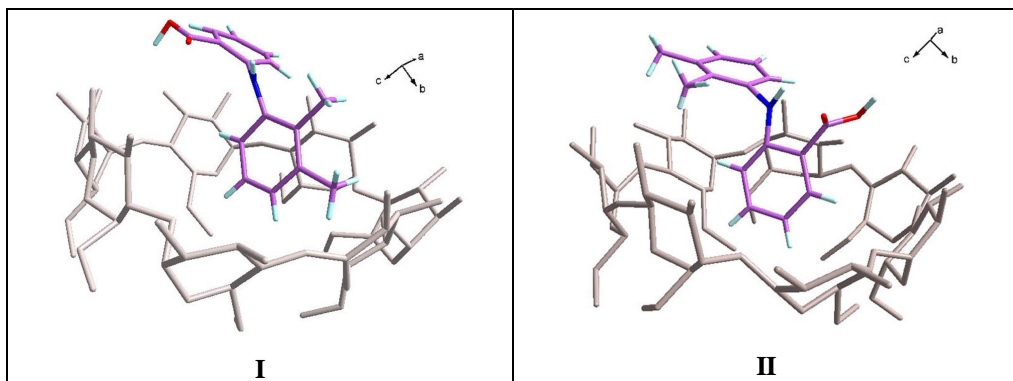


**Fig. 5.** The partial inclusion of xylyl moiety (**I**) and benzoic acid moiety (**II**) in the  $\beta$ -CD cavity

### Conclusions

The mefenamic acid sodium salt :  $\beta$ -cyclodextrin inclusion complex has been studied in aqueous solution by  $^1\text{H}$  NMR and in solid state by high-resolution synchrotron powder diffraction technique and molecular mechanics calculations. The induced chemical shifts in the NMR spectra prove the existence of a bimodal binding between MF-Na and  $\beta$ -CD and give values for the binding constants. The coexistence of the two 1:1 complexes also in solid state is confirmed by high-resolution powder diffraction data. The crystal structure that is more likely to be found in the solid state is suggested by RR agrees with the solution furnished by  $^1\text{H}$  NMR.

### Acknowledgements

The research was supported by the Romanian Ministry of Education, Research and Youth and the BIOTECH programme (Project 01-8-CPD-041).

### REFERENCES

1. T. Loftsson, D. S. Petersen, *Pharmazie*, **52**, 783 (1997).
2. J. Szejtli, "Cyclodextrin Technology", Kluwer, Academic Publishers, Dordrecht, 1988
3. T. Hladon, J. Pawlaczyk, B. Szafran, *J. of Incl. Phenom. and Macrocyclic Chemistry*, **35**, 497 (1999).
4. M. Bogdan, Mino R. Caira, Diana Bogdan, C. Morari, S. I. Fărcaș, *J. Incl. Phenom. and Macrocyclic Chem.* (in press)
5. G. Fronza, A. Mele, E. Redenti, P. Ventura, *J. Pharm. Sci.*, **81**, 1162 (1992)
6. N. Sadlej-Sosnowska, L. Kozerski, E. Bednarek, J. Sitkowski, *J. Incl. Phenom. and Macrocyclic Chem.*, **37**, 383 (2000)
7. N. Funasaki, H. Yamaguchi, S. Ishikawa, S. Neya, *Bull. Chem. Soc. Japan*, **76**, 903 (2003)
8. M. Bogdan, M.R. Caira, S.I. Fărcaș, *Supramolec. Chem.* **14** (5), 427 (2002)
9. K. Ikeda, K. Uekama, M. Otagiri, *Chem. Pharm. Bull.*, **23**(1), 201 (1975)
10. Mihaela Pop, C. Goubitz, Gh. Borodi, M. Bogdan, D.J.A. De Ridder, R. Peschar, H. Schenk, *Acta Crystallographica* **B58**, 1036 (2002)

**MASS SPECTROMETRY, CHROMATOGRAPHY, ATOMIC AND MOLECULAR SPECTROSCOPY**

**NEW CONCEPTS AND SENSING MATERIALS FOR THERMAL CONDUCTIVITY DETECTORS IN GAS CHROMATOGRAPHY**

**ADRIAN BOT, RODICA TURCU, IZABELLA PETER, VIOREL COSMA, VASILE SURDUCAN**

*National Institute for Research & Development of Isotopic and Molecular Technologies, POBox 700, 3400 – Cluj-Napoca, România.*

**ABSTRACT.** We report two new detector designs, which improve the sensitivity of TCD in order to make it suitable for trace analysis and with capillary columns:

- a half bridge "classic" thermal conductivity detector consisting by two microcells – sample measuring and carrier reference – with conducting polymers based temperature-sensitive resistors;
- a new concept of differential thermal conductivity detector based on pyroelectric effect, consisting by two cavities in a single block, each with a polyvinylidene fluoride (PVDF) pyroelectric transducer.

The thermal conductivity detector (TCD) was the first detector used in gas chromatography and, despite the general dissatisfaction with the problem of his relative low sensitivity, it still remains, after more that 50 years, one of the most commonly used detectors, even though more sensitive and specialized detectors have been developed. The advantage of the TCD lies in the detection of gases such as CS<sub>2</sub>, H<sub>2</sub>S, SO<sub>2</sub>, CO, NO, NO<sub>2</sub> and CO<sub>2</sub> in gas-solid chromatographic analysis on packed columns. Some of the advantages of TCD are its simplicity, stability, versatility and low cost; one of his best features is the ease of quantitative analysis.

The internal volume of the thermal conductivity detector is relatively large, thus the necessity to use high flow rate of column effluent (15-50 ml/min); this represents an incompatibility with the new modern opened capillary columns, wich operates at lower flow rate [1, 2].

**The thermal conductivity detector with polypyrrole ribbon filaments**

The TCD consists of a metallic block containing a cavity through which the gas flows. A heated element is positioned upon the thermal conductivity of the gas. For practical considerations a differential method is usually used that requires two cavities and two heated elements. Only carrier gas flows trough one cavity and the column effluent through the other. The two most commonly used detector transducers are resistive wires (metallic filaments) and thermistors (beads of metallic oxide). Their operation is similar except that filaments have a positive coefficient of resistance and thermistors have a negative coefficient of resistance. The choice between thermistor or filament is usually based on working temperature considerations - thermisors for ambient or sub-ambient and filaments for higher temperatures. Once the decision has been made to use filaments, the selection is based on the corrosiveness or oxidation characteristics of the materials to be analyzed. Filaments are fabricated from a variety of metals, the most common being tungsten; other materials are nickel, rhenium-tungsten and gold plated tungsten.

Based upon our experience in obtaining and manufacturing for different applications of conducting polymers, we have designed a new TCD with polypyrrole ribbon filaments used as temperature-sensitive transducers.

**Table 1.****Physical properties of some materials used as temperature-sensitive transducers**

Physical properties	Tungsten	Nickel	Thermistor	Polypyrrole
Density $10^{-3} \delta$ [kg m <sup>-3</sup> ]	19,3	8,9	3,5	1,6
Specific heat $10^{-2} c_p$ [J kg <sup>-1</sup> K <sup>-1</sup> ]	1,33	4,44	7,5	11
Thermal conductivity $\lambda$ [W m <sup>-1</sup> K <sup>-1</sup> ]	173	90	30	0,3
Electrical resistivity $10^{-8} \rho$ [ $\Omega$ m]	5,4	6,9	$\approx 60.000$	$\approx 12.500$
Temperature coefficient $\alpha$ [K <sup>-1</sup> ]	0,0048	0,0068	- 0,16	- 0,0039

The Table 1. presents some of the physical properties of films made by naphthalensulfonate doped polypyrrole [3, 4] compared with actually used materials. As we can see, the polypyrrole film has a relative low temperature coefficient, which represents a disadvantage, but the assembly of properties allow appropriate design solutions which guaranties the good performances of the detector.

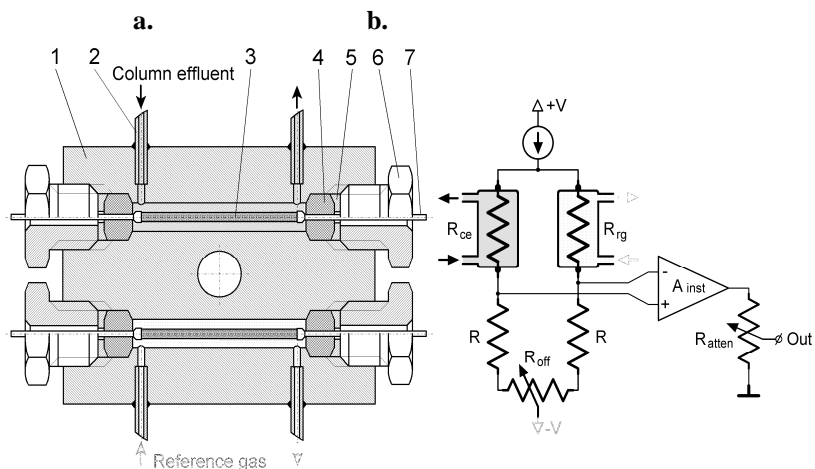


**Fig. 1.** The detection cell with polypyrrole ribbon temperature-sensitive resistors (a) and the electrical scheme of the detection circuit (b).

The Figure 1.a. presents a transverse section of the TCD block (1) with the two cavities - one for the column effluent and the other for reference gas. The temperature -sensitive elements are made by polypyrrole film - 0,015x1,4x16 mm ribbon (3); the resistance legs are made by gold plated Kovar  $\varnothing 0,6$  mm (7) and are electrical insulated from the cell block by Teflon passage rings (4), which assure also the pneumatic insulation of the cavities - the cell must be perfect gastight.

The two polypyrrole ribbon filaments (as good as possible electrically and mechanically matched) are connected into two arms of a Wheatstone Bridge (Fig.1.b.); two conventional resistors ( $R$ ) comprise the remainder of the bridge. When the thermal conductivity of the gas in one of the cavities changes as a result of the sample being eluted from the column, the temperature and the resistance of the detector element in that cavity change and an imbalance of the bridge appear. An instrumentation amplifier ( $A_{inst}$ ) amplifies the small signal. The readout can be a potentiometric recorder or a DAQ system. The matching in/out is done by the digital resistive attenuator ( $R_{atten}$ ). With the same gas passing trough both cavities the network is balanced by the offset potentiometer ( $R_{off}$ ) so the electrical output is zero.



Polypyrrole films (PPY) were obtained by electrochemical polymerization in galvanostatic conditions. Among the different types of ions used for in-situ doping polymerization of PPY we selected the following organic ions which results in stability and good mechanical properties of the polymer: p-toluensulfonate ( $TS^-$ ) and naphthalensulfonate ( $NS^-$ ). The ions concentration in the synthesis solution was varied in the range 0.01-0.1 M. The electropolymerization was carried out on stainless steel electrodes by using current densities in the range 0.11- 4 mA/cm<sup>2</sup>. The as-synthesized PPY films were peeled off from the electrode, washed and dried. Flexible freestanding PPY films with good mechanical properties and thickness in the range 10-20 $\mu$ m were obtained. The electrical conductivity of PPY films measured by the standard four contacts methods by using painted silver contacts has values in the range 37- 92 S/cm.

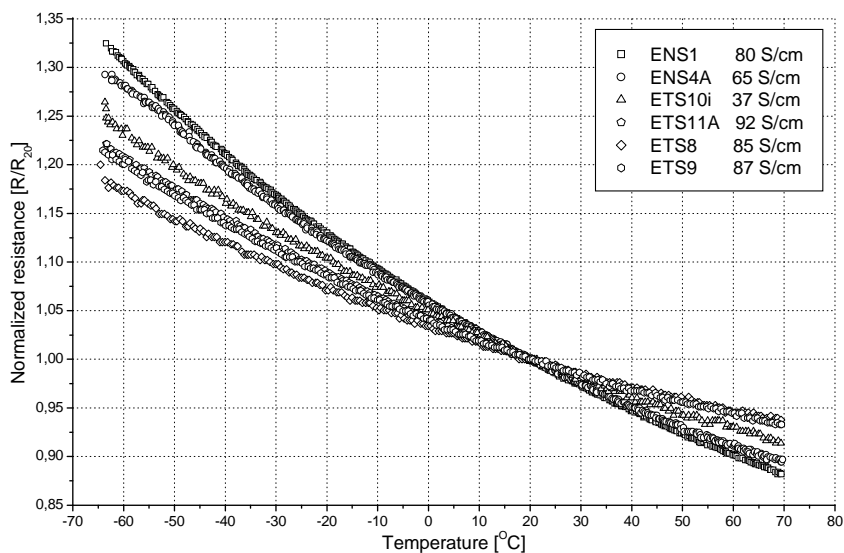


**Fig. 2.** The slope of the electrical resistance vs. temperature for some polypyrrole films.

A better stability of the electrical properties was obtained for PPY doped with  $NS^-$  ions as compared with  $TS^-$  doped ones, due to the compactness of the resulting structure for  $NS^-$  doped polymer. The temperature dependence of the electrical resistance for PPY films doped with both types of ions ( $TS^-$  and  $NS^-$ ) shows a reversible behavior in the temperature range  $-100 \div +120$  °C; at higher temperatures ( $140 < T < 250$  °C) irreversible changes of the polymers properties or the films degradation could appear.

From the figure 2 one can see that the slope of the resistance vs. temperature dependence is higher for the samples doped with  $NS^-$  ions as compared with  $TS^-$  doped ones. This means that the activation energy of the interchains charge transport process is higher for  $NS^-$  doped PPY. This fact can be attributed to the structural differences between the two doping ions ( $NS^-$  and  $TS^-$  respectively) which strongly influence the PPY morphology and consequently the interchains distances. The control of the resistance vs. temperature variation can be done mainly by two synthesis parameters: the nature and the concentration of the doping ions. In order to obtain a strongly variation of the resistance vs. temperature for PPY films, the synthesis should be performed with lower concentrations of  $NS^-$  doping ions.

Table 2.

**Estimated performances of polypyrrole ribbon filaments compared with metallic filaments and thermistor beads**

Performance	Tungsten filament Ø0,025mm	Nickel filament Ø0,033mm	Thermistor bead Ø1,2mm	Polypyrrole ribbon 0,015x1,4x 16 mm
Weight (without legs) m [µg]	3,45	2,36	2,20	0,504
Lateral surface $S_l$ [mm <sup>2</sup> ]	26,5	32,1	3,9	42
Resistance @ 25°C R [Ω]	40	25	8000	100
Resistance variation at 1mW power input $\Delta R_{1mW}/R$ [%]	0,0105	0,00649	0,0965	0,00704
Power consumed at 100°C $P_{100}$ [W]	0,89	1,16	0,48	0,41
Power losses trough legs $\Delta P_{100}$ [W]	0,18	0,12	0,08	0,02
Excellence coefficient of sensitivity $S_l \times \Delta R_{1mW}$	0,278	0,208	0,280	0,296
Excellence coefficient of power consumption $1 / (P_{100} + \Delta P_{100})$	0,93	0,78	1,78	2,32

We have presented in the Table 2 some of the estimated performances of the ribbon polypyrrole filaments compared with metallic wires and thermistor beads; we have defined two excellence coefficients – one of sensitivity and the other of power consumption – which allow a better comparison between the new design and the classic TCD's.

The new device can operate at cell temperatures between  $-100 \div +115^\circ\text{C}$  and we estimate an increase of sensitivity more than ten times compared with hot-wire filaments or thermistor beads made TCD. Moreover this detector has a few advantages related to the low temperature differential between sensitive resistors and cell block and low power consumption, which allow a major decrease of cavity volume, thus the using of lower column effluent flow rate (0,5÷2 ml/min).

The conducting polymer has a superior chemical resistance and doesn't degrade to different chemical agents – especially corrosive or oxidizing conditions.

### **The thermal conductivity detector with pyroelectric transducers**

One of the most sensitive thermoelectric transducers at this moment is the pyroelectric sensor, still it has two disadvantages. First, all the pyroelectric materials are also piezoelectric, thus a major source of electric noise due to mechanical vibrations. Second, the pyroelectric sensor is a dynamic transducer, i.e. it can measure only a change of temperature not a stable one.

Considering the distribution of samples in the column effluent a dynamic process (usually a Gaussian distribution), we have designed a thermal conductivity detector based on pyroelectric effect, consisting by two cavities in a single block (Figure 3) each with a polyvinylidene fluoride (PVDF) pyroelectric transducer (8).

The temperature of the base block of the detector (2) is controlled with a principal thermoelectric module (10); the temperature difference between the wall of the microcells (4) and the substrate of the pyroelectric sensors is done with a second thermoelectric module (3). The Peltier elements assure the best temperature stability, which is the essential condition for the measuring performances of this detector. The temperature of the base and the cell blocks are measured with the integrated semiconductor sensors (7). The heat pumped by the thermoelectric modules is evacuated by the forced air convection cooled finned heat sink (1). The assembly of the detector is thermally insulated with the neoprene foam cover (9).

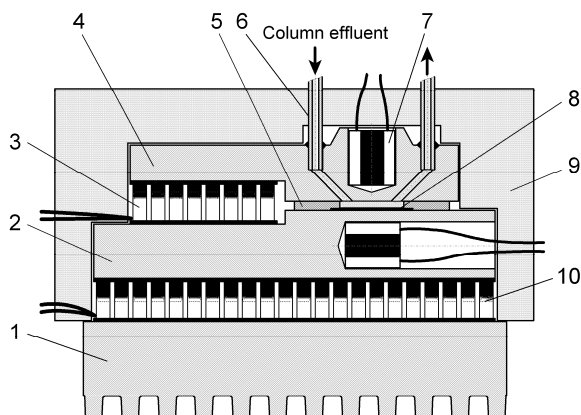


**Fig. 3.** The detection cell with polyvinylidene fluoride pyroelectric transducer (in this section on can see only one of two identical cavities with transducers)

When a component of the analyzed sample flow trough the measuring cell, the difference between its thermal conductivity and that of the carrier gas produce a variation of heat transfer, and, as a consequence, a temperature variation of the pyroelectric sensor which will generate an electrical charge (Figure 4).

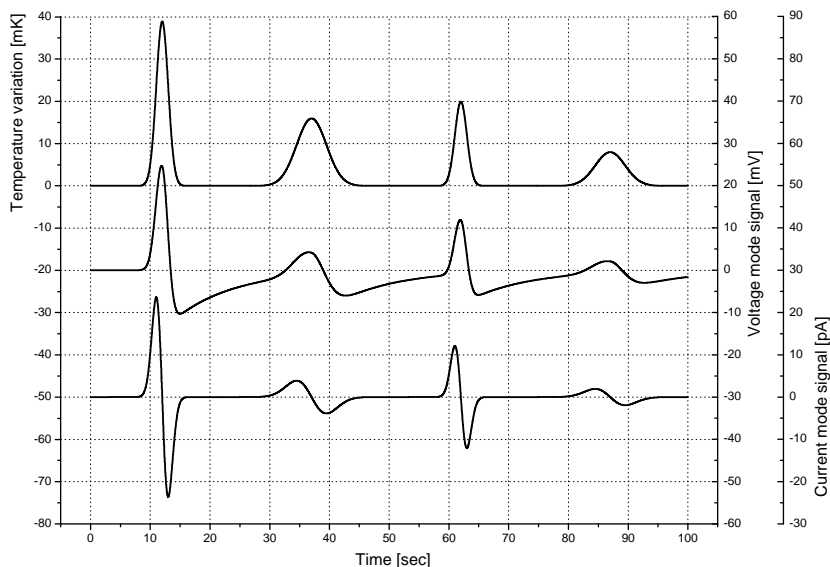


**Fig. 4.** The theoretical electrical response – voltage mode and current mode - of the pyroelectric PVDF transducer ( $25\mu\text{m}$ ,  $0,2\text{cm}^2$ ) at a chromatographic mode thermal excitation (four components with Gaussian distribution)

The resulted small current signal (tens of pA to nA) is voltage converted trough an electrometric amplifier. The reference cell serves to compensate the piezoelectric noise and the parasite signals due to the residual variation of the detector temperature and the variation of the flow rate. After the analog digital conversion, the electric signal is numerical processed and integrated in order to obtain the real chromatogram.

This *pyroelectric thermal conductivity detector* (PYTCD) can operate at two temperature ranges:  $-35 \div +70^{\circ}\text{C}$  and  $+50 \div +125^{\circ}\text{C}$ , depending upon the class of thermoelectric modules used. The PVDF sensors are gold-sheathed and the detector has a good chemical resistance. We estimate an increase of sensitivity more than hundred times compared with usual TCD's, at a temperature differential of just a few degrees. The thermal slew rate is very good and the volume of cell cavities is minimal - tens of  $\mu\text{l}$  - thus this detector can operate at very low flow rate of column effluent.

### Conclusions

To create an appropriate image of the technical performances of the new thermal conductivity detectors, we have presented in the Table 3. some of the estimated characteristics, compared with usually metallic wires filaments and thermistor beads based TCD's [5, 6, 7, 8]. On can see the improvements of the sensitivity and linearity, but mostly the major decreasing of the internal volume.

**Table 3.**

**Compared performances of the four types of thermal conductivity detectors**

Technical characteristics	Metallic wire filaments	Thermistor beads	Polypyrrole ribbon filaments	Pyroelectric transducers
Working temperature range [ $^{\circ}\text{C}$ ]	50÷450	-100÷50	-100÷115	-35÷70 50÷120
Sensitivity	$10^{-6}$	$10^{-7}$	$10^{-7}$	$10^{-8}$
Linearity	$10^{-4}$	$10^{-2}$	$10^{-4}$	$10^{-5}$
Thermal time constant [sec]	0,2	0,5	0,1	0,01
Internal volume [ml]	4	0,25	0,088	0,018
Gas flow rate [ $\text{ml min}^{-1}$ ]	15÷60	2÷8	0,5÷2	0,25÷1

All those performances make the new thermal conductivity detectors – with polypyrrole ribbon filament and with pyroelectric PVDF transducers - suitable for trace analysis and use with new modern capillary opened columns.

### REFERENCES

- David, D. J., *Gas Chromatographic Detectors*, John Wiley & Sons Inc., New York, 1974, p. 14-41;
- Grob, R. L., (editor), *Modern Practice of Gas Chromatography*, John Wiley & Sons Inc., New York, 1995, p. 281-291;
- Coldea, A., Turcu, R., Bot, A., Brie, M., *The Temperature Dependence of the Electrical Conductivity of polypyrrole Films Doped with Different Counterions*, Romanian Reports in Physics, Vol.52, Nos. 1-2, 2000, p. 127-138;
- Turcu, R., Brie, M., Frandas, A., Pruneanu, S., *Optical Studies on Free-standing Polypyrrole Films by the Photopyroelectric Method*, Appl. Phys., B62, 1996, p 499-502;
- Lechner-Fish, T. J., Yang, X., *A Microvolume Thermal Conductivity Detector for Online Gas Analysis*, Sensors Application Buletin 042, Daniel Industries Inc. USA, 2000;
- Yu, C., *Micro-Machined Thermo-Conductivity Detector*, U.S. Patent 6,502,983 B2, USA, 2003;
- \* \* \* *Thermal Conductivity Elements for Gas Analysis, TCD Filaments and Thermistor Beads Data Sheets*, GOW-MAC Instrument Company USA, 2002;
- \* \* \* *Finnigan Thermal Conductivity Detector*, Product Bulletin No. 802, CE Instruments – ThermoQuest Corporation USA, 1997.

## POTPOURRI OF ION OPTICS

DAMASCHIN IOANOVICIU

*National Institute for Research - Development of Isotopic and Molecular Technologies Cluj-Napoca ROMANIA*

**ABSTRACT.** This overview deals with some special cases of angular, double and time ion focusing analyzers. These include inhomogeneous magnetic field sectors perfectly focusing wide ion beams, Wien filters with inhomogeneous fields operated independently or in double focusing configurations, analyzers with high mass dispersion using electric prisms and oblique incidence magnets. Flight time analyzers of various kinds are also reviewed as classical reflectrons with homogeneous fields but accounting for oblique incidence, cylindrical reflectrons, perfect velocity focusing in time by quadrupole trap configuration source combined with a field free space. Quadrupole filters and traps are just mentioned for some calculation procedures. The use of ion optics to describe metastable peak shapes and peak tails in mass spectra closes the review.

### Introduction

There are some ion optical solutions which were not applied to large scale or which, from various reasons, are still in a development stage, or are waiting for some technological refinement to become fully operational. Most of the ion optical solutions from this potpourri belong to these categories.

### Magnetic sectors focusing wide ion beams

The inhomogeneous magnetic fields decreasing with the radius with an index  $n=1$  can focus perfectly wide ion beams if the sector limits are cut by circular contours. This happens when the ion main path is circular [1] and also when the main path is a logarithmic spiral [2],[3].

The logarithmic spiral main path introduces an additional parameter helping to obtain better mass dispersion and then resolution. The main path written in polar coordinates has the form:  $r = r_0 e^{\alpha\theta}$  where  $\alpha = \sqrt{2mU/(eB_1^2 r_1^2)} - 1$  where  $m$  is the ion mass,  $U$  its energy,  $e$  its charge,

$B_1$  the magnetic field induction at  $r_1$  from the origin. The resolution of such a sector can be approximated with the formula:

$$\mathfrak{R} = l_2(e^{\alpha\theta} - 1)/(2\alpha s),$$

where  $s$  is the source slit width.

The “wedge” magnetic field, created by two plane pole faces, by its additional parameter  $K$  offers the possibility to better focus with respect to the homogeneous magnetic field. The field intensity changes with the distance  $r$ , to the axis  $z$ , the virtual intersection of the two pole face planes:  $B = B_1 r_1/r$ . The main path is given in a parametric form:  $r = r_1 e^{K \cos \psi}$ ;  $z = -r_1 K \int e^{K \cos \psi} \cos \psi d\psi$ . Here  $K = (\sqrt{2mU/e})/(B_1 r_1)$ ,  $\psi$  the angle between the ion velocity and the  $z$  axis.

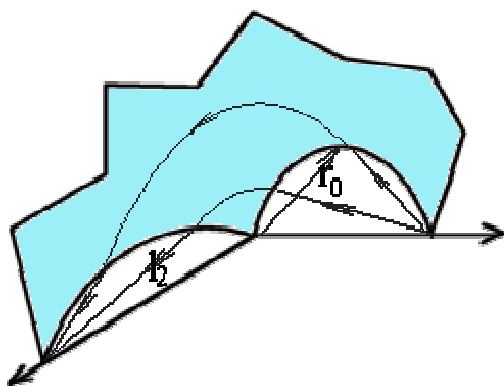


**Fig. 1.** Perfect angular focusing in an  $r^{-1}$  magnetic analyzer

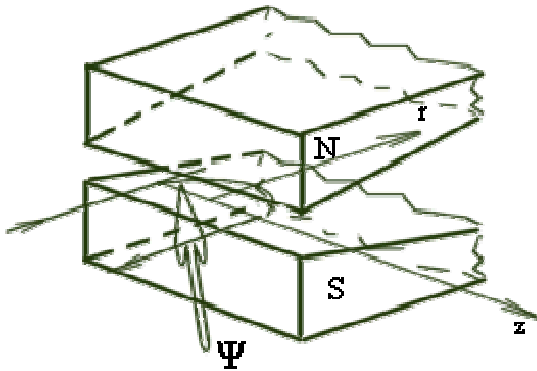


Fig. 2. "Wedge" field 180° deflecting analyzer

A complete matrix description of this kind of magnetic sectors, including the fringing effects was detailed in ref. 4. The outstanding focusing properties of the 180° deflecting sectors, known from ref. 5 were incorporated in the instrument of ref. 6. It attained a resolution of 1340 on  $m=2u$  peak, and an ion current of  $9 \times 10^{-12}A$ . It is worth to mention the outstanding properties of this geometry: radial angular focusing of second order (possibly of third order after some sources), stigmatic focusing with both radial and axial unit magnification. This layout is suitable for low mass isotopic analyzers, especially for deuterium as the sensitivity is extremely

high. Such a magnetic sector was proposed to be used in a proposal for time resolved ion momentum spectrometry [7], having obvious advantages compared with homogeneous magnetic sectors initially used with this purpose [8]. The limited use of inhomogeneous magnetic fields in mass spectrometry originates from the saturation effects impeding their use at high masses in instruments at convenient costs.

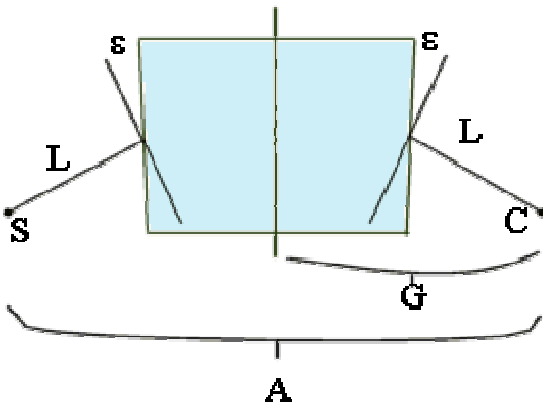


Fig. 3. Symbols for two symmetric halves of a homogeneous, oblique incidence, magnetic field analyzer

Homogeneous magnetic sectors seem to have no more focusing mysteries at the present time. However some doubt persists concerning fringing field accounting calculations by using fringing field integrals [9]. The second order radial angular aberration coefficient of a symmetric, oblique incidence, magnetic sector can be obtained in two ways: a) by multiplying the transfer matrices of the analyzer parts located between the collector and the analyzer's middle, and expressing this by the matrix elements of this second half  $A_{\alpha\alpha s}$  or b) by multiplying all the transfer matrices from the collector to

the ion source  $A_{\alpha\alpha}$ .  $A_{\alpha\alpha s} \cdot A_{\alpha\alpha s} = 2G_{xx}G_{\alpha}^2$  Obviously, the difference  $\Delta = A_{\alpha\alpha s} - A_{\alpha\alpha}$  should vanish. Instead  $\Delta = Lt(1+Lt/2)v - (1+Lt)v/2$  with  $t = \tan \epsilon$ ,  $v = 2I_1 t^2/c^2$ ,  $\epsilon$  the incidence (emergence) angle,  $I_1$  the fringing field integral.

### Electrostatic and crossed field mass analyzers

Not only magnetic field sectors can handle curved axis beams. The spiral cylinder plate condensers can focus beams curved on axes of same shape [10].

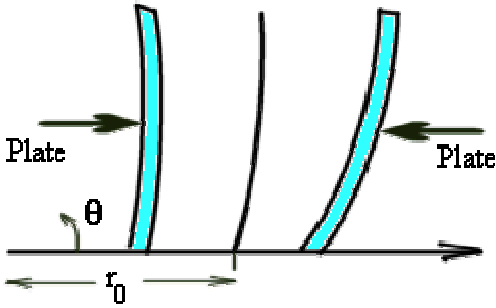


Fig. 4. Spirally shaped electrode condenser

The second order focusing theory has been developed in ref. 11. The main path inside this kind of deflector is expressed by:  $r = r_0 e^{\mu\theta}$  with  $\mu = \sqrt{2U/(eE_0 r_0)} - 1$  with  $E_0$  the  $r$  component of the electric field at  $r_0$ .

The Wien filter, the oldest particle analyzer, invented before 1897 [12], was resurrected by studies from ref 13 and the theory developed, including fringing field effects in ref. 14. Experimentally a Wien filter attained a resolution of 4100 on the  $C_2H_4^+ - N_2^+$  doublet, at a current of  $1.28 \cdot 10^{-16} A$  [15]

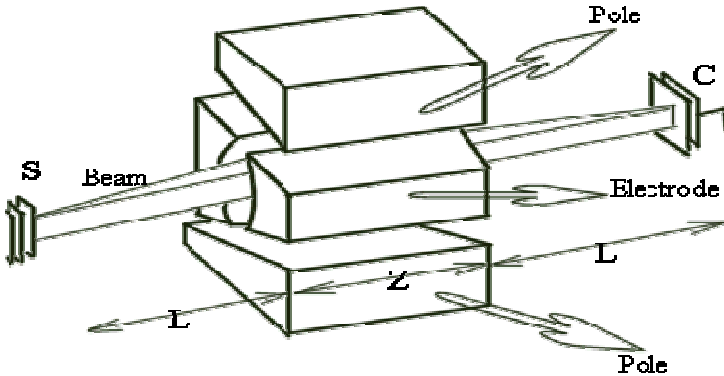


Fig. 5. Inhomogeneous field Wien filter

The length of the field free spaces, in front of and after the filter have the length  $L$  (symmetric case):  $L = 1/[Lk \tan(kZ/2)]$  with  $k = \sqrt{1/\rho(1/r_c - 1/r_e + 1/\rho)}$ ,  $\rho = \sqrt{2mU/(eB_0)}$ ,  $Z$  the filter effective length,  $r_c$  and  $r_m$  the axial radius of curvature of the electric potential surface and of the magnetic force line at the ion main path. The resolution can be estimated with the simple formula:  $\mathfrak{R} = 1/(k^2 \rho s)$ . The basic data of the Wien filter mass spectrometer were:  $L = 41$  cm,  $r_m = 10$  cm and  $Z = 30$  cm. The greatest, of about 4 m length, was working at Michigan State University. The study of Wien filter was extended to electric and magnetic crossed field sectors, including fringing field effects in ref. 16. By this last we stepped in the area of double focusing mass spectrometry. The Wien filter can be associated with an electrostatic condenser to ensure double, angular radial and energy focusing simultaneously as theory shows [17] and as it was incorporated in real world instruments [18], [19].

An estimative formula for the resolution is:  $\mathfrak{R} = r_0/(2 - c)(1/M_{es} - 1)/s$ . The used symbols are:  $c = r_e/r_0$ ,  $M_{es}$  the magnification of the electric sector. The basic parameters of the spectrometer described in ref. 18 are:  $r_0 = 20$  cm,  $\phi_e = 31.8^\circ$ ,  $l_1 = 40.2$  cm  $\mathfrak{R} = 5600$  on the  $C_2H_4 - N_2$  doublet. Double focusing can be obtained also by using part of the gap of a magnetic sector to create a Wien filter there.

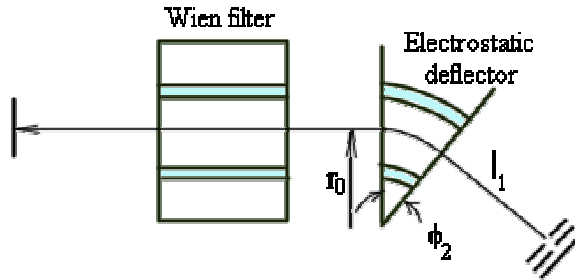


Fig. 6. Wien filter – electrostatic condenser double focussing geometry

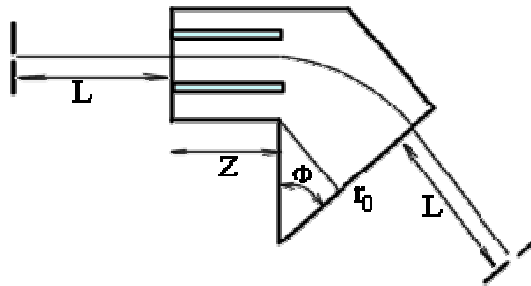


Fig. 7. Compact Wien filter – homogeneous magnetic field double focussing mass spectrometer

For homogeneous fields the theory was developed in ref. 20. The resolution may be calculated with the following formula:  $\mathfrak{R} = r_0 / (s + r_0 \delta + A_{\alpha\alpha} \alpha^2 + 2A_{\alpha\delta} \alpha \delta + \dots)$ .  $r_0$  is the main path radius inside the magnetic field,  $A_{ij}$  are aberration coefficients. An instrument which keeps half Dempster's spectrometer geometry for magnetic deflection has the theoretical resolution:  $\mathfrak{R} = 1 / (s/r_0 + \alpha^2 + 4\alpha\delta + 3\delta^2/4)$ . Such an instrument was operated at resolution 170, for 56 mm main path radius, ion current of  $1.6 \times 10^{-8}$  A, in perfect agreement with the instrument and beam parameters [21]. Partial pressure gauges were proposed based on the theory developed for Wien filters created and combined with wedge field sectors to create high sensitivity stigmatic, double focusing (triple focusing) geometries [22]. Compact oversimplified geometries including Wien filters and magnetic sectors in the same gap were analyzed from the aberration point of view [23].

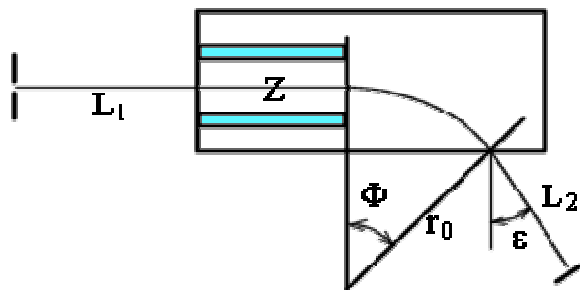


Fig. 8. Oversimplified Wien filter – homogeneous magnet double focussing geometry



An attempt to create double focussing mass spectrometers of high resolution by increasing mass dispersion was made by using Kelman's electric prisms [24]. The theory developed in ref. 25 was incorporated in a mass spectrometer attaining a resolution of 11000 with a remarkably high sensitivity [26].

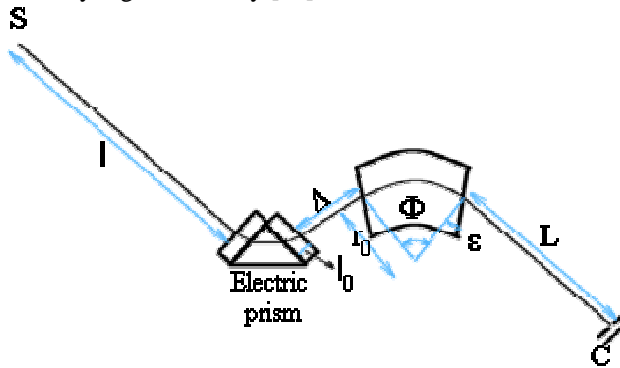


Fig. 9. High mass dispersion double focussing mass spectrometer including an electric prism

The field free spaces, one of them including also the electric prism electrodes can be calculated with the formula:  $L/r_0 = (t-M)/(1-t^2)$  and to estimate the resolution we can use the formula:  $\mathfrak{R} = r_0(1 - M)/[2s(1-t)]$  The parameters of the constructed instrument were:  $\epsilon = 31.73^\circ$ ,  $\phi = 90^\circ$ , electric deflection in the prism  $54.3^\circ$ ,  $M = -0.287$ , mass dispersion  $D_\gamma = 42.91$  cm for  $r_0 = 25$  cm.

**A word on quadrupoles**

Dynamic mass analyzers as quadrupoles and quadrupole traps represented an occasion for new theoretical approaches: a direct calculation method for ion trajectories using only the initial conditions for the filter [27] and a peak shape/resolution calculation for the trap [28].

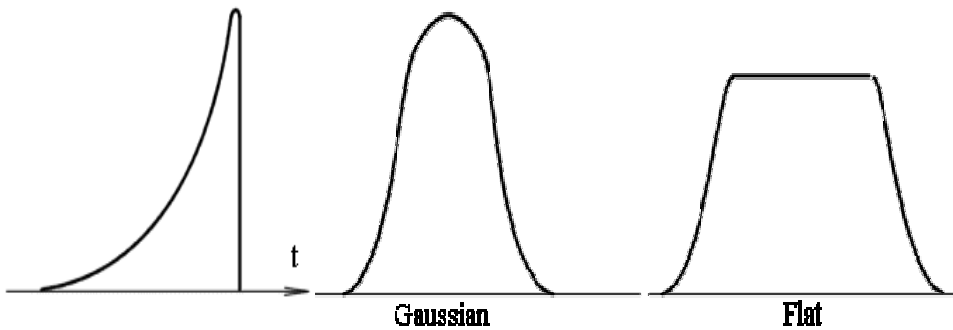


Fig. 10. Peak shape of axially ejected ions from a quadrupole trap

Fig. 11. Gaussian metastable peak in a double focussing mass spectrometer

Fig. 12. Flat topped peak in a single focussing mass spectrometer

**More about time-of-flight mass analyzers**

Time-of-flight mass spectrometry is not only a fashion but, among many others, it allowed Tanaka to accede to the Chemistry Nobel Prize of 2002. Much effort was spent to improve this branch of mass spectrometric instrumentation and the ion optical solutions with this purpose were reviewed successively in 1994 [29], 1995 [30], 1998 [31] and 2001 [32].

theory of already routinely used homogeneous electric field mirror mass spectrometers with one or two stages was refined to account even for third order contributions and the detector position effect in resolution formulas [33] Matrix formalism was adopted to describe the single and double stage mirror time-of-flight mass spectrometer performance, having oblique packet incidence [34], [35]. This method was already used to describe flight time through various other ion optical elements as electrostatic deflectors, magnetic sectors, electric and magnetic quadrupoles in a second order approximation [36]. Such combined transversal-longitudinal (flight time) transfer matrices were reviewed also in ref. 37.

The resolution and mass scale modification in post source focusing applied to linear time-of-flight mass spectrometers was analyzed in ref. 38.

Initial velocity ion focusing in time is mandatory for ions resulted from matrix assisted laser desorption/ionization. The delayed ion extraction from the source used at the present time could be replaced by a perfect velocity focusing procedure. The ion source shaped as a Paul trap is fed by high voltage pulses correlated with the ionizing laser pulses [39], [40]. This configuration ensures perfect velocity focusing for ions created on the end cap tip, after a flight over a field free space of appropriate length. Resolutions estimated to about 50,000 could be obtained by this procedure for high mass ions [41].

### Metastable peak shapes

Ion optics is also a way to describe the shape of the metastable peaks resulted with internal energy release. Metastable peaks of gaussian, flat topped and dish topped shape result from the energy released and the instrumental parameters in single and double focusing static mass spectrometers [41], [42].

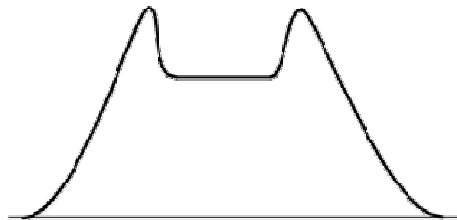


**Fig. 13.** Dish topped metastable peak

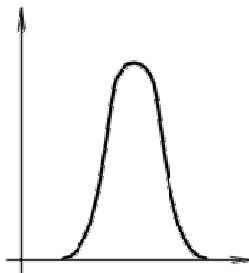


**Fig. 14.** Gaussian metastable peak in a TOF mass spectrometer.

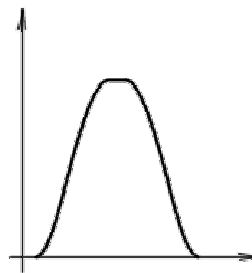


**Fig. 15.** TOF mass spectrometer detected metastable peak with a small flat top.

A sample of the formulas describing the metastable peak shape is given next:  $i_a = I_0 \gamma l / 2 [ 2\sigma - (\sigma+v)\ln(\sigma+v) - (\sigma-v)\ln(\sigma-v) ]$ , the symbols used being  $\sigma = \Delta / (\mu D_x l)$ ,  $v = v / (\mu D_x l)$   $\mu = \sqrt{m_3 T / (m_2 U)}$  for the disintegration  $m_1^+ \Rightarrow m_2^+ + m_3$ .  $i_a$  is the ion current detected for the metastable peak,  $I_0$  is the parent ion current,  $l$  the length of the path part from that the metastable ions are collected,  $\Delta$  half the detector slit width,  $T$  is the energy released during the process,  $v$  the coordinate of the beam axis on the collector. In time-of-flight mass spectrometers with single stage reflectrons the metastable peak shapes can be related also to the irrespective geometric parameters and to the released energy [43]. Two specific metastable peak shapes for reflectrons are given in Fig. 14 and Fig. 15.

**Peak tails in mass spectra**

Of major importance for isotopic analysis are the peak tails produced by elastic scattering of ions on residual gas molecules. An ion optical procedure first used by Menat [44] to calculate such tails in electromagnetic separators was generalised for static sectors and other ion optical elements operated independently or in tandem [45], [46]. The general form of the tail current  $i^+$  depends of the scattering cross section  $\sigma_o$ , on the current which generates the tail  $I^+$ , on the residual gas molecules per unit volume  $n_r$ , on the slit width  $\Delta$ , and on the position of the slit with respect to the main path of the scattered beam, measured in relative mass difference  $\Delta m/m$ :  $i^+ = \sigma_o I^+ n_r \Delta (m/\Delta m)^{1.69} C$  For the Mattauch-Herzog double focusing mass spectrometers, the coefficient  $C$  has the explicit form:  $C = 7.16(1.11 + \Delta f/r_{0e} + 0.6r_{0e}/r_{0m})$  Besides the main path radii of the electric and magnetic deflection, it depends on the distance between the deflectors  $\Delta f$ . For the Nier-Johnson geometry, another very popular double focusing mass spectrometer configuration  $C = 19.6$ .

Obviously this kind of interactions blurs the ion packet contour in time-of-flight mass spectrometers. These effects were estimated in ref. 47. The shapes of tails in linear and reflectron time-of-flight mass spectrometers are given in Fig. 16.

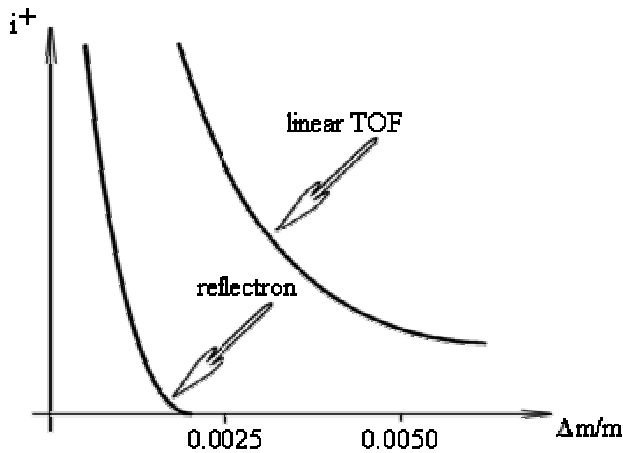


Fig. 16. Peak tail shapes in linear and reflectron time-of-flight mass spectrometers

### Conclusion

Ion optics has an undeniable role to play in the future development of mass spectrometry. As in the field of engineering, from a lot of patents only some arrive to be applied and even fewer become of general notoriety. So happens to ion optical solutions too.

### REFERENCES

1. A. F. Malov, V. A. Suzdalev, E. Fedoseev, Zh. Tekhn. Fiz. 35, 914 (1965)
2. D. Ioanoviciu, Int. J. Mass Spectrom. Ion Phys. 5, 29 (1970)
3. D. Ioanoviciu, Int. J. Mass Spectrom. Ion Phys. 11, 185 (1973)
4. D. Ioanoviciu, Int. J. Mass Spectrom. Ion Phys. 18, 289 (1975)
5. J. O'Connel, Rev. Sci. Instrum. 32, 1314 (1961)
6. D. Ioanoviciu, V. Mercea, C. Cuna, P. Ardelean, J. Sci. Instrum. 6, 129 (1973)
7. D. Ioanoviciu, M. I. Yavor, C. Cuna, B. Erdelyi, Rapid Commun. Mass Spectrom. 9, 1238 (1995)
8. C. G. Enke, J. T. Stults, J. F. Holland, J. D. Pinkston, J. Allison, J. T. Watson, Int. J. Mass Spectrom. Ion Processes 46, 229 (1983)
9. D. Ioanoviciu, Adv. Mass Spectrom. 10, 857 (1986), J. F. J. Todd editor J. Wiley Sons
10. V. G. Kovalenko, B. V. Polenov, Zhurn. Tekhn. Fiz. 44, 878 (1974)
11. D. Ioanoviciu, Int. J. Mass Spectrom. Ion Phys. 41, 229 (1982)
12. W. Wien, Verhandl. Deut. Phys. Ges. 16, 165 (1897)
13. L. Wahlen, Nucl. Instrum. Methods 38, 133 (1985)
14. D. Ioanoviciu, Int. J. Mass Spectrom. Ion Phys. 169 (1973)
15. D. Ioanoviciu, C. Cuna, Int. J. Mass Spectrom. Ion Phys. 25, 117 (1977)
16. D. Ioanoviciu, Int. J. Mass Spectrom. Ion Phys. 15, 89 (1974)
17. D. Ioanoviciu, C. Cuna, Int. J. Mass Spectrom. Ion Phys. 15, 79 (1974)
18. S. Taya, K. Tokiguchi, I. Kadnomata, H. Matsuda, Nucl. Instrum. Methods 150, 165 (1978)
19. C. Cuna, D. Ioanoviciu, Int. J. Mass Spectrom. Ion Processes 54, 333 (1983)
20. D. Ioanoviciu, C. Cuna Vacuum 24, 245 (1974)
21. D. Ioanoviciu, C. Cuna, Rapid Commun. Mass Spectrom. 9, 512 (1995)
22. D. Ioanoviciu, C. Cuna, A. Pamula, Cl. Fatu, D. Vonica, Vacuum 43, 559 (1992)
23. D. Ioanoviciu, Nucl. Instrum. Methods Phys. Res. A363, 406 (1995)
24. V. M. Kelman, I. V. Rodnikova, M. I. Uteev, P. A. Finoghenov, Zhurn. Tekhn. Fiz. 40, 1467 (1970)
25. D. Ioanoviciu, Adv. Mass Spectrom. 10, 899 (1986) J. F. J. Todd ed. J. Wiley Sons
26. D. Ioanoviciu, C. Cuna, Int. J. Mass Spectrom. Ion Processes 74, 129 (1986)
27. D. Ioanoviciu, Rapid Commun. Mass Spectrom. 11, 1383 (1997)
28. D. Ioanoviciu, A. Ioanoviciu, Nucl. Instrum. Methods Phys. Res. A427, 161 (1999)

29. D. Ioanoviciu, *Int. J. Mass Spectrom. Ion Processes* 131,43 (1994)
30. D. Ioanoviciu, *Rapid Commun. Mass Spectrom.* 9, 985 (1995)
31. D. Ioanoviciu, *Romanian J. Physics* 43, 421 (1998)
32. D. Ioanoviciu, *Int. J. Mass Spectrom.* 206, 211 (2001)
33. D. Ioanoviciu, *Rapid Commun. Mass Spectrom.* 7, 1095 (1993)
34. D. Ioanoviciu, G. E. Yefchak, C. G. Enke, *Int. J. Mass Spectrom. Ion Processes* 94, 281 (1989)
35. D. Ioanoviciu, C. Cuna, *J. Mass Spectrom.* In press
36. T. Matsuo, H. Matsuda, D. Ioanoviciu, H. Wollnik, V. Rabbel, *Int. J. Mass Spectrom. Ion Phys.* 42, 157 (1982)
37. D. Ioanoviciu, *Adv. Electronics Electron. Phys.* 73, ed. P. W. Hawkes, Acad Press 1989, pp.1
38. D. Ioanoviciu, *J. Amer. Soc. Mass Spectrom.* 6, 889 (1995)
39. D. Ioanoviciu, *Nucl. Instrum. Methods Phys. Res. A*427, 157 (1999)
40. D. Ioanoviciu, *Rapid. Commun. Mass Spectrom.* 12, 1925 (1998)
41. D. Ioanoviciu, C. Cuna, V. Cosma, *Proc. 27<sup>th</sup> Ann. ARA Congress, Polyt. Int. Press* 2003, pp. 1343
42. D. Ioanoviciu, *Int. J. Mass Spectrom. Ion Phys.* 23, 315 (1977)
43. D. Ioanoviciu, C. Cuna, V. Mercea, *Int. J. Mass Spectrom. Ion Phys.*, 23, 307 (1977)
44. D. Ioanoviciu, G. E. Yefchak, C. G. Enke, *Int. J. Mass Spectrom. Ion Processes* 104, 83 (1991)
45. M. Menat, *Canad. J. Phys.* 42, 164 (1964)
46. D. Ioanoviciu, *Canad. J. Phys.* 48, 1735 (1970)
47. D. Ioanoviciu, *Int. J. Mass Spectrom. Ion Phys.* 12, 115 (1973)
48. D. Ioanoviciu, *Nucl. Instrum. Methods Phys. Res. A*363, 454 (1995)

## SURFACE-ENHANCED RAMAN SPECTROSCOPY AND THEORETICAL INVESTIGATIONS OF DICLOFENAC SODIUM

**T. ILIESCU**,<sup>1</sup> **M. BOLBOACA**,<sup>1</sup> **S. AȘTILEAN**,<sup>1</sup> **D. MANIU**,<sup>1</sup> **W. KIEFER**<sup>2</sup>

<sup>1</sup>Physics Department, Babes-Bolyai University, 3400 Cluj-Napoca, Romania

<sup>2</sup>Institut für Physikalische Chemie, Universität Würzburg, D-97074 Würzburg, Germany

**ABSTRACT.** Raman and surface-enhanced Raman (SER) spectroscopies have been applied to the vibrational characterisation of diclofenac sodium (DCF-Na). Theoretical calculations (DFT) of two DCF-Na conformers have been performed to find the optimised structure and computed vibrational wavenumbers of the most stable one. SER spectra in silver colloid at different pH values have been also recorded and analysed. Good SER spectra have been obtained in acidic and neutral environments, proving the chemisorption of the DCF-Na molecule on the silver surface. In the investigated pH range the carboxylate anion has been bonded to the silver surface through the lone pair oxygen electrons. The phenyl rings orientation with respect to the silver surface has been changed on passing from acidic to neutral pH from a tilted close to flat to a more perpendicular one.

### Introduction

Diclofenac sodium, is a sodium salt of an aminophenyl acetic acid and is a well-known representative of nonsteroidal anti-inflammatory drugs (NSAIDs) [1,2]. DCF-Na has limited water solubility, especially in gastric juice and is unstable in aqueous solution [3]. This limited solubility in acidic medium engenders problems in its oral bioavailability and it is a drawback in terms of its formulation in controlled release devices. A possibility to overcome these limitations is the complexation of the DCF-Na with  $\beta$ -cyclodextrin that leads to the formation of a 1:1 guest-host complex [3]. Knowledge of the structure of DCF-Na molecule is essential to understand its pharmaceutical action. Many spectroscopic and non-spectroscopic techniques were used to study this molecular species. The FT-IR spectrum of DCF-Na was obtained and analysed by Szejtli [4] and Kovala-Demertzi et al [5]. Other methods like calorimetry [6-8], UV spectrophotometry [9], gas [10,11] and liquid chromatography [12,13] and NMR spectroscopy [14] were used to study DCF-Na molecular structure. From the literature is not completely established, which part of the DCF-Na molecule is included in the  $\beta$ -cyclodextrin, when a 1:1 guest-host complex is formed. Furthermore, the possibility to obtain 2:1 guest-host complex, which imply the inclusion of different parts of the DCF-Na molecule into two  $\beta$ -cyclodextrin entities, was also indicated [15]. We suppose that the adsorption of the DCF-Na- $\beta$ -cyclodextrin complex on a metallic surface can contribute to the elucidation of these problems. But first of all it is necessary to obtain more information about the possibility of adsorption of the free DCF-Na molecule on the silver surface.

In the present work a relatively detailed experimental and theoretical study of the DCF-Na molecule has been performed. The first part of the study presents the investigation of the DCF-Na molecule from an analytical (Raman spectroscopy) and theoretical (DFT calculations) point of view. Surface-enhanced Raman (SER) spectra of DCF-Na in silver sol at different pH values are also recorded and analysed in order to elucidate the adsorption behaviour of the molecules on colloidal silver particles.

## Experimental Section

**Sample and Instrumentation.** Diclofenac sodium was purchased from TERAPIA S.A. (Cluj-Napoca) and all other chemicals involved in substrate and sample preparation were purchased from commercial sources (Aldrich) as analytical pure reagents. The FT-Raman spectrum of the polycrystalline sample was recorded with a Bruker IFS 120HR spectrometer equipped with a FRA 106 Raman module. Radiation of 1064 nm from a Nd:YAG laser was employed for excitation. The spectral resolution was  $2\text{ cm}^{-1}$ .

The SER spectra were recorded with a Spex 1404 double monochromator equipped with a charged coupled device camera system (Photometrics Model 9000). The 514.5 nm wavelength of a Spectra Physics argon ion laser was used for excitation. The spectra were collected in the back-scattering geometry with a spectral resolution of  $2\text{ cm}^{-1}$ . A sodium citrate silver colloid, prepared according to the literature [16] was employed as SERS substrate. Small amounts of diclofenac sodium  $10^{-1}\text{ M}$  ethanol solution were added to 3 ml silver colloid. NaCl solution ( $10^{-2}\text{ M}$ ) was also added (10:1) for producing a stabilization of the colloidal dispersion and an activation of the silver colloid that yields to a considerable enhancement of the SER spectra. The final concentration was approximately  $6.8 \cdot 10^{-3}\text{ M}$ . NaOH and HCl were used to obtain the desired pH values.

**Computational Details.** Theoretical calculations of the structure and vibrational wavenumbers of the investigated compound were performed using the Gaussian 98 program package [17] Density functional theory (DFT) calculations were carried out with Becke's 1988 exchange functional [18] and the Perdew-Wang 91 gradient corrected correlation functional (BPW91) [19] and Becke's three-parameter hybrid method using the Lee-Yang-Parr correlation functional (B3LYP) [20]. The 6-31G\* Pople split-valence polarization basis set was used in the geometry optimization and normal modes calculations at all theoretical levels. At the optimized structure of the examined species no imaginary frequency modes were obtained, proving that a local minimum on the potential energy surface was found.

## Results and Discussion

**Theoretical Calculations.** Due to the flexibility of the acetate group the DCF-Na molecule allows for several conformers. DFT calculations have been performed at the RHF/6-31G\*, BPW91/6-31G\* and B3LYP/6-31G\* levels of theory on two of the most probable conformers in order to find out the most stable one. The optimized geometries of these two conformers at the BPW91/6-31G\* theoretical level are illustrated in Fig. 1.

Analytical harmonic vibrational modes have been calculated in order to ensure that the optimized structures correspond to minima on the potential energy surface. The calculations performed on both isomers at all theoretical levels demonstrate, in agreement with the experimental data obtained from X-ray diffraction experiments on tetrahydrate diclofenac sodium crystals [21] that the conformer 2 is energetically more stable by an energy difference of 17.997 kJ/mol (RHF), 29.946 kJ/mol (BPW91) and 26.596 kJ/mol (B3LYP), respectively.

The FT-Raman spectrum of DCF-Na in the range from 3200 to  $100\text{ cm}^{-1}$  with the calculated unscaled Raman intensities are illustrated in Fig. 2a.

The observed Raman bands with their vibrational assignment accomplished with the help of theoretical calculations are presented in Table 1.

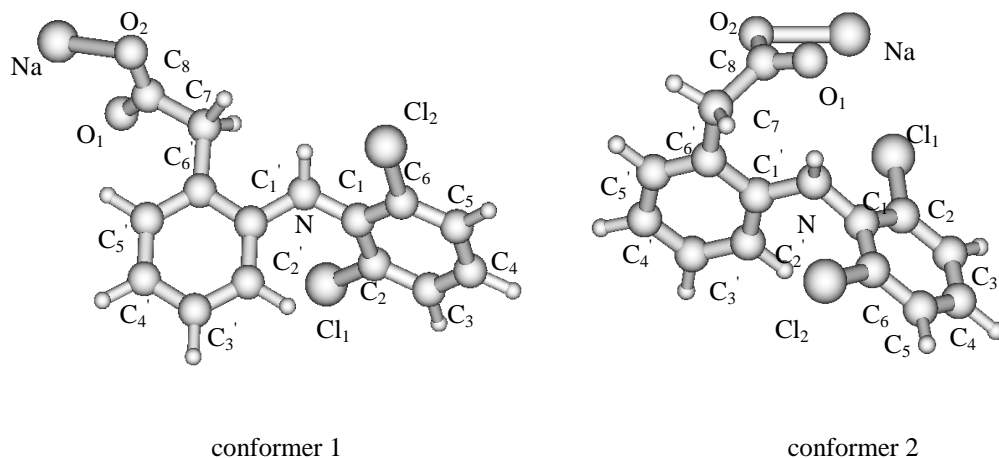


**Fig. 1.** Optimized geometries of two conformational isomers of the diclofenac sodium molecule obtained at the BPW91/6-31G\* level of theory.

The development of density functional theory (DFT) has provided an alternative means of including electron correlation in the study of the vibrational wavenumbers of moderately large molecules [22,23]. The DFT hybrid B3LYP functional tends also to overestimate the fundamental modes in comparison to the BPW91 method, therefore scaling factors have to be used for obtaining a considerable better agreement with the experimental data [24]. Thus, according to the work of Rauhut and Pulay [25] a scaling factor of 0.963 has been uniformly applied to the B3LYP calculated wavenumber values from Table 1.

The observed disagreement between the theory and experiment could be a consequence of the anharmonicity and of the general tendency of the quantum chemical methods to overestimate the force constants at the exact equilibrium geometry [25]. Nevertheless, as one can see from Table 1 the theoretical calculations reproduce well the experimental data and allow the assignment of the vibrational modes.

As one can see from Fig. 2a the dominant bands of the FT-Raman spectrum of polycrystalline DCF-Na appear at 1605, 1585 and 1578  $\text{cm}^{-1}$  and are given by phenyl ring stretching vibrations and asymmetric OCO stretching mode, respectively. The ring breathing vibrations determine also intense bands at 1073 and 1046  $\text{cm}^{-1}$  (see Table 1). The in-plane deformation vibrations of the CH groups of both rings give rise to Raman bands at 1160 and 1150  $\text{cm}^{-1}$  (bending vibrations) and 1281, 1250 and 1235  $\text{cm}^{-1}$  (rocking vibrations). The medium intense Raman bands at 517 and 533  $\text{cm}^{-1}$  are determined by the out-of-plane deformation vibrations of the phenyl rings. The bands attributed to the out-of-plane deformation vibrations of the CH groups occur in the 840-950  $\text{cm}^{-1}$  spectral range of the Raman spectrum. In the high wavenumber region between 3069 and 2890  $\text{cm}^{-1}$  six bands assigned to the NH and CH stretching mode are observed. Weak bands at 1398 and 637  $\text{cm}^{-1}$  assigned to the symmetric stretching and in-plane deformation vibration of the carboxylate group can be also seen in the Raman spectrum. The missing of the carbonyl stretching band in the 1800-1600  $\text{cm}^{-1}$  spectral range confirms the presence of the carboxylate group in the DCF-Na specie in solid state.



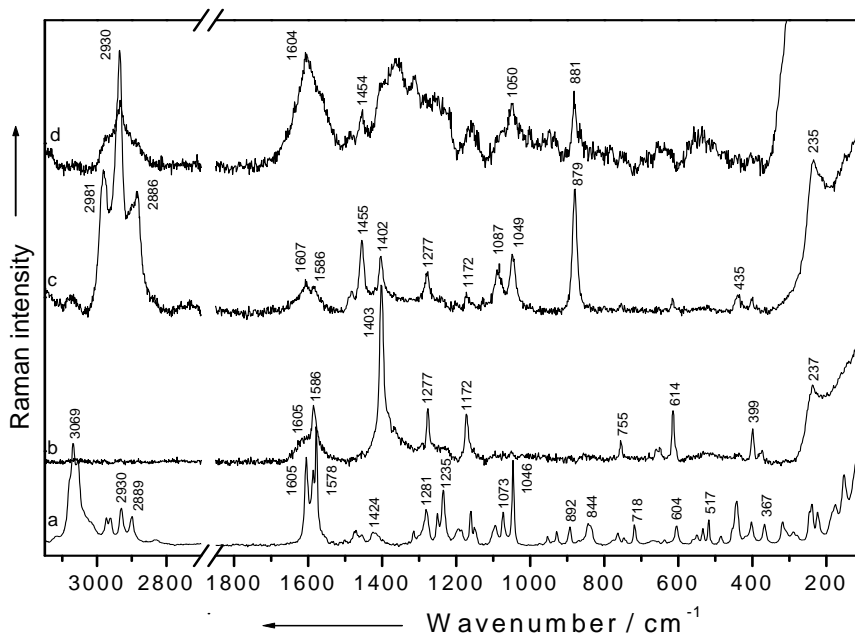


Fig. 2. FT-Raman (a) and SER spectra on silver colloid at pH 2 (b), pH 6 (c), pH 10 (d) of diclofenac sodium

Table 1

Experimental (FT-Raman) and calculated wavenumbers (in  $\text{cm}^{-1}$ ) of diclofenac sodium.

Raman	Calc. <sup>a</sup>	Calc. <sup>b</sup>	Calc. <sup>c</sup>	Vibrational assignment
152ms	143	149	147	ring 2 out-of-plane def.
175ms	183	161	178	C-O-Na def + C <sub>6,7,8</sub> def + C <sub>7</sub> H <sub>2</sub> def
223m	210	217	218	ring 2 out-of-plane def.
239m	231	240	242	C-O-Na def + C <sub>7</sub> H <sub>2</sub> rock
288m	291	277	299	ring 1 out-of-plane def + C <sub>1</sub> NC <sub>1</sub> def
318m	321	334	323	C <sub>1</sub> NC <sub>1</sub> def + C <sub>6,7,8</sub> def + C-Cl def
367m	354	356	357	
402m	394	397	391	O <sub>1</sub> C <sub>8</sub> O <sub>2</sub> def + Cl <sub>1</sub> C <sub>2,3</sub> , Cl <sub>2</sub> C <sub>6,5</sub> def + C <sub>7</sub> H <sub>2</sub> def
417sh	429	425	423	ring 2 out-of-plane def + Na-O stretching
442ms	442	446	443	
484m	483	476	470	NH def
517m	518	524	522	ring 2 + 1 out-of-plane def
533m	534	537	524	
549m	540	539	536	C <sub>6,7,8</sub> def + C <sub>7</sub> H <sub>2</sub> def
604m	587	599	589	ring 1 + 2 in-plane def
637w	645	630	621	O <sub>1</sub> C <sub>8</sub> O <sub>2</sub> def + C <sub>7</sub> H <sub>2</sub> def
653w	655	644	647	C <sub>1</sub> NC <sub>1</sub> def + ring 1 out-of-plane def
718w	722	724	731	CH wagging (ring 2 + 1)
747m	753	748	741	
763m	760	762	759	C-Cl stretching + ring 1 + 2 in-plane def
774sh	763	766	768	

Raman	Calc. <sup>a</sup>	Calc. <sup>b</sup>	Calc. <sup>c</sup>	Vibrational assignment
844m	838	848	837	CH twist (ring 2 + 1)
868w	861	866	867	
892m	877	894	893	
928m	927	927	929	C <sub>7,8</sub> stretching
940sh	940	934	936	CH twist (ring 2 + C <sub>7</sub> H <sub>2</sub> )
952m	962	954	956	
1046s	1059	1051	1050	ring 2 breathing
1073ms	1074	1081	1066	ring 1 breathing
1094m	1094	1094	1085	C <sub>7</sub> H <sub>2</sub> wagging + CH bend (ring 1 + 2)
1150m	1151	1149	1150	CH bend (ring 1 + 2)
1160ms	1158	1167	1162	
1186m	1191	1188	1187	CH rock (ring 1)
1193m	1196	1197	1197	C <sub>7</sub> H <sub>2</sub> twist
1235s	1213	1243	1221	C <sub>1</sub> NC <sub>1</sub> s. stretching + CH rock (ring 1 + 2) + C <sub>7</sub> H <sub>2</sub> wagging
1250m	1260	1269	1250	C <sub>6,7</sub> stretching + CH rock (ring 1 + 2)
1281ms	1272	1284	1277	CH rock (ring 1 + 2) + C <sub>7</sub> H <sub>2</sub> wagging
1303sh	1298	1307	1296	C <sub>1</sub> NC <sub>1</sub> a. stretching + CH rock (ring 1 + 2) + C <sub>7</sub> H <sub>2</sub> wagging
1327vw	1316	1320	1311	ring 1 stretching + C <sub>7</sub> H <sub>2</sub> wagging
1360vw	1358	1357	1363	ring 2 stretching + C <sub>7</sub> H <sub>2</sub> wagging
1398vw	1404	1385	1406	C <sub>7,8</sub> stretching + O <sub>1</sub> C <sub>8</sub> O <sub>2</sub> s. stretching
1417m	1433	1426	1437	CH rock (ring 1) + NH def
1424m	1448	1448	1441	C <sub>7</sub> H <sub>2</sub> bend
1454m	1451	1455	1456	C <sub>1</sub> N stretching + CH rock (ring 1)
1470m	1468	1468	1471	C <sub>1</sub> N stretching + CH rock (ring 2)
1481sh	1473	1482	1481	CH rock (ring 1 + 2) + NH def
1501vw	1526	1524	1531	
1553sh	1565	1558	1551	ring 1 stretching
1578vs	1596	1572	1575	O <sub>1</sub> C <sub>8</sub> O <sub>2</sub> as. stretching
1585s	1605	1588	1599	ring 1 + 2 stretching
1605s	1623	1615	1612	
2829m	2887	2850	2858	CH stretching (C <sub>7</sub> )
2900m	2936	2918	2949	CH stretching (ring 2)
2929m	3003	2950	3009	
2961m	3012	2987	3061	CH stretching (ring 1)
2973m	3026	3002	3084	
3054s	3080	3081	3092	NH stretching
3069s	3098	3092	3107	

\*Abbreviation: w-weak, m-medium, s-strong, v-very, sh-shoulder. Calculated with: <sup>a</sup>RHF/6-31G\*, <sup>b</sup>BPW91/6-31G\*, <sup>c</sup>B3LYP/6-31G\*, ring 1 = phenyl ring with Cl atoms.

**Adsorption on the Silver Surface.** In many cases the application of the conventional Raman spectroscopy is limited by the weak intensity of the Raman scattering light, especially in solution at low concentration, and the interference of the fluorescence. One way to overcome these disadvantages is surface-enhanced Raman spectroscopy [26-28]. The origin of the enhancement of Raman scattering cross section at rough surface has been an active field of research. The general consensus attributes the observed enhancement to 192

contribution from two mechanisms: one electromagnetic enhancement and a chemical effect [26,28,29]. In order to know the action of the potential drugs, such as our derivative, it is very important to find out if the structure of the adsorbed specie is the same as that of the free molecule. In these investigations the silver surface serves as an artificial biologic interface [30]. SER spectra of DCF-Na on silver colloid at different pH values together with the Raman spectrum of the polycrystalline sample are presented in Fig. 2. Good SER spectra were obtained in acidic and neutral medium, while at alkaline pH values the spectra present very broad bands. The shift in the peak position and the change in the relative intensities of the SERS bands with respect to the corresponding Raman bands indicates a chemisorption process on the silver surface. The assignment of the vibrational modes of DCF-Na to the SERS bands at different pH values is summarised in Table 2.

**Table 2**  
Wavenumbers (in  $\text{cm}^{-1}$ ) and assignment of the vibrational modes of diclofenac sodium to the SERS bands at different pH values.

Raman	SERS			Vibrational assignment
	pH 2	pH 6	pH 10	
	237s	235s		Ag-Cl + Ag-O stretching
367m	373w			$\text{C}_1\text{NC}_1$ def + $\text{C}_{6,7,8}$ def + C-Cl def
402m	399m	399m		$\text{O}_1\text{C}_8\text{O}_2$ def + $\text{Cl}_1\text{C}_{2,3}$ , $\text{Cl}_2\text{C}_{6,5}$ def + $\text{C}_7\text{H}_2$ def
442ms		435w		ring 2 out-of-plane def
533mw			537br	ring 2 + 1 out-of-plane def
604m	614m	616w		ring 1 + 2 in-plane def
637w	647w		649wbr	$\text{O}_1\text{C}_8\text{O}_2$ def + $\text{C}_7\text{H}_2$ def
653w	651w		649wbr	$\text{C}_1\text{NC}_1$ def + ring 1 out-of-plane def
747vw	755w	754vw		CH wagging (ring 2 + 1)
868w		879vs	882s	CH twist (ring 2 + 1)
1046s		1049s	1050s	ring 2 breathing
1073ms		1087ms		ring 1 breathing
1160ms	1172m	1172w	1155mbr	CH bend (ring 1 + 2)
1281ms	1277m	1277m		CH rock (ring 1 + 2) + $\text{C}_7\text{H}_2$ wagging
1327vw			1316m	ring 1 stretching + $\text{C}_7\text{H}_2$ wagging
1398vw	1403vs	1402m	1392br	$\text{C}_{7,8}$ stretching + $\text{O}_1\text{C}_8\text{O}_2$ s. stretching
1454m		1455s	1454mw	$\text{C}_1\text{N}$ stretching + CH rock (ring 1)
1470sh		1480w	1484w	$\text{C}_1\text{N}$ stretching + CH rock (ring 2)
1578vs	1586ms	1586m		$\text{O}_1\text{C}_8\text{O}_2$ as. stretching
1605vs	1606sh	1607m	1604sbr	ring 1 + 2 stretching
2890mw		2886s	2888sh	CH stretching ( $\text{C}_7$ )
2930m		2934vs	2931s	CH stretching (ring 2)
2973w		2981	2970sh	CH stretching (ring 1)
3069s			3062wbr	NH stretching

\*Abbreviation: w-weak, m-medium, s-strong, v-very, sh-shoulder, br-broad, ring 1= phenyl ring with Cl atoms.

As one can see from Fig. 2 the C=O stretching mode is absent in all SER spectra. The lack of this band evidences the presence of the carboxylate group also in DCF-Na adsorbed state, not only in the solid state.

Arancibia and Escadar [31] have determined from potentiometric and spectrophotometric measurements the  $pK_a$  value for the carboxylic group in DCF ( $pK_a = 4.9$ ). Taking into account the  $pK_a$  value of 4.9, an excess of DCF-Na molecules with carboxylic group (protonated form) is expected to be present at pH 2. As one can see from Fig. 2b the C=O stretching band typical for the carboxylic group is missing in the SER spectrum at this pH value. The absence of this band could be due to the lowering of the  $pK_a$  value at the silver surface [32] and indicates the existence of a direct carboxylate–surface interaction. The high intensity of the symmetric and asymmetric  $COO^-$  stretching bands present in the SER spectrum at 1403 and 1586  $cm^{-1}$  is a proof of the existence of the carboxylate group in the DCF-Na adsorbed state and of its proximity to the silver surface. In the SER spectrum at pH 2 are also present weak bands at 637 and 399  $cm^{-1}$  that contain contributions of the in-plane  $COO^-$  deformation vibrations (see Table 2).

By inspecting Fig. 2 and Table 2 blue shifts by 5 and 8  $cm^{-1}$  of the symmetric and asymmetric  $COO^-$  stretching bands were observed in the SER spectrum of DCF-Na molecule in acidic medium in comparison to the Raman spectrum, which confirm the binding of this molecular specie on the silver surface *via* oxygen lone pair electrons of the carboxylate group.

According to the surface selection rules for Raman scattering [29] the vibration of the adsorbed molecules, which has a polarizability tensor component normal to the surface, will be preferentially enhanced. Stretching vibrations are assumed to have the large component of the polarizability along the bond axis. The very high intensity of the symmetric and asymmetric stretching bands of the  $COO^-$  group observed in the SER spectrum of DCF-Na at pH 2 indicates the perpendicular or least tilted orientation of this group with respect to the silver surface.

It is known [33] that the molecules with nitrogen ring atom can form a pair with the chlorine ion and this pair is bonded to the silver surface. By looking at the SER spectrum recorded at pH 2 we assume that the caboxylate group of the DCF-Na is directly bond to the silver surface, otherwise a strong change in the peak position of the Ag-Cl stretching mode would occur.

The vibrations specific to phenyl rings are also present in the SER spectrum in acidic medium. The stretching vibration of both rings gives rise to a broad shoulder at 1606  $cm^{-1}$ . The in-plane CH and ring deformation vibrations were observed in the SER spectrum at 1277, 1172, and 614  $cm^{-1}$  (see Table 2). The shifts of these bands compared to the corresponding Raman bands confirm the interaction between phenyl rings and the silver surface. The out-of-plane deformation vibrations of CH groups of both rings present in the Raman spectrum in the spectral range between 850 and 950  $cm^{-1}$  are not active in the SER spectrum at pH 2. If we closely examine the conformation of the DCF-Na molecule (Fig. 1) and the enhancement of the in-plane vibrations of phenyl rings we assume a tilted close to flat orientation of these rings with respect to the silver surface. According to the surface selection rule<sup>36,43</sup> one would expect the CH ring stretching modes to be present in adsorbed state of DCF-Na molecules with weak intensity. The absence of these bands in the SER spectrum can be explained by the barely contribution of these modes to the  $\alpha_{zz}$  polarizability component (z being the axis perpendicular to the surface). A similar situation was found for the adsorbed phtalazine [34] where CH stretching modes are very weak, even though the molecule stands up on the surface. A deformation of the DCF-Na molecule in adsorbed state could also occur.

SER spectra recorded at close to neutral and alkaline pH values (Figs. 2c and 2d) show new bands in comparison to the spectrum obtained in acidic environment. Very

intense bands are developed in the high wavenumber region around  $2900\text{ cm}^{-1}$ . The peak at  $1607\text{ cm}^{-1}$ , present as a shoulder in the spectrum at pH value of 2, became in the SER spectrum at pH 6 even more intense than the band at  $1586\text{ cm}^{-1}$ . New peaks are also developed at  $1480$ ,  $1455$ ,  $1087$ ,  $1049$ ,  $879$ , and  $435\text{ cm}^{-1}$ . These bands arise also in the SER spectrum at pH 10 but with broader shape probably determined by different adsorption sites in alkaline medium. By considering the  $\text{pK}_a$  value for the carboxyl group ( $\text{pK}_a = 4.9$ ), we suppose that the carboxylate form is present in both neutral and alkaline environments, therefore we will further analyse only the SER spectrum at pH value of 6.

The appearance of new bands in the SER spectrum at pH 6 indicates the change in orientation of the adsorbed DCF-Na molecule with respect to the silver surface. The bands attributed to the symmetric and asymmetric stretching modes of the carboxylate group appear at  $1586$  and  $1402\text{ cm}^{-1}$  in the SER spectrum at this pH value, but with lower intensities compared to those observed in the SER spectrum at pH 2 (see Figs. 2b, 2c). This feature of the above-mentioned bands is a proof that the interaction between the carboxylate group and the silver surface *via* lone pair electrons of the oxygen atom exists also in neutral and alkaline environments, but it is weaker than in acidic medium.

The bands at  $1049$  and  $1087\text{ cm}^{-1}$  due to the ring breathing vibrations are intense and broadened in the SER spectrum at pH 6 compared to the Raman spectrum. The band assigned to the  $\text{C}_1\text{N}$  stretching vibration appears at the same position as in the Raman spectrum ( $1455\text{ cm}^{-1}$ ), but its intensity is very increased. The behavior of this band can be considered as an evidence of the large distance between this group and the metal surface. The  $\text{C}_1\text{N}$  stretching band is also observed in the SER spectrum at  $1480\text{ cm}^{-1}$ , but with low intensity. The presence in the SER spectrum of the very intense bands specific to the CH ring stretching modes (around  $2950\text{ cm}^{-1}$ ), the breathing ( $1049$  and  $1087\text{ cm}^{-1}$ ) and stretching ( $1607\text{ cm}^{-1}$ ) vibrations of the phenyl rings allows us to conclude a more perpendicular orientation of phenyl rings with respect to the silver surface at pH 6 as compared with that taken from the adsorbed molecule in acidic medium.

## Conclusions

DFT calculations have been performed at the RHF/6-31G\*, BPW91/6-31G\* and B3LYP/6-31G\* levels of theory on the two most probable conformers of diclofenac sodium. The conformer with the natrium atom closer to the phenyl ring substituted by chlorine atoms was found to be energetically more stable by an energy difference of  $17.997\text{ kJ/mol}$  (RHF),  $29.946\text{ kJ/mol}$  (BPW91) and  $26.596\text{ kJ/mol}$  (B3LYP), respectively. Optimised structural parameters of the diclofenac sodium calculated by various theoretical methods agree well with experimental X-ray diffraction values. The assignment of the vibrational modes was also accomplished and a good agreement was obtained between the theoretical vibrational wavenumbers and the experimental FT-Raman data.

Good SER spectra were obtained in acidic and neutral environments indicating the chemisorption of the diclofenac sodium molecule on the silver surface. At all studied pH values diclofenac sodium molecule was bonded to the silver surface through lone pair oxygen electrons of the carboxylate group, which has a perpendicular or least tilted orientation with respect to the silver surface. By analysing SER spectra at different pH values a change of the phenyl rings orientation with respect to the metal surface from a tilted close to flat to a more perpendicular one was concluded.

## REFERENCES

1. Tunçay, M.; Çaliş, S.; Kaş, H. S.; Ercan, M. T.; Peksoy, I.; Hincal, A. A. *Int. J. Pharmaceutics* **2000**, *195*, 179.
2. Kovala-Demertzi, D.; Mentzafos, D.; Terzis, A. *Polyhedron* **1993**, *12*, 1361.
3. Pose-Vilairnova, B.; Santana-Penin, L.; Echezarreto-Lopez, M.; Perez-Marcos, M. B.; Vila-Jato, J. L.; Torres-Lambandiera, J. J. S. T. P. *Pharma. Sciences* **1999**, *9*, 231.
4. Szejtli, J. "Cyclodextrins and their inclusions complexes", Budapest 1982. pp.323, 116.
5. Kovala-Demertzi, D.; Mentzafos, D.; Terzis, A. *Polyhedron* **1995**, *22*, 221.
6. Sastry, C. S.; Rao, A. R. M.; Prasad, T. H. V. *Anal. Lett.* **1987**, *20*, 349.
7. Sane, R. T.; Eamant, R. S.; Nayak, V. G. *Indian Drugs* **1987**, *24*, 349.
8. Sastry, C. S.; Tipirneni, A. S. R. P.; Synyanarayana, M. V. *Analyst* **1989**, *114*, 513.
9. Arrawal, Y. K.; Upadyay, V. P.; Menou, S. K. *Indian J. Pharma. Sci.* **1988**, *50*, 58.
10. Henning, B.; Stenp, A. A.; Benecke, R. *Pharmazie* **1987**, *42*, 861.
11. Schneider, W.; Degen, P. G. *J. Chromatogr.* **1981**, *217*, 263.
12. Gaudyeau, D.; Beleou, J. C.; Quincon, M. T.; Savel, E. *J. Pharm. Sci.* **1989**, *78*, 247.
13. Godbilou, J.; Gauron, S.; Metayer, J. P. *J. Chromatogr.* **1985**, *338*, 151.
14. Abdel Fattah, S. A.; El-khateeb, S. Z.; Abdel Razeg, S. A.; Tawakkol, M. S. *Spectrosc. Lett.* **1988**, *21*, 533.
15. Mucci, A.; Schenetti, L.; Vandelli, M. A.; Rouzi, B.; Forni, F. *J. Chem. Research* **1999**, 414.
16. Lee, P. C.; Meisel, D. J. *J. Phys. Chem.* **1992**, *86*, 539.
17. Frisch, M. J.; Trucks, G. W.; Schlegel, H. B.; Scuseria, G. E.; Robb, M. A.; Cheeseman, J. R.; Zakrzewski, V. G.; Montgomery, J. A. Jr.; Stratmann, R. E.; Burant, J. C.; Dapprich, S.; Millam, J. M.; Daniels, A. D.; Kudin, K. N.; Strain, M. C.; Farkas, O.; Tomasi, J.; Barone, V.; Cossi, M.; Cammi, R.; Mennucci, B.; Pomelli, C.; Adamo, C.; Clifford, S.; Ochterski, J.; Petersson, G. A.; Ayala, P. Y.; Cui, Q.; Morokuma, K.; Malick, D. K.; Rabuck, A. D.; Raghavachari, K.; Foresman, J. B.; Ciolowski, J.; Ortiz, J. V.; Stefanov, B. B.; Liu, G.; Liashenko, A.; Piskorz, P.; Komaromi, I.; Gomperts, R.; Martin, R. L.; Fox, D. J.; Keith, T.; Al-Laham, M. A.; Peng, C. Y.; Nanayakkara, A.; Gonzales, C.; Challacombe, M.; Gill, P. M. W.; Johnson, B.; Chen, W.; Wong, M. W.; Andres, J. L.; Head-Gordon, M.; Repogle, E. S.; Pople, J. A. *Gaussian 98*, Revision A7, Gaussian Inc.: Pittsburgh, PA 1998.
18. Becke, A. D. *Phys. Rev.* **1988**, *A 38*, 3098.
19. Perdew, J. P.; Wang, Y. *Phys. Rev.* **1992**, *B 45*, 13244.
20. Becke, A. D. *J. Chem. Phys.* **1993**, *98*, 1372.
21. Reck, G.; Faust, G.; Dietz, G. *Pharmazie* **1988**, *43*, 771.
22. Hutter, J.; Luthi, H. P.; Dieterich, F. *J. Am. Chem. Soc.* **1994**, *116*, 750.
23. Barone, V.; Adamo, C.; Lejl, F. *J. Chem. Phys.* **1995**, *117*, 4167.
24. Wong, M. W. *Chem. Phys. Lett.* **1996**, *256*, 391.
25. Rauhut, G.; Pulay, P. *J. Phys. Chem.* **1995**, *99*, 3093.
26. Moskovits, M. *Rev. Mod. Phys.* **1985**, *57*, 783.
27. Campion, A.; Kambhampati, P. *Chem Soc. Rev.* **1998**, *27*, 241.
28. Lombardi, J. R.; Birke, R. L.; Lu, T.; Xu, J. *J. Chem Phys.* **1986**, *84*, 4174.
29. Creighton, J. A. *Surf. Sci.* **1983**, *124*, 208.
30. Dryhurst, C. G. "Electrochemistry of Biological Molecules", Academic press, New York, 1977, p. 473.
31. Arancibia, J. A.; Escadar, G. M. *Analyst* **1999**, *124*, 1833.
32. Schmidt, P. H.; Plieth, W. *Ber. Bunsenges Phys. Chem.* **1987**, *91*, 323.
33. Iliescu, T.; Vlassa, M.; Caragiui, M.; Marian, I.; Astilean, S. *Vibr. Spectrosc.* **1995**, *8*, 451.
34. Moskovits, M.; Suh, J. *J. Phys. Chem.* **1984**, *88*, 5526.

# SOLID-STATE NMR TECHNIQUES FOR STRUCTURAL INVESTIGATIONS OF PROTEINS

CLAUDIU FILIP

*National Institute for Research and Development of Isotopic and Molecular Technology, Cluj-Napoca, Romania*

**ABSTRACT.** Applications of Solid-State NMR spectroscopy to structural investigation of large proteins requires extending its techniques from selectively to uniformly labeled compounds. Here we present two novel MAS NMR pulse sequences for simultaneous measurement of carbon-nitrogen distances in uniformly  $^{13}\text{C}$ ,  $^{15}\text{N}$ -labeled solids..

## Introduction

Solid-state nuclear magnetic resonance (SS-NMR) spectroscopy currently undergoes a remarkable evolution from being mainly physics-oriented method for studying small molecules in inorganic or organic materials toward biology-oriented applications handling complex clusters of atoms for structure analysis of large bio-molecules. Recent advances in magic-angle-spinning (MAS) SS-NMR instrumentation and methodology [1] have greatly contributed to extending its applicability from selectively to multiply  $^{13}\text{C}$ ,  $^{15}\text{N}$  labeled peptides and proteins. In a first step of obtaining full 3D structures for large proteins, site-specific resonance assignments are a source of valuable structural information. Whereas NMR experiments for sequential resonance assignments generally exploit the strongest spin-spin interactions and are relatively straightforward to implement in uniformly  $^{13}\text{C}$ ,  $^{15}\text{N}$  labeled systems, long-range distance measurements in these systems are more complicated. The nuclei form a tightly coupled network via through-space (dipolar coupling) and through-bond (J-coupling) spin-spin interactions; consequently, the strongest couplings can interfere with the accurate determination of the weaker ones. In the following we present new MAS NMR pulse sequences for *simultaneous* measurement of multiple carbon-nitrogen distances in uniformly  $^{13}\text{C}$ ,  $^{15}\text{N}$  labeled solids. The experiments are demonstrated in model U- $^{13}\text{C}$ ,  $^{15}\text{N}$  labeled tri-peptides N-formyl-L-Met-L-Leu-L-Phe (MLF), where 26  $^{13}\text{C}$ - $^{15}\text{N}$  distances up to  $\sim 5\text{-}6 \text{ \AA}$  were determined.

## Long-range distance constraints in uniformly $^{13}\text{C}$ , $^{15}\text{N}$ -labeled polypeptides

The pulse sequences employ transferred echo double resonance (TEDOR) for  $^{13}\text{C}$ - $^{15}\text{N}$  coherence transfer and  $^{15}\text{N}$  and  $^{13}\text{C}$  frequency labeling for site-specific resolution, and as such build on several previously described 3D TEDOR experiments. The novel feature of the 3D TEDOR pulse sequences presented here is that they are specifically designed to circumvent the detrimental effects of homonuclear  $^{13}\text{C}$ - $^{13}\text{C}$  J-couplings on the measurement of weak  $^{13}\text{C}$ - $^{15}\text{N}$  dipolar couplings. Homonuclear J-couplings: (i) generate undesirable anti-phase and multiple-quantum (MQ) spin coherences, which lead to spurious cross-peaks and phase-twisted lines in the 2D  $^{15}\text{N}$ - $^{13}\text{C}$  correlation spectra, and thus degrade the spectral resolution and prohibit the extraction of reliable cross-peak intensities and (ii) significantly reduce cross-peak intensities for strongly J-coupled  $^{13}\text{C}$  sites (e.g., CO and  $\text{C}^\alpha$ ). The first pulse sequence (Fig. 1a) employs z-filter periods to suppress the anti-phase and MQ coherences and generates 2D spectra with pure absorption mode peaks for all TEDOR mixing times. The second sequence (Fig. 1b) uses band-selective  $^{13}\text{C}$  pulses to refocus J-couplings between  $^{13}\text{C}$  spins within the selective pulse bandwidth and  $^{13}\text{C}$  spins outside the bandwidth.

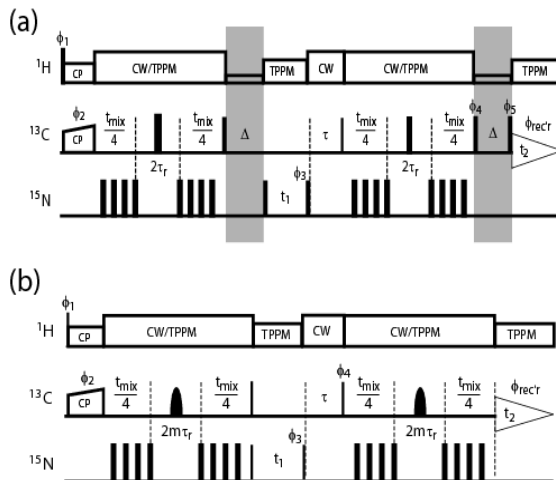


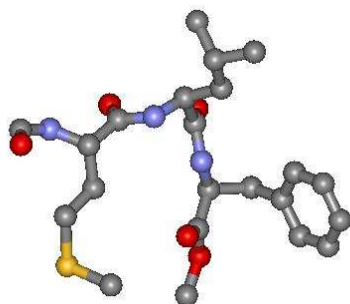
**Fig. 1.** Z-Filtered (ZF) and band-selective (BASE) 3D TEDOR pulse sequences. Narrow and wide solid rectangles represent  $\pi/2$  and  $\pi$  pulses, respectively. In (a) the modifications to the recently described 3D TEDOR experiment [ ] are highlighted by gray rectangles. The modifications consist of two z-filter periods,  $\Delta$ , which eliminate undesired multiple quantum and anti-phase spin coherences generated by  $^{13}\text{C}$ - $^{13}\text{C}$  J-evolution (see text for details). In (b) band-selective  $^{13}\text{C}$  Gaussian  $\pi$  pulses refocus  $^{13}\text{C}$ - $^{13}\text{C}$  J-couplings to nuclei outside the  $\pi$  pulse bandwidth

The NMR spectra were recorded at 11.7 T (500.1 MHz  $^1\text{H}$ , 125.8 MHz  $^{13}\text{C}$ , 50.7 MHz  $^{15}\text{N}$ ) using a triple-resonance MAS probe. The spinning frequency of 10.0 kHz was used in the all experiments and regulated to  $\pm 5$  Hz and the samples were centerpacked in the rotors to minimize the effects of rf inhomogeneity. The  $^{13}\text{C}$ ,  $^{15}\text{N}$  labeled tri-peptide N-formyl-L-Met-L-Leu-L-Phe (MLF) represents an excellent model system for the 3D TEDOR experiments as its three-dimensional structure (see Figure 2) has been already determined using X-ray crystallography [2].

Using a zero order approximation [3] we proceed to describe the 3D TEDOR experiments by neglecting all orientation dependent terms. In summary, the main features of the simulation model are: (i) for the  $i^{\text{th}}$   $^{13}\text{C}$  nucleus coupled to  $N_i$   $^{15}\text{N}$  spins all  $N_i$   $^{13}\text{C}$ - $^{15}\text{N}$  distances are determined by simultaneously fitting the experimentally observed buildup of cross-peaks located at  $(\Omega_{N_k}, \Omega_{C_i})$ ,  $k = 1, 2, \dots, N_i$ , using eqs (3)-(5) in Ref. [3] with  $N_i + 2$  fit parameters ( $N_i$  dipolar coupling constants,  $D_{ik}$ , a relaxation rate,  $\Gamma_i$ , and an amplitude scaling factor,  $\Lambda_i$ ), (ii) no knowledge of dipolar tensor orientations and no powder averaging are required, and (iii) the cross-peak intensities at long mixing times are inversely proportional to the number of  $^{15}\text{N}$  spins,  $N_i$ , simultaneously coupled to the  $^{13}\text{C}$  nucleus,  $V_{ik}(t_{\text{mix}}) \propto (2^{N_i})^{-1}$ , which places a practical limit on the magnitude of the weakest  $^{13}\text{C}$ - $^{15}\text{N}$  couplings that can be determined using 3D TEDOR methods (for the tri-peptide investigated in this work  $^{13}\text{C}$ - $^{15}\text{N}$  dipolar couplings corresponding to distances in the 4-6 Å regime could be determined).

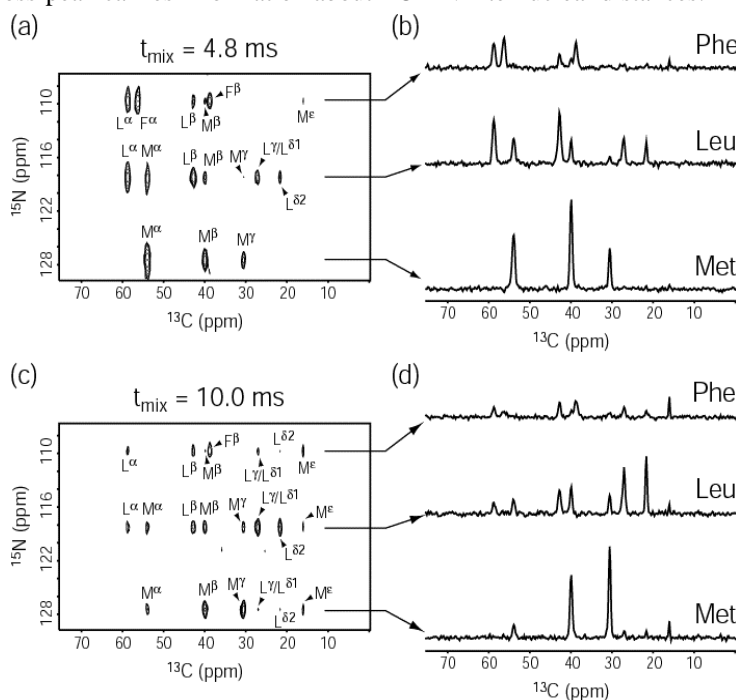
We note that for ZF-3D TEDOR the buildup of cross-peaks for the  $i^{\text{th}}$   $^{13}\text{C}$  nucleus also depends on the coupling topology of the  $m_j$  J-coupled  $^{13}\text{C}$  nuclei. These parameters are held constant in the simulations since  $^{13}\text{C}$ - $^{13}\text{C}$  J-couplings in peptides do not vary significantly for different types of couplings (i.e., CO- $\text{C}^\alpha$ ,  $\text{C}^\alpha$ - $\text{C}^\beta$ , etc.) [4].





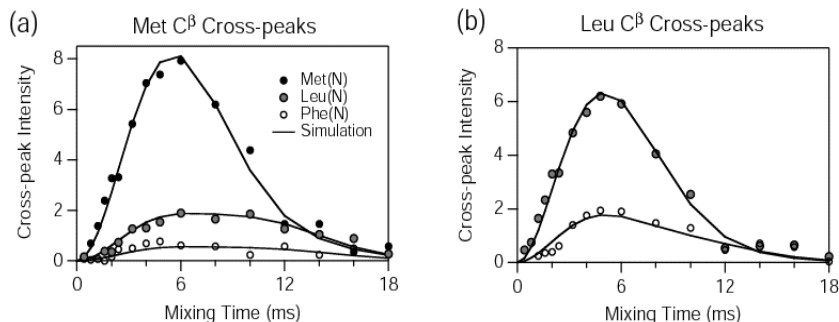
**Fig. 2.** X-ray crystal structure of N-formyl-L-Met-L-Leu-L-Phe-OMe (MLF)

Figure 3 shows representative 2D  $^{15}\text{N}$ - $^{13}\text{C}$  correlation spectra in N-formyl-[U- $^{13}\text{C}$ ,  $^{15}\text{N}$ ]L-Met-L-Leu-L-Phe for the ZF-3D TEDOR experiment. A large number of dipolar correlations ( $\sim 20$ ) are observed in the aliphatic  $^{13}\text{C}$  spectral region for longer mixing period (Figure 10c), and each cross-peak carries information about  $^{13}\text{C}$ - $^{15}\text{N}$  internuclear distances.



**Fig. 3.** Representative two-dimensional slices from broadband 3D TEDOR experiments in N-formyl-[U- $^{13}\text{C}$ ,  $^{15}\text{N}$ ]L-Met-L-Leu-L-Phe. The 2D spectra shown in (a) and (c) (with the 1D slices corresponding to Met, Leu and Phe  $^{15}\text{N}$  resonances shown in (b) and (d)) were recorded at 500 MHz  $^1\text{H}$  frequency and  $\omega_r/2\pi = 10 \text{ kHz} \pm 5 \text{ Hz}$  using the pulse sequence in Figure 1a with the z-filter delays of  $\Delta = 200 \mu\text{s}$ . Additional experimental parameters are described in the text. The 3D data set consisted of 16 2D spectra acquired for TEDOR mixing times up to 18 ms and incremented in a non-linear fashion in order to maximize the information content and minimize the duration of the experiment. Each 2D spectrum was acquired as (19, 1024) complex points in  $(t_1, t_2)$ , with time increments of (800, 20)  $\mu\text{s}$  resulting in acquisition times of (14.4, 20.5) ms. Each FID was 128 scans, with a 3 s recycle delay, yielding a total measurement time of  $\sim 67 \text{ h}$ .

The  $^{13}\text{C}$  and  $^{15}\text{N}$  resonance assignments for MLF have been presented in previous studies [5]. The 3D TEDOR cross-peak buildup curves for selected  $^{13}\text{C}$  sites corresponding to distances in the 2.5-6 Å range are shown in Figure 4. Similar experiments were performed using the BASE-3D TEDOR pulse sequence [3] (spectra not shown) and the results are presented in the Table.



**Fig. 4.** 3D TEDOR cross-peak buildup curves in *N*-formyl-[ $U$ - $^{13}\text{C}$ ,  $^{15}\text{N}$ ]L-Met-L-Leu-L-Phe. The buildup curves were acquired using the pulse sequence in Figure 1a and correspond to cross-peaks observed for the Met  $\text{C}^\beta$  (a) and Leu  $\text{C}^\beta$  (b) resonances in the 2D correlation spectra in Figure 3. For each  $^{13}\text{C}$  the experimental buildup curves corresponding to the Met (●), Leu (●) and Phe (○)  $^{15}\text{N}$  sites were fit (—) using analytical expressions based on the zeroth order Bessel function approximation. The values of  $^{13}\text{C}$ - $^{13}\text{C}$   $J$ -coupling constants used in the fits were 55 Hz for  $^1J_{\text{CO-C}^\alpha}$  and 34 Hz for all other  $J$ -couplings. The cross-peak buildup curves shown in the figure correspond to carbon-nitrogen distances in the 2.5-6 Å regime. Similar simulations were performed for the remaining cross-peaks (c.f. Figure 3) and the  $^{13}\text{C}$ - $^{15}\text{N}$  internuclear distances are summarized in the table.

**Table**
**Internuclear C-N distances N-formyl-L-Met-L-Leu-L-Phe-OMe (MLF)**

atoms		$r_{\text{C-N}}$ (Å)		
		ZF-3D TEDOR	BASE 3D TEDOR	X-ray
Met(N)	Met( $\text{C}^\gamma$ )	—	2.5	2.40
	Met( $\text{C}^\alpha$ )	1.5	—	1.46
	Met( $\text{C}^\beta$ )	2.5	2.6	2.50
	Met( $\text{C}^\gamma$ )	3.8	—	3.04
	Met( $\text{C}^\epsilon$ )	5.3	—	5.71
	Leu( $\text{C}^{\delta 2}$ )	6.1	—	6.28
Leu(N)	Met( $\text{C}^\gamma$ )	—	1.3	1.33
	Met( $\text{C}^\alpha$ )	2.6	—	2.44
	Met( $\text{C}^\beta$ )	3.2	3.2	3.20
	Met( $\text{C}^\gamma$ )	5.0	—	4.56
	Met( $\text{C}^\epsilon$ )	5.8	—	5.93
	Leu( $\text{C}^\gamma$ )	—	2.4	2.46
	Leu( $\text{C}^\alpha$ )	1.5	—	1.46
	Leu( $\text{C}^\beta$ )	2.6	2.6	2.50
	Leu( $\text{C}^{\delta 2}$ )	3.9	—	3.63
Phe(N)	Met( $\text{C}^\gamma$ )	—	3.4	3.41
	Met( $\text{C}^\beta$ )	3.9	3.8	4.06

atoms	$r_{C-N}$ (Å)		
	ZF-3D TEDOR	BASE 3D TEDOR	X-ray
Met(C <sup>γ</sup> )	5.6	—	5.43
Met(C <sup>ε</sup> )	5.2	—	5.62
Leu(C <sup>γ</sup> )	—	1.3	1.34
Leu(C <sup>α</sup> )	2.3	—	2.43
Leu(C <sup>β</sup> )	3.2	3.1	3.12
Leu(C <sup>δ2</sup> )	6.0	—	5.38
Phe(C <sup>γ</sup> )	—	2.7	2.37
Phe(C <sup>α</sup> )	1.4	—	1.47
Phe(C <sup>β</sup> )	2.6	2.6	2.53

### Conclusions

In conclusion, we have presented two 3D TEDOR NMR pulse sequences for the simultaneous measurement of multiple carbon-nitrogen distances in uniformly <sup>13</sup>C, <sup>15</sup>N labeled in site-specific fashion. The novel feature of the sequences is that they are compensated for the detrimental effects of <sup>13</sup>C-<sup>13</sup>C J-couplings on the measurements of long-range carbon-nitrogen distances. The experiments are robust and straightforward to implement in practice. Qualitatively, the presence of <sup>13</sup>C-<sup>15</sup>N correlations in the 2D spectra in itself provides direct information about three-dimensional structure. More accurate distance measurements were performed using a simple analytical simulation model, which accounts explicitly for multiple spin-spin couplings contributing to cross-peak buildup.

**Acknowledgment.** The author acknowledges financial support from the Romanian Academy by the Research Grant No. 22 /2003.

### REFERENCES

- [1] A.E. Benett, R.G. Griffin, S. Vega, *Solid State NMR IV: Methods and Applications of Solid-State NMR*, Springer, Berlin (1994)
- [2] E. Gavuzzo, F. Mazza, A. Scatturin, *Int. J. Pept. Protein Res.*, **34**, 409 (1989)
- [3] C.P. Jaroniec, C. Filip, R.G. Griffin, *J. Am. Chem. Soc.*, **124**, 10728 (2002)
- [4] J. Cavanagh, W. Fairbrother, A.G. Palmer, N. Skelton, *Protein NMR spectroscopy: Principles and Practice*, Academic Press, San Diego (1996)
- [5] C.P. Jaroniec, B. Tounge, J. Hertzfeld, R.G. Griffin, *J. Am. Chem. Soc.*, **123**, 3507 (2001)

## TLD USING IN CERAMICS DATING

C. COSMA, V. BENEĂ

*Faculty of Physics, Babes-Bolyai University, 3400-Cluj-Napoca, Romania*

**ABSTRACT.** Thermoluminescence dating is based on the measurement of the amount of light that is released upon thermal or optical stimulation, by minerals such as quartz and feldspar. The light signal is a measure of the radiation dose that has accumulated in these minerals through time. In our work we will present some preliminary results connected with the samples and device (Harshaw-2000) preparation for thermoluminescence of feldspar separated from ceramic samples with age well known. For external doses was used TLD-100 with high sensibility (LiF-Mg-Cu-P)

### 1. INTRODUCTION

Thermoluminescence (TL) dating is a radiometric method based on the fact that trace amounts of radioactive atoms, such as uranium and thorium, in rock, soil, and clay produce constant low amounts of background ionizing radiation. The atoms of crystalline solids, such as pottery and rock, can be altered by this radiation. Specifically, the electrons of quartz, feldspar, diamond, or calcite crystals can become displaced from their normal positions in atoms and trapped in imperfections in the crystal lattice of the clay molecules. These energy charged electrons progressively accumulate over time. When a sample is heated to high temperatures in a laboratory, the trapped electrons are released and return to their normal positions in their atoms. This causes them to give off their stored energy in the form of light impulses (photons). This light is referred to as thermoluminescence. What is actually determined is the amount of elapsed time since the sample had previously been exposed to high temperatures. In the case of a pottery vessel, usually it is the time since it was fired. For the clay or rock lining of a hearth or oven, it is the time since the last intense fire burned there.

The effective time range for TL dating is now about 300,000 years down to a few decades. Theoretically, this technique could date samples as old as the solar system, if we could find them.

### 2. PRINCIPLES OF TL DATING

Thermo luminescence dating is based on the measurement of the amount of light that is released upon thermal or optical stimulation, by minerals such as quartz and feldspar. The light signal is a measure of the radiation dose that has accumulated in these minerals through time.

When they are exposed to sunlight during transportation in the air the latent thermoluminescence signal in the quartz and feldspar grains is bleached down to a negligible level and the thermoluminescence "clock" is set to zero. After deposition of the grains and burial under new sediment, their latent thermoluminescence signal accumulates again because they absorb the natural ionising radiation that is emitted by the surrounding sediment. The flux of ionising radiation ( $\alpha$  -,  $\beta$  -,  $\gamma$  -rays) is produced by the very low concentrations of uranium ( $^{235}\text{U}$ ,  $^{238}\text{U}$ ), thorium ( $^{232}\text{Th}$ ), potassium ( $^{40}\text{K}$ ) and  $^{87}\text{Rb}$  in the sediments. A small amount is cosmic radiation. The total radiation dose that is accumulated in this way is called the palaeodose.

The age that is determined corresponds to the time span between the removal of the thermoluminescence signal by sunlight just before deposition and the removal of the newly accumulated palaeodose by thermal or stimulation in the laboratory. Stimulation by heat is called thermoluminescence (TL).

The age equation can be written as:

$$\text{Age } (a) = \frac{\text{Palaeodose (Gy)}}{\text{Annual radiation dose (Gy/a)}}$$

Thus, luminescence dating involves the determination of two major parameters: the palaeodose and the annual dose.

Reliable age determinations can be obtained from 0.1ka to 200 ka. Typical errors are in the range of 5 to 10 %.

Essentially, the palaeodose is evaluated by comparing the natural TL intensity of the sample with the increase of TL output induced by known amounts of additional radiation. By extrapolating the growth curve until it intersects the initial TL intensity of the sample, the dose accumulated since the initialising event can be found.

In this procedure a complication arises because, in general, the growth curves are not straight lines. While it is possible to observe the form of the growth curve for TL intensities greater than the natural level, the manner in which the TL grew from its initial state is not revealed. This difficulty is answered by measuring a second growth curve, using portions of the sample in which the initial state of the TL has been recreated by heating or exposure to light. The form of this second growth curve is then taken as the correct line to use when extrapolating the first growth curve. It should be noted that this assumption is ultimately untestable by scientific investigation, but can only be justified through the dating of known age samples.

The purpose of environmental dosimeter in TL dating is to measure the gamma and cosmic ray contribution to the total radiation dose received by the TL sample during its burial at the archaeological or geological site. In the case of flint and calcite, this contribution is commonly a major part of the total dose. Moreover, it is often the uncertainties in determining this contribution that govern the overall error limits of the TL date. The on-site environmental dosimeter is therefore an important part of the dating procedure.

In contrast to alphas and betas, the range of gamma rays is approximately 0.3 m, and therefore much greater than the dimensions of most TL samples. This means that the contribution to the total radiation dose, which comes from gammas, is dependent mainly upon the radioactive content of the sediment surrounding the TL sample, and only slightly upon the radioactivity of the sample. Like the alpha and beta rays, gamma radiation derives from the decay of naturally occurring radionuclides present in the ground, such as potassium-40 and members of the uranium and thorium decay series. Together with the contribution from cosmic rays, which is a minor one, the gamma component of the total radiation dose is referred to as the *environmental dose*.

The purpose of environmental dosimetry is to estimate the mean rate at which the TL sample has received its environmental dose during burial. Ultimately this can only be an estimate, because measurements record only the present day radiation environment. One concern is therefore the temporal variability of the burial conditions, which, as discussed below, is often associated with changes of ground water content. The other main concern is spatial variability, since it is rare to find sites that are homogeneous in their radioactivity. It is these spatial variations that are the principal subject for investigation in the field.

### 3. EXPERIMENTAL METHOD

The method most commonly used for environmental dosimetry is the small copper capsules containing a sensitive TL phosphor (LiF-Mg-Cu-P). These capsules are left buried in the sediment for a period of several months, and then returned to the laboratory where the TL acquired by the phosphor during its burial is measured.

An alternative method used for environmental dosimetry is the portable gamma spectrometer. This usually consists of a crystal scintillation detector with electronics for sorting gamma rays according to the quantity of energy they deposit in the crystal. The detector is housed in a cylinder of 55 mm diameter, and is inserted to a depth of 0.3 m or more into the sediment under study using an auger. Counting times are generally between 15 mins and an hour, depending on the radioactivity of the environment. The resulting spectrum of gamma energies is analysed to determine the concentrations of uranium, thorium and potassium in the sediment.

Upon arrival in the laboratory TL samples normally consist of two parts: the sample to be dated and a modern analogue sample for the surface residual correction. Both specimens are carefully sieved to separate the 90 - 125 micrometre grain size fraction, chemically cleansed in dilute HCl, etched in 40% w/w HF and finally subjected to heavy liquid separation. The sample so prepared consists of better than 99% pure quartz grains.

The quartz from the specimen under investigation is divided into two parts one of which is heavily bleached under a UV sunlamp. This exposure effectively removes all of the previously acquired TL leaving only what is termed as the "unbleachable TL". Aliquots of both the bleached and the unbleached quartz are deposited onto a series of aluminium planchettes and a number of these are incrementally irradiated using a calibrated 90Sr plaque source. Each planchette, complete with its sample aliquot, is heated to 500°C at a controlled rate and in an oxygen free atmosphere. The light emitted (TL) is recorded and in this way it is possible to establish a TL growth curve which relates TL output and the absorbed radiation dose. With reference to this curve the measured naturally accumulated sample TL may be converted to absorbed radiation units (Palaeodose P). The surface residual TL correction is determined from the modern analogue sample by means of a similar procedure and this correction is applied to the palaeodose value. In the absence of a suitable modern sample the laboratory induced unbleachable TL level is assumed which has the effect of maximising the resultant TL age determined. In the case of an older sample this correction may only represent a small proportion of the total age.

The radiation dose received annually by the sample is measured by means of calibrated thick source alpha counting which determines the specific activity of the uranium and thorium decay chains assuming that secular equilibrium exists. This process requires that the sample be crushed to an extremely fine grain size such that all of the short range alpha particles may be detected. The crushed sample is placed in immediate contact with a scintillation screen which is sealed in an alpha counting cell which in turn is positioned on a photomultiplier tube assembly. Because certain of the daughters within the uranium and thorium decay chains are gaseous it is necessary to wait a period of three weeks before introducing the cell into the counter. This period allows the decay chains to be re-established. The amount of potassium present in the sample is determined by means of atomic emission spectroscopy and the rubidium content by X-ray fluorescence. Thus, assuming the cosmic contribution and applying a correction for the modifying effect of the sample moisture content, the radiation dose received upon an annual basis (ARD) may be computed and the depositional age of the sample determined from the equation shown.

#### **4. RESULTS AND DISCUSSION**

As we can see from Table 1 and Fig.1 an exact linear dependence of TLD signal on absorbed dose was obtained. This result determines the constant of calibration of 370  $\mu\text{C}/\text{Gy}$  which will be used for these chips for archeological background of buried samples.

In table 2 a comparison between TL and C-14 method of age determination is shown [2].

**Table 1**

**Calibration of LiF: Mg, Cu, P detectors exposure to  $^{60}\text{Co}$  gamma rays**

TLD	Dose rate (Gy/min)	Exposure time (min)	Absorbed dose (Gy)	Background signal ( $\mu\text{C}$ )	Average TL signal ( $\mu\text{C}$ )
LiF:Mg,Cu,P (TLD100H)	0,1557	0,25	0,0778	0,245	28,5
		0,5	0,1557		57,5
		1	0,3113		117,4
		2	0,6226		235,7
		4			459,8

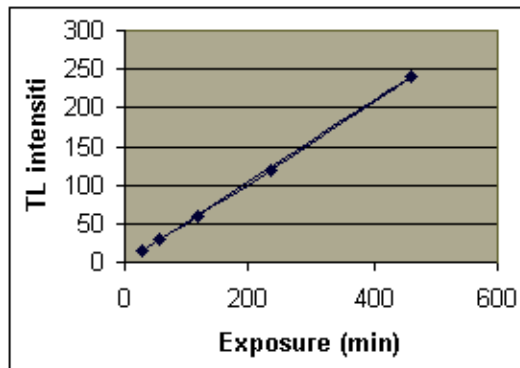


**Fig. 1.** Thermoluminescence (TL) against exposure to  $^{60}\text{Co}$  gamma rays for LiF:Mg,Cu,P (TLD-100)

**Table 2**

**Determination TL age**

	Paleodose (rad)	Annual dose (rad/yr)	TL age (BP)	C-14 age (BP)
Ceramic 1	1190 ( $\pm 4.7\%$ )	0.512 ( $\pm 6.9\%$ )	2570 $\pm$ 190	2320 $\pm$ 80
Ceramic 2	1650 ( $\pm 6.1\%$ )	0.453 ( $\pm 6.4\%$ )	3640 $\pm$ 320	
Ceramic 3	2570 ( $\pm 7.2\%$ )	0.613 ( $\pm 5.1\%$ )	4190 $\pm$ 370	4000 $\pm$ 65
Ceramic 4	3150 ( $\pm 4.7\%$ )	0.539 ( $\pm 4.2\%$ )	5840 $\pm$ 350	5230 $\pm$ 200

## REFERENCES

1. G. V a s a r u, C. C o s m a, *Metode de datare prin fenomene nucleare naturale*, Editura Dacia, Cluj-Napoca, 1998
2. M. J. A i t k e n, M. S. T i t e, J. R e i d, *Thermoluminescence Dating of Ancient Ceramics*, Nature, 202, 1032, 1964
3. P. H. B e n o i t, C. P. H a r t m e t z, *The Induced Thermoluminescence and Thermal History of Plagioclase Feldspars*, American Mineralogist, 86, 780, 2001
4. V. M e j d a h l, *Feldspar inclusion dating of ceramics and burnt stones, reprint nov. 1982, Proceedings of 3<sup>rd</sup> specialist seminar on TL and ESR dating, Helsingor, 1982*

5. W. Wang, Z. Zhou, *Thermoluminescence dating of Chinese pottery*, *Archeometry*, 25, 99-106, 1983
6. M. Schvoerer, A. Dantant, *Dataion par thermoluminescence*, *Gif-sur-Yvette*, 25 – 30 sept. 1999
7. A. Lang, A. Koderer, R. H. Behrends, G. A. Wagner, *Optical dating of anthropogenic sediments at the arhiological site of Herrenbrunnenbuckei, Bretten-Bauerbach, Germany*, *Arhaeometry* 41, 2, 387-411, 1999
8. M. Schoerer, P. Lamarque, J.F. Rouanet *Thermoluminescence - Dataion absolute par thermoluminescence*, *Etude d'une serie d'echantillons d'origine arhaeologique, don't deux fragments de gres brules provenant de niveaux magdaleniens IV et VI*, *Compte Rendue Acad. Sc. Paris*, 279, serie B-191. 1974
9. B. Erdelyi, I. Kasa, F. Beorillo, Z. Kiralaly, *Thermoluminescence Dating of the "Mas de Valero" site (Formiche Bajo, Ternet, Spaon)*, 27-29, vol. *Arhaeometry Proc. Of the 25<sup>th</sup> International Symposium*, Edit. Y. Moniatis, Oxford, 1989



## MAGNETIC AND IR SPECTROSCOPIC BEHAVIOUR OF SOME GLASSES CONTAINING GADOLINIUM AND NEODYMIUM IONS

**E.CULEA<sup>1</sup>, I.BRATU<sup>2</sup>, LIDIA POP<sup>1</sup>**

<sup>1</sup> *Technical University of Cluj-Napoca, Physics Dept., str. C. Daicovicu, nr. 15, 3400 Cluj-Napoca, Romania e-mail: eugen.culea@phys.utcluj.ro*

<sup>2</sup> *National Institute for Research and Development of Isotopic and Molecular Technologies, str. Donath, nr. 65-103, 3400 Cluj-Napoca, Romania*

**ABSTRACT.** Glasses of the  $xR_2O_3(1-x)(3Bi_2O_3 \cdot PbO)$  vitreous system with  $R = Gd$  and  $Nd$  and  $0 \leq x \leq 0.30$  were obtained and studied by IR spectroscopy, density and magnetic susceptibility measurements. IR and density measurements show that addition of  $R$  ions produces structural changes and these ions play a network modifier role in the host glass matrix. Magnetic susceptibility data show that the  $R^{3+}$  magnetic ions are present as isolated species for low  $x$  values and as both isolated and exchange coupled species for higher  $x$  values.

### Introduction

Rare-earth elements in glass have been widely studied due to their important applications for optical telecommunication, laser technology and immobilisation of radioactive materials [1].

A lot of studies were reported over the past several decades on the spectroscopic properties of  $Nd^{3+}$  ions incorporated in a large variety of vitreous matrices [1-4]. The important interest concerning these glasses is related to the capacity of the  $Nd^{3+}$  ions in producing strong infrared fluorescence radiations, which make these materials possible candidates in high power laser applications.

Glasses containing other rare-earth elements such as gadolinium were studied especially due to their interesting structural and magnetic properties [5, 6].

On the other hand, glasses based on  $Bi_2O_3$  heavy metal oxide attracted a great deal of interest due to their important applications in the field of glass ceramics, layers for optical and electronic devices, thermal and mechanical sensor, reflecting windows, etc. [7, 8]. Due to the small field strength of  $Bi^{3+}$  ions,  $Bi_2O_3$  cannot be considered as a network former oxide. However, in combination with other oxides (i.e.,  $B_2O_3$  or  $PbO$ ), glass formation is possible in a relatively large composition range [8]. The interest for  $Bi_2O_3$  as a network forming oxide is increased by the fact that bismuth ions are known to have more than one stable coordination generating several structural units.

In this view, we considered the  $3Bi_2O_3 \cdot PbO$  glass matrix to be a very interesting host for the gadolinium and neodymium ions. In order to obtain information concerning magnetic and spectroscopic properties of bismuthate glasses containing gadolinium and neodymium ions we studied the  $xR_2O_3(1-x)(3Bi_2O_3 \cdot PbO)$  glass system, where  $R = Gd$  and  $Nd$ , by means of IR spectroscopy, magnetic susceptibility and density measurements.

### Experimental

Samples of the  $xR_2O_3(1-x)[3Bi_2O_3 \cdot PbO]$  vitreous system where  $R = Gd$  and  $Nd$  and  $x = 0.02, 0.05, 0.10, 0.15$  and  $0.20$  (in addition,  $x=0.25$  and  $0.30$ , for the  $R=Nd$  samples) were obtained using reagent grade  $Bi_2O_3$ ,  $PbO$ ,  $Gd_2O_3$  and  $Nd_2O_3$ . First, the base  $3Bi_2O_3 \cdot PbO$  glass was prepared by mixing suitable amounts of  $Bi_2O_3$  and  $PbO$  and melting the mixture

at 1100°C for 15 minutes. The melt was quenched on a refractory steel block. The obtained base glass was crushed and powdered. Appropriate amounts of  $Gd_2O_3$  or  $Nd_2O_3$  and  $3Bi_2O_3 \cdot PbO$  glass powder were mixed and milled in an agate ball mill for 30 minutes. Then, the mixtures were melted at 1100°C for 15 minutes. The glass samples were obtained by pouring the melts on stainless steel.

X-ray diffraction investigation of the samples did not reveal crystalline phases.

IR spectra were recorded in the  $400 \div 2000 \text{ cm}^{-1}$  range with an EQUINOX 55 spectrophotometer using the KBr pellet technique.

Magnetic susceptibility measurements were performed on a Faraday type balance in the 80 to 300 K temperature range.

Density measurements were performed using the picnometric method with water as the reference immersion liquid.

### Results and discussion

Fig.1 shows the infrared absorption spectra recorded for some of the  $xR_2O_3(1-x)[3Bi_2O_3 \cdot PbO]$  glasses with  $R = Nd$ .

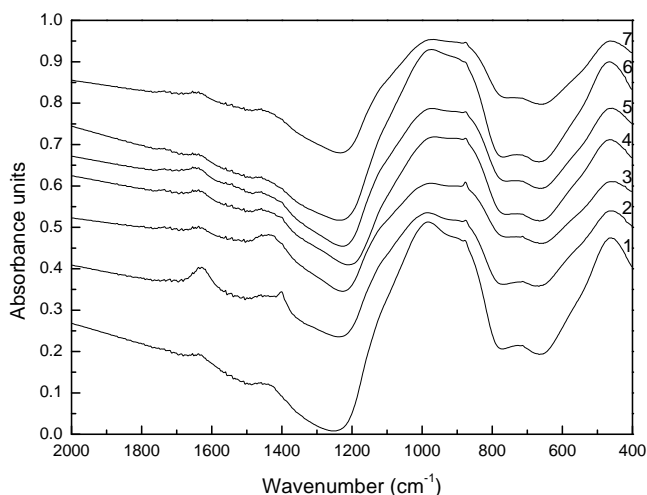


**Fig. 1.** IR absorption spectra of some of the  $xR_2O_3(1-x)[3Bi_2O_3 \cdot PbO]$  glasses with  $R = Nd$  ( $x=0$  (1),  $x=0.05$  (2),  $x=0.10$  (3),  $x=0.15$  (4),  $x=0.20$  (5),  $x=0.25$  (6) and  $x=0.30$  (7)).

A simple inspection of the spectral features of the spectra presented in Fig.1 shows that they are those characteristic of the base glass matrix,  $3Bi_2O_3 \cdot PbO$ , and no dramatic changes occur with increasing the  $Nd_2O_3$  content,  $x$ , of the samples. The same spectral features and weak modifications determined by varying the rare-earth oxide content were evidenced for the glasses with  $R = Gd$ .

Some of the IR spectral features observed for the  $xR_2O_3(1-x)[3Bi_2O_3 \cdot PbO]$  glasses studied by us are associated to the structural units involving the  $Bi^{3+}$  cation. Thus, several fundamental vibrational bands, such as those at about 460, 600 and  $855\text{ cm}^{-1}$ , are assigned to the Bi-O group [9-11].

The absorption band from  $855\text{ cm}^{-1}$  represents the convolution of the absorption bands reported for different bismuthate glasses at 847 and  $860\text{ cm}^{-1}$ , assigned to the total symmetric stretching vibrations of the  $[BiO_3]$  and  $[BiO_6]$  polyhedra, respectively [9-11]. In bismuthate glasses the  $[BiO_3]$  polyhedra play the glass network former unit role while the  $[BiO_6]$  play the glass network modifier unit role [10]. Based on the IR spectra obtained for the  $xR_2O_3(1-x)[3Bi_2O_3 \cdot PbO]$  glasses, we assumed that the structure of these glasses is built up of both  $[BiO_3]$  and  $[BiO_6]$  structural units.

The increase of the  $R_2O_3$  content,  $x$ , of the  $xR_2O_3(1-x)[3Bi_2O_3 \cdot PbO]$  samples determines the increase of the absorption band at  $855\text{ cm}^{-1}$  and its slow shift to  $850\text{ cm}^{-1}$ . This suggests the increase of the amount of  $[BiO_3]$  structural units with increasing  $x$  and is due to the increase of the number of nonbridging oxygens provided by the  $R^{3+}$  ions, having as effect the conversion of  $[BiO_6]$  into  $[BiO_3]$  structural units. Thus, the presence of gadolinium or neodymium ions influences the surrounding of the  $Bi^{3+}$  cations favourizing the formation of  $[BiO_3]$  units. In this view we mention two important facts that were previously reported [9]: (i) the bonding strength of Bi-O is higher in the  $[BiO_3]$  units than that in the  $[BiO_6]$  units and (ii) the degree of the connectivity of the glass network increases with increasing number of  $[BiO_3]$  polyhedra.

The IR absorption band from  $460\text{ cm}^{-1}$  is also related to the  $[BiO_6]$  polyhedra [11]. The increase of the  $Nd_2O_3$  content of the  $xR_2O_3(1-x)[3Bi_2O_3 \cdot PbO]$  glasses with  $R=Nd$  determines a slow shift of this band to higher wave numbers, namely to  $471\text{ cm}^{-1}$  for  $x=0.30$ . This is due to the increase of the degree of distorsion of the  $[BiO_6]$  polyhedra with increasing the  $Nd_2O_3$  content of the samples.

The IR spectra of the  $xR_2O_3(1-x)[3Bi_2O_3 \cdot PbO]$  glasses contain also some spectral features that are not related to the structural units involving  $Bi^{3+}$  cations. Thus, the absorption band at about  $700\text{ cm}^{-1}$  is due probably to the vibrations of the Nd-O group (the IR spectra of the crystalline  $Nd_2O_3$  shows an absorption band at  $655\text{ cm}^{-1}$  assigned to the Nd-O vibrations).

The structural changes observed by varying the  $R_2O_3$  content of  $xR_2O_3(1-x)[3Bi_2O_3 \cdot PbO]$  glasses and evidenced by the IR investigation suggest that the gadolinium and neodymium ions play a network modifier role in these glasses. Such a behaviour was previously reported for other rare earth ions glasses, too [12].

Fig.2 shows the variation of density as function of the neodymium ion content of the  $xR_2O_3(1-x)[3Bi_2O_3 \cdot PbO]$  glasses. The estimated error for the determined density values was less than  $0.02\text{ g/cm}^3$ .

The addition of the heavy rare-earth ions to an inert glass matrix would lead to a linear increase of the density with respect to  $x$  due to the higher number such accommodated in the host matrix. Fig.2 shows a very non-regular density-rare-earth oxide content dependence of the  $xR_2O_3(1-x)[3Bi_2O_3 \cdot PbO]$  glasses. This behaviour suggests that a more complicated mechanism, implying also the structural changes that occur with increasing rare-earth oxide content of the samples, must be considered to explain the density-composition dependence. Thus, density data support the assumption based on the IR spectroscopy data that increasing the rare-earth oxide content of the  $xR_2O_3(1-x)[3Bi_2O_3 \cdot PbO]$  glasses produce structural changes in the host glass matrix.

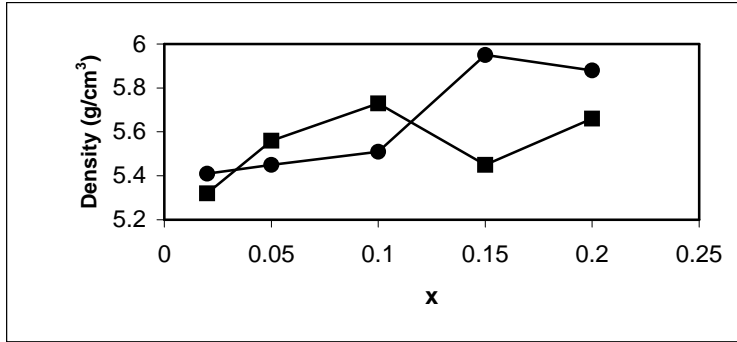


**Fig. 2.** Compositional variation of the density for some of the  $xR_2O_3(1-x)[3Bi_2O_3 \cdot PbO]$  glasses with  $R = Nd$  (●) and  $R=Gd$  (■).

Fig.3 presents the dependence of the reciprocal magnetic susceptibility,  $\chi^{-1}$ , as function of temperature for some of the  $xR_2O_3(1-x)[3Bi_2O_3 \cdot PbO]$  glasses with  $R=Gd$ . The data collapse to straight lines indicating a Curie or a Curie-Weiss type behaviour, described by

$$\chi^{-1} = (T - \theta_p) / C \quad (1)$$

where  $C$  is the Curie constant and  $\theta_p$  is the paramagnetic Curie temperature and  $T$  is the temperature. The same behaviour was found for all the  $xR_2O_3(1-x)[3Bi_2O_3 \cdot PbO]$  glasses studied in the present paper.

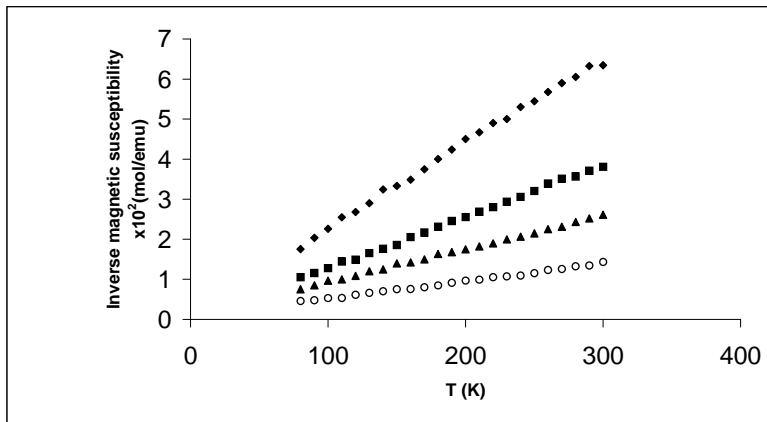


**Fig. 3.** Compositional variation of the density for some of the  $xR_2O_3(1-x)[3Bi_2O_3 \cdot PbO]$  glasses with  $R = Gd$  ( $x=0.02$  (◆),  $x=0.05$  (■),  $x=0.10$  (▲) and  $x=0.15$  (o)).

The magnetic behaviour of the  $xR_2O_3(1-x)[3Bi_2O_3 \cdot PbO]$  glasses was assumed to be due to the presence of the  $R^{3+}$  ions. The  $3Bi_2O_3 \cdot PbO$  host glass matrix was found diamagnetic and the experimental magnetic susceptibility data obtained for the  $xR_2O_3(1-x)[3Bi_2O_3 \cdot PbO]$  glasses were corrected taking into account this diamagnetic contribution.

The compositional dependence of the paramagnetic Curie temperature,  $\theta_p$ , is given in Fig.4.

The analysis of magnetic susceptibility data and of the data presented in figure 4 suggests that for the  $xR_2O_3(1-x)[3Bi_2O_3 \cdot PbO]$  glasses with  $0.02 \leq x \leq 0.05$  the magnetic  $R^{3+}$  ions are isolated and no magnetic order is present. The glasses with  $x > 0.05$  show a mictomagnetic type behaviour, where both isolated and exchange coupled neodymium ions are present in the glass matrix.

The negative and small values of the paramagnetic Curie temperature  $\theta_p$  ( $|\theta_p| \leq 9$  K for the  $R=Gd$  samples and  $|\theta_p| \leq 25$  for the  $R=Nd$  samples) for  $x > 0.05$  (see Fig.4) suggest that the exchange interactions between the  $R^{3+}$  ions are weak and predominantly antiferromagnetic.

The C values were used to calculate the magnetic moment of the  $R^{3+}$  ions present in the  $xR_2O_3(1-x)[3Bi_2O_3 \cdot PbO]$  glasses,  $\mu$ . The obtained  $\mu$  values were very close to the values corresponding to the free  $R^{3+}$  ions, namely  $3.68\mu_B$  for neodymium and  $7.9\mu_B$  for gadolinium, where  $\mu_B$  is the Bohr magneton [13, 14]. This behaviour is in agreement with the assumption of weak antiferromagnetic interactions between the  $R^{3+}$  ions.

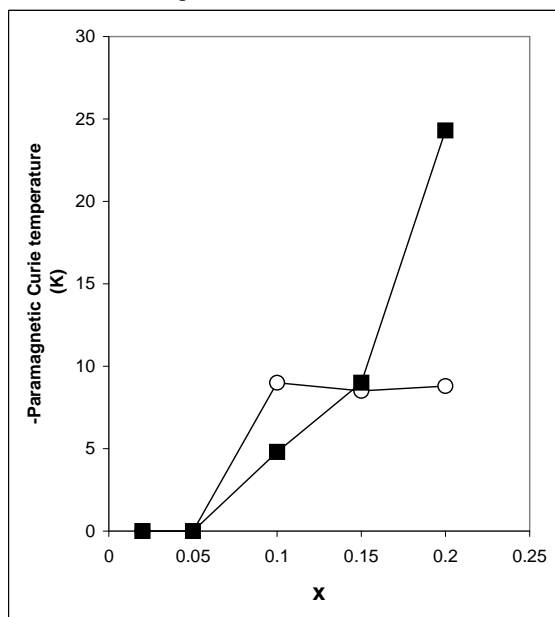


**Fig. 4.** Compositional variation of the paramagnetic Curie temperature of  $xR_2O_3(1-x)[3Bi_2O_3 \cdot PbO]$  glasses with  $R=Gd$  (○) and  $R=Nd$  (■).

No composition dependence of  $\mu$  was observed for the  $xR_2O_3(1-x)[3Bi_2O_3 \cdot PbO]$ , in agreement with the data reported for other oxide glasses containing other oxide glasses containing neodymium and gadolinium ions [15, 16].

Finally, note that the structural modifications produced by increasing the neodymium and gadolinium ion content of the  $xR_2O_3(1-x)[3Bi_2O_3 \cdot PbO]$  glasses seems to exert a neglectable influence on their magnetic behaviour.

## Conclusions

IR spectroscopic investigation of  $x\text{R}_2\text{O}_3(1-x)[3\text{Bi}_2\text{O}_3\cdot\text{PbO}]$  glasses with  $\text{R}=\text{Gd}$  and  $\text{Nd}$  shows that variation of the rare-earth oxide content of the samples,  $x$ , produce some structural changes of the host glass matrix. Density data support this assumption.

Magnetic susceptibility data show that at low rare-earth oxide content ( $x\leq 0.05$ ) the  $x\text{R}_2\text{O}_3(1-x)[3\text{Bi}_2\text{O}_3\cdot\text{PbO}]$  glasses present a Curie type paramagnetic behaviour, while for higher  $x$  values present a Curie-Weiss type behaviour.

## REFERENCES

1. B.Karthikeyan, S.Mohan, *Structural, optical and glass transition studies of  $\text{Nd}^{3+}$  doped lead bismuth borate glasses*, Physics B, 334 (2003) 298-302.
2. G.A.Kumar, E.de la Rosa-Cruz, A.Martinez, N.V.Unnikrishnan, K.Ueda, *Influence of borate content on the radiative properties of  $\text{Nd}^{3+}$  ions in fluorophosphate glasses*, J. Phys. Chem. Solids, 64 (2003) 69-76.
3. H.Li, J.D.Vienna, M.qian, Z.Wang, J.G.Darb, D.K.Peeler, *Neodymium (III) in alumino-borosilicate glasses*, J. Non-Cryst. Solids 278 (2000) 35-57.
4. J.D.Vienne, B.J.Riley, M.J.Schweiger, D.E.Smith, D.K.Peeler, I.A. Reamer, *Property Data for Simulated Americium/Curium Glasses*, PNNL-13009, Pacific Northwest National Laboratory, Richland, Washington, 1999.
5. S.Simon, I.Ardelean, S.Filip, I.Bratu, I.Cosma, *Structure and magnetic properties of  $\text{Bi}_2\text{O}_3\text{-GeO}_2\text{-Gd}_2\text{O}_3$  glasses*, Solid State Commun. 116 (2000) 83-86.
6. E.Culea, A.Pop, I.Cosma, *Magnetic behaviour of  $x\text{Gd}_2\text{O}_3(1-x)\text{Na}_2\text{B}_4\text{O}_7$  glasses*, J.Magn.Magnetic Mat. 157 (1996) 163-165.
7. A.Pan, A.Ghosh, *A new family of lead-bismuthate glass with a large transmitting window*, J. Non-Cryst. Solids 271 (2000) 157-161.
8. K.Kobayashbi, *Development of IR transmitting glasses*, J. Non-Cryst. Solids 316 (2003) 403-406.
9. H.Zheng, R.Xu, J.D.Mackenzie, *IR spectroscopic properties of some lead bismuthate glasses*, J. Mater. Res. 4 (1989) 911.
10. V.Dimitrov, Y.Dimitriev, A.Montenero, J. Non-Cryst. Solids 180 (1994) 51.
11. L.Baia, R.Stefan, W.Kiefer, J.Pop, S.Simon, *Structural investigation of cooper doped  $\text{B}_2\text{O}_3\text{-Bi}_2\text{O}_3$  glasses with high bismuth oxide content*, J. Non-Cryst. Solids 303 (2002) 379.
12. E.Culea, T.Ristoiu, I.Bratu, D.Ristoiu, *Structural and magnetic behaviour of some borate glasses containing europium ions*, Mat.Sci.& Engn. B 75 (2000) 82-85.
13. E.Burzo, *Fizica materialelor magnetice*, Edit. Academiei, 1979, pg.232.
14. A.Clare, *Rare Elements in Glasses*, Key Engineering Materials, edited by J.E.SHELBY, Vol.94-95 (Trans.Tech.publications) 1994, pp.161-181.
15. E.Culea, I.Bratu, *IR spectroscopic and magnetic behaviour of  $x\text{Nd}_2\text{O}_3(1-x)\text{Na}_2\text{B}_4\text{O}_7$  glasses*, Acta Materialia 49 (2001) 123-125.
16. T.Ristoiu, E.Culea, I.Bratu, *Spectroscopic and magnetic behaviour of some borate glasses containing gadolinium ions*, Materials Letters 41 (1999) 135-138.

**BIOPHYSICS AND ENVIRONMENTAL PHYSICS****RATCHET MOTION AND QUANTUM MOTORS IN BIOLOGICAL SYSTEMS****DAN GRECU<sup>1</sup>, ANCA VISINESCU<sup>1</sup>, IOAN TURCU<sup>2</sup>**<sup>1</sup> *Department of Theoretical Physics, National Institute of Physics and Nuclear Engineering, Magurele, P.O.Box MG-6, 76900 Bucharest, Romania, e-mail: dgrecu@theor1.theory.nipne.ro*<sup>2</sup> *National R&D Institute for Isotopic and Molecular Technologies, P.O.Box 700, RO-400293, Cluj-Napoca 5, Romania*

**ABSTRACT.** Molecular motors are nanometric cyclic machines able to convert chemical energy into mechanical work. The energy converted at each cycle is only several times larger than the average energy of the thermal bath, and consequently the fluctuations are very large and important, and their physical description must be necessarily stochastic. There are several mechano-chemical coupling mechanisms, all of them working far from equilibrium molecular states. One of the most frequently coupling mechanisms used by biomolecular motors is the Brownian ratchet mechanism. Essentially the motion is driven by chemically released energy, the motor kinetic being described as a vectorial transport biased by non-equilibrium fluctuations. Our purpose is to summarize few existing results emphasizing the appropriate mathematical models for two simple molecular ratchet motors: the particle transport in asymmetric fluctuation potentials and the enzyme DNA polymerase.

**Introduction**

In his well-known Lectures in Physics (vol.1, ch. 46) R. Feynman has used the ratchet model to prove that a useful work cannot be extracted from equilibrium fluctuations. But this is not the case when we have to deal with non-equilibrium noise. It was shown by Magnasco [1] that in an asymmetric potential, work can be extracted from non-equilibrium fluctuations and such a system can work as a molecular motor. Since than this very attractive idea was studied by many authors [2]-[18], as it represents an attractive theoretical model for the unidirectional movement of kinesin and myosin molecules along structural filaments.

Let us consider a Brownian particle in one dimension, whose motion is governed by the Newtonian equation

$$m \ddot{x} + V'(x) = -\eta \dot{x} + \xi \quad (1)$$

where  $x(t)$  is the position of the particle,  $m$  its mass,  $V(x)$  is a periodic (period  $L$ ) asymmetric potential,  $\eta$  friction coefficient and  $\xi(t)$  is a Gaussian white noise of zero mean  $\langle \xi(t) \rangle = 0$  and satisfying the fluctuation-dissipation relation.

$$\langle \xi(t_1) \xi(t_2) \rangle = 2\eta k_B T \delta(t_1 - t_2) \quad (2)$$

Here  $k_B$  is Boltzmann's constant and  $T$  the temperature of the surrounding bath at equilibrium. A typical saw-tooth form for  $V(x)$  (see fig.1) is considered as an example of the asymmetric potential.

In many cases the inertial effects can be neglected and the dynamics of the state variable  $x(t)$  is governed by an overdamped Langevin equation

$$\eta \dot{x} = -V'(x) + \xi(t) \quad (3)$$

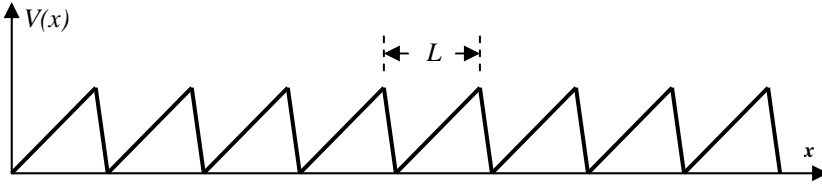


Fig. 1. Asymmetric saw-tooth potential

The quantity of foremost interest is the average particle current

$$\langle \dot{x} \rangle = \left\langle \lim_{t \rightarrow \infty} \frac{x(t) - x(0)}{t} \right\rangle \quad (4)$$

Taking into account the periodicity property of  $V(x)$  it can be written also as

$$\langle \dot{x} \rangle = - \lim_{t \rightarrow \infty} \frac{1}{t} \int_0^t dt' \int_0^L dx \frac{V'(x)}{\eta} P(x, t') \quad (5)$$

where  $P(x, t)$  is the probability density associated to the random process described by (2) (it is periodic in space and normalized to unity in the unit cell  $[0, L]$ ). It can be proved that in the long time limit the system described by (3) will evolve towards a Boltzmann steady state solution and this implies that the net current vanishes. In other words we find once again that no preferential direction of the random Brownian motion exists at thermal equilibrium, even if the potential in which the particles move is asymmetric.

This is no more true if an additional colored noise  $Z(t)$  is applied to the particle. We assume that the correlations in  $Z(t)$  are over long time intervals compared to the thermal fluctuations time scale. That in this case a net current to the left is obtained, can be seen from a very simple reasoning. Let us assume that the effect of  $Z(t)$  is to place the particle in two distinct configurations. In the first (denoted by (a)) the particle is just in the potential  $V(x)$  and localized near one of the minima of  $V(x)$ . After a time  $\tau_1$  particle's state is switched to a free one (denoted by (b)) and the particle start to diffuse nearly uniform to the left and to the right. After a time  $\tau_2$  particle's state is switched back to the state (a) (the time scales of the switches are small compared to the equilibrium time in  $V(x)$  and the diffusion time  $\frac{\xi L^2}{k_B T}$ ). Because the diffusion in state (b) starts from a region closer to the

basin of attraction of the next left unit cell, it is a higher probability that the particle will be captured in the next left cell than in the right one. The result is a net flow of probability to the left and a steady current in this direction. In this scenario both the anisotropy of the potential  $V(x)$  and the non-white property of the noise play an essential role, and it will be referred as the "flashing ratchet".

Another possibility is to assume that the temperature  $T$  of the Gaussian white noise is subjected to periodic temporal modulation with period  $\tau$ , i.e.

$$\langle \xi(t_1) \xi(t_2) \rangle = 2\eta k_B T(t) \delta(t_1 - t_2) \quad (6)$$

A simple example is

$$T(t) = \bar{T} \left( 1 + A \left( \text{sign} \frac{2\pi t}{\tau} \right) \right) \quad (7)$$



where  $\text{sign}(x)$  denotes the signum function and we assume  $|A| < 1$ . Then the temperature jumps from  $\bar{T}(1-|A|)$ ;  $\bar{T}(1+|A|)$  at every half period  $\frac{\tau}{2}$ . This situation will be called “thermal ratchet”. In the first interval the thermal energy is kept at the value  $k_B \bar{T}(1-|A|)$  much smaller than the potential barrier and the particle is localized in a minimum of the potential  $V(x)$ . Then the thermal energy jumps to  $k_B \bar{T}(1+|A|)$  much larger than the potential barrier and the particle starts to diffuse freely. The same argument as before leads us to the conclusion that a net current to the left will appear. The energy necessary to produce these jumps of the temperature might come from the hydrolysis of the adenosine triphosphate. The ATP hydrolysis energy is quickly converted into a very irregular vibrational motion of the fast internal degrees of freedom of the enzyme, giving rise of the local temperature. This excess heat spreads out after that and the temperature falls down and the process repeats again in a stochastic manner.

If we denote by  $P_+(t)$  the probability of the potential to be in the state  $V_+ = V(x)$  at time  $t$ , and by  $P_-(t)$  the probability to be in the state  $V_- = 0$  (flashing ratchet) they were satisfying a master equation

$$\frac{\partial}{\partial t} \begin{pmatrix} P_+ \\ P_- \end{pmatrix} = \gamma \begin{pmatrix} -b & a \\ b & -a \end{pmatrix} \begin{pmatrix} P_+ \\ P_- \end{pmatrix} \quad (8)$$

Here  $\gamma$  defines the correlation time scale of the flashing,  $\tau_c = \gamma^{-1}$ , and the numbers  $a$  and  $b$  are specifying the steady state probabilities of the potential,  $\frac{a}{a+b}$  to be in the state  $V_+$  and  $\frac{b}{a+b}$  in the state  $V_-$ .

The joint probability density of the particle to be found in the point  $x$  with the potential in one  $V_+$  or  $V_-$  state,  $\rho_{\pm}(x, t)$ , satisfies a coupled Fokker-Planck equation

$$\frac{\partial}{\partial t} \begin{pmatrix} \rho_+(x, t) \\ \rho_-(x, t) \end{pmatrix} = \begin{pmatrix} K_+ - b\gamma & a\gamma \\ b\gamma & K_- - a\gamma \end{pmatrix} \begin{pmatrix} \rho_+ \\ \rho_- \end{pmatrix} \quad (9)$$

where the position evolution operator is given by

$$K_{\pm} = \frac{1}{\xi} \frac{\partial}{\partial x} \left( \frac{(1 \pm 1)}{2} \frac{\partial V}{\partial x} + k_B T \frac{\partial}{\partial x} \right) \quad (10)$$

Periodic boundary conditions on  $[0, L]$  are considered. The marginal density for the position process is  $\rho(x, t) = \rho_+ + \rho_-$  and is normalized to unity. It satisfies a continuity equation

$$\frac{\partial \rho}{\partial t} + \frac{\partial J}{\partial x} = 0 \quad (11)$$

and the steady-state current is given by  $J = \lim_{t \rightarrow \infty} j(x, t)$  and must be independent of  $x$ .

Analytical calculations can be done only in some limiting situations, namely for a “slow flashing” limit when (small  $\gamma$ )  $J$  can be expanded as

$$J = \gamma J^{(1)} + \gamma^2 J^{(2)} + \dots \quad (12)$$

or a fast flashing limit ( $\tau_c \rightarrow 0$ ) when

$$J = \tau_c J_{(1)} + \tau_c^2 J_{(2)} + \dots \quad (13)$$

In both limit of very slow flashing ( $\gamma \rightarrow 0$ ) or very fast one ( $\tau_c \rightarrow 0$ ) we see that  $J \rightarrow 0$ . In the first case the current tends to the averaged current produced in each potential configuration, which is zero, while in the second case the result current would correspond to an averaged potential, which also vanishes. Consequently there is a optimal flashing rate  $\gamma$  giving a maximum current. Indeed, the numerical calculations give a net current to the left ( $J < 0$ ), depicted in fig.2. This is in complete agreement with the heuristic argument given above.

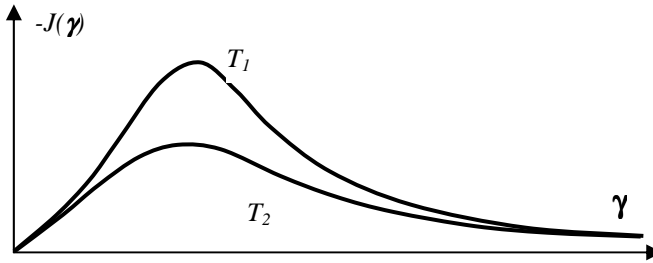


**Fig. 2.** The current  $J$  as a function of  $\gamma$  for two different temperatures  $T_1 < T_2$

The next step would be to move from the classical world and to take into account quantum effects. Recently a quantum ratchet was built [19]. The device, fabricated by nanolithography techniques, consists in an aluminum-doped gallium arsenide (GaAs/AlGaAs) quantum dot with a triangular shaped cavity, and the results support the idea that quantum effects can be observed. A first theoretical treatment [20] considers a quantum Brownian particle – an electron- at low temperature, moving in a periodic ratchet potential under the influence of quantum noise. The potential is tilted to the left and right by a slowly force (periodic or random in time). The theory predicts a finite current, even at very low temperature, an effect due to quantum tunneling. Many quantum devices could be constructed using these new concepts and the modern techniques of nanolithography.

## REFERENCES

1. M.O. Magnasco, *Phys. Rev. Lett.* **71**, 1477 (1993)
2. C.R. Doering, W. Horsthemke, J. Riordan, *Phys. Rev. Lett.* **72**, 2984 (1994)
3. C.R. Doering, *Nuovo Cimento D* **17**, 685 (1995)
4. M.O. Magnasco, *Phys. Rev. Lett.* **72**, 2656 (1994)

5. J. Prost, J.F. Chawin, L. Peliti, A. Adjari, *Phys. Rev. Lett.* **72**, 2652 (1994)
6. A. Adjari, D. Mukamel, L. Peliti, J. Prost, *J. Physique I* **4**, 1551 (1994)
7. R.D. Astumian, M. Bier, *Phys. Rev. Lett.* **72**, 1766 (1994)
8. M.M. Millonas, M.I. Dykman, *Phys. Lett. A* **185**, 65 (1994)
9. M.M. Millonas, *Phys. Rev. Lett.* **74**, 10 (1995)
10. R. Bartussek, P. Reimann, P. Hänggi, *Phys. Rev. Lett.* **76**, 1166 (1996)
11. P. Reimann, *Phys. Reports*, **270**, 149 (1997)
12. M. Bier, *Phys. Lett. A* **211**, 12 (1996)
13. F. Jülicher, A. Adjari, J. Prost, *Rev. Mod. Phys.* **69**, 1269 (1996)
14. H. Kamegawa, T. Hondou, F. Takagi, *Phys. Rev. Lett.* **80**, 5251 (1998)
15. J.M.R. Parrondo, *Phys. Rev. E* **57**, 7297 (1998)
16. C.R. Doering, *Physica A* **254**, 1 (1998)
17. P. Reimann, P. Hänggi, *Appl. Phys. A* **75**, 169 (2002)
18. P. Reimann, R. Bartussek, R. Häussler, P. Hänggi, *Phys. Lett. A* **215**, 26 (1996)
19. H. Linke, W. Sheng, A. Löfgren, Hongqi Xu, P. Omling, P.E. Lindelot, *Europhys. Lett.* **44**, 341 (1998)
20. P. Reimann, M. Grifoni, P. Hänggi, *Phys. Rev. Lett.* **79**, 10 (1997)

## CHARACTERISATION OF ORGANIC POLLUTANTS DETECTED IN SOMES RIVER BY GC/MS

Z. MOLDOVAN<sup>(1)</sup>, D J. M. BAYONA<sup>(2)</sup>

<sup>(1)</sup> *National Institute of Research and Development of Isotopic and Molecular  
Technology, 400293 Cluj-Napoca, P.O.B. 700, Romania  
E-mail: zaha@oc1.itim-cj.ro*

<sup>(2)</sup> *Instituto de Investigaciones Químicas y Ambientales de Barcelona,  
c/J. Girona 18-26, Spain*

### INTRODUCTION

The directives of the European Community indicates that all wastewater in the territories of the European Union have to be properly collected and subjected to biological treatment before being discharged in rivers waters. However in Romania the majority of wastewater, from high populated cities and industrial complex zones, is still discharged into surface waters without proper treatment. In respect to this, one of priority tasks is to determine the environmental distribution of organic pollutants in the surface waters

The present paper purpose is the mass spectrometric characterization of organic pollutants to evaluate the Structure of contaminant in the Somes-Tisa basin, from Transylvania (Romania) region and 2) study of photo-degradation processes of some types of pollutants on TiO<sub>2</sub> aerogels. In studied area it is some potential sources of pollution as:

-On the river Somes long of 250 km are as residents around of 800 000 people resulting an important quantity of synthetic compounds from domestic activity.

-In this area it is industrial activity as pharmaceutical, food, pulp and paper production as well as metallurgical production known as main sources of organic contaminants.

### EXPERIMENTAL

#### *a) Sample Preparation*

*Sample collection:* The 500 ml surface water (river water) from 1m under surface were collected and were stored at 5°C for maximum 5 days. For every sample 200 ml was acidified with 2N HCl to pH 2. *Cartridge condition:* Oasis 60mg cartridge (Waters) was conditioned with 6 ml dichloromethane, 6 ml acetonitrile and 6 ml of HPLC water. *Sample elution/1/:* Samples were percolated through the cartridge at a flow of 3 ml/min. The cartridge were rinsed with 1ml HPLC water (at a flow of 3ml/min) and dried by vacuum for 50 min. The elution was carried out with 2.5 ml of acetonitrile-dichloromethane (1:1) and 3.2 ml of dichloromethane. After elution the extract was transferred to vials and the excess of solvent was evaporated under a stream of nitrogen and than dissolved in iso-octane. The IS diphenilamine of 2 ppb were added at initial sample.

*b) Instrumentation.* The GC/MS analyses were performed using a Fisons MD 800 mass spectrometer operated in the EI mode to 70 eV. The source temperature was 230°C and emission current 300 µA. A HP-5MS (30x0.25mm) with 0.25µm film thickness containing 5% phenyl methyl siloxane was programmed from 90°C(1min) to 120°C at 10°C/min, from 120°C to 200°C at 3.50C/min and than to 315°C at 5°C/min (keeping this temperature for 11 min.)

### RESULTS AND DISCUSSION

The following families of compounds were detected:

1) *Steroidal* compounds (13 compounds) of type 5 $\beta$ -stanols C27 (*coprostanol*) C28 (*campestanol*) and C29 (*stigmastanol*) with base peak to m/z 215. The compound from 47.06 min is shown in the Fig.1. Their precursors, 5 $\beta$ -stenols as C27 (*cholesterol*), C28 (*campesterol*) and C29 (*Sitosterol*) are shown by ion chromatogram to m/z 213. They have a high chemical stability and are used as molecular biomarkers/2/ of human activity. The ratio of 5 $\beta$ -*colestanol* (*coprostanol*) to 5 $\beta$ -*Stigmastanol* is a precise indicator of fecal input/3/. In our samples the ratio was 4.2 resulting that they originating main from omnivore fecal mater (human+porcine).

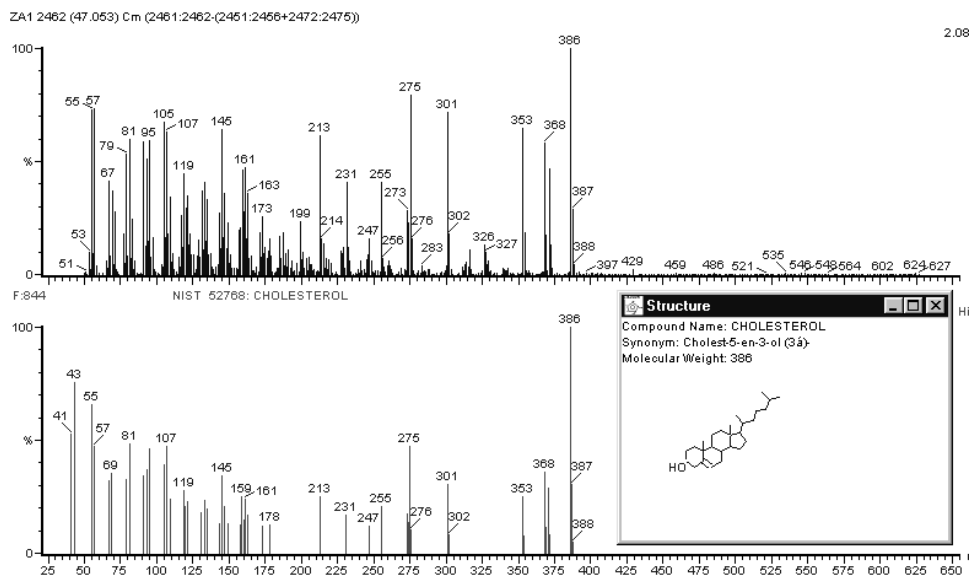


Fig. 1. Identification of compound from t=47.053(Cholesterol)

2) *Phthalate acid esters (PAEs)* esters widely used in different industrial activities. Their main application are as plasticizers for PVC resins, adhesives and cellulose film coating /4/. Analytical data about presence and levels of PAEs in surface water can be used to identification of contamination sources. The relative high abundance of unsaturated C22 amide, probable 17-docosenoicamide is to be mentioned.

3) A family of 8 *polyetoxyolate* compounds was detected. They have diagnostic ions m/z 89, 133, 177 (generally) and m/z=M-113 (specific). The probable structure and denomination will be presented in a future paper. The identification was made based on comparison of obtained MS with library MS.

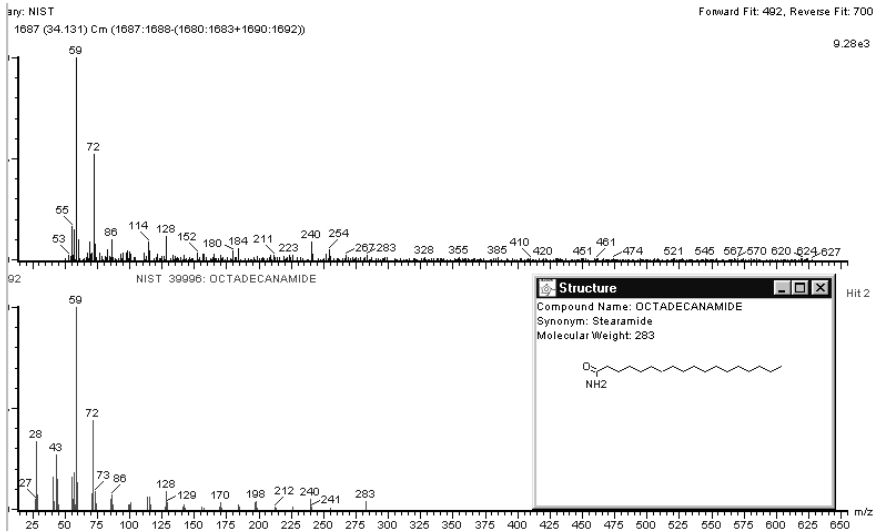
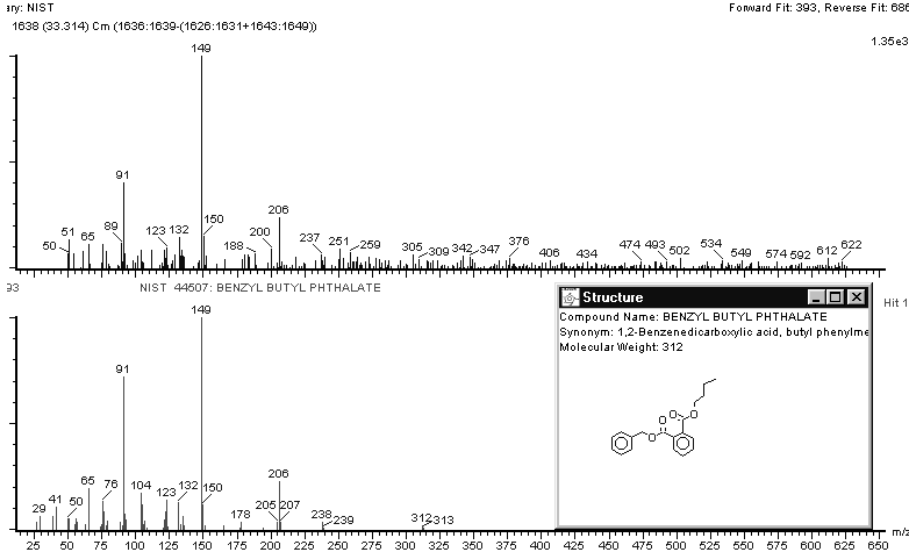
4) An important class of compounds is identified as *antioxidants* (14 compounds). They are compounds with high-branched chains/5/. Their probable structure will be also presented.

5) A number of 3 compounds were identified as *long chain amides* in the range C18-C22 (Fig. 3).

Their profile can be obtained by selected ion at m/z 149 (5 compounds). The high abundance of *Di-2-ethylhexyl phthalate (DEHP)* is to be mentioned.

6) A number of 9 pharmaceutical *compounds* were detected. They originated from municipal wastewater. These compounds could lead to ground water and soil and consequently accelerate the development of resistance in many disease organisms. Some mass spectra of

compounds identified as pharmaceuticals are shown. The *caffeine* (Fig. 4) is originating from coffee drink or as pharmaceuticals used as stimulant. The cocaine metabolite is present in smaller abundance and probable is originated from the consume of *cocaine* as a prohibit drug. *Triclosan* is a pharmaceutical used as antimicrobial. The compound *N-(2,3)-dihydro-1,5-dimethyl-3-oxo-2-Phenyl-1H Pyrazol-4-yl) Acetamide* is an analgesic and anti-inflammatory product. *Apazone (Azapropazone)* is a pharmaceuticals from Pyrazole class used for the treatment of Rheumatism inflammatory and Rheumatism articulate. Pentoxifylline is a xantine derivative used as a hemorrheologic agent/6/. The *Ethanoic acid, Bis(cyclohexylidenehydrazide)* is a compound of type *Cuprizone* used in Brain Pathology/7/.



## POLLUTANTS DETECTED IN SOMES RIVER BY GC/MS

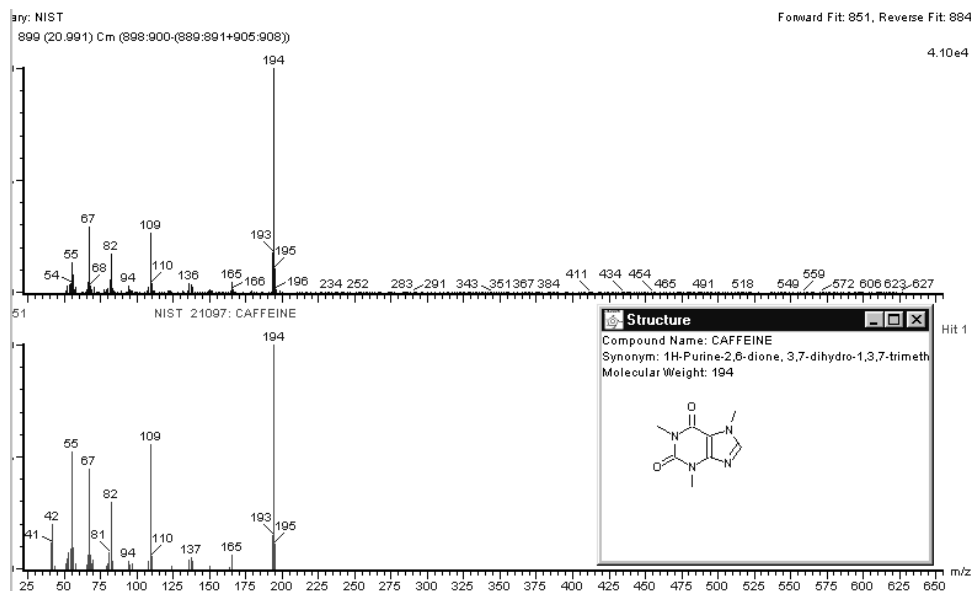


**Fig. 4.** Identification of the compound from t=20.991 (Caffeine)

7) A number of 5 compounds were identified as *long chain fatty acids* in the range C12-C18. Relative high abundance can be seen for the acid C16 and C18.

8) Some natural products as *Decanedioic acid dibutylester*, *Squalene* and *Vitamin E Acetate* were also detected in relative high concentration (*Squalene* 3.395 $\mu$ g/l)

9) The *alkyl esters of phosphoric acid* were identified in concentration of 1.067 $\mu$ g/l (*Phosphoric acid tri-iso-butyl ester*) and 0.107  $\mu$ g/l (*Phosphoric acid tri-n-butyl ester*).

## REFERENCES

- 1) Silvia Lacorte, Ingrid Guiffard, D. Fraisse and Damia Barcelo, *Anal. Chem.*, 72, (2000) 1430-1440
- 2) Cristina Maldonado, J. Dachs and J. M. Bayona, *Environ. Sci. Technol.* 33 (1999) 3290
- 3) R. P. Eveson and P. H. Bethell, *Archaeological Chemistry, ACS Symposium Series*, 1996, 157-172.
- 4) M. Guidoti, G. Macilenti and C. Cremisini, *Environmental International*, 23 (1997) 337
- 5) Z. Moldovan, and J. M. Bayona, *Rapid Comm. Mass Spectrom.* 14, (2000) 379-389
- 6) Patricia McCloskey, *Medications*, Springhouse Corporation, II Series, *Springhouse, Pennsylvania* 1994
- 7) G. K. Matsushima and P. Morell, *Brain Pathology* 11, (2001). 107-116

## MULTI - ELEMENT DETERMINATION BY NEUTRON – INDUCED PROMPT GAMMA – RAY ANALYSIS

**D. BĂRBOS, M. MLADIN, A DATCU**

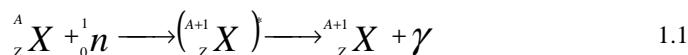
*Institute for Nuclear Research- Pitești*

### 1. Introduction

A prompt gamma neutron activation analysis (PGNAA) is an elemental and isotopic analytical technique in which prompt gamma – ray emitted within  $10^{-14}$ s after neutron capture reaction are measured. Although this analytical methodology is similar to instrumental neutron activation analysis (INAA), PGNAA is characterized by its capability for nondestructive multi – elemental analysis and by its ability to analyze elements that cannot be determinate by INAA. In addition, due to the negligibly low residual radioactivity after analyzing by PGNAA, same sample can be used for the other analytical methods.

According to calculation [1] the analytical sensitivity of PGNAA is higher than INAA under the same neutron and gamma – ray measurement conditions.

PGNAA technique is based on the interaction of the neutrons with the nuclei contained in a sample. Upon capturing a thermal neutron, a target nucleus gains energy, which produce a compound nucleus in an excited state. This process may be represented symbolically by the form:



Where  ${}^A_Z X$  is target and  ${}^{A+1}_Z X$  compound nuclei. The compound nucleus ( ${}^{A+1}_Z X$ )\* is produced in an excited state. The  $\gamma$  denotes the prompt gamma ray emitted from the instantaneous decay of the compound nuclide. These neutron capture gamma ray are usually emitted in less than  $10^{-13}$ s.

### 2. System construction

#### 2.1 Neutron and gamma filter and collimator

ACPR – TRIGA reactor is a LWR in an open pool and uses a fuel of mixed zirconium – hydride and 20%  ${}^{235}\text{U}$  enriched. This type of reactor can be operated at a maximum power peak of 20000MW in pulsed mode and 500kW maximum power level in steady – state mode.

Thermal neutron flux in central experimental hole is about  $10^{13}$ n/cm<sup>2</sup>\*s when reactor is operated in steady – state mode.

This reactor is provided with two (radial and tangential) horizontal beam tubes.

PGNAA system is linked to the radial beam tube of ACPR reactor. This solution was chosen because neutron diffractometer was linked at the radial beam tube of TRIGA – SSR reactor.

In Fig.1 schematic layout for neutron and gamma-ray filter and collimator is presented.



The filter is composed by a sintered nuclear graphite plug (L= 1413mm and  $\Phi=200$ mm) in which a two-diameter hole was bored. Over a length of 450mm hole diameter is 101.2mm and over the rest the length it is 100mm. In the largest diameter portion a silicon single crystal having a length of 450mm and diameter of 101mm was inserted. Silicon single crystal acts as a filter by rejecting most of the fast neutrons and gamma rays and in the same time transmitting most of thermal neutrons. The total cross – section decrease to a minimum value close to 0.05MeV energy[2]. Thermal neutron transmission factor for silicon single crystal at room temperature is about 40%. Our computation showed that a 50% increase of thermal neutron flux transmission could be reached if the single crystal is cooled to 77K.

If a bismuth single crystal would replace the silicon single crystal, the results would be more striking. If we note the ratio:

$$R = \Phi(E < 10\text{eV}) / \Phi(0.4\text{eV} > E < 10\text{eV})$$

It results:

- for silicon single crystal at 300K: R = 71
- for silicon single crystal at 77K: R = 96
- for bismuth single crystal at 300K: R = 5580
- for bismuth single crystal at 77K: R = 35700

Neutron beam collimation is obtained by using four collimators placed in the rear side of neutron filter. The first is filled with borated paraffin (30% B) with a length of 575mm. The second collimator consists of several annuli of lead with overall length of 575mm. The hole bored in this collimator is cone – shaped with the final inner diameter of 50mm.

Behind this collimator is a beam shutter. The third collimator is made of lead annuli with the inner diameter of 50mm and the length of 115mm. The fourth collimator is water filled cylinder and inside is a circular hole of 50mm diameter . Last collimator element has 1000mm length. The effect obtained with these collimators is a narrow neutron beam directed inside the beam catcher. This mixed collimator (graphite, boron paraffin, lead and water) has another advantage: low neutron and gamma background around the direct neutron beam.

## 2.2. Detectors

The gamma–ray detection system consist of an HpGe detector of 16% efficiency (detector model GC1518) with 1.85 keV resolution capability. The HpGe is mounted with its axis at 90° with respect to the incident neutron beam at distance about 200mm from the sample position.

In order to increase sample – detector distance up to 400mm the Dewar vessel is placed on a mobile pathway.

An inner Pb shielding of 100 thickness and 135 mm length surrounds the HpGe detector. The incident gamma –ray beam from the irradiated sample must pass through a 50mm diameter collimator and 135mm length.

Since the gamma – ray detector is susceptible to damage by either fast or thermal neutrons, the end cap of HpGe detector is surrounded by a fused LiF (35%  $^6\text{Li}$  enriched) cup with thickness of 30mm. The isotope  $^6\text{Li}$  absorbs thermal neutron primarily by reaction  $^6\text{Li}(n,\alpha)^3\text{He}$  and this reaction has the advantage that the reaction product is in ground state and no gamma – ray will emitted.

In the gamma–ray spectrum is possible to appear the 693keV peak caused by inelastic fast neutron scattering to the first excited state in  $^{72}\text{Ge}$ . A second peak at 595keV is a measure of the capture of thermal neutron by HpGe detector.

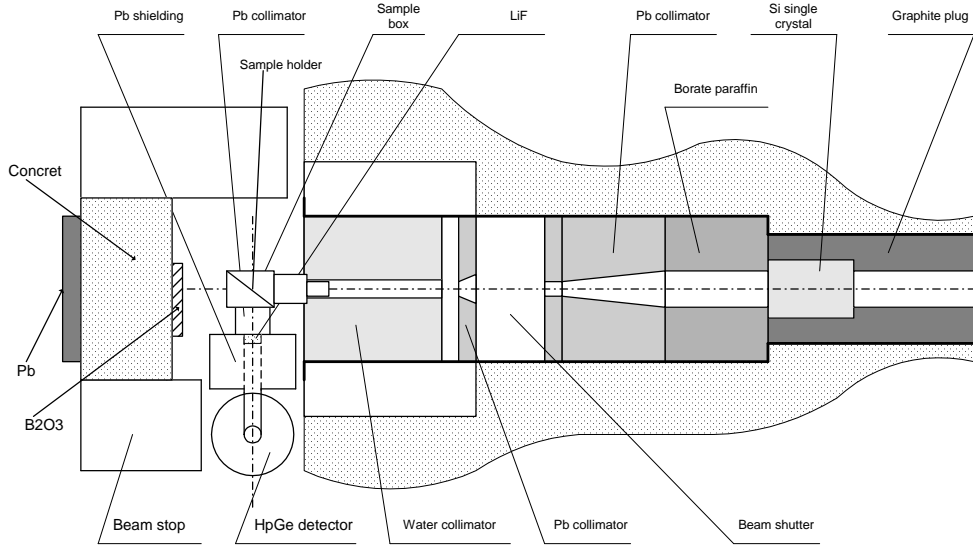


**Fig. 1.** Schematic layout of PGNAA facility at TRIGA - ACPR reactor

### 3. Characteristics of the system

#### 3.1. Neutron beam

Neutron beam position and shape in the sample holder location was determined by  $^{109}\text{Cd}$  foil irradiation for 46min. The obtained image was transferred to MG2 radiography. In this film was observed a circular spot, with 50mm diameter, a good contrast and slightly diffuse edge and homogenous as shown in Fig.2. The analysis of this image shown thermal neutron beam good collimation in circular beam with 50mm diameter right at 300mm distance from collimator exit. It was not observed any other impression besides the central spot.

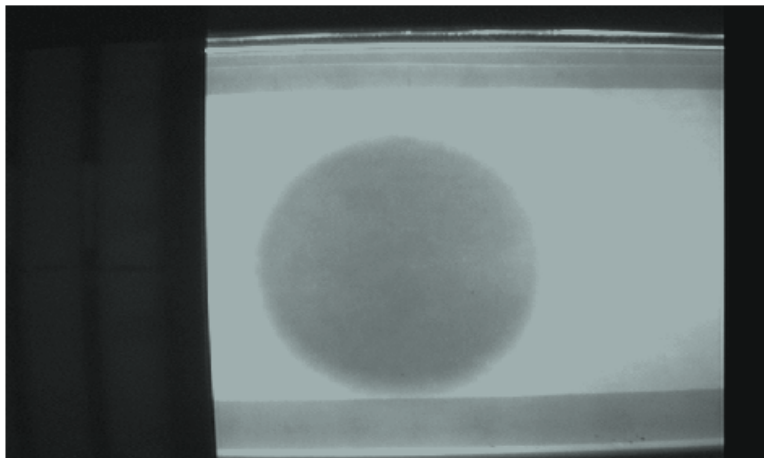


**Fig. 2.** Neutron beam radiographic image

Thermal neutron flux at the sample position was measured by foil activation method. There were irradiated two Au 100% thin foils. One of them was covered with 1mm thickness cadmium. The bare foil was irradiated 1h and cadmium covered foil 4h at 100kW reactor power level. From foil induced activity was computed thermal neutron flux with neutron energy lower than cadmium cut-off ( $E < 0.05\text{eV}$ ):

$$\Phi_{\text{scd}} = 7.52 \cdot 10^5 \text{ n/cm}^2/\text{s}$$

and cadmium ratio is:  $R_{\text{Cd}} = 80$ .

**3.2. Measurements results**

$^{10}\text{B}$  and  $^{157}\text{Gd}$  concentrations in samples extracted from Cernavoda NPP shut – down systems were determined by reporting the count rate/gram of the peaks of the analysed samples to the standard ones. Irradiation time was 1000s and sample weight ranged between 0.014 – 0.065g. Isotopes determination accuracy was less than 4%.

Measurements for method sensitivity determination were done for B, Gd and Sm. For this a number of aqueous dilutions, which contained the specified elements in various concentrations, were prepared .In figures 3,4 and 5, the curves which show the counts rate versus elemental concentration, are represented. Sensitivities and concentrations are presented in Table 1.

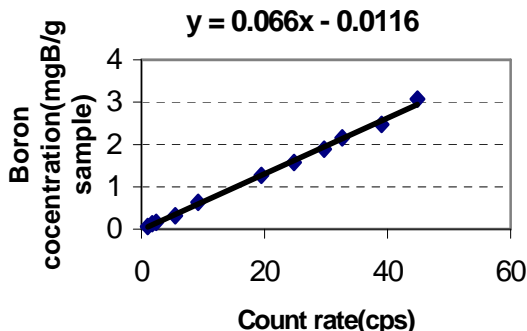


Fig. 3. Boron solution calibration curve

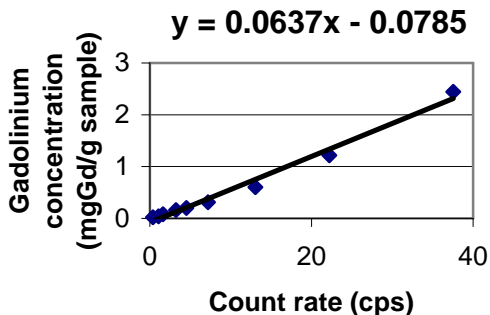


Fig. 4. Gadolinium solution calibration curve

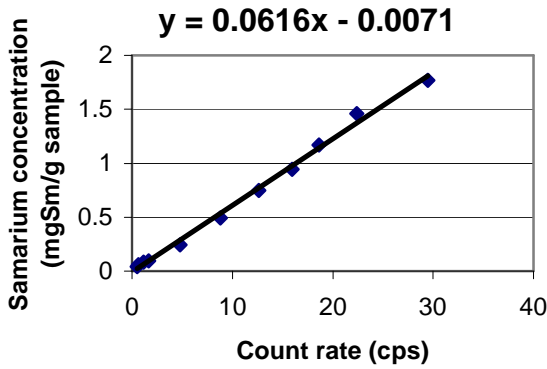


Fig. 5. Samarium solution calibration curve

Table 1.

Element	Concentration (mg /g sample)	Sensitivity (cps/mg)
B	0.06 – 3.072	8
Gd	0.024 – 2.44	10
Sm	0.0404 – 1.77	8

## CONCLUSIONS

To improve the PGNAA system performance thermal neutron flux intensity has to be increased. This can be achieved through reactor power raise up to 250 – 300kW and through replacement of silicon single crystal with a bismuth one.

For the same aimed acquisition system, which can be operated in Compton, suppression mode is needed.

## REFERENCES

1. Isenhour, T.L., G.H. Morrison, *Det. Anal. Chem.* 38(1966)/162
2. Hanna, A.G. -, *Nucl. Inst. And Meth.* 188(1981) 619-627
3. D. Barbos, M. Mladin, *R. I.* 2056/1993

## BIOMEDICAL APPLICATIONS OF GAS CHROMATOGRAPHY- MASS SPECTROMETRY

MONICA CULEA, ONUC COZAR, DUMITRU RISTOIU

*Univ. Babeș-Bolyai, Dept. of Atomic, Nuclear and Environmental  
Physics, 1 Kogalniceanu str, 3400 Cluj-Napoca, Romania; e-mail:  
mculea@phys.ubbcluj.ro*

**ABSTRACT.** Qualitative and quantitative determinations of some aroma compounds, lipids, vitamins, drugs, amino acids from biological media by using a gas chromatography-mass-spectrometric technique (GC/MS) are presented. Stable isotopic labeled homologous compounds or compounds from the same chemical class were chosen for the internal standard. Good validation parameters were obtained for precision, accuracy (C.V.<10%), linearity in the range of interest (mean  $r = 0.99$ ), the limit of detection and quantitation, selectivity and specificity. Chromatography was performed on a 5% phenyl methylpolysiloxane column (15 or 30 m x 0.25 mm I.D., 0.25  $\mu\text{m}$ ) operated in suitable temperature programs.

### Introduction

In the last years the number of procedures using extraction of organic compounds from different matrices has increased. Trace analyses involve pretreatment: of the samples, extraction and concentration procedure to increase the analyte concentration to within instrument sensitivity. The extraction procedure, internal standard selection and method validation are the steps to follow for quantitative analyses by using gas chromatography-mass spectrometric technique (GC-MS).

The preconcentration step could be: (1) solvent extraction, (2) headspace analysis, (3) purge and trap, (4) solid phase extraction (SPE) (column and discs) (5) solid phase microextraction (SPME) and some other modern technique.

### Experimental

#### *Extraction procedure*

*Liquid-liquid extraction (LLE):* The sample is shaken with an immiscible organic solvent, hexane, light petroleum, oxygenated and chlorinated solvents. The organic layer is injected into the chromatograph.

*Solid-phase extraction (SPE):* SPE sequence involves the following steps: (1) activation (conditioning) of the sorbent (2) sample introduction, (3) washing (4) elution of the compounds, (5) regeneration of the column. Ethyl acetate, methanol, acetone and hexane are the most frequently used solvent for desorption. Solid phase microextraction (SPME), microwave (MWE) extraction, ultrasonic (USE) extraction, supercritical fluid extraction (SFE) are some new extraction procedures.

Table 1 presents a comparison of different extraction procedure applied to a mixture of aroma compounds. 30  $\mu\text{l}$  standard *mixture* in 0.9 ml hydroalcoholic solution, 0.9 ml distilled water and 0.3ml *solvent*\* in a screw cap vessel. After extraction, 1 $\mu\text{l}$  3-hepten-2-one (ES) was added to the supernatant and analyzed.

#### *Apparatus*

A Hewlett Packard GC 5890 couplet with MS engine 5989B in the EI mode was used for compounds identification. The GC was equipped with a HP-5MS capillary column 30m x 0.25mm, 0.25 $\mu\text{m}$  film, in the temperature program: 50  $^{\circ}\text{C}$  (2') to 250  $^{\circ}\text{C}$  or 300  $^{\circ}\text{C}$  with a rate of 8  $^{\circ}\text{C}/\text{min}$ , helium flow rate 1ml/min. A Thermo Finnigan GC-MS equipped with a Rtx-5MS

(15m $\times$ 0.25mm, 0,25 $\mu$ m) column was also used in similar conditions. The GC/MS interface line and the ion source were maintained to 200 $^{\circ}$ C or 250  $^{\circ}$ C. Electron energy was 70eV and electron emission 300 $\mu$ A.

Table 1

**Comparative extraction procedure for some aroma compounds**

LLE	SPE	MWE	USE
Sample+ solvent* mix 1.5min; centrifuge 2 min	RP-18 or TSC cartridges; 3ml methanol 3ml distilled water; sample, wash; dry: 10 min., elution: 3 $\times$ 0.3ml solvent*	2.45Hz, 4 sec, 60 $^{\circ}$ C, solvent*	1 min, 60 $^{\circ}$ C, 1ml solvent*

\*Solvent: mixture ethyl acetate: hexane: dichloromethane, 5/1/1

Table 2

**Extraction procedure for amino acids (AA) and drugs from plasma**

Theoph. and caffeine	Amino acids extraction	AA derivatization	
1ml serum + drug 10 $\mu$ g IS <sup>1</sup> (5ml screw-cap vial)2ml solvent <sup>2</sup> , 0.5gNaCl,mixed 1min,centrif.3min,conc.	cation exchange resin Dowex 50W-X8 100mesh, 40 $\times$ 2mm column; Elution: 2ml 3M NH <sub>4</sub> OH; Evaporate	1.esterification:50 0 $\mu$ l butanol: acetyl chloride, 5:1,v/v, 1h, 100 $^{\circ}$ C	2.acetylation 200 $\mu$ l TFAA <sup>3</sup> , 60 $^{\circ}$ C, 20 min, cool, dry, 1ml ethyl acetate

<sup>1</sup>IS=<sup>15</sup>N-theophylline; <sup>2</sup>solvent=chloroform:isopropanol 20:1,v/v; <sup>3</sup>TFAA=trifluoroacetic anhydride; Resin is kept into refrigerator with distilled water and 1N NaOH; H+ form made with 1N HCl. Free AA are analyzed by adding 1ml 1N acetic acid to 0.5ml plasma. Total AA are analyzed after protein hydrolysis: 6NHCl at 110 $^{\circ}$ C overnight.

**GC-MS analytical method**

GC-MS is a high sensitive and specific technique used in organic analysis. In the selective ion monitoring (SIM) mode, using a few selected ions, the sensitivity is increased by one or two orders of magnitude SIM-GC/MS is very useful in quantitative work and is usually achieved by isotopic dilution (ID). Quantitation is performed by addition of known amounts of internal standards to the sample before extraction. The method will compensate for sample losses in the clean-up stage, assuming that the losses of the standard are identical with those of the analyte.

*Method validation:* The regression curves obtained for some standards in the range 0 – 24ng were: gave good linearity and r>0.99.

*Precision* gave relative standard deviation (R.S.D.) for LLE and SPE lower than 3% (n=5). *Recovery* for LLE was 81% (n=3) and for SPE 92% (n=4). *Accuracy* for 20ng shows a R.S.D.mean value of 5% and for 24ng of 6%. The *sensitivity* was lower than 100pg at a ratio S/N=10 and *L.O.D.* was 10pg, S/N=10.

The recovery results (Fig.2) for the standard mixture are the following:

MWE (103%) > USE (101%) > SPE (92%) > LLE (80.8%)

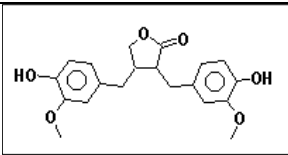
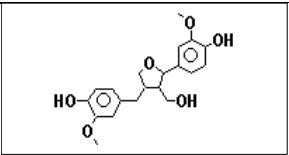
Table 3

**Comparative recovery mean values between two extraction procedures (n=4).**

Crt. No.	Compounds	t <sub>R</sub> (min)	LLE(%)	SPE (C-18)(%)
1	3-hepten-2-one	8.33	76.03	85.19
2	fenchone	11.4	79.12	87.55
3	phenyl ethyl alcohol	12	76.13	92.85
4	terpinen-4-ol	12.8	80.97	90.76

Crt. No.	Compounds	t <sub>R</sub> (min)	LLE(%)	SPE (C-18)(%)
5	citronellol	13.6	82.62	89.84
6	carvone	14	83.96	94.01
7	anisaldehyde	14.4	87.50	102.45
8	methyl myristate (ES)	21		
	mean values		<b>80.91</b>	<b>91.81</b>

	matairesinol		lariciresinol
---	--------------	---	---------------

## Results

### Active principles in herbs

The method was applied to characterize some active principles in a bitter (Floratonic) extract (12 herbs extract) and different herbs with therapeutic effects. Bitter shows sedative, antiseptic, antiinflammatory, carminativ, antirheumatic, antidepressive and tissue regenerating effects. Terpenoid, azulene, coumarin derivatives and polyphenols are responsible for some of these properties. The high levels of lignan flavonoids lariciresinol (250µg/ml) and matairesinol in “Floratonic” bitter may contribute to the protective effect on coronary heart diseases and arteriosclerosis. The plant lignans, as well as their mammalian metabolites enterolactone and enterodiol, have antioxidative properties.

The main volatile compounds identified by the GC-MS analysis of *Mentha piperita L.* were: menthol, menthone, isomenthone, 1,8 cineole, menthyl acetate, limonene, β-myrcene, carvone. *Mentha piperita L.* oil had the active principles: menthol, menthone, isomenthone, menthyl acetate, α-pinene, β-pinene, champhor, limonene, linalool, piperitone (Fig.1). *Mentha crispa L.* showed carvone as major component. The oil is used for the flavoring of pharmaceutical and cosmetic preparations and in medicine as a carminative and gastric stimulant. Vitamin F, E and C in seabuckthorn fruit have been determined in fruit and fruit oil. Esterification of the fatty acids with methanol:acetyl chloride is similar as step 1 in table 2. Dry fruits (400mg/ml) were extracted in 70% ethanol overnight and 0.5mg IS (methylundecenoate) was added to 40mg sample.

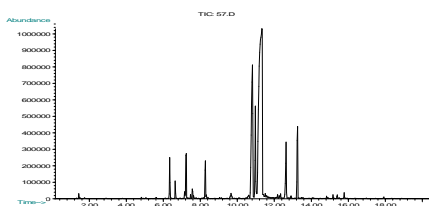


**Fig. 1.** *Mentha piperita L.* oil chromatogram; menthol is the major compound.

The methods presented are suitable for determination and control of organic compounds in medicinal herb. No major differences were observed between LLE and SPE in the plant extracts studied. Terpenic compounds, polyunsaturated fatty acids and flavonoids are some of the compounds responsible for antiinflammatory, antioxidant, anticarcinogenic activity of plants used in traditional medicine.

**Table 4**

Vitamin F determination in seabuckthorn dry fruits							
FAME	mg/g	mg/g	mg/g	mg/g	Mean mg/g	S.D.	R.S.D.,%
methyl undecenoate (C11:1)IS	12.50	12.50	12.50	12.00	12.38	0.25	2.02
methyl palmitoleate(C16:1)	9.90	12.37	9.51	11.18	10.74	1.30	12.11
methyl palmitate(C16:0)	15.05	18.42	15.02	16.96	16.36	1.65	10.06
methyl linoleate (C18:2)(9,12)	2.88	3.64	3.01	3.53	3.26	0.38	11.63
methyl oleate (C18:1)(9)	12.15	14.59	12.85	14.73	13.58	1.28	9.42
methyl stearate (C18:0)	3.61	4.41	4.17	4.45	4.16	0.39	9.30
total	43.59	53.44	44.55	50.84	48.11	4.79	9.96
Vitamin F	28.13	28.23	27.77	28.02	28.04	0.20	0.70

The high value of palmitoleic acid in these fruits make the oil very useful in cosmetics for skin protection. In wheat germs the vitamin F measured was 200mg/g, but palmitoleic acid is very small. Vitamin C (determined by silitation and GC analysis) in the dry fruits was 24,9mg %. Vitamin E of 0.06% in fruit oil was measured versus cholesterol as internal standard.

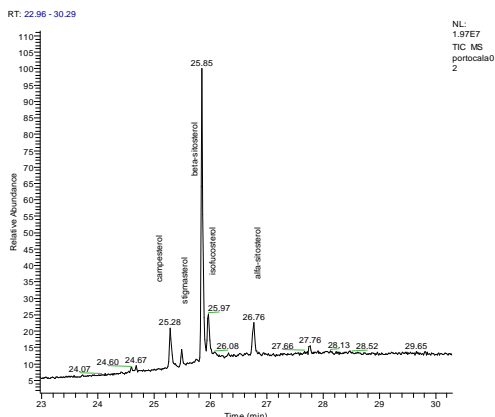


**Fig. 2.** Sterol profile for orange juice: cholesterol, campesterol,  $\beta$ -stigmasterol,  $\beta$ -sitosterol (the major compound), isofucosterol,  $\alpha$ -sitosterol.

Sterol profiles measurement by GC/MS could be used for adulteration detection of the fruit juices. Juice marker for orange and grapefruit (stigmastero, campesterol), pineapple (ergostanol and stigmasterol markers), passionfruit (beta-sitosterol) could be easily extracted: ethanol: juice: hexane, 8/10/1.5, mixed 2 minutes, centrifuged 5 minutes and analyzed (Fig. 3).

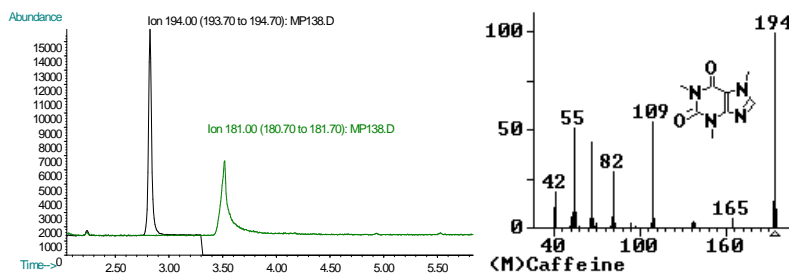


**Fig. 3.** Caffeine determination by GC/MS in the SIM mode (first peak)



### Drugs

GC/MS applications for measuring drugs are very important: purity control, pharmacokinetic studies, metabolic studies, clinical applications for treatment and diagnosis. Caffeine clearance is a novel approach for assessing hepatic microsomal function. 10 µg/ml <sup>15</sup>N-theophylline has been used as internal standard. The temperature program was: 200-250°C with a rate of 10°C/min. The method was validated in the range 0-20µg/ml caffeine. The regression curve obtained in GC/MS assay gave  $r=0.95$ . Precision gave R.S.D values lower than 5% for 5µg/ml (n=7) and lower 12% for 3µg/ml(n=7). Accuracy shows values lower than 6%. Sensitivity measured at a signal/noise 4/1 was 0.5µg/ml.

*Study population:* A dose of 4mg/kg p.o. was used. Blood caffeine concentrations were measured before dose and timed intervals at 0, 30 min, 1, 3, 6, 9 and 12 h. Caffeine clearance, measured in patients with cirrhosis and chronic hepatitis, was reduced and half live time was increased in children with liver disease as compared with control. The pharmacokinetic parameters were calculated with the formulas:

$$K_{el}=(\ln C_1-\ln C_2)\Delta t; t_{1/2}=\ln 2/k_{el}; Cl=k_{el}\times V_d$$

where:  $k_{el}$  is the elimination constant;  $C_1$  and  $C_2$  are the maximum plasma concentration and minimum plasma concentration of caffeine,  $t_{1/2}$  is the half-live time and  $V_d$  is the distribution volume of 0.6l/kg body weight. Fig.4 presents the ion chromatograms in the SIM mode for the molecular ions and basic peaks for the both components, caffeine (m/z 194) and the internal standard (m/z 181).

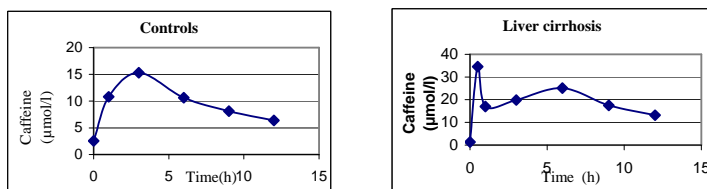


Fig. 4. The elimination curve of caffeine in control and cirrhotic patient

The method is simple, precise and rapid, useful in the analysis of xantines. Isotopic labeled internal standard used avoids metabolites overlapping. Significant changes ( $p<0.01$ ) were observed in caffeine metabolism in children with decompensated cirrhosis. The clearance values of  $0.41\pm 0.56\text{ml min}^{-1}\text{kg}^{-1}$  and half-life times of  $14.34\pm 14$  are changed because of the reduction in “functioning hepatocyte mass”. The control values for clearance and half-life time were  $1.5\pm 0.46$  and  $t_{1/2}=5\pm 1.8$  in literature and our data of  $1.36\pm 0.23$  and  $t_{1/2}=5.13\pm 0.85$  (n=10). Patients with noncirrhotic liver disease showed intermediate values ( $Cl=1.2\pm 0.46$  and  $t_{1/2}=6.62\pm 2.44$ ) but *higher values of caffeine plasma concentrations*, as shown in the figure above. (Control<sub>max</sub>=20 µmoles/l ; hepatic disease<sub>max</sub>=120 µmoles/l).

Important other clinical or metabolic applications have been developed by GC/MS technique with precise quantitation of drugs from plasma, saliva or tissues: theophylline for severe asthma or apnea treatment, anaesthetics (procaine, tetracaine, dibucaine, lidocaine) for pharmacokinetic and metabolic studies.

### Amino acids quantitation

Amino acids are components of proteins. They are nonvolatile and for GC-MS measurements they need to be derivatized as presented in table 2, column 2-4,. Normally, most living things can synthesize some of the amino acids (*non-essential*) from other food components

and other amino acids, but those that cannot be produced internally (*essential*) must be provided in the diet. They can be found in foods (infants formulas, cheese, beer, wine, grapes, honey, soy flour), in plasma, blood, urine, tissues. The assessment of amino acids quantity was made for metabolic studies (Gly and Ser interconversion), diagnoses (serum AA level for phenylketoneuria where Phe must be limited or maple syrup urine disease where Ile, Leu, Val are problematic), drug control (Trofopar), plant and food characterization, transmembranar transport study.

Amino acids determination by SIM-GC-MS in some leaves ethanol extracts is presented. By using  $^{15}\text{N}$ -Gly as internal standard and by monitoring the peaks  $m/z$  154 (for Gly) and 155 (for  $^{15}\text{N}$ -Gly), the unlabeled Gly was determined and then all the other separated amino acids, taking in account the response factors obtained with standards of the amino acids. Free amino acids levels measured in Fagus, Ginkgo biloba and Hedera helix leaf extracts are presented in table 5.

**Table 5****Quantitative determination of amino acids ( $\mu\text{g/g}$ ) from plant extracts**

	M	Fagus	Ginco biloba	Hedera helix
Ala (alanine)	89	46.57	88.63	
Gly (glycine)	75	37.16	225.91	155.91
Val (valine)	117	97.34		154.23
Leu (leucine)	131	12.88	95.71	100.31
Ileu (isoleucine)	131	14.17	193.43	80.84
Pro (proline)	115	2363.56	3289.03	2441.15
Asp (aspartic acid)	133	82.4	322.08	1891.68
Phe (phenylalanine)	165		151.18	136.34
Glu (glutamic acid)	146	492.8	416.65	
Lys (lysine)	146		85.15	
Tyr (tyrosine)	181			195.24
Met (methinine)	149	26.37		

The major amino acid is proline, which has an important role in protein syntheses and in tissue regeneration.

*AA transmembranar transport*

The isotopic dilution GC/MS technique has been used to study  $^{15}\text{N}$ -glycine transmembranar transport. Small influx was detected for glycine in red cells. The presence of some ingredients increased the amino acid influx. The washed cells suspended in the incubated medium contained  $^{15}\text{N}$ -Gly in the range 1-10mM. Incubation of 20 ml suspension was made in a rotary shaker at  $37^\circ\text{C}$ , followed by centrifugation at 3000xg. 10% trichloroacetic acid was used to hemolyse, then centrifuge and finally 0.2ml supernatant solution was analyzed. The peaks  $m/z$  154 and 155 of trifluoroacetyl-butyl ester derivatives of Gly and  $^{15}\text{N}$ -Gly were measured for transport calculation ( $^{15}\text{N}$ -Gly was used also as internal standard), where  $p$ =sample( $\mu\text{g.ml}$ );  $S$ =internal standard ( $\mu\text{g}$ );  $V$ =sample volume (ml);  $C$ ,  $C_s$ ,  $C_p$ =mol ratio of  $^{15}\text{N}$  Gly, atom%, for the half part of the sample where internal standard was added and sample, respectively. The quantity of  $^{15}\text{N}$ -Gly ( $\mu\text{M}$ ) was calculated as  $pC_p$ .

$$p = \frac{S(C_s - C)}{V(V - C_p)}$$

The presence of an electric field, incubation temperature, time of incubation, concentration, drugs, NaCl, could influence the glycine transport. The efflux of  $^{14}\text{N}$ -Gly was calculated together with the influx of  $^{15}\text{N}$ -Gly into the cell.

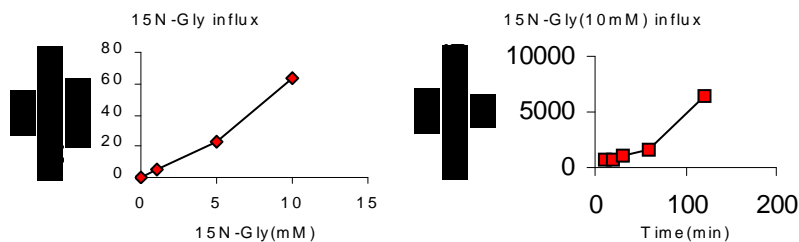


**Fig. 5.**  $^{15}\text{N}$ Gly influx versus concentration of  $^{15}\text{N}$ -Gly and incubation time

### Conclusions

After about half century of applications, GC-MS technique demonstrates that still remains an important tool for many studies, including biomedical field.

### REFERENCES

1. M. Culea, M. Apetri, C. Gherman, *Analysis of Aroma Compounds by Gas Chromatography and Gas Chromatography/Mass Spectrometry: Comparative Extraction Methods*, Roum.J. Physics. 46 (2001) 7-8.
1. 32. M. Culea, N. Palibroda, P. Panta Chereches, M. Nanulescu, "Comparative of isotopic dilution methods for determination of heophylline in the plasma and saliva of infants and children", *Chromatographia*, 53 (2001) S387-S-390.
2. M. Culea, S. Neamtu, N. Palibroda, M. Borsa, S. Nicoară: *Study of amino acid transmembranar transport in human red cell and rat hepatocyte*, *Journal of Molecular Structure*, 348 (1995) 377-380.

## STATIONARY AND NONSTATIONARY CHARACTERISTICS OF THE ATOMIC VIBRATIONS IN PROTEINS

V. V. MORARIU

*National Institute for Research & Development of Isotopic and Molecular Technologies P.O.Box 700, 3400 Cluj-Napoca, Romania, e-mail: vvm@L40.itim-cj.ro*

### 1. INTRODUCTION AND SCOPE

The structural characteristics of the proteins are stored in the Protein Data Bank and they include the coordinates and the temperature factors of all atoms. The temperature factor  $T_f$  is related to the amplitude of the atomic vibration and is some time referred to as the atomic mobility or flexibility. Most of the attention of the molecular biologists is directed to the structural data. These are concerned with the description of the position, bonds, secondary structure, the characteristics of the active sites etc., while much less attention is paid to the atomic mobilities. There are attempts to relate the atomic mobility to the protein activity but no simple rule was possible to extract from experimental data. For example enzymatic activity of various mutants of a bacteria did not correlate in a simple way with the atomic mobilities (1). It was puzzling to find that increased activity was associated to either increase or decrease of the atomic mobility.

We have started a systematic analysis of the temperature factors of proteins in order to understand their organization and significance for the stability and functional role of the proteins. We regard the data as series of numbers which are often referred to as fluctuation. They are suitable for specific mathematical methods of analysis which can reveal what kind and amount of order does exist in these series (2-10). This previous work can be summarized as follows:

-The temperature factors series of protein backbone atoms resulting from the X ray diffraction analysis of crystal data were analyzed by fast Fourier transform, detrended fluctuation analysis (DFA), and correlation dimension. The spectral analysis of 50 randomly selected proteins revealed the presence of a long-range correlation characterized on average by a power law  $P \approx 1/f^{1.79}$  (9). The DFA showed evidence for long range correlation extending over an average 48 atoms length, equivalent to 16 amino acid residues. The mean value of the scaling exponent was about 1.35. Beyond this range, the scaling exponent decreased significantly.

-The correlation dimension analysis revealed the presence of a strange attractor having an average dimension of 4.34. A similar analysis of the temperature factor for proteins in solution, as resulting from the NMR analysis, revealed that the spectral scaling exponent was lower in solution than in crystal form. This was expected from our model described in reference 10. The attractor dimension was lower by about one unit for proteins in solution compared to the crystal form.

Therefore the nature of at least one of the independent variables controlling the vibrations is dependent on the form of aggregation. Higher values of the scaling exponents were associated to the inactive or tense state of the protein. Lower values of the scaling exponent were associated to higher enzyme activity regardless of higher or lower flexibility. While the molecular biologist's view stresses the relation of particular sites in the protein to its function, the present analysis underlines the unity of the protein molecule. We proposed an Iterative Correlator with Random Seeds as a method to generate series characterized by a low dimensional attractor ( $D \approx 4.65$ ) and scaling properties described by a power law  $P = 1/f^a$  where  $0 < a \leq 2$  (10). The method basically introduces an interaction factor between the terms of the series. The higher the interaction factor the higher is the correlation exponent.

This previous work was practically focused on the characteristics of the stationary component of  $T_f$  fluctuation (as the DFA eliminated the non-stationary part). The scope of the present paper is to characterize the non-stationary component. This component dominates the series, as they have much higher amplitudes than the stationary component.

## 2. THE STRUCTURE OF THE NON-STATIONARY FLUCTUATION OF THE TEMPERATURE FACTOR SERIES

The series of the temperature factor refer to the protein main chain atoms: N-C $_{\alpha}$ -C. The oxygen atoms are excluded from the series as they are not located in a linear succession in the series. An example of a series for cytochrom c, a small protein is illustrated in fig.1. The left part of the plot represents the amino terminal part of the main chain. The plot is characterized by several peaks of increased mobility ( $T_f$ ) numbered between 1 and 5. Complementary to these peaks are the “valleys” i.e. relative minimum values, indicated on the plot by letters (a to f). A polynomial fit of the plot shows that the middle part is characterized (on average) by a maximum (which in turn is modulated by the peaks a-f). Another example is illustrated in fig.2 for calmodulin, a calcium binding protein, which has a longer main chain. The assign of the peaks is somewhat arbitrary, one always may question why smaller peaks are not counted etc. At the same time, it can be noticed that two different proteins have quite a similar structure of the main chain atoms mobility. First there is a similar mobile core in both proteins and a similar structure as far as the peaks and minima are concerned. All these features belong to the non-stationary characteristics of the series. I checked a number of proteins belonging to the all alpha class and also of alpha plus beta class and all revealed a similar structure of the series. These proteins, appart from those illustrated in fig.1-3 included the following (Protein Data Bank codes): 3hbb, 1axa, 1711, 1atr, 1a4u, 1a42, 1bfp, 2siv, 1aol, 1gpa, 1bhe, 1eob, 1j6z, 1h4w, 1gct, 1dzg, 1a48, 1i6i, a total number of 20 widely different proteins. A few of them revealed a double core structure such as chaperone - a very big molecule (fig.3). However such a structure was not limited to very large molecules. For example lysozyme, an about 500 main chain atoms also revealed a double

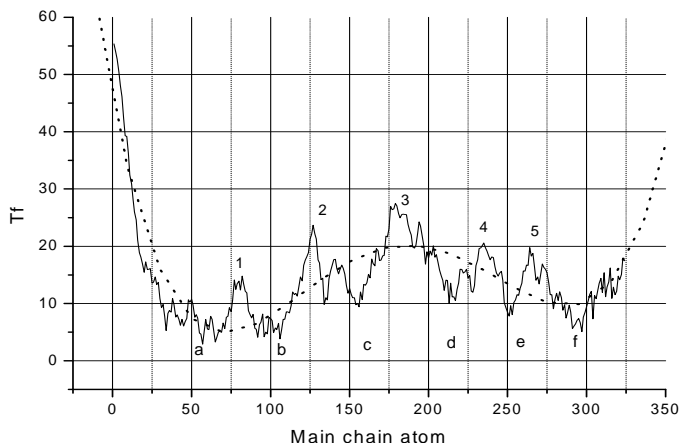


**Fig. 1.** The temperature factor series for cytochrom c (Protein Data Bank: 1ycc). The plot is fitted with a polynomial curve. The main peaks for increased values are marked from 1-5 while the relative minima are indicated by letters (a-f).

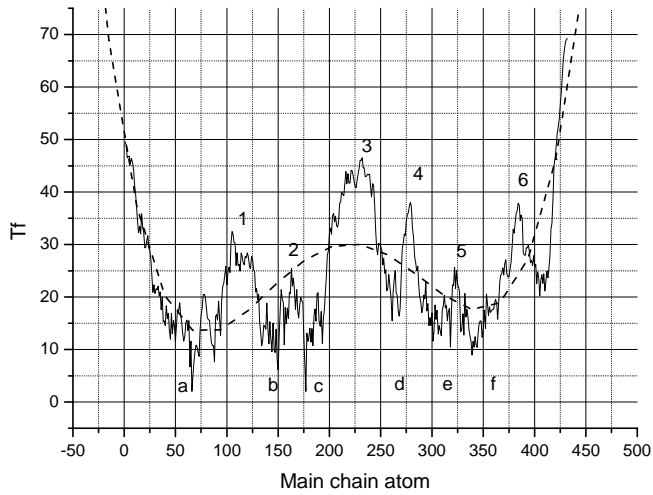


**Fig. 2.** The temperature factor series for calmodulin (Protein Data Bank: 1cll).  
The significance of other marks as in fig.1.

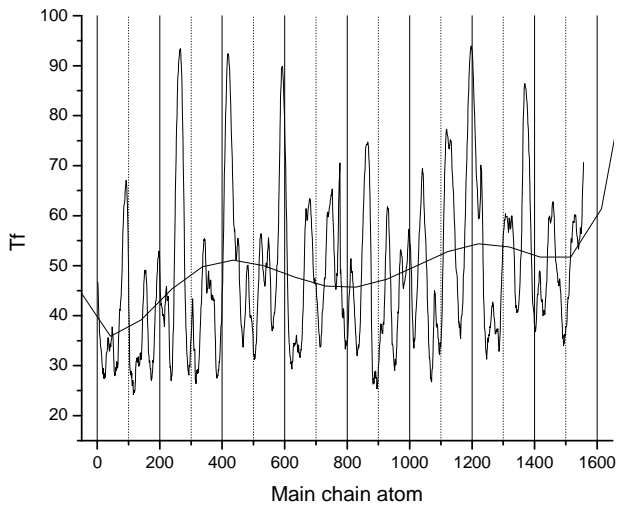


**Fig. 3.** The temperature factor series for chaperone, a four chains protein (Protein Data Bank code: 1gme).  
Polynomial fitting of the data revealed a double core structure. Roughly around six major peaks can be counted for each core, similar to single core proteins (see fig. 1-2).

core (not illustrated). Turning back to chaperone one can notice that each mobile core is modulated by a similar (approximately) number of peaks as for smaller proteins. Chaperone consists of four chains while alcohol dehydrogenase, a double chain protein presents only a single mobile core. To sum up a single mobile core is present both in single chain or double chain proteins while a four chain protein revealed a double core. On the other hand hemoglobin which, consists of two pairs of chains, have each chain characterized by a single core. Therefore, at present, we cannot draw a definite conclusion concerning the rule governing the number of mobile cores in relation to the number of chains.

On the other hand the number of peaks which modulate the core seems to increase with the length of the main chain. Again, it is somewhat arbitrary to identify and count the peaks yet our attempt illustrated in fig. 4 revealed that a roughly linear relationship exists between the number of peaks and main chain length. The scattering of data is normal considering the lack of precision in estimating the number of peaks. The correlation of data is reasonably good ( $R=0.900$  and  $p<0.0001$ ).

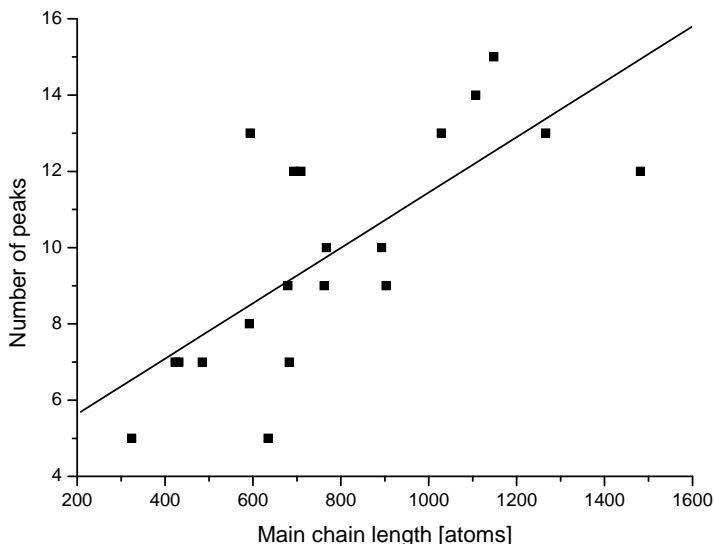


**Fig. 4.** The number of mobile peaks which modulate the protein mobile core *versus* the main chain length. It shows that longer main chain proteins are characterized by increasing number of mobile peaks or, alternatively, by an increased number of rigid segments.

### 3. THE GOLDEN NUMBER IN THE STRUCTURE OF NON-STATIONARY FLUCTUATION

Another way at looking to the data is to estimate the width of the mobile core *versus* the length of the main chain. The width is defined as the distance between the two minima expressed as number of atoms of the main chain. In the case of double core proteins there are two widths. The data are included in fig. 5. A linear relationship is again noticed. However the second core, where is present, follows a slower increase with the main chain length. Any way this linear dependence tells us that the ratio of the protein main chain length  $L$  to the width of the core  $\Delta$  is constant for each core.

The calculations for the proteins mentioned above, revealed that for the single and for the first core we have:  $(L/\Delta)_1 = 1.57 \pm 0.047$  which has the upper limit 1.62. This, in turn, is within the range of 1.618..., equivalent of  $\Phi$  - the golden number. In the case of double core proteins each core is characterized by a ratio  $(L/\Delta)_2 = 1.272 \pm 0.028 = \sqrt{1.618} = \sqrt{\Phi}$ . In other words the mobile core structure of a protein seems to be controlled by the golden mean proportion. The golden mean has very special mathematical properties although, formally, is just one of the roots of the equation  $x^2 - x - 1 = 0$ . It seems that it has an enormous impact in the mental activity of man while there is increasing evidence for its presence in the structure of the physical and living (biological) world (11-13).

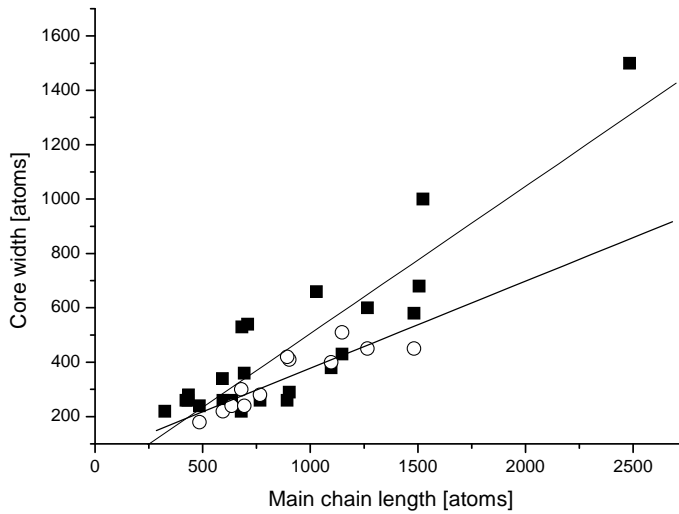
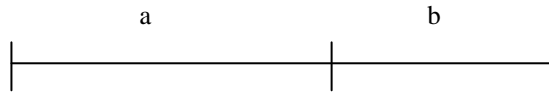


**Fig. 5.** The width of the core increases as the length of the protein main chain increases. Black squares: single core proteins and the first core of double core proteins; open circles: the width of the second core for double core proteins.

Dividing a segment into a golden mean proportion implies the following condition:



where  $(a+b)/a=a/b$ . If  $a=1$ , then  $b=0.618$ . In the case of the protein main chains we have for a single core protein:



where  $(a+b_1+b_2)/a=a/(b_1+b_2)$ . Here segment “a” represents the mobile core. Therefore the length of the core has a specific length in relationship with the length of the main chain. This is an empirical finding which might tell us that the stability of the protein is ensured by this golden mean structure although at this time it is not at all clear what is its fundamental meaning or what does it mean in physical terms. I have also checked whether there is a specific relationship between  $b_1$  and  $b_2$  or against the value of  $a$ . The estimation of these lengths from the protein data had a low precision. Consequently it was not possible to draw precise conclusions on this matter.

In the case of double core proteins the length of each core is in a  $\sqrt{\Phi}$  proportion in respect to the length of the whole main chain. Again we find a specific rule in the organization of these type of proteins.

#### 4. CONCLUSIONS

We found several properties of the non-stationary fluctuation of the temperature factors of the protein main chains which have never been reported before. They are:



- The mobility of the atoms in the protein main chain is characterized by one or double mobile cores.
- Each mobile core is modulated in turn by peaks of relative increased mobility of much shorter range than the length of the core.
- The number of the modulating peaks is proportional to the length of the main chain.
- The ratio of the core width to the length of the main chain is the golden mean for single core proteins and square root of the golden mean for the double core proteins.

## REFERENCES

1. T. Graycar, M. Knapp, G. Ganshaw, J. Dauberman, R. Bott, *Engineered Bacillus lentus subtilisins having altered flexibility*, J.Mol.Biol., 1999, 292, 97-109
2. A. Isvoran, D. Dolha, V. V. Morariu, *Attractor control of the stability of lysozymes* Int.J.Chaos Theory and Applications, 2000, 5, 1
3. A. Isvoran, V. V. Morariu, *An attractor controls the spatial fluctuations of human lysozyme*, Studia Univ. Babes-Bolyai, Special issue, 2000, 277-287
4. A. Isvoran, V. V. Morariu, *Comparison of the behavior of sea hare myoglobin when it forms two different complexes*, Chaos, Solitons and Fractals 2001, 12, 1041-1045
5. A. Isvoran, V. V. Morariu, *Analysis of the nonlinear behavior of ascaris trypsin inhibitor from NMR data* Chaos, Solitons and Fractals, 2001, 12, 1485-1488
6. A. Coza, V. V. Morariu, *Scaling characteristics of the structure of human haemoglobin*, Studia Univ. Babes-Bolyai, Special issue, 2001, 461-464
7. V. V. Morariu, L. Gheorghe, *Characteristics of the atomic vibration of cytoskeleton proteins*, Studia Univ. Babes-Bolyai, Special issue, 2001, 475-479
8. V. V. Morariu, *Scaling in the temperature factor of proteins*, Studia Univ. Babes-Bolyai, Special issue, 2001, 209-215
9. V. V. Morariu, A. Coza, *Nonlinear properties of the atomic vibrations in protein backbones*, Physica A, 2003, 320, 461-474
10. A. Coza, V. V. Morariu, *Generating 1/f noise with a low dimensional attractor characteristics: its significance for atomic vibrations in proteins and cognitive data*, Physica A, 2003, 320, 449-460
11. V. V. Morariu, Charles Card, *The archetypal hypothesis of C.G.Jung and W.Pauli and the number archetypes: an extension of the concept to the golden mean*, J. for Interdisciplinary and Cross Cultural Studies, 1998, 1, 1-7
12. I. Ciofu, *The golden number – a matrix of evolution ?* (in Romanian), Ed.Coresi, Bucuresti, 1994
13. M. Ghyska, *The geometry of art and life*, Dover, New York, 1977

## INTENSITY FLUCTUATING PATTERN OF LIGHT SCATTERED ON MICROPARTICLES

**I. TURCU<sup>\*</sup>, CRISTIAN V. L. POP, SILVIA NEAMTU**

*National Institute of R & D for Isotopic and Molecular Technologies,  
P.O.Box 700, RO-400293, Cluj-Napoca 5, Romania*

**ABSTRACT.** Our results characterize the time dependent speckle pattern obtained by stochastic interference of light, coherently scattered by microparticles. The information is obtained by capturing images by a CCD camera and also by measuring the intensity of scattered light by a photodetector. The image analysis is done in statistic terms the relevant parameters being the maximum value and the area of local light intensity maxima. The measured electric signal is a fluctuating current that captures the microparticles dynamics. There are two processes controlling the dynamics: the sedimentation in gravitational field, and additionally, a random Brownian motion.

The measured currents were separated conventionally in two components: a *dc* component corresponding to the average current, and an *ac* time dependent component describing the fluctuations. The experimental dependence of the mean light intensity scattered at small angle on scattering centers density is a peak-type curve. The fluctuations of the scattered light intensity are very important in the maximum neighborhood becoming comparable to the mean scattered light intensity. The characteristic time scale of the fluctuating component becomes shorter as the cell density increases.

The detection process has important effects on current fluctuations and it is important to discriminate between intrinsic dynamic characteristics of the interference pattern and artifacts coming from the experimental set-up. The artifacts are mainly due to the averaging effect of the detectors. In the far field experiments, the photo-detector captures a single interference speckle and gives the correct fluctuating dynamics. By decreasing the distance between the sample and detector, the detecting process switches from the single speckle to many speckles detection.

### INTRODUCTION

Light-scattering techniques are often used to investigate static or dynamic properties of microparticles. Low power lasers with various wavelengths in the visible or IR domains are the usual light sources used in experiments. The literature in the field covers a diversity of aspects ranging from fundamental problems related to rigorous or approximate theoretical approaches [1,2] to medical applications with diagnostic purposes [3-5] (see reference 6 for a comprehensive review).

Laser light scattered coherently by microparticles located at random positions, having random orientation, and moving in a complex manner in suspensions give a time-varying speckled interference pattern. The scattering phenomenon is a stochastic interference process providing information on both static and dynamic parameters of the investigated system.

In a light-scattering experiments there are, basically, two ways to obtain information:

- capturing images by a CCD camera;
- measuring the intensity of scattered light and converting the light intensity into an electric signal by a photo-detector.

---

<sup>\*</sup>E-mail: iturcu@L40.itim-cj.ro

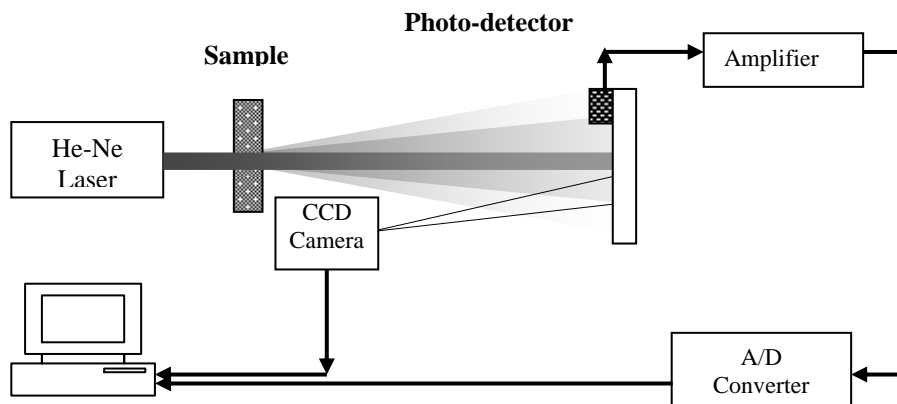


**Fig. 1.** The experimental set-up

As the speckle pattern is only partially captured by a photo-detector, the received information is incomplete. The detected current features fluctuations that contain encrypted information about the static and dynamic properties of the scatterers.

The purpose of the paper is to develop the appropriate experimental set-up and to investigate the static and dynamic properties of the scattered light upon interaction with suspensions of human red blood cells.

The human red blood cells are used as model microparticles but the results are similar for a wide variety of microparticles: yeast, bacteria, milk, natural juices, molecular aggregates in suspensions etc.

## METHODS

For all experiments, blood was obtained from healthy male donors, was collected on sodium citrate 3.8% and was used after one or two hours. The erythrocytes were separated from the blood plasma by centrifugation at 4000 rpm for 10 min and were washed three times in an isotonic saline buffer (145 mM NaCl, 5 mM KCl, 5mM Hepes, pH 7.4). The red blood cells were diluted in isotonic saline with haematocrit (volume fraction) values in the range  $10^{-6}$  – 0.4.

The used light source was a 633 nm linearly polarized continuous-wave He-Ne laser (Uniphase model 1125P) with a power of 5 mW. The beam diameter at  $1/e^2$  was 0.81 mm and the beam divergence 1 mrad. The laser beam was directed onto a 1 mm thick quartz cuvette containing the blood sample.

The intensity of the light scattered at small angles was captured as a digitized image by a CCD camera and also was converted in an electric signal by a photodiode. The typical distance between photodetector and the cuvette was  $D = 1$  m, but in order to capture single and multiple speckles, measurements were performed also at 5 and 0.5 m respectively. The sensitive area of the photodiode is  $A \approx 0.2$  cm<sup>2</sup> corresponding to a solid angle  $\Delta\Omega \approx 2 \times 10^{-5}$  sr. The detector measuring the scattered light is positioned in the forward direction at  $2^\circ$  off-axis. Measured value was corrected for the refractive index mismatch on the water/air interface.

The detected current is amplified and transferred to a PC by an A/D 12-bits converter having  $\nu = 20$  Hz sampling rate. The measurements at each haematocrit took less than 4 minutes (until  $2^{12}$  data are accumulated) and no significant sedimentation was observed during this time.

The current signals were separated conventionally in two components: a **dc** component corresponding to the average current, and an **ac** time dependent component describing the fluctuations:

$$i(t) = i_{dc} + i_{ac}(t) \quad ; \quad i_{dc} = \langle i \rangle \quad ; \quad i_{ac}(t) = i(t) - \langle i \rangle \quad (1)$$

The bracket denotes the time averaging operator over the measuring time  $T$ :

$$\langle i \rangle = \frac{1}{Tv} \sum_{n=1}^{Tv} i(n/v) \quad (2)$$

If the fluctuations are very fast, a rigorous approach is to consider also the averaging effect of the photo-detector. At the moment, we focus only on fluctuations with characteristic times longer than 50 ms and the averaging effect of the detector can be neglected.

### RESULTS AND DISCUSSION

In the following, we present the experimental results and we propose some mechanisms able to explain the effect of different parameters on the investigated phenomena. The relevant parameters are of two types: sample-related characteristics (microparticles density, optical and molecular properties of microparticles and of the suspending medium) and geometric parameters pertaining to the experimental set-up (distance between sample and photo-detectors, detection angle, detector area, etc.).

We will first analyze the properties of the light intensity speckle pattern. A typical image capturing the speckle pattern is given in Fig.2. The image analysis is done in statistic terms, the relevant parameters being the maximum value and the area of local light intensity maxima. The probability distribution of speckle maximum intensity values is given in Fig.3. As one can observe the distribution is Poissonian.

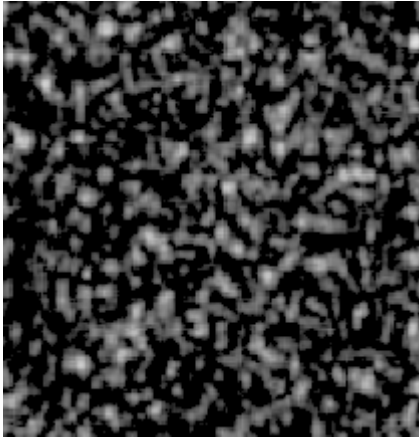


Fig. 2. Stochastic interference pattern

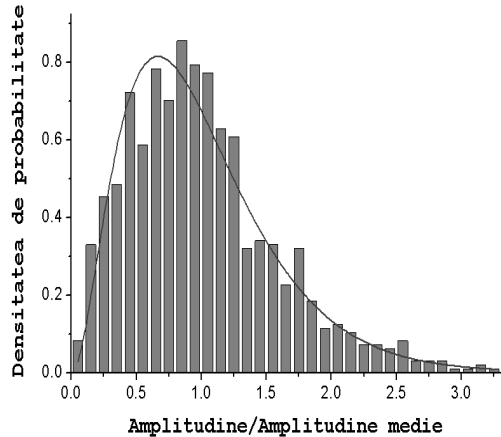


Fig. 3. Amplitude probability distribution

The probability distribution of speckle area has similar properties. The difference is given by the dependence of the two distributions on scattering centers concentration. The mean area (and also its distribution) is almost insensitive to scatterer concentration while the mean intensity increase linearly in the single scattering domain (small concentrations), attend a maximum and then decrease in the multiple scattering domain.

We present in the following the effect of scattering centers density on the static and dynamic characteristics of the time dependent photocurrent.

The dependence of the **dc** component of  $i(t)$ , on haematocrit is a peak function. Neglecting the noise, the photocurrent starts from zero, increases until a maximum value is reached at  $H_m$ , and then decreases asymptotically to a small saturation value characteristic for the isotropic scattering regime.

For very dilute suspensions ( $10^2 - 10^3$  cells/mm<sup>3</sup> corresponding to very small haematocrit values of  $H = 10^{-5} - 10^{-4}$ ) and for a cuvette thickness  $d = 1$  mm for example, the probability of double scattering events is very small, the scattering being essentially a single scattering process. The forward scattering anisotropy is very high and the light intensity scattered at small angle increases with increasing cell density.

When the concentration is high enough so that the rate of multiple scattering events becomes comparable with the rate of single scattering, the process switches to multiple scattering. The scattered light loses gradually its anisotropy and consequently the amount of light scattered at small angle decreases. Nevertheless, the total scattered light continues to increase until all incident photons are scattered and their propagation directions are distributed almost isotropically.

Depending on the external suspending medium, different values for the erythrocytes scattering cross-section was reported: from  $63.82 \mu\text{m}^2$  in plasma up to values by about 25 – 50 % higher ( $95 \mu\text{m}^2$ ;  $81.24 \mu\text{m}^2$ ) in osmotically balanced saline solution (0.9% NaCl). Usually the erythrocyte scattering cross-section is in the domain  $60 < \sigma_s < 90 \mu\text{m}^2$  (depending on the properties of the suspending medium) and the erythrocyte volume is  $v_e \approx 90 \mu\text{m}^3$ . For a sample thickness  $d = 1$  mm the upper value of the single scattering domain is somewhere in the range  $10^{-3} - 1.5 \cdot 10^{-3}$  (0.1 – 0.15%).

One can observe in Fig. 4 that the fluctuations of the scattered light intensity are very important in the maximum neighborhood becoming comparable with the scattered light intensity mean values. The characteristic time scale of the fluctuating component becomes shorter as the cell density increases from very small values up to physiologic values.

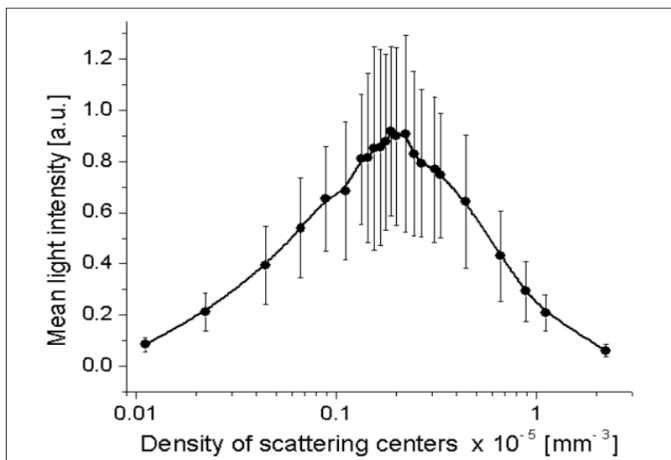


**Fig. 4.** Density dependence of the **dc** photocurrent for erythrocytes suspended in saline buffer. The fluctuations (given by the error bars) are comparable with the mean value.

The  $H$  dependence of **dc** current does not change significantly (up to an irrelevant rescaling effect) with distance  $D$  between sample and photo-detectors, as long as  $\theta$  is kept unchanged. Changes are observed rather in the fluctuating behavior of **ac** component. The explanation is related to the different number of speckles captured by the photo-detector. Since both the average number of speckles in a solid angle  $\Delta\Omega$ , and the sensing area  $A$  of the detector are constant, any change in  $D$  modifies the solid angle as  $\Delta\Omega = A/D^2$ . Consequently, the detector captures more or less speckles, depending on distance  $D$ .

Fig. 5 show the typical fluctuating behavior of  $i(t)$  measured at two distances  $D$  for the same  $H$  value. For small distances,  $\Delta\Omega$  is large enough so that the electric signal is the sum of many interference speckles and the fluctuations are distributed almost symmetrically about to the mean value. By decreasing the distance  $D$  one increase the number of captured speckles and the ratio of **ac** to **dc** components of  $i(t)$  decreases.

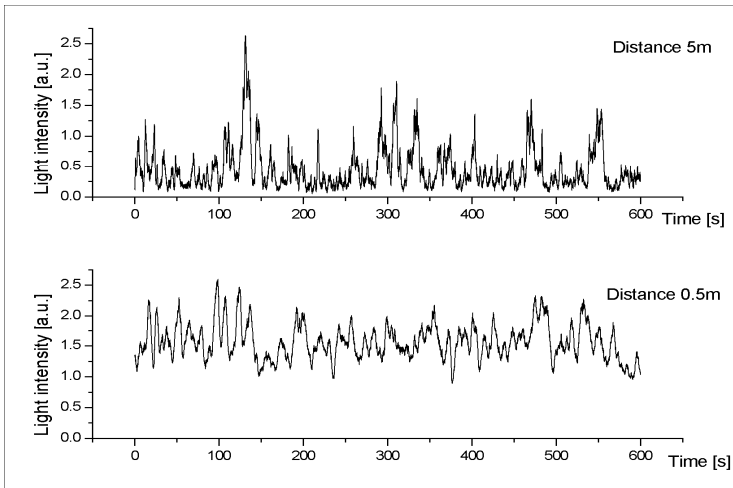


**Fig. 5.** Photocurrent fluctuations for single (upper curve) or multiple speckles (lower curve) capturing limits. The same time dependent stochastic interference pattern gives different photocurrent fluctuations.

For large distances, to the limit of single speckle, the scattered light captured by photo-detector is either a single bright light maximum or a dark spot, depending on constructive or destructive interference, respectively. The current fluctuations are asymmetric increasing from and decreasing to a baseline corresponding to the dark photocurrent. At intermediate distances one finds mixtures of the described limits.

Our results allow us to conclude that the most relevant parameter controlling the dynamics of scattering process is the density of erythrocytes suspension. The artifacts are mainly due to the averaging effect of the detectors. In the far field experiments, the photo-detector captures a single interference speckle and give the correct fluctuating dynamics. By decreasing the distance between the sample and detector, the detecting process switches from the single speckle to many speckles detection and the fluctuations amplitude of the measured photocurrent decrease by an artificial smoothing.

The effect of multiple scattering is easily observed in the dependence of scattered light intensity on the scatterer density. Both **dc** and **ac** components of the photocurrent have peak-type dependencies. The maximum of the corresponding curves indicates the entrance into the multiple scattering regime.

### ACKNOWLEDGMENTS

This research was supported by Romanian Education and Research Ministry, BIOTECH Program, research project 01-8-CPD-042.

### REFERENCES

1. A. Serov, W. Steenbergen, and F. de Mul, *Prediction of the photo-detector signal generated by Doppler-induced speckle fluctuations: theory and some validations*, J. Opt. Soc. Am. A **18**, (2001) 622-630.
2. X. Wang, G. Yao, and L.-H. Wang, *Monte Carlo model and single-scattering approximation of polarized light propagation in turbid media containing glucose*, Appl. Opt. **41** (4), (2002) 792–801.
3. W. Steenbergen, R. Kolkman, D. Faber and F. de Mul, *Scattering properties of whole blood under simple shear*, in *Optical Diagnosis of Biological Fluids V*, A. V. Priezzhev and T. Asakura, eds., Proc. SPIE **3923**, (2000) 99-108.
4. V. Voeikov, S. Kondakov, E. Buravleva, I. Kaganovsky, and M. Reznikov, *Computerised video-enhanced high temporal resolution of erythrocytes sedimentation rate (ESR-graphy) reveals complex dynamic and self-organising properties of whole blood*, in *Optical Diagnosis of Biological Fluids V*, A. V. Priezzhev and T. Asakura, eds., Proc. SPIE **3923**, (2000) 99-108.
5. A. K. Dunn, A. Devor, H. Bolay, M. L. Andermann, M. A. Moskowitz, A. M. Dale, and D. A. Boas, *Simultaneous imaging of total cerebral hemoglobin concentration, oxygenation, and blood flow during functional activation*, Opt. Lett. **28** (1), (2003) 28-30.
6. J. D. Briers, *Laser Doppler, speckle and related techniques for blood perfusion mapping and imaging*, Physiol. Meas. **22**, (2001) R35–R66.

## OVERVIEW ON MICROWAVES POWER APPLICATIONS IN MOLECULAR PHYSICS

**E. SURDUCAN<sup>2</sup>, V. SURDUCAN<sup>2</sup>, C. NEAMTU<sup>2</sup>, S.V. FILIP<sup>2</sup>, G. NAGY<sup>2</sup>,  
C. VILICHE<sup>1</sup>, M. POSTOLACHE<sup>1</sup>**

*1- Babes Bolyai University – Chemistry Faculty, Cluj-Napoca*

*2- National Institute for Research and Development of Isotopic and  
Molecular Technologies, 71-103 Donath Street, POB 700, Cluj Napoca,  
email:manu@130.itim-cj.ro*

**ABSTRACT.** The non-conventional microwave power treatments is a well-known method in chemical and physical processing of materials. The microwave power applications are very attractive because of the energy saving rate (2 to 1000 comparatively with classical processes). The microwave technologies are very elaborate and specific to the nature of the treated materials.

Our purpose is to present the principal results of our work in this field:

- in material processing: sample dehydration, chemical reactions, probe digestion and extraction, microwave plasma assisted reactions
- the microwaves treatments apparatus realised and used for non-conventional processing applications: microwave power generator design and microwaves power control solutions, unimodale and multimodale treatment cavities design, microwave plasma applicator, microwave s sample preparation unit for digestion and extraction, processing technologies for reproducible treatments, microwave absorption's and microwave power distributions in treatments processes, probe temperature measurements considerations, data base for microwave treatments

These results has the purpose to underline the microwaves power treatments advantages and to present the complexity of this domain and the directions of the future developments.

### **1. Basis of the microwave treatments**

The base principles of microwave treatments are: (one) the direct energy transfer of microwave energy on the probe to be treated and (second) the selectivity of microwave absorption by the dielectric loss of the probe. These two characteristics imply a time rate of treatments between 2 to 1000 comparatively with classical processes. Other attractive characteristic of microwave treatments is the possibility of microwave power control by a local PC or microcontroller.

These are the “good” side of microwave treatments. The other side of the problem are: the reproducibility of the treatments, temperature control of the process, the complexity if the microwave unit (including the acknowledge of the microwave theory of the field distributions, and the microwave treatment prescriptions) and not in the last time, the biological protection of the user.

In this paper we intent to present briefly all these aspects related to specific applications in molecular physics.



## 2. Microwave treatments applications

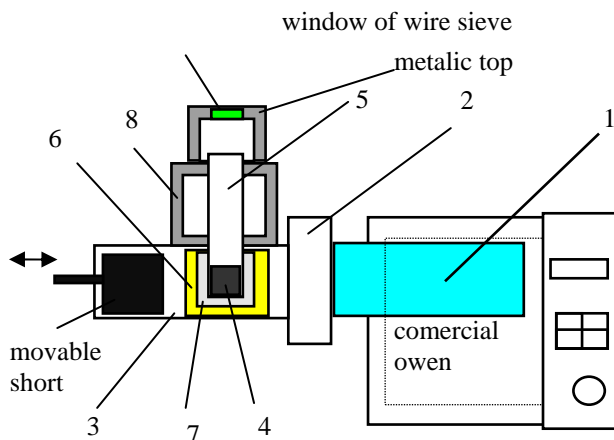


**Fig. 1.** A modified microwave comercial owen



**Fig. 2.** Experimental microwa-ve unit [1, 7] for chemical reaction with two cavities : multimodale  $TM_{333}$ , and

The first microwave device, which we have used in microwave treatments, was a modified microwaves commercial owen. The microwave owen is a multimodal microwave cavity in which the incident power has a particular distribution (fig.3). If the probe to be treated has a great volume, this multimodal cavity is OK to do a treatment because many part of the local power distribution intersect the volume of the probe. If the probe is small, the position of the probe in the multimodal cavity is critical and if by hazard the position of the probe coincide with one of the local power distribution only a fraction of the incident power is used in the process of the treatment. Our modification of the microwave owen consist in the use of one unimodal cavity and in the possibility to adapt de microwave power transfer in this unimodal cavity. In fact we use only the microwave generator and the electronic control system of the owen. In the figure 1 it is the microwave line arrangement (it is one of the most versatile configuration). The waveguide (1) pass out of the owen the microwave power. (2) is one inductive movable iris and (3) is one waveguide with movable short circuit. The unimodale cavity is formed between the short and the iris.

**Tabel 1.**

**Comparative results of the fenoxiacetic acid sinteze in microwave activation (700 W, 2.45 Ghz) and classic by thermal effect**

Acid fenoxiacetic	Microwave activation			Classical activation		
	Time (min.)	efficiency (%)	fusion temperature (°C)	Time (min)	efficiency (%)	fusion temperature (°C)
Ac. fenoxiacetic	0.5	70	94-96	240	73	99-100
Ac. 2,4-di-tBu-fenoxiacetic	0.66	64	166-167	240	60	165
Ac. 1,4-fenilendioxidiacetic	0.66	58	251-253	180	68-72	251
Ac. 1,3-fenilendioxidiacetic	0.4	60	190	180	62	194
Ac. 2-nitro-fenoxiacetic	4	70	157-159	660	46	156
Ac. 2-Me-5-iPr-fenoxiacetic	1	62	140-142	-	53.8	149
Ac. 2,3-dimetil-fenoxiacetic	0.4	55	162-163	-	60	160

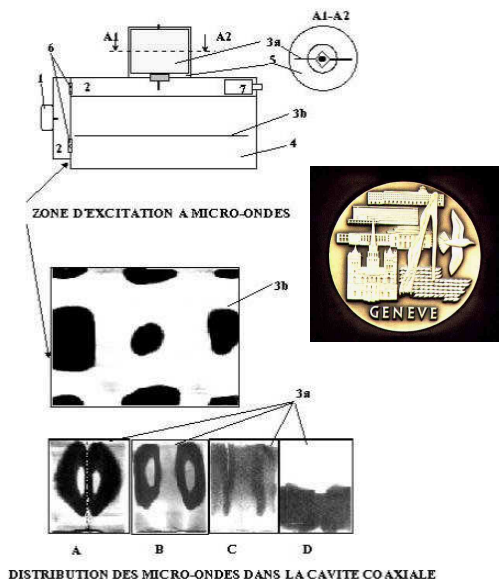


**Fig. 3.** Microwave power field distribution in the commercial oven (3b) and unimodale cavity (3a)-emptie (A), with TFLON vessel (B), filed with water (C), partially filed with water (D) [5]

The probe (4) is located in the center of this volume in one quartz test tube (5) (D=20mm, h=200mm). To homogenize de microwave field, the quartz tube is placed inside on ceramic (80% Al<sub>2</sub>O<sub>3</sub>) or quartz vase (6) (D=40mm, h=34mm) surrounded by alumina (99% Al<sub>2</sub>O<sub>3</sub>) powder (7). The filter (8) is to stop the microwave power to pass out via the quartz tube direction. For biological protection is better to use one metallic top cover (with one window of wire sieve), bat in most experimental arrangement this is an inconvenient [ 22, 23].

In chemical reaction it is important to know the microwave energy used. In the unimodal cavity all the microwave power is distributed in one volume (ellipsoid centered in the geometry of the cavity) (fig.2,3).

The results of the first chemical reactions studied are presented in the Table 1 [11,12,13,18,19].

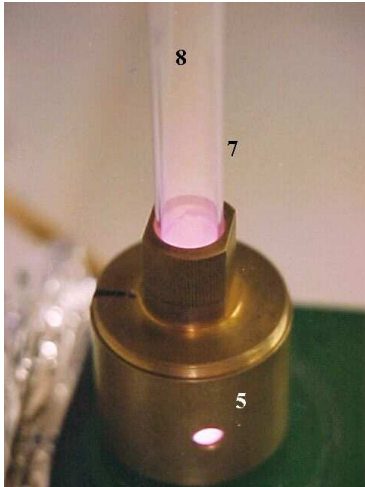


**Fig. 4.** Microwave plasma generator



**Fig. 5.** Microwave plasma unit for surface activation

*Reactive plasma discharges* (fig.4) are widely used to process materials. Among plasma sources, in the microwave plasma generator the microwave power is coupled to the plasma across a dielectric window, rather than by direct connection to an electrode immersed in the plasma as in classical RF plasma sources. The plasma (8) is confined in the maximum microwave power density distributions of the microwave cavity (5) [17]. This microwave power density distribution can be observed by the use of the microwave thermographic transducer [4, 5].

*Microwave plasma* are used in a process for activating ethylene-propylene- diene rubber in microwave plasma, which consists in polarizing the graphite addition-containing rubber surface in air plasma, priming the same in a microwave field, in the absence of the microwave radiation inside the treatment enclosure, at a pressure of 0.1 ... 0.5 mbars and a flow rate of 1 ... 5 l/min, for 15 ... 60 min, the volume ratio rubber/treatment enclosure being of 1/5. Rubber activation is ensured without structural volume changes thereof even in case the samples have an intricate topography, while also making sure that on filtering the microwaves in the activation enclosure, the sample does not interact with the microwave radiation [10,16].

*The process and device for heating fluids* (fig.4) without dielectric losses, in the high power microwave field, may be employed in the technological processes for the treatment in the high power microwave field of the fluids which cannot be heated normally by the absorption of high power microwave radiation, such as gases, non-polar liquids or gas-liquid mixtures. The device for heating the fluids without dielectric losses in the high power

microwave field employs an indirect or combined heating process. In an enclosure for treatment with microwaves (1,2), the fluid passes through a zone with highly microwave-absorbing material (3), such as a sponge conductor or dielectric-conductive combination having a spongy structure.

The microwave absorption by the material having dielectric loss results in the heating thereof, and consequently, by passing the fluid through this material, an indirect heating is achieved. The modification of the dielectric properties of the fluid due to heating the same may lead to a direct absorption of microwaves into the processed fluid. Thus, a combined heating is achieved [6,9,20,21].

*Microwave assisted digestion and extraction* represent the most complex unconventional treatment procedure, mostly because [3,14,15]:



**Fig.6.** Microwaves cavity for heating lossless material [6] (nonpolar solvents)



**Fig. 7.** Microwave unit for chemical treatments with microcontroller and RS232 PC interface

- Probe decomposition reaction is taking place in strong acids or mixture of strong acids and water ( $H_2O_2$ ); microwave absorption is taking place directly and selective in the probe-acids mixture.

- Microwave energy distribution inside the reaction chamber is a function of probe nature (including the probe, acids mixture and vessel) and microwave incident power distribution

- The samples are digested into closed vessels where the pressure can be up to 10 atm.

- The mixture is overheat up to 250C and TEFLON vessel can be destroyed;

- Pressure and temperature measurements inside the microwave reaction chamber are very difficult, usual temperature sensors are destroyed by the microwave field and pressure sensors by the acids.

- After a finished treatment and sample cooling the treatment vessels have an internal pressure up to 5atm

We have designed a microcontroller based, microwave digestion assisted unit (fig.7), project covered by three Romanians patents [7,8,9], internationally awarded, which solve most of the problems above. Digestion results (table 2) are the same (or better) than using an USA digestion equipment (CEM).

*Wine is an important food commodity and is traded across the whole world. This*

drink can contain significant levels of heavy metals originating from the soil, (agricultural practices and atmospheric pollution for instance) or production process. Samples (100 ml) were weighed in a Teflon capsule and placed in a microwave digester for 45 min, followed by digestion with  $HNO_3$  65% and  $H_2O_2$  30% for 15 min and dilution with  $H_2O$ .

Classic method is dry mineralization. Samples of wine (100ml) were evaporated to dryness 12 hours with  $HNO_3$  65%. The white residue was dissolved in  $HNO_3$  65% followed by dilution with  $H_2O$  to 25 ml. Analysis in both methods was by AAS with atomization by air/acetylene (Table no.3).

**Table 2**

**Atomic absorption spectrometry (AAS) results of the digested probe**

METHOD	Cu ( $\mu\text{g/g}$ )	Pb ( $\mu\text{g/g}$ )	Zn ( $\mu\text{g/g}$ )
Procedure I	176,58	677,91	453,7
Procedure II	191,65	726,78	490
Procedure III	275,81	763,03	515,87
CEM	248	838	426

Table 3

## AAS analysis of the vine

SAMPLE	METHOD	Cu (mg/l)	Pb(mg/l)	Zn(mg/l)
RED WINE	UNPROCESSING	0.02615	0.4115	0.4816
	CLASSIC	0.1738	0.039	0.80325
	<b>MICROWAVE</b>	<b>1.57415</b>	<b>0.201</b>	<b>9.43</b>
WHITE WINE	UNPROCESSING	0.02585	0.39	0.3162
	CLASSIC	0.15855	0.01	0.46535
	<b>MICROWAVE</b>	<b>0.7926</b>	<b>0.102</b>	<b>2.7672</b>

### 3. Future perspective

Microwaves processing of the probes for analyze is considered to be the future method for probe processing in the following 10 years. The complexity of the microwave treatment prescriptions will be solved by data bases stored in personal computers or local memory; network or genetic algorithms will solve the best solution for a particular process [2].

## BIBLIOGRAPHY

1. E.Surducu, V.Surducu, Gabriela Nagy, Sorin Filip, "APPAREIL DE TRAITEMENTS PAR MICRO-ONDES" GENEVA – PALEXPO, The 30th International Exhibition of Inventions, New Techniques and Products, 1th – 5th Mai 2002, **Bronze medal, class A**
2. V.Surducu, E.Surducu, C.Neamtu, "Microcontroller based interface unit for 5 KW microwave oven", Studia Universitatis "Babes-Bolyai", Physica, Special Issue vol. 2, Proc. of the 2<sup>nd</sup> Conf. with International Participation "Isotopic and Molecular Processes"- PIM 2001, Cluj-Napoca, Romania, Sept. 27-29, 2001, 294-299 (2002)
3. E.Surducu, C. Neamtu, V.Surducu, G. Nagy, S.Filip, "Microwave power - assisted sample preparation. Extraction studies "Studia Universitatis "Babes-Bolyai", Physica, Special Issue vol. 2, Proc. of the 2<sup>nd</sup> Conf. with International Participation "Isotopic and Molecular Processes"-PIM 2001, Cluj-Napoca, Romania, Sept. 27-29, 2001, 428-432 (2002)
4. E.Surducu, V.Surducu, C. Neamtu, "Studies of the microwaves distributions in microwave power applications", Studia Universitatis "Babes-Bolyai", Physica, Special Issue vol. 2, Proc. of the 2<sup>nd</sup> Conf. with International Participation "Isotopic and Molecular Processes"- PIM 2001, Cluj-Napoca, Romania, Sept. 27-29, 2001, 433-438 (2002)
5. E.Surducu, V.Surducu, "Le traducteur thermographique pour les microondes de puissance" GENEVA – PALEXPO, The 29th International Exhibition of Inventions, New Techniques and Products, 11th – 15th April 2001, Geneva, **Bronze medal, class A**
6. E.Surducu, V.Surducu, "Procede et dispositif pour le chauffage par micro-ondes des fluides sans pertes dielectrique" EUREKA-BRUSSEL The 50th Anniversary World Exhibition of Innovation Research and New Technology, 13-18 nov.2001, **Gold medal**

7. E.Surducan, V.Surducan, G.Nagy, S.Filip "*Instalatie de tratament in camp de microunde cu control de mod*" Brevet nr. **RO 116514 B1**/ian. 2001
8. E.Surducan, V.Surducan "*Traductor termografic pentru radiatie de microunde de putere*", Brevet nr. **RO116506** /ian. 2001
9. E.Surducan, V.Surducan, "*Dispozitiv pentru incalzirea fluidelor fara pierderi dielectrice in camp de microunde de putere*" Brevet nr. **RO 116515 B1**/ian. 2001
10. E.Surducan, S.Filip, V.Surducan, "*Metoda de activare a cauciucului de tip EPDM in plasma de microunde*" Brevet nr.**RO 116624 B1**/martie 2001
11. S.V. Filip, E. Surducan "*Procedure of acridone synthesis* "The Second Inventors' Olympiad - GENIUS 2000, International Fair of Inventions, 4th - 7th May 2000, Budapest
12. S.V. Filip, E. Surducan "*Procedure of acridone synthesis*" GENEVA – PALEXPO, The 28th Int. Exhib.of Invent. New Techn. and Products, 12th – 16th April 2000, Geneva
13. S.Filip, E.Surducan., "*Procedeu de sinteza a acridonei in camp de microunde*", Brevet nr **RO 114616 B1**, 30. 06. 1999
14. Gabriela Nagy, E. Surducan, U.Stanescu, C.Bele, D. Dadarlat, D. Bicanic, "*Microwave Degradation Of Sunflower Oil*" Romanian Reports in Physics, Vol. 51, Nr. 7-8-9 (1999)
15. D. Dadarlat, G. Nagy, U. Stanescu, C. Bele, M. Chirtoc, A. Frandas, I. Bratu, V. Surducan, E. Surducan, D. Bicanic "*Combined Photothermal and Classical Methods for the Study of Early Spoilage of Some Edible Oils*" Adv. Food Sci. 21, 177-183 (1999)
16. E. Surducan, V. Surducan, S.V. Filip, Gabriela Nagy, Camelia Neamtu "*Aplicatii ale interactiei microundelor cu substanta*" Revista Asociatiei pt. Colaborari Interdisciplinare a Specialistilor din Transilvania ASCI, Nr. 3 (1999)
17. E. Surducan, V.Surducan, "*The microwave power distribution measurements in the plasma generator cavity (TM100)*", Romanian Reports in Physics, Vol. 51, Nr.7-8-9 (1999)
18. S. Filip, I.A. Silberg, E. Surducan, V. Surducan, "*Microwave - assisted preparation of phenothiazines by thionation of diphenylamines* Synthetic Comm., 28, 337-345 (1998)
19. G.Nagy, S. V. Filip, E. Surducan, V. Surducan, "*Solvent-free synthesis of substituted phenoxyacetic acids under microwave radiation* Synthetic Comm., 27, 3729-3736 (1997)
20. E. Surducan, V. Surducan, S. V. Filip, C. Neamtu, "*Temperature influence on microwave absorption for polar liquids*" Balkan Phys. Lett., vol.5 (1997)
21. E.Surducan, V. Surducan, S. V. Filip, G. Nagy, "*Microwave absorption measurements on metal powder*" Balkan Phys. Lett., vol.5 (1997)
22. S.V. Filip, G. Nagy, E. Surducan, V. Surducan, "*Microwave appl. in organic synthesis. Microwave - assisted prep.of Diphenylamines in Dry media*" Balkan Phys. Lett., vol. 5 (1997)
23. S. Filip, E. Surducan, M. Vlassa, I. Silberg, G. Jucan, "*Microwave-assisted acridones preparation using an inorganic acidic solid support*" Heterocyclic Comm., 2, 431-434 (1996)

**ISOTOPIC SEPARATION, LABELLED COMPOUNDS AND APPLICATIONS****ANALYSIS OF MEASUREMENT ERRORS INFLUENCE ON  
EXPERIMENTAL DETERMINATION OF MASS  
AND HEAT TRANSFER COEFFICIENTS****FLOAREA POP, CORNELIA CROITORU, MIHAI CULCER,  
MARIANA ILIESCU, GHEORGHIE TITESCU,  
IOAN STEFANESCU, MARIUS PECULEA<sup>1</sup>***National Institute of Research-Development for Cryogenic and Isotopic  
Technologies ICSI Ramnicu Valcea, Romania, office@icsi.ro  
<sup>1</sup>Romanian Academy, Bucharest*

**ABSTRACT.** The paper analyses the influence of measurement errors of temperatures and concentrations at experimental determination of the mass and heat transfer coefficients. Calculus model for these coefficients, data obtained on the water distillation experimental plant, calculus model for measurement errors and the results of effected studies regarding measures errors influence are presented.

On experimental determination of mass and heat transfer coefficients have been used the relations

$$\frac{1}{A_1} \cdot \frac{d(L \cdot x)}{dz} = K'_y (y - y^*) \quad (1)$$

$$\frac{1}{A_1} \cdot c_{pl} \cdot \frac{d(L \cdot t_l)}{dz} = K'_t \cdot (t_v - t_l) + \frac{dL}{dz} \cdot c_{pl} \cdot t_l \quad (2)$$

The experimental column, with inner diameter of 108 mm have been equipped with B7 structured packing, on a height of 14 m. This column offers the possibility to measure vapour temperatures and concentrations in 12 points, figure 1. The quantities that have been measured are: temperatures, pressures, flow rate and isotopic concentrations. For errors propagation analysis were used just parameters measured on each packing stratum, vapour temperature, isotopic concentration respective, values presented in table 1. Isotopic concentrations were determined by densimetry, measurement errors being of  $\pm 0.02\%$ . Temperatures were measured with Fe-Co thermocouples, that have  $\pm 0.1^\circ\text{C}$  measurement errors. For the variation of these parameters with packing height, have been used approximate relations. For each packing stratum were calculated mass and heat transfer coefficients, using relations (1) and (2). These values are presented also in table 1.

Maximum errors at experimental determination of mass and heat transfer coefficients were calculated with relation:

$$e_K = \pm \sqrt{\left(\frac{\partial K'}{\partial t}\right)^2 \cdot \Delta t^2 + \left(\frac{\partial K'}{\partial x}\right)^2 \cdot \Delta x^2} \quad (3)$$

Partial derivatives on calculates using the next relation:

$$\frac{dK'_y}{dz} = \frac{\partial K'_y}{\partial x} \cdot \frac{dx}{dz} + \frac{\partial K'_y}{\partial t} \cdot \frac{dt}{dz} \quad (4)$$

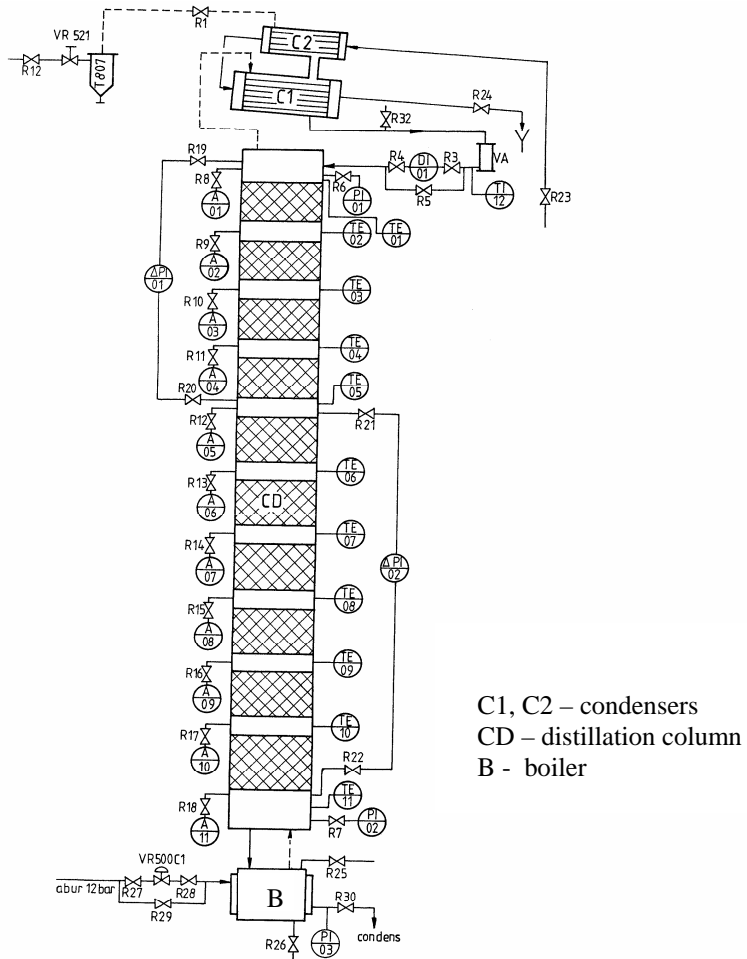


Fig. 1. Schematic diagram of the experimental water distillation plant

Using relation (4) were calculated maximum errors possible errors at experimental determination of the mass and heat transfer coefficients. These values are also presented in table 1.

Table 1

Nr. strat	Measured and calculated values					
	x	t	$K_y \text{ exp}$ kmol/m <sup>3</sup> .s	$e_{K_y}$	$K_t \text{ exp}$ kW/m <sup>3</sup> .grd	$e_{K_t}$
1	0.59	53,3	4.94E-02	1.42E-03	9.80E+00	9.87E-01
2	1.11	53.3	2.05E-01	1.40E-03	1.95E+00	1.56E-01
3	1.95	55.1	1.86E-01	2.52E-03	1.58E+00	1.31E-01
4	4.0	57.4	1.55E-01	3.78E-03	2.44E+00	8.78E-03
5	6.38	61.2	1.60E-01	7.28E-03	5.75E-01	5.19E-01



MEASUREMENT ERROR INFLUENCE ON MASS AND HEAT TRANSFER COEFFICIENTS

Nr. strat	x	t	Ky exp	$e_{Ky}$	Kt exp	$e_{Kt}$
	0,59	53,3	kmol/m <sup>3</sup> .s		kW/m <sup>3</sup> .grd	
6	15.8	63.85	1.47E-01	2.06E-02	7.77E-01	2.09E+00
7	29.52	62.8	1.35E-01	1.56E-02	1.34E+00	1.71E+00
8	41.76	63.8	1.24E-01	4.59E-02	5.20E+00	8.69E+00
9	51.46	62.2	1.15E-01	1.97E-02	-1.40E+01	2.84E+00
10	72.55	65.8	1.05E-01	1.44E-02	-1.46E+00	6.60E-01

Figures 2 and 3 show suggestively how large are the errors that can appear on experimental determinations.

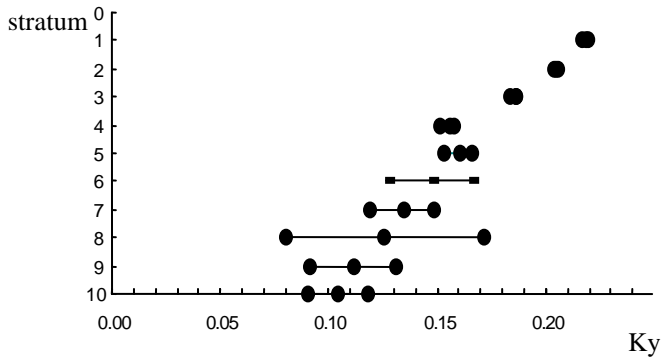


**Fig. 2** Error domains for Ky  
Ky [=] kmol/m<sup>3</sup>.s

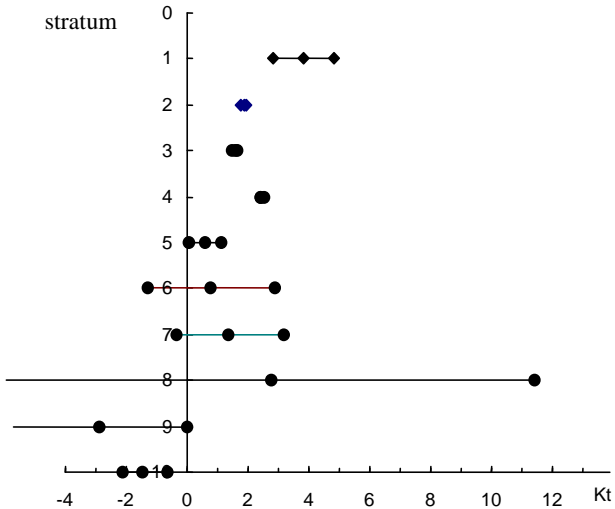


**Fig. 3** Error domains for Kt  
Kt [=] kW/(m<sup>3</sup>.grd)

The column having pellicular boiler, durring the experiments appeared superheatings of the column bottom. This ending effect have not been taken into consideration on the coefficients calculus, fact emphasised by negative values of heat transfer coefficient. In the same area measurement errors are the biggest. Being used in design, it is very important to know with high precision these transfer coefficients. Large errors on determination can lead to under or overestimation of packing performances. If the under estimation leads to increasing of investment costs, overestimation leads to decreasing of production capacity.

## REFERENCES

- [1] F. Pop, M. Peculea, C. Croitoru, *Experimental Determination of the Height of Transfer Unit at the Hydrogen Isotopic Distillation on Ordered Packing, B7 Type*, Revue Roumaine de Chimie, nr. 2, 1999
- [2] Tiron M., *Prelucrarea statistica si informationala a datelor de masurare*, Editura Tehnica, Bucuresti, 1976
- [3] C. Croitoru, F. Pop, Gh. Titescu, M. Culcer, M. Iliescu, *Experimentari asupra transferului de masa si caldura in coloane echipate cu umplutura ordonata tip B7*, Raport de cercetare, INC-DTCI ICSI Rm. Valcea, 2001

## **NEW IMPROVED HYDROPHOBIC Pt-CATALYST FOR HYDROGEN ISOTOPES SEPARATION**

**GH. IONITA, IRINA POPESCU, TEODORA RETEGAN and IOAN STEFANESCU**

*National Institute of Cryogenics and Isotopic Separation,  
P.O. Box 10, Rm-Valcea, 1000, Romania*

**ABSTRACT.** Based on the long experience of the authors, in the preparation, testing and evaluation of the performances of hydrophobic catalysts, and based on the reviewed references, this paper presents up-to-date R&D activities on the preparation methods and applications of the hydrophobic catalysts, in deuterium and tritium separation. The objectives of the paper are: (1) to provide a database for selection of the most appropriate catalyst and catalytic packing for above mentioned processes, (2) to evaluate the potentiality of hydrophobic Pt-catalysts in the deuterium and tritium separation (3) to assess and to find a new procedure for preparation of a new improved hydrophobic catalyst. The merits of the hydrophobic catalysts are shown in comparison to hydrophilic catalysts.

As results of the review some general conclusions about the applications of hydrophobic catalysts in environmental field are as follow: (1) the hydrophobic Pt-catalysts packed in the trickle bed reactors showed a high catalytic activity and long stability; (2) the utilization of the hydrophobic Pt-catalysts for tritium removal from liquid and gaseous effluent in nuclear field was entirely confirmed on industrial scale; (3) the extension of the utilization of the hydrophobic Pt-catalysts in other new processes, which take place in presence of liquid water or high humidity are subjected to testing.

### **I. INTRODUCTION**

The hydrophobic catalysts were initially conceived for the deuterium enrichment and tritium separation by hydrogen-liquid water isotopic exchange in nuclear field. For this process, the conventional hydrophilic catalysts become inefficient due to loss of their activity upon the direct contact with liquid water or by capillary condensation of water vapor. Therefore, it was necessary to prepare a catalyst, which repels the liquid water but allows the transport of the gaseous reactants and reaction products to and from catalytic active centers. In principle, the mode of preparation of hydrophobic catalysts is similar to that of conventional hydrophilic catalysts. The main differences between them consist of support nature, wet-proofing method and active metal deposition method [2-6]. The main research was focused on the improvement of the catalyst' activity and stability, on their geometry as well as on the decrease of their cost price. High performances have been proved in hydrogen isotopes separation process and recently, by the new applications in environmental field the interest for this type of catalysts became of large topical interest.

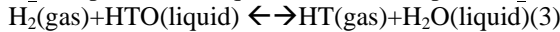
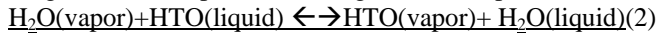
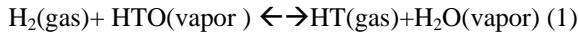
This paper, reviews a wide range of preparative methods and applications of hydrophobic catalysts for the removal of tritium from liquid and gaseous effluents. Also is presented a proposal for a new improved hydrophobic Pt-catalyst for hydrogen isotopes separation.

### **II. PROGRESS CONCERNING THE ENGINEERING APPLICATIONS OF THE HYDROPHOBIC Pt- CATALYSTS IN ENVIRONMENTAL FIELD**

#### ***II.1 Tritium Removal from Aqueous Effluents***

During spent nuclear fuel reprocessing and generally during nuclear activities involving tritium, significant quantities of intermediate and low-level liquid waste are generated. The detritiation of aqueous waste stream by hydrogen-water isotopic exchange were intensively researched and developed.

A demonstration pilot based on cryogenic distillation coupled with catalytic exchange on platinum on carbon and TEFLON (Pt/C/PTFE) hydrophobic catalyst in liquid phase is under testing in Romania [5] having as main goal the detritiation of heavy water from CANDU nuclear power plant from Cernavoda. The key point in all these processes for removal of tritium from aqueous effluents is the activity and stability of hydrophobic catalyst, which promote the isotopic exchange, in two steps:



To promote reaction (1), over 100 catalysts with hydrophobic properties have been prepared and tested [1-5]. The main types of tested and selected catalysts for hydrogen isotope separation process are summarized in Table 1. The high performances of hydrophobic Pt-catalysts and their long stability to promote reaction (1) was demonstrated on plant scale, in the process of the tritium recovery from heavy water used as moderator in CANDU reactors.

The experiments carried-out by some authors [6] showed that by diluting the currently hydrophobic catalyst with hydrophilic materials, the liquid hold-up increased, the water distribution was improved and the performances of the mass transfer between water vapors and liquid water increased considerably.

The main mixed catalytic packing types selected after long experiments in some country for tritium removal by isotopic exchange on hydrophobic catalysts are presented in the Table 1[1-5]. Usually the selected packings are operated at atmospheric pressure and at the temperatures bellow 80° C in columns of less 10 m height. Finally, it was also proved that an arrangement of the packing in ordered bed was more efficient than that in random bed.

## II. 2 Cleanup of the Airborne Tritium at Nuclear Facilities

Oxidation of tritium on catalyst surface followed by adsorption of tritiated water vapor in a molecular sieve drier was a widely accepted method for the recovery of airborne tritium to ensure that environmental releases from tritium handling facilities are minimized. The tritiated hydrogen-oxygen recombination (to cleanup of airborne tritium at tritium handling facilities) with platinum/silica and platinum/carbon hydrophobic catalyst showed a decontamination factors of  $10^3$  to  $10^6$  and a stability of the catalyst up to 120 days.

## III. DISCUSSIONS

Properties of hydrophobic catalysts like lifetime, catalytic activity, mechanical stability and susceptibility to poisoning and leaching are higher than of hydrophilic catalysts.

Table 1.

The main types of hydrophobic catalysts and mixed packing tested and selected for tritium removal by H<sub>2</sub>-H<sub>2</sub>O isotopic exchange

COUNTRY	Tested catalyst types and metal content (wt%)	Selected catalyst type and its stability	The type of selected mixed packing
CANADA	0.5%- Pt / Al <sub>2</sub> O <sub>3</sub> [6] 0.4%- Pt / PTFE 0.1-0.4%- (Pt / C)/PTFE (emulsion)	0.1% - (Pt/C)/PTFE After 170 days running the catalyst lost 13 % off initial activity	1) A matrix of platinized hydrophobic carbon and PTFE deposited on corrugated screening and wound with alternate layers of hydrophilic cotton cloth

NEW IMPROVED HYDROPHOBIC Pt-CATALYST FOR HYDROGEN ISOTOPES SEPARATION

COUNTRY	Tested catalyst types and metal content (wt%)	Selected catalyst type and its stability	The type of selected mixed packing
	Pt / zeolite Pt / SiO <sub>2</sub>		2) Random packing consisting of 50% 0.37% Pt/C PTFE catalyst and 50% hydrophilic packing
INDIA	1% - (Pt /C)/PTFE [4] 1% - (Pt/Al <sub>2</sub> O <sub>3</sub> )/PTFE [4] 1% - (Pt/zeolite)/PTFE[4]	1% - Pt/C/ PTFE Minimum some weeks	
JAPAN	1.5% - Pt/PTFE [3] 0.1-2% - Pt/SDBC [1, 3] 1.2-1.4% - Pt/SDBC-film type Pt /FC-PTFE Pt/Al <sub>2</sub> O <sub>3</sub> [1]	0.5% - Pt/SDBC (Kogel catalyst) 13 years in separated bed reactor process without any regeneration	1) Separated beds of 0.5%Pt/SDBC catalyst and Mac Mahon hydrophilic packing in which the liquid water is not in contact with the catalyst. 2) 1.5%Pt/PTFE rings (7 x 3 x 0.8 mm) and mists water (particle size 5 m) in con-current with H <sub>2</sub> gas
GERMANY	0.4% - Pt/C/PTFE [2]	0.4% - Pt/C/PTFE	-
ROMANIA	0.1-1% - Pt/C/PTFE [5] 0.1-2% - Pt/SDB 0.1-2% - Pt/SDB/PS 0.5% - Pt/SDB/PTFE	0.45% - Pt/C/PTFE One year half in LPCE process, without any regeneration	Alternated beds of 0.45% Pt/C/PTFE and thermo-chemical activated metal hydrophilic packing
BELGIUM	Pt; Pd; Ni; Pt-Ni; Pt-Pd; deposited on carbon or TEFLON (over 30 different types)	1% - Pt/C/ PTFE 5000 hours	67% etched Dixon packing and 33% Pt/C /PTFE catalyst
RUSSIA	0.8% - Pt/Polysorb Pd/Al <sub>2</sub> O <sub>3</sub>	0.8% - Pt/Polysorb	Alternated beds of granulated platinum / Polysorb catalyst and hydrophilic metallic packing (Levin's packing)
U.S.A	0.1% - Pt/C/PTFE (Canadian catalyst)	0.1% - Pt/C/PTFE	Ordered packing consisting of Pt/C/PTFE dispersed on corrugated stainless steel screen mesh with a cotton fabric overlaid on the screen and wound in a cylindrical shape

Their applicability to tritium removal from wastewater effluents from nuclear activities was proved on industrial scale and the extension of their application for similar process which take place in presence of liquid water or humid air was proved in many laboratory experiments.

From the analysis of reported data it is beyond any doubt, that platinum under 1 wt% remains the best active metal and the Teflon the most effective wet-proofing agent. In all applications, the hydrophobic Pt-catalysts showed a high activity, long stability, as well as an easy and repeatable way for their regeneration. The high efficiency in tritium removal from liquid and gaseous at low temperature on hydrophobic catalyst can be explained only by their hydrophobic property. By using of hydrophobic support, liquid water and the water vapor (as reaction product or from atmosphere) would not be adsorbed on the surface, thus the active sites would not be blocked, and catalyst activity can be maintained long time even at lower temperature. When a catalyst becomes hydrophobic, the reactants (hydrogen, hydrocarbon, oxygen etc.) may be more readily adsorbed on the surface of the catalyst where it can react.

Recording all available data concerning preparative methods and test results of the hydrophobic catalysts we consider that hydrophobic Pt-catalyst can be improved. Our proposal for a new improved hydrophobic Pt-catalyst is a method based on the direct polymerisation of the PTFE on the Pt/C support (hydrophilic catalyst) followed by the pressing in a convenient shape. In this way the PTFE surrounding the catalytic active particles and its hydrophobicity will be increased keeping on the same time initial high platinum dispersion.

#### IV. SUMMARY

Compared with conventional hydrophilic catalysts, the pollutants removal from liquid and gaseous effluent by means of hydrophobic catalyst offers a higher efficiency; lower operation temperature and pressure and energy requirements as well as lower costs.

According to available references data, the most catalytic active metal is platinum deposited on hydrophobic support or made wet-proofed by using Teflon. In the most applications, to improve its performances it is recommended the utilization of hydrophobic catalysts as ordered mixed catalytic packing in a trickle bed reactor. Due to their unique property, the hydrophobic Pt-catalyst may thus provide a cost effective environmentally attractive option to manage the complete removal of pollutants from liquid and gaseous effluents.

We propose a new preparative method for an improved hydrophobic Pt-catalyst used for hydrogen isotopes separation.

#### REFERENCES

1. Shimizu, M.; Kiyota, S.; Ninomya, R. *Hydrogen Isotope Enrichment by Hydrophobic Pt-Catalyst in Japan and Western Countries*. Proc. International Symposium on Isotope Separation and Chemical Exchange Uranium Enrichment, Tokyo, 1990.
1. Fieck, H. J.; Romaker, J.; Schindewolf, U. *Tritium-Anreicherung durch Isotopen-Austausch zwischen Wasserstoff und Wasser mittels Hydrophoben Catalysators für die Kernbrennstoff-Wiederaufbereitung*. Chem. Eng. Tech. 1980, 52, 892.
2. Asakura, Y.; Tsuchiya H.; Yusa, H. *Deuterium Exchange between Water Mists and Hydrogen Gas in a Hydrophobic Catalyst Bed*. Nuclear Science and Engineering. 1981, 79
3. Belapurkar, A. D.; Gupta N. M.; Iyer, R. M. *PTFE Dispersed Hydrophobic Catalysts for Hydrogen-Water Isotopic Exchange*. Applied Catalysis. 1988, 43, 1.
4. Ionita, G.; Stefanescu, I. *The Separation of Deuterium and Tritium on Pt/SDBC/PS and Pt/C/PTFE Hydrophobic Catalysts*. Fusion Technology. 1995, 28, 64.
5. Butler, J. P.; Rolston, J.; H Stevens, H. *Novel Catalyst for Isotopic Exchange between Hydrogen and Liquid Water*. ACS Symp. 1978, Series 68, 93.

## NEW IMPROVED COUNTER-CURRENT MULTI-STAGE CENTRIFUGAL EXTRACTOR FOR SOLVENT EXTRACTION PROCES

**GHEORGHE IONITA<sup>1</sup>, ASASHI KITAMOTO<sup>2</sup>, DUMITRU MIRICA<sup>1</sup>, CROITORU CORNELIA<sup>1</sup>, IOAN STEFANESCU<sup>1</sup> and RETEGAN TEODORA<sup>1</sup>**

*1-National Institute for Cryogenics and Isotopic Separation Rm-Valcea, P.O. Box 10, Romania, E-mail: ionita@icsi.ro*

*2-Tokyo Institute of Technology, O-Okayama, Meguro-ku, Tokyo, 152 Japan*

**ABSTRACT.** Total actinide recovery, lanthanide/actinide separation and the selective partitioning of actinide from high level waste (HLW) are nowadays of a major interest. Actinide partitioning with a view to safe disposing of HLW or utilization in many other applications of recovered elements involves an extraction process usually by means mixer-settler, pulse column or centrifugal contactor. This last, presents some doubtless advantages and responds to the above mentioned goals. A new type of counter-current multistage centrifugal extractor has been designed and performed. Similar apparatus still not found from other published paper yet. The counter-current multi-stage centrifugal extractor was a cylinder made of stainless steel with an effective length of 346 mm, the effective diameter of 100 mm and a volume of 1.5 liters, having horizontal position as working position. The new internal structure and geometry of the new advanced centrifugal extractor (Fig.1) consists in nine cells (units): five rotation units(R), two mixing units (M), two propelling units (P) and two final plates (S) assures the counter-current running of the two phases. The central shaft (CS) having the rotation cells fixed on it is connected by an intermediary connection to an electric motor of high rotation speed.

The new designed extractor has been tested at 500-2800 rot/min for a ratio of the aqueous/organic phase =1. The results showed that the performances have been generally good and the design demand was reached. New designed counter-current multistage centrifugal extractor may be a promising idea to increase extraction rate of radionuclides and metals from liquid effluents.

### Introduction

The separation by extraction of transuranium elements and long-lived nuclides (<sup>99</sup>Tc, <sup>129</sup>I etc) from high level radioactive waste is the key point in radioactive waste management as integrant part of partitioning- transmutation concept. What kind of extraction process can realize such fine partitioning of the high level waste with small radioisotopes inventory, with high recovery and with negligibly secondary wastes. In conventional extractors are needed to improve the separation factor to level of commercial importance. A more compact size, high throughput and high extraction efficiency as well as the minimization of solvent radiolysis and rapidly achieve steady state operation are necessary. Some strong advantages which determine an major interest for this type of extractor. At present time, the most countries with nuclear fuel processing programs are involved to some degree with centrifugal extractor development.

### Counter-Current Multistage Centrifugal Extractor

A new type of centrifugal extractor having a counter-current flowing of phases, an horizontal working position and special inner geometry have been designed and tested. Similar apparatus has not been found in the published papers yet. The counter-current multistage centrifugal extractor is a stainless steel cylinder with a 1.55 l capacity, having more settling and mixing cells set on the central shaft.

This can be rotated up to 2800 rpm by means an electric motor connected at central shaft by special connection piece. In the mixing zone, the two phases are mixed. The TBP extracts (in the same time) the radionuclides or metal of interest. In the settling zone the two phases are separated. A special geometry of the cells at the both ends of extractor assures the evacuations of organic and aqueous phase. The conceptual layout of advanced counter-current multistage centrifugal extractor is showed bellow.

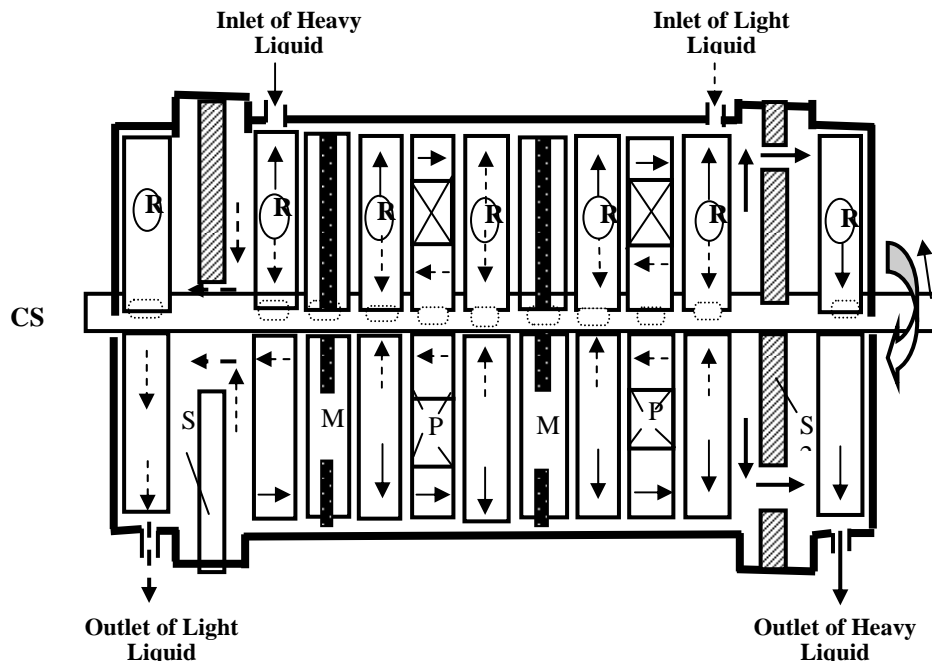


Fig. 1. Conceptual layout of advanced counter-current multi-stage centrifugal extractor.

### Experimental and Results

Preliminary tests concerning the mechanical behaviour showed a good balance and stability. Than the preliminary tests of the hydrodynamics of the two phases show the countercurrent flowing and a good separation of organic and aqueous phases. However some disturbing phenomena (remixing of phases, emulsion formation etc) could be avoided only in extreme operation conditions. In order to improve the separation performances and to avoid such phenomena a new inner geometry of settling and mixing zone has been proposed and performed. The hydrodynamic properties of two phases and separation performances of new improved centrifugal extractor were studied for a wide range of operation parameters: 500-2800 rotations per minute, 5-35 sec., residence time, 0.1- 5.0 organic/aqueous flow rate ratio. The influence of the operation parameters on separation performances and on the formation of third phase are presented and discussed in order to select the optimal operation parameters. A separation level for organic and aqueous phases upper of 93% and also a good efficiency for mixing zones (fig.1) have been obtained for whole range of operation parameters.

The disturbing phenomena could be partially avoided. The operating stability of the multi-stage centrifugal extractor is quite good and is very well showed in the figure 2. Some studies concerning the extension of number of stages and specific aspect for each application are still necessary.



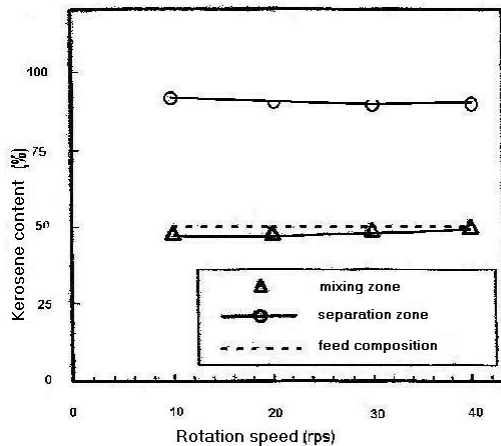


Fig.1.1. The mixing and outlet composition of the organic phase

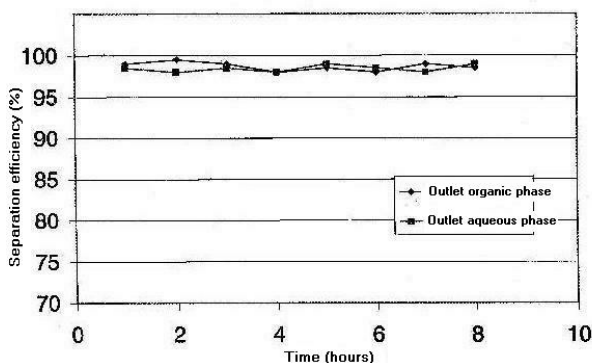


Fig.1.2. The operating stability of the multi-stage centrifugal extractor

### Conclusion

The new type of counter-current centrifugal extractor showed satisfactory results, it meet the design demand and by its advantages it could be a promising equipment for solvent extraction in chemical and nuclear industry.

### BIBLIOGRAPHY

1. R. A. Leonard, G. J. Bernstein, A. A.Ziegler and R. H. Pelto, "Annular Centrifugal Contactors for Solvent Extraction," Separation Science and Technology, 15(4), 925-943, (1980).
2. R. A. Leonard, "Recent Advances in Centrifugal Contactor Design," Separation Science and Technology, 23 (12&13), 1473-1487, (1988).
3. S.F.DeMuth and J.D.Randolph, "Uranium and Zirconium Mass Transfer Testing of 5.5-CM-Diam Centrifugal Contactors," Separation Science and Technology, 23 (12&13), 1489-1502, (1988).

## THE RECOVERY OF GOLD FROM CHLORIDE SOLUTIONS USING THE SELECTIVE ION EXCHANGE RESIN IONAC SR3

**MIHAELA PAVEL<sup>1</sup>, DAMIAN AXENTE<sup>2</sup>**

<sup>1</sup> Mining Research Development and Engineering Institute S.C. CEPROMIN S.A., Deva 2700, 22 Decembrie Street 37A; E-mail: mihapavel@scientist.com

<sup>2</sup> National Institute for Research and Development of Isotopic and Molecular Technologies, 3400 Cluj-Napoca, Donath Street 65-103; E-mail: axente@s6.itim-cj.ro

**ABSTRACT.** Strong base anion resins are not sufficiently selective to separate precious metals from large amounts of accompanying metals, present in hydrometallurgical gold solutions. The present work studied the recovery of precious metals from hydrometallurgical chloride solutions with high content of Pb, Cu, Zn, and Fe by an ion exchange process. Using the selective ion exchange resin IONAC SR3 gold recovery reached 92.43 %.

### Introduction

Ion exchange resins are still very little used commercially for gold extraction from hydrometallurgical leach solutions, despite the advantages of resins (higher equilibrium loading, easier elution of gold, no periodic thermal reactivation for organics removal etc.) over activated carbon [1,2]. Selective ion exchange resins, like IONAC SR3, can chelate gold and silver, but not interact with alkaline and alkaline earth metals or transition metals such as copper and zinc [3].

### Experimental

*Materials:* Synthetic and real leach solutions (obtained by the leaching of a metallurgical residue in highly concentrated acidic and oxidant calcium chloride solutions) were employed in the research works.

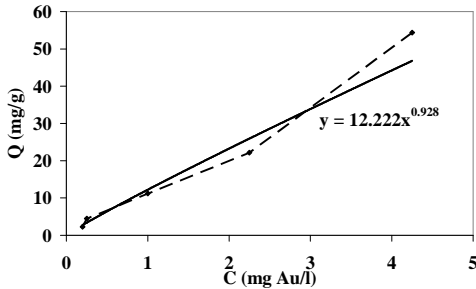
The ion exchange resin IONAC SR3, supplied by Sybron Chemicals Inc., is a highly selective chelating resin, containing isothiuronium chloride active groups. It was used for gold adsorption in chloride form, without any pre-treatment. Substances used for the test work, were all of reagent grade.

*Testing apparatus and procedure:* The adsorption and desorption tests were conducted in stirred glass vessels. All solutions before and after adsorption or desorption test were assayed for gold with an atomic adsorption spectrometer VARIAN SpectrAA 200.

### Results and discussions

*The adsorption isotherm* - Data to plot down the gold adsorption isotherm on the IONAC SR3 resin, at 25<sup>0</sup>C, has been obtained by stirring, for 24 hours, volumes of 100 ml of synthetic solutions, with a 0.95 pH and containing 113 mg/l Au, 0.64 mg/l Ag, and 59.3 mg/l Cu, and quantities of resin between 0.2g and 5g . The obtained results have shown that the resin / solution contact time of 24 hours has been sufficient for reaching the equilibrium point, while the gold concentrations on the resin and in the solution, remained practically constant after 16 hours.

The variation from Fig. 1,  $Q = f(C)$  can be approximated with the most lightly straight line  $y = 12,222 \times 0,928$  (computer drawn), according to Freudlich's equation [4]:



$$Q = k C^n \text{ or } \log Q = \log k + n \log C \quad (1)$$

where:  $Q$  and  $C$  are gold concentrations in the resin and solution;  $k$  and  $n$  are constants. Experimental values for 25 °C, were:  $k=12.222$  and  $n=0.928$ .

Gold concentrations of the resin phase ranged from 2.26 mg/g to 54.4 mg/g for resin/solution ratios of 1/20 ÷ 1/500.

**Fig. 1.** Isotherm for gold chloride adsorption on IONAC SR3 selective resin (25°C, 400 rpm, 113 mg Au/l, resin/solution= 1/500 – 1/20, pH=0.75, 3 g/l NaClO)

*The adsorption rate of AuCl<sub>4</sub><sup>-</sup> on the resin* was influenced by the initial gold concentration in the solution (Fig. 2), stirring rate (Fig. 3), temperature (Fig. 4) and resin/solution volume ratio (Fig. 5).

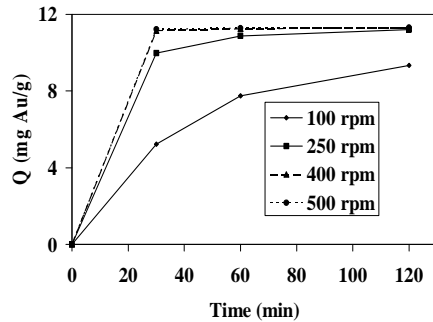
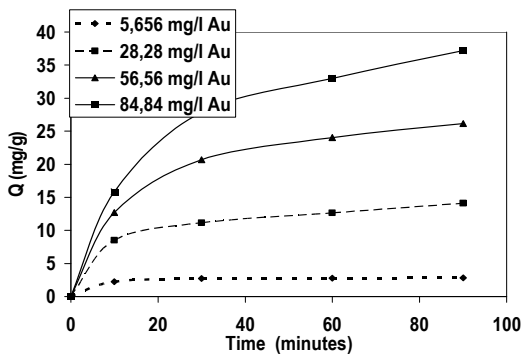


**Fig. 2.** Effect of initial gold concentration (resin/solution = 1/500, 400 rpm, 25°C)

**Fig. 3.** Effect of stirring rate (113 mgAu/l, 25°C, resin/solution=1/100)

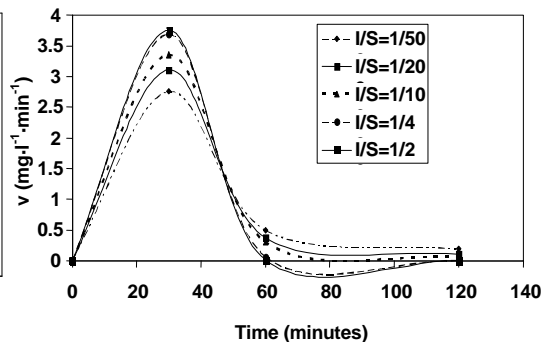
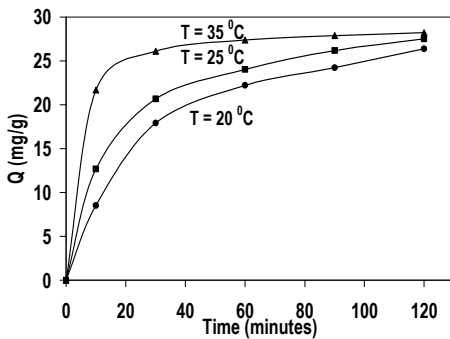


**Fig. 4.** Effect of temperature (56.56 mg Au/l, resin/solution=1/500, 400 rpm)

**Fig. 5.** Effect of resin / solution ratio (113 mg Au/l, 25°C, 400 rpm)

**The influence of "impurities"** - Because hydrometallurgical solutions usually contain chlorides and sulphates of heavy metals (Fe, Cu, Pb, Zn) in much higher concentrations than gold and silver, the effect of such „impurities” on the adsorption of precious metals on the selective resin IONAC SR3 has also been studied.

The results showed that precious metal adsorption efficiencies from solution containing 56.56 mg/l Au, 0.32 mg/l Ag, 1056 mg/l Cu, 905 mg/l Zn, 805 mg/l Fe, 1010 mg/l Pb, 5 g/l NaOCl and 300 g/l CaCl<sub>2</sub> on IONAC SR<sub>3</sub> resin are over 97% and haven't been affected by the presence in high concentrations of Cl<sup>-</sup> or heavy metals ions.

**The desorption of gold retained on the selective resin IONAC SR3** - The desorption of gold retained on the selective resin IONAC SR3 has been carried out with acid (HCl 3%) thiourea (30 – 50 g/l) solutions. In the desorption stage, Au<sup>3+</sup> is reduced to Au<sup>+</sup>, which is complexed by thiourea, thus forming a cationic complex Au[Tu]<sub>2</sub><sup>+</sup>, which is then eliminated into the solution. Desorption experiments took place at 25 °C, by stirring (400 rpm) for 120 minutes, 1g of resin containing 27,5 mg Au/g and 0,16 mg Ag/g, with 50 - 75 ml of acid thiourea solution. The results showed that the gold's elution efficiency rises with the thiourea concentration and the volume of the used solution. Usually, the purpose is to obtain solutions as concentrated in gold as possible in order to increase the energetic efficiency in the next stage, the electrolysis.

**Precious metal recovery from real hydrometallurgical solutions** - Table 1 shows that after 180 minutes of resin / real solution contact at 30 °C, the resin had adsorbed 97% of the gold present in the solution. After the desorption with thiourea, the pregnant solution contained 2.46 times more gold and 1.15 times more silver than the initial one, and did not concentrate on the other heavy metals. The total gold recovery (sorption and desorption stages) from the real hydrometallurgical chloride solution reached 92.43 %.

**Table 1.**  
Recovery of precious metals from a real hydrometallurgical chloride solution using IONAC SR3 selective resin

Parameters	Time (min)	Adsorption/Desorption Efficiency on IONAC SR3 Selective Resin (%)					
		Au	Ag	Cu	Pb	Zn	Fe
<b>Adsorption</b> 1g resin / 200 ml solution, 30 °C, 400 rpm	0	0	0	0	0	0	0
	10	59,00	45,7	12,57	4,84	21,1	3,15
	30	72,79	49,0	16,17	7,56	22,2	5,40
	60	83,33	51,9	20,21	8,64	22,8	6,21
	90	90,48	57,1	20,97	10,3	23,6	6,28
	120	92,25	60,7	20,99	11,4	23,8	6,40
	180	97,20	66,5	21,15	13,0	24,8	6,48
<b>Desorption</b> 1 g resin / 75 ml solution of 50 g/l thiourea, 3% HCl; 28 °C, 400 rpm	0	0	0	0	0	0	0
	10	74,50	55,3	0,05	4,32	1,53	0,77
	30	89,68	60,4	0,05	4,58	1,78	0,98
	60	92,4	62,8	0,06	4,80	1,97	1,33
	90	93,3	63,0	0,06	5,11	2,19	1,57
	120	94,4	64,4	0,07	5,35	2,52	1,76
	150	95,1	64,9	0,08	5,65	2,72	1,93

## Conclusions

Gold contained in hydrometallurgical chloride solutions can be recovered by the selective ion exchange resin IONAC SR3. The gold adsorption isotherm on the resin was described by the Freundlich's equation. The adsorption rate of AuCl<sub>4</sub><sup>-</sup> on the resin was influenced by the initial gold concentration in the solution, stirring rate, temperature and

resin/solution ratio. Under the conditions of resin/solution ratio = 1/200 and a stirring speed of 400 rpm at 30 °C, more than 97% of gold could be recovered by the resin in 180 minutes contact with a hydrometallurgical solution of 33.3 mg Au/l, 70.2 mg Ag/l and high Cu, Pb, Zn și Fe concentrations. After desorption (28 °C, 50 g/l thiourea, 3 % HCl), the pregnant solution contained about 2.5 times more gold than the initial one, and did not concentrate in heavy metals. The efficiency of gold recovery ion exchange process from the chloride hydrometallurgical solution has been over 92%.

## REFERENCES

1. Harris, W. I., Stahlbush, J. R., Pike, W. C. And Stewens, R. R., *Reactive Polymers*, 17, 1992, pp. 21-27;
2. Lukey, G. C., Van Deventer, J. S. J., Shallcross, D. C., *Hydrometallurgy*, 59, 2001, pp. 101-113;
3. Sybron Chemicals Inc. Brochure, *IONAC SR3, Selective Ion Exchange Resin for Gold Recovery*, 2000.
4. Nenițescu, C. D., *Chimie generală*, Ed. Didactică și Pedagogică, București, 1979, p. 294.

## EVALUATION OF THE ISOTOPIC THERMAL DIFFUSION FACTOR FROM MORSE - MORSE – SPLINE – VAN DER WAALS INTERMOLECULAR POTENTIAL

I. COROIU, H. R. COROIU

*Technical University, 3400 Cluj-Napoca, Romania,  
e-mail: coroiu@phys.utcluj.ro*

The isotopic thermal diffusion factors have been calculated from an improved intermolecular potential, Morse-Morse-Spline-van der Waals (MMSV) potential, proposed by R.A. Aziz *et al.* [J.Chem.Phys., 94(2), 1034 (1991)]. The results are tabled over a large temperature range,  $kT/\epsilon$  from 0.1 to 400. The treatment was completely classical and no corrections for quantum effects were made. These results would be employed for isotope separations of different spherical and quasispherical molecules.

### Introduction

The stable isotopes are now used extensively in physics, chemistry, geology, hydrology, biology, biochemistry, medicine and so on.

The thermodiffusion represents one of the most used methods for isotope separations, not only at a laboratory and small-scale production level, but also at a more extent scale.

Evaluation of the transport properties such as: viscosity, thermal conductivity, diffusion coefficient and thermal diffusion factor of various gases is related to the properties of their molecules. Each of the transport coefficients of the gas or gas mixture can be expressed in terms of well defined integrals over the intermolecular potential for each of the possible binary encounters in the system. Thus, provided that the intermolecular pair potential for the interactions of the molecules is known, it is possible to calculate the transport properties of the gas to any desired degree of accuracy at any temperature.

The isotopic thermal diffusion factor was calculated from Lennard-Jones  $n$ - $m$  function potential, Buckingham-Corner potential, modified Buckingham (exp-six) potential and other intermolecular potential functions [1-3]. These intermolecular potential forms have steeper repulsive walls to describe adequately the transport properties of spherical and quasispherical molecules.

The purpose of this paper is to calculate the isotopic thermal diffusion factor from a relatively new intermolecular potential, the Morse–Morse–Spline–van der Waals (MMSV) potential [4], that incorporates the  $C_6$  dispersion coefficient [5].

### Results and discussions

The Morse–Morse–Spline–van der Waals (MMSV) functional form is given by:

$$V(r) = \epsilon V^*(x)$$

where:

$$\begin{aligned}
 V^*(x) &= \exp[-2\beta_1(x-1)] - 2\exp[-\beta_1(x-1)], \quad 0 \leq x \leq 1 \\
 &= \exp[-2\beta_2(x-1)] - 2\exp[-\beta_2(x-1)], \quad 0 \leq x \leq x_1 \\
 &= \alpha_1 + (x-x_1)\{\alpha_2 + (x-x_2)[\alpha_3 + (x-x_1)\alpha_4]\}, \quad x_1 \leq x \leq x_2 \\
 &= -\left(\frac{C_6}{x^6} + \frac{C_8}{x^8} + \frac{C_{10}}{x^{10}}\right), \quad x \geq x_2
 \end{aligned}$$

and  $x=r/r_m$ .

To estimate the isotopic thermal diffusion factor from Morse–Morse–Spline–van der Waals potential form, initial it must to calculate different reduced collision integrals and some combination of these.

We calculated the reduced collision integrals for this new intermolecular potential form, over a large reduced temperature range ( $kT/\epsilon$  from 0.1 to 400).

For calculation of the reduced collision integrals we have chosen the programme catalogue number ACQN, authors H. O’Hara and F. J. Smith [6]. This programme was adapted to run in double precision on IBM computers by P. D. Neufeld and R. A. Aziz and subsequent adapted by us [7] to run on P.C.

The programme contains an efficacious calculation method with a high degree of simplicity and accuracy. This method advanced by Clenshaw and Curtiss computes the definite integrals through the integrand growth in a finite series of Cebishev polynomials and the integration of each term of the series.

The inherent computational error is estimated to be of the order of 0.1% except for very small  $T^*$ , where it may be larger.

Further on, we were computed the following combination of the reduced collision integrals:

$$\begin{aligned}
 A^* &= \Omega^{(2,2)*} / \Omega^{(1,1)*}, \quad B^* = \frac{5\Omega^{(1,2)*} - 4\Omega^{(1,3)*}}{\Omega^{(1,1)*}}, \quad C^* = \Omega^{(1,2)*} / \Omega^{(1,1)*}, \\
 E^* &= \Omega^{(2,3)*} / \Omega^{(2,2)*}, \quad F^* = \Omega^{(3,3)*} / \Omega^{(1,1)*}, \quad K^* = \frac{35/4 - 3B^* - 6C^*}{5 - 6C^*}
 \end{aligned}$$

The isotopic thermal diffusion factor was estimated for the same large reduce temperature range for:

Table 1.

The isotopic thermal diffusion factors from MMSV intermolecular potential

$T^*$	$[\alpha_0]_1$	$[\alpha_0]_1^K$	$[\alpha_0]_2^K$
<b>0.01</b>	0.305695	0.310088	0.310902
<b>0.05</b>	0.325028	0.330662	0.330200
<b>0.10</b>	0.374781	0.383815	0.379970
<b>0.50</b>	0.338081	0.341079	0.347042
<b>1.00</b>	0.336914	0.345332	0.339197

$T^*$	$[\alpha_0]_1$	$[\alpha_0]_1^K$	$[\alpha_0]_2^K$
<b>1.20</b>	0.381536	0.392786	0.384571
<b>1.40</b>	0.430093	0.444233	0.434588
<b>1.60</b>	0.468312	0.473950	0.472973
<b>1.80</b>	0.501136	0.520644	0.508516
<b>2.00</b>	0.532582	0.554325	0.541878
<b>2.50</b>	0.601576	0.627701	0.616775
<b>3.00</b>	0.650064	0.679249	0.670526
<b>3.50</b>	0.681728	0.713110	0.706036
<b>4.00</b>	0.704868	0.737900	0.732287
<b>4.50</b>	0.723234	0.757497	0.753305
<b>5.00</b>	0.738809	0.774050	0.771182
<b>6.00</b>	0.760782	0.797598	0.796572
<b>7.00</b>	0.777111	0.814863	0.815646
<b>8.00</b>	0.788542	0.826997	0.829007
<b>9.00</b>	0.797073	0.836130	0.839140
<b>10.00</b>	0.802759	0.842306	0.845890
<b>12.00</b>	0.811334	0.851556	0.856088
<b>14.00</b>	0.817873	0.858591	0.863901
<b>16.00</b>	0.822619	0.863716	0.869612
<b>18.00</b>	0.826072	0.867473	0.873798
<b>20.00</b>	0.828782	0.870432	0.877100
<b>25.00</b>	0.833682	0.875776	0.904041
<b>30.00</b>	0.836998	0.879384	0.887213
<b>35.00</b>	0.839179	0.881769	0.889944
<b>40.00</b>	0.840693	0.883431	0.891863
<b>50.00</b>	0.842648	0.885576	0.894378
<b>60.00</b>	0.843763	0.886799	0.895849
<b>70.00</b>	0.844413	0.887512	0.896735
<b>80.00</b>	0.844779	0.887912	0.897258
<b>90.00</b>	0.844974	0.888123	0.897562
<b>100.00</b>	0.845050	0.888204	0.897712
<b>200.00</b>	0.843938	0.886940	0.896621
<b>300.00</b>	0.842492	0.885309	0.894918
<b>400.00</b>	0.841339	0.884007	0.893509

(i) the first - order Chapman – Cowling approximation,

$$[\alpha_0]_1 = \frac{15(6C^* - 5)(2A^* + 5)}{2A^*(16A^* - 12B^* + 55)}$$

(ii) the first – order Kihara approximation,

$$[\alpha_0]_1^K = \frac{15(6C^* - 5)}{16A^*}$$

(iii) the second – order Kihara approximation,

$$[\alpha_0]_2^K = [\alpha_0]_1 f_\alpha^{K(2)}$$



with  $f_{\alpha}^{K(2)} = 1 + \delta_{\alpha}$ , and

$$\delta_{\alpha} = \frac{(7-8E^*)}{9} \left\{ \left[ \frac{2A^*}{\left(\frac{35}{4}\right) + 7A^* + 4F^*} \right] \left[ K^* + \frac{1}{2} \left( \frac{7(5-6C^*) + A^*(7-8E^*)}{5+2A^*} \right) \right. \right. \\ \left. \left. \times \left[ \frac{\left(\frac{35}{8}\right) + 28A^* - 6F^*}{21A^*} \right] \right] - \frac{5}{7} \left[ K^* - \frac{7}{5} \left( \frac{5-6C^*}{5+2A^*} \right) - \frac{3(7-8E^*)}{10} \right] \right\}$$

The obtained values are given in the Table 1.

### Conclusions

We present the calculation from MMSV intermolecular potential of the isotopic thermal diffusion factors:  $[\alpha_0]_1$  - the first-order Chapman–Cowling approximation,  $[\alpha_0]_1^K$  - the first-order Kihara approximation and  $[\alpha_0]_2^K$  - the second-order Kihara approximation. The obtained values are tabulated over a large reduced temperature ( $T^* = kT/\epsilon$ ) range from 0.1 to 400. These values can be used for isotope separations of some spherical and quasispherical molecules.

### REFERENCES

1. J.E. Lennard-Jones, Proc.Roy.Soc., 106A, 1924, p.463-470.
2. R.A. Buckingham, J.A. Pople, Trans.Faraday Soc., 51, 1955, p. 1173-1181.
3. C.G. Maitland, E.B. Smith, Chem.Phys.Lett., 22, 1973, p. 443-449.
4. R.A. Aziz, M.J. Slaman, W. Taylor, J. Hurley, J.Chem.Phys., 94, 1991, p. 1034.
5. A. Kumar, G. R. G. Fairley, W. J. Meath, J.Chem.Phys., 83, 1985, p.70-75.
6. H. O'Hara, F.J. Smith, Comp.Phys.Comm., 3, 1971, p.47-51.
7. I. Coroiu, D.E. Demco, Z. Naturforsch. 52a, 1997, p. 748-756

## INTERACTIVE STUDENTS TRAINING AND EVALUATION SOFTWARE FOR RADIOISOTOPES

**MIHAELA LIGIA UNGUREȘAN, LORENTZ JÄNTSCHI**

*Technical University of Cluj-Napoca*

<http://mihaela.academicdirect.ro>,

<http://lori.academicdirect.ro>

**ABSTRACT.** The present paper is focused on interactive students work with computer for detailed understanding of radioactive disintegration, fission and fusion, as well as corrects writing of nuclear reactions. A PHP program has been done to verify veracity of some equations of nuclear reactions, general questions about radioisotopes, as well as the observation of some reactions that are animated, and this is available through http Internet protocol at the address: [http://academicdirect.ro/virtual\\_library/molecular\\_dynamics/radio\\_isotopes/](http://academicdirect.ro/virtual_library/molecular_dynamics/radio_isotopes/)

**Keywords:** radioisotopes, PHP program, nuclear reaction.

### 1. Introduction

The isotopic marked compounds induce an activity sphere that offers many synthetic and applicative possibilities. The marked compounds have numerous applications, the principal direction of their use at this moment being the syntheses reagents, biosynthetic substrates, the establishment of metabolic schemes, the study of adsorption phenomenon, in vivo and in vitro clinical tracers diagnosis, toxicological and pharmacological studies, as well as establishment of mechanism reactions.[1]

From the discovery of radioactivity until now there were discovered more than 1200 radionucleuses.[2, 3]. *The radioactivity* is defined as the property of nucleuses (of some nuclides) to emit spontaneously  $\alpha$ ,  $\beta^\pm$  particles or to suffer an electronic capture and  $\gamma$  disintegration.[4]

Heavy charged particles can suffer three types of interactions:[5] (i) collision with atomic electrons (the most important); in these collisions the  $\alpha$  radiation lose its energy in proportion of more than 98% and the effects of collision are excitation (detectors used in study of  $\alpha$  radiations: ZnS), ionization (complete removal of electrons from atoms or molecules, originating positive and negative ions) and dissociation, (ii) braking in electric field of nucleus (reemission of  $\gamma$  and X radiations), (iii) nuclear reactions that are taking place with a very low probability, of aproximatively  $10^{-3}$  %.

### 2. Software

A client server application was build. For implementation of the software, HTML language was choused to the easiness to run and use. Only a computer with windows operating system and Microsoft Internet Explorer  $\geq 4.0$  is enough to run all \*.htm\* files.

Also, a set of php programs for evaluation of students was implemented. PHP (post-processed hypertext) language is a very easy to use and is a server-dedicated software. The php page request is send to web server, and the server using mod\_php module process the page, compile the program, execute the instructions and send to the client-processed data in html format.

### Implementation

A entry interface was putted into a web server at URL (see fig. 1).

*See reactions* link leads to a page, which contain a set of nuclear reactions tabulated into a table with three columns. The page is under constructions and it contains until now a number of 25 reactions. Every reaction is animated one and is saved into GIF format. In figure 2 is presented an example of this type (...) captured in few moments of evolution.

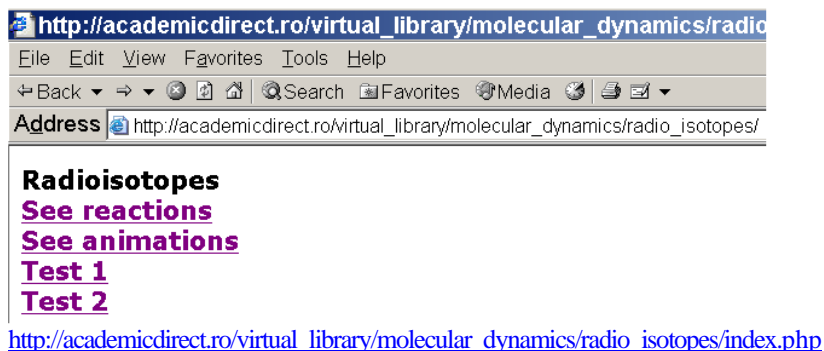


Fig. 1. The entry point interface into web program

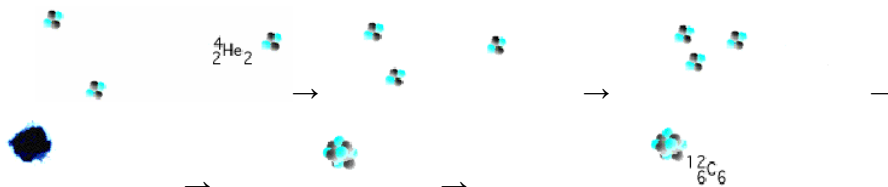


Fig. 2. Fusion of three molecules  ${}^4_2\text{He}$

*See animations* link leads into a page with a picture with a nuclear plant, most frequent artificial source of nuclear reactions. When user move the mouse pointer over the image, the image source is modified and page shows a technological scheme of a nuclear reactor.

The page, at URL: [http://academicdirect.ro/virtual\\_library/molecular\\_dynamics/radio\\_isotopes/filme/](http://academicdirect.ro/virtual_library/molecular_dynamics/radio_isotopes/filme/) it contain a select control which allow to chouse a audio-video file saved as \*.avi.

Selection of one avi file makes that the source of picture to be replaced with selected animation. The animation starts then user moves the mouse pointer into movie area and it plays at two times. The repetition is possible by moving again the mouse pointer into movie area.

*Test1* link goes to a test with 6 questions and every with 4 answers. User chouse the correct answer for every question and submit data to the server. The php program verifies answers and computes the resulted score and displays it onto the client browser.

*Test2* link goes to a set of 10 nuclear reactions equations. The mission of the user is to chouse the correct atomic number (Z) and mass number (A), element (X) or particle from a list with more than one value (see figure 4).

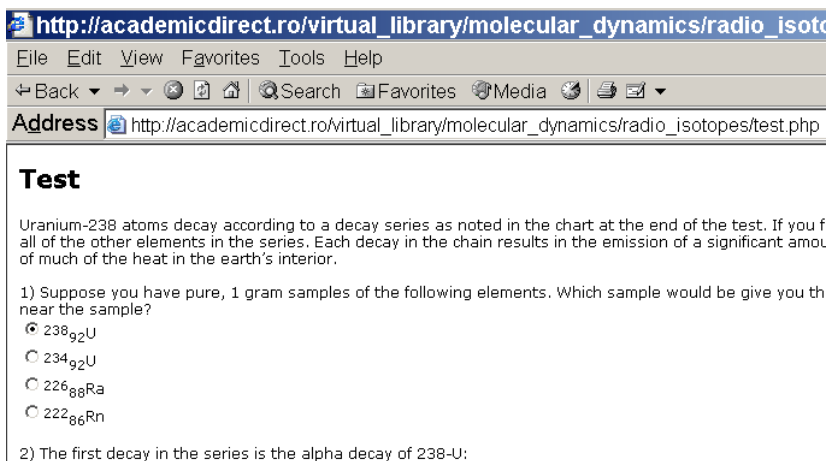


Fig. 3. Test for knowledge checking

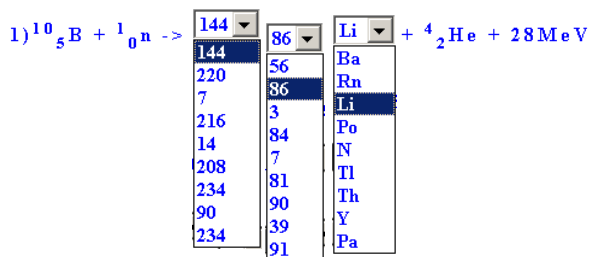


Fig. 4. Nuclear reaction equation

### 3. Conclusions

The program leads to a more efficient activity of teaching learning at chapter “Nuclear reactions”, by the specific dynamism of animations and through immediate evaluation, shorting the time of assimilation the new notions.

The client-server interface determines the program to be able to be executed from anywhere, using any computer bound to Internet, which determine that this application to be ideal for distance education also.

Study of radioisotope and of these reactions has distinct applications in biology. A particular interest presents radioisotope that emit  $\beta$  particles with low energy, especially carbon-14 ( $^{14}\text{C}$ ), phosphorus-32 ( $^{32}\text{P}$ ), tritium ( $^3\text{H}$ ), because they are incorporated in a great number of organic substances, which represent forerunners for different synthesis.[6] The use of marked substances with radioisotopes ( $^{32}\text{PO}_4$ , timidina- $^3\text{H}$ , citozina- $^3\text{H}$ , uridina- $^3\text{H}$ , metionina- $^{31}\text{S}$ ) has remarkable results on biosyntheses of some cellular chemical constituents and it's possible to explain the moment and the mechanism of genetic material retorting [7, 8], the fundamental biochemical processes, genetic recombination by cross-over procedure.[9, 10]

It was studied closely the nitrogen metabolism at different plants: the absorption of azotate compounds, the protein metabolism, the settling of nitrogen from air, as well as the establishment of comprising time of nitrogen in aminoacides, proteins and chlorophyll, in different parts of the plant.[11, 12] Between the most interesting applications of oxygen-18 are the investigations on the light effect in respiration of green plants, the mechanism of Hill reactions, mechanism de splitting phosphatic and phosphorilitic, formation of adenosine triphosphate in oxidative phosphorilation, source of oxygen in respiratory CO<sub>2</sub>. [13, 14]

## REFERENCES

1. Murgulescu I. G., Păun J., *Introducere in Chimia-Fizică, vol. I-3, Nucleul Atomic, Reacții Nucleare, Particule Elementare*, Ed. Academiei, București, 1982.
2. Balaban A.T., Galateanu I., Georgescu G., Simionescu Ligia, *Labelled Compounds and Radiopharmaceuticals Applied in Nucleare Medicine*, Ed. Acad., Bucuresti, Romania and John Wiley and sons LTD, 1986.
3. Melander L., *Isotope effects on reaction rate*, The Roald Press Comp., New York, 1980.
4. Bodner George M., Rhea Tony A., *Natural sources of ionizing radiation*, J. Chem. Educ., 61, 687, 1984.
5. Străjescu M., Cosma M., *Chimie anorganică pentru elevi și absolvenți de licee*, Cluj-Napoca, Ed. Dacia, 1975.
6. Kushwaha S.C., Suzue G., Subbarayan C., Porter J., *J. Biol. Chem.*, 18, 47084717, 1970.
7. Tamaș V., Neamțu G., *Pigmenți carotenoidici și metaboliti, vol 1*, Ed. Ceres, București, 1986.
8. loch K., *Steroids*, 57, 378-383, 1992.
9. Davies B.H., *Pure Appl. Chem.*, 35, 1-28, 1973.
10. Brechbihler-Bader S., Coscia C.J., Loew P., Sczepanski C., Arigoni D., *J. Chem. Soc. Chem. Commun.*, 136-137, 1968.
11. Ciulei I., Istudor V., Palade M., *Analiza farmacognostica și fitochimica a produselor vegetale* ", Ed. Didactică și Pedagogică, București, 1997.
12. Pandian S., Saengchjan S, Raman T.S. *Biochem. J.*, 196, 675-681, 1981.
13. Corol Delia Irina, Toma N., Dorobanțu I. I., *Izotopii Stabili și Radioactivi în determinarea etapelor biosintezei beta-carotenului*, Institutul National de C&D pentru Fizica si Inginerie Nucleara Horia Hulubei, 204-203, București, 2002.
14. Goodwin T.W., *Chemistry and Biochemistry of Plant Pigments*, Academic Press, London, 1965.

## ACID-BASE TITRATION NUMERICAL SIMULATOR

**LORENTZ JÄNTSCHI<sup>1</sup>, DELIA GLIGOR<sup>2</sup>, MIHAELA LIGIA UNGUREȘAN<sup>1</sup>**

<sup>1</sup> *Technical University of Cluj-Napoca*

<sup>2</sup> *Babes-Bolyai University of Cluj-Napoca*

<http://lori.academicdirect.ro>,

<http://mihaela.academicdirect.ro>

**ABSTRACT.** The analytical methods of qualitative and quantitative determination of ions in solutions are very flexible to automation. The present work is focus on modeling the process of titration and presents a numerical simulation of acid-base titration. A PHP program to compute all iterations in titration process that solves a 3<sup>rd</sup> rank equation to find value of pH for was built and is available through http internet protocol at the address: [http://academicdirect.ro/virtual\\_library/molecular\\_dynamics/radio\\_isotopes/](http://academicdirect.ro/virtual_library/molecular_dynamics/radio_isotopes/)

The method allows expressing the value of pH in any point of titration process and permits to observe the equivalence point of titration.

**Keywords:** Titration, Acid-base reactions, Simulation, Mathematical modeling of chemical processes, Server side processing.

### 1. Introduction

The process of titration is a recurrent process that can be watched by permanent measurement of a simple property such as mass, current intensity, tension, volume [1, 2, 3] or a complex property such as adsorption, heat of reaction [4, 5, 6], which need a complex evaluation.

Currently, is sent over the two milliards of probes to laboratories of medical clinics and this number growing. Most of these tests include the determination of glucose, urea, proteins, sodium, calcium,  $\text{HCO}_3^-/\text{H}_2\text{CO}_3$ , uric acid and pH [7, 8, 9].

The science of environment is focused on chemical, physical and biological changes through contaminating or modifying natural parameters of air, water, soil, alimentary products and residues [10, 11, 12].

### 2. Analytical Measurements

Any simple or complex the measurements can be, the assurance, utility, precision, interpretation and achievement of them depend of the analyst, that must be preoccupied -by making analysis and in same time by the how - why and where are the finally results of analysis used.

The analyst has the obligation to make determination based on sure, reproducible and verified procedures.

The first step in design of an analytical process is to establish the objective to follow.

Only by clear identification of proposed scope it can imagined logic way that lead to correct solving of the problem [13, 14].

A big responsibility for the analyst is to choose an analytical method that is leading to best solving of followed scope.

There exist cases when freedom of choosing is limited. The analysis of water or pharmaceuticals must make through legal standard approved procedures. If more than one similarly probe exists, such as quality control, the automation becomes possible [15].

### 3. Neutralization

An easy way to make an analytical method for quantitative determinations is trespassing from an acid solution to a basic one, known as neutralization.

In this case, evolution of reaction can be watched through pH measurements, continuously, when a known volume of titrating solution is added.

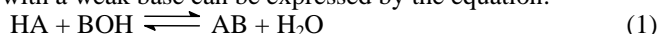
Usually, a strong acid or a strong base is solution added, but in biochemical processes, most of the acids and bases are weak. This is the reason for choosing a weak acid and a weak base for titration modeling.

The plot of the pH as function of added standardized solution is the titration curve. Many data result from a titration curve.

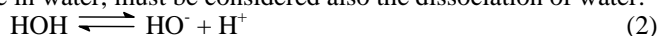
Most important for the quantitative determinations is volume of titrating solution necessary for neutralization ( $\text{pH} = \text{pOH} = 7$  at  $25^\circ\text{C}$ ) [16].

### 4. Reaction Modeling

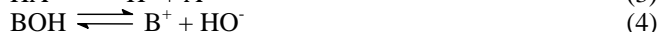
A weak acid titration with a weak base can be expressed by the equation:



If the titration is made in water, must be considered also the dissociation of water:



The processes of acid and base dissociation are:



Also, salt are in equilibrium with his ions:



The titration starts with adding of a small quantity of base in acid. In solution are present the species  $\text{H}^+$ ,  $\text{HO}^-$ ,  $\text{HA}$  and  $\text{A}^-$ . From acid dissociation (equation 3) it result:

$$[\text{H}^+]\cdot[\text{A}^-] = K_a\cdot[\text{HA}] \quad (6)$$

and from water dissociation (equation 2):

$$[\text{H}^+]\cdot[\text{HO}^-] = K_w \quad (7)$$

where  $[\cdot]$  is the molar concentration operator ( $[\text{H}^+]$  is the molar concentration),  $K_a$  is acidity constant and  $K_w$  is water constant of dissociation. If are applied the mass balance for the acid (see equations 3-5), it results:

$$C_a = [\text{HA}] + [\text{H}^+] - [\text{HO}^-] \quad (8)$$

where  $C_a$  is analytical concentration of the acid.

If are applied the mass balance for the salt, it results:

$$C_s = [\text{A}^-] - [\text{H}^+] + [\text{HO}^-] \quad (9)$$

where  $C_s$  is analytical concentration of the salt.

With proper substitutions a 3<sup>th</sup> rank equation of pH are obtained (Brönsted equation):

$$x^3 + (K_a + C_s) \cdot x^2 - (K_w + C_x \cdot K_a) \cdot x - K_w \cdot K_a = 0 \quad (10)$$

where  $x = [\text{H}^+]$ .

The equation (10) has a unique solution in (0,1) interval and note that:

$$C_s = C_b \cdot V_x / (V_a + V_x) \quad (11)$$

$$C_x = (C_a \cdot V_a - C_b \cdot V_x) / (V_a + V_x) \quad (12)$$

where  $C_b$  is analytical concentration of the base,  $V_x$  is added volume of base,  $C_x$  is analytical concentration of acid after adding of  $V_x$  volume of base and  $V_a$  is initial volume of acid.

The equation (10) with substitutions (11) and (12) can be solved numerically.

At equivalence point, all (1-4) equations must be considered. With an small hydrolysis  $C_s = [B^+] = [A^-]$  and:

$$x = \sqrt{\frac{K_w \cdot K_a \cdot (K_b + C_s)}{K_b \cdot (K_a + C_s)}} \quad (13)$$

With a similar deduction, the equation of  $[H^+]$  is given by:

$$x^3 + (K_w/K_b + C_x) \cdot x^2 - (K_w + C_s \cdot K_w/K_b) \cdot x - K_w^2/K_b = 0 \quad (14)$$

where the expressions of  $C_x$  (base excess) and  $C_s$  are:

$$C_x = (C_b \cdot V_x - C_a \cdot V_a) / (V_a + V_x) \quad (15)$$

$$C_s = C_a \cdot V_a / (V_a + V_x) \quad (16)$$

For obtaining a concrete model of titration, let consider the case of  $NH_3$  ( $k_b = 1.79 \cdot 10^{-5}$ ) solution titrate with  $CH_3COOH$  ( $k_a = 1.76 \cdot 10^{-5}$ ). Remark that  $NH_3$  is a typically weak base and  $CH_3COOH$  is a typically weak acid.

## 5. Program Projecting

Once you have an operating system installed, the next step is to choose a proper programming language for software developing.

In terms of programming, portability of resulted program can be a problem. As example, if we are chose to implement the algorithm in Visual Basic, the execution of the program is restricted to Windows machines. If Perl is our choice, a Unix-based machine is necessary to run program. If we choose to implement the program in C language, we will have serious difficulties to compile the programs on machines running with different operating systems. The complexity of program building is also a serious reason in language chousing. Is known that C based languages is poor in simplicity and necessity more time to expend for application building than other languages.

Other question requires an answer: We want a server-based application or client based application, a server side application or a client side application.

As example, a client side application can have disadvantage of execution on client, and dependence of processing speed by power of client machine. If we prefer this variant, a java script or visual basic script is our programming language.

A server side application requires a web server installed. The area of web servers is also a large set, but few have multiplatform capability. If we want a full-featured web server, Apache is our solution.

Under Apache, we have the possibility to execute programs already compiled in C, Fortran and Java, under Unix machines we can directly execute Perl programs, and, most important, under all operating system platforms we can execute PHP programs if we previously install php language and module binaries.

The advantage of PHP programs consist in his portability under most of operating system platforms and internal compilation feature that do not necessity the compilation "by hand" from the user. The pointer mechanism is absolute. Thus, a variable used as a string, can be exploited as an integer or real if the value represent a number such that. Class constructing is also available and PHP posses a strong library of database connectivity. Modular programming, recursivity and graphics are at home! Module loading of compiled programs in other languages and execution of binary programs is also available. A very easy mechanism to link PHP scripts to HTML scripts make PHP language to be one of the best. Shell executing commands make PHP a useful platform for system administration (PhpSysInfo, WebAdmin, PhpMyAdmin, PhpPgAdmin).



## 6. Program Implementation

An html form interface for choosing acid, base, adding quantity, volumes, and concentrations allow user to select a weak acid and a weak base (fig. 1).

The user select desired options and press submit button (Make) to send data through a post method to *titration.php* located in same directory. For substances, values that are sending are constants of equilibrium.

The *titration.php* program computes iteratively for every added quantity of base the coefficients for equation (10) until the equilibrium is reached and then calculates pH through relation (13) and after that computes iteratively the coefficients for equation (14). For every case of coefficients determination (equations 10 and 13) the third rank equation is solved searching the solution by halving the current interval starting with [0, 1] interval (that correspond to a real value of pH) until the difference are analytically insignificant (four digits) [17].

The resulted values of pH for every added quantity of base are tabulated and send to the client (user). The values can now be exported to any table-based program to make graphics.

Fig. 1. [http://academicdirect.ro/virtual\\_lybrary/molecular\\_dynamics/titration/v1.1/](http://academicdirect.ro/virtual_lybrary/molecular_dynamics/titration/v1.1/)

## 7. Applications

The *index.php* and *titration.php* programs are consecutively runs for different acids and bases, and the results are plotted in following figures for the values  $C_a=C_b=0.01$  M;  $V_b=2 \cdot V_a=20$  ml;  $V_x=x \cdot 0.1$  ml;  $x=0..200$  it result:

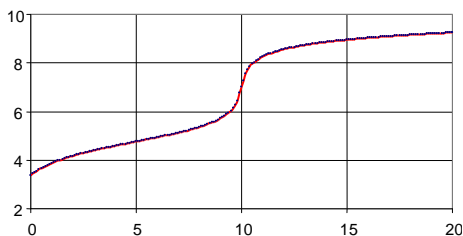
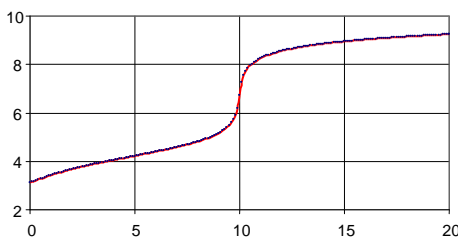
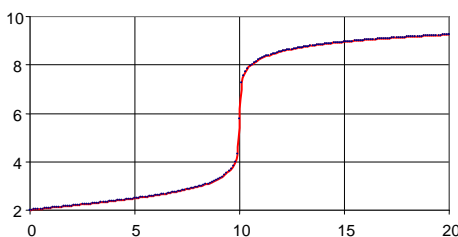


Fig. 2.  $\text{pH} = \text{pH}(V_x)$  for  $K_a = 1.76 \cdot 10^{-5}$  (HAc),  $K_b = 1.79 \cdot 10^{-5}$  ( $\text{NH}_3$ )



**Fig. 3.**  $\text{pH} = \text{pH}(V_x)$  for  $K_a = 6.3 \cdot 10^{-5}$  (ArCOOH),  $K_b = 1.79 \cdot 10^{-5}$  ( $\text{NH}_3$ )



**Fig. 4.**  $\text{pH} = \text{pH}(V_x)$  for  $K_a = 4.2 \cdot 10^{-1}$  (Picric acid),  $K_b = 1.79 \cdot 10^{-5}$  ( $\text{NH}_3$ )

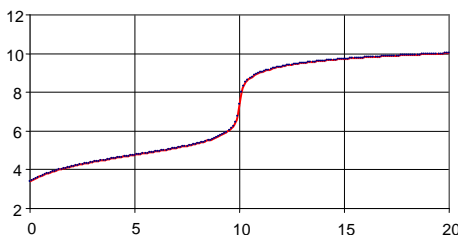


**Fig. 5.**  $\text{pH} = \text{pH}(V_x)$  for  $K_a = 1.76 \cdot 10^{-5}$  (AcCOOH),  $K_b = 1.1 \cdot 10^{-4}$  (AgOH)

### 5. Conclusions and Remarks

Looking at the figures (fig. 2, as example), we can observe the variation of dependency through process.

First, variation is faster, because does not exist enough salt formed to create salt-acid tampon solution.

Second, the variation of the pH is higher until the equivalence point than after the equivalence point, because before equivalence point, forming of salt is continuous and formation of salt increase tampon strength (see fig. 6).

The titration process is simple in appearance but shows to be complex in details. Even the simple case of titration of monobasic base ammonia with a mono-protic acid, such as acetic acid, we must manipulate complex equations (like 10 and 13).

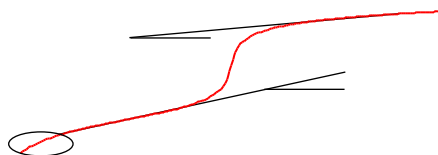


**Fig. 6.** Analysis of a titration curve

The method allows investigating more complex processes such as reaction of polyacids with poly-bases. If no approximation will be made, equations that are more complex will be necessary and superior rank equations will appear to be solved.

Anyway, the advantages of the method are higher than disadvantages resulted from complexity of calculus. Lack of approximations permits to express pH in all domain points with maximum accuracy.

## REFERENCES

1. Martin Todd M., Gupta Ram B., Roberts C. B., Measurements and Modeling of Cloud Point Behavior for Poly(propylene glycol) in Ethane and in Ethane + Cosolvent Mixtures at High Pressure, *Industrial & Engineering Chemistry Research*, 39, 2000, p. 185 – 194.
2. Lelia M., Miguel P., Carlos L., Félix R. M., José S. U., *Viscosity Measurements for the Binary Mixtures of 1,2-Dichloroethane or 1,2-Dibromoethane with Isomeric Butanols*, *Journal of Chemical & Engineering Data*, 45, 2000, p. 86 - 91.
3. Dunstan Dave E., Stokes Jason, *Diffusing Probe Measurements of Polystyrene Latex Particles in Polyelectrolyte Solutions: Deviations from Stokes-Einstein Behavior*, *Macromolecules*, 33, 1, 2000, p. 193-198.
4. Roncin Jean-Yves, Launay Françoise, Bredohl Harald, Dubois Iwan, *The Vacuum Ultraviolet Absorption Bands of the Pink Afterglow Spectrum of Molecular Nitrogen Revisited at High Resolution*, *American Society, JMSP*, 194, 2, 1999, p. 243-249 .
5. Cedeño F., Prieto María M., Xiberta J., *Measurements and Estimate of Heat Capacity for Some Pure Fatty Acids and Their Binary and Ternary Mixtures*, *Journal of Chemical & Engineering Data*, 45, 2000, p. 64-69.
6. Dai Wenbin, Kojima Kazuo, Ochi Kenji, *Measurement and Correlation of Excess Molar Enthalpies of Carbon Dioxide + 2-Butanol and 2-Propanol Systems at the Temperatures 303.15 K and 308.15 K and at Pressures from 7.0 to 8.5 MPa*, *Journal of Chemical & Engineering Data*, 45, 2000, p. 6-10.
7. Chakraborty Debashis, Chandrasekhar Vadapalli, Bhattacharjee Manish, Krätzner Ralph, Roesky Herbert W., Noltemeyer Mathias, *Metal Alkoxides as Versatile Precursors for Group 4 Phosphonates: Synthesis and X-ray Structure of a Novel Organosoluble Zirconium Phosphonate*, *Inorganic Chemistry*, 39, 2000 p. 23-26.
8. Gabelnick Aaron M., Capitano Adam T., Kane Sean M., Gland John L., *Propylene Oxidation Mechanisms and Intermediates Using in Situ Soft X-ray Fluorescence Methods on the Pt(III) Surface*, *Journal of the American Chemical Society*, 122, 1, 2000, p. 143-149.

9. Chapman Wendy Webber, Fizman Marcelo, Chapman Brian E., Haug Peter J., *A Comparison of Classification Algorithms to Automatically Identify Chest X-Ray Reports That Support Pneumonia*, American Society, JBIN, 34, 1999, p. 4 -14.
10. Jackson Togwell A., West M. Marcia, Leppard Gary G., *Accumulation of Heavy Metals by Individually Analyzed Bacterial Cells and Associated Nonliving Material in Polluted Lake Sediments*, Environmental Science & Technology, 33, 21, 1999, p. 3795-3801.
11. Bishop G. A., Stedman D. H., Hektner M., Ray J., *An In-Use Snowmobile Emission Survey in Yellowstone National Park*, Environ. Sci. & Techn., 33, 21, 1999, p. 3924-3926.
12. Fernández P., Vilanova Rosa M., Grimalt O., *Sediment Fluxes of Polycyclic Aromatic Hydrocarbons in European High Altitude Mountain Lakes*, Environmental Science & Technology, 33, 21, 1999, p. 3716-3722.
13. Sârbu C., Jäntschi L., *Validarea și Evaluarea Statistică a Metodelor Analitice prin Studii Comparative. I. Validarea Metodelor Analitice folosind Analiza de Regresie*, Revista de Chimie, București, 49(1), 1998, p. 19 - 24.
14. Nașcu H., Jäntschi L., Hodișan T., Cimpoiu Claudia, Câmpan Gabriela (1999), *Some Applications of Statistics in Analytical Chemistry*, Reviews in Analytical Chemistry, Freud Publishing House, XVIII(6), 1999 p. 409-456.
15. Jäntschi Lorentz, *Automat Server Side Processing of Statistical Data*, UNITECH'02 International Scientific Conference, Gabrovo, Bulgaria, 2002, p. 185-189.
16. Jäntschi L., Nașcu H., *Numerical Description of Titration*, AQTR, 13, Cluj-Napoca, 2002, p. 259-262.
17. Nașcu H., Jäntschi L., Hodișan T., Cimpoiu Claudia, Câmpan Gabriela, *Some Applications of Statistics in Analytical Chemistry*, Reviews in Analytical Chemistry, Freud Publishing House, XVIII(6), 1999, p. 409-456.

## SIMULATION OF KINETICS CHEMICAL REACTIONS

**MIHAELA LIGIA UNGUREȘAN, LORENTZ JĂNTSCHI**

*Technical University of Cluj-Napoca*

<http://mihaela.academicdirect.ro>,

<http://lori.academicdirect.ro>

**ABSTRACT.** The present paper presents the mathematical simulation of the kinetics of simple and complex reactions, using the program PHP is available through http Internet protocol at the address: [http://academicdirect.ro/virtual\\_library/molecular\\_dynamics/kinetics/](http://academicdirect.ro/virtual_library/molecular_dynamics/kinetics/)

The program makes the activity of teaching and learning about the kinetics of chemical reactions to be more efficient, the students being able to determine from the graphics of concentration depending on time, for slow as well as fast reactions, the reaction rate,  $t_{1/2}$ , the reaction order.

**Keywords:** Chemical kinetics, reaction order, simulation, rate law.

### 1. Introduction

The chemical kinetics[1] is about the rate and mechanism of chemical reactions. The research of the reaction mechanisms starts from establishing the experimental rate law that involves the dependence of rate law on the concentration of the reactants, products and catalyses, on temperature and on the interpretation of the activation parameters.[2] The kinetic study of a reaction involves: establishing the rate law, identifying the rate constants, establishing the reaction mechanisms according to the rate law, establishing the dependences of the reaction rates depending on time.

### 2. Software

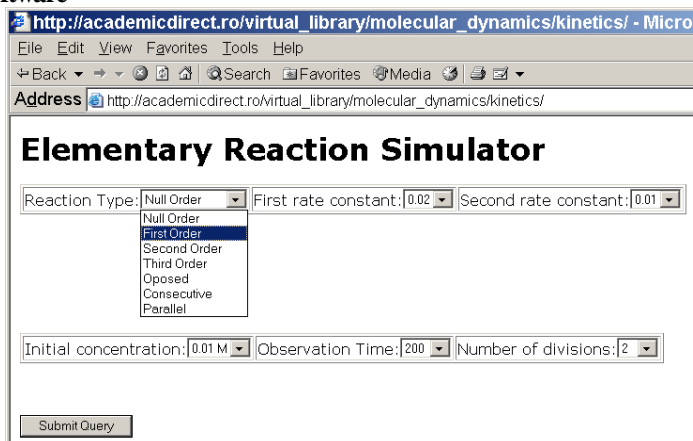


**Fig. 1.** [http://academicdirect.ro/virtual\\_library/molecular\\_dynamics/kinetics/](http://academicdirect.ro/virtual_library/molecular_dynamics/kinetics/)

A client server application was build. For implementation of the software, HTML language was choused from reason of easy to run and use. Only a computer with windows operating system and Microsoft Internet Explorer  $\geq 4.0$  is enough to run all \*.htm\* files. A set of php programs for computing

simulated values was implemented. PHP (post processed hypertext) language is a very easy to use and is a server dedicated software. The php page request is send to web server, and the server using mod\_php module process the page, compile the program, execute the instructions and send to the client process data in html format. Depending on the option chosen by the user, the program generates columns of calculated values and displays them (fig. 2). The data are modifiable so that the user, as he wishes, can modify the calculated values in simulation, introducing his own values (resulted for instance from experimental measurements).[3, 4]

84	176.000000	0.000347	0.009653
85	170.000000	0.000334	0.009666
86	172.000000	0.000321	0.009679
87	174.000000	0.000308	0.009692
88	176.000000	0.000296	0.009704
89	178.000000	0.000284	0.009716
90	180.000000	0.000273	0.009727
91	182.000000	0.000263	0.009737
92	184.000000	0.000252	0.009748
93	186.000000	0.000242	0.009758
94	188.000000	0.000233	0.009767
95	190.000000	0.000224	0.009776
96	192.000000	0.000215	0.009785
97	194.000000	0.000207	0.009793
98	196.000000	0.000198	0.009802
99	198.000000	0.000191	0.009809
100	200.000000	0.000183	0.009817
101			records
3			variables
<input type="button" value="Submit Query"/>			

**Fig. 2.** [http://academicdirect.ro/virtual\\_library/molecular\\_dynamics/kinetics/graph.php](http://academicdirect.ro/virtual_library/molecular_dynamics/kinetics/graph.php)

The mathematical functions that are used represents the concentrations of reactants at a certain moment, of the reactants, intermediates, as well as of the reaction products, the variable  $x$  being representing the time,  $c$  being the initial concentration, and  $k, k_1, k_2$  being rate constants. The expressions of the integrated forms of the rate laws are expressed for reaction of zero order, first, second, third, opposed, parallel and consecutive reactions[5] are presented as follows.

```
function ordin1($x,$k,$c){return $c*exp(-$x*$k);}function ordin1p($x,$k,$c){return $c*(1.0-exp(-$x*$k));}
function ordin1c1($x,$k1,$k2,$c){return $c*exp(-$x*$k1);}
function ordin1c2($x,$k1,$k2,$c){return $c*$k1*(exp(-$x*$k1)exp($x*$k2))/(k2-$k1);}
function ordin1c3($x,$k1,$k2,$c){return $c*(1.0-$k2*exp(-$x*$k1))/(k2-$k1)+$k1*exp(-$x*$k2)/(k2-$k1);}
function ordin1p1($x,$k1,$k2,$c){return $c*exp(-$x*(k1+k2));}
function ordin1p2($x,$k1,$k2,$c){return $k1*$c*(1.0-exp(-$x*(k1+k2)))/(k1+k2);}
function ordin1p3($x,$k1,$k2,$c){return $k2*$c*(1.0-exp(-$x*(k2+k1)))/(k2+k1);}
function ordin2($x,$k,$c){return $c/(1.0+$k*$x);}function ordin2p($x,$k,$c){return $c- $c/(1.0+$k*$x);}
function ordin01($x,$k,$c){if ($k*$x<$c) return $k*$x; else return $c;}
function ordin02($x,$k,$c){if ($k*$x<$c) return $c-$k*$x; else return 0.0;}
```

## SIMULATION OF KINETICS CHEMICAL REACTIONS

```
function ordin31($x,$k,$c1,$c2,$c3){return $c1-$k*$c1*$c2*$c3*$x;}
function ordin32($x,$k,$c1,$c2,$c3,$c4){return $c4+$k*$c1*$c2*$c3*$x;}
function ordinr1($x,$k1,$k2,$c1,$c2){return $c1-($k1*$c1-$k2*$c2)*$x;}
function ordinr2($x,$k1,$k2,$c1,$c2){return $c2-($k2*$c2-$k1*$c1)*$x;}
```

The data in fig. 2 are taken over by a program of graphic representation (fig. 3). The program allows choosing the options wanted (number of pixels, margins, background, pixels size, image type). Based on the options chosen by the user, the program makes the graphic (fig. 4).

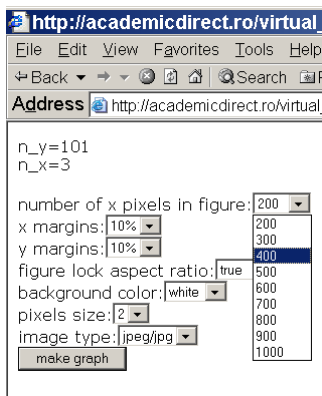


**Fig. 3.** [http://academicdirect.ro/virtual\\_library/molecular\\_dynamics/kinetics/do.php](http://academicdirect.ro/virtual_library/molecular_dynamics/kinetics/do.php)

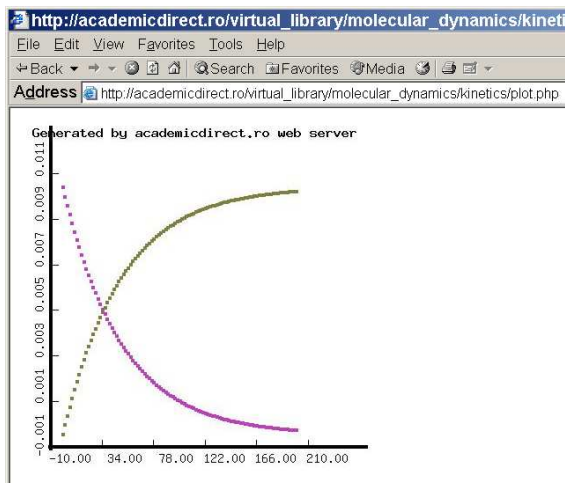


**Fig. 4.** [http://academicdirect.ro/virtual\\_library/molecular\\_dynamics/kinetics/plot.php](http://academicdirect.ro/virtual_library/molecular_dynamics/kinetics/plot.php)

We present as follows a few code sequences for displaying the graphic on browser client:

```

$n=$HTTP_POST_VARS['n'];//number of records; $m=$HTTP_POST_VARS['m'];//number of variables
for($k=0;$k<$m;$k++){ $temp=sprintf("x_%d",$k); $x[$k]=split('/',,$HTTP_POST_VARS[$temp]);//x values }
$x_size = $HTTP_POST_VARS['p'];//number of x pixels in figure; $k = $HTTP_POST_VARS['k'];
//figure lock aspect ratio; $b = $HTTP_POST_VARS['b']; //background color; $z = $HTTP_POST_VARS['z'];
//pixels size; $t = $HTTP_POST_VARS['z'];//line size; $r = $HTTP_POST_VARS['r'];//x margins; $s =
$HTTP_POST_VARS['s']; //y margins; switch($HTTP_POST_VARS['g']){case'png':header("Content-
type:image/png"); imagepng($image);break;case 'gif': header ("Content-type: image/gif"); imagegif($image);
break;case 'jpg': header ("Content-type: image/jpeg");imageinterlace($image,1); imagejpeg($image);}
//Content-type
    
```

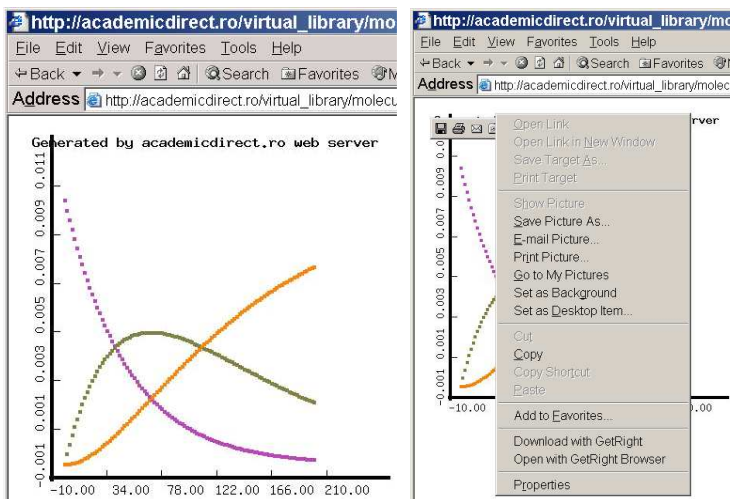


Fig. 5. The graphic representation of the consecutive reactions of the first order

The graphic obtained can be saved on the disk, as we can observe in fig.5. [6]

### 3. Conclusions

Considering the advantages of implemented software technology the programming language and the program itself is the one of the best choice now available. The program is successfully used for student practice in field of chemical kinetics. The program permits to observe more efficient the evolution of reaction in real time.

### REFERENCES

1. Canagaratna S. G., *The definition of the rate of a chem.l reaction*, J. Chem. Ed., 50,1973, p. 200.
2. Ball David W., *Kinetics of Consecutive Reactions: First Reaction, First-Order; Second Reaction, Zero Order*, J. Chem. Ed., 75, 1998, p. 917.
3. Kay G., *Bateman Eqs. Simplified for Computer Usage*, J. Chem. Ed., 65, 1988, p. 970.
4. Chesick John P., *Interactive program system for integration of reaction rate equations*, J. Chem. Ed., 65, 1988, p. 599.
5. Marasinghe P. A. B., Wirth L. M., *A graphical solution of the second-reaction rate constant of a two-step consecutive first-order reaction*, J. Chem. Educ., 69, 1992, p. 285.
6. Jäntschi L., *Automat Server Side Processing of Statistical Data*, UNITECH'02 International Scientific Conference, Gabrovo, Bulgaria, 2002, p. 185-189.



## **DEUTERIUM - DEPLETED WATER. EFFECTS ON LIVING ORGANISMS**

**STEFANESCU IOAN, TITESCU GHEORGHE, TAMAIA RADU**

*National Institute of Research – Development for Cryogenics  
and Isotopic Technologies, 1000 Ramnicu Valcea*

**ABSTRACT.** Deuterium-depleted water represents water that has an isotopic content smaller than 145 ppm D/(D+H) which is the natural isotopic content of water. DDW is a non-toxic product. Knowing that deuterium content of water has a big influence on living organisms, beginning with 1996 NIR-DCIT Rm.Valcea cooperated with Romanian specialized institutes for biological effect's evaluation of DDW. The investigations lead to the conclusion that DDW caused a tendency towards the increase of the basal tone, accompanied by the intensification of the vasoconstrictor effects. Animals treated with DDW showed an increase of the resistance both to sub lethal and to lethal gamma radiation doses. DDW stimulates immune defense reactions. Investigations regarding artificial reproduction of fish with DDW fecundated solutions confirmed favorable influence in embryo growth stage and resistance in next growth stages. One can remark the favorable influence of DDW on biological process at plants in various ontogenetic stages.

**Keywords:** stable isotopes, deuterium depletion, production, biological effects

### **INTRODUCTION: WATER IN NATURE**

In nature we can find water (H<sub>2</sub>O - hydrogen oxide) in three states: liquid water, solid water (ice) and gaseous water (water vapors). Water's properties are taken as standard in order to state fundamental physics properties.

No matter in what physical state, water molecule has an angular structure and it is composed from one oxygen atom and two hydrogen atoms. The distance between one oxygen atom and one hydrogen atom (O-H) is 0.96 Å and the valence angle H - O - H is 104.5°.

### **DEUTERIUM - DEPLETED WATER**

Deuterium - depleted water is distilled water, microbiological pure, with an isotopic deuterium concentration smaller than the concentration of natural water (145 ppm D/D+H).

Deuterium - depleted water (DDW) is a non-toxic product. It is the result of many researches developed through years by a research team from Romania, researches that lead to the realization of a patent for a technique and an installation for DDW production.

The technique used for DDW production is continuous under vacuum distillation of natural water through distillation columns equipped with high performance structured packing. The technology applied and the installation available in Romania assure the production of deuterium - depleted water with any desired concentration in the domain 20 -120 ppm D/D+H.

### **WHY DEUTERIUM - DEPLETED WATER?**

A usual question whose answer can be found in the heart of Nature. A team of explorers found in the high of Tibet a village whose people seems to come from another time; their health and longevity are significantly higher than the average. This fact amazes and put two questions: how and why?

It was obvious that live in a world without pollution and stress could have such effects but it was also another important factor: drinking water. The only drinking water available in region was water from an ancient iceberg. The analyze of this water showed a deuterium content much smaller than usual.

Further investigations showed that deuterium - depleted water similar to those found in Tibet can be found also in the polar ice calotte.

### **WHEN SCIENCE ASKS**

Starting from the certitude that heavy water (which is the opposite of deuterium - depleted water) has destructive effects on living cells was made the assumption that DDW could have the opposite effects.

The scientific base was already stated since it is well know that the joints between deuterium and another atoms are much stronger than the joints of hydrogen. This fact lead to the slow down or even to the stopping of many biochemical processes from living cell. It is the reason for which too much deuterium in living cells lead to the decrease of immunity.

The normal question was if it is important the level of deuterium from nature and the maintenance of a natural concentration in human body during live. The simplest way to answer this question was to investigate if the increase and the decrease of deuterium content have any effect in living cells (in plants, animals, and humans).

### **EXPERIMENTAL RESULTS**

The researches made by a Hungarian team showed that living cells could feel the change of deuterium level and react by changing the biochemical processes. Further more, the researchers affirms that the decrease of deuterium content could modify the metabolism of living cell and could stop the development of tumoral cell and even make the tumor disappear.

In the same time, in Romania were developed researches that lead to the following conclusions:

- deuterium depletion determine the decrease of growing rate of transplanted tumors;
- deuterium depletion increases the vascular reactivity;
- deuterium depletion stimulates some uncommon immunity systems;
- deuterium depletion increases organism's resistance to lethal, under-lethal radiation doses;
- deuterium depletion stimulates artificial reproduction of fish;
- deuterium depletion stimulates germination, growth, and development of plants.

## SAFETY SYSTEM IN A HEAVY WATER DETRITIATION PLANT

**OVIDIU BALTEANU, CARMEN MARIA RETEVOI,  
IULIANA STEFAN**

*Institute of Cryogenics and Isotope Technologies Rm.Valcea*

**ABSTRACT.** *In a CANDU – 600 reactor from a nuclear power plant a quantity of 1500 KCi/year of tritium is generated, 95% being in the D<sub>2</sub>O moderator which can achieve a radioactivity of 80 – 100 Ci/kg. Tritium in heavy water contributes with 30 ±50% to the doses received by operation personnel and up to 20% to the radioactivity released in the environment.*

The large quantity of heavy water used in this type of reactors (500 tones) make storage very difficult, especially for environment.

The extraction of tritium from tritiated heavy water of CANDU reactors solve the following problems: the radiation level in the operation area, the costs of maintenance and repair reduction due to reduction of personnel protection measures, the increase of NPP utilisation factor by shutdown time reduction for maintenance and repair, use the extracted tritium for fusion reactors and not for the last, lower costs and risk for storage heavy water waste.

Heavy water detritiation methods, which currently reached the industrial or pilot plant, are based on catalyst isotope exchange, electrolysis and cryogenic distillation. The technology developed at Institute of Cryogenics and Isotope Separation is based upon catalytic exchange between water/tritiated water and hydrogen/deuterium, followed by cryogenic distillation of hydrogen and its isotopes.

The nature of the fluids that are processed into detritiation heavy water plant requires the operation of the plant in maximum-security condition in order to protect the working staff and the environment. The paper presents the safety system solutions chose in order to solve this task in abnormal functioning and in case of terrorist activity as well a simulation of an incident and the response of the protection system. The application software is using LabView platform that is specialised on control and factory automation applications.

### **1. Introduction**

Conventional systems use a large number of equipment, very expensive, as well as the viability and accuracy are basis demands. On the other hand, the systems become more complex solving demands like redundancy, failure to safety or diversity. Like a result, operation and maintenance become more complicated and more expensive. Solution for these problems is to develop a reliable and flexible on-line diagnosis system, comprise by two computers and a small number of discrete equipment.

### **2. ICIT Heavy Water Detritiation Plant Safety system**

The ICIT plant for tritium and deuterium separation is an experimental project for extraction of the tritium from heavy water, based on catalytic exchange followed by cryogenic distillation (figure 1). ICIT institute intends to develop another experimental plant based on direct electrolysis and catalytic exchange.

The purpose of the security and control system is to ensure for population an irradiation risk under the prescription limits and to obtain a lower possible risk (ALARA principle). The safety system architecture must assure an active and passive, direct and/or indirect protection. The concept for security system design is based upon basic and maxim credible accidents which can appears in functioning. These categories of events comprise leakage from pipes and equipment and partial or total failure of the plant modules.

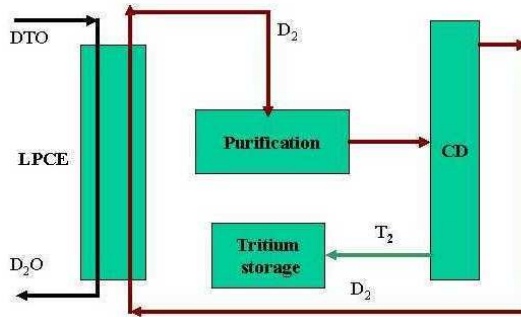


Fig. 1. Block diagram for ICIT detritiation plant

At ICIT experimental heavy water detritiation plant, control and security systems are entirely separated and these are using different type of equipment. Security system are designed in respect with "defence in depth" concept [1], which includes the use of redundancy, diversity, separation and failure to safety or fail-safe behaviour for its components and individual systems. Safety system design make possible to action in different way as well as the incidents is smaller or bigger. Thus, the technological process will not be shutdown if the equipment faults are not rising the security risk, even if the efficiency of the plant is lower.

The main objective of security system is controlling the ventilation system, which exhaust the air inside the plant and auxiliary facilities to the stack through a collector. The air that is exhausted through stack is continuously analysed by a tritium monitor (proportional counter) who is the main security equipment. By the other hand two tritium monitor (ionisation chambers) are placed inside the plant. These three monitors are playing a principal role in security system which shutdown the plant and starts the emergency ventilation and tritium recovery unit.

Whole security system is connected to the plant command and control system in order to take control of a process in abnormal condition. The connection between both systems is made at device control level (figure 2).

In present, our laboratory from ICIT Institute develops a highly integrated security system for Pilot Plant - virtual safety system. Thus the number of equipment which are used for this system are significant reduced, with benefits in maintenance and operation plant.

At this moment, virtual safety system has operational the part which monitoring the parameters limits, the equipment state, fire and integrity sensors and generate the specific procedure for each type of events. The virtual system loads the signals from classic security system through serial communication. Software applications assure signal conversion and comparison, as well as manage the information, generate the reports and select the specific procedure for each event. A "symptom oriented" philosophy software design reach the two goals which are for interest: to assure efficiency and viability for security system and to prevent fault events or major operation errors through alarm procedure and events prognosis. As well as the computer equipment is used for essential monitoring functions, a dual computer arrangement is used for redundancy [2].

In the following we present virtual security system action in case of major damage - completely loss of the radioactive inventory, through simultaneous or consecutively damage of plant modules.

## SAFETY SYSTEM IN A HEAVY WATER DETRITIATION PLANT

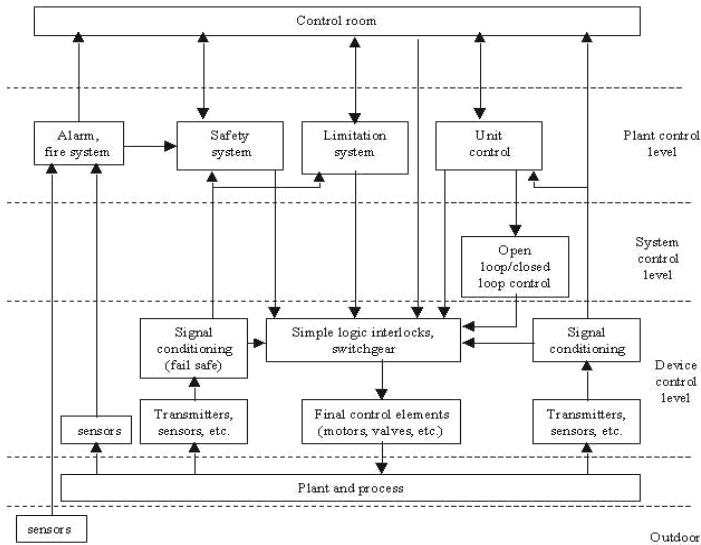


**Fig. 2.** Security and control system interconnection

If the limits for air evacuation are exceeded, the main tritium monitor mounted on the stack gives the following commands: ventilation system is stopped and evacuation stack is shut; the isotopic exchange and purification modules are shut-down; the emergency ventilation and recovery unit are started; the cryogenics distillation module is shut-down sequential; modules are emptying by process liquids.

The graphic interface of the software application assure a good plant surveillance and allow sequential monitoring for events and dynamic assistance for each step of a specific procedure which must be applied. The operator is informed step by step about the actions that he must make as well as about the consequences of his actions (figure 3). As is shown, are three distinct alarm zones: zone1 - equipment which release the alarm (and also presents the equipment state), zone 2 - specific operation procedure and zone 3 - the state of equipment in each step of the procedure.

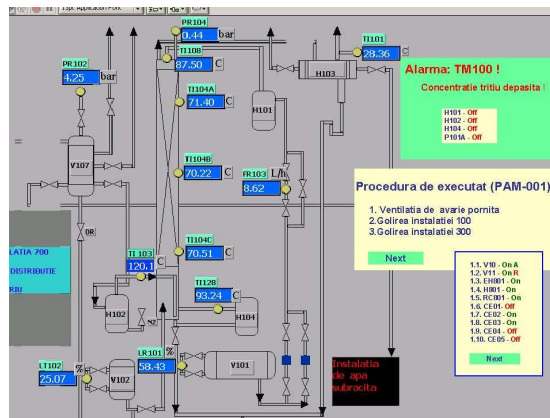


**Fig. 3.** Monitoring station - Alarm to TM100

### **3. Results**

The system is flexible, easy to use and the improvements needed by any technological process experiment could be done in short time and low costs. Such a system can replace a dedicated hardware and software for industrial process, regarding especially the experimental character of this plant. Information on the plant state is also essential in the dynamic prioritisation and conditioning of alarm message. The base in software design is to assure a good interface between hardware and software with high-speed connection.

### **REFERENCES**

1. W. Aleite, "*Defence in a depth by 'Leittechnique' systems with graded intelligence*", Proc. Symp. Nuclear Power Plant Control and Instrumentation 1982, Munchen, Germany, 1982, IAEA Vienna, 1983, 301-319.
2. N. M. Ichiyen, N. Yanofsky, "*Computer's key role in CANDU control*", Nucl. Eng. Int., **25**, 1980, pp 28-32.

## DATA ACQUISITION SYSTEM FOR OPTIMIZATION AND CONTROL THE PROCESSES FROM ISOTOPIC EXCHANGE COLUMN

**CARMEN MARIA RETEVOI, IULIANA STEFAN,**  
**ANISIA BORNEA, OVIDIU BALTEANU**

*National Institute of Research-Development for Cryogenic and  
Isotope Separation Technologies, Rm. Valcea*

**ABSTRACT.** One of the problems in a tritium separation installation is controlling the temperature of the isotopic exchange column. To maintain a constant column temperature, the signal from the monitoring system (sensors) is used to control a power supply for the electrical heat exchangers. Other parameters measured in the flow circuit are the pressure, water level in the column and boiler temperature. The computer to be used for the control is equipped with LabView software, a data acquisition board, and a signal conditioner. Also, we developed a new monitoring system for detritiation installation using National Instruments products, FieldPoint Modules, LabView 6.1 and serial board, configuring for RS-485, usefully for long distance.

### **1 Introduction**

The raise of tritium level concentration in heavy water determines some problems in operation of nuclear reactor and also for the environment. Therefore it is very important to decrease the tritium level in heavy water and in this way most owners of Candu reactors are making researches and develop technologies for heavy water detritiation. As it is well known after several years of functioning the radioactive level in the moderator attained such a value that imposes heavy water detritiation. The technology developed at the Institute of Cryogenics and Isotope Separations is based on catalytic isotope exchange between water and hydrogen gas both carrying various isotopes of hydrogen: normal hydrogen, deuterium, and tritium. This isotope exchange is followed by cryogenic distillation separating the various isotopes of hydrogen gas. The detritiation process was simulated using as working fluids water with a small content of deuterium and a gaseous mixture of hydrogen and deuterium.

In order to describe the isotopic exchange process water-vapor-hydrogen gas, we consider an exchange column and described the processes: distillation and catalytic isotope exchange distinctively. The distillation layer is realized with ordered package B7 type of phosphorous bronze. The hydrogen gas with water vapor saturate is circulated in countercurrent with water on the distillation layer and it's realized the isotopic exchange by distillation. The catalyst layer is realized with the catalyst PT/C/PTFE. The hydrogen gas and the water vapors are circulated in co-current on the catalyst layer and it's realized the isotopic exchange by catalyst isotopic exchange. The distillation and the isotopic exchange alternate along the column. Also for monitoring the isotopic exchange column is necessary to control the temperature very carefully. For that we made an automation system with data acquisition and control which provide all data for analyze. The design of the process calls for a constant catalytic exchange temperature that must be maintained at a value of 90<sup>0</sup>C. To achieve this, the plant is equipped with electrical heat exchangers for heating the gas (hydrogen) and the heavy water. The control is achieved using an array of sensors and controllers. The sensors used for monitoring the process are type J thermocouples. The control systems use different sensors of

the same type but better quality. The temperature control is achieved by controlling the electrical power fed to the heaters. Besides sensing the fluid temperatures at various points, we also monitor the vapor pressure and the heavy water level in the column. The level is controlled via two dosing pumps, which work alternately to feed water to the column.

## 2. Performances

We monitored the temperature of hydrogen inside the heat exchanger and at the input of column and made sure these are lower than the maximum safe temperatures (90°C and 150°C respectively). The security system monitors the pressure of the nitrogen used for cooling the electrical resistance rods inside the heaters. For temperature measurement, we used thermocouple type J, and the FieldPoint module FP-TC-120. The new system developed has module FP 1001 connected to the serial board, configured for RS-485 from computer. The real advantage is that we can connect all necessary FieldPoint modules to make the monitoring of entire installation. In this way we reduced the costs and are easy to use. The FP-1001 connected to the serial port type C114H is configured with address 10. The equilibrium constants for the various reactions inside the column are calculated using the formulas:

$$\begin{aligned} K1 &= 4.0231 - 0.01951 * T + 5.91595 * 10^{-5} * T^2 - 6.69797 * 10^{-8} * T^3; \\ K2 &= 12.64976 - 0.05189 * T + 1.51192 * 10^{-4} * T^2 - 1.67942 * 10^{-7} * T^3; \\ K3 &= 1.1423 - 0.00599 * T + 1.85109 * 10^{-5} * T^2 - 2.11582 * 10^{-8} * T^3; \\ K &= 3.51363 + 0.00195 * T - 4.16545 * 10^{-6} * T^2 + 3.94311 * 10^{-9} * T^3; \end{aligned}$$

The connection between FP-1001 module and PC is realized through serial board C114HI, with output configuration for RS-485, in half-duplex mode. Serial board connector has 25 pines, and pine with number 8 is connected at pine Rx+ to the FP-1001 module. Tx-pine is connected to the pine 2 of serial board connector. With FieldPoint Explorer we configured very quickly the parameters of FieldPoint modules, including ranges, power-up states and Ethernet IP address. We realized also interactively read and write data from I/O modules to tests and verify proper operation.

Because FieldPoint Systems also include a free OPC server for industry-standard connectivity, we integrated the systems with software that has OPC-client. OPC uses DCOM technologies, so client application can access data from remote OPC server over the network.

Figure 1 shows the “front panel” from LabView and shows how the temperature is controlled and also how we calculate the equilibrium constants, as a function of the acquired temperature.

## 3 Conclusions

The experimental dates obtained at the tritium isotopic exchange proved that the speed constants are half of the deuterium speed constants.

These experimental dates and the computed values of the speed constants represented an image about catalyst performances of the deuterium and tritium isotopic exchange. The mathematical model and the experimental dates permitted to design an isotopic exchange column for deuterium and tritium exchange for liquid to gas phase. Because LabView has the same development tools and language capabilities as a standard computer language such as C – looping and case structure – it is well suited for modeling and simulation.



The purpose of this application is to accomplish the monitoring and increasing level security, for protection in detritiation installation. We realized experiments with LabVIEW, as an OPC client by connecting to an OPC FieldPoint server through DataSocket connection. This procedure is used to connect VIs to devices on any OPC server, such as FieldPoint. With DataSocket we can efficiently pass data over the Internet, and respond to multiple users without the complexity of low-level TCP programming.

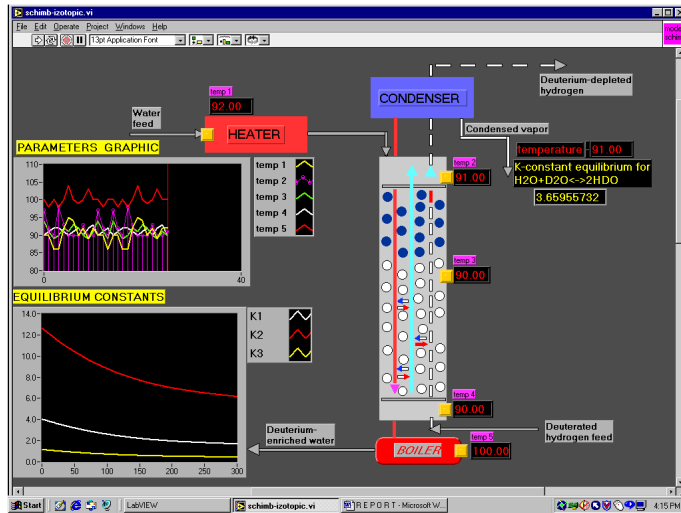


Fig. 1. Front Panel from LabView. Monitoring the isotopic exchange column

Figure 2 shows the “front panel” displaying the equilibrium isotherm and the operating line plot.

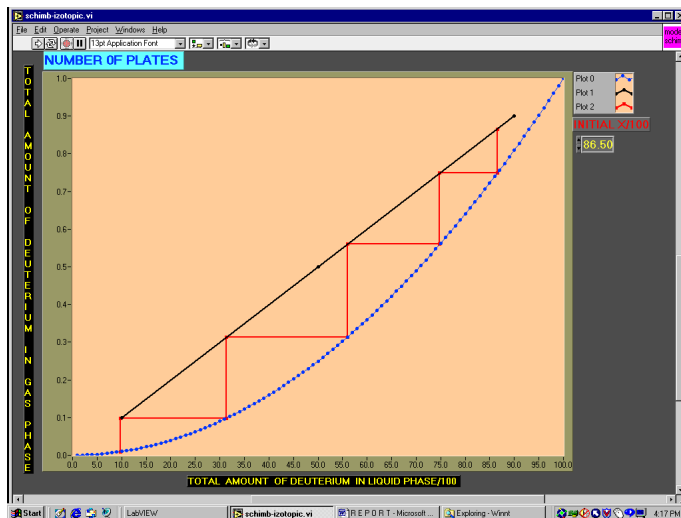


Fig. 2. front panel in LabView for equilibrium isotherm

## REFERENCES

1. Hall T. Martin & Meg. L. Martin – “*LabView for Automotive, telecommunications, semiconductor, Biomedical and other applications*”, Prentice Hall PTR, Upper Saddle River, NJ 07458, 2000, USA, pages 185-190, ISBN 0-13-019963-X
2. Cohen K. - *The Theory of isotope separation*, Editura Mc. Graw-Hill, New- York, 1951;
3. Masami Shimizu, T.Doi, A.Kitamoto, Y.Takashima - *Numerical Analysis on Heavy Water Separation Characteristics for a Pair of Dual Temperature Multistage - Type H<sub>2</sub> / H<sub>2</sub>O - Exchange Columns*. Journal of Nuclear Science and Technology, 17(6), pp.448 - 460 (June 1980);
4. Masami Shimizu, A.Kitamoto, Y.Takashima - *Numerical Analysis on Heavy Water Separation Characteristics for Pair of Bythermal Trickle- Bed Type H<sub>2</sub> / H<sub>2</sub>O - Exchange Columns*. Journal of Nuclear Science and Technology, 20(3), pp.254-263 (March 1983);

## DATA ACQUISITION AND CONTROL SYSTEM FOR A HEAVY WATER DETRITIATION PLANT

**IULIANA STEFAN, CARMEN RETEVOI, LIVIU STEFAN, OVIDIU BALTEANU**

*National Institute of Research-Development for Cryogenic and Isotope  
Separation Technologies, Rm. Valcea POBox 10-4, Rm. Valcea 1000,  
Romania, Phone:+40 250 736979, Fax:+40 250 732746*

**ABSTRACT.** The importance of detritiation of heavy water from CANDU type reactors is well known, as is the implications of detritiation in fusion processes and installations. The nature of the fluids that are processed in detritiation requires the operation of the plant in maximum security conditions in order to protect the working staff and environment. The paper presents how the data acquisition and control system could be made for an experimental heavy water detritiation plant. The plant must be designed to be operated without any working staff in the technological space. The purpose of the security and control system is to ensure for the population an irradiation risk below the prescription limits. The radiological risk is the tritium leakage that can be gas, vapors or liquid.

**Keywords:** data acquisition, control system, detritiation, tritium separation.

### 1. Introduction

The scope of the experimental plant for tritium and deuterium separation is to extract tritium from heavy water. The heavy water is used as moderator in the CANDU type nuclear reactor and after a period of operation an accumulation of tritium appears. The high concentration of tritium create some problems for safety operations of the plant and also for the population and environment.

Solving these problems means that a heavy water detritiation plant must be built and linked to the moderator circuits of the CANDU power plant. This type of plant can be assimilated as a nuclear facility, involving special regulation and safety systems, respecting the nuclear laws of ROMANIA, EU and international safety regulations, including IAEA Vienna specifications. Like any nuclear facility, a special safety system is provided, with special hardware and software that supervises the technological process and safety equipment.

The tritiated heavy water is received from the nuclear power plant and introduced into the process. The output result is a low concentration of tritium in the heavy water. This water is returned to the moderator circuits and so the safety regarding to the concentration level of tritium in the heavy water is re-established[1,2]. At the same time, this plant can constitute the basis for obtaining high purity tritium that can be used in future fusion reactors or other laboratory research.

### 2. System Description

Under normal operating condition of the detritiation plant, no operating personnel is allowed to enter in the technological area. Therefore, the monitoring, analysis and control systems must use remote controlled equipment. The plant building must include a control room and a data acquisition chamber which contain respectively the monitoring and control computers, and the sensors and control equipment. In the control room digital computers

are used for status monitoring, plant control and alarm annunciation. The digital computers communicate and manage all the other components of the system using software applications (LabView platform) with a friendly interface [1,2].

The measured values generated by process variables are converted into electrical or pneumatic signals, which are then transmitted to subsidiary units used for indication, control and protection functions. Before transmission, sensor signals are usually converted to standard signal levels (e.g. 4-20 mA or 0-10 V). For remote transmission of signals the 4-20 mA current signal is more common because of its higher noise immunity. Voltage signals (such as 0-10 V) are generally used within the control room for recorders and indicators[3].

During operation, the data acquisition can be done by a digital computer that provides signals from a network interface module of type FieldPoint which connects an RS-485 network to I/O modules and manages communications between the host computer and the I/O modules with a rate of 115.2 kb/s[4].

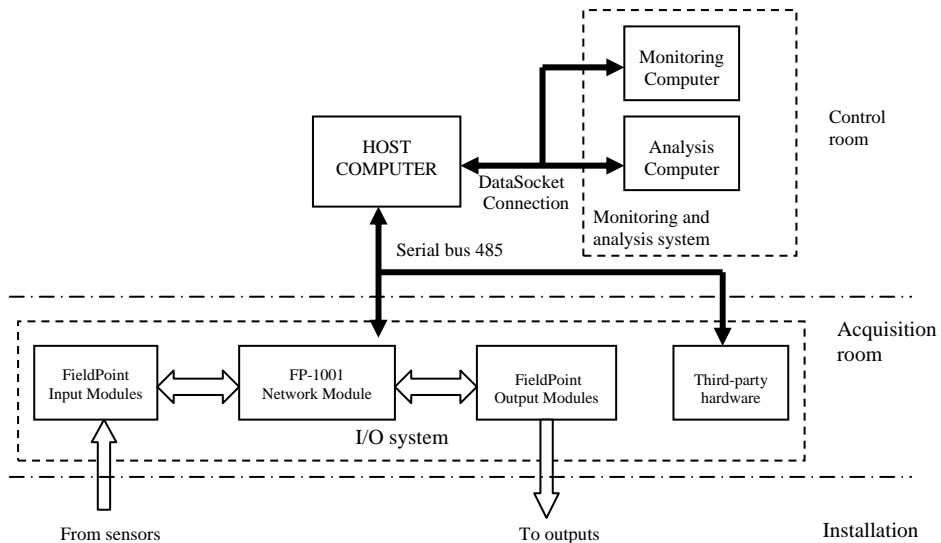


**Fig. 1.** Architecture of acquisition and control system

The input modules receive signals from transmitters (flow, pressure, level), push buttons, contacts, and limit switches. The measured values of the parameters are recorded and displayed in the control room for a continuous indication of the parameters and give a systematic view of the control status. These data are compared with predefined limits and if one parameter is out of these limits, a visual and acoustic alarm will be actuated. The software that controls inputs and outputs contains a logical structure based on control analysis of the technological process. Using implemented logic and signals from the technological process, a decision is taken and an output command is sent to execution. This action can be corrective (for technological process) or preventive (safety of the plant).

For cryogenic temperature measurement (e.g. temperatures from a cryogenic distillation column at about 23 Kelvin) carbon resistance temperature sensors can be used. In

order to measure variation of the sensor resistance with temperature, a four-wire measurement method can be used, which offers the best accuracy. For higher temperatures (e.g. temperature from the isotopic exchange column) type J thermocouples can be used [1,2].

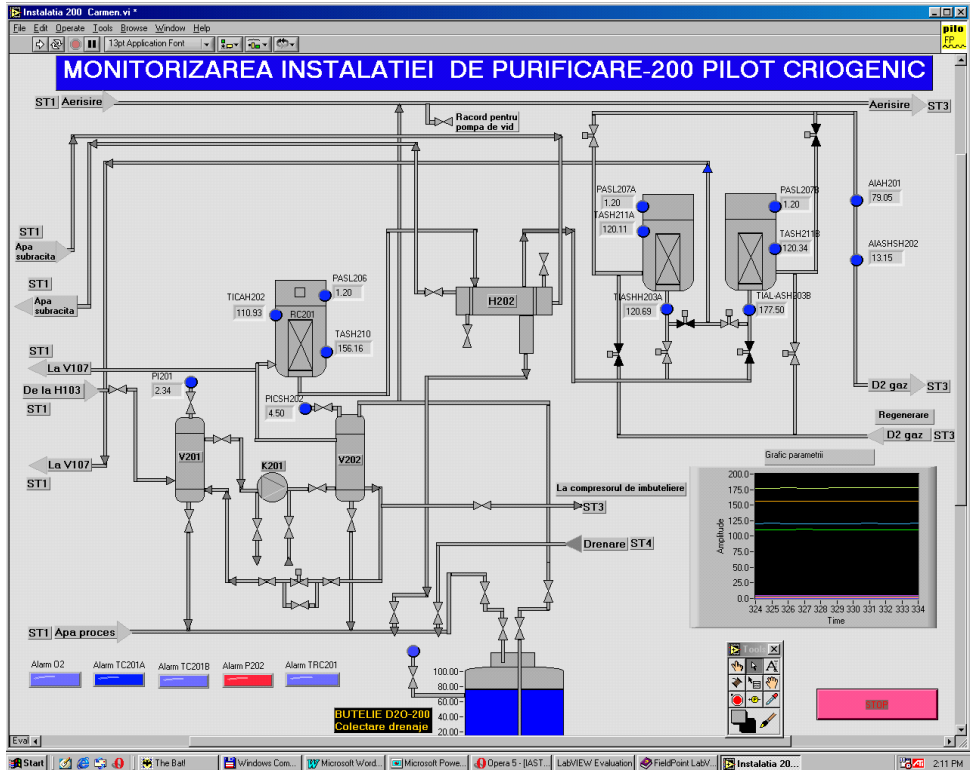


Fig. 2. Example of status monitoring using LabView Platform

The parameter display computer assists control room personnel in evaluating the control status of the plant by providing a continuous indication of the parameters or derived variables that are representative of that status.

It is important to consider the experimental nature of the plant, and therefore all data equipment is flexible and easy to adapt to the technological process.

This type of data acquisition system can be used as the basis for the measurements that are needed in most tritium experiments. In the case of industrial plant, dedicated equipment must be considered.

The control system provides the following functions:

- Ensures that all controlled parameters in the experimental plant remain within prescribed limits during all operational modes;
- Enables changes in set points to be made without excessive transients;
- Allows operation of remote equipment under automatic and manual control.

The main advantages of such a system are the continuous surveillance of the plant status with a display of main plant parameters, and making corrective and safety decisions regarding the technological process[3].

### 3. Conclusions

The system is flexible, easy to use and the improvements needed by any technological process experiment could be done in a short time and with low costs. Such a system can replace dedicated hardware and software for industrial processes, especially regarding the experimental character of this plant. Information on the plant state is also essential in the dynamic prioritization and conditioning of alarm messages. The basis of the software design is to assure a good interface between hardware and software with high-speed connection.

### REFERENCES

1. *Reference technical project of tritium separation plant*, Internal Report, ICIT, Romania, 2001, pp. 68-77
2. *Security final report of tritium separation plant*, Internal Report, ICIT, Romania 2002, pp. 50-58
3. *Modern Instrumentation and Control for Nuclear Power Plants: A Guidebook International Atomic Energy Agency*, Vienna, 1999, pp. 142-147
4. *FP 1000/1001 User Manual*, National Instruments Corporation, April 1999, pp 2-10

## ORIGIN AND FLOW DYNAMIC OF GROUNDWATER IN MOVILE CAVE AREA, ROMANIA, BASED ON ENVIRONMENTAL ISOTOPES

**LUCIA FEURDEAN, VICTOR FEURDEAN, MIHAI GLIGAN**

*National Institute for R&D of Isotopic and Molecular Technologies,  
PO Box 700, 3400 Cluj-Napoca 5, Romania, luci@140.itim-cj.ro*

**ABSTRACT.** As a conservative tracer in carbonate rocks deuterium was used to determine the un-elucidated problems of the water origin in cave. The values of  $\delta^2\text{H}$  and  $\delta^{18}\text{O}$  plotted on GMWL (Craig line) indicate the meteoric origin of groundwater in Movile Cave area. The  $\delta^2\text{H}$ - $\Delta\text{dens}$  correlation of samples delineated three isotopically water types. Time series of the deuterium concentration from groundwater samples exhibit a distinct seasonal effect with lower deuterium concentration in summer than in winter. The water of Movile Cave is the result of the mixing of two end members that have different hydrogen isotope ratios. The spatial variation of the deuterium content delineated the areas with vertical inflow and the flow path of groundwater from deep aquifer. The discharge of the deep aquifers occurs through faults and karstic channels into overlying aquifer. The Movile Cave and Karaoban Lake are connected and the cave water discharge by overflow mechanism that offers to cave the isolation of atmosphere.

The stable isotopes content of waters collected from study area provided important information about the unusual subterranean ecosystem of Movile Cave that is based on chemoautotrophic conditions. Located near the Mangalia City, the Movile Cave is closed system, which has groundwater rich in  $\text{H}_2\text{S}$  (8-12 mg/l) and an atmosphere poor in oxygen (7-10%), rich in  $\text{CO}_2$  (2-3.5%) and containing significant amount of  $\text{CH}_4$  (1-2%). Climate is semiarid; the land topography is smooth. The detritic Palaeozoic formation is overlain by a 450-500m thick stack of mainly carbonate rocks belonging to the Jurassic, the Cretaceous and the Eocene; over them the

fossiliferous limestones of Sarmatian age have been deposited in a thickness of 60-150m. Loess deposits covering limestones represent the Quaternary. The tectonic structure indicates the three faults (figure 1). Rocks classified according to their hydrological function include:

- The unconfined aquifer in the Sarmatian karstified limestones.
- The confined aquifer in the Eocene and Mesozoic limestones, which are fractured and karstified and represent a unitary complex interconnected with upper lying aquifer.

As a conservative tracer in carbonate rocks, deuterium was used to determine the un-elucidated problems of the water origin in cave. The average value of  $\delta^2\text{H}$  for all samples is  $-85\text{‰}$ , for the most samples (76%) the  $\delta^2\text{H}$  values are lower than  $-80\text{‰}$  and is isotopically more light than the waters from the semiarid lowland of the Dobrogea district that are over  $-76\text{‰}$  (figure 2 and 3).

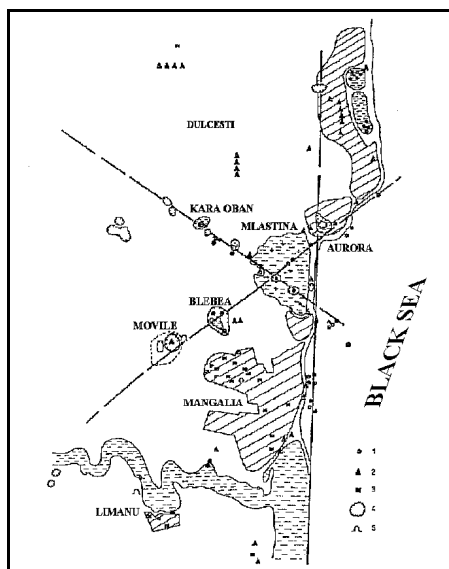


**Fig. 1.** The Mangalia area.

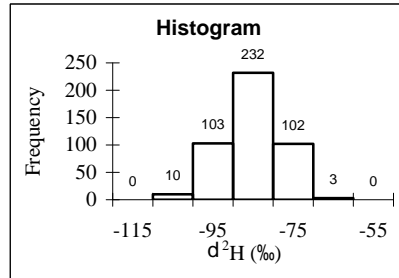


Fig. 2. Histogram of  $\delta^2H$  values

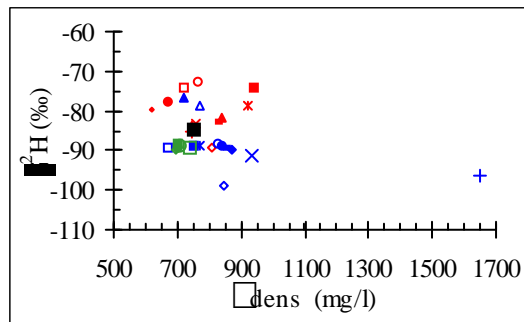


Fig. 3.  $\delta^2H$ - $\Delta$ Dens diagram

**The  $\delta^2H$ - $\Delta$ Dens correlation.** The distribution of the average values in the diagram delineate the existence of three isotopically water types:

- Type I that have low deuterium content ( $\delta^2H < -88\text{‰}$ ) and the samples come from wells concerning the Barremian-Jurassic aquifer and from the springs emerging in Karaoban area.
- Type II represents waters with deuterium content about mean recorded value of about  $-85\text{‰}$ . These samples are from domestic wells, Movile Cave and few springs.
- Type III represents waters with higher deuterium content ( $\delta^2H > -80\text{‰}$ ) that come from drink water wells and from southwestern part of area, in proximity of Mangalia Lake.

The  $\delta^2H$  values lower than  $-80\text{‰}$  are not specific to low land of Romania. The low  $\delta^2H$  values can be attributed to the following factors:

- the infiltration of winter meteoric water or high altitude water,
- the paleoclimate effect,
- the isotopic exchange between water and other hydrogen compounds.

**The  $\delta^2H$ - $\delta^{18}O$  covariance.** The data of hydrogen and oxygen isotopic contents for the samples from Movile area (fig. 4) form a linear band that can be described by equation with the slope of 8. The isotope data for samples collected from the Sarmatian aquifer ( $\delta^2H = 8.29\delta^{18}O + 10.7$ ;  $r^2 = 0.7863$ ) fit the Craig line ( $\delta^2H = 8\delta^{18}O + 10$ ) reasonable well despite the mathematical differences between the local line and global meteoric line. The  $\delta^2H$ - $\delta^{18}O$  covariance indicates the meteoric origin of groundwater from Movile area and reflects small kinetic effects during evaporation-condensation of precipitation that are the input of groundwater. The recorded isotopic content ranges between isotopically very light water and isotopically normal water for the lowland of Romania.



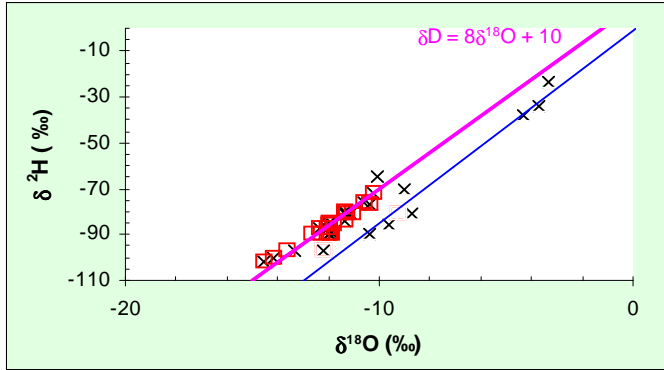


Fig. 4. The  $\delta^2\text{H}$ - $\delta^{18}\text{O}$  covariance.

**The  $\delta^2\text{H}$ -time correlation.** The seasonal variation of deuterium content from precipitation input is reproduced after damping and delay in the seasonal variation of  $\delta^2\text{H}$  values from groundwater.

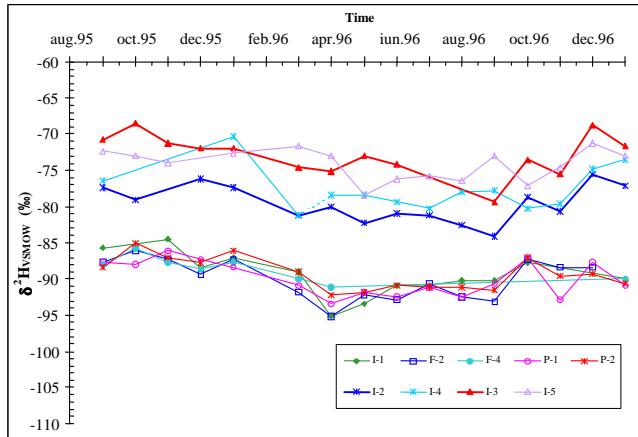
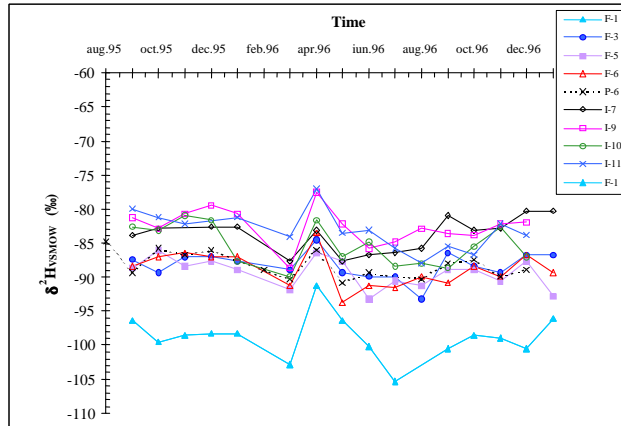


Fig. 5. Seasonal variation.

The seasonal effect is great preserved in groundwater flowing in fractured rocks (conduit flow or flow through subterranean passage partial filled with water) and damped in groundwater moving in homogenous porous media and/or long travel way. Similarity in the behavior of deuterium time series of different samples shows the same origin and path flow of groundwater. The different distances between recharge and sampling points or the different flow rates can produce the  $\delta^2\text{H}$  value shift in time and the peaks of discharge can be recorded at different moments. The recorded peaks on the background isotopic concentration of the  $\delta^2\text{H}$ - time series are caused by the storm discharge that strongly affects the flow system by the input concentration at the discharge moment.

The time series of  $\delta^2\text{H}$  values from groundwater of Movile Cave area indicate the following:



**Fig. 6.** Seasonal variation.

- Well outlined in time series (fig. 5), the seasonal effect of  $\delta^2\text{H}$  values from precipitation excludes the possibility of the paleoclimatic origin of groundwater and indicates a strong link with isotopic composition of precipitation, but a lower deuterium concentration in summer than in winter;
- This six-month shift of the isotopic composition variations with respect to normal succession of seasonal maximum and minimum values of precipitation and low  $\delta^2\text{H}$  average values are due to the water recharge from higher altitude (from the Balkan Plateau) and the long way of subterranean movement.
- The analogy of the variation in time (fig. 6, 7), with or out temporal shifting of the peaks, emphasized the membership at mixing system and/or the genetic relationship between water sources;
- The large peaks of  $\delta^2\text{H}$  values recorded in late spring months and in early summer months for the F1 and F11 samples (fig. 7) are due to the event water (rain falling on the site with altitude of 1000m and a rapid flow through alternative pathway is the most probably).

**The mixing lines.** On the  $\delta^2\text{H} - \Delta\text{Dens}$  average values, from possible straight lines are corroborated with other criteria represent a mixing system. The alignment of samples suites must be corroborated with evolution in time of  $\delta^2\text{H}$ . The diagram (fig. 8) suggests that the water from Movile Cave belongs to a mixing water system. One end member is isotopically light water and another end member is isotopically enriched water.

**The spatial variation of  $\delta^2\text{H}$  values.** The closed isolines of equal concentration of deuterium indicate vertical movement of water. The most low  $\delta^2\text{H}$  values were recorded for samples F1 and F11 from aquifer caught in Mesozoic limestones. The map of isolines of equal concentration (fig. 9) delineates the zones with the movement of water by vertical (closed lines) and horizontal (open lines). The water movement by vertical is for the following samples:

- from the aquifer caught in Mesozoic limestone (F1, F2);
- from the springs and well on the Karaoban site;
- for samples from Movile Cave.

ORIGIN AND FLOW DYNAMIC OF GROUNDWATER IN MOVILE CAVE AREA

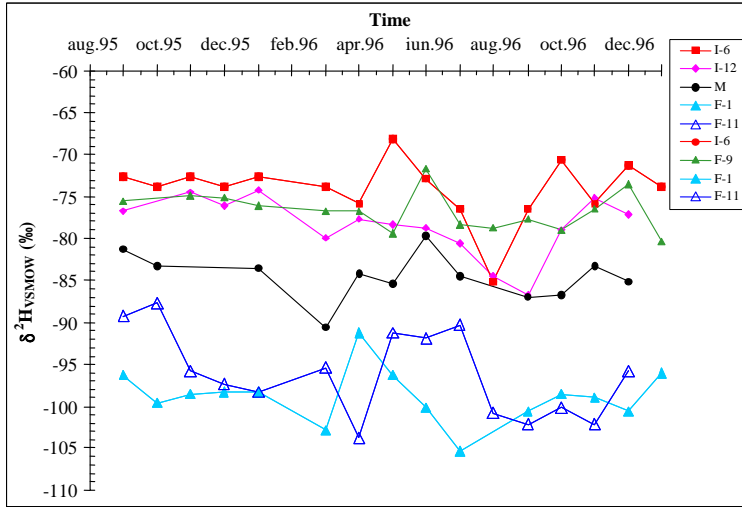


Fig. 7. Time variation.

The horizontal movement of water was determined for water caught in Sarmatian limestone. The movement direction is along the faults toward Mangalia swamp for deep groundwater and from WSW toward Black Sea from Sarmatian aquifer. The water of Movile Cave is a mixing of waters from Karaoban site, WSW wells and domestic fountains. Movile Cave is the buffer system between the confined aquifer (from depth) and unconfined aquifer and the connection between them is of siphon type. The isolines show the same mixing system as a mixing lines.

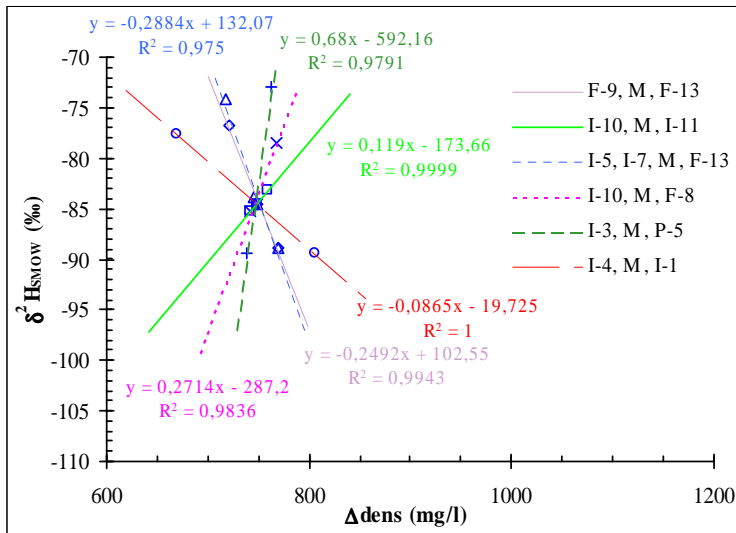


Fig. 8. Mixing line for cave water.

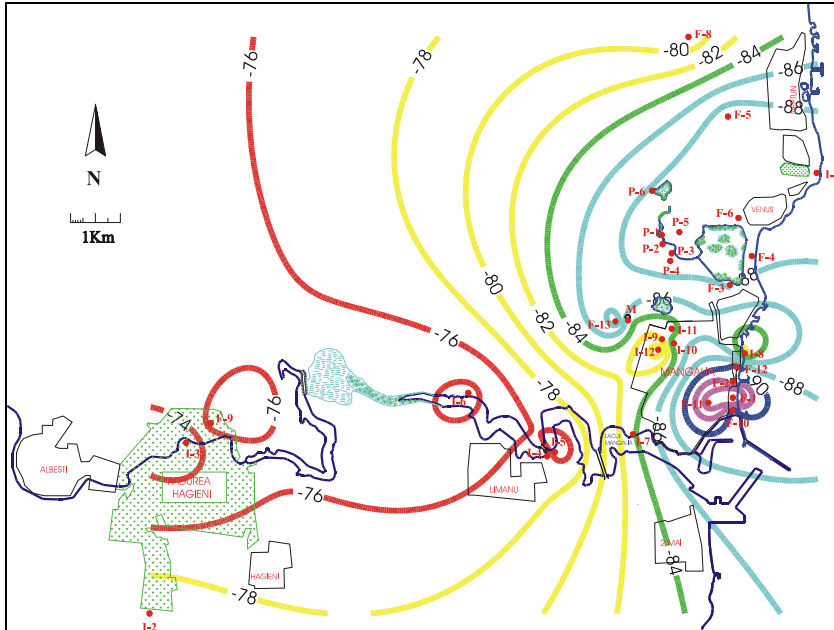


Fig. 9. Spatial variation of  $\delta^2\text{H}$  average values.

### Conclusions

- Water of Movile Cave area is of meteoric origin.
- Water from cave area come from high altitude (Balkan Plateau) site and flow in deep is slow and discharge occurs through faults that establish hydraulic connections with Sarmatian aquifer, but the springs across the impermeable formation, too. The Movile Cave is the buffer system between the confined aquifer (from depth) and unconfined aquifer and the connection between them is of siphon type.

### REFERENCES

1. Craig H. *Isotope variations in meteoric waters*. Science, 133 (1961): 1702-1703.
2. Sarbu S. M., Kane T. C. and Kinkle B. K. *A chemoautotrophically based groundwater ecosystem*. Science, 272 (1996): 1953-1955.
3. Feurdean L., Feurdean V. and Oraseanu I. *The use of deuterium as natural tracer to point out groundwater flow from karst area. Case study*. In *New Approaches Characterizing Groundwater Flow* (eds. Seiler & Wöhnlich): 2001, 59-63.

## PHOSPHOLIPID MODEL-MEMBRANES STUDIED BY FTIR SPECTROSCOPY

FERIDE SEVERCAN<sup>1</sup>, DANA DOROHOI<sup>2</sup>

<sup>1</sup> *Middle East University of Ankara, Biology Department, Ankara, Turkey, E-mail <feride@metu.edu.tr>*

<sup>2</sup> *"Al.I.Cuza" University, Faculty of Physics, 6600 Iasi, Romania, E-mail <ddorohoi@uaic.ro>*

**ABSTRACT.** Local fluidity of the acyl chains in model-membrane of the type dipalmitoylphosphatidyl glycerol (DPPG) and DPPG/GS containing peptide gramicidin S (GS) in different amounts is revealed by FTIR CH<sub>2</sub> symmetric and asymmetric stretching modes of phospholipid acyl chains. The influence of temperature as well as of the peptide content on GS/DPPC and GS/DPPG model-membrane fluidity, described by order parameter, has been studied.

A mathematical model was developed to describe the thermotropic main transition of the model membrane. Experimental data were fitted by functions obtained in this model.

### 1. Introduction

The inner compartment of the cells and organelles is isolated from the outer media by the biological membranes consisting in principal from phospholipids such as dipalmitoylphosphatidylcholine (DPPC) and dipalmitoylphosphatidylglycerol (DPPG).

The biological functions of membranes are assured by a large variety of processes. The fluidity of the lipid constituents is one of the most important factors associated with morphological changes in the biological membranes. DPPG is usually considered as model membrane in trials to evidence the perturbative action of temperature and/or of drugs inducing the lipid fluidization [1,2].

As well as DPPC [3-5], DPPG is an amphiphilic phospholipid with two hydrophobic fatty acid chains separated from a charged head group by a glycerol backbone. This phospholipid forms bilayers separated by water with the interior fatty acid chains oriented in parallel to each other and the phospholipid head faced out, in contact with water. The stability of the phospholipid membranes is assured by minimization of hydrophobic interactions and by maximization of the hydrophilic ones.

The nature of phospholipid interactions influences the mechanism of membrane penetration by some peptides, like antibiotics. When these interactions have an electrostatic nature [6], such as in the case of DPPG and Gramicidin S (GS) [7,8], membrane destabilization can occur by pores formation or by detergent like mechanism [9,10], favoring the leakage of the cellular content [11].

A variety of physical methods has demonstrated the presence of defects in the packing of lipid molecules in the solid bilayer. A pretransition and a main phase transition were evidenced [12,13]. At the main phase transition the defects are the sites of initial melting of the lipids forming small pools of fluid lipid molecules. Therefore both fluid and solid domains coexist at the main phase transition temperature. As temperature is raised beyond, the remaining solid lipids will rapidly and cooperatively melt in a first order

process into an all fluid phase. When temperature of fluid lipid is gradually lowered, the pathway from solid to fluid phase does not exactly retrace the pathway from solid to fluid phase, because of the difference in the free energies of the solid and fluid domains formed in one direction from those formed in the other. DPPC model membrane hysteresys of main phase has been evidenced by M. Geith [13].

The transition between the gel phase and the liquid crystalline phase of the model membrane is essentially induced by temperature [13-18], by the defects in the bilayer structure, or by the chemical reagents [18,19].

There is a main phase transition temperature at which the number of the systems in the gel phase equalizes the number of the systems in the liquid crystalline phase. Close to the main phase transition the membrane permeability is the greatest.

The studies on drug influence on the model membranes are beneficial for the understanding of the mechanisms of the human erythrocytes lysis [20] under antibiotic action.

## 2. Theoretical notions

Let us consider a system consisting from  $N$  subsystems that can have only two thermodynamic phases gel and liquid crystalline ones. Let suppose that the transition between these phases is a reversible thermodynamic transformation:

$$\text{Gel phase} \Leftrightarrow \text{Liquid crystalline phase} \quad (1)$$

Relation (1) suggests that by the increasing temperature of the system, subsystems can pass in the liquid crystalline phase and, by the system cooling, the subsystems can return in the gel phase.

Let be  $N_g$  the number of the subsystems in the gel phase and  $N_l$  the number of the subsystems in the liquid crystalline phase. These numbers are dependent on temperature and satisfy the equation:

$$N_g + N_l = N \quad (2)$$

At low temperatures, when the system is in the gel phase, we can consider that  $N_g$  tends to  $N$ , while at the temperature higher than the melting point  $N_g$  is near zero, because the system passed in its liquid crystalline phase and  $N_l$  tends to  $N$ .

Such a condition is satisfied by phospholipid acyl chains from the system DPPG/GS with various concentrations of GS. DPPG/GS systems support a reversible thermodynamic transformation of the type (1). For a fixed value of the GS molar ratio,  $N$  has a fixed value. By temperature increasing,  $N_l$  increases and  $N_g$  decreases as relation (1) predicts. Cooling the samples to lower temperatures,  $N_g$  increases and  $N_l$  decreases, to assure the returning of the system at its gel phase.

The reversibility of the transformation (1) has been experimentally demonstrated [13] by using wavenumber modification of  $\text{CH}_2$  stretching mode measured in the DPPC/GS systems. So, by temperature increasing the wavenumbers of the  $\text{CH}_2$  stretching mode increased, showing a sharp modification at  $41.5^\circ\text{C}$ , the melting point of DPPC, and then, at the sample cooling, they decreased in the same way to the values of the wavenumbers corresponding to the gell phase.

For the sample in the gel phase, supposing that all the subsystems are ordered, one can write:

$$N(\varepsilon_g^f - \varepsilon_g^i) \cong h \cdot c (\bar{\nu}_g - \bar{\nu}_0) \quad (3)$$

where  $\mathcal{E}_g^f$  and  $\mathcal{E}_g^i$  are the interaction energy of a pair of subsystems in the final (f) and initial (i) states of the spectral transition, when the molecules are in the gel phase (g):  $\bar{\nu}_g$  is the wavenumber measured in the gel phase of the system and  $\bar{\nu}_0$  is the wavenumber measured in the gas phase of the same system.

A similar relation can be written for the liquid crystalline phase of the system:

$$N(\mathcal{E}_l^f - \mathcal{E}_l^i) \cong h \cdot c (\bar{\nu}_l - \bar{\nu}_0) \quad (4)$$

by using the interaction energies,  $\mathcal{E}_l^f$  and  $\mathcal{E}_l^i$ , between two molecule from the liquid crystalline phase in the vibration states (f and i) participating to the IR transition and the wavenumbers  $\bar{\nu}_l$  and  $\bar{\nu}_0$  corresponding to the system in its liquid crystalline phase and in gas phase.

For the system at a given temperature T, different from  $T_m$ , one can define the ratios of the molecules from the gel and liquid crystalline phases, by:

$$p_g \equiv \frac{N_g}{N} \text{ and } p_l \equiv \frac{N_l}{N} \quad (5)$$

The ratios  $p_g$  and  $p_l$  satisfy the relation:

$$p_g + p_l \equiv 1 \quad (6)$$

One the other hand, for the system at a given temperature T, having  $N_g$  subsystems in the gel phase and  $N_l$  subsystems in liquid crystalline phase, one obtains:

$$N_g (\mathcal{E}_f^g - \mathcal{E}_i^g) + N_l (\mathcal{E}_f^l - \mathcal{E}_i^l) \cong h \cdot c (\bar{\nu} - \bar{\nu}_0) \quad (7)$$

$\bar{\nu}$  is the wavenumber measured for the system at temperature T. From equations (7), (3), (4) and (5) one obtains:

$$p_g \equiv \frac{\bar{\nu}_l - \bar{\nu}}{\bar{\nu}_l - \bar{\nu}_g} \quad (8)$$

$$p_l \equiv \frac{\bar{\nu} - \bar{\nu}_g}{\bar{\nu}_l - \bar{\nu}_g} \quad (9)$$

It results that the ratios of the subsystems in the gel phase ( $p_g$ ) and in the liquid crystalline phase ( $p_l$ ) from the system at temperature T can be estimated by the wavenumbers of the IR bands. The measurements refer to the system in the gel phase ( $\bar{\nu}_g$ ), in the liquid crystalline phase ( $\bar{\nu}_l$ ) as well as in an intermediate phase ( $\bar{\nu}$ ). The intermediate phase is represented by a mixture of these phases. Wavenumber  $\bar{\nu}$  increases with the temperature increasing. So, the equations (8) and (9) are indicators of the  $p_l$  increasing and of the  $p_g$  decreasing by temperature increasing.

In equations (8) and (9) wavenumber  $\bar{\nu}$  depends both on temperature and on molar ratios of GS from the studied systems. It results that the variation of the wavenumber  $\bar{\nu}$  when these parameters are modified determines the manner in which the number of the molecules varies from the gel and liquid crystalline states.

Relations (8) and (9) show that at the increasing temperature, if the wavenumber  $\bar{\nu}$  increases, the relative number of the subsystems in the liquid crystalline phase must increase in the same way with the decreasing of the relative number of the subsystems in the gel phase.

It also results that the derivatives versus temperature of the wavenumbers in the intermediate state could be considered as indicators of the variation of the relative numbers of the subsystems in the gel and in the liquid state at one fixed temperature.

The derivatives of the numbers  $p_g$  and  $p_l$  versus temperature are linear functions of the wavenumber derivative versus temperature:

$$\frac{\partial p_g}{\partial T} \equiv -\frac{1}{\bar{\nu}_l - \bar{\nu}_g} \frac{\partial \bar{\nu}}{\partial T} \quad (10)$$

$$\frac{\partial p_l}{\partial T} \equiv \frac{1}{\bar{\nu}_l - \bar{\nu}_g} \frac{\partial \bar{\nu}}{\partial T} \quad (11)$$

From equations (10) and (11) it results that, the manner in which the number of the subsystems from the studied system varies can be monitored by the wavenumber derivatives versus temperature in the points from the understudied temperature range.

The higher are the wavenumber derivative values, the faster are the thermodynamic phase transitions of the type (1).

## 2. Materials and methods.

DPPG and GS were purchased from Sigma Chemical Co St. Luis Mo,. They were used without purification. Multilamellar vesicles DPPG and DPPG/GS were obtained from DPPG dried films, phosphate buffer and stocks of drug-ethanol solutions, using the procedure proposed by F. Severcan et al [4]. DPPG/GS vesicles with a drug concentration of 1-10 mol% were used in this study.

The FTIR spectra of multilamellar DPPG and DPPG/GS systems were registered with a FTIR Bomeme BM 157 spectrometer, using CaCl<sub>2</sub> cells. A Unicam Specac Temperature Controller was used for temperature modifying. The FTIR spectra were averaged from 100 scans. The water vaporous influence was eliminated by subtracting the FTIR spectra of buffer solution from the model membrane spectrum, at each studied temperature. Experimental data were obtained in a large interval of temperature [27.1-70] °C.

## 4. Results and Discussion

In order to estimate derivatives (10) and (11) for the DPPG/GS systems, we used the wavenumbers of the CH<sub>2</sub> stretching vibrations that appear near 2850 cm<sup>-1</sup> (asymmetric stretching mode) and near 2917 cm<sup>-1</sup> (symmetric stretching mode) in the gel phase of the samples.

With temperature increasing, the corresponding bands slowly shift to the higher frequencies. Significant changes in the values of the wavenumbers of these bands appear at the melting point temperature. Then wavenumbers increase very slowly with the temperature increasing. Fig. 1 illustrates the shapes of the modifications of the wavenumbers of the CH<sub>2</sub> symmetric mode versus temperature.

Fig.1 shows us that DPPG and DPPG/GS model membranes have two distinct thermodynamic phases. One phase at low temperatures, named gel phase, in which the system is characterized by the smallest value of the wavenumber and the other phase, at high temperatures, named liquid crystalline phase and characterized by the highest value of the wavenumber. Thermodynamic transition (1) takes place between these phases.



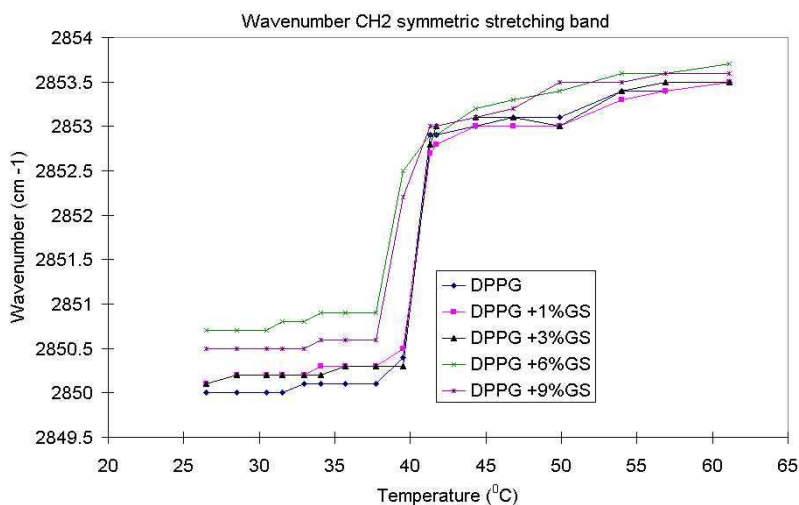


**Fig. 1.** Wavenumber of the symmetric stretching band vs temperature

These experimental data permit us to use (8) and (9) in order to estimate the relative number of the subsystems from the gel  $p_g$  and liquid crystalline  $p_l$  phases at the fixed temperature.

**Table 1**  
Wavenumber derivatives for symmetric stretching vibration of  $\text{CH}_2$  groups of DPPG

Nr.	T(K)	Gramicidin content (mol%)				
		0	1	3	6	9
1	301.5	0	0	0.05	0.05	0
2	303.5	0.05	0	0	0.05	0
3	304.5	0.1	0	0.1	0	0.2
4	306	0.07	0.07	0	0.07	0
5	307.1	0.09	0.09	0.09	0	0.18
6	308.7	0.06	0	0	0	0
7	310.7	0	0.1	0.05	0.15	0
8	312.5	0.11	0.28	0.28	<b>1.72</b>	<b>1.67</b>
9	314.3	<b>2.61</b>	<b>2.33</b>	<b>2.56</b>	0.61	0.61
10	314.7	0.25	0.25	0.25	0.25	0.25
11	317.3	0.11	0.11	0.12	0	0.08
12	319.8	0.04	0.04	0.08	0.08	0.04
13	322.9	0.06	0.03	0	0.07	0.1
14	327	0.02	0.02	0.02	0.05	0
15	329.9	0.03	0	0	0	0.1
16	334.1	0.02	0.02	0.07	0.02	0

The values of the derivatives contained in Table 1 show us that:

In the ranges (26.5-39.5) °C and (41.7-61.1) °C, the derivatives have small positive values, showing no significant changes are in the system from point of view of the numerical values  $N_g$  and  $N_l$ .

$P_1$  values rapidly increase beginning to 39.5 °C and become constant at 41.7 °C. The values of the derivatives in 41.7 °C are indeed small. It results that the thermodynamic transition (1) between the two phases of the system gives rise in the domain (39.5-41.7) °C for all the studied systems.

The values of the wavenumbers derivatives are significantly high at 41.3 °C, for GS concentrations 0, 1, 3 mol % indicating a fast modification of the ratios  $p_g$  and  $p_l$  at this temperature. Thus, for the molar ratios 0, 1 and 3 mol%, the main phase transition happens at 41.3 °C. It results that for the molar concentrations in the range (0-3] mol%, GS do not modify the melting point of the DPPG/GS systems.

Contrarily, for 6 and 9 mol% GS in the systems DPPG/GS, the values of the wavenumber derivatives are significant at 39.5 °C and decrease at 41.3 °C. For these samples, the melting point can be considered as being at 39.5 °C, decreased with approximately 1.8 °C compared with pure DPPG.

In Fig.2 are plotted the derivatives of the wavenumbers versus the temperature for asymmetric stretching vibration mode of CH<sub>2</sub> acyl chains that offer the same information such as Table 1. From these graphs it results that for concentrations 0,1 and 3 mol% GS, the number of the subsystems from the gel phase rapidly modifies at 41.3 °C, while for the molar concentrations 6 and 9 mol%, the number of the subsystems from the gel phase modifies rapidly at 39.50C. One can affirm that the high concentration such as 6 and 9mol% of GS in the DPPG/GS mixtures determines the decreasing of the main point temperature.

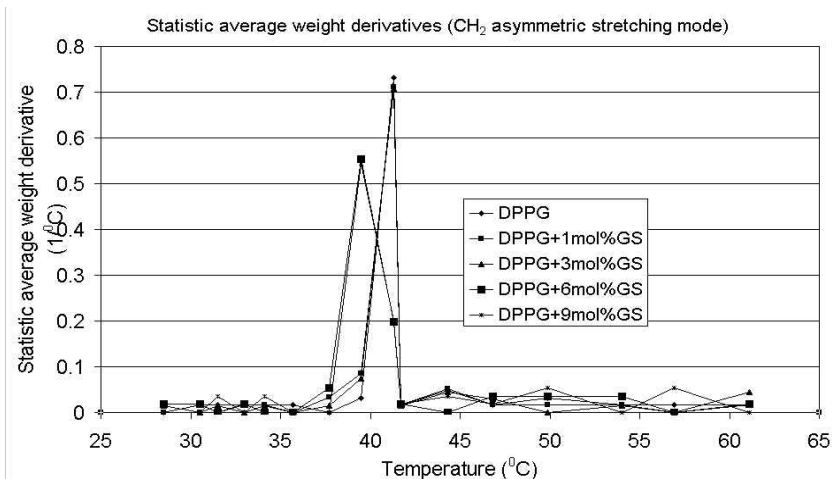


**Fig. 2.** Wavenumber derivatives for asymmetric stretching vibration of CH<sub>2</sub> group

Numerical values of the wavenumber derivatives show that the main point temperature decreases with about 2 °C for the DPPG/GS systems with high molar concentrations of peptide. The concentration role is evidenced only for the big molar ratios of GS in membrane model and only in the temperature range (39.5-41.7) °C. Our results are in agreement with those obtained in [18].

The hypothesis that GS increase permeability of the membrane by the increase of the curvature stress in the bilayers of DPPG, is also supported by the derivative values of the bandwidths expressed in the temperature range (39.5-41.7) °C, near the mean point of the thermodynamic transition of the type (1).

Using the derivatives of the ratios  $p_g$  and  $p_l$  versus temperature we calculated the number of the subsystems from the gel and from the liquid crystalline phases. The values of  $N_g$  for the studied DPPG/GS systems, computed for a system composed from one hundred subsystems, are plotted in Fig.3.

One can estimate the main point of transition (1) for pure DPPG as being at 41.5 °C. For DPPG/GS systems with molar ratios of peptide smaller than 3 mol% the main phase temperature is lowered at 41 °C and, finally DPPG/GS systems with molar ratios of peptide higher than 6 mol% pass in liquid crystalline phase at 38.8 °C.

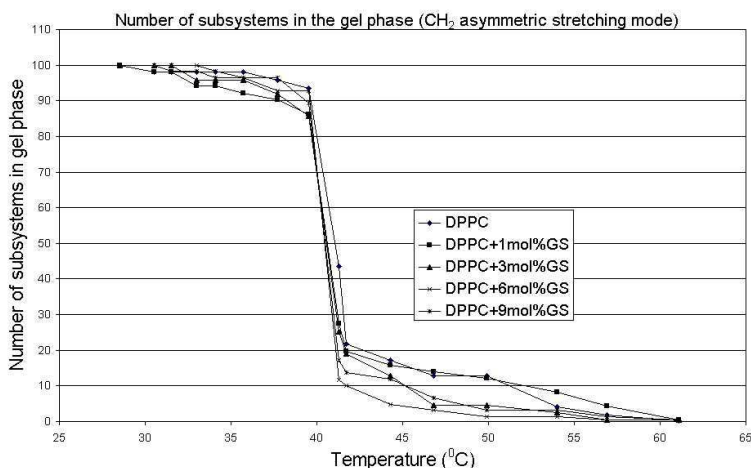


**Fig. 3.** Number of the subsystems from the gel state vs temperature for CH<sub>2</sub> asymmetric stretching mode.

## 5. Conclusions

The proposed model gives results in accordance with the previous ones and permits to obtain quantitative information about the thermodynamics of the lipid/peptide systems. The modifications in the model membrane fluidity are expressed as functions on the wavenumbers of CH<sub>2</sub> vibrations in DPPG acyl chains, directly dependent on the order degree in the local bilayer.

This study shows that the compromise between order and disorder that characterises model membranes is extremely vulnerable to the antibiotics.

## Acknowledgement

Dana Dorohoi gratefully acknowledges partial financial support of this study by Tubitak Committee of Turkey in a NATO PC-B Programme

## REFERENCES

1. M. K. Jain, Introduction to Biological Membranes, John Willey and Sons, (1988), 59.
2. D. G. Cameron, H. L. Casal, H. H. Mantch, Biophysical Journal, 38, (1982), 172.
3. J. T. Woodward and J. A. Zasadzinski Phys. Rev. E 53, (1996), 3044.
4. D. Papahadjapoulos, K. Jacobson, S. Nirand J. Isak, Biochim. Biophys. Acta, 311, (1973), 330.

5. K. Yee, C. Yee, A. Gopal, Anja von Nahmen, J. A. Zasadzinski, J. Majewski, G. S. Smith, P. B. Hobes and K. Kjaer, *J. Chem. Phys.*, 116/2, (2002), 774.
6. Derek Marsh, *Biomembranes*, in *Supramolecular Structure and Function*, (G. Pitaf and J.N.Herak, eds.), Plenum Press, New York and London, (1983), 127.
7. G. F. Gause, M. G. Brashnikova, *Nature*, 154, (1944), 704.
8. N. Izumia, T. Kato, H. Aoyaga, M. Waki, M. Kondo (Eds.), *Relationship between the primary structure and activity of Geamicidin S and Torycidines*, in *Synthetic Aspects of Biologically Active Cyclic Peptides; Gramicidin S and Thoricines*, Halsted Press, New York, (1979), 49.
9. R. M. Epand, *Biochim. Biophys. Acta*, 1376, (1998), 353.
10. K. Lohner, E. J. Prenner, *Biochim. Biophys. Acta*, 1462, (1999), 141.
11. T. Katsu, H. Kobayashi, T. Hirota, Y. Fujita, K. Sato, and U. Hagay, *Biochimica et Biophysica Acta*, 899, (1997), 57.
12. M. Jackson, H. H. Mantch, *Spectrochimica Acta Reviews*, 15, (1993), 53.
13. M. Geith, *Interactions of GS peptide with DPPC model membrane and the effect of vitamin D<sub>2</sub> steroid. A FT-IR and thermodynamic study*, PhD Thesis, METU, Ankara, Turkey, (1999).
14. E. J. Prenner, R. N. A. H. Lewis, L. H. Kodejewski, R. S. Flach, R. Mendelson, R. S. Hodges and R. N. Elhaney, *Biochim. Biophys. Acta*, 1417, (1999), 211.
15. R. N. A. H. Lewis, E. J. Prenner, L. H. Kodejewski, C. R. Flach, R. Mendelsohn, R. S. Hodges, and R. N. McElhaney, *Biochemistry*, 38, (1999), 15183.
16. E. J. Prenner, R. N. A. H. Lewis and R. N. McElhaney, *Biochimica et Biophysica Acta*, 1462, (1999), 201.
17. F. Severcan, N. Kazanci, U. Baykal, S. Suzer, *Biosc. Rep.* 15, (1995), 221.
18. F. Severcan, H. O. Durmus, F. Eker, P. I. Haris, B. G. Akinoglu, *Talanta*, 53, (2000), 205.
19. S. Tokmak, D. Dorohoi, P. I. Haris and F. Severcan, *Interactions of GS with lipid membranes*, The XIII Biofizic Congresi, 3-7 Eylul, 2001, Eskisir, Turkey, Abstract Book, p. 129.
20. F. Severcan, S. Tokmak, C. Agheorghiesei and D. Dorohoi, *An. Univ. Al.I. Cuza, Iasi, s. Chimie, T.X, nr.2*, (2002), 259.
21. T. Katsu, C. Ninomiya, M. Kuroko, H. Kobayashi, T. Hirota and Y. Fujita, *Biochimica et Biophysica Acta*, 939, (1998), 57.

## ON THE DETERMINATION OF THE CRYSTALLIZATION ENERGY IN NON-ISOTHERMAL PROCESSES BY USING EVOLUTIONARY ALGORITHMS

**IOAN ZAHARIE<sup>1</sup>, DANIELA ZAHARIE<sup>2</sup>**

<sup>1</sup> *Physics Department, University "Politehnica" Timișoara, Piața Regina Maria nr.1, 1900 Timișoara, e-mail: izaharie@etv.utt.ro*

<sup>2</sup> *Computer Science Department, West University of Timisoara, bv. V. Parvan, no. 4, 1900 Timisoara, e-mail: dzaharie@info.uvt.ro*

**ABSTRACT.** In the present paper the non-isothermal crystallization kinetics of  $\text{Fe}_{60}\text{Gd}_{10}\text{Cr}_{10}\text{B}_{20}$  amorphous alloys is investigated by differential thermal analysis (DTA). By X-ray diffraction (XRD) we established the crystalline phases which appeared in the non-isothermal crystallization process. By using an evolutionary algorithm we determined the peak temperatures for each DTA curve and we determined the values of the crystallization energy.

### Introduction

The DTA method belongs to the class of experimental methods which allow to characterize the amorphous alloys through the variation with the temperature of a physical or chemical quantity (e.g. heat capacity). The energy changed by the system with the environment during the transformation is proportional with the fraction of the alloy that crystallized. Measuring, at different heating rates, a physical quantity which is proportional to the transformed fraction of the alloy one can find the dependence on temperature and time of the transformed alloy fraction, i.e. the *transformation kinetics*. The aim of this work is to determine the crystalline phases and the crystallization energies for  $\text{Fe}_{60}\text{Gd}_{10}\text{Cr}_{10}\text{B}_{20}$  amorphous alloys. The crystalline phases are determined using XRD while the crystallization energies are computed starting from the peak temperatures. To obtain the peak temperatures, the experimental data have been fitted with a linear combination of some kernel functions [1]. The optimization problem involved in the least squares method have been solved by using an evolutionary optimization algorithm, an adaptive variant [2] of the differential evolution method [3].

### Theory

When an amorphous alloy is heated at a constant heating rate,  $\alpha$ , crystal nuclei are formed and grow until, finally, whole amorphous alloy is crystallized. The rate of change of the volume fraction of crystals,  $X$ , precipitated in the amorphous alloy, is expressed by [4]:

$$\frac{dX}{dt} = A \alpha^{-(n-1)} (1-X)^k \exp\left(-\frac{m\varepsilon}{RT}\right) \quad (1)$$

where  $A$  is a constant,  $n$ ,  $m$ ,  $k$  are numerical factors characterizing the crystallization mechanism and  $\varepsilon$  is the activation energy for crystalline phases growth. The rate of change of  $X$  reaches its maximum at a temperature  $T_i$  corresponding to the peak of the DTA curve. From the maximum condition applied in (1) it follows:

$$\frac{\alpha^n}{T_i^2} = \frac{AkR}{m\varepsilon} (1-X_0)^{k-1} \exp\left(-\frac{m\varepsilon}{RT_i}\right) \quad (2)$$

where  $X_0$  is the volume fraction of the crystal at the temperature  $T_i$ . For bulk nucleation, the exponent  $k$  is 1 thus  $(1 - X_0)^{k-1}$  is always equal to 1, while for surface nucleation  $k$  is 2/3 and the term  $(1 - X_0)^{k-1}$  can be regarded as constant when comparing with the change of the exponential term. From these remarks it results that the equation (2) can be rewritten as:

$$\ln\left(\frac{\alpha^n}{T_i^2}\right) = -\frac{m\mathcal{E}}{RT_i} + const. \quad (3)$$

If the mechanism which controls the crystallization is known, one can plot the dependence of  $\ln(\alpha^n/T_i^2)$  versus  $(-1/(RT_i))$ . The slope of the plotted line is  $m\mathcal{E}$  which divided by  $m$  produces the crystallization energy. If the mechanism is not known then we use equation (3) to study the recorded DTA curves. The obtained values of the crystallization energy will be analyzed to decide what mechanism was involved in the crystallization of the amorphous alloy. The crystallization process of an amorphous alloy is not based only on one mechanism, so we cannot associate a unique value to the activation energy [5]. The alloy crystallization involves different mechanisms, each one being dominant for a given value of the temperature. Great values of the activation energy suggest the participation of a great number of atoms to the crystallization mechanism.

### Experimental setup and data analysis

The amorphous alloy that we analyzed has been obtained by single-roller technique with a cooling rate of the order of  $10^5$  to  $10^6$ [Ks<sup>-1</sup>]. The samples have been realized of amorphous alloy diluted in aluminium oxide in such a proportion that the two crucibles have the same value of the heat capacity,  $C_p$ . The non-isothermal annealing was realized at constant annealing rates 9 K/min, 12K/min, respectively 15 K/min on a *Derivatograph C*. To identify the precipitated crystalline phases we recorded the diffractogram X on a DRON using radiation  $K\alpha$  of Mo with  $\lambda = 0.71 \text{ \AA}$ . To determine the peak temperatures, the data obtained by DTA have been processed as follows. First, the data have been preprocessed by normalization (such that the area of the region defined by the DTA curve is 1) and then by a linear transformation which brings the data points into  $[-3, 3] \times [0, 3]$ . Then the preprocessed data have been fitted with a linear combination,

$\sum_{i=1}^p h_i f_i(x)$ , of kernel functions,  $f_i$ . Due to the particularities of the experimental data we selected as kernel function the bi-Gaussian which depends on three parameters as follows:

$$f_i(x) = \exp\left[-\frac{(x - z_i)^2}{2w_{i1}^2}\right], \text{ for } x < z_i \text{ and } f_i(x) = \exp\left[-\frac{(x - z_i)^2}{2w_{i2}^2}\right], \text{ for } x \geq z_i. \text{ To find}$$

the parameters  $\{h_i, z_i, w_{i1}, w_{i2}\}_{i=1, \dots, p}$  the least squares method can be used. When the kernel functions have complicated expressions the global minimization problem arised by the least squares method become difficult, thus traditional optimization methods are no more appropriate. To solve the optimization problem we propose the use of an evolutionary method which proved to be a robust and efficient technique in global optimization over continuous domains: the differential evolution algorithms [2],[3].

### Results and discussion

Using the ASTM cards in analysing the X diffractogram (Figure 1(a)) we found the following crystalline compounds: 1-Fe<sub>3</sub>B, 2-Fe<sub>2</sub>B, 3-FeB, 4-Fe<sub>2</sub>Gd, 5-Gd<sub>2</sub>B<sub>5</sub>, 6-CrB. This result suggests the presence of 6 crystallization processes. Thus we fitted the experimental data using

the model presented in the previous section for  $p=6$ . The plots of the data, fitted curve and the kernel functions associated to peaks are presented in Figures 1(b), 1(c) and 1(d). The peak temperatures obtained by the fitting process are presented in Table 1. Starting from the peak temperatures in Table 1 and using relation (3) we found the activation energies presented in Table 2.

**Table 1**

Peak temperatures determined by fitting						
$\alpha$ [K/min]	$T_{i1}$ [K]	$T_{i2}$ [K]	$T_{i3}$ [K]	$T_{i4}$ [K]	$T_{i5}$ [K]	$T_{i6}$ [K]
9	893.913	934.530	964.404	967.370	978.061	1041.850
12	900.755	938.484	965.860	966.554	988.317	1053.270
15	908.357	949.193	973.490	975.151	1051.400	1104.100

**Table 2**

Process	The activation energy values			
	$\epsilon$ [eV] $n=1, m=1, k=2/3$	$\epsilon$ [eV] $n=2, m=1, k=1$	$\epsilon$ [eV] $n=3, m=2, k=1$	$\epsilon$ [eV] $n=4, m=3, k=1$
1	$2.31 \pm 0.24$	$4.79 \pm 0.49$	$3.63 \pm 0.37$	$3.24 \pm 0.33$
2	$2.28 \pm 0.84$	$4.73 \pm 1.67$	$3.59 \pm 1.26$	$3.21 \pm 1.12$
3	$3.68 \pm 1.86$	$7.52 \pm 3.72$	$5.68 \pm 2.80$	$5.07 \pm 2.48$
4	$3.24 \pm 2.77$	$6.64 \pm 5.54$	$5.02 \pm 4.16$	$4.48 \pm 3.69$
5	$0.34 \pm 0.25$	$0.85 \pm 0.51$	$0.68 \pm 0.38$	$0.63 \pm 0.34$
6	$0.52 \pm 0.31$	$1.22 \pm 0.62$	$0.96 \pm 0.46$	$0.88 \pm 0.41$

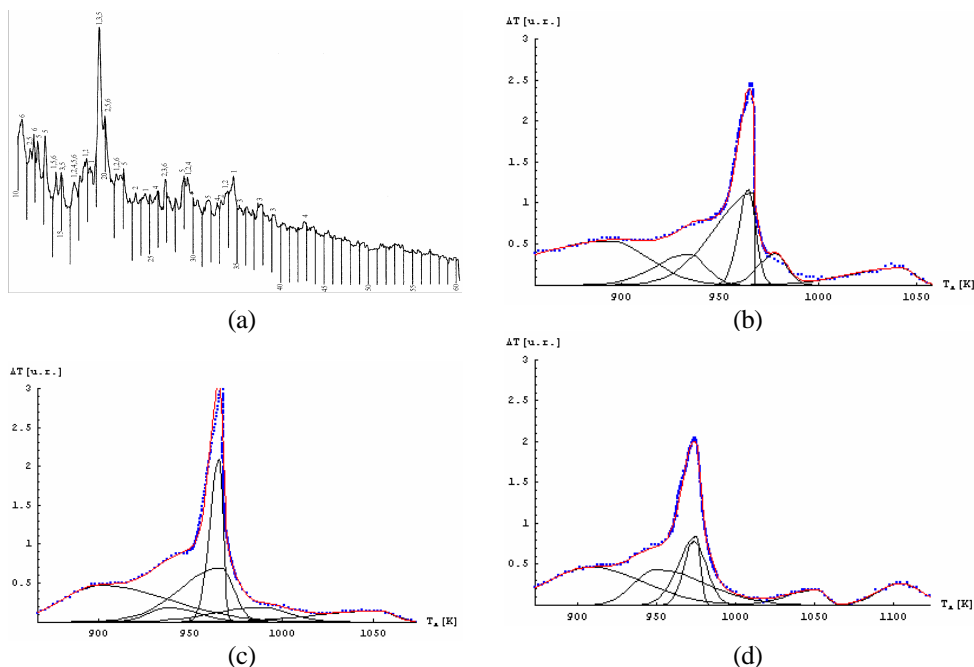


**Fig. 1.** (a) X diffractogram for the sample annealing with heating rate 9K/min; (b),(c),(d) Peaks fitting for data recorded at heating rates: 9K/min, 12K/min, 15K/min

Since the smallest values of the crystallization energy are for surface crystallization we can conclude that the alloy crystallization has been realized by surface nucleation. This can be explained by the fact that the alloy has been very well pressed when it has been introduced into crucible so it has been partitioned in very small pieces leading to an increase of its overall surface. Since the DTA treatment was not very appropriate, the registered data did not allow us to associate correct values of the energy to the crystalline phases. Further work will address the study of the applicability of the proposed data analysis method for different amorphous alloys.

**Acknowledgements.** The authors thank Dr.A.Jianu for supplying the amorphous alloys.

## REFERENCES

- [1] D i M a r c o, V. B., B o m b i G. G.; *Mathematical functions for the representation of chromatographic peaks*, Journal of Chromatography A, 931, 2001, 1-30.
- [2] Z a h a r i e, D.; *Control of Population Diversity and Adaptation in Differential Evolution Algorithms*, in R.Matousek, P.Osmera (eds.) Proc.of Mendel 2003, 2003, 41-46.
- [3] S t o r n, R., P r i c e, K.; *Differential Evolution – A Simple and Efficient Heuristic for Global Optimization over Continuous Spaces*, Technical Report TR-95-012, ICSI, 1995.
- [4] M a t u s i t a, K., S a k k a, S.; *Kinetic Study on Crystallization of Glass by Differential Thermal Analysis – Criterion on Application of Kissinger Plot*, J.of Non-Cryst. Solids, 38&39, 1980, 741-746.
- [5] K a l o s h k i n, S. D., T o m i l i n, I. A.; *The Crystallization Kinetics of Amorphous Alloys*, Termochimica Acta, 280/281, 1996, 303-317.



## PRODUCTION OF CARBON NANOTUBES BY THE CATALYSED VAPOUR PHASE PYROLYSING PROCESS

**AL. DARABONT<sup>1</sup>, K. KERTÉSZ<sup>1</sup>, C. NEAMȚU<sup>2</sup>, ZS. SÁRKÖZI<sup>1</sup>,  
L. TAPASZTÓ<sup>1</sup>, L.P. BIRÓ<sup>3</sup>, Z.E. HORVÁTH<sup>3</sup>, A.A. KOÓS<sup>3</sup>,  
Z. OSVÁTH<sup>3</sup>, Z. VÉRTESY<sup>3</sup>**

<sup>1</sup> Babeş-Bolyai University, Faculty of Physics, str. Kogălniceanu nr.1, Cluj-Napoca, 3400, Romania

<sup>2</sup> National Institute for Research and Development of Isotopic and Molecular Technologies, 71-103 Donath St., P.O. Box 700, Cluj-Napoca, 3400, Romania

<sup>3</sup> Hungarian Academy of Sciences, Research Institute for Technical Physics and Materials Science, P.O. Box 49, H-1525, Budapest, Hungary

**ABSTRACT.** This paper confirms that single-walled carbon nanotubes (SWCNTs) and multi-walled carbon nanotubes (MWCNTs), as well as bundles of well aligned MWCNT films can be obtained simultaneously by injecting a solution of ferrocene in benzene into a reaction furnace in Ar atmosphere. We have also justified that using a solution of ferrocene in thiophene, the reaction products contain Y-junction CNTs. There are data concerning the home made experimental set-up used. The reaction product was analysed on the basis of TEM, STM, FESEM and XRD studies. Besides the CNTs, the reaction product contains as byproducts Fe and Fe<sub>3</sub>C, which can be eliminated by the described purification process. Some CNTs are partially filled with Fe-catalyst.

### INTRODUCTION

Since the discovery in 1991 [1] of the carbon nanotubes (CNTs), they have been promising candidates for various applications. Thus, they are effective emitters for field emission due to the large current density at low threshold voltages [2]. The small size and high toughness make them suitable for new advanced scanning probes [3]. As CNTs are generally metallic or semiconducting, depending on the helicity and diameter [4], they can be used to construct nanoelectronic devices. In particular the Y and T shaped CNT junctions are considered likely to be the basic building units for this purpose. The CNTs are up to 100 times stronger than steel, able to withstand repeated bending, buckling and twisting, which results in building lightweight metal-matrixes [5, 6] and polymer composites [7]. They have also potential use as molecular pressure sensors [8] and chemical sensors [9].

There are many methods of producing CNTs, as electric arc discharge [10], laser evaporation [11], chemical vapour deposition (CVD) [12, 13], plasma-enhanced CVD [14] etc. Amongst the CVD methods, pyrolysis of hydrocarbons in the presence of a metal catalyst constitutes a simple and efficient process [15]. Generally, two methods are used to introduce the carbon source material into the pyrolysis furnace: either as a vapour in a gas stream (Ar) [15] or by liquid injection using an atomizer (sprayer) [16]. We used the latter method to produce CNTs at laboratory level.

### EXPERIMENTAL

The scheme of the home made experimental spray-pyrolysis set-up used for the synthesis of CNTs is represented in Fig. 1. This set-up uses the single step synthetic route, which involves the spray-pyrolysis of ferrocene-benzene or ferrocene-thiophene solutions in an

Ar atmosphere. The essential parts are: a) an 1 meter long quartz tube (the reactor) with  $\sim 20$  mm inner diameter, which supports well the  $1000^{\circ}\text{C}$  temperature, and at the same time plays the role of support for the catalyst particles resulting from the active solution and for the final product; b) a sprayer (atomizer) of the active solution, which consists of a glass nozzle (capillary) with 0.65 mm inner diameter at the end, surrounded by another glass tube with 2 mm inner diameter also at the end. The outer glass tube of the nozzle directs the carrier gas (Ar) flow around the nozzle. We consider that the surface area between the inner- and outer tube has a decisive role in the spraying process of the solution. In our case this area was  $3.14\text{ mm}^2$ .

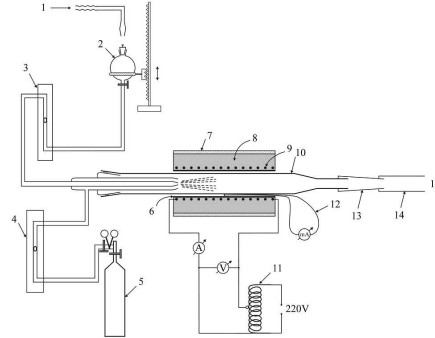


**Fig.1.** Scheme of the spray-pyrolysis set-up. 1-gas inlet; 2-container for the solution; 3-solution flow-meter; 4-gas flow-meter; 5-Ar gas cylinder; 6-alumina tube; 7-porcelaine tube; 8-thermal and electrical insulation; 9-heating element; 10-quartz tube; 11-autotransformer; 12-Pt-Pt(Rh) thermocouple; 13-teflon tube; 14-rubber tubing; 15- outlet to the air.

At the beginning of each experiment the quartz tube is flushed with Ar, to eliminate the oxygen from the reaction chamber. Then the tube is gradually preheated to temperatures between  $750$ – $975^{\circ}\text{C}$  and the Ar flow-rate is set at the desired value. The ferrocene-benzene or ferrocene-thiophene solution is introduced into the sprayer and pulverized into the reaction chamber by the Ar gas flowing around the nozzle. The flow-rate of the solutions is adjusted. The final product (the carbonaceous material deposited on the wall of the reactor chamber) is analysed by means of Transmission Electron Microscopy (TEM), Scanning Tunnelling Microscopy (STM), Field Emission Scanning Electron Microscopy (FESEM) and X Ray Diffraction (XRD).

We have performed growth experiments at different values of furnace temperature, solution concentration, and solution flow-rate. The values of the investigated parameters are resumed in Table 1. In addition, we investigated as carbon source material also thiophene (sample S14), because in the literature this material is known as promoting Y-junction growth of CNTs [17]. The parameters of this growth process were: 1 ml/min solution flow-rate, 3 g ferrocene/ 50 ml thiophene solution concentration,  $875^{\circ}\text{C}$ .

## RESULTS AND DISCUSSION

Systematic analysis of TEM images of the samples makes possible to determine the most suitable values of the investigated parameters. These are:  $875$ – $925^{\circ}\text{C}$  temperature range,  $\sim 1$  ml/min ferrocene-benzene solution flow-rate,  $\sim 3$  g ferrocene in 50 ml benzene catalyst concentration, while

**Table 1**

Investigated parameters.

sam- ple	catalyst quantity (g) in 50 ml benzene		solution flow-rate (ml/min)		temperature ( $^{\circ}\text{C}$ )	
	1 ml solution /min, $875^{\circ}\text{C}$ , 500l Ar/h	sample	3 g ferrocene /50ml benzene, $875^{\circ}\text{C}$ , 500l Ar/h	sample	1 ml solution/min, 3 g ferrocene/50ml benzene, 500l Ar/h	
S1	4.5	S6	0.5	S11	825	
S2	1.5	S7	2	S12	925	
S3	2.5	S8	1	S13	975	
S4	3.5	S9	3	S15	775	
S5	1.5	S10	0.5	S8	875	

in all experiments a constant Ar flow-rate of 500l/h was maintained. TEM and FESEM images of the most characteristic samples are given in Fig. 1–3. The TEM images also indicate that the samples, beside the CNTs, contain impurities as: Fe, Fe<sub>3</sub>C, and a small amount of amorphous carbon (as byproducts). A considerable part of byproducts may be removed by heating the samples first in dilute nitric acid for several hours, than in distilled water, finally the samples are washed with distilled water. The purification process do not affect the catalyst particles encapsulated in the CNTs (compare Fig. 1 a) with b)). Fig. 2 (FESEM image of sample S9) indicates that the sample contains large areas of aligned CNT films. The diameters of MWCNTs decrease with increasing growth temperature. It is probable, that the SWCNTs visibles in STM appears as the result of an overgrowth of fine particles and fibrous materials which appears on the top of the aligned nanotube films, and this overgrown material contains the SWCNTs [18]. Fig. 3 gives a characteristic TEM image of sample S14, obtained using thiophene as carbon source material and ferrocene as catalyst. Thus, we have obtained Y-type CNTs, which confirm that the presence of sulphur atoms promote the formation of ramified CNTs [17].

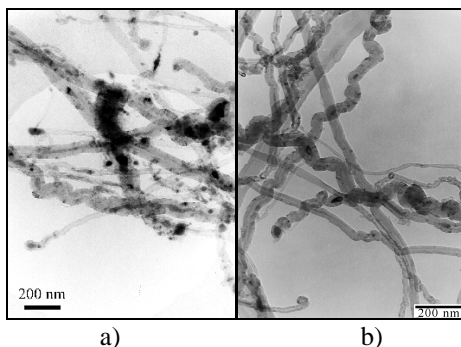


**Fig.1.** Characteristic TEM images of sample S8 a) before and b) after the purification treatment.

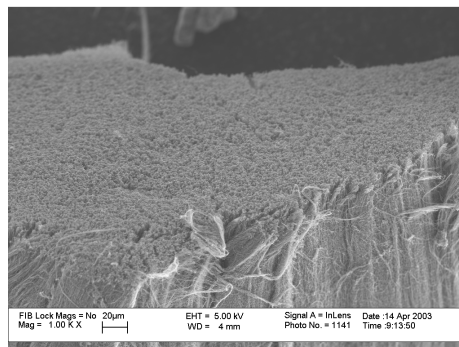


**Fig.2.** Characteristic FESEM image of S9.



**Fig. 3.** Characteristic TEM image of sample S14.

## CONCLUSIONS

The used spray-pyrolysis method yields both MWCNTs and SWCNTs. The prepared samples contain also bundles of well aligned CNTs. Probable the SWCNTs are included in the overgrown material which appears on the top of the aligned CNT films. Pyrolysis of thiophene with ferrocene yields Y-junction CNTs.

The purification of the samples in hot, dilute nitric acid and in distilled water eliminates the byproducts as Fe, Fe<sub>3</sub>C deposited between the tubes, but the impurities encapsulated in the tubes are not affected. The spray-pyrolysis method is a promising technique for production of large quantities of CNTs.

## REFERENCES

- 
1. S. Iijima, *Nature* 354 (1991) 56.
  2. Q. H. Wang, I. D. Corrigan, J. Y. Dai, R. P. H. Chang, A. R. Krauss, *Appl. Phys. Lett.* 70 (1997) 3308.
  3. H. Y. Dai, J. H. Hafner, A. G. Rienzler, D. T. Colben, R. F. Smally, *Nature* 384 (1996) 147.
  4. T. W. Ebbesen, H. J. Lezec, H. Hiuru, J. W. Bennett, H. F. Gaemi, T. Thio, *Nature* 382 (1996) 54.
  5. S. Dong, X. Zhang, *Trans. Nonferrous Metal Soc. China* 9 (1999) 457.
  6. T. Kuzumaki, K. Miyazawa, H. Ichinose, K. Ito, *J. Mater. Res.* 13 (1998) 2445.
  7. P. Calvert, *Nature* 399 (1999) 210.
  8. J. R. Wood, I. L. D. Wagner, *Appl. Phys. Lett.* 76 (2000) 2883.
  9. J. Kong, N. R. Franklin, C. W. Zhon, M. G. Chapline, S. Peng, K. Cho, H. Y. Dai, *Science* 287 (2000) 622.
  10. T. W. Ebbesen, P. M. Ajayan, *Nature* 358 (1992) 220.
  11. A. Tess, R. Lee, P. Nikolaev, H. J. Dai, P. Petit, J. Robert et al., *Science* 273 (1996) 483.
  12. M. Joseyacaman, M. Mikiyoshida, L. Rendon, J. G. Santiesteban, *Appl. Phys. Lett.* 62 (1993) 657.
  13. M. Endo, K. Takeuchi, K. Kobori, K. Takahashi, H. W. Kroto, A. Sarkar, *Carbon* 33 (1995) 873.
  14. Z. F. Ren, Z. P. Huang, J. W. Xu, J. H. Wang, P. Bush, M. P. Siegal et al., *Science* 282 (1998) 1105.
  15. C. Journet, T. Bernier, *Appl. Phys. A* 67 (1998) 1.
  16. R. Sen, A. Govindaraj, C. N. R. Rao, *Chem. Phys. Lett.* 267 (1997) 276.
  17. F. L. Deepak, A. Govindaraj, C. N. R. Rao, *Chem. Phys. Lett.* 345 (2001) 5.
  18. Ch. Singh, M. S. P. Shaffer, A. H. Windle, *Carbon* 41 (2003) 359.

## ON SURFACE MORPHOLOGY AND COMPOSITION CHANGES OF URANIUM SAMPLES AFTER HYDROGEN ABSORPTION

**DAN CHICEA, JOHN DASH<sup>1</sup>**

*University Lucian Blaga of Sibiu, Str. Dr. Ion Ratiu nr. 7-9, Sibiu,  
dan.chicea@ulbsibiu.ro.*

*1-Physics Department, Portland State University, Portland,  
Oregon 97207, U.S.A., dashj@pdx.edu*

**ABSTRACT.** Natural uranium foils were loaded with hydrogen by aqueous electrolysis. The topography and composition of the surfaces of the samples were determined. Results reveal that surface patterns changed from granules on the surface having a typical size of 2 - 4 microns to surface pits having a typical size less than one micron. The surface composition changed as a result of the hydrogen loading process. The results show that the thorium and protactinium concentration increased slightly in the natural uranium samples due to hydrogen loading.

### 1. Introduction

The purpose of this work was to determine the surface morphology and possible changes in composition resulting from hydrogen loading. Experiments were designed and performed to load hydrogen into metallic, natural uranium foils. Thorium and protactinium concentrations were measured before and after hydrogen loading. The Th/U ratio in a sample can be used to determine the age of the sample, as in [1]. The electrolysis parameters are presented in the next section. Other sections present the surface morphology changes that resulted from electrolytic loading of hydrogen. absorption. Then thorium and protactinium concentration changes, as determined with an energy dispersive spectrometer (EDS) attached to a scanning electron microscope (SEM), are presented.

### 2. Hydrogen loading parameters

Details about the electrolysis cell and parameters are presented in [2].

**Table 1.**

**Electrolysis parameters of the five experiments that were performed.  
All of the samples were from the same batch of natural uranium foil.**

Sample	Current(A)	Voltage (V)	Current density (mA/cm <sup>2</sup> )	Electrolysis Time (h)	Total electric charge (C)
S2	1.50	4.00	1790	5	27000
DC1	0.075	2.95	50	72	19440
DC2	0.400	2.87	370	206	296640
DC3	0.035	2.39	26	65	8159
DC4	0.150	2.53	54	66	35640

Electrolysis was chosen as H loading method because it is very effective and has a low cost. Table 1 presents the electrolysis conditions and parameters for the five experiments that were performed.

### 3. Surface morphology changes as a result of hydrogen loading

A typical image of the natural uranium surface before electrolysis is presented in Fig. 1. The surface is nonuniformly fissured and granulated, with granule sizes up to 3-4  $\mu\text{m}$ .

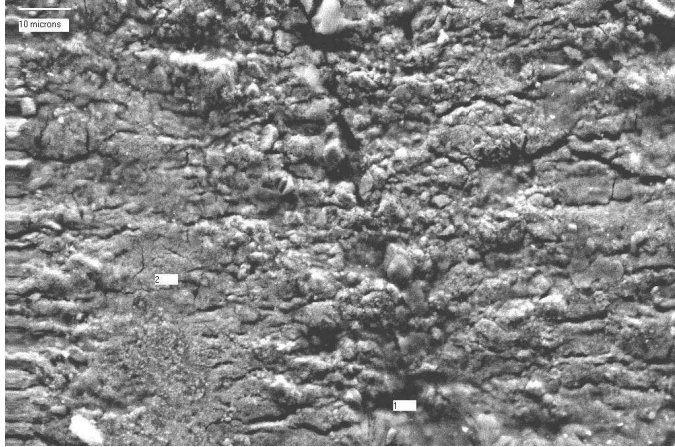


**Fig. 1.** A magnified image of the unelectrolyzed natural uranium surface.

A magnified image of the surface of sample DC1, after absorbing hydrogen, is presented in Fig. 2. Sample DC1 presents evidence of pitting, which may be caused by the formation of uranium hydride and erosion. The surface is covered with pits having a typical size of about 1  $\mu\text{m}$ . The main difference in the topography of the surface is that the granules protrude above the surface while on the electrolysed sample the surface is pitted.

### 4. Thorium and protactinium concentration changes

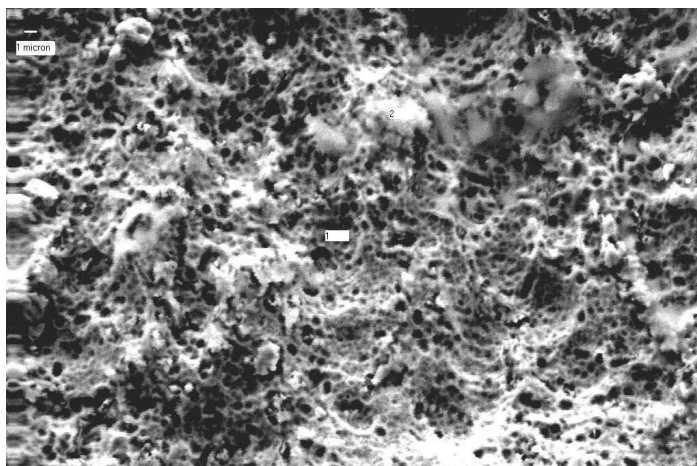
The concentration of several elements was measured on an as-received natural uranium sample (the control) and on each sample after loading it with hydrogen using electrolysis. The concentration of thorium and protactinium was assessed using the OXFORD EDS spectrometer, attached to an ISI Model SS40 SEM. The concentrations presented in the tables and the standard deviations, hereafter sigma, are atomic concentrations. First only thorium and uranium were selected on the list for the quantitative analysis.

Table 2 presents the average values of thorium concentrations and the average standard deviations ( $\sigma$ ).

**Table 2.**

**Average thorium concentration and standard deviation for the control natural uranium sample (S1) and for the samples that were loaded with hydrogen.**

Sample	Th (%)	$\sigma$ Th (%)	Number of spectra	Average counts
S1( control)	0.96	0.43	14	480321
DC1	1.05	0.37	13	537439
DC2	1.24	0.43	13	522777
DC3	1.95	0.68	10	180598
DC4	1.56	0.63	23	583748



**Fig. 2.** A magnified image of the DC1 uranium surface after hydrogen loading by electrolysis.

The averages are calculated for each sample separately. Table 2 shows that there is an increase of the thorium concentration for the hydrogen-loaded uranium samples compared with the control.

Analyses for protactinium are given in Table 3. The protactinium concentrations are all smaller than two standard deviations. Therefore, there is no significant amount of protactinium in any of the samples, within the sensitivity of the EDS method.

The concentrations that are written on the SEM analysis sheet are not the absolute concentrations. For example, 1% Th means that the ratio Th/U is 1/99, 0.5% Pa means that the ratio Pa/U is 0.5/99.5.

**Table 3.**  
**Protactinium average concentrations and standard deviations for the control natural uranium sample (S1) and for the samples that were loaded with hydrogen.**

Sample	Pa ( % )	$\sigma$ Pa ( % )	Number of spectra	Counts
S1 (control)	0.53	0.41	6	736849
DC1	0.5	0.83	16	490949
DC2	0.78	0.63	16	500043
DC3	0.08	0.9	10	180598
DC4	0.81	0.63	22	607998

## 5. Discussion

The experiments performed so far show that the thorium content increased for all of the hydrogen-loaded uranium samples compared with the as-received control. These results are consistent with gamma ray spectroscopy results on the same samples, which show, for four of five hydrogen-loaded samples, that the 92.4 keV  $^{234}\text{Th}$  peak contains significantly more counts per gram-hour than the as-received control [2].

Thorium concentration in different samples and in uranium was measured using several methods. In [3] alpha – beta coincidence was used to determine the Th and U. X-ray photoelectron detection was used in [4], a spectrophotometric method was used in [5] and [6]. In spite of our efforts to find references on thorium concentration changes as a result of hydrogen absorption, no paper was found on the subject. No work reporting on SEM and EDS analysis of metallic uranium samples was found either, therefore we can not compare our results with similar work.

## REFERENCES

1. R. Toenjes, H. Schatz, K. L. Kratz, B. Pfeiffer, T. C. Beers, J. Cowan, V. Hill, *Tuning The Clock, Uranium And Thorium Chronometers Applied To Cs 31082-001*, Astrophysical Ages And Time Scales, ASP Conference Series, Vol. TBD, 2001.
2. J. Dash, D. Chicea, *Changes In The Radioactivity Of Natural Uranium Samples After Hydrogen Loading*, 5-th General Conference of the Balkan Physical Union, Section 1, Nuclear Physics and Nuclear Energy.
3. R B Galloway, *Uranium and thorium series determination in natural samples by a beta-alpha coincidence technique*, Measurement Science and Technology, Volume: 1, 1990, pp. 725.
4. J. C. Fuggle, A. F. Burr, L. M. Watson, D. J. Fabian and W. Lang, *X-ray photoelectron studies of thorium and uranium*, Journal of Physics F: Metal Physics, Volume: 4, 1974, PP. 335.
5. R. D. Gardner, A. W. Mosen, H. Hurd, *The Determination of small amounts of thorium in the presence of uranium, titanium, and tungsten*, Los Alamos Scientific Laboratory internal report, LA-1948, June 1955.
6. *The spectrophotometric determination of thorium in uranium*, Los Alamos Scientific Laboratory, internal report, LA-1897, 1955.



## **GAS PERMEATION THROUGH POLYAMIDES AND POLYIMIDES POLYMERS MEMBRANES**

**T.D. SILIPAS<sup>1</sup>, V. TOSA<sup>1</sup>, DANA GARGANCIUC<sup>2</sup>, GH. BATRINESCU<sup>2</sup>,  
GABRIELA ROMAN<sup>2</sup>, B. ALBU<sup>2</sup>**

<sup>1</sup>*National Institute for R&D of Isotopic and Molecular Technologies,  
P.O. Box 700, Cluj-Napoca, Romania*

<sup>2</sup>*CCMMM, CP 15-43, 206 Splaiul Independentei, Bucarest, Romania*

**ABSTRACT.** We measured the permeation rate and the separation factor for different gases. After finding the permeation rates, a correlation between the obtained data and the type of polymer and method used for membrane preparation, has been performed. The results have been compared to an asymmetric ACA membrane produced by SEPAREX.

Membrane based gas separation processes [1], over the last three decades, have proved their potential as better alternatives to traditional separation processes. The conventional processes, for example absorption, cryogenic distillation, and pressure swing adsorption (PSA) are energy intensive, as well as responsible for some environmental pollution. An illustrative cost comparison of an ethyl cellulose membrane system with a standard PSA approach for 35% oxygen enrichment of air shows a reduction of 47% in capital costs, and 38% in operating costs for the membrane based process. The membrane based separation processes are not only cost effective and environmentally friendly, but also, with many novel polymeric materials available, offer much more versatility and simplicity in customized system designs.

Gas transport properties of polymer membranes [2] are not only important to industrial production of high purity gases, but also plays a role in the application of membranes as barrier materials for food packaging and beverage industry. It is therefore important to know the permeation rates of atmospheric gases through these membranes.

The polyamides and polyimides membranes were prepared at CCMMM Bucharest by using various conditions, e.g. with or without support, having a symmetric or asymmetric structure. The aim was to explore and find the best conditions for the gas separation process. To characterize the polymer membranes to permeation we used the manometric method as specified in ASTM D-1434/82. We used an experimental set-up designed and built [3] in the NIRDIMT Cluj. In principle we measured the increase of pressure in a given volume, as a result of gas permeation through the membrane.

In order to have an efficient separation process, when compared to other separation methods, the membrane must fulfill simultaneously the two performance criteria, namely high flux and high selectivity for the gas in question. Once these criteria are fulfilled the membrane must have good chemical stability with respect to the gases involved and good mechanical properties in order to be proof against as high as possible pressure gradients between the two sides of the membrane. The requirement to have the above conditions fulfilled simultaneously restrict in a considerable manner the area of the available methods to prepare the membrane.

The measurement of the membrane permeability for various pure gases means a characterization of its performance in terms of flux and selectivity. This measurement is in fact a quality test, which is done immediately after membrane preparation. That is why it is recommended to test the membrane for at least one "fast" gas, such as H<sub>2</sub> or He, and a "slow" gas, N<sub>2</sub> usually. If

the permeation is big for He or H<sub>2</sub>, typical values being in the range  $5 \cdot 10^{-5}$  cm<sup>3</sup>/cm<sup>2</sup>.sec.cmHg, and the selectivity for H<sub>2</sub>-N<sub>2</sub> is also big, say above 25, then the membrane can be accepted as good, and can be considered as a starting point for the scaling-up in a separation module.

The membrane we prepared are in the class of heterocyclic polymers, the choice of this class confers solubility in organic solvent, that is, a higher and easier processing. We used two different kinds of thermostable heterocyclic polymers: fluorinated polyamides and polyimides. We obtained membranes with a good mechanical resistance, uniform in appearance. We could divide the prepared membranes in 6 categories: asymmetric membranes with and without support, with adjuvant, obtained by reticulation, composites and obtained using controlled evaporation (symmetric membranes).

**Table 1.**  
**Permeation flux Q at 50°C through The SEPAREX asymmetric membrane (ACA)**

	GAS			Q
	At. mass (uam)	Boiling temp. (K)	Mol. diameter (Å)	(cm <sup>3</sup> /cm <sup>2</sup> *sec.cmHg) 10 <sup>-5</sup>
He	4.06	4.25	2.58	19.2
CO <sub>2</sub>	44.0	194.6	3.99	6.9
O <sub>2</sub>	32.0	90.2	3.43	1.4
N <sub>2</sub>	28.0	77.0	3.68	0.29

To measure the flux of gas through the membrane we used the manometric method, as described in ASTM D-1434/82, under the regime of stationary permeation, operating on a home made experimental set-up. We used four gases He, N<sub>2</sub>, O<sub>2</sub> of purity 99,5 %, and CO<sub>2</sub> of purity better than 99%. The area of the membrane varied between 2.02 and 2.8 cm<sup>2</sup>, and the working pressure on one side of the membrane was, depending on the type of membrane, in the range from 120 Torr to atmospheric pressure.

We considered useful to compare our membrane to a commercial one, already used for gas separations. In this sense we also measured an asymmetric membrane prepared from cellulose acetate, produced by SEPAREX (Table 1).

We analyzed and measured a number of over 20 membranes, the results being synthesized as follows:

For polyamides membranes, depending on membrane type, the permeation flux is two orders of magnitude higher for asymmetric membranes than for the symmetric ones. Even for the asymmetric membranes the separation factor is slightly diminished, these are superior to symmetric membranes (see Fig. 1)

The presence of adjuvants in the membrane structure is beneficial for the polyamide membrane, the values for the permeation flux and separation factor are enhanced (see Fig. 2).

For polyimide membrane the values for the permeation flux are in the range from 4,56 to 7,23 \*10<sup>-6</sup> cm<sup>3</sup>/cm<sup>2</sup>.s.cmHg, and the selectivities in the range from 54,33 to 73,55. These values indicate that the permeation is the result of a solving-diffusion process, not a transport process through a porous membrane. This is a first positive result and it demonstrates that the preparation procedure was correct. The differences between the above values could be attributed to different preparation process. The influence in the case of using a support is not significant, the values obtained for the flux and separation factor being in the range of experimental errors.

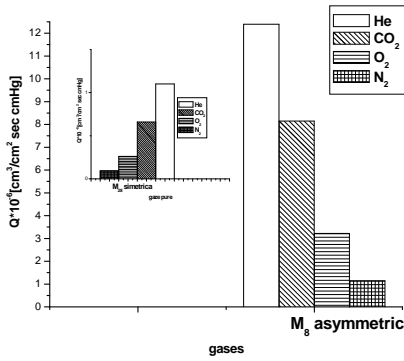


Fig. 1. Permeation flux Q for a symmetric and an asymmetric membrane

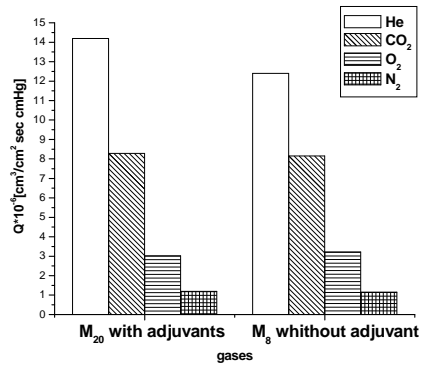


Fig. 2. Permeation flux Q for a membrane with and without adjuvants

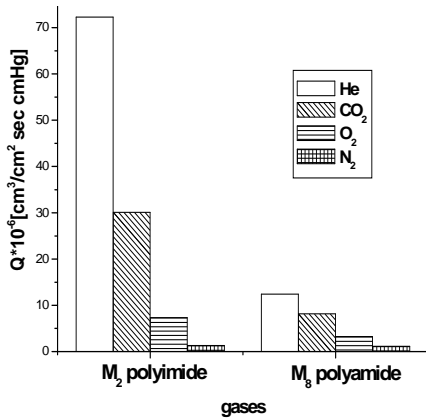


Fig. 3. Permeation flux Q through polyamide and polyimide membranes

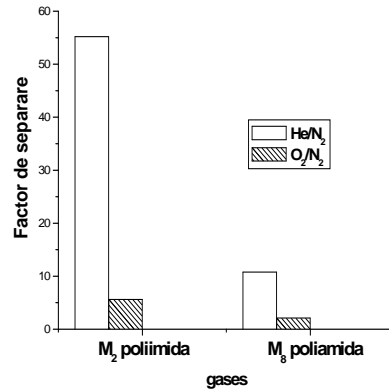


Fig. 4. Separation factors through polyamide and polyimide membranes

We illustrate in Fig. 3 and Fig. 4 a comparison between the polyamide and polyimide membranes in terms of flux and separation factor respectively. The polyimide membranes, as compared to the polyamide membranes have permeation flux 5 times higher and a separation factor almost 7 times higher (see membrane 4, for example), for a mixture He-H<sub>2</sub>, which indicate clearly their superiority.

## REFERENCES

- [1] S. Alexander Stern, *Journal of Membrane Science*, 94 (1994),1-65.
- [2] E. Sada, H. Kumazawa, P. Xu, S. T. Wang, *J. Polymer Sciences:part B: Polymers Physics*, 28, (1990), 113-125
- [3] A. Barbu, T. D. Silipas, I. Bratu, *Journal of Molecular Structure*, 410-411, (1997), 233-236.

## SYNTHESIS OF METALLIC AND SEMICONDUCTING NANOSTRUCTURES

**STELA PRUNEANU, LILIANA OLENIC, G. MIHAILESCU, D. LUPU,  
A. R. BIRIS, L. RADU-TUDORAN<sup>1</sup>**

*National Institute of R&D for Isotopic and Molecular Technologies,  
O.P.5, P.O. BOX 700, 3400 Cluj-Napoca, Romania*

*<sup>1</sup>Babes-Bolyai University, Faculty of Biology and Geology, Clinicilor  
Street, No. 5-7, 3400 Cluj-Napoca, Romania*

**ABSTRACT.** Metallic and semiconducting nanostructures were obtained by template synthesis, using nanoporous alumina membranes as matrix.

We have combined two deposition methods (chemical and electrochemical) in order to obtain gold nanostructures within the pores of membranes. On the other hand alumina membranes filled by cobalt particles were used as template for nanocarbon production by CVD method. The nanocomposites were characterized by SEM and TEM methods.

### INTRODUCTION

Template synthesis method has been playing an important role in fabrication of many kinds of nanowires and nanotubes. Alumina membranes prepared by electrochemical oxidation of aluminium, represents the appropriate material for synthesizing the desired nanostructures. By using alumina membranes for template synthesis, nano-fibrils, nano-wires or nano-tubules of metals [1,2], semiconductors [3,4] and carbon [5] have been prepared.

Gold and other metals have been deposited into porous alumina membranes by chemical or electrochemical reduction of the appropriate salt solution. We have combined the two methods, in order to obtain gold nano-wires of about 100 nm diameter and of 3  $\mu\text{m}$  length.

We have used further the alumina membrane filled by cobalt for obtaining carbon nanostructures by CVD (chemical vapor deposition) method.

### EXPERIMENTAL

High purity aluminium foil was vertically mounted between the two parts of an electrochemical cell. One compartment was filled with acidic solution (0.3M oxalic acid) and the other with distilled water. The oxidation was performed at constant voltage (70V) and low temperature (4...6<sup>0</sup> C) for about 3 hours. The membrane was then filled by gold, as following described.

#### *a) Chemical deposition of gold*

After preparation, the membrane was thoroughly washed with water and then immersed for 2 minutes in a mixture of  $\text{SnCl}_2$  and HCl. After that, the membrane was activated by treatment with a solution of  $\text{PdCl}_2$  in HCl (2 minutes) followed by the treatment with an ammoniacal solution of  $\text{AgNO}_3$  (2 minutes).

The Ag coated membrane was then immersed in the gold deposition bath, that contains formaldehyde as reducing agent. Au displaced the Ag particles, since gold is a more noble metal. The Au particles were catalytic sites for the oxidation of formaldehyde and the concurrent reduction of Au (I) to Au (0). The gold deposition process lasted for about 5 hours.

*b) Electrochemical deposition of gold*

The next step was the electrochemical deposition of gold. This was performed in a three-electrode cell, by cyclic voltammetry. The potential was varied between 0...1.5V/SCE at a scan rate of 100 mVsec<sup>-1</sup>, for about 5 hours.

At the end of these processes, the pores of alumina membrane were filled with gold nanowires. In order to evidence these nanowires, alumina template was removed by etching in a solution of 2M NaOH.

*c) Electrochemical deposition* was used for filling the alumina membrane *by cobalt* particles. Further the alumina membrane with reduced catalyst was used in CVD experiments according to the reference material (6). The catalyst was heated from room temperature to 550 °C under pure nitrogen flow (94 ml/min).

The cobalt oxide was reduced in additional hydrogen flow (6 ml/min) for two hours after which the hydrogen stream was stopped and the temperature raised to 650<sup>0</sup> C in nitrogen flow. At this temperature, acetylene was admitted in the mixture stream at 6 ml/min for one hour and the sample was cooled under a nitrogen stream.

## RESULTS AND DISCUSSIONS

Typical TEM pictures of alumina template, prepared in oxalic acid as described above, are presented in fig.1a. The picture evidences the porous morphology of the membrane, having the pore diameter of around 100 nm. The diameter is larger than one expects and this is due to the pore wall dissolution that take place during barrier layer removal. The TEM picture evidences the morphology of the membrane fracture, showing the channels.

The gold fibers prepared by template synthesis can be seen in the SEM image from figure 1b. The diameter of electroplated gold nanoparticles is equivalent to the pore diameter of alumina template membrane. The amount of gold deposited into the pores depends on the different pore diameters and time of electrolysis. The lengths and the aspect ratios of the gold fibers are analyzed by SEM. Gold nano-wires of about 100 nm diameter and 3 µm length have been produced.

Figure 2a presents the SEM image of the carbon deposit obtained by CVD method after dissolution of the template membrane.

The SEM analysis points out a high quantity of carbonic product (1) on the porous oxide (2).

The characteristics of the carbonic product have to be analyzed by TEM method.

The sample was purified by dissolving the aluminium oxide in NaOH 10% for 20 hours followed by washing and dissolution of catalyst (Co) in HCl 37% (boiling for 2 hours). Figure 2b show the TEM image of nanocarbon structures. The presence of bundles of aligned straight carbon nanotubes with uniform thickness having approximately 17 nm outer diameter and approximately 8 nm inner diameter. This fact reveals that the nanostructures are multi wall nanotubes.

Our results are similar to those obtained in reference material (6). Nanofibers of about 25 nm diameters are also present in the carbon deposit, grown probably on the initial deposit of aligned nanotubes.

## CONCLUSIONS

By combining a chemical and an electrochemical method we have prepared gold nanostructures, using alumina membrane as template. Aligned multi-wall carbon nanotubes of rather high aspect ratio were obtained on nanoporous alumina membranes filled by cobalt. Metallic and semiconducting nanostructures obtained by us are similar with those obtained in reference material.

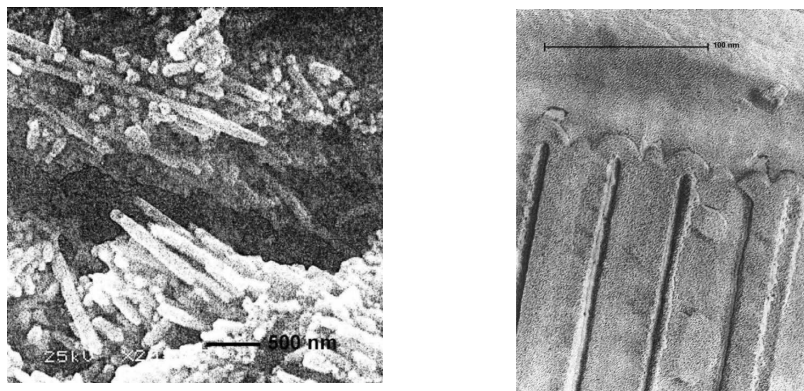


**Fig. 1. a)** TEM picture of alumina membrane showing the pores morphology; **b)** SEM picture of gold nanostructures, after dissolution of alumina template

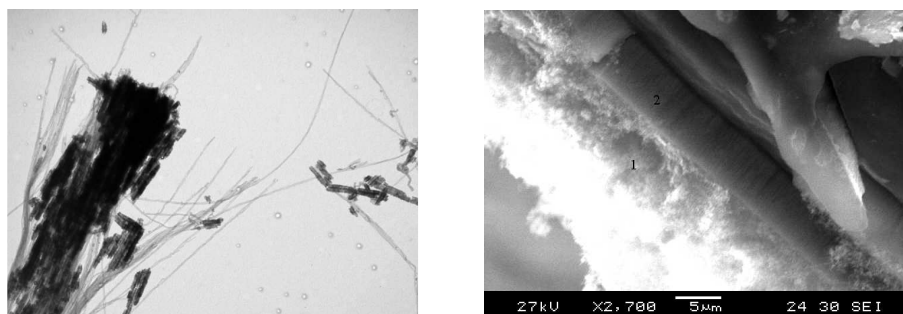


**Fig. 2.a)** SEM picture of carbonic product obtained on the surface of alumina membranes, filled by cobalt: (1) carbonic product (2) alumina membrane; **b)** TEM pictures of carbonic product obtained on the surface of alumina membrane, filled by cobalt

## REFERENCES

1. M. Wirtz, S. Yu, C. R. Martin, *Analyst*, 2002, vol. 127, 871-879.
2. J. C. Hulteen, V. P. Menon and C. R. Martin, *J. Chem. Soc., Faraday Trans.*, 1996, 92, 4029.
3. B. B. Lakshmi, P. K. Dorhout and C. R. Martin, *Chem. Mater.*, 1997, 9, 857.
4. J. D. Klein, R. D. I. Herrick, D. Palmer, M. J. Sailor, C. J. Brunlik and C. R. Martin, *Chem. Mater.* 1993, 5, 902.
5. R. V. Parthasarathy, K. L. N. Phani, C. R. Martin, *Adv. Mater.* 1995, vol. 7, 896-897.
6. Y. C. Sui, J. A. Gonzales-Leon, A. Bermudes, I. M. Saniger, *Carbon*, 2001, 39, 1709

## STUDY OF INTERNAL HEAT TRANSFER IN STAINLESS STEEL-WATER TWO-PHASE THERMOSYPHONS

D. RISTOIU, C. COSMA, T. RISTOIU<sup>1</sup>, D. CENAN<sup>1</sup>

*University Babes-Bolyai, Faculty of Physics, 1 M. Kogalniceanu, RO  
3400 Cluj-Napoca, Romania, dristoiu@phys.ubbcluj.ro  
<sup>1</sup>Technical University Cluj-Napoca, RO 3400 Cluj-Napoca, Romania.*

**ABSTRACT.** A two-phase closed thermosyphon is a typical wickless gravity assisted heat pipe. Thermosyphonic heat exchanger has been widely used in the field of heat recovery, air conditioning, solar energy, aerospace and nuclear reactor. There are many parameters which can be optimum in finned heat pipe heat exchanger, such as working fluid; filling ratios; tilt angles; wind velocity at both sides of heating section and cooling section; space length between two fins; fin height; length ratio of heating section to cooling section etc.. The paper describes the effect of the fluid property on the heat transfer characteristics of the thermosyphon by taking in account the filling ratio. The experimental stainless steel-water heat pipe is 2 m in length and 35 mm in diameter. The electrical power to heat evaporator is adjustable. The chosen filling ratios are 30%, 20%, 15% and 10%. The critical heat transfer rate and the thermal resistance are determinate in the range of the isothermal operation.

### INTRODUCTION

A heat pipe and a two-phase thermosyphon are passive two-phase heat transfer devices that have large quantities of heat transfer with a minimal temperature difference. The most important advantages of heat pipes and two-phase closed thermosyphons are that they can operate by capillary force in a wicking structure and a gravity force etc. without an external power.

The analysis of heat pipe operation rapidly becomes much more complicated if one considers the retarding force of viscosity in both the liquid and vapor, or such phenomena as supersonic shock waves or boiling, both of which can limit the performance at high power. A great deal of research has been focused on this behavior [1-3], and a thorough understanding of these effects is necessary when *designing* a heat pipe.

For the present article, however, we take the point of view of the potential user for whom the heat pipe is a sealed tube with rather unusual thermal properties, even though it appears from the outside to be a simple metallic rod. The basic difference is that a solid rod of copper, for example, conducts heat by diffusion, and a constant, geometry-independent thermal conductivity can be defined for the material. A heat pipe, however, conducts heat by transport of the vapor and therefore is more properly thought of as a heat *current* device rather than a simple thermal resistor.

The remarkably low thermal resistance of heat pipes means that careful attention must be paid to minimizing the thermal resistance associated with the interface between the heat pipe and either the heat source or heat sink. This problem is addressed elsewhere [2-3].

### Experimental apparatus and procedure

Figure 1 show the schematic illustration of the experimental setup. The thermosyphon used in the experiment was made of a stainless steel tube of 32 mm i.d. The working length of the thermosyphon was 2000 mm and consists of 2 parts; a lower part compose from of 700 mm

plus 200 mm used as the evaporator and respectively as the adiabatic section and a upper part of 1100 mm as the condenser section. The ratio of the evaporator section length to the diameter ( $L_e/d$ ) is set to be 22.

The goal of the measurements was to establish steady state heat flow at various power levels, average temperatures, and filling ratio, in an effort to map out the thermal characteristics of the heat pipe. A number of precautions were taken to measure these parameters accurately and to prevent loss of heat from the system. The working fluid is distilled water and the chosen filling ratio are 30%, 20%, 15% and 10%.

In order to measure the temperature profile along the heat pipe, seven thermocouples (0.25 mm dia., Type E) were attached with epoxy at equally spaced intervals (Figure 1). Heater wire (0.125 mm dia. Manganin,  $42\Omega$ ) was wound directly on a 700 mm section at one end of the heat pipe, defining it as the evaporator section. A condensing portion was formed at the other end by a water jacket.

The water supplied to the inlet was precooled or preheated, as required, and the flow rate was measured carefully ( $\pm 5\%$ ). The amount of heat removed by the water was then calculated by

$$Q_{out} = V C(T_{avg}^{water}) \Delta T^{water} \tag{1}$$

where  $V$  is the volume flow rate,  $C(T_{avg}^{water})$  is the heat capacity per unit volume at the average temperature

$$T_{avg}^{water} = (T_{in} + T_{out})/2 \tag{2}$$

and the temperature difference is defined as

$$\Delta T^{water} = T_{out} - T_{in} \tag{3}$$

The heater was driven with a variable transformer and the electrical heat input was calculated as

$$P_e = E^2/R \tag{4}$$

where  $E$  is the root-mean-square voltage measured at the heater windings and  $R$  is the electrical resistance. With the above precautions with respect to insulation, less than  $\sim 10\%$  of the input heat was lost from the system, i.e.,  $Q_{out} \approx 0.9 P_e$ . As the exact location of the heat leak is not known, the power  $P$  conducted by the heat pipe is taken to be the average of  $Q_{out}$  and  $P_e$ .

**Experimental results and discussion**

From the temperature distributions and heat transfer rates, the thermal resistance of the thermosyphon  $T_R$  defined by

$$T_R = \Delta T/Q \tag{5}$$

is obtained.  $\Delta T$  is the temperature difference between the evaporator and the condenser section. The typical result is shown in Fig.2, where  $T_R$  is plotted against  $Q$ . The thermal resistance decreases with the increase of  $Q$  and then reaches a constant value, which will be denoted as the nominal thermal resistance  $T_{Ro}$ . As  $Q$  increases further,  $T_R$  increases discontinuously. This state

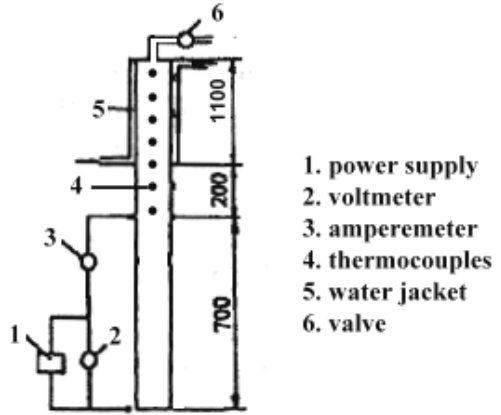


Fig.1 Experimental apparatus



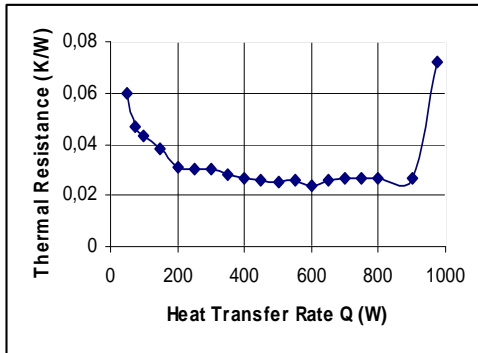


Fig. 2. Relation between the heat transfer rate and the thermal resistance

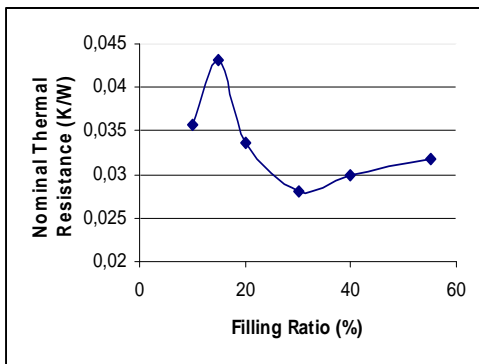


Fig. 3. Relation between the filling ratio and the nominal thermal resistance

gives the operating limit, and heat transfer rate at this limit is defined as critical heat transfer rate  $Q_C$ . In the case of small  $Q$ , i.e. less than 100 W, the thermal resistance is larger than  $T_{Ro}$  resulted from the high thermal resistance of natural convection which is the dominant heat transfer mechanism in the evaporator for small heat fluxes. With the increase of  $Q$  over those values, the thermal resistance is almost constant at  $T_{Ro}$ . This is because vigorous boiling occurs in the evaporator in this situation.

The dependence of the nominal thermal resistance on the filling ratio is shown in Fig. 3. The nominal thermal resistance is dependent on the filling ratio with a maximum at the 15% filling ratio and a minimum at the 30%. Average values of nominal thermal resistances are obtained to be 0.033 K/W.

### Conclusion

The measurements reported here illustrate a number of points regarding heat pipes. For power levels below a certain maximum power, the plot of temperature drop  $\Delta T$  vs. heat transport  $Q$  is linear, allowing one to define a thermal resistance  $T_R$ . The value of  $T_R$  is typically 60 times lower than for a simple tube of copper of the same dimensions. As discussed in a number of references [2-3], the value of  $T_R$  for the heat pipe is determined by details of the working fluid, wick construction,

filling ratio, etc., but it is fairly independent of the length of the heat pipe.

There exists the range of the filling ratio at which the thermosyphon shows the better performance, i.e. the critical heat transfer rate is higher and the thermal resistance is lower. The temperatures of all parts of the thermosyphon section were, in the condition of isothermal state.

### REFERENCES

1. P. D. Dunn, and D. A. Reay, Heat Pipes, 3rd Edition, Pergamon Press, 1982.
2. G. P. Peterson, An Introduction to Heat Pipes: Modeling, Testing, and Applications, John Wiley and Sons, Inc., 1994.
3. S. D. Garner, Heat Pipes for Electronics Cooling Applications, Electronics Cooling, Vol. 2, No. 3, September 1996, pp 18-23.
4. Dussinger, Pete, Development of Residential Gas-Fired Furnaces using Heat Pipe Heat Exchangers, Final Report, Gas Research Institute, July 1992.
5. R. T. Dobson, Thermal characterization of a two-phase closed thermosyphon, Refrigeration and Air Conditioning, January 2000, pp.55-59.

## **MODULAR - MICROWAVE POWER SYSTEM, BASED ON MICROCONTROLLER UNIT**

**V. SURDUCAN, E. SURDUCAN, C. NEAMTU**

*National Institute of Research and Development for Isotopic and Molecular Technology, Donath 75-103, Cluj-Napoca, Romania*

The “Modular-microwave power system” was designed for fine adjustment and control of any microwave power generator, based on continuous wave magnetron, with output power of max. 1000W. The destination for such power generators covers many scientific or industrial applications, from drying, microwave assisted digestion, polymerization, sample extractions etc. For scientific and other sensitive applications, it's imperative to control precisely both the output power and the energy of the microwave generator. The scientific key for this complex power and energy adjustment is the use of a smart device, like a personal computer, or a standalone microcontroller unit, to control the microwave generator's power supply. An user-friendly interface, having only four functional buttons and a large LCD display with 2 rows and 16 characters/row, assures the input parameters for the time pulse (energy) and power. A real time clock measuring the programming time and generates the markers for energy adjustment. Two different programming modes are implemented: a local mode and a programmed mode via an optoisolated RS232/485 interface, using an external personal computer unit. Various resolutions for the microwave output power may be achieved, with a simple and stalwart procedure by switching the power supply coils of the high voltage transformer. Sample's temperature can be logged and collected on the PC using some smart temperature sensors connected to one measurement bus.

### **Design consideration**

Our goal was to design and manufacture an universal microwave power system, being able to generate inside the microwave coaxial chamber, a range between low microwave power (beyond 50W for small sample volumes) to high microwave power (900W for large sample volumes), in different effective power steps using the same magnetron (900W/2.45GHz) and the same microwave circuit, because the microwave sample preparation for small (less than 6ml) and very small sample volumes are requiring an expensive and specialized microwave digestors. This has the effect of decreasing the system cost and increase of versatility. It was necessary to modulate the output energy in a precisely time quantum, because 50W of absorbed microwave power radiation is still too much for small sample volumes. Thus, the probe may be irradiated with any possible energy, by using a Pulse Width Modulation technique [fig.2], with four different amplitude energy pulses. If the pulse width is small enough and the pulse rate is extremely stable, then a precise power is generated in the probe chamber as the fig. 1 shows. However the user must know how much from this microwave radiation was absorbed by the probe, and for this purpose we have designed and patented a microwave thermal transducer [1]. Another problem in such systems may be the noise generation into the mains, the technique used to suppress this noise is zero crossing firing for the power semiconductor devices involved in driving the mains load. The mains zero crossing is synchronised with the rising edge of the power pulse width. [fig.2].

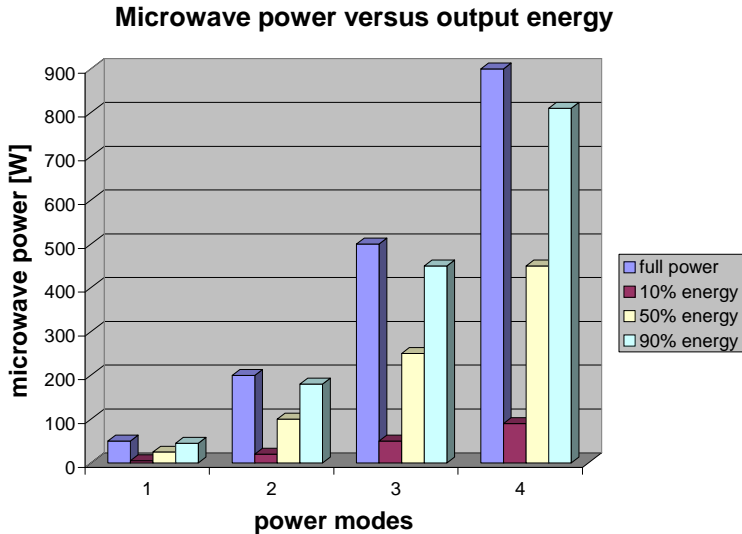


Fig. 1 The microwave generator output power versus 10% to 90% energy mode incident

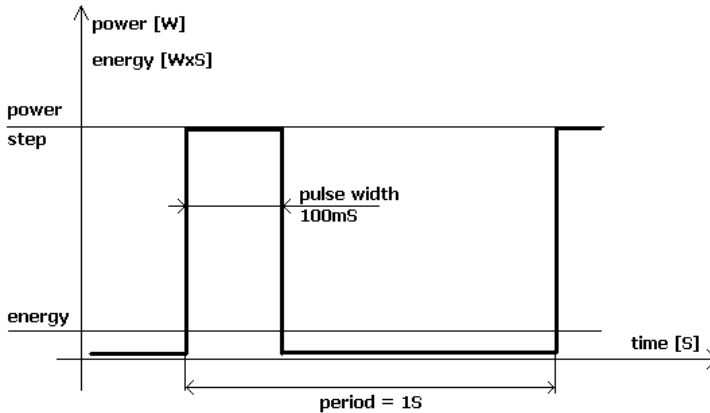


Fig. 2 Puls Width Modulation output technique for 10% output energy. The signal period is kept constant while the pulse width is increased until it equals the period time for 100% energy mode.

**Power design and control overview**

The generator [fig.3] is designed using a 900W CW magnetron [1]. The microwave power is extracted using a TE microwave guide and a coaxial adapter to the reaction chamber [2]. The chamber temperature is measured using a digital temperature sensor. The power supply [3] is entirely electronically controlled, both the anode voltage and the filament voltage can be directly controlled by the required program sequence. The system controller [4] is built with a PIC16F628 microcontroller. It uses a smart LCD driver [4b] with HD44780 which is able to display all the important parameters: the output power level (in relative power steps), the output energy (in percent indications), the treatment time (in minutes/seconds) and the chamber temperature (celsius

degree). All settings can be set from a small four buttons functional keyboard [4a]. A functional keyboard is sharing the button functions and displaying those on the LCD. When a button is pressed the microcontroller is running the specific routines and change the button function for the next push. Some buttons may have the same function in different screens displayed, other buttons may have different functions as the software requires. From one screen, the PC communication menu may be set. In this mode the whole generator control is under the PC command via the RS232 interface [5]. To avoid the computer breakdown, because of possible leakage currents from the high voltage modules, the RS232 interface is fully optoisolated.

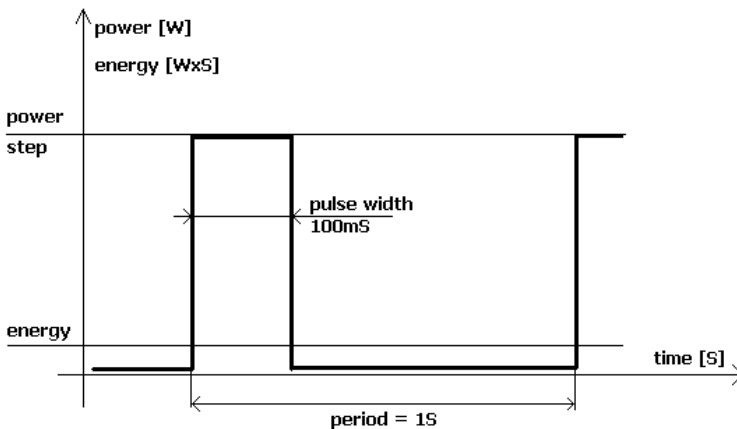
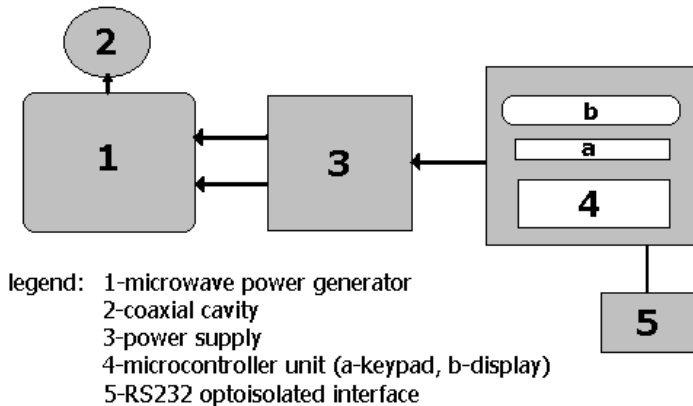
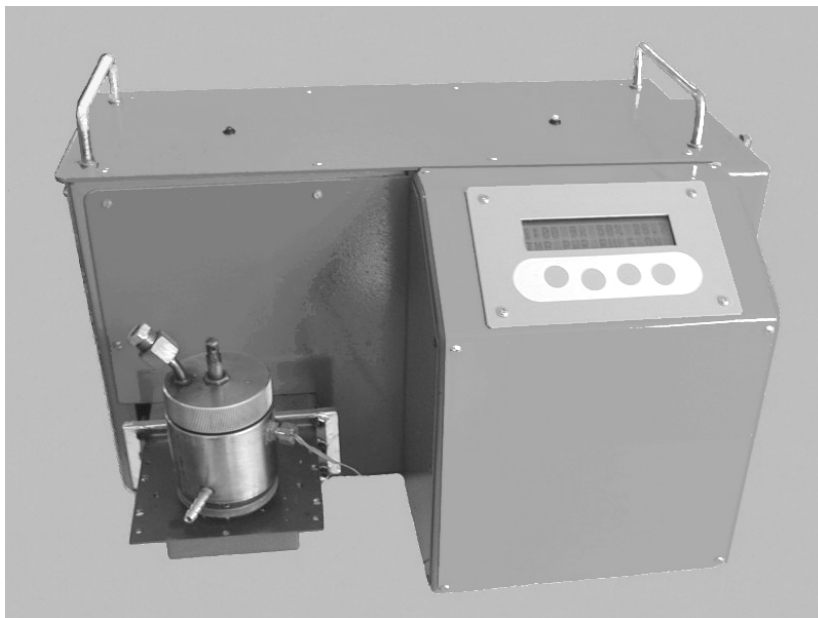


Fig. 3. Modular microwave power system, block diagram

### Conclusions

The modular-microwave power system can be used in any microwave application which request variable output power and energy. With a small firmware reconfiguration the system can be used in totally different applications. This is possible because of some logic/analogic reserved input/ output ports in the microcontroller unit and interchange features of the microwave circuit. One usage example is our versatile and cheap microwave digestion system [fig.4].



**Fig. 4.** Microwave digestion unit using the modular microwave power system

## BIBLIOGRAPHY

1. E.Surducan, V.Surducan, *Thermographic Transducer for Microwave Power Radiation*, Patent RO116506 / jan.2001

## WINE PROBES PROCESSING IN MICROWAVE POWER FIELD FOR ANALYSES

CLAUDIA VILICHE<sup>1</sup>, E.SURDUCAN<sup>2</sup>, V.SURDUCAN<sup>2</sup>

*1- Babes Bolyai University – Chemistry Faculty, Cluj-Napoca*

*2- National Institute for research and developemnet of Isotopic and Molecular Technologies, 75-103 Donath Street, POB 700, Cluj Napoca, email:manu@130.itim-cj.ro*

Wine is an important food commodity and is traded across the whole world. This drink can contain significant levels of heavy metals originating from the soil, (agricultural practices and atmospheric pollution for instance) or production process. Samples (100 ml) were weighed in a teflon capsule and placed in a microwave digester for 45 min, followed by digestion with HNO<sub>3</sub> 65% and H<sub>2</sub>O<sub>2</sub> 30% for 15 min and dilution with H<sub>2</sub>O to 25 ml. Classic method is dry mineralization. Samples of wine (100ml) were evaporated to dryness 12 hours with HNO<sub>3</sub> 65%. The white residue was dissolved in HNO<sub>3</sub> 65% followed by dilution with H<sub>2</sub>O to 25 ml. Analysis in both methods was by atomic absorption spectrometry (AAS) with atomization by air/acetylene.

The analysis results (fig.1) denote that the microwaves method of samples preparation perform total digestion of the molecular compounds in the less time as in the standard method.

The wine is the alcoholic natural drink, obtained through the fermentation of musts from grapes. It is the favorite drink of men by reason of olfactory and gustatory sensation that is offered. But his properties can be influenced by different factors like, the pollution with heavy metals. Wine contains part of these elements from adhesive substance on grapes (soil, pesticide, herbicide, fungicide), from the applicated treatment on must and wine (sulphitations, fining, filtering, etc), from the contact with vessels and with the installations for preservation, conditioning and stabilization of wines (Fe, Cu, Mn, etc). Some of mineral substances, like mercury, lead, copper, zinc and cadmium in high concentration become dangerous for men. To prevent toxic effects on human health, many of the producing countries have systems to controlate their products.

Low concentration of heavy metals in environmental samples may require preconcentration prior to detection. One of the decomposition methods is the mineralization in open vessels (classic method) and the second is processing in microwave power field (modern method).

The analyzed wine samples were “Feteasca Neagră” and “Feteasca Albă”, 2000 production, from the vineyard Dealu Mare in the Prahova county.

### **The wine samples mineralisation in open vessels (Fig. 1).**

The wine (100ml) was evaporated into a crucible to dryness on the sand bath. Temperature must be constant and low, because the wine at high temperatures boils over. The crucible must be overlooked because the ashes can be burned and destroyed. The residue from the crucible was ached step by step to 500-550<sup>0</sup>C into electric furnace. Then residue was dissolved in 2 ml HNO<sub>3</sub> 65% and the operation was repeated. In this stage the sample must became a white ash without coal. Then ash was dissolved in 10ml HNO<sub>3</sub> 65% and evaporated on the sand bath till the half of the initial volume. The contain of crucibles passes quantitative in to a 25 ml graduated flask and completed with distillate water. In parallel, blank sample was processed in the same way, to eliminate impurity errors of reactives.

### **The wine samples processing in microwave power field (Fig.2).**

In the first stage was made a preconcentration of samples. The alcohol and water must be eliminated because they interfered negative in the process of processing (growing temperature and pressure). The microwave oven is foressed with a 40ml cell. The sample (25 ml) was placed

in to a TEFLON capsule and applied the microwave treatment. Because the wine at high temperature boils, at the process installation it was added a vacuum pump. The pre-concentration treatment was 90 min. with 50% microwave energy for each sample of 25 ml until 100ml. After that treatment the sample (10ml) was weighed and digested with  $\text{HNO}_3$  65%-10 ml and  $\text{H}_2\text{O}_2$  35%-5 ml in microwave digester up to 30 min. with 10%, 20%, 30% microwave energy. This stage is very dangerous because reactivities mixed and sample to high temperature boils. The digestion process was considered finish when sample trough in color-less sample. The sample was then diluted to 25ml. In parallel, blank sample was processed in the same way.

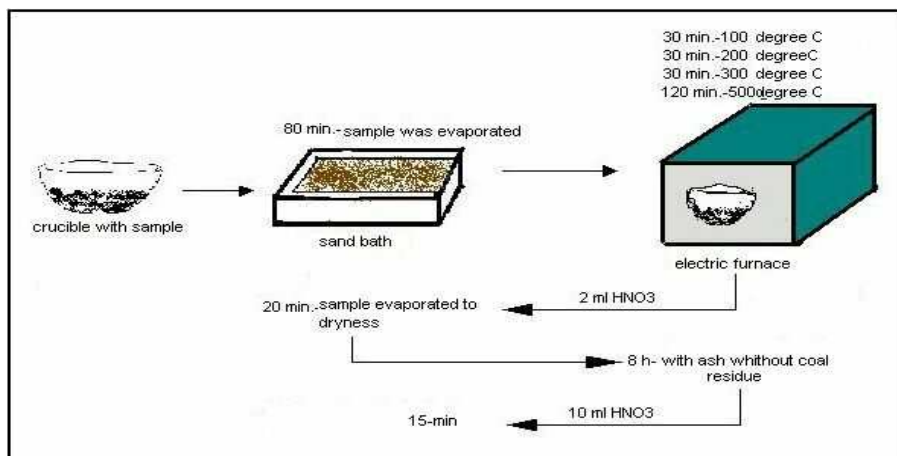


**Fig. 1.** Processing stages in classic method (preparation in open vessels)

Analysis was performed in flame atomic absorption spectrometry (FAAS). Cu, Pb, and Zn were determined at 375,24 nm, 217,83 nm and 213,90 nm using an air/acetylene flame. The results obtained were depended on a three category of samples which analysed: an unprocessed wine, a wine digested in open vessels and a wine digested in microwave oven. The concentration value for each sample was represented in the table 1.



**Fig. 2.** Microwave treatment configurations

**Table 1****The Cu, Pb, Zn concentrations values in unprocessed wine, red and white wine samples**

SAMPLE	METHOD	Cu (mg/l)	Pb (mg/l)	Zn (mg/l)
RED WINE	UNPROCESSING	0.02615	0.4115	0.4816
	CLASSIC	0.1738	0.039	0.80325
	MICROWAVE	<b>1.57415</b>	<b>0.201</b>	<b>9.43</b>
WHITE WINE	UNPROCESSING	0.02585	0.39	0.3162
	CLASSIC	0.15855	0.01	0.46535
	MICROWAVE	<b>0.7926</b>	<b>0.102</b>	<b>2.7672</b>

### Conclusions

The analysis results (fig.3) denote:

- The optimal microwave preparation conditions are: pre-concentration of sample time up 45 min.; 10-5ml HNO<sub>3</sub>/H<sub>2</sub>O<sub>2</sub> as solvent, digesting time 15 min.;
- The samples are digested into closed vessels; the pressure can be up to 10 atm.;
- The microwave method was preferred because to the shorter treatment time (hour rather than 12 hour);
- The low concentration of Cu and Zn in unprocessing samples is probably because matrix effect;
- The application of microwave digestion may improve the preparation. For this reason Cu, Pb, Zn concentrations were high;
- The concentration of heavy metals was much higher in red wine than in white;

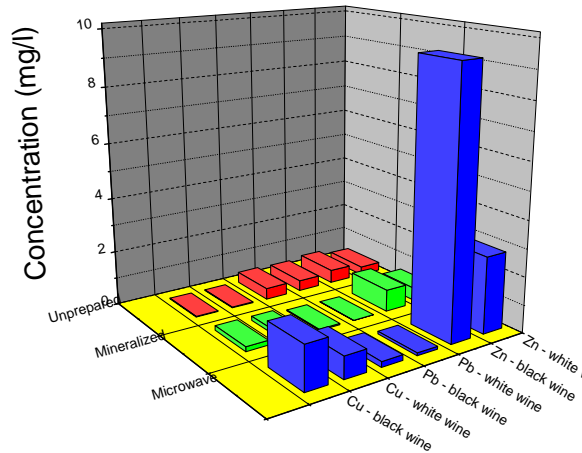


**Fig. 3.** Graphics of the Cu, Pb, Zn concentrations values in unprocessed wine, red and white wine samples

### BIBLIOGRAPHY

1. Dorel Modoran, *Wine and Distillate Drink Tehnology*, ICPIAF Publishing book, Cluj-Napoca, 2002;
2. Monitorul Oficial al Romaniei, *STAS 7588-75, STAS 6182/5-79, STAS 7588-66*;
3. E. Surducan, V. Surducan, G. Nagy, S. Filip, *Thermographic Transducer for Microwave Power Radiation*, Patent Ro 116514 B1/jan. 2001.



## MICROWAVE DIELECTRIC RESONATOR (DRO) TRANSDUCER FOR MOLECULAR DYNAMICS STUDIES

**E. SURDUCAN, V. SURDUCAN**

*National Institute for Research and Development of Isotopic  
and Molecular Technologies, 71-103 Donath Street, POB 700,  
Cluj Napoca, email:manu@130.itim-cj.ro*

In most of the physical and chemical processes the complex permittivity of the materials changes as the process evolves in time. The dynamics of the permittivity as function of time and temperature can provide useful information about a particular process and it can also be used as control feedback.

We propose a new transducer based on the microwave resonant method, using a multilayer dielectric resonator as part of a microwave oscillator (DRO). The probe represents one layer of a multilayer dielectric resonator. Any change in the electric or magnetic properties of the probe will affect the resonance frequency and Q factor, and as a result the total power generated by the oscillator.

In the transducer concept the DRO is coupled with one microcontroller unit. After proper calibration, the change in microwave power emitted by DRO can be directly related to the state of the monitored and/or controlled process. To prove out the concept, preliminary measurements were performed to monitor the polymerization of macrofiller composite diacrilic resin, vitrification of ovalbumine and the gypsum hydration.

### **1. MICROWAVE DIELECTRIC RESONATOR TRANSDUCER**

The key of the dielectric resonator method, used in this transducer (DRO-T) is the dielectric resonant oscillator (DRO). The DRO is a microwave generator, frequency stabilized with one dielectric resonator DR. Microwave frequencies depend on the dielectric resonator permittivity and his geometrical shape. The active device (GUNN diode, FET) is coupled to the dielectric resonator for maximum output level at the frequency  $f_0$ . Any change in frequency or in the quality factor Q of the resonator modifies the microwave output power.

For this method, the microwave resonator is a dielectric multilayer resonator composed by a base dielectric resonator DR ( $\epsilon_{rDR} = (20...70)$ ) and a dielectric sample layer DS ( $\epsilon_{rDS} < \epsilon_{rDR}$ ) which contents the sample support (Teflon cell) and the sample (liquid, solid or mixture of liquid and solid) [1].

The transducer is composed by DRO and a system controller based on PIC16F876 microcontroller (fig.1). The role of the system controller is to perform a digital acquisition of the microwave output of the DRO, to storage a set of data in a buffer memory and to send the data, via RS232, to a personal computer PC (fig.1). The firmware of the system controller can also compute the data (average, liniarise) and to command a feet-back or display the data (for stand-alone applications).

### **2. EXPERIMENTAL MEASUREMENTS**

There are presented three kinds of experiments:

- studies of the macrofiller composite diacrilic resin polymerization,
- vitrification of ovalbumine (liquid phase, permittivity-temperature modification)
- and the gypsum hydration vitrification (permittivity - time dependence)

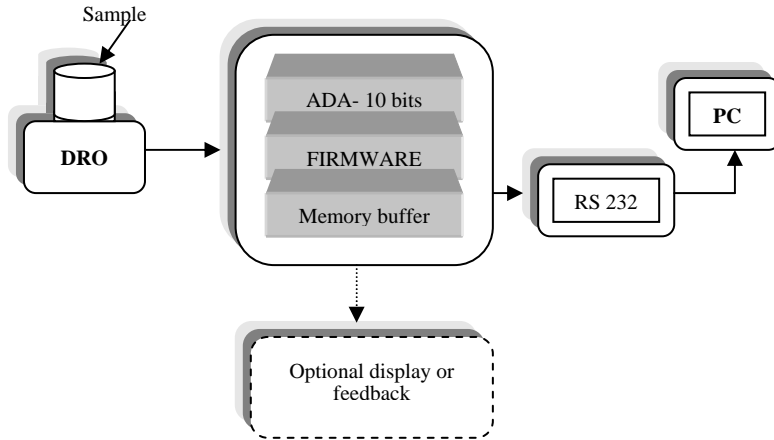


**Fig. 1.** DRO-T transducer configuration

Polymer vitrification is a chemical process with an evolution in time. Any change in dielectric properties of the sample is transferred to the microwave frequency and Q -factor of oscillator and modifies the value of microwave output power level. A process with an evolution in time can be well studied by a real time measurement of the microwave output power modification. For dental material is necessary to know the polymerization time after the two component resins is mixed. In fig.2, the diagram of microwave output frequency versus time characterises the time evolution of the polymerization process. The temperature was also measured using a PN- junction transducer at a same system controller.

Ovalbumine is a glair component and spare protein. The exposures of spherical proteins to high temperature result in a physical modification named denaturation, involving the decrease of solubility and lose of the specific biological activity. For this experiment additional IR source was used for thermal exposure of the sample (not shown in fig.1). The microwave - temperature diagrams (fig.3) show the value of 54.4 °C as the temperature of the beginning of the ovalbumine denaturation.

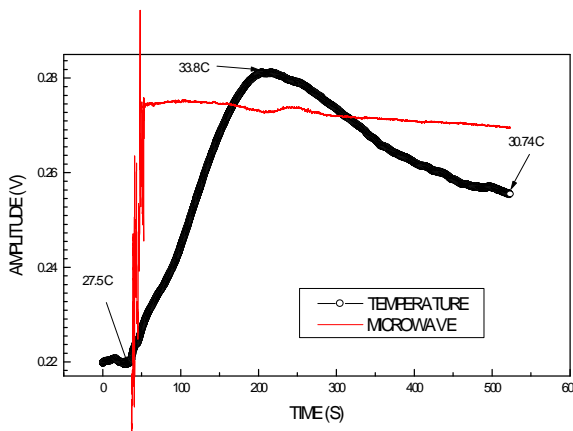


**Fig. 2.** The dynamic of polymerization process studied by DRO-T transducer

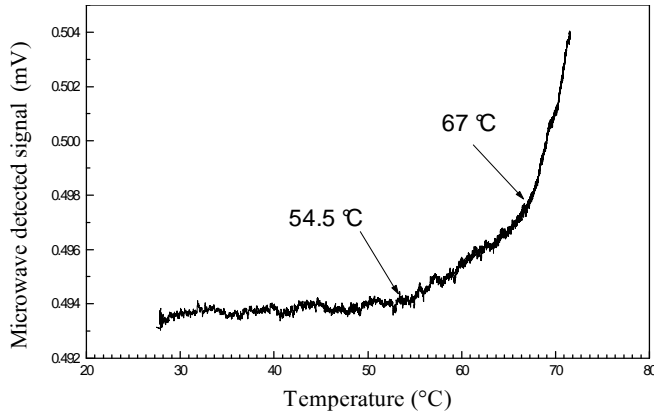


**Fig. 3.** The ovalbumine denaturation monitorized by DRO-T transducer

The gypsum hydration studies are similar to the dental polymer vitrification. In this case the microwave DRO measurements show that the hydration of the gypsum starts after 350s from the mixing of the water with the gypsum. (fig.4) The temperature evolution of the reaction was measured using an additional temperature transducer at the same controller system (not shown in fig.1).

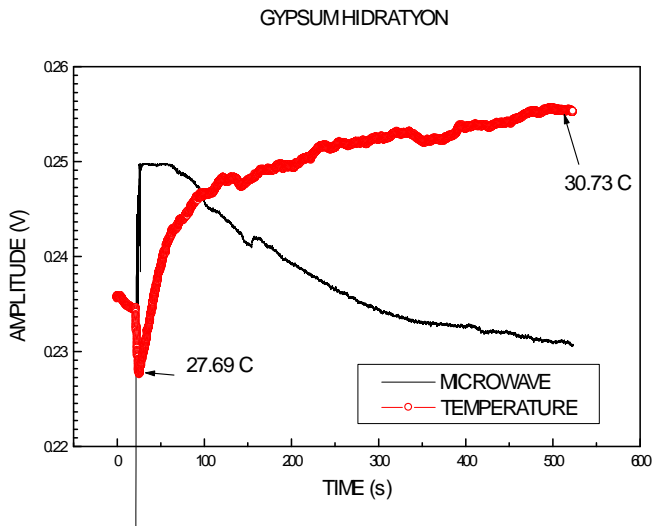


**Fig. 4.** Gypsum hydration measurement by DRO-T transducer

### 3. CONCLUSION

The microwave multilayer dielectric resonator oscillator method DRO is very sensitive to the dielectric cavity modification, not only on the permittivity modification, but also on the volume change. One must have a careful attention to the multilayer arrangement. The ADA 10 bits acquisition must be correlate with a preamplifier of microwave signal for some applications (this is the case of dynamics presented in fig.2) or the transducer must be used for one applications at a time.

The results obtained with the restacril, ovalbumine and gypsum show that this method is specify for the study of slow process dynamics and this transducer has the potential to monitorise these kind of applications.

### **BIBLIOGRAPHY**

1. E. Surducan, V.Surducan, C.Avram, S.V.Filip, G.Nagy, C.Neamtu, "*Microwave dielectric method for the study of the processes dynamics*" Romanian Journal of Physics, no. 50-52 (1998)

## POLYPYRROLE – ZEOLITES COMPOSITES FOR ELECTROANALYTICAL APPLICATION

**IZABELLA PETER<sup>1</sup>, RODICA TURCU<sup>1</sup>, ADRIAN BOT<sup>1</sup>, IONEL CHICINAS<sup>2</sup>,  
RODICA GRECU<sup>3</sup>, LIANA MURESAN<sup>4</sup>, IONEL CATALIN POPESCU<sup>4</sup>**

<sup>1</sup>*National Institute of R & D for Isotopic and Molecular Technologies,  
3400, Cluj – Napoca*

<sup>2</sup>*Technical University, <sup>2</sup>Materials Science and Technology Department,  
3400, Cluj-Napoca*

<sup>3</sup>*Chemistry Institute “Raluca Ripan”, 3400 Cluj-Napoca, Romania*

<sup>4</sup>*Department of Physical Chemistry, “Babes-Bolyai” University, 3400 Cluj-  
Napoca, Romania*

### INTRODUCTION

Polypyrrole (PPy) has been studied in the form of thin films deposited on the electrode surfaces [1]. Polypyrrole films can be prepared by anodic electropolymerization of pyrrole in either aqueous or nonaqueous media using a variety of electrochemical techniques like potentiometry. The deposited polypyrrole films have high conductivity, good environmental stability and a large variety of potential technological applications like: battery electrodes, corrosion protection and biological sensors [2-4].

Zeolites [5-6] are crystalline open framework oxide structures (classically aluminosilicates but now encompassing many elemental compositions) with pore size between 0, 3 and more than 3 nm. The topologies of these systems include 1-D channels, intersecting 2-D channels and 3-D open frameworks.

### EXPERIMENTAL

Pyrrole (Py) was vacuum – distilled and stored in darkness prior to use. All the other reactants were analytical grade and were used as – received: para – toluensulfonic acid (p-TSO), lithium perchlorate (LiClO<sub>4</sub>) and zeolite (Bayer Zeolith). Chemical composition of these zeolites is Na<sub>j</sub>[(AlO<sub>2</sub>)<sub>j</sub>(SiO<sub>2</sub>)<sub>192-j</sub>] x z H<sub>2</sub>O (z = 260, j = 77 ÷ 96, Si/Al = 1 ÷ 1,5, 3-D channels and the main channels = 4, 3 Å).

An AUTOLAB electrochemical analyzer was used in experiments. Electrochemical experiments were performed in a three-electrode cell. The counter electrode was platinum foil (1 cm<sup>2</sup>) while the reference electrode was saturated calomel electrode (SCE). All potentials reported are referenced to the SCE. A platinum electrode (θ = 5 mm) and an inox electrode (4 cm<sup>2</sup>) were used as the working electrode for electrochemical studies. Prior to each experiment, the platinum and the inox electrodes were polished with microalumina down to 6 ÷ 15 μm.

Polypyrrole films were electrodeposited on platinum or inox working electrode by applying a controlled electropolymerization potential of + 0,8 V in a solution containing the monomer (Py), the dopant (p-TSO, LiClO<sub>4</sub>, K<sub>3</sub>Fe(CN)<sub>6</sub>), the zeolite and the electrolytes (LiClO<sub>4</sub>).

The polymerization conditions for the synthesis of the Ppy-Ze composites are given in Table 1.

The morphology of the resulting Ppy-Ze composites was determined by scanning electron microscopy (SEM) by using a JSM 5600 LV (JOEL) microscope. Also the EDX tool associated with SEM provides information about the general and local stoichiometry.

Infrared spectra in the range 400 – 7800 cm<sup>-1</sup> were recorded by a JASCO 610 spectrophotometer on the film.

**Table 1****The polymerization condition for the synthesis of the Ppy-Ze composites**

Sample	Thickness ( $\mu\text{m}$ )	Py/zeolit molar ratio	Dopant	Dopantconc (M)	Polim. time (s)	Conductivity (S/cm)
PPY-Z1a	70	$1.35 \times 10^3$	p-TSO	0.1	3600	28
PPY -Z1b	70	$1.35 \times 10^3$	p-TSO	0.1	3600	28
PPY -Z2a*	-	$0.54 \times 10^3$	LiClO <sub>4</sub>	0.1	1800	-
PPY -Z3a*	-	$1.35 \times 10^3$	LiClO <sub>4</sub>	0.1	1800	-
PPY -Z4a	26	$1.35 \times 10^3$	p-TSO	0.1	1800	71
PPY -Z4b	50	$1.35 \times 10^3$	p-TSO	0.1	1800	38
PPY -Z5a	12	$1.35 \times 10^2$	p-TSO	0.1	1800	18
PPY -Z5b	16	$1.35 \times 10^2$	p-TSO	0.1	1800	26
PPY -Z <sub>Fe</sub> 6a	64	$1.35 \times 10^3$	LiClO <sub>4</sub>	0.1	1800	1.7
PPY -Z <sub>Fe</sub> 6b	42	$1.35 \times 10^3$	LiClO <sub>4</sub>	0.1	1800	1
PPY Z7a	40	$1.35 \times 10^3$	K <sub>3</sub> Fe(CN) <sub>6</sub>	0.1	1800	2
PPY -Z7b	45	$1.35 \times 10^3$	K <sub>3</sub> Fe(CN) <sub>6</sub>	0.1	1800	5

*a* – the surface of PPy-Ze films from the counter electrode; *b* – the surface of PPy-Ze films from the solution

The electrical conductivity,  $\sigma$ , of the Ppy-Ze composite films was determined by the four contacts method.

The Ppy-Ze composite films have been characterized by its cyclic voltammogram (CV). At define time periods, CVs of the electrode were recorded over potential scan limits of - 0,2 V ÷ + 0,8 V.

## RESULTS AND DISCUSSION

### *Morphology of the polypyrrole – zeolites composites films*

In Figure 1 is shown the morphology of the Ppy-Ze1 composite. The morphology of the composites surface contain micronic globular particles, forming a cauliflower – like structure and fibrillar aggregates with about 5 – 10  $\mu\text{m}$  in diameter and tens  $\mu\text{m}$  in length The cauliflower – like morphology is typical from electrochemically prepared PPy. The presence of the zeolite in the polymerization solution results in the formation of a fibrillar superstructure. This superstructure appears due to the formation of the cationic radicals in the zeolite channels, who determine an other structural organization of a polymeric chain as compared with that obtained in the absence of the zeolite.

The elemental analysis with EDX spectrophotometer for the PPy-Ze1 sample is showed in Table 2, and the spectrum of relative intensity of X radiation specific for the elements from sample is showed in Figure 2.

**Table 2**

### Elemental analysis of PPy-Ze1

Element	App Conc.	Intensity Corn.	Weight%	Weight% Sigma	Atomic%
C K	180.30	0.6624	46.61	3.25	54.47
N K	15.99	0.1218	22.49	5.00	22.54
O K	50.43	0.3946	21.89	2.03	19.20
Al K	0.31	0.9510	0.06	0.08	0.03

Si K	0.73	0.9881	0.13	0.09	0.06
S K	28.61	0.9840	4.98	0.42	2.18
Cl K	18.08	0.8060	3.84	0.36	1.52
Totals			100.00		

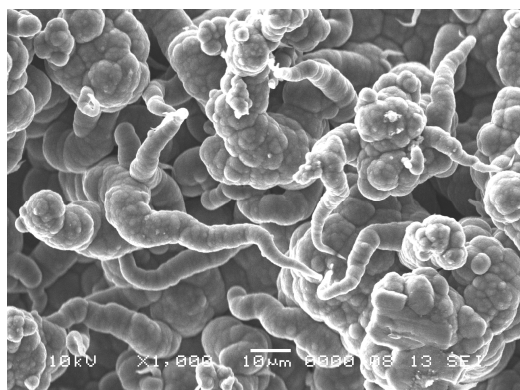


**Fig. 1.** SEM image of PPy-Ze1

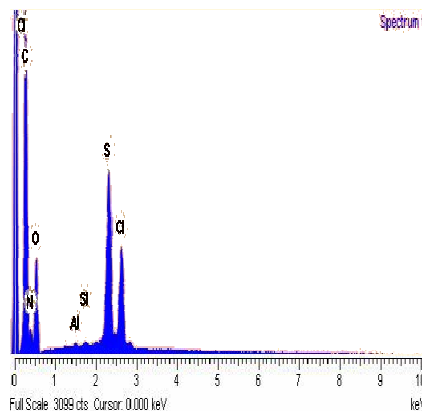


**Fig. 2.** EDX spectrum of PPy-Ze1

### *Structural characterization*

In Figure 3 are presented the FTIR spectra of the beginning zeolite NaX. It is observe that the characteristic bands are located round  $3400\text{ cm}^{-1}$  and  $100\text{ cm}^{-1}$  and it is attributed for the OH stretching vibration and the  $\text{SiO}_2$  groups.

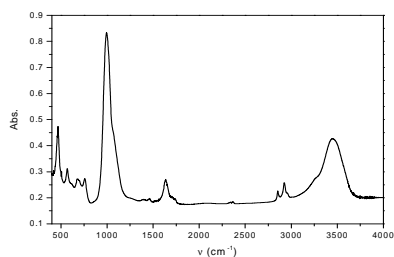


**Fig. 3.** FTIR spectra of the beginning zeolite

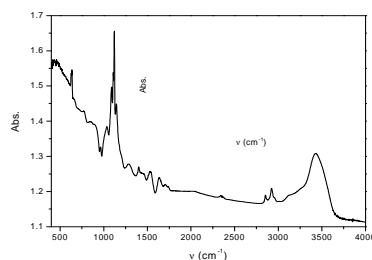


**Fig. 4.** FTIR spectra of PPy-Ze<sub>Fe6a</sub>

The Figure 4 showed the FTIR spectrum of PPy-Ze<sub>Fe6a</sub> synthesized by electrochemical polymerization with zeolite that contains  $\text{Fe}^{3+}$ .

If we compare the FTIR spectra shown in Figures 3 and 4, we observe the appearance of the characteristic absorption bands of PPy located at  $1535$ ,  $1450$ ,  $1281$ ,  $963\text{ cm}^{-1}$ . The absorption bands between  $1000 - 1150\text{ cm}^{-1}$  observed in same spectra are attributed to  $\text{SiO}_2$  groups from zeolite,  $\text{ClO}_4^-$  dopant and the oxidized pyrrolic. Also, a new band was observed at  $1400\text{ cm}^{-1}$ . This band was assigned to absorbed monomer in the zeolite channels and that remained unpolimerized.

**Electrochemical characterization**

Cyclic voltammograms for a PPy-Ze1 film are shown in Figure 5. The voltammograms show the polymerization of the polypyrrole. The zeolite incorporation is characterized by a high capacitive behavior.

If one compares the voltammogram plotting in the presence and in the absence of the zeolite, the difference is significant to a 30-th cycle (Figure 6).

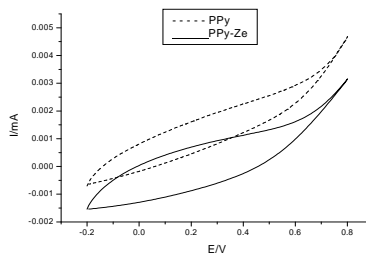
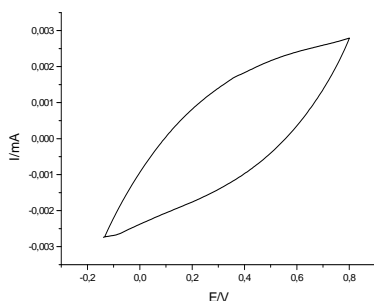


**Fig. 5.** Cyclic voltammogram of PPy-Ze1 film    **Fig. 6.** Cyclic voltammogram of a PPy and PPy-Ze films

The voltammetric results therefore suggest the zeolite insertion in the polymeric matrix.

In conclusion, this study demonstrates that the synthesis of pyrrole in the presence of zeolite can form intrazeolite polypyrrole by electrochemical polymerization reaction.

**REFERENCES**

1. G. B. Street, *Handbook of Conducting Polymers*, T. A. Stotheim (ed), Marcel Dekker, New-York, Vol 1, 1986, 265-291;
2. C. A. Ferreira, S. Aeyach, M. Delamar, P. C. Lacaze, *J. Electroanal. Chem.*, **35**, 1990, 284
3. N. C. Fould, C. R. Lowe, *Anal. Chem.*, **60**, 1988, 2473
4. F. Mizutani, M. Asai, *Bull Chem. Soc. Jpn.*, **61**, 1988, 4458
5. R. M. Barrer, *Hydrothermal Chemistry of Zeolites*, Academic Press, London, 1982
6. M. E. Davis, R. Lobo, *Chem. Mater.*, **4**, 1992, 458



## COMPLEMENTARY METHODS FOR MONITORING THERMAL PHENOMENA ASSOCIATED WITH THE POLYMERISATION PROCESS OF EPOXIDIC RESINS

**MIHAI CHIRTOC<sup>1</sup>, ILEANA CHIRTOC<sup>1</sup>, EMANOIL SURDUCAN<sup>1</sup>,  
VASILE SURDUCAN<sup>1</sup>, CAMELIA NEAMTU<sup>1</sup>, CRISTIAN V.L. POP<sup>1</sup>,  
DANE BICANIC<sup>2</sup> and M. WUBBENHORST<sup>3</sup>**

<sup>1</sup> National R&D Institute for Isotopic and Molecular Technologies, POB 700,  
3400 Cluj-Napoca 5, Romania

<sup>2</sup> Wageningen Univ. and Res. Center, Dreijenlaan 3, Transitorium, 6703 HA  
Wageningen, The Netherlands

<sup>3</sup> Delft Univ. of Technology, Dept. Chem. Technol. and Mat. Sci., Julianalaan  
136, 2628 BL Delft, The Netherlands

Acrylic resins used in modern dental treatment undergo considerable changes of their thermal, mechanical and optical properties during the process of polymerisation. The curing history affects the long-term stability of the resin and it is believed to be responsible, to some extent, for its dimensional changes [1]. The exothermic reaction associated with the curing process leads to local temperature increase the magnitude of which depends on the heat evacuation rate to the surrounding medium. Overheating should be avoided for two reasons: in order to achieve a homogeneous polymeric material and, what is even more important, to avoid the damage to the coronal pulp of the tooth [2].

The real-time temperature profiles obtained during curing of several acrylic resins allowed for a comparative evaluation regarding the hardening time and the maximum developed temperature. Next, by using a microwave method, we showed that the parameters of the sample (i.e., dielectric constant) are correlated with the temperature increase. Finally, a photothermal (PPE) method is used to investigate the variation of thermal parameters due to phase transitions taking place upon curing.

We developed a simple, differential calorimetric technique for temperature monitoring of the polymerisation reaction. A low power silicon diode biased with a constant forward current of 0.5 mA was used as a temperature transducer [3]. A second, identical diode was placed in the proximity of the mixing vessel to compensate for the effect of ambient temperature drift. A typical differential temperature profile is shown in Fig. 1. The time origin corresponds to the mixing of the liquid and powdered constituents. The initial cooling effect (1-2°C) is produced by partial evaporation of the volatile liquid component of the mixture. This represents no danger for the integrity of the tooth. At time  $t_{on}$  is the on-set of the polymerisation process, which is associated with heat release.

This may lead to heating of the coronal pulp above the threshold of 42°C resulting in irreversible damage. Eventually the temperature reaches a maximum  $\Delta T_{max}$  followed by an exponential decrease with a time constant  $T_T$ , depending on the rate of heat loss by conduction. Nine materials (abbreviated as A,B,C,...I) were investigated, classified into four categories (I-IV) according to their origin and application destination: materials for extraoral purposes (A,B,C, group I), for temporary relining in the mouth (D,E, group II), for provisional crowns and inlays (F, group III), and for articulator and impression tray (G,H,I, group IV).

The total curing time  $t_{on}+t_{max}$  is the maximum time interval during which the material can still be modelled before hardening. It varies between  $\approx 4$  min. for material I and  $\approx 11$  min. for material C. On the average, group II has the longest time before hardening (7-8 min.), and the opposite is true for group IV, with 4-5 min.

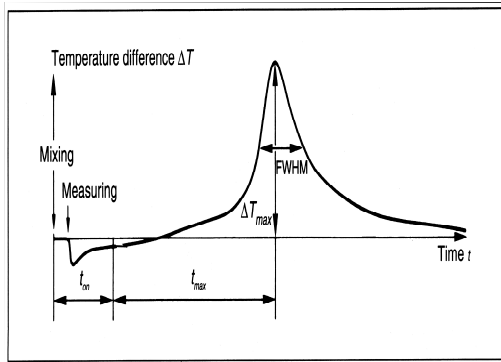


**Fig. 1.** Typical temperature evolution during curing of epoxidic resins.

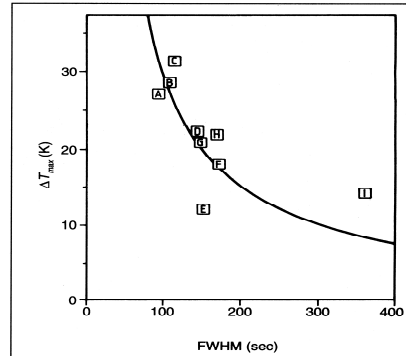


**Fig. 2.** Maximum temperature increases  $\Delta T_{max}$  vs. peak width FWHM.

The product of  $\Delta T_{max}$  and the peak width FWHM (full peak width at half maximum) gives an estimation of the peak area, which in turn is proportional to the total energy released during the polymerisation. The fit (solid line) in Fig. 2 represents a hyperbola satisfying the equation:

$$\Delta T_{max} \text{ FWHM} = 3000 \text{ deg.s.} \quad (1)$$

The hyperbolic fit indicates that the product of these two quantities is approximately constant for most of the investigated materials. The majority of the investigated materials are positioned close to this hyperbola suggesting that their reaction energies are comparable. Therefore, the choice of a product generating lower temperature increase can be made only at the expense of accepting a longer exposure of the tooth at that temperature. A favourable finding is the fact that only the materials destined for repair and casting outside the mouth (group I) show higher temperature increases (by about  $10^{\circ}\text{C}$ ) than the other groups.

The dynamics of permittivity  $\epsilon$  as function of time and temperature provides useful information about a particular chemical process and can be used also as feedback information to control that process. We propose a new method to study dielectric properties of materials using a dielectric resonant oscillator (DRO). It is composed of a microwave generator (GUNN diode, FET), coupled to a multilayer dielectric resonator and tuned at frequency  $f_0$  for maximum output level. The sample (dielectric intermediate layer, DI) is part of the resonator. Changes in its  $\epsilon$  affect  $f_0$  and the  $Q$  factor, resulting in variations of the total power generated by the oscillator. After proper calibration, this information can be related to various sample properties that evolve in time. In Fig. 3 the minimum of the microwave signal coincides with the onset of polymerisation process, indicated by the rise in temperature. This demonstrates the correlation between temperature and other sample-related properties during curing.

A photothermal method known as the photopyroelectric (PPE) technique has been implemented for in-situ studies of the thermal effusivity  $e=(ck)^{1/2}$  and diffusivity  $\alpha=k/c$  of a mixture of di-glycidyl ether of bis-phenol A (DGEBA) epoxy resin and diamino-diphenyl-methane (DDM) hardener during isothermal curing at  $25^{\circ}\text{C}$  [4]. Alternatively, the sample properties can be represented by the volume specific heat  $c$  and the thermal conductivity  $k$ . The experimental set up is based on a  $L_p=9 \mu\text{m}$  thin PVDF polymer film (area  $A$  and pyroelectric coefficient  $p$ ) which is in close contact with a thicker layer  $L_s$  of initially uncured epoxy resin. A sinusoidally modulated He-Ne laser (radiation flux  $H$ ) acts as periodic heat source of heat waves with frequency  $f$ . Depending on the side of the PPE cell that is being irradiated, two experimental configurations are available, with front-detection (FPPE, the sensor-side is irradiated), and back-detection (BPPE, the sample-side is irradiated).

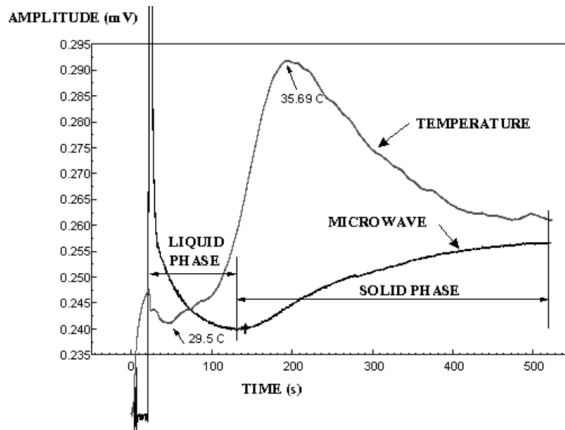


**Fig. 3.** Microwave signal and the temperature (measured by a p-n junction) during the polymerisation process of Restacril dental filling material.

For the theoretical model we consider the bilayer structure of the PPE cell, in the one-dimensional heat propagation approximation [5]. In the case of the detector alone without the sample, the current signal is given by:

$$I_0 = H A p / (c_p L_p) \tag{2}$$

In the FPPE configuration, for a thermally thick sample deposited on a thermally thin detector (at low modulation frequency), one has:

$$I_F = (1+i) H A p (\pi f)^{1/2} / e_s \tag{3}$$

The thermal effusivity  $e_s$  can be obtained from eq. (3) normalised to eq. (2).

In the BPPE configuration, the signal is:

$$I_B = I_0 \exp[-(1+i)L_s/\mu_s] \tag{4}$$

where  $\mu_s = (\alpha_s / (\pi f))^{1/2}$  is the thermal diffusion length in the sample. The eq. (4) can be rewritten as eq. (5) and then  $\alpha_s$  can be determined both, from the slope of the amplitude and phase vs.  $f^{1/2}$ :

$$\ln(|I_B/I_0|) = \varphi_B = -L_s (\pi f / \alpha_s)^{1/2}; \alpha_s = L_s^2 \pi / (\text{Slope})^2 \tag{5}$$

In the end, by combining  $e_s$  and  $\alpha_s$  one obtains  $c_s$  and  $k_s$ , Fig. 4.

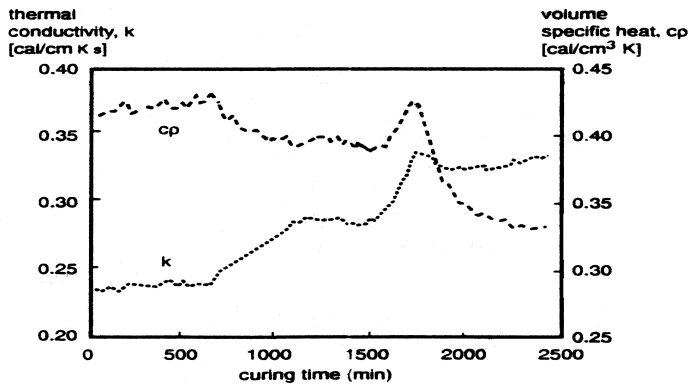


**Fig. 4.** Volume specific heat  $c_s$  and thermal conductivity  $k_s$  during curing of DGEBA-DDM epoxy resin at 25°C. The glass transition is marked by a stepwise decrease of  $c_s$ .

The experimental phenomena observed in this study are the following:

-The thermal effusivity shows a marked increase until it drops when the rubber-to-glass transition is passed, i.e. when the molecular network that is being formed vitrifies into the glassy state;

-The volume specific heat is rather constant in time until vitrification occurs, when a stepwise decrease shows up;

-The thermal conductivity increases steadily in the pre-vitrification state due to increase of crosslink density;

-The thermal conductivity has no discontinuity at the glass transition, and there is no indication for a significant (phononic) lattice heat transfer component in  $k$ .

#### **Acknowledgements**

This research was supported by Romanian Education and Research Ministry, BIOTECH Program, research project 01-8-CPD-042

Part of this work was carried out with the support of the Dutch Organization for Scientific Research (NWO) for one of the authors (M.C.)

#### **REFERENCES**

1. M.L. Hitge, P.J. Torfs, and D.D. Bicanic, *J. Biomech.* **24**, 961 (1991).
2. R. Labella, M. Braden, and K.W. Davy, *Biomaterials* **13**, 937 (1992).
3. M. Chirtoc, D.D. Bicanic, M.L. Hitge, and W. Kalk, *Int. J. Prosthodontics* **8**, 259 (1995).
4. M. Wübbenhorst, J. van Turnhout, and L. Alili, *Ferroelectrics* **165**, 153 (1995).
5. M. Chirtoc and G. Mihailescu, *Phys. Rev. B*, **40**, 9606 (1989).

## OPTICAL AND STRUCTURAL INVESTIGATIONS OF ORDERED METALLIC NANOSTRUCTURES FOR SERS EXPERIMENTS

M. BOLBOACA<sup>1</sup>, L. BAIA<sup>1</sup>, I. CHICINAS<sup>2</sup>, D. MANIU<sup>1</sup>,  
T. ILIESCU<sup>1</sup>, S. ASTILEAN<sup>1</sup>

<sup>1</sup>Physics Faculty, Babes-Bolyai University, Cluj-Napoca, Romania

<sup>2</sup>Department of Materials Science and Technology, Technical University, Cluj-Napoca, Romania

**ABSTRACT** We employ scanning electron microscopy in combination with transmission and reflectivity spectroscopy to characterize the structural, morphological and optical properties of thin gold film deposited on polystyrene colloidal crystal. We make interesting correlations between the optical response, nanometer-scale morphology and surface-enhanced Raman scattering (SERS) activity of nanostructured film.

### Introduction

Nanostructured metallic substrates offer the possibility of enhancing the electromagnetic field close to surfaces by factors up to  $10^3$  due to surface plasmon excitation [1]. Thereby, Raman signals from molecules adsorbed at these substrates are enhanced by up to six orders of magnitude. This surface-enhanced Raman scattering (SERS) offers high sensitivity and the possibility of detecting monolayers of molecules [2]. For this reason and the additional typical high selectivity of Raman scattering due to the fingerprint nature of the molecular spectra, SERS has a large potential for new developments in chemical and biochemical sensor applications [3].

Optimization of the Raman amplification is of major interest for applying the SERS technique in ultrasensitive molecular detection. A wide variety of substrates has been found to exhibit SERS [4]. In contrast to irregular metallic substrates (roughened metal electrodes, metal island films and colloidal metal films), regularly arranged metallic nanoparticles and metallic gratings can offer the possibility for a more systematic and reproducible study of the plasmon resonance contribution to SERS.

The rapid development of the nanofabrication technique has made possible to produce well-controlled and highly ordered nanostructured metallic surfaces. Two types of nanofabrication techniques, i.e., lithography and template synthesis, play a dominant role for this purpose. Electron, ion, or light beam lithography can make highly ordered periodic arrays with optimized particle size, shape, and interparticle spacing. However, these point-by-point approaches make the fabrication process very slow and cost-consuming. In contrast, nanostructured surfaces with a large area can be prepared more easily and quickly by the template synthesis technique, especially when combined with the self-assembly method and nanosphere lithography.

In this paper, we applied the second route of nanofabrication to produce metallic nanostructures with SERS activity. Nanostructures exhibit valuable SERS properties due to highly ordered metallic features created by covering regular arrays of polystyrene nanospheres with a gold film. We were able to make correlations between optical response, nanometer-scale morphology and the amplification of surface-enhanced Raman scattering (SERS) spectra of rhodamine 6G molecules adsorbed on the substrate.

### Experimental

a) *Nanostructures preparation.* The nanostructures were prepared in two steps, according to the drop-coat method of nanosphere ordering as described in literature [5]. Firstly, a suspension of polystyrene nanospheres of 220 nm diameter was drop-coated onto the a glass

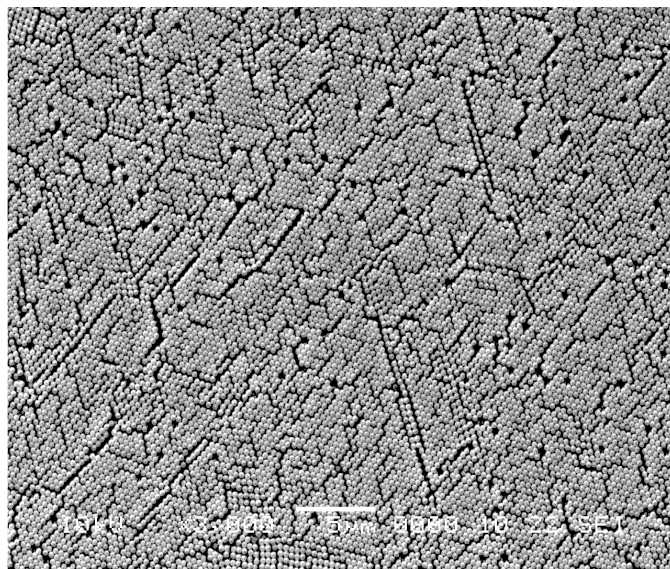
slide where they, after water evaporation, self-assembled into hexagonally close-packed two-dimensional (2D) colloidal crystals. Then, the substrate was mounted into the vacuum chamber of a vapour deposition system and gold films of 64 nm thickness were thermally evaporated onto the substrate under a pressure of  $5 \times 10^{-6}$  Torr.

For recording the SERS spectra, a drop of rhodamine 6G in methanol solution ( $10^4$  M concentration) was evaporated on the substrate. Rhodamine 6G and all materials involved in substrate preparation were purchased from commercial sources as analytical pure reagents.

*b) Experimental measurements.* Scanning electron microscopy investigations were performed with an JEOL JSM 5600-LV scanning electronic microscope. Transmission and reflectivity spectra were measured at normal incidence using a Perkin Elmer Lambda 9 uv-vis-nir spectrometer. The SERS measurements were performed on a Dilor Labram system by using an Olympus LMPlan FI 50 microscope objective and two laser lines for excitation (514 nm and 633 nm respectively). The FT-Raman spectrum of Rhodamine 6G was recorded with a Bruker IFS 120HR spectrometer equipped with a FRA 106 Raman module and a Nd:YAG laser for excitation with the 1064 nm line.

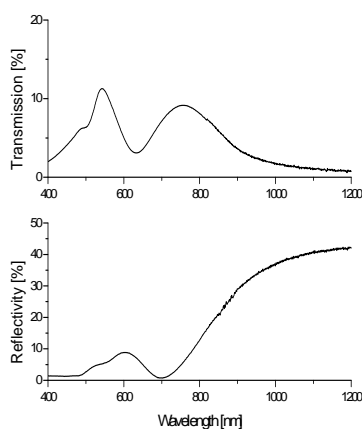
### Results and discussion

Figure 1 shows the scanning electron microscopy (SEM) picture the nanospheres assembly covered with a gold film. Depositing a thin film of metal over the nanospheres assembly produces regular arrays of quasi-interconnected metallic triangular nanoparticles. The ordered domains range from a few to tens of  $\mu\text{m}$ . Figure 2 shows the transmission and reflection spectra of nanostructured gold film recorded at normal incidence. The optical spectra reflect the interplay between two distinct optical responses of nanostructure: (a) localized surface plasmon (LSPR) modes associated with individual nanoparticles and (b) delocalized modes associated with the plasmon propagation on quasi-continuous corrugated film. Both characteristics enhance the versatility of SERS substrate.



**Fig 1.** SEM images of typical nanostructured gold film produced by metal coating crystalline assemblies of 220 nm polystyrene nanospheres.

The SERRS spectrum of Rh6G recorded with the 514 nm laser line (where molecules exhibit an electronic absorption maximum) together with SERS spectrum recorded with the 633 nm laser line, demonstrates the great capability of this substrate to provide Raman enhancements. We mention that these spectra were collected from the same region of substrate and two different laser lines. The differences between the SERRS and SERS spectra can be explained by considering the resonant contribution to the overall SERS enhancement. Previous theoretical studies [6,7] on aggregate structures suggest that the electromagnetic field effects responsible for SERS on solid substrates are localized in the interstitial regions of the arrays, and are accompanied by field depletion outside of these areas. This implies that the majority of the SERS signal measured from our sample is due to the excitation of very small percentage of adsorbate situated at these interstitial sites, and the individual enhancements are likely greater the surface-averaged measurements [8].



**Fig. 2.** Transmission and reflectivity spectra of nanostructured gold film

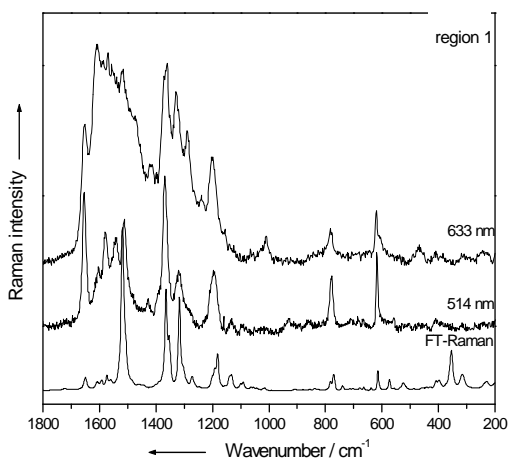


**Fig. 3.** FT-Raman, SERRS and SERS spectra of Rh6G adsorbed on nanostructured gold film

### Conclusions

The absorption and reflectivity spectroscopy together with scanning electron microscopy have been performed in order to characterize the structural and optical properties of nanostructured gold film. The film deposited on colloidal crystal of polystyrene spheres exhibits structural periodicity, strong optical resonances and reproducible SERS properties. The approach of nanofabrication we employed here, provides great opportunity for not only optimizing the SERS activity but also searching for a new class of SERS active materials.

### REFERENCES

1. U. Kreibig and M. Vollmer, *Optical Properties of Metal Clusters*, Springer, (1995).
2. M. Moskovits, *Rev. Mod. Phys.* **57**, 783, (1985).
3. K. Kneipp, H. Kneipp, I. Itzkan, R. D. Dasari, M. S. Feld, *Chem. Rev.*, **99**, 2957 (1999).
4. T. Vo-Dinh, *Trends in Analytical Chemistry*, **17** (8&9), 557, (1998).
5. C. L. Haynes and R. P. Van Duyne, *J. Phys. Chem. B* **105**, 5599 (2001).
6. N. Felidj, J. Aubard, G. Levi, J.R. Krenn, A. Hohenau, G. Schider, A. Leitner, F. R. Aussenegg, *Appl. Phys. Lett.*, **82**, 3095, (2003).
7. F. J. Garcia-Vidal, and J. B. Pendry, *Phys. Rev Lett.*, **77**(6), 1163, (1996).
8. S. Astilean, M. Bolboaca, T. Iliescu, D. Maniu, to be published in *Romanian Journal of Physics* (2003).

## THEORETICAL INVESTIGATIONS OF THE SURFACE POLARITONS DENSITY OF STATES ON SILVER SURFACES

**C. MORARI<sup>1</sup>, S. ASTILEAN<sup>2</sup>**

<sup>1</sup> *National Institute for Research and Development of Isotopic and Molecular Technologies, R-3400 Cluj-Napoca, P.O. 5, Box 700, Romania*

<sup>2</sup> *Physics Faculty, 'Babes-Bolyai' University, Cluj-Napoca, RO-3400, Romania*

**ABSTRACT.** We present the implementation of a recently proposed method for solving the reduced Rayleigh equations at the metal-vacuum interface. Our implementation allows us to perform an extensive study of the surface plasmon polaritons properties (band structure and density of states are described). Several results are listed in order to illustrate the capabilities of our software.

### Introduction

Conventional photonic crystals are artificial three-dimensional periodic dielectric structures that inhibit the propagation of electromagnetic waves of certain wavelengths [1]. In recent years, there has been a growing interest in employing surface-plasmon polaritons (SPP) propagating across rough surfaces for the same purpose.

In the present paper we report the results obtained for computing the density of states of the SPP's for a nanostructured silver surface. The theoretical model implemented by us was recently introduced by Kretschmann and Maradudin. It describes the propagation of the SPP's across periodic metal-vacuum interface and dielectric vacuum interface. Both band structure and density of states are reported, for several lattice parameters of the nanostructured surface. The results show the existence and the properties of the band gap in all the structures under investigation. Among the possible application of these results one of the most important is to give a deeper understanding of the phenomena involved in the SERS.

### Method

Several methods were proposed in literature to compute the band structure of the SPP's [2,3]. Recently, Kretschmann and Maradudin proposed a nonperturbative approach based on the reduced Rayleigh equation, to study absolute photonic band gaps in the frequency spectrum of surface-plasmon polariton for periodic metal-vacuum interfaces [4]. In their model, a double periodic rough interface separates the metal (or dielectric) region  $x_3 < \zeta(x_{II})$  from the vacuum region  $x_3 > \zeta(x_{II})$ . In the relations above we have  $x_{II} = (x_1, x_2, 0)$ .

The profile function  $\zeta(x_{II})$  is describing an array of hemielipsoids with radius  $R$  and height,  $HR$  and it has the form (see Figure 1)

$$\zeta(x_{II}) = \sum_l S(x_{II} - x^l) \quad (1)$$

where  $S(x_{II})$  is the analytical equation that describe the profile given in Figure 1.



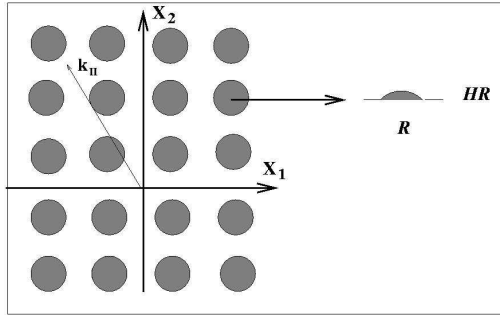


**Fig. 1.** Schematic view of the  $x_3=0$  plane for a square array of hemispheres.  $\mathbf{k}_{||}$  is the wavevector of the surface plasmon polaritons. A detail on the profile function is given in the right side.

By asking to the electric field at the interface, governed by the reduced Rayleigh equation [5] to satisfy the Bloch-Floquet theorem, they arrived at the equations that governs the propagation of surface polariton across the interface. The solvability condition for the set of equations describing the eigenstates of SPP's is that the determinant of the coefficients vanishes

$$D(\omega, k_{||}) = 0 \tag{3}$$

Eq. 3 provides the dispersion relations for the surface polariton,  $\omega(\mathbf{k}_{||})$ . The corresponding density of states can be calculated using the relation

$$\sigma(\omega) = \sum_{branch, k_{||}} \delta(\omega - \text{Re}(k_{||})) \tag{4}$$

where the first summation index is running over the branches  $\omega(\mathbf{k})$  computed by using Eq. 4.

**Results**

We performed a study of the dependence of the DOS with the filling factor, for a hexagonal lattice. Two ways for changing the filling factor were taken into account: (a) the lattice parameter was changed, while the radius of the profile function (R) was maintained constant; (b) the radius of the profile function (R) was changed for a given value of the lattice parameter. For all calculation the height of the profile function, H, was maintained constant:  $H=0.4$ . The results for the first set of calculations are summarised in figure 2, and those for the second set are given in figure 3. The parameters used for the calculations are also indicated. The value of the band gap was  $\Delta E = 0.260$  eV (figure 3 left) and  $\Delta E = 0.275$  eV (Figure 3 right). The results are in good agreement with the results of Maradudin and Kretschman, showing that our implementation is correct.

The existence of a band gap due to the presence of nanostructures on the silver surface is proven theoretically. The position and the parameters of the band gaps depend both on lattice parameters and the shape of the profile function as shown in Figures 2 and 3.

A future application of these results will be to check, by experimental methods, the connection between the theoretical DOS and the SERS spectra on the nanostructured surfaces, as suggested by Gaponenko [6]. According to its studies, a connection between the peaks of the SPP's DOS and the SERS scattering amplitude must occur on nanostructured surfaces.

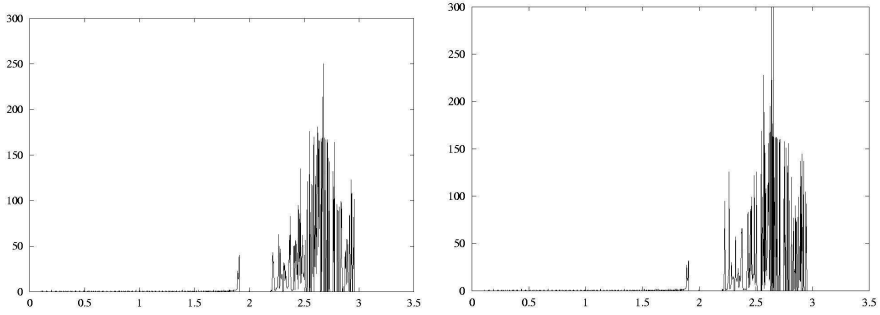


**Fig. 2.** The DOS for several lattice parameters, a. The numerical values of the lattice parameters are  $a=0.19$  nm (left) and  $a=0.2$  nm (right).  $R=0.07$ .

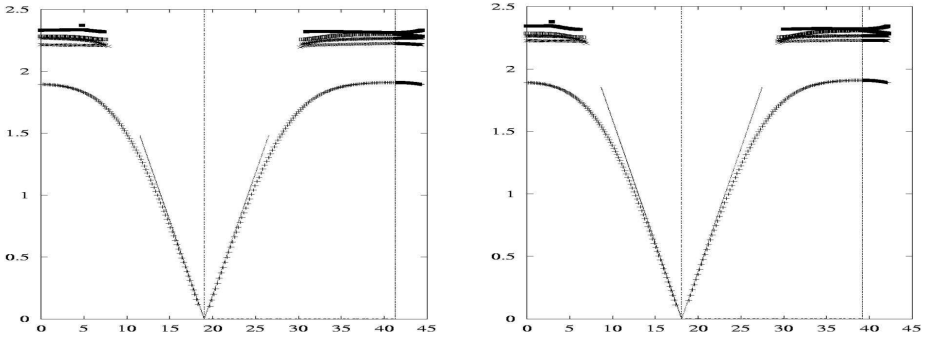


**Fig. 3.** The band structure of the SPP's for the DOS given in Figure 2.

### Conclusion

We implemented a new and efficient algorithm that allows us to compute the density of states for the surface plasmon polaritons at the metal-vacuum interface. The method is nonperturbative and has a good numerical accuracy. Our simulations show clearly the existence and the origin of the band gap that occurs into the SPP's spectra on nanostructured surfaces.

### REFERENCES

1. J. D. Joannopoulos, P. R. Villeneuve, S. Fan, *Nature* **386**, 143 (1997).
2. P. C. Chaumet, A. Rahmani, G. W. Bryant, *Phys. Rev. B*, **67** 165404 (2003).
3. T. Sondergaard, S. I. Bolhevoinyi, *Phys. Rev. B*, **67** 165405 (2003).
4. M. Kretschmann, A.A. Maradudin, *Phys. Rev. B*, **66**, 245408 (2002).
5. G. C. Brown, V. Celli, M. Haller, A. Marvin, *Surf. Sci.* **136**, 381 (1984).
6. S. V. Gaponenko, *Phys. Rev. B*, **65** 140303 (2002).

## INVESTIGATIONS OF THE PENICILIN - $\beta$ -CYCLODEXTRINE COMPLEX BY SEMIEMPIRICAL METHODS

**C. I. MORARI<sup>1</sup>, C. IONESCU<sup>2</sup>**

<sup>1</sup> National Institute for Research and Development of Isotopic and Molecular Technologies, R-3400 Cluj-Napoca, P.O. 5, Box 700, Romania

<sup>2</sup> I. Hatieganu University of Medicine and Pharmacy, Faculty of Pharmacy, Dept. of Biochemistry and Clinical laboratory, R-3400, Cluj-Napoca, Romania

**ABSTRACT.** Two simulation of the  $\beta$  - CD penicilin docking complex are presented. The calculations were performed at semiempirical level (PM3 and AM1). The values of binding energies of the complexes and the MOPAC charge analysis are discussed for both models.

### Introduction

Penicillin V is a narrow spectrum, b-lactamase-labile antibiotic. Still, being acid-stable (unlike penicillin G, for instance) it can be orally given, consequently providing a better compliance of the patients. The aim of the present study is to design a new orally form of administration for penicillin V with enhanced stability to b-lactamases; this is consequent with the fact that resistance of bacteria to b- lactam antibiotics may be associated with enzymes termed b-lactamases. Susceptible penicillins are converted to the corresponding penicilloic acid which is inactive. On the other hand, alterations in the molecule (by substitution) can produce penicillins with changes in microbiological and/or pharmacological properties. Our idea is to complex the penicillin with  $\beta$ -cyclodextrin, a modern and more and more used vehicle for drugs from different classes. It has been demonstrated that cyclodextrins may improve absorption, stability and bioavailability.

Obtaining a good simulation of the processes involving the interaction between a drug molecule and a cyclodextrin represents a difficult task. Among the difficulties involved by these calculations the size of the system and the presence of hydrogen bonds are to be mentioned. In order to overcome these problems and still to keep a good level of accuracy, we performed a study of the docking process of the peniciline into beta - CD by using the semiempirical PM3 and AM1 methods. Our aim was to give a numerical simulation of the process.

The steps of the simulations were: (i) the geometry for the peniciline was optimized; (ii) the complex  $\beta$ -CD - peniciline was set up using the MOLDEN package; (iii) the equilibrium geometry and the binding energy were computed. All the calculations were performed using the GAMESS package. The binding energies and the Mopac charges are reported. Altogether, these results allow us to draw valuable conclusions about the nature and the strength of the forces into the complex.

### Computational method

The molecular modeling of the host - guest interaction by semiempirical methods was performed in three steps:

(i) The Z matrices for the equilibrium structures of CD and penicilin were builded up. The structure  $\beta$  - CD was taken from Cambridge Structural Database [1]. We considered that this structure changes very little during the complexation process. As a consequence of this approach, no further theoretical optimization were performed on these structures. The initial structure of penicilin was builded up using the Hyperchem 5 program. This initial structure was optimized at ab initio level by using the PM3 approach; for all calculations the GAMESS package was used [3]. The resulting structure of penicilin is depicted in Figure 1.

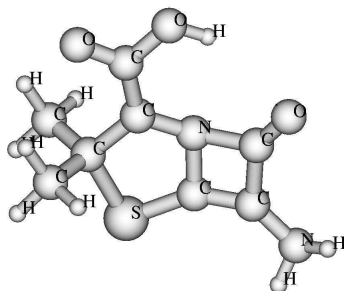


**Fig. 1.** Molecular structure of penicilin

(ii) The optimization strategy consisted in keeping frozen all the internal coordinates of the CD, while the relative orientation CD - penicilin and the internal geometry of the penicilin molecule were optimized. The semiempirical methods PM3 and AM1 were used to this end [4].

### Results

Table 1 summarize the results of Mopac charge analysis [4] of the complex CD - penicilin for different computational models. The binding energy for the complex are also given in eV. The small value of the Mopac charge acquired by penicillin shows that the nature of the binding interaction is probably a Van der Waals - like interaction. The binding energy is sufficiently large to enshure the stability of the complex at the room temperature ( $k_B T = 0.026$  eV at room temperature).

**Table 1**

**Binding energy of the complex and the sum of the total Mopac charges over the atoms of penicilin for different computational models (PM3 and AM1)**

Computational model	Binding energy [eV]	Mopac charge of penicilin
AM1	0.20	-0.0018
PM3	0.46	-0.006

The resulting equilibrium PM3 and AM1 geometries are given in Figures 3 and 4.

It can be seen that in the complex the penicilin lies close to the symmetry axis of the CD molecule, for both computational models. A possible explanation of this behavior is that the long range forces are dominant into the complex. This situation leads to a complex that follows the symmetry of the CD molecule since at large distance the binding forces appear to be averaged.

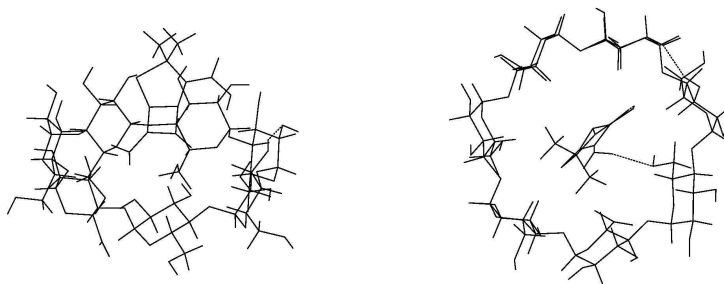


**Fig. 3.** Equilibrium geometries, PM3 level for  $\beta$ -CD + penicilin complex. Left: lateral view. Right: top view.

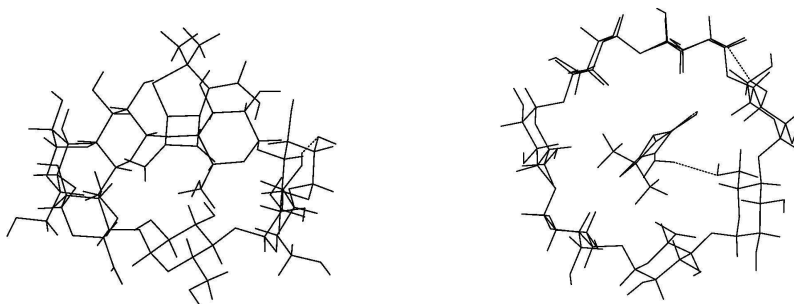


**Fig. 4.** Equilibrium geometries, AM1 level for  $\beta$ -CD + penicillin complex. Left: lateral view. Right: top view.

### Conclusion

A theoretical investigation of the stability of the  $\beta$ -CD + penicillin complex was performed. Semiempirical PM3 and AM1 methods were employed to investigate the nature of the interaction inside the complex. The binding energies are 10-20 times larger than the thermal energy ( $k_B T = 0.026$  eV at room temperature). These values suggest that the complex is stable at room temperature. The Mopac population analysis shows that the charge transfer plays a negligible role in the docking process. Using the geometry of the system we propose as the main contribution to the binding forces of the system the long range components of the intermolecular potential.

### REFERENCES

1. Cambridge Structural Database and Cambridge Structural Database System, Version 5.18, October 1999, Cambridge Crystallographic Data Centre, University Chemical Laboratory, Cambridge, England.
2. J.-P. Blaudeau, M. P. McGrath, L. A. Curtiss, L. Radom *J. Chem. Phys.* **107**, 5016-5021 (1997)
3. M. W. Schmidt, K. K. Baldrige, J. A. Boatz, S. T. Elbert, M. S. Gordon, J. H. Jensen, S. Koseki, N. Matsunaga, K. A. Nguyen, S. J. Su, T. L. Windus, M. Dupuis, J. A. Montgomery, *J. Comput. Chem.*, **14** 1347-1363 (1993)
4. J. J. P. Stewart, *J. Computer-Aided Molecular Design* **4**, 1-105 (1990)

## ALUMINA BASED COMPOSITE MATERIAL FOR CATALYTIC PURPOSES

**ANA-MARIA KASZONI PRICOP<sup>1</sup>, ELISABETH-JEANNE POPOVICI<sup>1</sup>,  
DORU ROIBAN<sup>1</sup>, TRAIAN URSALEŞ<sup>1</sup>, RODICA GRECU<sup>1</sup> and EMIL INDREA<sup>2</sup>**

<sup>1</sup>*“Raluca Ripan” Institute for Research in Chemistry, 30 Fantanele, 3400 Cluj-Napoca, Romania; e-mail: kaszoni@icrr.cj.edu.ro*

<sup>2</sup>*National Institute for R&D of Isotopic & Molecular Technology 3400 – Cluj-Napoca, P.O. Box 700, Romania*

**ABSTRACT.** Alumina based composite material could be used as porous absorbing layer for coatings on ceramic or metallic substrates in order to manufacture the catalytic supports. The paper presents some of our results referring to the preparation and characterisation of alumina hydrate (boehmite) that are to be used as binder for the preparation of alumina coatings on metallic substrates. Thermal analysis, X-ray diffraction and FTIR investigation were used to characterise the prepared alumina samples.

**Key words:** boehmite, alumina, catalysts, support.

### INTRODUCTION

Alumina-based composite materials are generally used as catalytic substrate in order to increase the surface area and the mechanical resistance of catalysts. Alumina-based compositions could be also used as coatings on ceramic or metallic substrate for the manufacture of honeycomb type-catalysts that are largely used for medium protection.

In order to manufacture a catalytic support with metallic skeleton (CSMS), a study was initiated referring to the formation of alumina coatings on metallic substrate (ACOMS). ACOMS could be prepared from suspensions containing alumina (porous material), boehmite (binder) and water (dispersing medium). Crystalline structure, particle morphology and size and hydration degrees could influence the binding ability of boehmite and as the result, the ACOMS adherence. The boehmite quality is extremely sensitive to the synthesis conditions [1-3].

The paper presents some of our results referring to the preparation and characterisation of boehmite (alumina hydrate) that is to be used for the manufacture of CSMS.

### EXPERIMENTAL PART

Samples of alumina hydrates were prepared by adding diluted nitric acid to sodium aluminate solutions obtained by the reaction of either aluminium powder or aluminium nitrate with sodium hydroxide solution. The nitric acid solution was slowly added, under continuous agitation, until the medium pH was 9. The separated gel was centrifuged, washed and dried at 110°C for 24 hours. The dried gel was washed with ammoniac aqueous solution, dried and then dispersed into iso-propanol.

Alumina hydrate samples were investigated by thermal analysis (Paulik-Erdely OD-102 Derivatograf; heating rate = 6°C/min), X-ray diffraction (DRON 3M Diffractometer; CuK<sub>α</sub> radiation) and FT-IR spectroscopy (JASCO-610 Spectrophotometer; KBr disks).

## RESULTS AND DISCUSSION

Two series of alumina hydrate samples ( $\text{Al}_2\text{O}_3 \cdot x\text{H}_2\text{O}$ ) were prepared by the acidulation of some diluted sodium aluminate solutions. The aluminate solutions were prepared either from aluminium powder, or from aluminium nitrate. The two synthesis routes that are schematically presented below, generate two alumina hydrates types possessing different physical characteristics.

- Sample code **B<sub>2</sub>**                       $\text{Al}(\text{NO}_3)_3 \cdot 9\text{H}_2\text{O} \rightarrow \text{Na}[\text{Al}(\text{OH})_4] \rightarrow \text{Al}_2\text{O}_3 \cdot x\text{H}_2\text{O}$
- Sample code **B<sub>3</sub>**                       $\text{Al} \rightarrow \text{Na}[\text{Al}(\text{OH})_4] \rightarrow \text{Al}_2\text{O}_3 \cdot x\text{H}_2\text{O}$

The thermal analysis illustrates the thermal behaviour of the two-alumina hydrate series. The thermogravimetric (TG), differential thermogravimetric (DTG) and differential thermal analysis (DTA) curves of the samples are depicted in **figure 1**.

The experimental thermal weight losses of the two samples, 33.5 % for **B<sub>2</sub>** and 31.2 % for **B<sub>3</sub>** are quite equal and almost twice the theoretical value (15%) of the anhydrous boehmite  $\text{AlO}(\text{OH})$ . Visible differences do appear between the thermal curve shape and the position of the characteristic endothermic peaks. The **B<sub>2</sub>** sample shows a strong endothermic peak at about 300°C whereas the **B<sub>3</sub>** sample presents a relatively weaker one at about 160°C. The observed endothermic effect and the corresponding weight variation are correlated with the remove of chemical and physical bonded water, respectively. One can presume that **B<sub>2</sub>** correspond to aluminium hydroxide (considered alumina trihydrate  $\text{Al}_2\text{O}_3 \cdot 3\text{H}_2\text{O}$ ) whereas **B<sub>3</sub>** is boehmite (considered alumina monohydrate  $\text{Al}_2\text{O}_3 \cdot \text{H}_2\text{O}$ ). Large amounts of adsorbed water are present in both sample series.

The FTIR spectra of the two series of alumina hydrate put also in evidences the different physical characteristics of the samples (**figure 2**).

The FTIR spectra suggest that **B<sub>2</sub>** sample is well-crystallised as compared with **B<sub>3</sub>** sample. The structure of the spectrum in the high frequencies domain suggests the simultaneous presence of adsorbed water, crystallisation water and free OH groups. For the **B<sub>2</sub>** series, the pair of bands at 980 and 1020  $\text{cm}^{-1}$  could be associated with the characteristic vibrations of the Al-OH bonding. The wide absorption band with maximum at 3470.28  $\text{cm}^{-1}$  is due to the vibration of  $\text{H}_2\text{O}$  molecules, which take part in hydrogen bonding with  $\text{Al}_2\text{O}_3$  surface [4].

In the case of the **B<sub>3</sub>**, an intense broad band at 3426.4  $\text{cm}^{-1}$  was observed. This suggests a high content of unstable  $\text{H}_2\text{O}$  [4]. Al-O-H bending mode is expected in the region 900-1100  $\text{cm}^{-1}$  [5].

The FTIR analysis proved the existence of two types of alumina hydrates. **B<sub>2</sub>** sample seems to possess an  $\text{Al}_2\text{O}_3 \cdot 3\text{H}_2\text{O}$  structure whereas **B<sub>3</sub>** sample an  $\text{AlO}(\text{OH})$  (boehmite) structure. This supposition is confirmed by the XRD patterns (**figure 3**). Sample **B<sub>2</sub>** possesses high cristallinity degree and the spectrum corresponds to aluminium hydroxide with monoclinic structure of bayerite type. In spite of the fact that **B<sub>3</sub>** show very low cristallinity, the bands of aluminium oxy-hydroxide with orthorhombic structure of boehmite type could be noticed. In fact, the reflection lines at 13.6 (6.5 Å) and 14.5 (6.1 Å) degree suggest that the material is a mixture of boehmite and pseudoboehmite. The latter one is a water-rich variety of boehmite that can be XRD recognised from the shift of the (020) reflection from 6.1 Å towards higher values [1, 2].

## CONCLUSIONS

The alumina hydrate samples could be classified in two basic categories that are easily recognised by their FTIR spectra, thermal analysis curves and XRD patterns. In our experimental conditions, the aluminium → sodium aluminate → alumina hydrate synthesis route proved to be appropriate for the synthesis of boehmite for the formation of alumina coatings on metallic substrate (ACOMS).

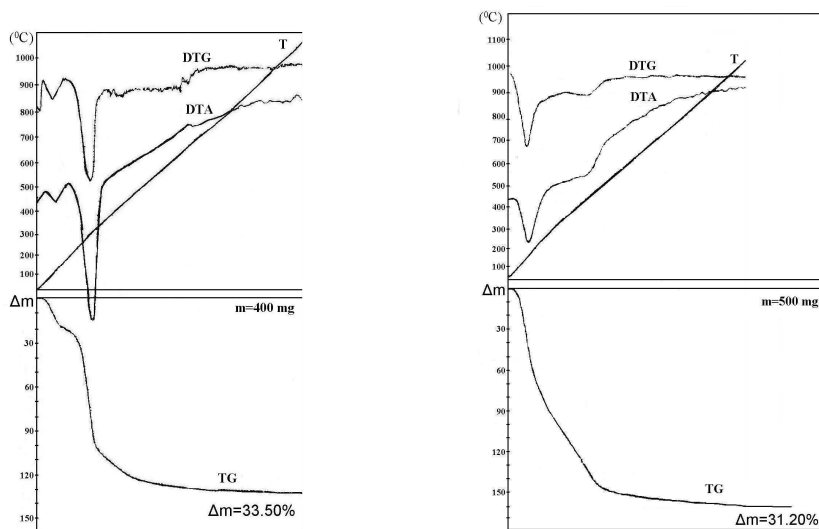


**Fig. 1.** The thermal analysis curves of the two type of alumina hydrate namely **B<sub>2</sub>** series (left) and **B<sub>3</sub>** series (right)

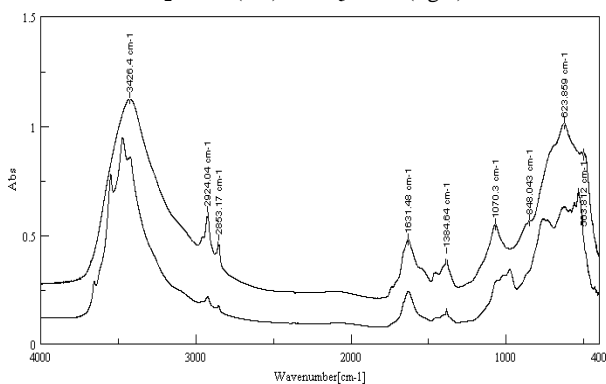


**Fig. 2.** FTIR spectra of the two type of alumina hydrate namely **B<sub>2</sub>** (up) and **B<sub>3</sub>** (down)

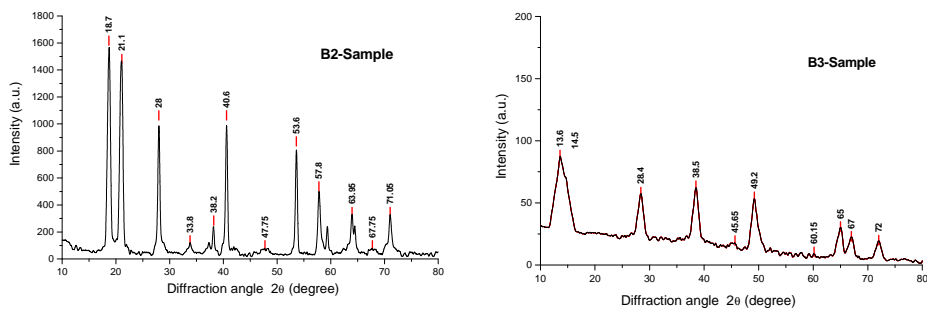


**Fig. 3.** XRD spectra of the two type of alumina hydrate namely **B<sub>2</sub>** (left) and **B<sub>3</sub>** (right)



**Acknowledgements:**

The work was supported by MATNANTECH National Research Program, under contract no. 109/2002.

**REFERENCES**

1. Decker JR Lewis, Oberlander Richard, “*Alumina dispersion behaviour*”, US 4360449, **1982**, 1-8p;
2. Sanchez-Moises, Ernest Michael, Laine Norman, “*Spheroidal alumina particles and catalysts employing the particles as a support*”, US 4390456, **1983**, 1-25p.
3. Ohashi Yuji, Segawa Hideo, Tsukada Takayuki, “*Method of manufacturing pseudo-boehmit*”, US6429172, **2000**, 1-15p;
4. Chuiko, A. A., Kruglitskii, N.N. Shimanskii, A. P., “*Chemistry of the Surface of Finally Divided Aluminium Oxide studied by an IR spectroscopic method*”, Zhurnal Fizicheskoi Qhimii, **1975**, 49 (2), 435-439;
5. Krishna Priya, G. Padmaja P., Warriar K.G.K., “*Dehydroxylation and high temperature phase formation in sol-gel boehmite characterized by Fourier transformed infrared spectroscopy*”, J. Mater. Sci. Letters, **1997**, 16, 1584-1587.

## SYNTHESIS AND CHARACTERISATION OF SOME NEW CALIX[n]ARENE DERIVATIVES

**TRAIAN-NICOLAE URSALES<sup>1</sup>, ELISABETH-JEANNE POPOVICI<sup>1</sup>, IOAN SILAGHI-DUMITRESCU<sup>2</sup>, NICOLAE POPOVICI<sup>1</sup> and ADINA URSALES<sup>1</sup>**

<sup>1</sup> "Raluca Ripan" Institute for Research in Chemistry, Fantanele 30, PO Box 702, R- 3400 Cluj-Napoca; e-mail: TUrsales@email.ro

<sup>2</sup> Faculty of Chemistry and Chemical Engineering, Babes-Bolyai University, R-3400 Cluj-Napoca, Romania

**ABSTRACT.** The synthesis of new calix[n]arene derivatives was attempted by selective alkylation with dichlorophenylphosphin oxide and 2-butenyl bromide, in the presence of sodium hydride as a base. The results of FT-IR, <sup>1</sup>H-NMR and <sup>31</sup>P-NMR spectroscopic investigations are in good agreement with the expected structure and purity of such prepared material.

**Keywords:** calixarene, dichlorophenylphosphin oxide, E-2-butenyl bromide, alkylation.

### Introduction

Calix[n]arene are cyclic oligomers of phenol-formaldehyde condensates. This class of compounds has generated a particular interest because of their natural basket-shaped cavities associated with versatile recognition properties towards ions and neutral molecules as well<sup>1-3</sup>. By selective functionalisation at the OH phenolic groups (lower rim) and/or in the para positions of the phenol ring (upper rim), specific receptors for cations<sup>4</sup>, anions<sup>5</sup> and neutral molecules<sup>6</sup> could be prepared.

With the purpose to obtain some new calixarenes derivatives with increased ability to extract lanthanide ions, the selective alkylation of p-tertbutyl calix[n]arenes with dichlorophenylphosphin oxide and 2-butenyl bromide was attempted. The paper presents our results referring to the synthesis and characterisation of some new compounds from this class.

### Experimental part

The calixarene derivatives were prepared in the presence of sodium hydride (NaH), by the reaction between calix[4], calix[6], and calix[8]arenes with E-2-butenyl bromide (crotyl bromide) and dichloro-phenylphosphin oxide, in acetonitril or dimethylformamide- tetrahydrofuran medium. The syntheses were performed at reflux, under inert atmosphere. FT-IR (KBr pellets; JASCO-615 Spectrometer), <sup>1</sup>H-NMR (tetramethylsilane; 80MHz Bruker Spectrometer) and <sup>31</sup>P-NMR (phosphoric acid; 200MHz Bruker Spectrometer) investigation methods were used in order to check out the purity of as prepared products.

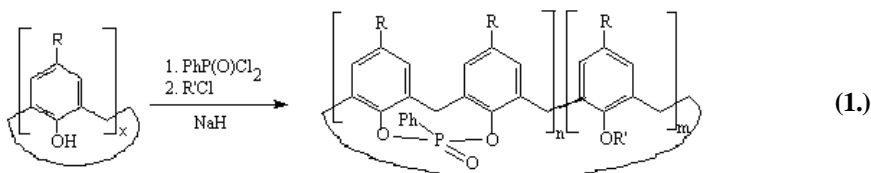
### Results and discussions

The starting calixarenes were prepared by adapting the synthesis method described in the literature<sup>7-9</sup>. The simultaneous alkylation of calixarenes with dichlorophenylphosphin oxide and crotyl bromide give rise to some derivatives that possess two types, of substituting groups at the lower rim (**reaction 1**).

Elemental analysis, <sup>1</sup>H-NMR, <sup>31</sup>P-NMR and FT-IR (**figure 1-3**) investigations confirmed the formation of the new calix[n]arenes derivatives. The main characteristics of the new products are as follows:

#### Compound I

*Elemental analysis:* MW=862, calculated for C<sub>58</sub>H<sub>71</sub>O<sub>4</sub>P; C= 79.02 %; H= 8.49%, P= 4.23 % found; C= 80.74 %; H= 8.24%, P= 3.59% calculated.



**I.** R = t-Bu; R' = Crotyl; n = 1; m = 2; **II.** R = t-Bu; R' = Crotyl; n = 1; m = 4; **III.** R = t-Bu; R' = Crotyl; n = 1; m = 6

*FT-IR:* (KBr,  $\text{cm}^{-1}$ ):  $\nu_{\text{CH}=\text{CH}}$ : 3023.84 and 965.68  $\text{cm}^{-1}$ ;  $\nu_{\text{P}=\text{O}}$ : 1201.43  $\text{cm}^{-1}$ ;  $\nu_{\text{P-O-C}}$ : 970.00  $\text{cm}^{-1}$ ;  $\nu_{\text{P-C}}$ : 694.25  $\text{cm}^{-1}$ ;  $^1\text{H-NMR}$  ( $\delta_{\text{ppm}}$ ,  $\text{CDCl}_3$ , ppm): 6.75-7.24(m, 13H,  $\text{C}_6\text{H}_2$  and  $\text{C}_6\text{H}_5$ ); 5.60-5.80 (m, 4H,  $\text{CH}=\text{CH}$ ); 4.23-4.42(m, 8H,  $\text{ArCH}_2\text{Ar}$ ); 2.86-3.40(m, 4H,  $-\text{OCH}_2$ ); 0.69-1.78(m, 42H,  $=\text{CH}-\text{CH}_3$  and tBu).

$^{31}\text{P-NMR}$  ( $\delta_{\text{ppm}}$ ,  $\text{CDCl}_3$ , ppm): 22.85; and -10.42 (2 s, 1P).

#### Compound II

*Elemental analysis:* MW=1294, calculated for  $\text{C}_{88}\text{H}_{111}\text{O}_4\text{P}$ ; C= 80.01 %; H= 8.69%, P= 3.21 % found; C= 81.61 %; H= 8.57%, P= 2.39% calculated.

*FT-IR:* (KBr,  $\text{cm}^{-1}$ ):  $\nu_{\text{CH}=\text{CH}}$ : 3021.91 and 966.64  $\text{cm}^{-1}$ ;  $\nu_{\text{P}=\text{O}}$ : 1203.36  $\text{cm}^{-1}$ ;  $\nu_{\text{P-O-C}}$ : 955.64  $\text{cm}^{-1}$ ;  $\nu_{\text{P-C}}$ : 694.98  $\text{cm}^{-1}$ ;  $^1\text{H-NMR}$  ( $\delta_{\text{ppm}}$ ,  $\text{CDCl}_3$ , ppm): 6.93-7.26(m, 17H,  $\text{C}_6\text{H}_2$  and  $\text{C}_6\text{H}_5$ ); 5.62(m, 8H,  $\text{CH}=\text{CH}$ ); 3.86(m, 12H,  $\text{ArCH}_2\text{Ar}$ ); 1.85(m, 8H,  $-\text{OCH}_2$ ); 1.55(d, 8H,  $^3\text{J}_{\text{HH}}=7, 12\text{Hz}$ ); 1.26(s, 54H, tBu).

$^{31}\text{P-NMR}$  ( $\delta_{\text{ppm}}$ ,  $\text{CDCl}_3$ , ppm): 22.62 (s, 1P).

#### Compound III

*Elemental analysis:* MW=1726, calculated for  $\text{C}_{118}\text{H}_{151}\text{O}_4\text{P}$ ; C= 81.79 %; H= 8.92%, P= 2.29 % found; C= 82.04 %; H= 8.75%, P= 1.79% calculated.

*FT-IR:* (KBr,  $\text{cm}^{-1}$ ):  $\nu_{\text{CH}=\text{CH}}$ : 3023.84 and 968.57  $\text{cm}^{-1}$ ;  $\nu_{\text{P}=\text{O}}$ : 1204.81  $\text{cm}^{-1}$ ;  $\nu_{\text{P-O-C}}$ : 947.84  $\text{cm}^{-1}$ ;  $\nu_{\text{P-C}}$ : 693.28  $\text{cm}^{-1}$ ;

$^1\text{H-NMR}$  ( $\delta_{\text{ppm}}$ ,  $\text{CDCl}_3$ , ppm): 7.49(m, 5H,  $\text{C}_6\text{H}_5$ ); 6.94(s, 16H,  $\text{C}_6\text{H}_2$ ); 5.50(m, 12H,  $\text{CH}=\text{CH}$ ); 4.08(d, 8H,  $\text{ArCH}_2\text{Ar}$ ,  $^3\text{J}_{\text{HH}}=6, 9\text{Hz}$ ); 3.72(d, 8H,  $\text{ArCH}_2\text{Ar}$ ,  $^3\text{J}_{\text{HH}}=7, 08\text{Hz}$ ); 2.70(m, 12H,  $-\text{OCH}_2$ ); 1.45(d, 18H,  $=\text{CH}-\text{CH}_3$ ,  $^3\text{J}_{\text{HH}}=6, 0\text{Hz}$ ); 1.25(s, 72H, tBu).

$^{31}\text{P-NMR}$  ( $\delta_{\text{ppm}}$ ,  $\text{CDCl}_3$ , ppm): 21.84 (1s, 1P).

In the  $^1\text{H-NMR}$  spectra of the parent calixarenes, the OH group signals appear at 9.5-10.2 ppm. The disappearance of the signals in the spectra of the new derivatives confirmed the full functionalisation of the starting calixarenes.

New signals at 5.5-5.8 ppm appeared, which were correlated with the presence of the protons from the  $\text{CH}=\text{CH}$  groups of the crotyl groups. The protons of  $-\text{OCH}_2$  and  $=\text{CH}-\text{CH}_3$  groups give signal at ~ 1.8-2.8 ppm and near the tert-butyl protons, respectively. The protons from the phenylphosphinoyl bridge give broad signals in the aromatic zone of the calixarene skeleton (6.7-7.5 ppm). The phosphorus presence in the new compounds was put in evidence by the specific signals (21.84-22.85 ppm) from the  $^{31}\text{P-NMR}$  spectra.

FTIR spectra revealed the disappearance of the OH groups from the parent calixarenes. The specific OH vibrations of the p-tert-butylcalix[4]arene, p-tert-butylcalix[6]arene and p-tert-butylcalix[8]arene (3173, 3150 or 3140  $\text{cm}^{-1}$ , correspondingly) could not be noticed in the spectra of the compound I, II or III. New vibration bands for the substituting groups could be observed, namely: 1201.43  $\text{cm}^{-1}$  (P=O), 970.00  $\text{cm}^{-1}$  (P-O-C) and 3023.84 and 965.68  $\text{cm}^{-1}$  (crotyl groups) for compound I; 1203  $\text{cm}^{-1}$  (P=O), 956  $\text{cm}^{-1}$  (P-O-C) and 3022  $\text{cm}^{-1}$  and 967  $\text{cm}^{-1}$  (crotyl groups) for compound II and 1201  $\text{cm}^{-1}$  (P=O), 970  $\text{cm}^{-1}$  (P-O-C), and 3024  $\text{cm}^{-1}$  and 966 (crotyl groups) for compound III.

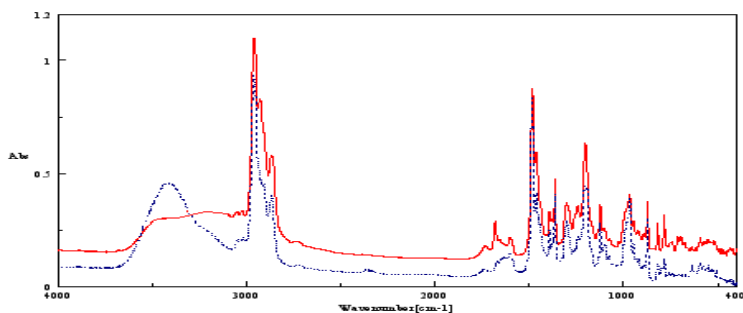


**Fig. 1.** FT-IR spectra of mono(phenylphosphinoxide)-bis(2-butenyl)-p-tertbutylcalix[4]arene (I) (straight line) as compared with the original p-tertbutylcalix[4]arene (dashed line).

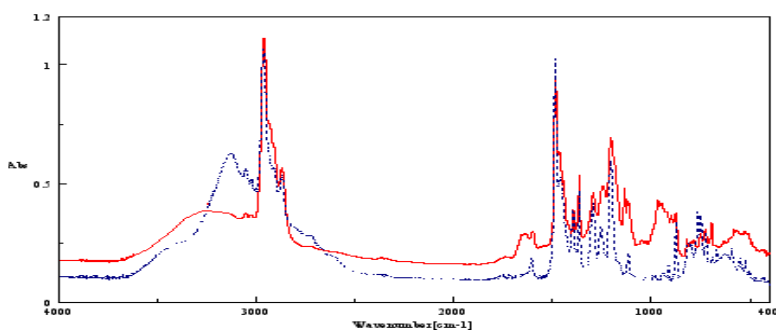


**Fig. 2.** Infrared spectra of mono(phenylphosphinoxide)-tetra(2-butenyl)-p-tertbutylcalix[6]arene (II) (straight line) as compared with the original p-tertbutylcalix[6]arene (dashed line).

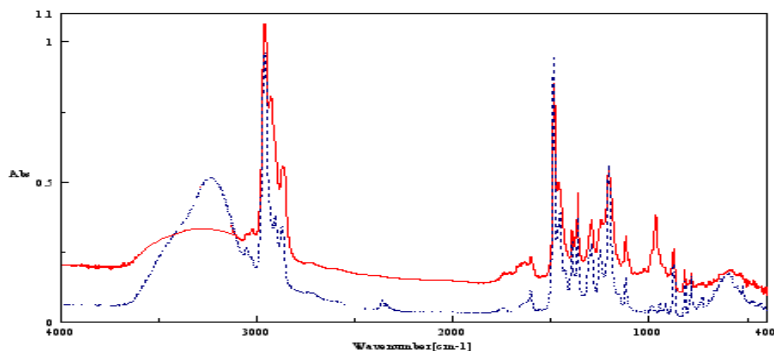


**Fig. 3.** Infrared spectra of mono(phenylphosphinoxide)-hexa(2-butenyl)-p-tertbutylcalix[8]arene (III) (straight line) as compared with the original p-tertbutylcalix[8]arene (dashed line).

### Conclusions

The spectroscopic investigations confirmed the formation of calixarenes derivatives containing one phenylphosphinoxide bridge group and 2, 4 or 6 crotyl groups, respectively. These new compounds, which were not previously described in the literature, possess large utilisation potential. The presence of “p” electrons of the oxygen (P=O group) and  $\pi$  electrons (crotyl group) could increase the ability of the new calixarene derivatives to extract rare-earth ions.

**Acknowledgements:**

The work was supported by CERES National Research Program, under contract no. 42/2001.

**REFERENCES**

1. C. D. Gutsche, "Calixarenes revisited", Royal Society of Chemistry, London, **1998**, p. 3.
2. R. Ungaro, "Calixarenes in Action", Imperial College Press, London, **2000**, p. 1.
3. V. Böhmer, *Calixarene-Makrocyclen mit (fast) unbegrenzten Möglichkeiten*, *Angew. Chem., Int. Ed. Engl.*, **1995**, *34*, p. 713.
4. V. W. Yam, K. K. W. Lo, "Recent advances in utilization of transition metal complexes and lanthanides as diagnostic tools", *Coordination Chem. Reviews*, **1999**, *184*, p. 157.
5. E. M. Georgiev, N. Wolf, D. M. Roundhill, "Lower rim alkylammonium-substituted calix[4]arenes as  $\text{-proton-switchable-}$  extractants for chromate and dichromate anions", *Polyhedron*, **1997**, *16*, p. 1581.
6. L. J. Bauer, C. D. Gutsche, "Calixarenes 15. The formation of Complex of Calixarenes with Neutral Organic Molecules in Solution", *J. Am.Chem. Soc.*, **1985**, *107*, p. 6063.
7. C. D. Gutsche, M. Iqbal, "*P-tert-butylcalix[4]arene*", *Org.Synthesis*, **1989**, *68*, p. 234.
8. C.D.Gutsche, B. Dhawan, M. Leonis, D. Stewart, "*P-tert-butylcalix[6]arene*", *Org. Synthesis*, **1989**, *68*, p. 238.
9. J. H. Munch, C.D. Gutsche, "*P-tert-butylcalix[8]arene*", *Org. Synthesis*, **1989**, *68*, p. 243.

## MICROWAVE ASSISTED SOLVENT EXTRACTION OF SOME BIOACTIVE COMPOUNDS FROM *VACCINIUM MYRTILLUS* L. LEAVES

**SIMONA COBZAC<sup>1</sup>, OLAH NELI<sup>3</sup>, CARMEN BATTU<sup>1</sup>,  
S. GOCAN<sup>1</sup>, E. SURDUCAN<sup>2</sup>**

<sup>1</sup> Univ. Babeș-Bolyai, Facultatea de Chimie și Inginerie Chimică, Cluj-Napoca

<sup>2</sup> Nat. Inst. of R&D for Isotopic and Molec. Techn, POB 700, Cluj-Napoca, Romania

<sup>3</sup> SC PlantExtrakt SRL, Radaia, Romania

**ABSTRACT.** The *Vaccinium myrtillus* L. leaves are useful in curing different diseases due to its hipoglycemiant, diuretic and antibacterial action. This paper presents the identification and quantification of arbutine and flavonoids (caffeic acid, chlorogenic acid and hyperoside) from leaves extracts obtained in different conditions. Microwave extraction procedure was realised with different power, time and solvents compositions. The obtained results were compared to identify the changes in number of extracted compounds or the degradation of compounds. The quantitative content of arbutine and flavonoids were determined by TLC – photodensitometry using the calibration curve method. The results were compared to evaluating the extraction performance. The quality and quantity of bioactive compound is varying with extraction condition.

### Introduction

Extraction of bioactive compound from plant tissue is the most important step in the preparation of plant material for chromatographic analysis. The technique and solvents involved must assure a good (total) transfer of compounds from solid matrix to liquid matrix to obtain a representative, selective and pure extract. The main techniques used today are the Soxhlet extraction and the maceration. The last few years were introduced some modern techniques e.g. sonication, accelerated solvent extraction (ASE), pressurized solvent extraction (PSE), microwave-assisted extraction (MAE), and superfluid extraction (SFE) [1, 2]. The obtained extract can be analyzed using chromatographic techniques gas-liquid chromatography (GLC) for volatile compounds and HPLC and thin layer chromatography (TLC) for the other of compounds. Generally, because the drawbacks of HPLC, for routine plant extracts TLC is widely used. The condition of TLC analysis for plants extracts are established considering the contained active compounds [3-8].

### Experimental

The plant extracts was obtained using three different extraction techniques: Soxhlet extraction, hot solvent extraction and microwave assisted extraction. *Bioactive compound extraction.* The dried *Vaccinium myrtillus* (Fares Bio Vital, București) leaves were grinded using a blender and seaved using the seave no. 2. The lipophilic compounds and chlorophile were Soxhlet-extracted with CCl<sub>4</sub>. Flavonoids and arbutin were extracted in three different ways with methanol. For each type of extraction techniques a quantity (2 gr) of epuised plant material were **weighed**.

*Extract A* – obtained after concentration the Soxhlet extract with a rotavapor and adjusting the final volume to 10 mL.

*Extract B* – were obtained by refluxing the plant material 30 min. with 25 mL methanol. After centrifugation the volume were reduced by rotavapor and than the final volume was bring up to 10 ml.

*Extract C* – the plant material was subjected two times to microwave extraction with 10 mL methanol (table 1). The unified methanolic extracts were evaporated using a rotavapor and than bring up to a final volume of 10 mL.

**Table 1.**

**Condition for microwave assisted extraction of *Vaccinium myrtillus* leaves.**

Power factor	Time (sec)	Temperature range ( <sup>o</sup> C)
9x80	240	32-50
9x80	240	50-75,3

Metanolic solutions (1mL) of arbutine, caffeic acid, chlorogenic acid and hyperoside were also subjected to a microwave treatment to determine if the microwave radiations induce changing in molecular structure.

*TLC separation, identification and quantitation conditions* TLC separation was performed using Kieselgel 60 F<sub>254</sub> plates (Merck) and a solvent mixture of ethyl acetat - methanol – water (77:13:10, v/v) as mobile phase. The migration distance was 12 cm. The samples (A, B and C Extracts) and the reference solutions (caffeic acid-1.05 mg/mL, chlorogenic acid-0.97 mg/mL, arbutin-5 mg/mL and hyperosid-1.03 mg/mL) were manual applied as bands (20µL) and respective as spots (10µL) using a Hamilton microsyringe. For quantitation were applied 20 µL spots from reference solution with different concentration. After development the plates were dried in a gentile air stream and the obtained chromatograms were inspected in UV light (254 nm) and after spraying with NTS + PEG 400 at 366 nm. The photodensitograms were obtained by scanning the plates at 254 nm in reflection mode with a Desaga CD 60 apparatus. The in-situ UV-Vis spectra were obtained in the 200 – 500 nm range. The total flavonoids was also determined using the aluminum chloride spectrophotometric method. The absorbance were determined after 15 min. at 430nm. The calibration curve was achieved using rutin as reference compound.

### Results and discussion

In figure 1 are presented the chromatograms of A, B and C Extracts near the reference solution at 254 and 366 nm and in figure 2 the photodensitograms at 245nm. In the table 2 are presented the equations for calibration curve for the analised compounds and for rutin.

The analysis of the reference solution subjected to microwave treatment show no change in molecular structure. The results obtained after quantitative TLC determination for the analysed bioactive compound and for the flavonic total content are presented in table 3.

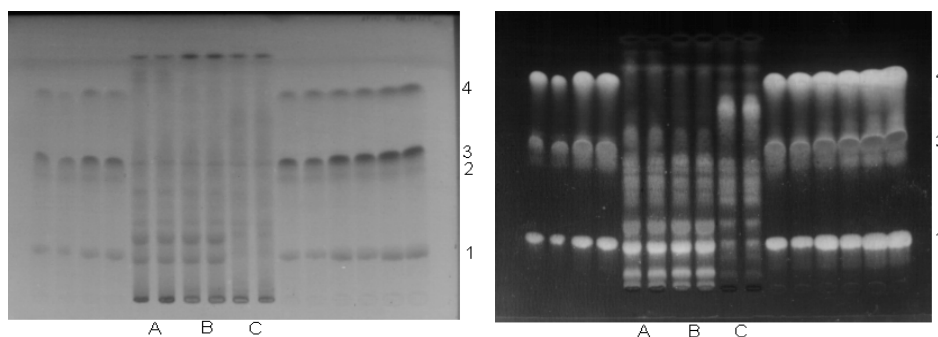


**Fig. 1.** The chromatograms for Soxhlet extract - A, refluxing extract -B, microwave extract -C and reference solution of chlorogenic acid (1), arbutin (2), hyperosid (3), caffeic acid (4) at 254 nm and 366 nm.

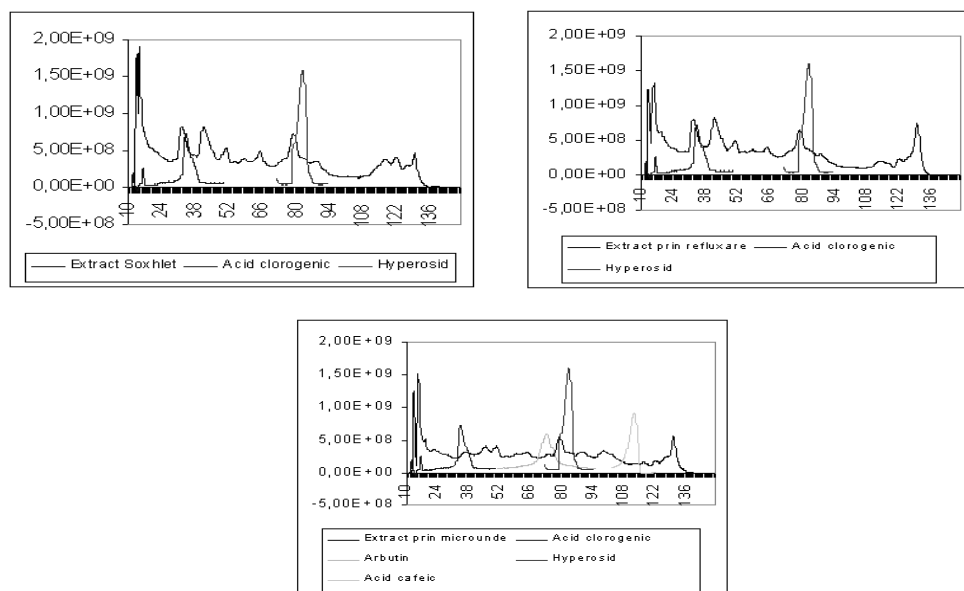


Fig. 2. The photodensitograms for A, B and C extracts overlapped on the reference solution (1, 2, 3,4) at 254 nm.

**R<sub>f</sub> values and calibration curve equation for the analyzed compound and rutin.**

Table 2.

Compound	R <sub>f</sub>	Calibration curve equation	r <sup>2</sup>
Chlorogenic acid	0.18	$Y=924.98(\pm 780.14)+6466.71(\pm 1772.41)X$	0.989
Caffeic acid	0.82	$Y=345.4(\pm 1445.11)+8290.98(\pm 3032.97)X$	0.981
Hyperosid	0.57	$Y=59.5(\pm 1224.09)+991.12(\pm 295.26)X$	0.987
Arbutin	0.49	$Y=676.65(\pm 1624.29)+12398.42(\pm 3490.08)X$	0.988
Rutin	---	$Y=0.06(\pm 0.12)+1.92(\pm 1.1)X$	0.982

**The determinate bioactive components concentration in the three different types of extracts.**

Table 3.

Sample	Concentration (mg/mL)				Total Flavonoids
	Chlorogenic acid	Caffeic acid	Hyperosid	Arbutin	
A	0.42	---	0.26	---	0.48
B	0.44	---	0.24	---	0.39
C	0.07	0.02	0.09	0.89	0.16

### Conclusions

The chromatograms presented in figure 1 and the results from table 4 show a great similarity between extract A (Soxhlet) and B (refluxing). The microwave extract differs very much from the previous two and can be observed a change in the quantity of extracted compounds (caffeic acid and arbutin). In the same time the microwave extraction is less efficient due to small quantity in total flavonoids. It is clear that the extraction technique have a great influence in the nature and quantity of extracted compound.



## BIBLIOGRAPHY

1. Sz. Nyiredy, K. Glowniak, *Planar Chromatography In Medicinal Plant Research*, Planar Chromatography, Ed.Sz.Nyiredy, Springer, Budapesta, 2001, 550.
2. J. Namiesnik, T. Goreki, *Sample Preparation For Chromatographic Analysis Of Plant Material*, J. P. C.-Modern TLC, **13** (2000), 404.
3. DAB, Ed X, Deutscher Apotheker Verelag, Stuttgart, 1991
4. HAB, Homeopatisches Arzneibuch, 2000, Deutscher Apotheker Verelag, Stuttgart, Govi Verlag, Pharmazeutischer Verlag, GmbH, Eschborn, 2000.
5. H. Wagner, S. Bladt, E. M. Zgainski, *Drogen Analyse, DC Analyse von Arzneidrogen*, Springer Verlag, Berlin, 1983.
6. M. Wichtel, *Teedrogen und Phytopharmaka*, 3 Auflage, Wissenschaftliche Verlag, Stuttgart, 1997.
7. S. Cobzac, G. Cimpan, N. Olah, S. Gocan, *The Quantitative Determination Of Rutin In Different Glycerinic Plant Extracts By SPE And TLC/Densitometry*, J. P. C.-Modern TLC, **12** (1999), 26
8. S. Gocan, S. Cobzac, *Determinarea Cantitativa A Hiperosidului Din Maceratul Glicerinic De Betula Verrucosa Prin CSS/Fotodensitometrare*, Revista de Chimie, **47** (1996), 54.

## UPTAKE OF URANYL IONS BY CHITOSAN AND CELLULOSE DERIVATIVES

MARGARETA BAKO<sup>1</sup>, SIMINA DREVE<sup>2</sup>, I. BRATU<sup>2</sup>, E. INDREA<sup>2</sup>

<sup>1</sup>*"Babes-Bolyai" University, Faculty of Physics, 1 Kogalniceanu st, Cluj-Napoca, Romania*

<sup>2</sup>*National R&D Institute of Isotopic and Molecular Technologies, P.O. Box 700, R-400293 Cluj-Napoca 5, Romania*

**ABSTRACT.** Deacetylated chitosan blends were prepared from natural chitin sources by chemical treatment. The structure was confirmed by chemical tests and infrared spectroscopy analysis. The uranyl sorption performances in comparison to the cellulose derivatives uranyl sorption properties were studied using the quantitative complexation method of the uranyl ions with Arsenazo III, followed by spectrophotometric analysis. The uptake of uranium (as uranyl ions) by chitosan, in comparison with other cellulose derivatives was determined and the sorption factors were calculated. The correlation between the sorption factors and the chitosan and cellulose derivatives structure obtained by infrared spectroscopy was established.

### Introduction

As part of continuing program of quantitative determinations of radionuclides in the environment [1,2], some new sorbents for uranium (VI), as uranyl ions, were studied.

Polysaccharides as cellulose and cellulose derivatives are convenient, natural and cheap chelating agents. Cellulose is a well known sorbent of natural origin for uranium (VI), in diluted effluents. The substitution of cellulose functional groups with mono-chloro-acetic-acid allows the synthesis of carboxy-methyl-cellulose (CMC) [3]. Chitin is a high molecular weight linear polymer of N-acetyl-D-glucosamine (N-acetyl-2-amino-2-glucopyranose) units linked by  $\beta$ -D bonds, a highly insoluble material resembling cellulose.

### Experimental

Natural chitosan was obtained by chemical treatment of chitinolytic biomaterials with 0,1 N HCl, followed by separation and deacetylation of the resulted chitin with 0,1 N NaOH, and by neutralisation, filtration and drying in normal conditions [4].

FT IR spectrum of the obtained chitin, see Fig. 1, was compared with the one mentioned elsewhere [5]. At present infrared studies of the uranyl biosorption by materials of biological origin are widely studied and described in the literature [6].

On going from chitin one obtains chitosan by a deacetylation process. This material was used in the present paper for the sorption of the uranyl ions.

FT IR spectra were obtained with an UR 20 Carl Zeiss spectrophotometer in the 4000 - 400  $\text{cm}^{-1}$  spectral range by using the well-known KBr pellet technique.

In order to find the sorption performances of chitosan, cellulose and its derivatives, 10 g of each sample was treated with 1000 ml of uranyl nitrate hexahydrate solution,  $(\text{UO}_2)(\text{NO}_3)_2 \times 6\text{H}_2\text{O}$ , Merck quality, this volume containing  $10^{-2}$  gU.

For the cellulose samples a parallel experiment was carried out on microcrystalline cellulose and, respectively, on amorphous cellulose.

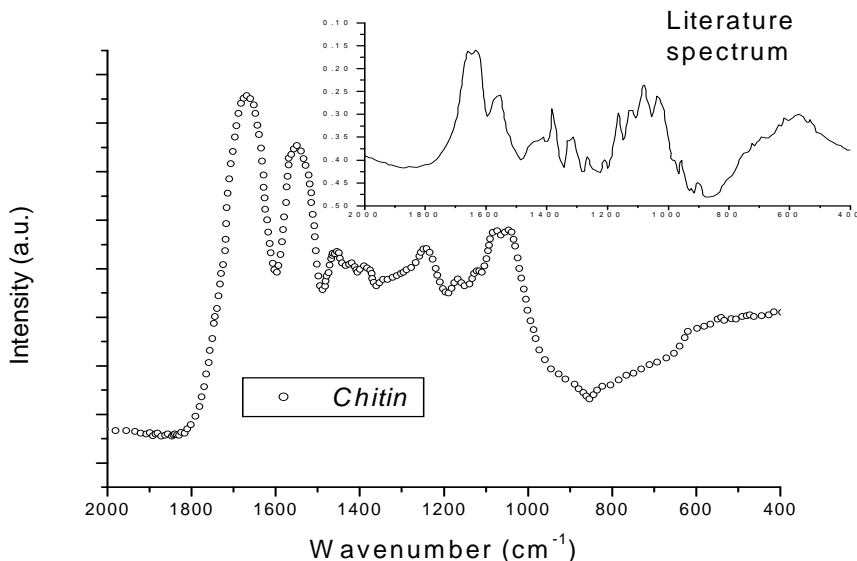


Fig. 1. Infrared spectrum of experimentally obtained chitin, compared with the literature [5].

Volumes of 100 ml solution were taken at certain periods of time, and the uranium (VI) content was measured using the Arsenazo III complexation method [7]. Uranium was determined by spectrophotometry at 655 nm using a calibration curve obtained with uranium (VI) standard solutions [8].

The absorption factors were calculated using the relation (1).

$$F = Q_u/Q_p \quad (1)$$

where  $F$  = the absorption factor ( $\mu\text{g/g}$ );  
 $Q_p$  = the weight of the sample (g);  
 $Q_u$  = the weight of uranium absorbed ( $\mu\text{g}$ ).

### Results and Discussion

The sorption isotherms of uranyl ions in chitosan, cellulose and carboxy-methyl-cellulose are presented in the Fig. 2.

Generally the uptake of uranium (VI) in chitosan, cellulose and cellulose derivatives are between 65  $\mu\text{g/g}$ . Chitosan and CMC derivative is uptaking 1.5-1.6 times more uranium than the amorphous cellulose (AC). The experimental results showed that microcrystalline cellulose (MCC) is a better sorbent for uranium (VI) than the amorphous variety of the same substance. These results are in good agreement with the literature data [9].

A wide range of factors are occurring in uranium sorption: the crystalline structure, the granulation, the volume and the polarity of the functional groups, the steric factors, etc. In our case the carboxy-methyl groups grafted on the cellulose skeleton for the CMC derivative, and respectively the amino group grafted on the cellulose skeleton for chitosan, make the two compounds better sorbents for uranyl ions than cellulose.

Uranium uptake by chitosan can be substantially improved by increasing the deacetylation factor [10].

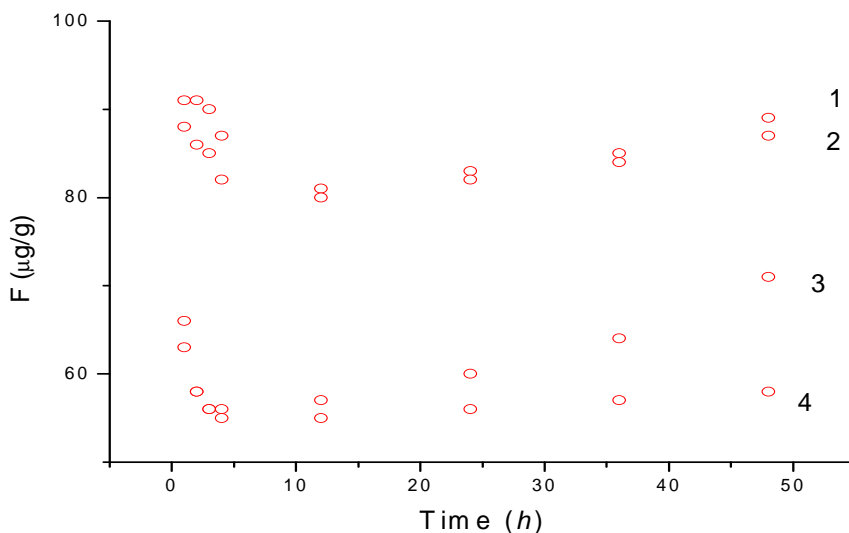


**Fig. 2.** Sorption isotherms of uranyl ions in chitosan, cellulose and carboxy-methyl-cellulose: 1- CMC; 2- chitosan; 3- MCC; 4- AC.

## REFERENCES

- [1] S. Dreve, I. Chereji, S. Boscaneanu, *J. Radioanal. Nucl. Chem.* 249 (3), (2001), 677.
- [2] P. Kolhe, R. M. Kannan, *Biomacromolecules*, 4(1), (2003), 173.
- [3] A. Cenan, C. Marutoiu, V. Slavescu, *Rev. Chim.*, 48, 2, (1997), 154.
- [4] T. Yoshino, Y. Machida, H. Onishi and T. Nagai, *Drug Dev Ind Pharm*, 29, 4, (2003), 417.
- [5] E. Guibal, Ch. Roulph, P. Le Cloirec, *Envir. Sci. & Technol.*, 29 (1995), 2496-2502.
- [6] M. Jansson-Charrier, I. Saucedo, E. Guibal, P. Le Cloirec, *Reactive & Funct. Polym.*, 27 (1995), 209-221.
- [7] A. S. Al Ammar, H. M. Basher, *J. Radioanal. Nucl. Chem., Lett.*, 159, (1992), 281.
- [8] S. Dreve, I. Chereji, S. Boscaneanu, "Absorption of uranyl ions in cultures of *Saccharomices cerevisiae*", *J. Radioanal. Nucl. Chem.* 249 (3), (2001), 677-679.
- [9] E. Guibal, I Saucedo, J. Roussy, P. Le Cloirec, *Reactive Polymers*, 23, (1994), 147.
- [10] E. Guibal, M. Jansson-Charrier, I. Saucedo, and P. Le Cloirec, *LANGMUIR*, 11, (1995), 591.

## TEMPLATE-BASED PREPARATION OF NANOSTRUCTURED POLYVINYLFORMALDEHYDE THIN-FILM

**SIMINA DREVE<sup>1</sup>, E. INDREA<sup>1</sup>, I. BRATU<sup>1</sup>, MARGARETA BAKO<sup>2</sup>,  
GH. MIHAILESCU<sup>1</sup>, LILIANA OLENIC<sup>1</sup>, STELA PRUNEANU<sup>1</sup>,  
V. ZNAMIROVSKY<sup>2</sup>, L. BARBU TUDORAN<sup>3</sup>**

<sup>1</sup> *National R&D Institute of Isotopic and Molecular Technologies, P.O. Box 700, R-3400 Cluj-Napoca 5, Romania*

<sup>2</sup> *'Babes-Bolyai' University, Faculty of Physics, 1 Kogalniceanu st., 3400 Cluj-Napoca, Romania*

<sup>3</sup> *'Babes-Bolyai' University, Faculty of Biology & Geology, 5-7 Clinicilor st., 3400 Cluj-Napoca, Romania*

**ABSTRACT.** One application which is frequently mentioned for nanometer-sized semiconductor crystals is the conversion of the optical into electric signals. At the basis of such transducers is the nanostructured thin layer of polymer, having deposited on it different doped films, following the application purpose. We have recently demonstrated the feasibility of a polyvinylformaldehyde nanostructured "brush-type" thin-film covered with a silver layer. The polyvinylformaldehyde nanostructured thin-film was prepared using the template deposition technique on anodic aluminium oxide film, which allowed the control of the thickness and the structure of the polymeric film. By chemical and evaporation techniques a silver thin layer was deposited on the film surface. The chemical tests, the determination of dielectric characteristics, and the determination of the optical properties in correlation with the thickness were done.

X-ray and electronic microscopy microstructural investigations were performed for the plastic thin-film with and without silver thin layer. The data were correlated with the specimen preparation methods.

### Introduction

Polymeric thin films, as polypyrrole, polyaniline, polyvinylformaldehyde, polythiophene (and their derivatives) are explored as promising basis-materials for the fabrication of microsensors, or to immobilise chemosensitive compounds [1].

The principles for the synthesis and preparation of polymeric nanostructured thin films generally follow specific techniques, upon the final purpose of sensing and ability to transfer the information. It is reported that [2,3] the microstructure can be achieved and controlled by various fabrication techniques, such as the use of thin film preparation technique on a template support.

### Experimental

For experimental purposes all the used reagents were A. R. grade. A solution with the specific mass of 1.230 g/cm<sup>3</sup> of polyvinylformaldehyde, C<sub>10</sub>H<sub>18</sub>O<sub>12</sub>, (Merck quality) in dichlorethane was prepared. Separately, a pure alumina nanostructured membrane, (disk shape with 3 cm diameter) was prepared via the anodisation of aluminium metal in acidic solution [4]. This membrane contains cylindrical pores of uniform diameter of 50 nm. On the top of the alumina nanostructured support the chemical deposition of a thin silver film was performed, in order to realise the conductive layer of the assembly [5].

A separation funnel, consisting in a reservoir and a capillary separated by a valve, was filled with the solution of known concentration. A cleaned piece of thin glass having fixed on it the alumina nanostructured silvered face up was mounted under the capillary of the separation funnel. The solution is allowed to escape at a controlled flow rate. The solvent readily evaporates from the solution and a thin polyvinylformaldehyde layer of high homogeneity sticks to the alumina disk. The alumina template membrane was removed and the resulting material of polyvinylformaldehyde covered with silver were washed with double distilled water and dried in normal conditions.

### Results and discussion

The preparation of the polyvinylformaldehyde-silver (PVF-silver) assembly using different parameters of deposition allowed identifying the several types of nanostructured polymeric films that were characterised:

PVF1-Ag particles of 80-130 nm deposited on a smooth surface of polymer;

PVF2-„brush-type” structure 50-70 nm fibrils covered with silver thin layer;

PVF3-ordered structure with pores of 0,5-2  $\mu\text{m}$ ;

PVF4-disordered structure with pores of 1-2  $\mu\text{m}$ .

**Optical characterisation.** The UV/VIS and IR measurements (Carl-Zeiss Jena spectrophotometer) revealed the variation of thickness of the assembly between 0.35-3.0  $\mu\text{m}$ . The assemblies having a total thickness of 2.5 nm present optical absorption property in the blue wavelength region. The variation of the reflection coefficient in IR domain was determined, and it was evidenced and it's relatively values decrease with the roughness of the assembly. The chemical tests, the determination of dielectric characteristics, and the optical properties in correlation with the thickness will be detailed elsewhere [6].

**Structural characterisation.** The X-ray diffraction patterns of the polymeric film without the silver deposited layer indicate a disordered structure of the polymeric chains. For the nanostructured PVF-silver assembly the X-ray diffraction analysis revealed, Fig. 1, the characteristic cubic structure of the Ag layer. The maximum intensity of the corresponding maxim is for the (111) structure, indicating that the Ag crystals have the tendency to develop on the normal crystallographic direction of the (111) plane.

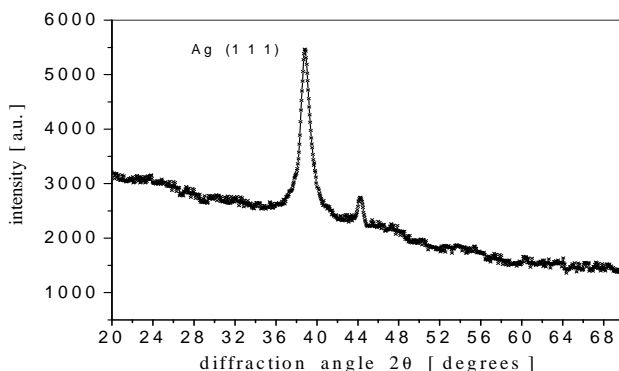


**Fig. 1.** The X-ray diffraction pattern of the PVF-Ag nanostructured thin film.

The Fourier analysis of the Ag (111) and (200) X-ray diffraction lines indicated relatively small dimensions Ag microcrystals (approx.  $D_m = 100 \text{ \AA}$ ) covering the polyvinylformaldehyde “brush-type” thin film.

**Electronic microscopy.** The four different types of nanostructured polymer-silver assemblies were investigated and the SEM images are presented in the fig.2-5. The images show that there is a good correlation between the preparation parameters of the assembly and the shape and dimensions of the nanostructures.

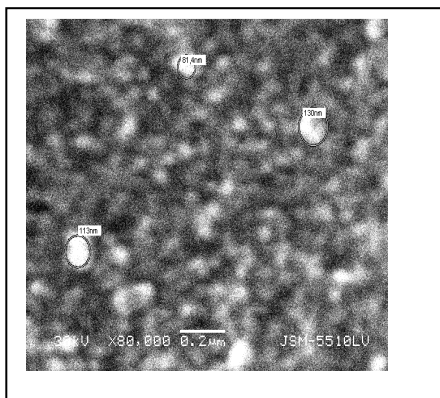


**Fig. 2.** SEM image of the PVF1 assembly Ag particles of 80-130 nm layer

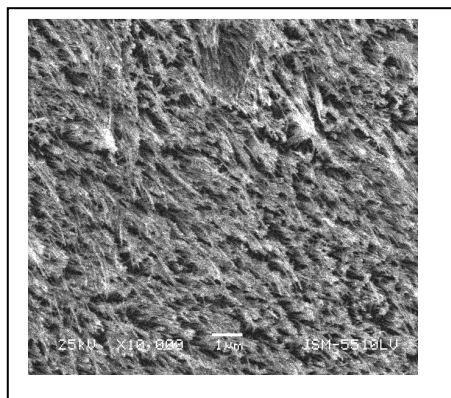


**Fig. 3.** SEM image of the PVF2 assembly-„brush-type” structure 50-70 nm fibrils covered with silver thin

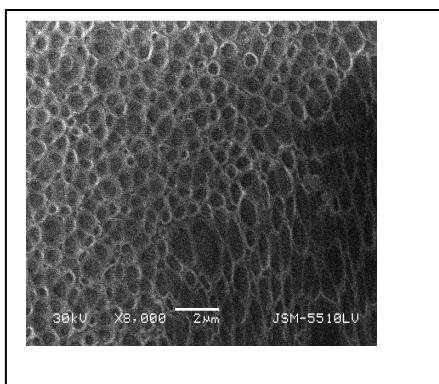


**Fig. 4.** SEM image of the PVF3 assembly structure with pores of 0,5-2 μm

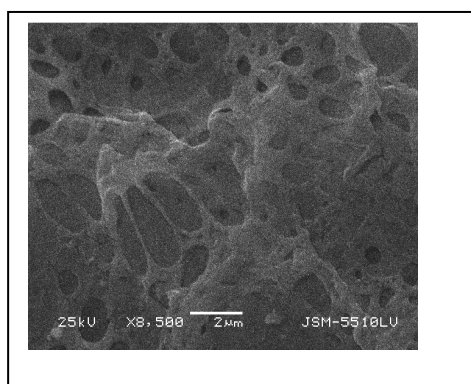


**Fig. 5.** SEM image of the PVF1 assembly ordered disordered structure with pores of 1-2 μm

### Conclusions

The results are in good agreement with the literature data [7] and the new “brush-type” polyvinylformaldehyde-silver nanostructured thin-film assembly can be used as basis for the fabrication of sensing multilayer device [8].

## BIBLIOGRAPHY

1. M. Nishizawa, K. Mukai, S. Kuwabata, C. R. Martin, H. Yoneyama, *J. Electrochem. Soc.*, 144(6), 1997, 1923.
2. H. T. Sun, M. T. Wu, P. Li and X. Yao, *Sens. Actuators*, 19 (1989) 61.
3. I. Shimizu, H. Arai and T. Seiyama, *Sens. Actuators*, 7 (1985) 11.
4. Evelina Palibroda, A. Lupsan, Stela Pruneanu, M. Savos, *Thin Solid Films*, 256 (1995) 101.
5. Stela Pruneanu, Liliana Olenic, G. Borodi, G. Sigartau, G. Mihailescu, *Proceeding of International Semiconductor Conference*, Sinaia, Roumania, 2002.
6. Simina Dreve, Emil Indrea, "Nanostructured "brush"-shape Ag deposited on submicronic resin film", in press.
7. H. Schmidt, M. Mennig, *Institut für Neue Materialien Report*, Saarbrücken, Germany.
8. F. Faupel, R. Wilecke, A. Tran, *Materials Science and Engineering: R: Reports*, 22(1), 1998, 1-55.



## STUDY OF SOME CERAMIC SYSTEMS BASED ON SILICIUM OXIDE

I. COROIU<sup>1</sup>, E. CULEA<sup>1</sup>, AL. DARABONT<sup>2</sup>, I. BRATU<sup>3</sup>, GH. BORODI<sup>3</sup>

<sup>1</sup> Technical University, 3400 Cluj-Napoca, Romania, e-mail: coroiu@phys.utcluj.ro

<sup>2</sup> Babes-Bolyai University, 3400 Cluj-Napoca, Romania

<sup>3</sup> National Institute for Research and Development of Isotopic and Molecular Technologies, 3400 Cluj-Napoca, P.O. Box 700, Romania

**ABSTRACT.** Increased interest in silicate systems containing different rare earth oxides has resulted from their important applications. Glass-ceramics of 0.95SiO<sub>2</sub>-0.05Na<sub>2</sub>O composition containing 15% molar Gd<sub>2</sub>O<sub>3</sub> were obtained by sol-gel method, and heat-treated at 250°C, 500°C and 1000°C. The samples were studied by means of X-ray diffraction, IR spectroscopy and magnetic susceptibility measurements.

### Introduction

Sol-gel processes have been intensively developed since they were found to be suitable for preparing materials and designed devices with specific properties [1-3]. In comparison with ordinary ceramics, gel-derived ceramics offer the advantage of good chemical homogeneity and purity and a better control of physical and chemical properties.

Silicate systems containing different rare earth oxides, obtained by sol-gel techniques, are important in various fields of technology [1-4] including laser, optical fibre and optical waveguides in telecommunication applications, microelectronics and catalysis.

The purpose of this paper was to study the structure of 0.95SiO<sub>2</sub>-0.05Na<sub>2</sub>O glass-ceramic containing 15% molar Gd<sub>2</sub>O<sub>3</sub>, heat-treated at 250°C, 500°C and 1000°C by X-ray diffraction, IR spectroscopy and magnetic susceptibility measurements.

### Experimental

Samples of xGd<sub>2</sub>O<sub>3</sub>(1-x)(0.95SiO<sub>2</sub> 0.05Na<sub>2</sub>O) composition, where x=0, and 0.15, were prepared starting from tetraethoxysilane (99.9% purity, purchased from Fluka Chemika) as source of silica, sodium peroxide and respectively, gadolinium oxide. Gd<sub>2</sub>O<sub>3</sub> (99.99% purity) and Na<sub>2</sub>O<sub>2</sub> (99,95% purity) were purchased from Aldrich and Merck, respectively.

The sodium peroxide and gadolinium oxide were converted to the corresponding nitrates, NaNO<sub>3</sub> and Gd(NO<sub>3</sub>)<sub>3</sub>. The water solutions of these nitrates were evaporated on a water bath (100°C). The tetraethoxysilane was mixed with ethanol and water in molar ratio 1:3:1, and then stirred for 1 hour at room temperature. After this hydrolysis, the sodium nitrate and the gadolinium nitrate were added to give a H<sub>2</sub>O/tetraethoxysilane ratio of 20. Before this operation, the nitrates were again dissolved in water. The obtained solution was stirred about 1 hour with magnetic agitator and then dried at 60°C.

The achieved gel was heat-treated at 500°C and 1000°C in air under normal pressure. For thermal treatment the samples were prepared in the following way: the gel was dried at 250°C, crumbled and pressed at 200kgf/cm<sup>2</sup> as discs with a diameter of Φ=22mm and a thickness of approximately 1mm. The thermal treatment both at 500°C and 1000°C was made for about 48 hours.

The X-ray diffraction measurements were carried out on a DRON 3 diffractometer using  $\text{CuK}\alpha$  radiation. The diffraction patterns were compared to standard patterns for phase's identification.

Infrared absorption spectra were measured at room temperature ( $\sim 20^\circ\text{C}$ ) in the  $400\text{--}4000\text{ cm}^{-1}$  range with a resolution of  $4\text{ cm}^{-1}$  using a FT-IR Vector 25 Bruker type infrared spectrophotometer and the KBr pellet technique.

Magnetic susceptibility measurements were performed operating a Weiss type magnetic balance in the temperature range  $80\text{--}300\text{ K}$ . The accuracy of the temperature control was less than  $\pm 0.1\text{ K}$  over the whole range and the overall accuracy of the measurements of magnetic moment was less than  $\pm 0.5\%$ .

### Results and discussions

The X-ray diffraction patterns of the samples heat-treated at  $250^\circ\text{C}$ ,  $500^\circ\text{C}$  and  $1000^\circ\text{C}$ , points out that the thermal treatment has a great importance for the evolution of the crystallization process. The samples heat-treated at  $250^\circ\text{C}$  and  $500^\circ\text{C}$  present wholly amorphous phase.

The indexed X-ray powder diffraction patterns of the studied samples heat-treated at  $1000^\circ\text{C}$  are shown in Fig.1. It has been ascertained that an extensive crystalline phase was developed for  $x=0$ . This crystalline phase decreases for  $x=0.15$ .

The presence of the gadolinium oxide in the  $0.95\text{SiO}_2\text{--}0.05\text{Na}_2\text{O}$  matrix slows down this process.

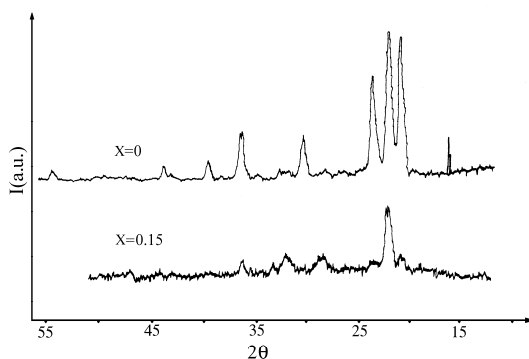


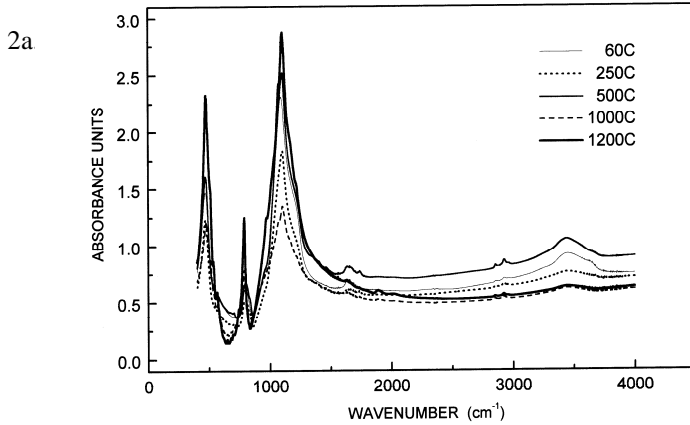
**Fig. 1.** X-ray diffraction patterns for the  $x\text{Gd}_2\text{O}_3\text{--}(1-x)(0.95\text{SiO}_2\text{--}0.05\text{Na}_2\text{O})$  samples, with  $x=0$  and  $x=0.15$ , heat-treated at  $1000^\circ\text{C}$ .

The increase of the amorphous phase in the presence of gadolinium oxide agrees with the previously reported data [4], showing that the addition of the gadolinium ions generates structural changes of the host glass ceramic matrix. Thus, the gadolinium ions play a network modifier role of the glass ceramic structure.

The crystalline phase formed for  $x=0$  is tridymite, crystallised in monoclinic system with the  $a=18.49\text{Å}$ ,  $b=4.99\text{Å}$ ,  $c=25.83\text{Å}$  and  $\beta=177.55^\circ$  lattice parameters. For  $x=0.15$  the crystalline phase diminishes and consists in a mixture of tridymite (crystallised in orthorhombic system with  $a=5.046\text{Å}$ ,  $b=8.236\text{Å}$ ) and cristobalite (crystallised in tetragonal system with  $a=4.971\text{Å}$ ,  $b=6.918\text{Å}$ ).

STUDY OF SOME CERAMIC SYSTEMS BASED ON SILICIUM OXIDE

The IR absorption spectra of the  $x\text{Gd}_2\text{O}_3(1-x)(0.95\text{SiO}_2\cdot 0.05\text{Na}_2\text{O})$  samples, with  $x=0$  are displayed in Fig.2a and with  $x=0.15$ , heat-treated at  $1000^\circ\text{C}$ , in Fig.2b.



2b.

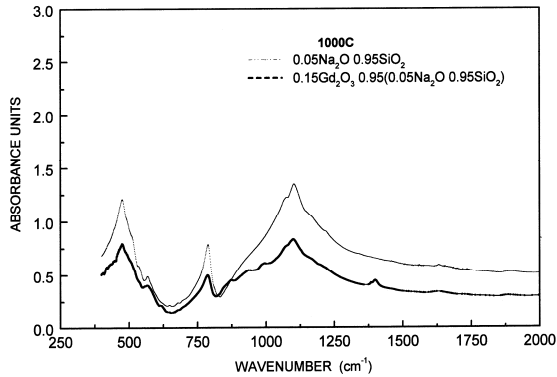


Fig. 2

The IR data of the studied samples reveal the main features characteristic of the silicate chains[5]: a sharp absorption band at  $465\text{-}473\text{ cm}^{-1}$  (bending vibrations of Si-O-Si linkages), a slightly broadened absorption band at  $550\text{-}581\text{ cm}^{-1}$  (ring vibrations of six or more than six-members rings composed of  $[\text{SiO}_4]^{4-}$  tetrahedral units), a weak absorption band at  $789\text{-}801\text{ cm}^{-1}$  (symmetric stretching vibration of [O-Si-O] bonds) and a strong and broad absorption band at  $1083\text{-}1100\text{ cm}^{-1}$  (antisymmetric stretching vibrations of bridging oxygen's), which modify with respect to the heat treatment temperatures.

The absorption band at  $3420\text{ cm}^{-1}$  is correlated with the molecular water.

The  $40\text{ cm}^{-1}$  shift of the symmetric stretching vibration of O-Si-O bonds for the  $x=0.15$  (see Fig. 2b) are denotative of the strengthening of the glass ceramic network with increasing the gadolinium oxide content [6].

Figure 3 shows the temperature dependence of the inverse magnetic susceptibility for the  $x=0.15$  samples, heat-treated at 250°C, 500°C and 1000°C. The data collapse to straight lines indicating a Curie-Weiss type magnetic behavior following the

$$\chi^{-1} = (T - \theta_p) / C$$

law [7], where  $C$  is the Curie constant and  $\theta_p$  is the paramagnetic Curie temperature.

Magnetic susceptibility data point weak ferromagnetic interactions between the  $Gd^{3+}$  ions. Increasing the heat treatment temperature decrease the intensity of these interactions.

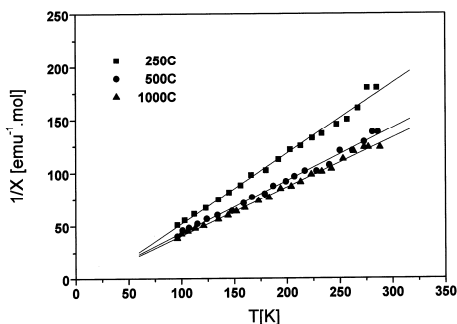


Fig. 3. Temperature dependence of the inverse magnetic susceptibility of the  $x=0.15$  samples

### Conclusions

Samples of  $xGd_2O_3(1-x)(0.95SiO_2 \ 0.05Na_2O)$  composition, where  $x=0$  and  $0.15$  were obtained and studied.

X-ray diffractograms show that addition of gadolinium oxide diminishes the amount of crystalline phase in the samples.

IR data show that the heat treatment produce structural changes of the studied glass ceramic.

Magnetic susceptibility measurements estimate weak ferromagnetic interactions between the  $Gd^{3+}$  ions that decrease with the heat treatment temperature.

### REFERENCES

1. R.J.P. Corriu, D. Leclercq, *Angew. Chem. Int. Ed. Engl.* 35, 13/14, 1996, p. 1420.
2. B. Karmakar, G. De, D. Ganguli, *J. Non-Cryst. Solids*, 272, 2-3, 2000, p. 119.
3. J.D.L. Meixner, P.N. Dyer, *J. Sol Gel Sci. Technol.*, 14, 1999, p. 223.
4. E. Culea, I. Milea, *J. Non-Cryst. Solids* 189, 1995, p. 246.
5. C.I. Merzbacher, W.B. White, *J. Non-Cryst. Solids*, 130, 1991, p. 18.
6. F. Xianping, W. Minquan, X. Guohong, *Mater. Sci. Eng.*, B12, 1993, p. 55.
7. E. Culea, A. Pop, I. Cosma, *J. Magn & Magn. Mat.*, 157/158, 1996, p. 163.

**MASS SPECTROMETRY, CHROMATOGRAPHY, ATOMIC AND MOLECULAR SPECTROSCOPY**

**ION OPTICAL SOLUTIONS INVOLVED IN FORENSIC MASS SPECTROMETRY**

**D. IOANOVICIU<sup>1</sup>, C. CUNA<sup>1</sup>, A. PAMULA<sup>1</sup>, I. ALBERT<sup>1</sup>, T. NEDA<sup>2</sup>**

<sup>1</sup> *National Institute for Research-Development of Isotopic and Molecular Technologies Cluj-Napoca*

<sup>2</sup> *Sapientia University Cluj-Napoca*

**ABSTRACT.** The ion optical solutions to obtain a major detection limit increase for explosive detectors is discussed. An ion source having high sensitivity and focusing transversally will be combined with a very efficient time-of-flight analyzer using cylindrical electrostatic mirror. A limit of detection in the range of p. p. t. is expected for TNT and RDX.

**Introduction**

Explosive detection is a major branch of the Forensic Science. A big number of reviews and books deal with the methods of the forensic science. All those include research directed to refine explosive detection methods in the present context of the increased importance dedicated to fight terrorism. Reviews as: Journal of Forensic Sciences, The American Journal of Forensic Medicine and Pathology, Forensic Science International, Forensic Science Review, J. of Forensic Science Society, Canadian Society of Forensic Science are may be the most known, with the highest impact factor, to mention only a few of those publishing articles belonging to forensic science. We cannot omit some fundamental works as Forensic Science Handbook edited by Richard Saferstein, representative person for this field, Analytical Methods in Forensic Chemistry by Ho (Harwood editions 1990).

The explosive detection is the field of application of various methods but the obtained results did not offer an ultimate solution to the problem at a satisfactory level. Absorption atomic spectrophotometry has been used to detect antimony and barium from the residuum of gun shots [1] as well as the inductively coupled plasma in an atomic emission spectrometer for the determination of barium [2]. High-resolution liquid chromatography was used to analyze the difeniamine traces from firing weapons [3]. Neutron activation served to study bullets [4], [5]. Nitroglycerine derived explosives were analyzed by gas chromatography coupled with a mass spectrometer [6]. Magnetic nuclear resonance was also used with this purpose [7]. Raman spectra were obtained from explosive particles [8]. Explosive traces were detected in glow discharge connected to a quadrupole trap [9]. The detection of trinitrotoluene was reported with a glow discharge ion source coupled to a quadrupole-time-of-flight tandem mass spectrometer [10]. The same ion source type was bound to a model MAT TSQ-700 triple quadrupole mass spectrometer to identify explosives [11]. In this way the spectra of TNT, PETN and RDV were obtained [12]. The research in this project is directed to construct and test an explosive detector of high sensitivity allowing to eliminate from the luggage flux of those containing hidden bombs and to impede in this way of terrorist attacks and the smuggling of explosives. The detector will be designed to quickly examine explosion residues, giving hints to guide the forensic investigations. Such detectors are useful for check points at the border, as well as all those which are investigating crimes and events where firearms were used.

**General description of the new principle**

The final goal of this research is to realize a functional model of an ultrasensitive explosive detector having superior performances compared to other existing detectors based on mass spectrometric analyzers. The ultrasensitive detector will include in a compact assembly the ion source, the electrostatic mirror and the ion detector. A sensitivity increase of several magnitude orders is expected by combining the following procedures:

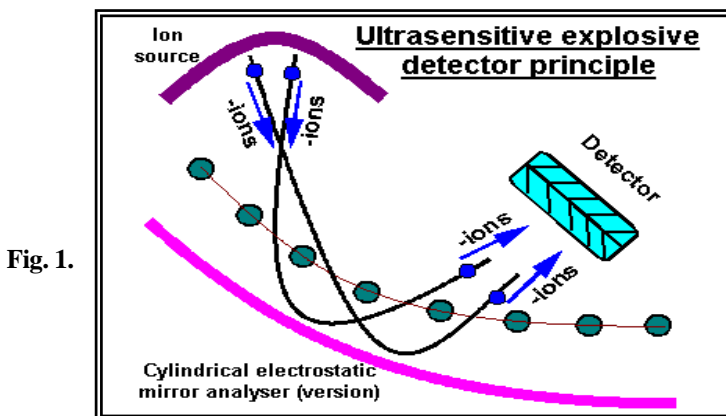


Fig. 1.

The ion source will be so designed that the ions will be generated from a variable thickness region, located between spherical, cylindrical or plane surfaces. The ion extraction from the region of generation will allow their focusing in transversal direction at the ion detector site. Because the explosive substance molecules have a high electron attachment cross-section inside the ion source an electron retarding system will be accommodated by using multiple ionizing filaments. The electrons will be slowed down during the ionizing time lapse to ease the electron attachment process. The ionization in this regime will be maintained during the ion accumulation, its duration being established by tests.

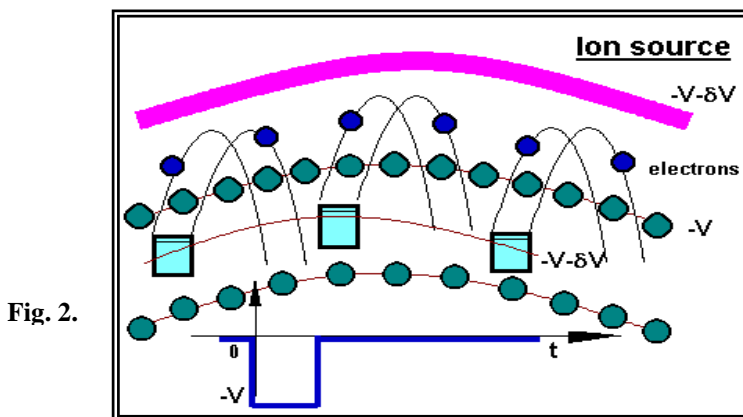


Fig. 2.

The ion production time lapse will be followed by their extraction. The voltages ensuring the ion extraction will be correlated with the static voltages applied to the cylindrical or spherical electrodes of the electrostatic mirror in such a way that the longitudinal (time) focusing be accomplished simultaneously with the transversal (space) one. An additional sensitivity increase will be added by this focusing procedure. The use of multichannel plates with spherical surfaces will be also considered with the same purpose.

The mass analyzer will be selected based on an in depth analysis of the ion optical properties of various configurations which could include electrostatic mirrors with one and two stages, with homogeneous field or with inhomogeneous fields of parabolic or exponential type as well as the possibilities to use linear analyzers with or without post source focusing.

The basic parameters of the electronic units are function of the mass analyzer solution adopted.

The ion detection will be performed with channel multipliers or with electron multipliers specially designed to have short time response. Most probably a double channel plate chevron system will be adopted. The time response should be in the range of picoseconds. The accumulation of the mass spectra will be obtained on a personal computer by an interface transient integrator plate. A vacuum system will be evacuated by turbomolecular pumps started by mechanical vacuum pumps, the pressure inside the vessel being measured by vacuum gauges.

For the ultrasensitive explosive detector a sensitivity level in the p. p. t. range is expected for trinitrotoluene (TNT) and cyclotrimethylene trinitramine (RDX).

### Ion optical solutions

The ion optical solution will be the result of comparison of various versions of time of flight analyzers with electrostatic mirror operating the ion source in impulse regime. The ion optical study of the ion motion inside the fields is based on the analysis of the trajectories inside the homogeneous, quadrupole, exponential, spherical and cylindrical fields [13]. Besides the methods of ion path simulation on computer, the matrix language will be also used by including a line and a column with the time dependent elements. By this last procedure the instrumental properties result from the multiplication of matrices expressing the properties of various ion path portions.

This can be done also by computer programming. To describe ion motion in accelerating and decelerating electric fields we start with the formula expressing the flight time as function of the ion energy at the ion entry and exit inside and from the applied field.

### Linear TOF

In a mass spectrometer with ion source operated with continuous extracting and accelerating voltages position time focusing is obtained, called often "space focusing". The flight time differences due to different points of formation are suppressed by using a field free space of  $D$  length, after the ions leave the source. This distance results from the ion source geometric and operating parameters.

$$D = 2v^2[vd_a - d_b/(1 + v)]$$

Where  $d_a$  and  $d_b$  are the distance over that the extraction and acceleration takes place respectively,  $v$  the ratio between the reference ion velocity at the source exit and when leaving the extraction region, ratio set by the applied electric fields.

The resolution of a time-of-flight mass spectrometer with ion optics focusing at first order is given by the formula:

$$\mathfrak{R} = D_\gamma / (t_0 + \Delta t_v + \Delta t_2)$$

where  $D_\gamma = t_\Sigma/2$  is the temporal coefficient of mass dispersion,  $t_\Sigma$  the total flight time of the reference ion from formation to detection,  $\Delta t_v$  the "turn around" time of an ion starting against the extracting field,  $\Delta t_2$  is the temporal aberration resulted from the incomplete compensation of the initial position effects.. The detailed expressions of the above enumerated quantities are:

$$D_\gamma = [d_a(1 + v^2) + d_b(1 - v)/(1 + v)]$$

$$\Delta t_v = -2v^2 d_a v_0 / v_s^2, \Delta t_2 = [d_a(3 - v^2) + d_b(v - 1)(v + 2)/v(1+v)] / (4v v_s) \delta^2$$

Here  $v_s$  is the velocity of the reference ion in the field free space,  $v_0$  the initial ion velocity, resulted from the thermal molecular motion before ionization,  $\delta$  the relative energy difference of the ions formed at different initial sites.

### Homogeneous field reflectrons

The time-of-flight analyzers having electrostatic mirrors allow energy focusing of the ions of the packets, of first or second order, depending upon the number of used homogeneous field stages.

The time-of-flight mass spectrometer configuration assembled from an ion source with a single accelerating field and an analyzer with mirror with two stages needs a field free space of L length to be included in the ion path.

$$L = 2[2\eta^2 d_1 + (\eta^2 - 1)d_s]/(\eta^2 - 3)$$

The involved quantities are:  $d_1$  the depth of the mirror's first stage (decelerating),  $d_s$  the depth of the extraction-accelerating space in the ion source and  $\eta$  is the ratio between the reference ion velocity on the field free space and that after the deceleration inside the first stage of the mirror. To find out the resolution of the two stage mirror time of flight mass spectrometer in the formula we substitute for  $D_\gamma$  by the expression:

$$D_\gamma = L(1 - 1/\eta^2)/v_s$$

Because the second order aberration disappears, we have to account for that of third order  $\Delta t_3$  by a term of this order in the relative energy spread of the ions from the packet  $\delta_p$ :

$$\Delta t_3 = (\eta^2 - 1)L\delta_p^3/(8v_s)$$

If for the ion packet energy focusing is used a single stage mirrors the temporal focusing condition of first order is satisfied if:

$$L = 2(d_s + 2d_1)$$

The ion flight time being:

$$t_\Sigma = 2L/v_s$$

The resolution formula contains in this case the second order aberration:

$$\Delta t_2 = \delta_p^2(d_s/2 + d_1)/v_s$$

the third order aberration being neglected.

### Delayed extraction

The temporal focusing of the ions with respect to their initial velocities is accomplished by applying the extraction of the ions delayed with respect to the instant of their formation. This focusing procedure must be used for the detection of ions result from matrix assisted laser desorption/ ionization. For a simple geometry, composed from an ion source with two homogeneous electric fields, the extraction one established after some delay with respect to the ionization instant, and from a field free space, the delay  $\tau$  results from the formula:

$$\tau = 2d_a v^4 / \{v_s [D/2 + v^2(d_b/1 + v - v d_a)]\}$$

The focusing is accomplished exactly only for ions of a given mass, approximately for the neighbouring masses. This because  $\tau$  depends of the reference ion velocity.

The presence of the term in  $v_o^2$  severely limits the mass resolution accounting for the initial velocity distribution widths resulted for ions generated by matrix assisted laser desorption/ ionization. In the literature values between 450 m/s and 750 m/s were reported.

An original ion optical solution is that combining a hyperbolic electrode ion source and a field free space [14]. The electrodes must be fed by high voltage pulses which will be performed by high voltage commutators as those offered by the company Behlke, Germany. This configuration insures complete initial velocity focusing for the ions created from the tip of the end cap ion source electrode.

During  $T_c$  the high voltage pulse the potential  $\Phi$  inside the ion source is that of a Paul ion trap:

$$\Phi = \Phi_o(z^2 - r^2/2)/z_o^2$$

where  $\Phi_o$  is the height of the applied pulse,  $2z_o$  the distance between the end electrodes. The perfect velocity focusing condition is satisfied for a field free space of length L:

$$L = z_o[\tau\omega \sin(\omega T_c) - \cos(\omega T_c)]$$

With the parameter  $\omega$  defined by the relation:



$$\omega = (2e\Phi_0/m)^{1/2}/z_0$$

For the ions emitted from an area described for a circle of radius  $\delta r$  on the electrode tip, the length of the packet at the detector site will be:

$$\Delta t_d = [\delta r^2 L/(\delta r^2 + 4z_0^2) + L t_0 v_0 + v_0 \delta r^2/(4z_0^2 \omega \sin(\omega T_c))]/[\omega z_0 \sin(\omega T_c)]$$

The mass time dispersion coefficient of this geometry takes the form:

$$D_\gamma = [T_c + \sin(\omega T_c)/\omega + \tau T_c \omega/\sin(\omega T_c)]L/(2z_0)$$

### Electrostatic condenser TOF

To select the ion-optical solution the properties of the electrostatic condensers must be also accounted for. The properties of the toroidal condensers are given by the transfer matrix elements. The temporary matrix elements are given and only those of first order.

$$(t/x) = 2 \sin[\Phi_e(2 - \lambda)^{1/2}]/[v_s(2 - \lambda)^{1/2}], (t/\alpha) = 2\{1 - \cos[\Phi_e(2 - \lambda)] R_c/[v_s(2 - \lambda)]\}$$

$$(t/\gamma) = R_c\Phi_e/(2v_s), (t/\delta) = \{2[\Phi_e - \sin\Phi_e(2 - \lambda)^{1/2}/(2 - \lambda)^{1/2}]/(2 - \lambda) - \Phi_e/2\}R_c/v_s$$

These elements form the last line of the first order transfer matrix of the toroidal condenser.

$$\begin{array}{c|ccc|ccc} \begin{array}{c} x \\ \alpha \\ \gamma \\ \delta \\ t \end{array} & & \begin{array}{c} x/x \\ \alpha/x \\ 0 \\ 0 \\ (t/x) \end{array} & \begin{array}{c} x/\alpha \\ \alpha/\alpha \\ 0 \\ 0 \\ (t/\alpha) \end{array} & \begin{array}{c} x/\gamma \\ \alpha/\gamma \\ 1 \\ 0 \\ (t/\gamma) \end{array} & \begin{array}{c} x/\delta \\ \alpha/\delta \\ 0 \\ 1 \\ (t/\delta) \end{array} & \begin{array}{c} 0 \\ 0 \\ 0 \\ 0 \\ 1 \end{array} \end{array}$$

### Cylindrical mirror TOF

The study of the electrostatic mirrors with cylindrical electrodes indicates the possibility to obtain second order position temporal focusing with a single grid. In this way a better sensitivity can be obtained by maintaining high resolution.

To estimate the resolution the ion packet length at the detector  $\delta t$  was calculated:

$$\delta T = |b_{\delta\delta}| \delta^2 + |b_{\delta\delta\delta}| \delta^3$$

for the first order focusing case with respect to the energy spread  $\delta$ .

We distinguish two classes of configurations. One of them represents those geometries for that  $r_b$ , the radius where the reference ion stops inside the electrostatic field, is greater than the radius  $r_0$  of the grid which limits the mirror.

Then:

$$b_{\delta\delta} = [a^2 r_0 (a^2 - 1/2) + 2a^5 r_b I_c + 3L_f/8]/v$$

With:

$$a^2 = \ln(r_b / r_0)$$

$$I_c = \int_0^a \exp(-x^2) dx \quad si \quad L_f = 4a^2(r_0 + 2ar_b I_c)$$

the last relationship being the consequence of the first order energy focusing condition. The configurations for  $r_b > r_0$  do not offer the possibility of second order focusing, therefore the coefficient  $b_{\delta\delta\delta}$  calculation was omitted.

For the geometries with  $r_b < r_0$ , when the grid convexity is directed towards the ion source the following expressions result for the temporal aberration coefficients:

$$b_{\delta\delta} = \left\{ 3L_f / 8 + b^2 \left[ 2b^3 r_b I_d - r_b (b^2 + 1/2) \right] \right\} / v$$

and

$$b_{\delta\delta\delta} = \left\{ -5L_f / 16 + \left( \frac{b^2}{3} \right) \left[ r_o \left( b^4 + \frac{b^2}{2} + \frac{3}{4} \right) - 2b^5 r_b I_d \right] \right\} / v$$

where:

$$b^2 = -\ln(r_b / r_o),$$

$$I_d = \int \exp(x^2) dx,$$

$$L_f = 4b^2 (r_o - 2br_b I_d).$$

A numerical exploration of the two aberration coefficients values allowed to cancel the first for  $r_b/r_o=0,7013$  when  $L_f/r_o=0,6188$ . In these conditions also the third order aberration coefficient is very small:

$$b_{\delta\delta\delta} = -0,0775 r_o/v$$

### Conclusions

The ultrasensitive explosive detector will make an important step on the way of refining the means to keep under control the traffic through the check points on highways as well as through airports. By improving the detection limit of the explosives it will help to better fight terrorism and to speed up forensic investigation procedures.

### REFERENCES

- [1] - Koons RD, Havekost DG, Peters CA, J. Forens, *Sci* 32, 846 (1987)
- [2] - Koons RD, Havekost DG, Peters J. Forens, *Sci* .33, 35 (1988)
- [3] - J. B. F. Lloyd, *Anal. Chem.* 59, 1401 (1987)
- [4] - V. P. Guinns, S. R. Fler, C. L. Heye, T. H. Jourdan, *Radioanal. Nucl. Chem.* 114, 265 (1987)
- [5] - J. M. Cohen, R. R. Pla, M. I. Mila, C. D. Gomer, J. Trace, *Microprobe tech.* 6, 113 (1987)
- [6] - D. T. Burns, R. J. Lewis, *Anal. Chem. Acta* 307, 89 (1995); D. T. Buons, R. J. Lems, *Anal. Chem. Acta.* 300, 221 (1995)
- [7] - C. Cheng s.a., J. Forensic, *Sci.* 40, 31 (1995)
- [8] - S. A. McLuckey, D. E. Georinger, K. G. Asano, G. Vaidyanthan, J. L. Stephenson, *Rapid Commun. Mass Spectrom.* 10, 287 (1996)
- [9] - S. A. McLuckey, G. L. Glesh, K. G. Asano, *Anal. Chem. Acta* 225, 25 (1989); B. C. Grant s.a., *ASMS Conf on MS and Allied Topics Nashville TN 1991*, p. 166
- [10] - G. L. Glesh s.a., *Proc first Int. symp. On Explosive Detection Technology, Atlantic City New York 1991*, p 642
- [11] - D. Ioanoviciu, *Int. J. Mass Spectrom.* 206, 211 (2001)
- [12] - D. Ioanoviciu, C. Cuna, V. Cosma, *Proc. 27<sup>th</sup> Congress Amer. Rom. Academy, Polyt. Int. Press 2003*, pp1343

## MULTIFUNCTIONAL ION DETECTOR FOR A THERMAL IONIZATION MASS SPECTROMETER

A. PAMULA, I. DOBOCAN, N. GLIGAN, ADRIANA BENȚA

*Natioanal Institute for Research and Development  
of Isotopic and Molecular Technologies*

**ABSTRACT.** A three mode operating ion detector was designed and built for a thermal ionization mass spectrometer. It allows ion detection:

- on a Faraday cage
- on a secondary electron multiplier after the conversion of incident ions in secondary electrons
- on a secondary electron multiplier by direct bombardment of the first dynode by the incoming ions

### Introduction

In a thermal ionisation mass spectrometer, the ion beams energy ranges, usually, in between 5 – 10 keV. If, for sensitivity reason, a secondary electron multiplier is used, than the first dynode is subject to a very hard heavy ion bombardment, which, in time, leads to the alteration of its surface. As a result, an amplification loss occurs. To avoid this, an ion-electron conversion outside the multiplier is proposed.

The ion optics of the detection system was numerically modelled [1] and the system was designed and build up in the Mass Spectrometry Laboratory of the institute.

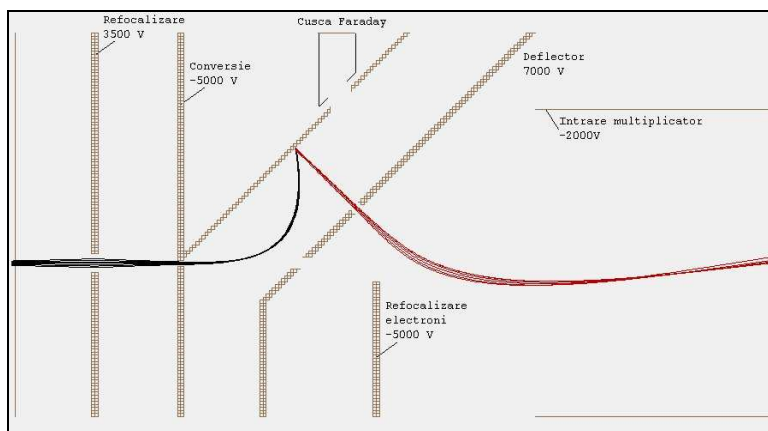


**Fig. 1.** Numerical modelling of the multifunctional ion detector. Ion and electron trajectories are shown for the ion-electron conversion mode.

The detector was mounted in the analyser chamber of the SMIT-1 thermal ionisation mass spectrometer. An adjustable resolution slit (0 – 1 mm) was placed in front of it. The width of this slit can be adjusted from the exterior via a micrometric screw. Figure 2 shows the adjustable slit mounted in front of the detector.

A throughput assembly was built to supply the necessary potentials to the detector electrodes. The throughputs were realised from tubular ceramic insulators of 70 mm long and 10 mm exterior diameter. Epoxy resins ensured the tightening. The assembly can be outgassed at 80° C. The typical vacuum in the mass spectrometer tube is  $3,5 \times 10^{-7}$  torr.



**Fig. 2.** The adjustable slit mounted in front of the detector.



**Fig. 3.** The multifunctional detector mounted in the spectrometric tube of the SMIT-1 apparatus.

### Performance testing

The starting potential values supplied to the detector electrodes were those determined by numerical modelling (figure 1).

With all the electrodes grounded except the re-focussing electrode maintained at 3500 V, the spectrometer was tuned on the  $^{238}\text{U}^+$  ion. The secondary electron multiplier was supplied with 2.1 kV, corresponding to a gain of approximately  $10^4$ . A stable output signal of 1.524 V (mean value) was observed. The standard deviation of the values registered in 60 sec. interval was  $\sigma = 0,005\text{V}$ . This value represents fluctuations of the output signal caused both by electrical noise. A 5000 V potential was applied on the conversion and electron re-focussing electrodes, while maintaining unchanged the voltage on the deflection electrode (0.0 V). The output signal becomes zero. Then, the potential of the deflection electrode was gradually risen; watching the electrometer output signal. At 6900 V on the deflection electrode we got a stable output signal of 1.225 V (mean value). The intensity and the standard deviation of the output signal remains in the same range of magnitude as in the case of the direct detection of the ions.

At 3850 V on the deflection electrode we obtain a signal on the Faraday cage. This signal is about  $10^4$  times less intense than in the preceding situation

### Conclusions

- The potentials determined by numerical modelling are in very good agreement with those experimentally determined
- In the ion-electron conversion mode, the detected signal has the same magnitude order as the signal registered in the direct ion detection mode. The ion-electron conversion should be preferred to avoid a hard bombarding of the first dynode of the secondary electron multiplier.
- The ion-electron conversion doesn't alter the accuracy of the measurements.
- The multifunctional detector requires a very limited number of different voltages.
- The system being non-dependent of the multiplier type, the detector could fit any mass spectrometer functioning with ion energies of several keV.

### REFERENCE

1. David A. Dahl and Anthony D. Appelhans "Ion Optics Through the Eyes of SIMION 6.0", An Asms Short Course, Portland ASMS Conference, May 11-12, 1996

## PHOTOSYNTHETIC FRACTIONATION OF CARBON ISOTOPES

**STELA CUNA<sup>1</sup>, GABRIELA MURESAN<sup>1</sup>, ONUC COZAR<sup>2</sup>,  
NICOLAE LUPSA<sup>1</sup>, VALENTIN MIREL<sup>1</sup>**

<sup>1</sup> *National Institute of Research and Development for Isotopic  
and Molecular Technologies, Cluj Napoca*

<sup>2</sup> *Babes-Bolyai University Cluj Napoca*

**ABSTRACT.** Variation in carbon isotopic composition among plant species could be used to distinguish among photosynthetic pathway types, to determine the water-use efficiency, and the adaptation of the plant at the environmental stress. The method that we have proposed to establish the photosynthetic fractionation from the plants consists of two stages. In the first stage the organic matter is converted to CO<sub>2</sub> by dry combustion in an excess of oxygen. In the second stage the stable carbon isotope ratios (<sup>13</sup>C/<sup>12</sup>C) is measured with high precision by mass spectrometry with double collector. We have analyzed the carbon isotopic composition of five plants (*Malus domestica*, *Zea mays*, *Robinia pseudoacacia*, *Juglans regia* and *Castanea sativa*), and we have determined the linearity and precision of the method, and the most propitious size of the sample to be analyzed. The precision was ± 0.2 ‰ for 10 mg of dry plant used for combustion. The photosynthetic pathway for these plants was different, and we have joined them with C<sub>3</sub> and C<sub>4</sub> type of the photosynthesis.

### **Introduction**

The use of carbon isotope ratios in plant ecological and physiological research has increased significantly [1]. The two stable isotopes of carbon (<sup>13</sup>C and <sup>12</sup>C) are not equally distributed in natural compounds because of isotope fractionation occurring during physical, chemical and biological processes involved in the carbon cycle. Normally plants are depleted in <sup>13</sup>C compared to atmospheric CO<sub>2</sub> because of carbon isotope fractionation occurring during photosynthetic CO<sub>2</sub> fixation. Carbon isotope discrimination (Δ) is a measure of this process and depends on fractionation during diffusion and during enzymatic carboxylation reactions. In plants possessing C<sub>3</sub> photosynthetic pathways the major components contributing to the overall fractionation are the differential diffusibility of CO<sub>2</sub> across the stomatal pathway and the fractionation by Rubisco carboxylase (δ<sup>13</sup>C range between -35‰ and -22‰). Variation in composition among plants with the C<sub>4</sub> photosynthetic pathway is less than in C<sub>3</sub> plants (δ<sup>13</sup>C from -20‰ to -8‰) because there is another carboxylase (PEP carboxylase) that fixed carbon during photosynthesis [2]. Then, carbon isotope abundance becomes a classical means to distinguish between different photosynthetic pathways and to study their geographical, taxonomic and ecological distributions.

### **Materials and methods**

Carbon isotope discrimination was analyzed in the leaves of five plant species: *Malus domestica*, *Robinia pseudoacacia*, *Juglans regia*, *Castanea sativa*, and *Zea mays*.

Sample collection was straightforward. We have collected the samples at the same time of the day, because diurnal changes in starch and sugar contents can affect carbon isotope ratio. To further minimize sample variation in population-level studies, samples were collected from the same canopy position. There can be δ<sup>13</sup>C<sub>air</sub> gradients that could potentially confound interpretation of plant isotopic values, especially in dense canopies. After harvesting, the five plant samples were dried immediately at a 70°C to avoid loss of organic materials. Samples were stored at room temperature after drying for later determination of their isotopic composition.

Because of instrumental requirements, carbon from plant must be converted to CO<sub>2</sub> for stable isotope ratio measurements. Conversion of organic samples (plant's leaves) to CO<sub>2</sub> for isotopic analysis is accomplished by dry combustion in an excess of oxygen. We have chosen the simplest and fastest method that involves the combustion of individual sample in sealed quartz tubes. Because each sample is prepared in its own container, there is no chance for memory effects. For combustion we used 3 mg, 5 mg, 7 mg, and 10 mg of dried leaves from each five plants. The dried tissues have grounded to pass through a 40-mesh screen [3].

The materials and devices needed for this method was: quartz tubes for combustion and for sample boats, CuO as the oxygen source, furnace, and a vacuum system for purification and measurement of CO<sub>2</sub> generated by combustion

The CO<sub>2</sub> was separated from the other combustion products by cryogenic distillation. We used a simple vacuum line who consists of a diffusion pump to provide a high vacuum, a tube cracker for breaking the combustion tube under vacuum, a purification trap for cryogenic distillation of the combustion products, a manometer for measuring the volume of CO<sub>2</sub> produced, and a port for attaching sample bulbs.

CO<sub>2</sub> purified was analyzed with a mass spectrometer equipped with a double inlet system and double collector, type Atlas 86 designed by Varian MAT. The CO<sub>2</sub> gas generated from the sample was admitted to the sample side of the dual-inlet system, and a reference gas of known carbon isotope composition was admitted to the standard side of the inlet. Then, sample and standard gases were alternately admitted to the ion source of the mass spectrometer, and the isotopic composition of the sample was repeatedly and rapidly compared with that of the standard.

### Results and discussions

The results of the measurements are presented in Table 1, Table 2 and Fig. 1.

Table 1

The variation of  $\delta^{13}\text{C}$  with sample size

Sample size	Malus domestica $\delta^{13}\text{C}$ ‰	Castanea sativa $\delta^{13}\text{C}$ ‰	Robinia pseudoacacia $\delta^{13}\text{C}$ ‰	Juglans regia $\delta^{13}\text{C}$ ‰	Zea mays $\delta^{13}\text{C}$ ‰
3mg	-27.02	-26.63	-26.20	-25.54	-10.17
5mg	-	-26.57	-27.27	-26.62	-10.03
7mg	-26.91	-27.52	-25.28	-	-9.60
10mg	-26.66	-27.49	-25.30	-26.12	-9.25

We have taken 3 mg, 5 mg, 7 mg and 10 mg from each plant to see the variation of carbon isotopic composition ( $\delta^{13}\text{C}$ ) with sample size (Table 1). The results show this variation is about 1‰ for any plant. This means that it is possible that some errors can appear during sample preparation because biochemical heterogeneity within the sample. Heterogeneity in ground leaves arises because of incomplete grinding and mining and small differences in metabolic activity among different leaves in a bulked sample.

Table 2

The variation  $\delta^{13}\text{C}_{\text{vs. PDB}}$  of studied plants

No.	Sample	$\delta^{13}\text{C}_{\text{vs. PDB}}$ [‰]	Photosynthetic group
1	Malus domestica	-26.86	C <sub>3</sub>
2	Castanea sativa	-27.06	C <sub>3</sub>
3	Robinia pseudoacacia	-26.01	C <sub>3</sub>
4	Juglans regia	-26.01	C <sub>3</sub>
5	Zea mays	-9.76	C <sub>4</sub>

## PHOTOSYNTHETIC FRACTIONATION OF CARBON ISOTOPES

The amount of sample required will depend largely on volume of the mass spectrometer inlet system and carbon content of the sample. We think that sample size of 5 mg for plant tissue should be adequate. In Fig. 1 there is one example of variation of the  $\delta^{13}\text{C}$  with sample size.

The variation  $\delta^{13}\text{C}$  between  $\text{C}_3$  and  $\text{C}_4$  plants is shown in Table 2. The 1-4 plants with an average  $\delta^{13}\text{C} = -26.48\text{‰}$  are  $\text{C}_3$  plants. In this group of plants the isotopic fractionation of carbon in leaves is caused by ribulose biphosphate carboxylase (Rubisco) [1], [2]. Zea mays belongs to  $\text{C}_4$  plants because for this plant  $\delta^{13}\text{C}$  is  $-9.76\text{‰}$  and this means that isotopic fractionation of carbon is caused by PEP carboxylase.

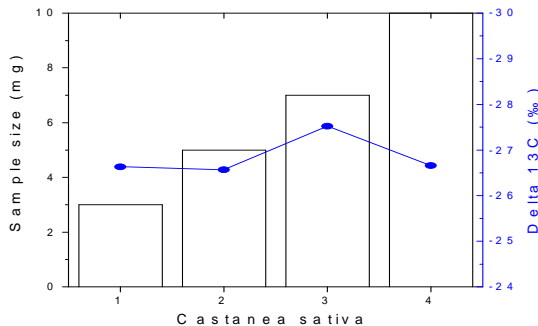


**Fig. 1.** The variation  $\delta^{13}\text{C}$  with sample size in *Castanea sativa*

The carbon isotopic composition is approximately the same for the plants  $\text{C}_3$  that means this studied plants had the same source of  $\text{CO}_2$  because photosynthetic rate is linearly related to ambient  $\text{CO}_2$  concentration. Also, these values reflect the fact that we have collected the samples at the same time of the day. There is a little difference in  $\delta^{13}\text{C}$  values between *Juglans regia* (nut tree) and *Castanea sativa* (chestnut tree). The lower  $\delta^{13}\text{C}$  value in *Juglans regia* indicates a lower intercellular  $\text{CO}_2$  concentration because the species of nut trees occurs on much drier site those chestnut trees.

### Conclusions

We have analyzed the carbon isotope composition of five plant species by isotope ratio mass spectrometry (IRMS). Carbon was extracted from leaves as  $\text{CO}_2$  by combustion and purified by cryogenic distillation. The precision of measurements was  $\pm 0.2\text{‰}$  for 10 mg of dry plant used for combustion. The photosynthetic pathway of the studied plants was different, and we have joined *Malus domestica*, *Robinia pseudoacacia*, *Juglans regia* and *Castanea sativa* with  $\text{C}_3$  type of photosynthesis and *Zea mays* with  $\text{C}_4$  type of the photosynthesis.

The results obtained are in good agreement with the model predicts in literature.

## REFERENCES

- [1] E. Brugnoli, G. D. Farquhar "Photosynthetic fractionation of carbon isotopes" in "Photosynthesis: Physiology and Metabolism", pp. 399-434, R. C. Leegood, T.D. Sharkey and S. von Caemmerer (eds.), Kluwer Academic Publishers, The Netherlands, 2000
- [2] G. D. Farquhar, J. R. Ehleringer, K. T. Hubick, "Carbon isotope discrimination and photosynthesis, *Annu. Rev. Plant Physiol. Plant Mol. Biol.*, 40, 503-537, 1989
- [3] T. W. Boutton "Stable carbon Isotope Ratios of Natural materials: Sample preparation and Mass Spectrometric Analysis" in *Carbon Isotope Techniques*, pp. 155-170, D. C. Coleman, B. Fry (eds.), Academic Press Inc., San Diego, 1991

## TRITIUM ENRICHMENT OF ENVIRONMENTAL WATERS BY ELECTROLYSIS

IOSIF CHEREJI, WOLFANGO PLATINO<sup>1</sup>, STELA CUNA, NICOLAE LUPSA, GABRIELA MURESAN, VALENTIN MIREL, PETRE BERDEA, CALIN BACIU<sup>2</sup>

*National Institute of Research & Development for Isotopic and Molecular Technologies P.O. Box 700, 3400 Cluj-Napoca, Romania*

<sup>1</sup>*University of Roma Tre, Department of Physics, Roma, Italy*

<sup>2</sup>*Biology-Geology Faculty, Babes-Bolyai University Cluj-Napoca*

**ABSTRACT.** In order to enrich the tritium in the water samples by minimum 10 times we have developed a battery of 5 electrolysis cells. The procedure includes before the enrichment a primary distillation of the samples and after the enrichment a final distillation. The enrichment factor for the tritium content ( $\beta$ ) was calculated by means of the enrichment factor for the deuterium content ( $\alpha$ ) that was measured before and after the electrolysis by mass spectrometry. That is valuable in the limits of  $\pm 5\%$  errors. In order to obtain a desired final volume in every cell we have developed a programmable electronic system that can interrupt the current through any cell in which the desired volume of electrolyte is attained. We have obtained an enrichment factor of 20 for the electrolyzed water samples.

### Introduction

Tritium ( $^3\text{H}$ ) possess great significance for isotope hydrology in addition to the stable isotopes  $^2\text{H}$  and  $^{18}\text{O}$  [1]. Tritium is a pure low-energy beta emitter ( $E_{\text{max}}=18.6$  keV) with a half-time of 12.43 years. Tritium activities are described in terms of tritium units (TU) where 1TU=1 atom of tritium per  $10^{18}$  atoms of hydrogen. In the northern hemisphere, tritium concentration in precipitation vary from a few hundred to a few thousand TU; in surface waters concentration are slightly lower (100-200 TU) than current precipitation due to dilution with older ground water, while ground water concentration range from zero to several hundred TU.

It is established that useful hydrological and meteorological information can be obtained from measurements of the natural tritium content of precipitation, surface water and ground water. Also, tritium is one of the most important global contaminant produced not only by nuclear bomb tests but always in increasing amount by fission reactors and fuel reprocessing as well. Tritium contamination of the environment may be utilized as a tracer in hydrological investigation, e.g. dating of underground waters. Routine tritium analysis in water samples for hydro-geological and hydrological studies are performed by liquid scintillation spectrometry. At present some degree of enrichment is essential to obtain adequate net tritium count rates for most hydrological samples. Electrolysis is generally used for the enrichment process [2]

### Materials and methods

In order to enrich the tritium in the environmental water samples, we have developed a battery of 5 electrolysis cells [1,3]. The wall (anode) of the cells is made of stainless steel tube. At the top a brass ring serves as mounting aid and as the electrical anode connection. The cathode is made of mild steel tube. The produced gas flows through a stainless steel tube welded to the cathode, that also provides the electrical connection by the help of a brass ring. From there the gas is released to the atmosphere through a long and narrow plastic tube and a silica-gel trap which absorbs the evaporated and sprayed water.

The procedure for electrolytic tritium enrichment of water requires that both the isotopic fractionation during the sample treatment, and the contamination with other water possibly of



distillation of the samples and after the enrichment a final distillation. During distillation the temperature should be high and the recovery of water close to unity. The distillation and electrolysis cells reservoirs should be separated from the room air as it usually contains water vapor with a higher  $^3\text{H}$  concentration than that of the sample. This is the reason to connect a long and narrow PVC tube as a diffusion barrier both to the condensation flask of the distillation apparatus and to the electrolysis cells. In order to obtain a desired final volume in every cell we have developed a programmable electronic system that can interrupt the current through any cell in which the desired volume of electrolyte is attained.

Each cell was filled with 330 ml of the sample water containing 5g NaOH 1%. The cells were connected in series and a voltage corresponding to 2.2-2.7 volts per cell was applied across them from the battery-charger. We have used a cooling bath with running tap water ( $4-8^{\circ}\text{C}$ ) in order to minimize the quantity of evaporated and sprayed water. A total charge of about 915 Ah is needed theoretically for a volume reduction of about 305 ml of water. When the necessary charge has passed through the cells, the current was switched off and the cells were disconnected to stop reverse current to pass through the cells as this has been found to damage the cathode surface [1]. The cells were then removed from the cooling bath and the enriched samples poured out of the cells into glass flasks and distilled without neutralizing them.

### Results and discussion

We have chosen three water samples with different content of tritium for electrolysis enrichment: tap water, precipitation water, and moisture from nuclear laboratory. We have taken two replicates A and B from the same sample. The sample A and B was distilled and electrolyzed separately: the first electrolysis for low enrichment, and the second electrolysis for high enrichment

The enrichment factor  $(EF)_T$  for the tritium content in the electrolyzed water samples is calculated by means of the enrichment factor  $(EF)_D$  for the deuterium content. The enrichment factor  $(EF)_D$  is:

$$(EF)_D = \frac{D_f}{D_i} \quad (1)$$

where  $D_i$  and  $D_f$  are the deuterium content measured before and after electrolysis by mass spectrometry.

Taking accounting for the relation between the enrichment factor  $(EF)_D$  and the separation factor  $\alpha$  for the deuterium isotope :

$$(EF)_D = \left( \frac{V_i}{V_f} \right)^{\frac{\alpha-1}{\alpha}}$$

where  $V_i$  is initial volume of sample introduced in cell for electrolysis, and  $V_f$  is final volume of sample after electrolysis, we can calculate the separation factor  $\alpha$  for the deuterium isotope.

$$\alpha = \frac{\lg \frac{V_i}{V_f}}{\lg \frac{V_i}{V_f} - \lg (EF)_D}, \quad (2)$$

The separation factor  $\beta$  for the tritium isotope was calculated using the Bigeleisen relation:

$$\ln \beta = 1,41 \ln \alpha \quad (3)$$

That is valuable in the limits of  $\pm 5\%$  errors. Finally, the enrichment factor for tritium  $(EF)_T$  is deduced from the similar relation:

$$(EF)_T = \left( \frac{V_i}{V_f} \right)^{\frac{\beta-1}{\beta}} \tag{4}$$

The results are presented in Table 1 and Tables 2.

**Table 1**

First electrolysis, low enrichment					
Sample	Tap water		Precipitation water		Moisture from nuclear lab
Cell No.	1	2	3	4	5
$V_i$ [ml]	330	330	330	330	355
$V_f$ [ml]	25	25	25	25	50
$D_i$ [ppm]	143.17	143.17	130.66	130.66	143.29
$D_f$ [ppm]	1334.7	1496.3	1462.0	1393.0	1348.7
$(EF)_T$	<b>11.3</b>	<b>12.4</b>	<b>11.4</b>	<b>11.0</b>	<b>11.3</b>

**Table 2**

Second electrolysis, high enrichment					
Sample	Tap water		Precipitation water		Moisture from nuclear lab
Cell No.	1	2	3	4	5
First stage					
$V_i$ [ml]	330	330	330	330	305
$V_f$ [ml]	25	25	25	25	50
Second stage					
$V_i$ [ml]	330	330	330	330	-
$V_f$ [ml]	25	25	25	25	-
$D_i$ [ppm]	143.7	143.7	130.66	130.66	
$D_f$ [ppm]	2579.2	2633.1	2570.8	2443.0	
$(EF)_T$	<b>21.6</b>	<b>22.5</b>	<b>21.3</b>	<b>23.0</b>	<b>22.5</b>

By using this procedure for tritium enrichment it is easy to see that the overall precision of the method is governed by the Bigeleisen relation and that it is important to assure, as it is possible, a constant value for the initial and final volume ratio  $V_i/V_f$ .

The values of the enrichment factor for tritium  $(EF)_T$  are in range of 11.0-12.4 for the low enrichment, and 21.3-23.0 for high enrichment. The results are in very good agreement with the literature [2].

The tritium (deuterium) separation factor  $\beta$  ( $\alpha$ ) depends of quality of the cathode surface. In spite of its initial chemical treatment (IAEA procedure), the best quality is attainable only after a great number of runs (about 50-60 runs). So, as our cells were not used until now for more than 20 runs, it is explicable the variances of the  $(EF)$  in spite of our effort to maintain constant the volume ratio for each of the cells into a run.

**Conclusions**

The usual improvement of the detection sensitivity by an order (or more) of magnitude for the tritium content of water samples is performed by electrolysis.

We have distilled three water samples (tap water, precipitation water, and moisture from nuclear laboratory) and placed them in electrolysis cells for two electrolyses: the first electrolysis for low enrichment, and the second electrolysis for high enrichment.

## TRITIUM ENRICHMENT OF ENVIRONMENTAL WATERS BY ELECTROLYSIS

The values of the enrichment factor for tritium  $(EF)_T$  was in range of 11.0-12.4 for the low enrichment, and 21.3-23.0 for high enrichment. The results are in very good agreement with the literature.

This paper was accomplished with the support of the EU funds under the contract TARI-HPRI-CT-2001-00149

### REFERENCES

- [1] J. F. Cameron, B. R. Rayne, *Apparatus for concentration and measurement of low tritium activities*, Proc. Sixth Int. Conf. Rad. Trit. Dating, CONF-650.652, 1965, pp. 454-464
- [2] G. T. Cook, Ch. J. Passo, and B. Carter in: *Handbook of radioactivity analysis*, ed. Michael F. L'Annunziata, Academic Press New York, 1995, pp. 358-365
- [3] D. J. Groeneveld, *Tritium analysis of environmental waters*, PhD Thesis, Univ. Groningen, 1977.

## THE STRUCTURAL CHARACTERISATION OF FOSSIL RESINS BASED ON MASS SPECTRA OBTAINED IN GC/MS MODE ON PYROLISED SAMPLE

**Z. MOLDOVAN, CORINA IONESCU<sup>1</sup>, FLORINA TUSA,  
N. PALIBRODA and A. PAMULA**

*National Institute of Research and Development of Isotopic and Molecular Technology,  
400293 Cluj-Napoca, P.O.B. 700, Romania, e-mail: zaha@ocl.itim-cj.ro*

*<sup>1</sup>University "Babes-Bolyai" Cluj-Napoca, Str. M. Kogalniceanu 1, 3400 Cluj-Napoca*

### **Introduction**

The purpose of the present papers is the application of the pyrolysis gas chromatography in combination with mass spectrometry (Py-GC-MS) to characterisation of the fossilised resins. Fossilised resins of conifers are known as amber. The most significant deposit of amber in Europe occurs along the southern shores of the Baltic Sea<sup>1</sup>. Amber from these deposits is known as Baltic amber. Other sources of amber lie in Romania (known as Romanit), North America, Canada and China. While Baltic amber has been extensively investigated from many years only few works have been published on Romanit<sup>2</sup>.

Pyrolysis gas chromatography in combination with mass spectrometry has shown to be powerful techniques for analysing a wide variety of polymeric samples<sup>3</sup>. The utility of these methods varies from obtaining simple fingerprinting information to the identification of characteristic pyrolysis product. The results obtained on a particular sample depend of the pyrolytic methods and several other experimental conditions such as pyrolysis temperature, sample size, type of column, flow rate and temperature variations<sup>4</sup>.

In order to achieve reproducible results, it is necessary to attain pyrolysis at a controlled temperature followed by efficient trapping of pyrolysis products onto column. Curie-point pyrolysis is characterised by a rapid inductive heating ( $5000 \text{ K s}^{-1}$ ) of a ferromagnetic wire containing a small mount of sample material (10 $\mu\text{g}$ ).

To increase the sensitivity of method controlled temperature program was used for a quantity of sample of few mg. The decomposition products were identified using mass spectra data base or mass spectra information about molecular mass or unsaturation degree. The sample is characterised by molecular distribution vs. unsaturated degree ( $z=0$ ;  $z=-12$ ).

### **Experimental**

#### *Sample preparation*

A quantity of 1-3mg Romanian amber was ground to a powder and then heated for 1 min at 575<sup>o</sup>C. The decomposition products were washed with 3ml of CH<sub>2</sub>Cl<sub>2</sub>. After concentration at 0.5 ml the sample was injected in GC. The sample of fossil resin (Romanite) was collected from an East-Carpathian place of Romania.

#### *Instrumentation*

Py-CG-MS analyses were performed using a Perkin Elmer Gas Chromatograph (model 990) coupled to a double focusing mass spectrometer MAT 311.

*GC condition.* A homemade GC column was used. The column characteristic was the following: 2m length, internal diameter 4mm, stationary phase OV-17 (polymer of methyl silicone). The column was heated from 60<sup>o</sup>C to 300<sup>o</sup>C with 8<sup>o</sup>C/min and maintained 10 min at the final temperature.

The ion source of the mass spectrometer was operated to electron energy of 70eV, current emission of 100  $\mu$ A and to a temperature of 180<sup>0</sup>C.

### Results and discussions

The GC/MS chromatogram (total ion current) obtained in the conditions as in experimental is shown in the Fig. 1 and the identification of the compounds is shown in the Table 1.

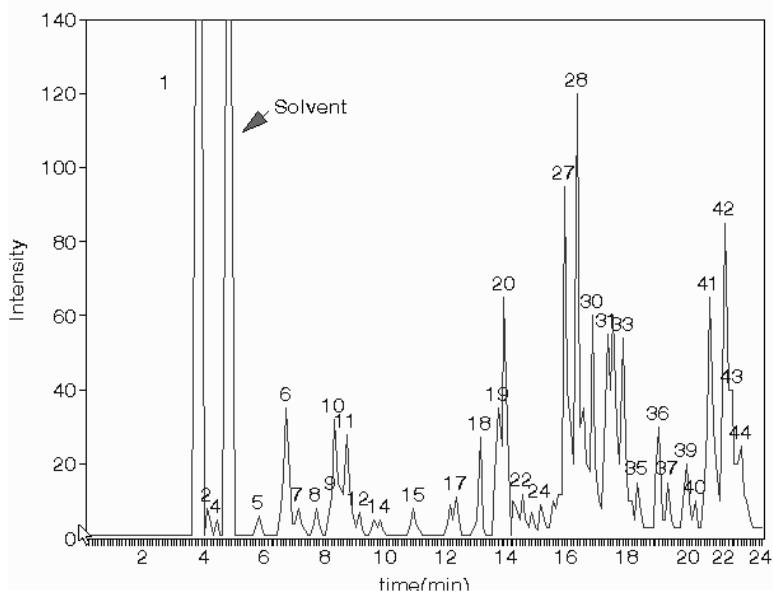


**Fig. 1.** The TIC chromatogram of the compounds obtained by pyrolysis of resin sample

The most prominent components are a variety of diterpenoid acids. Among them are the octahydrotrimethyl and octahydrotetramethyl-naphthalenes and their carboxylate derivatives. More numerous are completely or partially aromatized compounds, including alkyl-benzene, cymene and naphthalene. Our results are in good correlation with early reported composition of fossil resins<sup>2/</sup>. For every compound the unsaturation degree ( $z$ ) were estimated. The distribution of the compounds vs.  $z$  is shown in the **Table 2**.

The main contribution of the detected compounds are situated between  $z = -4$  and  $z = -10$  with the maximum on  $z = -6$ . The obtained distribution is shown in the **Fig.2**

**Table 1.**

**The identification of compounds resulting from pyrolysis of the fossilised resin (Romanite).  
The number corresponds to the peak number from Fig 1**

1. M=70: C <sub>5</sub> H <sub>10</sub> ( $z=0$ ), 1,2 dimethyl trans-cyclopropene
2.-5?
6 .M=92: C <sub>7</sub> H <sub>8</sub> ( $z=-6$ ), Toluene+M=110:C <sub>8</sub> H <sub>14</sub> ( $z=-1$ ), 4,5 dimethyl 1,3 hexadiene
7. M=124: C <sub>9</sub> H <sub>16</sub> ( $z=-1$ ), 2,4 Heptadiene
8. M=108: C <sub>8</sub> H <sub>12</sub> ( $z=-4$ ), 2,4,6 octatriene, all trans
9. M=136: C <sub>10</sub> H <sub>16</sub> ( $z=-4$ ), 3,7 dimethyl-1,3,6 trioctene (beta ocmene).
10. M=106: C <sub>8</sub> H <sub>10</sub> ( $z=-6$ ), (m+p)-xylene
11. M=124: C <sub>9</sub> H <sub>16</sub> ( $z=-2$ ), 3,3,5 trimethylcyclohexene+M=136: C <sub>10</sub> H <sub>16</sub> ( $z=-4$ ) Camphene (2:3)
12. M=122: C <sub>9</sub> H <sub>14</sub> ( $z=-4$ )

THE STRUCTURAL CHARACTERISATION OF FOSSIL RESINS

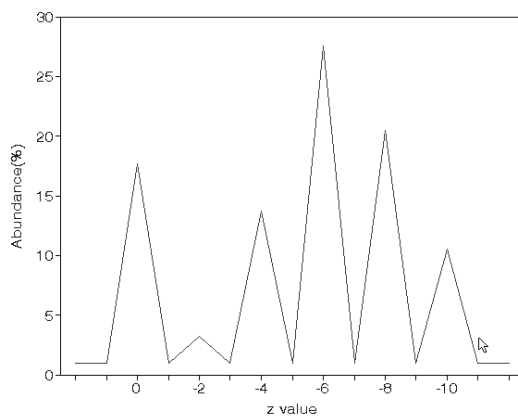
13. M=120:C<sub>9</sub>H<sub>12</sub> (z=-6), isopropylbenzene (Cumene)  
 14. M=138:C<sub>10</sub>H<sub>18</sub> (z=-2), trepan  
 15. M=134: C<sub>10</sub>H<sub>14</sub> (z=-6), (m+p) methylisopropylbenzene (cymene)+M=120(z=-6), 1methyl, 3ethylbenzene  
 16.?  
 17. M=134: C<sub>10</sub>H<sub>14</sub> (z=-6), o-cymene  
 18. M=162: C<sub>12</sub>H<sub>18</sub> (z=-6), C<sub>6</sub>-Benzene  
 19. M=176: C<sub>13</sub>H<sub>20</sub> (z=-6), C<sub>7</sub>-Benzene  
 20. M=178:C<sub>13</sub>H<sub>22</sub> (z=-4), 1,2,3,4,4a,5,8,8a-octahydro-1,4a,6-trimethylnaphtalene  
 21.-26?  
 27. M=192:C<sub>14</sub>H<sub>24</sub> (z=-4): 1,2,3,4,4a,7,8,8a octahydro-1,4a,5,6-tetramethylnaphtalene  
 28. M=190: C<sub>14</sub>H<sub>22</sub> (z=-6), C<sub>4</sub>-hexahydronaphtalene  
 29. M=202: C<sub>15</sub>H<sub>22</sub> (z=-8), Sesquiterpena+M=190:C<sub>14</sub>H<sub>22</sub> (z=-6)  
 30. M=204: C<sub>15</sub>H<sub>24</sub> (z=-6), C<sub>5</sub>-hexahydronaphtalene+M=202:C<sub>15</sub>H<sub>22</sub> (z=-8), C<sub>5</sub>-tetrahydronaphtalene.  
 31. M=204: C<sub>15</sub>H<sub>24</sub> (z=-6) C<sub>5</sub>-hexahydronaphtalene +M=202:C<sub>15</sub>H<sub>22</sub> (z=-8) C<sub>5</sub>-tetrahydronaphtalene.  
 (1:1)  
 32. M=202:C<sub>15</sub>H<sub>22</sub> (z=-8), 1,2,3,4 tetrahydro-1, 6-dimethyl-4-(1-methylethyl) naphthalene  
 33. M=204:C<sub>15</sub>H<sub>24</sub> (z=-6) C<sub>5</sub>-hexahydronaphtalene+M=202:C<sub>15</sub>H<sub>22</sub> (z=-8) C<sub>5</sub>-tetrahydronaphtalene  
 (3:2)  
 34.?  
 35. M=202:C<sub>15</sub>H<sub>22</sub> (z=-8)  
 36. M=186: C<sub>4</sub>-Dihydronaphtalene (z= -10)  
 37. M=202: C<sub>5</sub>-Tetrahydronaphtalene (z= -8)  
 38.?  
 39. M=244: C<sub>18</sub>H<sub>28</sub> (z=-8), C<sub>8</sub>-Tetraline  
 40.?  
 41. M=258:C<sub>19</sub>H<sub>30</sub> (z=-8), C<sub>9</sub>-Tetraline  
 42. M=242:C<sub>18</sub>H<sub>26</sub> (z=-10), C<sub>8</sub>-Dihydronaphtalene  
 43. M=256:C<sub>19</sub>H<sub>28</sub> (z=-10), C<sub>9</sub>-Dihydronaphtalene  
 44. M=256:C<sub>17</sub>H<sub>36</sub>O, Hydroxy-C<sub>8</sub>-Tetraline

Table 2

The compound distribution as a unsaturated degree (z=0, z=-12)

Nr. peak	A	%	z=0	z=-2	z=-4	z=-6	z=-8	z=-10	z=-12	z=x
1	220,00	17,68	17,68	0	0	0	0	0		0
2	20,00	1,61								1,61
3	8,00	0,64								0,64
4	12,00	0,96								0,96
5	7,00	0,56								0,56
6	32,00	2,57		1,54		1,03				
7	8,00	0,64		0,64						
8	6,00	0,48			0,48					
9	6,00	0,48			0,48					
10	31,00	2,49				2,49				
11	26,00	2,09		0,84	1,25					
12	7,00	0,56			0,56					
13	2,00	0,16				0,16				
14	2,00	0,16		0,16						
15	6,50	0,52				0,52				
16	8,00	0,64								0,64
17	9,00	0,72				0,72				
18	22,00	1,77				1,77				
19	32,00	2,57				2,57				

Nr. peak	A	%	z=0	z=-2	z=-4	z=-6	z=-8	z=-10	z=-12	z=x
20	59,00	4,74			4,74					
21	2,00	0,16								0,16
22	3,00	0,24								0,24
23	1,00	0,08								0,08
24	6,00	0,48								0,48
25	6,00	0,48								0,48
26	3,00	0,24								0,24
27	77,00	6,19			6,19					
28	106,0	8,52				8,52				
29	36,00	2,89				1,44	1,44			
30	56,00	4,50				3	1,5			
31	51,00	4,10				2,05	2,05			
32	53,00	4,26					4,26			
33	49,00	3,94				1,58	2,36			
34	3,00	0,24								0,24
35	13,00	1,04					1,04			
36	29,00	2,33						2,33		
37	16,00	1,29					1,29			
38	3,00	0,24								0,24
39	19,00	1,53					1,53			
40	4,00	0,32								0,32
41	62,00	4,98					4,98			
42	82,00	6,59						6,59		
43	20,00	1,61						1,61		
44	21,00	1,69				1,69				
<b>Total</b>	<b>1244,5</b>	<b>100</b>	<b>17,7</b>	<b>3,18</b>	<b>13,71</b>	<b>27,54</b>	<b>20,45</b>	<b>10,53</b>	<b>0</b>	<b>6,90</b>



**Fig. 2.** The distribution of compounds vs. unsaturated degree (z)

## REFERENCES

- 1) Walter Schumann, *Guide des Pierres et Mineraux*, Delachaux & Niestle, Lausanne, 1985, p 184
- 2) A. Banerjee, V. Ghiurca, B. Langer and M. Wilhelm, *Archologisches Korrespondenzblatt* 29 (1999) p 593-606
- 3) W. J. Irwin, *Analytical Pyrolysis*, Marcel Decker, New York, 1982
- 4) E. C. Stout, C. W. Beck, and K. B. Anderson, *Phys. Chem. Minerals* (2000), 27, 665-678.

## DETERMINATION OF CHEMICAL STRUCTURE OF POLYMERS BY PY-GC/MS

**Z. MOLDOVAN, PH. BETTEN\*, N. PALIBRODA and ILEANA CHIRTOC**

*National Institute of Research and Development of Isotopic and  
Molecular Technology, 400293 Cluj-Napoca, P.O.B. 700, Romania,  
e-mail: zaha@oc1.itim-cj.ro*

*\*Mannkiewicz Gebr. & Co., Georg-Wilhelm Strasse 189, D-21107  
Hamburg, Germany*

### Introduction

The paper discusses the pyrolysis of polymeric materials in a "Curie-point" pyrolyser and the analysis of the scission products by coupled gas chromatography-mass spectrometry. There have studied the water-soluble copolymers with complex structure. The scission products were separated on a homemade chromatograph column and than introduced on-line in mass spectrometer. The formed compounds were identified based on mass spectra data base as well as based on fragmentation rules of organic compounds/1,2,3/. The pyrolysis temperature was of 600°C for 4s.

By examination of mass spectra of compounds results from extract from liquid sample and of the compounds results from pyrolysed material (solid part obtained by dried sample) the structure of the solvent as well as the structure of copolymer was determined.

### Experimental

#### *Sample preparation*

The 1ml of sample was taken and introduced in 3 ml Chloroform. After shaken 1 min and then after 30 min three fractions could be seen. Every fraction was analyzed by high resolution mass spectrometry (HRMS), coupled system gas chromatography-mass spectrometry (GC/MS) or by Py-GC/MS.

#### *Instrumentation*

The thermal decomposition of the sample was performed in a "Curie-point" pyrolyser (Fisher Labor, Germany) at 600°C for a time of 4s.

The time separation of the scission products were obtained by GC on a homemade column of the following characteristics: l=2m, d=0.4 cm having a filling of silanised G Chromosorb 80/100 mesh with 10% of polymer SE-30, methylsilicon polymer. The temperature was programmed from 60°C to 300°C at 12°C/min.

The identification of the products were made based of mass spectra obtained in CG/MS mode. The GC/MS analyses were performed using a MAT 311 mass spectrometer operated in Electron Impact mode to 70 eV. The ion source temperature was of 180°C and emission current 100µA.

### Results and discussions

The chromatogram obtained for the products of pyrolysis (fraction 2) are shown in the Fig. 1. The compounds were identified by using mass spectra library of known compounds. Also some compounds were identified based on discussion of the main ions visible in mass spectra as well as their relative intensity.

The identified compound are shown in the Table 1



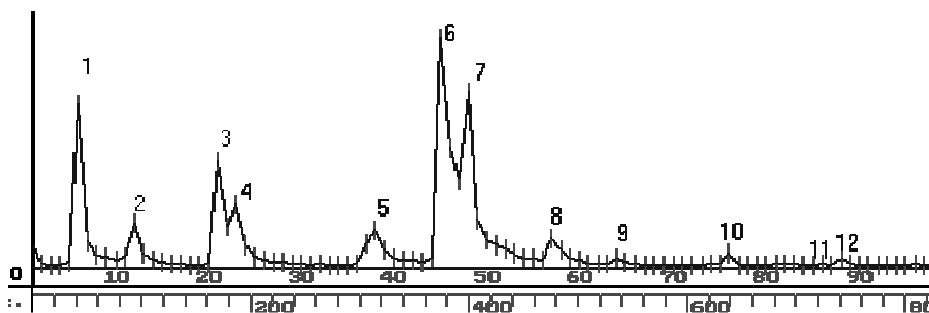


Fig. 1. GC separation of the pyrolysis products from polymer unfractionated sample

Our determination process follow the scheme:

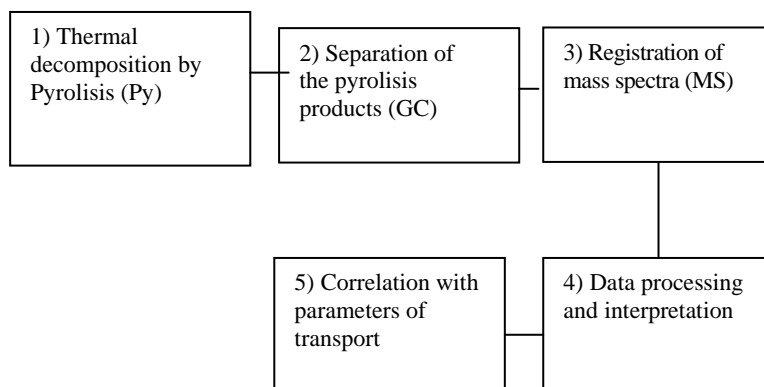


Table 1.

The identified compound resulting by thermal decomposition of the sample (pyrolysis to 600<sup>0</sup>C).

Nr. crt	compound	Peak number(Fig 1)	fraction
1	CO <sub>2</sub>	1	2
2	Butene		2,3
3	Acetaldehyde		2
4	Ammonium		1
5	Propionaldehyde		2
6	1,2 Propyleneglycole		1
7	2-Butoxyethanol		2,3
8	Styrene	6	2
9	Alkylbenzene M=190		1,2,3
10	Dioxan		3
11	Toluene	4	2
12	Alfa-methyl-Styrene	7	2
13	Beta-methyl-Styrene	8	2
14	Alkylbenzene ethoxylate		1
15	Unknown, m/z 109, 151, 169		2,3

Based on the information from Table 1 the folowing structure of product was obtained:

**A. Solvent composition:**

- 1) The **water** is the main compound;
- 2) **Ammonium** is in a concentration around of 1% with respect to water (confirmed by high-resolution mass spectrometry);
- 3) **2-butoxy ethanol** is also an important compound in solvent;
- 4) **propylene glycol (1,2 propane diol)**;
- 5) **An unknown** compound (with characteristic ions 109 and 151) used probably as non-ionic surfactant. This compound is unstable when the temperature is increasing.

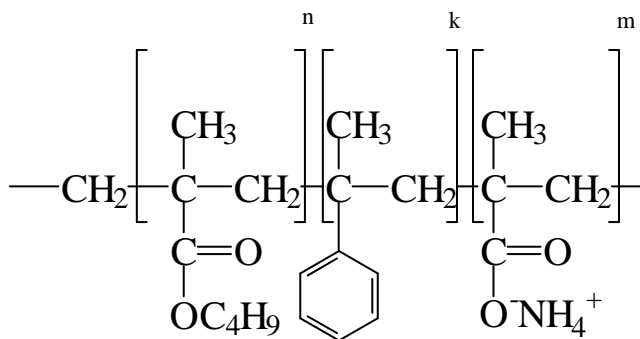
**B. Polymer composition:**

The following group of compounds were identified as scission pyrolysis products after chromatographic separation and based on mass spectra obtained in GC/MS mode:

- 1) **Toluene**;
- 2) **Ethyl Benzene**;
- 3) **Styrene as main compound**;
- 4) **Alfa-methyl styrene**.
- 5) Other **oxygenated compounds**.

On the base of identified compounds after pyrolysis results that the polymer is a styrene-based copolymer.

The probable structure of the polymer is shown in the Scheme 1.



**Scheme 1.** Probable structure of investigated polymer

**REFERENCES**

1. I.Q.N.Porter and J. Baldas, *Mass Spectrometry of Heterocyclic compounds*, Wiley-Interscience, New York, 1971
2. F. W. McLaferty and F. Turecek, *Interpretation of Mass Spectra*, University Science Books, Mill Valley, 1993
3. Z. Moldovan, Cristina Maldonado and J.M.Bayona, *Rapid. Commun. Mass Spectrom.* 11, 1077-1082 (1997)

## KINETIC ENERGY RELEASE IN SOME THIOPHOSPHORYLIC p-CARBOXYBENZENE SULFONAMIDES

\* S. NICOARĂ<sup>1</sup>, N. PALIBRODA<sup>2</sup>, Z. MOLDOVAN<sup>2</sup>, M. CULEA<sup>3</sup>,  
O. COZAR<sup>3</sup>, I. FENESAN<sup>4</sup>

<sup>1</sup> *Physics Dept., T.U.C-N, C. Daicoviciu str., 15, 3400 Cluj-Napoca,*

\* *snicoara@phys.utcluj.ro, or simona.nicoara@personal.ro*

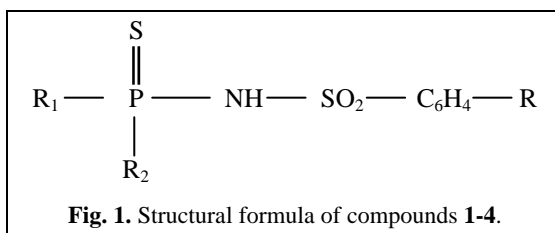
<sup>2</sup> *Nat. Inst. R.&D. Isot. Molec. Tech., Donath str., 103, 400293 Cluj-Napoca*

<sup>3</sup> *Physics, "Babeș-Bolyai" Univ., Kogălniceanu 1, 3400 Cluj-Napoca*

<sup>4</sup> *Chemistry Inst. "Raluca Ripan", Donath str., 103, 3400 Cluj-Napoca*

**ABSTRACT.** The kinetic energy release  $T$  in metastable ions transitions that correspond to the main EI fragmentations, is presented and interpreted for compound (1), as the representative of a series consisting of: p-carboxymethylbenzene sulfonamide of the O,O- diethylthio-phosphoric acid (1), p-carboxylbenzenesulfonamide of the O,O- diethyl-thiophosphoric acid (2), 2-(p-carboxymethylbenzenesulfonamido)-2-thio-no-(5,5-dimethyl-1,3,2-dioxaphosphorinane) (3) and 2-(p-carboxyl-ben-zenesulfonamido)-2-thiono-(5,5-dimethyl-1,3,2-dioxaphosphorinane) (4).

The 70 eV mass spectra were recorded and the metastable ions were analyzed in the MIKE mode, on a MAT-311 double focusing mass spectrometer. The peak width at 50 % height has been used to calculate the kinetic energy  $T_{50}$  released during the metastable ions transitions. The  $T_{50}$  values and the peak shapes are discussed, related to the type of the



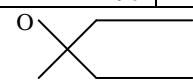
fragmentation mechanism proposed.

### Introduction

This paper aims to discuss the mass spectral data, for a series of thiophosphorylic compounds containing p-carboxybenzene-sulfonamido moieties, synthesized at the Chemistry Institute "Raluca Ripan" of Cluj-Napoca, having the structural formula given in figure 1 and Table 1 below:

**Table 1.**

**The compounds 1-4.**

Compound (mass)	1 (367)	2 (353)	3 (379)	4 (365)
Inlet temp. T (°C)	150	170	190	200
R <sub>1</sub> (mass)	C <sub>2</sub> H <sub>5</sub> O (45)	C <sub>2</sub> H <sub>5</sub> O (45)		
R <sub>2</sub> (mass)	C <sub>2</sub> H <sub>5</sub> O (45)	C <sub>2</sub> H <sub>5</sub> O (45)		
R (mass)	COOCH <sub>3</sub> (59)	COOH (45)	COOCH <sub>3</sub> (59)	COOH (45)

Thiophosphorus organic compounds have been extensively studied, owing to their wide range biologic potential, as plant growth regulators, pesticides, antiviral and therapeutic agents [2-4]. The compounds (**1-4**) belong to a series of substances with proven enzyme-inhibition activity, with potential therapeutic effect on metabolic and neurological disorders [5]. Among other spectroscopic techniques, the mass spectrometry is a reliable tool in the structural characterization of organophosphorus compounds [6-10]. In MS, the determination of the kinetic energy release  $T$ , in metastable ions analysis is helpful in ion structure studies, as they provide information on the mechanism and energetics of the fragment ions reactions [11-15].

The kinetic energy release may originate in two different sources:  $E^{++}$ , the non-fixed excess energy of the activated complex, and  $E_o^{\ddagger}$ , the reverse reaction crytical energy [11,13]. Their contributions  $T^{++}$  and  $T^{\ddagger}$  respectively, to the total translational energy, depend on the precursor ion structure, on the reaction mechanism and products. The relative contribution of  $T^{++}$  and  $T^{\ddagger}$  to  $T$  influence the metastable peak shape, thus allowing a correlation with the reaction mechanism [11,13,14]. Simple fission and reactions controlled by the statistical partitioning of the excess energy  $E^{++}$  are associated with a Gaussian peak, the squared ratio of the average (22 % height peak width) to the most probable (61 %) energy release,  $r = (w_{22}/w_{61})^2$  is equal to 3. If, on the contrary,  $E_o^{\ddagger}$  controls the fragmentation, and if the fraction of it appearing as kinetic energy covers only a small range of values,  $r < 3$ , the peak is narrower than a Gaussian one. Wider peaks, with  $r > 3$ , most likely indicate two or more mechanisms in the fragmentation of the metastable ion.

### Experimental

The measurements were made on a VARIAN MAT-311 double focusing mass spectrometer (60  $\mu$ A electronic emission, 70 eV electron energy, 150  $^{\circ}$ C ion source temperature, 800 resolution). The solid sample inlet system was maintained at different evaporating temperatures, depending on the compound: 150  $^{\circ}$ C (**1**), 170  $^{\circ}$ C (**2**), 190  $^{\circ}$ C (**3**), and 200  $^{\circ}$ C (**4**). The metastable ions analysis under slow scanning of the electric sector voltage (MIKE mode) was preferred for the calculus of the kinetic energy release, owing to the wider mass range of the daughter ions, and to the better quality of the ion optics and of the graphical signal, compared to the performance in the HV scanning.

### Results and discussion

The 70 eV mass spectra of the four compounds and their fragmentation pattern were discussed elsewhere [7]. Figure 2 shows an example of the peak shapes recorded in the MIKE mode for the transitions  $a$ ,  $m/z$  (244+R)  $\rightarrow$   $b$ ,  $m/z$  (216+R);  $a \rightarrow c$ ,  $m/z$  (188+R), and  $a \rightarrow n$ ,  $m/z$  (119+R), the ions being presented in the fragmentation pattern [7]. For single charged ions:  $m_1^+ \rightarrow m_2^+ + m_3^0$ , the kinetic energy release  $T$  (J) was calculated according to the relationship [11, 13-16]:

$$T \cong 5,62 \cdot \left( w_c / U_0 \right)^2 \cdot m_1^2 / m_2 m_3 \text{ (eV)} \quad (1)$$

with a 2970 V accelerating voltage;  $U_0$  = the electric sector voltage for the main ion beam, an average  $s = 20,76$  V/min electric sector scanning rate, and  $p = 120$  mm/min paper speed. Here  $w_c$  is the peak width, corrected with respect to the main ion beam width at 50 % and with respect to the ions masses [14,15]. Table 2 contains the MIKE experimental data recorded for the ions in the mass spectrum of compound **1** (R= COOCH<sub>3</sub>, 59 Da).

The metastable ion *a*, *m/z* 303 in compound **1** successively eliminates two neutral C<sub>2</sub>H<sub>4</sub> molecules, resulting the ions *b*, *m/z* 275 and *c*, *m/z* 247 [7]. The high values  $\langle T \rangle$  in each of these transitions (317,1 meV and 268,3 meV), the non-Gaussian peak shapes (such as in figure 1 with  $r=2,01$ ), and the high stability of the neutrals eliminated correspond to the type of fragmentations supported by the reverse activation energy  $E_o^r$ , as described in the literature [13]. The ion *a* may also generate the ion *c*, *m/z* 247, by losing two neutral ethene molecules. The process seems to involve two fission mechanisms, as supported by the peak in figure 2 ( $r = 3,13$ ), and by a relatively high  $\langle T \rangle = 71,9$  meV. This value and the stability of the neutral molecules simultaneously eliminated, suggests that  $E_o^r$  is important, thus  $T^r$  providing the dominant contribution to *T*. The ion *c* further undergoes the rearrangement of a H from hydroxyl to N, through a four member transition state, and loses a neutral radical HO<sub>2</sub>PS. The value  $\langle T \rangle = 32,4$  meV and the wide peak shape ( $r = 3,9 > 3$ ) suggests that the H transfer mechanism may stimulate the whole structure *c*, and that the excess energy  $E^{++}$  probably provides the main part of the kinetic energy *T*. The ion *a* may also generate the ion *n*, *m/z* 178 through a complex mechanism via several rearrangements with the multiple neutrals elimination: 2 H<sub>2</sub>O molecules, the C<sub>2</sub>H<sub>4</sub> molecule and the PS radical. The peak shape, close to a Gaussian one (Fig. 2) with  $r = 2.9$ , and  $\langle T \rangle = 51,6$ meV, could indicate a reaction driven by both  $E_o^r$  and  $E^{++}$ . The ion *n* may be produced via another reaction channel from the ion *b*, by the elimination of 2 neutral H<sub>2</sub>O molecules and of the neutral C<sub>6</sub>H<sub>4</sub> radical. The reaction, involving the migration of more than one atom, with a wide peak ( $r= 3,22$ ), and a kinetic energy release of 51,5 meV, may be controlled by  $E_o^r$  as well as by the excess energy  $E^{++}$ .

The simple fission of the O-P and P-N bonds in ion *b* result in the ion *q*, *m/z* 108. The corresponding MIKE peak shape is Gaussian ( $r=3,03$ ) and, the small value of  $\langle T \rangle = 37,6$  meV, suggests that  $T^{++}$  could have a dominant contribution to the total *T*. The ion *b* may also undergo the migration of a H atom from the NH group onto the aryl, through a three member transition state, losing a neutral radical, to yield the stable ion *p*, *m/z* 136. The MIKE peak shape close to Gaussian ( $r \cong 3,1$ ) and a relatively small amount  $\langle T \rangle = 28,8$  meV, indicates a dominant contribution of  $E^{++}$  in the activated complex.

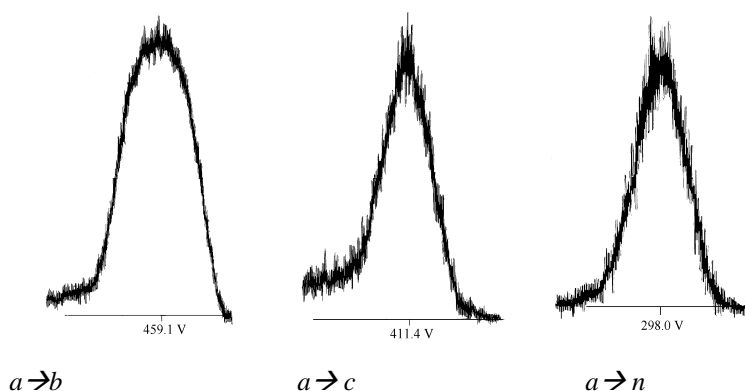


Fig. 2. MIKE peaks of the  $a \rightarrow b$ ,  $a \rightarrow c$  and  $a \rightarrow n$  transitions

**Table 2.**

MIKE data for (**1**),  $M_R = 59$  Da;  $U_o =$  main ion ( $m_1$ ) beam electric sector voltage = 504,8 V;  $U =$  electric sector voltage for recording the daughter ion ( $m_2$ );  $\sigma =$  standard deviation for 3-4 consecutive determinations of the kinetic energy release;  $\langle T \rangle =$  average of 3-4 determinations of the  $T_{50}$ . The coefficient  $r = (w_{22}/w_{61})^2$ .

$m_1/z$ (Da)	U (V)	$m_2/z$ (Da)	$\langle T \rangle \pm \sigma$ (meV)	$\langle r \rangle$
<i>a</i> , m/z 303	459,1	<i>b</i> , m/z 275 (216+R)	317,1+12,1	2,01
	411,4	<i>c</i> , m/z 247 (188+R)	71,9+1,6	3,13
	298,0	<i>n</i> , m/z 178 (119+R)	51,6+3,5	2,90
<i>b</i> , m/z 275	454,7	<i>c</i> , m/z 247 (188+R)	268,3+13,5	2,40
	327,4	<i>n</i> , m/z 178 (119+R)	56,7+5,2	3,36
	299,8	<i>o</i> , m/z 163 (104+R)	51,5+3,2	3,36
	278,1	<i>d</i> , m/z 151 (92+R)	35,6+1,7	3,10
	250,4	<i>p</i> , m/z 136 (77+R)	28,8+1,3	3,12
	198,4	<i>q</i> , m/z 108	37,6+1,7	3,03
<i>c</i> , m/z 247	469,5	<i>f</i> , m/z 230	33,0+4,7	3,32
	442,1	<i>g</i> , m/z 216	30,5+4,4	3,33
	309,6	<i>d</i> , m/z 151 (92+R)	32,4+3,6	3,90

The simple fission of the O-C bond in the metastable ion *c*, eliminates a neutral OH radical. The value  $\langle T \rangle = 33,0$  meV and the peak shape ( $r$  greater than, but close to 3), may indicate that the fission influences most of the activated complex of the structure *c*, the final product *h*, m/z 230, probably being very unstable, as its abundance is reduced (10 %) in the mass spectrum. The ion *c* also eliminates the neutral  $\bullet\text{OCH}_3$  radical. The product ion *n*, m/z 216 gives a low abundance peak in the mass spectrum of compound **1**. The peak shape ( $r \approx 3,3$ ), indicates that the whole structure *c* may be stimulated to vibration, prior to the radical loss, and  $\langle T \rangle = 30,5$  meV, suggests that its main source could be  $T^{++}$ , originating in the excess energy of the activated complex  $E^{++}$ .

### Conclusions

The kinetic energy release in the ion fragmentations apparently originated in the reverse critical energy  $E_o^r$  for the higher values  $T \in (70, 318)$  meV; in the excess energy of the activated complex  $E^{++}$ , for small values  $T \in (28, 37)$  meV; and possibly a balanced contribution of  $T^{++}$  and  $T^r$  to  $T$ , in the medium range of values,  $T \approx 50$  meV.

### REFERENCES

1. A. Scozzafava, F. Briganti, C.T. Supuran, I. Fenesan, R. Popescu, V. Muresan, S. Farcas, *Main Group Metal Chemistry*, **19** (1996) 503.
2. C. Fest and K. J. Schmidt: "The Chemistry of Organophosphorus Pesticides", Springer Verlag, Berlin, Heidelberg, New-York (1973).
3. L. Almasi, "Les composés thiophosphororganiques", Ed/ Masson, Paris (1976).

4. I. Fenesan, I. Chioreanu, A. Hantz, Al. Alexandru, R. Popescu, *FARMACIA*, **XXXI**, Nr. 3 (1988) 143.
5. C. T. Supuran, V. Muresan, R. Popescu, I. Fenesan, *Main Group Metal Chemistry*, **18**, 11 (1995) 629.
6. S. Safe and O. Hutzinger: "Mass Spectrometry of Pesticides and Pollutants", CRC Press, Cleveland (1976).
7. S. Nicoara, M. Culea, *Rapid Comm. Mass Spectrom.*, **16** (2002) 1180.
8. Monica Culea, N. Palibroda, Z. Moldovan, Simona Nicoară, I. Fenesan, R. Popescu, V. Muresan, E. Postoiu and V. Znamirovski, *Rapid Commun. Mass Spectrom.*, **12** (1998) 1808.
9. Simona Nicoară, Monica Culea, N. Palibroda, O. Cozar, I. Fenesan, A. Hantz, *Rapid Commun. Mass Spectrom.*, **9** (1995) 61.
10. I. Fenesan, R. Popescu, C. T. Supuran, Simona Nicoară, Monica Culea, N. Palibroda, Z. Moldovan and O. Cozar, *Rapid Commun. Mass Spectrom.*, **15** (2001) 721.
11. R. G. Cooks, J. H. Beynon, R. M. Caprioli, G. R. Lester: "Metastable Ions", Elsevier, Amsterdam (1973).
12. J. H. Beynon and R. K. Boyd, *Adv. Mass Spectrom.*, **78** (1978) 1115.
13. Z. Moldovan, N. Palibroda, V. Mercea, G. Mihăilescu, *Org. Mass Spectrom.*, **20** (1985) 77.
14. Z. Moldovan: "Studiul proceselor de ciocnire la molecule poliatomice prin spectrometrie de masă", teza de doctorat (1984)
15. Simona Nicoară: "Spectrometria de masă cu impact electronic în investigarea structurii moleculelor unor compuși organici biologici activi", teza de doctorat (1997).
16. S. Nicoară, Z. Moldovan, N. Palibroda, M. Culea, I. Fenesan, R. Popescu, C. Bele, *Studia Univ. Babeş-Bolyai, Physics*, XLVII, nr. 1. 2002= 37-48.

## SUPERCRITICAL FLUID EXTRACTION OF *ACORUS CALAMUS* L. ANALYSIS BY GAS CHROMATOGRAPHY- MASS SPECTROMETRY

SIMION GOCAN<sup>1</sup>, SIMONA COBZAC<sup>1</sup>, EDA PRODAN<sup>1</sup>,  
VLADIMIR CIOVARNACHE<sup>2</sup>

<sup>1</sup> *Universitatea Babeș-Bolyai, Facultatea de Chimie și Inginerie Chimică,  
Cluj-Napoca*

<sup>2</sup> *I. C. P. T. Câmpina, Prahova*

**ABSTRACT.** The composition of the supercritical fluid extraction (SEF) of European calamus (*Acorus calamus* L.) was investigated by gas chromatography-mass spectrometry (GC-MS). A total of 27 major components was detected, e. g. asarone, shyobunone and acorenone. The results show considerable qualitative and quantitative difference between the compounds extracted in supercritical conditions that an essential oil obtained by steam distillation from the same variety of plant.

### Introduction

Essential oils of *Acorus calamus* L. (*A. calamus*) are highly complex mixtures. In the early papers there was reported that the essential oil of the root of *A. calamus* is composed of  $\alpha$ -pinen, champhen, champhor, borneol, and sesquiterpene [1], reducing sugars, tannins, resins, sterol, and 1,5% essential oil [2]. Stahl and Keler [3] determined the  $\beta$ -asarone content from 45 commercial Calamus drugs. They classified *A. calamus* in four major groups, according to their  $\beta$ -asarone content determined by gas liquid chromatography (GLC). The material mostly used in Italy for aromatisation contains only 5% of  $\beta$ -asarone and no  $\alpha$ -asarone [4]. Analysis of the components of the rhizome volatile oils from *A. calamus* (sweet flag) Chinese plants showed that  $\beta$ -asarone is the major component [5]. The gas chromatography-mass spectrometry (GC-MS) method was developed for asarone isomer determination from the *A. calamus*, *A. europaeum* essential oils of Romanian origin and alcoholic extract of *A. calamus* [6]. Keler and Stahl [7] evaluated the essential oil extracted from American diploid using two different procedures for isolation of sesquiterpenes. The ether extract of the steam distillate of the rhizomes was separated by repeated silica gel chromatography. The methanol extract and the ether extract were analyzed by GLC [8]. The essential oil, obtained by means of the steam distillation, was chromatographed on silicagel. After elution of monocyclic ketones (shyobunone, epishyobunone and isoshyobunone) with petroleum ether – diethyl ether (10:1) calamendiol was eluted with ratio (5:1) and a new sesquiterpene diol and isocalamendiol was eluted with ratio (3:10). Preisocalamendiol isolated from *A. calamus* can be considered as an intermediate for isocalamendiol. Acoragermacrone was isolated from rhizomes of *A. calamus* [9-12]. Röst and Bos [13] were briefly discussed the systematic meaning of the chemistry of Acorus oils. On the basis of the totality of gas liquid chromatograms of leaf top oils and rhizomes oils seven compounds were chosen for the analysis of the taxonomic potential of the oil composition. From *A. calamus* rhizome was isolated in addition to sitosterol, the new phenyl propane derivative 1(p-hydroxyphenyl)-1-(O-acetyl)prop-2-ene [14], calamensesquiterpineol [15]. A new tricyclic sesquiterpene (calamenone) and two sesquiterpenes (calamendiol, isocalamendiol) was isolated from roots of *A. calamus* L [16]. The *A. calamus* L. essential oil obtained by steam distillation from rhizome of the Romanian plant was investigated by GC-MS [17,18]. Mazza [19,20] obtain the essential oil of European *A. calamus* L by steam distillation of fresh rhizome, or unpeeled dried rhizome, pre-separated by LSC and analyzed by GC-MS.

The present paper reports on the replacement of steam distillation or alcoholic extraction with supercritical fluid extraction (SFE) and the analysis of the extract by GC-MS.



## Experimental

**Instrumentation.** A Hewlett-Packard 7680 T extractor equipped with an auxiliary pump, HP 1050, for the modifier, was used for supercritical fluid extraction. A Hewlett-Packard 5890 Plus GC, coupled with a MSD 5972 mass spectrometer was used for separation and identification.

**Supercritical fluid extraction.** Sample was 2g of *Acorus calamus* L. prepared as powder rhizome obtained from Plantextrakt (Cluj, Romania). Extraction condition: density 0.78 g/mL; pressure 150 bar; chamber temperature 40°C; flow rate 1.0 mL/min; extraction fluid CO<sub>2</sub>; equilibration time 2.00 min; extraction time 12.10 min; thimble volume swept 2.0. Extraction trapping conditions: nozzle temperature 50°C; trap temperature 45°C; trap packing ODS; void volume compensation 1.0 mL. Fraction output: rinse solvent 1.8 mL acetone 2 mL/min; nozzle temperature 50°C.

**Separation and identification conditions.** A Hewlett-Packard 5890 Plus gas chromatograph, coupled with a MSD 5972 mass spectrometer, equipped with a capillary column HP-1 (30 m x 0,32 mm i. d.) with a 4 µm film thickness was use for separation of volatile components under the following conditions: column temperature, held 50°C for 2 min then increasing at 20°C/min to 280°C, run time 30 min; injector temperature 250°C; splitless, valve off 0.5 min flow split 10 mL/min; carrier gas (helium) flow-rate 1.4 mL/min, v = 43 cm/s. For electron impact ionization the source temperature was 200°C, and electron energy was 70 eV.

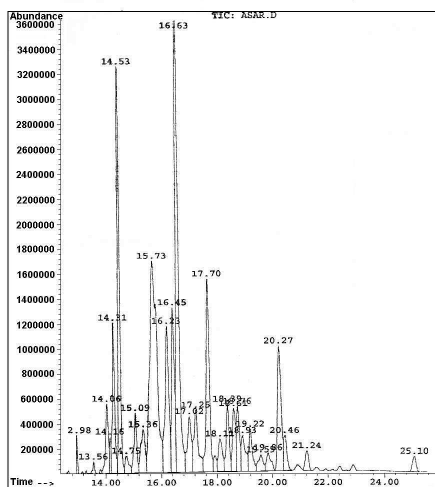


**Fig. 1.** The gas chromatogram for the supercritical fluid extract from European *Acorus calamus* L

## Results and discussion

The supercritical fluid extraction with CO<sub>2</sub> has provided a sample with a great number of extracted compounds. Table 1 shows the analytical results and Fig. 1 the gas chromatogram for the supercritical fluid extract from European *Acorus calamus* L.

The complete identification of the compounds was very difficult. The identification of the compounds was performed on the basis of their MS spectra, by comparison with the spectra library (Wiley and NIST). The European extract from *A calamus* L. is characterized by a higher amount of  $\beta$ -asarone. Even a superficial examination of the results [19, 20] clearly shows considerable qualitative and quantitative differences between the volatile fraction of an alcoholic extract [20] and that an essential oil from the same variety obtained by steam distillation [19].

The results from Table 1 shows considerable qualitative and quantitative difference between an extract obtained in supercritical conditions, an essential oil from the same variety of plant [19] and the volatile fraction of an alcoholic extract [20].

Table 1.

**The composition of *Acorus Calamus L.* extract obtained through supercritical fluid extraction and analyzed by GC-MS**

No	Compound	Molecular ion (m/z)	t <sub>R</sub> (min)	Concentration (%)
1	Methyl eugenol Benzene,1,2-dimethoxy-4-(1-propenil)	178	12.98	0.46
2	Benzene,1-(1,5-dimethyl-4-hexenyl)-4-methyl Criptoacorone	202	13.56	0.12
3	$\alpha$ -Selinene	208	14.05	2.12
4	Preisocalamendiol	204	14.16	0.48
5	Asarone	220	14.31	4.48
6	Benzene,1,2,4-trimethoxy-5-(1-propenil) Calamenol	208	14.53	10.40
7	Non identified	220	14.75	0.52
8	Non identified	225	15.09	1.79
9	Shyobunone, Iso shyobunone, Epishyobynone	193	15.36	1.91
10	(+)-3,8-Dimethyl-5-(1-methyllethylidene)-1,2,3,4,5,6,7,8-octahydroazulene-6-one	220	15.73	18.31
11	Calacone 1,4-Trans-1,7-trans-acorenone	218	16.23	6.20
12	Non identified	222	16.45	5.39
13	Calamendiol	220	16.63	16.23
14	Non identified	203	17.02	2.15
15	Non identified	238	17.26	2.40
16	Unknown sesquiterpene	223	17.70	6.81
17	Non identified	179	18.11	0.36
18	Isoacorone	236	18.39	1.24
19	Acorone	218	18.61	2.10
20	Non identified	236	18.76	2.05
21	Unknown sequiterpene	236	18.93	2.14
22	Non identified	187	19.22	1.07
23	Non identified	236	19.60	1.29
24	Non identified	208	19.86	0.36
25	Non identified	252	20.28	5.43
26	Non identified	268	21.24	0.42
27	Non identified	207	25.10	0.75

The supercritical extract contains (table 1): asarone (10.40%), sesquiterpeneketone, e. g. shyobunone and its isomers (18.31%), sesquiterpenes, e. g. calamendiol (2.40%). Also, contain in high concentration *trans*-acorenone (18.31%).

### Conclusion

In this way the supercritical extract from *A. calms L.* can be analyzed directly without any preparation, permitting easier identification of the individual components.

REFERENCES

1. G. P. Pivnenko, R. K. Chargovets, O. V. Chaiko, M. F. Loknitskaya, T. Khar'Kov, *The chemical and antibacterial properties of the essential oil of Accorus root*, Farmatsevt. Inst. 1957, No. 1 294-299; Refrat. Zühr. Khim., Biol. Khim., 1958, Abstr. No. 27435; C. A.,53(1959), 4425a.
2. B. C. Bose, R. Vijayvargirja, A. Q. Saifi, S. K. Sharma, *Chemical and Pharmacological Studies of Acorus calamus*, J. Am. Pharm. Assoc., Sci. Ed., **49**(1960), 32-34.
3. E. Stahl, K. Keller, *Über den unterschiedlichen  $\beta$ -Asarongehalt handelsüblicher Kalmusdrogen*, Pharmazie, **36**(1981), 53-57.
4. L. Usseglio-Tomasset, *Gas-chromatographic examination of some essential oils of Acorus calamus,[aromatic calamus]* Industrie Agrarie, **4**(1966), 153-156.
5. H Yuanzheng, H Zougying, C Yannuai, W Yialin, *Analysis of the components of the rizome volatile oils from Chinese Acorus plants and rational use of resource*, Sepu, **11**(1993), 267-270;C. A.,120 (1994) 46437.
6. R. Oprean, M. Tamas, L. Roman, *Comparison of GC-MS and TLC techniques for Asarone isomers determination*, J. Pharm. Biomed. Anal., **18**(1998), 227-234.
7. K. Keller, E. Stahl, *Zusammensetzung des aterischen Oles von B-Asaronfreim Kalamus*, Planta Medica, **47**(1983), 71-74.
8. S. Yamamura, M. Iguchi, A. NishiYama, M. Niwa, *Sesquiterpenes from Acorus calamus L.*, Tetrahedron, **27**(1971), 5419-5431.
9. M. Iguchi, A. Nishiyama, *Isolation and structures of three new sesquiterpenes*, Tetrahedron Lett., **51**(1968), 5315-5318.
10. M. Iguchi, A. Nishiyama, H. Koyama, S. Yakamura, Y. Hirata, *Isolation and structure of isocalamendiol*, Tetrahedron Lett., **42**(1969), 3729-3732.
11. M. Iguchi, A. Nishiyama, S. Yakamura, Y. Hirata, *Preisocalemendiol, a possible precursor of isocalamendiol*, Tetrahedron Lett., **43**(1970), 855-857.
12. M. Iguchi, M. Niwa, A. Nishiyama, S. Yakamura, *Isolation and structure of acoragermacrone*, Tetrahedron Lett., **29**(1973), 2759-2762; C. A. 79 (1973) 126651n.
13. L. C. M. Röst, R. Bos, *Biosistematic Investigations with Acorus L.*, Planta Medica, **36**(1979), 350-361.
14. A. K. A. Chowdhury, T. Ara, M. F. Hashim, M. Ahmed, *A new fenilpropane derivative from Acorus calamus*, Pharmazie, **48**(1993), 786-787.
15. W. Lijun, S. L. Ling, L. Maixiang, *The structural analysis of a new cristal sesquiterinpenol in Acorus calamus*, Zhougguo, Yaowu Huaxue Zazhi, **3**(1993), 201-202;C. A., 121(1994), 78242s.
16. W. Lijun, S. L. Ling, L. Maixiang, Y. Hua, Z. R. Jiang, L. Yang, T. Zhiyne, Z. Qitai, N. Toshio, *Constituents of the roots of Acorus calamus L.*, Yakugaku Zasshi, **114**(1994), 182-185. C. A., 121(1994), 53966t.
17. R. Oprean, M. Tamas, R. Sandulescu, L. Roman, *Essential oils analysis. I. Evaluation of essential oils composition using both GC and MS fingerprints*, J. Pharm. Biomed. Anal., **18**(1998), 651-657.
18. R. Oprean, L. Oprean, M. Tamas, R. Sandulescu, L. Roman, *Essential oils. II. Mass spectra identification of terpene and phenilpropane derivatives*, J. Pharm. Biomed. Anal., **24**(2001), 1163-1168.
19. G. Mazza, *Gas chromatographic and mass spectrometric studies of the constituents of the rhizome of Calamus*, J. Chromatogr., **328**(1985), 179-194
20. G. Mazza, *Gas chromatographic and mass spectrometric studies of the constituents of the rhizome of Calamus*, J. Chromatogr., **328**(1985), 195-206.

## MASS SPECTROMETRY CHARACTERIZATION OF SOME *n*-OCTADECYL CHEMICALLY MODIFIED ADSORBENTS USED AS STATIONARY PHASES IN TLC

**Z. MOLDOVAN<sup>1</sup>, VIRGINIA COMAN<sup>2</sup> and MIUȚA FILIP<sup>2</sup>**

<sup>1</sup> *National Institute for Research & Development of Isotopic and Molecular Technology, 71-103 Donath Street, RO-400293 Cluj-Napoca, Romania, E-mail: zaha@ocl.itim-cj.ro*

<sup>2</sup> *"Raluca Ripan" Institute for Research in Chemistry, 30 Fântânele Street, RO-400294 Cluj-Napoca, Romania, E-mail: v.coman@icrr.cj.edu.ro*

**ABSTRACT.** Some chemically modified stationary phases have been prepared by organosilanization reactions using silica gel R and different aluminas as inorganic support and some trifunctional modifiers. The characterization of these stationary phases by mass spectrometry puts in evidence the presence of the adequate chains on the surface of modified silica gel and aluminas, respectively.

**Key Words:** Chemically modified stationary phases, *n*-octadecyl silica gel R, *n*-octadecyl alumina, thin layer chromatography

### INTRODUCTION

The chemically modified stationary phases with organic compounds are widely used in chromatography to increase the selectivity and the efficiency of the chromatographic separations [1-3].

The silica gel R samples were modified with *n*-octadecyltrichlorosilane [1] and some different alumina samples (alumina R and alumina 150 T) were modified with *n*-octyl, *n*-octadecyl, 3-mercaptopropyl, N-(2-aminoethyl)-3-aminopropyl trifunctional modifier [2, 3]. The characterization of stationary phases by mass spectrometry is not frequently met in literature [4-6]. The pyrolysis coupled by mass spectrometry method applied to the modified stationary phases permitted the characterization of the attachment agent functionality and of the "end-capping" phases [5].

In this paper, a mass spectrometry method is described for the characterization of *n*-octadecyl silica gel R and of two alumina types *n*-octadecyl chemically modified used as stationary phases in thin layer chromatography.

### EXPERIMENTAL

The unmodified and chemically modified silica gel R was prepared at the "Raluca Ripan" Institute for Research in Chemistry, Cluj-Napoca, Romania.

Aluminium oxide 150 acidic type T (acidic alumina) and *n*-octadecyltrichlorosilane were purchased from E. Merck (Darmstadt, Germany). Aluminium oxide N (basic alumina) was supplied by Macherey-Nagel (Düren, Germany).

The chemically modified stationary phases have been obtained by the organosilanization reaction using different trifunctional modifiers.

The mass spectra were registered on a FINIGAN MAT 311 spectrometer with double focusing. The experimental conditions have been the following: electron energy 70 eV, emission current 100  $\mu$ A, ion source temperature 180°C. The sample has been introduced directly in the ion source and heated up to 350°C in approximately  $10^{-6}$  torr vacuum. The mass spectra of all samples have been continuously registered.

## RESULTS AND DISCUSSION

An ideal representation of the modifications performed by the silanization reaction of hydroxylated surface of supports, with *n*-octadecyltrichlorosilane modifier is given in Figure 1.

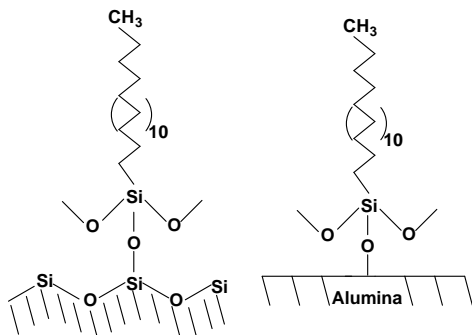


**Fig. 1.** Ideal representation of *n*-octadecyl chemically modified silica gel and alumina, respectively.

The mass spectra of unmodified and chemically modified samples were performed. The comparative mass spectrometry study of these stationary phases puts in evidence the presence of the *n*-octadecyl chain on the surface of modified adsorbent. The  $m/z$  values (where  $m$  is mass number and  $z$  is number of electron loss by ionization) for all studied samples have been in the range 16-300 Daltons.

The characteristic mass spectra for *n*-octadecyl silica gel R is presented in Figure 2. Similar results were obtained for alumina samples.

Since the *n*-octadecyltrichlorosilane modifier has been used for the chemical modification of silica gel R, acidic alumina and basic alumina, the  $m/z$  36 ion characteristic for HCl has been observed for all samples.

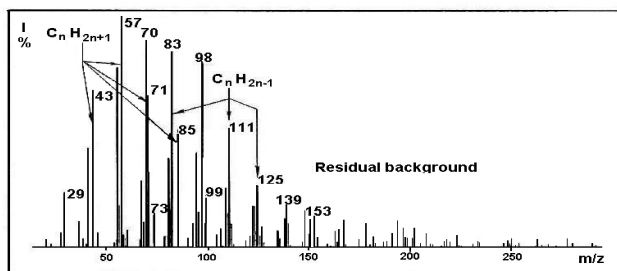


**Fig. 2.** Mass spectra in maximum intensity point for *n*-octadecyl silica gel R.

For both type of chemically modified stationary phases (*n*-octadecyl silica gel and *n*-octadecyl alumina), the main ions observed in the mass spectra are:  $m/z$  18 due to the presence of  $-OH$  residual groups and  $m/z$  between 29 and  $M-15$  of *n*-alkyl part ( $M$  is the mass number of R). The last ions proceed from the *n*-alkyl chain fragmentation bonded on stationary phases.

The fragmentation rules of hydrocarbons with normal chain determine the presence in the mass spectrum of ions which correspond to the  $C_nH_{2n+1}$  (29, 43, 57, 71, ...,  $M-15$ ) series. These ions are accompanied by those of  $C_nH_{2n-1}$  (27, 41, ...) series due to the molecular hydrogen loss [7].

The periodicity of ions with a mass difference of  $\Delta m = 14$  ( $CH_2$ ) must be mentioned. The ion intensity with  $m/z$  over than 57 is decreasing when their mass number is increasing.

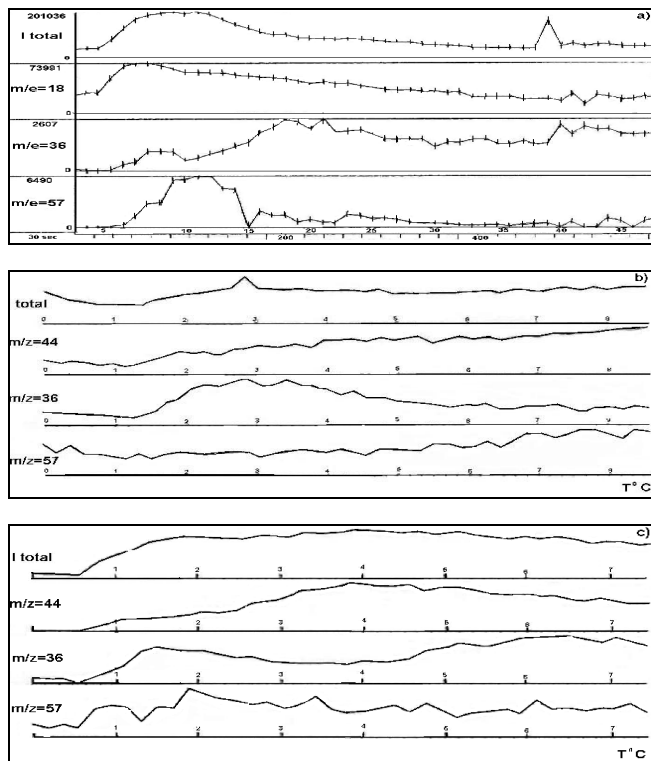


**Fig. 3.** Intensity of characteristic ions *versus* temperature for: a) *n*-octadecyl silica gel R b) *n*-octadecyl alumina T c) *n*-octadecyl alumina N

The variation of characteristic ions of  $m/z$  18 (water), 57 (organic part) and 36 (hydrochloric acid) *versus* temperature for all samples has been studied (Figure 3).

In all cases, the  $[C_4H_9]^+$  ion with  $m/z$  57 presents high abundance and can be used to show the quantity of organic part released *versus* temperature.

The released water by the heating of samples in the mass spectrometer proves that the reaction of some  $-OH$  groups with the trifunctional modifier takes place. The water quantity is increased at the unmodified phase comparatively with those modified.

### CONCLUSIONS

The present study shows that the unmodified and *n*-octadecyl modified adsorbents can be characterized by mass spectrometry by drawing the characteristic ion intensity as a temperature function.

The data obtained by mass spectrometry are in agreement with those obtained by elemental analysis, specific surface area measurements, FTIR spectroscopy and thermoanalytical study. All these data indicate the change of the hydrophilic character of unmodified surface of adsorbent into hydrophobic one. The 2-3 functionality of *n*-octadecyltrichlorosilane modifier is confirmed too.

### ACKNOWLEDGEMENT

The authors thank to MEC-CNCSIS for the financial support of Grant No. 318/2002.

## REFERENCES

1. V. Coman, C. Măruțoiu, Gh. Marcu and M. Brie, *Obtaining and Characterization of Chemically Modified Silica Gel R IV. n-Octadecyl Silica Gel R (Obținerea și caracterizarea silicagelului R modificat chimic IV. Silicagel R n-octadecil)*, Rev. Chim. (Bucharest), 1997, 48, 33-39.
2. C. Măruțoiu, M. Filip, C. Tigae, V. Coman, R. Grecu and Gh. Marcu, *Synthesis and Characterization of Chemically Modified Alumina R with n-Octyl for Use as a Stationary Phase in TLC*, J. Planar Chromatogr.-Mod. TLC, 2003, 16, 183-185.
3. M. Filip, V. Coman, R. Grecu and Z. Moldovan, *Characterization of Some Chemically Modified Acidic Alumina Samples for TLC*, Proceedings of the International Symposium on Planar Separations, Budapest, Hungary, 21-23 June 2003, 231-242.
4. S. Héron and A. Tchaplă, *Propriétés et caractérisation des phases stationnaires et phases mobiles de chromatographie liquide à polarité de phases inversées*, Analusis, 1993, 21, 327-347.
5. R.E. Aries, C.S. Gutteridge and R. Macrae, *Pyrolysis - Mass Spectrometry Investigations of Reversed-Phase High-Performance Liquid Chromatography Phases*, J. Chromatogr., 1985, 319, 285-297.
6. K.K. Unger, *Packings and Stationary Phases in Chromatographic Techniques*, K.K. Unger (Editor), Marcel Dekker, Inc., New York and Basel, 1990, Chapter 6, 331-470.
7. F. W. McLafferty, F. Turecek, *Interpretation of Mass Spectra*, University Science Books, Mill Valley, 1993.

## **VACUUM SYSTEM PROTECTION AND AUTOMATION UNIT (VSPAU) DESTINED TO MODERNIZE THE IZOTOPIC ANALYSYS MASS SPECTROMEETER**

**NICOLAE LUPSA, VALENTIN MIREL, STEFAN POPESCU**

*National institute for Research and Development of Isotopic and Molecular  
Technologies, P.O.Box 700, 3400 Cluj-Napoca 5, Romania*

The high vacuum protection ensurance is necessarily so that the izotopic analys mass spectrometer correctly work and require boths: the using of the high performance vacuum pumps and the nonstop working of them. If there are no some condition assured during pumps running, they get out of order. For this reason there is of capital importance the existence of a electronic unity destined to keep working the pumps if only the necessarily conditions are acomplished.

The isotopic analysis spectrometer vacuum system is made up by two distinct subsystems: one wich assures the vacuum in the magnetic analisys chamber and another which assures the vacuum in the inlet subsystem.

The first subsystem is made up of preliminary vacuum pump, one turbomolecular pump, air electrovalves and separation electrovalves, two gauges for preliminary vacuum measurement at the preliminary vacuum pump input, respectively at the turbomolecular pump output and a high vacuum gauge for vacuum measurement in the chamber analyser.

The second subsystem is structured also by preliminary vacuum pump, one spreading pump, air electrovalves and separation valves, two preliminary gauges and a high vacuum gauge.

The V.S.P.A.U. consist of several parts like:

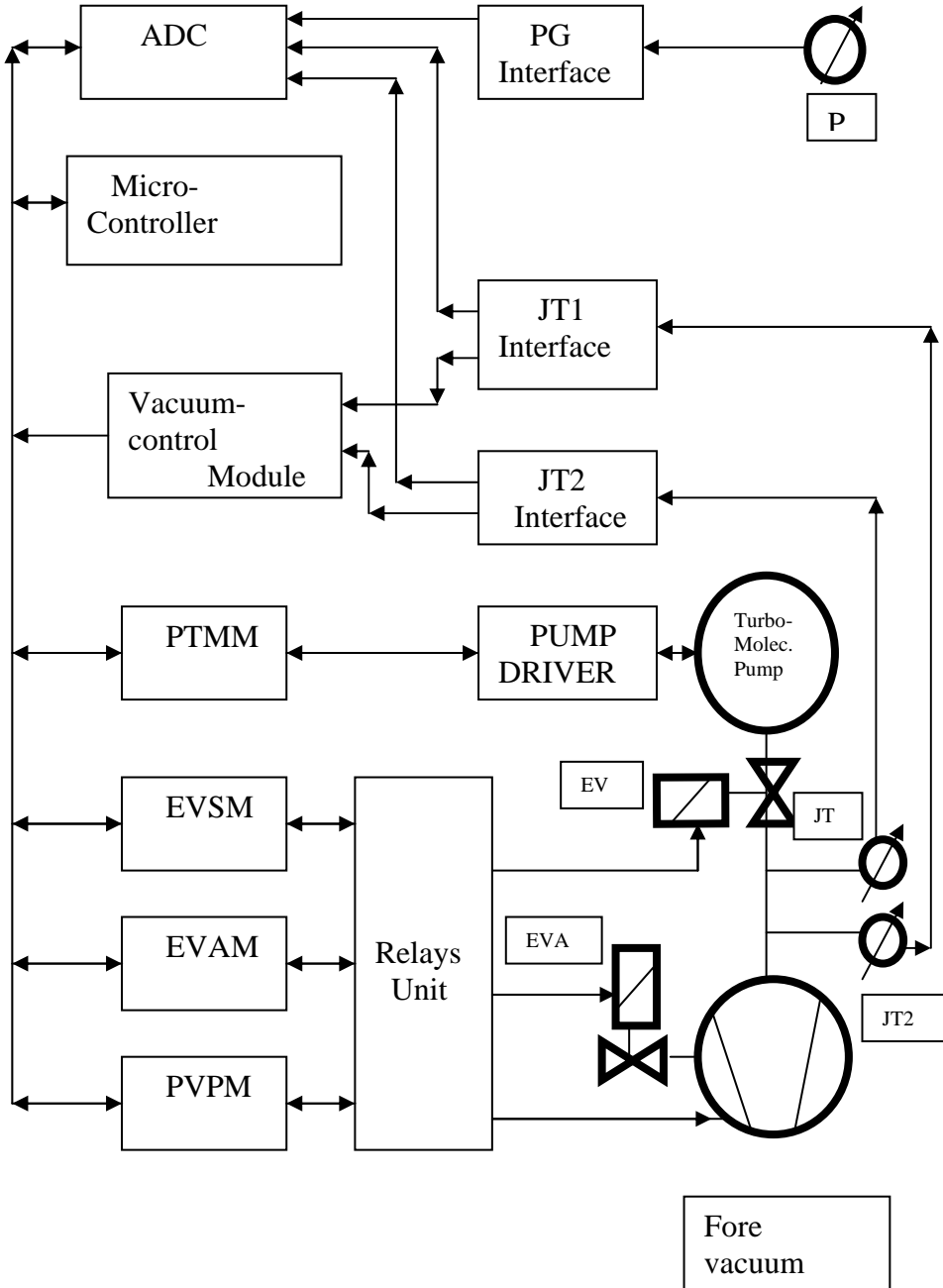
- the electronic circuitry for vacuum poms and for electrovalves action,
- the electronic relays for overload protection,
- the vacuum measure circuitry coresponding to the vacuum gange,
- the logic circuitry which assures pump working conditions check (protection function) and the corect starting, respectively stoping sequences (automation function).
- assures the correct shut down of mass spectrometer in case of accidental net voltage fall (power suplay interrupt protection), and the automatic restarting when the net voltage restarts,
- for the VSPAU building we have designed and realized the electronic relays for overload protection as well we used the CMOS integrated circuits in local protection logic of the power components (pumps, electro valves, heating resistors).

By means of some dedicated microcontrollers starting sequences and restarting protocols for the two vacuum systems are achived.



VACUUM SYSTEM PROTECTION AND AUTOMATION UNIT

The block diagram for VSPAU is the following:



The major functions of the unit are accomplished by the following modules:

**1. Vacuum control module.**

- a) It manages the logical signals from the vacuum gauges and made the command signals in correlation with the other system components.
- b) Memorises all the abnormal events.

**2. PVPM**

This module checks and assures the proper vacuum pump with protection at short circuits and overload.

**3. EVSM**

Manages the separation valve during the start, stop and restart after failure process of the mass spectrometer.

**4. EVAM**

This module drives and checks the air electro-valve and memorises the failure events.

**5. PTMM**

Makes the connection the micro-controller module and the turbo-molecular unit giving the Start- Stop commands and checking the signals from it.

All of these modules are interconnected with the microcontroller unit by a bus system.

The micro-controller unit manages:

- Start sequence commands
- Stop sequence commands
- Acquire the signals from the vacuum gauges
- Linearise the transfer function of the vacuum gauges
- Digital display for the vacuum system parameters.

## HPLC DETERMINATION OF SOME ANTIBIOTICS

**VIRGINIA COMAN<sup>1</sup>, VERONICA AVRAM<sup>1</sup>, LOREDANA SORAN<sup>1</sup>,  
RODICA GRECU<sup>1</sup>, Z. MOLDOVAN<sup>2</sup> and HAJNALKA FARKAS<sup>3</sup>**

<sup>1</sup> "Raluca Ripan" Institute for Research in Chemistry, Department of Chromatography, 30 Fântânele Street, RO-400294 Cluj-Napoca, Romania, E-mail: v.coman@icrr.cj.edu.ro

<sup>2</sup> National Institute for Research & Development of Isotopic and Molecular Technology, 71-103 Donath Street, RO-400293 Cluj-Napoca, Romania

<sup>3</sup> "Babeș-Bolyai" University, Faculty of Chemistry and Chemical Engineering, 11 Arany Janos Street, RO-400028 Cluj-Napoca, Romania

**ABSTRACT.** The determination of antibiotics presents some difficulties because of their thermal instability. The HPLC method at room temperature is preferred in the last decade. This work presents a simple HPLC method for the determination of some antibiotics (ampicillin, cefuroxime, lincomycin, penicillin, gentamicin, oxacillin and chloramphenicol). The registering of chromatograms was performed with a high performance liquid chromatograph JASCO – 980 (JASCO, Japan) equipped with an UV-VIS detector (190–400 nm). The BORWIN Soft has processed the HPLC data. For all antibiotics the calibration curves were registered in the concentration range of 0.2–1.0 mg/ml.

### Introduction

The antibiotics are considered to be a group of chemical substances obtained from the cellular metabolism or through partial synthesis, some of them reproduced by synthesis, which in highly diluted solutions have the property to stop the development and even to destroy some microorganisms [1]. Traditionally, microbiological methods have been used for analysis of antibiotics; these methods are time-consuming (entailing bacterial culture) and normally non-specific. More recently, other methods have been described, including GC with different detectors, HPLC and TLC; these have been shown to be fast, accurate, and specific for many antibiotics. Most of these methods are used for the evaluation of raw material in the pharmaceutical industry, where the moiety to be evaluated is almost always free from interference [2].

At present, high performance liquid chromatography (HPLC) is the most important separation method and the most important analytical technique as well [3]. HPLC is an excellent tool for the determination of antibiotics [4].

A HPLC system, using a strong cation exchanger and isocratic elution, was developed for the separation of the main components of gentamicin (C<sub>1</sub>, C<sub>1a</sub>, C<sub>2</sub>, C<sub>2a</sub>) and C<sub>2b</sub> (sagamicin) in less than 20 minutes. The detection was performed by postcolumn derivatization with *o*-phthalaldehyde and a fluorescence detector. The detection limit was 10 ng for gentamicin C<sub>1</sub>. Some commercial gentamicin samples were analyzed. The stationary phase was two columns Nucleosil 100-10 SA, 250 x 4.6 mm ID each; eluent: 1.1 M KCl solution, adjusted to pH 3.0 with HCl, flow rate 2 mL/min; detection: fluorescence, excitation 338 nm and emission 455 nm [5].

A reversed phase liquid chromatographic method for the analysis of some penicillins and cephalosporins of closely related structure is described. The influence of eluent pH and NaCl concentration on the resolution of ampicillin and epicillin is discussed.

The method can be applied to the selective analysis of synthetically produced antibiotics and their pharmaceutical preparations. Because of the high sensitivity (10<sup>-7</sup> g/cm<sup>3</sup>) the method can also be used for the analysis of penicillins in physiological fluids. The stationary phase was column Nucleosil 100-5 CN, 250 x 3 mm ID; eluent: 0.05 M phosphate buffer pH 7 + CH<sub>3</sub>OH (7:3.6, v/v); flow rate: 3.2 mL/min; detection: UV 220 nm [6].

## EXPERIMENTAL

This work presents a simple HPLC method for the determination of some antibiotics, such as: ampicillin, chloramphenicol, oxacillin and penicillin (ANTIBIOTICE, Iași), cefuroxime (SCHEIN, USA), lincomycin (LEK, Slovenia), gentamicin (KRKA, Slovenia).

The chromatograms were performed using a high performance liquid chromatograph (Jasco, Japan) equipped with a HPLC pump (Model PU-980), a low pressure gradient unit (Model LG-980-02), an in-line degasser (Model DG-980-50) and an UV-VIS detector (Model UV-970/975).

The solutions of studied antibiotics were prepared in HPLC grade water.

The samples were introduced by manual injection with Hamilton Rheodyne Syringe (50  $\mu$ L) in a valve of 20  $\mu$ L loop.

To find the optimum UV wavelength for the detection of mentioned antibiotics, the UV-VIS spectra were registered on UNICAM UV4 spectrometer.

For the determination of these antibiotics, the following experimental HPLC parameters were established: wave length 220 nm; column NUCLEOSIL 120-C18, 5  $\mu$ , 25 $\times$ 0.4 cm; mobile phase acetonitrile – water with ammonium acetate buffer 80 mM, in the ratio 20:80 (v/v); flow rate of 1 mL/min.

Some antibiotics were detected also at 270 nm (cefuroxime, chloramphenicol) and 250 nm (gentamicin) in order to improve the HPLC detection limit.

The BORWIN Soft has processed the HPLC data. For all antibiotics, the calibration curves were registered in the concentration range of 0.2–1.0 mg/ml.

## RESULTS AND DISCUSSION

The ampicillin, cefuroxime, lincomycin, penicillin, gentamicin, oxacillin, chloramphenicol can be separated by this method because they have different retention times in the same HPLC conditions. The chromatogram is given in Figure presented below.

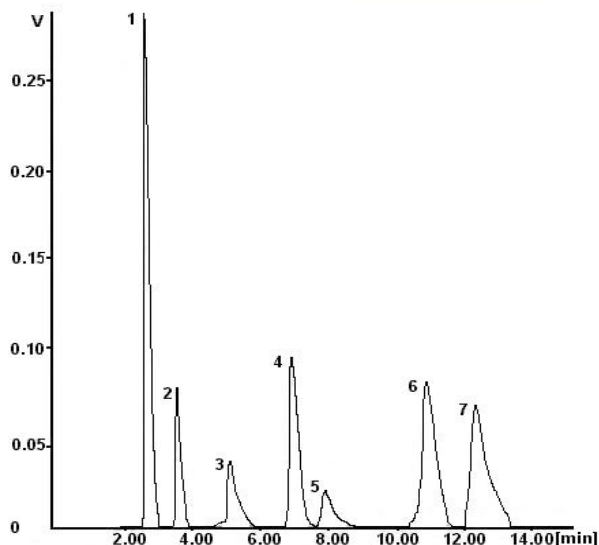


**Figure.** HPLC chromatogram of studied antibiotics: 1-ampicillin; 2-cefuroxime; 3-lincomycin; 4-penicillin; 5-gentamicin; 6-oxacillin; 7-chloramphenicol.

The calibration curves were performed by plotting peak area *versus* known injected amount of compounds. These are straight lines with the correlation factors of  $r > 0.995$ .

The retention times, detection limits and correlation factors for studied antibiotics are given in the table below.

**Table**  
**Retention times (RT), detection limits (DT) and correlation factors (r) for studied antibiotics.**

No.	Antibiotic	RT [min]	DL [ $\mu\text{g/ml}$ ]	r
1	Ampicillin	2.70	50.0	0.99567
2	Cefuroxime	3.58	12.5	0.99972
3	Lincomycin	5.12	50.0	0.99960
4	Penicillin	7.00	3.1	0.99895
5	Gentamicin	7.95	50.0	0.98335
6	Oxacillin	11.01	0.8	0.99573
7	Chloramphenicol	12.46	12.5	0.99925

### CONCLUSIONS

A HPLC method was performed for the determination of seven antibiotics, namely: ampicillin, chloramphenicol, oxacillin, penicillin, cefuroxime, lincomycin and gentamicin.

The HPLC conditions of this method are: column NUCLEOSIL 120–C18, 5  $\mu$ , 25 $\times$ 0.4 cm; mobile phase acetonitrile – water with ammonium acetate buffer 80 mM (20:80, v/v); flow rate of 1 mL/min; detection at 220 nm.

The quantitative determination of mentioned antibiotics are possible using the calibration curves.

This HPLC method can be used for the identification of antibiotics from different matrices (biological media, food products etc), for the verifying of antibiotic identity and to put in evidence the possible modifications during the storage.

### ACKNOWLEDGEMENTS

This work was financial supported by VIASAN Program (Contract No. 059/2001) of the National Plan for Research-Development and Innovation.

### REFERENCES

- [1] M. Balş, *Clinical Laboratory in Infections (Laboratorul clinic în infecții)*, Medical Publishing House, Bucharest, 1982, 259–310.
- [2] M. Vega, G. Garcia, R. Saelzer, R. Villegas, *HPTLC Analysis of Antibiotics in Fish Feed*, *J. Planar Chromatogr.*, 1994, 7, 159–161.
- [3] V. R. Meyer, *Practical High-Performance Liquid Chromatography*, III<sup>th</sup> Edition, John Wiley & Sons Ltd., Chichester, 1998.
- [4] \*\*\*, *LC Applications*, Macherey-Nagel, 1996, 90-101.
- [5] G. Seidl, H.P. Nerad, *Gentamicin C: Separation C<sub>1</sub>, C<sub>1a</sub>, C<sub>2</sub>, C<sub>2a</sub> and C<sub>2b</sub> Components by HPLC Using Isocratic Ion-Exchange Chromatography and Postcolumn Derivatization*, *Chromatographia*, 1988, 25, 169–171.
- [6] V. Hartmann, M. Rödiger, *Application of HPLC to the Analysis of Penicillins and Cephalosporins*, *Chromatographia*, 1976, 9, 266–272.

## M.O. CALCULATIONS OF VIBRATIONAL SPECTRA OF SOME UREIDES AND THIOUREIDES; THEORETICAL CONTRIBUTIONS TO C=S GROUP LOCALIZATION ON I.R. SPECTRA

CORINA ANCA SIMION

*"Horia Hulubei" National Institute for Physics and Nuclear Engineering, 407 Atomistilor St. PO Box MG – 6, R 76900, Magurele, Bucharest*

Using computational Chemistry program HyperChem 5.02<sup>(1)</sup>, two series of compounds starting with urea and thiourea have been investigated.

This paper presents the results on the following (thio)ureas and (thio)ureides: (thio)urea, methyl(thio)urea, phenyl(thio)urea, and formyl(thio)urea respectively.

Simulation stages on HyperChem 5.02. Program:

1. “building” of compound structure
2. “constraints...” on N atoms to tetrahedral and on C(O, S) atoms to trigonal
3. “restraints...” for H intramolecular bond formation and for the phenyl orientation between parallel and perpendicular positions relatively to the six membered pseudo heterocycle plane H-N-C(S, O)-N-C-O (for ureide type compounds)
4. introducing “Periodic Box” conditions
5. geometry optimization using **MM<sup>+</sup>**: Polak-Ribiere optimizer, RMS (Gradient) of 0.1 kcal/mol.Å; single point calculations
6. geometry optimization using **semi empirical AM1 / PM3** methods: Polak-Ribiere optimizer, RMS (Gradient) of 0.1 kcal/mol. Å (then 0.01 kcal/mol. Å), accelerated convergence, singlet state, RHF, total charge zero, spin multiplicity of one; single point calculations
7. calculating vibrations and performing a vibrational analysis (all normal modes of vibration must have only positive values for a molecule reaching minima on EPS).

The aim of the MO calculations was a theoretical study of band positions of the C=S group in the vibrational spectra of thioureides. For a correct attribution of signals, the homologues in ureide serie were taken into account. The original data concerning a general characterization of these molecules, and frequencies assignments by type of bonding in i.r. spectra versus literature data are presented in Table 1<sup>(2)</sup>, and a comparative study for C=O and C=S bond values<sup>(3, 4)</sup> is described in Table 2.

The attributions for the C—H (aromatic) and N—H bonds in phenyl(thio)urea were made by comparison with the values obtained from the thiocarbanilide and N-Benzoyl-N'-phenylthiourea simulations.

Table 1.

General assignments for (thio)ureides; intercomparison with experimental and literature data (relative intensities in brackets)<sup>(2)</sup>

AM1 frequencies	PM3 frequencies	Experimental frequencies (Kbr)	Frequencies in literature data (5,6)	Attributions
347-443(w); 690(i); 478-666(mi); 744(m); 752(wm); 904(wm); 943-1228(wm); 1314(m)	357-463(w); 469-670(m); 756-774(m); 921(m); 950-1226(m); 1049(m); 1304(m)	440(w); 690(i); 500-680(mi); 740(i); 780(i); 910(w); 940-1100(wm); 1040(w); 1340(w)	350-450(wm); 690-710(i); 730-770(i); 900(w); 950-1225(w); 1045(w); ~ 1300(w)	bending bonds; skeleton
1296(m); 1573(i)	1477(i); 1622(i)	1490(m); 1610(i)	1471-1613(-i)	CS stretching in thioureides
1345-1453(wm)	1383(m); 1435(w)	1370(m); 1400(m); 1450(m)	~ 1380(m); 1430-1470(m); ~1460(m)	C-H bending bonds in CH <sub>2</sub> , CH <sub>3</sub>
1441; 1670-1791(w;mi)	1574-1785(mi)	1460(vw); 1500(vw); 1580(m); 1600(m); 1650-2000(vw)	1450; 1500(vw); 1580(-i); 1600(mi); 1650-2000(vw)	C-H bending bonds in phenyl; aromatic overtones
1482; 1560(mi)	1535(m)	1520-1560(m, broad)	1475-1580(wm)	N-H bending bonds; Band II (CO)
1631(m); 1992(vi)	1896(vi)	1690(vi)	1600-1850(vi)	CO stretching; Band I (CO)
3002-3107; 3157(wm)	2887-3056(i)	2850-2920(mi)	2853-2962(mi)	C-H stretching in CH <sub>2</sub> , CH <sub>3</sub>
3110; 3175-3200(mi)	3063-3169(mi)	3030(m)	3010-3040(m)	C-H aromatic stretch
3284; 3386(i)	3182(w); 3312(m)	3180(mi); 3260(mi)	3280-3330 and 3060-3100(mi) in solid state 3400-3500(mi) in solutions	N-H stretching

Table 2.

Comparative study of band frequencies in (thio)ureas and (thio)ureides

Compound	Calculated frequencies, cm <sup>-1</sup>	Attributions
Thiourea	1155	skeleton
	1482	C=S
	1644	C=S
	1703	N—H
	1704	N—H
Urea	1176	skeleton
	1242	skeleton
	1592	C=O
	1707	N—H
	1716	N—H
Formylthiourea	1975	C=O
	1093	skeleton
	1302	skeleton
	1353	C=S
	1387	C—H (CHO)
	1604	C=O
	1643	C=S
1717	N—H	
2003	C=O	

Compound	Calculated frequencies, cm <sup>-1</sup>	Attributions
Formylurea	1219	skeleton
	1315	skeleton
	1378	C—H (CHO)
	1575	C=O
	1602	C=O
	1705	N—H
	1977	C=O
Methylthiourea	2005	C=O
	1109	skeleton
	1205	skeleton
	1340	C=S
	1364	C—H (CH <sub>3</sub> )
	1371	C—H (CH <sub>3</sub> )
	1384	C—H (CH <sub>3</sub> )
	1462	N—H
	1603	N—H
1675	C=S	
Methylurea	1707	N—H
	1212	skeleton
	1368	C—H (CH <sub>3</sub> )
	1372	C—H (CH <sub>3</sub> )
	1386	C—H (CH <sub>3</sub> )
	1454	N—H
	1553	C=O
	1608	N—H
1712, 1970	N—H, C=O	

Table 3.

**Comparative study of band frequencies in (thio)ureas and (thio)ureides (part two)**

Compound	Calculated frequencies, cm <sup>-1</sup>	Attributions
Phenylthiourea	1252	skeleton
	1327	skeleton
	1333	C=S
	1380	N—H
	1449	N—H
	1555	C—H (aromatic)
	1588	C—H (aromatic)
	1638	C=S
	1690	C—H (aromatic)
	1707	N—H
	1744	C—H (aromatic)
	1778	C—H (aromatic)
	Phenylurea	1255
1330		skeleton
1356		N—H
1446		N—H
1523		C—H (aromatic)
1576		C—H (aromatic)
1608		C=O
1689		C—H (aromatic)
1706		N—H
1745		C—H (aromatic)
1780		C—H (aromatic)
1964		C=O

In all compounds, the thiocarbonyl signals appear in the generally accepted interval data tables. For the carbonyl group, a combined signal has been obtained over 1850 cm<sup>-1</sup> associated with the corresponding signal in amido-acids. For all compounds, the  $\nu_{\text{CO}}/\nu_{\text{CS}}$  ratio remains in the 1.14 – 1.60 range as suggested by literature data<sup>(5,6)</sup>.



## BIBLIOGRAPHY

1. HyperChem; Release 5.02. For Windows 95/NT. Molecular Modeling System, Hypercube, Inc., 1997.
2. Simion C. A., *Vibrational analysis and infrared spectra of N[1-<sup>13</sup>C]capronyl-N'-phenylthiourea (<sup>12</sup>C, <sup>13</sup>C, <sup>14</sup>C) using computational chemistry*, *Proceedings of the 8th International Symposium on the Synthesis and Applications of Isotopes and Isotopically Labelled Compounds*, Wiley & Sons, Ltd, NY, 2003 (in press).
3. Mecke H., Mecke R. and Lüttringhaus D., *Z. Naturforsch.*, 1955; 105B: 367-375.
4. Bellamy L.J., *The Infra-red Spectra of Complex Molecules*, Edited by London: Methuen & Co. Ltd.; New York: John Wiley & Sons, Inc., 1959.
5. Jones R.N., *Infrared spectra of organic compounds: Summary charts of principal group frequencies*, NRC Bulletin No.6, Ottawa, 1959.
6. Avram M. and Mateescu Gh. D., *Infrared Spectroscopy. Applications in Organic Chemistry*, Wiley Interscience, New York, 1972.

## FT- IR SPECTROSCOPY FOR LIGNINS CHARACTERIZATION

<sup>1</sup>GEORGETA CAZACU, <sup>2</sup>CARMEN- MIHAELA POPESCU, <sup>3</sup>V. I. POPA,  
<sup>2</sup>GH. SINGUREL, <sup>1</sup>CORNELIA VASILE

<sup>1</sup>*“Petru Poni” Institute of Macromolecular Chemistry, Aleea Gr. Ghica Vodă  
41 A, 6600-Iași, Romania*

<sup>2</sup>*“Al. I.Cuza” University, Optics-Spectroscopy Depart., Bd. Carol I, 11, 6600-Iași,  
Romania*

<sup>3</sup>*“Gh. Asachi” Technical University, Iasi, Romania*

**ABSTRACT.** FT-IR spectroscopy was applied to obtain new structural information and characterization of various native lignins and chemically modified lignins. The relative content of different functional groups was appreciated by normalized intensities and deconvolution of the bands.

### INTRODUCTION

Lignins characterisation is a very difficult task, because of its diversity in respect both with provenience and method of separation. The elaboration of well-defined analytical methods is very important for its introduction as raw material in industry. The heterogeneity of lignin is caused by variation in polymer composition, size, cross linking, functional groups, linkage type between the phenylpropane monomers (p- hydroxy phenyl, guaiacyl and siringyl units). The major chemical functional groups in lignin include: hydroxyl, methoxyl, carbonyl and carboxyl. [1,2]

Taking into account these general information about structure of lignin is very evident that FT-IR spectroscopy can be a very useful tool for characterisation of different native lignins or chemically-modified lignins.

### EXPERIMENTAL

#### *Materials*

The studied lignin samples received from ATO- Netherlands and Granit- Switzerland were classified in two groups: lignin from woody plants and lignin from annual plants (see column 1, Table 1). The methods of delignification were also different. Several samples were chemically modified by oxidation or nitration (NL) reaction using a mixture of nitric acid and acetic acid.

#### *Method*

The IR spectra were recorded for solid samples in KBr tablets using a FT-IR Bomem MB-104 spectrometer (Canada) with a resolution of 4 cm<sup>-1</sup>. The concentration of the sample in the tablets was constant of 2.5 mg samples/ 482 mg KBr. Processing of the spectra was done by means of Grams/ 32 program. The normalised intensity was evaluated for main bands characteristic to lignin structure, such as: 3450 cm<sup>-1</sup>(ν<sub>OH</sub>), 2920 cm<sup>-1</sup>(ν<sub>asCH<sub>2</sub></sub>,guaiacyl- siringyl), 2840 cm<sup>-1</sup>(ν<sub>sCH<sub>2</sub></sub> ,guaiacyl- siringyl), 1730 cm<sup>-1</sup>(ν<sub>C=O</sub> non conjugated ketone and aromatic ester), 1658 cm<sup>-1</sup>(ν<sub>C=O</sub> aryl ketone p-substituted, guaiacyl), 1510 cm<sup>-1</sup> and 1425 cm<sup>-1</sup>(ν<sub>C=C</sub> aromatic ring, guaiacyl- siringyl), 1325 cm<sup>-1</sup>(ν<sub>s</sub> siringyl ring),1275 cm<sup>-1</sup>(ν<sub>s</sub> guaiacyl ring, ν<sub>asC-O-C</sub>),1220 cm<sup>-1</sup> (ν<sub>s</sub> siringyl ring),1030 cm<sup>-1</sup> (δ<sub>C-H</sub> guaiacyl aromatic ring and δ<sub>C-OH</sub> primary alcohol), and 860 cm<sup>-1</sup> (γ=CH aromatic ring ,guaiacyl- siringyl).[3]

Shoulders and complex bands were deconvoluted for a good assessment.

### RESULTS AND DISCUSSION

The spectral data of the studied lignins are given in table 1.

It can be remarked that the strongest hydrogen bonds are present in lignin from Pine and Curan lignin and also in lignosulfonates whose  $3450\text{ cm}^{-1}$  band is very strong. The bands at  $1275\text{ cm}^{-1}$  and  $1220\text{ cm}^{-1}$  ( $1330\text{ cm}^{-1}$ ) (Fig.1a,b,c) assigned to guaiacyl, respectively siringyl ring increase/decrease in the series studied of lignin from woody plants.

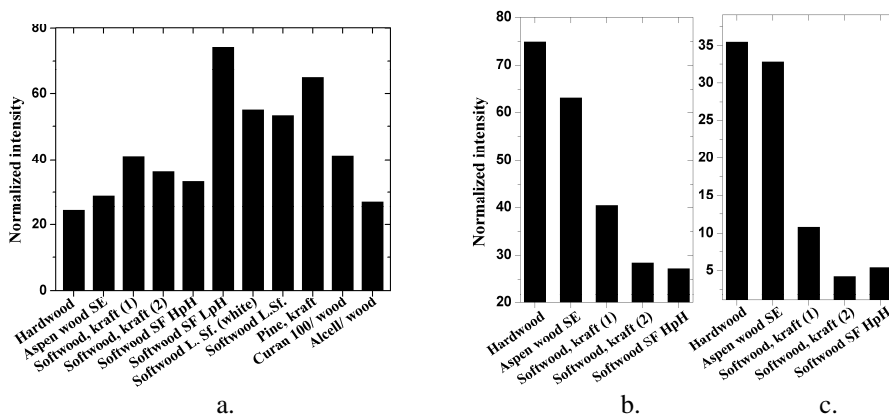


**Fig. 1.** Variation of the normalised intensities of the bands at  $1275\text{ cm}^{-1}$ (a),  $1220\text{ cm}^{-1}$ (b) and  $1330\text{ cm}^{-1}$ (c)

The lignin from annual plants have much complex IR spectra, the bonds at  $2840\text{ cm}^{-1}$  and  $1325\text{ cm}^{-1}$  are stronger than those of woody plants (see Table 1). The oxidation leads to the destruction of aromatic ring because of introduction of carbonyl and carboxyl groups. The bands at  $1275\text{ cm}^{-1}$  ( $\nu_s$  guaiacyl ring) (Fig.2a),  $1510\text{ cm}^{-1}$  ( $\nu_{C=C}$  aromatic ring, guaiacyl- siringyl) (Fig.2b) and  $1700\text{ cm}^{-1}$  ( $\nu_{C=O}$  non conjugated ketone) (Fig.2c) decrease in the series studied of lignin from flax.

**Table 1.**

**FT-IR results for lignins of various origins and for chemically modified lignins**

vs - very strong, s - strong, m - medium, w - weak, vw - very weak, NL A-fraction precipitated with dioxane, NL B-fraction precipitated with ethyl ether/ dichloroethane, NL C-fraction precipitated with water and NL D- residue

Names	$E_H$ (the energy of hydrogen bond)	$3450\text{ cm}^{-1}$ $\nu$ OH	$2920\text{ cm}^{-1}$ $\nu_{as}$ $\text{CH}_2$ guaiacyl - siringil	$2840\text{ cm}^{-1}$ $\nu_s$ $\text{CH}_2$ guaiacyl - siringil	$1730\text{ cm}^{-1}$ $\nu$ C=O non conjugated ketone and aromatic ester	$1658\text{ cm}^{-1}$ $\nu$ C=O aryl ketone p-substituted guaiacyl	$1510\text{ cm}^{-1}$ $\nu$ C=C aromatic ring; guaiacyl - siringil	$1425\text{ cm}^{-1}$ $\nu$ C=C aromatic ring; guaiacyl - siringil	$1325\text{ cm}^{-1}$ $\nu_s$ siringil ring and $\nu$ C-O	$1275\text{ cm}^{-1}$ $\nu_s$ guaiacyl ring; $\nu_{as}$ C-O-C aromatic ester	$1220\text{ cm}^{-1}$ $\nu_s$ siringil ring	$1080\text{ cm}^{-1}$ $\delta$ C-H guaiacyl aromatic ring and $\delta$ C-OH primary alcohol	$866\text{ cm}^{-1}$ $\gamma$ =CH aromatic ring; guaiacyl - siringil [...]
Lignins from woody plants													
Hardwood organosolv	3.08	m	m	m	—	m	s	m	w	v w	m	w	v v w
Aspen wood/ SE	3.17	s	m	m	—	—	m	m	w	v w	m	w	—

Names	$E_H$ (the energy of hydrogen bond)	$\nu_{OH}$	$\nu_{as} CH_2$	$\nu_s CH_2$	$\nu_{C=O}$ non conjugated ketone and aromatic ester	$\nu_{C=O}$ aryl ketone p-substituted guayacil	$\nu_{C=C}$ aromatic ring: guayacil - siringil	$\nu_{C=C}$ aromatic ring: guayacil - siringil	$\nu_{C=O}$ aromatic ring and $\nu_{C-O}$	$\nu_{as} C-O-C$ aromatic ester	$\nu_s$ siringil ring	$\delta_{C-H}$ guayacil aromatic ring and $\delta_{C-OH}$ primary alcohol	$\gamma=CH$ aromatic ring: guaiacil - siringil [...]
Softwood, kraft (1)	3.25	v s	m	—	—	w	m	v w	v v w	w	w	w	v v w
Softwood, kraft (2)	3.25	v s	—	—	v w	m	m	w	v v w	w	w	w	v v w
Softwood SF HpH	3.59	m	—	—	v v w	m	v w	w	v v w	w	w	w	—
Softwood SF LpH	3.25	m	m	—	—	w	s	w	—	m	m	m	v v w
Softwood L.Sf. (white)	3.34	v v s	m	—	v w	m	m	v w	v w	m	m	s	v v w
Softwood L.Sf.	3.59	m	—	—	v w	m	w	m	—	m	s	s	—
Pine, kraft	3.77	m	m	m	—	w	m	v w	vw	m	m	m	v w
Curan wood	3.68	m	w	w	v v w	w	w	v v w	—	w	w	w	v v w
Alcell/ wood	3.25	m	m	m	—	m	s	m	w	v w	m	m	v w
Lignins from annual fibre crops													
Flax SF (1)	3.34	s	v s	s	—	m	m	v v w	v w	m	m	m	v v w
Flax SF(2)	3.51	s	v s	s	—	m	m	w	v w	m	m	m	vw
Flax oxidized	3.42	s	v s	m	m	m	m	v w	v w	w	m	w	v v w
PF 3035/ Flax	3.42	s	s	s	—	m	m	v w	v v w	w	m	w	v v w
Straw	2.99	v s	m	w	m	m	m	w	vw	w	m	m	—
BPD/ Straw	3.08	s	m	m	m	—	m	w	v v	m	m	m	—
Sisal	3.17	s	m	m	w	—	m	w	w	v v w	w	w	v v w
Sisal/ Soda pulping	3.25	s	s	m	m	s	m	w	w	v v w	m	m	v v w
PF 3074/ Hemp	3.42	s	s	m	m	m	v w	v w	w	w	w	w	v v w
Hemp	3.42	v s	s	m	w	m	w	v w	v w	v w	v w	v w	v v w
Jute	2.99	s	s	m	m	m	m	w	v w	v w	m	m	v v w
Abaca	2.65	v s	m	m	—	—	s	m	w	—	s	w	w
Nitrolignins													
NL A	2.75	m	v w	v v w	—	v s	—	—	v s	—	—	—	—
NL B	3.15	m	m	w	s	s	—	—	s	—	m	—	—
NL C	3.71	m	w	v v w	—	v s	—	—	s	m	—	—	—
NL D	4.24	m	m	m	m	—	—	—	m	m	m	v w	—

The presence of the -NO<sub>2</sub> and -ONO<sub>2</sub> groups was possible to be evidenced only after deconvolution (Fig. 3b-d), they appearing in spectrum as very weak peaks (880 cm<sup>-1</sup>), or shoulders (1277 cm<sup>-1</sup>, 1544 cm<sup>-1</sup>), or overlapped with other bonds (1614 cm<sup>-1</sup>) (Fig. 3a).

Therefore FT-IR spectroscopy can be successfully used in the characterisation of complex molecules as lignin, having in view that its structure depends on the raw material, extraction/separation procedure and chemical modification.

## FT- IR SPECTROSCOPY FOR LIGNINS CHARACTERIZATION

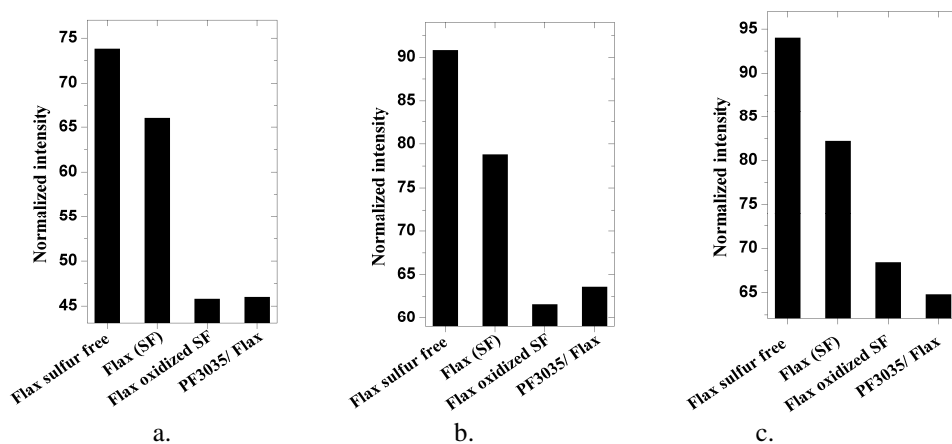


**Fig. 2.** Variation of the normalised intensity of the bands at 1275cm<sup>-1</sup>(a), 1510 cm<sup>-1</sup>(b) and 1700 cm<sup>-1</sup>(c)

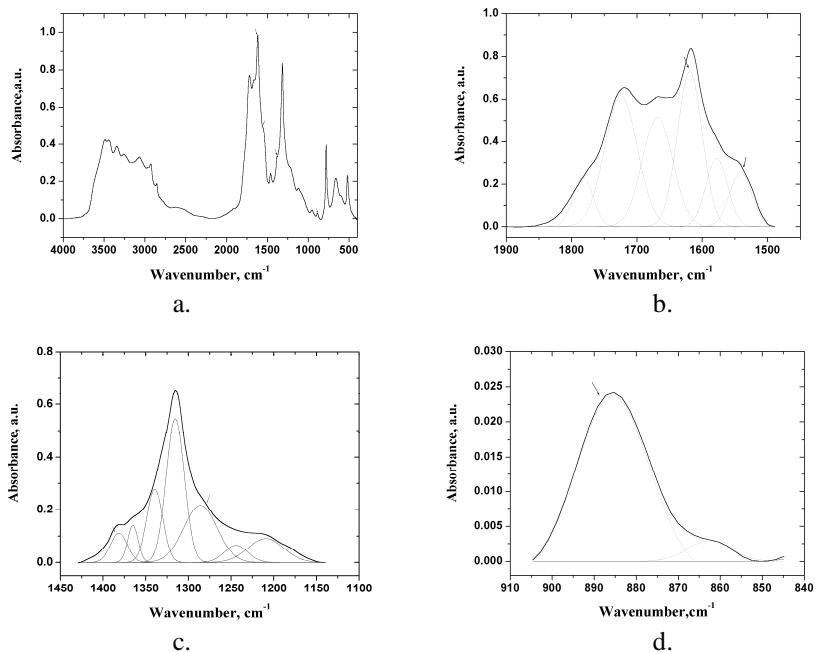


**Fig. 3.** FT-IR spectra of nitrolignin(a) and deconvolutions for 1900-1450 cm<sup>-1</sup>(b), 1450-1100 cm<sup>-1</sup>(c) and 910-840 cm<sup>-1</sup>(d) regions of the spectra

## REFERENCES

1. R.J.A.Gosselink, A.Abächerli, H.Semke, R.Malherbe, P.Käuper and J.E.G.van Dam, *Characterisation of sulfur-free lignins from alkaline pulping of annual fibre crops*, Fifth International Forum of ILI, Bordeaux France, September 7, 2000
2. A.Abächerli, *New lignins from agricultural plants*, Idem.
3. A.Bermello, M.del Valle, U.Orea and L.R.Carballo, *Characterisation by IR spectrometry of lignins of three eucalyptus species*, Intern. J. of Polym. Mat., 51: 557-566p, 2002

## SPECTROSCOPICAL STUDY OF SOME SYSTEMS CONTAINING LIQUID CRYSTALLINE COMPONENTS

**MARIA-CRISTINA POPESCU<sup>1</sup>, CORNELIA VASILE<sup>1</sup>, DANIELA FILIP<sup>1</sup>,  
DOINA MACOCINSCHI<sup>1</sup>, GH. SINGUREL<sup>2</sup>**

<sup>1</sup> *Romanian Academy, "P. Poni" Inst. of Macromolecular Chemistry, 41A  
Grigore Ghica Vodă Alley, Iași-ROMANIA*

<sup>2</sup> *"Al. I. Cuza" University, Optics and Spectroscopy Department, 11 Blvd. Carol I,  
Iași- ROMANIA*

**ABSTRACT.** The FT-IR spectroscopy was applied to determine interactions and transition temperature of two different kinds of systems CP/PEA and CP/ PTHF exhibiting properties liquid crystals.

### INTRODUCTION

FT-IR spectroscopy is a valuable technique to study both low molecular weight and polymer liquid crystals (LCs) (especially polyurethanes) [1-2], and also to estimate of interactions and morphological changes in polymer blends such as: poly(arylene phosphine oxide)/bisphenol A poly(hydroxy ether) [3], poly(styrene-co-vinylphenol)/poly( $\epsilon$ -caprolactone) [4] and polysaccharides/maleic copolymers [5]. In order to combine the properties in the components of a blend it is necessary to investigate the phase behaviour.

The FT-IR spectroscopy was used to evidence the colesteryl palmitate influence on the transition temperature of some polymeric systems exhibiting crystal-liquid.

### 1. EXPERIMENTAL PART

#### 1.1. Materials

As semi-crystalline isotropic polymeric compound are used poly(ethylene adipate) (PEA) and poly (tetrahydrofuran) (PTHF).

PEA is a commercial product purchased from Fibrex SA Savinesti, Romania ( $\overline{M}_n = 2000$  g/mol), PTHF is a BASF product, ( $\overline{M}_n = 2000$  g/mol) and CP was used as a low molecular additive. It is a product purchased from Nopris SRL, Cluj Napoca, Romania

#### 1.2. Blends preparation

Semi-crystalline PEA, PTHF and CP were separately dissolved in 1,2-dichloroethane (DCE) to form 0.8 g/dL solutions. Then, the solutions were mixed in the following CP/ PEA and CP/PTHF ratios (wt/wt): 1) 2/ 98, 2) 4/ 96, 3) 6/ 94, 4) 10/ 90, 5) 16/ 84, 6) 32/ 68, 7) 64/ 36 and 8) 80/ 20. The mixtures of solutions were stirred for 5 h. After that, the solvent was slowly evaporated at room temperature. In order to remove the residual solvent and moisture, the samples were dried in a vacuum oven at 50 °C for 2-6 days and total removal was checked by IR spectroscopy.

#### 1.3. Investigation method

FT-IR spectra at different temperatures were recorded for solid samples in KBr tablets using a FT-IR Bomem MB-104 spectrometer (Canada) with a resolution of 4 cm<sup>-1</sup>. The

concentration of the sample in the tablets was constant of 3 mg/ 500 mg KBr. The behaviour of the samples was followed both on heating and on cooling using a heating/cooling rate of 1°C/min. Processing of the spectra was done by means of Grams/32 program [Galactic Industry Corporation].

## 2. RESULTS AND DISCUSSION

As expected, the spectra of the blends obtained at room temperature contain the bands corresponding to the both components. With the aim of establishing if the blending determined spectral changes, the pure components spectra were taken into account and on the basis of additivity law. The calculated spectra of the blends were obtained and were compared with the experimental ones recorded at room temperature. For an immiscible blend the additive spectrum is overlapped with the experimental one while for a miscible or partially miscible blend could appear differences (frequency shifts, band broadening) changes in the intensity of some bands caused by intermolecular interactions between components. The differences could be attributed to some conformational changes, too. In the case of CP/PEA blends can remark differences between experimental and calculated spectra in 2750-3100  $\text{cm}^{-1}$ , 1350-1500  $\text{cm}^{-1}$  and 1000-1350  $\text{cm}^{-1}$  regions (fig 1.A.)

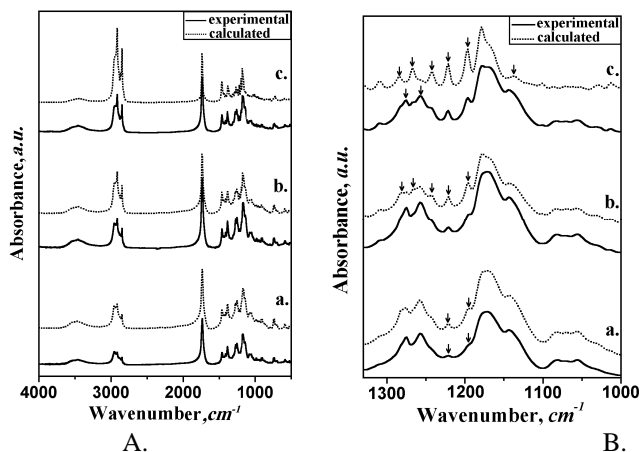


**Fig. 1.** Experimental and calculated spectra in 500-4000  $\text{cm}^{-1}$  region (A) 1100-1350  $\text{cm}^{-1}$  region (B) of 10 CP/90 PEA (a), 32 CP/68 PEA (b) and 80 CP/20 PEA (c), respectively.

For the some blends (32 wt % CP) in the 1100-1350  $\text{cm}^{-1}$  region (fig 1.B) the experimental spectrum of the blends with prevalent content of CP is a composed spectra of the overlapped bands of components, those of PEA being much better evidenced, while the calculated spectra are as expected similar with that of CP.

In the case of CP/PTHF blends it can be remarked differences between experimental and calculated spectra in 2750-3100  $\text{cm}^{-1}$  and 900-1800  $\text{cm}^{-1}$  regions. In this case the differences are not so evident as in the case of CP/PEA. To evidence the difference we subtract calculated spectra from experimental spectra. (Fig. 2)

These spectral modifications could be attributed to the interactions between components, conformational changes or phase transitions.

In order to elucidate this aspect, further information was obtained from the spectra recorded on heating up to 100 °C followed by cooling down to room temperature (heating/cooling rate 1°C/min).

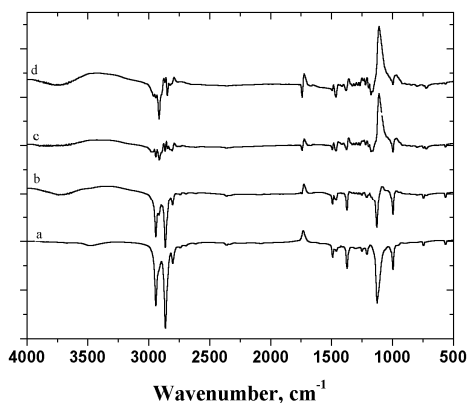


**Fig. 2.** Difference spectra of 8 CP/92 PTHF (a), 32 CP/68 PTHF (b), 64 CP/36 PTHF (c) and 80 CP/20 PTHF (d)

The most sensitive bands at variation of temperature are the bands at: 1257 and 1275  $\text{cm}^{-1}$  for PEA, 1267, 1242, 1221 and 1196  $\text{cm}^{-1}$  for CP and 1012  $\text{cm}^{-1}$  and 998  $\text{cm}^{-1}$  for PTHF, which are also present in the blends. These bands disappear by heating at transition temperature and reappear on cooling, at approximately the same temperature, the phenomenon being reversible.

Correlating these data with those obtained by DSC [6] we might assign these bands to the crystalline structure of the components of the blends. The melting of the crystalline phase is thus the phase transition evidenced by IR spectroscopy.

For the determination of the transition temperature, the curves of the dependence of integral absorption of these bands on temperature were fitted to a Boltzmann function (using Origin 6.1 program).

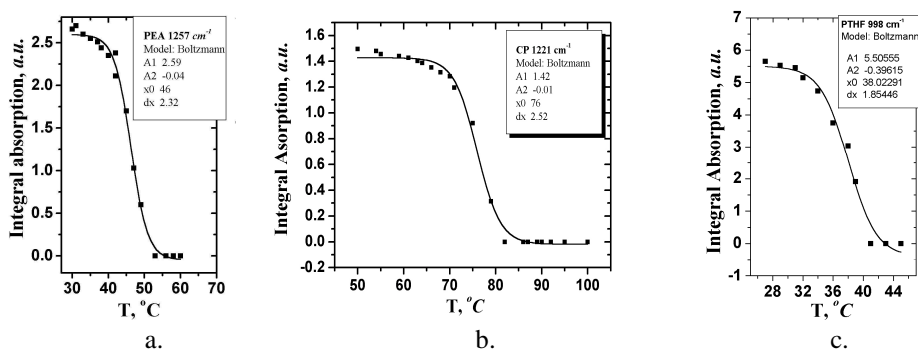


**Fig. 3.** Dependences on temperature of the integral absorption of the bands at 1257  $\text{cm}^{-1}$  (PEA) (a), 1221  $\text{cm}^{-1}$  (CP) (b) and 998  $\text{cm}^{-1}$  (PTHF) (c)

In fig 3. the values of the integral absorbances at different temperatures of the bands at 1257 for PEA, 1221  $\text{cm}^{-1}$  for CP and 998  $\text{cm}^{-1}$  for PTHF were represented by dots, solid line representing the Boltzmann fitted curve. By fitting procedure  $A_1$ ,  $A_2$ ,  $x_0$  and  $dx$  parameters are obtained. The value corresponding to  $x_0$  means the value of transition temperature. These above mentioned bands appear in the spectra of the blends, too. Following the same procedure, the values of transition temperatures of the blends were obtained and are shown in table 1.



**Table 1.**

The values of the transition temperatures obtained by fitting procedure of integral absorbance-temperature dependence curves from CP/PEA blends (a) and CP/ PTHF blends (b).

wt % CP	$t_1, ^\circ\text{C}$	$t_2, ^\circ\text{C}$
0	46	
16	49	69
32	50	70
64	50	71
80	51	74
100		76

wt % CP	$t_1, ^\circ\text{C}$	$t_2, ^\circ\text{C}$
0	38	
8	34	74
32	34	77
64	37	78
80	38	79
100		76

The data obtained by IR are in a good agreement with DSC data [6].

## REFERENCES

1. M. Brecl, T. Malavasic, *J. Polym. Sci., Part A*, 35, 2871, 1997;
2. D. Filip, Gh. Singurel, C. I. Simionescu, A. Socoliuc, D. Macocinschi, *Mater Plast*, (Bucharest, Romania) 39,(1) 62-66, (2002);
3. S. Wang, H. Zhuang, H. K. Shobha, T. E. Glass, M. Sankarapandian, Q. Ji, A. R. Shultz, J. E. McGrath, *Macromolecules*, **34**(23), 8051 (2001);
4. S. W. Kuo, F. C. Chang, *Macromolecules*, **34**(22), 7737 (2001);
5. G. G. Bumbu, C. Vasile, M. C. Popescu, H. Darie, G. C. Chițanu, Gh. Singurel, A. Carpov, *J. Appl. Polym. Sci.*, vol.88,2585-2597 (2003);
6. D. Filip, C. I. Simionescu, D. Macocinschi, I. Paraschiv, *J. Therm. Anal.*, **65**, 821 (2001).

## SPECTROSCOPIC INVESTIGATION OF Cu(II) MOLECULAR COMPLEXES OF ATENOLOL AND METOPROLOL TARTRATE

**FELICIA POP-GOZMAN<sup>1</sup>, I. BRATU<sup>2</sup>, O. COZAR<sup>3</sup> and M. BOJITA<sup>4</sup>**

<sup>1</sup>University of Oradea, Faculty of Pharmacy, 1 Armatei Romane st., Oradea, Romania

<sup>2</sup>National R&D Institute of Isotopic and Molecular Technologies, P.O. Box 700, R-400293 Cluj-Napoca 5, Romania

<sup>3</sup>Babes-Bolyai' University, 1 Kogalniceanu st., Cluj-Napoca, Romania

<sup>4</sup>Iuliu Hatieganu' University of Medicine and Pharmacy, 4 Clinicilor st., Cluj-Napoca, Romania

**ABSTRACT.** FT-IR spectroscopic data of atenolol and its copper complex suggest that NH<sub>2</sub> and carboxyl groups are involved in the coordination of the metal ion.

Powder EPR spectra of these complexes show a square-planar symmetry around the metal ion with a CuN<sub>2</sub>O<sub>2</sub> chromophore in xOy plane. A small tetragonal-octahedral distortion is present in the case of CuATE compound.

### Introduction

Atenolol (C<sub>14</sub>H<sub>22</sub>N<sub>2</sub>O<sub>3</sub>) and metoprolol tartrate (C<sub>15</sub>H<sub>25</sub>NO<sub>3</sub>)<sub>2</sub>.C<sub>4</sub>H<sub>6</sub>O<sub>6</sub> molecules are the most frequently used drugs in the treatment of cardiovascular diseases. In the last few years some molecular copper complexes of different drugs (cardiovasculares, antiinflammatories) are used because their activity is enhanced. For a better understanding of their activity, structural investigation [1-10] by different spectroscopic methods (FT IR and EPR spectroscopy) was done.

### Experimental

Molecular complexes of atenolol (ATE) and metoprolol tartrate (MET) with Cu(II) were obtained on going from the starting salts (sodium benzoate and copper sulphate) by co-precipitation procedure. After drying, the powder complexes were analysed by classical KBr pellet technique with an EQUINOX 55 Bruker FT IR spectrometer in the 400 - 4000 cm<sup>-1</sup> spectral domain. The EPR spectra of the samples in the powder form were registered in the X band using an ADANI-USA spectrometer.

### Results and Discussion

A comparative study of the FTIR spectra of ligands (ATE and MET) and the corresponding complex, see Figs. 1 and 2, established the molecular groups involved in the complexation. Analysing the FTIR spectrum of ATE one can see that the frequency of the band at 3351 cm<sup>-1</sup> and assigned to NH<sub>2</sub> group is shifted to 3441 cm<sup>-1</sup> in the spectrum of copper complex; it is possible that some hydrogen bonds are broken during the complexation process. The band at 1631 cm<sup>-1</sup> in the FTIR spectrum of ATE, assigned to carbonyl group is shifted to 1602 cm<sup>-1</sup> in the spectrum of the complex. It is quite evident that the complexation is produced through this molecular group.

Powder EPR spectra of Cu (II) atenolol (ATE) and Cu (II) metoprolol tartrate (MET) complexes obtained at room temperature exhibit the absorption signals typical of randomly oriented single state (S=1/2) species having axial symmetry (Fig. 3). The ground state for paramagnetic electron is d<sub>x<sup>2</sup>-y<sup>2</sup></sub> orbital. By comparing the shape of these EPR spectra with those obtained for others copper complexes with nitrogen and oxygen ligands we have concluded that the local symmetry around metal ions is of square-planar type with a CuN<sub>2</sub>O<sub>2</sub> chromophore in the xOy plane [1].

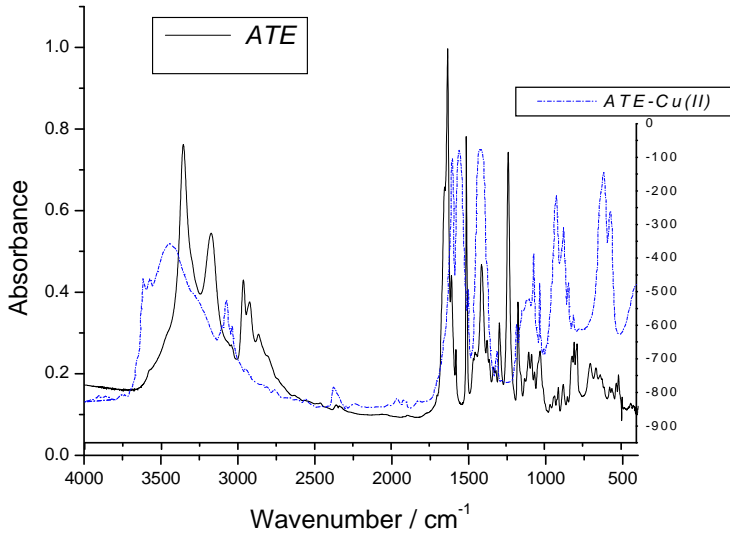


**Fig. 1.** FT IR spectra of ATE and its copper complex

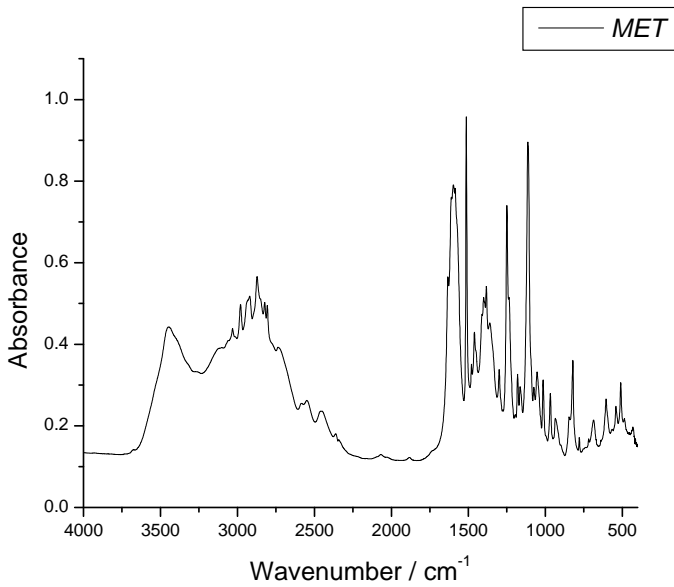


**Fig. 2.** FT IR spectra of MET.

The characteristic EPR parameters for CuATE compound are the following  $g_{//}=2.268$ ,  $g_{\perp}=2.078$ ,  $A_{//}=165$  G and  $g_{//}=2.268$ ,  $g_{\perp}=2.095$ ,  $A_{//}=145$  G for CuMET.

The  $g_{//}$  values suggest the presence of a small tetragonal-octahedral distortion in the case of CuATE compound [10].

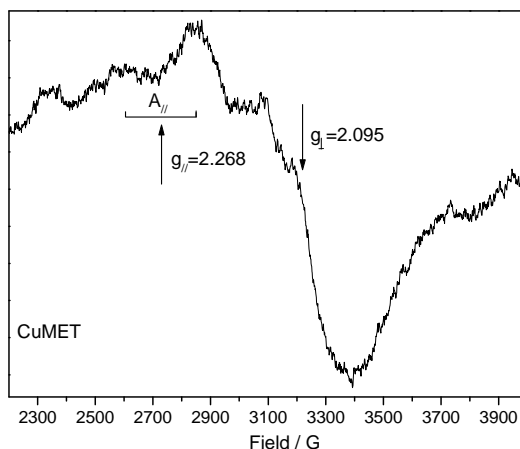


Fig. 3. Powder EPR spectrum of CuMET at room temperature.

### Conclusions

The FT-IR data obtained for ATE and MET drugs and their copper compounds suggest that  $\text{NH}_2$  and carboxyl groups are involved in the complexation (coordination) of the metal ions.

Powder EPR spectra of these complexes show a square-planar symmetry around the metal ions with a  $\text{CuN}_2\text{O}_2$  chromophore in xOy plane. A small tetragonal-octahedral distortion is present in the case of CuATE compound.

### REFERENCES

- [1] O.Cozar, L.David, V.Chis, C.Cosma, V.Znamirovski, G.Damian, *Appl. Magn. Reson.*, 8(1995), 235.
- [2] E.Forizs, L.David, O.Cozar, C.Craciun, M.Venter, M.Kilyen, *J.Molec.Structure*, 408/409 (1997), 195-199.
- [3] O.Cozar, L.David, V.Chis, E.Forisz, C.Cosma, G.Damian, *Fressenius Journal of Analytical Chemistry*, 355(1996), 701.
- [4] E.Forizs, L.David, O.Cozar, C.Craciun, M.Venter, M.Kilyen, *J.Molec.Structure*, 408/409(1997), 195-199.
- [5] A. Torregiani, P. Taddei, M.R. Tosi, V. Tugnolo, *J. Molec. Struct.*, 565-566 (2001), 347-352.
- [6] G. Facchin, M.H. Torre, E. Kremer, O.E. Piro, E.J. Baran, *Z. Naturforsch.* 53b (1998), 871-874.
- [7] G. Facchin, M.H. Torre, E. Kremer, *Z. Anorg. Allg. Chem.*, 624 (1998), 2025-2028.
- [8] E.Forizs, L.David, O.Cozar, V.Chis, G.Damian, *J. of Molecular Structure* 482(1) (1999), 143-147
- [9] E.Forizs, L.David, O.Cozar, V.Chis, R.Tetean, M.Todica, *Appl.Mag.Resonance* 16(1999), 499-506.
- [10] O. Cozar, I. Bratu, L. David, C. Craciun, A. Hernanz, R. Navarro, M. de la Fuente, C. Balan, *Appl.Mag.Resonance*, 21(2001), 71-78.

## NMR STUDY OF HOMO- AND HETEROASSOCIATION OF AROMATIC MOLECULES IN AQUEOUS SOLUTION. NUMERICAL SIMULATIONS

DIANA BOGDAN<sup>1</sup>, C. MORARI<sup>1</sup>, M. BOGDAN<sup>1</sup>

<sup>1</sup>National Institute for Research and Development of Isotopic and Molecular Technologies, P.O. Box 700, Donath Str. # 71-103, 400293 Cluj-Napoca 5, Romania Tel. +4-0264-584037, Fax: +4-0264-420042

**ABSTRACT.** Investigation of the homo- and heteroassociation of different molecules and their competitive binding to receptors deal with some important aspects of molecular interactions. Although there have been a number of attempts, to develop models of homo- and heteroassociation of aromatic molecules, there are often limitations in their use because rather approximate expressions for equilibrium concentrations are used. In this report, we analyse different models in which indefinite aggregates exist for both self- and heteroassociation between molecules in solution. Using these models based on numerical simulations a NMR analysis was developed in order to determine the structural and thermodynamic parameters of molecular homo- and heteroassociation in solution using the chemical shifts variation of different protons as a function of concentration.

### Introduction

Investigation of the homo- and heteroassociation of different molecules and their competitive binding to receptors deal with some important aspects of molecular interactions. From a pharmacological point of view, association complexes and competitive binding may influence the activity of drugs when used in combination or in the interaction of drugs with aromatic molecules from food sources.

Although there have been a number of attempts, in recent years, to develop models and analyses of homo- and heteroassociation of aromatic molecules, there are often limitations in their use. The model developed by Baxter *et al.* [1] for the heteroassociation of aromatic molecules is not applicable to the general case because rather approximate expressions are used for equilibrium monomeric concentrations of one of the components in the mixed solution. Models used for the interpretation of optical spectroscopic data of the association of aromatic molecules either to not take into account the formation of  $n$ -mer aggregated for all the components present in the mixed solution or only consider formation of a 1:1 heterocomplex without taking into account the self-association of aromatic molecules in solution [2].

For these reasons, in the present paper we intend to present a general model for analysis of indefinite association of molecules in solution, based on NMR spectroscopy.

NMR spectroscopy has some advantages over optical investigations of molecular complexation because it can be used to determine both the equilibrium and structural details of multicomponent complex formation in solution [3]. The NMR analysis has been developed based on chemical shift measurements of one species as a function of concentration. The analytical expression was obtained without any approximations or restrictive hypotheses.

### Theory

#### *Isodesmic model*

The isodesmic model – also known as the indefinite non-cooperative model – is based on the assumption that solute molecules associate to form stacks (superior order oligomers),  $A_n$ ,  $n \in (2, \infty)$ , where the value of equilibrium constant,  $K_n$ , for each step are assumed to be equal:

$$K = K_2 = K_3 = \dots = K_n, (n \rightarrow \infty).$$

In this case, based on superior order oligomers formation reactions, it is possible to express the concentration of the  $n$ -mer as a function of association constant,  $K$ , and the concentration of monomer,  $[A]$ , as follows

$$[A_n] = K^{n-1} [A]^n \quad (1)$$

Defining the total concentration,  $[A_0]$ , as

$$[A_0] = [A] + 2 [A_2] + 3 [A_3] + \dots + i [A_i] + \dots = \frac{[A]}{(1 - K[A])^2} \quad (2)$$

we obtain for  $[A]$  the following expression

$$[A] = \frac{1}{2K^2[A_0]} \left\{ 2K[A_0] + 1 - \sqrt{4K[A_0] + 1} \right\} \quad (3)$$

The general accepted hypothesis in the case of isodesmic non-cooperative model considers that the chemical shifts for each nucleus observed by NMR and belonging to a molecule at the end of the oligomer ( $\delta_e$ ) is the arithmetical average of the chemical shifts corresponding to the monomer ( $\delta_m$ ) and to the molecule intercalated into the  $n$ -mer ( $\delta_i$ ). Hence

$$\delta_e = \frac{\delta_m + \delta_i}{2} \quad (4)$$

Therefore:

$$\delta_{obs} - \delta_m = (\delta_i - \delta_m) \frac{2K[A_0] + 1 - \sqrt{4K[A_0] + 1}}{2K[A_0]} \quad (5)$$

It is worth of mentioning that the isodesmic non-cooperative model cannot distinguish between the dimerisation process and the indefinite association model. The only differences being that

$$K = 2K_2 \text{ and } \delta_i - \delta_m = \delta_{dimer} - \delta_m.$$

Eq. (4) defines a parameter  $f = \frac{1}{2}$  in the following equivalent equation

$$\delta_e = (1 - f) \delta_m + f \delta_i \quad (6)$$

In the general case, the parameter  $f$  from eq. (7) can be defined as

$$0 \leq f \leq 1 \quad (8)$$

In a molecule, the environment of nuclei is different, so that they may have different values for the  $f$  parameter. In this case, besides the parameters  $K$  and  $\delta_i$ , the equation which describes the observed chemical shift variation as a function of concentration will also contain  $f$  as a fit parameter. By performing a simple mathematical calculus, the following expression for  $\delta_{obs}$  can be

$$\delta_{obs} = \frac{[A]}{[A_0](1 - K[A])} \left\{ (1 + K[A](1 - 2f)) \delta_m + K[A] \left( \frac{2f - K[A](2f - 1)}{1 - K[A]} \right) \delta_i \right\} \quad (9)$$

The total concentration,  $[A_0]$ , is given by eq. (2), yielding the solution (3). In this case, the final expression of the observed chemical shift may be written as:

$$\delta_{obs} = (1 - K[A]) \{ 1 - K[A](2f - 1) \} \delta_m + K[A] \{ 2f - K[A](2f - 1) \} \delta_i \quad (10)$$

where:

$$K[A] = \frac{2K[A_0] + 1 - \sqrt{4K[A_0] + 1}}{2K[A_0]} \quad (11)$$

In the case when  $f = \frac{1}{2}$ , the eq. (10) come down to eq. (5), which is characteristic for the isodesmic usual accepted model.

### Heteroassociation

The heteroassociation study was performed using two different molecules A and B. We considered that the concentration of A molecules is very low (aprox. 1 mM) and at this concentration the A molecules are essentially monomeric. Even so, there are many different species present in solution, of which the only components that have been considered are B molecules stacks containing one A molecule either at the end or intercalated at some point within the stack.

The B molecule is assumed to stack according to the isodesmic model with association constant  $K_m$ . These interactions are assumed to be unaffected by the presence of A molecules elsewhere in the stack.

Thus:



all have the same equilibrium constant,  $K_m$ .

On addition of B molecules to a solution of monomeric A molecules, the A molecules may associate at the ends of B stacks with association constant,  $K_e$



$$\begin{aligned} B_n + A &\leftrightarrow B_n A \\ K_e &= \frac{[AB]}{[B][A]} = \frac{[B_2A]}{[B_2][A]} = \frac{[B_n A]}{[B_n][A]} \end{aligned} \quad (14)$$

or A molecules may intercalate into B stacks with association constant,  $K_s$



$$\begin{aligned} B_n + A &\leftrightarrow B_{n-1}AB \text{ or } B_{n-2}AB_2 \text{ or } BAB_{n-1} \\ K_s &= \frac{[BAB]}{[B_2][A]} = \frac{[B_2AB]}{[B_3][A]} = \dots = \frac{[B_{n-1}AB]}{[B_n][A]} \end{aligned} \quad (16)$$

For these expressions, equations for the concentrations of each species can be derived in terms of the concentrations of monomers. For example

$$\begin{aligned}
 [B_n] &= K_m^{n-1} [B]^n \\
 [B_n C] &= K_m^{n-1} K_e [M]^n [A]
 \end{aligned}
 \tag{17}$$

As is usual in the isodesmic model, it is assumed that the change in chemical shift of an A molecule at the end of a stack is only half that for intercalation into a stack. Hence

$$\delta_e = \frac{\delta_i + \delta_m}{2} .
 \tag{18}$$

where

$\delta_e$  – the proton chemical shift of A molecule associated at the end of a B stack

$\delta_i$  – the proton chemical shift of A molecule intercalated into a B stack

$\delta_m$  – the chemical shift of monomeric A

Following the procedure outlined by Baxter *et al.* [1], we obtain for the observed chemical shift of A the expression

$$\delta = \delta_m + \delta_m \frac{[A] - [A]_0}{[A_0]} + \delta_m \frac{[A][B]}{[A_0](1 - K_m [B])} \left\{ \frac{\delta_i + \delta_m}{2} K_e + \delta_i K_s K_m [B] \right\} .
 \tag{19}$$

To complete the derivation, the concentration of monomeric A and B molecules must be calculated.

The concentration of monomeric A molecule is given by

$$[A] = \frac{[A]_0 \{1 - K_m [B]\}}{1 - K_m [B] + K_e [B] + K_s K_m [B]^2} .
 \tag{20}$$

For the monomeric B molecule, Baxter *et al.* [1] made an approximation considering the concentration of monomeric B in the absence of A, namely

$$[B] \approx [B]_0 \left\{ \frac{2}{1 + (4K_m [B]_0 + 1)^{1/2}} \right\}^2
 \tag{21}$$

We have calculated the exact expression for [B] and obtained

$$[B]_0 = [B] \frac{1 + K_e [A] + K_s K_m [A][B](2 - K_m [B])}{(1 - K_m [B])^2} .
 \tag{22}$$

### Experimental

We used the following values:

$$K_m = 100 \text{ M}^{-1}$$

$$K_s = 4 \text{ M}^{-1}$$

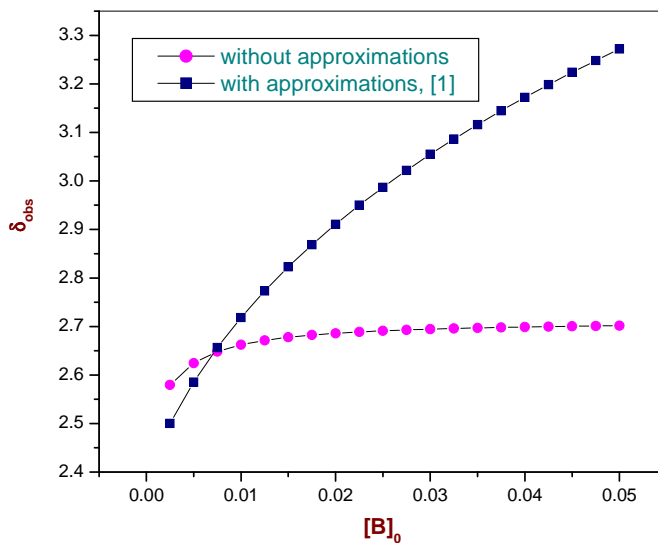
$$K_e = 8 \text{ M}^{-1}$$

$$[A_0] = 1 \text{ mM}$$

$$\delta_m = 2.5 \text{ ppm}$$

$$\delta_i = 3.3 \text{ ppm}$$





## REFERENCES

1. N. J. Baxter, M. P. Williamson, T. H. Lilley, E. Haslam, *J. Chem. Soc. Faraday Trans.*, **92**, 231 (1996).
2. R. W. Larsen, R. Jasuja, R. Hetzler, P. T. Muraoka, V. D. Andrada, D. M. Jameson, *Biophys. J.*, **70**, 443 (1996)
3. D. B. Davies, A. N. Veselkov, *J. Chem. Soc. Faraday Trans.*, **92**, 3545 (1996)

## ABOUT THE EXTRAORDINARY REFRACTIVE INDEX IN VIS – IN ADP SINGLE – CRYSTALS

DANIELA DOLHA

*Department of Physics, Faculty of Physics, The West University of  
Timișoara, Bd. V. Pârvan No. 4, Timișoara, RO – 1900, România*

**ABSTRACT.** The Ammonium dihydrogen phosphates are single-crystals with electrooptical properties, shortly known as ADP, are used in high power nonlinear optical devices. The crystals are uniaxial, so they having different properties when a beam of light passes through the crystalline samples. For each applications of these single – crystals is required a precise knowledge of the crystal's refractive index as a function of wavelength. The crystalline plates resulted by Z-cutting from the prismatic region of the crystal were brought to optical transparency. The paper shows that dependence of the extraordinary refractive index by the wavelength for the single – crystals of ADP in VIS, using a Herzberger dispersion formulae.

### INTRODUCTION

The ammonium dihydrogen phosphates are single-crystals with electrooptical properties, shortly known as ADP crystals, used for frequency conversion in high power nonlinear optical devices.

The single - crystals of ADP are uniaxial, so they having different properties when a beam of light passes through the crystalline samples obtained from these single – crystals. These single - crystals were grown from a supersaturated ADP solution using a seed obtained from solution or by a preferential cutting from an ADP single-crystal previously grown. [1] The growing method were the same used also for the growing of the KDP single crystals, another ferroelectric crystal with a similar structure as ADP and with electrooptical properties, the conventional method of slow cooling [2,3]. The crystals were grown from a supersaturated solution of ammonium dihydrogen phosphate, from a temperature wanted for started the growing process, which is around 80 Celsius degrees. The temperature were cooled in different steps, very slowly, and the growing process was stopped when the further growing of the single – crystals was limited by the size of the crystallization vessel [2,3].

### WORKING METHOD

When a beam of light passes through the ADP crystal, two beams results with different properties. One of them is called the ordinary beam which is characterized by an ordinary refractive index, and the other is called extraordinary and is characterized by an extraordinary refractive index.

For each applications of these single – crystals is required a precise knowledge of the crystal's refractive index as a function of wavelength. The crystals were grew from solution, so the crystalline plates resulted by Z-cutting from the prismatic region of the crystal used for detaching a physical – chemical method using water. The obtained crystalline plates were brought to optical transparency [4] to be better used for further analysis.

From different kind of dispersion formula presented in the speciality literature – that of Herzberger, Zernike, Sellmeier - it have been used a Herzberger dispersion formulae. The values of the refractive index for different values of the wavelength were calculated [5]:

$$n = A + BL + CL^2 + D\lambda^2 + E\lambda^4 \quad (1)$$

where:

$$L = \frac{1}{\lambda^2 - 2,8 \cdot 10^6} \quad (2)$$

The values of the A,B,C,D,E coefficients from the Herzberger dispersion formula, used to calculate the extraordinary refractive index in the single- crystal of ADP, at the temperature of 24.8 °C are given in table 1.

**Table 1.**  
The values of the A, B, C, D, E coefficients from the Herzberger dispersion formula

A	B	C	D	E
1.476613	$2.552032 \cdot 10^5$	$-1.661894 \cdot 10^{11}$	$-1.792370 \cdot 10^{-10}$	$6.965756 \cdot 10^{-19}$

## RESULTS

For 15 values of the wavelength from the Visible domain, between 400 nm and 800 nm was calculated the values of the extraordinary refractive index, using the Herzberger dispersion formula and the coefficients which are shown in table 1.

The dependence of the obtained values for the extraordinary refractive index by the wavelength between 400 and 800 nm were plotted and is shown in figure 1:

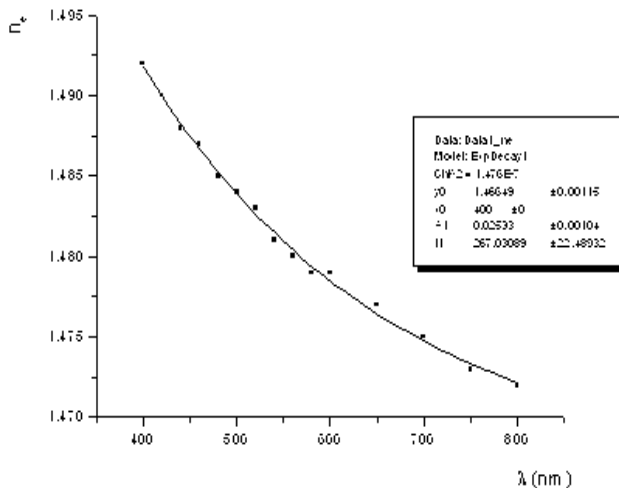


**Fig. 1.** The dispersion of the extraordinary refractive index in VIS for the ADP single – crystal

The curve which fit better with the distribution of the obtained values is a first degree exponential one with the equation:

$$y = y_0 + A_1 e^{-(x-x_0)/t_1} \quad (3)$$

and the parameters are shown in the figure.

With the obtained values for the extraordinary refractive index could be calculated the values of transmission and the absorption coefficient for different ADP crystalline samples. The extraordinary refractive index decreases exponentially with the increase of the wavelength [6].

## CONCLUSIONS

1. The growing method were the same used also for the growing of the KDP single – crystals, the conventional method of slow cooling
2. The curve which fit better with the distribution of the obtained values is a first degree exponential one
3. The extraordinary refractive index decreases exponentially with the increase of the wavelength and it allowed to calculate the values of the refractive index for any value from the analyzed range of wavelength.

## REFERENCES

1. Daniela Dolha et al., *About the Growing of Single-crystals from solution Using Different Kind of Seeds*, presented at the Physics Annual Conference, november 2002, in press
2. Volkman L., *Analele Universității Timișoara, Seria Fizică*, Universitatea Timisoara, 1985, vol. XXIII, 69-72
3. Volkman L. et.all., *Annals of West University of Timișoara, ser. Chem.*, 1998 , vol. 7, 119 – 123
4. Daniela Dolha, *vol. simpozionului “Tinerii și cercetarea multidisciplinară”*, 1999, 177-179
5. \*\*\* *Handbook of Optical Constants of Solids II*, Academic Press United Kingdom , 199, 1005-1021
6. Daniela Dolha, *About the internal transmission and absorption coefficient as a function of wavelength in electrooptic single-crystals*, Ukrainian Journal of Physics, 2001, T.46, No.3, 296-297

## **AB INITIO DENSITY FUNCTIONAL THEORY STUDY OF CF<sub>2</sub>HCL AND ITS ISOTOPIC SPECIES**

**A. BENDE<sup>1,2</sup> and V. TOSA<sup>1</sup>**

<sup>1</sup> *National Institute of Research and Development of Isotopic and Molecular Technologies, Str. Donath, No: 71-103, P.O. Box 700, Ro-3400, Cluj-Napoca, Romania*

<sup>2</sup> *Molecular Biophysics Department, German Cancer Research Centre, Im Neuenheimer Feld 280, D-69120 Heidelberg, Germany*

**ABSTRACT.** The geometrical parameters, permanent dipole moments and harmonic vibrational frequencies of CF<sub>2</sub>HCl (Freon22) and its isotopic species (D and <sup>13</sup>C) has been calculated in four different basis sets (cc-pVDZ, cc-pVTZ, aug-cc-pVDZ and aug-cc-pVTZ) at the density functional theory (DFT) method using B3LYP and B3PW91 exchange-correlation functionals. The results are compared with the experimental values. The calculated values are found to be in good agreement with the available experimental data, and explanations are offered for discrepancies. This confirms the accuracy of the ab initio DFT study in the geometry structure and other molecular parameter calculation.

### **Introduction**

The experimental and computer simulation spectra of laser-induced infrared multiple photon excitations (IRMPE) of CF<sub>2</sub>HCl for the purpose of selective isotopic enrichment have been studied [1, 2, 3] as a possible solution for laser isotope (D and <sup>13</sup>C) separation. In order to understand the multiple photon excitation mechanism, an accurate study of equilibrium geometry, permanent and induced dipole moments, harmonic vibrational frequencies and their assignments is required.

The experimental geometry structure was determined very early in 1962 from microwave spectra by *McLay et al.* [4] and *Beeson et al.* [5] while the infrared (IR) and Raman spectra of CF<sub>2</sub>HCl and their isotopic species (D and <sup>13</sup>C) were obtained by *Magill et al.* [6] in 1986 and the band assignment and isotopic shifts were briefly discussed in their paper. Our aim is to obtain a good agreement for geometry and frequencies using DFT methods in order to get much more description for other molecular parameters which cannot be compared with the experimental data and which are necessary in IRMPE spectra simulation.

### **Results and Discussion**

The calculations were carried out in Heidelberg on Hewlett-Packard cluster. The standard B3LYP and B3PW91 DFT type calculations (full geometry optimization and harmonic vibrational frequencies) were performed by the Gaussian98 [7] computer code using cc-pVDZ, Aug-cc-pVDZ, cc-pVTZ and Aug-cc-pVTZ Dunning's correlation consistent basis sets. The calculated results are summarized in three tables. Table 1 show the results obtained for the equilibrium, geometry and permanent dipole moments of the CF<sub>2</sub>HCl at the DFT method. The bond distances are given in Å, the bond angles are given in Degree and the permanent dipole moments are given in Debye. Table 2 contain the harmonic vibrational frequencies for protonated (H) and deuterated (D) species given in cm<sup>-1</sup> while in Table 3 are presented the same results but for <sup>12</sup>C and <sup>13</sup>C isotopic species.

As it can be observed from Table 1, the calculated geometry parameters (bonds and angles) are in a very good agreement with the experimental values. Increasing the number of the basis functions, the bond lengths and bond angles do not change that much, but the values of the permanent dipole components ( $\mu_a$  and  $\mu_c$ ) have an important basis set dependence.

**Table 1**  
**The geometrical parameters (in Å and Degree) and permanent dipole moments (in Debye) of CF<sub>2</sub>HCl computed at DFT method, using cc-pVDZ, Aug-cc-pVDZ, cc-pVTZ, Aug-cc-pVTZ basis sets.**

Basis	Method	r <sub>1</sub>	r <sub>2</sub>	r <sub>3</sub>	α <sub>1</sub>	α <sub>2</sub>	α <sub>3</sub>	α <sub>4</sub>	μ <sub>a</sub>	μ <sub>c</sub>
cc-	B3LYP	1.099	1.797	1.343	108.44	110.40	109.54	108.54	.277	1.415
-pVDZ	B3PW91	1.099	1.785	1.340	108.59	110.30	109.56	108.53	.292	1.428
Aug-cc-	B3LYP	1.095	1.788	1.353	109.41	110.09	109.57	108.10	.012	1.498
-pVDZ	B3PW91	1.096	1.778	1.347	109.34	110.07	109.58	108.17	.060	1.461
cc-	B3LYP	1.087	1.788	1.341	108.78	110.22	109.62	108.37	.145	1.429
-pVTZ	B3PW91	1.089	1.776	1.336	108.78	110.15	109.67	108.42	.150	1.411
Aug-cc-	B3LYP	1.086	1.784	1.344	109.11	110.10	109.67	108.20	.027	1.463
-pVTZ	B3PW91	1.089	1.774	1.339	108.99	110.08	109.69	108.32	.069	1.422
Exp.		1.080	1.747	1.367	108.99	110.74	110.20	107.63	.120	1.430

**Table 2**  
**The harmonic vibrational frequencies (in cm<sup>-1</sup>) of CF<sub>2</sub>HCl and its deuterated species computed at DFT method, using cc-pVDZ, Aug-cc-pVDZ, cc-pVTZ, Aug-cc-pVTZ basis sets.**

	B3LYP									
	cc-pVDZ		Aug-cc-pVDZ		cc-pVTZ		Aug-cc-pVTZ		Exp.	
	H	D	H	D	H	D	H	D	H	D
v <sub>1</sub>	3125.7	2306.9	3175.0	2321.6	3129.3	2307.5	3130.2	2309.2	3020.5	2260.5
v <sub>2</sub>	1295.1	1107.6	1289.6	1071.0	1319.5	1097.1	1314.5	1085.1	1313.2	1102.8
v <sub>3</sub>	1119.2	993.7	1082.7	988.7	1125.6	1009.1	1097.8	1004.9	1109.0	1012.7
v <sub>4</sub>	776.2	716.9	781.1	722.7	794.2	722.0	777.7	722.1	809.3	750.0
v <sub>5</sub>	591.1	586.3	578.4	573.9	600.4	589.4	590.7	586.0	596.3	592.1
v <sub>6</sub>	398.9	395.8	397.3	394.2	400.9	397.8	400.3	397.3	412.9	410.9
v <sub>7</sub>	1364.9	1198.4	1335.0	1123.8	1374.0	1164.9	1362.7	1142.0	1351.3	1161.0
v <sub>8</sub>	1153.2	961.7	1094.9	952.0	1128.8	974.5	1109.7	969.2	1127.5	969.0
v <sub>9</sub>	357.5	354.7	355.3	352.6	359.2	356.4	358.3	355.5	365.4	365.0
	B3PW91									
v <sub>1</sub>	3137.7	2316.0	3150.3	2323.5	3129.5	2307.8	3130.2	2308.2	3020.5	2260.5
v <sub>2</sub>	1300.3	1121.9	1293.5	1089.0	1319.8	1113.4	1315.2	1104.1	1313.2	1102.8
v <sub>3</sub>	1133.2	999.4	1100.1	993.9	1125.6	1012.0	1116.3	1008.3	1109.0	1012.7
v <sub>4</sub>	791.7	729.8	797.1	735.6	794.2	734.9	793.6	734.6	809.3	750.0
v <sub>5</sub>	597.3	592.4	585.5	580.3	600.4	595.6	597.4	592.6	596.3	592.1
v <sub>6</sub>	406.1	402.9	403.9	400.6	407.6	404.4	406.9	403.7	412.9	410.9
v <sub>7</sub>	1367.0	1214.8	1336.8	1145.6	1372.3	1183.2	1362.2	1164.3	1351.3	1161.0
v <sub>8</sub>	1170.6	964.6	1118.1	955.1	1149.5	975.9	1134.1	971.3	1127.5	969.0
v <sub>9</sub>	362.4	359.6	359.5	356.8	363.3	360.5	362.2	359.4	365.4	365.0

The CF<sub>2</sub>HCl is an asymmetric top molecule having C<sub>s</sub> molecular symmetry with two types of vibrational bands (v<sub>1</sub>-v<sub>6</sub>: A' and v<sub>7</sub>-v<sub>9</sub>: A''). The A' symmetry vibrations give rise to polarized Raman and IR absorption bands of mixed *a/c* type, which in general have well defined central *Q* branch. While the A'' vibrations give rise to *b* type bands having central minima (only *P* and *R* branch) in IR absorption and Raman bands of similar shape.

In case of deuterated species (Table 2) it can be observed an important isotopic shift in vibrational frequencies especially for higher values, but at the same time we have to mention that this frequency values and their isotopic shifts are quite sensitive on the applied functional and basis set. As we are interested in IRMPE using CO<sub>2</sub> laser the two most important values are v<sub>3</sub> and v<sub>8</sub>. Both frequency values are well separated in the absorption band from their isotopic species.

**Table 3**  
**The harmonic vibrational frequencies (in cm<sup>-1</sup>) of <sup>12</sup>CF<sub>2</sub>HCl and its <sup>13</sup>C isotope computed at DFT method, using cc-pVDZ, Aug-cc-pVDZ, cc-pVTZ, Aug-cc-pVTZ basis sets.**

B3LYP										
	cc-pVDZ		Aug-cc-pVDZ		cc-pVTZ		Aug-cc-pVTZ		Exp.	
	<sup>12</sup> C	<sup>13</sup> C	<sup>12</sup> C	<sup>13</sup> C	<sup>12</sup> C	<sup>13</sup> C	<sup>12</sup> C	<sup>13</sup> C	<sup>12</sup> C	<sup>13</sup> C
v <sub>1</sub>	3125.7	3111.3	3175.0	3137.6	3129.3	3116.7	3130.2	3120.9	3020.5	3010.6
v <sub>2</sub>	1295.1	1289.0	1289.6	1286.3	1319.5	1312.7	1314.5	1310.2	1313.2	1307.2
v <sub>3</sub>	1119.2	1091.1	1082.7	1054.7	1125.6	1083.5	1097.8	1073.3	1109.0	1083.5
v <sub>4</sub>	776.2	754.9	781.1	755.7	794.2	754.5	777.7	755.6	809.3	788.9
v <sub>5</sub>	591.1	586.7	578.4	574.2	600.4	589.4	590.7	586.8	596.3	592.3
v <sub>6</sub>	398.9	397.8	397.3	395.9	400.9	398.9	400.3	399.1	412.9	412.8
v <sub>7</sub>	1364.9	1357.5	1335.0	1331.6	1374.0	1366.9	1362.7	1359.4	1351.3	1346.0
v <sub>8</sub>	1153.2	1125.9	1094.9	1064.7	1128.8	1101.2	1109.7	1083.4	1127.5	1101.0
v <sub>9</sub>	357.5	355.1	355.3	354.0	359.2	357.1	358.3	356.7	365.4	363.0
B3PW91										
v <sub>1</sub>	3137.7	3125.6	3150.3	3137.9	3129.5	3116.2	3130.2	3118.1	3020.5	3010.6
v <sub>2</sub>	1300.3	1293.0	1293.5	1289.6	1319.8	1313.4	1315.2	1310.8	1313.2	1307.2
v <sub>3</sub>	1133.2	1102.9	1100.1	1072.1	1125.6	1099.5	1116.3	1090.7	1109.0	1083.5
v <sub>4</sub>	791.7	769.9	797.1	771.7	794.2	771.4	793.6	772.4	809.3	788.9
v <sub>5</sub>	597.3	592.2	585.5	580.4	600.4	595.5	597.4	593.2	596.3	592.3
v <sub>6</sub>	406.1	404.6	403.9	402.8	407.6	406.1	406.9	405.8	412.9	412.8
v <sub>7</sub>	1367.0	1357.0	1336.8	1332.9	1372.3	1364.8	1362.2	1358.7	1351.3	1346.0
v <sub>8</sub>	1170.6	1140.3	1118.1	1087.9	1149.5	1121.9	1134.1	1107.0	1127.5	1101.0
v <sub>9</sub>	362.4	359.9	359.5	358.5	363.3	361.4	362.2	360.8	365.4	363.0

In case of <sup>12</sup>C and <sup>13</sup>C isotopes (Table 3) this frequency shifts are much smaller. Only v<sub>3</sub> and v<sub>8</sub> give considerable isotopic shift.

On the other hand it can be observed an important discrepancy between the theoretical and experimental frequency values due to the anharmonic effects. Taking into account the experimental anharmonic corrections [8] the calculated values are in a very good agreement with the experimental results. Moreover comparing only the calculated and measured isotopic shifts this agreement is more accurate.

Considering the above results we found that in case of geometry parameters the method and basis set dependence are not so important that in case of permanent dipole moments and harmonic vibrational frequencies, the best approach for all these parameters can be obtained with B3LYP exchange-correlation functional using cc-pVTZ basis set. Comparing theoretical results with the experimental values we could establish the accuracy of the applied *ab initio* calculation (the choice of a suitable method and basis set). Using this calculation we are able to get other important molecular parameters (force constants, induced dipole moments, etc.) which cannot be easily obtained by experimental methods. The knowledge of these molecular data are necessary as starting data to model the infrared multiphoton process in CF<sub>2</sub>HCl and their isotopic species.

## REFERENCES

1. A. Bende, V. Tosa, *Rom. Rep. in Phys.*, **51**(7-8-9-10), 917 (1999).
2. I. Deac, V. Cosma, V. Tosa, *J. Mol. Struct.* **266**, 405 (1992).

3. V. Tosa, S. Solimeno, R. Bruzzese, C. de Lisio, *J. Mol. Struct.* **267**, 269 (1992).
4. D. B. McLay, C. R. Mann, *Can. J. Chem.*, **40**, 61 (1962).
5. E. T. Beeson, T. L. Weatherly, Q. Williams, *J. Chem. Phys.*, **37**, 2926 (1962).
6. J. V. Magill, K. M. Gough, W. F. Murphy, *Spectrochim. Acta*, **42A**, 705, (1986).
7. J.M. Frisch, G.W. Trucks, H.B. Schlegel, G. E. Scuseria, M. A. Robb, J. R. Cheeseman, V. G. Zakrzewski, J. a. Jr. Montgomery, R. E. Stratmann, J. C. Burant, S. Dapprich, J. M. Millam, A. D. Daniels, K. N. Kudin, M. C. Strain, O. Farkas, J. Tomasi, V. Barone, M. Cossi, R. Cammi, B. Mennucci, C. Pomelli, C. Adamo, S. Clifford, J. Ochterski, G. A. Petersson, P. Y. Ayala, Q. Cui, K. Morokuma, D. K. Malick, A. D. Rabuck, K. Raghavachari, J. B. Foresman, J. Cioslowski, J. V. Ortiz, A. G. Baboul, B. B. Stefanov, G. Liu, A. Liashenko, P. Piskorz, I. Komaromi, R.omperts, R. L. Martin, D.J. Fox, T. Keith, M. A. Al-Laham, C. Y. Peng, A. Nanayakkara, C. Gonzalez, M. Callacombe, P.M.W. Gill, B. W. Johnson, W. Chen, M. W. Wong, J. L. Andres, C. Gonzalez, M. Head-Gordon, E. S. Replogle, J. A. Pople, Program Gaussian98, Gaussian Inc., Pittsburgh PA, 1998.
8. A. Brown, D.C. McKean, J. L. Duncan *Spectrochim. Acta*, **44A**, 553, (1988).



## VIBRATIONAL AND EPR ANALYSIS OF NEW COMPLEXES OF PYRAZINAMIDE WITH Cu(II)

**T. JURCA<sup>1</sup>, S. CAVALU<sup>1</sup>, S. CINTA PINZARU<sup>2</sup>, V. SIMON<sup>2</sup>**

<sup>1</sup> University of Oradea, Faculty of Medicine and Pharmacy, P-ta 1 Decembrie 10, 3700 Oradea, Romania

<sup>2</sup> Babes-Bolyai University, Faculty of Physics, Kogalniceanu No. 1, Cluj-Napoca, 3400, Romania

**ABSTRACT.** Three new mixed complexes combinations of pyrazinamide (pyrazinecarboxamide) have been prepared and analyzed by UV-VIS, FT-IR, FT-Raman and EPR spectroscopy:  $[\text{Cu}(\text{PZA})_n\text{X}_m]$ , where  $\text{X} = \text{C}_6\text{H}_5\text{COO}^-$ ,  $\text{Cl}^-$  and  $[\text{Hg}(\text{SCN})_4]^{2-}$ .

PZA can coordinate through the pyrazine ring nitrogens, the  $>\text{C}=\text{O}$  and/or  $-\text{NH}_2$  groups. FT-IR and FT-Raman techniques are diagnostic of the coordination mode of PZA in complexes. Complementary EPR investigation allowed the supposition that  $[\text{Cu}(\text{PZA})_2(\text{C}_6\text{H}_5\text{COO})_2 \cdot 4\text{H}_2\text{O}$  complexes are hexacoordinated, while in the case of  $[\text{Cu}(\text{PZA})_2]\text{Cl}_2$  and  $[\text{Cu}(\text{PZA})_2][\text{Hg}(\text{SCN}_4)]$  the corresponding complexes are tetraordinated.

### Introduction and Experimental

Pyrazinamide (Pyrazine-2-carboxamide) has the following chemical formula  $\text{C}_5\text{H}_5\text{N}_3\text{O}$  and is reagent from Trans Medical Pharma GmbH, Germania.

The C,H,N,S analysis results for the investigated complexes are (found/calc.):

$[\text{Cu}(\text{PZA})_2](\text{C}_6\text{H}_5\text{COO})_2 \cdot 4\text{H}_2\text{O}$ : C%45,12/45,85; N% 13,85/13,37; H%4,368/4,458;

$[\text{Cu}(\text{PZA})_2]\text{Cl}_2 \cdot 2\text{H}_2\text{O}$ : 30,10/30,6; N%21,07/22,04; H%3,04/3,15;

$[\text{Cu}(\text{PZA})][\text{Hg}(\text{SCN}_4)]$ : C%16.94/17.41; N%15.94/15.80; S%20.84/20.64; H%0.862/0.806

The FT-IR spectra of pyrazinamide and their complexes with cooper (II), were recorded in the region  $4000\text{--}400\text{ cm}^{-1}$  by a Bruker EQUINOX 55 spectrometer, using a diamond ATR unit.

The EPR spectra of studied complex combinations were recorded on an EPR-E-4 spectrometer.

### Results and Discussion

Based on the elemental analysis the metal to ligand ratio is found to be 1:1 for  $[\text{Cu}(\text{PZA})][\text{Hg}(\text{SCN}_4)]$  and 1: 2 for  $\text{Cu}(\text{PZA})_2\text{Cl}_2$  and  $[\text{Cu}(\text{PZA})_2](\text{C}_6\text{H}_5\text{COO})_2 \cdot 4\text{H}_2\text{O}$ .

The IR data show that the amide  $\text{NH}_2$  of PZA does not take part in coordination, but forms weak hydrogen bonds, probably with guest water molecules. In the IR spectra the ring-breathing mode of PZA is observed at  $1015 \pm 10\text{ cm}^{-1}$  and around  $1035\text{ cm}^{-1}$  for Me-PZA complexes. The amides, containing nitrogen atom having lone pair electron to donate, have absorption  $\nu_{\text{C}=\text{O}}$  at  $1640\text{--}1700\text{ cm}^{-1}$ . The IR spectra of the Me-PZA compounds show negative shifts of  $\nu_{\text{C}=\text{O}}$ .

The EPR spectrum recorded from  $[\text{Cu}(\text{PZA})][\text{Hg}(\text{SCN}_4)]$  ( $\text{Cu}^{2+}$  ion, electronic configuration  $[\text{AR}] 3d^9$ , fundamental ground state spectral term  ${}^3D_{5/2}$ ) occurs from resonant centers disposed in an elongated octahedron vicinity, with rhombic symmetry.

The values of the spectroscopic splitting factor for are:  $g_1 = 2.19$ ;  $g_2 = 2.06$ ;  $g_3 = 2.02$ .

It is evident that the unpaired electron is localized in the  $d_{x^2-y^2}$  orbital.

**Table 1.**  
**The assignment of some of the most characteristic IR bands**

Tent. Assig.	PZA	Me-PZA complexes		
		Cu(C <sub>6</sub> H <sub>5</sub> -COOH) <sub>2</sub>	CuHg(SCN) <sub>4</sub>	CuCl <sub>2</sub>
$\nu_{as}$ NH <sub>2</sub>	3410s	3610w	3440w	3430s
$\nu_s$ NH <sub>2</sub>	3140m	3170m	3100s	3110m
$\nu_{CH}$	3080	3065m	3080w	3070m
$\nu_{C=O}$ (1)	1705s	1915w	1670m	1700s
$\delta_{NH_2}$ (2)	1600m	1590m	1630m	1590m
$\nu_{ring}$	1570	1585m	1580m	1585m
$\nu_{ring}$	1530	1545s	1540w	1510w
$\nu_{CN}$ (III)	1375s	1380s	1370w	1385s
$\delta_{CH}$	1150w	1180w	1180w	1170m
$\Delta NH_{2t}$	1090m	1085w	1090w	1080w
$\delta_{ring}$	870w	850w	860w	870m
$\Delta NH_{2w}$	665w	680m	675w	670w

The EPR spectrum recorded from [Cu(PZA)<sub>2</sub>]Cl<sub>2</sub>, occurs from resonant centers disposed in an elongated octahedron vicinity, with rhombic symmetry, having different ligands along the three x, y, z axes.

The values of the spectroscopic splitting factor are:  $g_1 = 2.22$ ;  $g_2 = 2.02$ ;  $g_3 = 2.00$ . The ESR spectrum of [Cu(PZA)<sub>2</sub>](C<sub>6</sub>H<sub>5</sub>COO)<sub>2</sub> · 4H<sub>2</sub>O is anisotropic having a  $g_{\perp}$  parameter value of 2.06 and a  $g_{\parallel}$  value of 2.25. The spectrum shown the Cu<sup>2+</sup> ion occurs in a tetragonal field with axial symmetry.

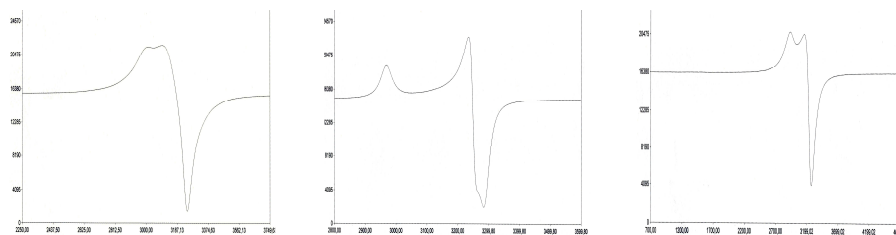
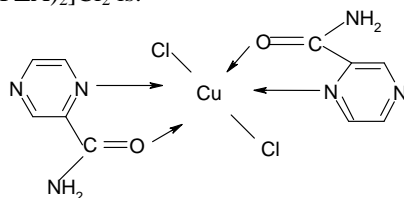


**Fig. 1.** The ESR spectra of [Cu(PZA)] [Hg(SCN)<sub>4</sub>], Cu(PZA)<sub>2</sub>Cl<sub>2</sub> and [Cu(PZA)<sub>2</sub>](C<sub>6</sub>H<sub>5</sub>COO)<sub>2</sub> · 4H<sub>2</sub>O

### Conclusion

We may conclude that the coordination through the –C=O and aromatic nitrogen ring groups in the Me-PZA complexes is implied by the FT-IR spectra. A similar coordination mode of PZA was observed in lanthanide complexes and adsorbed species on metal surfaces. The proposed structure for Cu(PZA)<sub>2</sub>Cl<sub>2</sub> is:



## REFERENCES

- [1] E. Akalin, S. Akyuz, *J. Mol. Struct.* **463/464** (2001), 579.
- [2] V. Lavini, A.S. Maia, I.S. Paulino, U. Schuchardt, W. Oliveira, *J. Inorg. Chem. Commun.* **4** (2001), 582.
- [3] Sevim Akyuz, *Journal of Molecular Structure*, 12754, 2002
- [4] *Analele Universitatii Oradea, Fascicula Stiinte farmaceutice*, Vol I (2002).
- [5] N. Ekici, Z. Kantarci, S. Akyuz, *J. Inclusion Phenom.* 10 (1991) 9.
- [6] M. Bakiler, I.V. Maslov, S. Akyuz, *J. Mol. Struct.* 476 (1999) 21.

# A NEW ANALYTICAL METHOD FOR TRACE DETECTION AT FEMTOGRAM LEVEL EMPLOYING SURFACE-ENHANCED RAMAN SPECTROSCOPY

**NICOLAE LEOPOLD<sup>1</sup>, ONUC COZAR<sup>1</sup>,  
CONSTANTIN COSMA<sup>1</sup>, BERNHARD LENDL<sup>2</sup>**

<sup>1</sup> Faculty of Physics, Babes-Bolyai University, Kogalniceanu 1, 400084, Cluj-Napoca, Romania

<sup>2</sup> Institute of Chemical Technology and Analytics, TU Vienna, Getreidemarkt 9-164/AC, 1060 Vienna, Austria

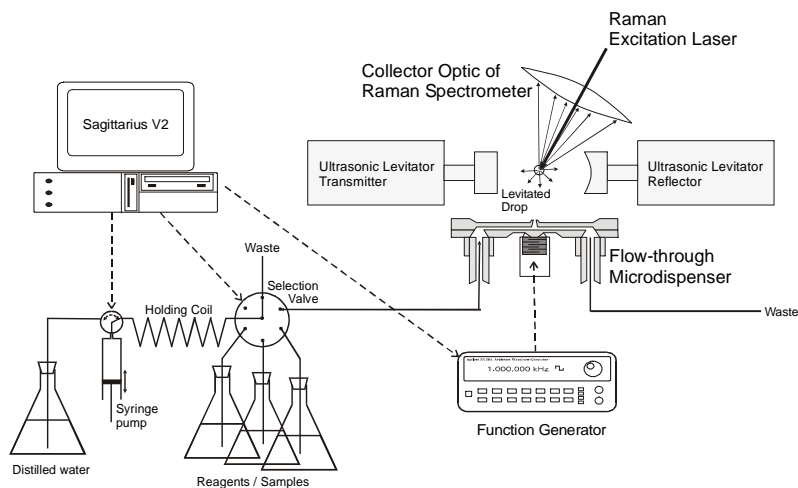
**ABSTRACT.** We report a new strategy for on-line monitoring of chemical reactions in ultrasonically levitated, nanoliter-sized droplets by Raman spectroscopy.

## Introduction

Recently, the development of a microflow cell for SERS analysis where the silver colloid is prepared using the lab-on-a-chip concept and applied to semiquantitative measurements has been reported. In the present paper, a new and versatile setup for carrying out on-line Raman monitoring of chemical reactions in acoustically levitated nanodroplets is described. The setup is used for trace analysis of organic substances using surface-enhanced Raman scattering (SERS).

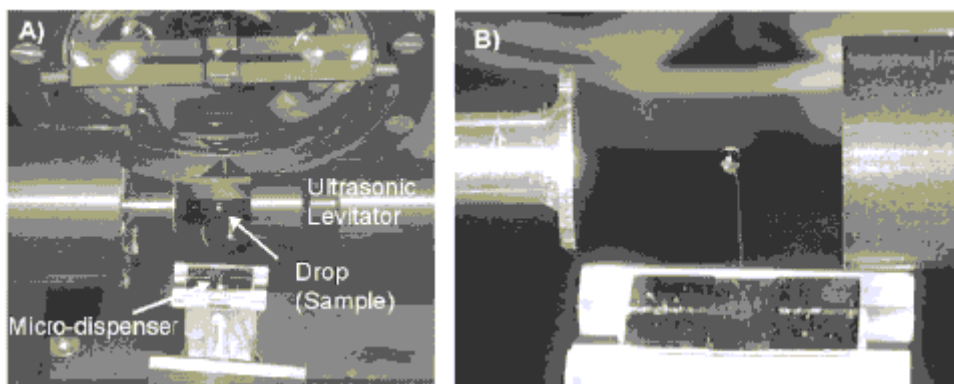
## Experimental Setup

Figure 1 shows the experimental setup used for in situ preparation of a SERS substrate in levitated nanodroplets and on-line monitoring by FT-Raman spectroscopy.



**Fig. 1.** Experimental setup comprising a flow-through microdispenser coupled to an automated flow system, an ultrasonic levitator and a FT-Raman spectrometer.

As can be seen in the figure, the computer-controlled flow system enabled sequential introduction of the different solutions (reagents and analytes) into the microdispenser, to dose the proper amounts, in streams of 60-pL droplets, into the node of the acoustic trap. A picture of the Raman spectrometer including the acoustic trap, as well as a closeup of the microdispenser can be seen in Figure 2.



**Fig. 2.** A) Image of the ultrasonic levitator holding a droplet in a node that is aligned with the collection optics of the Raman spectrometer. B) Detail showing the microdispenser sending a stream of droplets (60 pL each) to the levitated nanodroplet.

### Airborne SERS Spectroscopy

An automated flow system was employed for the continuous supply of the different reagents in order to obtain a levitated droplet for SERS measurements. First, 432 nL of  $1.1 \times 10^{-3}$  M silver nitrate was dosed by the microdispenser into the acoustic node of the ultrasonic levitator, followed by 48 nL of a solution of  $3 \times 10^{-2}$  M hydroxylamine containing 0.1 M NaOH. Both reagents were dispensed at a rate of 200 droplets (60 pL each) per second. In this way, the silver ions are reduced in the levitated drop yielding a silver sol, which serves as an airborne SERS substrate. To the obtained colloid, 12 nL of a  $10^{-5}$  M 9-aminoacridine solution containing 0.2 M NaCl was added. The evolution of the system with time is presented in Figure 3.

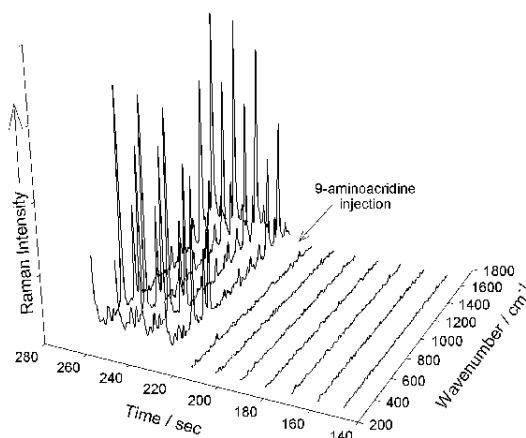


**Fig. 3.** Time evolution of the processes in the droplet as monitored by FT-Raman spectroscopy, comprising silver sol synthesis followed by injection of the analyte

The different processes in the droplet do not produce any significant signal in the recorded spectra due to the low concentration ( $10^{-3}$  M range) of the reagents employed for the synthesis of the silver sol and the extremely small cross section for Raman scattering. However, after the addition of 9-aminoacridine (~220 s), well-defined SERS spectra were obtained. The whole process, comprising synthesis of the SERS substrate and recording of the SERS spectra, took ~4 min.

During this time, the levitated droplet is exposed to the action of the laser and evaporation of the solvent takes place if the laser power is too high. To avoid this effect, the laser power was set to 100 mW. The analytical performance of the SERS substrate was tested using 9-aminoacridine as the model compound.

As the microdispenser allows for highly accurate dosing of the amount of analyte, different concentrations of 9-aminoacridine up to  $4 \times 10^{-7}$  M were dosed into the levitated droplet by following the procedure described above.

The obtained spectra are presented in Figure 4 and clearly show the dependence of the SERS signals on the concentration of the analyte.

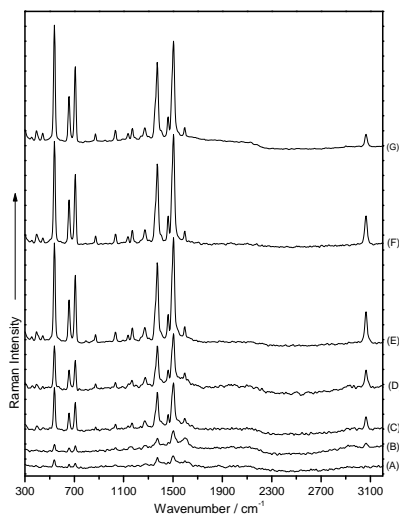


**Fig. 4** FT-SERS spectra of different amounts/ approx. concentration of 9-aminoacridine in a levitated drop containing silver colloids: (A)  $23 \times 10^{-15}$  g /  $2 \times 10^{-10}$  M, (B)  $46 \times 10^{-15}$  g /  $4 \times 10^{-10}$  M, (C)  $230 \times 10^{-15}$  g /  $2 \times 10^{-9}$  M, (D)  $460 \times 10^{-15}$  g /  $4 \times 10^{-9}$  M, (E)  $4.6 \times 10^{-15}$  g /  $4 \times 10^{-8}$  M, (F)  $46 \times 10^{-15}$  g /  $4 \times 10^{-7}$  M. (G) FT-SERS spectrum from  $4 \times 10^{-7}$  M 9-aminoacridine obtained with a Lee-Meisel silver sol measured in a cuvette.

## Conclusion

The versatility of the presented approach allows addressing different application areas in chemistry. For instance, the presented system for generation of SERS-active droplets can in principle be combined with liquid chromatographic techniques using a second microdispenser. Furthermore, when a dispersive, more sensitive Raman spectrometer is used, direct monitoring of arbitrary chemical reactions in liquids can be easily achieved in the presented format. Therefore, applications in different fields including combinatorial chemistry can be envisioned too.

## REFERENCES

1. Nicolae Leopold, Michael Haberkorn, Thomas Laurell, Johan Nilsson, Josefa R. Baena, Johannes Frank and Bernhard Lendl, *Anal. Chem.* **2003**, *75*, 2166-2171.
2. Nicolae Leopold, Bernhard Lendl, *J. Phys. Chem. B.* **2003**, *107* (24) 5723 – 5727.
3. N. Leopold, J.R. Baena, M. Bolboaca, O. Cozar, W. Kiefer, B. Lendl, „Raman, IR and surface-enhanced Raman spectroscopy of papaverine. An automatized setup for in situ synthesis of the silver substrate and recording of the SERS spectra“, submitted.

## CHARACTERIZATION BY FTIR SPECTROSCOPY OF DIFFERENT ALUMINA SAMPLES USED IN TLC

**RODICA GRECU, VIRGINIA COMAN and MIUȚA FILIP**

*"Raluca Ripan" Institute for Research in Chemistry, Department of Chromatography, 30 Fântânele Street, RO-400294 Cluj-Napoca, Romania, E-mail: r.grecu@icrr.cj.edu.ro; v.coman@icrr.cj.edu.ro*

**ABSTRACT.** The acidic alumina 150 T and basic alumina N used as stationary phase in TLC have been chemically modified by organosilanization reaction using the *n*-octadecyltrichlorosilane and 3-mercaptopropyltrimethoxysilane as trifunctional modifiers.

The study of these stationary phases by FTIR spectroscopy puts in evidence the presence of the modifier on the alumina surface. To improve the sensibility of infrared method, the difference and second derivative spectra were also analysed in order to find out the effect of the modifier on the alumina surface properties.

**Key Words:** Chemically modified alumina, *n*-octadecyl alumina, 3-mercaptopropyl alumina, FTIR spectroscopy, TLC.

### INTRODUCTION

A lot of thin layer chromatographic separations are performed on chemically modified stationary phases in order to increase their selectivity and efficiency [1].

The infrared spectroscopy is a common method used to characterize the chemically modified stationary phases [1-6]. In literature, infrared studies on chromatographic aluminas have mainly concentrated on the hydroxyl groups and Al-O-Al linkages created during the dehydration process [5]. Diffuse reflectance infrared Fourier transform (DRIFT) spectra have been used to the characterization of chemically modified aluminas [6].

In this paper, *n*-octadecyl and 3-mercaptopropyl chemically modified aluminas (acidic alumina 150 T and basic alumina N) used as stationary phases in thin layer chromatography are studied by FTIR spectroscopy.

### EXPERIMENTAL

Aluminum oxide 150 acidic type T (acidic alumina) *n*-octadecyltrichlorosilane and 3-mercaptopropyltrimethoxysilane were purchased from E. Merck (Darmstadt, Germany). Aluminium oxide N (basic alumina) were supplied by Macherey-Nagel (Düren, Germany).

The modification of alumina surface was achieved by the organosilanization reaction of superficial O-H groups of alumina samples with *n*-octadecyltrichlorosilane as well as 3-mercaptopropyltrimethoxysilane [4].

Infrared spectra of samples were registered on a JASCO-610 FTIR spectrometer using KBr pellet technique. To improve the sensibility of IR method, the difference and second derivative spectra were also analyzed.

### RESULTS AND DISCUSSION

The differences in the structure of acidic and basic alumina are well evidenced by their infrared spectra presented in Figure 1. The broad band centered at  $3433\text{ cm}^{-1}$  assigned to  $\nu(\text{OH})$  vibrations, results from the overlap of several bands due to the hydroxyl groups from the alumina surface and the adsorbed water on KBr matrix.

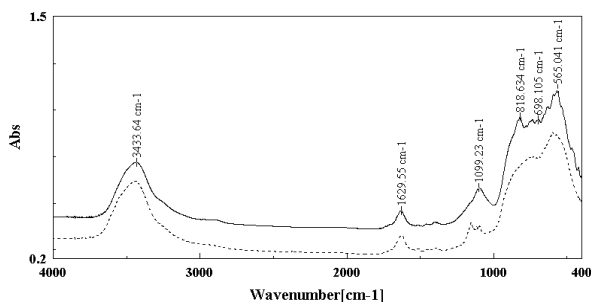


**Fig. 1.** FTIR spectra of acidic (top) and basic (bottom) unmodified alumina (KBr) pellet technique.

A tentative assignment of the prominent bands from the spectrum of unmodified aluminas is given in Table 1.

**Table 1**

**The assignments of some vibrational modes for acidic alumina and basic alumina.**

Vibrational mode	Peak position [cm <sup>-1</sup> ]	
	Acidic alumina	Basic alumina
v (Al-O-Al)	565.0	599.2
v (Al-OH)	698.1	734.2
	735.7	
	818.6	
δ (OH)	~1100	~1100

Because the FTIR spectra were registered in transmission, on sample prepared using the KBr pellet method, no information on the modification (reduction) of the superficial OH groups number of alumina as effect of the silanization reaction can be obtained.

New bands noticed especially in the 2800-3000 cm<sup>-1</sup> range of spectrum confirm the presence of the organic part of the modifier on the surface of alumina: v<sub>as</sub>(CH<sub>2</sub>) at ~ 2925 cm<sup>-1</sup> and v<sub>asym</sub>(CH<sub>2</sub>) at ~ 2855 cm<sup>-1</sup>. The band at 2960 cm<sup>-1</sup> is assigned to v<sub>as</sub>(CH<sub>3</sub>) and this fact confirms that, due to steric reasons, the functionality of the modifier is 2 and 3.

Due to low concentration of the modifier on the surface, - the intensity of the new bands - is weak. The presence of modifier is better confirmed by the difference spectrum (see Figure 2). The bands observed at ~ 1470 cm<sup>-1</sup>, 950 and 1062 cm<sup>-1</sup> were assigned to δ(CH<sub>2</sub>) and v(AlO), v(SiO) attesting the formation of Al-O-Si bridges by attaching of silane derivative onto alumina.

In the case of 3-mercaptopropyl modified aluminas the expected bands due to the Al-O-Si vibrations have been put in evidence comparing the second derivative FTIR spectra (Figure 3) of chemically modified and unmodified alumina. The bands assigned to CH<sub>2</sub> groups, having a very low intensity in the spectra of 3-mercaptopropyl modified aluminas can also be easily observed using the second derivative spectra.

**CONCLUSIONS**

The presence of organic part of the modifier on alumina surface is evidenced by the new bands (v(CH) vibrations of CH<sub>2</sub> and CH<sub>3</sub> groups) observed in the 2800-3000 cm<sup>-1</sup> range. These bands are better noticed in the difference spectrum of unmodified and chemically modified alumina.

The second derivative of FTIR spectra improves the sensibility of infrared method in the study of the chemically modified chromatographic adsorbents specially when the organic chain of modifier is short like in case of 3-mercaptopropyl.



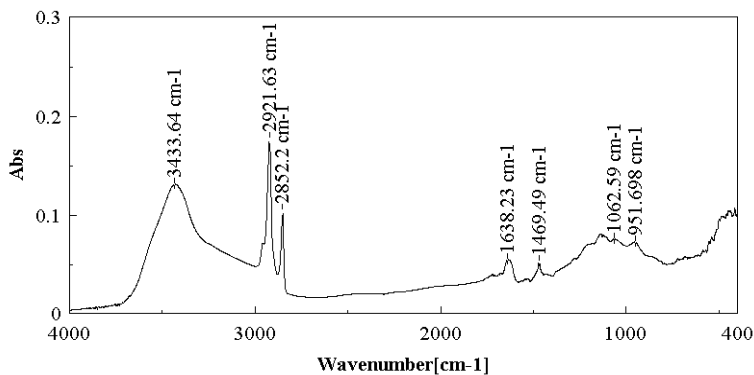


Fig. 2. Difference spectrum of *n*-octadecyl acidic alumina and acidic alumina.

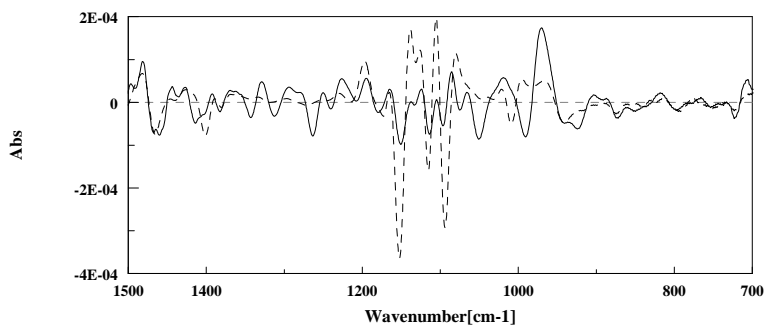


Fig. 3. Second derivative spectrum of 3-mercaptopropyl basic alumina (–) and basic alumina (..).

#### ACKNOWLEDGEMENT

The authors thank to MEC-CNCSIS Grant Program for the financial support.

#### REFERENCES

1. S. Héron and A. Tchaplă, *Propriétés et caractérisation des phases stationnaires et phases mobiles de chromatographie liquide à polarité de phases inversée*, *Analisis*, 1993, 21, 327-347.
2. V. Coman, *Silicon Compounds Used as Stationary Phases in Liquid Chromatography*, (Ph. D. Thesis), Cluj-Napoca (Romania), 1997.
3. C. Măruțoiu, M. Filip, C. Tigăe, V. Coman, R. Grecu and Gh. Marcu, *Synthesis and Characterization of Alumina R Chemically Modified with *n*-Octyl for Use as a Stationary Phase in TLC*, *J. Planar Chromatogr.-Mod. TLC*, 2003, 16, 183-185.
4. M. Filip, V. Coman, R. Grecu and Z. Moldovan, *Characterization of Some Chemically Modified Acidic Alumina Samples for TLC*, *Proceedings of the International Symposium on Planar Separations*, Budapest (Hungary), 21-23 June 2003, 231-242.
5. J. J. Pesek and M. T. Matyska, *Modified Aluminas as Chromatographic Supports for High-Performance Liquid Chromatography- Review*, *J. Chromatogr. A*, 2002, 952, 1-11.
6. H. Azour, J. Derouault, P. Lauroua and G. Vezon, *Fourier Transform Infrared Spectroscopic Characterization of Grafting of 3-Aminopropyl Silanol onto Aluminum/Alumina Substrate*, *Spectrochimica Acta. Part A*, 2000, 56, 1627-1635.

## EVALUATION OF APPLE QUALITY BY REFLECTANCE SPECTROMETRY

**DORU ROIBAN, ELISABETH-JEANNE POPOVICI, ANA-MARIA KASZONI PRICOP, LAURA SILAGHI-DUMITRESCU and RODICA GRECU**

*“Raluca Ripan” Institute for Research in Chemistry, 30 Fantanele, 400294-Cluj Napoca, Romania, roiband@icrr.cj.edu.ro*

**ABSTRACT** Attempts were made to use the reflectance spectroscopy in order to evaluate the apple quality. The aim of the study was to illustrate the spectral differences between different apple varieties from Bistrita County.

**Key words:** apple, chromatic characteristics.

### INTRODUCTION

There is a continuous demand for developing alternative fruit storage techniques as well as for finding non-destructive methods for food quality control. In this context, an ample investigation was initiated in order to develop an ozone-based apple storage method. For this purpose, the quality of the as treated apples is evaluated and compared with the quality of the traditional deposited fruits [1]. In this investigation, the apple chromaticity is attempted as one of the experiment markers. Chromatic quality of apples at the beginning of the storage period was evaluated on the basis of diffuse reflection spectra.

The current investigation put in evidence the spectral differences between the three apple varieties from Bistrita County i.e. JONATHAN, GOLDEN SPUR and GOLDEN fruits.

### EXPERIMENTAL PART

*Sample preparation:* Thin round disks were cut from the apple surface. The disks were slightly concave, had 32 mm diameter and 1.0 – 1.5 mm thickness. By using an original, special designed device, 2 ÷ 4 uniform round disks were cut out from each apple, and then slightly pressed onto 50x50 mm glass plates. For each investigated variety, at least ten apple fruits were measured.

*Colour measurement:* Diffuse reflection spectra were registered with an UNICAM UV4 Spectrometer, with RSA-UC-40 integrating sphere accessory. The reflectance was registered in visible domain (380-780 nm) in comparison with a white standard (SPECTRALON; 0.3104; 0.3189; 0.3707 coordinate). The measurements were performed with Illuminant C (10°), by using CHROMA v1.0 software. By computing the diffuse reflection spectra with the sensitivity of human eye, trichromatic coordinate and CIELAB 76 colour parameters were calculated and the apple colour evaluated.

### RESULTS AND DISCUSSION

The diffuse reflection spectra of three apple varieties from Bistrita County were registered and mathematical processed in order to appreciate the fruit colours, in numerical terms. Reflectance spectra of some representative GOLDEN SPUR, GOLDEN and JONATHAN apples are depicted in **figure 1**. The colour parameters in CIELAB system permitted the apple placement inside the colour circle whose diameters are the blue-yellow and red-green coordinates (**figure 2**).

Chromatic system CIELAB 76 works with the following parameters: L-lightness, a - red-green coordinate, b - blue-yellow coordinate, c-chroma index  $[c = (a^2 + b^2)^{1/2}]$  and h - hue angle.

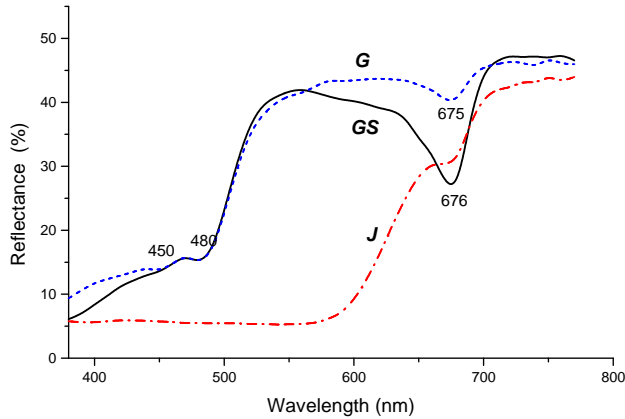


**Fig. 1.** Diffuse reflection spectra of GOLDEN SPUR (GS), GOLDEN (G) and JONATHAN (J) apples.

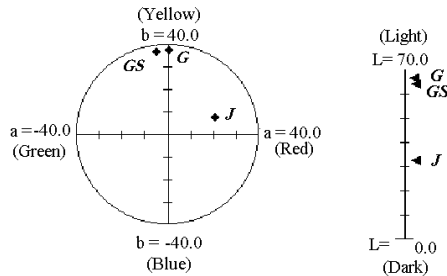


**Fig. 2.** The CIELAB colour parameters of GOLDEN SPUR, GOLDEN and JONATHAN apples

One can observe that:

- GOLDEN SPUR (GS) apples present two absorption peaks at 480 nm (weak) and 676 nm (strong), respectively, and reflect well the colour in 520÷ 640 nm domain (GS fruits show green colour); CIELAB coordinates are noticed in the green yellow quadrant, near the yellow axis.
- GOLDEN (G) apples have two relatively weak absorption peaks, situated in 400-500 nm domain and 675 nm; G-fruits reflect well the light in 520÷650 nm domain, region which is more expanded than for GS apple (G-fruits show gold yellow colour); CIELAB coordinates are observed in the yellow-red quadrant.
- JONATHAN (J) apples have a maximum of absorption at 676 nm (surprisingly in the same domain with GOLDEN SPUR apples) and have an intense absorption in 380÷570 nm region; J-apples strongly reflect the light in the 700÷780 nm domain (J-fruits show red colour); CIELAB coordinates are situated in yellow - red quadrant, closer to the red axis.
- The highest lightness values are observed for GOLDEN varieties.

The reflectance spectra could be used to calculate the three x, y, z chromatic coordinates that permit the sample placement in the chromatic CIE diagram (Commission International de l’Eclairage), inside the triangle whose corners are the red, green and blue saturated colours [2,3].

The colour coordinates were calculated from the diffuse reflectance spectra of all apple samples. The variation limits of the colour coordinates in the two chromatic systems are given in **table 1**. The minimum and maximum values for x and y coordinates are represented on the CIE

chromatic map (**figure 3**). The large variability of JONATHAN apples in comparison with GOLDEN SPUR and even GOLDEN apples is put in evidence.

**Table 1**

**CIELAB coordination variation domain and three-chromatic coordinates for the three sort of apples**

<i>Apple variety</i>	<b>GOLDEN SPUR</b>	<b>GOLDEN</b>	<b>JONATHAN</b>
<b>CIELAB 76 – Coordinates</b>			
coordinate red-green (a)	-9,10 ÷ 2,56	- 0,63 ÷ 16,69	- 2, 03 ÷ 52,57
coordinate blue-yellow (b)	31,74 ÷ 47,04	34, 06 ÷ 51,80	- 3,10 ÷ 39,34
chroma index (c)	31,97 ÷ 47,09	34,04 ÷ 51,80	17,21 ÷ 39,56
Lightness (L)	59,88 ÷ 69,85	58,65 ÷ 71,64	30,11 ÷ 69,44
<b>Chromatic Coordinates</b>			
x	0,3869 ÷ 0,4116	0,3948 ÷ 0,4521	0,3943 ÷ 0,4618
y	0,4126 ÷ 0,4455	0,3859 ÷ 0,4400	0,3110 ÷ 0,3838

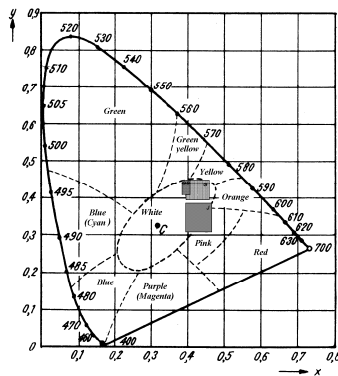


**Fig. 3.** The colour of GOLDEN SPUR, GOLDEN and JONATHAN apples in CIE coordinate map

### CONCLUSIONS

On the basis of reflectance spectra, the apple colour can be expressed in numerical terms, fact that facilitates the evaluation of fruit quality. The trichromatic coordinate system illustrates the differences between the apple varieties whereas CIELAB system seems to be more accurate in evaluating the differences between the sorts of the same variety, i.e. to illustrate their variability. The study revealed that instrumental colorimetry could be used as a non-destructive technique to appreciate the apple quality before and during the storage period.

### Acknowledgments

The work was supported by AGRAL Research National Program, under contract 124/2002.

### REFERENCES

1. Lowasz T, “Change Of Physiological Condition And Composition Of Apples During Storage”, Magyar Kemia Folyoirat, **1997**, 103, 130-135;
2. Francis F.J., “Color Quality Evaluation Of Horticultural Corps, Hort. Science, **1980**, 15, 58-59;
3. Varady Burgetti C, Lukacs Gy., “Application Of Instrumental Colorimetry In The Determination Of The Optimum Picking Times Of Different Apple Varieties”, Hungarian Scientific Instruments, 1985, 60, 49-55.

## SPECTROSCOPIC CHARACTERISATION OF CADMIUM SULPHIDE THIN LAYERS DEPOSITED ON ITO COATED GLASS

**MARIA LĂDAR<sup>1</sup>, ELISABETH-JEANNE POPOVICI<sup>1</sup>, LIGIA PASCU<sup>1</sup>,  
RODICA GRECU<sup>1</sup>, IONEL CĂTĂLIN POPESCU<sup>2</sup> and EMIL INDREA<sup>3</sup>**

<sup>1</sup> "Raluca Ripan" Institute of Research in Chemistry, 30 Fantanele,  
400294 Cluj-Napoca, Romania

<sup>2</sup> Faculty of Chemistry and Chemical Engineering "Babes-Bolyai"  
University 400028 Cluj-Napoca

<sup>3</sup> National Institute for R&D of Isotopic & Molecular Technology  
400293 Cluj-Napoca, Romania

**ABSTRACT.** By chemical bath deposition, CdS thin films were grown onto ITO coated glass. Crystalline structure and optical properties were investigated by XRD and UV-VIS spectroscopy. The main CdS/ITO/glass characteristics were correlated with the conditions of growing and post-growth treatment.

**Key words:** cadmium sulphide; thin films; ITO coated glass; chemical bath deposition

### INTRODUCTION

Cadmium sulphide (CdS) is commonly used as n-type semiconducting layer in different kind of "sandwich" heterostructures such as CdTe/CdS/ITO/glass with interesting optoelectronic properties. Different techniques could be used for CdS thin films preparation such as: chemical bath deposition, sputtering, chemical vapour deposition or electrodeposition [1]. Among them, chemical bath deposition (CBD) is a simple and low-cost method and produces uniform, adherent and reproducible films. Moreover, CBD is a low temperature technique and can be used for CdS deposition onto a wide range of substrates.

Thin films of cadmium sulphide were grown by chemical bath deposition on indium tin oxide (ITO) coated glass platelets, using the multilayer technique already mentioned in our previous works [2,3]. Cadmium sulphide films properties are extremely sensitive to preparation conditions [4,5]. The aim of this work is to study the influence of different preparative parameters on film quality and, consequently, on some of the structural and optical characteristics of CdS/ITO/glass structures.

### EXPERIMENTAL PART

Cadmium sulphide layers were chemical bath deposited onto ITO coated glass pieces from Optical Filters Ltd. Prior the deposition, the platelets (50mm x 25mm x 1mm) were ultrasonically cleaned with acetone/ethanol mixture and dried.

CdS films were formed in many successively deposition steps that always were performed in renewed chemical bath (CB) prepared from cadmium acetate, NH<sub>3</sub> aqueous solution, sodium citrate and distilled water. The deposition bath was continuously stirred and heated at 70°C. The glass platelets were immersed into the deposition bath, by vertically suspending them around the stirrer. After the thermal equilibrium was reached, thiourea solution was added under stirring.

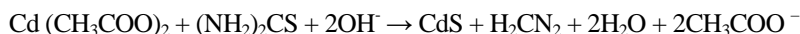
The multi-layer deposition procedure was as follows. The wet glass platelets were immersed into the hot chemical bath. The platelets were taken out after 1.0 hr, washed and reintroduced into a renewed hot CB. Deposition parameters were: [Cd<sup>2+</sup>] = 3x10<sup>-3</sup>M; [C<sub>6</sub>H<sub>5</sub>O<sub>7</sub><sup>3-</sup>] = 1.2x10<sup>-1</sup>M; [NM<sub>3</sub>] = 3x10<sup>-1</sup>M; [thiourea] = 3.10<sup>-2</sup>M; pH = 10.5÷11.0;

All samples were washed, dried and annealed in air, at 350°C.

Cadmium sulphide thin films were characterised by thickness, crystalline structure and UV-Vis transmittance spectra. XRD patterns were obtained by means of a standard DRON-3M Diffractometer. Optical investigations were performed with UNICAM Spectrometer UV4. The film thickness was evaluated by the micro-weighing method [3].

## RESULTS AND DISCUSSION

CdS/ITO/glass samples were prepared by chemical bath deposition method, from cadmium acetate and thiourea solutions. The chemical bath deposition of films involves the decomposition of alkaline solutions containing thiourea in the presence of a metal salt, as follows:



Chemical bath contains also some chelating agents such as ammonia or sodium citrate, whose role is to control the CdS film-growing rate.

CBD method was adapted for multilayer CdS film formation onto ITO coated glass platelets. CdS/ITO/glass samples, with 1, 2 or 4 consecutively deposited CdS layers, were prepared and characterised. Composition of the as prepared heterostructures, packing density, growing rate and thickness of CdS films are presented in table 1.

**Table 1**

**General characteristics of some heterostructures containing ITO and CdS films**

Samples code	Heterostructures	CdS film type	Total dep. time n x m*	Packing density (mg/cm <sup>2</sup> )	Film thickness (nm)	Growing rate (nm/min)
ITO 0	ITO/glass	-	0	0	20**	0
ITO1.0	CdS/ITO/ glass	Mono-layer	1 x 2 h	0.088	15	0.1
ITO 2.1	CdS/ITO/ glass	Multi-layer	2 x 1h	0.480	100	0.8
ITO 2.3	CdS/ITO/ glass		4 x 1h	1.424	295	1.2
ITO 2.5	CdS/ITO/ glass		4 x 1h	1.296	270	1.1

\* where: n = number of layers, m = deposition time; \*\*- manufacturer measurement

The increase of cadmium sulphide film thickness with the total deposition time could be noticed. Moreover, for the same deposition time, the multilayer film (ITO 2.1.) is almost 7 times thicker than the corresponding monolayer one (ITO1.0). The use of a high number of successively deposited layers (coatings) determines the increase of the film thickness. One can note that, for various heterostructures, the growing rate is different, increasing with the number of coatings.

UV-Vis spectroscopy (figure 1 and figure 2) and X-ray diffraction (figure 3 and figure 4) were used to investigate the optical and structural properties of different CdS/ITO/glass heterostructures. The transmission spectra of the heterostructures that contain multilayer CdS films, illustrate the decrease of film transparency parallel with the film thickness increases (figure 1). As for the post-growing thermal treatment, this one seems to increase the film transmittance (figure 2).

One can be noted that the ITO coated glass substrate shows a high transparency on the entire visible domain.

The crystalline structure of the thermally treated CdS/ITO/glass heterostructures was investigated by X-ray diffraction. Beside the strong bands of the cubic indium-tin oxide, the characteristic bands of the hexagonal crystalline structure (greenokite type) of the cadmium sulphide could be noticed (figure 3). The cristallinity of the films are rather high due to the post-growing thermal treatment.

In order to compare de effect of multiple layers on the crystalline structure of CdS films, XRD spectra were normalised, in rapport with (222) peak of the indium-tin oxide (figure 4). The spectra normalisation put in evidence the increase of the three XRD characteristic bands of cadmium sulphide, i.e. (100), (002), (101). This fact could be explained by the presence of a higher CdS amount on the surface of ITO coated glass platelets.

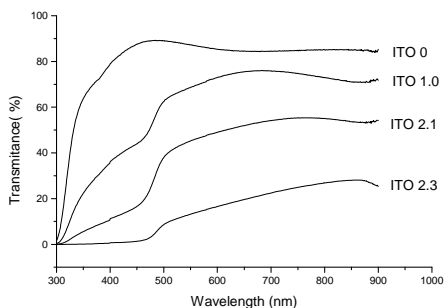


**Fig. 1.** Transmission spectra of CdS/ITO/glass samples with multilayered CdS film

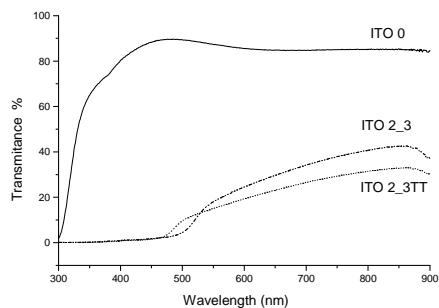


**Fig. 2.** Transmission spectra of CdS/ITO/glass samples before and after the thermal treatment

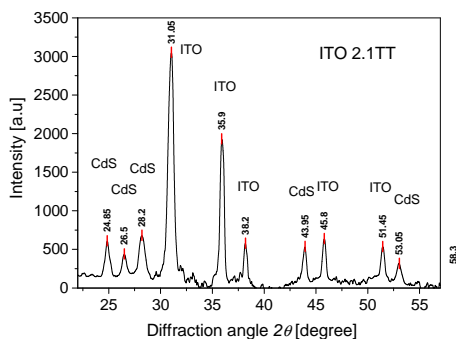


**Fig. 3.** XRD spectra for CdS/ITO/glass sample after the thermal treatment

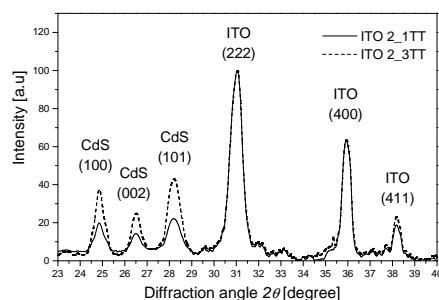


**Fig. 4.** XRD spectra for CdS/ITO/glass samples with multilayer CdS films

## CONCLUSIONS

The bath composition and the special CBD technique used in our experiments proved to be convenient for the deposition of adherent and homogeneous films with controllable thickness onto the ITO coated glass substrate. UV-Vis and XRD investigation illustrated the quality of the as prepared CdS/ITO/glass heterostructures.

## Acknowledgements:

The work was supported by CERES National Research Program, under contract no. 28/2002.

## REFERENCES

1. P.O Brien, T. Saeed, "Deposition and characterization of cadmium sulfide thin films by chemical bath deposition", *Journal of Crystal Growth*, **158**, **1996**,497-594
2. L. Pascu, E.-J. Popovici, E. Indrea, R. Grecu, L.Pacurar, "Studies on thin films CdTe/CdS structures", *Proceeding of SPIE*, vol.4068, **2000**, 117-123;
3. L. Pascu, E.-J. Popovici, C. Dan, R. Grecu, L. Pacurar, E. Indrea, "Studies on thin films CdTe/CdS heterostructures. Chemical bath deposited cadmium sulphide layers", *Proceeding of SPIE*, vol.4430, **2001**, 267-274;
4. I. O. Oladeji, L. Chow, "Optimization of chemical bath deposited cadmium sulfide thin films", *J. Electrochem. Soc.*, **144**, **1997**, 2342-2346
5. M. Stoev, A. Katerski, "XPS and XRD study of photoconductive CdS films obtained by a chemical bath deposition process", *J. Mater. Chem.*, **6**(3), **1996**, 377-380

## INVESTIGATION OF OPTICAL PROPERTIES OF CHEMICAL BATH DEPOSITED ZINC SULPHIDE THIN FILMS

**RODICA GRECU<sup>1</sup>, ELISABETH-JEANNE POPOVICI<sup>1</sup>, MARIA LĂDAR<sup>1</sup>,  
LAURA SILAGHI-DUMITRESCU<sup>1</sup> and E. INDREA<sup>2</sup>**

<sup>1</sup> "Raluca Ripan" Institute for Research in Chemistry, 30 Fântânele Street,  
RO-400294 Cluj-Napoca, Romania, E-mail: rgrecu@icrr.cj.edu.ro

<sup>2</sup> National Institute for R & D of Isotopic and Molecular Technologies,  
67-103 Donath; RO-400293 Cluj-Napoca

**ABSTRACT.** Thin films of zinc sulphide have been prepared by chemical bath deposition in alkaline ammonia solutions from zinc acetate and thiourea, using successive depositions. The obtained films are amorphous. The evolution of optical characteristics of ZnS films after the annealing process was dependent on the number of deposited layers.

### INTRODUCTION

Zinc sulphide is a binary II–VI semiconductor compound that is of interest in the technology of solar cells, photoconductive sensors and many others optical devices. Various techniques have been employed to prepare ZnS thin films, such as, metal-organic chemical vapour deposition [1], chemical bath deposition [2, 3], SILAR method [4], electrodeposition etc. The chemical bath deposition (CBD) is an "electroless" technique that is attractive as low cost method. Unfortunately, the deposition parameters strongly influence the properties of the films: homogeneity, adherence to the support, crystalline structure, optical characteristics etc.

The aim of this paper is to study the optical properties of some multilayer ZnS films prepared by CBD method. The transmittance (T) and the reflectance (R) of the films in the UV-Vis region, the value of the band gap energy ( $E_g$ ) calculated from the transmittance spectra, and also the effect of the annealing process are reported.

### EXPERIMENTAL

The ZnS films were prepared using a chemical bath containing zinc acetate (0.03 M), thiourea (0.60 M), sodium citrate (0.12 M) and ammoniac (0.30 M). Films were grown on optical glass slides in optimised conditions: temperature 84-86<sup>0</sup> C, pH 9.5-10.5. Thick samples were produced by successive deposition of 1 h layers. After each deposition, samples were carefully washed and immersed into renew chemical bath. The optical glass slides of 30 x 45 x 1 mm used as support were cleaned using a special procedure.

Film thickness was determined by micro gravimetric weight difference method.

The post-growth treatment of the samples consisted in 1 hour air annealing at 350<sup>0</sup>C, in an electrical furnace.

Transmission spectra at normal incidence were recorded in the wavelength range of 300-900 nm using an UNICAM UV4 double beam spectrophotometer. Reflectance spectra at 8<sup>0</sup> angle (specular reflectance included) and 0<sup>0</sup> (diffuse reflectance) incidence were obtained using the integrating sphere RSA-UC-40 accessory of the spectrometer.

### RESULTS AND DISCUSSION

Study of materials by means of optical absorption provides information on the quality of the thin films and some optical constants.



A series of ZnS/glass/ZnS structures was prepared by a multi-step technique. The figure from sample notation indicates the number of the deposited layers by successively immersion of glass substrate into the chemical bath. The optical behaviour of samples was evaluated before and after the post-growth thermal treatment (samples noted adding TT). Optical measurements were performed on ZnS/glass/ZnS or ZnS/glass structures.

*Zinc sulphide films characterization*

XRD spectra showed that the as-grown zinc sulphide films possesses an amorphous structure. Contrary to our expectation, the thermal post-growth treatment (1 h, 350°C in air) did not significantly changed the structural arrangement of film particles.

The optical transmittance of as-grown or annealed films, with different thickness is presented in Figure 1. As expected, the film transmission decreases as the thickness increases. In spite of the fact that during the annealing period the film thickness decreased, no improvement in the film transmittance could be observed. For instance, the thermal treatment reduces the transmittance of the sample S10 to about 30 % (see Figure 1). The pattern of interference fringes suggests that the films do not have uniform thickness.

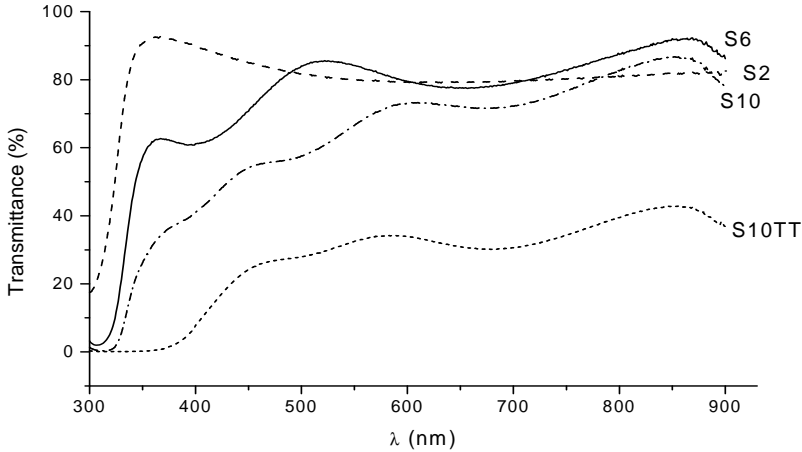


**Fig. 1.** Transmission spectra (corrected for glass absorption) of ZnS/glass/ZnS samples. The thickness of films is: 54 nm (S2), 208 nm (S6), 361 nm (S10) and 289 nm (S10TT)

The specular reflectance of samples calculated as difference of reflection measured at 8° (specular included) and 0° (diffuse reflectance) incidence decreased as the number of layers increased (Figure 2). The consequence of the thermal treatment on the mirror type reflection of ZnS films was a slight improvement (sample S2) or an important reduction (sample S10).

The evolution of optical characteristics of zinc sulphide films by the annealing process must be related to their multilayer structure that determined a grainy material and formation of powdery layers between uniform adherent layers.

*Optical constants of the films*

Zinc sulphide is a direct band gap semiconductor, so that the absorption coefficient  $\alpha$  can be related to the photon energy by:

$$(\alpha h\nu)^2 = A(h\nu - E_g)$$

where A is a constant and  $E_g$  is the optical energy gap.

From the transmittance spectra of ZnS/glass structures, the value of  $E_g$  was estimated by extrapolation of the straight line in the plot of  $(\alpha h\nu)^2$  versus the photon energy  $h\nu$  (Figure 3). The band gap of as-grown films is 3.6-3.75 eV, comparable to values reported by other authors for CBD prepared ZnS films [2].

The decreasing of band gap to 3.4–3.5 eV in the annealed films confirms the powdery nature of these films and suggests a possible contamination with zinc hydroxide.

The refractive index was calculated from the transmittance spectra according to Swanpoel's method, which assumes transparent and uniform films exhibiting interference patterns. The value of  $n$  (2.40-2.50) systematic higher than data reported in literature for ZnS films (1.95-2.23, depending on deposition method [4]) or the bulk material ( $n \sim 2.3$ ) shows that the studied films are not enough uniform to give accurate values of maxim and minima of transmittance used in the calculus formula.

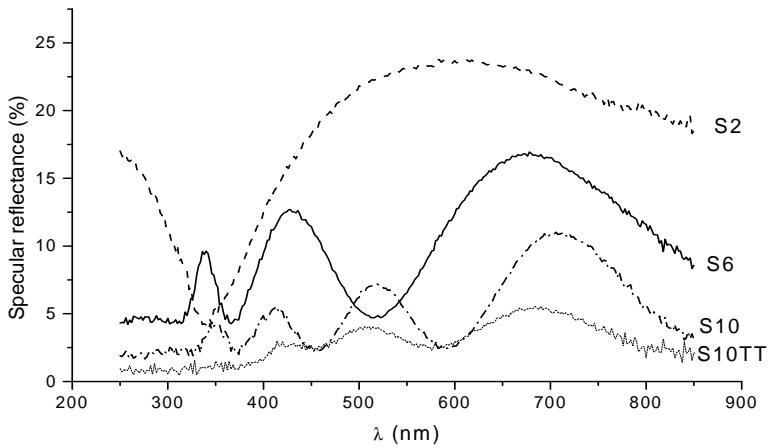


Fig. 2. Specular reflectance of ZnS/glass/ZnS samples.

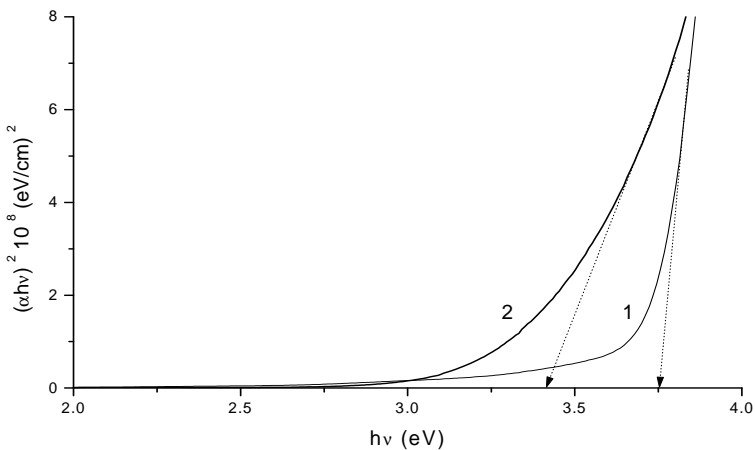


Fig. 3. Plot of  $(\alpha h\nu)^2$  vs.  $h\nu$  of sample S6 (ZnS/glass) as-grown (1) and annealed (2)

### CONCLUSIONS

The investigation of the absorption and reflectance spectra of ZnS thin films grown on glass support, by CBD method using successive depositions, showed that the samples are amorphous and have a high transmittance in the visible region of spectra. The air thermal treatment at 350<sup>o</sup> C did not improve the optical properties of the films with a too large number of layers.

### ACKNOWLEDGMENT

The work was supported by MECT (CNCSIS Grant nr. 717/2003), Romania

### REFERENCES

1. O. Osasona, A. Djebach, I. A. O. Ojo, M. A. Eleruja, A. V. Adedeji, C. Jeynes and E. O. B. Ajayi, *Preparation and characterization of MOCVD thin films of zinc sulphide*, Optical Materials, 7, 1997, 109-117
2. J. M. Dona, J. Herrero, *Process and Film Characterization of Chemical-Bath-Deposited ZnS Thin Films*, J. Electrochem. Soc., 141, 1994, 205-210
3. I. C. Ndukwe, *Solution growth, characterization and applications of zinc sulphide thin films*, Solar Energ. Mater. Solar Cells, 40, 1996, 123-131
4. S. Lindroos, Y. Charreire, D. Bonnin, M. Leskela, *Growth and characterization of zinc sulfide thin films deposited by the successive ionic layer adsorption and reaction (SILAR) method using complexed zinc ions as the cation precursor*, Materials Research Bulletin, 33, 1998, 453-459

## STRUCTURAL INVESTIGATIONS OF IRON DOPED $\text{Bi}_2\text{O}_3\text{-GeO}_2$ GLASSES BY MEANS OF MICRO-RAMAN AND INFRARED SPECTROSCOPIES

L. BAIA<sup>1</sup>, R. STEFAN<sup>2</sup>, W. KIEFER<sup>1</sup> and S. SIMON<sup>2</sup>

<sup>1</sup> *Institut für Physikalische Chemie, Universität Würzburg, D-97074 Würzburg, Germany*

<sup>2</sup> *Physics Department, Babes-Bolyai University, 3400 Cluj-Napoca, Romania*

**ABSTRACT.** Samples belonging to  $97\%[\text{xBi}_2\text{O}_3(1-\text{x})\text{GeO}_2]3\%\text{Fe}_2\text{O}_3$  glasses system with different Bi/Ge nominal ratios ( $0.20 \leq \text{x} \leq 0.875$ ) have been investigated by means of micro-Raman and infrared spectroscopy. The influence of iron cations on vitreous  $\text{Bi}_2\text{O}_3$  and  $\text{GeO}_2$  network as well as the structural changes around bismuth and germanate atoms have been evidenced by comparing spectra recorded at different concentrations. In order to determine the influence of the dopant on the bismuth-germanate matrices structure the recorded spectra have been compared with the already published data on undoped  $\text{Bi}_2\text{O}_3\text{-GeO}_2$  glasses.

### Introduction

Glasses containing  $\text{Bi}_2\text{O}_3$  in combination with  $\text{GeO}_2$  have been investigated for their applications as materials for low loss fibers and for IR transmitting windows [1], being also suggested their use as active medium for Raman fiber optical amplifiers [2].

On the basis of Raman and infrared investigations it has been reported that  $\text{GeO}_2$  is present in the structure of various glasses as  $[\text{GeO}_4]$  tetrahedra and/or  $[\text{GeO}_6]$  octahedra [3, 4], while the  $\text{Bi}_2\text{O}_3$  structure is built up from pyramidal  $[\text{BiO}_3]$  and/or octahedral  $[\text{BiO}_6]$  structural units [5, 6]. On the other hand, it is well established that the structure and properties of glasses containing transition metal ions depend critically on the relative proportions of the different valence states. Therefore, the structural changes induced by the modification of the Bi/Ge nominal ratios and the presence of  $\text{Fe}_2\text{O}_3$  as dopant are of great interest from the structural point of view.

The goal of the present study was to obtain by means of Raman and infrared spectroscopy specific data regarding the local structure of iron doped  $\text{Bi}_2\text{O}_3\text{-GeO}_2$  glasses and to evidence the changes of both  $\text{Bi}_2\text{O}_3$  and  $\text{GeO}_2$  structural units. Furthermore, our interest was to find out the influence of the dopant on the bismuth-borate matrices structure.

### Experimental

The samples were prepared using as starting materials  $\text{Bi}_2\text{O}_3$ ,  $\text{GeO}_2$  and  $\text{Fe}_2\text{O}_3$  of reagent grade purity (99.9%). The components have been mixed in proportions corresponding to the desired compositions, then they were melted in sintered corundum crucibles. The mixtures have been heated in an electric furnace at  $1100^\circ\text{C}$  and maintained at this temperature for 10 min, then they were quickly undercooled at room temperature by puring onto stainless steel plates. All the samples have been analyzed by X-ray diffraction and no crystalline phase was evidenced.

The Raman measurements were performed on a Dilor Labram system equipped with an Olympus LMPlan Fl 50 microscope objective, an 1800 lines/mm grating and an external laser with an emission wavelength of 514 nm. In the recording of the micro-Raman spectra a power of 100 mW on the sample has been employed. The spectral resolution was about  $4\text{ cm}^{-1}$ .

For infrared measurements the glasses were powdered and mixed with KBr in order to obtain thin pellets with a thickness of about 0.3 mm. The infrared spectra were recorded with a Bruker IFS 25 spectrometer; the spectral resolution in this case was  $2\text{ cm}^{-1}$ .

### Results and discussion

The infrared spectra of the investigated glasses, which are presented in Fig. 1a, are dominated by three broad bands centered in the spectral regions around  $400\text{-}530\text{ cm}^{-1}$ ,  $700\text{-}820\text{ cm}^{-1}$  and  $840\text{-}900\text{ cm}^{-1}$  and one shoulder at  $980\text{ cm}^{-1}$ . The most important condition for the existence of  $[\text{BiO}_3]$  and  $[\text{GeO}_6]$  polyhedra is the presence of absorption bands around  $830$  and  $680\text{ cm}^{-1}$ , respectively [3, 7]. The missing of these bands leads to the idea that the  $\text{Bi}_2\text{O}_3$  and  $\text{GeO}_2$  structures are built up from  $[\text{BiO}_6]$  and  $[\text{GeO}_4]$  polyhedra. For  $x = 0.20$  one observes that the main contribution to the bands observed in the infrared spectrum is due to germanate structural units vibrations. Thus, the only infrared band given by bismuthate unit vibrations appears as a Bi-O bond vibration together with a symmetric Ge-O-Ge stretching vibration, giving a very broad band centered around  $530\text{ cm}^{-1}$ , while the convoluted bands at  $745$  and  $815\text{ cm}^{-1}$  are given by asymmetric stretching vibrations of Ge-O-Ge and symmetric stretching vibrations of O-Ge-O [3]. The high frequency feature at  $980\text{ cm}^{-1}$  arises from the asymmetric stretching vibration of Ge-O-Ge bridges involving both O and Ge motions [8]. By increasing the  $\text{Bi}_2\text{O}_3$  concentration,  $x = 0.40$ , and comparing the infrared spectra of the investigated doped glasses with high and medium  $\text{GeO}_2$  content,  $x = 0.20$  and  $0.40$ , with those of the already published data on  $\text{Bi}_2\text{O}_3\text{-GeO}_2$  glasses [3] one can see that, while for  $x = 0.20$  all spectral features are very similar, for the doped glasses with  $x = 0.40$  an obvious spectral change appears in the small wavenumber region. The broad band around  $520\text{ cm}^{-1}$ , which present an asymmetrical form, can be observed instead of two distinguished bands at  $430$  and  $540\text{ cm}^{-1}$ , which were attributed in the above-mentioned study to the Bi-O stretching vibrations in  $[\text{BiO}_6]$  octahedral units and to the symmetric Ge-O-Ge vibrations in  $[\text{GeO}_4]$ . This broad band is the result of the appearance of other vibrations in this spectral range and could be regarded as a consequence of the existence of different Bi-O bond lengths in distorted  $[\text{BiO}_6]$  polyhedra [9]. It indicates the influence of the  $\text{Fe}^{2+}$  or/and  $\text{Fe}^{3+}$  cations on the bismuthate structure for the doped glasses with  $x = 0.40$ .

It can be observed that the increase of the  $\text{Bi}_2\text{O}_3$  content and consequently the decrease of the  $\text{GeO}_2$  concentration,  $x \geq 0.60$ , leads to a significant vanishing of the infrared band at  $815\text{ cm}^{-1}$  attributed to the symmetric stretching vibrations of O-Ge-O, this spectral behaviour could be interpreted as a modification of the linkages between  $[\text{GeO}_4]$  tetrahedra. This assumption is proved both by the shift of the band from  $745\text{ cm}^{-1}$  for  $x = 0.40$  to  $721\text{ cm}^{-1}$  for  $x = 0.80$ , this latter band being related to the vibrations of the isolated  $[\text{GeO}_4]$  tetrahedral, as well as the appearance, especially for  $x = 0.80$ , of two distinguished bands at  $460$  and  $875\text{ cm}^{-1}$  due to Bi-O bond vibrations.

The micro-Raman spectra of the investigated glasses system illustrated in Fig. 1b are dominated in the  $50\text{-}180\text{ cm}^{-1}$  spectral region by intense bands attributed to the vibrations involving the  $\text{Bi}^{3+}$  cations motion in  $[\text{BiO}_6]$  polyhedra [10], contributions of some  $\text{Ge}^{4+}$  motions to these vibrations being also possible. The broad Raman band observed at  $420\text{ cm}^{-1}$  for  $x = 0.20$  is due to a symmetric stretching vibration of the bridging oxygen atoms in the  $\text{GeO}_2$  network structure, while the small band at  $780\text{ cm}^{-1}$  could be assigned to the Ge-O and Ge-O-Ge stretching vibrations in  $[\text{GeO}_4]$  tetrahedral [10]. By increasing the  $\text{Bi}_2\text{O}_3$  content,  $x = 0.40$ , the assumption made before concerning the existence of different Bi-O bond lengths in distorted  $[\text{BiO}_6]$  polyhedra is confirmed by the appearance of a very broad band at  $380\text{ cm}^{-1}$  attributed to the Bi-O-Bi vibrations. The missing of this Raman band in the already investigated undoped  $\text{Bi}_2\text{O}_3\text{-GeO}_2$  glasses [10] confirms the influence of the  $\text{Fe}^{2+}$  or/and  $\text{Fe}^{3+}$  cations on the  $\text{Bi}_2\text{O}_3$  network. For  $x \geq 0.60$  the Raman spectra show distinguished and narrow bands in the  $200\text{-}600\text{ cm}^{-1}$  spectral region due to the Bi-O-Bi and Bi-O vibrations, the appearance of these spectral features demonstrating the occurrence of a structural ordering process of the  $[\text{BiO}_6]$  octahedral units. For  $x = 0.875$ , the disappearance of the  $780\text{ cm}^{-1}$  Raman band assigned to the Ge-O and Ge-O-Ge stretching vibrations indicates the iron dopant influence on the bismuthate and germanate units, the incorporated iron cations favouring the appearance of the mentioned structural ordering process of the  $[\text{BiO}_6]$  units and of the depolymerization process of the  $\text{GeO}_2$  structure in the investigated doped glass structure. The

ordering of the bismuthate structural units is further proved by the significant decrease in half-width of the Raman bands, in which the  $\text{Bi}^{3+}$  cations motion is involved, and that arise in the low wavenumber region between 50 and  $180\text{ cm}^{-1}$ . By comparing the behaviour of the Raman bands for  $x \leq 0.40$  with that observed for  $x \geq 0.60$  one can observe a stabilizing effect of the glass structure formation for the first above-mentioned compositional range.

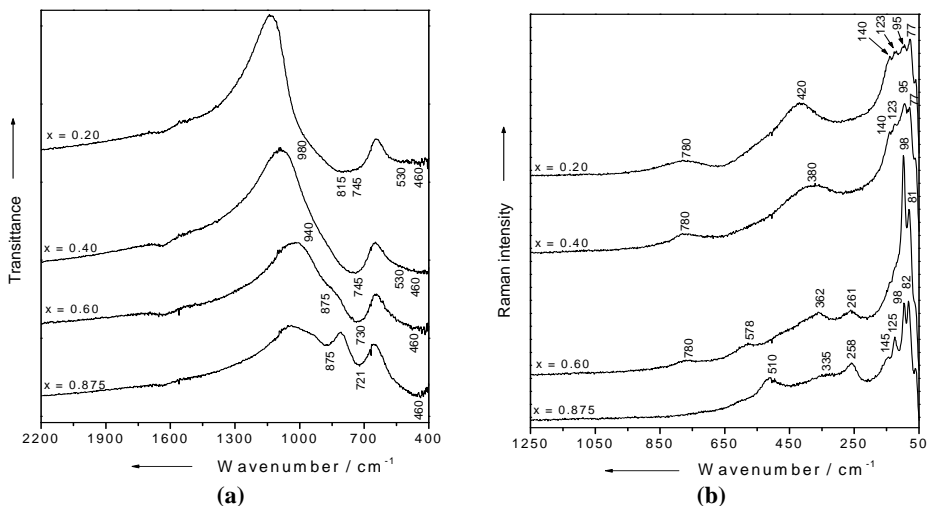


Fig. 1. Infrared (a) and micro-Raman spectra (b) of 97% $[\text{xBi}_2\text{O}_3(1-\text{x})\text{GeO}_2]$ 3% $\text{Fe}_2\text{O}_3$  glasses

### Conclusion

On the basis of infrared and micro-Raman investigations of iron doped  $\text{Bi}_2\text{O}_3\text{-GeO}_2$  glasses system it was evidenced that  $\text{Bi}^{3+}$  cations are incorporated in the glass network as  $[\text{BiO}_6]$  octahedra, while germanium takes part as  $[\text{GeO}_4]$  tetrahedra. The influence of the iron cations on the  $\text{Bi}_2\text{O}_3$  and  $\text{GeO}_2$  structures is represented by the appearance of different Bi-O bond lengths for low and medium  $\text{Bi}_2\text{O}_3$  content ( $x = 0.20$  and  $x = 0.40$ ), and by the occurrence of an ordering process of the  $[\text{BiO}_6]$  polyhedra and consequently the existence of a depolymerization process of the  $\text{GeO}_2$  structure for higher  $\text{Bi}_2\text{O}_3$  content ( $x = 0.60$  and  $x = 0.875$ ). Moreover, a stabilizing effect of the glass structure formation has been observed for  $x \leq 0.40$ .

### REFERENCES

1. K. Nassau, D. L. Wood, D. L. Chadwick, *Appl. Optics*, 21, 1982, 4276.
2. C. Lin, *Opt. Comm.*, 4 (1983) 2.
3. V. Dimitrov, Y. Dimitriev, A. Montenero, *J. Non-Cryst. Solids*, 180, 1994, 51.
4. W. C. Huang, H. Jain, *J. Non-Cryst. Solids*, 40, 1994, 180.
5. S. Hazra, S. Mandal, A. Ghosh, *Phys. Rev. B* 56, 1997, 8021.
6. L. Baia, D. Maniu, T. Iliescu, S. Simon, S. Schlücker, W. Kiefer, *Asian J. Physics*, 9, 2000, 51.
7. P. Pernice, A. Arone, M. Catauro, A. Marotta, *J. Non-Cryst. Solids*, 210, 1997, 23.
8. S. K. Sharma, D. W. Matson, J. A. Philpotts, T. L. Roush, *J. Non-Cryst. Solids*, 68, 1984, 99.
9. R. Betsch, W. White, *Spectrochimica Acta*, 34A, 1977, 5051.
10. P. P. Lottici, A. Antonioli, C. Razzeti, A. Montenero, *The Physics of Non-Crystalline Solids*, eds. L.D. Pye et al., Taylor & Francis, London, 1992, p. 101.

## SPECTRAL INVESTIGATION ON TERBIUM ACTIVATED YTTRIUM OXYSULPHIDE PHOSPHORS

LAURA MURESAN<sup>1</sup>, ELISABETH-JEANNE POPOVICI<sup>1</sup>, AMALIA  
HRISTEA<sup>1</sup>, EMIL INDREA<sup>2</sup> and MARILENA VASILESCU<sup>3</sup>

<sup>1</sup>“Raluca Ripan“ Institute for Research in Chemistry, 30 Fantanele, 3400-Cluj-Napoca, Romania; ella-m@personal.ro

<sup>2</sup>National Institute for R&D of Isotopic & Molecular Technology, 3400- Cluj Napoca, Romania

<sup>3</sup>“I.G. Murgulescu” Institute of Physical Chemistry of Romanian Academy, 202 Spl.Independentei, Bucuresti, Romania

**ABSTRACT.** Samples of terbium activated yttrium oxysulphide phosphors were prepared by solid-state reaction route. The structural characteristics and photoluminescence (PL) properties were evaluated on the basis of X-ray diffraction patterns and excitation or emission spectra. The paper investigates the influence of the synthesis conditions on optical and structural properties of Y<sub>2</sub>O<sub>2</sub>S: Tb phosphor.

**Key words:** phosphor; yttrium oxysulphide; luminescence

### INTRODUCTION

Under different types of radiation such as UV and X-ray, terbium activated yttrium oxysulphide shows bright green luminescence related to the terbium ion presence. Terbium activated yttrium oxysulphide (Y<sub>2</sub>O<sub>2</sub>S: Tb) phosphor is of great interest for the manufacture of X-ray intensifying screens for medical diagnosis [1,2]. The utilisation of oxysulphide phosphors depends on the powder particle size distribution and luminescent properties that are adjusted during the phosphor synthesis stage [3]. Phosphor parameters are extremely sensitive to synthesis conditions.

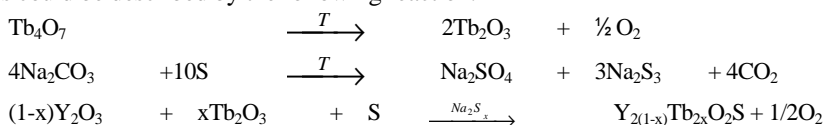
In order to establish the optimum synthesis conditions for the manufacture of an efficient phosphor for X-ray intensifying screens, the correlation composition-structure-properties was studied for samples prepared by solid state reaction route. The paper presents the influence of some preparative conditions on the structural and photoluminescence properties of Y<sub>2</sub>O<sub>2</sub>S: Tb phosphor.

### EXPERIMENTAL PART

Homogeneous mixtures of Y<sub>2</sub>O<sub>3</sub>, Tb<sub>4</sub>O<sub>7</sub>, Na<sub>2</sub>CO<sub>3</sub>, sulphur and Na<sub>3</sub>PO<sub>4</sub> were fired at 1200<sup>0</sup>C for 4 hours, air (closed system). Samples were carefully washed with diluted hydrochloric acid, dried and sieved. Phosphor samples were characterised by emission and excitation spectra registered, under UV excitation, with 204 Perkin Elmer Spectrofluorimeter and by X-ray diffraction spectra taken with Philips PW 1050 Diffractometer.

### RESULTS AND DISCUSSION

Phosphor synthesis was performed by solid state reaction from mixtures containing oxide material (Y<sub>2</sub>O<sub>3</sub>, Tb<sub>4</sub>O<sub>7</sub>) and sulphuring flux mixture (Na<sub>2</sub>CO<sub>3</sub>, S, Na<sub>3</sub>PO<sub>4</sub>). The phosphor synthesis could be described by the following reaction:



Some of the synthesis conditions and general characteristics of phosphor samples are presented in table 1.

**Table 1****General characteristics of terbium activated yttrium oxysulphide samples**

Sample code	Sulphuring mixture Na <sub>2</sub> CO <sub>3</sub> : Na <sub>3</sub> PO <sub>4</sub> :S	Phosphor formula	Powder colour	Photoluminescence colour
Y <sub>2</sub> O <sub>2</sub> S: Tb samples prepared with different amounts of terbium oxide				
Y11	2 : 0.2 : 6.5	Y <sub>1.99</sub> Tb <sub>0.01</sub> O <sub>2</sub> S	Dark cream	White green
Y12	2 : 0.2 : 6.5	Y <sub>1.97</sub> Tb <sub>0.03</sub> O <sub>2</sub> S	Brick-red	Yellow green
Y13	2 : 0.2 : 6.5	Y <sub>1.95</sub> Tb <sub>0.05</sub> O <sub>2</sub> S	Light grey	Bright green
Y01	2 : 0.2 : 6.5	Y <sub>1.93</sub> Tb <sub>0.07</sub> O <sub>2</sub> S	Light cream	Bright green
Y15	2 : 0.2 : 6.5	Y <sub>1.9</sub> Tb <sub>0.1</sub> O <sub>2</sub> S	White	Bright green
Y <sub>2</sub> O <sub>2</sub> S: Tb samples prepared with various amounts of sulphur in the sulphuring flux mixture				
Y16	2 : 0.2 : 0	Y <sub>1.97</sub> Tb <sub>0.03</sub> O <sub>2</sub> S	Dirty cream	Dirty green
Y17	2 : 0.2 : 2	Y <sub>1.97</sub> Tb <sub>0.03</sub> O <sub>2</sub> S	Light cream	Light green
Y18	2 : 0.2 : 4	Y <sub>1.97</sub> Tb <sub>0.03</sub> O <sub>2</sub> S	Orange	Yellow-green
Y19	2 : 0.2 : 6	Y <sub>1.97</sub> Tb <sub>0.03</sub> O <sub>2</sub> S	White	White
Y20	2 : 0.2 : 8	Y <sub>1.97</sub> Tb <sub>0.03</sub> O <sub>2</sub> S	White	White-green

Photoluminescence (PL) properties of as prepared samples were checked by emission spectra. The presence of terbium ions into the yttrium oxysulphide phosphors generates four principal emission bands in the visible spectrum, the strongest one showing a maximum at about 545 nm (**figure 1** and **figure 2**).

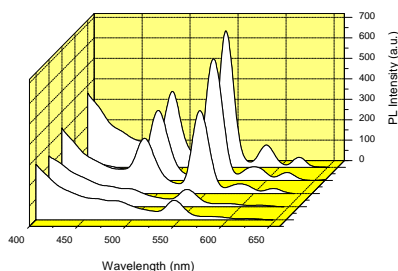


**Fig. 1.** PL spectra of samples prepared with various activator amounts

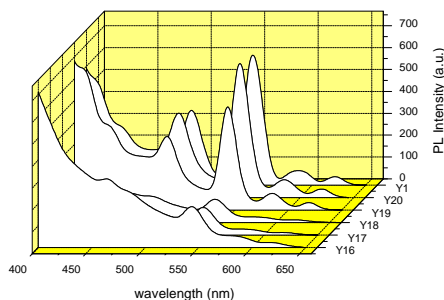


**Fig. 2.** PL spectra of samples prepared with variable sulphuring flux mixture

These bands could be assigned to the following electronic transition that occur between the excitation and the fundamental levels of the terbium ions:  $^5D_4 \rightarrow ^7F_6$  (~487 nm);  $^5D_4 \rightarrow ^7F_5$  (~544 nm);  $^5D_4 \rightarrow ^7F_4$  (~585 nm) and  $^5D_4 \rightarrow ^7F_3$  (~620 nm). The emission bands relative ratio determines the apparent PL colour.

The overall PL emission depends of activator concentration i.e. large terbium amounts determines the intensification of the specific green bands (**figure 3**). The increase of sulphur content into the sulphuring flux mixture is in the favour of yttrium oxide conversion into the desired yttrium oxysulphide host lattice thus resulting in an increase of the green emission (**figure 4**).

All samples possess a good excitability at around 310 nm. The excitation maximum is influenced by the preparative conditions.



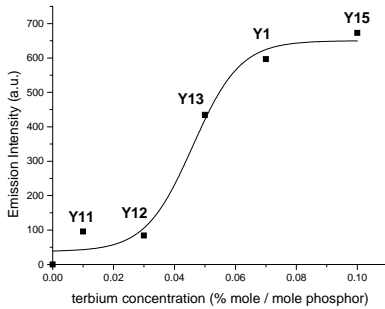


**Fig. 3.** Influence of the activator amount on PL emission ( $I_{545nm}$ )

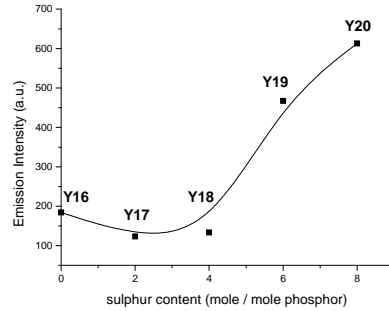


**Fig. 4.** Influence of the host lattice sulphuration degree on PL emission ( $I_{545nm}$ )

X-ray patterns illustrate the change of the crystalline structure from cubic yttrium oxide to hexagonal yttrium oxysulphide; the later is observable at samples prepared with more than 6 mole S/ mole phosphor. The formation of a multiphase luminescent material was put in evidence (**figure 5**).

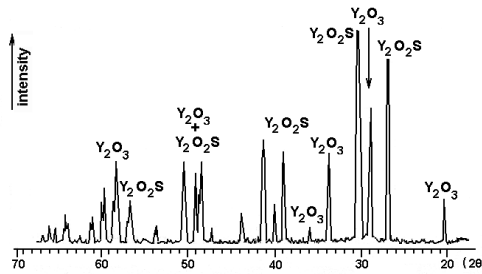


**Fig. 5.** X-Ray diffraction spectra for Y20 phosphor sample ( $CuK_{\alpha}$  radiation)

## CONCLUSIONS

The preparation conditions such as the quality of oxide mixture, concentration of terbium activator and composition of the sulphuring mixture, thermal synthesis conditions and conditioning regime are factors that influence the morpho-structural and photoluminescence characteristics of  $Y_2O_2S: Tb$  phosphor. The optimum concentration into the host lattice and the recommended sulphur amount into the sulphuring flux mixture could be established for the indicated thermal synthesis regime.

## Acknowledgements:

The work was supported by MATNANTECH National Research Program, under contract no. 70/2001.

## REFERENCES

1. H. Degenhardt, "Utilisation de substances luminophores a la base de terre rares dans les ecrans renforceurs al la haute definition", *Electromedica*, **1980**, 3, 76-79;
2. G. Blasse, B.C. Grabmaier "Luminescence materials", **1994**, Berlin- Heidelberg
3. Y. Shu-Hong, H. Zhao-Hui, "Synthesis and formation mechanism of  $La_2O_2S$  via a Novel solvothermal-pressure-Relief Process", *Chem. Mater.* **1999**, 11, 192-194.

## MICROSTRUCTURAL INVESTIGATIONS OF NEW VITREOUS MATERIAL FOR CERAMIC INDUSTRY

CEZARA VOICA<sup>1</sup>, LIANA GAGEA<sup>3</sup>, E. INDREA<sup>2</sup>, SIMINA DREVE<sup>2</sup>, I. BRATU<sup>2</sup>

<sup>1</sup>*S.C.CEROC S.A., 1 Treboniu Laurean st., 3400 Cluj-Napoca, Romania*

<sup>2</sup>*National R&D Institute of Isotopic and Molecular Technologies, P.O. Box 700, R-3400 Cluj-Napoca 5, Romania*

<sup>3</sup>*Babes-Bolyai' University, 1 Kogalniceanu st., Faculty of Chemistry, Cluj-Napoca, Romania*

**ABSTRACT.** Colorants and glazes in ceramic industry is using vitreous materials named "frits", containing usually rather large amounts of lead. The necessity of ecological and safe products imposed lately the synthesis of new frits lead-free, having as much as possible, the same structure and properties.

We report here a new frit-type vitreous lead-free material for fabrication of colorants and glazes in ceramic industry. The chemical composition of the oxidic mixtures for the classical frit F1 and for the new frit and the technological procedures for fabrication are presented.

The physical properties as melting point and dilatation coefficient, the specific surface and the optical properties were determined in correlation with the microstructural characteristics.

### Introduction

In traditional ceramics the presence of lead in frits have a very important role: to give the hardness and shining properties and to realise the dispersion of the decorating colours in thin layers. Despite this important properties the problems of the use of lead in frits composition (low chemical resistance, pollution, toxicity) imposed the elaboration of new frits, replacing the lead oxide with other compounds, but keeping the same physical properties. The present work present the preparation of a new frit-type vitreous material with bismuth oxide, having the capacity to replace the frit with lead and having more convenient physico-chemical properties for use in industrial ceramic.

### Experimental

In order to prepare the new frit-type material usual raw materials from the production process were taken, adjusting the quantities upon the chemical composition and following the usual production process. The important modification of the recipe was the replacement of the lead oxide, PbO, with bismuth oxide, Bi<sub>2</sub>O<sub>3</sub>, the molar ratios of the chemical compounds in the frit material being presented in table 1.

### Thermal derivatography

To establish the technological firing conditions the thermal analysis of the new material was performed, with a thermal analyser type MOM Q 1500. The two frits have an almost similar thermal behaviour, and results. Between 160<sup>0</sup> and 175<sup>0</sup> C the same endothermal effects are observed, due to the loss of water from the mixed raw materials. Over 600<sup>0</sup> C the effects are very weak, and the loss of weight is low. A calcinations over 800<sup>0</sup> C assure the melting and the stability of the fondant. The new prepared frit have the loss of weight at calcinations decreased with 1.5% than the leaded frit, at the correspondent calcinations temperatures. The thermal analysis curves are represented in fig. 1.

**Table 1.**  
**Molar ratios of the chemical compounds in the frit.**

Oxydes	Molar ratio	
	leaded frit (1)	bismuth frit (2)
K <sub>2</sub> O	0,053	0,076
Na <sub>2</sub> O	0,433	0,619
CaO	0,034	0,049
MgO	0,014	0,019
ZnO	0,165	0,237
PbO	0,301	-
B <sub>2</sub> O <sub>3</sub>	1,422	2,033
Al <sub>2</sub> O <sub>3</sub>	0,201	0,288
Fe <sub>2</sub> O <sub>3</sub>	0,002	0,003
Bi <sub>2</sub> O <sub>3</sub>	-	0,206
SiO <sub>2</sub>	3,051	4,363
TiO <sub>2</sub>	0,002	0,003

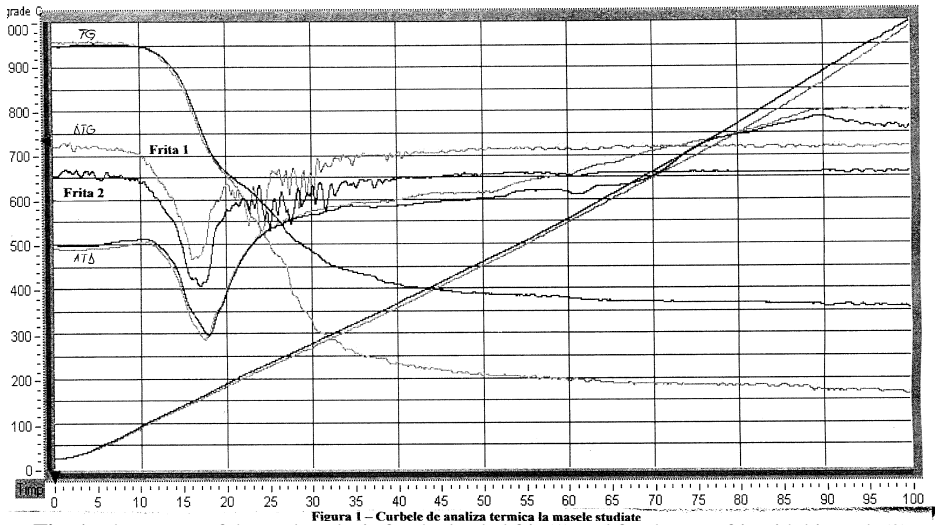


**Fig. 1.** The curves of thermal analysis for the leaded frit (1) and for the new frit with bismuth (2).

**Thermal microscopy**

The thermal microscopy analysis was performed on the two frits, using a microscope of high temperatures LEITZ, between 900<sup>0</sup> C and 1300<sup>0</sup> C. The results are presented in table 2.

**Table 2.**

**Thermal microscopy results for the leaded (1) and bismuth (2) frits.**

Nr.	Temperature (°C)	900		1100		1300	
		1	2	1	2	1	2
1	Sample	1	2	1	2	1	2
2	Low-melting-point	690	690	675	690	685	710
3	Low-softening point	780	790	750	815	780	835
4	Melting	870	870	850	880	855	920
5	Softening interval	90	100	75	125	95	125
6	Melting interval	90	80	100	65	75	85

As it can be seen after 1100<sup>0</sup> C the thermal behaviour of the two kind of vitreous material is different, and the frit with bismuth is more suited for practical applications because it has larger melting intervals so it assure a better aderence to the ceramic support at a better shining.

### Structural characterisation

The long-range order characteristic for the crystalline state is not occurring in the vitreous state, where the short-range order is typical [1]. For the crystalline structures there are correlations between two atoms disposed at arbitrary large distances one to other. In the non-crystalline solids like glasses there is a local order, a short-range order, characterised only for the first coordination spheres of the component atoms, i.e. at the distances at which the interatomic forces are acting. The local order in glass and crystalline compounds of the same composition has both similarities and differences. The differences are assigned to the loss of long range order, to the deviation from a perfect crystalline structure. The order extension degree can be investigated using the analysis technique of atom electron distribution functions obtained form X-ray scattering measurements. There are also glass systems wherin the local structure is extended at more than some coordination spheres imposing a middle or intermediate range order [2]. The non-crystalline state of a compound can occur in a large structural variety depending on the preparation conditions. This is due to the fact that during the vitreous sample preparation the “freezing” process of the atoms arrangement has an important effect on the atom bonds and atom relaxation energy barriers. Along with the neutron scattering the X-Ray scattering from disordered materials is largely used to investigate their local structure [3-7].

The X-ray scattering patterns were obtained by means of standard DRON-3M powder diffractometer, working at 40 kV and 30 mA, and equipped with scintillation counter with single channel pulse height discriminator associated counting circuitry. The Cu K<sub>α</sub> radiation, Ni filtered, was collimated with Soller slits. X- ray scattering patterns were recorded in a step-scanning mode with  $\Delta 2\theta = 0.10^0$  steps. The analysed samples, disposed as a powered disk with diameter of 12 mm and thickness about 2 mm, were investigated by means of a X ray scattering experiment, using a goniometer in Bragg-Brentano reflection alignment.

The structure of the lead oxide, PbO, and bismuth oxyde, Bi<sub>2</sub>O<sub>3</sub> vitreous systems was investigated by analysing the atomic radial distribution function obtained from X ray scattering data using a PEDX program [8]. The computation steps consist first in the determination of radial distribution function  $4\pi r^2 \rho(r)$ . The preliminary processing of scattering data implies the determination of the total experimental coherent scattering function  $I_T(s_k) : I_T(s_k) = [I_{exp}(s_k) - I_F(s_k)] \cdot A(s_k)/P(s_k)$

The atom pairs correlation function  $g(r)$  shows maxima and their position, width and area are determined by the distribution of atom pairs in the structural disordered sample (Fig. 2). The real space distance corresponding to the maxima determined from the data obtained in this study may be compared with results reported for other similar systems [9,10] and allow to identify the atom pairs orderly disposed in the the SiO<sub>2</sub> matrix vitreous systems. They are summarised in Table 3.

**Table 3**

Coordination sphere	Atom pairs	Distance (Å)
I	Si – O	1.69
II	O – O	2.93
III	Si - Si	3.21

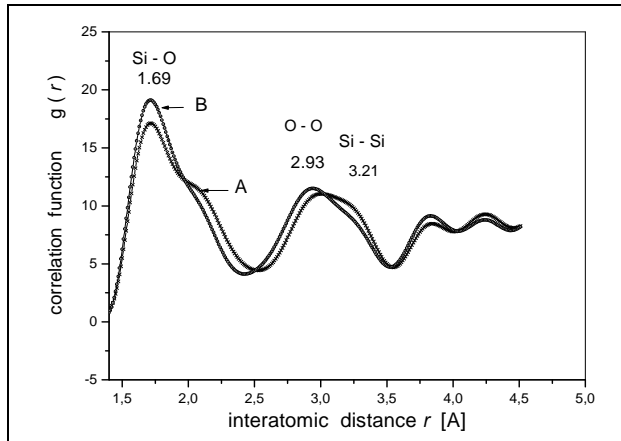


**Fig. 2.** The atomic pair correlation function  $g(r)$  for samples of the lead oxide, A, and bismuth oxide, B, vitreous systems.

Inspecting the data obtained for the samples with lead oxide,  $\text{PbO}$ , and bismuth oxide,  $\text{Bi}_2\text{O}_3$ , from the analysis of atom pairs correlation function  $g(r)$  one remarks the occurrence of Si – O pair as a first coordination formation, well composed at a distance of 1.69 Å. In  $\text{SiO}_2$  vitreous systems, the basic structural building block is the same as the crystalline silicates, the  $\text{SiO}_4$  tetrahedron [10]. The distances  $r$  between O - O and Si – Si pairs are ranging from 2.6 to 3.5 Å. The bismuth addition to the  $\text{SiO}_2$  matrix frits vitreous system preserves the vitreous structure, that evidences the high ability of the precursor glass to accept relatively high  $\text{Bi}_2\text{O}_3$  content without structural changes.

## REFERENCES

1. J. Zarzycki, *Glasses and Vitreous State*, Cambridge University Press, 1991
2. R.E. Youngman, S.T. Haubrich, J. W. Zwanziger, M. T. Janicke and B. F. Chmelka, *Science* 269, 1416 (1995)
3. D.L. Price and M.-L. Saboungi, *Anomalous X-Ray Scattering from Disordered Materials, Local Structure from Diffraction*, eds., S. J. L. Billinge and M. F. Thorpe, Plenum Press, New York, 1998.
4. D. L. Price, M.-L. Saboungi, A. C. Barnes, *Phys. Rev. Lett.* 81,15, 3207 (1998)
5. K. Suzuya, D. L. Price, C.-K. Loong, S. W. Martin, *J. Non-Cryst. Solids*, 232-234, 650 (1998)
6. M. Nofz, B. Himmel, Th. Gerber, F. Ehrentreich, *J. Non-Cryst. Solids*, 143, 191 (1992)
7. B. Himmel, J. Weigelt, Th. Gerber, M. Nofz, *J. of Non-Cryst. Solids*, 136, 27 (1991)
8. PEDX: a program for radial-distribution function analysis of energy-dispersive X-ray diffraction data from disordered materials (authors: V. Petkov, Department of Solid State Physics, Sofia University, Sofia – 1126, Bulgaria and Y. Waseda, Institute for Advanced Materials, Tohoku University, Sendai 982, Japan).
9. J. Swenson, L. Börjesson, R.L. McGreevy, W.S. Howells, *Phys. Rev.* B55, 17, 11236 (1997)
10. R.L. Mozzi and B.E. Warren, *J. Appl. Crystallogr.*, 2, 164-172 (1969).

## SILICA-LIME-PHOSPHATE VITROCERAMICS WITH IRON

D. ENIU<sup>1</sup>, S. SIMON<sup>2</sup>

<sup>1</sup>*University of Medicine and Pharmacy, Faculty of Pharmacy,  
3400 Cluj- Napoca, Romania*

<sup>2</sup>*Babes-Bolyai University, Faculty of Physics, 3400 Cluj-Napoca,  
Romania*

**ABSTRACT.** Glass transition and crystallisation temperatures determined from thermal analyses indicate the structural evolution of samples in function of composition. The glass stability is enhanced by Fe<sub>2</sub>O<sub>3</sub> addition to silica-lime-phosphate host glass up to 20 mol %. Electron paramagnetic resonance and magnetic susceptibility results inform on the surrounding and magnetic interactions between iron ions. The Fe<sup>3+</sup>-EPR data indicate that the size of ferromagnetic particles increases after heat treatment and their surroundings become more ordered due to the partial crystallisation of samples. The magnetic susceptibility increases by heat treatment and depends on the treatment temperature.

### Introduction

The use of calcium phosphate glasses and glass ceramics as bone substitutes has become common in orthopedic surgery [1]. Ferromagnetic calcium phosphate glass ceramics are successfully applied to reinforce the bone and to decrease the recurrence of tumors by hyperthermic treatment [2]. In this samples is essential the development of ferromagnetic crystallites in iron rich phases.

The aim of this paper is to evidence the structural effects caused by iron addition to calcium-silica-phosphate glasses, the vicinity and magnetic interactions of iron ions of CaO-P<sub>2</sub>O<sub>5</sub>-SiO<sub>2</sub>-Fe<sub>2</sub>O<sub>3</sub> glass and glass ceramic samples.

### Experimental

The starting materials used to obtain 45(3.34 CaO-P<sub>2</sub>O<sub>5</sub>)(55-x)SiO<sub>2</sub>-xFe<sub>2</sub>O<sub>3</sub> glasses were CaCO<sub>3</sub>, CaHPO<sub>4</sub>·2H<sub>2</sub>O, SiO<sub>2</sub> and Fe<sub>2</sub>O<sub>3</sub> of reagent grade purity. The oxide mixtures corresponding to the desired compositions (0 ≤ x ≤ 30 mol %) were melted in corundum crucibles at 1550°C for 10 minutes in an electric furnace Carbolite type RHF 1600, in air, under normal conditions. The melts were quickly undercooled by pouring onto stainless steel plates at room temperature. Specimens of the glass samples were heat treated with a rate of 4°C/min from the room temperature to 1000, 1100 and 1200°C in air. They were maintained at the treatment temperature for 30 minutes and then were slowly cooled in the furnace down to the room temperature.

The electron paramagnetic resonance (EPR) spectra were recorded on a 300 ESP Bruker spectrometer, in X band, at room temperature on powder samples.

The magnetic susceptibility was measured between 80K and 300K with a 10<sup>-8</sup> emu/g sensitivity Faraday-type magnetic balance.

Thermal analysis measurements were carried out using a MOM derivatograph with a rate of 10°C/min.

### Results and discussion

The structural evolution of samples in function of composition was first checked by determining the glass transition and crystallisation temperatures from differential thermal analyses. The data obtained show that the glass transition temperature, T<sub>g</sub>, increases by addition of iron to the calcium-silica-phosphate matrix up to 20 mol % (Fig. 1). One observes that glass transition temperatures are very close for the sample without iron and that with lowest iron content, while T<sub>g</sub> has the same value for the samples with 20 and 30 mol % Fe<sub>2</sub>O<sub>3</sub> contents.

With respect to glass stability, expressed by the difference between the crystallization temperature and glass transition temperature, it was found an increase up to  $x = 20$  Fe<sub>2</sub>O<sub>3</sub> mol %.

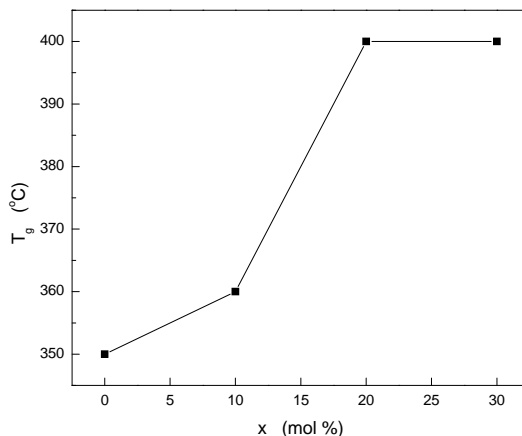


**Fig. 1.** The composition dependence of glass transition temperature.

The local atomic order and the valence state of iron in oxide glass matrices play a major role in determining the physical properties of glasses, inclusively their capability to aggregate in clusters [3]. For glass compounds used as precursor materials of ferromagnetic biomaterials with applications in hyperthermic treatments the iron atoms segregation in clusters is very important. Both cluster size and sample magnetic susceptibility are to be enlarged in view of this therapy.

The EPR spectra of the investigated samples consist in a large, relatively symmetric line. This feature is specific to disordered oxide systems with high Fe<sub>2</sub>O<sub>3</sub> content wherein spherical ferromagnetic monodomain particles are formed [4], most probably magnetite particles. The resonance line at  $g \approx 2.0$  is shifted to lower values of the magnetic field when the iron oxide content increases. This result could be assigned to the occurrence of ferromagnetic multidomain particles in the samples with higher Fe<sub>2</sub>O<sub>3</sub> content. The width of  $g \approx 2.0$  line increases with Fe<sub>2</sub>O<sub>3</sub> content from 830 Gs, for  $x = 10$ , to 2780 Gs, for  $x = 30$ , and suggests that the size of ferromagnetic particles are distributed on a relative large values range, but on the other hand they are small enough to be not detected by X-ray diffraction analyse. The size of these particles and the local order are increased by the crystallisation heat treatment. This is also reflected by EPR spectra evolution as can be seen from Figure 2. The spectrum of the heat treated sample contains beside the line typical of untreated glass sample an additional narrow line ( $\Delta B = 195$  G) arising from Fe<sup>3+</sup> ions disposed in the crystalline phase well developed during the applied heat treatment.

The highest local concentration for iron inside the samples was obtained from ESCA measurements [5] for the glass ceramic resulting by the treatment applied at 1000°C. The magnetic susceptibility,  $\chi$ , increases by heat treatment, e.g. for the sample with  $x = 10$  mol %, at room temperature,  $\chi$  increases from 35 to 150 ( $10^{-3}$  emu/mol). The temperature dependence of the reciprocal magnetic susceptibility for this composition is illustrated in Figure 3. The magnetic susceptibility reaches the largest value after the heat treatment applied at 1100°C.

Both SiO<sub>2</sub> and P<sub>2</sub>O<sub>5</sub> are glass formers. Pure vitreous SiO<sub>2</sub> and P<sub>2</sub>O<sub>5</sub> consist in a continuous random network of quasi-tetrahedral SiO<sub>4</sub> and PO<sub>4</sub> units wherein silicon, respectively phosphorous is four coordinated. In these glasses CaO and Fe<sub>2</sub>O<sub>3</sub> act as glass network modifiers.

The thermal diffusivity of these samples has a good stability in the temperature range including the interval of interest for therapy by hyperthermia [6].

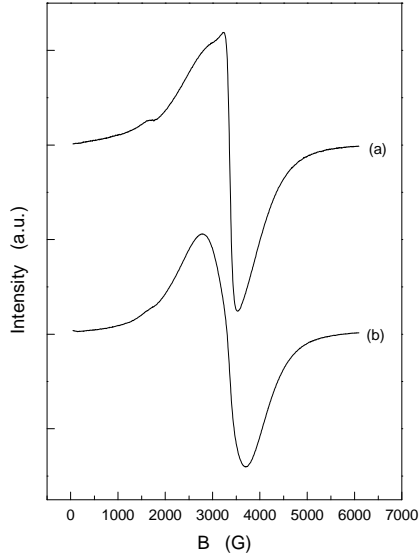


**Fig. 2.** EPR spectra of (a) glass ceramic and (b) glass samples.

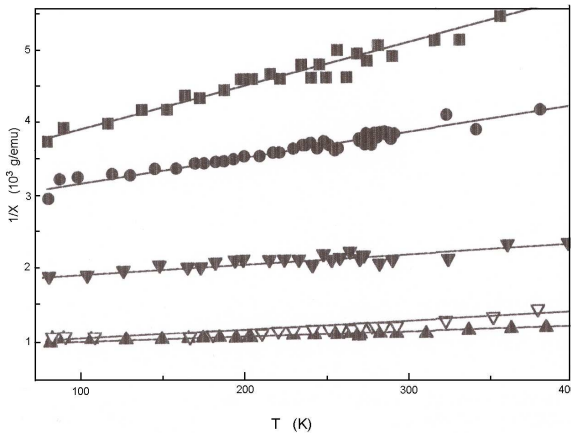


**Fig. 2.** Temperature dependence of reciprocal susceptibility for  $45(3.34 45(3.34 \text{CaO} \cdot \text{P}_2\text{O}_5)45\text{SiO}_2 \cdot 10\text{Fe}_2\text{O}_3$  samples heat treated at different temperatures: untreated (■),  $1000^\circ\text{C}$  (●),  $1100^\circ\text{C}$  (▲),  $1200^\circ\text{C}$  (▼).

### Conclusion

The glass stability is enhanced by  $\text{Fe}_2\text{O}_3$  addition to silica-lime-phosphate host glass up to 20 mol %. With increasing  $\text{Fe}_2\text{O}_3$  content the samples contain beside monodomain also multidomain ferromagnetic particles. The size of these particles increases and their local structure becomes more ordered in vitroceramic samples obtained by heat treatment. The magnetic susceptibility rises up to five times in the partially crystallised samples.



**REFERENCES**

1. A. Dupraz, T. P. Nguyen, M. Richard, G. Daculsi, N. Passuti, *Biomaterials*, 20, 663 (1999)
2. M. Babinkova, D. Leszczynska, P. Sourivong, P. Cicmanec, P. Babinec, *J. Magn. Magn. Mater*, 225, 109 (2001)
3. F. D'Acapito, S. Mobilio, J. R. Regnard, E. Cattaruzza, F. Gonella, P. Mazzoldi, *J. Non - Cryst. Solids*, 232-234, 364 (1998)
4. D. L. Griscom, *J. Non-Cryst. Solids*, 67, 81 (1984)
5. V. Simon, S. G. Chizbaian, M. Neumann, D. Eniu, E. Indrea, A. Torok-Kiss, S. Simon, *Mod. Phys. Lett. B.*, 14, 21, p.767 (2000)
6. S. Simon, D. Eniu, A. Pasca, D. Dadarlat, V. Simon, *Mod.Phys.Lett.B*, 15, 21, 921 (2001).

## THE INCLUSION COMPLEX OF NIMODIPINE WITH $\beta$ -CYCLODEXTRIN. FT IR SPECTROSCOPY AND X-RAY DIFFRACTION STUDIES

MIHAELA TOMA<sup>1</sup>, I. BRATU<sup>2</sup>, A. HERNANZ<sup>3</sup>, GH. BORODI<sup>2</sup>,  
O. COZAR<sup>1</sup> and GH. BORA<sup>4</sup>

<sup>1</sup> "Babes-Bolyai" University, Faculty of Physics, 1 Kogalniceanu st., Cluj-Napoca

<sup>2</sup> National Institute for R&D of Isotopic and Molecular Technologies, P.O. Box 700,  
Cluj-Napoca

<sup>3</sup> UNED, Depto de CC y TT Fisico-Quimicas, 28040 Madrid, Spain

<sup>4</sup> "Terapia", 126 Fabricii st., Cluj-Napoca

### Introduction

Nimodipine (C<sub>21</sub>H<sub>26</sub>N<sub>2</sub>O<sub>7</sub>) (NIMO) is frequently used as antianginal, anti-hypertensive or cerebral vasodilator pharmon. There are two main disadvantages in its use: it is practically insoluble in water and light sensitive in solution. Cyclodextrin (CD) derivatives may be used as inclusion complex-forming agents to increase the solubility of drugs and different dyes are also available to prevent the photodegradation of these molecules. In order to avoid this inconvenient and to increase the solubility, inclusion complexes (IC) of cyclodextrins with this drug are prepared and investigated. Different procedures, largely recommended in the literature [1], were employed to obtain IC: physical mixtures (*pm*), coprecipitation (*co*), kneading (*kn*) and freeze-drying (*fd*). The *kn* and *co* methods were already used [2-4] to prepare IC of nimodipine. A systematic study of the FT IR and XRD spectra of the IC complexes was done in order to establish which one of these procedures is the more efficient and how the molecule is included in the CD torus.

### Experimental

ICs of NIMO with  $\beta$ -CD in 1:1 molar ratio was obtained by commonly used methods: *fd*, *co*, *kn* and *pm*. They were solved in a (1:1) mixture of water and ethanol, being submitted to the specific procedure in each case:

- for *co* procedure the solutions were stirred at 60°C for 24 hours;
- for *kn* procedure the mixtures were kneaded at room temperature for at least 40 minutes by adding small quantities of mixture of solvents until a solid powder resulted;
- for the *fd* procedure the solutions were frozen at -15°C and then dried under vacuum.

FT IR spectra were obtained with a Bomem DA 3 spectrometer in the 4000 to 400 cm<sup>-1</sup> spectral range by using the well-known KBr pellet technique.

XRD spectra were obtained with a DRON 3 diffractometer by using the Cu-K $\alpha$  radiation.

### Results and Discussion

#### FTIR spectra

Based on some fundamental references [5, 6], one can attribute the main absorption bands that appeared in these spectra, see Figs 1-3.

A detailed analysis of these spectra reveals the following spectral changes if one compares the corresponding spectra of *pm*, *co*, *kn* and *fd* complexes:

- the  $\nu$  (O-H) stretching band of  $\beta$ -CD is shifted, Fig. 1, from 3379 cm<sup>-1</sup> in pure  $\beta$ -CD or *pm* system to 3384 cm<sup>-1</sup> for the complexes obtained by *co*, *fd* and *kn* methods. One can observe that the  $\nu$ (O-H) massif change its intensity distribution on going from pure  $\beta$ -CD to IC systems specially in the high frequency wing of this profile.

- the  $\nu$  (N-H) stretching band of NIMO and *pm* system is located at  $\sim 3297\text{ cm}^{-1}$ ; this band is shifted to  $3277.6\text{ cm}^{-1}$  for the *IC* systems obtained by *co* and *kn* methods. In the mean time, the band located at  $\sim 3218\text{ cm}^{-1}$  remains unchanged in frequency upon complexation. This frequency shift can be explained by the restricted mobility of the NH group in the *IC* as compared to the *pm* or pure Nimodipine.

In the  $1900\text{-}1500\text{ cm}^{-1}$  spectral region, Fig 2, the  $\nu$  (C=O) stretching band profile having two components, one at  $1700.3$  and other at  $1693.9\text{ cm}^{-1}$ , is located in the spectra of pure Nimodipine and *pm* system. These components are shifted to  $\sim 1702$  and  $1696.4\text{ cm}^{-1}$ , respectively for the *IC* systems obtained by *co*, *kn* and *fd* methods. The inversion of the intensities in this band doublet is observed also. This inversion in intensity can be explained by the breaking of the hydrogen bonds upon complexation. The higher frequency component is assigned to the CO bonds involved in fewer hydrogen bonds whereas the lower one belongs to CO groups involved in higher number of hydrogen bonds.

The out-of-plane bending, centred on  $904.5\text{ cm}^{-1}$  (NIMO and *pm*), Fig. 3, is shifted to  $907.3\text{ cm}^{-1}$  for *co*, *kn*, and *fd* samples. The out-of-plane deformation of the aromatic ring, centred on  $678.5\text{ cm}^{-1}$ , is not shifted upon complexation but its intensity is decreased showing the restriction in the mobility of the drug molecule in the neighborhood of the host molecule.

One can conclude that the functional groups mainly involved in the inclusion process are the N-H and C=O molecular groups. During the complexation process some water molecules are expelled from the inner part of the CD truncated conus [7], being demonstrated by the intensity decrease in the  $\nu$ (O-H) high frequency profile wing. By comparing the high frequency wings of the O-H stretching massifs for the  $\beta$ -CD, and the *pm*, *co*, *kn* and *fd* systems, one can conclude that more water molecules are expelled during the complexation processes in the case of *fd* system.

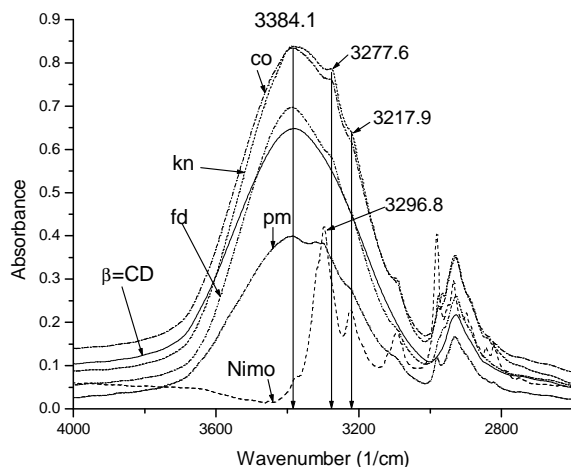


**Fig. 1.** FT IR spectra ( $4000\text{-}2600\text{ cm}^{-1}$ ) of NIMO (dashed line),  $\beta$ -CD (solid line) and their *IC*: dash-dot (*co*), dash-dot-dot (*fd*), short-dash (*kn*), short-dash-dot (*pm*)

#### XRD measurements

Analyzing the XRD diffraction patterns of NIMO,  $\beta$ -CD, their physical mixture (*pm*) and *IC*s obtained by the already mentioned methods (*co*, *fd* and *kn*), see Figs. 4-6, one can conclude that these spectra contain lines at the same diffraction angles but of different intensities, i.e. relative intensity changes are obtained.

Although the literature data indicates that only amorphous state is obtained in the case of *fd IC*, our data show that crystalline phase was obtained also. By comparing different methods of preparation, it looks that the smallest crystallites were obtained by using the *kn* method.

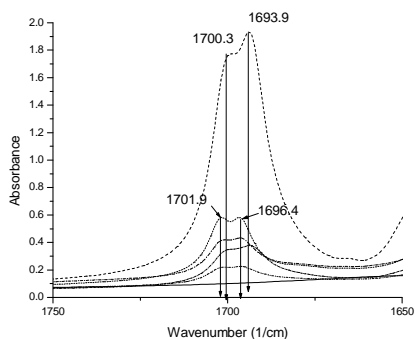


**Fig. 2.** FT IR spectra (1750-1650 cm<sup>-1</sup>) of NIMO (dashed line), β-CD (solid line) and their IC: dash-dot (*co*), dash-dot-dot (*fd*), short-dash (*kn*), short-dash-dot (*pm*)

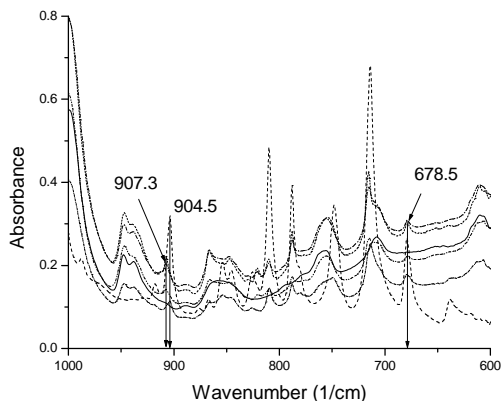


**Fig. 3.** FT IR spectra (1000-600 cm<sup>-1</sup>) of NIMO (dashed line), β-CD (solid line) and their IC: dash-dot (*co*), dash-dot-dot (*fd*), short-dash (*kn*), short-dash-dot (*pm*)

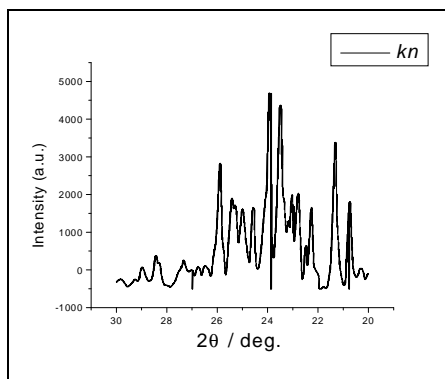
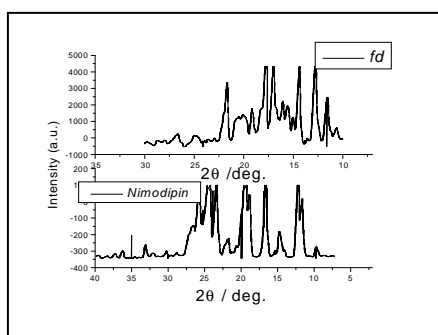
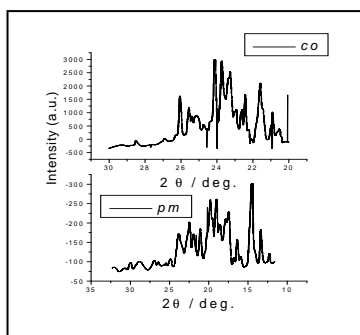


**Fig. 4-6.** X-ray diffraction patterns of the IC obtained by using different preparation methods.

## REFERENCES

- [1] Szejtli, J., *Chem. Rev.*, 98 (1998), 1743-1753.
- [2] Chowdary, K. P. R. Kamalakara, Reddy G., *Indian Drugs* 38(11), (2001), 555-558.
- [3] Gyeresi, A., Tokes, B., Regdon, G., Kata, M., Nagy, G., in Szejtli, J., Szenté, L. (Editors), *Proc. Intern. Symp Cyclodextrins*, 8th, Budapest, Mar. 31-Apr. 2, (1996), 345-348.
- [4] Mielcarek, Jadwiga, *Acta Poloniae Pharmaceutica*, (1995), 52(6), 465-70.
- [5] N.B. Colthup, L.H. Daly, St. E. Wiberley, "Introduction to infrared and Raman spectroscopy, Acad. Press, New York, 1975.
- [6] N.P. Roeges, "A guide to the complete interpretation of infrared spectra of organic structures", Wiley, Chichester, 1984.
- [7] A. Hernanz, J.M. Gavira, I. Bratu, *Vibr. Spectr.* 32(2), (2003), 137-146.

## XPS INVESTIGATION OF BISMUTH GALLATE GLASSES CONTAINING IRON

V. SIMON<sup>1</sup>, LAURA BARZĂ<sup>1</sup>, S.G. CHIUZBĂIAN<sup>2</sup>, M. NEUMANN<sup>2</sup>

<sup>1</sup>*Babes-Bolyai University, 3400 Cluj-Napoca, Romania*

<sup>2</sup>*University of Osnabrück, Physics Department, 49069 Osnabrück, Germany*

**ABSTRACT.** Atomic environment of  $x\text{Fe}_2\text{O}_3 \cdot (80-x)\text{Bi}_2\text{O}_3 \cdot 20\text{Ga}_2\text{O}_3$  glasses ( $0 \leq x \leq 20$  mol %) was investigated with respect to electronic structure of the samples. Data obtained from Bi 4f, Ga 2p, Fe 2p, and O 1s core-level photoelectron spectra indicate changes in the local order on the account of partial substitution of bismuth atoms by iron atoms. The bismuth cations behave essentially as network formers while the iron and gallium ones acts as network modifiers. The number of nonbridging oxygens depends on  $\text{Fe}_2\text{O}_3$  content introduced in samples.

### Introduction

Current interests in functional glasses include gallium based systems, which have useful optical properties. Due to their high optical nonlinearity, high magneto-optic effect and extended IR transparency heavy metal gallate glasses are of technological importance for potential application in optical switching, optical isolators (Faraday rotators) used to avoid self-focusing in high power laser systems, IR windows and sensors [1-3]. Bismuth gallate glasses appear to be promising host materials for waveguide devices in the microwaves telecommunication windows, broad band amplifier and high power laser applications [4-7].

An attractive reason in studying these glasses also consists in the fact that they do not contain any conventional glass formers such as  $\text{SiO}_2$ ,  $\text{B}_2\text{O}_3$ ,  $\text{P}_2\text{O}_5$ ,  $\text{GeO}_2$ , etc. The interesting properties of these glasses are mainly due to the high polarisability and the relatively low field strengths of heavy metal cations as compared to conventional glass formers.

The present study is focused on the atomic environment of an iron-bismuth-gallate glass system investigated by X-ray photoelectron spectroscopy (XPS).

### Experimental

The starting material used to prepare  $x\text{Fe}_2\text{O}_3 \cdot (80-x)\text{Bi}_2\text{O}_3 \cdot 20\text{Ga}_2\text{O}_3$  glass samples with  $x = 0, 5, 10$  and 20 mol % were analytically pure reagents  $\text{Fe}_2\text{O}_3$ ,  $\text{Bi}_2\text{O}_3$  and  $\text{Ga}_2\text{O}_3$ . They were obtained by melting oxide mixtures of desired compositions in sintercorundum crucibles at 1200°C for 30 minutes in an electric furnace in air. The melts were quickly undercooled at room temperature by pouring onto stainless steel support and pressing in form of thin plates. The bismuth-gallate matrix is metallic yellow. By addition of iron to this matrix the glasses become reddish brown. All samples have been analysed by X-ray diffraction and no crystalline phase was evidenced.

XPS measurements were performed using a PHI 5600ci Multi Technique system with monochromatised Al  $K_{\alpha}$  radiation from a 250 W X-ray source ( $h\nu = 1486,6$  eV). During the measurements the pressure in the analysis chamber was in the  $10^{-9}$  Torr range. Low energy electron beam was used to achieve charge neutrality at the sample surface. High resolution core level scans were acquired for the Fe 2p, Bi 4f, Ga 2p and O 1s photoelectron peaks. The position and full width at half maximum of photoelectron peaks were estimated using spectra simulation based on summation of lorentzian and gaussian functions.

### Results and discussion

In the attempt to identify the local environment of the different elements in heavy metal glasses several techniques are employed. The X-ray photoelectron spectroscopy (XPS) is used to obtain information on binding energy of the glass component elements from their photoelectron

peaks [8]. XPS survey spectra recorded from the fractured surface of investigated  $\text{Fe}_2\text{O}_3\text{-Bi}_2\text{O}_3\text{-Ga}_2\text{O}_3$  glasses permit to determine the elemental chemical composition of samples (Table 1).

**Table 1.**  
**Atomic percentage of the elements experimentally obtained from XPS analysis on the surface of the fractured samples (exper. on surf.) along with the nominal values expected for the bulk samples (nominal in bulk).**

x mol %	Fe (signal 2p)		Bi (signal 4f)		Ga (signal 2p)		O (signal 1s)	
	nominal in bulk	exper. on surf	nominal in bulk	exper. on surf	nominal in bulk	exper. on surf	nominal in bulk	exper. on surf
	at %							
0	0	0	32	36.73	8	1.98	60	61.29
5	2	0	30	30.62	8	4.59	60	64.79
10	4	1.43	28	29.90	8	4.33	60	64.34
20	8	4.16	24	25.30	8	4.16	60	66.38

One observes that the values obtained for iron and gallium are much lower compared to the nominal concentrations that could suggest a migration of these atoms from the surface into the inner of the samples. On the other hand this result points out the modifier behaviour for these cations, in contrast with the conclusion drawn by Man et al. [4] from Raman spectroscopy data. They consider both  $\text{Bi}^{3+}$  and  $\text{Ga}^{3+}$  cations as glass network formers.

The high resolution Fe 2p, Bi 4f and Ga 2p core level XPS experimental spectra are well fitted by the curves obtained from summation of Fe  $2p_{1/2}$  with Fe  $2p_{3/2}$ , Bi  $4f_{5/2}$  with Bi  $4f_{7/2}$ , respectively of Ga  $2p_{1/2}$  with Ga  $2p_{3/2}$  lines.

The positions of photoelectron peaks in Bi 4f high resolution spectra are shifted to some higher energies relative to pure Bi 4  $f_{7/2}$  (157 eV) and Bi 4  $f_{5/2}$  (162.31 eV) but the spin orbit splitting is very close to 5.3 eV. The binding energies are close to the values reported for other bismuth oxide compounds [9-11]. The full width at half maximum (FWHM) of photoelectron peaks increases with the iron content. The decrease of FWHM is believed to be a reduction in the site distribution or disorder of the glass [8]. In this case the composition dependence of FWHM in our samples indicates an increase of the disorder degree with the iron content.

The network of multicomponent bismuth - transition metal glasses is built up of both  $[\text{BiO}_6]$  octahedral and  $[\text{BiO}_3]$  tetrahedral units [12]. Similar to the glasses with conventional glass network formers in bismuth gallate glasses the structural units are connected by means of bridging oxygens. The O 1s spectra from all samples are presented in Figure 1. The peaks are not symmetric and denote the presence of bridging (BO) and non-bridging (NBO) oxygen atoms. The BO photoelectron peak occurs at higher binding energy and NBO photoelectron peak at lower binding energy.

The fraction of NBO relative to the total number of oxygens  $O_t$  was estimated from the areas corresponding to O 1s photoelectron peaks. One observed a decrease of the fraction  $\text{NBO}/O_t$  from 0.74 in  $80\text{Bi}_2\text{O}_3\text{-}20\text{Ga}_2\text{O}_3$  bismuth-gallate matrix to 0.29 by addition of a low  $\text{Fe}_2\text{O}_3$  content (5 mol %) and then  $\text{NBO}/O_t$  increases again by further addition of iron.

According to the recent approach of Dimitrov and Komatsu [13] the oxides could be simply classified based on the correlation between electronic polarisabilities of the entering ions and their binding energies determined by XPS. It was established that O 1s binding energy of different oxides varies in 528.0- to 533.5-eV range and its value corresponds to different degree of ionicity in the M-O bonds. The O 1s binding energy for the oxide glass samples  $\text{Fe}_2\text{O}_3\text{-Bi}_2\text{O}_3\text{-Ga}_2\text{O}_3$  ranges between 529.57 and 532.97 eV range and according to Dimitrov model they are semicovalent compounds with a ionic component.

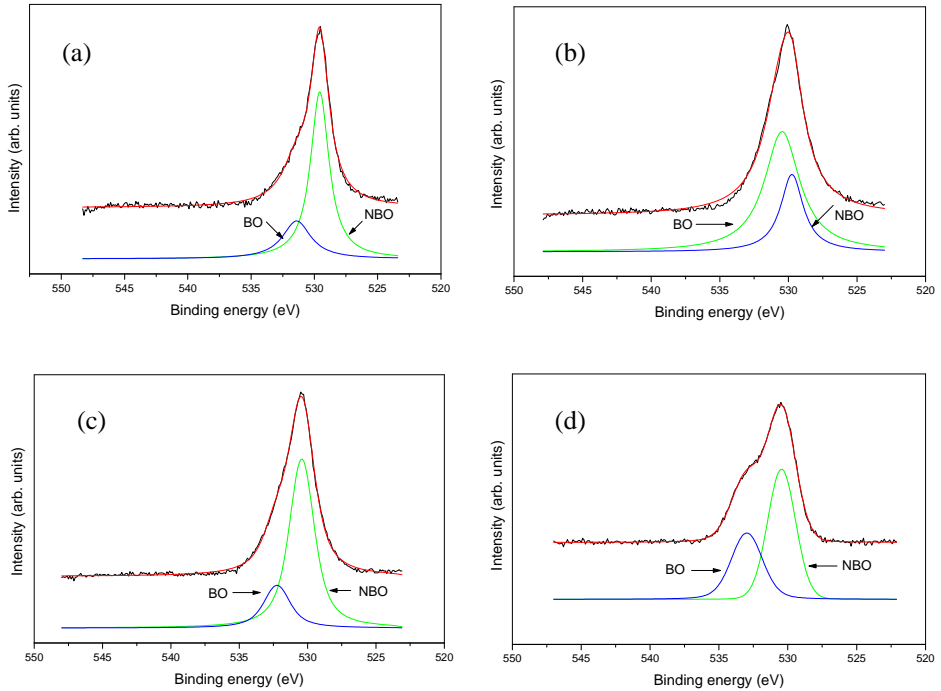


**Fig. 1.** O 1s core level photoelectron spectra of  $x\text{Fe}_2\text{O}_3 \cdot (80-x)\text{Bi}_2\text{O}_3 \cdot 20\text{Ga}_2\text{O}_3$  glasses (a)  $x = 0$ , (b)  $x = 5$ , (c)  $x = 10$  and (d)  $x = 20$ .

The polarisability of the samples is related to the bismuth ions and decreases with the substitution degree of bismuth by the iron atoms.

### Conclusion

XPS investigation of heavy metal  $x\text{Fe}_2\text{O}_3 \cdot (80-x)\text{Bi}_2\text{O}_3 \cdot 20\text{Ga}_2\text{O}_3$  glasses shows that the binding energy and full-width at half-maximum in core level spectra are modified by introducing iron, that denotes changes in the atomic environments and an increase of the disorder degree. In the investigated glass system  $\text{Bi}^{3+}$  cations are formers while  $\text{Ga}^{3+}$  and  $\text{Fe}^{3+}$  are modifiers of the glass network. By addition of a low iron content to  $\text{Bi}_2\text{O}_3\text{-Ga}_2\text{O}_3$  host glass the number of nonbridging oxygens is diminished and it increases again by further addition of iron. According to the polarisability model these glasses are semicovalent compounds, partially ionic.

### REFERENCES

1. A. C. Hannon, J M Parker, B Vessal, *J Non-Crystalline Solids*, 232-234, 51 (1998)
2. A. C Hannon, J M Parker, B Vessal, *J Non-Cryst Solids*, 196, 187 (1996)
3. M. J. Weber, *Journal of Applied Physics*, 63, 8, 3118 (1988)
4. S. Q. Man, E.Y.B. Pun, P.S. Chung, *J. Opt. Soc. Am. B*, 17, 1, 23 (2000)
5. S. Q. Man, S.F. Wong, E.Y.B. Pun, *J. Opt. Soc. Am. B*, 19, 8, 1839 (2002)



XPS INVESTIGATION OF BISMUTH GALLATE GLASSES CONTAINING IRON

6. T. Murata, M. Torisaka, H. Takebe, K. Morinaga, *J. Am. Ceram. Soc.*, 81, 8, 2135 (1998)
7. S. Q. Man, E. Y. B. Pun, P. S. Chung, *Appl. Phys. Lett.*, 77, 4, 483 (2000)
8. I. A. Gee, D. Holland, C. F. McCoville, *Phys. Chem. Glasses*, 42, 6, 339 (2001)
9. V. Simon, H. Bako-Szilagy, M. Neumann, S. Chiuzbaian, S. Simon, *Mod. Phys. Lett. B*, 17, 7, 291 (2003)
10. W. E. Morgan, W. J. Stec, J. R. van Wazer, *Inorg. Chem.*, 12, 4, 953 (1973)
11. V. I. Nefedov, D. Gati, B. F. Dzhurinskii, N. P. Sergushin, Ya. V. Salyn, *Russ. J. Inorg. Chem.*, 20, 2307 (1975)
12. H. Zheng, R. Xu, J. D. Mackenzie, *J. Mater. Res.*, 4, 911 (1989)
13. V. Dimitrov, T. Komatsu, *J. Solid State Chem.*, 163, 100 (2002).

***BIOPHYSICS AND ENVIRONMENTAL PHYSICS*****THE INFORMATION CONTENT OF DNA AND THE ORIGIN OF LIFE****V. V. MORARIU**

*National Institute for Research and Development of Isotopic and Molecular Technologies, P.O.Box 700, 400293 Cluj-Napoca 5, Romania, e-mail: vvm@L40.itim-cj.ro*

The first form of terrestrial life is estimated to be 3.5-3.85 billion years old. The younger age evidence for life was fossilized microbes from a rock formation in Australia while the older one, from the carbon isotopes in a ratio characteristic of living organisms in rocks from an island off the coast of Greenland.

Evolution led to new species, which, in time, gradually increased in complexity. This is quantified in the increasing molecular weight of the species DNA. Delsemme converted the molecular weight in quantity of information and constructed an information vs. time linear plot to be referred as Delsemme plot. This illustrates how the information content of the DNA increased in time for the main classes of species. I have reconstructed Delsemme's plot and represented it on a double logarithmic diagram (fig.1).

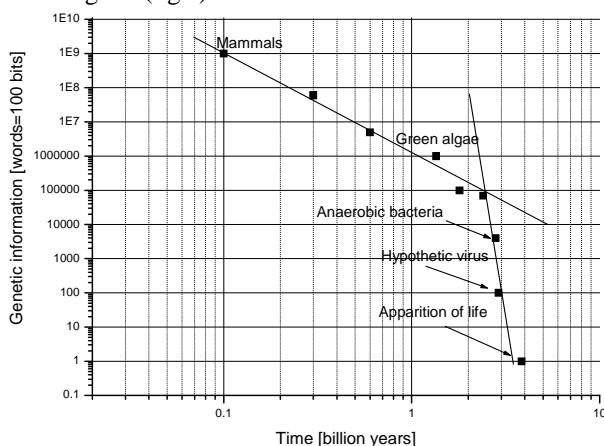


**Fig. 1.** Reconstructed Delsemme's plot. It illustrates the increase of DNA information during evolution. Some of the species are mentioned on the plot. Time is expressed in years by present.

Some contradictions or unclear aspects can be noted in Delsemme's plot. The hypothetic virus or the protobion, according to Delsemme, represents an emergent form of life before the first bacteria. Although it is specifically mentioned as being a hypothetic primitive form of life, something alike to a virus, the reason for including it on the plot is not clear. Also it is not at all clear why its age is set at 3 billion years by present (b.p.). Further the apparition of life is mentioned on the same plot at 3.8 billion B.P. and it corresponds to information of one word (100 bits). This would have been an even simpler form of virus than the hypothetic virus or protobion. Again this aspect is not discussed in the original paper. However it contradicts the finding of fossilized microbes as a simple form of virus could not leave such fossilized traces. Also it is doubtful that the original form of life could have existed with such a low amount of information.

The younger species can be connected with a straight line in Delsemme's plot while the older ages clearly show that evolution of life must have proceeded with a much greater speed, as shown by the straight line with the higher slope (fig.1). In fact there is a gap between the apparition of life and the anaerobic bacteria where the actual forms of life remain unknown.

Another problem is to whether a break exists between the prebiotic evolution and post biotic evolution as far as the DNA information content is concerned. We may reasonably suppose that the first form of life must have evolved on a background of existing molecules and structures and they did not differ too much (the protocell and the environment respectively). In other words the information content of nucleic acids during prebiotic and the first forms of life must have been within a close range. Again, the information during the prebiotic evolution of nucleic acids was not considered in the original Delsemme's paper.

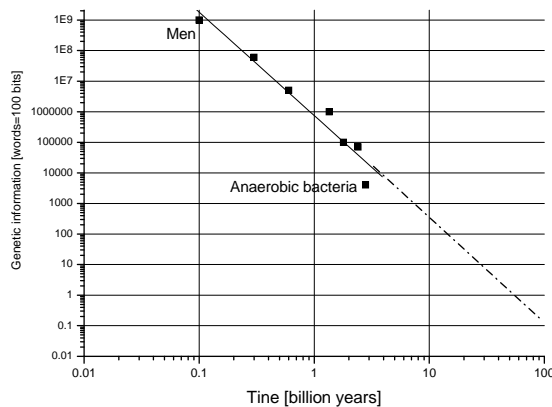
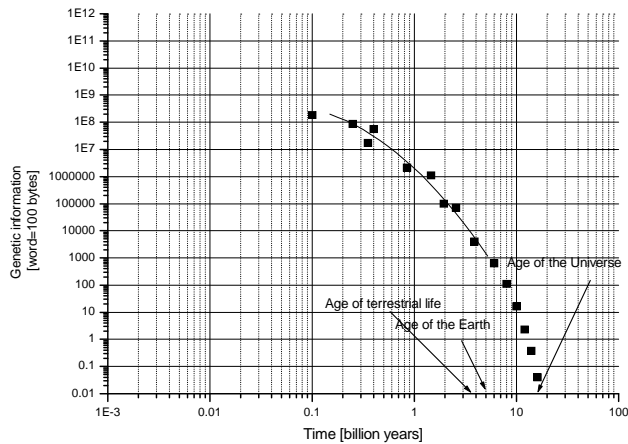


Fig. 2. Linear extrapolation of Delsemme's double logarithmic plot.

A simple linear extrapolation of Delsemme's double logarithmic plot to older ages goes to nowhere. Although we do not know the information content of the DNA in the first form of life on Earth and what was its prebiotic evolution we must turn to the lowest possible information of the earliest molecules. The first significant information was one bit. We can see on the plot (fig.2) that the linear extrapolation goes behind 100 billions of years when reaching one bit of information. This is meaningless when the age of the Earth is around 5 billion of years and the age of the Universe is established within the range of  $12.5 \pm 3$  and  $15.6 \pm 4.6$  billion years (2). The conclusion is that the evolution of DNA must have not been linear (on the double log plot). In mathematical terms such a hypothetic linear plot is equivalent to a fractal rule. However Nature is full of multifractal structures, or in other words, of a nonlinear plot. This is why we performed a polynomial fitting of the data available from Delsemme's plot. There is no much difference between the linear fitting and the polynomial fitting within the limited range of the known evolution period. However it makes a significant difference when further extrapolating the polynomial curve to older ages.

This is illustrated in fig.3. We can notice that the minimum information of 1 bit is attained at about the time of Big Bang. This does not mean that the origin of information starts exactly at the time of Big Bang. Perhaps it starts at a later date but the precision of the extrapolation at such an old age cannot tell more than that. The consequences of these findings are:

First, it shows that it is plausible to think of the evolution of the terrestrial life as an integral part of the evolution in the Universe.



**Fig. 3.** Polynomial fitting of the available evolution data (continuous curve) and extrapolation (isolated data) of Delsemme's plot. Very low information could have characterized the early stages of the molecular evolution before the smallest DNA molecule appeared. It shows that an information content of 1 bit occurs at about the time of the Big Bang.

Second, it links the prebiotic evolution (low information content) to the post-biotic stages as a continuous process. In other words, in terms of the information content, the apparition of life does not represent a sort of a "Big Bang", at least according to the precision of this estimation. One could possibly argue that the first form of life was RNA and not DNA based (3). However this does not exclude the parallel evolution of DNA.

Third, it tells that the life is of extraterrestrial origin. This implies that life must have been seeded on Earth and this is in agreement with various ideas of panspermia (4).

Fourth, it suggests that at present the evolution of DNA is almost slowed down to an end, and therefore little changes are expected in the future. However we know that even very small differences of DNA make a significant difference in the species such as between a monkey and a human being.

Fifth, it predicts that any other forms of extraterrestrial life must follow a similar course. This does not mean that similar species might exist outside Earth. All what can be said is they could have similar DNA information content regardless of the place in the Universe.

Finally it should be mentioned that the present analysis and conclusions are to be regarded with great caution while they can be the basis for further discussions on the subject. Nevertheless they represent a coherent picture in agreement with other findings and ideas mentioned in the literature (5-6).

## REFERENCES

1. A. H. D e l s e m m e, *Les cometes et l'origine de la vie*, 5<sup>e</sup> Reunion Regionale Europeenne d'Astronomie, Liege, 28 juillet-1<sup>er</sup> aout, 1980, publiee dans "Variability in Stars and Galaxies" *Age of the Universe*, <http://www.astro.ucla.edu/~wright/age.html>
2. J. F. Joyce, *The antiquity of RNA-based evolution*, Nature, 2002 (No.6894) 214- 221. *Cosmic Ancestry*, <http://www.panspermia.org>
3. P. R e a n e y, *Scientists Claim Evidence of Life in Outer Space*, Science Reuters, 2001 July 31.
4. N. R. P a c e, *The universal nature of biochemistry*, Proc. Natl. Acad. Sci. USA, Vol. 98, Issue 3, 805-808, January 30, 2001

## THEORETICAL SIMULATION OF THE RAMAN SPECTRA OF DNA BASES

**C. I. MORARI, C. M. MUNTEAN**

*National Institute for Research and Development of Isotopic and Molecular  
Technologies, 400293 Cluj-Napoca, P.O. 5, Box 700, Romania*

**ABSTRACT.** Our present study reports the Raman spectra of each DNA bases (adenine, cytosine, thymine and guanine). The simulations were performed at ab initio level using the DZ gaussian basis set. The steps of the simulations were the following: (i) optimisation of the geometry for each DNA base; (ii) computing the hessian matrix and the IR spectra for each DNA base; (iii) computing the Raman intensities by using the ab initio polarisabilities. All the calculations were performed using the GAMESS package. Each simulation is reported separately for adenine, cytosine, thymine and guanine. As a first approach for the Raman spectrum of the whole DNA molecule we use the overlap of these four spectra.

### Introduction

DNA is a very important biological molecule since it carries the genetic code. The famous double helix structure has emphasized the relationship between structure and function. In the specific case of DNA, understanding the processes by which specific binding sites are recognized by drugs, mutagens, proteins and other molecules would represent a fundamental step towards understanding its biological activity.

Raman spectroscopy was presented as an alternative structural approach for the study of nucleic acids and their complexes, particularly for investigating the aqueous solution structures and the interactions of large oligonucleotides, native nucleic acids and their biological assemblies, like chromosomes and viruses. The high information content of Raman spectra is reflected in the many new insights that have been obtained into the conformation, composition, interaction and functioning of DNA molecules.

As a first approach of comparing the experimental results of DNA molecule with theoretical calculations, our present study reports the Raman spectra of each separate DNA base (adenine, cytosine, thymine and guanine) and the overlap of these four spectra.

### Computational methods

In order to compute the normal modes of a polyatomic molecule, we have to build the Hessian matrix  $F^{ij}$  [1]. The eigenvalues for the vibrational modes are the results of the following system

$$\sum_j (F^{ij} - \delta^{ij} \lambda_k) l_{jk} = 0 \quad (1)$$

which can be solved by asking to its determinant to vanish.

$$\det(F^{ij} - \delta^{ij} \lambda_k) = 0 \quad (2)$$

The final vibrational frequencies are

$$\nu_k = \lambda_k^{1/2} / 2\pi \quad (3)$$

where  $\lambda_k$  are the frequencies resulting from the Eq. (1).

All the calculation presented below are performed using the GAMESS implementation of this scheme [2].

The structure for all DNA components were optimized using the DZ basis set [3]. The resulting geometries are depicted in Figures 1 and 2.

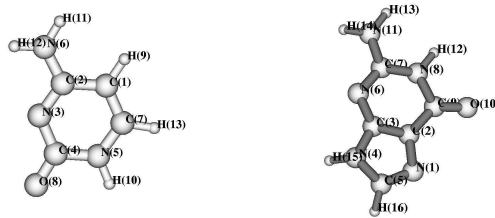


**Fig. 1.** The structures of cytosine (C) and guanine (G).}

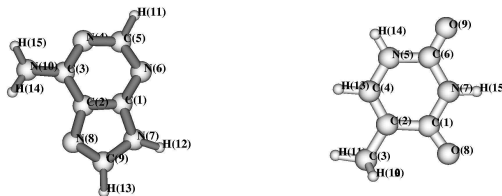


**Fig. 2.** The structures of adenine (A) and thymine (T)

## RESULTS

The vibrational analysis was performed by computing the Hessian matrix and the force constants for all normal modes of each DNA base. The computed frequencies were scaled with a factor of 0.89 in order to remove the effect of the harmonic oscillator approach upon the computed frequencies [4]. The resulting spectra are given in Figures 3 and 4. The Figure 5 is the overlap for all 4 spectra computed independently.

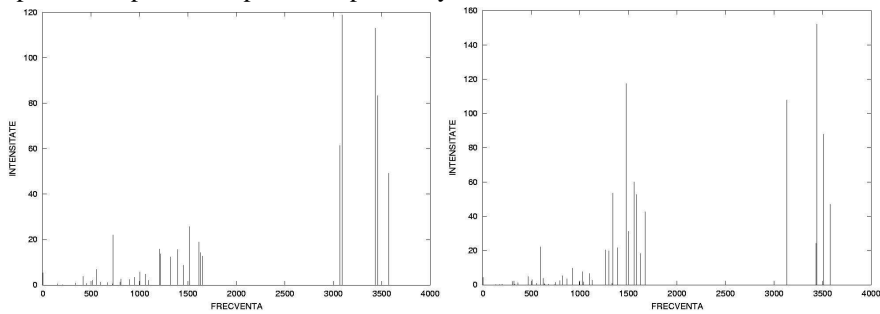


**Fig. 3.** The Raman spectra of cytosine (left) and guanine (right)

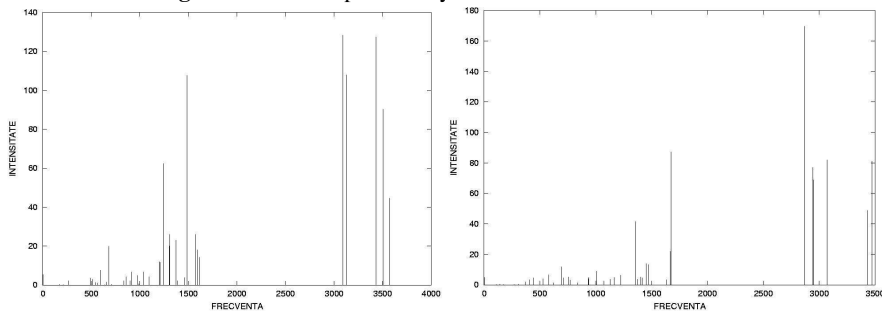


**Fig. 4.** The Raman spectra of adenine (left) and thymine (right)}

## THEORETICAL SIMULATION OF THE RAMAN SPECTRA OF DNA BASES

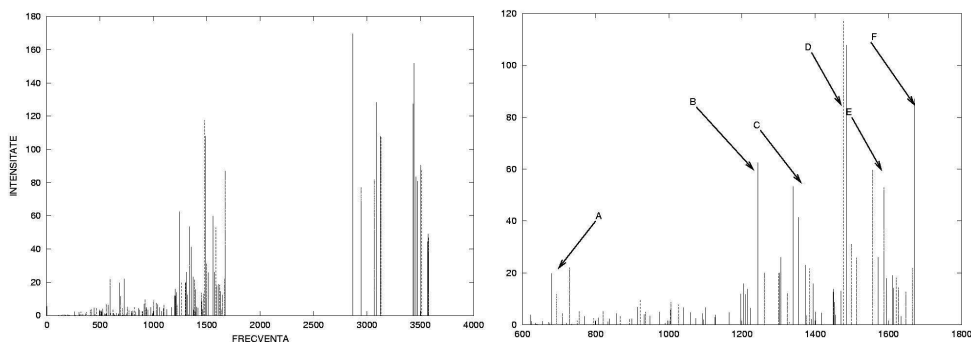


**Fig. 5.** Overlap of the spectra given in the Figures 3 and 4. Left: the complete calculation. Right: details for the region  $600\text{ cm}^{-1}$  -  $1800\text{ cm}^{-1}$ .

The significant breathing modes are  $681\text{ cm}^{-1}$  (G)  $727\text{ cm}^{-1}$  (A),  $749\text{ cm}^{-1}$  (T) and  $784\text{ cm}^{-1}$  (C) [5]. These values are reproduced by our calculations (see Figures 3 and 4). The bands at  $1376\text{ cm}^{-1}$  (T,A, G, marker "C" in Figure 5),  $1489\text{ cm}^{-1}$  (G, A, "D" in Figure 5),  $1578\text{ cm}^{-1}$  (G, A, "E" in Figure 5) shows a good correlation with the experimental results. The band located near  $1668\text{ cm}^{-1}$  which was assigned to coupled C=O stretching and N-H deformation modes of T, G and C do exists in the theoretical spectra of thymine (marker "F").

Significant differences between the theoretical and experimental spectra occur for the intensities of the Raman bands (markers "B", "C", and "D", Figure 5.) A possible explanation for these changes are the changes in the polarizability of the whole DNA molecule compared to the polarizabilities of its components.

### Conclusion

An ab initio simulation of the Raman spectra for the DNA bases was performed. The results confirm the previously experimental assignments. Significant difference of the Raman intensity for the simulated and experimental spectra exist. This is a clear indication of the influence of the interactions between base pairs and of the solvent effects upon the computed Raman intensities.

### REFERENCES

1. I. N. Levine, "Quantum Chemistry", Prentice Hall, 2000.
2. M. W. Schmidt, K. K. Baldrige, J. A. Boatz, S. T. Elbert, M. S. Gordon, J. H. Jensen, S. Koseki, N. Matsunaga, K. A. Nguyen, S. J. Su, T. L. Windus, M. Dupuis, J. A. Montgomery, *J. Comput. Chem.* **14**, 1347-1363 (1993).
3. T. H. Dunning, Jr., P. J. Hay in "Methods of Electronic Structure Theory", H. F. Haefer III, Ed. Plenum Press, N.Y. 1977.
4. A. P. Scott, L. Radom, *J. Phys. Chem.* **100**, 16502-16513 (1996).
5. C. M. Muntean, "Teza de doctorat", Cluj, 2002.

## FOOD ADDITIVES STUDY: VIBRATIONAL APPROACH

**S. CÎNȚĂ PINZARU<sup>1</sup>, N. PEICA<sup>2</sup>, I. PAVEL<sup>2</sup>, W. KIEFER<sup>2</sup>**

<sup>1</sup> Babes-Bolyai University, Physics Faculty, Kogalniceanu 1, RO 3400 Cluj-Napoca, Romania

<sup>2</sup> Institut für Physikalische-Chemie, Am Hubland, DE 97074 Würzburg, Germany

**ABSTRACT.** E 102 food additive is characterised by means of FT-IR, FT-Raman and SERS spectroscopy in order to check the detection limit, process control and monitoring the dye content in food. The dye presence was detectable under nanomolar level using SERS on silver colloid.

### Introduction

Recent studies [1,2] showed that food additives are responsible for a large number of health affections like allergic reactions, migraine, blurred vision, etc. Asthmatics and aspirin intolerant sufferers appear to be particularly at risk. Tests have shown that in large doses, such compounds will raise the plasma histamine levels of healthy adults. Determination of tolerance level (maximum level of additive allowed in food) requires sensitivity, selectivity and fast experimental protocol involved in the process control. Such requirements are provided by the resonance Raman (RR) or surface enhanced Raman scattering (SERS) techniques. In order to detect, control and monitor the food additives, FT-IR, FT-Raman, RR, and SERS spectroscopy were employed here. For example, E 102 additive (Fig. 1) is characterised in order to get insight into its vibrational behaviours in different environments. E 102 often give rise to a phenomenon named “metachromasia”, in the presence of anions and other macromolecule.

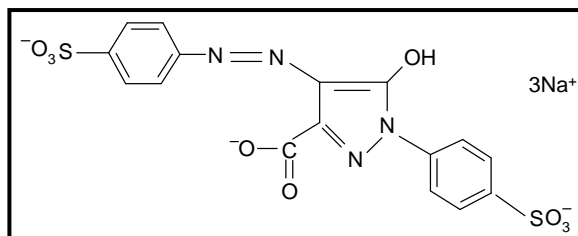


**Fig. 1.** The molecular structure of the E 102.

This is a characteristic colour change when certain tissue elements are stained by cationic dye. Therefore, the first step in the characterisation of this molecule would require its free state, than its aqueous solutions at different pH values or adsorbed onto a surface and finally, in conjunction with other cationic dyes up to the tissue level. The preliminary study is presented in this paper. E-102 in Europe or FD&C Yellow Number 5, the molecule consists essentially of trisodium 5-hydroxy-1-(4-sulfonatophenyl) (4-sulfonatophenylazo)-H-pyrazole-3-carboxylate and subsidiary colour matters together with sodium chloride and/or sodium sulphate as the principal uncoloured components. E 102 is described as the sodium salt. The calcium and the potassium are also permitted.

### Experimental

FT-IR and FT-Raman spectra of E 102 solid powder were recorded using an Equinox 55 FT-IR Bruker spectrometer with an integrated FT-Raman FRA 106 S module. SERS spectra of E 102 on silver colloid [3] were obtained on a Labram integrated Raman system. An Ar<sup>+</sup> laser



(514.5 nm) coupled by optic fiber to the 50x NA 0.7 objective of the microscope was used. Peltier cooled CCD detection was performed. For the SERS samples, E 102 solutions in distilled water and sodium citrate-reduced Ag colloid were freshly prepared. On the freshly prepared Ag colloid 0.3 ml  $10^{-1} \text{ mol l}^{-1}$  NaCl solution was added in order to adjust the aggregation status and hence the optimal enhancement of the Raman signal. All reagents used were of analytical purity.

### Results and Discussions

An interesting behaviour in the electronic absorption was observed since the bands of E 102 and the silver colloid presents the same position (Fig. 2). Moreover, adding the E 102 solution to the colloid, the plasmon resonance remains unchanged. This fact reflects that the modification in the aggregation status of silver particles with the adsorbed molecules is unchanged.

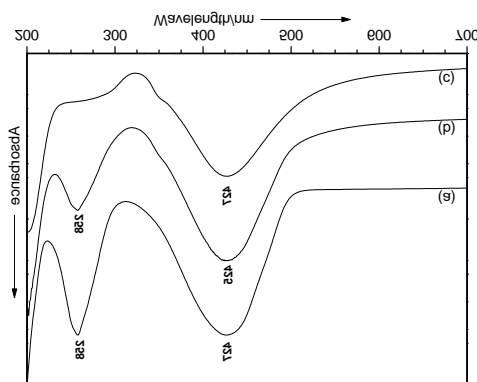


**Fig. 2.** Comparative UV-VIS spectra of E102  $10^{-1} \text{ mol l}^{-1}$  aqueous solution (a), E102 with Lee Meisel (b), and Lee- Meisel Ag sol (c).

The vibrational spectra of E 102 are presented in Fig. 3. The most prominent FT-IR bands were observed at 692, 1007, 1035 (fingerprint), 1124, 1154, 1179, 1475, 3422  $\text{cm}^{-1}$ , besides the medium intensity bands at 714, 836, 1346, 1413, 1555, 1562, 1598, 1642, 1725  $\text{cm}^{-1}$ . The FT-Raman spectrum reveals a sharp marker band at 1601  $\text{cm}^{-1}$  (*para*-substituted benzene stretching), several intense bands at 1136, 1365 and 1503  $\text{cm}^{-1}$  assigned as  $\text{SO}_3$  asym. stretch and  $\text{N}=\text{N}$  stretch for *trans*- and *cis*- form respectively. Bands with medium intensity at 622, 633, 1051, 1095, 1181, 1219, 1419, 1691  $\text{cm}^{-1}$  were also observed.

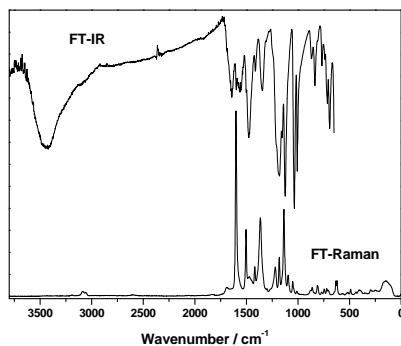


**Fig. 3.** FT-IR (micro-ATR) and FT-Raman spectra of E 102, solid powder.

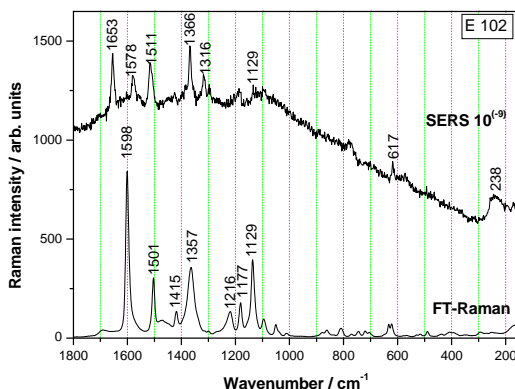


**Fig. 4.** SERS spectrum of E 102 on Ag colloid at picomolar concentration in comparison with its corresponding FT-Raman spectrum.

As a monoazo compound, E 102 reveals the characteristic azochromophore group  $-N=N-$  subject to azo hydrazone form in appropriate solutions [4, 5]. The vibrational behaviour of the aqueous solution will be discussed into a next paper.

SERS spectrum of the title compound obtained at usual concentration of about  $10^{-5}$ - $10^{-6}$  mol/l presents roughly the same band positions and intensities as the corresponding Raman spectrum of aqueous solution (not given here), reflecting a most probably physisorption on the nanoparticles.

Fig. 4 presents the SERS spectrum of E 102 on Ag colloid at picomolar concentration. As we can see in comparison with the FT-Raman spectrum, large differences are present either in band positions or relative intensities. The adsorbed species presents intense SERS bands at 1366, 1511 and 1653  $\text{cm}^{-1}$ , bands involved into the adsorption process through the azo and C=O functional groups.

### Conclusions

FT-IR and FT-Raman spectra of E 102 were recorded and used as data bank for further applications in trace analysis of food.

With a conventional SERS setup E 102 was found to be detectable under nanomolar level ( $10^{-10}$  mol  $\text{l}^{-1}$ ). A strong chemical interaction of E 102 with the colloidal particles was concluded mainly at very low concentrations.

The surface selection rules along with our theoretical results are subject to explain the adsorbate structures on the metal surface at different concentrations and pH values. SERS and SERRS may be promising techniques for detecting and monitoring the presence of such additives in food.

### REFERENCES

1. M. Bhatia, *J. Clinical Psychiatry*, 61 (7) (2000), 473-476.
2. M. Worm, W. Vieth, I. Ehlers, W. Sterry, T. Zuberbier, *Clinical Exp. Allergy* 31 (2), 2001, 265-273.
3. P. C. Lee and D. Meisel; *J. Phys. Chem.*; 86, 1982, 3391-3395.
4. P. Sett, N. Paul, S. K. Brahms and S. Chattopadhyay, *J. Raman Spectrosc.*, 30, 1999, 611-618.
5. G. McAnally, C. McLaughlin, R. Brown, D. C. Robson, K. Faulds, D. R. Takley, W. E. Smith and D. Graham, *Analyst*, 127, 2002, 834-841.

## THE IMPORTANCE OF THE SKIN GALVANIC RESPONSE ON CERTAIN POINTS

**NICOLAE-MARIUS BÂRLEA, ADINA MAN**

*Technical University of Cluj-Napoca, Physics Department, Str. C. Daicoviciu  
15, ROMANIA, E-mail: mbirlea@phys.utcluj.ro*

**ABSTRACT.** A safe and inexpensive body diagnosis can be done by skin level electric measurements. An instrument that can do this reliably and effectively is the ElectroDermal Screening Device (EDSD) that is basically an ohmmeter. The low voltage emitted by this device causes a response at the acupuncture point, which reflects the condition of the associated system. Thus, it could be used in diagnosis and monitoring of a patient's health status. In this paper we describe our experimental device and the measurements we did on a few healthy and sick persons, mainly on the distal points (points situated near the nails of the fingers or toes). We compared the acupuncture point measurements of healthy persons to those of persons who had conventionally diagnosed diseases. Apparently very simple this method requires adequate research for solving the technical problems and more important, the basic functioning mechanism.

### INTRODUCTION

The body diagnosis can be done by skin level electric measurements with an instrument that is basically an ohmmeter, the ElectroDermal Screening Device (EDSD).

Electrodermal screening (EDS) has been developed in Germany [1] by Dr. Reinhold Voll, 50 years ago, and is now estimated to be used by more than 100,000 medical doctors and healthcare practitioners around the world. Voll was an early investigator who applied low voltage currents to acupuncture points in humans. Voll's original goal was therapeutic electroacupuncture but he noted that the low voltage emitted by his device caused a response at the acupuncture point, which reflected the condition of the associated system. Thus, it could be used in diagnosis and monitoring of a patient's health status, becoming known as electroacupuncture according to Voll (EAV). This was the revolutionary aspect of EAV, which has led to development of EDST (ElectroDermal Screening Test).

Dr. Voll compared the acupuncture point measurements of healthy patients to those of patients who had conventionally diagnosed diseases. He found that the electrical conductivity of healthy acupuncture points measured within a given normal range, while readings outside of this range revealed disturbances in the tissues and organs traditionally associated with these points.

### THE DEVICE AND THE MEASUREMENT PROCEDURE

EDSD's basic design and functional use imply that the instrument delivers 10-12  $\mu\text{A}$  of direct current at a maximum voltage of 1-1.25 V. Since the ionization potential of hydrogen atoms is 1.36 volts, this is perfectly safe [2]. The device's meter is calibrated to read from 0 to 100 so that the standard skin resistance of 100 k $\Omega$  reads 50. Zero represents infinite resistance and 100 indicates zero resistance at this electrical potential.

The *testing probe* is an insulated body with a tip of brass or silver connected to the positive side of the circuit. This, held by the operator, is pressed firmly on the patient's skin at the measurement point. A brass hand electrode is held by the patient and connected to the negative side of the circuit. (Figure 1)

Point location must be accurate (Figure 2), and the probe must be applied at the correct angle. Appropriate pressure must be applied (create a temporary dimple) during measurement

which may take as long as 60 seconds. It may be slightly uncomfortable but should not be painful. Moistening the probe tip and the hand electrode ensures good electrical contact. Repeated measurements, the time taken for each and the time between them affects readings.

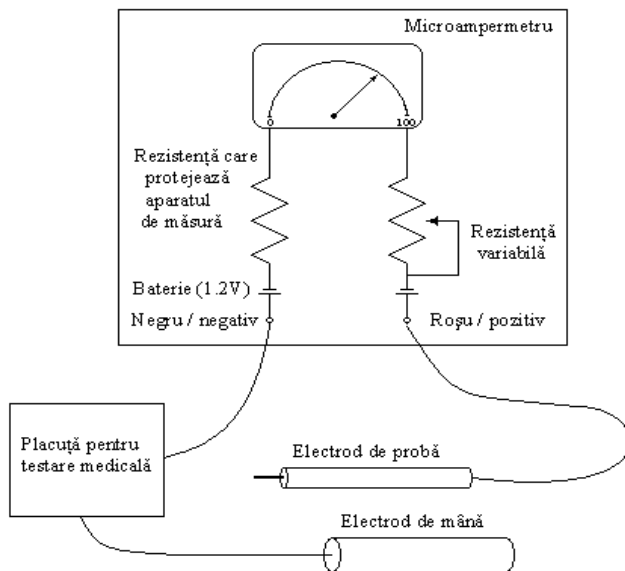


Fig. 1. The basic design of the Electrodermal Screening Device (EDSD).

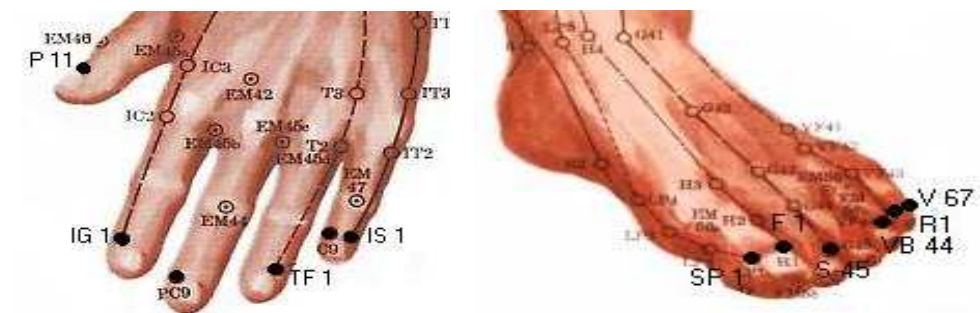


Fig. 2. Jing Points (distal) placement on fingers and toes.

We do the measurements on the Jing distal points because they are located near the nails' angle of the fingers and toes.

### THE EXPERIMENTAL MEASUREMENTS

Table 1 presents the measurements made on Jing points of a healthy person (23 years female, April 2003) with Ni testing electrode and reference electrode on the tongue (the most stable readings) at different day moments. On notice diurnal variation of point electrical resistance.

Table 2 presents the measurements made on Jing point Spleen-Pancreas SP1 of 10 different subjects of various ages, the subject number 4 being diabetic.

Table 1.

Daytime variations of the electrical current through distal points of a healthy subject.

Hour	P11	IG1	VS9	TF1	C9	IS1	SP1	F1	S45	VB44	R1	V67
10	52	44	54	44	58	52	56	54	58	52	44	46
11	44	48	60	40	46	46	68	58	52	54	52	50
12	48	48	48	46	44	50	52	48	50	40	46	48
13	54	48	44	46	48	44	60	54	54	58	48	48
14	52	46	50	50	46	46	58	60	48	54	42	52
15	56	52	58	58	58	58	58	58	54	56	52	52
16	52	58	52	48	52	44	62	60	44	48	42	54
17	52	52	50	54	46	48	62	58	48	64	48	56
18	52	52	50	52	44	48	58	52	46	48	56	52
19	52	52	60	48	60	44	68	68	44	56	46	52

Table 2.

The electrical current through SP1 point for 10 subjects (subject 4 with diabetes mellitus)

Subject	1	2	3	4	5	6	7	8	9	10
SP1 value	42	48	56	28	46	54	52	58	62	56

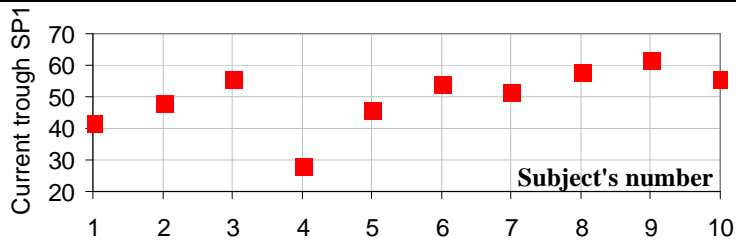


Fig. 3. The electrical current through SP1 point (Spleen-Pancreas) for 10 subjects (subject 4 with diabetes).

The measurements made on the distal point P11 (Lung) of a young subject (male) after an medical intervention on lung, clearly show growing values with time passed after the medical intervention (table 3).

Table 3.

Electric current through point P11 for a human subject after a medical intervention on lung.

Days after intervention	1	2	3	4	5	6
Electric current value on P11	30	38	40	40	46	48

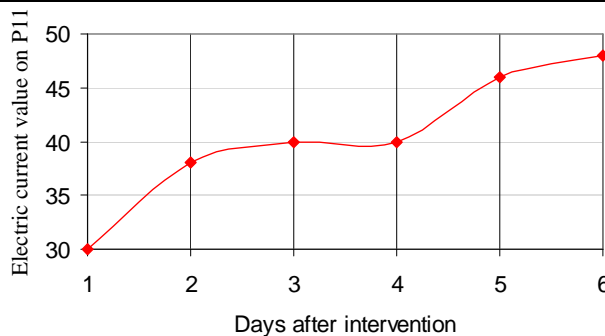


Fig. 4. Electric current time evolution on point P11 after a medical intervention on lung.

## CONCLUSION

The measurements made with our device show that the body diagnosis can be done by the electric measurements at the skin level. It could be used in diagnosis and monitoring of a patient's health status. The most important goal of the method is to detect the imbalances early, before a lesion to occur on an organ. Anything that alters system function or structure changes the energy flow through the body "wiring" and the EDSM measures the resistance and polarization at the affected acupuncture points. It thus provides a picture of the balance of related systems that are interconnected through the "wiring". Robert O. Becker has proved the existence of a direct current system in the human body [3] that modulates the nerve reactivity and the healing mechanisms. This system may explain the acupuncture points activity [4, 5] and offers a good base for further investigations.

## REFERENCES

1. Voll R. "*Twenty years of electroacupuncture diagnosis in Germany: a progressive report*" Am. J. Acupunct. 1975;3:7-17
2. Tsuei Julia, "*The Science of Acupuncture-Theory and Practice*" IEEE Engineering in Medicine and Biology, May/June 1996, 52-57.
3. Becker R. O., Selden G. "*The Body Electric: Electromagnetism and the foundation of life*" New York, Quill, 1985.
4. Becker R. O., Reichmanis M, Marino A. "*Electrophysiological correlates of acupuncture points and meridians*", Psychoenergetic Systems 1976;1:195-212.
5. Dumitrescu I. Fl., "*The man and the electrical medium. Surface bioelectrical phenomena.*" Ed. Stiintifica si Enciclopedica, Bucharest 1976.

## **SIMULATION OF FLUCTUATING INTERFERENCE PATTERN FOR LIGHT SCATTERED ON ERYTHROCYTES IN SUSPENSION**

**CRISTIAN V.L. POP<sup>1,\*</sup>, IOAN TURCU<sup>1</sup>, CALIN VAMOS<sup>2</sup>**

<sup>1</sup> *National Institute for R&D of Isotopic and Molecular Technologies,  
P.O.Box 700, RO-400293 Cluj-Napoca, Romania*

<sup>2</sup> *"T. Popoviciu" Institute of Numerical Analysis, Romanian Academy,  
P.O.Box 68, Cluj-Napoca, Romania*

**ABSTRACT.** We present new software able to simulate the stochastic interference in light scattering experiments. The software works in two stages. First an interference image is generated which capture the static aspects of the pattern. The fluctuating dynamics of the light intensity is simulated in the second stage.

The simulated data given by the software can be compared with experimental data, the similarity being a potential tool for identification of relevant parameters.

### **INTRODUCTION**

The speckled light scattered by erythrocytes in suspension provide information on both static and dynamic parameters of the investigated system. A very complex time dependent speckle pattern is obtained so that a numerical simulation of stochastic light interference, coherently scattered on human red blood cells, is a useful tools. The main goal of the paper is to present the developed software able to simulate light scattering experiments.

### **DESCRIPTION OF THE MODEL**

The software gives two type of information. First an interference image is generated which capture the static aspects of the pattern. After that for a small domain from the interference pattern (the photo-detector area) the fluctuating dynamics of the light intensity is also simulated.

For images simulation the input data are the parameters of the scattering centers (erythrocytes concentration, mean sedimentation rate, random velocity of scatterers) and the geometry of the experimental set-up (sampling rate, sample - detector distance, detector area, detecting angle). Software generates the interference image with a controlled spatial resolution, the scatterers' density being the main parameter of the simulation.

From simulated images one obtain the whole speckle pattern in the first step and its detailed characterization in a second step. Local interference maxima are identified and for each local maximum the program give the maximum value of light intensity and the speckle area. The stochastic properties of the obtained image originate from the random distribution of scattering centers.

There are two processes controlling the red blood cells dynamics: (i) the sedimentation in gravitational field, simulated by a Stokes dynamics, and (ii) the random Brownian motion. Uncorrelated random Brownian velocities, distributed isotropically and randomly distributed angular velocities, giving the dynamics of the azimuthal angle, simulate the random dynamics.

### **NUMERICAL MODEL**

The procedural flowcharting contains several steps. The software starts with a 3D generation of particle (erythrocytes) random distribution. In a second step the stochastic interference of light scattered by suspended erythrocytes is simulated:

---

\*E-mail: [popcl@L40.itim-cj.ro](mailto:popcl@L40.itim-cj.ro)

- square planar lattice generation – screen simulation;
- simulation of speckle interference pattern on screen.

Dynamics simulation is performed in the third step and is given by combining two independent motions:

- a constant velocity simulating the mean sedimentation rate;
- random velocities with Gaussian distributions on each axis for hydrodynamic and Brownian dynamics simulation.

In the last step software simulates the time dependent electric signal captured by a photo-detector:

- a small area is selected on the screen – photo-detector simulation
- at each discrete time step the values of light intensity on each pixel are added to give the simulation of temporal signal evolution.

## RESULTS

A schematic view of the simulated experiment is presented in Figure 1.

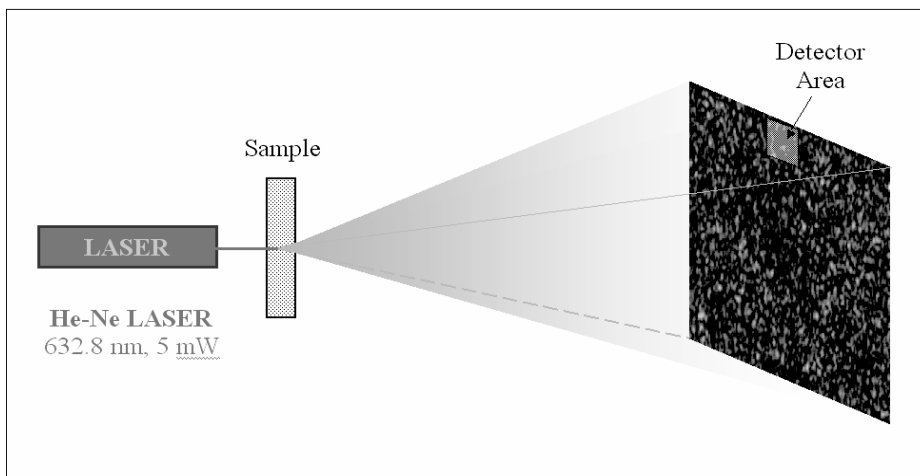


**Fig. 1.** The intensity speckle pattern of laser light scattered by erythrocytes in suspension.

The statistics of the simulated interference pattern gives an exponential decay for the light intensity probability and a Poisson distribution for the probability of speckle maximum light intensity (amplitude) as shown in Figure 2.

The interference pattern shows bright and dark speckles mixed in a random manner. A detail with high resolution is given in Figure 3 (photo-detector simulation).

The simulated electric signal given by the photo-detector is shown in Figure 4. In a laser light scattering experiment the dynamics of the particles is converted in signal fluctuations. The sedimentation in gravitational field, simulated by a Stokes dynamics is the main source of the slow fluctuations with large amplitude while the random Brownian motion gives the fast fluctuations.

The simulated data given by the software can be compared with experimental data (Figure 4), the similarity being a potential tool for identification of relevant parameters.

## ACKNOWLEDGMENTS

This research was supported by Romanian Education and Research Ministry, BIOTECH Program, research project 01-8-CPD-042.



FLUCTUATING INTERFERENCE PATTERN FOR LIGHT SCATTERED ON ERYTHROCYTES

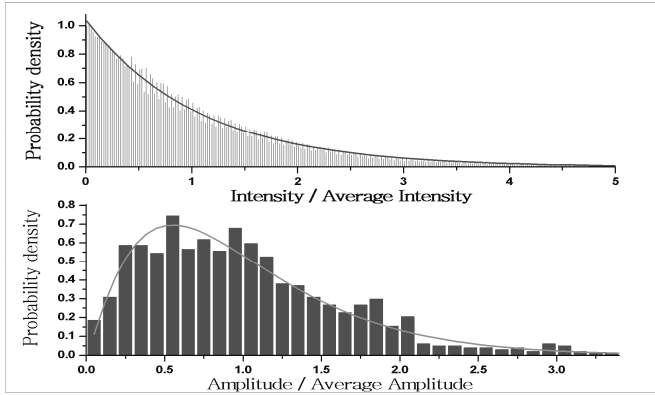


**Fig. 2.** Probability distribution for simulated scattered light intensity

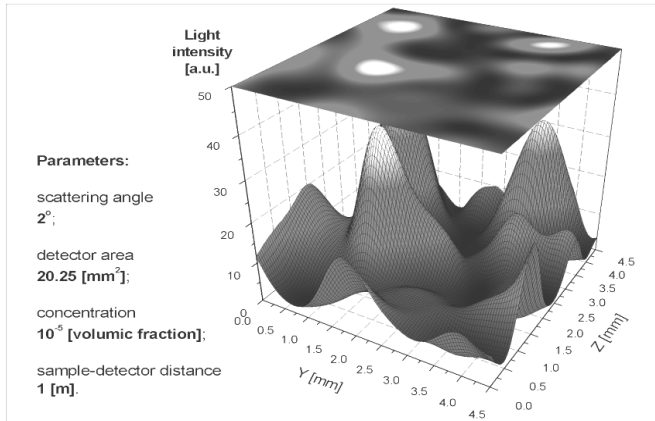


**Fig. 3.** The simulated light intensity scattered on detector area

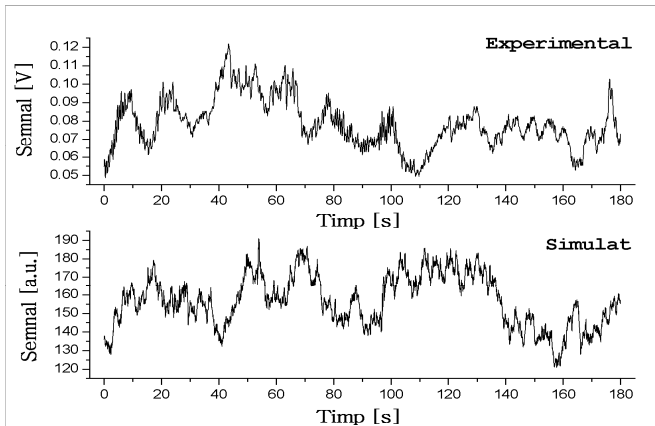


**Fig. 4.** The signal time dependent fluctuations. Parameters: concentration 10<sup>-5</sup> [volumic fraction]; sample-detector distance 1m; sampling rate 20Hz; detection angle 2°; detector area 20.25 mm<sup>2</sup>.

## REFERENCES

1. A. Serov, W. Steenbergen, and F. de Mul, *Prediction of the photo-detector signal generated by Doppler-induced speckle fluctuations: theory and some validations*, J. Opt. Soc. Am. A **18**, (2001) 622-630.
2. J. D. Briers, *Laser Doppler, speckle and related techniques for blood perfusion mapping and imaging*, Physiol. Meas. **22**, (2001) R35–R66.
3. C. V. L. Pop, C. Vamos, I. Turcu, *Numerical simulation of speckled light scattered by red blood cells in suspensions*, 4<sup>th</sup> European Biophysics Congress, July 5-9, Alicante, Spain, Eur. Biophys. J. **32**, 3 (2003) 220.

## SIMULATION OF THE MOLECULAR DYNAMICS OF A POLYPEPTIDE IN VACUUM

**ADRIANA ISVORAN**

*West University of Timisoara, Blvd. V. Pirvan no. 4,  
1900 Timisoara, e-mail: adriana.physics.uvt.ro*

**ABSTRACT.** The aim of this paper is to show a way to build the melittin polypeptide and to analyse its geometrical properties using the molecular dynamics simulation method. The dimensions of the melittin obtained by simulation are in good agreement with those calculated using files that contains experimental structural data that are deposited in the banks of data for proteins

### Introduction

Mellitin is a toxin from *Apis mellifera* venom. It is a polypeptide which contains 26 amino acids and it is known that it produces a selective perturbation of the membrane permeability and fluidity [1]. When we study the interactions between the peptides and lipids in the membrane cell it is necessary to have some information about the dimension and charges of the peptides that can be incorporated into the membrane core because the biological membranes are very sensitive at the geometrical properties of peptides. The aim of this paper is to show the way to build the melittin molecule and to study its geometrical properties using the simulation of the molecular dynamics technique.

### Method

The principles of the molecular dynamics simulation are shortly presented here [2]. Molecular dynamics is a method used for studying of the movements and spatial configuration evolution of the molecular systems. The formalism of the molecular dynamics technique uses the second Newton's law in order to describe the movements of the molecule in time.

$$\vec{F}_i = m_i \vec{a}_i = m_i \frac{d^2 \vec{r}_i}{dt^2} \quad (1)$$

where  $F_i$  is the force acting of the atom  $i$ ,  $m_i$  is the mass of the atom  $i$  and  $a_i$  is its acceleration. The force acting on each atom can be determined from the potential energy:

$$F_i = - \frac{dE}{dr} \quad (2)$$

and the potential energy can be calculated using the molecular mechanics technique:

$$E = E_b + E_{nb} \quad (3)$$

where  $E_b$  is the energy term for the interactions between the bonded atoms and  $E_{nb}$  is the energy term for the interactions between the non-bonded atoms. Usually these terms are given as follow

$$E_b = E_{bl} + E_{\theta} + E_{\omega} \quad (4)$$

$$E_{nb} = E_e + E_w \quad (5)$$

whits  $E_{bl}$  the energy due to the changes in the bond length,  $E_{\theta}$  is the energy due to the flexion of the bond,  $E_{\omega}$  is the energy due to the molecule rotation around a bond,  $E_e$  is the energy due to the electrostatics interaction between the non-bonded atoms and  $E_w$  is the energy due to the wan der Waals interactions.

Molecular dynamics allows the study of atoms trajectories if we know the acting force on each atom, but a little different approach is considered. The position vector of the atom  $i$  at the moment  $t+\Delta t$  can be determined if we know it at the moment  $t$

$$\vec{r}_i(t + \Delta t) = \vec{r}_i(t) + \frac{d\vec{r}_i(t)}{dt} \cdot \Delta t + \frac{d^2\vec{r}_i(t)}{dt^2} \cdot (\Delta t)^2 + \dots \quad (6)$$

The acceleration is determined from the equation (1), the speed is determined from

$$\vec{a}_i = \frac{d\vec{v}_i}{dt} \quad (7)$$

and the position of the atom  $i$  at the moment  $t$  from

$$\vec{v}_i = \frac{d\vec{r}_i}{dt} \quad (8)$$

For building the melittin molecule I use the version 27b4 of CHARMM (Chemistry at HARvard Macromolecular Mechanics) force field [3]. The steps used for building the system are: building the “psf” file using the parameters and topology of the amino acids, minimization of the polypeptide in 50000 steps of 1 fs each; heating the polypeptide at 300 K in 30 steps of 10 K each, equilibration of the polypeptide for 100 ps, performing molecular dynamics for 1 ns. The used cutoff radius for the non-bonded atoms interactions was 12 Å.

## Results

The stability of the constructed polypeptide can be tested using its energy diagram. This diagram is presented in the figure 1 and we notice that the system is stable beginning with the equilibration step. The changes in the volume of the melittin and in its radius of gyration are shown in the figure 2 and in the figure 3 respectively.

From these figures we notice a dramatic change in the volume and radius of gyration of mellitin after the transition between the unfolded and folded states. After the polypeptide folding the changes in the radius of gyration are not significant. For the volume we notice some important fluctuation every 200 ps. I compare the results obtained by simulation with those obtained using experimentally techniques. We can find structural data for melittin polypeptide using the Protein Data Bank of Brookhaven National Laboratory (<http://www.rcsb.org>), codes entry 2MLT (data obtained by X ray crystallography) and 1D9P (data obtained by NMR method).

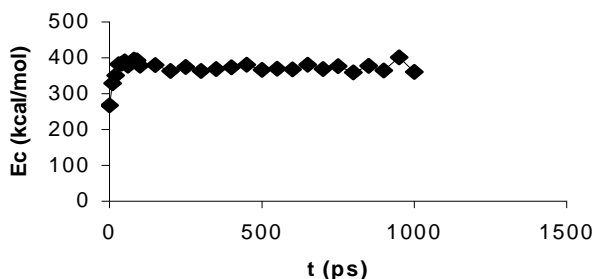


**Fig. 1.** The energy diagram for 1 ns dynamics of melittin

The values for the volume obtained using the pdb files are  $V=2533,675 \text{ \AA}^3$  from the X-ray file and  $V=6072,342 \text{ \AA}^3$  from the NMR data. The volume obtained from the X-ray file is in good agreement with the values obtained by simulation because we must take into account that for obtaining the structure using X-ray crystallography we need a crystal and

we work at very low temperature. The temperature for simulation was 300 K. The disagreement between the volume value obtained from the NMR data file and those obtained from simulation can be explained by the fact that the NMR study is made for the polypeptide in solution and the simulation is made in vacuum.

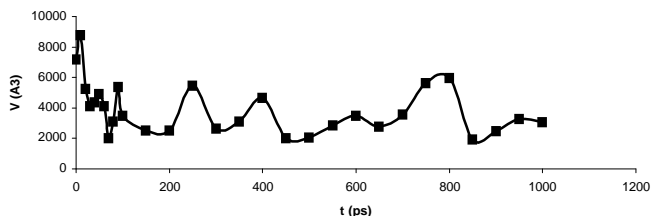


**Fig. 2.** The changes in the volume of melittin for 1 ns

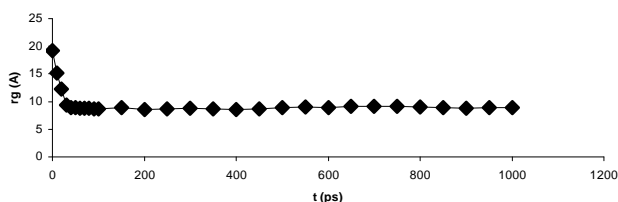


**Fig. 3.** The changes in the radius of gyration for melittin during 1 ns dynamics

### Discussions and conclusions

The results presented here show that the simulation of the molecular dynamics is a powerful technique for studying macromolecular systems and it can be applied for many aims. It can offer information on the folding and unfolding of the proteins, on the interactions between the side chains of the amino acids, on the interactions between the proteins and lipids in the cell membrane, and so on.

The results obtained from simulation for polypeptide melittin concerning its structural properties are in good agreement with the experimental data. The constructed polypeptide is stable, so we can use it further to analyse its interactions with the lipids and to study the molecular mechanism responsible for the changes in the membrane permeability in the melittin presence.

### REFERENCES

1. Paula I Watnick et al, *Characterization of the traverse relaxation rates in lipids bilayers*, Proc. Nat. Acad. Scie. USA, Biophysics, 1990, 87, 2082-2086
2. Caroline Joubert, *Simulation de la dynamique moléculaire des interactions spécifiques entre la protéine membranaire PMP1 et les lipides chargés négativement*, Rapport de stage, CEA Saclay, 2002
3. MacKerel et al, *CHARMM-force field used in molecular mechanics*, Academic Press, 1999

## ATR FT-IR INVESTIGATIONS OF SECONDARY STRUCTURE OF LYOPHILIZED PROTEINS IN WATER AND DEUTERATED WATER

G. DAMIAN

*“Babeș-Bolyai” University, Department of Physics, Cluj-Napoca,  
Str.Kogalniceanu No.1A, Romania, e-mail: dgrig@phys.ubbcluj.ro*

**ABSTRACT.** The conformational and structural changes due to lyophilization of bovine hemoglobin, casein and trypsin at neutral pH value, have been studied by FT-IR spectrometry using an Attenuated Total Reflectance (ATR) accessory. Changes in the amide bands in Fourier transform infrared spectra of proteins are generally attributed to alterations in protein secondary structure. In this study, spectra of these different proteins in the solid state lyophilized from H<sub>2</sub>O and D<sub>2</sub>O solution were analyzed. The second-derivative analysis of infrared spectra permits direct quantitative analysis of the secondary structural components of proteins by integration and curve fitting. By using D<sub>2</sub>O as solvent leads to a shift of the amide I band between 2 and 9 cm<sup>-1</sup> to lower frequencies depending on the particular protein.

### INTRODUCTION

The study of preparation of lyophilized (freeze-dried) proteins products is essential to obtain the requisite stability during months or even years at ambient temperature [1-3]. By freezing-drying process, in proteins are generates a variety of stresses which tend to denature their secondary structure. The denaturation of secondary structure refers to changes in ratio among three common structures, namely alpha helices, beta sheets, and turns. A number of “other” secondary structures types have been proposed, however they represent a small fraction of residues and may not be a general structural principle of proteins.

Infrared spectroscopy is one of the most used technique for studying stress-induced alterations in protein conformation and for quantitation of protein secondary structure[4–10]. By establishing the frequencies of all IR-active amide modes of each element of the secondary structure together with their respective molar extinction coefficients, it is possible to determine the secondary structure of any given protein precisely from its vibrational spectrum. In this paper conformational and structural changes due to lyophilization of bovine hemoglobin, casein and trypsin from H<sub>2</sub>O and D<sub>2</sub>O solution have been studied by FT-IR spectrometry using an Attenuated Total Reflectance (ATR) accessory.

### MATERIALS AND METHODS

The powder proteins were obtained from Sigma and used without further purification. The protein was rehydrated in phosphate buffer physiological saline at a final concentration of 10<sup>-3</sup> mol/l. The pH and pD range was adjusted at neutral values adding a small amount of NaOH and NaOD respectively. A small amount of 5 ml from each sample was lyophilized for 30 hours at -5<sup>0</sup> C and than used as powder sample.

The FT-IR spectra of proteins were recorded in the region 4000-800 cm<sup>-1</sup> by a Bruker EQUINOX 55 spectrometer, using an Attenuated Total Reflectance accessory with a scanning speed of 32 cm<sup>-1</sup> min<sup>-1</sup> and the spectral width 2.0 cm<sup>-1</sup>. The internal reflection element was a ZnSe ATR plate (50 x 20 x 2 mm) with an aperture angle of 45°. A total of 128 scans were accumulated for each spectrum.

In the Fourier domain derivative, the second-derivative analysis of infrared spectra permits direct quantitative analysis of the secondary structural components of proteins. By this procedure, the signal to noise ratio of the spectrum is minimized and is amplified disproportionately in the weak features of the spectrum. Thus, the areas corresponding to the different types of secondary

structure are quantitatively and qualitatively evaluated by integration and curve fitting. The second derivatives of all spectra were calculated using the OPUS spectrometer software. Before starting the fitting procedure, the obtained depths of the minima in the second derivative spectrum and, subsequently, the calculated maximum intensities were corrected for the interference of all neighboring peaks. The curve fitting is performed by stepwise iterative adjustment towards a minimum root-mean-square error of the different parameters determining the shape and position of the absorption peaks.

## RESULTS AND DISCUSSION

Lyophilization induced significant structural alterations in proteins, characterized by a decrease in the  $\alpha$ -helix and a significant increase in the  $\beta$ -sheet content. The best structural information from infrared band of proteins is the amide I band appearing between 1600 and 1700 $\text{cm}^{-1}$  with a maximum for most proteins at around 1654–1674  $\text{cm}^{-1}$ , which arises primarily from the stretch vibration of the peptide C=O group. Normal mode analysis reveals that the C=O stretching couples slightly with CN stretching, CCN deformation and NH bending. Each type of secondary structure (i.e.  $\alpha$ -helix,  $\beta$ -sheet,  $\beta$ -turn and disordered) gives rise to different C=O stretching frequencies [6-10], and, hence, results in characteristic band positions. In the Fourier domain derivative, the second-derivative analysis of infrared spectra permits direct quantitative analysis of the secondary structural components of proteins [6-8]. In figure 1 are presented the inverted second derivative of the lyophilized studied proteins and in the Tables I-III, its relative areas and assignments of the secondary structure. Unfortunately, the HOH bending motion of water almost coincides with the amide I band and makes studies in protonic aqueous solution difficult [11]. This problem is overcome by using  $\text{D}_2\text{O}$  as solvent. Involved in different secondary structure elements via hydrogen bonding to the peptide NH group, the experimentally observed amide I band envelopes a multitude of single bands with different frequencies which can be resolved as described above.

**Table I**  
Relative Areas and Assignments of Infrared Second Derivative Amide I Band of lyophilized Bovine Hemoglobin from water and deuterated water.

H <sub>2</sub> O		D <sub>2</sub> O		Assignments
$\nu$ ( $\text{cm}^{-1}$ )	Areas (%)	$\nu$ ( $\text{cm}^{-1}$ )	Areas (%)	
1685	17.1	1674	3.2	turn
1667	2.6	1661	6	turn
1655	52.3	1651	63.1	$\alpha$ -helix
1635	9	1633	21.9	$\beta$ -sheet
1619	19.1	1616	6	$\beta$ -sheet

**Table II**  
Relative Areas and Assignments of Infrared Second Derivative Amide I Band of lyophilized Casein from water and deuterated water

H <sub>2</sub> O		D <sub>2</sub> O		Assignments
$\nu$ ( $\text{cm}^{-1}$ )	Areas (%)	$\nu$ ( $\text{cm}^{-1}$ )	Areas (%)	
1683	6			turn
1676	9.5	1673	9	turn
1668	12.1	1660	24.1	turn
1652	36.23	1640	57.3	$\alpha$ -helix
1644	4.8			unordered
1637	16.9			unordered
1626	1.6	1627	2.8	$\beta$ -sheet
1613	12.2	1609	6.8	$\beta$ -sheet

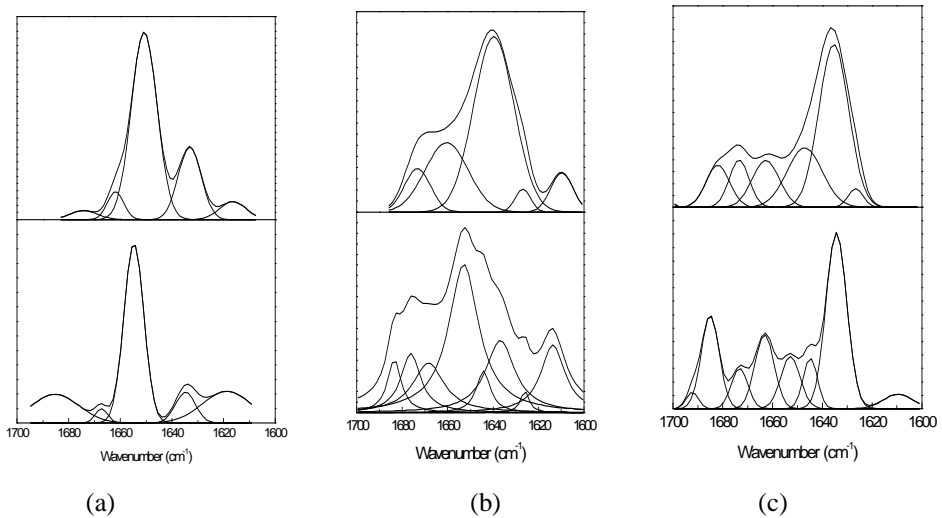


**Fig. 1.** Curve-fitted inverted second-derivative amide I spectra of lyophilized (a) hemoglobin, (b) casein and (c) trypsin from D<sub>2</sub>O (upper) and H<sub>2</sub>O (lower)

**Table III**  
**Relative Areas and Assignments of Infrared Second Derivative Amide I**  
**Band of lyophilized Trypsin from water and deuterated water**

H <sub>2</sub> O		D <sub>2</sub> O		Assignments
$\nu$ (cm <sup>-1</sup> )	Areas (%)	$\nu$ (cm <sup>-1</sup> )	Areas (%)	
1692	2.1			aggregate
1685	17.2	1682	9.5	turn
1673	6.8	1673	9	turn
1663	14.5	1663	12.2	$\alpha$ -helix
1653	10.4			unordered
1645	7.3	1647	20.1	unordered
1634	37.6	1635	46.4	$\beta$ -sheet
1610	4.1	1626	2.7	$\beta$ -sheet

## CONCLUSIONS

Fourier transform infrared spectroscopy is an important method to determine changes in secondary structure of proteins in the processes, which involve their denaturation. Among the spectral regions arising out of coupled and uncoupled stretching and bending modes of amide bonds, the amide I spectral band is the most sensitive to the variations in secondary structure folding.

## REFERENCES

1. J. F. Carpenter, B. S. Chang, *Lyophilization of protein pharmaceuticals*, in: K. E. Avis, V. L. Wu (Eds.), *Biotechnology and Biopharmaceutical Manufacturing, Processing and Preservation*, Interpharm Press, Buffalo Grove, IL, 1996, pp. 199–264.
2. Joly, M. (1965). *A Physico-chemical Approach to the Denaturation of Proteins. Molecular Biology series* Vol. 6. (Eds. Horecker, B., Kaplan, N. O., Scheraga, H. A.), Academic Press, London



3. Harwalker, V. R. and Kalab, M., *Milchwissenschaft*. 40(1985); 31-34.
4. A. Dong, S.J. Prestrelski, S.D. Allison, J.F. Carpenter, *J. Pharm. Sci.* 84 (1995) 415-424.
5. D. M. Byler, H. Susi, *Biopolymers* 25 (1986) 469-487.
6. H. Susi, D. M. Byler, *Methods Enzymol.* 130 (1986) 290- 311.
7. W. K. Surewicz, H. H. Mantsch, *Biochim. Biophys. Acta* 953 (1988) 115-130.
8. S. Krimm, J. Bandekar, *Adv. Protein Chem.* 38 (1986) 181-364.
9. A. Dong, W. S. Caughey, *Methods Enzymol.* 232 (1994) 139-175.
10. H. H. Mantsch, D. Chapman, *Infrared Spectroscopy of Biomolecules*, Wiley-Liss, New York.
11. K. Rahmelow K, W. Hübner, *Appl. Spectrosc.* 51(1997), 160-170.

## LOW INTENSITY GAMMA RADIATION EFFECTS IN YOUNG PLANTLET ASSIMILATORY PIGMENTS

MIHAELA RĂCUCIU<sup>1</sup>, DORINA CREANGĂ<sup>2</sup>

<sup>1</sup> University „Lucian Blaga” of Sibiu, Faculty of Science, Physics Department, Ion Rațiu Street, no. 7-9, e-mail: mracuciu@yahoo.com.

<sup>2</sup> University „Al.I.Cuza” Iasy, Faculty of Physics, Bd. Copou, no. 11

**ABSTRACT.** In this paper we studied the low intensity gamma radiation effects in young plantlets of *Chelidonium majus*. Experimental observation aimed: seed germination, assimilatory pigments contents, absorption and fluorescence of the photosynthesis pigments. It was observed the fluctuation of the assimilatory pigments concentrations in function on the irradiation time. We have recorded the absorption and fluorescence spectra for acetone extracts, made measurements and accomplish comparative interpretation.

### Introduction

*Chelidonium majus*, on the *Papaveraceae* family, was the object of many scientific researches [1] due to its rich contents in alkaloids with numerous therapeutic applications. Some physical factors, such as gamma irradiation, can have different effects for different radiation doses [2]. In the *Chelidonium majus* cases such effects are little known. On this reason, we proposed to study the gamma radiation effects on the *Chelidonium majus*, through the spectrophotometry methods. We have studied the absorption and fluorescence spectra for acetone extracts.

### Material and methods

The *Chelidonium majus* caryopsides have been irradiated with gamma radiation from a 10mCi Cobalt source, for different irradiation times, expressed in hours: 0,5h, 1h, 1,5h, 2h, 6h, 16,5h. After germination, from the plantlets of exposed samples and control ones, pigment extraction in 85% acetone were prepared for the spectrophotometrical assay of the assimilatory pigments contents.

We have studied the absorption spectra using the SPECORD UV-VIS spectrophotometer. After recording of the absorption spectra, we have calculated the A-chlorophyll concentration ( $C_{Cla}$ ), B-chlorophyll concentration ( $C_{Clb}$ ) and carotene pigments concentration ( $C_{ct}$ ) (in mg of pigment/g of green tissue), according to [3] on the basis of the light extinction at the  $15.080\text{ cm}^{-1}$ ,  $15.500\text{ cm}^{-1}$  and  $21.190\text{ cm}^{-1}$ . The fluorescence spectra of chlorophyll solutions (diluted in 1/10 ratio) were recorded using an adequate fluorescence installation described in [5]. For the excitation of fluorescence we have used the  $23.740\text{ cm}^{-1}$  radiation, to observe the red fluorescence band and  $29.720\text{ cm}^{-1}$  radiation, to observe the blue fluorescence band.

### Results and discussion

The absorption spectra for samples 1-4 are showed in Figure 1. For the other samples similar spectra were recorded.

We observed that in these spectra don't appear evidently modifications for different samples in comparison to the control. This can be explained on the basis of the values given in Table I (the molar extinction for both chlorophyll types are concordant with [3], [7]). The values from Table I show us that the A-chlorophyll concentrations ( $C_{Cla}$ ) are bigger than the B-chlorophyll concentrations ( $C_{Clb}$ ) and carotenoid pigment concentrations ( $C_{ct}$ ).

The values from Table I are presented in the graphic form in Figure II.

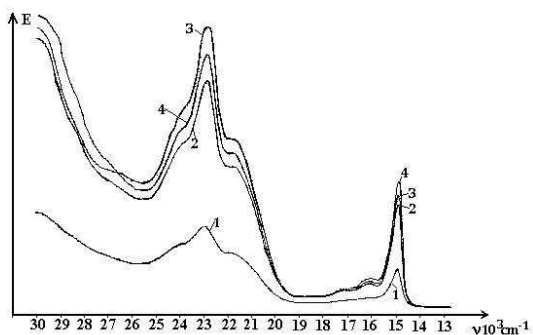


Fig. 1. Absorption spectra for the samples 1-4

Table I.

The concentration values to assimilatory pigments contents for control and samples

Test	Irradiation times (h)	C <sub>Cl<sub>a</sub></sub> (mg/g)	C <sub>Cl<sub>b</sub></sub> (mg/g)	C <sub>Cl<sub>c</sub></sub> (mg/g)
1-control	0	0.4603	0.046	0.214
2	0,5	0.603	0.127	0.248
3	1	0.533	0.066	0.256
4	1,5	0.456	0.04	0.204
5	2	0.588	0.107	0.119
6	6	0.396	0.063	0.179
7	16,5	0.684	0.064	0.237

We didn't obtained a definite dependence of the pigment concentration on the irradiation times (or radiation dose). We observed the fluctuations of the pigment concentrations in function on the irradiation times, these fluctuations being more important in A-chlorophyll. This supposition seems to be sustained also by the fluorescence spectra. In the registered absorption spectra we observed that there is a band to about 30.000 cm<sup>-1</sup> (333,3 nm) which [8] is assigned to the carotenoid pigments. The fluorescence spectra of the diluted acetone solution (in 1/10 ratio) have two fluorescence bands: a blue range band with the maximum at 23000 cm<sup>-1</sup> and a red range band with the maximum at 14.600 cm<sup>-1</sup>.

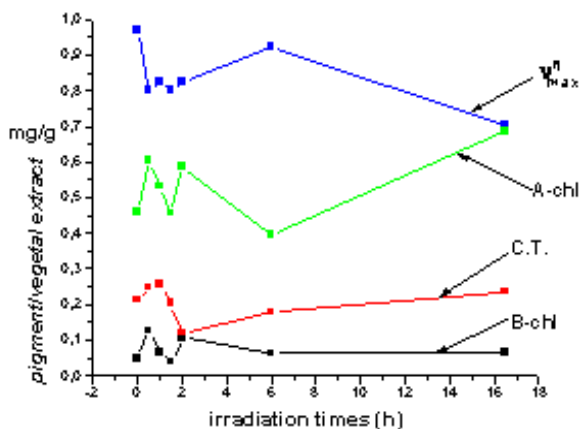


Fig. 2. The fluctuations of the concentrations for different the irradiation times

The red range band is narrower than the other one. These fluorescence bands, according to [3], [7], [8] are due to A-chlorophyll and B-chlorophyll, as the carotenoid pigments don't have significant fluorescence in these wave number ranges. In Figures 3, 4, 5, 6 are showed absorption and fluorescence bands for control and exposed sample 2 (samples corresponding to 0,5 h – irradiation time). We observed in these figures that fluorescence bands in the blue range is the same for the control and exposed sample, but while the fluorescence band is a smooth band, the absorption band is a structured one (Figure 3 and 4).

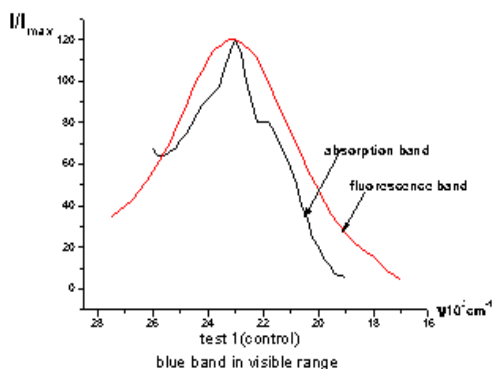


Fig. 3. control sample 1

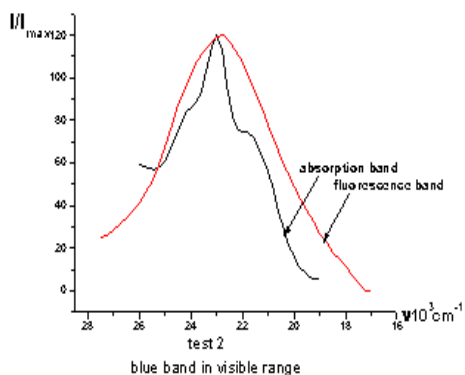


Fig. 4. exposed sample 2

It's interesting that the maximum frequency for the fluorescence band in the blue range alternates in opposition with the A-chlorophyll concentration, for different irradiation times (see Figure 2).

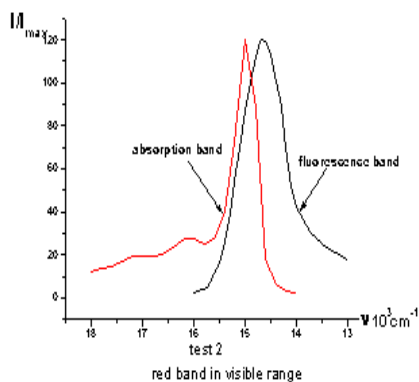


Fig. 5. control sample 1

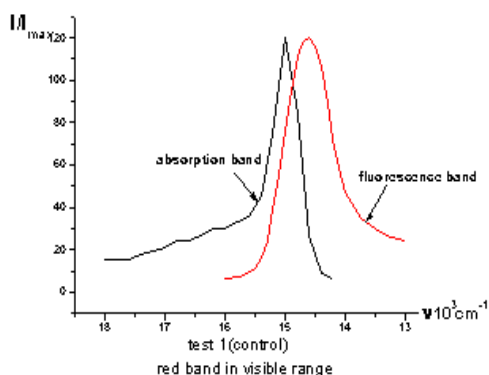


Fig. 6. exposed sample 2

The fluorescence band in red range is very narrow so that we can't say very much about it, but it seems to be less sensitive to the A – chlorophyll concentration fluctuations. In the red range, the fluorescence band doesn't coincide with the absorption band for the control and exposed sample (Figure 5 and 6).

### Conclusions

It's possible that exposure to low activity gamma radiation source, for different irradiation times, have an influence on the plant cell nuclei inhibiting or stimulating differently the synthesis of A-chlorophyll and B-chlorophyll molecules. This way could be explained the different modifications of these pigment concentrations in exposed samples in comparison to the control ones. These studies represent preliminary investigations regarding a larger experimental projected designed to the elucidation of the gamma radiation action in young plant cells.

### REFERENCES

1. Colombo M. L., Bosisio E., *Pharmacological activities of Chelidonium majus L. (Papaveraceae)*, Pharmacological Research, 1996, 33(2): 127-134.
2. Ghiorghiuță G. I., *Radiobiologie vegetală*<sup>3/4</sup>, Ed. Academiei, București, 1987.
3. Rabinowitch E. I., *Spectroscopy and Fluorescence of Photosynthetic Pigments, Kinetics of Photosynthesis*, Interscience Publishers, Inc., New York, 1951.
4. DeRose V. J., Latimer M. J., Zimmermann J., Mukerji I., Yachandra V. K., Sauer K., Klein M. P., *Fluoride substitution in the Mn cluster from Photosystem II: EPR and X-ray absorption spectroscopy studies*, Chemical Physics, 1995, 194 (2-3): 443-459.
5. Vlahovici A., Druță I., Andrei M., Cotleț M., Dinică R., Journal of Luminescence, 82, 155, 1999.
6. Knox R. S., *Excited-state equilibration and the fluorescence-absorption ratio*, Acta Physica Polonica, 1999, 95, 85-103.
7. Sălăgeanu N., *Fotosinteza*, Ed. Academiei, 1981.
8. Mircea Știrban, *Procese primare în fotosinteză*, Cluj, 1981.

## DEUTERIUM DEPLETION IN BLOOD, BLOOD PLASMA AND NEOPLASM TISSUE FROM PATIENTS. DIAGNOSIS AND TREATMENT IMPLICATIONS

P. BERDEA<sup>1</sup>, STELA CUNA<sup>1</sup>, M. CAZACU<sup>2</sup>, M. TUDOSE<sup>2</sup>

<sup>1</sup> National Institute of Research-Development for Isotopic and Molecular Technologies, 71-103 Donath St. 400293 Cluj-Napoca, Romania, e-mail: cuna@oc1.itim-cj.ro

<sup>2</sup> University Hospital of the Railway Society, 18 Bilascu St., 3400 Cluj-Napoca

**ABSTRACT.** The water deuterium content in blood plasma, blood cells and neoplasm tissue of the patients with different cancer diseases is depleted in deuterium compared with the average deuterium content of healthy human. The water deuterium content of blood plasma of the cancerous patients is depleted in deuterium (-85.6‰) compared with healthy humans (about -37‰). The blood cells water also is deuterium depleted by 19‰ compared with the blood plasma. The highest depletion in deuterium was found in the blood plasma extract (-510‰) from patient drinking deuterium depleted water (-840‰) 36 days long.

The experimental method consists of three steps: 1. separation of plasma and blood cells by centrifugation; 2. water extraction by vacuum distillation; 3. isotopic analyses of water by mass spectrometry.

Diagnosis implication: The deuterium depletion of blood coagulate compared with blood plasma is correlated with cancer disease.

Treatment implication: We obtained more deuterium depletions in the blood plasma and in the tumour fluid from cancerous patients using deuterium depleted water as drinking water.

### 1. INTRODUCTION

Human blood serum of healthy human is enriched in deuterium compared with the average deuterium content of local drinking water (1). For human patients having different cancer diseases the deuterium content of blood plasma is diminished or close to the average deuterium content of drinking water and more depleted compared with healthy humans (2). Such a variation of deuterium content of human blood serum is correlated with cancer disease status of the patients.

The variations of deuterium concentration in human fluids as: blood, urine depends on deuterium contents of drinking water and diet. Compared with drinking water, human blood serum in Central Europe is enriched by 30‰ in deuterium. Change of location frequently induces a change in the isotopic content of the blood (1).

We report here another deuterium fractionation in water deuterium of blood cell from patients with different cancer diseases: the deuterium depletion of blood coagulate compared with blood plasma is correlated with cancer disease status of patient.

More important deuterium depletion is noticed in the blood plasma and the tumour fluid of cancerous patients using deuterium depleted water as drinking water.

### 2. MATERIALS AND METHODS

#### 2.1. Deuterium fractionation of water in the blood cells for patients with different cancer diseases

The samples were supplied by The University Hospital of the Railway Society from Cluj-Napoca, as human blood from patients with different cancer diseases. The witness samples were obtained from volunteers, healthy students, and were collected in the same conditions.

The experimental method for blood processing consists of three steps: a) separation of plasma and blood cells by centrifugation; b) water extraction by vacuum distillation; c) deuterium concentration analyses of water by mass spectrometry.

**2.2. The deuterium depletion in blood plasma and tumour water extract for patients treated with deuterium depleted water**

We used deuterium depleted water (-840‰ ± 30‰) 1.5 litre / day / patient as drinking water. The blood collection and deuterium content analysis were performed as shown above.

The deuterium content analyses of water is carried out using a mass spectrometer SMAD-1.

The deuterium content is expressed as deuterium/protium ratio: R=D/H, in ppm units, where D is the number of deuterium atoms, and H is the number of protium atoms. It is also expressed as δ values, in “part per thousand”(‰)

$$\delta = (R/R_S - 1) 1000,$$

where: R is the deuterium/protium ratio of the sample, R<sub>S</sub> is the same ratio of the international V-SMOW standard (Vienna Standard Mean Ocean Water).

The precision of the determination of δ values was ±2‰.

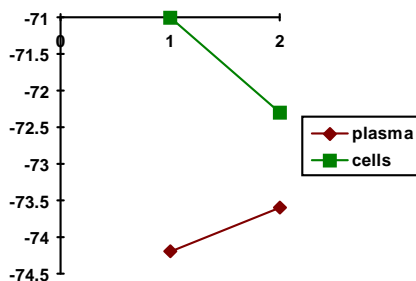
**3. RESULTS AND DISCUSSIONS**

Table 1 presents the deuterium content of blood: plasma (δ<sub>p</sub>), cells (δ<sub>c</sub>), and deuterium fractionation of water in cells, (δ<sub>p</sub> - δ<sub>c</sub>), for patients with different cancer diseases, in stage 4.

**Table 1**  
**Deuterium fractionation of water in the blood cells for patients with different cancer diseases;**  
**δ<sub>p</sub> - blood plasma deuterium content; δ<sub>c</sub> - blood cells deuterium content;**  
**(δ<sub>p</sub> - δ<sub>c</sub>) - deuterium fractionation of water in blood cells**

No	Patient	Neoplasm location	δ <sub>p</sub> (‰)	δ <sub>c</sub> (‰)	δ <sub>p</sub> - δ <sub>c</sub> (‰)
1	T.	thyroid	-65.2 ± 1.5	-90.3 ± 1.7	25.1 ± 2.3
2	C.V.	oesophagus	-63.9 ± 1.1	-80.6 ± 1.3	16.7 ± 1.7
3	B.	stomach	-65.2 ± 1.0	-84.5 ± 1.2	19.3 ± 1.6
4	B.P.	pancreas	-65.2 ± 1.3	-81.9 ± 1.0	16.7 ± 1.6
Average deuterium fractionation of water in the blood cells: 19.45 ± 3.96(‰)					

Human serum, in Central Europe, is enriched by 30 ‰ compared with the drinking water average deuterium content. The deuterium content of the blood plasma of healthy humans (about -37 ‰) was higher compared with the average deuterium content of the drinking water.



**Fig. 1.** The deuterium content, as δ(‰) of the blood plasma and the blood cells of healthy humans.

Our results (2) and Table 1 reveal that the deuterium content of blood plasma for patients with cancer disease is lower or very close to the average deuterium content of the drinking water (-69‰).

Table 1 presents the deuterium fractionation in water from blood cells from patients with different cancer diseases. The inside water of this blood cells is depleted in deuterium compared with plasma. At the contrary, the deuterium content of cell inner water is higher or close to the plasma deuterium content of healthy volunteers ( Fig.1). This may have a consequence in the cancer diagnosis.

**3.1. The deuterium depletion in blood plasma and tumour water extract from patients treated with deuterium depleted water.**

Deuterium depleted water proved the inhibitory effect in the proliferation of tumours cells for animals and human, or in plant growth (3, 4, 5, 6). Fig. 2 presents the deuterium depletion of blood plasma and tumour water for a patient with pancreas tumour, treated with deuterium depleted water (-708‰) 5 days long. The course of deuterium depletion in the blood plasma and the inner fluid from tumour proved the efficiency of the treatment.

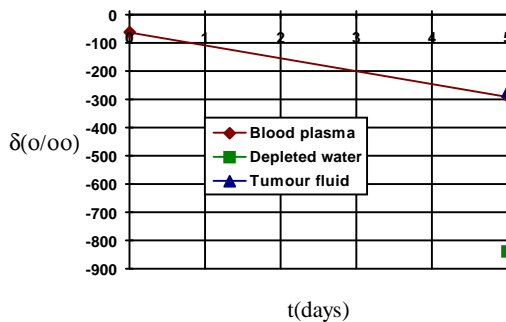


**Fig. 2.** Deuterium content in blood plasma and tumour fluid from patients with pancreas cancer before and after 5 days long drinking deuterium depleted water(DDW)

The effect of deuterium depleted water was the diminishing of the blood deuterium content to about one half after 5 weeks of treatment, as shown in Figure 3.

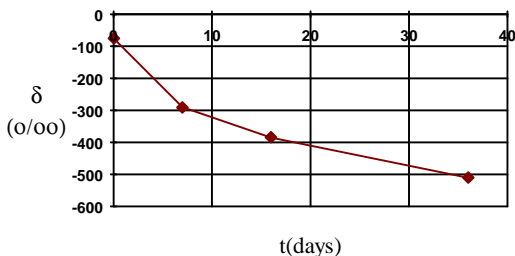


**Fig. 3.** Course of deuterium depletion in blood plasma of patient treated with deuterium depleted water (-839.5‰).

**4. CONCLUSIONS**

The tumours cells induce deuterium depletion. Consequently, the deuterium content of plasma, blood cells or tumour inner water for neoplasm patients is depleted in deuterium compared with the values obtained for healthy subjects. The human blood serum of healthy human is enriched in deuterium compared with the average deuterium content of local drinking water (1). For



patients heaving different cancer diseases the deuterium content of blood plasma is diminished compared with the deuterium content of the drinking water and even more depleted in the blood cell water. Such a variations in the deuterium content of human blood plasma is correlated with cancer disease status. This result can be used in the cancer diagnosis and treatment.

## REFERENCES

1. U. Zimmermann, and U. Cegla, *Der Deuterium-und Sauerstoff-18-Gehalt der Körperflüssigkeit des Menschen und seine Änderung bei Ortswechsel*, Die Naturwissenschaften, **60**, (1973), 243
2. P. Berdea, Cuna Stela, Cazacu M., Tudose M., *Deuterium variation of human blood serum*, Studia Universitatis Babeş-Bolyai, Physica, Special Issue, 2, pp. 256-258,(2001)
3. Stela Cuna, P. Berdea, M. Cazacu, M. Tudose, *Watching tumours evolution by using deuterium content of the blood as a marker*, Alternatives 2002, International Workshop on Promotion of the Three Rs Concept in Relation to Animal Experimentation in Hungary, Bulgaria, Romania and Slovenia,(abstr. p.36), 27-30 Oct., 2002, Balatonfüred, Hungary
4. G. Somlyai, G. Jancso, G. Jakli, K. Vass, B. Barna, V. Lakics and T. Gaal, *Naturally occurring deuterium is essential for the normal growth rate of cells*, FEBS 317, (1993), 1-4
5. D. Ieremia, Rodica Dumitrescu, Elena Nes, *Restriction of cellular growth by deuterium deprivation*, IV-th Natl.Conf. of Biophys., 16-18 Oct. Cluj-Napoca (Abstract), (1997), MR-7
6. P. Berdea, Cristina Dobrota, C. Cosma, Stela Cuna, *Growing rate decrease of the maize embryos sprouted in deuterium-depleted water (20 ppm)*, Colloquium Spectroscopicum Internationale XXXI, Ankara, Turkey, sept. 5-10, (1999), (Abstr.), 123

## THE EFFECT OF HIGH MAGNETIC FIELD ON $\text{Li}^+$ TRANSPORT THROUGH HUMAN ERYTHROCYTE MEMBRANES

**C. BINDEA<sup>1</sup>, GABRIELA BINDEA<sup>2</sup>, ST. POPESCU<sup>1</sup>, T. SIMPLACEANU<sup>1</sup>**

<sup>1</sup>National Institute for Research and Development of Isotopic and Molecular Technologies, P.O.Box 700, 400293 Cluj-Napoca

<sup>2</sup>Dept. of Biology, "Babes-Bolyai" University, Cluj-Napoca, Romania

**ABSTRACT.** Human erythrocytes were exposed to magnetic field in the 0.59-0.62 T intensity domain and the  $\text{Li}^+$  influx and efflux through erythrocyte membrane was measured. The  $\text{Li}^+$  influx by passive diffusion mechanism increased linearly with the time exposure, and by  $\text{Na}^+ - \text{K}^+$  pump mechanism decreased linearly, depending on the time exposure. The total  $\text{Li}^+$  efflux and  $\text{Li}^+$  efflux by countertransport  $\text{Li}^+ - \text{Na}^+$  mechanism decreased linearly with the time.

**Key Words:** ion transport,  $\text{Li}^+$  transport, passive diffusion,  $\text{Na}^+ - \text{K}^+$  pump, countertransport  $\text{Li}^+ - \text{Na}^+$ , erythrocytes and magnetic field.

### INTRODUCTION

The transport of lithium ions through human erythrocyte membranes is known to occur by the following mechanisms: (a) passive diffusion along its electrochemical gradient; (b) active transport by the  $\text{Na}^+ - \text{K}^+$  ATPase pump as  $\text{Li}^+$  compete with  $\text{K}^+$  at the external site of the pump; (c) by  $\text{Li}^+ - \text{Na}^+$  countertransport which is responsible for the  $\text{Li}^+$  efflux against its electrochemical gradient and therefore the presence of  $\text{Na}^+$  ions in the extracellular medium is essential to this transfer [1], and (d) passive transport associated with bicarbonate ions which is responsible for about 30% of the  $\text{Li}^+$  influx in integral blood. The  $\text{Li}^+$  transport through erythrocyte membranes gained much interest in connection with lithium therapy in manic depression [2]. Our own investigations have been concerned with the influence of general anesthetics on  $\text{Li}^+$  transport, particularly of a procaine based drug and also its influence on lithium therapy of manic depression [2,3].

The present work is concerned with  $\text{Li}^+$  transport through erythrocyte membranes under the influence of high magnetic field. Only the first three transport pathways (a,b,c) have been investigated as our samples were limited to washed cells.

### MATERIALS AND METHODS

Human blood in citrate was collected from apparent healthy subjects. The whole blood was exposed to magnetic field in the 0,59-0,62 T intensity domain. A minimum of two samples were exposed to the same time at room temperature. The experimental method we used for  $\text{Li}^+$  transport mechanism through human erythrocyte membranes was similar to that described by Canessa ... [4]. We adapted it to the investigation of drug and gamma radiation effects on the  $\text{Li}^+$  influx and efflux through human erythrocytes membranes [3,5].

The effect of high magnetic field on  $\text{Li}^+$  influx was calculated using the  $(\Delta\text{Li}^+_{\text{influx}}/\text{influx}_c) \times 100$ , where  $\Delta\text{Li}^+_{\text{influx}} = (\text{Li}^+_{\text{influx}})_{\text{magnetic field exposed}} - (\text{Li}^+_{\text{influx}})_{\text{control}}$ .

The effect of high magnetic field on  $\text{Li}^+_{\text{efflux}}$  was expressed as a relative effect  $\Delta K/K_{\text{control}}$ , where  $K(\text{constant}) = \text{Li}^+_{\text{efflux}}/\text{Li}^+_{\text{erythrocyte}}$  and  $\Delta K$  is the difference between the two constants for exposed magnetic field samples and controls, respectively.

### RESULTS AND DISCUSSION

The  $\text{Li}^+_{\text{influx}}$  by passive diffusion mechanism increased linearly with the time exposure (fig. 1) and by  $\text{Na}^+ - \text{K}^+$  pump mechanism decreased linearly, depending on the time exposure (fig.2).

THE EFFECT OF HIGH MAGNETIC FIELD ON  $\text{Li}^+$  TRANSPORT

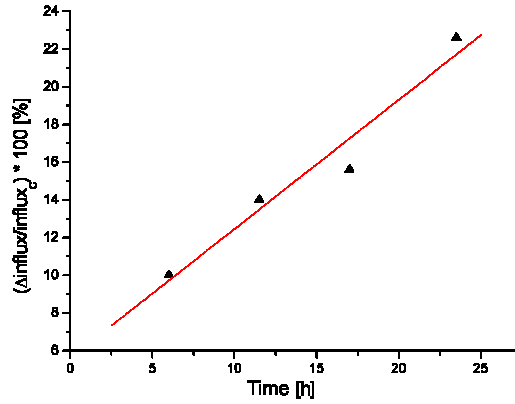


Fig. 1.

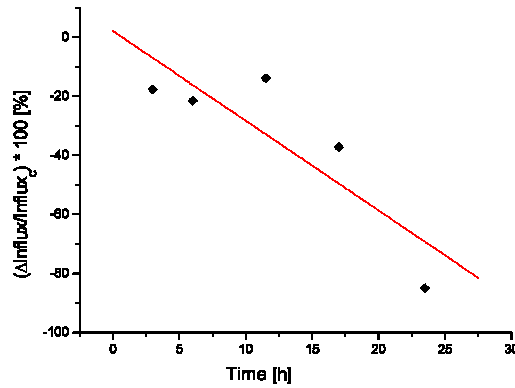


Fig. 2.

The total  $\text{Li}^+$  efflux (fig.3) and  $\text{Li}^+$  efflux by countertransport  $\text{Li}^+\text{-Na}^+$  mechanism (fig.4) decreased linearly with the exposure time.

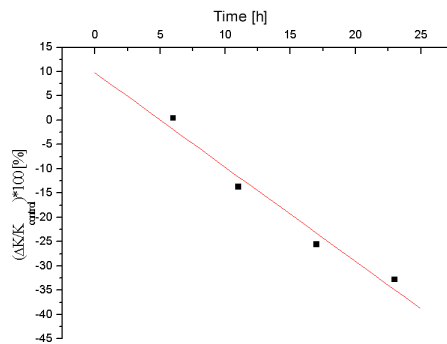


Fig. 3.

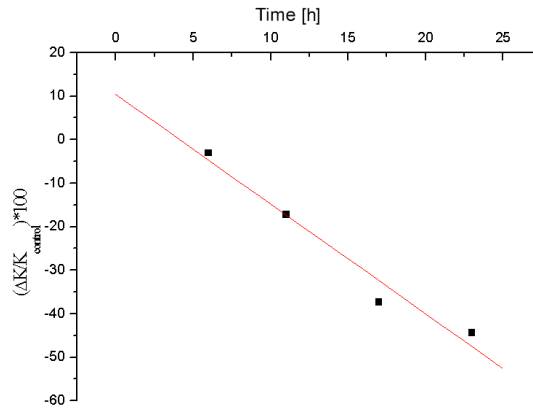


Fig. 4.

There has been obtained an increase of about 25% of the  $\text{Li}^+$  influx by passive diffusion in the human erythrocytes exposed to a magnetic field compared the  $\text{Li}^+$  influx in the non exposed control erythrocytes using the same mechanism.

The  $\text{Li}^+$  influx through the  $\text{Na}^+\text{-K}^+$  pump mechanism in the human erythrocytes exposed to the magnetic field has been diminished with about 50% compared with the  $\text{Li}^+$  influx through the same mechanism from the non exposed control erythrocytes.

The  $\text{Li}^+$  efflux through the  $\text{Li}^+\text{-Na}^+$  countertransport mechanism from the human erythrocytes exposed to the magnetic field has been diminished with about 50% compared with the  $\text{Li}^+$  efflux through the same mechanism from the non exposed control erythrocytes.

We may conclude that there is an effect of the magnetic field upon the channel protein ( $\text{K}^+$ ,  $\text{Na}^+$ ) and  $\text{Na}^+\text{-K}^+$  ATPase.

## REFERENCES

1. J. M. Benoist, *Therapie* **37**, 1982, 615-628
2. C. Bindea, D. Baciu, V. V. Morariu, S. Rândașu, *Biomedical Letters* **55**, 1997, 141-146
3. C. Bindea, Alexandra Chifu, *Rev. Roum. Biochim.* **24**, 1987, 185-192
4. M. Canessa, N. Adragna, S. Solomon, M. Connolz, D. C. Tosteson, *N. Engl. J. Med.* **302**, 1986, 772-776
5. C. Bindea, V. V. Morariu, I. Chereji, *Cytobios* **93**, 1998, 23-31

## THE EFFECT OF LOW MAGNETIC FIELD ON $\text{Li}^+$ INFLUX IN HUMAN ERYTHROCYTES

**GABRIELA BINDEA<sup>1</sup>, C. BINDEA<sup>2</sup>, ST. POPESCU<sup>2</sup>, T. SIMPLACEANU<sup>2</sup>**

<sup>1</sup>*Dept. of Biology, "Babes-Bolyai" University, Cluj-Napoca, Romania*

<sup>2</sup>*National Institute for Research and Development of Isotopic and Molecular Technologies, P.O.Box 700, 400293 Cluj-Napoca*

**ABSTRACT.** Human erythrocytes were exposed to two different magnetic field condition compared with terrestrial one (0.5 gauss): zero magnetic field, and 3 gauss magnetic field. In near null magnetic field no effect on  $\text{Li}^+$  influx through human erythrocyte membrane it was observed, for up to 45 hours exposure. After 71.5 h it was obtained a small increase of total  $\text{Li}^+$  influx and  $\text{Li}^+$  influx by passive diffusion mechanism. In 3.0 gauss magnetic field condition, for up to 14 hours exposure the  $\text{Li}^+$  influx by passive diffusion mechanism increased slight and by  $\text{Na}^+ - \text{K}^+$  pump mechanism decreased  $\approx 50\%$ .

**Key Words:** ion transport,  $\text{Li}^+$  transport, passive diffusion,  $\text{Na}^+ - \text{K}^+$  pump, erythrocytes and magnetic field.

### INTRODUCTION

The influx of lithium ion in human erythrocytes is known to occur by the following mechanisms: a) passive diffusion along its electrochemical gradient; b) active transport by the  $\text{Na}^+ - \text{K}^+$  ATPase pump as  $\text{Li}^+$  compete with  $\text{K}^+$  at the external site of the pump.

The most recent research on the ions transport through biomembranes is dedicated to the influences of the physical and environmental factors upon the transport mechanism.

Complex information on the effect of low-leveled magnetic field upon different biophysical processes might be found in bibliography connected to the field while their effect upon the ion transport through biomembranes is a restricted topic in terms of the information provided. The space-flights have increased interest towards these effects. The spaceman leaves behind gravity and atmosphere and comes to a very weak near null magnetic field.

The present work is concerned with  $\text{Li}^+$  influx in human erythrocyte by passive diffusion and  $\text{Na}^+ - \text{K}^+$  pump mechanism under the influence of near null magnetic field and 3.0 gauss magnetic field.

### MATERIALS AND METHODS

Human blood in citrate was collected from apparent healthy subjects. The whole blood was exposed to magnetic field in the 0,59-0,62 T intensity domain. A minimum of two samples were exposed to the same time at room temperature. The experimental method we used for  $\text{Li}^+$  transport mechanism through human erythrocyte membranes was similar to that described by Canessa ... [15]. We adapted it to the investigation of drug and gamma radiation effects on the  $\text{Li}^+$  influx and efflux through human erythrocytes membranes [9,16].

The effect of high magnetic field on  $\text{Li}^+$  influx was calculated using the  $(\Delta\text{Li}^+_{\text{influx}}/\text{influx}_c) \times 100$ , where  $\Delta\text{Li}^+_{\text{influx}} = (\text{Li}^+_{\text{influx}})_{\text{magnetic field exposed}} - (\text{Li}^+_{\text{influx}})_{\text{control}}$ .

### RESULTS AND DISCUSSION

The effect of zero magnetic field on the total  $\text{Li}^+$  influx is illustrated in Table 1.

The effect of zero magnetic field on the  $\text{Li}^+$  influx by passive diffusion mechanism is illustrated in Table 2.

The effect of zero magnetic field on the  $\text{Li}^+$  influx by  $\text{Na}^+ - \text{K}^+$  pump mechanism is illustrated in Table 3.

Table 1

T [h]	n	Total Li <sup>+</sup> influx [mmol/(I <sub>ERTR</sub> xh)]		$\frac{\Delta Influx}{Influx_c} \times 100$ [%]
		Control	Near null magnetic field	
11.5	4	2.59±0.06	2.64±0.12	2.2±3.6
23.5	5	2.53±0.12	2.59±0.16	2.4±3.1
46.0	7	1.95±0.26	1.96±0.33	0.5±3.1
71.5	5	1.51±0.07	1.66±0.05	10±1.5

Table 2

T [h]	n	Li <sup>+</sup> influx by passive diffusion [mmol/(I <sub>ERTR</sub> xh)]		$\frac{\Delta Influx}{Influx_c} \times 100$ [%]
		Control	Near null magnetic field	
11.5	4	1.88±0.07	1.92±0.11	1.7±2.4
23.5	5	1.78±0.15	1.83±0.21	2.2±4.4
46.0	7	1.75±0.23	1.76±0.35	0.6±3.9
71.5	5	1.28±0.04	1.43±0.04	11.7±1.1

Table 3

T [h]	n	Li <sup>+</sup> influx by Na <sup>+</sup> -K <sup>+</sup> pump [mmol/(I <sub>ERTR</sub> xh)]		$\frac{\Delta Influx}{Influx_c} \times 100$ [%]
		Control	Near null magnetic field	
11.5	4	0.70±0.09	0.73±0.09	4.1±8.4
23.5	5	0.75±0.16	0.77±0.15	1.9±5.4
46.0	7	0.21±0.02	0.20±0.02	0.9±8.0
71.5	5	0.23±0.02	0.23±0.02	0.5±5.9

In near null magnetic field no effect on Li<sup>+</sup> influx through human erythrocyte membrane it was observed, for up to 45 hours exposure. After 71.5 h it was obtained a small increase of total Li<sup>+</sup> influx and Li<sup>+</sup> influx by passive diffusion mechanism.

The effect of 3.0 gauss magnetic field on the Li<sup>+</sup> influx by passive diffusion mechanism is illustrated in Table 4.

Table 4

T [h]	n	Li <sup>+</sup> influx by passive diffusion [mmol/(I <sub>ERTR</sub> xh)]		$\frac{\Delta Influx}{Influx_c} \times 100$ [%]
		Control	3 gauss magnetic field	
3	3	1.61±0.37	1.67±0.39	3.2±1.7
6	2	1.63±0.15	1.73±0.14	6.5±1.5
14	2	1.27±0.10	1.58±0.11	26.6±22.2

The effect of 3.0 gauss magnetic field on the Li<sup>+</sup> influx by Na<sup>+</sup>-K<sup>+</sup> pump mechanism is illustrated in Table 5.

Table 5

T [h]	n	Li <sup>+</sup> influx by Na <sup>+</sup> -K <sup>+</sup> pump [mmol/(I <sub>ERTR</sub> xh)]		$\frac{\Delta Influx}{Influx_c} \times 100$ [%]
		Control	3 gauss magnetic field	
3	3	0.65±0.07	0.48±0.12	-25.8±12.5
6	2	0.62±0.12	0.43±0.23	-30.6±18.7
14	2	0.86±0.15	0.39±0.14	-56.8±9.2

In 3.0 gauss magnetic field condition, for up to 14 hours exposure the  $\text{Li}^+$  influx by passive diffusion mechanism increased slight and by  $\text{Na}^+\text{-K}^+$  pump mechanism decreased  $\approx 50\%$ .

We may conclude that there is an effect of the 3 gauss magnetic field upon the  $\text{K}^+$  channel protein, namely an increase of  $\text{Li}^+$  permeability, upon  $\text{Na}^+\text{-K}^+$  ATPase namely a decrease in its activity.

## REFERENCES

1. C. Brugnara, W. H. Churchill, *Transfusion* 32 (3), 1992, 246-252
2. V. A. Louginov, I. M. Timonin, B. I. Michenko, V. I. Klimovitski, *Axia. Kosm. Ekolog. Med.* 26 (5), 1992, 71-75
3. C. Bindea, T. Simplaceanu, I. Chereji, V. V. Morariu, *Analele Universitatii din Oradea, Fizica Tom IV*, 1996, 42-50
4. T. Simplaceanu, C. Bindea, I. Chereji, V.V. Morariu, *Analele Universitatii din Oradea, Fizica Tom IV*, 1996, 135-144
5. C. Bindea, T. Simplaceanu, I. Chereji, *Analele Universitatii din Oradea, Fizica Tom VIII*, 1998, 63-72
6. C. Bindea, T. Simplaceanu, S. Kreibik, S. Popescu, *Analele Universitatii din Oradea, Fizica Tom VIII*, 1998, 55-62
7. C. Bindea, T. Simplaceanu, S. Popescu, S. Kreibik, *Analele Universitatii din Oradea, Fizica Tom VIII*, 1998, 45-54
8. T. Simplaceanu, C. Bindea, S. Popescu, G. Cristea, *Analele Universitatii din Oradea, Fizica Tom VIII*, 1998, 233-244
9. C. Bindea, V. V. Morariu, I. Chereji, *Cytobios* 93, 1998, 23-31
10. Lorelai I. Ciortea, V. V. Morariu, Alina Todoran, S. Popescu, *Electro – and Magnetobiology*, 20 (2), 2001, 151-163
11. V. V. Morariu, Daniela Ciorba, Silvia Neamt, *Electro – and Magnetobiology* 19 (3), 2000, 289-302
12. Daniela Ciorba, V. V. Morariu, *Electro and Magnetobiology* 20 (3), 2001, 313-321
13. T. Simplaceanu, Dorina Bratfacean, C. Bindea, D. Panfil, St. Popescu, *Analele Universitatii din Oradea, Fizica Tom X*, 2000, 143-150
14. T. Simplaceanu, C. Bindea, Dorina Bratfacean, St. Popescu, D. Panfil, *Analele Universitatii din Oradea, Fizica Tom X*, 2000, 151-156
15. M. Canessa, N. Adragna, S. Solomon, M. Connolz, D. C. Tosteson, *N. Engl. J. Med.* 302, 1986, 772-776
16. C. Bindea, Alexandra Chifu, *Rev. Roum. Biochim.* 24, 1987, 185-192

## ADVANTAGES AND SHORTCOMINGS IN FT-RAMAN AND SURFACE ENHANCED RAMAN SCATTERING OF TWO DIFFERENT ENZYMES

**S. CAVALU<sup>1</sup>, S.CANTA-PANZARU<sup>2</sup>, W.KIEFER<sup>3</sup>**

<sup>1</sup>*University of Oradea, Faculty of Medicine and Pharmacy, Biophysics dept., P-ta 1 Decembrie nr.10, Oradea, 3700, Romania, scavalu@rdslink.ro*

<sup>2</sup>*Babes-Bolyai University, Physics Faculty, Optics and Spectroscopy Dept, Kogalniceanu 1, RO 3400 Cluj-Napoca, Romania*

<sup>3</sup>*Institut für Physikalische Chemie, Universität Würzburg, Am Hubland, 97074 Würzburg, Germany*

**ABSTRACT.** Mammalian peroxidases are fundamentally distinct from plant peroxidases. The resonant Raman spectrum, in the high frequencies region, is dominated by modes other than the heme oxidation state marker band ( $\nu_4$ ) which is the most intense of the porphyrin modes under Soret excitation. However, on passing from RR to SERRS, this marker band is upshifted and strongly enhanced. As shown in the RR spectrum of lactoperoxidase (powder sample), this enzyme exhibits only a fluorescent feature upon excitation with the green light, but the SERRS spectra were successfully obtained upon excitation both with the green and the red laser line.

### INTRODUCTION

An important field of application of lasers in medicine is related to laser spectroscopic characterization of biomedically relevant molecules and processes in order to study structural-functional properties. Laser spectroscopic methods can be applied non-invasively under ambient conditions in a biological environment. This work summarizes some interesting results concerning resonant Raman and SERRS investigations on silver nanoparticles of enzymes from two different classes: lactoperoxidase and horseradish peroxidase.

SERS techniques, due to the high sensitivity and selectivity, can be successfully used to investigate the versatility to adsorption and conformational changes of proteins which occur as a consequence of proteolysis, lyophilization or dehydration.[1]. In the case of hemic proteins, it is possible to investigate by means of SERRS *exclusively* the vibrations of the chromophore, without interference by scattering of the huge surrounding protein. As a further advantage, the fluorescence background, which can make normal Raman spectroscopy extremely difficult, has been quenched in many SERRS experiments by new nonradiative decay channels provided by the SERS-active metal.

### EXPERIMENTAL

**Chemicals.** Lactoperoxidase and horseradish peroxidase (type VI) were received from Sigma and used without further purification. Samples were prepared in phosphate buffer physiological saline at a final concentration of  $10^{-3}$  mol/l. A small amount of 5 ml from each sample was lyophilized for 30 hours at  $-50^{\circ}\text{C}$  and then used as powder Raman sample. Colloidal silver substrate was prepared according to the Lee-Meisel procedure [4]. The absorption maximum of the freshly prepared colloid was centered at 423 nm. For the SERRS measurements, a small amount of about  $10\ \mu\text{l}$   $10^{-2}$  mol/l protein solution was added to 2 ml colloidal silver, resulting in a final sample concentration of  $5 \times 10^{-5}$  mol/l.

**Apparatus.** A micro-Raman setup was employed in order to record the Raman spectra of lyophilized powder samples. The 514.5 nm and 630 nm line of an argon ion laser (Spectra Physics, Model 166) was applied for excitation. The scattered light was collected in back-scattering geometry by focusing a x50 objective (Olympus ULWD MSPlan50) on the entrance slit of a



spectrometer LabRam, Dilor with 1800 grooves/mm diffractive grating. The detection system consisted of a charge-coupled multichannel detector (CCD, SDS 9000 Photometrics). For the SERS spectra we used an x10 objective, a laser power of 1 mW and an exposure time of 1000 s with 4 overlaps. Each Raman spectrum is the result of 4 accumulations with 100 sec. exposure time using a laser power of about 12 mW. The spectral resolution was  $3\text{ cm}^{-1}$ .

## RESULTS AND DISCUSSION

The structure of the prosthetic group in lactoperoxidase and horseradish peroxidase is presented in fig.1. Native form of lactoperoxidase is six coordinated, high spin and the sixth ligand is suggested to be a water molecule or an alcoholic hydroxyl group[3]. The first coordination shell structure is different from that of horseradish peroxidase which is a high spin five coordinate heme system [4,5].

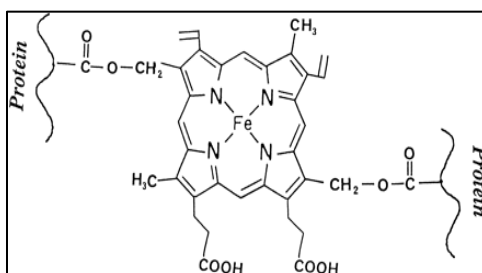


Fig. 1. Structure of the prosthetic group in lactoperoxidase and horseradish peroxidase .

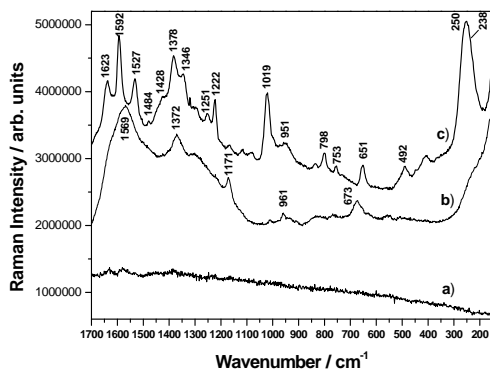


Fig. 2. RR spectrum of lactoperoxidase powder, the native protein (a), and SERRS spectra of lactoperoxidase at 630 nm (c) and 514 nm (b) excitation line.

As shown in fig.2., the RR spectrum of lactoperoxidase (powder sample) exhibit only a fluorescent features upon excitation with the green light, but the SERRS spectra were successfully obtain upon excitation both with the green and the red laser line .On can observe that upon the red light excitation, the resonant response offer much more details then the other one (fig.2). In the high frequencies region, the common features of the skeletal stretching modes of metalloporphyrin are present (table 1) and assigned to in plane vibrational modes  $\nu_{10}, \nu_2, \nu_{11}, \nu_{19}, \nu_3, \nu_4$ . Those frequencies, which are enhanced under the red light excitation in our SERRS spectrum, have been generally used to characterize the oxidation and spin state of the heme iron [6,4]. There are also contributions from the peripheral vinyl stretching vibrations, that might be overlapped the  $\nu_{10}$  band,

and the scissor modes of the two vinyls,  $\delta(=CH_2)$ . The assignments in Table 1 are based on the comparison with the solution spectra obtained under different excitation line [23,24]. In the low frequencies region we can notice an enhancement of the modes assigned to the phenyl ring breathing,  $\pi$  out of plane vibrations, pyrrole fold vibrations and especially the stretching vibration of the Fe-N<sub>histidine</sub> mode upon the red light excitation.

**Table 1.**  
Assignment of the main frequencies in RR and SERRS spectra of lactoperoxidase (native protein) upon excitation with 630 nm and 514 nm (ref.7,8). Abbreviations: w-weak, vw-very weak,

Assignments RR (solution. pH=7)	SERRS 630 nm	SERRS 514 nm
1622 $\nu_{10}$ , $\nu(C=C)$	1623 m	
1593 $\nu_2$	1592 vs	1569 vs
1560 $\nu_{11}$	---	
1527 $\nu_{19}$	1527 m	---
1484 $\nu_3$	1484 w	---
1428 $\delta(=CH_2)$	---	---
1373 $\nu_4$	1378 vs	1372 vs
1340 $\delta(=CH_2)$	1346 w	---
1212 $\nu_5, \nu_8$	1222 s	1222 vw
1170 $\nu(C-C)$	1171 w	1171 m
994 Phenyl breathing	1019 vs	---
752 $\pi$ out of plane	951 m	961 w
674 Pyrrole fold	798 m	---
496 $\nu(Fe-Nhis)$	753 w	---
	651 m	673 m
	492 m	---
	250 vs	240 sh

s-strong, vs-very strong, m-medium, sh-shoulder.

Fig. 3. presents the resonance Raman spectrum of horseradish peroxidase (native protein, powder sample) at 630 nm excitation together with the SERRS spectrum on silver sol at 514 nm excitation. As compared to the literature [7,9-11], RR spectrum of horseradish peroxidase upon red light excitation (630 nm) show a modified intensity pattern relative to that observed under Soret excitation (413 nm). This spectrum, in the high frequencies region, is dominated by modes other than the heme oxidation state marker band ( $\nu_4$ ) which is the most intense of the porphyrin modes under Soret excitation. However, on passing from RR to SERRS, this marker band is upshifted and strongly enhanced (Table 2). The band at  $1631\text{ cm}^{-1}$ , which has been proposed to be a vinyl stretching mode, appears almost invariably in Soret excited spectra [4,7], obscuring the  $\nu_{10}$  mode, a spin state marker frequency. This band is absent in our RR spectrum upon excitation with the green light. The  $\nu_2$ ,  $\nu_{10}$  and some other modes above  $1550\text{ cm}^{-1}$  (in the RR spectrum) involve expansion and contraction motion of the outer periphery of the porphyrin ring ( $\nu_{C-C}$ ) to a greater extent than  $\nu_4$  which is a ring breathing mode involving motions of atoms ( $\nu_{C-N}$ ) in the inner core. The selective enhancement of  $\nu_2$  and  $\nu_{10}$  modes might be therefore reflective of displacement of equilibrium nuclear positions in the excited state relative to the ground state of the heme periphery [5]. In the SERRS spectrum, only the  $\nu_{10}$ ,  $\nu_2$  and  $\nu_4$  stretching modes are selectively enhanced.

## CONCLUSIONS

Normal resonance Raman and SERRS spectroscopy allowed an interesting comparison between the results obtained with these techniques. On passing from RR to SERRS large differences can be observed both in band positions and relative intensities. SERRS technique is a very important tool for measuring small amounts (nmol, pmol and even lower) of proteins due to its high selectivity and huge enhancement of the Raman signal combined with (pre-) resonance amplification contribution. SERRS spectra of peroxidases under red light excitation offer much more details than the green light excitation.

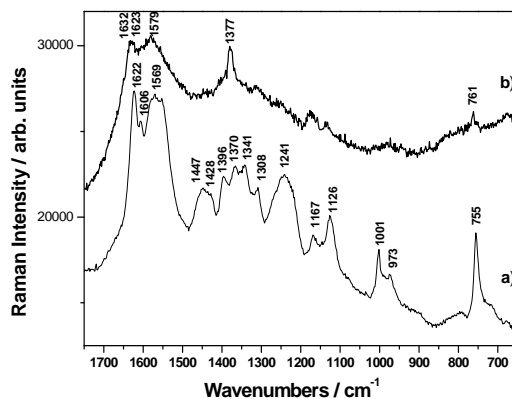


**Fig. 3.** Resonance Raman spectrum of horseradish peroxidase (native protein, powder sample) at 630 nm excitation (a) and SERRS spectrum on silver sol at 514 nm excitation (b).

**Table 2.**

**Assignment of the main frequencies in RR and SERRS spectra of horseradish peroxidase (native protein) upon excitation with 630 nm and 514 nm respectively (ref. 5,7,9,10).**

**Abbreviations: w-weak, s-strong, vs-very strong, m-medium**

RR solution (pH=7)	RR Powder 630 nm	SERRS 514 nm
1631 $\nu_{10}$	----	1632 m
1620 $\nu(\text{C}=\text{C})$	1622 vs	1623 m
1575 $\nu_2$	1569 m	1579 m
1430 $\delta(=\text{CH}_2)$	1447 s	1430 w
1374 $\nu_4(=\text{C}-\text{N})$	1370 m	1377 vs
1341 $\delta(=\text{CH}_2)$	1341 m	1341 w
1302	1308 m	1310 w
1238 $\delta(\text{C}-\text{H})$	1241 vs	----
1170 $\nu(\text{C}-\text{C})$	1167 m	1170 m
1127 $\nu(\text{C}-\text{C})$	1126 vs	1128 w
1000 ph breathing	1001 vs	---
973	973 m	---
755 } $\pi$ out of plane	755 vs	761 m

## REFERENCES

- [1] S. Canta-Panzaru, S.Cavalu, N. Leopold, W. Kiefer, *J. Mol. Struct.*, 565-566, (2001) 225-229.
- [2] P. C. Lee, D. Meisel, *J. Phys. Chem.*, 84, (1982), 3391.
- [3] L. A. Andersson, S.A. Bylkas, A. E. Wilson, *J. Biol. Chem.*, 271, 7, (1996), 3406-3412.
- [4] A. Feis, M.P. Marzocchi, M. Paoli, G. Smulevich, *Biochemistry*, 33, (1994), 4577-4583.
- [5] V. Palaniappan, J. Turner, *J. Biol. Chem.*, 264, 27, (1989), 16046-16053.
- [6] T. G. Spiro in *Iron Porphyrins II*, Lever and Gray (eds), Addison-Wesley Pub.Co, (1983), p.89.
- [7] T. Kitagawa, S. Hashimoto, J. Teraoka, S. Nakamura, H. Yajima, T. Hosoya, J. A. Manthey, N. J. Boldt, D. F. Bocian, S. I. Chan, *J. Biol. Chem.*, 261, 15, (1986), 6734-6741.
- [8] G. Smulevich, *Biospectroscopy* (1998), 4, S3-S17.
- [9] B.D.Howes, A. Feis, L. Raimondi, C. Indiani, G. Smulevich, *J. Biol. Chem.*, 276, 44, (2001), 40704-40711.
- [10] E. J. Bjerneld, Z. Foldes-Papp, M. Kall, R. Rigler, *J. Phys. Chem. B.* 106, (2002), 1213-1218.

## HEMOGLOBIN SOLUTIONS IN ULTRASONIC FIELD

ALINA RAPA<sup>1</sup>, SERVILIA OANCEA<sup>2</sup>, DANA DOROHOI<sup>3</sup>

<sup>1</sup>*C.A.Johnson High School Columbia SC (USA), e-mail: arapa@richlandone.org*

<sup>2</sup>*Univ. of Agronomy and Veterinary Medicine, Iasi, Romania, e-mail:lioancea@univagro-iasi.ro*

<sup>3</sup>*“A.I.Cuza” Univ, Faculty of Physics, Iasi, Romania*

**ABSTRACT.** High-frequency acoustic waves interact with living systems. Knowledge on the ultrasound propagation process through mammalian tissues is of the great interest for application in medicine, pharmacy and agriculture. In what hemoglobin is concerned, hemoglobin as well as the hematocrit and erythrocyte counting is of a great importance for screening and diagnosis related to anemia. This is the reason for us to study some experimental aspects linked with behavior of hemoglobin in ultrasonic field. Ultrasound velocity was interferometrically determined. Adiabatic coefficient of compressibility has been estimated from ultrasound velocity and the solution density. At 20°C, the ultrasound velocity in solutions increases with the concentration of cow blood hemoglobin in water solution, ranging between 1520-1620 m/s for concentration between 5-40 mg/cm<sup>3</sup>. For human hemoglobin ultrasound velocity in water solutions at 20°C ranged between 1492-1540 m/s, also increasing with concentration.

Concomitantly, an increase of absorption coefficient with concentration was determined. The water absorption was subtracted from the total absorption to obtain information on protein absorption.

### 1. Introduction

Knowledge on the ultrasound propagation process through mammalian tissues is of the great interest for application in medicine, pharmacy and agriculture [1], [2]. In what hemoglobin is concerned, hemoglobin as well as the hematocrit and erythrocyte counting is of a great importance for screening and diagnosis related to anaemia [3]. The development of atherosclerosis and the failure of vascular grafts are often associated with specific characteristic of local hemodynamics. Clinically, ultrasound velocity measurement can be used to estimate wall shear rate in vivo [4].

Investigation of blood properties from various species has attracted considerable interest and comparative studies have yielded interesting aspects about the behaviour of blood [5]. [6].

### 2. Materials and methods

We obtained the hemoglobin solutions by treating washed, packed red blood cell from cow blood with toluene to liberate the hemoglobin. By centrifugation, the stroma associated with toluene is separated from the heavier hemoglobin solution. Then a hemoglobin solution can be obtained by adding distilled water. The action of osmotic forces on the red blood cells causes hemolysis and free hemoglobin is distributed through the solution.

We didn't make spectral analysis in order to estimate the portion of oxihemoglobin or methemoglobin in the studied solutions, because the ultrasound absorption by these derivatives is substantially the same [7]. Ultrasound velocity was interferometrically determined using an ultrasound pulse method. A laboratory device designed and assembled in our laboratory was used to measure wave velocity and to test behaviour of ultrasonic wave in a hemoglobin sample (Fig.1). An ultrasonic oscillator gives a signal that propagates through the hemoglobin solution. The direct signal and the one propagated through the hemoglobin solution are simultaneously visualized on the oscilloscope screen [8]. Velocities were measured, for different US frequencies, using the value of propagation time through solution:

$$\Delta t = n \tau$$

where: -n represents the number of divisions that separates the two signals on the screen

-  $\tau$  is the time base of oscilloscope

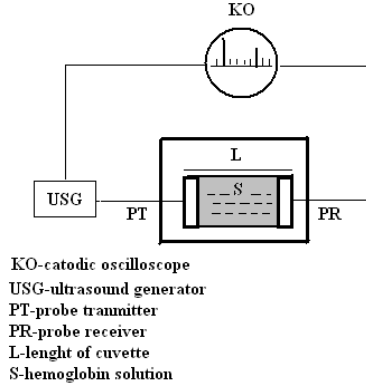


**Fig. 1.** Bloch schema for determination of the velocity and absorption coefficient of ultrasound in hemoglobin solutions

The ultrasound velocity is:

$$c = \frac{L}{\Delta t}$$

with L-the length of the propagation cell. Ultrasound absorption has been estimated in terms of absorption ( $\alpha$ ) per wavelength ( $\lambda$ ),  $\alpha\lambda$  in nepers. Absorption coefficient  $\alpha$  has been measured from the intensity I of two signals at the distance L related to the oscillator:

$$\alpha = \frac{\ln \frac{I_1}{I_2}}{L_2 - L_1}$$

The wavelength of US has been calculated with formula:

$$\lambda = \frac{c}{\nu}$$

where are ultrasound velocity and  $\nu$  the ultrasound frequency.

### 3. Results and discussion

The results of the measurements for US velocity are presented in Table 1.

**Table 1.**

**US velocity in hemoglobin solution.**

	1	2	4	7
5	1520.0	1523.0	1524.0	1524.3
10	1530.1	1530.4	1530.8	1531.2
15	1541.5	1541.5	1541.7	1542.0
20	1562.4	1562.5	1563.1	1563.3
25	1581.7	1582.2	1582.4	1582.7
30	1607.7	1608.2	1608.7	1609.3
40	1619.1	1619.3	1620.1	1620.8

The dependence of US velocity by Hb concentration (mg/cm<sup>3</sup>) for 1MHz is given in the Fig. 2.

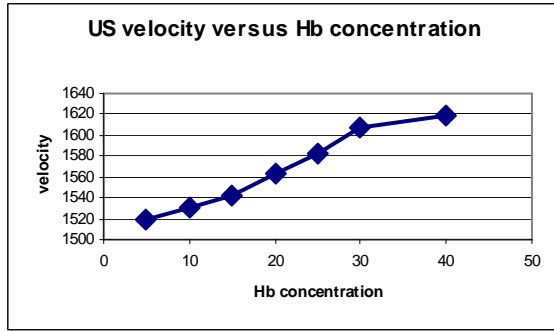


**Fig. 2.** US velocity versus Hb concentration for 1 MHz

The dependence of the US velocity from frequency of the ultrasonic wave is given in Fig. 3.

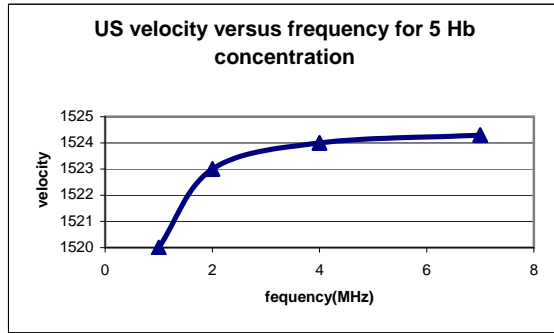


**Fig. 3.** US velocity as a function of frequency for 5 mg/cm³ concentration

For 40mg/cm³ concentration the dependence US velocity from frequency is given in Fig.4.

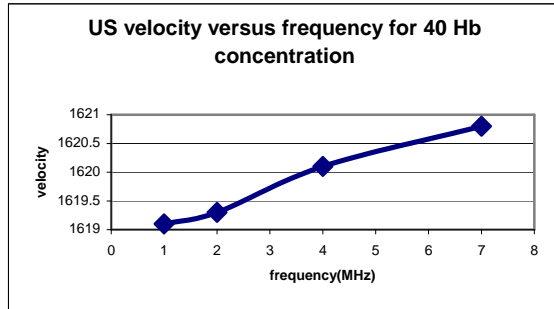


**Fig. 4.** US velocity as a function of frequency for 40mg/cm³ concentration

The results of the measurements for absorption are presented in Table 2 .

**Table 2.**

**US absorption ( $\alpha\lambda$  ) \* 10³ (nepers) in Hb solutions**

	1	2	4	7
5	0.64	0.71	0.80	1.00
10	0.74	0.78	0.81	1.20
15	1.82	2.10	2.20	2.50

## HEMOGLOBIN SOLUTIONS IN ULTRASONIC FIELD

	1	2	4	7
20	3.00	3.10	3.21	3.35
25	3.80	4.00	4.10	4.20
30	5.80	6.00	6.10	6.30
40	7.10	7.20	7.50	7.76

The US absorption versus Hb concentration for 1 MHz is given in Fig. 5.

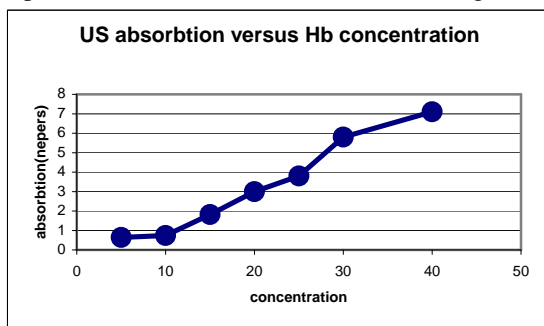


**Fig. 5.** US absorption versus Hb concentration for 1 MHz

### 4. Conclusions

1. Ultrasound velocity in hemoglobin solutions increases with the concentration of hemoglobin solution, these increases not being affected by ultrasound frequency.
2. Ultrasound velocity in hemoglobin solutions increases with the frequency but this dependence is different for different concentrations.
3. US absorption in hemoglobin solutions also increases with the concentration of hemoglobin solutions.

Further investigations will be developed in order to evaluate the US velocity and US absorption in hemoglobin solutions of blood for other animals.

### REFERENCES

1. B. Brown, E. J. Goodman, (1959), *Ultrasound de haute intensité*, Ed. Dunod.
2. V. Vasilescu, N. Iosif (editors), (1984), *Ultrasunetele in medicina si biologie*, Ed. Medicala, Bucuresti.
3. Y. Suzuki, (1998), *Anal Sci*, Vol.14,1013-1016
4. F. J. H. Gijzen, P. J. Brands, F. N. van de Vosse, J.D. Jansen, (1998), *J. of Vascular Investigation*, 4, 187-196
5. Windberger, U., Ribitsch, V., Resch, K., *The viscoelasticity of blood and plasma in pig, horse, dog, ox and sheep*, *Journal of Experimental Animal Science*, 1993/1994, 36: 89 – 95.
6. S. Oancea, A. Răpă, N. Cojocaru, V. Rusu, (2000), *Egyptian J. of the Biophysical Society*, Vol.6, No.1, 1-5.
7. E. L. Carstensen, H. P. Schwan, (1959), *J. Acoust. Soc. Amer.*, 31(3), 305-311
8. F. Severcan, D. Dorohoi, D. Creanga, (2001), *Studia Universitatis Babeş Bolyai Physica*, Special Issue, 165-175

## METABOLIC ACTIVITY OF BACTERIA IN ZERO MAGNETIC FIELD. THE INFLUENCE OF GEOMAGNETIC FLUCTUATIONS

**SILVIA NEAMTU<sup>1</sup>, V. V. MORARIU<sup>1</sup>, E. BOLDIZSAR<sup>2</sup>**

<sup>1</sup>National R&D Institute for Isotopic and Molecular Technologies, P.O. Box 700,  
400293 Cluj-Napoca

<sup>2</sup>Microbiology Department, University of Agricultural Sciences and Veterinary  
Medicine, Cluj-Napoca

**ABSTRACT.** The degradation of glucose, lactose and albumin by *Salmonella*, *E. Coli* and nonspecific bacteria activity in zero magnetic field (ZMF) and geomagnetic field as control was investigated using spectrophotometric and two electrophoresis methods. The results showed that ZMF conditions generally favor the bacteria activity and growth. Significant sensitivity of bacteria to natural variations of magnetic field was also observed. In the presence of major magnetic storms metabolic activity of gram(-) germs was inhibited.

### INTRODUCTION

Zero magnetic field (ZMF) is an important reference in studies concerning the effect of geomagnetic field (GMF) on living systems and also is a tool to investigate the sensitivity of organisms to an extremely change of magnetic environment (magnetic polarity reversal, spaceflight inframagnetic field, interplanetary very low magnetic field). There are few but significant evidences concerning cellular [1,2,3] and whole organism [4] response to the lack of static component of geomagnetic field. In order to enlarge the picture of the simplest organisms behavior in ZMF we investigated the metabolic activity of *Salmonella*, *E. Coli* and nonspecific gram(-) bacteria during the lag phase of cells multiplication. The effect obtained was compared with the results of bacteria growth tests (data not published) and was analyzed in respect with the variation of geomagnetic activity during the period of experiments. Our experimental set up consists of a coil that compensates the static component of geomagnetic field. However the natural fluctuations remain operative. Such analysis allows us to perceive or to remove the possible contribution of natural magnetic disturbance (magnetic storms) to the effect recorded and also to emphasize the sensitivity of bacteria or of any system investigated to inframagnetic field (nT, Hz).

### MATERIALS AND METHOD

Static geomagnetic field (0,47 G) has been compensated with a factor of 100 in a pair of Helmholtz coils oriented along geomagnetic field lines. A group of bacteria cultures was exposed in ZMF in the space delimited by the coils and another group to natural GMF environment as control, in the same room at a significant distance from the coil. The temperature was kept at 24°C.

Metabolic activity of bacteria was measured by the degradation of sugar and albumin substrate in the presence of specific bacteria (*Salmonella sp.* and *E. Coli sp.*) and gram(-) bacteria. *Salmonella* and *E. Coli* activity was investigated in media with a minimum content of nutritive substance but rich in sugars (glucose, lactose) in the presence of blue bromthymol. The degree of glucose and lactose degradation was estimated spectrophotometrically by the decrease of bromthymol absorption peak. The pH variation of the medium has been determined simultaneously.

Agarose and SDS polyacrilamide electrophoresis methods were used to estimate the effect of gram(-) germs on albumin substrate.

Variation of natural fluctuation of GMF represented by Ap index values of geomagnetic activity (GMA) was downloaded from National Geophysical Data Center, USA for each period of the experiment.



**RESULTS AND DISCUSSION**

The decrease of glucose and lactose concentration in *Salmonella* respectively *E. Coli* cultures as a consequence of metabolic activity of bacteria in GMF and ZMF conditions is illustrated in Fig. 1a and 2a. Concomitant change of pH in cells suspension is also presented in Fig 1b and 2b.

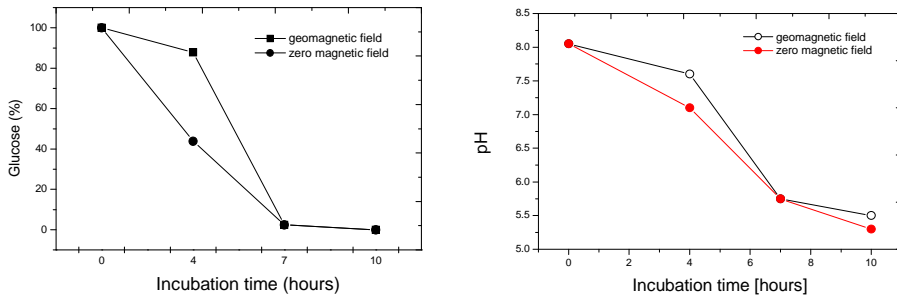


**Fig. 1a.** - Glucose degradation (a) and pH variation (b) in the presence of *Salmonella sp.* exposed in geomagnetic field and zero magnetic field at 24<sup>0</sup> C

After 4 hours glucose was significantly reduced in *Slamonella* cells suspensions exposed in ZMF (49,5% vs. GMF) and is entire metabolized after 7 hour in both magnetic environments. In the same time pH decrease attained 6,8% in ZMF. These results show the positive influence of ZMF on *Salmonella* germs activity and support the data obtained in the bacteria growth tests.

The decrease of lactose concentration and pH in *E. coli* cells suspension was less pronounced in ZMF conditions in respect with GMF. On the other hand, *E. coli* growth tests showed no changes. The sensitivity of bacteria to the changes of GMF seems to depend on the bacterial type.

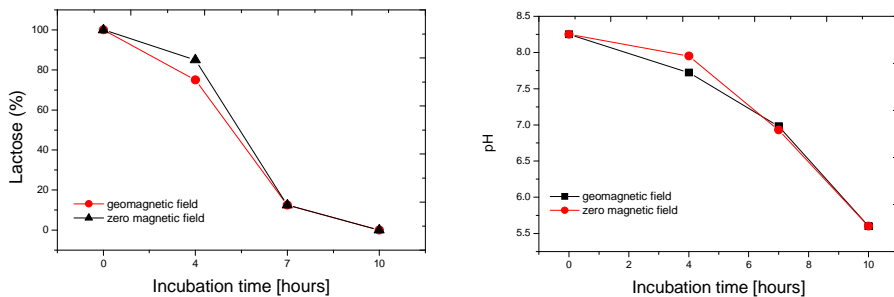


**Fig. 2.**– a) Lactose degradation and b) pH variation in presence of *E. coli* exposed in geomagnetic field and in zero magnetic field at 24<sup>0</sup>C

Bacteriological tests revealed the growth of gram(-) germs on the albumin as nutritive media. Both agarose gel electrophoresis and SDS poliacrylamide electrophoresis of albumin revealed significant increase of the degradation process in ZMF conditions. The increase of integrated aria of albumin band from 15% in GMF to ~25% in ZMF observed in the 5<sup>th</sup> incubation day (Fig.3) was explained by the appearance of new protein fractions due to the bacteria metabolic activity.

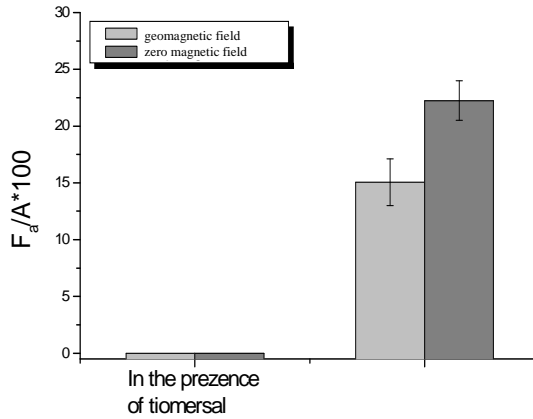


**Fig. 3.** – The percentage of new proteic fraction after 5 days of albumin incubation in geomagnetic field and in zero magnetic field with and without tiomersal

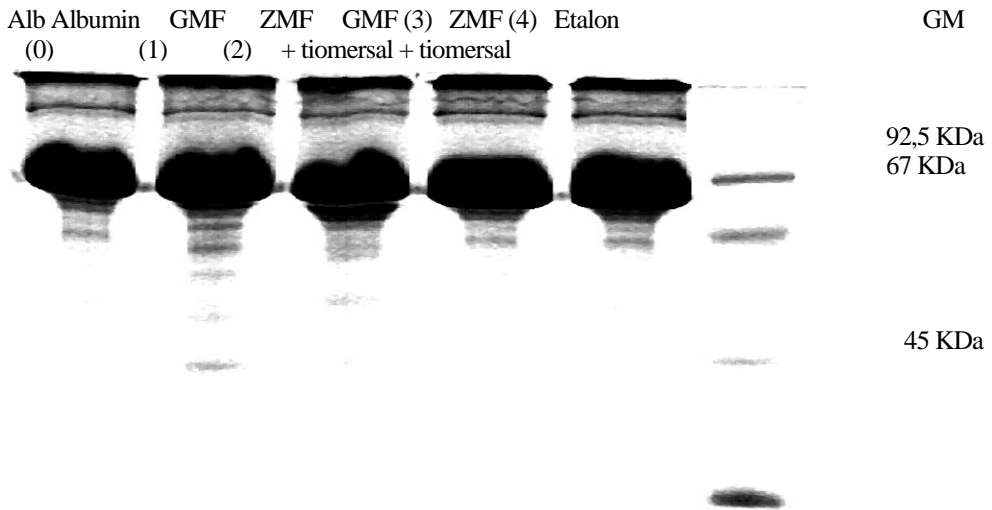


**Fig. 5.** - SDS poliacrylamide gel electrophoresis of albumin exposed 3 days in geomagnetic field and zero magnetic field with and without tiomersal as bactericide agent

The same results were obtained after 3 days of incubation using the second electrophoresis method. In the sample exposed to ZMF (Fig 4- poz 2) it was detected a protein fraction with molecular weight close to that of albumin, that emphasize significant degradation of the albumin molecule. The presence of small proteins showed less pronounced activity of bacteria in GMF (Fig 5- GMF(1)). A positive effect of ZMF on metabolic activity of gram(-) bacteria was also recorded in the cells growth experiments (data not shown).

Two series of investigations (albumin electrophoresis, bacteria growth tests) showed however no significant effects. The relation between biological effects recorded in ZMF and the



## **RADON EPIDEMIOLOGIC STUDIES. UNCERTAINTIES IN ASSESSING HEALTH RISKS FROM NATURAL RADIATION**

**ALEXANDRA FLORE, CONSTANTIN COSMA**

*“Babes-Bolyai” University, Faculty of Physics, Cluj-Napoca, 3400, Romania.*

**ABSTRACT.** Epidemiological studies of human health and natural radiation may provide a direct way of evaluating the estimates validity of risk at low doses that are based on groups with generally higher radiation doses. In the absence of direct quantitative evidence, risks have to be estimated by extrapolation from higher exposures where direct effects can be observed, sometimes received over a fairly short period of time.

Indoor radon is now believed to be the most important source of ionizing radiation in the environment.

However, uncertainties can effect the interpretation of these studies. Even though natural radiation forms the main source of radiation exposure for most people, obtaining reliable information from epidemiological studies of these exposures is not easy, because of low statistical power, confounding factors, combined effects with other agents, uncertainties in assessing exposure. This paper reviews some of these uncertainties, presents different types of epidemiologic studies, comparing their advantages and disadvantages, giving particular attention to residential radon and lung cancer.

### **Introduction**

During the last two decades, potential lung cancer risks due to inhalation of radon daughter products have been the subject of wide concern, not only because of the potential impact on the well-being of people living or working in high-natural environments, but also because of the high costs of radon remediation programs, for example, of uranium mining areas and private homes. Besides obvious economic, social, and psychological implications, the assessment of potential residential radon risks became an important test case for the validity of the linear-no-threshold LNT hypothesis, the related collective dose concept, and the value of epidemiological studies.

Indoor radon is now believed to be the most important source of ionizing radiation in the environment. Radon's adverse effects were first observed in miners, especially uranium miners, and now increased attention is being directed to its implications for the general population, in order to correctly estimate its health hazards. Based on miners' and some case control epidemiological studies, a large number of additional lung cancer in the population are due to residential radon, but also various recent studies (with never-smoking women in high-radon areas, as well as animal and cell experiments) indicate thresholds, perhaps even biopositive effects including the reduction of other types of cancer in areas with increased residential radon levels.

In the absence of direct quantitative evidence, risks have to be estimated by extrapolation from higher exposures where direct effects can be observed, sometimes received over a fairly short period of time. Particular examples are underground miners exposed to high levels of radon and the Japanese atomic bomb survivors. Epidemiological studies of human exposures to radiation, including residential radon, may provide means of assessing the validity of risk estimates based on the above extrapolation. But there are a lot of confounding factors and other agents that interfere because the subjects are placed in real life situation in a complex and changing human environment. In order to estimate the effects of radiation on population there have been developed models for low doses range from linear no-threshold to large thresholds, or considering hormesis [1], or the bystander effects [2].

## **2. Different types of epidemiological study**

For a study of natural radiation to be informative, it is necessary to maximize the statistical power [3] and to minimise the potential for bias or confounding factors. Bias represent systematic errors in the design or conduct of the study, while a confounding factor is the effect or one or more variables that are correlated with both the exposure and the disease outcome of interest.

### **2.1. Case-control study**

A case-control is an investigation that compares the exposure received by a group of persons with a disease (the cases) with a group of persons without the disease (the controls). It is not necessary to follow a large number of people for many years in order to identify the cases, and usually it is possible to obtain individual data on exposures by measurements in dwellings of radon or gamma radiation and the confounders by questionnaires. The bias may exist because of the retrospective nature of this type of epidemiological study, such as different participation rate in cases and controls, quality of information. Also the statistical power of one case-control study is not high.

Residential radon case-control studies have some advantages over other types of case-control studies in determining retrospective exposure, because a significant proportion of the radon exposure occurs in the home and the radon concentrations can be measured at some later date. Uncertainty in the estimating retrospective radon exposures increases when certain time periods in the 15 to 20-year time period before study are missing. For example some case-control studies in the USA [4] and Sweden, in order to reduce the bias due to estimating past exposure, measurements from glass items that were located in current and previous homes were performed. Only using the data containing integrated radon exposure over a longer period through glass measurements resulted in a statistically significant association between the radon gas and the risk of lung cancer.

### **2.2. Correlation study**

Known also as an “ecological” or “geographical” study, the correlation study is based on aggregated data for disease rates, exposures and possibly confounding factors. In the case of radon correlation study we look for a correlation between the lung cancer rate in certain geographical areas and the mean radon exposure in these areas. Since it is often possible to include large populations, the statistical power of correlation studies can be high. Smoking is an important bias/confounding factor in assessing the risk of lung cancer and also the differences between individual and aggregated levels versus aggregated exposure and confounders are important in the case of residential radon. [5]

### **2.3. Cohort study**

These studies are based on identifying a specific group of individuals and following them over time (prospectively or retrospectively) in order to determine mortality and disease incidence. The statistical power rises only if the cohort is followed for many years, but in the context of natural radiation, this study is not efficient. An important example is the study that has been conducted in China [6].

## **3. A discussion on statistical power**

In order to estimate at best the relationship between radon exposure and lung cancer mortality the statistical power should be increased. A possible approach could be the increase of the number of cases in a study by having a lot of persons with high/low exposure. Another one could be to quantify the results of existent studies, or by using their data to interpret them in different statistical models.

The meta-analysis method is based on the summary of different published studies in order to obtain an overall estimate of risk. The results of individual studies range from positive to negative correlations as shown in fig.1. For example, Cohen [5] observed that the higher exposure to domestic radon correlated with the lower incidence of cancer (negative correlation), whereas Lubin and Boice [7] have reported a positive one, in agreement with the extrapolated data from the underground miners.

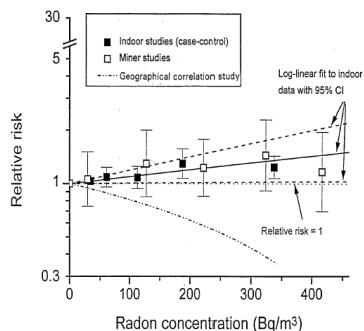


**Fig. 1.** – Summary relative risk from meta-analysis of indoor radon studies [8]

Also is used another method, called combined or parallel analysis, which consists in interpreting the raw data obtained in different studies and comparing them, in order to examine the importance of various factors and their relevance such as smoking, age, gender.

The most serious problem appears to be the retrospective evaluation of smoking habits, and the underestimation of use could invalidate some of the well-known case-control studies. There is a substantial evidence for a threshold, or a U-shaped response curve [9] that can explain the beneficial effects attributed to radon in balneology.

Also, at the molecular level new assumptions and effects are studied in order to get a better perspective of low dose response. The bystander effect [2], used originally to develop oncogenesis transformation in vitro, has been extended to low dose rates. Radiation response is considered as a superposition of bystander and the linear direct effects, and these data are fitted to the data from miners exposed to radon. The results suggest that, at low radon exposure, the risk could be dominated by bystander effects. There are new techniques and considerations to be made in order to better understand the significance of the epidemiological data thus increasing the statistical power of the studies. The environmental biodosimetry can give an estimate of cumulative lifetime dose, improving the accuracy and reducing the uncertainties in ecological risk assessment.

Implementing these methods to enhance the validity of risk estimates from the studies of natural radiation would provide in the future a better estimate of the lung cancer risks from residential radon.

## BIBLIOGRAPHY

- [1] Jawarowski, Z. *Beneficial Effects of Radiation and Regulatory Policy*. Hormesis and Radioadaptive Response Web Site <http://www.angelfire.com/mo/radioadaptive/>, Australian Physical & Engineering in Medicine, 20, 1997
- [2] Brenner, D. J., Sachs, R. K. *Bystander Effects May Dominate Domestic Radon Risk But Current Risk Estimates are Probably Okay*. *Radiat. Res.*, 158, 2002, 790-791
- [3] Muirhead, C. R. *Uncertainties in assessing health risks from natural radiation, including radon*. Elsevier. International Congress Series 1225, 231-237.
- [4] Field R. W, *A Review of Residential Radon Case-Control Epidemiologic Studies Performed in the US*, *Reviews on Environmental Health*, vol. 6, no.3, 2001, 151-167.
- [5] Cohen, B. L. *Test of the linear-no threshold theory of radiation carcinogenesis for inhaled radon decay products*. *Health Physics* 68, 1995, 157.
- [6] Tao, Z., Zha Y., et al., *Cancer mortality in high background radiation area of Yangjiang, China, 1979-1995*. *Natl. Med. J. China* 79, 1999, 487-492.
- [7] Lubin J. H. and Boice, J. D, *Lung Cancer Risk from residential Radon: Meta-analysis of Eight Epidemiological Studies*. *J. National Cancer Inst.* 89, 1997, 49-57.
- [8] Lubin, J. H. Rejoinder: *Cohen's response to "On the discrepancy between epidemiologic studies in individuals of lung cancer and residential radon and Cohen's ecologic regression"*. *Health Phys.*, 75, 1998, 29-30.
- [9] Becker, K. *residential radon and the LNT hypothesis*. Elsevier. International Congress Series 1225, 2002, 259-266

## MODELING THE PROPAGATION OF FEMTOSECOND LASER PULSES IN GASEOUS MEDIA

VALER TOSA

*National Institute for R&D of Isotopic and Molecular Technologies,  
P.O. Box 700, 3400 Cluj-Napoca, Romania*

**ABSTRACT.** A mathematical model for the propagation of femtosecond laser pulses in gaseous media is presented. The propagation of ultrashort laser field was solved in the paraxial approximation for a 3D geometry with axial symmetry. A Fourier transform coupled to a finite difference method was chosen to solve the propagation equation of the pulsed electromagnetic wave. The linear and nonlinear dispersion effects as well as the presence of the electron plasma due to the ionization of the atoms was taken into account. The atomic rate of ionization was calculated by various models proposed in the literature and is shown to influence fairly well the field configuration in the interaction region. The field configuration is found to be in good agreement with the experimental data of laser produced fluorescence in the interaction region.

The process of high-order harmonic generation (HHG) by rare-gas atoms in intense laser fields has become a reliable way to produce high-brightness, tabletop size, coherent radiation in the vacuum ultraviolet and soft-x-ray ranges (see 1 for a recent review). The unique properties of the harmonic emission have opened the way to relevant and new applications in i) atomic and molecular core-level 2–4, photo-ionization 5, and plasma 6 spectroscopy, ii) x-ray fluorescence analysis 7, iii) time-resolved solid state physics of surface states 8 and of UV photoemission spectroscopy 9, iv) nano- and micro-structured material characterization, such as porous silicon 10, v) XUV interferometry for the diagnostics of dense plasmas 6, 11, 12.

The propagation of femtosecond (fs) laser pulses in transparent media induces strong nonlinear behaviours. In particular, in a gaseous medium, where the pulse induces a considerable ionization plasma, the laser beam departs from its gaussian form, both in intensity and in phase. The harmonic field, generated by such a modified laser pulse will essentially depend on the driving field characteristics. Investigating these characteristics helps one to control and optimize the harmonic emission.

### NUMERICAL MODEL

Typical calculations of the harmonic field consist of three parts: a) the calculation of the driving field in the interaction region b) the microscopic response of the single atom to the driving field, which is then inserted as a source term in the c) propagation equation for the harmonic field. It is also important to adopt, within the model framework, an appropriate model for the ionization of the atoms in oscillating fields of ultrahigh intensity. In the following we will detail the description of the physical model adopted for the pulse propagation in ionized media and we will mention the analytical and numerical methods used for solving the propagation equations.

In an ionized gas pulse propagation is affected by diffraction, refraction, nonlinear self-focussing, ionization, and plasma defocusing. The pulse evolution in such media are described by the wave equation which can be written as:

$$\nabla^2 E_1(r, z, t) - \frac{1}{c^2} \frac{\partial^2 E_1(r, z, t)}{\partial t^2} = \frac{w^2}{c^2} (1 - \eta_{eff}^2) E_1(r, z, t) \quad (1)$$

where  $E_1(r, z, t)$  is the transverse electric field of the laser, of frequency  $\omega$ . Radial symmetry is assumed, therefore cylindrical coordinates are used throughout. The effective refractive index of the medium can be written as

$$\eta_{\text{eff}}(r, z, t) = \eta_0 + \eta_2 I(r, z, t) - \frac{\omega_p^2(r, z, t)}{2\omega^2} \quad (2)$$

The first linear term  $\eta_0 = I + \delta_i + i\beta_i$  accounts for the refraction ( $\delta_i$ ) and absorption ( $\beta_i$ ) while the second term describes a  $\chi^{(3)}$  process depending on laser intensity  $I$ , and known as the optical Kerr effect. Finally the third term contains the plasma frequency  $\omega_p = (4\pi e^2 n_e / m)^{1/2}$  and accounts for the presence of a density  $n_e$  of electrons (of mass  $m$  and charge  $e$ ) per unit volume. It is known that if diffraction, self focussing due to  $\eta_2$ , and defocusing due to plasma generation are properly balanced, a self guided optical beam can be formed and propagated over extended distances, i.e. many vacuum Rayleigh lengths. Keeping only the real terms in the refractive index, the propagation equation for  $E_I(r, z, t)$  becomes

$$\nabla^2 E_1(r, z, t) - \frac{1}{c^2} \frac{\partial^2 E_1(r, z, t)}{\partial t^2} = k^2 \left( \frac{\omega_p^2}{\omega^2} - 2(\delta_1 + \eta_2 I) \right) E_1(r, z, t) \quad (3)$$

The method adopted to solve this equation is described by Priori et al. and will only be mentioned briefly here. We write the equation in the moving frame, and, after performing the paraxial approximation, eliminate the temporal derivative by a Fourier transform, and obtain the equation:

$$\nabla^2 E_1(r, z, \omega) - \frac{2i\omega}{c} \frac{\partial E_1(r, z, \omega)}{\partial z} = \tilde{F} \left[ k^2 \left( \frac{\omega_p^2}{\omega^2} - 2(\delta_1 + \eta_2 I) \right) E_1(r, z, \omega) \right] \quad (4)$$

where  $\tilde{F}$  is the Fourier transform operator acting on the temporal coordinate. We mention that Priori et al. solved the same equation taking into account only for the electrons plasma term.

From the numerical point of view, the right hand side of Eq. (4) has both an implicit (through plasma frequency term and  $\eta_2 I$  term) and an explicit dependence on  $E_I$ . For this reason, Eq. (4) was solved selfconsistently in every  $\tilde{\Delta}z$  step as follows. After advancing the solution  $E(r, z, \omega)$  by a Crank-Nicolson scheme, we calculated  $E(r, z, t)$  by a back Fourier transform, thus evaluated again the right hand side term of Eq. (4), firstly in  $t$  domain and then in  $\omega$  domain. Crank-Nicolson scheme was applied again on the same step  $\tilde{\Delta}z$  and a new  $E(r, z, \omega)$  solution was obtained. The iteration was repeated until the difference between the new and the old solution was under an imposed threshold.

The energy lost by the pulse during propagation is made up of two contributions: the photoionization term represented by  $\beta_1$  and the energy consumed in ionization processes. By writing the energy balance for the ionization process we obtain the imaginary contribution to the refractive index as  $\gamma = (n_0 I_p w \lambda) / 4\pi I$ , where  $n_0$  is the atomic density,  $I_p$  the ionization potential, and  $w$  the ionization rate for an average intensity  $I$ . The energy loss was estimated for each  $(r, z)$  point after every successful integration step, and the dumped field was used in the next integration step. Energy loss by inverse bremsstrahlung (collisional absorption) was not considered here because the working gas pressure is low.

## RESULTS AND DISCUSSIONS

We will present in the following two typical results concerning the field configuration in the interaction region. Plotted in Fig. 1 is the peak intensity of the pulse after passing through a gaseous medium of constant density. In particular we have considered here Xe at 0.6 torr. The cell has a total length of 14 cm and is placed in a loose irradiation geometry produced by a lens with  $f=5$  m. Two positions of the cell with respect to the focus are calculated: one with the cell in the converging beam, with  $z_c = -25$  cm, the other with the input pinhole in the focus, i.e.  $z_c = 7$  cm. Here



$z_c$  represents the distance from the focus to the cell input pinhole. As one can see, the field configuration is rather different in the two cases: a convergent beam induces a flat configuration that persists even after 14 cm of propagation. This is due to the balance between the divergent lens created by the electron plasma and the convergence of the beam. When the cell is placed in the focus or after the focus, i.e. in the diverging beam, an initial flat radial distribution tends to form but is gradually destroyed with increasing  $z$ , as seen in Fig. 1.

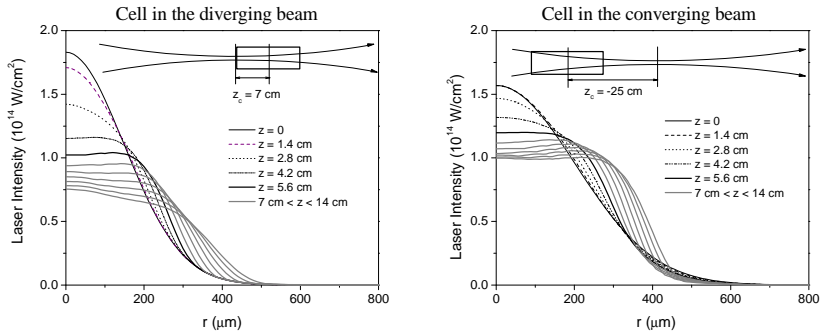


Fig. 1. The peak intensity of the laser pulse as a function of  $z$ , the distance from the cell input, and for two cell positions as specified on the graphs.

As distinct from the common self-guiding effect, where the field confinement is due to the total internal reflection at the guide boundaries, in this case [15] the effect is obtained due to a strong reflection of the trapped wave from the plasma boundary that is sharp as compared to the transverse scale. As shown recently [14, 15], these field configurations are particularly favorable for the generation of high order harmonics, leading to an optimisation of the conversion efficiency.

## REFERENCES

1. T. Brabec and F. Krausz, *Rev. Mod. Phys.* **72**, 545 (2000)
2. M. Drescher, M. Hentschel, R. Kienberger, M. Uiberacker, V. Y. A. Scrinzi, T. Wester, W. Albesloh, U. Kienberger, U. Heinzmann and F. Krausz, *Nature* **419**, 803 (2002).
3. R. Haight and P. Seidler, *Appl. Phys. Lett.* **65**, 517 (1994).
4. J. Larsson, E. Mevel, R. Zerne, A. L'Huillier, C.-G. Wahlstrom and S. Svanberg, *J. Phys. B:At. Mol. Opt. Phys.* **28**, L53 (1995).
5. M. Gisselbrecht, D. Descamps, C. Lyngša, A. L'Huillier, C.-G. Wahlstrom and M. Meyer, *Phys. Rev. Lett.* **82**, 4607 (1999).
6. W. Theobald, R. Hassner, C. Wulker, and R. Sauerbrey, *Phys. Rev. Lett.* **77**, 298 (1996).
7. M. Schnurer, Z. Cheng, M. Hentschel, G. Tempea, P. Kalman, T. Brabec and F. Krausz, *Phys. Rev. Lett.* **83**, 722 (1999).
8. R. Haight and D. Peale, *Phys. Rev. Lett.* **70**, 3979 (1993).
9. F. Quere, S. Guizard, G. Petite, P. Martin, H. Merdji, B. Carre and J.-F. Hergott, *Phys. Rev. B* **61**, 9883 (2000).
10. F.D. Filippo, C. de Lisio, P. Maddalena, G. Lerondel, T. Yao and C. Altucci, *Appl. Phys. A* **73**, 737 (2001).
11. P. Salieres, L. L. Deroff, T. Auguste, P. Monot, P. d'Oliveira, D. Campo, J.-F. Hergott, H. Merdji and B. Carre, *Phys. Rev. Lett.* **83**, 5483 (1999).
12. D. Descamps, J.-F. Hergott, H. Merdji, P. Salieres, C. Lyngsa, J. Norin, M. Bellini, T. Hansch, L'Huillier, and C.-G. Wahlstrom, *Opt. Lett.* **25**, 135 (2000).
13. E. Priori, G. Cerullo, M. Nisoli, S. Stagira, S. D. Silvestri, P. Villoresi, L. Poletto, P. Ceccherini, C. Altucci, R. Bruzzese, *Phys. Rev. A* **61**, 063801 (2000).
14. V. Tosa, E. Takahashi, Y. Nabekawa, K. Midorikawa, *Phys. Rev. A*, **67**, 063817 (2003)
15. E. Takahashi, V. Tosa, Y. Nabekawa, K. Midorikawa, *Phys. Rev. A*, **68**, 023808 (2003)

## **RADON CONTENT IN SCHOOLS FROM CLUJ AND ONEȘTI CITIES**

**C. COSMA, CORINA RUDEI, IRINA CIOBOTARU, KINGA HENING**

*“Babeș-Bolyai” University, Faculty of Physics, 3400-Cluj-Napoca, Romania*

**ABSTRACT.** This paper is based on a comparative analysis between the Radon concentrations obtained in Cluj-Napoca and Onești Cities with other measurements made in Romania, as Bucharest, Bihor, Stei and Oradea, measurements that were made in schools, kinder-gardens and dwellings. The values (numbers) obtained in the Transilvanian study are 2-3 times higher than the ones obtained in Moldova. The results from the three studies are almost similar. The differences are due to the geological differences, different measurement conditions and different periods in the year when the studies were made, type of buildings.

### **INTRODUCTION**

The main radionuclides that are important from the radiological protection point of view are radon, thoron and their short-life family products. Radon is present everywhere, in rocks, water, soil, it comes from solid and liquid materials, it's present in the air and in natural gases. Radon, because it is a radioactive gas and the only  $\alpha$  emitter of this type, is very mobile. The first indications of a possible radon prone area<sup>1</sup> for Cluj-Napoca City were the relatively high radon concentration (1 nCi/L) in the old water supply plant. The implication of this gas on our health is very serious. Through inhalation, Radon gets into our lungs, and through blood circulation it reaches the other organs. The irradiation its-self is not very dangerous, but the attached elements (radionuclides) on the respiratory paths are, from where they directly irradiate the bronchi and the bronchi mucus and also the bronchi epithelium that covers the interior surface of the lungs, so the irradiation is very significant. The risk of irradiation is higher if the concentration of Radon is increased.

Between the indoor radon exposure and the lung cancer risk seems to be a direct relation, that's why determinating radon concentrations in buildings is very important for characterizing the indoor air quality. The detectors used for this study are of CR-39 type, the most sensitive nuclear track detector investigated so far, because it gives an answer to all alpha energies. For the measurements of the Rn activity concentrations integrated in the time unit was used RadoSys2000.

In order to determinate the Rn concentrations in air and to make possible an analysis of lung cancer risk due to Rn exposure, we placed CR-39 detectors in 28 schools and high schools from Cluj-Napoca and 14 detectors in schools and kindergartens from Onești. The detectors were exposed in average for 35 days in secretariats, principles' offices and libraries, at appreciatively 1m from the ground. The measurements were made in warm season, spring to summer, and the appreciations for the whole year average is determinated due to other studies performed<sup>2</sup> which proved that radon concentrations are 2 or 3 times higher in winter seasons than in summer. The values obtained in the schools from Cluj-Napoca City are higher comparing to the ones obtained in Onești.

### **EXPERIMENTAL METHOD**

As the “ion explosion spike” model sustains, the forming mechanism of the tracks is the following: the charged particle on its trajectory ionizes the atoms of solid materials. There appear forces, which remove the ionized atoms creating numerous holes and interstitially defects. This process will take place if the big void charge does not decrease fast from the particles trajectory and if the appearing forces are high sufficiently to remove the atoms. With chemical methods these tracks can be observed with an optical microscope.

The CR-39 track detectors used for this study are made of plastic (polyetilen membranes) and they are sensitive to alpha radiation, with energies between 0.2-8Mev. The detector is placed inside of a small box called radapot, which allows the air inside. The volume of the radapot is

## RADON CONTENT IN SCHOOLS FROM CLUJ AND ONEȘTI CITIES

$V=0.0000402 \text{ m}^3$ . The radon daughters which contaminated the detector are then corrodated with a NaOH solution with a concentration  $C=7.02\text{mol}$  in a thermostat at  $t=90^\circ\text{C}$ . The developing time is 4.5h.

The tracks after the developing are read using the Radosys2000 system, where the electronic microscope is attached to the computer. The number of tracks from the detector is proportionally with the radon concentration from the radapot. From the tracks number, based on a calibration of Radosys2000, it can be calculated the concentration with an extent of  $V=0.0000402\text{m}^3$ .

### RESULTS AND DISSCUTION

After developing and measuring the detectors placed in the schools from Cluj-Napoca and Onești, with RadoSys2000 system, the results obtained are enclosed in the following table and graphic. The annual values were approximated by increasing the measured ones by 1,5, using the results and formulas deduced in other studies<sup>3,2</sup>, as they admitted that the for the values found in winter the ratio is 3:1and were due to slightly increased radon potential of the region, and on peoples' tendency to save heat in the cold season, on the other hand.

**Table 1**

**Measured and Estimated Radon Concentrations in Cluj-Napoca and Onești**

Place	Values	Geometric Average (Bq/m <sup>3</sup> )	Arithmetic average (Bq/m <sup>3</sup> )	0-100 Bq/m <sup>3</sup>	100-200 Bq/m <sup>3</sup>	>200 Bq/m <sup>3</sup>	Excess 200 Bq (%)
Cluj-Napoca	Summer Measured	83.49	91.85	20	6	2	0.071
	Annual Estimated	106.9	275.53	17	6	5	0.178
Onești	Summer Measured	75.438	113	10	4	-	-
	Annual Estimated	113.5	125.57	6	6	2	0.142

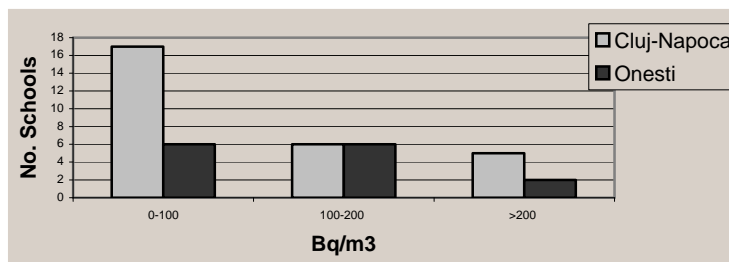


**Fig. 1.** Lognormal Distribution for Radon in Schools from Cluj-Napoca and Onești

The lognormal distribution obtained is limited between 39 Bq/m<sup>3</sup> and 556.5 Bq/m<sup>3</sup>, annual estimated values. Usually, in basements of buildings, the Rn concentration presents rather high values than in other places because the aerating process is very weak and it permits radionuclid accumulation, as the 556.5 Bq/m<sup>3</sup> value indicates, value that was obtained in a semi-basement space, in order to compare it with other obtained values. As the means show, the values obtained in Cluj-Napoca are higher than the ones obtained in Onești and the mean is near 300 Bq/m<sup>3</sup>, that can be rather alarming.

The “Public Health” Institute and “Joszef Stefan” Institute from Ljubliana, Slovenia realized a resembling study upon Rn concentrations in 100 schools and kindergartens from Bucharest. The measurements were made in wintertime and the track detectors were also placed

there for 35 days. A lognormal distribution was obtained, limited between  $43 \text{ Bq/m}^3$  and  $447 \text{ Bq/m}^3$ , an arithmetic average of  $146 \text{ Bq/m}^3$  and a geometric average of  $129.18 \text{ Bq/m}^3$ . The results from the three studies are almost similar. The differences are due to the geological differences, different measurement conditions, and different periods in the year when the studies were made, type of buildings. If we compare arithmetic means, we notice that Cluj-Napoca has the most increased Rn potential from these three studies, followed by Bucharest and Onești.

Indoor radon concentrations at ground floor level have been measured in 2001<sup>2</sup>, in Cluj-Napoca, in 46 detached houses, as well as in 35 flats in blocks, in cold season. The average values found were  $183.04 \pm 75.33 \text{ Bq/m}^3$  for houses and of  $69.64 \pm 23.47 \text{ Bq/m}^3$  for flats. The values found then were rather high and the average value found for houses in the cold season resembles those found in Ukraine<sup>3</sup> respectively in Sweden<sup>4</sup>. Indoor radon values in Cluj-Napoca City are 2-3 times higher than other values found in Romania<sup>5</sup>.

The influence of constructions materials upon indoor Rn concentrations is very well illustrated if we compare the measurements made in the schools from Cluj-Napoca with 80 measurements made in Stei area, a zone at 15 km far from an Uranium mine<sup>2</sup>; in a few homes, Uranium waste was used in constructions materials. The medium value obtained was  $240 \text{ Bq/m}^3$ , higher than the one obtained in the schools from Cluj-Napoca, it can be noticed a difference of  $148.15 \text{ Bq/m}^3$ . In Stei measurements, there can be observed rather high concentrations ( $234 \text{ Bq/m}^3$  and  $269 \text{ Bq/m}^3$ ), but also maximum values like  $1070 \text{ Bq/m}^3$  and  $1231 \text{ Bq/m}^3$ . In the schools measured in Cluj-Napoca, the values obtained are variant, from  $26 \text{ Bq/m}^3$  obtained in "School nr. 21" from Mănăștur ward to  $399 \text{ Bq/m}^3$  obtained in "Grup Școlar Transporturi" in Gheorghieni ward.

The radon measurements made in these schools contribute to a map of the Radon from the air for Romania, in order to establish for the future a maximum exposure admitted value for the population. It has been demonstrated that the lung cancer apparition risk due to Rn exposure is higher as the age is lower, that's why we have chosen placing the detectors in schools.

## REFERENCES

1. A. Szabo, *Ape și Gaze Radioactive în România*. Editura Dacia, Cluj-Napoca, 1978, p245
2. C. Cosma, D. Ristoiu, C. Cîndea, S. Râmboiu, *Season and building material influence on indoor radon concentration in houses from Transylvania*, Studia Universitatis Babeș-Bolyai, Physica, XLVI, 1, 2001, pag. 42
3. T. A. Pavelko, I. P. Los, *Indoor <sup>222</sup>Rn levels and irradiation doses on the territory of Ukraine*. Radiation Measurements, 25, 595, 1995
4. G. Perhagen, Z. Liang, et al., *J. Residential radon exposure and lung cancer in Swedish women*. Health Phys, 63, 179, 1991
5. C. Milu, R. Gheorghie et al. *Air exposure to radon and thoron daughters in Romanian houses*. Rom J Biophys 1993; 3: 157-162

## THE SEPARATION OF POLYCYCLIC AROMATIC HYDROCARBONS (PAHS) BY HIGH RESOLUTION GAS CHROMATOGRAPHY

**Z. MOLDOVAN, FLORINA TUSA**

*National Institute of Research and Development of Isotopic and Molecular Technology,  
400293 Cluj-Napoca, P.O.B. 700, Romania, e-mail: zaha@oc1.itim-cj.ro*

### Introduction

Environmental monitoring and analytical surveys indicate that appreciable amounts of dangerous chemicals are released in air, water and soil. Since a number of these compounds are known to possess carcinogenic or mutagenic activities, their presence in the environment has to be regularly monitored to ensure that the permitted levels are not exceeded. Products of combustion such as Polycyclic Aromatic Hydrocarbons (PAHs) are found in polluted environments, workplaces and different smokes. Some PAHs are known mutagens and carcinogens: benzo[a]pyrene, benzo[a]anthracene, dibenzo[a,b]anthracene. They can form DNA adducts in man and animals. These adducts are thought to probably increase the risk for lung cancer and possibly for kidney, bladder and other cancers/1,2/.

The purpose of this study was to develop a convenient analytical method for the simultaneous determination of a wide range PAHs in environmental samples. The complete separation of these compounds is very important due to the fact that some compounds are very dangerous for the man and animal health. A lot of analytical methods were developed in the last decade. Many of them are expensive and time consuming/3/. The paper presents a simple cost efficient method for the analysis of PAH in environmental samples.

### Results and discussions

The chromatographic separation of 17 compounds on a long capillary column and detection with Flame Ionization Detector (GC-FID) were performed. The temperature program for an optimum separation was used.

The relative response factor (with respect of naphthalene) for FID detector was calculated. The medium value for Detection Limit obtained for a signal of three times more high than noise signal was of 1 ng for every compound. A complete separation of all 17 compounds was obtained in a total time of 30 min.

In the **Fig. 1-17** the compounds structure as well as the characteristic mass spectra are shown. The absolute and relative response factors relative to FID detector are shown in the **Table 1**.

The separation was performed with at a resolution enough for a complete separation of all compounds. The complete GC separation is shown in the **Fig. 18**.

### Experimental section

#### Sample preparation

The samples were prepared by introduction of known quantity from every compound in a solvent mixture (n-hexane+ethyl ether 3:1).

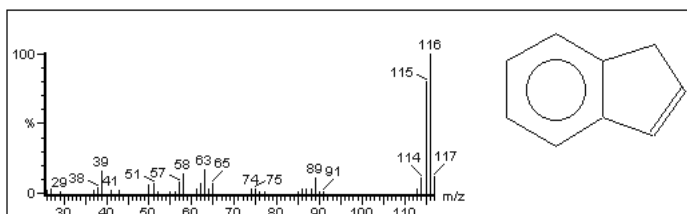


**Fig. 1.** Indene (M=116)

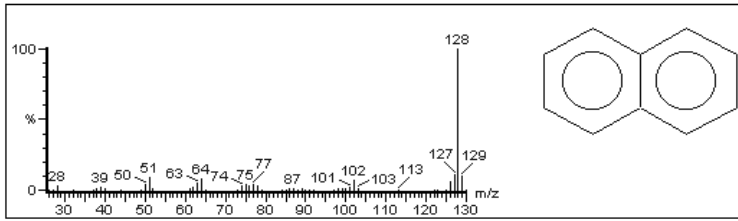


Fig. 2. Naphtalene (M=128)

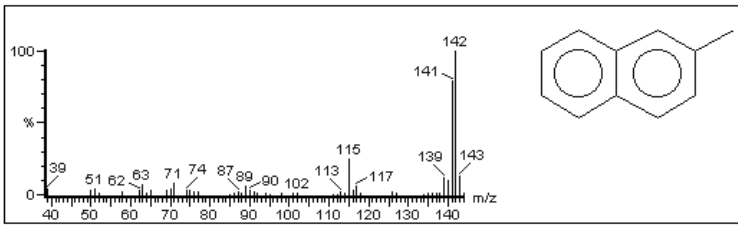


Fig. 3. 2 Methyl naphtalene (M=142)

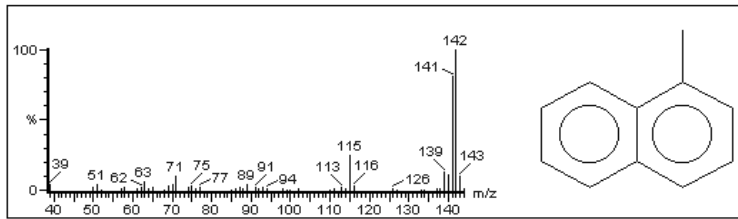


Fig. 4. 1 Methyl naphtalene (M=142)

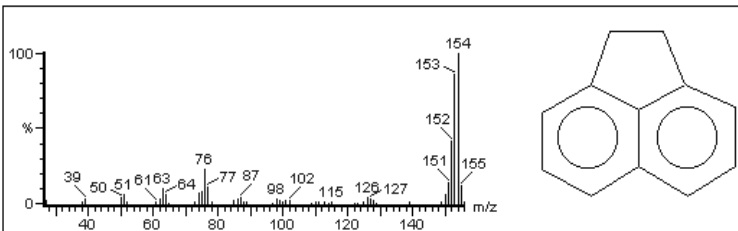


Fig. 5. Acenaphthene (M=154)

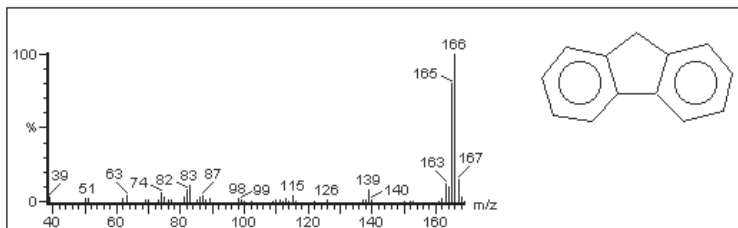


Fig. 6. Fluorene (M=166)

THE SEPARATION OF POLYCYCLIC AROMATIC HYDROCARBONS

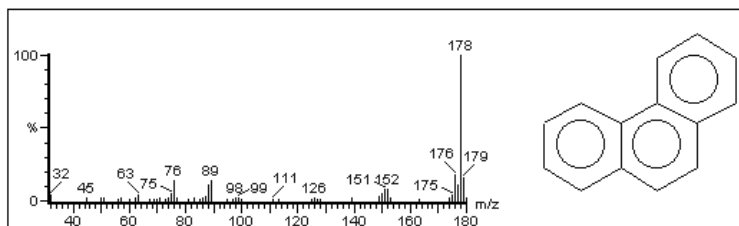


Fig. 7. Phenanthrene (M=178)

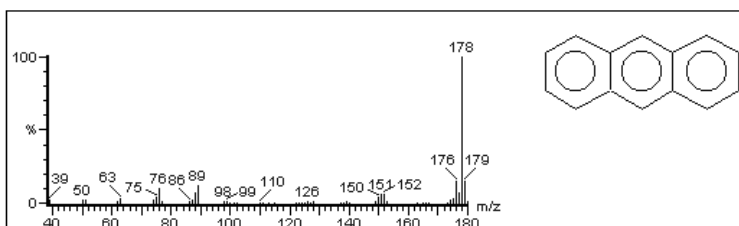


Fig. 8. Anthracene (M=178)

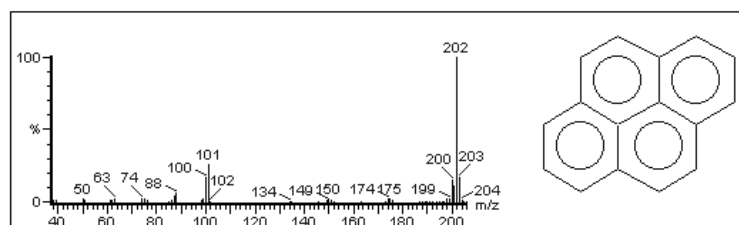


Fig. 9. Pyrene (M=202)

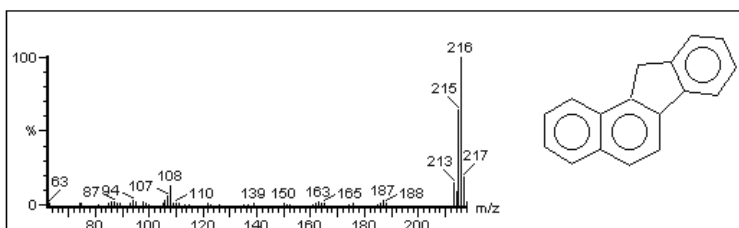


Fig. 10. 11H-Benzo- $\alpha$ -Fluorene (M=216)

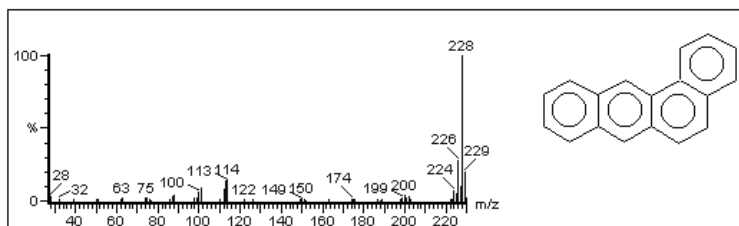
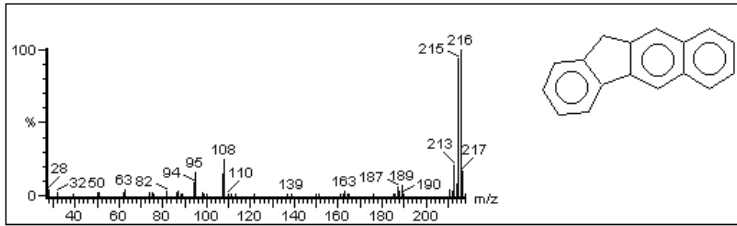
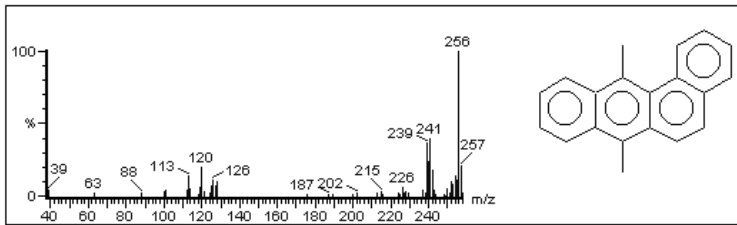


Fig. 11. 11H-Benzo- $\beta$ -Fluorene (M=228)



**Fig. 12.** Benz- $\alpha$ -Antracene (M=216)



**Fig 13.** 7,12 Dimethyl Benzo-A-Antracene (M=256)

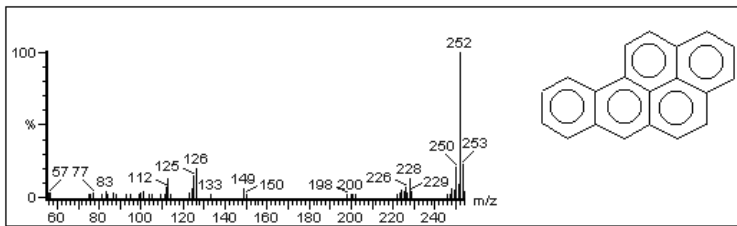


**Fig 14.** Benzo- $\alpha$ -Pyrene (M=252)

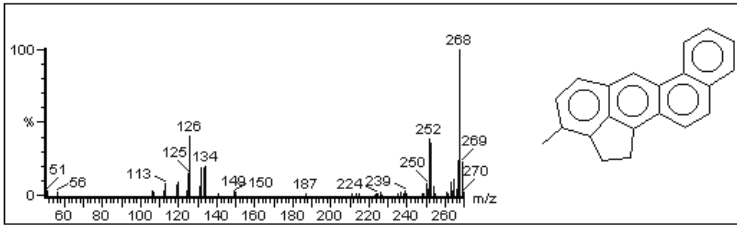


**Fig 15.** 3-Methyl Cholantrene (M=268)

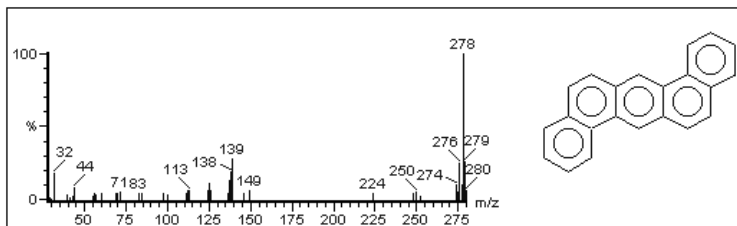


**Fig 16.** Dibenzo-AH-Antracene (M=278)



## THE SEPARATION OF POLYCYCLIC AROMATIC HYDROCARBONS

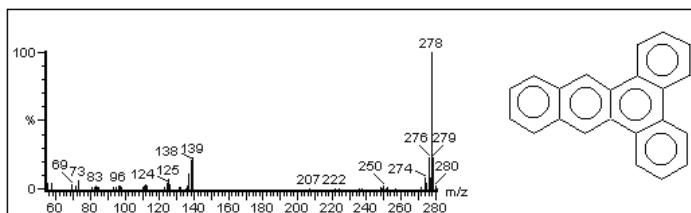


**Fig. 17.** Dibenzo-AC-Antracene (M=278)

### *Experimental condition*

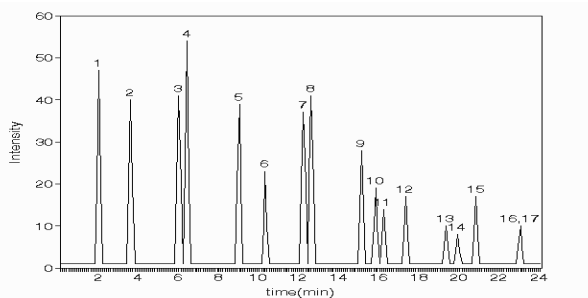
A HP-5MS (30x0.25mm) with 0.25 $\mu$ m film thickness containing 5% phenyl methyl siloxane was programmed from 125<sup>o</sup>C(5min) to 330<sup>o</sup>C at 15<sup>o</sup>C/min (keeping this temperature for 10 min.). The flow eluent was 6 ml/min (Helium). The used detector was FID.

**Table 1.**

**The FID response factors for PAHs. Absolute ( $F_i$ ) and relative ( $F_r$ ) values**

Nr.crt	Component	$F_i=A_i/m_i$	$F_r=F_i/F_N$
1	Indene	300.2	0.44
2	Naphtaline	682.5	1
3	2-Methyl-Naphtaline	233.3	0.34
4	1-Methyl-Naphtaline	510.6	0.75
5	Acenaphtene	552.8	0.84
6	Fluorene	467.7	0.69
7	Fenantrene	512.9	0.75
8	Antracene	388.3	0.57
9	Pyrene	455.5	0.67
10	11-H-Benzo [ $\alpha$ ] Fluorene	513.3	0.76
11	11-H-Benzo [ $\beta$ ] Fluorene	445.7	0.65
12	Benz [a] Antracene	354.6	0.51
13	7,12M <sub>2</sub> Benz [ $\alpha$ ] Antracene	37.5	0.05
14	Benzo [a] Pyrene	303.1	0.44
15	3-Methyl-Cholantrene	234.3	0.34
16+17	Dibenzo [a,h] Antracene+Dibenzo [a,c] Antracene	202.9	0.30

**Fig. 18.** GC separation of compounds 1-17



## REFERENCES

1. G. Vollmer, L. Gianoni, L. Olsen, B. Sokull-Klutgen and S.J. Munn, *Risk assessment, Occupational Exposure*, European Commission, Joint Research Centre, 2001
2. C. D. Simpson, W. R. Cullen, Kristine B. Quinlan and K. J. Reimer, *Chemosphere*, 31, 4143-4155, 1995
3. R. L. Grob, *Chromatographic analysis of the Environment*, Marcel Dekker, Inc., New York, 1983

## **DETERMINATION BY ICP SPECTROMETRY OF HEAVY METALS CONCENTRATION IN SOME CONCERNED AREALS OF ROMANIA**

**IOAN I. SUCIU, CONSTANTIN C COSMA**

*Babeș-Bolyai, University, Department of Physics, Mihail Kogălniceanu 1,3400;  
siioan@hotmail.com,amsoc@phys.ubbcluj.ro*

**ABSTRACT.** Determining the heavy metals in the soil is important taking into account the toxic potential of some of these elements. Centers of Chemical Industry, known as centers of pollution at least until 2000, have been established for determination. The samples have been driven grounded and homogenized. The analyses by ICP spectrometry is made in the EXPROGAZ MEDIAȘ laboratory using an IRIS ADVANTAGE spectrometer and processed in a first stage by the THERMO SPEC/CID Research soft. Following the preliminary qualitative analysis there have been identified the most frequent metals in the established sites. The quantitative analysis has had as an aim to determine the concentration for those, which have an acknowledged toxic potential: Co, Cr, Pb, etc. For some of samples, the results obtained by ICP spectrometry have been confronted with the results obtained by NAA and AAS. The concordance between them was excellent.

### **Introduction**

Determining the heavy metals in the soil is important taking into account the toxic potential of some of these elements. Centers of the Chemical Industry, known as centers of pollution at least until 2000, have been established for determination. In order to take the samples three points have been established, in each place avoiding the sites where there are ground sliding going (approximately) on or where the probability of alluvial deposits is very high [1]. At the established points there have been taken soil samples at depths of 5,15 and 25 cm. The samples gathered from Târnăveni, Copșa Mică and Câmpia Turzii (see fig.no.1) were transported and stored in containers of polyethylene. They were previously treated with a molar solution of HCl and rinsed with distilled water [2].

### **Materials and methods**

The samples have been driven grounded and homogenized. A medium sample has been kept for analyses. For the digestion the procedure was concordant with the MLS soft WAVE REPORT recommendations, regarding the soil samples. At the quantity of 0.250g of each sample there was added 3ml HNO<sub>3</sub> 65% and 3ml HF 40%. The mixture resulted was introduce into a microwave and digested. After that, in the recipient, there was added distilled water up to 50 ml.

The introduction in the plasma jet was made with a peristaltic pump, with 8 rolls and 3 grooves, having maximum speed of 200 spins/min, controlled by the computer. The analyses by ICP spectrometry is made in the EXPROGAZ MEDIAȘ laboratory using an IRIS ADVANTAGE spectrometer and processed in a first stage by the THERMO SPEC/CID Research soft.

Following the preliminary qualitative analysis there have been identified the most frequent metals in the established sites. The quantitative analysis has had as an aim to determine the concentration for those, which have an acknowledged toxic potential: Co, Cr, Pb, etc.

### **The results**

According to the nature of the industrial activities in the site, the presence of one or another of the researched elements is greater. The highest concentration of Cr was found near the Târnăveni's Chemical Platform and it is in direct connection with the sodium until 2000. The concentration outruns the alarm level in the sensitive areas [4]. The highest concentration of Pb

was found near the S.C **Industria Sârmiî S.A. Cîmpia Turzii**. The value outruns the alarm level in the less sensitive areas but is still under the intervention limit [4]. The highest concentration of Cu was found in the Copsa Mică area. It outruns the alarm level in the sensitive areas.



Fig. 1. Selected area

Table 1.

Maximum concentrations for analyzed samples (ppm)

The Element,	Târnăveni		Copsa Mică		Câmpia Turzii	
	Concentration	%RSD	Concentration	%RSD	Concentration	%RSD
Cr	<b>363</b>	0,1788	<b>103</b>	1,162	<b>61,7</b>	1,586
Co	<b>16,4</b>	14,65	—	—	—	—
Pb	<b>145,9</b>	2,379	<b>687,4</b>	2,726	<b>868,6</b>	1,229
Cu	<b>72,9</b>	1,079	<b>149,76</b>	2,241	<b>59,8</b>	1,292

Table 2.

The results obtained in Târnăveni area

Sample No.	Depth (cm)	Element	Wave length $\lambda$ (nm)	Concentration (ppm)	%RSD
1	5	Cr	267,716	258	0,7037
2	15	Cr	267,716	274	0,7986
3	25	Cr	267,716	259	0,6027
4	5	Cr	267,716	140	1,581
5	15	Cr	267,716	140	2,181
6	25	Cr	267,716	117	0,3282
7	5	Cr	267,716	<b>363</b>	0,1788
8	15	Cr	267,716	245	1,259
9	25	Cr	267,716	168	1,431

Table 3.

## The results obtained in Câmpia Turzii area

Sample No.	Deep (cm)	The element	Wave length (nm)	Concentration (ppm)	%RSD
1	5	Pb	220.353	0	0
2	15	Pb	220.353	0	0
3	25	Pb	220.353	0	0
4	5	Pb	220.353	0	0
5	15	Pb	220.353	0	0
6	25	Pb	220.353	<b>868,6</b>	<b>1,229</b>
7	5	Pb	220.353	0	0
8	15	Pb	220.353	673,5	1,290
9	25	Pb	220.353	837,2	2,459

Table 4

## The results obtained in Copșa Mică area

Sample No.	Deep (cm)	The element	Wave length (nm)	Concentration (ppm)	%RSD
1	5	Cu	224,700	52,3	1,115
2	15	Cu	324,754	140,48	2,273
3	25	Cu	324,754	<b>149,76</b>	2,241
4	5	Cu	327,396	72,16	0,2216
5	15	Cu	327,396	48,4	1,023
6	25	Cu	327,396	56,8	3,624
7	5	Cu	327,396	56,44	3,077
8	15	Cu	327,396	54,94	1,063
9	25	Cu	324,754	32,24	0,5862

### Conclusions

Determining the heavy metals concentration in the soil is important taking into account the high toxic potential of some of these elements. There may determine irritations, allergies, anemia and cancer. [3]

The determinations by ICP-OES spectrometry require a shorter time, has a good fidelity and presenting other advantages, too.

Some migration process towards to deep strata can also be spotted. The end of some industrial activities can explain this remark.

The results obtained have been rendered evident some higher concentrations, even exceeding of alert level in sensitive sites but they don't overrun the intervention level.

For some of samples, the results obtained by ICP spectrometry have been confronted with the results obtained by NAA and AAS. The concordance between them was excellent.

### REFERENCES

1. Gh. Rogobete, N. Oancea, *Pedologie generală și ameleorativă*, ed. Did. și Ped. București 1977
2. Malissa, Fresnius Z. *Anal Chem.* 319, 357-363/1984
3. Mogoș Gh. *Intoxicații acute*, ed. med. Buc. 1981, pp 475
4. *Monitorul Oficial al României* nr. 303 bis/ 6 XI 1997-O.M.756/1997
5. O. A. Culicov, M. Frontasyeva, E. Steinnes, *JNR Preprint* E14-2002-102, Dubna 2002
6. Cordoș E., A. Frentiu, T. Rusu, Vâtcă G. *Elemental speciation of Pb, Zn and Cu in sedimented dust and soil using cacacitively coupled plasma AES as detector*, *Analyst* (London), 120, pp 725-731

## THE ANALYSIS OF ATMOSPHERIC METHANE CONCENTRATION IN THE AREAL OF CLUJ

**C. CUNA, P. ARDELEAN, STELA CUNA**

*National Institute for Research and Development of Isotopic and Molecular Technologies, Cluj-Napoca, Romania*

**ABSTRACT.** The measurements of the atmospheric methane concentration in the surrounding of Cluj-Napoca are reported. Our data will contribute to the completion of the existing ones in aiming to realize a mathematical model of the atmospheric methane concentration. These measurements can be extended also to other gases of interest as CO, N<sub>2</sub>O, NO<sub>x</sub>.

### **Introduction**

The methane was recognized as one of the most important gases with low concentration in atmosphere, heaving a very significant contribution to the climatic changes of the Earth in the course of the last century [1,3].

The methane gas absorbs infrared radiation, this fact leading to the global climate warming. The methane also, has an important influence on the abundance and the distribution of OH radicals in troposphere, inducing changes in the chemical composition of the Earth atmosphere [1].

The methane influences the ozon concentration in troposphere and stratosphere [5] and it is a water source in stratosphere [6].

The analyses performed in the last period show a global average growth rate of the methane concentration of 1,1% per year [7].

This growth began approximately two centuries ago.

In the same time, with this relatively uniform growth of the methane concentration in the air, a seasonal variation of the methane concentration in atmosphere was observed, ascribed to the seasonal variation of the reaction rate of the methane with OH radicals.

The methane gas is produced by different activities in agriculture, by natural gases exploitation and by coal extraction (mining activities).

Mainly, the atmospheric methane concentration growth is ascribed to the growth of the horned cattle number, to the growth of the biomass quantity burnt yearly and to the growth of the rice cultivated surfaces, all these being potential sources of tropospheric methane emission.

Though the main atmospheric methane sources are known, the quantitative estimation of methane emission from these sources varies appreciably. The methane emission from biomass burning was measured in tropical and temperate regions using samples prelevated from different locations or using laboratory experiments [4].

The analyses were made by gas chromatographic.

The emission factors for CH<sub>4</sub>, varies between 1,65g/kg and 9,3g/kg. The emission factor is defined as the methane quantity liberated for 1kg fuel consumed. The quantity of methane liberated in the atmosphere was estimated at 500-600 terragrames (Tg), but there are some disagreements concerning this value.

Taking into consideration the methane importance in the chemistry of the atmosphere and in the energetic balance of the atmosphere it results that to survey the abundance and the distribution of CH<sub>4</sub> and other gases is a problem of great importance in the environmental science.

### **Methods of analysis**

The analytical objectives for environmental characterization imply in many cases very precise analyses at low concentrations, for methane, between 1,69-1,85 ppm. By their high selectivity and sensitivity, mass spectrometry and gas-chromatography are particularly recommended for this type of analysis.

The data regarding the methane concentration in the atmosphere are very important for the elaboration and the checking of the theoretical model concerning the methane transport phenomena in the troposphere.

A general appreciation is, the data concerning these concentrations are yet incompletes.

To eliminate the local influence on the methane concentration the samples were prelevated from four points of prelevations. One of these is situated in the central zone of the town, two prelevations points are placed on the outskirts, near the forest zone, with lower pollution and another point at 30 km from Cluj-Napoca, in a rural far-off zone, without industrial activities and road traffic.

To increase the precision of the analysis 2÷3 sample were prelevated from each prelevation point, and we used also an internal standard whose concentration was close to the atmospheric methane concentration.

### **Results and discussions**

The measurements were performed by gas chromatography and by mass spectrometry. We used a GCL-90 gas chromatograph with an improved detection system and with a molecular sive column 13x adapted for high performance measurements.

To obtain a great sensitivity, many preliminary determinations were made in order to obtain the best operation conditions for the chromatographic column dedicated to methane detection, a FID system was used, working with optimized parameters for trace detection.

The samples used for the mass spectrometric analysis were prepared by differentiated cooling. Single and double focusing mass spectrometers were used to perform this type of analysis. The improvements were made to the single focusing mass spectrometer in the vacuum line (TMH 261 turbomolecular pump) and in detection, data acquisition and processing.

To perform the mass spectrometric analysis the following steps must be made:

- the air sample prelevation
- the sample preparation for analysis by differentiated cooling method (with liquid nitrogen )
- the CO<sub>2</sub> elimination from the atmospheric air samples
- the preparation of the internal standard
- the mass spectrometric analysis

For the sample preparation we used a laboratory equipment with a high vacuum system and precise gauge for pressure measurement.

The following conditions must be observed:

- the standard and the sample must be introduced into the ion source at the same pressure
- high vacuum is necessary in the analyzer and in the ion source
- considering the high sensitivity requirements, the electron multiplier detector is recommended.

To obtain the values of concentration for different components the ionization efficiency for different substances given in the mass spectra catalogues were used.

To minimize the measurement errors, 4-5 determinations for each sample were made. The enrichment procedure influences the mass spectrometric analysis, producing a greater spreading of the values than in the case of chromatographic analysis.

## THE ANALYSIS OF ATMOSPHERIC METHANE CONCENTRATION

These latter types of analysis permit rapid determination and greater sensitivity.

Some internal standards were prepared with 2,5ppm, 1,7ppm and 1,5ppm values respectively, to cover all the range of concentrations to be measured.

In fig.1 are presented the results obtained for some methane concentrations measured from air samples prelevated in different locations.

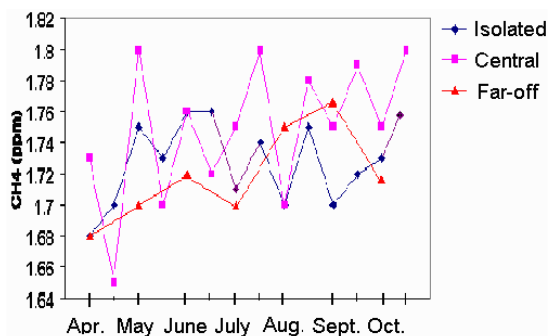


**Fig. 1.** The rhombuses show the concentrations obtained in the two isolated regions. The squares show the data obtained in the central part of the town and the triangles represent the methane concentrations of the sample prelevated from the far-off region, about 30km from the Cluj-Napoca.

Because the time interval in which the sample were prelevated and measured was relatively short one don't observe spectacular variations of the methane concentrations in air. These values are placed generally under the values reported by the scientific literature.

### Conclusions

The following characteristics can be observed:

- for the samples collected from the isolated region the concentration is near 1,7ppm, with relative small oscillations.
- for the sample prelevated in the central part of the town the values of the methane concentration and also the oscillations of these values are greater (2-3ppm).

These measurements permit to conclude that in the regions of sample prevalence the methane concentration in air is under the level reported by other authors for other geographic locations. To obtain a more complet vision on the phenomena concerning the seasonal variations (reaching a minimum in the cold period of the year) and the general evolution of the concentration it is necessary to perform the measurements on samples prelevated from a large geographic area and into a larger laps of time (minimum 2-3 years).

### REFERENCES

1. E. G. Brunke, H. E. Scheel and W. Seiler, *Atmos. Environ.*, 24A, (1990),585-595.
2. L. P. Steele, P. J. Fraser, R. A. Rasmussen, M. A. Khalil, T. J. Conwey, A. J. Crawford, R. H. Gammon, K. A. Masarie and K. W. Thoning, *J. of Atmos. Chem.*, 5, (1987), 125-171.
3. W. M. Hao and D. E. Ward, *J. Geophys. Res.*, 98, (1993), 20657-20661.
4. H. S. Johnston, *Ann. Rev. Phys. Chem.*, 35, (1984), 481-489.
5. D. H. Ehalt, *Naturwissenschaften*, 66, (1979), 307-315.
6. C. P. Rinsland, J. S. Levine and T. Miles, *Nature*, 318, (1985), 245-249.
7. B. Stauffer, G. Fisher, A. Nefted and H. Oeschger, *Science*, 229, (1985), 1386-1388.

## VIBRATIONAL STUDIES OF ADSORBED CARVONE ON SOME SURFACES

G. DAMIAN<sup>1</sup>, V. MICLĂUȘ<sup>2</sup>, I. MOLDOVAN<sup>1</sup>, M. PUJA<sup>1</sup>

<sup>1</sup>“Babeș-Bolyai” University, Department of Physics, Cluj-Napoca, Romania

<sup>2</sup>“Babeș-Bolyai” University, Department of Chemistry, Cluj-Napoca, Romania

**ABSTRACT.** FT-Raman and FT-infrared spectroscopy have been used to investigate the sorption mechanisms of carvone (C<sub>10</sub>H<sub>14</sub>O) onto Al<sub>2</sub>O<sub>3</sub>, and ZnO as a model for pollutant interactions with soil. The observed frequencies of the prominent maxima in the Infrared and Raman spectra of the carvone and sorbates carvone with the proposed assignments are presented. The band shifts due to adsorption effects were in the range of 15 cm<sup>-1</sup> to low frequencies.

### INTRODUCTION

The presence of great amount of particulate matters with various composition and structures in the Earth's atmosphere, such as insulator oxides (SiO<sub>2</sub>, Al<sub>2</sub>O<sub>3</sub>, ZnO, MgO, etc), involve the necessity of quantitative and qualitative studies on the interaction between this ones and volatile organic compounds. The chemical coupling between volatile organic compounds and particulate matter was mentioned in as of profound importance in understanding processes of the gas-aerosol chemical interactions [1, 6-7]. An understanding of the mechanisms by which organic contaminants adsorb to mineral surfaces will be critical in predicting their fate and transport in the environment [8]

In this paper, FT-Raman and FT-infrared spectroscopy have been used to investigate the sorption mechanisms of carvone (C<sub>10</sub>H<sub>14</sub>O) onto Al<sub>2</sub>O<sub>3</sub>, and ZnO as a model for pollutant interactions with soil [2-5]. Soil and clay environmental samples are complex, heterogeneous mixtures of minerals. Therefore, model systems such as alumina and mineral oxides are studied by vibrational spectroscopy so that a fundamental understanding of organic interactions with minerals can be obtained. Raman and Infrared spectroscopy are both vibrational spectroscopic techniques which are capable of probing the organic pollutant-mineral oxide interface. Even though both techniques provide vibrational spectroscopic information, they are complementary approaches. Raman spectroscopy of organic adsorption to mineral oxides is challenging given the limited sensitivity of the method. Infrared spectroscopy is considered to be more sensitive than Raman, but suffers from serious interferences due to oxide absorption. Along with relative immunity to oxide interference, Raman is also immune to water in the sample matrix. Since many mineral oxides are expected to have water hydrating their surfaces, they are more difficult to analyze via infrared spectroscopy, which shows strong vibrational bands for water.

### EXPERIMENTAL

The porous surfaces were dried four hours in air at 150°C before impregnation in order to remove free water. The samples have been prepared by stirring for two days a mixture of powder metallic oxides and liquid carvone.

The FT-IR spectra of carvone, surface supports and adsorbed carvone, were recorded in the region 4000-400 cm<sup>-1</sup> by a Bruker EQUINOX 55 spectrometer, using an Attenuated Total Reflectance accessory with a scanning speed of 32 cm<sup>-1</sup> min<sup>-1</sup> with the spectral width 2.0 cm<sup>-1</sup>. The internal reflection element was a ZnSe ATR plate (50 x 20 x 2 mm) with an aperture angle of 45°. A total of 128 scans were accumulated for each spectrum. The FT-Raman spectra were also recorded with the same instrument with a FRA 106 Raman module equipped with Nd-YAG laser source operating with 200 mW in the wave number range 3500-100 cm<sup>-1</sup>. The frequencies of all sharp bands are accurate to ±2 cm<sup>-1</sup>.



**RESULTS AND DISCUSSION**

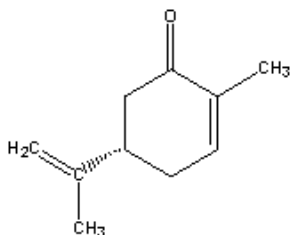


**Fig. 1.** Chemical structure of carvone

Carvone (2-Methyl-5-(1-methylethenyl)-2-cyclohexene-1-one ) is a caraway essential natural oil products (in the class of terpenes) occurring in plants as secondary metabolites which are highly volatile and exhibit very characteristic smells. This compound exhibits a number of interesting biological activities, e.g., antifungal, insecticidal and plant growth regulatory activities. Chemical structure of the studied carvone is presented in Figure 1. Commercial metal oxides with the following specific surface ( $m^2/g$ ) were used as surface supports:  $\gamma$ - $Al_2O_3$  -200, ZnO - 6.5

The recorded FT-IR and FT-Raman spectra of liquid carvone and adsorbed carvone on  $Al_2O_3$  and ZnO are shown in Figures 2 and 3.

The observed frequencies of the prominent maxima in the infrared and Raman spectra of the carvone and sorbates studied carvone with the proposed assignments are summarized in Table 1.

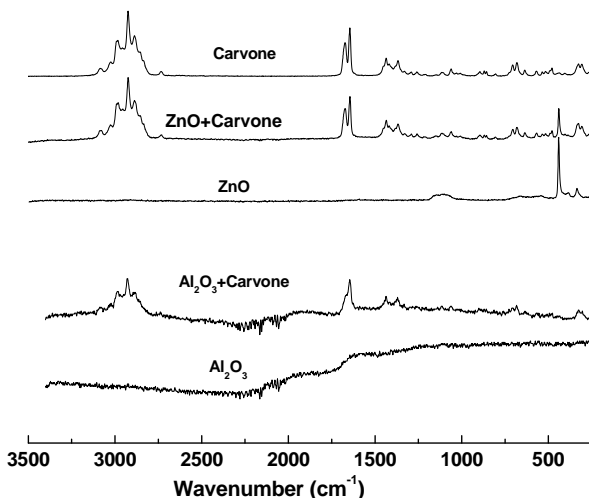


**Fig. 2.** FT-Raman spectra of carvone, adsorbed carvone on ZnO and  $Al_2O_3$

**Table 1**

**Main observed bands in Raman and Infrared spectra and most probable vibrational assignment of carvone**

Observed wavenumber ( $cm^{-1}$ )		Assignment
FT-Raman	FT-IR	
3085	3084	C -H stretching
2983	2970	aromatic C H stretch
2924	2923	methyl C-H asym./sym. stretch
		aromatic C H stretch
2734	2731	methyl C-H asym./sym. stretch
		aromatic C H stretch
1673	1673	C =C stretch
1644	1644	C =C stretch

Observed wavenumber (cm <sup>-1</sup> )		Assignment
FT-Raman	FT-IR	
1436	1634	C–C stretching , C-H bending
1367	1367	C–C stretching
1061	1058	ring vibrations
869	960	ring breathing
706	702	C–H out-of-plane bend
637		C-H bend
568		CCC out of plane bending
479		CCC out of plane bending/ C = O out of plane bending

Assignments were made on the basis of relative intensities, magnitude of frequencies, as well as literature data of molecules of similar structure.

The band shifts due to adsorption effects were in the range of 15 cm<sup>-1</sup> to low frequencies. The C–H stretching vibrations (around 2800 cm<sup>-1</sup> and 3100 cm<sup>-1</sup>) and the C–C deformation vibrations (1367 cm<sup>-1</sup>) are very similar for all aromatic compounds. Also, the characteristic bands of the ring vibrations (1060 cm<sup>-1</sup>) were used for identification of the sorbed products.

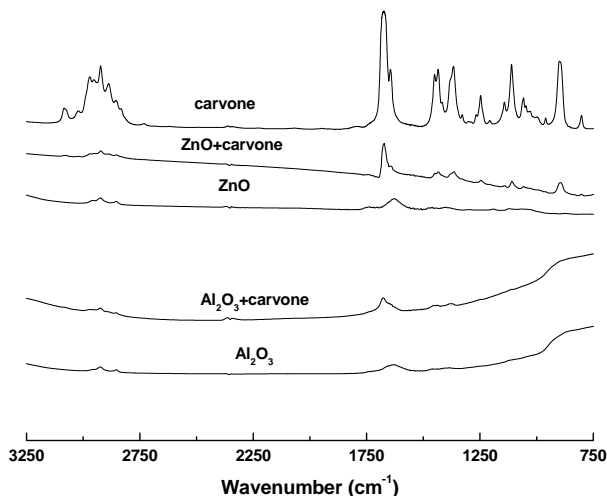


Fig. 3. FT-IR spectra of carvone, adsorbed carvone on ZnO and Al<sub>2</sub>O<sub>3</sub>

## REFERENCES

1. Z. Meng, D. Dabdub, J. H. Seinfeld, *Science*, **277**, 116 (1997)
2. V. S. Zakharenko, *Catalysis Today* 39 (1997) 243-249
3. Yu. M. Gershenzon, S. G. Zvenigorodskii, B. V. Rozenshtein, *Russ. Chem. Rev.* 59 (1990) 1601.
4. Prashant S. Chintawar, Howard L. Greene, *Applied Catalysis B: Environmental* 14 (1997) 37-47
5. G. Damian and V. Miclaus, *Studia Universitatis Babeș-Bolyai, Physica*, **XLV**,1,(2000)
6. K. Griesbaum, M. Hilß, J. Bosch, *Tetrahedron* 52, (1996) 14813
7. a) K. Griesbaum, V. Miclaus, I. C. Jung and R.-O. Quinkert, *Eur. J. Org. Chem.*, (1998) 627, b) K. Griesbaum, I. C. Jung, V. Miclaus, *Environ. Sci. Technol.*, 32 (1998) 647.
8. G. Damian, O. Cozar, V. Miclaus, Cs. Paizs, V. Znamirovski, V. Chis, L. David, *Colloids and Surfaces A*, 137, (1998) 1

## INFLUENCE OF RADIOACTIVE ISOTOPES UPON ENVIRONMENT

**ANISOARA PREDA, FELICIA VASUT, NICOLAE BIDICA, COSMIN DRAGOIU**

*National R & D Institute for Cryogenics and Isotopic Technologies – ICSI Rm. Valcea*

**ABSTRACT.** The main objection against nuclear power is the risk of “radioactivity” (radioactive isotopes) to the environment where it may cause humans health effects. We are concerned with the chemical aspects of the sources of releases and the migration of the radionuclides in the environment.

Their chemical properties, together with hydrology, determine how fast they will move from their point of entry into the groundwater to water resources used by man.

Most of the radionuclides produced in nuclear tests, accidents and the normal fuel cycle are short lived. Such releases occur from mining and milling operations, particularly of uranium ores, the nuclear fuel fabrication processes, normal operation of nuclear reactors, reprocessing of spent nuclear fuel, nuclear weapons production and recovery, transportation of nuclear material, testing of nuclear weapons and accidents, and from storage of nuclear wastes.

The types of radionuclides, in the atmosphere are dependent on their source, their mechanisms of production and the nature of the particular environment. While some species are gaseous, others are associated to particles with properties and half-life that are strongly dependent from the particle size and density. In the environment where released large amounts of nuclear fission products and actinides elements from nuclear weapons testing and from accidental and intention discharged from nuclear operations and fuel processing. The paper presents the influence of radionuclides upon the groundwater, air and soil and also the influence of this about the human health.

### 1. Introduction

The discovery of radioactivity a century ago opened up a new field in science, that of the atomic nucleus, which culminated 40 years later in the discovery of fission, and its practical consequences in the form of nuclear weapons and nuclear power reactors.

The three naturally occurring radioactive decay series are known as the thorium series, the uranium series and the actinium series. A fourth series, which originates in the synthetic element neptunium, is neptunium series.

Nuclear radiation is all around us in the environment. Low-level radiation is found in the oceans and waterways, the rocks and soils, the plant materials and in the atmosphere surrounding the planet. The radiation that we are exposed to can be said to come from two sources, that which occur naturally and that which is due to the activities of man.

### 2. Natural Radiation

#### *Terrestrial*

Radioactivity in nature comes from two main sources, terrestrial and cosmic. Terrestrial radioisotopes are found on the earth that came into existence with the creation of the planet. Although some are long gone, some radioisotopes take a long time to decay and become non-radioactive (on the order of hundreds of millions of years) and are still around today.

Radioactive elements found in rock, soil, water, air, and in food from the earth make their way in our bodies when we drink water, breath air or eat foods which contain them. These naturally occurring radioisotopes such as carbon-14, potassium-40, thorium-223, uranium-238, polonium-218, and tritium(hydrogen-3) expose us to radiation from within our bodies.

By far, the largest contributor to our daily exposure of radiation is the natural world, and the major form of natural radiation is radon gas. Radon-222 is a naturally occurring decay product of uranium-238 which is commonly found in soils and rocks. Radon-222 is a gas which is odorless, colorless, tasteless and chemically nonreactive. As it escapes from the soils and rocks of which it is trapped, it enters the water we drink and the air we breathe.

Since distribution of uranium in the earth's crust varies from place to place, so does the prevalence of radon gas. In areas where surface rocks contain a high concentration of uranium, radon gas could enter a home through a crack in the foundation. A concern for homeowners is the possibility that radon gas could accumulate to dangerous levels. This is especially a problem during the winter months when windows and doors are tightly shut.

Radon diffuses out of thorium and uranium minerals, and adds radioactivity to the ground water and to the atmosphere both by its own presence. Since Ra and Rn are among the most radio-toxic substances existing, causing bone and lung cancer at relatively low concentrations, special attention must be devoted to their appearance in nature. In many places water from hot mineral wells is considered beneficial to health both for bathing and drinking ("spas" or hot springs). The water may be warm due to radiogenic heating at the source (minerals rich in U or Th) and have a high content of dissolved radium and radon.

The average exhalation rate of radon from the ground is 5 – 50 mBq/m<sup>2</sup>s, leading to a near ground level radon concentration of 1 – 10 Bq/m<sup>3</sup>, but varies widely with ground conditions. The concentration in air above ground depends also on temperature and wind conditions.

Many ores contain small amounts of uranium. During processing, uranium and/or its daughters may enter the product, causing a radioactive contamination problem. For example, when apatite is used to produce phosphoric acid, the gypsum by-product contains all the radium originally present, producing a  $\gamma$ -ray and inhalation hazard from Rn-daughters, making it unsuitable for building material.

Radon concentration in indoor air may be quite high, depending on site and building material.

#### *Cosmic*

Another source of natural radiation comes from the interaction of **cosmic rays** with the earth's upper atmosphere. Cosmic rays permeate all of space and are composed of highly energized, positively charged particles as well as high energy photons. Approaching the earth at near the speed of light, most cosmic rays are blocked by the earth's protective atmosphere and magnetic field. As a byproduct of the interaction between cosmic rays (i.e. particles) and the atmosphere, many radioactive isotopes are formed such as **carbon-14**.

It is reasonable to assume that the production of <sup>14</sup>C in the atmosphere has been constant for at least a million years, which means that equilibrium exists between the rates of formation and decay of the <sup>14</sup>C in the atmosphere. Moreover, the half-life of <sup>14</sup>C is sufficient to allow equilibrium between the <sup>14</sup>C in the atmosphere, the oceans (including precipitations to ocean bottoms), and exchangeable carbon in natural materials. Thus from measurement of the specific radioactivity of carbon, it should be possible to determine when the sample became isolated from its natural environmental compartment.

Cosmic rays are also composed of high energy photons, and not all are prevented from reaching the earth's surface. It makes sense that the higher you are in altitude, the more you are exposed to cosmic radiation.

### **3.Nuclear Radiation from Human Activities**

Although radioisotopes occur naturally in the environment, activities of humans have brought this radiation closer to us all. For examples, the bricks, stones, cements and drywalls that we use for the building of our homes, schools, offices frequently contain uranium ores and are thus sources of radon.

The human production of tobacco products introduces another way for us to get exposure to radiation. Smokers receive a dose of radiation from polonium-210 which is naturally present in tobacco. Smokers also receive an additional dose of radiation from the decay product of radon gas, polonium-218. Polonium-218 clings to aerosols such as tobacco smoke, and eventually winds up in the lungs. Once in the lungs, polonium decays by alpha particle emission and in the process may damage cells.

Strontium-90 and cesium-137 are the radioisotopes which should be most closely guarded against release into the environment. They both have intermediate half-lives of around 30 years, which is the worst range for half-lives of radioactive contaminants. It ensures that they are not only highly radioactive but also have a long enough half-life to be around for hundreds of years. Strontium-90 mimics the properties of calcium and is taken up by living organisms and made a part of their electrolytes as well as deposited in bones. As a part of the bones, it is not subsequently excreted like cesium-137 would be. It has the potential for causing cancer or damaging the rapidly reproducing bone marrow cells.

Strontium-90 is not quite as likely as cesium-137 to be released as a part of a nuclear reactor accident because it is much less volatile, but is probably the most dangerous components of the radioactive fallout from a nuclear weapon.

Iodine-131 is a major concern in any kind of radiation release from a nuclear accident because it is volatile and because it is highly radioactive, having an 8 day half-life. It is of further concern in the human body because iodine is quickly swept up by the thyroid, so that the total intake of iodine becomes concentrated there. The thyroid has a maximum uptake of iodine, however, so some protection against iodine releases can be afforded by taking potassium iodide tablets to load up the thyroid to capacity so that radioactive iodine would be more likely to be excreted.

Most of the radionuclides produced in nuclear tests, accidents and in the normal fuel cycle are short lived.

As the amount of spent nuclear fuel increases, the contribution to the total plutonium in the environment could become more significant over a longer time, especially if nuclear waste disposal sites release actinide elements slowly to the environment. Whatever the sources of plutonium and other actinides, their presence a contamination of the environment by highly toxic material.

The majority of the plutonium from weapons testing was injected initially into the stratosphere. The plutonium originally in the weapon which survived the explosion would have been formed into high-fired oxide which would be expected to remain insoluble as it returned to earth. Such insoluble particles would have sunk in a rather short time into the bottom sediments of lakes, rivers, and oceans or would become incorporated in soils below the surface layer.

These observations indicate that the speciation of radionuclides in the atmosphere is dependent on their source, their mechanisms of production and the nature of the particular environment. While some species are gaseous, others are associated to particles with properties and suspension times that are strongly dependent on the particle size and density.

## REFERENCES

1. Gregory Choppin, Ian-Olov Liljenzin, Jan Rydberg *Radiochemistry and Nuclear Chemistry* Butterworth-Heinemann, 2002, 123-642
2. M. Negulescu, *Protectia mediului inconjurator*, Ed Tehnica, Bucuresti, 1995, 149-172
3. G. Ciplea, *Poluarea mediului ambient*, Ed. Tehnica Bucuresti, 1978, 165-175

## SEMICONDUCTOR GAS SENSOR FOR DETECTING AIR POLLUTION

**NICOLAE-MARIUS BÂRLEA, SÎNZIANA IULIA BÎRLEA**

*Technical University of Cluj-Napoca, Physics Department, Str. C. Daicoviciu 15,  
ROMANIA, E-mail: mbirlea@phys.utcluj.ro*

**ABSTRACT.** Over 50 million tin dioxide gas sensors have been used in domestic gas alarms since 1968 to 1990 only in Japan. Many other oxides are gas sensitive as LICKÉ iron oxides, chromium oxides, zinc oxide, etc. In this paper we characterize gas sensitive sensors made in our laboratory. A hot filament heats the oxide material of the gas sensor (deposited on a ceramic cylinder) to the functioning temperature (100-400°C). When it is exposed to an atmosphere containing a reducing gas (a gas which can interact with the oxygen from the air), the electric resistance of the semiconducting material is dramatically modified, even at very low gas concentrations. We present the influence of the supplied electric current to the sensor sensitivity and the response time and recovery time. The advantages for using semiconducting gas sensors for detection of the air pollution (toxic and/or flammable gases) are emphasized.

### INTRODUCTION

Air pollution by noxious exhaust gases from autovehicles' engines and from burning methane gas and oil is becoming a serious danger. For effective prevention of air pollution a stable and inexpensive sensor for detecting dangerous gases is needed.

In the scientific literature, various oxides were proposed as gas-sensor elements, like iron oxides, chromium oxides, zinc oxide, etc. Tin dioxide ( $\text{SnO}_2$ ) is by far the most popular semiconductor oxide used in semiconductor gas sensors, mainly for its ability to sense hydrocarbures and carbon monoxide. The tin dioxide is used as a thin film or as a thick film sintered powder. Naoyoshi Taguchi designed the semiconductor gas sensors based on tin dioxide in 1962 [1]. Only in Japan there have been used over 50 million Taguchi sensors in domestic gas alarms since 1968 to 1990 [3].

The main mechanism of operation is through surface electrical conductivity changes of the semiconductor induced by chemical reactions on the surface [4]. Atmospheric oxygen is chemisorbed on the surface primarily as  $\text{O}^-$ , and it ties the electronic carriers, decreasing the electrical conductivity of the N-type semiconductor sensor. Any reducing gases that may be present in the atmosphere will remove the chemisorbed oxygen, liberating electronic carriers into the conduction band of the semiconductor and enhancing its the electrical conductivity. Therefore any given mixture of atmospheric oxygen and a reducing gas will produce a unique sensor conductance for that gas concentration.

### THE DEVICE

As it is show in figure 1, the semiconductor sensor for gas detection made in our laboratory contains:

1. a cylindrical ceramic body ( $\text{Al}_2\text{O}_3$ )
2. a coiled filament for heating (stainless steel AISI 304, 50  $\mu\text{m}$  diameter),
3. a pair of platinum contacts,
4. the semiconductor material,  $\text{SnO}_2$ , deposited over the contacts,
5. a porous case for protection, made from sintered bronze balls, gas permissive,
6. a mounting base which connect the sensor's inner wires with external wires.

The inner hot filament heats the semiconducting material of the gas sensor (placed on the ceramic cylinder) to the functioning temperature (100-400°C). The platinum wires make a nonrectifying contact with the semiconductor (tin dioxide).

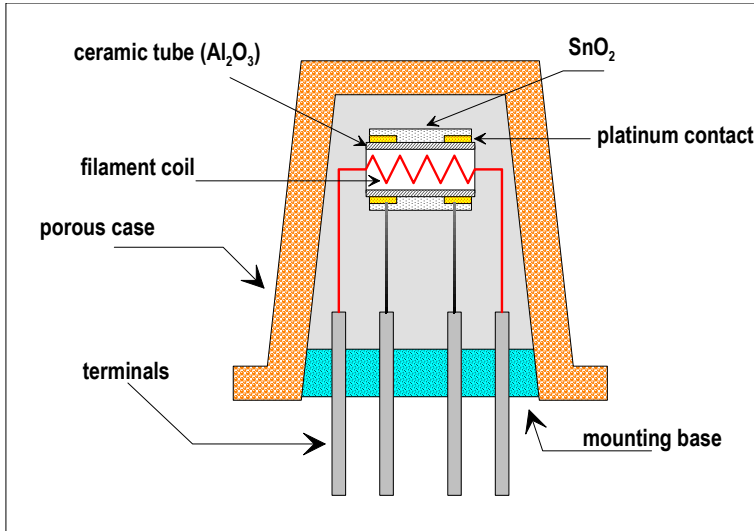


**Fig. 1.** Sensor's structure (protected by a porous bronze case and closed by a mounting base with the terminal leads):  $\text{Al}_2\text{O}_3$  cylinder with inner heater filament coil and external  $\text{SnO}_2$  semiconductor sensing material, which have two platinum contacts.

### THE EXPERIMENT

Our sensors were tested with carbon monoxide (CO), liquid petroleum gas (LPG, mainly butane) and methane gas. Known quantities of test gas were injected in the test chamber which volume was 20 ml. The electrical resistance of the sensor was recorded. After each test the chamber was washed with clean air and we waited that electrical resistance of the sensor to return at the clean air value. This protocol was repeated for each gas concentration and each supply voltage.

The heating current for the filament is provided by a monolithic adjustable three terminals voltage regulator (LM317). The output voltage is set by the adjustment potentiometer and measured with a digital voltmeter (3 ½ digits). The electrical resistance of the  $\text{SnO}_2$  thick film is measured by an ohmmeter (3 ½ digits) as shown in figure 2.

Sensor's sensitivity ( $R_{\text{air}}/R_{\text{gas}}$ ) for methane grows from 2,8V to 3,6V of the supply voltage, at 4V being slightly lower. For LPG the sensitivity grows from 2,2V to 3,1V and the sensitivity for CO grows from 2V to 3,5V. In table 1 we present a set of measurements for methane in air at a supply voltage of 3,6V.

Response time was determined with the aid of a chart recorder. As a rule, the recovery time (time needed to return at the clean air sensor's resistance) was longer than the response time (time needed for stabilizing the resistance's value in air with gas). Response time was longer for lower supply voltage (many seconds, even minutes) and became very short (under 1 second) at the greatest voltages.

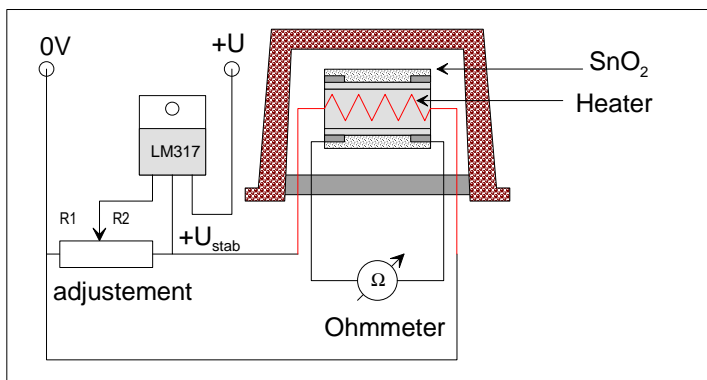


**Fig. 2.** Measurement set-up: the heater is biased by the stabilized tension from a monolithic adjustable three terminal voltage regulator (LM317) and the resistance is measured by an ohmmeter (3 ½ digits).

**Table 1.**  
The values of the electrical resistance of the gas sensor versus methane concentration

c (%CH <sub>4</sub> )	R(kΩ)	ln (c)	lnR
0 (clean air)	124	-	4,82
0,4	21	-0,916	3,04
0,8	14	-0,223	2,64
1,2	9,8	0,182	2,28
1,6	8,3	0,470	2,12
2	6,0	0,693	1,79
4	3,8	1,386	1,33
6	2,4	1,792	0,87
8	1,8	2,079	0,59

**CONCLUSION**

SnO<sub>2</sub> electrical conductance depends on reducing gas concentration [5]:

$$G = G_0 + \gamma p^S \tag{1}$$

where:

- "S" – an exponent (value close on 0,5),
- "γ" – a constant,
- "p" – partial pressure of the reducing gas,
- "G<sub>0</sub>" – clean air conductance (very low in general).

If we neglect the clean air conductance (G<sub>0</sub>) then the sensor's resistance (1/conductance) is:

$$R \sim p^{-S} \sim (\text{gas concentration})^{-S} \tag{2}$$

a useful relation, because the exponent "S" is an indicator of the quality of the gas sensitivity of the semiconductor material (greater "S", greater sensitivity). For the data in table 1, presented in a double logarithmic scale in figure 3, the parameter "-S" is 0,83, a good figure of merit.

The advantages for using semiconducting gas sensors for detection of the flammable and/or toxic gases are: high sensitivity, resistance to poisoning, robust construction, long life (over 10 years), no need for recalibration (low maintenance cost), low device's price (~ 20 \$).



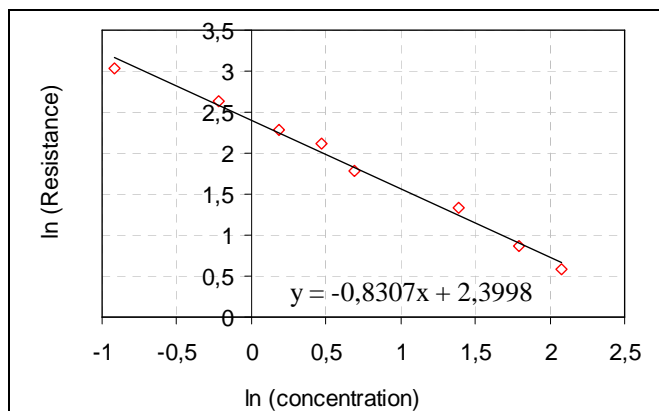


**Fig. 4.** Logarithm of sensor's resistance versus logarithm of gas concentration.

## REFERENCES

1. Naoyoshi Taguchi, US patent 3,644,795 (1972);
2. T. Seiyama et al. Anal. Chem. (1962) **34**, 1502-1503.
3. FIGARO products catalog, pag. 2, (1990).
4. S. Roy Morrison, "*Selectivity in semiconductor gas sensors*", Sensors and Actuators (1987) **12**, 425-440.
5. N. M. Bârlea "*Fizica senzorilor*", pag. 85, Editura Albastra, Cluj-Napoca, 2000.

## STRUCTURAL CHANGES IN DENTAL ALLOYS INVESTIGATED BY MICROSCOPY

**V. A. SZABO<sup>1</sup>, C. IONESCU<sup>2</sup>, V. SIMON<sup>1</sup>**

<sup>1</sup>*Babes-Bolyai University, Faculty of Physics, 3400 Cluj Napoca, Romania*

<sup>2</sup>*Babes-Bolyai University, Faculty of Biology and Geology, 3400 Cluj Napoca, Romania*

**ABSTRACT.** Dental alloys based on Ni-Cr, Au, stainless steel and special brasses were investigated in order to evidence structural changes induced both by modelling procedures and by the employ of these materials under mechanical stress and corrosion conditions. The metallographic examinations point out that the corrosion process is accelerated around the high mechanically stressed sites and welded joints.

### 1. Introduction

Metallic biomaterials are used as pins for anchoring tooth implants and as parts of orthodontic devices. The oral environment represents a combination of complex conditions: intraoral flora, variable alterations in pH and warm, moist environment, which, when subjected to fluctuating stresses during mastication, leads to irregular cyclic fatigue conditions that may be further exacerbated by stress corrosion processes. Such an aggressive environment can cause failure processes in metallic, ceramic, or polymeric materials. Even though numerous studies [1-4] have been performed, the mechanisms involved in these aging/wearing processes have not yet been completely explained.

The purpose of this study is to examine the wearing effect on some dental metallic biomaterials with respect to their microscopic structural changes, due to the fact that proper mechanical and corrosion resistance properties of dental metallic biomaterials are implicitly determined by their structure.

### 2. Experimental

The samples investigated in the present study are alloys based on Ni-Cr, Au, stainless steel and special brasses. The last one is an alloy consisting on 80-85 % Cu, 8.5-10% Al, 3-4 %Ni, 1.5 – 2.5 % Mn and 1 – 2% Fe, with a hardness of 130 HB. All samples were mirror polished and etched with nitrohydrochloric acid (3HCl:HNO<sub>3</sub>). The mosaic blocks dimensions, grain size dimension, interdendritic spaces dimensions, dislocation features and crystallinity were analysed on selected areas of the etched samples using a Nikon Eclipse E200 microscope. The computed images were recorded with a Nikon Kooply X995 camera.

### 3. Results and discussion

The metallographic examination allows to determine the changes induced in the wearied samples in relation to reference samples processed in similar conditions and of same composition. The results inform on processing quality, crystalline texture, corrosion level, crystallites deformation and homogeneity of welded joints.

Figure 1 shows two modifications occurred in a stainless steel dental material. One remarks that the crystallite boundaries are excessively corroded due both to a deficient processing and a weak corrosion resistance. At the same time are evidenced holes developed during the

corrosion process around structural defects. A dental crown of stainless steel of same composition, modelled at a proper temperature, has after aging the microstructure shown in Figure 2. It is well evidenced the austenite structure typical for stainless steels. The corrosion depth for this sample lies in the accepted limits of 1.5-5  $\mu\text{m}/\text{year}$ , estimated in vitro [6].

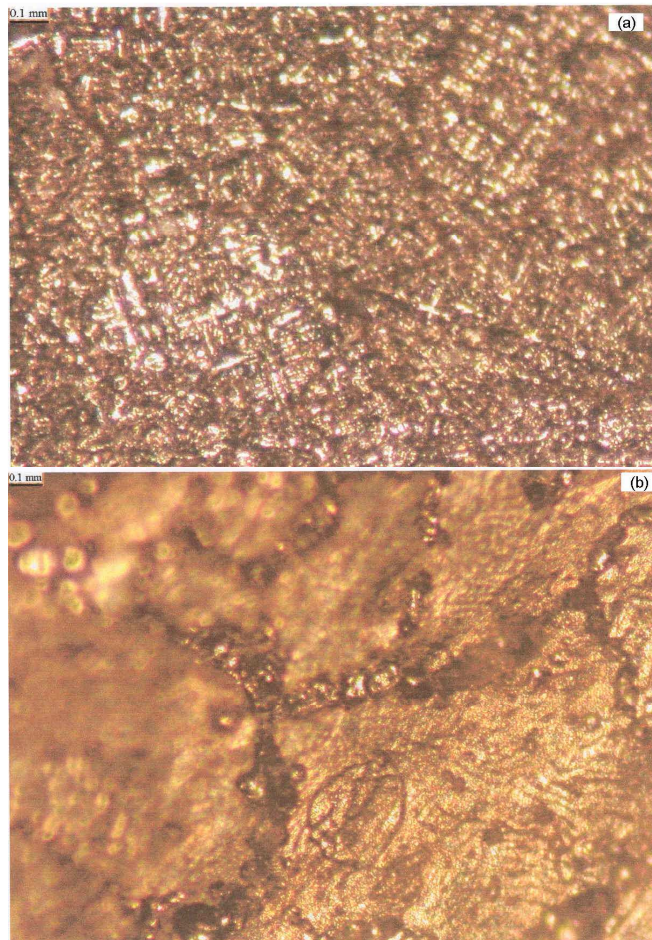


**Fig. 1.** Microstructure of a dental stainless steel. a.) reference b.)worned sample

A high stability is observed for dental alloys based on gold and Ni-Cr. As can be seen from Figure 3, the analysed Ni-Cr sample kept the dendritic structure of the crystallites with a good package and minimal corrosion effects.

In Figure 4 are depicted the microscopies obtained from welded samples of dental stainless steel. Such welds are necessary to repair cleaved or broken dental works.

One observes a good structural compatibility between the two materials in the first case (Fig. 4a), that will confer durability to the joint, and a structural incompatibility in the second case (Fig. 4b). In Figure 4a the crystallites are of comparable size in the two materials and the welded section will have similar mechanical properties with the host material.

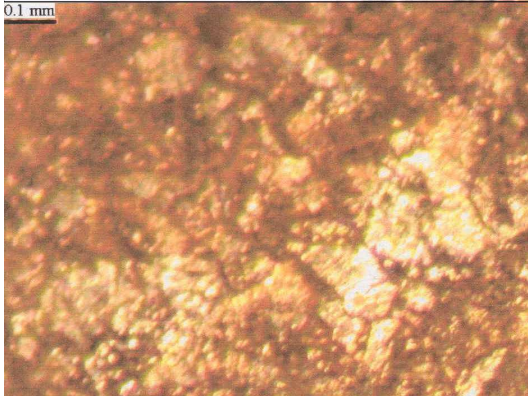


**Fig. 2.** Microstructure of a dental stainless steel wearied sample

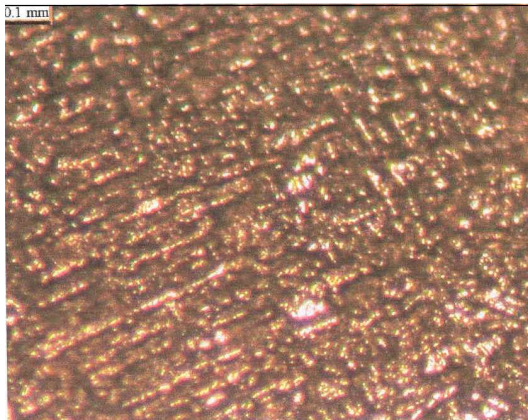


**Fig. 3.** Microstructure of a wearied dental crown of Ni-Cr alloy.

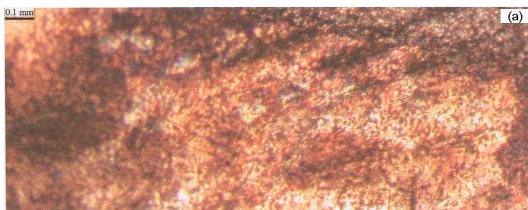


**Fig. 4.** Microstructure of a welded dental stainless steel. In the upper right corners is the stainless steel and the rest of images shows the weld material.

It was found that a very slight change in the composition of dental alloys has a strong influence on their weldability and in the welding zone was pointed out a very important change in the microstructure due to increasing micro-hardness [6,7].

#### 4. Conclusion

The grain morphology in metallic orthodontic devices is affected in all regions mechanically stressed during modelling. The crystallite textures for the same composition of stainless steels is influenced by the modelling temperature. An accelerated corrosion process occurs around the high mechanically stressed sites and at the welded joints. Among the investigated dental materials, excepting the gold alloys, the highest corrosion resistance and implicitly the highest bioresistance was observed for alloys based on Ni-Cr.

#### REFERENCES

1. H. J. Seol, T. Shiraishi, Y. Tanaka, K. Hisatsune, *J. Mater. Sci: Mater. Med.*, 13, 237 (2002)
2. M. Ohta, T. Shiraishi, M. Nakagawa, M. Matsuya, *J. Mater. Sci.*, 29, 2083 (1994)
3. T. Shiraishi, M. Ohta, M. Yamane, *Dent. Mater. J.*, 3, 193 (1984)
4. K. Yanaru, K. Yamaguchi, H. Kakigawa, Y. Kozono, *Dent. Mater. J.*, 22, 2 (2003)
5. F. Laurent, B. Grosgeat, L. Reclaru, F. Dalard, M. Lissac, *Biomaterials*, 22, 2273 (2001)
6. C. Bertrand, Y. Le Petitcorps, L. Albingre, V. Dupuis, *British Dental J.*, 190, 5, 255 (2001)
7. H. Y. Seol, T. Shiraishi, Y. Tanaka, E. Miura, K. Hisatsune, H. Kim, *Biomaterials*, 23, 4873 (2002)

## SOLID STATE CELLS FOR CARDIAC PACEMAKERS

GEORGETA TARALUNGA

*University of Agricultural Sciences and Veterinary Medicine, 3-5 Mănăștur  
Street, 3400 Cluj-Napoca, Romania*

**ABSTRACT.** A wide diversity of batteries are utilized such as implanted medical devices (pacemaker) and external devices for monitoring of bodily functions. For the safety of patients, it is used the solid state batteries which have a number of very desirable features. In this paper are presented the main characteristics of Ag/RbAg<sub>4</sub>I<sub>5</sub>/AgI<sub>3</sub> cell.

### INTRODUCTION

The advances in battery technology, electronics and medical knowledge have produced a wide variety of sophisticated implantable devices to treat ailments ranging from irregular heartbeat to pain and epilepsy. Also a great diversity of battery powered external devices are used to administer drugs, treat ailments and monitor bodily functions.

Generally, for the safety of patients, it is used the solid state batteries which have a number of very desirable features such as absence of any possible liquid leakage or gassing and the possibility of operation over a wide temperature range. The batteries with RbAg<sub>4</sub>I<sub>5</sub> solid electrolyte are made part from these galvanic cells.

The solid electrolyte RbAg<sub>4</sub>I<sub>5</sub> belong to the compounds-group of general formula MAg<sub>4</sub>I<sub>5</sub> (where M<sup>+</sup> = Rb<sup>+</sup>, K<sup>+</sup>, NH<sub>4</sub><sup>+</sup>) having an exceptionally high ionic conductivity (about 10<sup>-1</sup> S/cm) at room temperature. The structures of these solid electrolytes are not close-packed, but contain two- or three networks of passageways intercalated in crystalline structures.

The crystallographic structure of RbAg<sub>4</sub>I<sub>5</sub> was determined by X-ray diffraction. There are three crystalline modifications of RbAg<sub>4</sub>I<sub>5</sub>, labeled as the α, β and γ phases in order of decreasing temperature. The α form has a cubic crystal lattice of P4<sub>1</sub> 32 (O<sup>7</sup>) or P4<sub>3</sub> 32 (O<sup>6</sup>) symmetry, β form has a rhombohedral crystal lattice of R 32 (D<sub>3</sub><sup>7</sup>) symmetry and γ modification has a hexagonal structure of loss P 321 (D<sub>3</sub><sup>2</sup>) symmetry.

The high conductivity is due to a combination of a high concentration of mobile ions and a low activation energy for ionic motions from site to site. For these materials the silver ion is mobile specie and its transport into lattice takes place by a defect mechanism [1-4].

### EXPERIMENTAL DATA

The solid electrolyte RbAg<sub>4</sub>I<sub>5</sub> was prepared by an original method [5-7].

RbAg<sub>4</sub>I<sub>5</sub> samples were obtained by isothermal crystallization (at 55<sup>0</sup>C) from acetone solution containing a mixture of RbI and AgI in molar ratio 1:2. By gravimetric and chemical analyses, it was established that the prepared powder is RbAg<sub>4</sub>I<sub>5</sub> having a 98.894% purity. The structural characterization of the prepared RbAg<sub>4</sub>I<sub>5</sub> was performed by X-ray diffraction .

With RbAg<sub>4</sub>I<sub>5</sub> solid electrolyte prepared were realized two types (I- and II-type) of Ag/RbAg<sub>4</sub>I<sub>5</sub>/RbI<sub>3</sub> button cells. The cathodes for both types of batteries were performed from a mixture of RbI<sub>3</sub> (87.30%), graphite (6.75%) and RbAg<sub>4</sub>I<sub>5</sub> (5.95%), which was pressed. The anode for the I-type cell was an amalgamated silver disk of 0.02 mm thickness and for II-type cell a mixture of Ag powder (88.00%), graphite (8.00%) and RbAg<sub>4</sub>I<sub>5</sub> (12.00%), which was pressed. The cells were assembled by pressing of their components (anode, solid electrolyte and cathode) at 1700 kgf/cm<sup>2</sup> for 20 minutes.

**RESULTS AND DISCUSSION**

From X-ray diffraction pattern of obtained powder it comes that are present only specific diffraction lines of  $\alpha$ -RbAg<sub>4</sub>I<sub>5</sub> solid electrolyte.

The values of e.m.f. for I-type cells were situated in the range 590-600 mV and for II-type were 650-660 mV. The electrochemical behavior of RbAg<sub>4</sub>I<sub>5</sub> solid state cells was investigated by performance curves under constant load and galvanostatic regime.

From Fig.1, where are showed the discharge curves of I-type and II-type cells under constant resistance (R=100Ω), it can see that the II-type cell has higher characteristics than the I-type battery.

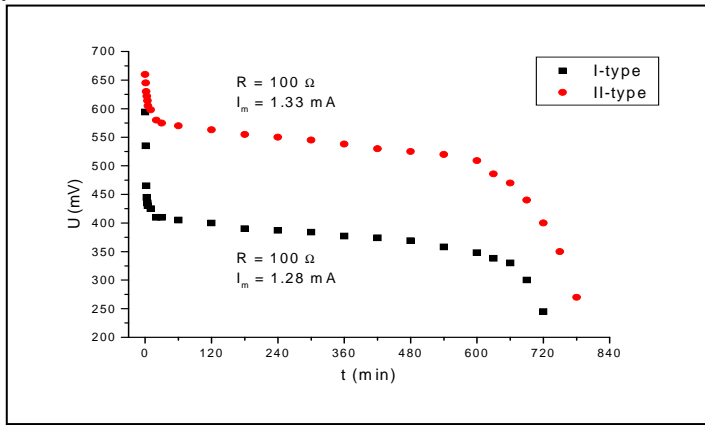


**Fig. 1.** Discharge curves of I-type and II-type cells under R=100Ω

Thus the discharge plateau of II-type was situated in the domain 525-575 mV, whereas for I-type in range 350-400 mV. The average discharge intensity was of 1.33mA for II-type and 1.28mA for I-type cell.

The batteries were discharged at two current densities:  $i=2\text{mA/cm}^2$  (Fig.2) and  $i=0.2\text{mA/cm}^2$  (Fig.3) in galvanostatic regime. From the discharge curves it can ascertain that at less current density ( $0.2\text{mA/cm}^2$ ) the discharge plateaus have higher values for I-type cell, close to those of II-type cell. At the current density of  $0.2\text{mA/cm}^2$  the total yielded energy was of 10.20mWh for I-type cell and 11.89mWh for II-type cell.

The electrochemical characteristics of Ag/RbAg<sub>4</sub>I<sub>5</sub>/RbI<sub>3</sub> cells are presented in Table 1, where from the experimental data were calculated: C- the mass capacities, W- the energy densities, and u- the utilization coefficients of active material (silver).

**Table 1**

**The electrochemical characteristics of batteries with RbAg<sub>4</sub>I<sub>5</sub> solid electrolyte**

Type cell	Mass [g]	Discharge regime	i [mA/cm <sup>2</sup> ]	C <sub>g</sub> [Ah/kg]	W <sub>g</sub> [Wh/kg]	u [%]
I	1.096	Load R=100Ω	2.52	13.80	5.92	55.2
II	1.037		2.63	16.49	9.79	66.0
I	0.995	galvanostatic	2	15.07	6.22	62.8
II	1.053			15.20	9.00	63.3
I	0.915	galvanostatic	0.2	20.22	11.15	84.3
II	0.954			20.44	12.46	85.2

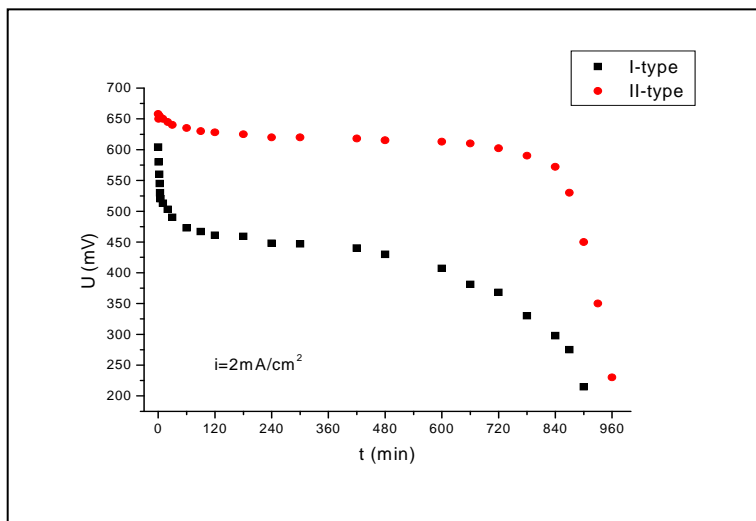


Fig. 2. Discharge curves of cells at  $i=2\text{mA}/\text{cm}^2$

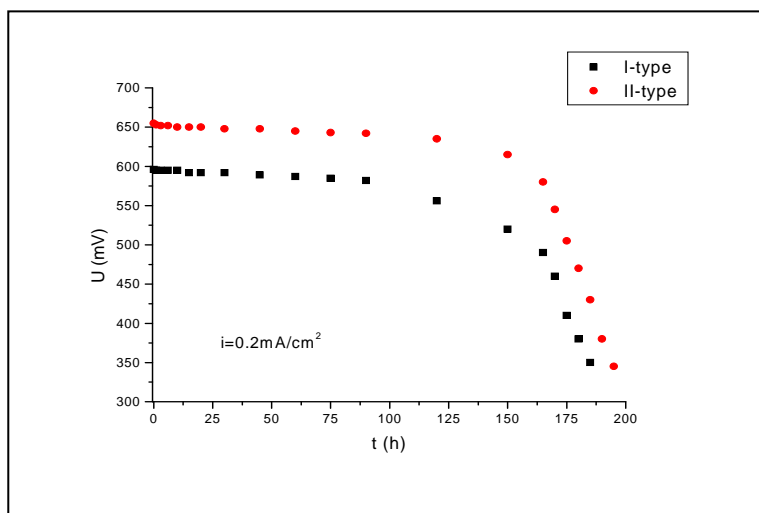


Fig. 3. Discharge curves of cells at  $i = 0.2\text{mA}/\text{cm}^2$

As can be seen from Table 1, the all calculated parameters are better for II-type cells than for I-type cells. The mass capacities and energy densities depend on the discharge regime, they are higher under galvanostatic at less current densities ( $0.2\text{mA}/\text{cm}^2$ ).

**CONCLUSIONS**

From the obtained results it can be establish that  $\text{Ag}/\text{RbAg}_4\text{I}_5/\text{RbI}_3$  batteries present good electrochemical characteristics to use in medical devices such as cardiac pacemaker.



## REFERENCES

1. Bradley, J. N., P. D. Greene., *Solid with high ionic conductivity in group I halide systems*, Trans. Faraday Soc., 1967, **63**, 424-429.
2. Funke, K., *Transport and relaxation in ionic crystal*, Ber. Bunsenges. Phys. Chem. 1989, **93**, 1197-1201.
3. Holmes, c.f., *The role of electrochemical power sources in modern health care*, The Electrochemical Society-Interface, 1999, **8**, 32-34.
4. Vincent, C.A., F. Bonino, M. Lazzari, B. Scrosati, *Modern Batteries*, Chap.7, edited by Edward Arnold (Publishers) Ltd., London, 1984.
5. Bolla, Cs. C., Georgeta Țarălungă, A. Borbely-Keri, L.D. Bobos, Silvia Avram, L. Oniciu, *Batteries with RbAg<sub>4</sub>I<sub>5</sub> solid electrolyte*, Batteries for Portable and Electric Vehicle Applications, A. Landgrebe Ed., the Electrochemical Society Inc. Pennington, N.J. USA, 1997, **18**, 518-523.
6. Bolla, Cs., ILDIKO SZEKELY, A. Borbely-Keri, L. Oniciu, Georgeta Țarălungă, *Pile galvanice miniaturizate*, In Producerea, Transportul si Utilizarea Energiei, vol. XIV, pp. 101-105, Cluj-Napoca, 1995.
7. Bolla, Cs. C., Ph. D. Thesis *Electroliti solizi și aprotici pentru pile galvanice neconvenționale*, "Babeș-Bolyai" University, Cluj-Napoca, 2001.

## ELECTRICAL FIELD ACTION ON LIPID BILAYER - MATHEMATICAL MODEL

**D. E. CREANGA**

*Univ. Al. I. Cuza, Fac. of Physics, 11 A Bd. Carol I, Iasi*

Lipid bilayer behavior was studied starting from the dependence of the rate of hydrophilic pore formation on the pore activation energy, that is depending on the area of a single lipid molecule as well as on the temporal parameters of the electrical field application and is increased under the action of an electrical field. The mathematical model proposed inhere describes the permeability of the lipid bilayer for different values of the electrical constraint. The main differential equation intended for the mathematical model development led finally to a cubic solution that takes various graphical forms for different values of the parameter  $d$ , related to the presence of a cation channel controlled by other cation species. The negative slope of the hysteresis type curve that was noticed for certain  $d$  values, may be taken as an indication of the self-adjusting phenomena underlying the charged species transport phenomena through membrane pores under the electrical field influence. Though not fitted yet with experimental data, the model may be useful in the study of therapeutical protocols where drug substances are ionized molecules.

### Phenomenological background

Artificial membranes consistent with lipid bilayers are convenient biophysical models used for the study of charged species transport. Permeability of lipid bilayers can be controlled using electrical fields, the rate of hydrophilic pore formation being calculated by Glasser et al. (1) as an exponential function of the activation energy,  $\Delta W$ , in dependence also of the single lipid area,  $s$ , the temperature  $T$  and the frequency of lateral fluctuations of the lipid molecule  $\nu$ . The pore activation energy was assumed proportional to the voltage drop  $u$ , pore radius  $r_0$  and the relative permittivity of water inside pore  $\epsilon_w$  and of the lipid molecule  $\epsilon_m$ . So, the rate of pore activation was found as being equal to:

$$\frac{dN}{dt} = \frac{\nu}{a} \left[ \frac{t_p}{t_i} \right] \exp \left[ -\frac{\Delta W^0}{kT} + \frac{\pi r_0^2 (\epsilon_w - \epsilon_m) \epsilon_0 u^2}{2dkT} \right] - \frac{N}{t_r} \quad (1)$$

where:  $N$  is the pore density,  $h$  is the layer thickness,  $\epsilon_0$  is the dielectric constant,  $k$  is Boltzmann's constant,  $\Delta W_0$  is the activation energy in the lack of the electrical field,  $t_p$ ,  $t_i$  and  $t_r$  being the electrical pulse duration, the interval between pulses and the pore resealing time. It is obvious that the electroporation rate is lower when a certain number of pores are already formed.

We propose the study of the lipid bilayer with protein incorporated so that ion channels permeable for a species of cations ( $C_1$ ) are present in the artificial membrane.

### Mathematical model

The mathematical model that was developed inhere assumes that ion channels are not voltage dependent but they are activated by a second species of cations  $C_2$  while in the two compartments separated by the lipid bilayer both cation species can be found.

- (i) The electrical field is applied in the direction of  $C_2$  ions gradient (for instance from the left to the right) so that electroporation facilitates  $C_2$  transport through the membrane.
- (ii) Once they pass through the membrane they are able to activate  $C_1$  channels so that the rate of cation concentration increase in the right compartment is enhanced significantly.
- (iii) As a consequence, a local field opposite to the external one is generated and the electroporation rate is slowed down rapidly as well as that of cation accumulation in the right side compartment.
- (iv) The attachment of  $C_2$  cations to the  $C_1$  ion channels diminishes cation concentration in the right side compartment.

The differential equation describing the above presumptions proposed in this article has the form:

$$\frac{dn}{dt} = \frac{v}{s} \left[ \frac{t_p}{t_i} \right] \frac{a.u.^2 \pi.r_0^2 (\epsilon_w - \epsilon_m) \epsilon_0}{2.k.h.T} + \frac{b.n^2}{1+c.n^2} - d.n \quad (2)$$

where the first term in the right side corresponds to the above (i) hypothesis, the nominator of the second term corresponds to the hypothesis (ii), the denominator of the second term expresses the presumption (iii) while the third term describes the (iv) assumption;  $a$ ,  $b$ ,  $c$  and  $d$  are the parameters describing the rates of the four processes invoked above. It is evident that instead of the exponential dependence the second order polynomial dependence was used.

### Result and discussion

The investigations aiming the describing of the stationary states, the left side of the equation (2) was taken as equal to zero so that, left side of the equation (2) vanishes and for calculation simplicity one can take all coefficients equal to the unit except that we focused on for the interpretation of the cation dynamics:

$$\frac{v}{s} \left[ \frac{t_p}{t_i} \right] \frac{a\pi.r_0^2 (\epsilon_w - \epsilon_m) \epsilon_0}{2khT} = 1, b = 1, c = 1, d \neq 1 \quad (2')$$

The equation (3) will be further discussed for different values of  $d$ :

$$u^2 + \frac{n^2}{1+n^2} - dn = 0 \quad (3)$$

The interesting cases were found for certain  $d$  values and for relatively small values of the independent variable ( $u$  - up to 1 kV). The initial value of cation concentration in the right compartment is taken formally as equal to zero. In all below graphs the independent variable,  $u$ , is noted with  $x$  while  $n$  is noted with  $y(x)$ . Monotone curve corresponds to the case of two complex solutions and was obtained for  $d$  higher than 0.65 (fig. 1). For  $d$  values lower than 0.65 the curve shape changes so that three distinct zones can be seen: between two zones with monotone shapes a negative slope curve zone appears, very narrow at the beginning but covering whole range between 0.25 and 0.0 (fig. 2-3) for  $d$  approximately equal to 0.6. The negative slope of the hysteresis type curve may be usually taken as an indication of the self-adjusting phenomena underlying the charged species transport phenomena through membrane pores under the electrical field influence.

In fig. 4 a turning point is visible having the coordinates (0;1). For lower  $d$  values the loop resulted in the small  $x$  values becomes smaller and smaller while the distance between the loop and the monotone branch situated at high  $y$  values becomes larger. For

further decreasing  $d$  values two distinct branches of  $y(x)$  are visible suggesting that the cation system can pass suddenly from one low-energy state to another state with higher energy and lower stability. The stable energetical states correspond to relatively low values of the electrical field,  $u$ , while it is enhancing from zero to about 0.25 kV. When the total electrical field is diminished following the generation of a local field of opposite direction, then the cation system can pass to an unstable state, its concentration remaining non-zeroed. After the activation of ion channels assuring membrane permeability for the second cation species the system may pass to a higher energetical state (for the same value of the external electrical field) non-stable because of the complexity of phenomena involved in the ion transport through the artificial membrane.

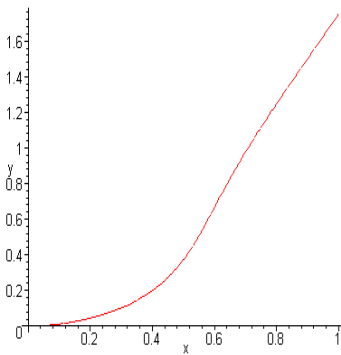


**Fig. 1.** Graphical plot of the solution  $y(x)$  obtained for  $d > 0.65$

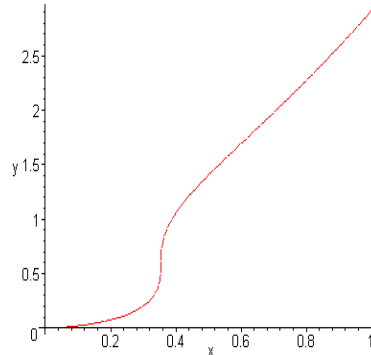


**Fig. 2.** Graphical plot of the solution  $v(x)$  obtained for  $d = 0.65$

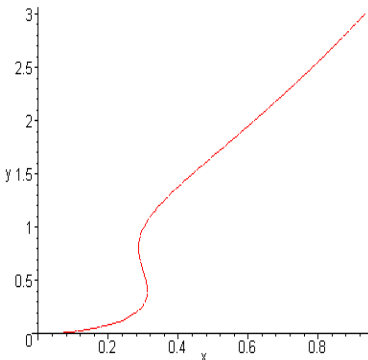


**Fig. 3.** The case of negative slope for  $d = 0.59$

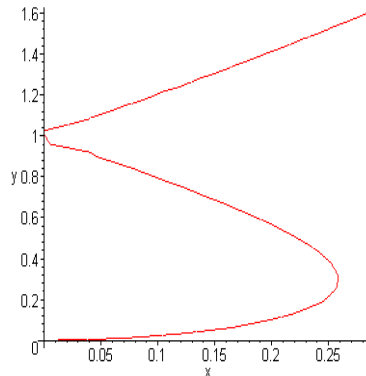


**Fig. 4.** The turning point revealed for  $d = 0.4998$

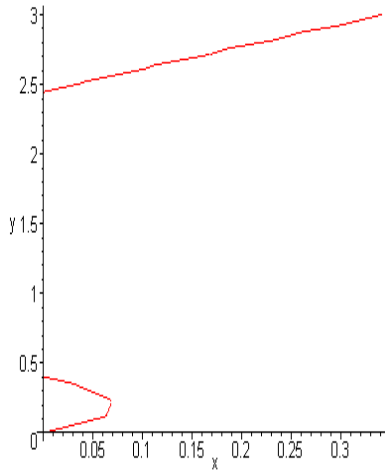


**Fig. 5.** Two distinct branch solutions for  $d=0.35$

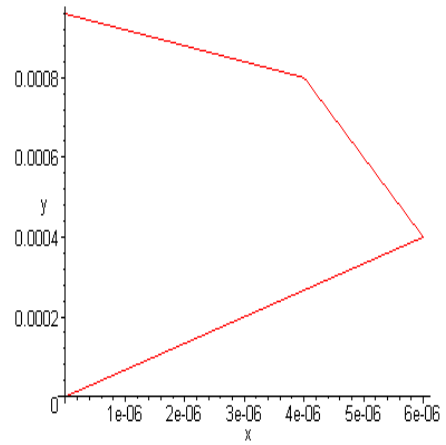


**Fig. 6.** The inferior branch of the solution.  $y(x)$  is very short and narrow for  $d=0.001$

### Conclusion

Non-linear behavior of ion concentration under the action of an electrical field could be revealed for certain values of the parameter corresponding to cation concentration diminution after attaching to ion channel cation-controlled. Electrical measurements with adequate devices, able to recorded time real data, could validate or not the proposed model.

### REFERENCES

1. Chizmadzhev, Y. A., Zarnitsin, V. G., Weaver, J. C., Potts, R. O., *Mechanism of electroinduced ionic species transport through a multilamellar lipid system*, Biophysical Journal, 1995, 68 (3), 749-765
2. Clarke, R. J., Zouni, A., Holzwarth, J. F., *Voltage sensitivity of the fluorescent probe RH421 in a model membrane system*, Biophysical journal, 1995, 68 (4), 1406-1416

## MATHEMATICAL APPROACH ON THE FREE $\text{Ca}^{+2}$ KINETICS IN THE MUSCLE CELL

D. E. CREANGA

*Univ. Al. I. Cuza, Fac. of Physics, 11 A Bd. Carol I, Iasi*

**ABSTRACT.** The theoretical model presented inhere was proposed to describe the in vivo circulation of  $\text{Ca}^{+2}$  ions through the plasma membrane as well as through the sarcoplasmic reticulum (SR) storage membranes, based on in vitro experimental findings. A set of differential equations was written and solutions were identified according to the “standard” bi-compartmental model. The time constants  $k_{12}$ ,  $k_{21}$  and  $k_{01}$  describing ion transport through the system compartments can be calculated.

### Theoretical background

The two-compartment physiological model is able to describe the kinetics of a labeled substance  $s$ , which is passing between two physiological compartments  $C_1$  and  $C_2$ , so that  $C_1$  communicates with  $C_2$  as well as with the physiological pool  $C_0$  while  $C_2$  is a closed compartment (communicating only with  $C_1$ ) [1]. According to the phenomenological model,  $s_1(t)$  and  $s_2(t)$  represent the quantities of the substance  $s$  that can be found at the time  $t$  in the compartment  $C_1$ , respectively,  $C_2$ ;  $k_{12}$  and  $k_{21}$  are the time constants characterizing the circulation of the substance  $s$  between the two compartments;  $k_{01}$  and  $\rho_{10}$  are the time constant for the passing of  $s$  into the physiological pool and respectively the turnover rate characterizing the physiological pool ability of replacing the substance  $s$  from the compartment  $C_1$ . In our case the calcium ions represent the substance  $s$ , labeled, studied during the movement from the SR stores (the compartment  $C_2$ ) toward the cytoplasm (the compartment  $C_1$ ) and reversibly, as well as during the calcium exchanges between cytoplasm and the extra-cellular medium ( $C_0$ ). The differential equation system, describing the communication between  $C_1$ ,  $C_2$  and  $C_0$  by means of the calcium ions is [1]:

$$\frac{ds_1(t)}{dt} = k_{12}s_2(t) - k_{21}s_1(t) - k_{01}s_1(t) \quad (1)$$

$$\frac{ds_2(t)}{dt} = k_{21}s_1(t) - k_{12}s_2(t) \quad (2)$$

with the initial conditions:

$$s_1(0) \neq 0, s_2(0) = 0 \quad (3)$$

written in the hypothesis that a certain amount of calcium ions that we follow enters the cell at the time  $t=0$ , throw the plasma membrane calcium channels and, therefor they are not arrived yet in the second compartment at this initial moment of time. We have to mention that the turnover process (corresponding to the  $\rho_{10}$  rate constant) does not explicitly appear in the equation system solutions, since the labeled ions are not yielded naturally. The solutions of the differential equation system written for the description of the labeled substance kinetics are:

$$s_1(t) = X_1 \exp(-\lambda_1 t) + X_2(t) \exp(-\lambda_2 t) \quad (4)$$

$$s_2(t) = X_3 [\lambda_1 \exp(-\lambda_1 t) - \exp(-\lambda_2 t)] \quad (5)$$

$$\text{where: } X_1 = \frac{s_1(0)(\lambda_1 - k_{12})}{\lambda_1 - \lambda_2} \quad (6) \quad X_2 = \frac{s_1(0)(k_{12} - \lambda_2)}{\lambda_1 - \lambda_2} \quad (7) \quad X_3 = \frac{s_1(0)k_{21}S_1}{(\lambda_1 - \lambda_2)S_2} \quad (8)$$

$$\text{that is: } s_1(t) = \frac{s_1(0)(\lambda_1 - k_{12})}{\lambda_1 - \lambda_2} \exp(-\lambda_1 t) + \frac{s_1(0)(k_{12} - \lambda_2)}{\lambda_1 - \lambda_2} \exp(-\lambda_2 t) \quad (9)$$

$$s_2(t) = \frac{s_1(0)k_{12}S_1}{S_2(\lambda_1 - \lambda_2)} [\lambda_1 \exp(-\lambda_1 t) - \exp(-\lambda_2 t)] \quad (10)$$

$$\text{where: } \lambda_1, \lambda_2 = \frac{k_{12} + k_{21} + k_{01} \pm \sqrt{(k_{12} + k_{21} + k_{01})^2 - 4k_{12}k_{01}}}{2} \quad (11)$$

S<sub>1</sub> and S<sub>2</sub> being the equilibrium values of the substance s mass in the two compartments C<sub>1</sub> and C<sub>2</sub>, and s<sub>1</sub>(0) is the initial amount of s in C<sub>1</sub>, (s<sub>2</sub>(0) = 0).

### The premises for the model application

The exponential form of the above system solutions suggested a correlation with the next experimental evidences reported in literature.

(i) First, the results reported in [2] where a fluorescent dye was used to evaluate the Ca<sup>+2</sup> taken up by smooth muscle skinned cells, that revealed the rapid decreasing of calcium concentration in the cells suspension. The experimental curve describing the calcium decay in the skinned cell suspension is similar to the graphic representation of s<sub>1</sub>(t) (equivalent to the calcium kinetics in cytoplasm, namely the compartment C<sub>1</sub>).

(ii) Further, it was found that the release of Ca<sup>+2</sup> ions from isolated triad vesicles (equivalent with the circulation from C<sub>2</sub> to C<sub>1</sub>), induced by a calcium ionophore was fit to a single exponential with a known time constant (corresponding to k<sub>12</sub>)[3].

(iii) Then, the depolarization-induced calcium release in isolated muscle triads (equivalent also to the circulation from C<sub>2</sub> to C<sub>1</sub>) is reported as being fitted by a sum of exponential: a fast one and a slow one, both having negative time constants[3]:

$$y = a + b \exp\left(-\frac{x}{T_1}\right) + c \exp\left(-\frac{x}{T_2}\right) \quad (12)$$

where the fast one is considered as the dominant, i.e.:

$$y \cong c \exp\left(-\frac{x}{T_2}\right) \quad (13)$$

In the above equations the symbol y is designing the calcium level, x is the time while T<sub>1</sub> and T<sub>2</sub> are the time constants.

(iv) In [2] is mentioned that in [4], the study of calcium extrusion from cytoplasm, led to the idea that: "...the plasma membrane calcium extrusion processes account for 20-40% of the calcium removal seen experimentally"[4]. Thus the SR pumps cover about 80-60% of the calcium removal from cytoplasm.

### Discussion

In Figure 1 one can see a comparison between the experimental curve representing only calcium decay in the cell suspension, obtained in [2] and the solution s<sub>1</sub>(t) representing the calcium kinetics in cytoplasm (compartment C<sub>1</sub>) provided by the theoretical model. The

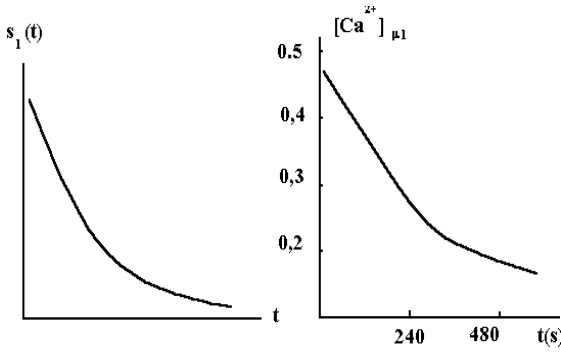


**Fig. 1.** A comparison between the theoretical  $Ca^{2+}$  kinetics in cytoplasm (left) and the experimental curve obtained in [2] (modified after [2]) (right).

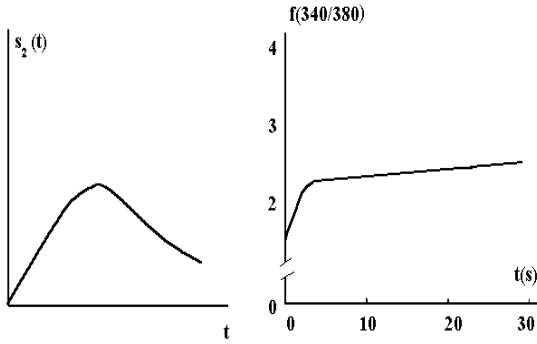


**Fig. 2.** The theoretical  $Ca^{2+}$  kinetics in the sarcoplasmic reticulum (left) and the depolarization-induced calcium release obtained by measuring the fura fluorescence ratio at 340 nm and 380 nm in a Fura-2 suspension of triad vesicles [modified after (3)] (right).

latest may be taken as corresponding to the calcium decay within the cytoplasm due to the  $Ca^{2+}$  pumps from plasma membrane and from the SR and also to the calcium release through SR (compartment  $C_2$ ) ion channels and to the calcium uptake from the extra-cellular medium (physiological pool,  $C_0$ ). In Figure 2 are given the experimental curve obtained in [3] for the calcium released in cytoplasm from SR stores upon depolarization together with the theoretical curve of the whole calcium kinetics in the cytoplasm. The analysis of Figures 1 and 2 reveals the following limitations of the model:

- if we take into account that calcium intrusion in the cytoplasm and calcium storage in SR vesicles are not in phase processes, then the theoretical curve from Figure 1 (left) can be taken as describing only the calcium kinetics during the time interval when the SR pumps occurs diminishing calcium level in cytoplasm;
- the theoretical curve from Figure 2 (left) corresponds to the overlapping of calcium intrusion in the cytoplasm from extra-cellular medium and calcium extrusion from SR storages followed by the action of calcium pumps from SR membranes, while

the experimental curve (right) corresponds *only to  $Ca^{2+}$  extrusion* from the SR storages through ion channels. So, in order to evaluate *in vivo* time constants of calcium ion transport, in the first stage  $k_{12}$  is to be determined from *in vitro* experiments designed for calcium release by ionophore action from isolated muscle triades. In the second stage  $T_2$  and  $c$  may be determined from *in vitro* experiments focused on depolarization-induced calcium release from isolated muscle triades. Then, if we approximate the two percentage values mentioned above [4] with 30% and respectively with 70%, and considering that the ratio may be applied to the time constants, we may obtain:

$$k_{21} \cong \frac{7k_{01}}{3} \tag{14}$$

In the hypothesis that the value of  $\rho_{10}$  could be considerable, so that the second term in (10) is negligible, we can obtain an approximation of  $y$  from (13) with  $s_2(t)$  from (10) and, following this:



$$c \equiv \lambda_1 s_1(0) \frac{S_1 k_{21}}{S_2 \sqrt{(k_{12} + k_{21} + k_{01})^2 - 4k_{12}k_{01}}} \quad (15)$$

and, from (11):

$$\frac{1}{T_2} = \lambda_1 = \frac{k_{12} + k_{21} + k_{01} + \sqrt{(k_{12} + k_{21} + k_{01})^2}}{2} \quad (16)$$

From (ii), (14) and (16) we could determine all the three rate constants while from (15) it results the value of the ratio:

$$s_1(0) \frac{S_1}{S_2} \quad (17)$$

The rate  $S_1/S_2$  gives the ratio of the calcium quantities in  $C_1$  and  $C_2$  when the dynamic equilibrium is established and could be related to the correspondent concentrations of calcium ions in the cytoplasm and respectively in the triad vesicles. The  $s_1(0)$  parameter corresponds to the arbitrarily established initial moment when hypothetical labeling of a certain amount of calcium ions is carried out.

### Conclusion

The model offers the possibility to evaluate the time constant  $k_{01}$  describing the *in vivo* calcium transport from cytoplasm to the extra-cellular medium, on the basis of the *in vitro* approximated time constants  $k_{12}$  and  $k_{21}$  (corresponding to  $\text{Ca}^{2+}$  circulation between cytoplasm and sarcoplasmic reticulum). It gives also an evaluation of the ratio between the calcium quantities (and then between the correspondent concentrations) in cytoplasm and sarcoplasmic reticulum at the dynamic equilibrium, characterizing calcium kinetics. The model should be improved by taken into account the timing of the intrusion and extrusion processes that are not simultaneous while new experimental evidences are expected to give experimental curves describing *in vitro* behavior of calcium ions within the muscle cell.

### REFERENCES

- (1) Gremy, F., Perrin, J., Elements de biophysique, Ed. Flammarion, Paris, 1970
- (2) Kargacin, M. E., Kargacin, G. J., *Direct measurement of  $\text{Ca}^{2+}$  uptake and release by the sarcoplasmic reticulum of saponin permeabilized isolated smooth muscle cells*, Journal of General Physiology, 1995, 106, 467-484
- (3) Kramer, J. W., Corbett, A. M., *The voltage dependence of depolarization-induced calcium release in isolated skeletal muscle triads*, Membrane Biology, 1995, 144: 217-230
- (4) Conney, R. A., Honeyman, T. W., Scheid, R. C., *Contribution of  $\text{Na}^+$  dependent and ATP-dependent  $\text{Ca}^{2+}$  transport to smooth muscle calcium homeostasis*, Sodium exchange: Proceedings of the Second International Conference, 1991, 639:558-560